



TECHNISCHE
UNIVERSITÄT
WIEN

DISSERTATION

Control of intramolecular charge transfer phenomena in functional organic materials

ausgeführt zum Zwecke der Erlangung des akademischen Grades eines
Doktors der technischen Wissenschaften unter der Leitung von

Univ.Prof. Dipl.-Ing. Dr.techn. **Johannes Fröhlich**

163 – Institut für Angewandte Synthesechemie

eingereicht an der **Technischen Universität Wien**
Fakultät für Technische Chemie

von

Dipl.-Ing. **Paul Kautny**, BSc.

0726487

Mühlgrundgasse 3/25, A-1220 Wien

Wien, März 2017

Abstract

Organic push-pull materials consisting of an electron donating and an electron withdrawing subunit within one π -conjugated molecule have been investigated extensively during the last decades due to a wide range of technologically relevant applications. Among those the most important are organic light emitting diodes, imaging, organic photovoltaics, dyes and nonlinear optical materials for two-photon absorption or second harmonic generation to name a few. The molecular properties of these materials are determined by their electronic structure, which is in turn dominated by the donor-acceptor interaction by means of intramolecular charge transfer (ICT). Therefore, controlling ICT is among the most important challenges in the development of new functional bipolar materials.

In this thesis new strategies to control the delicate interaction between electron donating and electron withdrawing groups in bipolar organic materials are developed. In particular three different approaches are pursued: i) modification of the donor unit to modulate the donor strength by planarization of triarylaminines and disruption of the conjugated system by introduction of strategic sterically demanding groups; ii) application of a Click-derived 1,2,3-triazole bridge, as functional linker between the donor and acceptor unit in order to control the electronic interaction of both groups; iii) investigation of ene-yne compounds, derived from thiophene ring fragmentation, as tunable building blocks to realize conjugation control by chemical modification of the methylthio-substituted ene-yne fragment.

Kurzfassung

In den letzten Jahren wurden funktionelle organische Moleküle hinsichtlich ihrer Verwendung in vielfältigen technologischen Anwendungen ausgiebig erforscht. Aromatische push-pull Moleküle, die aus einer elektronenreichen Donor- und einer elektronenarmen Akzeptor-Untereinheit aufgebaut sind, die durch ein konjugierte π -System miteinander verbunden werden, haben sich hierfür als besonders geeignet erwiesen. Im Speziellen deren Einsatz in Organischen Leuchtdioden, in der Organischen Photovoltaik, als Farbstoffe, oder als nichtlineare optische Materialien sind bereits weit entwickelt. Die molekularen Eigenschaften dieser organischen Moleküle werden durch deren elektronische Struktur bestimmt, die wiederum durch die Wechselwirkung zwischen der Donor- und der Akzeptor-Einheit geprägt wird. Daher ist es von enormer Bedeutung diese Wechselwirkung zu kontrollieren, um neue maßgeschneiderte Materialien zu entwerfen.

In dieser Arbeit werden neue Strategien entwickelt, um die Wechselwirkung zwischen den elektronenziehenden und den elektronenschiebenden molekularen Untereinheiten zu kontrollieren. Dabei werden drei unterschiedliche Ansätze verfolgt: i) Modifizierung der Stärke der Elektronendonoren durch die Planarisierung von Triarylamininen und die Unterbrechung des konjugierten π -Systems durch das Einführen sterisch anspruchsvoller Gruppen; ii) Anwendung von 1,2,3-Triazolen als funktioneller Verbindung zwischen Donor- und Akzeptoreinheit, um die elektronische Interaktion der beiden Gruppen zu kontrollieren; iii) Untersuchung von En-In Verbindungen, die sich durch Ringfragmentierung aus Thiophenen herstellen lassen, hinsichtlich ihrer Einsetzbarkeit als molekularer Baustein und der Möglichkeit durch gezielte chemische Modifizierung dieses Bausteins die π -Konjugation zu beeinflussen.

Danksagung

Zuerst möchte ich mich bei Prof. Johannes Fröhlich für die Möglichkeit bedanken diese Arbeit in seiner Arbeitsgruppe durchzuführen, sowie für all den Freiraum und die konstante Unterstützung die er mir dabei gewährte.

Besonderer Dank gebührt meinen langjährigen Laborkollegen Florian Glöcklhofer, Brigitte Holzer und Thomas Kader für die ausgezeichnete und unkomplizierte Atmosphäre im Labor, sowie für zahlreiche lustige Stunden auch außerhalb der Arbeitszeit.

Bei Daniel Lumpi möchte ich mich für das Heranführen an das wissenschaftliche Arbeiten, zahlreiche hilfreiche Diskussionen in den letzten Jahren und seine Freundschaft bedanken. Prof. Berthold Stöger danke ich für die unkomplizierte und freundschaftliche Zusammenarbeit und das Messen unzähliger Einkristalle. Bei Prof. Christian Hametner bedanke ich mich für das Durchführen zahlreicher NMR Experimente und viele Korrekturen.

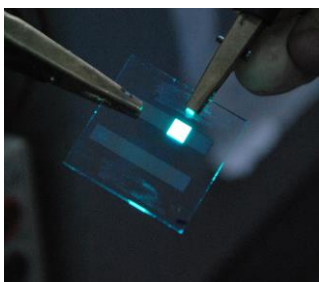
Diese Arbeit wäre in der Form, in der sie nun vorliegt, nicht ohne die Mitarbeit zahlreicher Studenten, die ich im Rahmen ihrer Diplomarbeiten, Bachelorarbeiten oder Wahlpraktika betreuen durfte, möglich gewesen. Dafür möchte ich mich herzlich für den großen Einsatz bei Dorian Bader, Johanna Eichelter, Paul Gauss, Thomas Kader, Daniel Koch, Helene Kriegner, Dongjian Liu, Daniel Möstl, Hannes, Puntcher, Martina Rüscher, Eva-Sophie Schönegger, Dominik Schopf, Thomas Schwartz und Michael Stibi bedanken. Bei meine Kollegen Johannes Binting, Christoph Denk, Ernst Horkel, Stefan Kronister, Stefan Lexmüller, Hannes Mikula, Markus Schwarz, Philipp Skrinjar, Barbara Sohr, Dennis Svatoněk, Julia Weber und allen anderen Mitgliedern der FGHF möchte ich mich für das angenehme Arbeitsklima bedanken. Auch die allgemeinen Mitarbeiter des IAS und der TU Wien, ohne die eine solche Forschungsarbeit nicht möglich wäre, sollen nicht unerwähnt bleiben. Im Speziellen möchte ich mich bei Sabine Stiedry und Tanja Halbarth für die vielen kleinen Dinge bedanken, die das Leben um so viel einfacher machen.

Allen Kooperationspartner, die zum Gelingen der Projekte, die in dieser Arbeit beschrieben werden, beigetragen haben, sei gedankt. Ebenso gebührt der TU Wien, dem Bundesministerium für Wissenschaft, Forschung und Wirtschaft und dem FWF für die finanzielle Unterstützung dieser Arbeit im Rahmen des Forschungsstipendiums, des Mobilitätsstipendiums „Kurzfristige wissenschaftliche Arbeiten im Ausland“, des Förderprogramms „Innovative Projekte“ und des FWF Projekts Nr. I 2589-N34 Dank.

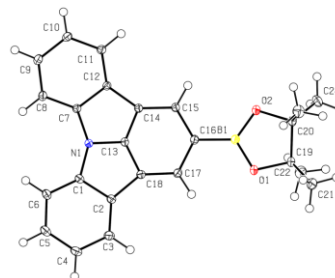
Ganz besonders möchte ich mich bei meinen Eltern Michaela und Rudolf Kautny bedanken. Ihr habt mich von klein auf stets gefördert und ohne eure Hilfe und euer Vertrauen wäre mir mein Studium und diese Arbeit nicht möglich gewesen. Vielen Dank für eure unbedingte Liebe! Ebenso möchte ich mich bei meiner Schwester Lena Kautny bedanken. Ihr gebt mir als Familie stets Sicherheit und den Rückhalt in allen Lebenslagen, den ich mir nur wünschen kann.

Gleichfalls gebührt mein Dank meiner Lebensgefährtin Rebecca Dieplinger. Du hast mich während des größten Teils meines Studiums und während meiner Doktorarbeit begleitet. Vielen Dank für das viele Verständnis und die Unterstützung während dieser Zeit, gerade in schwierigen Phasen! Vielen Dank, dass du mir meinen Blick immer wieder auf das Wesentliche lenkst und mit mir mein Leben neben der Arbeit teilst aus dem ich so viel Kraft schöpfen kann und vielen Dank vor allem für deine uneingeschränkte Liebe!

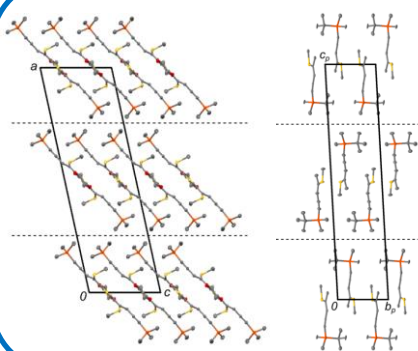
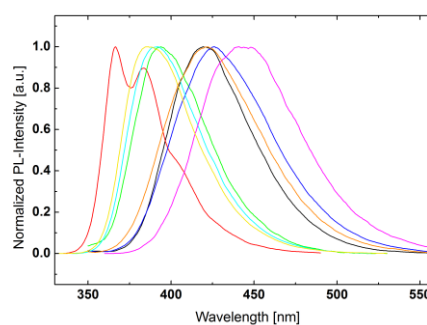
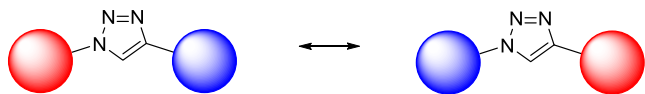
Highlights



Indolo[3,2,1-*jk*]carbazole was established as a novel building block for optoelectronic materials.



The **Click Linkage** methodology was introduced for the design of donor-acceptor materials with controlled molecular properties.



The potential of the **ene-yne** motive as a tunable building block and a structural template for crystal engineering was demonstrated.

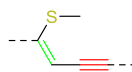


Table of contents

1. Introduction	15
1.1. Aims and structure of the thesis	17
1.2. Overview of contributions	18
1.3. Context of contributions	20
1.4. Statement of contribution	28
1.5. Summary and conclusion	31
1.6. Literature	32
2. Original works	37
2.1. Manuscript #1 Oxadiazole based bipolar host materials employing planarized triarylamine donors for RGB PHOLEDs with low efficiency roll-off	39
2.2. Manuscript #2 Structure-property studies of <i>P</i> -triarylamine-substituted dithieno[3,2- <i>b</i> :2',3'- <i>d</i>]phospholes	55
2.3. Manuscript #3 Indolo[3,2,1- <i>jk</i>]carbazole based planarized CBP derivatives as host materials for PhOLEDs with low efficiency roll-off	69
2.4. Manuscript #4 Controlling singlet-triplet splitting in carbazole-oxadiazole based bipolar phosphorescent host materials	81
2.5. Manuscript #5 Using dicyanoanthracene triflates as superior precursors: modifying properties by sterically hindered aryl substituents	97
2.6. Manuscript #6 Thieno[3,4- <i>c</i>]pyrrole-4,6-dione as novel building block for host materials in red PhOLEDs	107
2.7. Manuscript #7 Structure-property relationships in Click-derived donor-triazole-acceptor materials	117
2.8. Manuscript #8 Ethyne-linked push-pull chromophores: implications of crystal structure and molecular electronics on the quadric nonlinear activity	131
2.9. Manuscript #9 Functional organic click-materials: application in phosphorescent organic light emitting diodes	173
2.10. Manuscript #10 Thiophene ring-fragmentation reactions: Principles and scale-up towards NLO materials	187

2.11. Manuscript #11	199
Crystal chemistry of layered structures formed by linear rigid silyl-capped molecules	
2.12. Manuscript #12	219
Crystal chemistry of trialkylsilyl-capped (3Z)-4-(methylthio)-3-penten-1-yne: polymorphism, twinning and ambiguity of order-disorder descriptions	
2.13. Manuscript #13	231
Charge transfer states in triazole linked donor-acceptor materials: strong effects of chemical modification and solvation	
3 Appendix	247
3.1. Supporting Information - Manuscript #1	249
3.2. Supporting Information - Manuscript #2	279
3.3. Supporting Information - Manuscript #3	319
3.4. Supporting Information - Manuscript #4	335
3.5. Supporting Information - Manuscript #5	353
3.6. Supporting Information - Manuscript #6	377
3.7. Supporting Information - Manuscript #7	385
3.8. Supporting Information - Manuscript #8	413
3.9. Supporting Information - Manuscript #9	419
3.10. Supporting Information - Manuscript #10	435
3.11. Supporting Information - Manuscript #11	453
3.12. Supporting Information - Manuscript #13	465
3.13. Curriculum Vitae	479

1. Introduction

1.1. Aims and structure of the thesis

The aim of this thesis was to develop new methodologies to control intramolecular charge transfer (ICT) in organic donor-acceptor materials and the application of this knowledge in the design of novel functional materials. This thesis is written as a cumulative work consisting of 13 individual manuscripts. Among those eleven manuscripts are already published and two manuscripts have been submitted for publication. These manuscripts can be organized into three groups in which different approaches to control ICT are pursued:

- i) Planarization/deplanarization of triarylamines
- ii) Click linkage
- iii) Ene-yne materials

The applicant is first author or shared first author of nine of the manuscripts, second author of three of the manuscripts and corresponding author of four of the manuscripts. The contributions of the applicant to the individual manuscripts were manifold and a detailed description of the contribution of each coauthor to the respective manuscripts is given in section 1.4.

1.2. Overview of contributions

Part 1 - Planarization/deplanarization of triarylaminines

Manuscript #1

Paul Kautny, Daniel Lumpi, Yanping Wang, Antoine Tissot, Johannes Binting, Ernst Horkel, Berthold Stöger, Christian Hametner, Hans Hagemann, Dongge Ma, Johannes Fröhlich; [Oxadiazole based bipolar host materials employing planarized triarylamine donors for RGB PHOLEDs with low efficiency roll-off](#); *Journal of Materials Chemistry C*, **2014**, 2, 2069-2081.

Manuscript #2

Hannes Puntsher, Paul Kautny, Berthold Stöger, Antoine Tissot, Christian Hametner, Hans R. Hagemann, Johannes Fröhlich, Thomas Baumgartner, Daniel Lumpi; [Structure-property studies of P-triarylamine-substituted dithieno\[3,2-b:2',3'-d\]phospholes](#); *RSC Advances*, **2015**, 5, 93797-93807.

Manuscript #3

Paul Kautny, Zhongbin Wu, Johanna Eichelter, Ernst Horkel, Berthold Stöger, Jiangshan Chen, Dongge Ma, Johannes Fröhlich, Daniel Lumpi; [Indolo\[3,2,1-jk\]carbazole based planarized CBP derivatives as host materials for PhOLEDs with low efficiency roll-off](#); *Organic Electronics*, **2016**, 34, 237-245.

Manuscript #4

Paul Kautny, Zhongbin Wu, Berthold Stöger, Antoine Tissot, Ernst Horkel, Jiangshan Chen, Dongge Ma, Hans Hagemann, Johannes Fröhlich, Daniel Lumpi; [Controlling singlet-triplet splitting in carbazole-oxadiazole based bipolar phosphorescent host materials](#); *Organic Electronics*, **2015**, 17, 216-228.

Manuscript #5

Florian Glöcklhofer, Paul Kautny, Patrick Fritz, Berthold Stöger, Johannes Fröhlich; [Using dicyanoanthracene triflates as superior precursors: modifying properties by sterically hindered aryl substituents](#); *ChemPhotoChem*, **2017**, 1, 51-55.

Manuscript #6

Paul Kautny, Chenyang Zhao, Dominik Schopf, Berthold Stöger, Ernst Horkel, Jiangshan Chen, Dongge Ma, Johannes Fröhlich, Daniel Lumpi; [Thieno\[3,4-c\]pyrrole-4,6-dione as novel building block for host materials in red PhOLEDs](#); *Journal of Materials Chemistry C*, **2017**, 5, 1997-2004.

Part 2 - Click linkage

Manuscript #7

Paul Kautny, Dorian Bader, Berthold Stöger, Georg A. Reider, Johannes Fröhlich, Daniel Lumpi; [Structure-property relationships in Click-derived donor-triazole-acceptor materials](#); *Chemistry-A European Journal*, **2016**, 22, 18887-18898.

Manuscript #8

Paul Kautny, Helene Kriegner, Dorian Bader, Michal Dušek, Georg A. Reider, Johannes Fröhlich, Berthold Stöger; [Ethyne-linked push-pull chromophores: implications of crystal structure and molecular electronics on the quadric nonlinear activity](#); **submitted for publication**

Manuscript #9

Paul Kautny, Chenyang Zhao, Thomas Kader, Berthold Stöger, Ernst Horkel, Jiangshan Chen, Dongge Ma, Johannes Fröhlich, Daniel Lumpi; [Functional organic click-materials: application in phosphorescent organic light emitting diodes](#); *RSC Advances*, **2017**, 7, 12150-12160.

Part 3 - Ene-yne materials

Manuscript #10

Daniel Lumpi, Johannes Steindl, Sebastian Steiner, Victor Carl, Paul Kautny, Michael Schön, Florian Glöcklhofer, Brigitte Holzer, Berthold Stöger, Ernst Horkel, Christian Hametner, Georg Reider, Marko D. Mihovilovic, Johannes Fröhlich; [Thiophene ring-fragmentation reactions: Principles and scale-up towards NLO materials](#); *Tetrahedron*, **2017**, 73, 472-280.

Manuscript #11

Daniel Lumpi, Paul Kautny, Berthold Stöger, Johannes Fröhlich; [Crystal chemistry of layered structures formed by linear rigid silyl-capped molecules](#); *IUCrJ*, **2015**, 2, 584-600.

Manuscript #12

Daniel Lumpi, Paul Kautny, Berthold Stöger, Johannes Fröhlich; [Crystal chemistry of trialkylsilyl-capped \(3Z\)-4-\(methylthio\)-3-penten-1-yne: polymorphism, twinning and ambiguity of order-disorder descriptions](#); *Acta Crystallographica Section B*, **2016**, 72, 753-762.

Manuscript #13

Paul Kautny, Florian Glöcklhofer, Thomas Kader, Jan-Michael Mewes, Berthold Stöger, Johannes Fröhlich, Daniel Lumpi, Felix Plasser; [Charge transfer states in triazole linked donor-acceptor materials: strong effects of chemical modification and solvation](#); **submitted for publication**

1.3. Context of contributions

Bipolar π -conjugated organic molecules consisting of an electron donating and an electron withdrawing subunit are of crucial importance for a wide range of technological applications such as organic light emitting diodes (OLEDs),¹⁻⁶ organic photovoltaics (OPVs),⁷⁻¹⁰ dyes and nonlinear optical (NLO) materials¹¹⁻¹⁴ for two-photon absorption¹⁵⁻¹⁷ or second harmonic generation (SHG)¹⁸⁻²⁰ to name the most important. In the design of these functional organic materials, the incorporation of electron rich and electron poor building blocks, which act as donor and acceptor, respectively, within one molecule inevitably leads to electronic interactions between the two molecular subunits. Mediated by the conjugated π -system an intramolecular charge transfer (ICT) from the donor to the acceptor occurs.^{1,3,5,21,22} Accordingly, the spatial and energetic locations of the frontier molecular orbitals are changed.

There are manifold reasons for the combination of donor and acceptor subunits within one molecule. The induction of the ICT can be desirable in order to modify the molecular properties of the material or the individual properties of the separated building blocks can be required (e.g. to provide balanced charge transport properties²¹). In materials for OPVs an intense interaction between the donor and acceptor is desired. A donor-acceptor architecture can be applied to overcome the effective conjugation length in organic polymers^{7,9,10,23-26} or in the design of small molecule chromophores with a low optical gap^{7,8,21,27} in order to optimize the usage of the solar spectrum.

However, the situation can be a little bit more diverse for other applications. In the following paragraphs the most challenging requirements to control ICT in the design of functional materials are discussed with a focus on applications, which are relevant for this thesis. From the viewpoint of optical gap tuning, the situation is multifarious in the case of OLEDs. Similar to OPVs the donor-acceptor interaction can be employed to modulate the optical gap and thus tune the emission color.²⁸⁻³⁰ On the other hand, the overall conjugation has to be carefully controlled to retain the purity of the emission of blue chromophores.^{4,5} Frequently, these chromophores have to be modified to prevent aggregation effects in the solid state.^{4,29,31}

Traditional fluorescent emitters in OLEDs are limited to a maximum internal quantum efficiency of 25% due to spin statistics,³² as they are restricted to the conversion of excited singlet states.^{1,22,33} However, the recent emergence of novel mechanisms for the utilization of excited triplet states in OLEDs for the generation of light *via* fluorescence significantly enhanced the efficiency of organic emitters to a maximum internal quantum efficiency of 100%.^{34,35} In the case of thermally activated delayed fluorescence (TADF), the energy splitting between the first excited singlet and triplet state has to be minimized,^{3,6} whereas materials with hybridized local and charge transfer states (HLCT) can utilize high lying triplet states *via* hot exciton processes.³⁶ Both processes have in common that the interplay between the donor and the acceptor has to be exactly controlled to achieve the required properties of the excited states.

Generally, emitters in OLEDs are doped into host materials.^{1,2,4,22,33,37} These host materials provide an enhanced thermal stability as well as improved charge transport properties and prevent concentration-induced quenching of the excited states.^{1,2,4,38} In particular, the application of bipolar host materials with balanced charge transport properties proved to be advantageous.^{1,2,22,38} The optical gap of the host materials has to be higher compared to the dopant to confine the excited states on the emitter.^{39,40} Therefore, the interaction between the donor and acceptor subunit in host materials has to

be controlled. In particular in bipolar host materials for phosphorescent^{38,41-43} and TADF^{3,6} emitters also a high triplet energy of the host material has to be retained.^{1,2,22,33,37,44}

In the case of nonlinear optical materials for second harmonic generation^{11,14,18-20} a donor-acceptor architecture is required to provide a high polarizability of electrons in the conjugated π -system on the molecular scale.^{14,45,46} This polarization in a strong applied electric field occurs along the main charge transfer axis of the organic molecules.^{47,48}

Even very small variations in the molecular design of organic donor-acceptor materials significantly alter the photophysical and electrochemical properties of the material and thus its practical applicability. Consequently, one major aspect in the design of novel bipolar organic materials is the precise control of this kind of interaction. Therefore, it is of immense importance to exactly understand the electronic interplay between the donor and the acceptor unit and to develop methodologies to control the degree of the ICT in order to create new materials with tailored molecular properties.

The objective of this work is to investigate the effect of systematic variations of the molecular structure of donor-acceptor materials on the properties of the compounds and to develop new strategies to control the ICT. Obviously, the donor and acceptor group itself are factors that can be influenced to achieve this goal. Variation of the donor and acceptor strength can be employed to modulate the degree of ICT (Figure 1.3.1). Ultimately, the continuous decrease of the electron donating or accepting

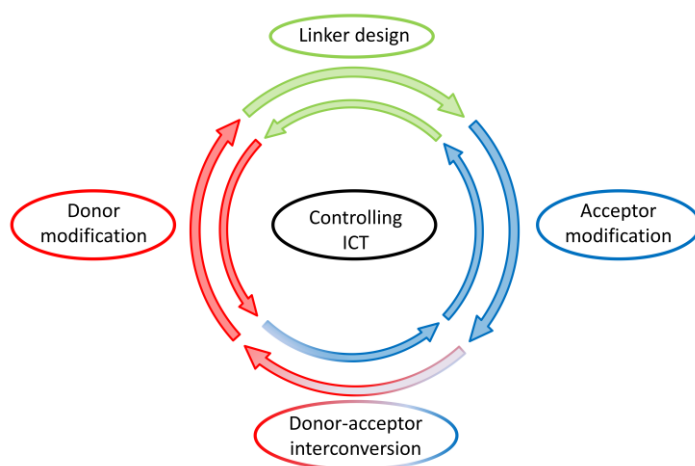


Figure 1.3.1 Schematic representation of various methodologies to control the ICT.

strength leads to the interconversion of donor groups to acceptor groups and vice versa (Figure 1.3.1). The ICT is mediated by the conjugated π -system of the linker, which connects the donor and acceptor group. Therefore, this bridging unit offers another target to influence the electronic interaction by proper molecular design (Figure 1.3.1). In course of this work three different approaches have been pursued to control ICT phenomena. Accordingly, the individual contributions of this thesis can be categorized into of three

groups, which are, however, often interconnected: (1) the planarization and deplanarization of triphenylamines; (2) the investigation of the Click linkage concept in donor-acceptor materials and (3) the application of ene-yne compound in functional materials. In the following, the contribution of each manuscript to the respective topic will be outlined and connected to preexisting literature.

Part 1 - Planarization/deplanarization of triarylamines

The pool of triarylamines (TAAs) is indisputably the primary source of electron donating groups for optoelectronic applications. In particular, triphenylamine (TPA) and 9-phenyl-9*H*-carbazole (PCz) are widely applied as donors in bipolar materials, which are used as emitters in fluorescent OLEDs or as

host materials in PhOLEDs.^{1-5,21,33,49-57} Furthermore, most hole-transporting materials are made up of those molecular building blocks.^{33,58-60}

However, in bipolar materials the electron donating effect of TPA and PCz leads to a strong ICT from the donor to the acceptor. Ultimately, this electronic exchange leads to a decreased bandgap and thus

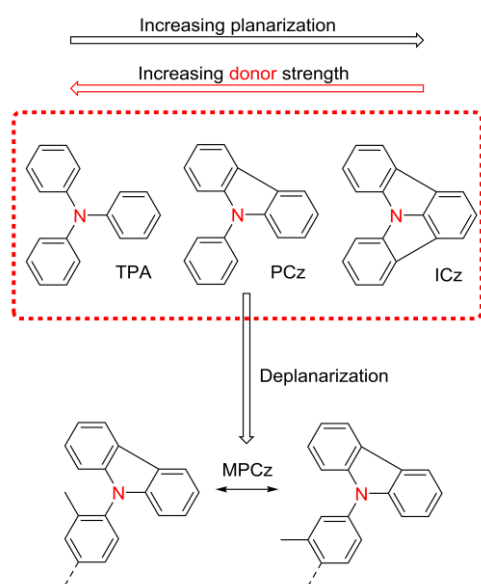


Figure 1.3.2 Schematic representation of the concept of planarization of triaryl amines as well as the introduction of methyl groups in order to deplanarize phenylcarbazoles.

red-shifted emission as well as low triplet energies (E_T s).^{1,2,15,33} Notably, this often undesired effect is more dominant in materials with TPA donors. The annulation and thus planarization of two phenyl substituents in PCz leads to a decreased donor strength, as the nitrogen lone pair contributes to the aromaticity of the pyrrole ring of the carbazole. Delocalization of the lone pair would consequently weaken the aromaticity of the pyrrole and is thus unfavored compared to TPA. To further decrease the donor strength of TAAs we aimed to expand this planarization and apply indolo[3,2,1-*jk*]carbazole (ICz) as electron donor in materials with large bandgaps and high E_T s for optoelectronic applications (Figure 1.3.2). In contrast to PCz, the lone pair in ICz contributes to the aromaticity of two pyrrole rings and thus its donor strength is further reduced. Therefore, the application of this new building block should allow for further control over ICT phenomena.

Another possibility to control the electronic interaction between donor and acceptor is the interruption of the conjugated π -system by the introduction of torsion between the aromatic moieties. Such a deplanarization can be induced by the installation of sterically demanding groups, a concept that has been previously described.^{39,61-63} Thus, the deplanarization of the molecular frame can assist the planarization of the carbazole donor unit (Figure 1.3.2).

Although there are numerous examples of the application of TPA and PCz as building blocks for functional organic materials, reports on ICz as a functional unit are extremely rare.⁶⁴⁻⁶⁷ This lack can be attributed to the troublesome synthesis of the ICz moiety⁶⁷⁻⁶⁹ until recently a new methodology based on a Pd-catalyzed C-H activation has been reported.⁷⁰ Based on this procedure we developed a novel protocol and the application of an N-heterocyclic carbene ligand^{71,72} allows for the reliable synthesis of ICz (**Manuscript #1**).

Beside higher yields at lower catalyst loading the improved methodology enables a two-fold ring closure and also converts chlorine precursors (Figure 1.3.3). Consequently, this

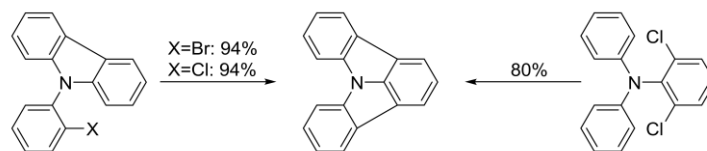


Figure 1.3.3 Synthesis of the ICz moiety by one-fold (left) or two-fold (right) Pd-catalyzed C-H activation.

methodology enabled us to incorporate ICz as donor in bipolar materials based on a TAA donor and an 1,3,4-oxadiazole acceptor (**Manuscript #1**). Notably, the fluorescence of the developed materials was blue shifted and the E_T s were increased with progressive planarization of the donor units (Figure 1.3.4). Suchlike developed compounds were successfully employed as host materials in red, green and blue PhOLEDs with low efficiency roll-off.

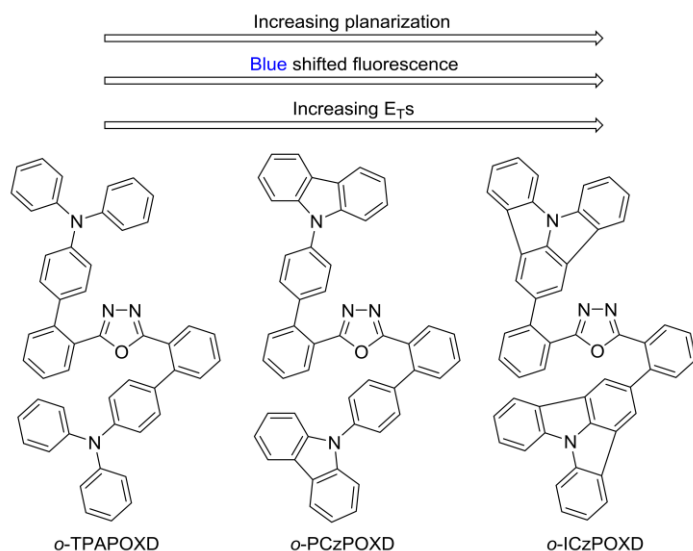


Figure 1.3.4 Molecular structures of bipolar host materials based on an 1,3,4-oxadiazole acceptor and TAA donor with increasing degree of planarization.

introduced concept is a starting point for the development of a new class of TADF materials.

Due to the observation of high E_T s of the bipolar materials with ICz donor and also their improved thermal stability we decided to investigate the incorporation of the ICz building block into the 9,9'-[(1,1'-biphenyl)-4,4'-diyl]bis[9H-carbazole] (CBP) scaffold (**Manuscript #3**). Beginning with the first reports on PhOLEDs⁷⁴ CBP is undoubtedly the most investigated host material.¹ However, CBP exhibits some major drawbacks, such as a rather low glass transition temperature (62 °C)⁷⁵ and a low E_T (2.56 eV)⁷⁶ resulting in an inferior thermal stability of OLED devices²⁸ and inefficient energy transfer to high energy blue phosphorescent emitters.^{76,77} Gradual planarization of the CBP scaffold by the introduction of the ICz moiety (Figure 1.3.5) led to novel CBP derivatives with improved thermal properties and E_T s above 2.80 eV. Suchlike prepared materials could be successfully employed as host materials in blue PhOLEDs with a high power efficiency.

Based on *o*-PCzPOXD (Figure 1.3.4) we investigated the impact of torsion due to steric hindrance on the molecular properties of host materials (**Manuscript #4**). For this purpose, methyl groups were introduced on the phenyl units of the phenylcarbazoles resulting in materials with significantly twisted conformations (Figure 1.3.6). The increased torsion resulted in a decreased overall conjugation and

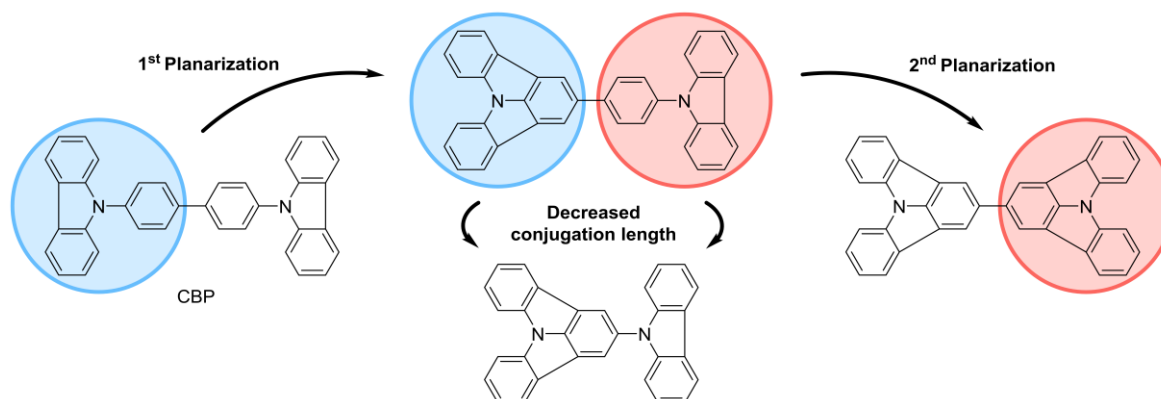


Figure 1.3.5 Schematized molecular design of novel host materials obtained from the CBP scaffold by gradual planarization of the phenylcarbazole moieties.

These results prompted us to investigate the ICz donor in combination with the dithieno[3,2-*b*:2',3'-*d*]phosphole oxide acceptor (**Manuscript #2**). The application of the weak ICz donor basically suppressed the ICT in these donor-acceptor materials. Additionally, the ICz based derivatives exhibited a very low singlet-triplet splitting (ΔE_{ST}) in comparison to various materials with carbazole donors. This feature is of particular interest as a low ΔE_{ST} allows for the upconversion of excited triplet states to excited singlet states. Therefore, triplet excitons can be harvested via TADF.^{3,6,34,73} Consequently, the

increased E_T s. Thus, the methyl substituted derivatives of *o*-PCzPOXD could be employed as host materials for deep blue PhOLEDs, further expanding the scope of this class of materials.

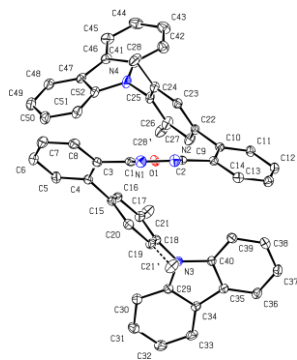


Figure 1.3.6 Molecular structure of methyl substituted *o*-PCzPOXD

The same strategy was applied in the preparation of 9,10-dicyanoanthracene (DCA) chromophores. DCA constitutes a promising candidate as fluorescent emitter in OLEDs with favorable emissive properties in solution.⁷⁸ However, the emission of DCA is compromised in the solid state due to intermolecular aggregation as a result of the highly planar structure of DCA, a phenomenon that is frequently observed for anthracene derivatives.^{4,31} Therefore, we introduced additional substituents to the DCA core (**Manuscript #5**). Twisted molecular conformations were targeted, to avoid a shift in the emission color due to an extended π -electron system. In such a way significantly improved emission from

crystalline powders were obtained compared to plain DCA.

Finally, single planarized PCz was employed as donor in bipolar materials in combination with the thieno[3,4-*c*]pyrrole-4,5-dione (TPD) acceptor (Figure 1.3.7). By employing the *meta* and *ortho* linkage concept,^{52-55,57,79,80} the molecular properties of the developed compounds could be tuned. Suchlike developed derivatives were successfully incorporated as host materials in efficient red PhOLEDs (**Manuscript #6**). While the TPD unit has been widely used in polymers for photovoltaic applications⁸¹⁻⁸⁵ and in organic field effect transistors,⁸⁶ our report on the TPD based host materials introduced this particular acceptor unit also to the field of OLED materials.

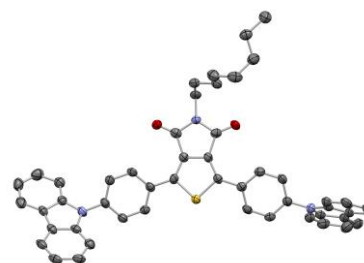


Figure 1.3.7 Molecular structure of a bipolar host material based on PCz and TPD.

Part 2 - Click linkage

Cu(I)-catalyzed azide-alkyne cycloaddition (CuAAC) is certainly the most successful example of Click chemistry.⁸⁷ CuAAC joins an organic azide and an alkyne by 1,2,3-triazole formation. This particular reaction has been widely employed in many fields of organic chemistry in recent years.⁸⁷⁻⁹¹ Nonetheless, reports on materials employing 1,2,3-triazoles as functional unit are relatively scarce, a lack that is somewhat surprising as 1,2,4-triazoles are frequently employed in functional organic materials as electron accepting moieties.^{54,92-95} So far the 1,2,3-triazole unit has been incorporated in push-pull materials for NLO materials,^{96,97} fluorophores,⁹⁸⁻¹⁰³ materials for two-photon absorption,¹⁰⁴ fluorescent metal sensors,¹⁰⁵⁻¹⁰⁹ and electro-optical materials.¹¹⁰⁻¹¹²

The prospect to use the intriguingly simple CuAAC approach to join two molecular subunits and to use the resulting 1,2,3-triazole as functional linker in materials for technological applications prompted us to explore the influence of the 1,2,3-triazole on the properties of donor-acceptor chromophores. Investigations on 1,2,3-triazole linked chromophores indicate a significant influence of the triazole substitution pattern on the photophysical and electrochemical properties of the compounds.^{99-103,109,113}

Nevertheless, no full combinatorial study on 1,2,3-triazole linked donor-acceptor materials can be found in literature. Therefore, we prepared, as a first step, a systematic series of structurally simple 1,2,3-triazole linked push-pull materials to gain insight into the effect of the 1,2,3-triazole substitution

pattern as well as donor and acceptor variations on the ICT (Figure 1.3.8) and thereby developed a structure-properties relationship for this particular molecular scaffold (**Manuscript #7**). Our

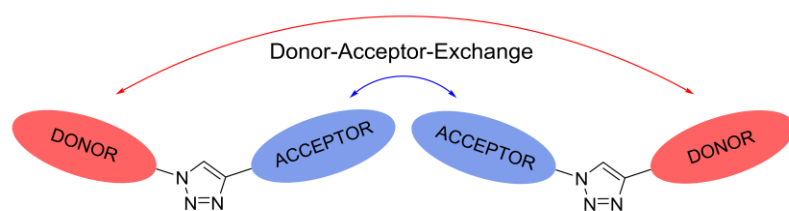


Figure 1.3.8 Schematic representation of the 1,2,3-triazole linked donor-acceptor materials.

investigations revealed that the triazole linker not only reduces the overall conjugation of the molecules in the ground state but may also increase the electron donating strength of the electron donor or establish an electron accepting group

itself, depending on the substitution pattern. Due to the successful application of triazole derivatives as NLO materials,^{96,97} selected compounds were also subjected to SHG measurements. High SHG efficiencies were recorded, thus further proving the potential of triazole derivatives for this purpose. Based on the design concept presented in Manuscript #7 we substituted the triazole by an acetylenic linker (**Manuscript #8**). The modified linkage mode between the donor and acceptor materials allowed for increased ICT as evidenced by a comprehensive photophysical characterization and thus potentially high SHG efficiency. Indeed a powdered crystalline sample of one of these materials (*N,N*-Dimethyl-4-[2-(2-pyrimidinyl)ethynyl]benzamine) exhibited extraordinarily high NLO activity, which was orders of magnitude higher compared to previously investigated materials.^{96,97} Furthermore, we could explain the high NLO activity of the material under investigation by a multidisciplinary approach based on the crystallographic and spectroscopic characterization in combination with computational methods.

Finally, the developed Click linkage methodology was applied in the synthesis of large band gap bipolar host materials for PhOLEDs (**Manuscript #9**). In this regard 1,2,3-triazoles were employed as linker between two electron donating groups and an electron withdrawing core (Figure 1.3.9). While the electron poor molecular subunit consisted of the 1,2,3-triazoles itself in combination with a pyridine or benzene unit, TAAs were applied as electron donors. Analogously to the simplified donor-acceptor materials of our basic investigations, the developed potential host materials indeed exhibited high band gaps resulting from the decreased conjugation due to the triazole linkage. Furthermore, the concept of planarization was again utilized in this work to tune the donor strength of the TAAs and to control the degree of ICT. Suchlike developed derivatives were successfully incorporated as host materials in solution processed green PhOLEDs.

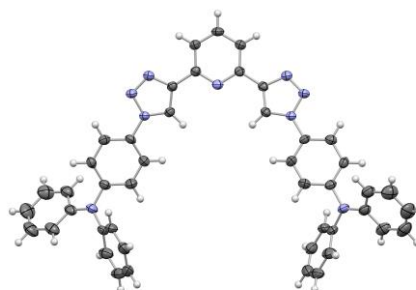


Figure 1.3.9 Molecular structure of an 1,2,3-triazole linked bipolar host material.

Part 3 - Ene-yne materials

Ene-yne compounds, derived from thiophene ring fragmentation (TRF)¹¹⁴⁻¹¹⁶ feature a versatile π -conjugated building block and have already been successfully employed in the design of NLO chromophores.^{96,97} Owing to the manifold functional groups present, the ene-yne scaffold offers various possibilities for chemical modification and is therefore an ideal building block to investigate the

effect of structural alterations on the ICT behavior of the molecules (Figure 1.3.10). Thus, conjugation control in bipolar ene-yne based materials could be realized by a proper molecular design using this particular scaffold as tunable unit to adjust the ICT. The aim of this part of the thesis is to investigate these effects and explore the potential of the ene-yne motive as building block for functional organic materials.

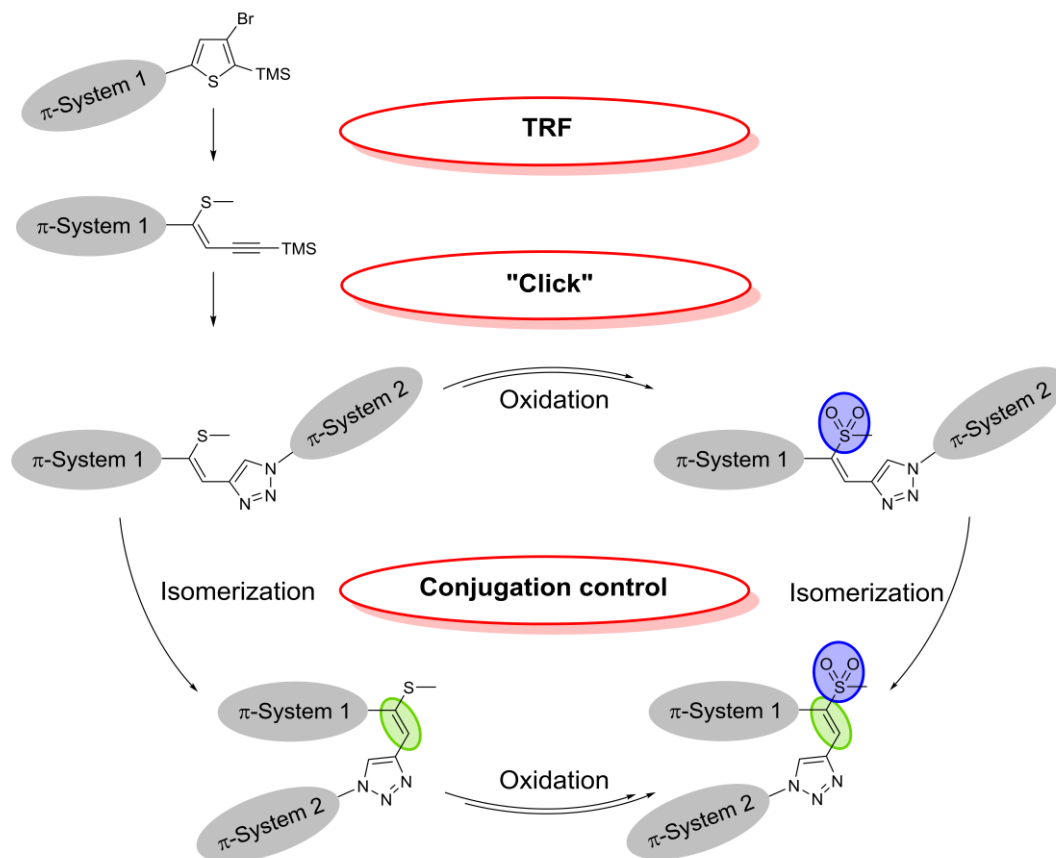


Figure 1.3.10 Synthetic approach towards ene-yne derivatives via TRF, modification of the alkyne via CuAAC and potential modifications to control the overall conjugation.

Oxidation selectively converts the thioether group (+M effect) to a sulfone (-M effect), thus converting an electron donating functional group to an electron withdrawing group. This donor-acceptor interconversion may enhance the weak intrinsic electron withdrawing properties of the triazole^{104,110,117} and induce or enhance ICT. Due to the cyclic structure of the thiophene, ring fragmentation selectively yields the *Z*-isomer of the ene-yne compound. Nonetheless, isomerization to the corresponding *E*-isomer can be readily achieved. The double bond configuration, however, not only impacts the overall electronic properties of the compounds but also the spatial alignment of the substituents. Due to the altered configuration significant steric interactions may occur, resulting in increased torsion angles. Thus, the double bond configuration constitutes a tool to influence the donor-acceptor interaction. While π -system 1 is determined by the fragmentation precursor, π -system 2 is introduced after the fragmentation step by functionalization of the alkyne. For this purpose CuAAC represents a suitable reaction and a potential application of the Click linkage concept. Moreover, other modification of the alkyne (e.g. Sila-Sonogashira coupling) are feasible as well. Furthermore, the nature of π -system 1 and π -system 2 is almost unrestricted and both can be employed as electron donating and/or accepting unit. These multifarious possibilities for structural modifications predestine the described scaffold to be employed in the design of functional organic materials with tailored molecular properties.

As a first step we deepened the knowledge of the mechanism of the thiophene fragmentation reaction. These systematic investigations culminated in an improved synthetic protocol with an enhanced selectivity and efficiency (**Manuscript #10**). Additionally, this methodology was implemented in a flow-chemistry protocol allowing for the convenient synthesis of the fragmentation product. Finally, a new Click derived chromophore based on a TRF product exhibited the highest NLO activity within this particular class of materials.^{96,97}

Employing this newly developed procedure we prepared a series of spacer extended *bis* ene-yne fragmentation products (Figure 1.3.11), which were derived by a tandem TRF (**Manuscript #11**). Such structures are valuable building blocks for further functionalization towards functional materials.

Notably, these materials also reliably crystallized in layered structures with the silyl groups forming the layer interfaces. This behavior is of particular interest, as layered structures with defined interactions between aromatic units within the individual layers are of tremendous importance in the field of organic electronics.¹¹⁸⁻¹²¹ Therefore, this molecular architecture displays the potential as a structure directing template for

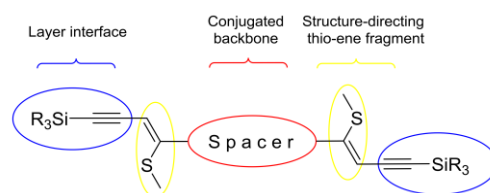


Figure 1.3.11 Schematized molecular structure of the spacer extended bis ene-yne derivatives derived by tandem TRF.

such layered materials. Based on these results we further investigated the crystallization behavior of TRF products and found, that the tendencies to form layered crystal structures is preserved in tandem fragmentation products without an aromatic spacer (**Manuscript #11**), but also in simple silyl capped methylthio substituted ene-yne derivatives with a low molecular weight (**Manuscript #12**).

Finally, we investigated the potential of the ene-yne scaffold to realize conjugation control employing a strong TPA donor. Again, the Click linkage concept was employed to attach the TPA donor to the ene-yne scaffold *via* an 1,2,3-triazole linker (**Manuscript #13**). Indeed, remarkable differences in the photophysical properties of the materials, depending on the double bond configuration in combination with the sulfur oxidation state were observed. Furthermore, the possibility to selectively prepare 1,4- or 1,5-substituted triazoles provides another possibility to control the properties of these materials (Figure 1.3.12). Assisted by theoretical methods we could therefore establish a structure-properties relationship for this versatile building block, revealing its potential for the design of materials with tailored properties.

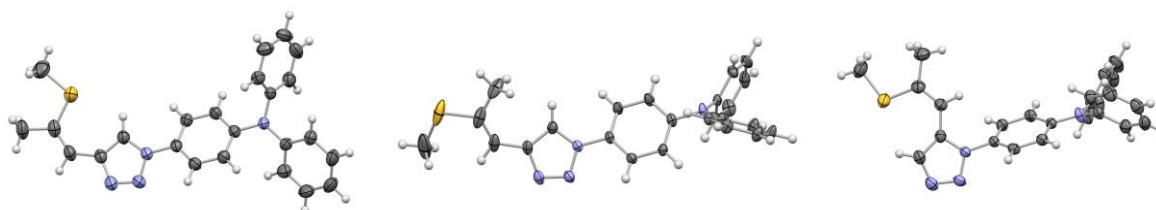


Figure 1.3.12 Molecular structures of different chromophores derived from TRF products applying the Click linkage concept. Different linkage modes and double bond configurations have been realized: left: Z, 1,4-substitution; middle: E, 1,4-substitution; right: Z, 1,5-substitution.

1.4. Statement of contribution

In this section the contributions of all coauthors to the individual tasks of the single projects are listed. Notably, the content of the same task of two manuscripts may differ (e.g. crystal growth will be included in the task synthesis unless significant time has been invested to grow crystals for a specific purpose). All authors are listed by their initials. The ordering is strictly alphabetic according to the second name of the authors and does not relate to the share of the respective task. If one author contributed 50% or more of the work to one task the initials are given in bold letters. In all cases all authors contributed to the manuscript correction and discussion. Working packages marked with an asterisk (*) are already part of the diploma thesis of the applicant. Working packages marked with two asterisks (**) have been initiated in and are to some extent part of the diploma thesis of the applicant.

CRG	Crystal growth
CRY	Crystal structure determination
DFM	OLED device fabrication and measurement
ECC	Electrochemical characterization, cyclic voltammetry
FIP	Final preparation of materials including extended purification techniques of materials for OLED fabrication
FLO	Flow chemistry
INC	Initiation and coordination of the project
MAN	Manuscript preparation
NLO	Measurement of nonlinear optical properties
PPC	Photophysical characterization, including UV/Vis absorption, photoluminescence and low temperature phosphorescence
SYN	Synthesis of the materials, including purification and routine characterization; (Co)supervision of the synthesis performed in course of bachelor thesis
THC	Thermal characterization, including differential scanning calorimetry and thermogravimetric analysis
THE	Theoretical calculations

Manuscript #1: Paul Kautny, Daniel Lumpi, Yanping Wang, Antoine Tissot, Johannes Binting, Ernst Horkel, Berthold Stöger, Christian Hametner, Hans Hagemann, Dongge Ma, Johannes Fröhlich; [Oxadiazole based bipolar host materials employing planarized triarylamine donors for RGB PHOLEDs with low efficiency roll-off](#); *Journal of Materials Chemistry C*, **2014**, 2, 2069-2081

CRY (**BS**), DFM (DM, **YW**), ECC* (**PK**), FIP (**PK**), INC (JF, PK, DL, DM), MAN (**PK**, DL), PPC* (HH, **PK**, DL, AT), SYN* (JB, CH, EH, **PK**, DL), THC (**PK**), THE (**EH**)

Manuscript #2: Hannes Puntsher, Paul Kautny, Berthold Stöger, Antoine Tissot, Christian Hametner, Hans R. Hagemann, Johannes Fröhlich, Thomas Baumgartner, Daniel Lumpi; [Structure-property studies of P-triarylamine-substituted dithieno\[3,2-b:2',3'-d\]phospholes](#); *RSC Advances*, **2015**, 5, 93797-93807

CRY (**BS**), ECC (PK, **HP**), INC (TB, JF, **DL**), MAN (TB, **PK**, DL), PPC (JF, HH, **PK**, AT), SYN (TB, CH, PK, **HP**), THE (**TB**)

Manuscript #3: Paul Kautny, Zhongbin Wu, Johanna Eichelter, Ernst Horkel, Berthold Stöger, Jiangshan Chen, Dongge Ma, Johannes Fröhlich, Daniel Lumpi; [Indolo\[3,2,1-*jk*\]carbazole based planarized CBP derivatives as host materials for PhOLEDs with low efficiency roll-off](#); *Organic Electronics*, **2016**, 34, 237-245

CRY (**BS**), DFM (JC, DM, **ZW**), ECC (**PK**), FIP (**PK**), INC (JC, JF, **PK**, DL), MAN (**PK**), PPC (**PK**), SYN (**JE**, PK), THC (**PK**), THE (**EH**)

Manuscript #4: Paul Kautny, Zhongbin Wu, Berthold Stöger, Antoine Tissot, Ernst Horkel, Jiangshan Chen, Dongge Ma, Hans Hagemann, Johannes Fröhlich, Daniel Lumpi; [Controlling singlet-triplet splitting in carbazole-oxadiazole based bipolar phosphorescent host materials](#); *Organic Electronics*, **2015**, 17, 216-228

CRG (**PK**), CRY (**BS**), DFM (JC, DM, **ZW**), ECC* (**PK**), FIP (**PK**), INC (JC, JF, **PK**, DL), MAN (**PK**), PPC (HH, **PK**, AT), SYN* (**PK**), THC (**PK**), THE (**EH**)

Manuscript #5: Florian Glöckhofer, Paul Kautny, Patrick Fritz, Berthold Stöger, Johannes Fröhlich; [Using dicyanoanthracene triflates as superior precursors: modifying properties by sterically hindered aryl substituents](#); *ChemPhotoChem*, **2017**, 1, 51-55.

CRG (**FG**), CRY (**BS**), INC (JF, **FG**), MAN (**FG**, PK, BS), PPC (PF, **PK**), SYN (PF, **FG**), THE (**PK**)

Manuscript #6: Paul Kautny, Chenyang Zhao, Dominik Schopf, Berthold Stöger, Ernst Horkel, Jiangshan Chen, Dongge Ma, Johannes Fröhlich, Daniel Lumpi; [Thieno\[3,4-*c*\]pyrrole-4,6-dione as novel building block for host materials in red PhOLEDs](#); *Journal of Materials Chemistry C*, **2017**, 5, 1997-2004.

CRY (**BS**), DFM (JC, DM, **CZ**), ECC (**PK**), FIP (PK, **DS**), INC (JC, JF, **PK**), MAN (**PK**), PPC (**PK**), SYN (PK, **DS**), THC (**PK**), THE (**EH**)

Manuscript #7: Paul Kautny, Dorian Bader, Berthold Stöger, Georg A. Reider, Johannes Fröhlich, Daniel Lumpi; [Structure-property relationships in Click-derived donor-triazole-acceptor materials](#); *Chemistry-A European Journal*, **2016**, 22, 18887-18898.

CRG (**PK**), CRY (**BS**), INC (JF, **PK**, DL), MAN (**PK**), NLO (**GR**), PPC (**PK**), SYN (DB, **PK**), THE (**PK**)

Manuscript #8: Paul Kautny, Helene Kriegner, Dorian Bader, Michal Dušek, Georg A. Reider, Johannes Fröhlich, Berthold Stöger; [Ethyne-linked push-pull chromophores: implications of crystal structure and molecular electronics on the quadric nonlinear activity](#); **submitted for publication**

CRG (**PK**), CRY (MD, **BS**), INC (JF, **PK**), MAN (**PK, BS**), NLO (**GR**), PPC (**PK**), SYN (DB, **PK, HK**), THE (**PK**)

Manuscript #9: Paul Kautny, Chenyang Zhao, Thomas Kader, Berthold Stöger, Ernst Horkel, Jiangshan Chen, Dongge Ma, Johannes Fröhlich, Daniel Lumpi; [Functional organic click-materials: application in phosphorescent organic light emitting diodes](#); *RSC Advances*, **2017**, 7, 12150-12160.

CRY (**BS**), DFM (JC, DM, **CZ**), ECC** (**PK**), FIP (**TK, PK**), INC (JC, JF, **PK, DL**), MAN (**PK**), PPC (**PK**), SYN** (**TK, PK**), THC (**PK**), THE (**EH**)

Manuscript #10: Daniel Lumpi, Johannes Steindl, Sebastian Steiner, Victor Carl, Paul Kautny, Michael Schön, Florian Glöcklhofer, Brigitte Holzer, Berthold Stöger, Ernst Horkel, Christian Hametner, Georg Reider, Marko D. Mihovilovic, Johannes Fröhlich; [Thiophene ring-fragmentation reactions: Principles and scale-up towards NLO materials](#); *Tetrahedron*, **2017**, 73, 472-280.

CRG (**DL**), CRY (**BS**), FLO (PK, MM, MS, **SS**) INC (JF, **DL**), MAN (PK, DL, MS), NLO (**GR**), SYN (VC, FG, CH, BH, EH, PK, DL, JS)

Manuscript #11: Daniel Lumpi, Paul Kautny, Berthold Stöger, Johannes Fröhlich; [Crystal chemistry of layered structures formed by linear rigid silyl-capped molecules](#); *IUCrJ*, **2015**, 2, 584-600

CRG (PK, **DL**), CRY (**BS**), INC (JF, **DL**), MAN (**BS**), SYN (PK, **DL**)

Manuscript #12: Daniel Lumpi, Paul Kautny, Berthold Stöger, Johannes Fröhlich; [Crystal chemistry of trialkylsilyl-capped \(3Z\)-4-\(methylthio\)-3-penten-1-yne: polymorphism, twinning and ambiguity of order-disorder descriptions](#); *Acta Crystallographica Section B*, **2016**, 72, 753-762

CRG (PK, **DL**), CRY (**BS**), INC (JF, **DL**), MAN (**BS**), SYN (PK, **DL**)

Manuscript #13: Paul Kautny, Florian Glöcklhofer, Thomas Kader, Jan-Michael Mewes, Berthold Stöger, Johannes Fröhlich, Daniel Lumpi, Felix Plasser; [Charge transfer states in triazole linked donor-acceptor materials: strong effects of chemical modification and solvation](#); **submitted for publication**

CRG (PK, **DL**), CRY (**BS**), INC (JF, **PK, DL, FP**), MAN (**PK, DL, FP**), PPC (**PK**), SYN (**FG, TK, PK, DL**), THE (JM, **FP**)

1.5. Summary and conclusion

In course of this thesis a reliable synthetic approach towards indolo[3,2,1-*jk*]carbazole has been developed and the applicability of this particular building block as electron donating moiety in functional organic materials has been demonstrated. In particular the utilization of the indolo[3,2,1-*jk*]carbazole in host materials for phosphorescent organic light emitting diodes proved to be promising. Therefore, this research adds another member to the family of triarylamine building blocks and increases the number of tools for organic chemists to design novel materials with tailored molecular properties. Furthermore, the Click linkage concept has been developed as a novel linkage mode for the connection of electron rich and electron poor molecular subunits in bipolar materials. These investigations on the effects of 1,2,3-triazole linkers on the molecular properties of push-pull chromophores revealed a tremendous impact on the photophysical behavior of the compounds. Suchlike prepared materials and compounds derived thereof exhibited not only very high nonlinear optical activity but the developed linkage mode could likewise be employed in the synthesis of large bandgap host materials for solution processed phosphorescent organic light emitting diodes. The intriguingly simple synthetic approach of this methodology in combination with the possibility to precisely control the electronic constitution of the molecules predestines the Click linkage for the design of functional organic materials, not only for optoelectronic applications but beyond. The Click linkage has also been employed in the functionalization of methylthio-substituted ene-yne compounds. A comprehensive control of the properties of these materials could be realized owing to manifold possibilities for molecular modifications offered by the methylthio-substituted ene-yne scaffold and the Click linkage. Notably, the ene-yne materials under investigation featured a rich crystal chemistry and reliably crystallized in layered structures. Thus, the ene-yne building block may provide a template in the design of functional organic materials with predetermined solid state arrangements, but also can be employed as versatile platform for selective modulation of the molecular properties by chemical modification.

1.6. Literature

1. Y. Tao, C. Yang and J. Qin, *Chem. Soc. Rev.*, 2011, **40**, 2943-2970.
2. A. Chaskar, H.-F. Chen and K.-T. Wong, *Adv. Mater.*, 2011, **23**, 3876-3895.
3. Y. Tao, K. Yuan, T. Chen, P. Xu, H. H. Li, R. F. Chen, C. Zheng, L. Zhang and W. Huang, *Adv. Mater.*, 2014, **26**, 7931-7958.
4. M. Zhu and C. Yang, *Chem. Soc. Rev.*, 2013, **42**, 4963-4976.
5. W.-C. Chen, C.-S. Lee and Q.-X. Tong, *J. Mater. Chem. C*, 2015, **3**, 10957-10963.
6. Z. Yang, Z. Mao, Z. Xie, Y. Zhang, S. Liu, J. Zhao, J. Xu, Z. Chi and M. P. Aldred, *Chem. Soc. Rev.* 2017, **46**, 915-1016.
7. A. Mishra and P. Bäuerle, *Angew. Chem., Int. Ed.*, 2012, **51**, 2020-2067.
8. J. Roncali, *Acc. Chem. Res.*, 2009, **42**, 1719-1730.
9. Y.-J. Cheng, S.-H. Yang and C.-S. Hsu, *Chem. Rev.*, 2009, **109**, 5868-5923.
10. H. Zhou, L. Yang and W. You, *Macromolecules*, 2012, **45**, 607-632.
11. M. J. Cho, D. H. Choi, P. A. Sullivan, A. J. P. Akelaitis and L. R. Dalton, *Prog. Pol. Sci.*, 2008, **33**, 1013-1058.
12. S.-i. Kato and F. Diederich, *Chem. Commun.*, 2010, **46**, 1994-2006.
13. L. R. Dalton, *Pure Appl. Chem.*, 2004, **76**, 1421-1433.
14. S. R. Marder, *Chem. Commun.*, 2006, 131-134.
15. G. S. He, L.-S. Tan, Q. Zheng and P. N. Prasad, *Chem. Rev.*, 2008, **108**, 1245-1330.
16. M. Pawlicki, H. A. Collins, R. G. Denning and H. L. Anderson, *Angew. Chem., Int. Ed.*, 2009, **48**, 3244-3266.
17. H. Myung Kim and B. Rae Cho, *Chem. Commun.*, 2009, 153-164.
18. L. R. Dalton, P. A. Sullivan and D. H. Bale, *Chem. Rev.*, 2009, **110**, 25-55.
19. T. Verbiest, S. Houbrechts, M. Kauranen, K. Clays and A. Persoons, *J. Mater. Chem.*, 1997, **7**, 2175-2189.
20. J. A. Delaire and K. Nakatani, *Chem. Rev.*, 2000, **100**, 1817-1846.
21. F. Dumur and F. Goubard, *New J. Chem.*, 2014, **38**, 2204-2224.
22. X. Yang, G. Zhou and W.-Y. Wong, *Chem. Soc. Rev.*, 2015, **44**, 8484-8575.
23. E. E. Havinga, W. ten Hoeve and H. Wynberg, *Polym. Bull.*, 1992, **29**, 119-126.
24. J. Roncali, *Chem. Rev.*, 1997, **97**, 173-206.
25. J. Roncali, *Macromol. Rapid Comm.*, 2007, **28**, 1761-1775.
26. X. Guo, M. Baumgarten and K. Müllen, *Prog. Polym. Sci.*, 2013, **38**, 1832-1908.
27. Y. Lin, Y. Li and X. Zhan, *Chem. Soc. Rev.*, 2012, **41**, 4245-4272.
28. Y. Shirota, *J. Mater. Chem.*, 2000, **10**, 1-25.
29. J. Gierschner and S. Y. Park, *J. Mater. Chem. C*, 2013, **1**, 5818-5832.
30. I. S. Park, S. Y. Lee, C. Adachi and T. Yasuda, *Adv. Funct. Mater.*, 2016, **26**, 1813-1821.
31. C. Adachi, T. Tsutsui and S. Saito, *Appl. Phys. Lett.*, 1990, **56**, 799-801.
32. M. A. Baldo, D. F. O'Brien, M. E. Thompson and S. R. Forrest, *Phys. Rev. B: Condens. Matter Mater. Phys.*, 1999, **60**, 14422-14428.
33. K. S. Yook and J. Y. Lee, *Adv. Mater.*, 2012, **24**, 3169-3190.
34. H. Uoyama, K. Goushi, K. Shizu, H. Nomura and C. Adachi, *Nature*, 2012, **492**, 234-238.
35. W. Li, D. Liu, F. Shen, D. Ma, Z. Wang, T. Feng, Y. Xu, B. Yang and Y. Ma, *Adv. Funct. Mater.*, 2012, **22**, 2797-2803.
36. D. Hu, L. Yao, B. Yang and Y. Ma, *Philos. Trans. R. Soc., A*, 2015, **373**.
37. H. Sasabe and J. Kido, *Eur. J. Org. Chem.*, 2013, **2013**, 7653-7663.
38. C.-L. Ho and W.-Y. Wong, *New J. Chem.*, 2013, **37**, 1665-1683.
39. S. Tokito, T. Iijima, Y. Suzuri, H. Kita, T. Tsuzuki and F. Sato, *Appl. Phys. Lett.*, 2003, **83**, 569-571.
40. R. J. Holmes, S. R. Forrest, Y.-J. Tung, R. C. Kwong, J. J. Brown, S. Garon and M. E. Thompson, *Appl. Phys. Lett.*, 2003, **82**, 2422-2424.
41. Y. Chi and P.-T. Chou, *Chem. Soc. Rev.*, 2010, **39**, 638-655.
42. C. Ulbricht, B. Beyer, C. Friebe, A. Winter and U. S. Schubert, *Adv. Mater.*, 2009, **21**, 4418-4441.
43. W. C. H. Choy, W. K. Chan and Y. Yuan, *Adv. Mater.*, 2014, **26**, 5368-5399.
44. S. O. Jeon and J. Y. Lee, *J. Mater. Chem.*, 2012, **22**, 4233-4243.
45. J. Zyss, *J. Chem. Phys.*, 1979, **71**, 909-916.
46. S. R. Marder, B. Kippelen, A. K. Y. Jen and N. Peyghambarian, *Nature*, 1997, **388**, 845-851.

47. J. L. Oudar, *J. Chem. Phys.*, 1977, **67**, 446-457.
48. J. L. Oudar and D. S. Chemla, *J. Chem. Phys.*, 1977, **66**, 2664-2668.
49. C. W. Tang and S. A. VanSlyke, *Appl. Phys. Lett.*, 1987, **51**, 913-915.
50. M. A. Baldo, D. F. O'Brien, Y. You, A. Shoustikov, S. Sibley, M. E. Thompson and S. R. Forrest, *Nature*, 1998, **395**, 151-154.
51. Z. Ge, T. Hayakawa, S. Ando, M. Ueda, T. Akiike, H. Miyamoto, T. Kajita and M.-a. Kakimoto, *Adv. Funct. Mater.*, 2008, **18**, 584-590.
52. Y. Tao, Q. Wang, Y. Shang, C. Yang, L. Ao, J. Qin, D. Ma and Z. Shuai, *Chem. Commun.*, 2009, 77-79.
53. C.-H. Chen, W.-S. Huang, M.-Y. Lai, W.-C. Tsao, J. T. Lin, Y.-H. Wu, T.-H. Ke, L.-Y. Chen and C.-C. Wu, *Adv. Funct. Mater.*, 2009, **19**, 2661-2670.
54. Y. Tao, Q. Wang, L. Ao, C. Zhong, C. Yang, J. Qin and D. Ma, *J. Phys. Chem. C*, 2010, **114**, 601-609.
55. Z. Ge, T. Hayakawa, S. Ando, M. Ueda, T. Akiike, H. Miyamoto, T. Kajita and M.-a. Kakimoto, *Org. Lett.*, 2008, **10**, 421-424.
56. S.-J. Su, H. Sasabe, T. Takeda and J. Kido, *Chem. Mater.*, 2008, **20**, 1691-1693.
57. Y. Tao, Q. Wang, C. Yang, C. Zhong, K. Zhang, J. Qin and D. Ma, *Adv. Funct. Mater.*, 2010, **20**, 304-311.
58. B. E. Koene, D. E. Loy and M. E. Thompson, *Chem. Mater.*, 1998, **10**, 2235-2250.
59. Y. Kuwabara, H. Ogawa, H. Inada, N. Noma and Y. Shirota, *Adv. Mater.*, 1994, **6**, 677-679.
60. Y. Shirota and H. Kageyama, *Chem. Rev.*, 2007, **107**, 953-1010.
61. Y. Zheng, A. S. Batsanov, V. Jankus, F. B. Dias, M. R. Bryce and A. P. Monkman, *J. Org. Chem.*, 2011, **76**, 8300-8310.
62. Y. Agata, H. Shimizu and J. Kido, *Chem. Lett.*, 2007, **36**, 316-317.
63. S. Gong, X. He, Y. Chen, Z. Jiang, C. Zhong, D. Ma, J. Qin and C. Yang, *J. Mater. Chem.*, 2012, **22**, 2894-2899.
64. C. Luo, W. Bi, S. Deng, J. Zhang, S. Chen, B. Li, Q. Liu, H. Peng and J. Chu, *J. Phys. Chem. C*, 2014, **118**, 14211-14217.
65. W. Cao, M. Fang, Z. Chai, H. Xu, T. Duan, Z. Li, X. Chen, J. Qin and H. Han, *RSC Adv.*, 2015, **5**, 32967-32975.
66. S. I. Wharton, J. B. Henry, H. McNab and A. R. Mount, *Chem. – Eur. J.*, 2009, **15**, 5482-5490.
67. C. Niebel, V. Lokshin, A. Ben-Asuly, W. Marine, A. Karapetyan and V. Khodorkovsky, *New J. Chem.*, 2010, **34**, 1243-1246.
68. H. G. Dunlop and S. H. Tucker, *J. Chem. Soc.*, 1939, 1945-1956.
69. S. I. Wharton, J. B. Henry, H. McNab and A. R. Mount, *Chem. – Eur. J.*, 2009, **15**, 5482-5490.
70. J. Lv, Q. Liu, J. Tang, F. Perdih and K. Kranjc, *Tetrahedron Lett.*, 2012, **53**, 5248-5252.
71. O. Navarro and S. P. Nolan, *Synthesis*, 2006, **2006**, 366-367.
72. N. Marion, O. Navarro, J. Mei, E. D. Stevens, N. M. Scott and S. P. Nolan, *J. Am. Chem. Soc.*, 2006, **128**, 4101-4111.
73. M. Godumala, S. Choi, M. J. Cho and D. H. Choi, *J. Mater. Chem. C*, 2016, **4**, 11355-11381.
74. D. F. O'Brien, M. A. Baldo, M. E. Thompson and S. R. Forrest, *Appl. Phys. Lett.*, 1999, **74**, 442-444.
75. M. H. Tsai, Y. H. Hong, C. H. Chang, H. C. Su, C. C. Wu, A. Matoliukstyte, J. Simokaitiene, S. Grigalevicius, J. V. Grazulevicius and C. P. Hsu, *Adv. Mater.*, 2007, **19**, 862-866.
76. C. Adachi, R. C. Kwong, P. Djurovich, V. Adamovich, M. A. Baldo, M. E. Thompson and S. R. Forrest, *Appl. Phys. Lett.*, 2001, **79**, 2082-2084.
77. I. Tanaka, Y. Tabata and S. Tokito, *Chem. Phys. Lett.*, 2004, **400**, 86-89.
78. S. Schoof, H. Güsten and C. Von Sonntag, *Berichte der Bunsengesellschaft für physikalische Chemie*, 1978, **82**, 1068-1073.
79. Y. Tao, Q. Wang, L. Ao, C. Zhong, J. Qin, C. Yang and D. Ma, *J. Mater. Chem.*, 2010, **20**, 1759-1765.
80. M.-Y. Lai, C.-H. Chen, W.-S. Huang, J. T. Lin, T.-H. Ke, L.-Y. Chen, M.-H. Tsai and C.-C. Wu, *Angew. Chem., Int. Ed.*, 2008, **47**, 581-585.
81. C. Piliego, T. W. Holcombe, J. D. Douglas, C. H. Woo, P. M. Beaujuge and J. M. J. Fréchet, *J. Am. Chem. Soc.*, 2010, **132**, 7595-7597.
82. T.-Y. Chu, J. Lu, S. Beaupré, Y. Zhang, J.-R. Pouliot, S. Wakim, J. Zhou, M. Leclerc, Z. Li, J. Ding and Y. Tao, *J. Am. Chem. Soc.*, 2011, **133**, 4250-4253.
83. C. B. Nielsen, R. S. Ashraf, B. C. Schroeder, P. D'Angelo, S. E. Watkins, K. Song, T. D. Anthopoulos and I. McCulloch, *Chem. Commun.*, 2012, **48**, 5832-5834.

84. M.-C. Yuan, M.-Y. Chiu, S.-P. Liu, C.-M. Chen and K.-H. Wei, *Macromolecules*, 2010, **43**, 6936-6938.
85. X. Guo, N. Zhou, S. J. Lou, J. Smith, D. B. Tice, J. W. Hennek, R. P. Ortiz, J. T. L. Navarrete, S. Li, J. Strzalka, L. X. Chen, R. P. H. Chang, A. Facchetti and T. J. Marks, *Nat. Photonics*, 2013, **7**, 825-833.
86. X. Guo, R. P. Ortiz, Y. Zheng, M.-G. Kim, S. Zhang, Y. Hu, G. Lu, A. Facchetti and T. J. Marks, *Am. Chem. Soc.*, 2011, **133**, 13685-13697.
87. A. Qin, J. W. Y. Lam and B. Z. Tang, *Chem. Soc. Rev.*, 2010, **39**, 2522-2544.
88. V. V. Rostovtsev, L. G. Green, V. V. Fokin and K. B. Sharpless, *Angew. Chem., Int. Ed.*, 2002, **41**, 2596-2599.
89. F. Amblard, J. H. Cho and R. F. Schinazi, *Chem. Rev.*, 2009, **109**, 4207-4220.
90. J. E. Hein and V. V. Fokin, *Chem. Soc. Rev.*, 2010, **39**, 1302-1315.
91. C. W. Tornoe, C. Christensen and M. Meldal, *J. Org. Chem.*, 2002, **67**, 3057-3064.
92. D. Liu, D. Li, M. Wang and W. Li, *J. Mater. Chem. C*, 2016, **4**, 7260-7268.
93. M.-k. Leung, Y.-H. Hsieh, T.-Y. Kuo, P.-T. Chou, J.-H. Lee, T.-L. Chiu and H.-J. Chen, *Org. Lett.*, 2013, **15**, 4694-4697.
94. J. Zhuang, W. Su, W. Li, Y. Zhou, Q. Shen and M. Zhou, *Org. Electron.*, 2012, **13**, 2210-2219.
95. J. Zhuang, W. Li, W. Su, M. Zhou and Z. Cui, *New. J. Chem.*, 2014, **38**, 650-656.
96. D. Lumpi, B. Stöger, C. Hametner, F. Kubel, G. Reider, H. Hagemann, A. Karpfen and J. Fröhlich, *CrystEngComm*, 2011, **13**, 7194-7197.
97. D. Lumpi, F. Glöckhofer, B. Holzer, B. Stöger, C. Hametner, G. A. Reider and J. Fröhlich, *Cryst. Growth Des.*, 2014, **14**, 1018-1031.
98. J. Li, M. Hu and S. Q. Yao, *Org. Lett.*, 2009, **11**, 3008-3011.
99. S. S. Bag and R. Kundu, *J. Org. Chem.*, 2011, **76**, 3348-3356.
100. A.-S. Cornec, C. Baudequin, C. Fiol-Petit, N. Plé, G. Dupas and Y. Ramondenc, *Eur. J. Org. Chem.*, 2013, **2013**, 1908-1915.
101. J. Shi, L. Liu, J. He, X. M. Meng and Q. X. Guo, *Chem. Lett.*, 2007, **36**, 1142-1143.
102. P. D. Jarowski, Y.-L. Wu, W. B. Schweizer and F. Diederich, *Org. Lett.*, 2008, **10**, 3347-3350.
103. A. Wild, C. Friebe, A. Winter, M. D. Hager, U.-W. Grummt and U. S. Schubert, *Eur. J. Org. Chem.*, 2010, **2010**, 1859-1868.
104. M. Parent, O. Mongin, K. Kamada, C. Katan and M. Blanchard-Desce, *Chem. Commun.*, 2005, 2029-2031.
105. R. M. Meudtner, M. Ostermeier, R. Goddard, C. Limberg and S. Hecht, *Chem. – Eur. J.*, 2007, **13**, 9834-9840.
106. Y. H. Lau, P. J. Rutledge, M. Watkinson and M. H. Todd, *Chem. Soc. Rev.*, 2011, **40**, 2848-2866.
107. J. J. Bryant, Y. Zhang, B. D. Lindner, E. A. Davey, A. L. Appleton, X. Qian and U. H. F. Bunz, *J. Org. Chem.*, 2012, **77**, 7479-7486.
108. D. Schweinfurth, K. I. Hardcastle and U. H. F. Bunz, *Chem. Commun.*, 2008, 2203-2205.
109. S. Ast, T. Fischer, H. Muller, W. Mickler, M. Schwichtenberg, K. Rurack and H. J. Holdt, *Chem. – Eur. J.*, 2013, **19**, 2990-3005.
110. M. K. Kim, J. Kwon, T.-H. Kwon and J.-I. Hong, *New J. Chem.*, 2010, **34**, 1317-1322.
111. M. Juricek, M. Felici, P. Contreras-Carballada, J. Lauko, S. R. Bou, P. H. J. Kouwer, A. M. Brouwer and A. E. Rowan, *J. Mater. Chem.*, 2011, **21**, 2104-2111.
112. I. Stengel, A. Mishra, N. Pootrakulchote, S. J. Moon, S. M. Zakeeruddin, M. Grätzel and P. Bäuerle, *J. Mater. Chem.*, 2011, **21**, 3726-3734.
113. G. de Miguel, M. Wielopolski, D. I. Schuster, M. A. Fazio, O. P. Lee, C. K. Haley, A. L. Ortiz, L. Echegoyen, T. Clark and D. M. Guldi, *J. Am. Chem. Soc.*, 2011, **133**, 13036-13054.
114. S. Gronowitz and T. Frejd, *Chem. Heterocycl. Compd.*, 1978, **14**, 353-367.
115. B. Iddon, *Heterocycles*, 1983, **20**, 1127-1171.
116. T. L. Gilchrist, *Advances in Heterocyclic Chemistry*, ed. R. K. Alan, Academic Press, 1987, Volume 41, 41-74.
117. Y. Zhu, S. Guang, X. Su, H. Xu and D. Xu, *Dyes Pig.*, 2013, **97**, 175-183.
118. J. E. Anthony, D. L. Eaton and S. R. Parkin, *Org. Lett.*, 2002, **4**, 15-18.
119. J. E. Anthony, *Angew. Chem., Int. Ed.*, 2008, **47**, 452-483.
120. C. Wang, H. Dong, W. Hu, Y. Liu and D. Zhu, *Chem. Rev.*, 2012, **112**, 2208-2267.
121. W. Wu, Y. Liu and D. Zhu, *Chem. Soc. Rev.*, 2010, **39**, 1489-1502.

2. Original works

2.1. Manuscript #1

Oxadiazole based bipolar host materials employing planarized triarylamine donors for RGB PHOLEDs with low efficiency roll-off

Paul Kautny, Daniel Lumpi, Yanping Wang, Antoine Tissot, Johannes Bintinger, Ernst Horkel, Berthold Stöger, Christian Hametner, Hans Hagemann, Dongge Ma, Johannes Fröhlich

Journal of Materials Chemistry C, **2014**, 2, 2069-2081

Reproduced with the kind permission of the Royal Society of Chemistry.

PAPER

Oxadiazole based bipolar host materials employing planarized triarylamine donors for RGB PHOLEDs with low efficiency roll-off†

Cite this: *J. Mater. Chem. C*, 2014, 2, 2069Paul Kautny,^a Daniel Lumpi,^{*a} Yanping Wang,^b Antoine Tissot,^c Johannes Binting,^a Ernst Horkel,^a Berthold Stöger,^d Christian Hametner,^a Hans Hagemann,^c Dongge Ma^b and Johannes Fröhlich^a

A series of 6 novel triarylamine-containing oxadiazole compounds (*o*-PCzPOXD, *o*-ICzPOXD, *o*-TPATOXD, *o*-PCzTOXD, *o*-ICzTOXD, *o*-CzTOXD) have been designed, synthesized and characterized concerning applications as host materials in PHOLED devices. To further improve the *ortho*-linkage concept, the impact of incorporating planarized electron-donating triarylamine (TAA) structures on intramolecular charge transfer was examined. The effect was evaluated for two series of electron-accepting oxadiazole scaffolds, realizing *ortho*-linkage on the benzene (POXD) and the thiophene (TOXD) cores. Thermal analysis shows increased glass-transition temperatures for planarized structures indicating an improved morphological stability. A higher degree of planarization also results in significantly increased singlet and triplet energy values, revealing the impact on the intramolecular charge transfer. Employing the developed materials, red (*o*-TPATOXD: CE_{\max} : 28.8 cd A⁻¹, EQE_{\max} : 16.9%), green (*o*-PCzPOXD: CE_{\max} : 62.9 cd A⁻¹, EQE_{\max} : 17.1%) and blue (*o*-PCzPOXD: CE_{\max} : 29.8 cd A⁻¹, EQE_{\max} : 13.4%) devices were achieved showing remarkably low efficiency roll-off for planarized donors. Hence, this is the first report of efficient blue devices for this specific class of host materials. It is proposed that the results correlate with an increasing *ortho*-linkage effect and decreasing donor strength of the TAA moiety by planarization and, thus, tackling one of the major challenges in PHOLED research: improving both triplet energy and compound stability.

Received 26th November 2013
Accepted 4th January 2014

DOI: 10.1039/c3tc32338b

www.rsc.org/MaterialsC

Introduction

Organic Light Emitting Diodes (OLEDs) and their application in display technology represent the most advanced technology among the rapidly growing field of organic electronics.^{1–7} Since the groundbreaking work of Forrest *et al.* from 1998 (ref. 8 and 9) great efforts have been made in developing Phosphorescent Organic Light Emitting Diodes (PHOLEDs) typically employing heavy transition metal complexes.^{10,11} In contrast to fluorescent OLEDs phosphorescent emitters are capable of

harvesting triplet and singlet excitons simultaneously and, thus, can theoretically achieve 100% internal quantum efficiency.^{12,13}

However, high concentration of triplet excitons leads to triplet-triplet annihilation at high current rates resulting in efficiency roll-off.¹⁴ Thus, phosphorescent emitters are generally widely dispersed in an organic host material. Efficient host materials have to fulfill some basic requirements:⁷ (i) higher triplet energy (E_t) value than that of the dopant to effectively confine triplet excitons on the phosphorescent emitter; (ii) suitable HOMO/LUMO levels to facilitate charge injection; and (iii) morphological stability for durable and long lasting devices.

Bipolar host materials have received great attention in recent years, due to their balanced charge transport properties resulting in broad charge recombination zones. However, combining donor and acceptor subunits in one molecule ultimately lowers the E_t as a result of the intramolecular charge transfer.⁷ Therefore, the molecular design of bipolar host materials focuses on the interruption of the conjugated π -system in order to reduce donor-acceptor interactions and thus to retain high E_t values. Among the most efficient ways to separate the molecular subunits is the introduction of specific linkage modes.⁷ Particularly, *ortho*-linkage of donor and

^aInstitute of Applied Synthetic Chemistry, Vienna University of Technology, Getreidemarkt 9/163, A-1060 Vienna, Austria. E-mail: daniel.lumpi@tuwien.ac.at

^bState Key Laboratory of Polymer Physics and Chemistry, Changchun Institute of Applied Chemistry, Chinese Academy of Sciences, Changchun, 130022, China

^cDépartement de Chimie Physique, Université de Genève, 30, quai E. Ansermet, 1211 Geneva 4, Switzerland

^dInstitute of Chemical Technologies and Analytics, Vienna University of Technology, Getreidemarkt 9/164, A-1060 Vienna, Austria

† Electronic supplementary information (ESI) available: NMR spectra, TGA/DSC analyses, cyclic voltammetry, phosphorescence as well as electroluminescence spectra, DFT calculations and crystallographic information. CCDC 955416–955418. For ESI and crystallographic data in CIF or other electronic format see DOI: 10.1039/c3tc32338b

acceptor subunits, inducing twisted molecular conformations, proved to be a highly efficient strategy to achieve large triplet bandgap materials.¹⁵

In this contribution we reveal the enhancement of the effect of *ortho*-linkage by applying increasingly planarized triarylamine donors (from *N,N*-diphenylbenzenamine (TPA) to 9-phenyl-9*H*-carbazole (PCz) and indolo[3,2,1-*jk*]carbazole (ICz)) to an established phenyl-oxadiazole-phenyl (POXD) acceptor. The corresponding triphenylamine compound (***o***-TPAPOXD) has been previously demonstrated to be highly efficient as the host in red and green PHOLED devices.^{16,17} Utilizing the planarized arylamines we were able to increase singlet as well as triplet energies resulting in higher efficiencies and significantly reduced efficiency roll-off in non-optimized red, green and blue PHOLED devices. We propose that these findings correlate with an increasing *ortho*-linkage effect due to steric impact and decreasing donor strength of the triarylamine moiety by planarization as a result of the contribution of the nitrogen lone-pair to the aromaticity of the formed pyrrole subunit(s). To prove the developed concept, TPA, PCz, ICz as well as carbazole (Cz) donors were also applied to a new thiophene-oxadiazole-thiophene (TOXD) acceptor moiety confirming the trends.

By employing the developed materials red (***o***-TPATOXD: CE_{\max} : 28.7 cd A⁻¹, EQE_{\max} : 16.9%), green (***o***-PCzPOXD: CE_{\max} : 62.9 cd A⁻¹, EQE_{\max} : 17.1%) and blue (***o***-PCzPOXD: CE_{\max} : 29.8 cd A⁻¹, EQE_{\max} : 13.4%) devices have been obtained.

Hence, we report on an efficient approach to gain control of intramolecular charge transfer, significantly affecting singlet as well as triplet energies, by the planarization of electron donating triarylamine moieties. As a result, novel host materials have been designed, synthesized and characterized exhibiting remarkably low efficiency roll-off, which is of technological relevance for both single doped devices and multi-color based white PHOLEDs.

Results and discussion

Synthesis

The synthesis of target host materials and precursors primarily relies on organo-lithium assisted and transition-metal catalyzed (Ullman condensation, Suzuki cross-coupling) reactions. The first part describes the synthetic pathways towards planarized triarylamine (TAA) structures phenylcarbazole and indolocarbazole particularly focusing on C–H activation as an efficient approach to acquire the desired planarization. In the second part the realization of the *ortho*-linkage on the benzene (**5a–c**) core and subsequently the thiophene core (**8a–d**), achieved *via* a Halogen Dance (HD) reaction, is outlined.

Boronic esters of triphenylamine (**3a**) and phenylcarbazole (**3b**) were obtained in analogy to the literature.^{18–20} The synthesis of indolocarbazole boronic ester (**3c**) is based on a recently developed methodology utilizing C–H activation.²¹ Compared to previously reported procedures this synthetic approach towards indolo[3,2,1-*jk*]carbazole **2** (Scheme 1) is shorter (less steps), more efficient and does not rely on the application of special equipment (*e.g.* vacuum flash pyrolysis).^{22,23} Although good yields of 83% (15 mol% Pd(OAc)₂ catalyst) were accomplished

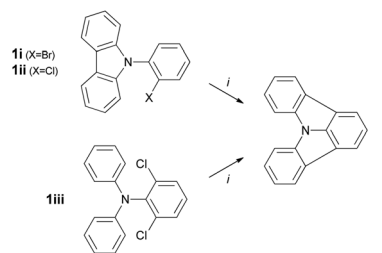
the reduction of catalyst loads drastically decreased the reaction conversion. The use of 5 mol% Pd(OAc)₂ even limits the product formation to trace amounts.²¹ Hence, we report on an improved procedure at significantly reduced catalyst amounts (2 mol%) towards indolo[3,2,1-*jk*]carbazole employing Pd(PPh₃)₄ and K₂CO₃ (71% yield). In fact, the application of a (NHC)Pd(allyl)Cl^{24,25} catalyst (2 mol%) further improves the yields to 94% (Scheme 1 and Table 1). Moreover, the substrate scope could be broadened to chlorine derivatives (no conversion for Pd(PPh₃)₄, Table 1).

Particularly, the demonstrated two-fold C–H activation of chlorine derivatives allows for a convenient and selective synthesis of a variety of novel target structures, broadening the scope of accessible indolo[3,2,1-*jk*]carbazole moieties.

Selective bromination (NBS, 54%)²³ of **2** and organo-lithium assisted transformation (*n*-BuLi, isopropyl pinacol borate, 69%) yielded the indolocarbazole pinacol boronic ester **3c**. The crystal structure (see the ESI† for details) discloses the desired planarity of this TAA type structure. **3c** (ref. 26) crystallizes with one crystallographically unique molecule in the asymmetric unit located on a general position. The aromatic system is close to flat: the N atom is located 0.1573(5) Å from the least square (LS) plane defined by the C atoms of the benzene rings.

The dibrominated POXD (benzene-oxadiazole-benzene structure) precursor **4** was synthesized according to the literature.²⁷ The conversion towards target compounds **5a–c** was accomplished utilizing TAA boronic esters **3a–c** applying a standard Suzuki protocol (Scheme 2).²⁸ Good to excellent yields of 85% and 93% were achieved for **5a** and **5b**, respectively; the lower yield of **5c** (39%) is attributed to a lower solubility affecting both reaction conversion and work-up.

In contrast to the POXD series the dibrominated TOXD (thiophene-oxadiazole-thiophene structure), precursor **7i**, is unavailable in the literature. The *ortho*-substitution pattern is realized by applying a double-sided halogen dance (HD)^{29–31}

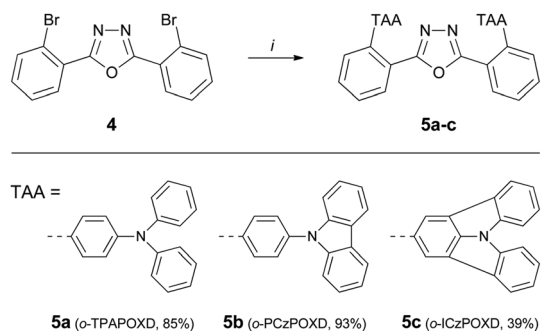


Scheme 1 Synthetic pathways towards indolo[3,2,1-*jk*]carbazole **2**: (i) (NHC)Pd(allyl)Cl (2 mol%), K₂CO₃ (2.0 eq.), DMA (0.2 M), 130 °C, 1–2 h.

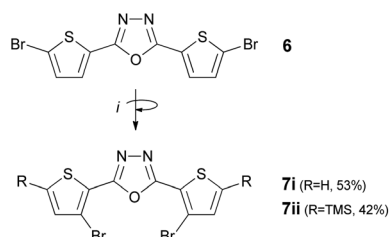
Table 1 Results of the C–H activation of substrates **1i–iii**

Substrate	Pd(PPh ₃) ₄	(NHC)Pd(allyl)Cl
1i	71% ^a	94% ^a
1ii	n.c. ^b	94% ^a
1iii	n.c. ^b	80% ^a

^a Isolated yields. ^b No conversion (GC-MS).



Scheme 2 Synthesis of POXD based host materials **5a–c**: (i) boronic acid ester **3a–c** (2.5 eq.), K_2CO_3 (5.0 eq., 2 M aq.), $\text{Pd}(\text{PPh}_3)_4$ (5 mol%), THF (~0.5 M), reflux.

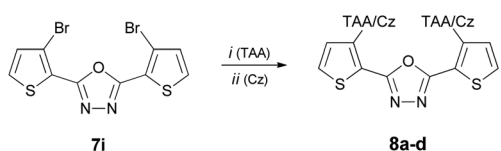


Scheme 3 Halogen dance reaction towards *ortho*-substitution patterns (**7i,ii**): (i) THF, $-25\text{ }^\circ\text{C}$, LDA (2.4 eq.), 30 min stirring prior to addition of electrophiles (MeOH and TMS-Br).

methodology (Scheme 3) starting from **6** (synthesized according to the literature). Due to coordinating and activating effects of the oxadiazole moiety³² the lithium diisopropylamide (LDA) induced metallation selectively takes place in the respective *ortho*-positions. Subsequently, a rearrangement of the bromine atoms (“halogen dance”), resulting in the thermodynamically most stable organo-lithium intermediate, yields the desired *ortho*-substitution pattern.

As a consequence, this approach enables direct introduction of substituents R in the 5-positions by addition of suitable electrophiles (R), which has been demonstrated utilizing TMS-Br to yield the silylated compound **7ii**. Hence, specific alterations of material properties *e.g.* solubility (for *e.g.* solution processing) can be achieved; however, reaction conditions were not further optimized in this study.

The triarylamine and carbazole cap structures are attached to the TOXD core *via* Suzuki cross-coupling reaction^{33–35} and Ullmann condensation,^{36–38} respectively (Scheme 4).



Scheme 4 Synthesis of TOXD based host materials **8a–d**: (i) Suzuki cross-coupling: boronic acid ester **3a–c** (3.0 eq.), KO^tBu (3.0 eq.), $(\text{NHC})\text{Pd}(\text{allyl})\text{Cl}$ (2 mol%), $i\text{PrOH-H}_2\text{O}$ (3 : 1, 5 mM), rf; (ii) Ullmann condensation: carbazole (3.0 eq.), K_2CO_3 (3.0 eq.) and $\text{CuSO}_4 \cdot 5\text{H}_2\text{O}$ (6.4 mol%), $230\text{ }^\circ\text{C}$.

The Suzuki reaction utilizing TAA precursors **3a–c** was shown to proceed with good to moderate yields using $\text{Pd}(\text{PPh}_3)_4$. However, improved yields and more reliable results could be obtained by applying $(\text{NHC})\text{Pd}(\text{allyl})\text{Cl}$,²⁴ (55–74%) which generally turned out to be a highly efficient catalyst for thiophene–benzene cross-coupling. Attempts of Buchwald–Hartwig reactions in order to introduce the carbazole did not give satisfactory results, which led to a solvent-free Ullmann procedure²⁰ using $\text{CuSO}_4 \cdot 5\text{H}_2\text{O}$ as the catalyst.

Thermal properties

The thermal stability of the target host materials was investigated by TGA. High decomposition temperatures (T_d – determined from 5% mass loss) between $392\text{ }^\circ\text{C}$ and $426\text{ }^\circ\text{C}$ were observed for all materials. Glass transition temperatures (T_g) were analyzed by DSC. While *o*-TPAPOXD exhibits glass transition at $94\text{ }^\circ\text{C}$ ¹⁶ the values for *o*-PCzPOXD ($125\text{ }^\circ\text{C}$) and *o*-ICzPOXD ($152\text{ }^\circ\text{C}$) are significantly higher indicating improved morphological stability of thin films in PHOLED devices. Within the TOXD series *o*-PCzTOXD also features higher glass transition at $135\text{ }^\circ\text{C}$ compared to *o*-TPATOXD ($101\text{ }^\circ\text{C}$) or *o*-CzTOXD ($106\text{ }^\circ\text{C}$) while no glass transition was detected for *o*-ICzTOXD. In general, the incorporation of the thiophene linker (TOXD derivatives) resulted in slightly higher glass transition temperatures in relation to the corresponding POXD compounds. Higher T_g values for PCz and ICz compounds compared to that of the TPA structure are attributed to an increased rigidity of the TAA moieties. All observed values are distinctly higher compared to that of CBP ($62\text{ }^\circ\text{C}$ (ref. 7)).

Photo-physical properties

Fig. 1 (left) displays the UV/VIS absorption and photoluminescence (PL) spectra of *o*-PCzPOXD and *o*-ICzPOXD as well as “reference compound” *o*-TPAPOXD. Spectra of the TOXD series are depicted in Fig. 1 (right). The optical bandgaps (opt. BG), determined from absorption onsets, are summarized in Table 2.

The absorption bands of *o*-TPAPOXD and *o*-TPATOXD at 305 nm are assigned to triphenylamine centered $n-\pi^*$ transition.³⁹ All carbazole containing compounds exhibit sharp absorption peaks around 290 nm , which are attributed to the $n-\pi^*$ transition of the carbazole moiety.⁴⁰ Indolocarbazole containing *o*-ICzTOXD and *o*-ICzPOXD features a related $n-\pi^*$ transition below 300 nm . Longer wavelength absorption bands result from $\pi-\pi^*$ charge transfer transitions from electron-donating arylamines to electron-accepting oxadiazole.⁴¹ Strikingly, the absorbance of charge transfer transition is significantly lower for *o*-PCzPOXD and *o*-ICzPOXD compared to that of *o*-PCzTOXD and *o*-ICzTOXD, indicating that the partial disruption of the conjugated π -system by *ortho*-linkage is more effectively realized on the benzene spacer.

For the TOXD series also a significant blue shift of the absorption onset from *o*-TPATOXD ($\sim 450\text{ nm}$) to *o*-PCzTOXD and *o*-ICzTOXD (both located at $\sim 400\text{ nm}$) has been observed, indicating increased optical bandgaps as a result of planarized TAA donors.

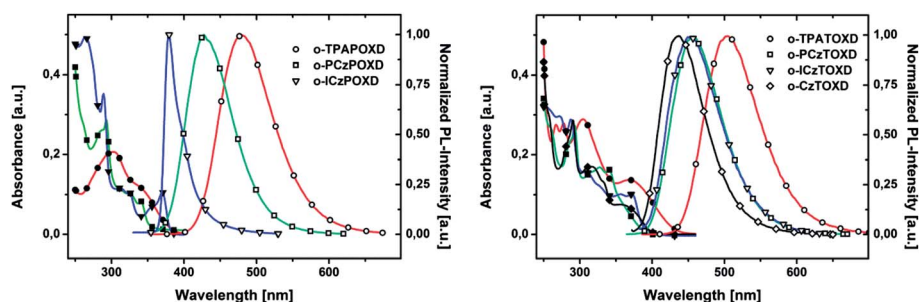


Fig. 1 Absorption (full symbols) and PL (hollow symbols) characteristics of host materials **5a–c** (POXD series, left) and **8a–d** (TOXD series, right); recorded in a 5 μM solution in DCM at r.t.

Photoluminescence (PL) spectroscopy revealed a fluorescence emission maximum of **o**-TPAPOXD located at 479 nm. A significant blue shift of the emission maxima is observed for both **o**-PCzPOXD (428 nm) and **o**-ICzPOXD (379 nm). These results impressively demonstrate the impact of planarizing TAA donors by shifting the singlet emission by up to 100 nm ($\Delta E = 0.68$ eV). Similar trends were observed for the TOXD series (**o**-TPATOXD (502 nm), **o**-PCzTOXD (456 nm) and **o**-ICzTOXD (452 nm)). We propose that these findings correlate with an increasing *ortho*-linkage effect (more twisted conformation) and decreasing donor strength of the TAA moiety (ICz < PCz < TPA) by planarization. The alteration in donor strength is attributed to the fact that the lone pair of the nitrogen increasingly contributes to the aromaticity (PCz and ICz). **o**-CzTOXD shows an emission maximum at 436 nm; the deep blue emission characteristic is due to the less extended conjugated π -system compared to the TAA structures. Clearly, all POXD compounds exhibit blue shifted emission with respect to the thiophene analogs (TOXD) indicating a more effective donor–acceptor separation for the benzene spacer.

Phosphorescence spectroscopy (77 K) revealed that planarization also impacts triplet emission, although the effect is less pronounced compared to singlet emission. The E_t values, deduced from the highest vibronic sub-band of the phosphorescence spectra, of **o**-TPAPOXD, **o**-PCzPOXD and **o**-ICzPOXD were determined to be 2.49 eV (2.46 eV (ref. 16)), 2.62 eV and

2.83 eV, respectively. Compared to the POXD series the E_t values of the TOXD materials **o**-TPATOXD (2.21 eV), **o**-PCzTOXD (2.29 eV), **o**-ICzTOXD (2.37 eV) and **o**-CzTOXD (2.39 eV) are shifted to lower energies.

Although the E_t values significantly increase as a consequence of planarization for both series, host materials of the TOXD series are restricted to low energy emitters. In contrast, the triplet energies of the POXD series are suitable for the construction of green devices.^{16,17} E_t values >2.60 eV for the PCz and ICz donor structures potentially broaden the scope even to blue phosphorescent emitters (e.g. FIrPic). Particularly the unexpectedly high E_t value (2.83 eV) for **o**-ICzPOXD reveals the effect of incorporating indolo[3,2,1-*j*]*k*carbazole structures; a possible explanation for these findings is given by DFT calculations (see below).

Additionally, lifetimes for the excited singlet and triplet states were determined. Most striking are the significantly longer triplet lifetimes (τ) found in the POXD series (**o**-TPAPOXD (~790 ms), **o**-PCzPOXD (~335 ms), **o**-ICzPOXD (~349 ms)) compared to those of the TOXD compounds; triplet lifetimes for the TOXD structures range from 8.2 to 12.3 ms. The sulfur atoms in the TOXD compounds are subject to stronger spin–orbit coupling which leads to somewhat relaxed selection rules for transitions between singlet and triplet states (i.e. shorter lifetimes of the triplet). Further details on photo-physical properties are given in the ESI.†

Table 2 Physical data of synthesized materials

	$T_g/T_c/T_m/T_d^a$ [°C]	opt. BG ^{b,c} [eV]	$\lambda_{\text{PL,max}}^c$ [nm]	HOMO/LUMO [eV]		E_T (eV)	
				Exp. ^d	Cal. ^e	Exp. ^f	Cal. ^g
o -TPAPOXD	94/—/270/432 (ref. 16)	3.24	479	−5.25/−2.41 (ref. 16)	−5.14/−1.77	2.49	2.63
o -PCzPOXD	125/n.o. ^h /252/395	3.51	428	−5.64/−2.50	−5.55/−2.04	2.62	2.83
o -ICzPOXD	152/231/308/404	3.26	379	−5.73/−2.50 ⁱ	−5.70/−1.84	2.83	2.88
o -TPATOXD	101/n.o. ^h /184/414	2.88	502	−5.30/−2.57	−5.19/−2.11	2.21	2.21
o -PCzTOXD	135/n.o. ^h /261/426	3.19	456	−5.66/−2.68	−5.57/−2.37	2.29	2.30
o -ICzTOXD	n.o. ^h /302/341/402	3.19	452	−5.68/−2.56	−5.70/−2.03	2.37	2.36
o -CzTOXD	106/n.o. ^h /211/392	3.11	436	−5.69/−2.66	−5.65/−2.39	2.39	2.33

^a Determined from TGA/DSC analysis; T_c : crystallization temperature. ^b Estimated from the absorption onset. ^c Measurement in DCM (5 μM) at r.t. ^d Calculated from onsets of oxidation and reduction peaks. ^e Calculated applying the density functional theory level (B3LYP/6-311 + G*). ^f Estimated from the highest energy vibronic transition in toluene at 77 K. ^g Calculated applying the time-dependent density functional theory level (B3LYP/6-311 + G*). ^h Not observed. ⁱ Calculated from HOMO level and absorption onset.

Electro-chemical properties

Electro-chemical properties (Table 2) of target materials were investigated by cyclic voltammetry (CV). Predominately determined by electron-rich triaryl amines, the HOMO energy levels span a narrow range of -5.73 eV to -5.64 eV with the exception of *o*-TPAPOXD and *o*-TPATOXD at -5.25 eV (ref. 16) and -5.30 eV, respectively. Thus, the incorporation of planarized TAA donors significantly lowers the HOMO energy levels. While *o*-TPATOXD shows reversible oxidation, all carbazole and indolocarbazole containing materials exhibit irreversible oxidation waves due to the instability of the formed cations.^{23,42,43} Quasi-reversible reductions were observed during cathodic scans; however, no significant reduction process was observed for *o*-ICzPOXD. The LUMO energy levels of the compounds are located between -2.68 eV and -2.41 eV. These values indicate no significant injection barrier for charge carriers from adjacent charge transporting layers.

Theoretical calculations

To investigate the geometrical and electronic properties of the target compounds at the molecular level studies applying density functional theory (DFT) and time-dependent DFT (TDDFT) calculations were conducted (for additional details see the Experimental section). According to DFT calculations, absolute HOMO/LUMO values are in the range of 5.14 – 5.70 eV/ 1.77 – 2.39 eV, which correlates with the experimental data; LUMO levels show a systematic shift of ~ 0.5 eV.

The contour plots for **5a** and **8a**, comparing the POXD with the corresponding TOXD compounds, are depicted in Fig. 2. As expected, HOMO levels are mainly located at one of the TAA

structures and the LUMOs at the oxadiazole containing cores (POXD and TOXD). This separation, particularly crucial for high triplet energies, was found to be more efficiently realized for the POXD series (benzene linker) for all substance pairs, which is in agreement with photo-physical data (Table 2). Inspecting the TPA (Fig. 2 (left)) and PCz (Fig. 3 (left)) scaffolds a similar trend is observed: a reduced HOMO/LUMO overlap is indicated for the more rigidified PCz *versus* the TPA structures. The comparison of the average tilting angles of the of POXD and the TOXD benzene to the TAA benzene core supports the aforementioned assumptions: 54.6° ($56.2^\circ/53.0^\circ$) *o*-TPAPOXD $<$ 58.7° ($62.2^\circ/55.2^\circ$) *o*-PCzPOXD $<$ 59.7° ($61.9^\circ/57.5^\circ$) *o*-ICzPOXD and 50.2° ($52.0^\circ/48.3^\circ$) *o*-TPATOXD $<$ 54.3° ($57.8^\circ/50.8^\circ$) *o*-PCzTOXD $<$ 54.9° ($57.0^\circ/52.8^\circ$) *o*-ICzTOXD (the exact tilting angle values for each side of the asymmetric molecules are given in brackets).

A remarkable result of the calculation was acquired for *o*-ICzPOXD (Fig. 3 (right)). While the HOMO is positioned at the TAA (ICz) scaffold (as expected), the LUMO is not located on the POXD core but on the opposing ICz moiety. Potentially, this fact is an explanation for the aforementioned unexpectedly high triplet energy observed as a result of the enhanced spatial separation and modified acceptor properties. This finding outlines the significant deviation in donor strength for the applied TAA structures and the effect on material properties. In contrast, the LUMO in the *o*-ICzTOXD remains located at the TOXD core (as observed for all other molecules), which corresponds to the detected triplet and singlet energy value relationships, thus, supporting the hypothesis for the LUMO located on the ICz core in *o*-ICzPOXD.

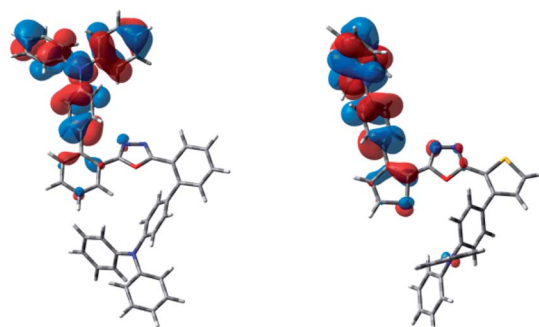
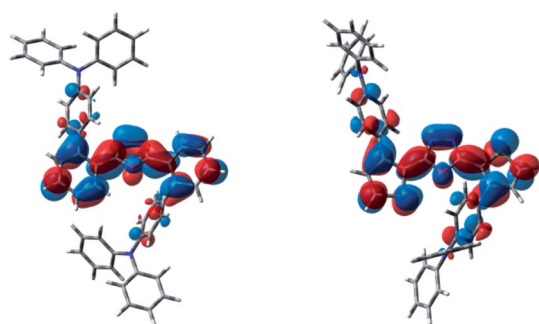


Fig. 2 HOMO (bottom) and LUMO (top) of *o*-TPAPOXD **5a** (left) and *o*-TPATOXD **8a** (right).

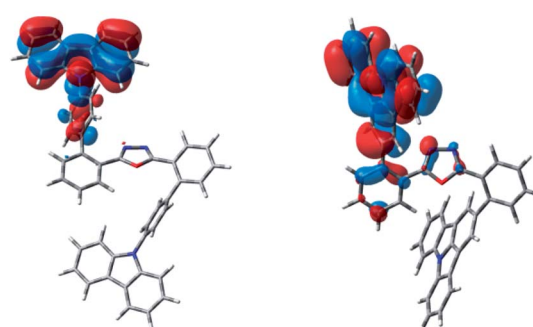
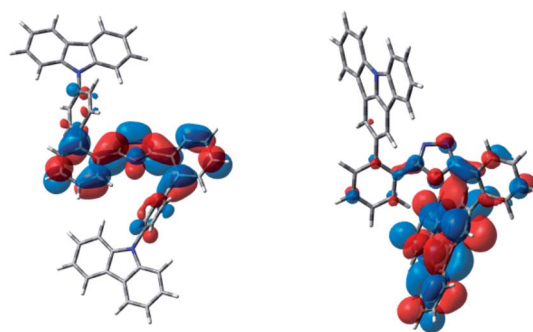


Fig. 3 HOMO (bottom) and LUMO (top) of *o*-PCzPOXD **5b** (left) and *o*-ICzPOXD **5c** (right).

Crystallography

***o*-PCzPOXD (5b)**⁴⁴ (Fig. 4 (left)) crystallizes with one crystallographically unique molecule in the asymmetric unit. The molecules are pseudo-symmetric by twofold rotation around an axis passing through the O atom of the oxadiazole ring. The PCz donor units are located on the side of the O atom of the oxadiazole ring. Due to steric interaction of these groups, the core benzenes (POXD) are strongly inclined to each other (angle between the LS planes: 60.95(3)°) and to the central oxadiazole ring (32.45(8)° and 33.64(8)°). The carbazole moieties are moderately inclined with respect to the core benzenes (15.58(9)° and 16.25(9)°). On the other hand the PCz-benzene rings are distinctly inclined to the POXD benzenes (53.49(6)° and 54.12(6)°) and carbazoles (56.38(5)° and 57.68(5)°).

***o*-PCzTOXD (8b)**⁴⁵ (Fig. 4 (right)) crystallizes with two crystallographically different molecules ($Z' = 2$) located in general positions. Both molecules are geometrically virtually equivalent. One thiophene ring is in *trans*- and one in *cis*-conformation with respect to the central oxadiazole ring. Thus, both PCz moieties face opposite directions. This is in contrast to the crystal structures of ***o*-PCzPOXD** and the solvates of the thiadiazole analog of ***o*-PCzTOXD** (as reported in earlier studies), in which the thiadiazole and thiophene rings are all in *trans*- and, therefore, the PCz units in *cis*-conformation.⁴⁶ The thiophene and oxadiazole rings in *cis*-conformation are practically planar with tilt angles of 3.17(10)° and 3.53(10)°. In contrast, the thiophenes in the *trans*-conformation feature distinct inclination to the oxadiazole ring (12.03(11)° and 11.44(11)°). While the carbazole connected *via* the PCz-benzene to the *cis*-located thiophene is nearly coplanar with the latter (3.17(8)°, 2.33(8)°), the *trans*-located thiophene is strongly inclined to the corresponding carbazole (76.91(9)°, 76.86(9)°). The PCz-benzenes on the other hand are, as in ***o*-PCzPOXD**, always strongly inclined to the neighboring aromatic moieties (tilt angles to thiophene: 45.82(10)–47.93(10)°; to carbazoles: 44.59(8)–61.06(8)°).

Charge transport properties

In order to study the influence of the four investigated arylamine-donors on charge transport properties within the TOXD series, hole-only devices (HODs; structure: ITO/MoO₃,

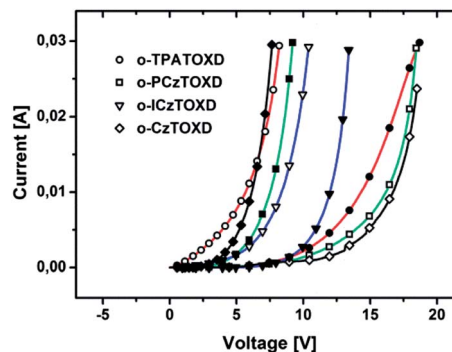


Fig. 5 Current–voltage (I – V) curves of hole- (hollow symbols) and electron-only (full symbols) devices.

(8 nm)/host (80 nm)/MoO₃ (8 nm)/Al) and electron-only devices (EODs; structure: Al/Li₂CO₃ (1 nm)/Be:Li₂CO₃ (30 nm)/host (80 nm)/Be:Li₂CO₃ (30 nm)/Li₂CO₃ (1 nm)/Al) were fabricated. It is noted that the HOMO levels of ***o*-CzTOXD**, ***o*-PCzTOXD** and ***o*-ICzTOXD** are nearly 0.4 eV lower compared to those of ***o*-TPATOXD**. This fact may hamper hole injection into the HODs; however, this displays the actual situation in the PHOLED devices. Current–voltage curves are shown in Fig. 5.

***o*-TPATOXD** exhibits good hole transport properties due to the presence of the triphenylamine moiety; significantly lower current density was observed in the EOD. In contrast carbazole based ***o*-CzTOXD** and ***o*-PCzTOXD** feature better electron

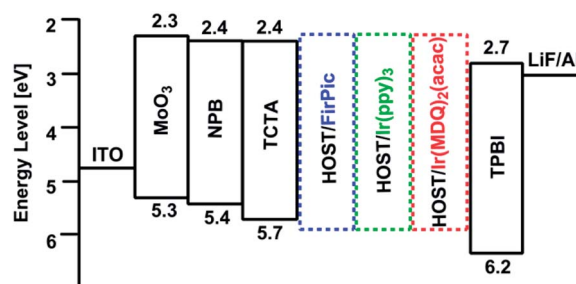


Fig. 6 Schematic energy level diagram of the device architecture employed in this work.

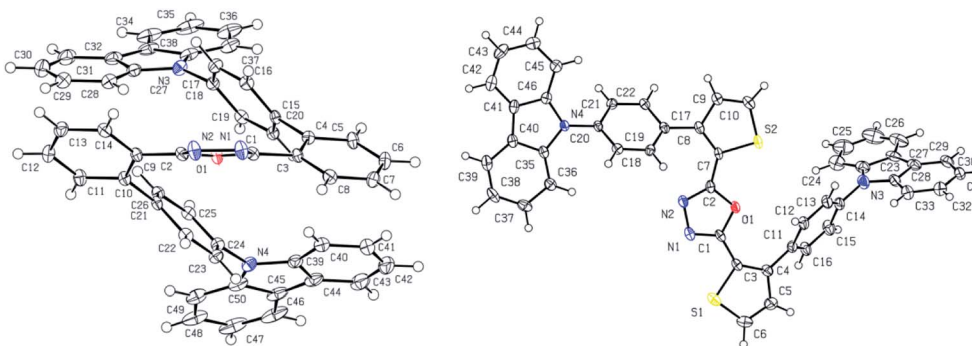


Fig. 4 Molecular structures of ***o*-PCzPOXD** (left) and ***o*-PCzTOXD** (right) – C, N, O and S atoms are represented by white, blue, red and yellow ellipsoids drawn at 50% probability levels, and H atoms by spheres of arbitrary radius. For ***o*-PCzTOXD** only one out of two unique molecules is shown.

transport properties. While *o*-PCzTOXD exhibits similarly low hole current density compared to *o*-CzTOXD, the current density in the EOD applying *o*-PCzTOXD is lower and therefore charge transport in *o*-PCzTOXD is more balanced than that in *o*-CzTOXD. For *o*-ICzTOXD the HOD shows higher current density than the EOD. Furthermore, carrier properties in *o*-ICzTOXD are more balanced compared to the other host materials. Thus, the incorporation of the indolocarbazole moiety resulted in the most bipolar character of *o*-ICzTOXD among this series of materials. The same trends were found for the POXD series with the exception of the EOD of *o*-ICzPOXD featuring hardly any electron transport. This finding can be explained by the

significantly altered orbital distribution of *o*-ICzPOXD as discussed in the theoretical part.

Electroluminescent properties

To evaluate the applicability of the POXD series as universal host materials for RGB PHOLED devices with a standard architecture of ITO/MoO₃ (8 nm)/NPB (50 nm)/TCTA (5 nm)/EML (10 nm)/TPBI (25 nm)/LiF (1 nm)/Al, in which the EMLs consist of coevaporated hosts *o*-TPAPOXD (I), *o*-PCzPOXD (II) or *o*-ICzPOXD (III) and guests Ir(MDQ)₂(acac) (R), Ir(ppy)₃ (G) or FIrPic (B), were fabricated. NPB is used as a hole transporting

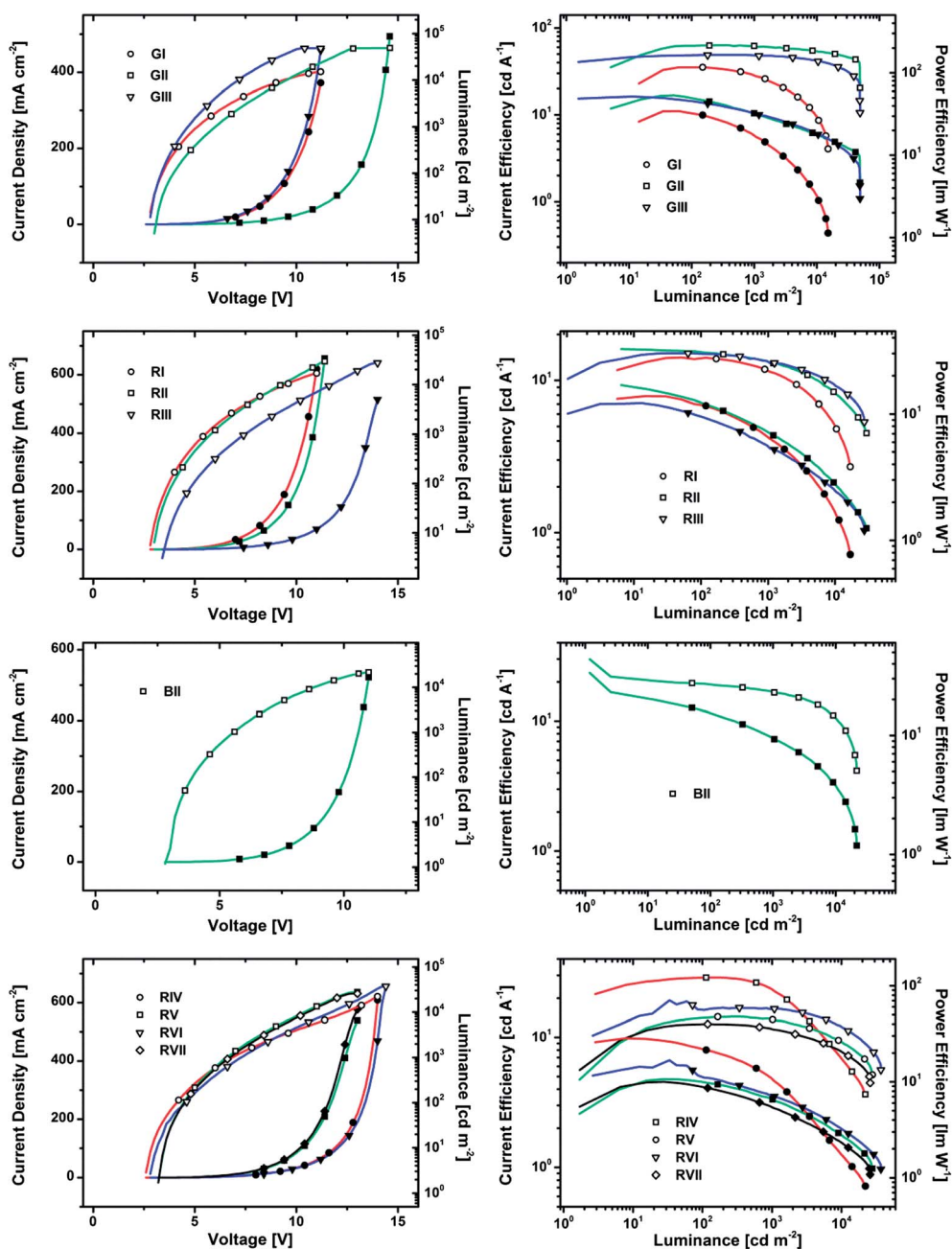


Fig. 7 Current density–voltage–luminance (full symbols: current density; hollow symbols: luminance) and current efficiency–luminance–power efficiency (full symbols: power efficiency; hollow symbols: current efficiency) curves of all devices investigated in this work.

layer while TPBI is applied as an electron transporting and hole blocking layer due to its low lying HOMO level.^{47–50} Additionally a thin TCTA layer is inserted between the hole transporting and emitting layers in order to confine triplet excitons more effectively in the EML as a result of a larger triplet energy of TCTA compared to that of NPB.⁴⁸ The standard device architecture including HOMO and LUMO levels of all employed materials is depicted in Fig. 6.

Current density–voltage–luminance and current efficiency–luminance–power efficiency curves for all devices are depicted in Fig. 7 and the electroluminescent properties of all fabricated PHOLED devices are summarized in Table 3. Among green devices the best efficiency was achieved for device GII (host material: **o-PCzPOXD**), giving a maximum current efficiency (CE) of 62.9 cd A⁻¹, a maximum power efficiency (PE) of 53.5 lm W⁻¹ and a maximum external quantum efficiency (EQE) of 17.1%, while lower values were obtained for GI and GIII with CE_{max} of 35.1 cd A⁻¹ and 48.8 cd A⁻¹, PE_{max} of 34.4 lm W⁻¹ and 51.6 lm W⁻¹ and EQE_{max} of 10.3% and 13.8%, respectively. We emphasize that significantly higher efficiencies were obtained by applying **o-PCzPOXD** and **o-ICzPOXD** in our standard device configuration compared to **o-TPAPOXD**. In fact, using **o-TPAPOXD** Tao *et al.*¹⁷ reported highly efficient green PHOLED devices reaching an EQE_{max} of 22.0% (vs. EQE_{max} of 10.3%) after optimization of the device architecture, thus revealing the potential of the newly developed materials within this paper. Notably, at an illumination relevant brightness of 1000 cd m⁻² devices GII and GIII retained high CE of 61.2 cd A⁻¹ and 48.1 cd A⁻¹. These values correspond to remarkably low efficiency roll-offs of 2.7 and 1.5%. Even at a brightness of 5000 cd m⁻² GII showed a CE of 56.8 cd A⁻¹ (9.7% roll-off), while GIII displayed a CE of 44.8 cd A⁻¹ (8.2% roll-off). In contrast a significantly higher overall efficiency roll-off of 55.3% for device GI, featuring CE of 28.2 cd A⁻¹ and 15.7 cd A⁻¹ at brightness of 1000 cd m⁻² and 5000 cd m⁻², was observed. This efficiency roll-off is attributed to the dominant hole transport properties of **o-TPAPOXD**, due to the TPA donor unit (more balanced charge transport for the planarized donor structures; see the section Charge transport properties). The unbalanced charge transport properties lead to accumulation of holes at the interface of the emissive and TPBI layer and a narrow exciton recombination

zone. Since triplet–triplet annihilation (TTA) is strongly dependent on the triplet exciton concentration the thickness of the recombination zone is of crucial importance and a major factor for efficiency roll-off in PHOLED devices at high current densities.⁵¹ Thus, the incorporation of planarized arylamine donors significantly decreases the efficiency roll-off as a result of more balanced charge transport properties resulting in broader recombination zones.

Red devices RI, RII and RIII showed similar performance exhibiting CE_{max} of 14.0 cd A⁻¹, 16.1 cd A⁻¹ and 15.0 cd A⁻¹, PE_{max} of 13.7 lm W⁻¹, 16.8 lm W⁻¹ and 12.2 lm W⁻¹ and EQE_{max} of 8.3%, 11.2% and 10.1%. In analogy to the green devices lower efficiency roll-off was observed for devices RII and RIII (incorporating planarized host materials) compared to RI.

Furthermore, blue device BII, utilizing **o-PCzPOXD** as the host, was fabricated displaying a CE_{max} of 29.8 cd A⁻¹, a PE_{max} of 33.5 lm W⁻¹ and an EQE_{max} of 13.4%. Thus, it was demonstrated that **o-PCzPOXD** is applicable as a universal host material in efficient red, green and blue PHOLED devices. However, low device performance has been observed for blue devices applying **o-ICzPOXD**. For these devices also the recorded emission could not be assigned to the FIrPic emitter only. Systematic investigation is necessary to understand these findings.

As a result of the lower triplet energies of the TOXD materials compared to those of the POXD series, **o-TPATOXD** (IV), **o-PCzTOXD** (V), **o-ICzTOXD** (VI) and **o-CzTOXD** (VII) were examined in red (R) devices only. Identical device architecture as for the POXD series was applied. Among this series of devices RIV exhibited the highest CE_{max} of 28.8 cd A⁻¹, PE_{max} of 28.4 lm W⁻¹ and EQE_{max} of 16.9%, while RV, RVI, and RVII displayed CE_{max} of 14.4, 19.2 and 12.6 cd A⁻¹, PE_{max} of 10.6, 16.7 and 10.0 lm W⁻¹ and EQE_{max} of 11.2%, 13.2% and 9.4%, respectively, displaying similar device performance as the corresponding POXD compounds. The same tendency for decreased efficiency roll-off observed for the POXD series was found for devices RIV–VII. While the CE of device RIV drops to 10.5 cd A⁻¹ at a brightness of 5000 cd m⁻², corresponding to an efficiency roll-off of 64%, current efficiencies for devices RV, RVI and RVII (incorporating planarized donors) decreased only by 24% to 27%.

Table 3 Electroluminescent properties of devices GI–III, BII and RI–VII

	V _{on} [V]	L _{max} [cd m ⁻²]	CE ^a [cd A ⁻¹]	PE ^a [lm W ⁻¹]	EQE ^a [%]
GI	2.8	15 049	35.0/28.2/15.7/35.1	32.3/17.1/6.3/34.4	10.3/8.1/4.7/10.3
GII	3.0	49 386	62.3/61.2/56.8/62.9	48.9/31.1/21.5/53.5	17.0/16.4/15.5/17.1
GIII	2.6	48 768	48.4/48.1/44.8/48.8	44.9/32.1/22.4/51.6	13.7/13.6/12.7/13.8
BII	2.8	21 710	18.9/16.7/13.4/29.8	15.3/9.4/5.6/33.5	8.5/7.5/6.1/13.4
RI	2.8	16 838	13.9/11.5/7.4/14.0	11.7/6.4/2.9/13.7	8.2/6.6/4.1/8.3
RII	3.0	29 615	15.3/13.2/10.1/16.1	12.4/7.2/4.0/16.8	10.6/9.1/6.7/11.2
RIII	3.0	27 517	14.9/12.9/10.8/15.0	9.4/5.3/3.3/12.2	9.1/6.9/5.3/10.1
RIV	2.6	22 160	28.7/22.6/10.5/28.8	21.4/10.1/3.0/28.4	16.8/13.2/6.0/16.9
RV	3.2	27 768	14.2/13.7/10.9/14.4	9.7/6.5/3.7/10.6	11.1/9.5/7.3/11.2
RVI	2.8	36 975	16.2/16.5/14.2/19.2	11.0/7.0/4.3/16.7	11.3/11.4/9.6/13.2
RVII	3.0	25 837	12.6/11.4/9.2/12.6	8.6/5.3/3.1/10.0	9.3/7.2/5.8/9.4

^a Measured at a brightness of 100 cd m⁻²/1000 cd m⁻²/5000 cd m⁻²/max.

Conclusion

In this study, the impact of planarizing TAA donors in bipolar host materials on the *ortho*-linkage effect was investigated in detail. Hence, oxadiazole based structures **5a–c** and **8a–d** have been designed, synthesized and examined regarding thermal, photo-physical and electro-chemical properties.

The straight-forward synthesis of target compounds relies on efficient cross-coupling and organolithium based procedures. In particular, the developed C–H activation protocol allows for a convenient and selective access to potential target scaffolds, clearly broadening the scope of accessible indolo[3,2,1-*jk*]-carbazole moieties.

For increasingly planarized TAA donor structures the following conclusions can be drawn: (i) improved morphological stability; (ii) elevated singlet and triplet energy values, which are attributed to an enhanced *ortho*-linkage effect and reduced donor strength of the planarized structures; and (iii) significantly reduced efficiency roll-off for all devices. Hence, the concept of planarization addresses major challenges in PHOLED research: improving both triplet energy and compound stability. In fact, triplet energies >2.60 eV enable the construction of efficient blue (FIrPic) PHOLEDs, which has not been reported for this specific substance class to date.

Improved PHOLED performance in standard device configurations compared to that of non-planarized reference compound **o**-TPAPOXD (EQE_{max} of 22.0% reported for optimized architecture)¹⁷ reveals the great potential of the developed compounds as highly efficient host materials.

Experimental section

General information

All reagents and solvents were purchased from commercial suppliers and used without further purification. Anhydrous solvents were prepared by filtration through drying columns; dry DMF was obtained from Acros. Column chromatography was performed on silica 60 (Merck, 40–63 μm). NMR spectra were recorded on a Bruker Avance DRX-400 spectrometer or a Bruker Avance 200 spectrometer. High resolution mass spectra (HRMS) were obtained from a Thermo Scientific LTQ Orbitrap XL hybrid FTMS (Fourier transform mass spectrometer) and Thermo Scientific MALDI LTQ Orbitrap interface; α -cyano-4-hydroxycinnamic acid was used as the matrix. Thermogravimetric (TG) and differential scanning calorimetry (DSC) measurements were carried out at a heating rate of 5 K min⁻¹ in a flowing argon atmosphere (25 ml min⁻¹). For the TG measurements, a Netsch TG 209 F9 Tarsus system, working with open aluminium oxide crucibles, was used. For the DSC measurements, a Netsch DSC 200 F3 Maia, working with aluminium pans with pierced lids, was employed. UV/VIS absorption and fluorescence emission spectra were recorded in DCM solutions (5 μM) with a Perkin Elmer Lambda 750 spectrometer and an Edinburgh FLS920, respectively. Time resolved experiments were performed using a Quantel Brilliant tripled Nd-YAG laser (355 nm, 20 Hz repetition rate, pulse width: ~5 ns). Spectra were measured using a SPEX

270 monochromator equipped with both photomultiplier and CCD. This set-up is controlled using a home-built Labview-based program which allows using different instruments such as photon counting devices, oscilloscopes, and additional mechanical shutters. For the measurement of the triplet emission, a mechanical shutter was triggered by the pulsed laser. A pretrigger period of 0.5 ms was followed by a 1 ms aperture and a rest time of 300–500 ms allowed obtaining the measurements shown in the ESI.† The slit of the monochromator was also opened further (up to 0.5 mm) to measure the triplet emission. Triplet energy (E_T) values were determined from the highest energy vibronic subband (first significant peak/shoulder) of the time-resolved low-temperature phosphorescence spectra. Cyclic voltammetry was performed using a three electrode configuration consisting of a Pt working electrode, a Pt counter electrode and an Ag/AgCl reference electrode and a PGSTAT128N, ADC164, DAC164, External, DI048 potentiostat provided by Metrohm Autolab B. V. Measurements were carried out in a 0.5 mM solution in anhydrous DCM (oxidation scan) and THF or DMF (reduction scan) with Bu₄NBF₄ (0.1 M) as the supporting electrolyte. The solutions were purged with nitrogen for 15 minutes prior to measurement. HOMO and LUMO energy levels were calculated from the onset of oxidation and reduction, respectively. The onset potential was determined by the intersection of two tangents drawn at the background and the rising of oxidation or reduction peaks.

Synthetic details

N,N-Diphenyl-4-(4,4,5,5-tetramethyl-1,3,2-dioxaborolan-2-yl)benzenamine (**3a**),^{18,19} 9-[4-(4,4,5,5-tetramethyl-1,3,2-dioxaborolan-2-yl)phenyl]-9*H*-carbazole (**3b**),^{19,20} 2,5-bis(5-bromo-2-thienyl)-1,3,4-oxadiazole (**4**),⁵² and 2,5-bis(2-bromophenyl)-1,3,4-oxadiazole (**6**)²⁷ were prepared according to published procedures.

9-(2-Chlorophenyl)-9*H*-carbazole (1ii). **1ii** was synthesized following procedures in the literature.²⁰ Carbazole (2.51 g, 15.0 mmol, 1.00 eq.), 1-bromo-2-chlorobenzene (3.45 g, 18.0 mmol, 1.20 eq.), K₂CO₃ (2.07 g, 15.0 mmol, 1.00 eq.) and CuSO₄·5H₂O (0.19 g, 0.75 mmol, 0.05 eq.) were added to a 250 ml three-necked round-bottomed flask. The mixture was heated with a heating jacket to 230 °C for 72 h. After cooling to r.t. H₂O (100 ml) was added and the mixture was extracted with toluene. The brown suspension was filtered and the remaining solvent removed *in vacuo*. Purification by crystallization from EtOH yielded **1ii** as a white solid (1.93 g, 6.9 mmol, 46%). ¹H NMR (400 MHz, CDCl₃): δ = 8.21 (d, J = 7.7 Hz, 2H), 7.73–7.71 (m, 1H), 7.56–7.44 (m, 5H), 7.35 (t, J = 7.5 Hz, 2H), 7.15 (d, J = 8.1 Hz, 2H) ppm. ¹³C NMR (100 MHz, CDCl₃): δ = 140.8 (s), 135.0 (s), 133.7 (s), 131.0 (d), 130.8 (d), 129.8 (d), 128.1 (d), 125.9 (d), 123.3 (s), 120.3 (d), 120.0 (d), 109.9 (d) ppm. Calculated: m/z : 277.07 [M]⁺. Found: MS (EI): m/z : 277.03 [M]⁺.

2,6-Dichloro-*N,N*-diphenylbenzenamine (1iii). Diphenylamine (1.02 g, 6.0 mmol, 1.00 eq.) was dissolved in dry DMF (18 ml). The solution was purged with argon, subsequently heated to 50 °C and NaH (0.43 g, 18.0 mmol, 3.00 eq.) was added quickly. The suspension was stirred for 5 min at 50 °C before 1,3-dichloro-2-fluorobenzene (1.49, 9.0 mmol, 1.50 eq.) was

added. Due to incomplete conversion (TLC) after stirring overnight additional NaH (0.14 g, 6.0 mmol 1.00 eq.) was added. After full conversion (TLC – 24 h) the reaction mixture was poured on H₂O, extracted with DCM repeatedly and the combined organic layers were dried over Na₂SO₄ and concentrated under reduced pressure. Column chromatography (PE) yielded **1iii** (0.79 g, 2.5 mmol, 42%) as a white solid. ¹H NMR (400 MHz, CD₂Cl₂): δ = 7.46 (d, *J* = 8.1 Hz, 2H), 7.29–7.22 (m, 5H), 6.99–7.96 (m, 6H) ppm. ¹³C NMR (100 MHz, CD₂Cl₂): δ = 145.7 (s), 140.7 (s), 137.6 (s), 130.2 (d), 129.6 (d), 129.3 (d), 122.6 (d), 121.0 (d) ppm. Calculated: *m/z*: 313.04 [M]⁺. Found: MS (EI): *m/z*: 313.01 [M]⁺.

Indolo[3,2,1-*jk*]carbazole (2). **1i/1ii/1iii** (1.0 eq.), (NHC)Pd(allyl)Cl^{24,25} (2 mol%) and K₂CO₃ (2.00 eq.) were dissolved in degassed *N,N*-dimethylacetamide (DMA, 0.2 M) under an argon atmosphere and heated to 130 °C until complete conversion (GCMS). The reaction mixture was poured on water and extracted with Et₂O. The combined organic layers were dried over anhydrous Na₂SO₄ and the solvent was removed under reduced pressure. Purification was accomplished by column chromatography (PE). Starting from **1i** (9.66 g, 30.0 mmol), (NHC)Pd(allyl)Cl (0.34 g, 0.60 mmol) and K₂CO₃ (8.29 g, 60.0 mmol) **2** was obtained as a white powder (6.78 g, 28.1 mmol, 94%). Starting from **1ii** (3.70 g, 13.3 mmol), (NHC)Pd(allyl)Cl (0.15 g, 0.27 mmol) and K₂CO₃ (3.67 g, 26.6 mmol) **2** was obtained as a white powder (3.02 g, 12.5 mmol, 94%). Starting from **1iii** (0.47 g, 1.5 mmol), (NHC)Pd(allyl)Cl (0.02 g, 0.03 mmol) and K₂CO₃ (0.43 g, 3.1 mmol) **2** was obtained as a white powder (0.29 g, 1.2 mmol, 80%). ¹H NMR (400 MHz, CD₂Cl₂): δ = 8.16 (d, *J* = 7.8 Hz, 2H), 8.06 (d, *J* = 7.4 Hz, 2H), 7.92 (d, *J* = 8.1 Hz, 2H), 7.62–7.55 (m, 3H), 7.38 (t, *J* = 7.7 Hz, 2H) ppm. ¹³C NMR (100 MHz, CD₂Cl₂): δ = 144.2 (s), 139.2 (s), 130.5 (s), 127.3 (d), 123.6 (d), 123.4 (d), 122.3 (d), 119.9 (d), 118.9 (s), 112.7 (d) ppm. Calculated: *m/z*: 241.09 [M]⁺. Found: MS (EI): *m/z*: 241.11 [M]⁺.

2-Bromoindolo[3,2,1-*jk*]carbazole. **2** (14.26 g, 59.1 mmol, 1.0 eq.) was dissolved in AcOH–CHCl₃ = 1 : 1 (300 ml) and heated to 55 °C. NBS (10.51 g, 59.1 mmol, 1.0 eq.) was added in small portions over a period of 1 h to the grey suspension. Since GC-MS analysis indicated incomplete conversion, more NBS (1.05 g, 5.9 mmol, 0.10 eq.) was added. After complete conversion the reaction mixture was poured on an aqueous NaOH solution (1000 ml, 6 M, 2 eq.) and extracted with DCM. The organic layer was dried over Na₂SO₄ and the solvent was removed *in vacuo*. Crystallization from ACN yielded 2-bromoindolo[3,2,1-*jk*]carbazole as a beige powder (10.30 g, 32.2 mmol, 54%). Physical data are in accordance with the literature.²³

2-(4,4,5,5-Tetramethyl-1,3,2-dioxaborolan-2-yl)indolo[3,2,1-*jk*]carbazole (3c). The synthesis of **3c** was accomplished analogously to published procedures.^{19,23} To a solution of 2-bromoindolo[3,2,1-*jk*]carbazole (10.25 g, 32.0 mmol, 1.00 eq.) in anhydrous THF (100 ml) under an argon atmosphere *n*-BuLi (14.1 ml, 2.5 M in hexanes, 35.2 mmol, 1.10 eq.) was added dropwise at –78 °C. Subsequently the reaction mixture was stirred at –80 °C for 1 h before Pinbop® (7.14 g, 38.4 mmol, 1.20 eq.) was added and the reaction mixture was allowed to warm to

room temperature slowly. After stirring overnight the solvent was removed under reduced pressure and the residue was partitioned between aqueous HCl (1 N) and DCM. The aqueous phase was extracted with DCM, and the combined organic layers were dried over anhydrous Na₂SO₄ and concentrated *in vacuo*. **3c** (8.10 g, 22.1 mmol, 69%) was isolated as a white solid after crystallization from acetonitrile. ¹H NMR (400 MHz, CDCl₃): δ = 8.58 (s, 2H), 8.14 (d, *J* = 7.7 Hz, 2H), 7.90 (d, *J* = 8.0 Hz, 2H), 7.56 (dd, *J* = 8.0, 7.6 Hz, 2H), 7.37 (dd, *J* = 7.7, 7.6 Hz, 2H), 1.46 (s, 12H) ppm. ¹³C NMR (100 MHz, CDCl₃): δ = 145.9 (s), 138.9 (s), 130.0 (s), 126.7 (d), 126.3 (d), 123.2 (d), 122.0 (d), 118.2 (s), 112.2 (d), 83.8 (s), 25.0 (s) ppm (C–B not detected). Calculated: *m/z*: 367.17381 [M]⁺, 368.18164 [M + H]⁺. Found: MS (MALDI): *m/z*: 367.17526 [M]⁺, 368.17856 [M + H]⁺.

General procedure for the Suzuki cross-coupling towards 5a–c. The reactions towards **5a–c** were performed under an argon atmosphere. **4** (1.00 eq.) and boronic acid ester **3a–c** (2.50 eq.) were dissolved in degassed THF (~0.5 M). Subsequently degassed 2 M aqueous K₂CO₃ (5.00 eq.) and Pd(PPh₃)₄ (5 mol%) were added. The reaction mixture was heated to reflux until full conversion of the dibromide (4–20 h, TLC). Afterwards the solution was poured on water and repeatedly extracted with DCM. The combined organic layers were dried over anhydrous Na₂SO₄ and concentrated under reduced pressure. The crude products were purified by column chromatography.

2',2''-(1,3,4-Oxadiazole-2,5-diyl)bis[*N,N*-diphenyl[1,1'-biphenyl]-4-amine] (5a). Starting from **4** (0.27 g, 0.70 mmol), **3a** (0.65 g, 1.75 mmol), 1.75 ml aqueous K₂CO₃ solution and Pd(PPh₃)₄ (40 mg, 35 μmol) **5a** (0.42 g, 0.59 mmol, 85%) was isolated after column chromatography (DCM) as a white solid. Physical data are in accordance with the literature.¹⁶

9,9'-(1,3,4-Oxadiazole-2,5-diyl)di(1,1'-biphenyl)-2',4-diylbis[9H-carbazole] (5b). Starting from **4** (0.19 g, 0.50 mmol), **3b** (0.46 g, 1.25 mmol), 1.25 ml aqueous K₂CO₃ solution (2.5 mmol) and Pd(PPh₃)₄ (29 mg, 25 μmol) **5b** (0.33 g, 93%) was isolated after column chromatography (DCM) as a white solid. ¹H NMR (400 MHz, CD₂Cl₂): δ = 8.14 (d, *J* = 7.7 Hz, 4H), 7.96 (d, *J* = 7.8 Hz, 2H), 7.69 (ddd, *J* = 7.6, 7.5, 1.1 Hz, 2H), 7.56–7.49 (m, 8H), 7.40–7.21 (m, 16H) ppm. ¹³C NMR (100 MHz, CD₂Cl₂): δ = 165.6 (s), 141.6 (s), 141.3 (s), 140.1 (s), 137.4 (s), 132.1 (d), 131.7 (d), 131.0 (d), 130.6 (d), 128.7 (d), 127.2 (d), 126.6 (d), 123.9 (s), 123.3 (s), 120.8 (d), 120.5 (d), 110.1 (d) ppm. Calculated: *m/z*: 704.25706 [M]⁺, 705.26489 [M + H]⁺, 727.24683 [M + Na]⁺. Found: MS (MALDI): *m/z*: 704.25807 [M]⁺, 705.26586 [M + H]⁺, 727.24966 [M + Na]⁺.

2,2'-(1,3,4-Oxadiazole-2,5-diyl)di-2,1-phenylene)bis[indolo[3,2,1-*jk*]carbazole] (5c). Starting from **4** (0.76 g, 2.0 mmol), **3c** (1.84 g, 5.0 mmol), 5 ml aqueous K₂CO₃ solution (10 mmol) and Pd(PPh₃)₄ (0.12 g, 0.1 mmol) **5c** (0.55 g, 0.8 mmol, 39%) was isolated after column chromatography (DCM) as a white solid. ¹H NMR (400 MHz, CD₂Cl₂): δ = 8.09 (d, *J* = 7.8 Hz, 4H), 7.98 (d, *J* = 8.1 Hz, 4H), 7.91 (s, 4H), 7.61 (dd, *J* = 7.7, 7.7 Hz, 4H), 7.50–7.30 (m, 10H), 7.01 (dd, *J* = 7.7, 7.7 Hz, 2H) ppm. ¹³C NMR (100 MHz, CD₂Cl₂): δ = 165.0 (s), 144.0 (s), 143.9 (s), 139.7 (s), 136.8 (s), 132.6 (d), 131.3 (d), 130.4 (s), 129.8 (d), 127.7 (d), 127.6 (d), 123.8 (d), 123.7 (s), 122.4 (d), 121.2 (d), 118.5 (s), 112.9 (d) ppm. Calculated: *m/z*: 700.22576 [M]⁺, 701.23359 [M + H]⁺, 723.21553

$[M + Na]^+$. Found: MS (MALDI): m/z : 700.22461 $[M]^+$, 701.23624 $[M + H]^+$, 723.21879 $[M + Na]^+$.

General procedure for double-sided halogen dance reactions. A protocol described in the literature⁵³ was adopted for the double-sided halogen dance reaction. Freshly prepared LDA was used. To a solution of diisopropylamine (2.40 eq.) in anhydrous THF (0.75 M), *n*-BuLi (2.40 eq., 2.5 M in hexanes) was slowly added at 0–5 °C and the solution was stirred for 30 min. Subsequently, the LDA solution was added dropwise to dibromide **6** (1.00 eq.) dissolved in anhydrous THF (25 mM) at –25 °C *via* a syringe. The temperature was maintained at –25 °C for 30 min before the reaction was quenched with an electrophile and warmed to room temperature. For work up the THF was removed under reduced pressure, the remaining oil was dissolved in DCM and washed with water. The aqueous phase was extracted with DCM, the combined organic layers were dried over anhydrous Na₂SO₄ and the solvent was removed *in vacuo*. Purification was accomplished by column chromatography.

2,5-Bis(3-bromo-2-thienyl)-1,3,4-oxadiazole (7i). Starting from DIPA (0.18 g, 1.8 mmol), *n*-BuLi (0.72 ml, 1.8 mmol), **6** (0.29 g, 0.75 mmol) and MeOH (0.25 ml) **7i** (0.16 g, 0.40 mmol, 53%) was yielded after column chromatography (light petrol : Et₂O = 60 : 40) as a white solid. ¹H NMR (400 MHz, CDCl₃): δ = 7.52 (d, *J* = 5.3 Hz, 2H), 7.16 (d, *J* = 5.3 Hz, 2H) ppm. ¹³C NMR (100 MHz, CDCl₃): δ = 159.2 (s), 132.8 (d), 130.2 (d), 120.9 (s), 114.0 (s) ppm. Calculated: m/z : 390.82046 $[M + H]^+$, 412.80240 $[M + Na]^+$. Found: MS (MALDI): m/z : 390.82188 $[M + H]^+$, 412.80376 $[M + Na]^+$.

2,5-Bis(3-bromo-5-trimethylsilyl-2-thienyl)-1,3,4-oxadiazole (7ii). Starting from DIPA (0.18 g, 1.80 mmol), *n*-BuLi (0.72 ml, 1.80 mmol), **6** (0.29 g, 0.75 mmol) and TMSBr (0.35 g, 2.25 mmol, 3.00 eq.) **7ii** (0.17 mg, 0.31 mmol, 42%) was yielded after column chromatography (light petrol : Et₂O = 95 : 5) as a colorless oil that solidified after an extended period of time at –30 °C. ¹H NMR (400 MHz, CDCl₃): δ = 7.22 (s, 2H), 0.37 (s, 18H) ppm. ¹³C NMR (100 MHz, CDCl₃): δ = 159.2 (s), 147.0 (s), 138.6 (d), 125.0 (s), 114.6 (s), –0.5 (q) ppm. Calculated: m/z : 534.89951 $[M + H]^+$, 556.88145 $[M + Na]^+$. Found: MS (MALDI): m/z : 534.90132 $[M + H]^+$, 556.88296 $[M + Na]^+$.

General procedure for the Suzuki cross-coupling reaction of 7i and boronic acid esters 3a–c. Target compounds **8a–c** were synthesized by a Suzuki cross-coupling procedure according to a published protocol.²⁴ Dibromide **7i** (1.00 eq.), boronic acid esters **3a–c** (3.00 eq.), KO^tBu (3.00 eq.) and (NHC)Pd(allyl)Cl^{24,25} (2 mol%) were suspended in ¹PrOH–H₂O (3/1, 5 mM) under an argon atmosphere. The mixture was heated to reflux until full conversion (4–20 h, TLC), poured on H₂O and repeatedly extracted with DCM. The combined organic layers were dried over anhydrous Na₂SO₄ and the solvent removed *in vacuo*.

4,4'-(1,3,4-Oxadiazole-2,5-diyl)-2,3-thiophenediyl]bis[*N,N*-diphenylbenzenamine] (8a). Starting from **7i** (1.76 g, 4.5 mmol), **3a** (5.01 g, 13.5 mmol), KO^tBu (1.51 g, 13.5 mmol) and (NHC)Pd(allyl)Cl (51 mg, 90 μmol) **8a** (1.97 g, 2.7 mmol, 61%) was isolated after column chromatography (light petrol : DCM = 35 : 65 → 0 : 100) as a yellow solid. ¹H NMR (400 MHz, CD₂Cl₂): δ = 7.56 (d, *J* = 5.1 Hz, 2H), 7.31–7.24 (m, 12H), 7.19 (d, *J* = 5.1 Hz, 2H), 7.12–7.03 (m, 12H), 6.98 (d, *J* = 8.5 Hz, 4H) ppm. ¹³C NMR

(100 MHz, CD₂Cl₂): δ = 160.9 (s), 148.4 (s), 148.0 (s), 145.4 (s), 131.8 (d), 130.6 (d), 129.9 (d), 129.6 (d), 128.8 (s), 125.4 (d), 123.9 (d), 122.9 (d), 118.9 (s) ppm. Calculated: m/z : 720.20120 $[M]^+$, 721.20903 $[M + H]^+$, 743.19097 $[M + Na]^+$. Found: MS (MALDI): m/z : 720.20177 $[M]^+$, 721.20580 $[M + H]^+$, 743.19167 $[M + Na]^+$.

9,9'-(1,3,4-Oxadiazole-2,5-diyl)bis(2,3-thiophenediyl-4,1-phenylene)]bis[9*H*-carbazole] (8b). Starting from **7i** (78 mg, 0.20 mmol), **3b** (222 mg, 0.60 mmol), KO^tBu (67 mg, 0.60 mmol) and (NHC)Pd(allyl)Cl (2.3 mg, 4 μmol) **8b** (78 mg, 0.11 mmol, 55%) was isolated after column chromatography (light petrol : DCM = 80 : 20) as a white solid. ¹H NMR (400 MHz, CD₂Cl₂): δ = 8.16 (d, *J* = 7.7 Hz, 4H), 7.74 (d, *J* = 8.4 Hz, 4H), 7.64–7.62 (m, 6H), 7.49 (d, *J* = 8.1 Hz, 4H), 7.40 (ddd, *J* = 8.2, 7.3, 1.2 Hz, 4H), 7.32–7.28 (m, 6H) ppm. ¹³C NMR (100 MHz, CD₂Cl₂): δ = 160.8 (s), 144.9 (s), 141.2 (s), 138.1 (s), 134.4 (s), 131.9 (d), 131.3 (d), 130.1 (d), 127.1 (d), 126.5 (d), 124.0 (s), 120.8 (d), 120.6 (d), 120.1 (s), 110.4 (d) ppm. Calculated: m/z : 716.16990 $[M]^+$, 717.17773 $[M + H]^+$, 739.15967 $[M + Na]^+$. Found: MS (MALDI): m/z : 716.17188 $[M]^+$, 717.17841 $[M + H]^+$, 739.16278 $[M + Na]^+$.

2,2'-(1,3,4-Oxadiazole-2,5-diyl)-2,3-thiophenediyl]bis[indolo-[3,2,1-*jk*]carbazole] (8c). Starting from **7i** (118 mg, 0.30 mmol), **3c** (330 mg, 0.90 mmol), KO^tBu (101 mg, 0.90 mmol) and (NHC)Pd(allyl)Cl (3.4 mg, 6 μmol) **8c** (158 mg, 0.22 mmol, 74%) was isolated after column chromatography (DCM) as a white solid. ¹H NMR (400 MHz, d₆-DMSO): δ = 8.03–8.00 (m, 8H), 7.93–7.87 (m, 6H), 7.57 (dd, *J* = 7.7, 7.7 Hz, 4H), 7.38–7.34 (m, 6H) ppm. ¹³C NMR (100 MHz, d₆-DMSO): δ = 159.9, 146.1, 142.5, 138.1, 132.5, 130.4, 129.2, 129.0, 127.1, 123.2, 121.9, 120.9, 117.8, 117.1, 112.7 ppm. Calculated: m/z : 712.13860 $[M]^+$, 713.14643 $[M + H]^+$, 735.12837 $[M + Na]^+$. Found: MS (MALDI): m/z : 712.13611 $[M]^+$, 713.14685 $[M + H]^+$, 735.129520 $[M + Na]^+$.

9,9'-(1,3,4-Oxadiazole-2,5-diyl)-2,3-thiophenediyl]bis[9*H*-carbazole] (8d). **7i** (2.16 g, 5.5 mmol, 1.0 eq.), carbazole (2.76 g, 16.5 mmol, 3.0 eq.), K₂CO₃ (2.28 g, 16.5 mmol, 3.0 eq.) and CuSO₄·5H₂O (88 mg, 0.35 mmol, 6.4 mol%) were mixed in a sealed reaction vial and heated to 230 °C. After cooling the reaction mixture was dissolved in CHCl₃, washed with water and the aqueous phase was extracted with CHCl₃. The combined organic layers were dried over anhydrous Na₂SO₄ and concentrated under reduced pressure. **8d** (0.81 g, 1.4 mmol, 26%) was isolated after column chromatography (light petrol : DCM = 85 : 15 → 78 : 22) as a white solid. ¹H NMR (400 MHz, CD₂Cl₂): δ = 8.13 (d, *J* = 7.7 Hz, 4H), 7.67 (d, *J* = 5.3 Hz, 2H), 7.36–7.23 (m, 10H), 7.04 (d, *J* = 7.9 Hz, 4H) ppm. ¹³C NMR (100 MHz, CD₂Cl₂): δ = 158.6 (s), 141.2 (s), 137.2 (s), 130.7 (d), 128.7 (d), 128.6 (d), 124.1 (s), 120.9 (d), 120.9 (d), 119.9 (s), 110.5 (d) ppm. Calculated: m/z : 564.10730 $[M]^+$, 565.11513 $[M + H]^+$, 587.09707 $[M + Na]^+$. Found: MS (MALDI): m/z : 564.10961 $[M]^+$, 565.11649 $[M + H]^+$, 587.09908 $[M + Na]^+$.

Computational details

All computations were performed using the Gaussian 09 package, revision A.02.⁵⁴ Density functional theory (DFT) and time-dependent (TD) DFT calculations were performed using the Becke three parameters hybrid functional with Lee–Yang–Perdew correlation (B3LYP),^{55,56} in combination with Pople

basis sets (6-31 G*, 6-311 + G*).⁵⁷ Geometry optimization was performed in the gas phase and without symmetry constraints. For the calculation of HOMO/LUMO levels, ground state (S_0) geometries were optimized applying the 6-311 + G* basis set. The determination of triplet energy (E_T) was achieved by the calculation of the T_1 excitation energy applying the TDDFT level and the 6-311 + G* basis to a S_0 geometry optimized at the DFT level using the 6-31 G* basis set.

Single crystal diffraction

Single crystals were obtained by recrystallization from hot solvents (**3c** – acetonitrile, **5b** – toluene, **8b** – toluene). Crystals of **3c**, **o-PCzPOXD (5b)** and **o-PCzTOXD (8b)** suitable for single-crystal diffraction were selected under a polarizing microscope, embedded in perfluorinated oil and attached to Kapton® micro-mounts. Intensity data were collected on a Bruker KAPPA APEX II diffractometer equipped with a CCD detector using MoK α radiation ($\lambda = 0.71072 \text{ \AA}$). Data were reduced with Saint-Plus⁵⁸ and an absorption correction was applied using the multi-scan approach implemented in SADABS.⁵⁸ All non-H atoms were located in the electron-density maps obtained by charge-flipping implemented in Superflip.⁵⁹ The structures were refined against F values using Jana2006.⁶⁰ H atoms were placed at computed positions and refined as riding on the parent C atoms. All non-H atoms were refined with anisotropic displacement parameters.

Device fabrication and measurement

The devices were fabricated on cleaned glass substrates pre-coated by 180 nm thick indium-tin-oxide (ITO) with a sheet resistance of 10 Ω per square. Prior to deposition, the surface of ITO was treated by oxygen plasma for 2 min, following a decrease in an ultrasonic solvent bath. All layers were deposited by thermal evaporation in a high vacuum system (pressure < 10⁻⁴ Pa) without breaking the vacuum. The device structures are described in the text. For the case of doping, the deposition rates of both host and guest were measured by a quartz crystal oscillator, and monitored by a frequency counter and calibrated by a Dektak 6M profiler (Veeco). The aluminum (Al) electrodes were deposited on the organic films through shadow masks. The overlap between ITO and Al electrode was 4 mm \times 4 mm as the active emissive area of the devices.

The current–voltage–brightness characteristics were measured by using a Keithley source measurement unit (Keithley 2400 and Keithley 2000) with a calibrated silicon photodiode. The electroluminescence (EL) spectra were measured by a Spectrascan PR650 spectrophotometer. All the measurements were carried out in ambient atmosphere at room temperature.

Acknowledgements

This work was supported in part by the Swiss National Science Foundation. The authors thank F.-A. Miannay and B. Lang (University of Geneva) for help with the picosecond lifetime measurements. The X-ray centre of the Vienna University of Technology is acknowledged for providing access to the

single-crystal diffractometer. G. Fafilek is acknowledged for support regarding the CV measurements, B. Holzer for collaboration during the synthetic experiments, K. Föttinger assisting the photo-physical analysis and J. Chen for fruitful discussions.

References

- 1 C. W. Tang and S. A. VanSlyke, *Appl. Phys. Lett.*, 1987, **51**, 913–915.
- 2 S. R. Forrest, *Nature*, 2004, **428**, 911–918.
- 3 Y. Sun, N. C. Giebink, H. Kanno, B. Ma, M. E. Thompson and S. R. Forrest, *Nature*, 2006, **440**, 908–912.
- 4 S. Reineke, F. Lindner, G. Schwartz, N. Seidler, K. Walzer, B. Luessem and K. Leo, *Nature*, 2009, **459**, 234–238.
- 5 M. C. Gather, A. Koehnen and K. Meerholz, *Adv. Mater.*, 2011, **23**, 233–248.
- 6 L. Xiao, Z. Chen, B. Qu, J. Luo, S. Kong, Q. Gong and J. Kido, *Adv. Mater.*, 2011, **23**, 926–952.
- 7 Y. Tao, C. Yang and J. Qin, *Chem. Soc. Rev.*, 2011, **40**, 2943–2970.
- 8 M. A. Baldo, D. F. O'Brien, Y. You, A. Shoustikov, S. Sibley, M. E. Thompson and S. R. Forrest, *Nature*, 1998, **395**, 151–154.
- 9 M. A. Baldo, S. Lamansky, P. E. Burrows, M. E. Thompson and S. R. Forrest, *Appl. Phys. Lett.*, 1999, **75**, 4–6.
- 10 P.-T. Chou and Y. Chi, *Chem. – Eur. J.*, 2007, **13**, 380–395.
- 11 Y. Chi and P.-T. Chou, *Chem. Soc. Rev.*, 2010, **39**, 638–655.
- 12 M. A. Baldo, D. F. O'Brien, M. E. Thompson and S. R. Forrest, *Phys. Rev. B: Condens. Matter Mater. Phys.*, 1999, **60**, 14422–14428.
- 13 C. Adachi, M. A. Baldo, M. E. Thompson and S. R. Forrest, *J. Appl. Phys.*, 2001, **90**, 5048–5051.
- 14 M. A. Baldo, C. Adachi and S. R. Forrest, *Phys. Rev. B: Condens. Matter Mater. Phys.*, 2000, **62**, 10967–10977.
- 15 Y. Tao, Q. Wang, C. Yang, Q. Wang, Z. Zhang, T. Zou, J. Qin and D. Ma, *Angew. Chem., Int. Ed.*, 2008, **47**, 8104–8107.
- 16 Y. Tao, Q. Wang, Y. Shang, C. Yang, L. Ao, J. Qin, D. Ma and Z. Shuai, *Chem. Commun.*, 2009, 77–79.
- 17 Y. Tao, Q. Wang, C. Yang, J. Qin and D. Ma, *ACS Appl. Mater. Interfaces*, 2010, **2**, 2813–2818.
- 18 H. B. Goodbrand and N.-X. Hu, *J. Org. Chem.*, 1999, **64**, 670–674.
- 19 R. Anemian, D. C. Cupertino, P. R. Mackie and S. G. Yeates, *Tetrahedron Lett.*, 2005, **46**, 6717–6721.
- 20 H. Xu, K. Yin and W. Huang, *Chem. – Eur. J.*, 2007, **13**, 10281–10293.
- 21 J. Lv, Q. Liu, J. Tang, F. Perdih and K. Kranjc, *Tetrahedron Lett.*, 2012, **53**, 5248–5252.
- 22 H. G. Dunlop and S. H. Tucker, *J. Chem. Soc.*, 1939, 1945–1956.
- 23 S. I. Wharton, J. B. Henry, H. McNab and A. R. Mount, *Chem. – Eur. J.*, 2009, **15**, 5482–5490.
- 24 N. Marion, O. Navarro, J. Mei, E. D. Stevens, N. M. Scott and S. P. Nolan, *J. Am. Chem. Soc.*, 2006, **128**, 4101–4111.
- 25 O. Navarro and S. P. Nolan, *Synthesis*, 2006, 366–367.

- 26 (**3c**): $C_{24}H_{22}BNO_2$, $M_r = 367.3$, trigonal, $R\bar{3}$, $a = b = 30.3853(6)$ Å, $c = 10.5350(2)$ Å, $V = 8423.5(3)$ Å³, $Z = 18$, $\mu = 0.081$ mm⁻¹, $T = 100$ K, 124 955 measured, 11 591 independent and 9475 observed [$I > 3\sigma(I)$] reflections, 253 parameters, wR (all data) = 0.060, $R[I > 3\sigma(I)] = 0.041$.†
- 27 X. Zheng, Z. Li, Y. Wang, W. Chen, Q. Huang, C. Liu and G. Song, *J. Fluorine Chem.*, 2003, **123**, 163–169.
- 28 S. Zrig, G. Koeckelberghs, T. Verbiest, B. Andrioletti, E. Rose, A. Persoons, I. Asselberghs and K. Clays, *J. Org. Chem.*, 2007, **72**, 5855–5858.
- 29 J. Froehlich, *Prog. Heterocycl. Chem.*, 1994, **6**, 1–35.
- 30 M. Schnuerch, M. Spina, A. F. Khan, M. D. Mihovilovic and P. Stanetty, *Chem. Soc. Rev.*, 2007, **36**, 1046–1057.
- 31 d. S. M. V. Nora, *Curr. Org. Chem.*, 2007, **11**, 637–646.
- 32 A. E. Lozano, M. L. Jimeno, J. de Abajo and J. G. de la Campa, *Macromolecules*, 1994, **27**, 7164–7170.
- 33 N. Miyaura, K. Yamada and A. Suzuki, *Tetrahedron Lett.*, 1979, 3437–3440.
- 34 N. Miyaura and A. Suzuki, *J. Chem. Soc., Chem. Commun.*, 1979, 866–867.
- 35 N. Miyaura and A. Suzuki, *Chem. Rev.*, 1995, **95**, 2457–2483; and references cited therein.
- 36 F. Ullmann, *Ber. Dtsch. Chem. Ges.*, 1903, **36**, 2382–2384.
- 37 F. Ullmann, *Ber. Dtsch. Chem. Ges.*, 1904, **37**, 853–854.
- 38 S. V. Ley and A. W. Thomas, *Angew. Chem., Int. Ed.*, 2003, **42**, 5400–5449; and references cited therein.
- 39 Z. Ge, T. Hayakawa, S. Ando, M. Ueda, T. Akiike, H. Miyamoto, T. Kajita and M.-a. Kakimoto, *Adv. Funct. Mater.*, 2008, **18**, 584–590.
- 40 Z. Ge, T. Hayakawa, S. Ando, M. Ueda, T. Akiike, H. Miyamoto, T. Kajita and M.-a. Kakimoto, *Org. Lett.*, 2008, **10**, 421–424.
- 41 Y. Tao, Q. Wang, C. Yang, C. Zhong, K. Zhang, J. Qin and D. Ma, *Adv. Funct. Mater.*, 2010, **20**, 304–311.
- 42 J. F. Ambrose and R. F. Nelson, *J. Electrochem. Soc.*, 1968, **115**, 1159–1164.
- 43 J. F. Ambrose, L. L. Carpenter and R. F. Nelson, *J. Electrochem. Soc.*, 1975, **122**, 876–894.
- 44 (**5b**): $C_{50}H_{32}N_4O$, $M_r = 704.8$, orthorhombic, $Pna2_1$, $a = 17.9874(4)$ Å, $b = 9.2989(8)$ Å, $c = 21.5822(9)$ Å, $V = 3609.9(4)$ Å³, $Z = 4$, $\mu = 0.078$ mm⁻¹, $T = 100$ K, 146 762 measured, 3589 independent and 10 547 observed [$I > 3\sigma(I)$] reflections, 496 parameters, wR (all data) = 0.044, $R[I > 3\sigma(I)] = 0.040$.†
- 45 (**8b**): $C_{46}H_{28}N_4OS_2$, $M_r = 716.9$, orthorhombic, $Pna2_1$, $a = 16.6992(7)$ Å, $b = 8.3716(3)$ Å, $c = 49.404(2)$ Å, $V = 6906.7(5)$ Å³, $Z = 8$, $\mu = 0.199$ mm⁻¹, $T = 100$ K, 124 623 measured, 15 888 independent and 12 302 observed [$I > 3\sigma(I)$] reflections, 955 parameters, wR (all data) = 0.036, $R[I > 3\sigma(I)] = 0.036$.†
- 46 B. Stoeger, P. Kautny, D. Lumpi, E. Zobetz and J. Froehlich, *Acta Crystallogr., Sect. B: Struct. Sci.*, 2012, **68**, 667–676.
- 47 M. Ikai, S. Tokito, Y. Sakamoto, T. Suzuki and Y. Taga, *Appl. Phys. Lett.*, 2001, **79**, 156–158.
- 48 D.-H. Lee, Y.-P. Liu, K.-H. Lee, H. Chae and S. M. Cho, *Org. Electron.*, 2010, **11**, 427–433.
- 49 M. E. Kondakova, T. D. Pawlik, R. H. Young, D. J. Giesen, D. Y. Kondakov, C. T. Brown, J. C. Deaton, J. R. Lenhard and K. P. Klubek, *J. Appl. Phys.*, 2008, **104**, 094501.
- 50 S. H. Kim, J. Jang, K. S. Yook, J. Y. Lee, M.-S. Gong, S. Ryu, G.-k. Chang and H. J. Chang, *J. Appl. Phys.*, 2008, **103**, 054502.
- 51 Q. Fu, J. Chen, H. Zhang, C. Shi and D. Ma, *Opt. Express*, 2013, **21**, 11078–11085.
- 52 L. G. Liu, Y. F. Xu, X. H. Qian and Q. C. Huang, *Chin. Chem. Lett.*, 2004, **15**, 7–10.
- 53 J. Froehlich, C. Hametner and W. Kalt, *Monatsh. Chem.*, 1996, **127**, 325–330.
- 54 M. J. Frisch, G. W. Trucks, H. B. Schlegel, G. E. Scuseria, M. A. Robb, J. R. Cheeseman, G. Scalmani, V. Barone, B. Mennucci, G. A. Petersson, H. Nakatsuji, M. Caricato, X. Li, H. P. Hratchian, A. F. Izmaylov, J. Bloino, G. Zheng, J. L. Sonnenberg, M. Hada, M. Ehara, K. Toyota, R. Fukuda, J. Hasegawa, M. Ishida, T. Nakajima, Y. Honda, O. Kitao, H. Nakai, T. Vreven, J. A. Montgomery, Jr, J. E. Peralta, F. Ogliaro, M. Bearpark, J. J. Heyd, E. Brothers, K. N. Kudin, V. N. Staroverov, R. Kobayashi, J. Normand, K. Raghavachari, A. Rendell, J. C. Burant, S. S. Iyengar, J. Tomasi, M. Cossi, N. Rega, N. J. Millam, M. Klene, J. E. Knox, J. B. Cross, V. Bakken, C. Adamo, J. Jaramillo, R. Gomperts, R. E. Stratmann, O. Yazyev, A. J. Austin, R. Cammi, C. Pomelli, J. W. Ochterski, R. L. Martin, K. Morokuma, V. G. Zakrzewski, G. A. Voth, P. Salvador, J. J. Dannenberg, S. Dapprich, A. D. Daniels, Oe. Farkas, J. B. Foresman, J. V. Ortiz, J. Cioslowski and D. J. Fox, *Gaussian 09, Revision A.2*, Gaussian, Inc., Wallingford, CT, 2009.
- 55 C. Lee, W. Yang and R. G. Parr, *Phys. Rev. B: Condens. Matter*, 1988, **37**, 785–789.
- 56 A. D. Becke, *J. Chem. Phys.*, 1993, **98**, 5648–5652.
- 57 R. Krishnan, J. S. Binkley, R. Seeger and J. A. Pople, *J. Chem. Phys.*, 1980, **72**, 650–654.
- 58 *Saint and SADABS*, Bruker Analytical X-ray Instruments, Inc., Madison, WI, USA, 2008.
- 59 L. Palatinus and G. Chapuis, *J. Appl. Crystallogr.*, 2007, **40**, 786–790.
- 60 V. Petříček, M. Dušek and L. Palatinus, *Jana2006: The crystallographic computing system*, Institute of Physics, Praha, Czech Republic, 2006.

2.2. Manuscript #2

Structure-property studies of *P*-triarylamine-substituted dithieno[3,2-*b*:2',3'-*d*]phospholes

Hannes Puntsher, Paul Kautny, Berthold Stöger, Antoine Tissot, Christian Hametner, Hans R. Hagemann, Johannes Fröhlich, Thomas Baumgartner, Daniel Lumpi

RSC Advances, **2015**, 5, 93797-93807

Reproduced with the kind permission of the Royal Society of Chemistry.

PAPER

Cite this: *RSC Adv.*, 2015, 5, 93797

Structure–property studies of *P*-triarylamine-substituted dithieno[3,2-*b*:2',3'-*d*]phospholes†

Hannes Puntscher,^{‡ab} Paul Kautny,^{‡a} Berthold Stöger,^c Antoine Tissot,^d Christian Hametner,^a Hans R. Hagemann,^d Johannes Fröhlich,^a Thomas Baumgartner^{*b} and Daniel Lumpi^{*a}

The synthesis of 10 novel *P*-substituted dithienophosphole oxide compounds applying phenylcarbazole and indolocarbazole donors is presented. Based on photo-physical and theoretical investigations, the study reveals that the pyramidal geometry of the phosphorus allows for the synthesis of charge transfer materials by introducing strong exocyclic donor groups but suppresses intramolecular charge transfer below a certain donor strength threshold, which is an appealing structural feature for the design of donor–acceptor materials. The triplet energies of the phenylcarbazole based compounds are in the range of 2.49–2.65 eV, sufficiently high for potential applications as host materials in PhOLEDs. By contrast, the introduction of indolocarbazole, the weakest employed donor, yields materials exhibiting a significantly higher triplet energy of up to 2.87 eV and a remarkably low singlet–triplet splitting (0.18 eV). In addition an interesting example of an intramolecular electronic through-space interaction has been observed for the *ortho*-linked phenylcarbazole derivative.

Received 12th July 2015
Accepted 26th October 2015

DOI: 10.1039/c5ra13651b

www.rsc.org/advances

1 Introduction

The development of functional π -conjugated organic materials for applications in organic electronics such as organic light emitting diodes (OLEDs),^{1–3} organic field effect transistors (OFETs),^{4–6} organic photovoltaics (OPVs)^{7,8} or sensors^{3,6} is a steadily evolving field of research due to the appealing possibility of tailoring the organic materials' intrinsic electronic properties by subtle modifications of their molecular framework.⁹ The incorporation of main group elements such as B,^{10–12} Si,^{13–15} Se,¹⁶ Te¹⁷ or P^{18–22} has proven to be a particularly valuable tool for designing materials featuring, *e.g.*, highly interesting optical properties, inaccessible through purely hydrocarbon-based compounds.

In this context, the dithieno[3,2-*b*:2',3'-*d*]phosphole scaffold (Fig. 1) has been thoroughly investigated as novel platform for functional materials in the last decade.²³ The electron lone pair

of the phosphorus atom within the phosphole structure has high *s*-character that hinders efficient interaction with the π -system.²³ Therefore, the aromaticity of phospholes is diminished compared to other five-membered heterocycles, such as pyrrole, thiophene or furan. Nevertheless, interactions between the σ^* -orbital of the exocyclic bond and the π^* -system of the ring lead to a certain degree of aromaticity and a high polarizability of the phosphole system.^{23,24} The resulting high tunability of the photo-physical and electro-chemical properties by chemical modification^{22,23,25} suggested the utility of this versatile building block for the fields of luminescent materials,^{26–31} polymers,^{32–34} coordination chemistry^{26,35} and self-organizing materials.^{36,37} In particular, oxidation of the phosphorus center is an appealing strategy to significantly enhance the electron-accepting properties of the dithieno[3,2-*b*:2',3'-*d*]phosphole moiety,^{21,24} which enables the application of this scaffold in donor–acceptor type materials.

Donor–acceptor materials are of specific interest for applications due to the possibility to selectively influence photo-physical and electro-chemical characteristics by intramolecular charge transfer (ICT)^{2,3,38–40} as well as bipolar charge transport properties in electronic devices.^{39,41} Thus, the

^aInstitute of Applied Synthetic Chemistry, Vienna University of Technology, Getreidemarkt 9/163, A-1060 Vienna, Austria. E-mail: daniel.lumpi@tuwien.ac.at

^bDepartment of Chemistry & Centre for Advanced Solar Materials, University of Calgary, 2500 University Dr. NW, Calgary, AB, T2N 1N4, Canada. E-mail: ttbaumga@ucalgary.ca

^cInstitute of Chemical Technologies and Analytics, Vienna University of Technology, Getreidemarkt 9/164, A-1060 Vienna, Austria

^dDépartement de Chimie Physique, Université de Genève, 30, quai E. Ansermet, 1211 Geneva 4, Switzerland

† Electronic supplementary information (ESI) available. CCDC 1407916. For ESI and crystallographic data in CIF or other electronic format see DOI: 10.1039/c5ra13651b

‡ Contributed equally to this work.

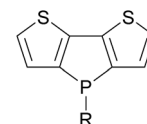


Fig. 1 Molecular scaffold of dithieno[3,2-*b*:2',3'-*d*]phosphole.

interaction of the molecular donor and acceptor subunits is of crucial importance. Phosphine oxide derivatives have been widely applied as functional materials in OLEDs.²¹ Particularly bipolar host materials for phosphorescent OLEDs (PhOLEDs) comprising phosphine oxide and carbazole^{42–44} or triphenylamine^{45,46} moieties were exhaustively investigated due to limited conjugation *via* the phosphine oxide as result of its tetrahedral geometry.²¹ Moreover, the coordination geometry of the phosphorus atom in the five-membered phosphole ring offers new opportunities to control electronic and photo-physical characteristics.^{22–24} Whereas direct substitution of the thiophene moieties allows for full conjugation with the main scaffold, the pyramidal structure of the PC₃ fragment prevents π -conjugation of the exocyclic substituent with the dithieno[3,2-*b*:2',3'-*d*] phosphole core.

Recently, the influence of exocyclic donor groups on the properties of dithieno[3,2-*b*:2',3'-*d*]phosphole based donor-acceptor materials has been investigated^{29–31} revealing efficient charge transfer from the donor to the dithieno[3,2-*b*:2',3'-*d*] phosphole oxide core.²⁹ Herein we report on the synthesis and characterization of a new series of dithieno[3,2-*b*:2',3'-*d*] phosphole oxides with phenylcarbazole or indolo[3,2,1-*jk*] carbazole substituents as exocyclic donor moieties; the experimental results have been correlated with DFT calculations. In order to further elucidate the influence of the donor-acceptor interaction on the photo-physical properties of the whole system, the influence of various substitution patterns, as well as planarization of the donor was investigated.

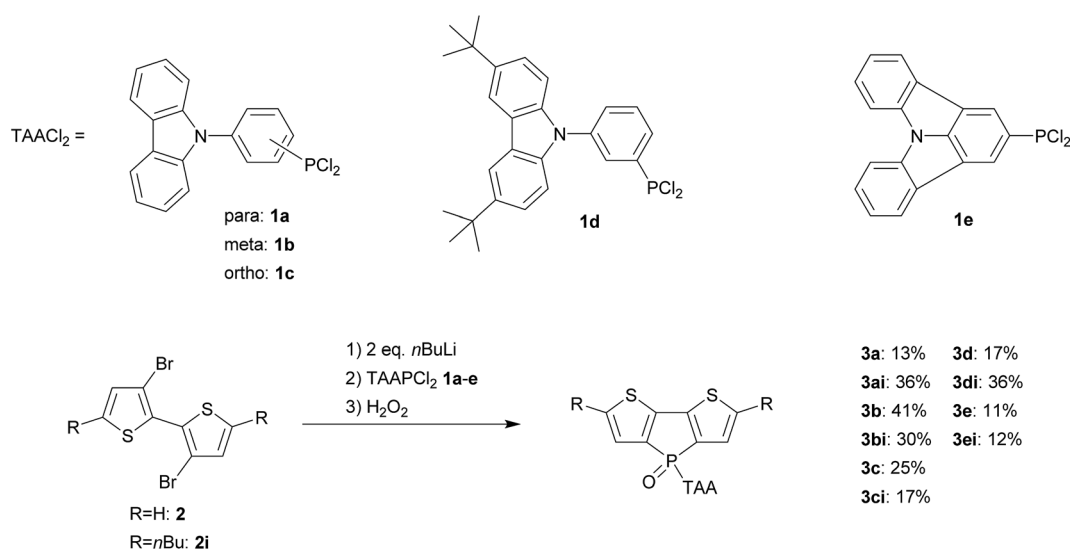
2 Results and discussion

2.1 Synthesis and characterization

Intrigued by the initial studies on systems with an exocyclic triphenyl amine substituent,²⁹ this work focuses on less electron-donating aryl amines such as phenylcarbazole (PCz; with *ortho*-, *meta*- and *para*-substitution pattern) and indolo

[3,2,1-*jk*]carbazole (ICz). Due to the increasing contribution of the nitrogen lone pair to the π -system of the pyrrole-like rings in the planarized triarylamine (TAA) subunits, the donor strength is reduced in the order triphenylamine > phenylcarbazole > indolocarbazole.⁴⁷ To circumvent possible insolubility issues as a result of the incorporation of increasingly planarized structural motives, the *n*-butyl substituted species **3ai–ei** were synthesized in addition to target molecules **3a–e** without alkyl substituents (Scheme 1). Furthermore, in the case of the *meta*-linked phenylcarbazole, *t*-butyl substituents were introduced at the 3- and 6-position of the carbazole unit in order to investigate the influence of these substituents on molecular properties, but to also enhance the electro-chemical stability of the latter.⁴⁸ Following established procedures, the synthesis of the dithienophospholes was accomplished by lithiation of the corresponding dibromobithiophenes **2** or **2i**, followed by conversion of the lithiated species with TAAPCl₂ **1a–e** at low temperature (Scheme 1). The TAAPCl₂ starting materials were prepared from the corresponding bromides (TAABr) *via* suitably adapted literature procedures²⁹ and were applied without further purification. For a streamlined synthetic process, the resulting trivalent phosphorus compounds were not isolated but directly oxidized by addition of excess H₂O₂ yielding target compounds **3a–3ei** in moderate to low yields after column chromatography.

The carbazole-based compounds **3a**, **3b** and **3d** exhibited ³¹P NMR chemical shifts at $\delta = 16.2$, 17.8 and 18.0 ppm, respectively, that are shifted somewhat upfield compared to the corresponding triphenyl amine-substituted dithienophosphole oxide (*cf.*: 19.1 ppm).²⁹ In contrast, indolocarbazole-substituted **3e** showed a slightly downfield-shifted ³¹P NMR resonance at $\delta = 22.2$ ppm that is, however, in line with related systems exhibiting exocyclic polyaromatic hydrocarbon (PAH) substituents.³⁰ By contrast, *ortho*-derivative **3c** featured a significantly upfield-shifted ³¹P NMR chemical shift at $\delta = 12.9$ ppm compared to its congeners **3a** and **3b**, indicating a distinctively different chemical environment of the phosphorus atom for



Scheme 1 Synthetic pathways towards carbazole and indolo[3,2,1-*jk*]carbazole functionalized dithienophosphole oxides **3a–3ei**.

this particular configuration. In all cases, the *n*-butyl substituents at the dithienophosphole core led to slightly (1–3 ppm) downfield-shifted resonances, which is in accordance with previous findings.²⁹ In addition, the successful formation of target compounds **3a–3ei** was also confirmed by ¹H and ¹³C NMR spectroscopy, as well as high-resolution mass spectroscopy (HRMS).

Moreover, single crystals of **3c** (ref. 49) suitable for X-ray crystallography were obtained from a CD₂Cl₂ solution upon slow evaporation of the solvent at room temperature (Fig. 2). Bond lengths and angles within the dithienophosphole oxide scaffold are in good accordance with previously reported *P*-phenyl substituted derivatives.^{29,30} Elongated double bonds and shortened single bonds indicate a high degree of conjugation of the planar scaffold (largest distance of 0.0457(10) Å from the least squares (L.S.) plane observed for the C6 atom). Notably, the carbazole unit deviates distinctly from planarity (distance of the C17 atom from the L.S. plane of 0.1211(10) Å). The most striking feature is the alignment of the dithienophosphole and the carbazole units (Fig. 2 (left)). Due to the *ortho*-linkage on the phenylene linker, the carbazole is forced in close vicinity to the dithienophosphole unit resulting in a parallel orientation (angle of L.S. planes of 8.26(2)°) of the two subunits. The shortest interatomic contact between both units is only 3.2424(12) Å (C4–C26) hinting toward strong intramolecular π–π interactions. In contrast, no such intermolecular interactions are observed with neighboring molecules (Fig. 2 (right)).

The particular spatial arrangement of the *ortho*-linked derivatives **3c** and **3ci** was verified in solution *via* NMR spectroscopy. Following a complete signal assignment (ESI[†]) using standard 2D methods, 1D and 2D NOESY spectra were recorded (ESI[†]). Significant NOE enhancement of the carbazole *ortho*-proton upon irradiation of both of the thiophene signals (and *vice versa*) clearly indicates close vicinity of the respective moieties in compound **3c**. A similar result was obtained for the same carbazole-H and the remaining thiophene proton for **3ci**. Thus, parallel alignment of carbazole and dithienophosphole

ring systems in the *ortho*-bridged molecules **3c** and **3ci** can be assumed in solution as well.

2.2 Photo-physical investigations

In order to investigate the photo-physical properties of the newly developed materials, UV/Vis absorption and photoluminescence spectra were recorded in dilute CH₂Cl₂ solutions; results are summarized in Table 1. The absorption spectra (Fig. 3 (top), ESI[†]) exhibit specific features of both chromophores – the dithienophosphole and carbazole moieties. Whereas the low wavelength region is dominated by well-resolved transitions at approximately 292, 326 and 338 nm, typical for phenylcarbazoles,⁵⁰ broad absorption bands, which can be attributed to the dithienophosphole unit,^{27,35,51} are observed at higher wavelengths (350–400 nm). Notably, peaks arising from the carbazole donors are insensitive to the presence/absence of the *n*-butyl groups at the dithienophosphole. In contrast, installation of the *t*-butyl groups at the 3- and 6-position leads to red-shifted carbazole absorption peaks for **3d** and **3di**. Related transitions are observed for the indolocarbazole-based materials **3e** and **3ei**. The absorption bands arising from the indolocarbazole unit are slightly blue-shifted compared to those of carbazole, which is in accordance with previously reported results.⁵² Similarly, the absorption of the dithienophosphole moieties are not influenced by the triaryl amines, with exception of **3c** and **3ci**, but the *n*-butyl substituents lead to a red-shift of the broad dithienophosphole peak. The optical bandgaps determined from the absorption onset of **3a/b/d/e** are located in a narrow range between 3.04 and 3.06 eV. The absorption onsets of *n*-butyl-substituted **3ai/3bi/3di/3ei** are shifted to energies between 2.85 and 2.87 eV likely due to the “+I” effect of the donating butyl substituent (*vide infra*). However, most striking is the observation that absorption onsets of *ortho*-derivatives **3c** and **3ci** are red-shifted by nearly 0.1 eV compared to their respective congeners. The same tendencies are found in emission spectra (Fig. 3 (bottom), ESI[†]). Whereas **3a/b/d/e** exhibit featureless emission maxima around

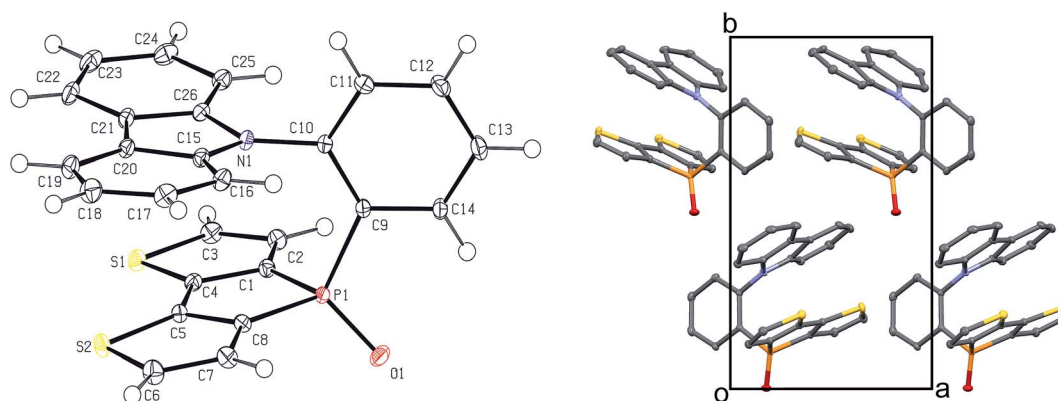


Fig. 2 Molecular structure of **3c** (left) in the solid state (50% probability level, H atoms are represented by white spheres of arbitrary radius); selected bond lengths [Å] and angles [°]: P1–C2: 1.8062(9); P1–C6: 1.7979(9); P1–C9: 1.8167(8); C1–C2: 1.4220(14); C1–C4: 1.3824(12); C2–C3: 1.3680(13); C4–C5: 1.4526(14); C5–C8: 1.3825(12); C6–C7: 1.3689(13); C7–C8: 1.4216(14); C2–P1–C6: 92.32(4); C2–P1–C9: 110.51(4); C6–P1–C9: 109.14(4); C2–P1–O1: 166.99(4); C6–P1–O1: 116.38(4); C9–P1–O1: 110.25(4); packing of **3c** (right) in the single crystal viewed along the *c*-axis (H atoms were omitted for clarity).

Table 1 Photo-physical properties of the synthesized materials

Compound	λ_{abs} [nm]	λ_{em} [nm]	E_{S}^a [eV]	E_{T}^b [eV]
3a	392/326/338/366(sh ^c)	454	3.04	2.65
3b	292/327/339/364	454.5	3.06	2.56
3c	293/323/337/374	471.5	2.96	2.53
3d	297/333/337/368(sh ^c)	456	3.04	2.57
3e	288/310/323/360	451.5	3.05	2.87
3ai	292/326/338/386	486.5	2.86	2.60
3bi	292/326/339/386	486.5	2.85	2.51
3ci	293/324/337/397	495.5	2.78	2.49
3di	297/333/346/386	487.5	2.85	2.51
3ei	286/308/323/367/ 389(sh ^c)	482	2.87	2.66

^a Estimated from the absorption onset. ^b Estimated from the highest energy vibronic transition in toluene at 77 K. ^c Shoulder.

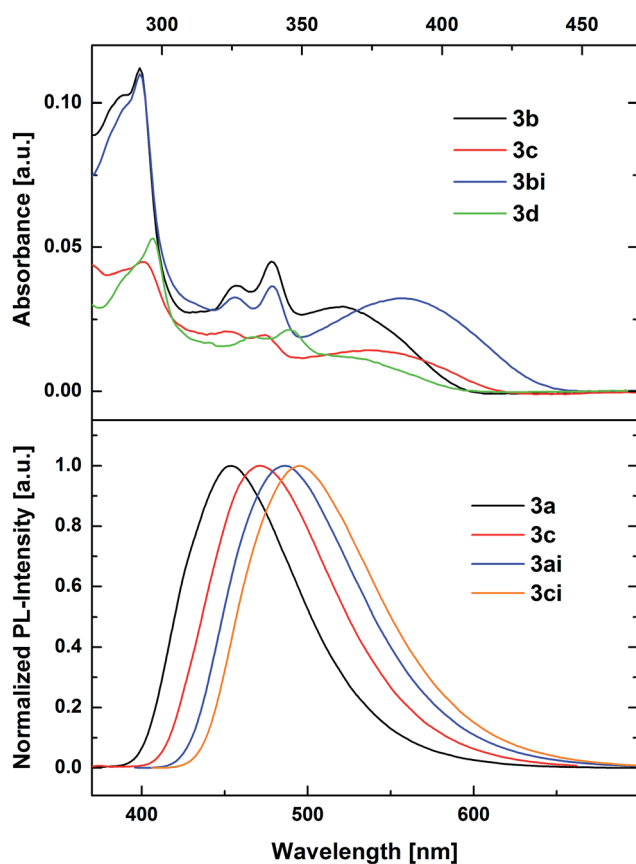


Fig. 3 Absorption spectra of **3b**, **3c**, **3d** and **3bi** (top) and normalized PL spectra of **3a**, **3c**, **3ai** and **3ci** (bottom). All spectra were recorded from 5 μM solution in DCM at r.t.

454 nm, the emission of the *n*-butyl substituted materials **3ai/bi/di/ei** is red-shifted by approximately 30 nm, due to the donor-effect if the alkyl groups (*vide infra*), while the emission maxima of **3c** and **3ci** are located at 471.5 and 495.5 nm, respectively. Remarkably, the emission of **3a/b/d/e** is identical to the purely phenyl-substituted dithienophosphole oxide (453 nm).³² Therefore, the addition of electron-rich aryl amines does not seem to influence the emission properties of the materials.

This is also supported by the DFT calculations that identify the dithienophosphole π^* -system as the LUMO for all species with largely comparable HOMO–LUMO energy gaps (*vide infra*). From these findings – as well as the fact that absorption and emission properties are independent of the kind of the adjacent subunit and linkage mode (with the exception of *ortho*-linkage) – we conclude that the electronic coupling of both chromophores is basically suppressed by linkage *via* the phosphorus atom. This finding is in disagreement with previous findings concerning triphenyl amine substituted dithienophosphole oxides that exhibit pronounced ICT,²⁹ but can be attributed to the fact that the donor-strength of the aryl amines applied in this study is significantly decreased compared to triphenyl amine.⁵² Therefore, the pyramidal nature of the phosphorus allows for the synthesis of charge transfer materials based on strong exocyclic donor groups but suppresses ICT below a certain donor strength threshold. This appealing structural feature for the design of donor–acceptor materials has also been confirmed *via* the DFT calculations (*vide infra*).

In contrast to the photo-physical properties of all other investigated materials in this study, those of the *ortho*-derivatives **3c** and **3ci** are distinctly different, indicating the presence of electronic interactions between the carbazole and dithienophosphole moieties. Due to the fact that these interactions are absent in *para*-linked **3a** and **3ai**, which exhibit the highest degree of conjugation between the two molecular subunits, electronic exchange *via* the phenylene linker can be ruled out. However, the close vicinity of the planar carbazole and dithienophosphole, which has been confirmed by NOE measurements, suggests through-space interaction of the aromatic groups that are also revealed by the theoretical calculations (*vide infra*).

Bipolar organic materials exhibiting limited ICT have received great attention in recent years due to potential applications as host materials for transition metal complexes in PhOLEDs.^{39,53} The incorporation of phosphorescent triplet emitters in electro-optical devices overcomes the limitation of purely fluorescent emitter and theoretically allows for 100% internal quantum efficiency.⁵⁴ These phosphorescent emitters have to be dispersed in an organic matrix for efficiency reasons. One major requirement of such host materials are high triplet energy (E_{T}) values in order to confine the excited states on the emitter. However, the combination of donor and acceptor subunits within one molecule lowers the E_{T} *via* ICT.^{39,53} Therefore, research focuses on the design and synthesis of donor–acceptor materials with decreased interaction between the molecular subunits. In this regard we investigated the E_{T} s of the developed materials. The E_{T} s were determined in frozen (solid) toluene solutions at 77 K from the highest vibronic transition of the delayed emission, and decrease in the order of *para* (**3a** = 2.65 eV/**3ai** = 2.60 eV) > *meta* (**3b** = 2.56 eV/**3bi** = 2.51 eV) > *ortho* (**3c** = 2.53 eV/**3ci** = 2.49 eV), respectively. These values are sufficiently high for applications as host materials in green and red PhOLEDs.³⁹ While the additional *t*-butyl substituents at the carbazoles in **3d** and **3di** do not influence the energy levels, all of the *n*-butyl-substituted compounds feature slightly decreased E_{T} s compared to the unsubstituted dithienophospholes.

However, the influence of the *n*-butyl substituents on the E_T s is lower compared to the corresponding optical bandgap E_S (Fig. 4). Notably, the ICz-substituted compound **3e** features a significantly higher E_T of 2.87 eV (Fig. 5), rendering the application in blue PhOLEDs possible. In contrast to all other materials **3e** exhibits vibronically well resolved phosphorescence (Fig. 5, ESI[†]), indicating a localized T_1 (3LE) state.⁵⁵ The transition from a charge transfer T_1 (3CT) state to a 3LE in case of **3e** can be explained by the weaker donor strength of the ICz moiety destabilizing the 3CT and thus might be the explanation for the significantly increased E_T of **3e**. In addition, the low singlet–triplet splitting of 0.18 eV makes this material particularly interesting. Recently, Adachi and coworkers introduced bipolar compounds with low singlet–triplet splitting as highly efficient electro-optical materials by means of thermally activated delayed fluorescence (TADF) due to thermal up-conversion of excited triplet states to singlet states.⁵⁶ Thus, the investigated approach of attaching exocyclic donors to dithienophosphole oxides *via* the pyramidal coordinated phosphorus may provide a new design concept for efficient TADF materials.

2.3 Theoretical calculations

In order to provide some deeper understanding of the experimentally determined photo-physics of the materials in this study, we have performed Density-Functional Theory (DFT) calculations at the B3LYP/6-31+G(d) level of theory using the Gaussian 09 suite of programs.⁵⁷ In order to save computing time, the butyl groups in the ‘i’ series of compounds were replaced with methyl substituents and the corresponding species are denominated as **3(a–e)i’**. The DFT data generally support the experimentally determined features, with most compounds showing similar photo-physics, and the *ortho*-carbazole substituted species being distinct from their congeners. As a common denominator, the LUMO orbitals of all investigated species comprise the π^* -system of the dithienophosphole scaffold, with the presence of the *n*-butyl groups being reflected in commonly increased energy levels by approximately 0.15 eV compared to their H-substituted relatives

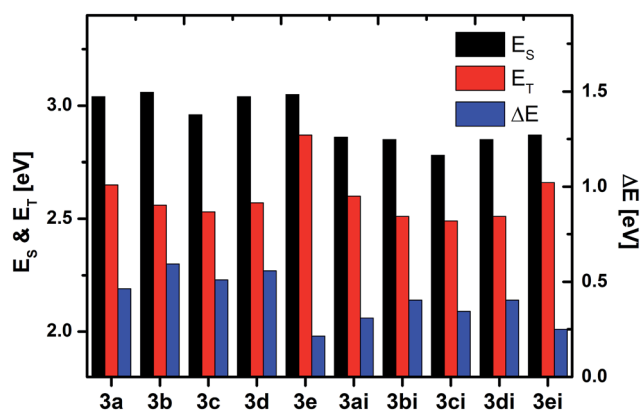


Fig. 4 Singlet energies (E_S), triplet energies (E_T) and singlet–triplet splitting of all synthesized materials.

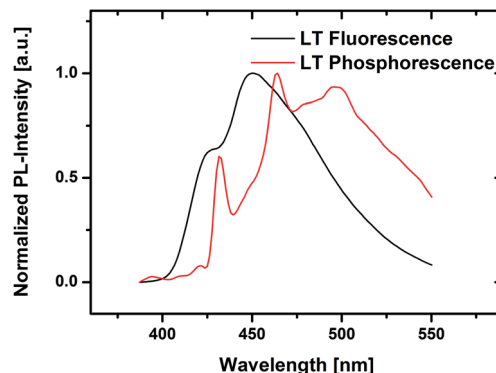


Fig. 5 Low temperature fluorescence and phosphorescence spectra of **3e** recorded at 77 K.

(Table 2). Another common denominator is the fact that the HOMO, HOMO–1 and HOMO–2 levels of all compounds are fairly close in energy for each compound ($\Delta E \sim 0.4$ eV) and consequently relevant for the observed experimental photo-physics. These orbitals respectively represent – to varying extents – the π -systems of the dithienophosphole and the triaryl amine scaffolds, as well as the π -bridge between the units in **3a,b,d,e** and **3(a,b,d,e)i’** (ESI[†]). It should also be mentioned in this context that the HOMO for **3a,b,d** and **3(a,b,d)i’** represents the π -system of the carbazole substituents with largely comparable energy levels ($E_{HOMO} \sim -5.7$ eV), a feature that has been confirmed by cyclic voltammetric (CV) measurements (Table 2).

Notably, the presence of the butyl substituents in the 2- and 6-positions of the dithienophospholes raises the energy of this unit’s π -system, which leads to a switch in the orbital order with the π -system of the corresponding carbazole unit. The calculations suggest that the raised level of the dithienophosphole π -system in the *para*- and *meta*-carbazole species (HOMO–1, instead of HOMO–2 in **3a,b,d**), in combination with the lowered LUMO levels is responsible for the red-shifted photo-physics of the ‘i’-series of compounds. This also indicates a reduced electronic communication between the two sub-chromophores. The effect of the *t*-butyl substituents in **3d** and **3di’** is reflected in the increased energies of the respective HOMO levels at $E_{HOMO} \sim -5.5$ eV (CV: **3d**: -5.54 eV; **3di**: -5.53 eV).

In the case of **3e** and **3ei’**, the observed slight blue shift is the result of increased LUMO levels, compared to those of **3a,b,d(i’)**. However, the donor-effect of the methyl substituent is evident in the respective HOMO levels (-5.92 eV for **3e** vs. -5.61 eV for **3ei’**). This particular electrochemical behavior has been confirmed by CV measurements. In contrast to all other pairs of molecules the aliphatic substituent at the dithienophosphole leads to an increase of the HOMO energy in case of **3ei** (-5.58 eV) compared to **3e** (-5.76 eV). Remarkably, the orbital sequence and electronic contributions to the frontier orbitals of the indolocarbazole-substituted species (particularly for **3ei**), approach those of the PAH-substituted species,³⁰ clearly reflecting the effect of the diminishing donor-strength of the exocyclic substituent. The DFT data for the latter suggest only

Table 2 Orbital energies and character of the frontier orbitals^a

Compd	$E_{\text{HOMO}-2}$ [eV] (character)	$E_{\text{HOMO}-1}$ [eV] (character)	E_{HOMO} [eV] (character)	E_{LUMO} [eV] (character)	E^{ox} [V] CV	E_{HOMO} [eV] CV
3a	-6.14 (π -S ₂ P)	-6.13 (π -cbz)	-5.76 (π -cbz-ph)	-2.24 (π^* -S ₂ P)	0.91	-5.71
3b	-6.13 (π -S ₂ P)	-6.12 (π -cbz)	-5.75 (π -cbz-ph)	-2.24 (π^* -S ₂ P)	0.90	-5.70
3c (<i>syn</i>)	-6.10 (π -S ₂ P-cbz)	-5.93 (π -S ₂ P-cbz)	-5.78 (π -S ₂ P-cbz)	-2.08 (π^* -S ₂ P)	0.86	-5.66
3d	-6.10 (π -S ₂ P)	-5.96 (π -cbz)	-5.55 (π -cbz-ph)	-2.21 (π^* -S ₂ P)	0.74	-5.54
3e	-6.47 (π -ICz)	-6.11 (π -S ₂ P-ICz)	-5.92 (π -S ₂ P-ICz)	-2.09 (π^* -S ₂ P)	0.96	-5.76
3ai	-6.10 (π -cbz)	-5.82 (π -S ₂ P-cbz)	-5.69 (π -S ₂ P-cbz)	-2.09 (π^* -S ₂ P)	0.94	-5.74
3bi	-6.09 (π -cbz)	-5.78 (π -S ₂ P)	-5.72 (π -cbz-ph)	-2.09 (π^* -S ₂ P)	0.88	-5.68
3ci' - <i>syn</i>	-6.05 (π -cbz)	-5.80 (π -S ₂ P-cbz)	-5.55 (π -S ₂ P-cbz)	-1.93 (π^* -S ₂ P)	0.85	-5.65
3ci' - <i>anti</i>	-5.93 (π -cbz)	-5.72 (π -S ₂ P-cbz)	-5.67 (π -S ₂ P-cbz)	-2.08 (π^* -S ₂ P)	—	—
3di	-5.93 (π -cbz)	-5.75 (π -S ₂ P)	-5.51 (π -cbz-ph)	-2.06 (π^* -S ₂ P)	0.73	-5.53
3ei	-6.41 (π -ICz)	-6.02 (π -ICz)	-5.61 (π -S ₂ P)	-1.95 (π^* -S ₂ P)	0.78	-5.58

^a S₂P: dithienophosphole; cbz: carbazole; ph: phenylene; ICz: indolocarbazole; E^{ox} : oxidation potential relative to Fc/Fc⁺.

limited ICT present in this system, which is in fact absent in the PAH-relatives.

As mentioned above, the photo-physics of the *ortho*-substituted congeners were found to be distinct from those of the rest of the series. For this reason we have performed some more detailed studies on these species, including time-dependent (TD) DFT calculations at the B3LYP/6-31+G(d) level of theory. To establish the presence of electronic through-space interactions, we have included a conformer of **3ci'**, in which the two sub-chromophores exhibit an *anti*-configuration, without the possibility of through-space interactions. In fact, the DFT calculations for **3ci'**-*anti* provide orbital energies, that are not much different from those of the *para*- and *meta*-linked relatives, albeit with the HOMO largely comprising the dithienophosphole π -system (with the addition of the phenylene bridge), and the HOMO-1 and HOMO-2 showing increasing contribution for the carbazole π -system with diminishing contribution from the dithienophosphole scaffold (Fig. 6).

However, while there is certainly also a resemblance between the shape/contributions of these orbitals in **3ci'**-*anti* with those of the two *syn*-configured conformers **3c** and **3ci'**-*syn*, the close proximity of the dithienophosphole and carbazole π -systems opens up through-space interactions in the latter. This is already reflected in orbital shapes and energies that deviate by about 0.1–0.2 eV from those of the other relatives (ESI, Table S2[†]). However, a much clearer picture is provided by the relevant transitions obtained from the TD-DFT calculations that show distinct differences between the *syn*- and *anti*-conformers (Fig. 6). For **3ci'**-*anti* the lowest energy absorption, corresponding to an excitation HOMO \rightarrow LUMO occurs at 352 nm, however with very low oscillator strength ($f = 0.0029$). Other transitions of note include HOMO \rightarrow LUMO+1 (340 nm; $f = 0.1201$), HOMO-1 \rightarrow LUMO (337 nm; $f = 0.0722$), with the most intense transition at 295 nm ($f = 0.1744$) corresponding to HOMO-1 \rightarrow LUMO+1 (the π^* -system of the phenylene bridge). In the case of the *syn*-conformers **3c** and **3ci'**-*syn*, the lowest energy transitions appear around 400 nm, in line with the experimental data, representing a mix of HOMO \rightarrow LUMO (95%) and HOMO-1 \rightarrow LUMO (5%) ($f = 0.0154$) for **3c** and

HOMO \rightarrow LUMO (2%) and HOMO-1 \rightarrow LUMO (96%) ($f = 0.1133$) for **3ci'**-*syn*. Both species show two further transitions of note, respectively, that appear at 375 nm for **3c** (HOMO-1 \rightarrow LUMO (92%), HOMO \rightarrow LUMO (4%); $f = 0.0608$), 380 nm for **3ci'**-*syn* (HOMO-1 \rightarrow LUMO; $f = 0.0208$), as well as 358.5 nm for **3c** (HOMO-2 \rightarrow LUMO; $f = 0.0313$) and 350 nm for **3ci'**-*syn* (HOMO-2 \rightarrow LUMO; $f = 0.0121$). These calculations are in line with the experimental data and rule out the *anti*-conformation to be relevant for the observed photo-physics and support the presence of through-space interactions resulting from *syn*-configuration.

3 Experimental section

3.1 General information

All reactions were carried out under nitrogen atmosphere, employing standard Schlenk techniques. Reagents and solvents were purchased from commercial suppliers and used without further purification unless noted otherwise. Anhydrous solvents were absolutized by an MBraun solvent purification system prior to use. NMR spectra were recorded on Bruker Avance-II/III 400 MHz Spectrometers; for compounds **3c** and **3ei** 2D NMR spectra for complete signal assignment (COSY, HSQC, HMBC) as well as 1D and 2D NOESY spectra were obtained on a Bruker Avance IIIHD 600 MHz spectrometer equipped with a Prodigy BBO cryo probe. A Thermo Scientific LTQ Orbitrap XL hybrid FTMS (Fourier Transform Mass Spectrometer) equipped with a Thermo Fischer Exactive Plus Orbitrap (LC-ESI+) and a Shimadzu IT-TOF Mass Spectrometer were used for high resolution mass spectrometry. UV/Vis absorption and fluorescence emission spectra were recorded in DCM solutions (5 μ M) with a Perkin Elmer Lambda 750 spectrometer and an Edinburgh FLS920, respectively. Time resolved experiments were obtained using a Quantel Brilliant tripled Nd-YAG laser (355 nm, 20 Hz repetition rate, pulse width ~ 5 ns). Spectra were measured using a SPEX 270 monochromator equipped with both photomultiplier and CCD. This set-up is controlled using a home-built Labview-based program which allows using different instruments such as photon counting, oscilloscope, and additional

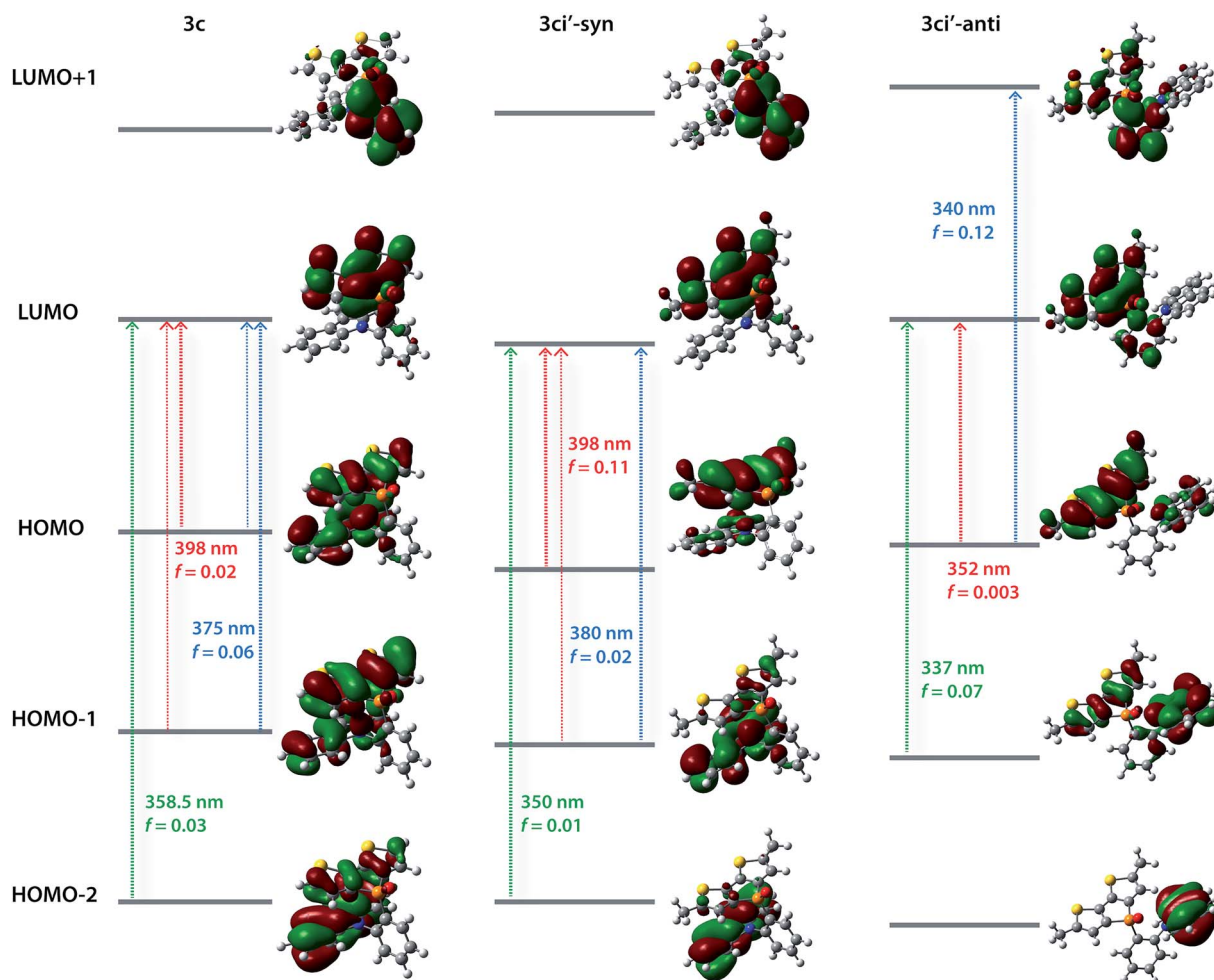


Fig. 6 TD-DFT calculation data for **3c**, **3ci'-syn** and **3ci'-anti** showing notable transitions as well as their intensity (f = oscillator strength). Thickness of arrow indicates weight to transition.

mechanical shutters. For the measurement of the triplet emission, a mechanical shutter was triggered by the pulsed laser. A pretrigger period of 0.5 ms was followed by a 1 ms aperture and a rest time of 300–500 ms allowed obtaining the measurements shown in the ESI.† The slit of the monochromator was also opened further (up to 0.5 mm) to measure the triplet emission. Cyclic voltammetry was performed using a three electrode configuration consisting of a Pt working electrode, a Pt counter electrode and an Ag/AgCl reference electrode and a PGSTAT128N, ADC164, DAC164, External, DI048 potentiostat provided by Metrohm Autolab B.V with ferrocenium–ferrocene (Fc/Fc^+) as standard. Measurements were carried out in a 0.5 mM solution in anhydrous DCM with Bu_4NBF_4 (0.1 M) as supporting electrolyte. The solutions were purged with nitrogen for 15 minutes prior to measurement. HOMO energy levels were calculated from the onset of the oxidation peaks. The onset potential was determined by the intersection of two tangents drawn at the background and the rising of the oxidation peaks. HOMO levels were calculated according to the equation $\text{HOMO} = -(4.8 + E^{\text{ox}})$, where E^{ox} is the oxidation potential relative to Fc/Fc^+ .

3.2 Synthetic details

Dibrominated bithiophenes **2** (ref. 58) and **2i** (ref. 31) were synthesized as described in literature. Dichlorophosphanes **1a–e** were prepared in analogy to a previously published procedure from the corresponding brominated precursors and were used crude without any further purification.²⁹

General procedure for the synthesis of TAA-substituted dithieno[3,2-*b*:2',3'-*d*]phospholes. The synthesis of TAA-substituted dithieno[3,2-*b*:2',3'-*d*]phospholes was accomplished according to established procedures.^{26,27,29,32,33,59} To a solution of **2/2i** (1 eq.) and TMEDA (2 eq.) in dry diethylether or THF (~0.25 M) under nitrogen atmosphere was added *n*-BuLi (2.5 M in hexane, 2 eq.) dropwise at -78 °C. The reaction mixture was stirred at -78 °C before a solution of dichlorophosphane **1a/b/c/d/e** (1 eq.) in dry THF (0.05–0.1 M) was slowly added. Subsequently the resulting mixture was allowed to warm to room temperature quickly, stirred for one hour and the solvent was removed under vacuum. The residue was dissolved in chloroform and excess of water and H_2O_2 (30%, 0.5–1 mL mmol^{-1}) was added. After stirring for 1.5 hours the organic

phase was dried over MgSO₄ before the solvent was removed and the crude product was purified by column chromatography.

4-(4-(9H-Carbazol-9-yl)phenyl)-4H-phospholo[3,2-b:4,5-b']dithiophene 4-oxide (3a). Starting from **2** (1.00 g, 3.1 mmol) and TMEDA (0.94 mL) in diethylether, *n*-BuLi (2.47 mL, 2.5 M), **1a** (0.75 g, 2.2 mmol, 0.71 eq.) and H₂O₂ (30%, 2 mL) product **3a** (130 mg, 0.29 mmol, 13%) was obtained as light yellowish solid after column chromatography (silica, ethyl acetate); undefined impurities (approx. 5–10%) were not separable from **3a** by repeated column chromatography. ³¹P {¹H} NMR (162 MHz, CD₂Cl₂): δ = 16.2 (s) ppm. ¹H NMR (400 MHz, CD₂Cl₂): δ = 8.14 (d, *J* = 7.6 Hz, 2H), 7.95 (dd, *J* = 12.7, 8.3 Hz, 2H), 7.68 (dd, *J* = 8.3, 2.4 Hz, 2H), 7.47–7.39 (m, 6H), 7.32–7.25 (m, 4H) ppm. ¹³C {¹H} NMR (100 MHz, CD₂Cl₂): δ = 146.5 (d, *J*_{CP} = 24.3 Hz), 142.1 (d, *J*_{CP} = 3.5 Hz), 140.8 (s), 139.4 (d, *J*_{CP} = 112.3 Hz), 133.2 (d, *J*_{CP} = 12.1 Hz), 129.4(4) (d, *J*_{CP} = 108.1 Hz), 129.4(1) (d, *J*_{CP} = 14.9 Hz), 127.5 (d, *J*_{CP} = 13.0 Hz), 126.7 (s), 126.4 (d, *J*_{CP} = 14.5 Hz), 124.2 (s), 121.0 (s), 120.9 (s), 110.3 (s) ppm. Calculated: *m/z* 453.04054 [M]⁺, 454.04837 [M + H]⁺, 476.03031 [M + Na]⁺. Found: MS (ESI): *m/z* 453.03978 [M]⁺, 454.04737 [M + H]⁺, 476.02944 [M + Na]⁺.

4-(4-(9H-Carbazol-9-yl)phenyl)-2,6-dibutyl-4H-phospholo[3,2-b:4,5-b']dithiophene 4-oxide (3ai). Starting from **2i** (0.80 g, 1.8 mmol) and TMEDA (0.58 mL) in diethylether, *n*-BuLi (1.46 mL, 2.5 M), **1a** (0.63 g, 1.8 mmol) and H₂O₂ (30%, 2 mL) product **3ai** (375 mg, 0.66 mmol, 36%) was obtained as yellowish solid after column chromatography (silica, ethyl acetate : hexanes = 1 : 1). ³¹P {¹H} NMR (162 MHz, CDCl₃): δ = 19.2 (s) ppm. ¹H NMR (400 MHz, CD₂Cl₂): δ = 8.14 (d, *J* = 7.7 Hz, 2H), 7.94 (dd, *J* = 12.7, 8.3 Hz, 2H), 7.68 (dd, *J* = 8.4, 2.3 Hz, 2H), 7.48–7.39 (m, 4H), 7.30 (ddd, *J* = 7.4, 7.4, 1.1 Hz, 2H), 6.91 (d, *J* = 2.0 Hz, 2H), 2.85 (t, *J* = 7.6 Hz, 4H), 1.69 (tt, *J* = 7.6, 7.6 Hz, 4H), 1.42 (qt, *J* = 7.6, 7.3 Hz, 4H), 0.95 (t, *J* = 7.3 Hz, 6H) ppm. ¹³C {¹H} NMR (100 MHz, CD₂Cl₂): δ = 150.8 (d, *J*_{CP} = 14.4 Hz), 144.4 (d, *J*_{CP} = 24.6 Hz), 141.9 (d, *J*_{CP} = 3.2 Hz), 140.8 (s), 137.6 (d, *J*_{CP} = 112.7 Hz), 133.2 (d, *J*_{CP} = 12.3 Hz), 130.2 (d, *J*_{CP} = 107.3 Hz), 127.4 (d, *J*_{CP} = 13.0 Hz), 126.7 (s), 124.2 (s), 122.9 (d, *J*_{CP} = 14.6 Hz), 121.0 (s), 120.9 (s), 110.3 (s), 34.2 (s), 30.6 (s), 22.7 (s), 14.1 (s) ppm. Calculated: *m/z* 565.16574 [M]⁺, 566.17357 [M + H]⁺, 588.15551 [M + Na]⁺. Found: MS (ESI): *m/z* 565.16518 [M]⁺, 566.17259 [M + H]⁺, 588.15436 [M + Na]⁺.

4-(3-(9H-Carbazol-9-yl)phenyl)-4H-phospholo[3,2-b:4,5-b']dithiophene 4-oxide (3b). Starting from **2** (1.41 g, 4.4 mmol) in diethylether, *n*-BuLi (3.49 mL, 2.5 M), **1b** (1.50 g, 4.4 mmol) and H₂O₂ (30%, 2 mL) product **3b** (0.81 g, 1.8 mmol, 41%) was obtained as light yellowish solid after column chromatography (silica, ethyl acetate). ³¹P {¹H} NMR (162 MHz, CDCl₃): δ = 17.8 (s) ppm. ¹H NMR (400 MHz, CD₂Cl₂): δ = 8.12 (d, *J* = 7.8 Hz, 2H), 7.89–7.81 (m, 2H), 7.79–7.75 (m, 1H), 7.73–7.68 (m, 1H), 7.41–7.36 (m, 4H), 7.32–7.23 (m, 6H) ppm. ¹³C {¹H} NMR (100 MHz, CD₂Cl₂): δ = 146.5 (d, *J*_{CP} = 24.5 Hz), 140.9 (s), 139.3 (d, *J*_{CP} = 112.7 Hz), 138.9 (d, *J*_{CP} = 15.7 Hz), 133.3 (d, *J*_{CP} = 105.8 Hz), 131.2 (d, *J*_{CP} = 14.0 Hz), 131.1 (d, *J*_{CP} = 2.7 Hz), 130.2 (d, *J*_{CP} = 10.3 Hz), 129.5 (d, *J*_{CP} = 15.1 Hz), 129.2 (d, *J*_{CP} = 12.2 Hz), 126.6 (s), 126.3 (d, *J*_{CP} = 14.6 Hz), 124.0 (s), 120.8(8) (s), 120.8(5) (s), 110.0 (s) ppm. Calculated: *m/z* 453.04054 [M]⁺, 454.04837 [M + H]⁺, 476.03031

[M + Na]⁺. Found: MS (ESI): *m/z* 453.04004 [M]⁺, 454.04705 [M + H]⁺, 476.02881 [M + Na]⁺.

4-(3-(9H-Carbazol-9-yl)phenyl)-2,6-dibutyl-4H-phospholo[3,2-b:4,5-b']dithiophene 4-oxide (3bi). Starting from **2i** (1.39 g, 3.2 mmol) in diethylether, *n*-BuLi (2.56 mL, 2.5 M), **1b** (1.10 g, 3.2 mmol) and H₂O₂ (30%, 2 mL) product **3bi** (0.55 g, 1.0 mmol, 30%) was obtained as light yellowish solid after column chromatography (silica, ethyl acetate : hexanes = 1 : 1). ³¹P {¹H} NMR (162 MHz, CDCl₃): δ = 19.1 (s) ppm. ¹H NMR (400 MHz, CD₂Cl₂): δ = 8.13 (d, *J* = 7.3 Hz, 2H), 7.91–7.67 (m, 4H), 7.41–7.35 (m, 2H), 7.33–7.26 (m, 4H), 6.90–6.88 (m, 2H), 2.84–2.79 (m, 4H), 1.70–1.61 (m, 4H), 1.44–1.34 (m, 4H), 0.94–0.89 (m, 6H) ppm. ¹³C {¹H} NMR (100 MHz, CD₂Cl₂): δ = 150.9 (d, *J*_{CP} = 14.4 Hz), 144.4 (d, *J*_{CP} = 24.5 Hz), 140.9 (s), 138.8 (d, *J*_{CP} = 15.3 Hz), 137.4 (d, *J*_{CP} = 112.8 Hz), 133.9 (d, *J*_{CP} = 104.3 Hz), 131.1 (d, *J*_{CP} = 13.8 Hz), 130.8 (d, *J*_{CP} = 2.6 Hz), 130.2 (d, *J*_{CP} = 10.3 Hz), 129.1 (d, *J*_{CP} = 14.6 Hz), 126.6 (s), 124.0 (s), 122.7 (d, *J*_{CP} = 14.6 Hz), 120.8 (s), 120.8 (s), 110.0 (s), 34.2 (s), 30.6 (s), 22.6 (s), 14.1 (s) ppm. Calculated: *m/z* 565.16574 [M]⁺, 566.17357 [M + H]⁺, 588.15551 [M + Na]⁺. Found: MS (ESI): *m/z* 565.16499 [M]⁺, 566.17241 [M + H]⁺, 588.15411 [M + Na]⁺.

4-(2-(9H-Carbazol-9-yl)phenyl)-4H-phospholo[3,2-b:4,5-b']dithiophene 4-oxide (3c). Starting from **2** (1.00 g, 3.1 mmol) and TMEDA (0.94 mL) in diethylether, *n*-BuLi (2.47 mL, 2.5 M), **1c** (1.06 g, 3.1 mmol) and H₂O₂ (30%, 1.5 mL) product **3c** (353 mg, 0.78 mmol, 25%) was obtained as light yellowish solid after column chromatography (silica, ethyl acetate). ³¹P {¹H} NMR (162 MHz, CDCl₃): δ = 12.9 (s) ppm. ¹H NMR (400 MHz, CD₂Cl₂): δ = 8.76 (ddd, *J* = 13.2, 7.8, 1.7 Hz, 1H), 7.82–7.83 (m, 3H), 7.81–7.69 (m, 1H), 7.24–7.20 (m, 1H), 7.13–7.04 (m, 4H), 6.75 (dd, *J* = 4.9, 3.5 Hz, 2H), 6.68 (dd, *J* = 4.9, 2.6 Hz, 2H), 6.44 (d, *J* = 7.84 Hz, 2H) ppm. ¹³C {¹H} NMR (100 MHz, CD₂Cl₂): δ = 145.8 (d, *J*_{CP} = 25.5 Hz), 142.4 (s), 138.9 (d, *J*_{CP} = 6.1 Hz), 137.2 (d, *J*_{CP} = 115.6 Hz), 137.2 (d, *J*_{CP} = 7.3 Hz), 134.6 (d, *J*_{CP} = 2.3 Hz), 132.8 (d, *J*_{CP} = 101.8 Hz), 132.0 (d, *J*_{CP} = 7.7 Hz), 130.4 (d, *J*_{CP} = 11.3 Hz), 128.3 (d, *J*_{CP} = 15.3 Hz), 126.1 (s), 125.4 (d, *J*_{CP} = 15.3 Hz), 123.4 (s), 120.2 (s), 120.0 (s), 110.2 (s) ppm. Calculated: *m/z* 453.04054 [M]⁺, 454.04837 [M + H]⁺, 476.03031 [M + Na]⁺. Found: MS (ESI): *m/z* 453.03945 [M]⁺, 454.04731 [M + H]⁺, 476.02871 [M + Na]⁺.

4-(2-(9H-Carbazol-9-yl)phenyl)-2,6-dibutyl-4H-phospholo[3,2-b:4,5-b']dithiophene 4-oxide (3ci). Starting from **2i** (1.00 g, 2.3 mmol) and TMEDA (0.69 mL) in THF, *n*-BuLi (1.83 mL, 2.5 M), **1c** (0.79 g, 2.3 mmol) and H₂O₂ (30%, 1.5 mL) product **3ci** (220 mg, 0.39 mmol, 17%) was obtained as light yellowish solid after column chromatography (silica, ethyl acetate : hexanes = 1 : 1). ³¹P {¹H} NMR (162 MHz, CDCl₃): δ = 14.1 (s) ppm. ¹H NMR (400 MHz, CD₂Cl₂): δ = 8.70 (ddd, *J* = 13.2, 7.9, 1.5 Hz, 1H), 7.90–7.81 (m, 3H), 7.75–7.73 (m, 1H), 7.18 (dd, *J* = 6.8, 5.9 Hz, 1H), 7.14–7.08 (m, 4H), 6.49–6.45 (m, 2H), 6.34 (d, *J* = 2.2 Hz, 2H), 2.55–2.42 (m, 4H), 1.53–1.44 (m, 4H), 1.34 (qt, *J* = 7.5, 7.5 Hz, 4H), 0.92 (t, *J* = 7.5 Hz, 6H) ppm. ¹³C {¹H} NMR (100 MHz, CD₂Cl₂): δ = 149.6 (d, *J*_{CP} = 14.8 Hz), 144.0 (d, *J*_{CP} = 25.3 Hz), 142.5 (s), 138.9 (d, *J*_{CP} = 5.4 Hz), 137.1 (d, *J*_{CP} = 6.9 Hz), 135.9 (d, *J*_{CP} = 116.0 Hz), 134.3 (d, *J*_{CP} = 2.3 Hz), 133.5 (d, *J*_{CP} = 100.3 Hz), 131.8 (d, *J*_{CP} = 7.7 Hz), 130.3 (d, *J*_{CP} = 11.0 Hz), 125.7 (s), 123.5 (s), 122.1 (d, *J*_{CP} = 14.6 Hz), 120.1 (s), 120.0 (s), 110.5 (s) 33.7 (s), 30.3 (s), 22.8 (s), 14.1 (s) ppm. Calculated: *m/z* 565.16574 [M]⁺,

566.17357 [M + H]⁺, 588.15551 [M + Na]⁺. Found: MS (ESI): *m/z* 565.16504 [M]⁺, 566.17275 [M + H]⁺, 588.15397 [M + Na]⁺.

4-(3-(3,6-Di-*tert*-butyl-9H-carbazol-9-yl)phenyl)-4H-phospholo[3,2-*b*:4,5-*b'*]dithiophene 4-oxide (**3d**). Starting from **2** (0.62 g, 1.9 mmol) and TMEDA (0.58 mL) in THF, *n*-BuLi (1.53 mL, 2.5 M), **1d** (0.87 g, 1.9 mmol) and H₂O₂ (30%, 1 mL) product **3d** (185 mg, 0.33 mmol, 17%) was obtained as light yellowish solid after column chromatography (silica, DCM : MeCN = 20 : 1). ³¹P {¹H} NMR (162 MHz, CDCl₃): δ = 18.0 (s) ppm. ¹H NMR (400 MHz, CD₂Cl₂): δ = 8.13 (d, *J* = 1.9 Hz, 2H), 7.86–7.74 (m, 3H), 7.68 (ddd, *J* = 7.7, 7.7, 3.7 Hz, 1H), 7.44 (dd, *J* = 8.7, 1.8 Hz, 2H), 7.38 (dd, *J* = 4.9, 3.5 Hz, 2H), 7.26–7.22 (m, 4H), 1.45 (s, 18H) ppm. ¹³C {¹H} NMR (100 MHz, CD₂Cl₂): δ = 146.6 (d, *J*_{CP} = 24.1 Hz), 144.0 (s), 139.4 (d, *J*_{CP} = 15.9 Hz), 139.2 (d, *J*_{CP} = 112.7 Hz), 139.2 (s), 132.9 (d, *J*_{CP} = 105.8 Hz), 131.1 (d, *J*_{CP} = 14.0 Hz), 130.7 (d, *J*_{CP} = 2.8 Hz), 129.6 (d, *J*_{CP} = 10.4 Hz), 129.5 (d, *J*_{CP} = 15.2 Hz), 128.8 (d, *J*_{CP} = 12.2 Hz), 126.4 (d, *J*_{CP} = 14.5 Hz), 124.3 (s), 124.0 (s), 116.9 (s), 109.4 (s), 35.2 (s), 32.3 (s) ppm. Calculated: *m/z* 565.16574 [M]⁺, 566.17357 [M + H]⁺, 588.15551 [M + Na]⁺. Found: MS (ESI): *m/z* 565.16500 [M]⁺, 566.17249 [M + H]⁺, 588.15648 [M + Na]⁺.

4-(3-(3,6-Di-*tert*-butyl-9H-carbazol-9-yl)phenyl)-2,6-dibutyl-4H-phospholo[3,2-*b*:4,5-*b'*]dithiophene 4-oxide (**3di**). Starting from **2i** (0.83 g, 1.9 mmol) and TMEDA (0.58 mL) in THF, *n*-BuLi (1.53 mL, 2.5 M), **1d** (0.87 g, 1.9 mmol) and H₂O₂ (30%, 1 mL) product **3di** (0.47 g, 0.7 mmol, 36%) was obtained as light yellowish solid after column chromatography (silica, DCM : MeCN = 20 : 1). ³¹P {¹H} NMR (162 MHz, CDCl₃): δ = 19.2 (s) ppm. ¹H NMR (400 MHz, CD₂Cl₂): δ = 8.13 (d, *J* = 1.8 Hz, 2H), 7.88–7.73 (m, 3H), 7.68 (ddd, *J* = 7.6, 7.6, 3.5 Hz, 1H), 7.43 (dd, *J* = 8.7, 1.9 Hz, 2H), 7.25 (d, *J* = 8.6 Hz, 2H), 6.89–6.88 (m, 2H), 2.82 (t, *J* = 7.6 Hz, 4H), 1.67 (tt, *J* = 7.6, 7.6 Hz, 4H), 1.45–1.34 (m, 22H), 0.92 (t, *J* = 7.3 Hz, 6H) ppm. ¹³C {¹H} NMR (100 MHz, CD₂Cl₂): δ = 150.9 (d, *J*_{CP} = 14.1 Hz), 144.5 (d, *J*_{CP} = 24.5 Hz), 143.9 (s), 139.3 (d, *J*_{CP} = 15.3 Hz), 139.2 (s), 137.3 (d, *J*_{CP} = 112.6 Hz), 133.6 (d, *J*_{CP} = 105.0 Hz), 131.0 (d, *J*_{CP} = 13.9 Hz), 130.4 (d, *J*_{CP} = 3.7 Hz), 129.7 (d, *J*_{CP} = 10.1 Hz), 128.6 (d, *J*_{CP} = 12.4 Hz), 124.3 (s), 124.0 (s), 122.7 (d, *J*_{CP} = 13.8 Hz), 116.9 (s), 109.5 (s), 35.2 (s), 34.2 (s), 32.3 (s), 30.6 (s), 22.7 (s), 14.1 (s) ppm. Calculated: *m/z* 677.29094 [M]⁺, 678.29877 [M + H]⁺, 700.28071 [M + Na]⁺. Found: MS (ESI): *m/z* 677.28998 [M]⁺, 678.29816 [M + H]⁺, 700.27997 [M + Na]⁺.

4-(Indolo[3,2,1-*jk*]carbazol-2-yl)-4H-phospholo[3,2-*b*:4,5-*b'*]dithiophene 4-oxide (**3e**). Starting from **2** (0.50 g, 1.5 mmol) in THF, *n*-BuLi (1.22 mL, 2.5 M), **1e** (0.52 g, 1.5 mmol) and H₂O₂ (30%, 2 mL) product **3e** (73 mg, 0.16 mmol, 11%) was obtained as light yellowish solid after column chromatography (silica, DCM : MeCN = 5 : 1). ³¹P {¹H} NMR (162 MHz, CDCl₃): δ = 22.2 (s) ppm. ¹H NMR (400 MHz, CD₂Cl₂): δ = 8.46 (d, *J* = 13.0 Hz, 2H), 8.15 (d, *J* = 7.8 Hz, 2H), 7.95 (d, *J* = 7.9 Hz, 2H), 7.62 (dd, *J* = 7.7, 7.7 Hz, 2H), 7.43–7.36 (m, 4H), 7.20 (dd, *J* = 4.8, 2.3 Hz, 2H) ppm. ¹³C {¹H} NMR (100 MHz, CD₂Cl₂): δ = 146.3 (d, *J*_{CP} = 2.3 Hz), 146.2 (d, *J*_{CP} = 23.6 Hz), 140.8 (d, *J*_{CP} = 111.0 Hz), 139.7 (s), 129.8 (s), 129.2 (d, *J*_{CP} = 14.6 Hz), 128.2 (s), 126.4 (d, *J*_{CP} = 14.5 Hz), 124.1 (s), 123.9 (d, *J*_{CP} = 108.1 Hz), 123.0 (s), 122.9 (d, *J*_{CP} = 14.5 Hz), 119.5 (d, *J*_{CP} = 17.5 Hz), 113.0 (s) ppm. Calculated: *m/z* 451.02489 [M]⁺, 452.03272 [M + H]⁺, 474.01466 [M + Na]⁺.

Found: MS (ESI): *m/z* 451.02445 [M]⁺, 452.03177 [M + H]⁺, 474.01384 [M + Na]⁺.

4-(Indolo[3,2,1-*jk*]carbazol-2-yl)-2,6-dibutyl-4H-phospholo[3,2-*b*:4,5-*b'*]dithiophene 4-oxide (**3ei**). Starting from **2i** (0.97 g, 2.2 mmol) in THF, *n*-BuLi (1.78 mL, 2.5 M), **1e** (0.76 g, 2.2 mmol) and H₂O₂ (30%, 2 mL) product **3ei** (152 mg, 0.27 mmol, 12%) was obtained as light yellowish solid after column chromatography (silica, DCM : MeCN = 20 : 1). ³¹P {¹H} NMR (162 MHz, CDCl₃): δ = 23.3 (s) ppm. ¹H NMR (400 MHz, CD₂Cl₂): δ = 8.45 (d, *J* = 12.9 Hz, 2H), 8.15 (d, *J* = 7.9 Hz, 2H), 7.94 (d, *J* = 8.2 Hz, 2H), 7.61 (dd, *J* = 7.7, 7.7 Hz, 2H), 7.40 (dd, *J* = 7.7, 7.7 Hz, 2H), 6.85 (s, 2H), 2.82 (t, *J* = 7.5 Hz, 4H), 1.66 (tt, *J* = 7.5, 7.5 Hz, 4H), 1.39 (qt, *J* = 7.5, 7.4 Hz, 4H), 0.92 (t, *J* = 7.4 Hz, 6H) ppm. ¹³C {¹H} NMR (100 MHz, CD₂Cl₂): δ = 150.6 (d, *J*_{CP} = 13.9 Hz), 146.3 (d, *J*_{CP} = 2.3 Hz), 144.0 (d, *J*_{CP} = 23.7 Hz), 139.7 (s), 138.9 (d, *J*_{CP} = 111.2 Hz), 129.8 (s), 128.2 (s), 124.7 (d, *J*_{CP} = 106.6 Hz), 124.1 (s), 123.0 (s), 122.9 (d, *J*_{CP} = 14.6 Hz), 122.8 (d, *J*_{CP} = 14.2 Hz), 119.4 (d, *J*_{CP} = 16.9 Hz), 113.0 (s), 34.2 (s), 30.6 (s), 22.6 (s), 14.1 (s) ppm. Calculated: *m/z* 563.15009 [M]⁺, 564.15792 [M + H]⁺, 586.13986 [M + Na]⁺. Found: MS (ESI): *m/z* 563.14933 [M]⁺, 564.15704 [M + H]⁺, 586.13880 [M + Na]⁺.

3.3 Computational details

Density-Functional-Theory (DFT) and Time-Dependent (TD) DFT calculations have been carried out at the B3LYP/6-31+G(d) level of theory using the GAUSSIAN 09 suite of programs.⁵⁷

3.4 Single crystal diffraction

Crystals of **3c** (ref. 49) suitable for single crystal diffraction were selected under a polarizing microscope, embedded in perfluorinated oil and attached to Kapton® mounts. Intensity data were collected in a dry stream of nitrogen at 100 K on a Bruker KAPPA APEX II diffractometer system. Since automatic unit-cell determination failed, reflection position were analyzed using the RLATT⁶⁰ tool. Two monoclinic domains related by reflection at (101) could be identified. They were integrated concurrently using SAINT-Plus⁶⁰ with overlap detection (HKLF5-style output file) and an empirical absorption correction using the multi-scan approach implemented in TWINABS⁶⁰ was applied. The crystal structures were solved by charge-flipping implemented in SUPERFLIP⁶¹ and refined against *F* with the JANA2006 (ref. 62) software package. The non-H atoms were refined with anisotropic displacement parameters (ADPs). The H atoms were placed at calculated positions and refined as riding on the parent C atoms. More details on data collection and refinement are summarized in the ESI.†

4 Conclusion

In summary, the synthesis and characterization of novel dithienophosphole oxide donor–acceptor materials, applying various phenylcarbazole and indolocarbazole derivatives, has been presented. The following major conclusion can be drawn:

(1) The intramolecular charge transfer through the phosphorus atom can be virtually suppressed by reducing the donor strength in the donor–acceptor scaffold;

(2) Compounds potentially suitable as host materials in PhOLED applications could be obtained (triplet energies up to 2.87 eV; singlet-triplet splitting of 0.18 eV);

(3) Through space interactions have been established for the *ortho*-phenylcarbazole structure.

The theoretical calculations support the aforementioned assumptions drawn from the experimental data.

As a result, the approach of increasing the planarization of the triarylamine type donor in stepwise fashion and, thus, decreasing the donor strength clearly broadens the scope of potential applications of the dithienophosphole oxide scaffold.

Acknowledgements

T. B. thanks the Natural Sciences and Engineering Research Council of Canada (NSERC) and the Canada Foundation for Innovation for financial support. This work was supported in part by the Vienna University of Technology research funds, the Austrian Federal Ministry of Science, Research and Economy and the Swiss National Science Foundation. The X-ray centre of the Vienna University of Technology is acknowledged for providing access to the single-crystal diffractometer. K. Föttinger is acknowledged for assisting the photo-physical analysis. The student exchange of H. P. was financially supported by the Joint Study Grant (TASSEP for Canada, 2012) and the KUWI Grant (Vienna University of Technology, 2013).

References

- 1 S. Reineke, M. Thomschke, B. Lüssem and K. Leo, *Rev. Mod. Phys.*, 2013, **85**, 1245–1293.
- 2 M. Zhu and C. Yang, *Chem. Soc. Rev.*, 2013, **42**, 4963–4976.
- 3 Y. Tao, K. Yuan, T. Chen, P. Xu, H. H. Li, R. F. Chen, C. Zheng, L. Zhang and W. Huang, *Adv. Mater.*, 2014, **26**, 7931–7958.
- 4 Q. Meng, H. L. Dong, W. P. Hu and D. B. Zhu, *J. Mater. Chem.*, 2011, **21**, 11708–11721.
- 5 C. A. Di, F. J. Zhang and D. B. Zhu, *Adv. Mater.*, 2013, **25**, 313–330.
- 6 L. Torsi, M. Magliulo, K. Manoli and G. Palazzo, *Chem. Soc. Rev.*, 2013, **42**, 8612–8628.
- 7 Y. J. Cheng, S. H. Yang and C. S. Hsu, *Chem. Rev.*, 2009, **109**, 5868–5923.
- 8 A. Facchetti, *Chem. Mater.*, 2011, **23**, 733–758.
- 9 J. G. Mei, Y. Diao, A. L. Appleton, L. Fang and Z. N. Bao, *J. Am. Chem. Soc.*, 2013, **135**, 6724–6746.
- 10 Z. M. Hudson and S. N. Wang, *Acc. Chem. Res.*, 2009, **42**, 1584–1596.
- 11 F. Jakle, *Chem. Rev.*, 2010, **110**, 3985–4022.
- 12 C. R. Wade, A. E. J. Broomsgrove, S. Aldridge and F. P. Gabbai, *Chem. Rev.*, 2010, **110**, 3958–3984.
- 13 J. W. Chen and Y. Cao, *Macromol. Rapid Commun.*, 2007, **28**, 1714–1742.
- 14 J. Ohshita, *Macromol. Chem. Phys.*, 2009, **210**, 1360–1370.
- 15 B. C. Schroeder, Z. G. Huang, R. S. Ashraf, J. Smith, P. D'Angelo, S. E. Watkins, T. D. Anthopoulos, J. R. Durrant and I. McCulloch, *Adv. Funct. Mater.*, 2012, **22**, 1663–1670.
- 16 X. M. He and T. Baumgartner, *RSC Adv.*, 2013, **3**, 11334–11350.
- 17 A. A. Jahnke and D. S. Seferos, *Macromol. Rapid Commun.*, 2011, **32**, 943–951.
- 18 T. Baumgartner and R. Reau, *Chem. Rev.*, 2006, **106**, 4681–4727.
- 19 J. Crassous and R. Reau, *Dalton Trans.*, 2008, 6865–6876.
- 20 Y. Matano and H. Imahoria, *Org. Biomol. Chem.*, 2009, **7**, 1258–1271.
- 21 S. O. Jeon and J. Y. Lee, *J. Mater. Chem.*, 2012, **22**, 4233–4243.
- 22 Y. Ren and T. Baumgartner, *Dalton Trans.*, 2012, **41**, 7792–7800.
- 23 C. Romero-Nieto and T. Baumgartner, *Synlett*, 2013, **24**, 920–937.
- 24 T. Baumgartner, *Acc. Chem. Res.*, 2014, **47**, 1613–1622.
- 25 M. G. Hobbs and T. Baumgartner, *Eur. J. Inorg. Chem.*, 2007, 3611–3628.
- 26 T. Baumgartner, W. Bergmans, T. Karpati, T. Neumann, M. Nieger and L. Nyulaszi, *Chem.–Eur. J.*, 2005, **11**, 4687–4699.
- 27 Y. Dienes, S. Durben, T. Karpati, T. Neumann, U. Englert, L. Nyulaszi and T. Baumgartner, *Chem.–Eur. J.*, 2007, **13**, 7487–7500.
- 28 M. Stolar and T. Baumgartner, *New J. Chem.*, 2012, **36**, 1153–1160.
- 29 C. J. Chua, Y. Ren and T. Baumgartner, *Org. Lett.*, 2012, **14**, 1588–1591.
- 30 C. J. Chua, Y. Ren and T. Baumgartner, *Organometallics*, 2012, **31**, 2425–2436.
- 31 C. J. Chua, Y. Ren, M. Stolar, S. Xing, T. Linder and T. Baumgartner, *Eur. J. Inorg. Chem.*, 2014, 1767–1774.
- 32 T. Baumgartner, T. Neumann and B. Wirges, *Angew. Chem., Int. Ed.*, 2004, **43**, 6197–6201.
- 33 S. Durben, Y. Dienes and T. Baumgartner, *Org. Lett.*, 2006, **8**, 5893–5896.
- 34 C. Romero-Nieto, S. Durben, I. M. Kormos and T. Baumgartner, *Adv. Funct. Mater.*, 2009, **19**, 3625–3631.
- 35 C. Romero-Nieto, K. Kamada, D. T. Cramb, S. Merino, J. Rodriguez-Lopez and T. Baumgartner, *Eur. J. Inorg. Chem.*, 2010, 5225–5231.
- 36 C. Romero-Nieto, M. Marcos, S. Merino, J. Barbera, T. Baumgartner and J. Rodriguez-Lopez, *Adv. Funct. Mater.*, 2011, **21**, 4088–4099.
- 37 Y. Ren, W. H. Kan, V. Thangadurai and T. Baumgartner, *Angew. Chem., Int. Ed.*, 2012, **51**, 3964–3968.
- 38 G. S. He, L.-S. Tan, Q. Zheng and P. N. Prasad, *Chem. Rev.*, 2008, **108**, 1245–1330.
- 39 Y. Tao, C. Yang and J. Qin, *Chem. Soc. Rev.*, 2011, **40**, 2943–2970.
- 40 A. Mishra and P. Bäuerle, *Angew. Chem., Int. Ed.*, 2012, **51**, 2020–2067.
- 41 Y. Shirota and H. Kageyama, *Chem. Rev.*, 2007, **107**, 953–1010.
- 42 X. Cai, A. B. Padmaperuma, L. S. Sapochak, P. A. Vecchi and P. E. Burrows, *Appl. Phys. Lett.*, 2008, **92**, 083308.

- 43 S. O. Jeon, K. S. Yook, C. W. Joo and J. Y. Lee, *Adv. Funct. Mater.*, 2009, **19**, 3644–3649.
- 44 H.-H. Chou and C.-H. Cheng, *Adv. Mater.*, 2010, **22**, 2468–2471.
- 45 P. K. Koech, E. Polikarpov, J. E. Rainbolt, L. Cosimbescu, J. S. Swensen, A. L. von Ruden and A. B. Padmaperuma, *Org. Lett.*, 2010, **12**, 5534–5537.
- 46 U. S. Bhansali, E. Polikarpov, J. S. Swensen, W.-H. Chen, H. Jia, D. J. Gaspar, B. E. Gnade, A. B. Padmaperuma and M. A. Omary, *Appl. Phys. Lett.*, 2009, **95**, 233304.
- 47 P. Kautny, Diploma thesis, Vienna University of Technology, 2013.
- 48 E. Mondal, W.-Y. Hung, H.-C. Dai and K.-T. Wong, *Adv. Funct. Mater.*, 2013, **23**, 3096–3105.
- 49 (**3c**): $C_{26}H_{16}NOPS_2$, $M_r = 453.50$, $T = 100$ K, monoclinic, space group $P2_1$, $a = 8.3295(6)$ Å, $b = 14.1464(10)$ Å, $c = 8.8132(6)$ Å, $\beta = 103.1530(19)^\circ$, $V = 1011.24(12)$ Å³, $Z = 2$, $\rho_{\text{calcd}} = 1.4894$ Mg m⁻³, $\mu = 0.363$ mm⁻¹, $\lambda = 0.71070$ Å, $\theta_{\text{max}} = 32.72^\circ$, 82 676 measured reflections, 7360 [$R(\text{int}) = 0.0407$] independent reflections, GOF on $F = 1.92$, $R_1 = 0.0198$, $wR_2 = 0.0272$ ($I > 3\sigma(I)$), $R_1 = 0.0201$, $wR_2 = 0.0273$ (all data), largest difference peak and hole 0.280 and -0.200 e Å⁻³. Twinned by twofold rotation about $[10\bar{1}]$ with a 63.75 : 36.25(7) volume ratio. CCDC reference number 1407916†
- 50 H. H. Li, Y. Wang, K. Yuan, Y. Tao, R. F. Chen, C. Zheng, X. H. Zhou, J. F. Li and W. Huang, *Chem. Commun.*, 2014, **50**, 15760–15763.
- 51 C. Romero-Nieto, S. Merino, J. Rodriguez-Lopez and T. Baumgartner, *Chem.-Eur. J.*, 2009, **15**, 4135–4145.
- 52 P. Kautny, D. Lumpi, Y. Wang, A. Tissot, J. Bintingier, E. Horkel, B. Stöger, C. Hametner, H. Hagemann, D. Ma and J. Fröhlich, *J. Mater. Chem. C*, 2014, **2**, 2069–2081.
- 53 A. Chaskar, H.-F. Chen and K.-T. Wong, *Adv. Mater.*, 2011, **23**, 3876–3895.
- 54 C. Adachi, M. A. Baldo, M. E. Thompson and S. R. Forrest, *J. Appl. Phys.*, 2001, **90**, 5048–5051.
- 55 Q. Zhang, B. Li, S. Huang, H. Nomura, H. Tanaka and C. Adachi, *Nat. Photonics*, 2014, **8**, 326–332.
- 56 H. Uoyama, K. Goushi, K. Shizu, H. Nomura and C. Adachi, *Nature*, 2012, **492**, 234–238.
- 57 M. J. Frisch, G. W. Trucks, H. B. Schlegel, G. E. Scuseria, M. A. Robb, J. R. Cheeseman, J. A. Montgomery Jr, T. Vreven, K. N. Kudin, J. C. Burant, J. M. Millam, S. S. Iyengar, J. Tomasi, V. Barone, B. Mennucci, M. Cossi, G. Scalmani, N. Rega, G. A. Petersson, H. Nakatsuji, M. Hada, M. Ehara, K. Toyota, R. Fukuda, J. Hasegawa, M. Ishida, T. Nakajima, Y. Honda, O. Kitao, H. Nakai, M. Klene, X. Li, J. E. Knox, H. P. Hratchian, J. B. Cross, V. Bakken, C. Adamo, J. Jaramillo, R. Gomperts, R. E. Stratmann, O. Yazyev, A. J. Austin, R. Cammi, C. Pomelli, J. W. Ochterski, P. Y. Ayala, K. Morokuma, G. A. Voth, P. Salvador, J. J. Dannenberg, V. G. Zakrzewski, S. Dapprich, A. D. Daniels, M. C. Strain, O. Farkas, D. K. Malick, A. D. Rabuck, K. Raghavachari, J. B. Foresman, J. V. Ortiz, Q. Cui, A. G. Baboul, S. Clifford, J. Cioslowski, B. B. Stefanov, G. Liu, A. Liashenko, P. Piskorz, I. Komaromi, R. L. Martin, D. J. Fox, T. Keith, M. A. Al-Laham, C. Y. Peng, A. Nanayakkara, M. Challacombe, P. M. W. Gill, B. Johnson, W. Chen, M. W. Wong, C. Gonzalez and J. A. Pople, *Gaussian 09, Revision A.02*, Gaussian, Inc., Wallingford CT, 2009.
- 58 J. Ohshita, M. Nodono, H. Kai, T. Watanabe, A. Kunai, K. Komaguchi, M. Shiotani, A. Adachi, K. Okita, Y. Harima, K. Yamashita and M. Ishikawa, *Organometallics*, 1999, **18**, 1453–1459.
- 59 Y. Ren, Y. Dienes, S. Hettel, M. Parvez, B. Hoge and T. Baumgartner, *Organometallics*, 2009, **28**, 734–740.
- 60 *SAINT and SADABS*, Bruker Analytical X-ray Instruments, Inc., Madison, WI, USA, 2008.
- 61 L. Palatinus and G. Chapuis, *J. Appl. Crystallogr.*, 2007, **40**, 786–790.
- 62 V. Petříček, M. Dušek and L. Palatinus, *Z. Kristallogr.*, 2014, **229**, 345.

2.3. Manuscript #3

Indolo[3,2,1-*jk*]carbazole based planarized CBP derivatives as host materials for PhOLEDs with low efficiency roll-off

Paul Kautny, Zhongbin Wu, Johanna Eichelter, Ernst Horkel, Berthold Stöger, Jiangshan Chen, Dongge Ma, Johannes Fröhlich, Daniel Lumpi

Organic Electronics, **2016**, 34, 237-245

Reproduced with the kind permission of Elsevier B. V.



Indolo[3,2,1-*jk*]carbazole based planarized CBP derivatives as host materials for PhOLEDs with low efficiency roll-off



Paul Kautny^{a,1}, Zhongbin Wu^{b,1}, Johanna Eichelter^a, Ernst Horkel^a, Berthold Stöger^c, Jiangshan Chen^{b,**}, Dongge Ma^b, Johannes Fröhlich^a, Daniel Lumpi^{a,*}

^a Institute of Applied Synthetic Chemistry, Vienna University of Technology, Getreidemarkt 9/163, A-1060 Vienna, Austria

^b State Key Laboratory of Polymer Physics and Chemistry, Changchun Institute of Applied Chemistry, Chinese Academy of Sciences, Changchun 130022, China

^c Institute of Chemical Technologies and Analytics, Vienna University of Technology, Getreidemarkt 9/164, A-1060 Vienna, Austria

ARTICLE INFO

Article history:

Received 11 January 2016

Received in revised form

18 April 2016

Accepted 21 April 2016

Keywords:

Blue PhOLED

High triplet energy

Low efficiency roll-off

Planarized CPB derivatives

Structure property relationship

ABSTRACT

Three novel planarized CPB derivatives (**ICzCz**, **ICzPCz**, **ICzICz**) have been synthesized and characterized concerning applications as host materials for PhOLEDs. The incorporation of fully planar indolo[3,2,1-*jk*]carbazole (ICz) in the CBP scaffold has been systematically investigated, revealing a significant impact on molecular properties, such as improved thermal stability ($t_g > 110$ °C), high triplet energies ($E_T > 2.81$ eV) and charge transport properties. Employing the newly developed materials as host materials, efficient green PhOLEDs (CE_{max} : 60.1 cd A⁻¹, PE_{max} : 42.1 lm W⁻¹, EQE_{max} : 15.9%) with a remarkably low efficiency roll-off of 5% at 1000 cd m⁻² as well as blue PhOLEDs (**ICzCz**) with a high PE of 26.1 lm W⁻¹ have been realized. Hence, the first comprehensive report on the application of ICz as integral building block for electroluminescent materials is presented, establishing this particular structural motive as versatile structural motive in this field.

© 2016 Elsevier B.V. All rights reserved.

1. Introduction

Starting with the groundbreaking work of Forrest et al., in 1998 [1,2], great efforts have been made in the development of phosphorescent organic light emitting diodes (PhOLEDs), due to their high internal quantum efficiency [3–8]. In contrast to fluorescent OLEDs, phosphorescent transition metal emitters harvest singlet and triplet excitons simultaneously. Therefore, PhOLEDs can theoretically achieve 100% internal quantum efficiency [9,10].

To avoid triplet-triplet annihilation at high current rates and consequently high concentrations of long living triplet excitons, phosphorescent emitters have to be widely dispersed in an organic host material [11,12]. Carbazole derivatives are among the most frequently employed host materials due to high triplet energies (E_T) and good charge transport properties [7]. Among those 4,4'-bis(9-carbazolyl)biphenyl (CBP - Scheme 1) has been widely utilized as

host material for various dopants in PhOLEDs [7,13]. However, CBP exhibits some major drawbacks, such as a low glass transition temperature (t_g : 62 °C) [14] and a low E_T (2.56 eV) [15] resulting in devices with inferior thermal stability [16] and inefficient energy transfer to high energy blue guest emitters [15,17]. Since the emission of blue light is inevitable for the application of PhOLEDs as lighting source many modifications have been suggested to overcome the intrinsic drawbacks of CBP. The main strategies focus on the interruption of the conjugated π -system in order to retain high E_T s and can be divided into three categories: (i) incorporation of a saturated carbon- or heteroatom-bridge [18–21]; (ii) sterically induced torsion [22–24] and (iii) shortening of the π -system [24–27].

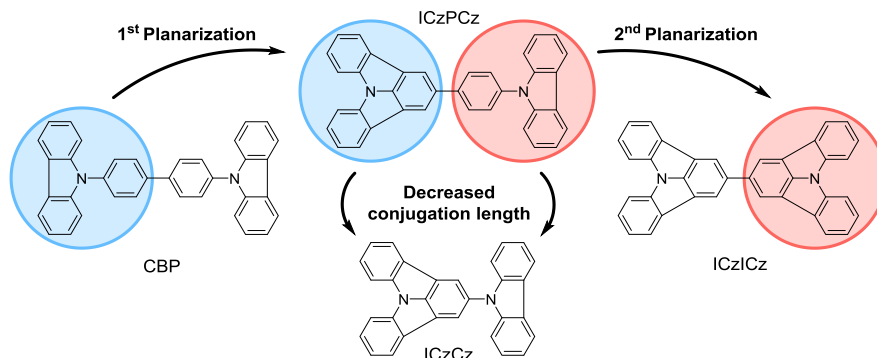
Recently, our group introduced the application of fully planar indolo[3,2,1-*jk*]carbazole (ICz) as electron donating moiety in bipolar host materials [28,29]. Inspired by our initial findings we aimed to further incorporate the ICz building block into the CBP scaffold benefitting from the effects of systematic planarization of the triarylamine moiety. Hence, the study reveals a novel design strategy for unipolar opto-electronic materials yielding thermally stable CBP derivatives in combination with high E_T values. Particularly recent improvements in synthetic accessibility of the ICz

** Corresponding author.

* Corresponding author.

E-mail addresses: jschen@ciac.ac.cn (J. Chen), daniel.lumpi@tuwien.ac.at (D. Lumpi).

¹ Contributed equally to this work.



Scheme 1. Schematized molecular design of target materials **ICzCz**, **ICzPCz** and **ICzICz** by gradual planarization of the phenylcarbazole moieties.

moiety [28,30] elevate the relevance of revealing the application scope ICz based materials.

2. Materials and methods

2.1. General information

All reagents and solvents were purchased from commercial suppliers and used without further purification. Anhydrous solvents were prepared by filtration through drying columns. Column chromatography was performed on silica 60 (Merck, 40–63 μm). NMR spectra were recorded on a Bruker Avance DRX-400 Spectrometer. A Thermo Scientific LTQ Orbitrap XL hybrid FTMS (Fourier Transform Mass Spectrometer) equipped with a Thermo Fischer Exactive Plus Orbitrap (LC-ESI+) and a Shimadzu IT-TOF Mass Spectrometer were used for high resolution mass spectrometry. Thermogravimetric (TG) and differential scanning calorimetry (DSC) measurements were carried out with a heating rate of 5 K/min in a flowing argon atmosphere (25 ml/min). For the TG measurements, a Netzsch TG 209 F9 Tarsus system with open aluminium oxide crucibles was used. For the DSC measurements, a Netzsch DSC 200 F3 Maia, working with aluminium pans with pierced lids, was employed. UV/Vis absorption and fluorescence emission spectra were recorded in DCM solutions (5 μM) with a Perkin Elmer Lambda 750 spectrometer and an Edinburgh FLS920, respectively. Time resolved low temperature phosphorescence spectra were recorded in solid solutions (1 mg/ml; toluene:EtOH = 9:1) at 77 K with a Perkin Elmer Instruments LS 50B luminance spectrometer. Cyclic voltammetry was performed using a three electrode configuration consisting of a Pt working electrode, a Pt counter electrode and an Ag/AgCl reference electrode and a PGSTAT128N, ADC164, DAC164, External, DI048 potentiostat provided by Metrohm Autolab B.V. Measurements were carried out in a 0.5 mM solution in anhydrous DCM with Bu_4NBF_4 (0.1 M) as supporting electrolyte. The solutions were purged with nitrogen for 15 min prior to measurement. HOMO energy levels were calculated from the onset of the oxidation peaks. The onset potential was determined by the intersection of two tangents drawn at the background and the rising of the oxidation peaks.

2.2. Synthetic details

2-Bromoindolo[3,2,1-*jk*]carbazole (**1**) [31], 9-[4-(4,4,5,5-tetramethyl-1,3,2-dioxaborolan-2-yl)phenyl]-9*H*-carbazole (**3**) [32] and 2-(4,4,5,5-tetramethyl-1,3,2-dioxaborolan-2-yl)indolo[3,2,1-*jk*]carbazole (**4**) [31] were synthesized according to previously published procedures whereas 9*H*-carbazole (**2**) was purchased by Apollo Scientific and used without further purification.

ICzCz. The synthesis of **ICzCz** was accomplished analogously to a published procedure [33]. **1** (3.20 g, 10.0 mmol, 1.00 eq.), **2** (2.50 g, 15.0 mmol, 1.50 eq.), K_2CO_3 (2.07 g, 15.0 mmol, 1.5 eq.) and $\text{CuSO}_4 \cdot 5\text{H}_2\text{O}$ (0.13 g, 0.5 mmol, 0.05 eq.) were ground and placed in a teflon autoclave, which was subsequently heated at 230 $^\circ\text{C}$ for 70 h. After cooling the solid was partitioned between CH_2Cl_2 and water and the aqueous phase was extracted with CH_2Cl_2 . The combined organic layers were dried over anhydrous Na_2SO_4 and concentrated *in vacuo*. **ICzCz** (2.45 g, 6.0 mmol, 60%) was isolated after column chromatography (light petrol: CH_2Cl_2 = 80:20 \rightarrow 50:50) as a yellowish white solid. ^1H NMR (400 MHz, CD_2Cl_2): δ = 8.24–8.20 (m, 4H), 8.16 (d, J = 7.7 Hz, 2H), 8.03 (d, J = 8.1 Hz, 2H), 7.65 (dd, J = 7.8, 7.8 Hz, 2H), 7.45–7.37 (m, 6H), 7.32 (ddd, J = 7.7, 6.6, 1.5 Hz, 2H) ppm. ^{13}C NMR (100 MHz, CD_2Cl_2): δ = 143.4 (s), 143.0 (s), 139.9 (s), 133.4 (s), 130.3 (s), 128.1 (d), 126.5 (d), 124.0 (d), 123.6 (s), 122.7 (d), 120.8 (d), 120.4 (d), 120.2 (d), 119.7 (s), 113.1 (d), 110.4 (d) ppm. Calculated: m/z 406.14645 $[\text{M}]^+$, 407.15428 $[\text{M}+\text{H}]^+$. Found: MS (ESI): m/z 406.14550 $[\text{M}]^+$, 407.15346 $[\text{M}+\text{H}]^+$.

ICzPCz. The Suzuki cross-coupling reaction towards **ICzPCz** was performed under an argon atmosphere. **1** (1.54 g, 4.80 mmol, 1.00 eq.) and boronic acid ester **3** (2.22 g, 6.00 mmol, 1.25 eq.) were dissolved in degassed THF (90 ml). Subsequently, 6 ml degassed aqueous K_2CO_3 (1.66 g, 12.00 mmol, 2.50 eq.) solution and $\text{Pd}(\text{PPh}_3)_4$ (0.28 g, 0.24 mmol, 0.05 eq.) were added and the reaction mixture was refluxed for 23 h (TLC). The solution was poured on water and repeatedly extracted with CH_2Cl_2 . The combined organic layers were dried over anhydrous Na_2SO_4 and concentrated under reduced pressure. **ICzPCz** (1.38 g, 2.86 mmol, 60%) was isolated after column chromatography (light petrol: CH_2Cl_2 = 80:20 \rightarrow 50:50) as a white solid. ^1H NMR (400 MHz, CD_2Cl_2): δ = 8.40 (s, 2H), 8.25 (d, J = 7.7 Hz, 2H), 8.19 (d, J = 7.7 Hz, 2H), 8.04 (d, J = 8.1 Hz, 2H), 7.98 (d, J = 8.1 Hz, 2H), 7.74 (d, J = 8.1 Hz, 2H), 7.63 (dd, J = 7.6, 7.7 Hz, 2H), 7.56 (d, J = 8.1 Hz, 2H), 7.49–7.41 (m, 4H), 7.33 (dd, 7.5, 7.3 Hz, 2H) ppm. ^{13}C NMR (100 MHz, CD_2Cl_2): δ = 144.3 (s), 143.0 (s), 141.5 (s), 139.8 (s), 137.2 (s), 136.8 (s), 130.5 (s), 130.1 (d), 127.9 (d), 127.7 (d), 126.6 (d), 123.9(2) (s), 123.8(6) (d), 122.5 (d), 120.8 (d), 120.5 (d), 119.8 (d), 119.3 (s), 113.0 (d), 110.4 (d) ppm. Calculated: m/z 482.17775 $[\text{M}]^+$, 483.18558 $[\text{M}+\text{H}]^+$. Found: MS (ESI): m/z 482.17699 $[\text{M}]^+$, 483.18510 $[\text{M}+\text{H}]^+$.

ICzICz. The Suzuki cross-coupling reaction towards **ICzICz** was performed under an argon atmosphere. **1** (1.54 g, 4.80 mmol, 1.00 eq.) and boronic acid ester **4** (2.20 g, 6.00 mmol, 1.25 eq.) were dissolved in degassed THF (90 ml). Subsequently, 6 ml degassed aqueous K_2CO_3 (1.66 g, 12.00 mmol, 2.50 eq.) solution and $\text{Pd}(\text{PPh}_3)_4$ (0.28 g, 0.24 mmol, 0.05 eq.) were added and the reaction mixture was refluxed 46 h (TLC). The precipitate was filtered and washed with THF and water. The filtrate and the aqueous phase

were combined resulting in further precipitation and filtered again. The solid was dissolved in CH_2Cl_2 , the solution dried over anhydrous Na_2SO_4 and concentrated under reduced pressure yielding **ICzICz** (2.00 g, 4.16 mmol, 87%) as a white solid. ^1H NMR (400 MHz, CD_2Cl_2): δ = 8.46 (s, 4H), 8.25 (d, J = 7.6 Hz, 4H), 8.00 (d, J = 8.0 Hz, 4H), 7.63 (dd, J = 8.0, 7.6 Hz, 4H), 7.42 (dd, J = 7.6, 7.6 Hz, 4H) ppm. ^{13}C NMR (100 MHz, CD_2Cl_2): δ = 143.9 (s), 140.3 (s), 139.8 (s), 130.7 (s), 127.5 (d), 123.8 (d), 122.4 (d), 120.9 (d), 119.2 (s), 113.0 (d) ppm. Calculated: m/z 480.16210 $[\text{M}]^+$, 481.16993 $[\text{M}+\text{H}]^+$. Found: MS (ESI): m/z 480.16120 $[\text{M}]^+$, 481.16977 $[\text{M}+\text{H}]^+$.

2.3. Computational details

All (TD)DFT computations were performed using the Gaussian 09 package, revision D.01 [34]. Density functional theory (DFT) and time-dependent (TD)DFT calculations were performed using the Becke three parameters hybrid functional with Lee–Yang–Perdew correlation (B3LYP) [35,36], in combination with Pople basis sets (6–31G*, 6–311 + G*) [37]. Geometry optimizations were performed in gas phase and without symmetry constraints. For the calculation of HOMO/LUMO levels, ground state (S_0) geometries were optimized applying the 6–311 + G* basis set. The determination of triplet energy (E_T) was achieved by the calculation of the T_1 excitation energy applying TDDFT level and the 6–311 + G* basis to a S_0 geometry optimized at DFT level using the 6–31G* basis set. Orbital plots were generated using GaussView [38].

2.4. Single crystal diffraction

A crystal of **ICzCz** suitable for single crystal diffraction was selected under a polarizing microscope, embedded in perfluorinated oil and attached to Kapton[®] micromounts. Intensity data were collected in a dry stream of nitrogen at 100 K on a Bruker KAPPA APEX II diffractometer system. Data were reduced using SAINT-Plus [39] and an empirical absorption correction using the multi-scan approach implemented in SADABS [39] was applied. The crystal structures were solved by charge-flipping implemented in SUPERFLIP [40] and refined against F with the JANA2006 [41] software package. The non-H atoms were refined with anisotropic displacement parameters. The H atoms were placed at calculated positions and refined as riding on the parent C atoms.

2.5. Device fabrication and measurement

All the devices were fabricated on glass substrates pre-coated with 180 nm indium tin oxide (ITO) with a sheet resistance of 10 Ω per square. The ITO substrates were degreased in an ultrasonic solvent bath and then dried at 120 °C for 30 min. Before loaded into the deposition chamber, the ITO surface was treated with UV-ozone for 15 min. All layers were grown in succession by thermal evaporation without breaking the vacuum ($<5 \times 10^{-4}$ Pa). The device structures were described in the text. The organic materials and metal oxide were evaporated at the rate in a range of 1–2 $\text{\AA}/\text{s}$, and the metals were evaporated at the rate of 8–10 $\text{\AA}/\text{s}$. The overlap between ITO and Al electrodes was 4 mm \times 4 mm which is the active emissive area of the devices. Current–voltage–brightness characteristics were measured by using a Keithley source measurement unit (Keithley 2400 and Keithley 2000) with a calibrated silicon photodiode. The EL spectra were measured on a Spectrascan PR650 spectrophotometer. EQEs were calculated from the luminance, current density, and EL spectrum, assuming a Lambertian distribution. All the measurements were carried out in ambient atmosphere.

3. Results and discussion

3.1. Molecular design

The aim of this work is to investigate the effects of a gradual planarization of the phenylcarbazole moieties of CBP on photo-physical and electrochemical properties of the resulting materials. Starting from CBP, the planarization of one phenylcarbazole yields **ICzPCz** and the introduction of a second ICz group leads to twofold planarized **ICzICz**, which has been identified as dimeric product upon electrochemical oxidation of ICz [42] previously. Moreover, shortening the conjugated π -system of **ICzPCz** by removal of one phenyl unit results in **ICzCz**, which can be regarded as a planarized *para* derivative of mCP (Scheme 1).

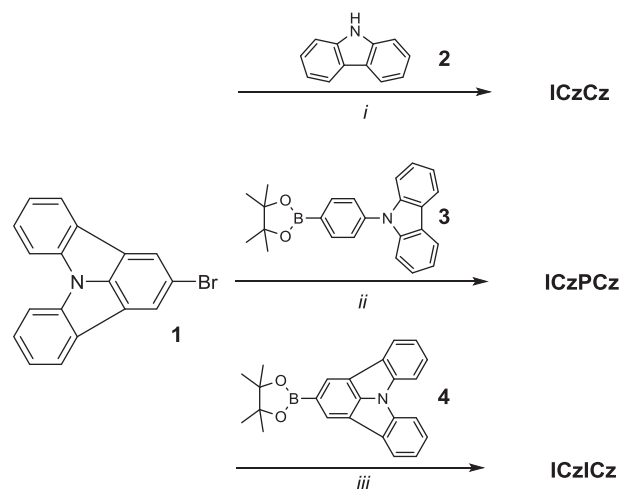
3.2. Synthesis

The synthetic approach toward **ICzCz**, **ICzPCz** and **ICzICz** is outlined in Scheme 2. **ICzCz** was obtained in 60% yield via Ullmann condensation of bromoindolocarbazole **1** and carbazole **2** in the presence of $\text{CuSO}_4 \cdot 5\text{H}_2\text{O}$ and K_2CO_3 . The synthesis of **ICzPCz** and **ICzICz** was accomplished in a Suzuki cross-coupling reaction employing **1** and the corresponding boronic acid esters **3** and **4**.

The chemical identity of the three title compounds was confirmed by ^1H and ^{13}C NMR measurements as well as high resolution mass spectroscopy. Additionally, single crystals of **ICzCz** [43] suitable for X-ray diffraction (Fig. 1) were grown from a CD_2Cl_2 solution by slow evaporation of the solvent at room temperature. The ICz moiety is virtually planar [maximum distance from the least squares (LS) planes: 0.043(2) \AA for C29]. The carbazole and ICz moieties are distinctly inclined [angle between LS planes: 54.07(5) $^\circ$].

3.3. Thermal properties

Thermal properties of the compounds were investigated by DSC and TGA (see supplementary material). All materials feature high thermal stability with decomposition temperatures (corresponding to 5% mass loss) higher than 344 °C. During DSC runs **ICzCz** and **ICzPCz** exhibited t_g values of 111 °C and 119 °C which are



Scheme 2. Synthetic approach toward **ICzCz**, **ICzPCz** and **ICzICz**. i: **1** (1 eq.), **2** (1.5 eq.), K_2CO_3 (2.5 eq., 2 M aqueous solution), $\text{CuSO}_4 \cdot 5\text{H}_2\text{O}$ (0.05 eq.), 230 °C, 70 h, 60%; ii: **1** (1 eq.), **3** (1.25 eq.), $\text{Pd}(\text{PPh}_3)_4$ (0.05 eq.), K_2CO_3 (2.5 eq., 2 M aqueous solution), THF, reflux, 23 h, 60%; iii: **1** (1 eq.), **4** (1.25 eq.), $\text{Pd}(\text{PPh}_3)_4$ (0.05 eq.), K_2CO_3 (2.5 eq.), THF, reflux, 46 h, 87%.

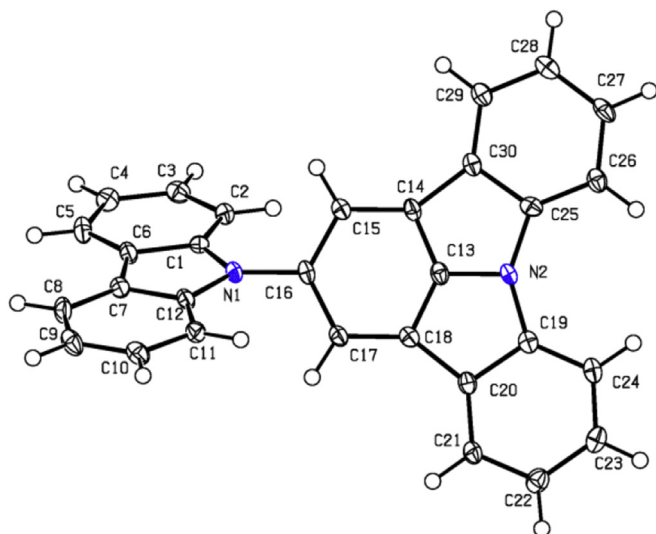


Fig. 1. Molecular structure of **ICzCz**; C and N atoms are represented by white and blue ellipsoids drawn at 50% probability levels, H atoms by spheres of arbitrary radius [44].

significantly higher compared to CBP (62 °C) [14]. The increased t_g values can be attributed to the high rigidity of the ICz motive. No t_g was observed in the case of **ICzICz** below the melting point 383 °C (decomposition).

3.4. Photophysical properties

To investigate the effects of the conducted molecular modifications on photophysical properties, UV/Vis absorption, photoluminescence as well as low temperature delayed photoluminescence were recorded. The spectra are displayed in Fig. 2. The compounds feature related absorption behavior with absorption onsets at 395 (**ICzCz**), 387 (**ICzPCz**) and 387 nm (**ICzICz**), corresponding to optical band gaps of 3.14, 3.21 and 3.21 eV, respectively. Compared to CBP (3.52 eV; see [supplementary material](#)) band gaps are reduced by more than 0.3 eV due to the lower band gap of the ICz building block in relation to phenylcarbazole [45], which benefits the fabrication of PhOLED devices with low driving voltage and high power efficiencies. All materials exhibit distinct absorption around 375 nm, which is attributed to the ICz motive. Furthermore, weak transitions at approximately 342 and 328 nm, typical values for phenylcarbazole derivatives [45], were observed for **ICzCz** and **ICzPCz**. Analogously, slightly blue-shifted absorption bands were found for **ICzICz** as shoulders at 332 and 316 nm. Prominent peaks below 300 nm are attributed to the $\pi-\pi^*$ transitions of the carbazole and/or ICz moieties [31,46]. Notably, in **ICzICz** the peak maximum at 292 nm is red-shifted compared to the other congeners; for **ICzCz** and **ICzPCz** this ICz derived transition is observed as shoulder in the absorption spectra. The corresponding carbazole related bands are located at lower wavelength.

ICzCz, **ICzPCz** and **ICzICz** exhibit photoluminescence with peak maxima at 404.5, 385.5 and 406 nm, respectively. Whereas **ICzCz** features unstructured emission, weak shoulders were observed at higher energies in the spectra of **ICzPCz** and **ICzICz**.

In order to gain insight into the photophysical properties of the potential host materials in the solid state, thin films were subjected to UV/Vis absorption and photoluminescence measurements (see [supplementary material](#)). Compared to measurements in solution absorption onsets are systematically red-shifted by approximately 10–20 nm due to intermolecular interactions. Emission spectra of

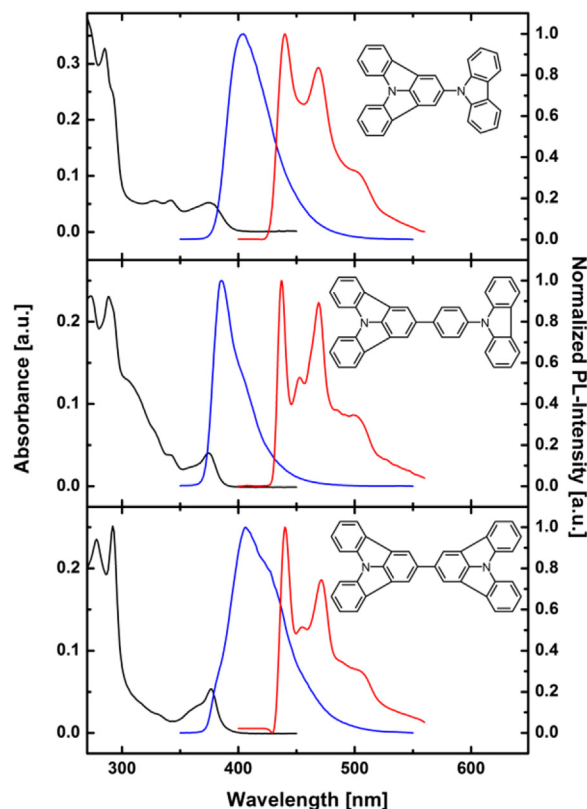


Fig. 2. UV–Vis absorption (black), normalized fluorescence spectra at room temperature (blue) and normalized phosphorescence spectra at 77 K (red) of **ICzCz** (top), **ICzPCz** (middle) and **ICzICz** (bottom). (For interpretation of the references to colour in this figure legend, the reader is referred to the web version of this article.)

thin films display a more diverse behavior. Whereas the emission of **ICzCz** is virtually identical in thin film and solution (peak maxima at 407 nm), thin film emission is slightly red-shifted in the case of **ICzPCz** (18.5 nm) and distinctly red-shifted for **ICzICz** (51 nm). Furthermore, additional low energy emission, indicating excimer formation upon photoexcitation, was observed around 550 nm, whereupon the intensity of this emission band increases from **ICzCz** to **ICzPCz** to **ICzICz**. These findings clearly indicate that the degree of excimer formation decreases in the order **ICzCz** < **ICzPCz** < **ICzICz**, which is in agreement with the tendency of planarized π -systems to aggregate in the solid state [47].

In contrast to room temperature fluorescence delayed phosphorescence spectra at 77 K exhibit well resolved vibronic peaks. Triplet energies calculated from the highest energy vibronic transition are 2.84, 2.82 and 2.82 eV for **ICzPCz**, **ICzCz** and **ICzICz**, respectively, which are significantly higher compared to CBP (2.56 eV) [15] and allow for the application of the developed ICz-hosts in blue PhOLED devices. Notably, the new host materials display a very low singlet-triplet energy splitting in the range of 0.28–0.39 eV. In fact, this is a particularly desirable feature, owing to a reduction of thermal losses during exciton transfer from the host to phosphorescent dopants retaining high power efficiency and enabling low driving voltage [8,48,49].

3.5. Electrical properties

The HOMO energy levels of the compounds were determined by cyclic voltammetric (CV) measurements (Fig. 3). All compounds exhibit irreversible oxidation, typically for carbazole and ICz materials [42,50]. HOMO levels were estimated from the onset of the

oxidation peak relative to ferrocene and are located at -5.56 eV for **ICzCz** and **ICzPCz**. However, in the case of **ICzICz** the HOMO is distinctly shifted to higher energy (-5.39 eV). A possible explanation for this unexpected electro-chemical behavior is given by DFT calculations (*vide infra*). LUMO levels were calculated from HOMOs and the optical bandgap determined from the UV/Vis absorption onset. The LUMO energy levels of **ICzCz** and **ICzPCz** are located at -2.42 and -2.35 eV, respectively, indicating no significant charge injection barriers from adjacent electron transporting layers. As a result of the increased HOMO level of **ICzICz** also the LUMO level is shifted to higher energy (-2.18 eV). The relevant photophysical and electrochemical data is summarized in Table 1.

3.6. Theoretical calculations

In order to provide a more detailed insight into the electronic properties of the developed materials at the molecular level, density functional theory (DFT) and time-dependent DFT (TDDFT) calculations were conducted using the Gaussian 09 software package [34]. Predicted HOMO and LUMO levels as well as E_T values are in good agreement with experimental data (Table 1). LUMO levels exhibit a systematic shift towards higher energies. Nevertheless, the tendency of increasing orbital energy from **ICzCz** to **ICzPCz** and **ICzICz** is reproduced by theoretical calculations.

The spatial distributions of HOMOs and LUMOs are significantly different in the investigated molecules (Fig. 4). Host materials **ICzCz** and **ICzPCz**, consisting of one indolocarbazole and carbazole moiety, feature distinctive separation of the HOMO and LUMO. Owing to the decreased donor strength of ICz [31], the LUMO is exclusively located on this particular molecular subunit in both compounds. Accordingly, the HOMO level spreads over the carbazole/phenyl-carbazole and extends to some degree to the adjacent phenyl ring and nitrogen atom of the ICz. In this regard, although both subunits are arylamines, the carbazole acts as donor group, whereas ICz exhibits slight acceptor properties, a feature that has previously been observed in bipolar host materials by our groups [31]. In contrast the frontier molecular orbitals are uniformly distributed over the entire molecule in symmetric **ICzICz**. These findings are consistent with the electrochemical analysis of the materials and determine the energetic location of the orbitals. Whereas the HOMO of **ICzCz** and **ICzPCz** are located at -5.56 eV, typical for materials with electronically isolated carbazole groups [24,31,51,52], the HOMO level of **ICzICz** at -5.39 eV is increased due to a higher degree of delocalization.

Furthermore, the torsion angle between the planar subunits is a crucial parameter influencing intermolecular interaction in thin films [47]. Although geometry optimization of the molecules is

carried out in the gas phase, the observed tendencies can be extrapolated to the solid state. Notably, the calculated torsion angle between the carbazole and ICz subunit in **ICzCz** is 73° and therefore significantly higher compared to the torsion angle between the indolocarbazoles in **ICzICz** (48°). This behavior can be attributed to the increased steric demand of the carbazole protons at C2 and C11 *meta* to the nitrogen atom (Fig. 1), which is not present in the case of ICz due to an altered annulation pattern. Analogously, the calculated torsion angle between the carbazole and the phenylene linker in **ICzPCz** is larger (61°) than between the phenylene linker and the ICz (42°). These results suggest an increased likelihood of intermolecular interaction of **ICzICz** molecules in the solid state compared to the other derivatives as consequence of a more planar overall molecular alignment [47], which is in line with enhanced excimer formation observed in **ICzICz** thin films (see supplementary material).

3.7. Electroluminescent properties

At first the applicability of the compounds as host materials in green PhOLEDs with the device architecture of ITO/MoO₃/TCTA: MoO₃ (20%, 50 nm)/TCTA (20 nm)/EML (20 nm)/BmPyPB (45 nm)/LiF/Al has been evaluated, whereby the EML was made up from 8 wt% green emitting Ir(ppy)₂(acac) doped into **ICzCz** (**GI**), **ICzPCz** (**GII**) or **ICzICz** (**GIII**). TCTA was used as a hole transporting layer and BmPyPB was employed as an electron transporting and hole blocking layer. Current density-voltage-luminance and current efficiency-luminance-power efficiency curves of device **GI-III** are displayed in Fig. 6 and key electroluminescent parameters are summarized in Table 2. Energy level diagrams of all devices are provided in the supplementary material. Exclusively green emission from Ir(ppy)₂(acac) was observed in all devices indication energy transfer from the host to the dopant (Fig. 5).

Devices **GI** and **GII** displayed similar performance, featuring high maximum current efficiencies (CE) of 60.1 cd A⁻¹ and 56.3 cd A⁻¹, maximum power efficiencies (PE) of 36.5 lm W⁻¹ and 35.4 lm W⁻¹ and maximum external quantum efficiencies (EQE) of 15.9 and 14.8% , respectively. However, it has to be noted that CBP based PhOLEDs with the same devices architecture exhibited higher efficiency (CE_{max}: 84.7 cd A⁻¹; Supplementary Material). Nonetheless, **GI** and **GII** displayed satisfying characteristics and more notably both devices exhibited remarkably low efficiency roll-off. At a brightness of 1000 cd m⁻², relevant for practical applications, the CEs of **GI** and **GII** were still as high as 57.2 cd A⁻¹ and 53.8 cd A⁻¹, corresponding to a negligible efficiency roll-off of 4–5%. Even at a high luminance of 5000 cd m⁻² the devices reached CEs of 54.1 cd A⁻¹ (**GI**; 10% roll-off) and 51.6 cd A⁻¹ (**GII**; 8% roll-off). The observed efficiency roll-off is lower than for the corresponding CBP based device and can be explained by the partial bipolar character of **ICzCz** and **ICzPCz** as suggested by the theoretical calculations. In contrast, the electroluminescent performance of device **GIII** was distinctly lower and the **ICzICz** based PhOLED reached a CE_{max} of 32.9 cd A⁻¹, a PE_{max} of 23.0 lm W⁻¹ and an EQE_{max} of 8.7%.

Subsequently, the ICz derivatives were probed as host materials for blue emitting FIrPic, according to the high E_T s of the materials. However, blue emission from FIrPic could not be observed in devices employing **ICzPCz** and **ICzICz** as host materials for the phosphorescent dopant. Exclusively **ICzCz** based device **BI** with the architecture of ITO/MoO₃/TAPC (60 nm)/mCP (5 nm)/**ICzCz**: FIrPic (20 nm, 20%)/TmPyPB (30 nm)/LiF/Al displayed the expected emission as displayed in Fig. 7. TAPC was employed as hole transporting layer, owing to its higher hole mobility rate compared to TCTA [53] and mCP functions as exciton blocking layer because of its high E_T [25]. TmPyPB instead of BmPyPB was used as electron

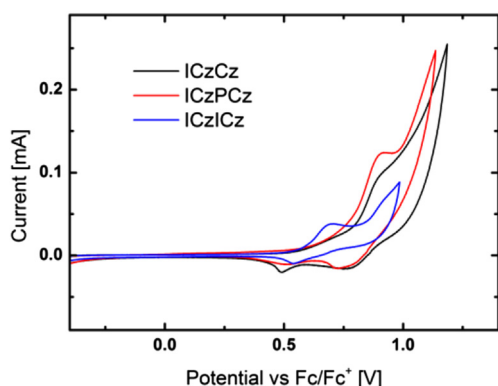


Fig. 3. CV curves of **ICzCz**, **ICzPCz** and **ICzICz**.

Table 1
Physical data of target materials.

	$T_g/T_{rc}/T_m/T_d$ [°C] ^a	Opt. BG [eV] ^{b,c}	$\lambda_{PL,max}$ [nm] ^c	HOMO/LUMO [eV]		E_T (eV)	
				exp. ^d	cal. ^e	exp. ^f	cal. ^g
ICzCz	111/156/253/344	3.14	404.5	−5.56/−2.42	−5.60/−1.91	2.82	2.87
ICzPCz	119/165/262/385	3.21	385.5	−5.56/−2.35	−5.60/−1.81	2.84	2.91
ICzICz	n.o. ^h /n.o. ^h /383 ⁱ /408	3.21	406.0	−5.39/−2.18	−5.62/−1.71	2.82	2.91

^a Determined from DSC/TGA analysis; T_{rc} : recrystallization temperature.

^b Determined from the absorption onset.

^c Measured in DCM (5 μ M) at r.t.

^d HOMO levels were calculated from the onset of the oxidation peak. CV-measurements were carried out in a 0.5 mM solution in anhydrous DCM with Bu₄NBF₄ (0.1 M) as supporting electrolyte; LUMO levels were calculated from HOMO levels and the optical bandgap.

^e Calculated applying density functional theory level (B3LYP/6–311 + G*).

^f Estimated from the highest energy vibronic transition in solid solutions of toluene/EtOH (9:1) at 77 K.

^g Calculated applying the time-dependent density functional theory level (B3LYP/6–311 + G*).

^h Not observed.

ⁱ Melts under decomposition.

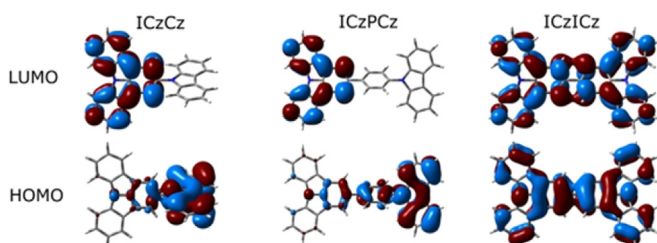


Fig. 4. Spatial distribution of HOMOs and LUMOs of the developed materials.

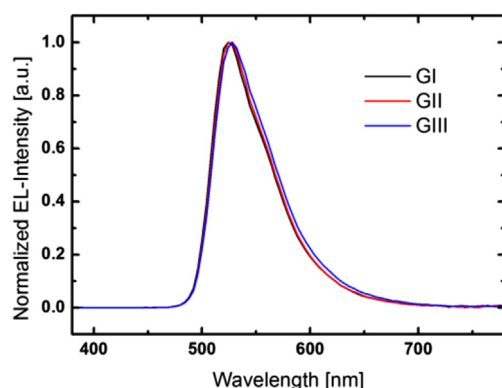


Fig. 5. Electroluminescence spectra of **GI**, **GI** and **GIII** at a driving voltage of 10 V.

transporting layer for **BI** due to its slightly higher E_T [6].

The surprising lack of FlrPic emission in devices with **ICzPCz** and **ICzICz** as host materials may be explained by the formation of excimers of the hosts in the emitting layer as result of the highly planar structure of the ICz moiety. Indeed red-shifted emission was observed in FlrPic doped **ICzICz** films (Figure S14). These excimers can act as triplet trapping sites, due to their low E_T and thus inhibit the confinement of triplet excitons on the phosphorescent emitter [54,55]. Notably, the tendency of **ICzPCz** and **ICzICz** to form excited dimers in the solid state is higher compared to **ICzCz** as suggested by thin film photoluminescence (see supplementary material). This fact is in line with the finding that FlrPic derived emission was exclusively observed in **BI** employing **ICzCz** as host materials. Among the three ICz derivatives **ICzICz** exhibits the highest tendency to aggregate in combination with red-shifted thin film emission (*vide supra*). Therefore, the high concentration of low triplet states in **ICzICz** thin films may not only impact blue devices

but also impedes the energy transfer to green emitting Ir(ppy)₂(acac) in **GIII** and represents a possible explanation for the decreased efficiency of **GIII** compared to **GI** and **GII**. In contrast to FlrPic doped films the emission in **GIII** exclusively originates from the dopant. However, the energy of excimer emission of **ICzICz** is close to the emission of Ir(ppy)₂(acac). Thus, energy transfer from emissive excimer states to Ir(ppy)₂(acac) is reasonable. However, the presence of non-emissive low lying triplet states could significantly decrease the emission efficiency. Intermolecular interactions of carbazole derived materials in thin films have recently been investigated and strongly depend on interchromophoric distances, a feature that can be efficiently addressed by subtle molecular modification [55]. This strategy can likewise be adapted to ICz based materials in order to minimize excimer formation.

Nevertheless, device **BI** showed a high performance with a CE_{max} of 32.8 $cd A^{-1}$ and an EQE_{max} of 14.0%. Analogously to the green devices, **BI** exhibited low efficiency roll-off retaining a CE of 29.4 $cd A^{-1}$ (10% roll-off) and 26.5 $cd A^{-1}$ (19% roll-off) at 1000 $cd m^{-2}$ and 5000 $cd m^{-2}$, respectively. Most notably device **BI** also featured a high PE_{max} of 26.1 $lm W^{-1}$. To the best of our knowledge, this value is among the highest compared to other biscarbazole derivatives connecting *via* the N atoms without an electron withdrawing subunit (Table 3). The high PE of **BI** is attributed to the small HOMO-LUMO gap and reduced singlet-triplet splitting of **ICzCz** compared to other CBP derivatives, thus allowing for efficient charge injection into the emitting layer and minimizing thermal energy losses upon exciton formation and energy transfer to FlrPic [8,48,49].

4. Conclusion

In this study the impact of incorporating fully planar indolo [3,2,1-*jk*]carbazole in the CBP scaffold has been systematically investigated. This strategy significantly improved the molecular properties of the target materials leading to: (i) better thermal stability owing to the rigid layout of the ICz motive; (ii) increased E_T s and low singlet-triplet splitting enabling the application as host materials in blue PhOLEDs with high PE; (iii) low efficiency roll-off at high brightness, which is attributed to the chemical structure incorporating both the ICz and Cz moiety in one molecule. With these results the applicability of the ICz as universal building block for functional organic materials is being established. Further work will focus on controlling the intermolecular interactions of ICz based materials in the solid state by molecular design for the development of highly efficient ICz based materials for electroluminescent devices.

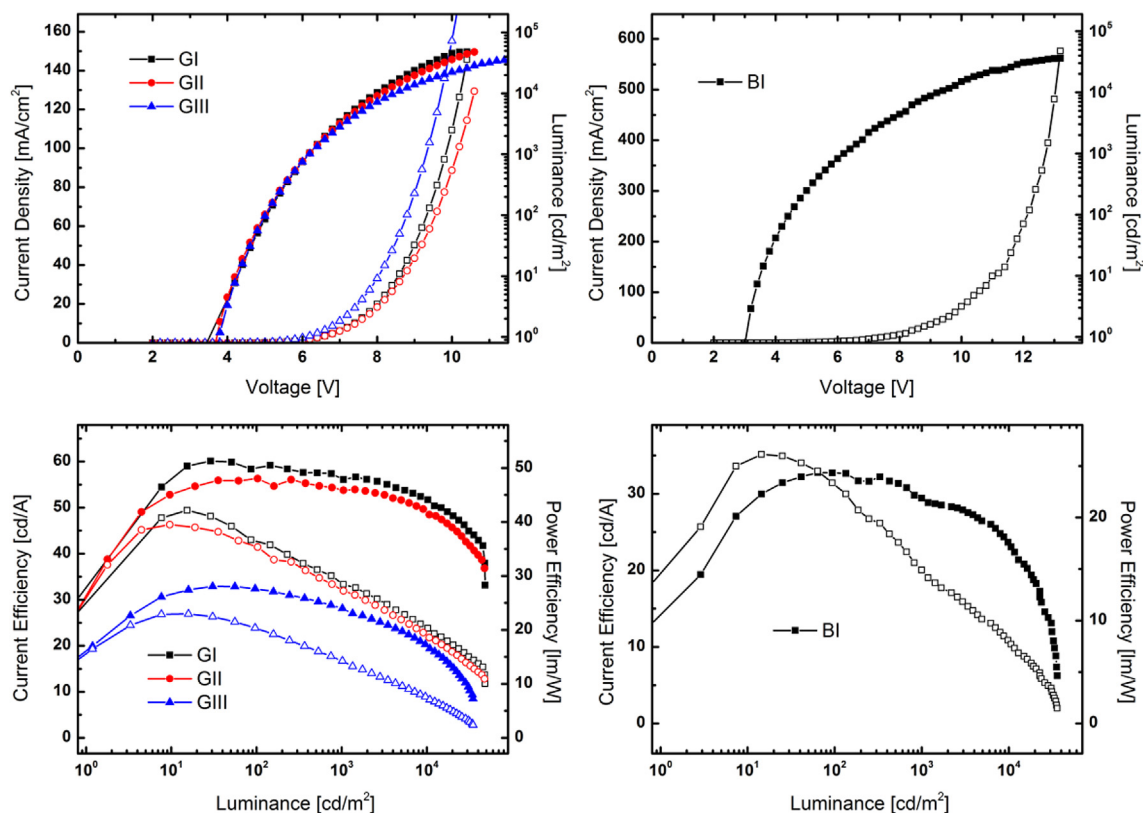


Fig. 6. Current density–voltage–luminance (hollow symbols: current density; full symbols: luminance) and current efficiency–luminance–power efficiency (full symbols: current efficiency; hollow symbols: power efficiency) curves of devices **GI–III** and **BI**.

Table 2
Electroluminescent properties of devices **GI–III** and **BI**.

	V_{on} [V]	CE [cd A^{-1}] ^a	PE [lm W^{-1}] ^a	EQE [%] ^a
GI	3.8	58.5/57.2/54.1/60.1	36.5/28.5/23.5/42.1	15.6/14.9/14.2/15.9
GII	3.8	56.3/53.8/51.6/56.3	35.4/27.2/21.9/39.5	14.8/14.1/13.5/14.8
GIII	3.8	32.4/28.1/23.5/32.9	20.3/14.1/9.6/23.0	8.6/7.4/6.1/8.7
BI	3.2	32.7/29.4/26.5/32.8	23.4/14.9/10.1/26.1	14.0/12.7/11.4/14.0

^a Measured at a brightness of 100 cd m^{-2} /1000 cd m^{-2} /5000 cd m^{-2} /max.

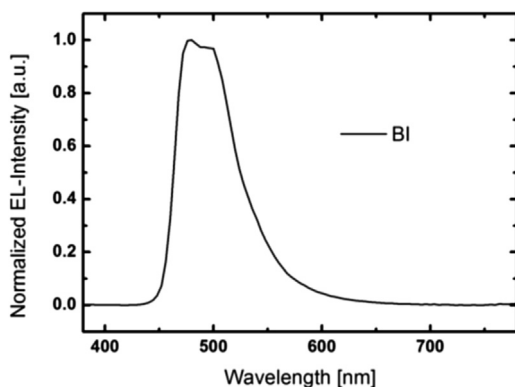


Fig. 7. Electroluminescence spectra of **BI** at a driving voltage of 10 V.

Table 3
Physical properties and device performance of FIrPic devices based on selected CBP derivatives.^a

Host	T_g [°C]	E_T [eV]	PE [lm W^{-1}] ^b	EQE [%] ^b	Ref.
CBP	62 [14]	2.56	6.3	5.7	[15]
mCP	60 [7]	2.90	9.3	12.3	[26]
CDBP	–	3.0	10.5	10.4	[22]
3CZPBP	110	–	17.3	16.5	[23]
o-CBP	82	3.00	25.3	14.2	[24]
CBPE	81	3.01	5.1	–	[20]
DCz	–	2.95	15.0	9.8	[19]
CTP-3	113	2.81	25.6	15.4	[27]
DCB	–	2.95	–	5.8	[18]
ICzCz	111	2.82	26.1	14.0	This work

^a Only CBP derivatives featuring two carbazole moieties connecting *via* the N atoms have been considered (see [supplementary material](#)).

^b Maximum power efficiency and external quantum efficiency.

Acknowledgement

This work was supported in part by the Vienna University of Technology research funds and the Austrian Federal Ministry of Science, Research and Economy. The X-ray centre of the Vienna University of Technology is acknowledged for providing access to the single-crystal diffractometer.

Appendix A. Supplementary data

Supplementary data related to this article can be found at <http://dx.doi.org/10.1016/j.orgel.2016.04.036>.

References

- [1] M.A. Baldo, D.F. O'Brien, Y. You, A. Shoustikov, S. Sibley, M.E. Thompson, S.R. Forrest, Highly efficient phosphorescent emission from organic electroluminescent devices, *Nature* 395 (1998) 151–154.
- [2] M.A. Baldo, S. Lamansky, P.E. Burrows, M.E. Thompson, S.R. Forrest, Very high-efficiency green organic light-emitting devices based on electrophosphorescence, *Appl. Phys. Lett.* 75 (1999) 4–6.
- [3] S.R. Forrest, The path to ubiquitous and low-cost organic electronic appliances on plastic, *Nature* 428 (2004) 911–918.
- [4] Y. Sun, N.C. Giebink, H. Kanno, B. Ma, M.E. Thompson, S.R. Forrest, Management of singlet and triplet excitons for efficient white organic light-emitting devices, *Nature* 440 (2006) 908–912.
- [5] S. Reineke, F. Lindner, G. Schwartz, N. Seidler, K. Walzer, B. Lussem, K. Leo, White organic light-emitting diodes with fluorescent tube efficiency, *Nature* 459 (2009) 234–238.
- [6] L. Xiao, Z. Chen, B. Qu, J. Luo, S. Kong, Q. Gong, J. Kido, Recent progresses on materials for electrophosphorescent organic light-emitting devices, *Adv. Mater.* 23 (2011) 926–952.
- [7] Y. Tao, C. Yang, J. Qin, Organic host materials for phosphorescent organic light-emitting diodes, *Chem. Soc. Rev.* 40 (2011) 2943–2970.
- [8] S. Reineke, M. Thomschke, B. Lüssem, K. Leo, White organic light-emitting diodes: Status and perspective, *Rev. Mod. Phys.* 85 (2013) 1245–1293.
- [9] M.A. Baldo, D.F. O'Brien, M.E. Thompson, S.R. Forrest, Excitonic singlet-triplet ratio in a semiconducting organic thin film, *Phys. Rev. B* 60 (1999) 14422–14428.
- [10] C. Adachi, M.A. Baldo, M.E. Thompson, S.R. Forrest, Nearly 100% internal phosphorescence efficiency in an organic light-emitting device, *J. Appl. Phys.* 90 (2001) 5048–5051.
- [11] M.A. Baldo, C. Adachi, S.R. Forrest, Transient analysis of organic electrophosphorescence. II. Transient analysis of triplet-triplet annihilation, *Phys. Rev. B* 62 (2000) 10967–10977.
- [12] C. Murawski, K. Leo, M.C. Gather, Efficiency roll-off in organic light-emitting diodes, *Adv. Mater.* 25 (2013) 6801–6827.
- [13] D.F. O'Brien, M.A. Baldo, M.E. Thompson, S.R. Forrest, Improved energy transfer in electrophosphorescent devices, *Appl. Phys. Lett.* 74 (1999) 442–444.
- [14] M.H. Tsai, Y.H. Hong, C.H. Chang, H.C. Su, C.C. Wu, A. Matoliukstyte, J. Simokaitiene, S. Grigalevicius, J.V. Grazulevicius, C.P. Hsu, 3-(9-carbazolyl)carbazoles and 3,6-di(9-carbazolyl)carbazoles as effective host materials for efficient blue organic electrophosphorescence, *Adv. Mater.* 19 (2007) 862–866.
- [15] C. Adachi, R.C. Kwong, P. Djurovich, V. Adamovich, M.A. Baldo, M.E. Thompson, S.R. Forrest, Endothermic energy transfer: a mechanism for generating very efficient high-energy phosphorescent emission in organic materials, *Appl. Phys. Lett.* 79 (2001) 2082–2084.
- [16] Y. Shirota, Organic materials for electronic and optoelectronic devices, *J. Mater. Chem.* 10 (2000) 1–25.
- [17] I. Tanaka, Y. Tabata, S. Tokito, Energy-transfer and light-emission mechanism of blue phosphorescent molecules in guest-host systems, *Chem. Phys. Lett.* 400 (2004) 86–89.
- [18] G.T. Lei, L.D. Wang, L. Duan, J.H. Wang, Y. Qiu, Highly efficient blue electrophosphorescent devices with a novel host material, *Synth. Met.* 144 (2004) 249–252.
- [19] D.R. Whang, Y. You, S.H. Kim, W.I. Jeong, Y.S. Park, J.J. Kim, S.Y. Park, A highly efficient wide-band-gap host material for blue electrophosphorescent light-emitting devices, *Appl. Phys. Lett.* 91 (2007).
- [20] J. He, H. Liu, Y. Dai, X. Ou, J. Wang, S. Tao, X. Zhang, P. Wang, D. Ma, Nonconjugated carbazoles: a series of novel host materials for highly efficient blue electrophosphorescent OLEDs, *J. Phys. Chem. C* 113 (2009) 6761–6767.
- [21] D.H. Hu, P. Lu, C.L. Wang, H. Liu, H. Wang, Z.M. Wang, T. Fei, X. Gu, Y.G. Ma, Silane coupling di-carbazoles with high triplet energy as host materials for highly efficient blue phosphorescent devices, *J. Mater. Chem.* 19 (2009) 6143–6148.
- [22] S. Tokito, T. Iijima, Y. Suzuri, H. Kita, T. Tsuzuki, F. Sato, Confinement of triplet energy on phosphorescent molecules for highly-efficient organic blue-light-emitting devices, *Appl. Phys. Lett.* 83 (2003) 569–571.
- [23] Y. Agata, H. Shimizu, J. Kido, Syntheses and properties of novel quarterphenylene-based materials for blue organic light-emitting devices, *Chem. Lett.* 36 (2007) 316–317.
- [24] S.L. Gong, X. He, Y.H. Chen, Z.Q. Jiang, C. Zhong, D.G. Ma, J.G. Qin, C.L. Yang, Simple CBP isomers with high triplet energies for highly efficient blue electrophosphorescence, *J. Mater. Chem.* 22 (2012) 2894–2899.
- [25] R.J. Holmes, S.R. Forrest, Y.-J. Tung, R.C. Kwong, J.J. Brown, S. Garon, M.E. Thompson, Blue organic electrophosphorescence using exothermic host-guest energy transfer, *Appl. Phys. Lett.* 82 (2003) 2422–2424.
- [26] S.J. Yeh, M.F. Wu, C.T. Chen, Y.H. Song, Y. Chi, M.H. Ho, S.F. Hsu, C.H. Chen, New dopant and host materials for blue-light-emitting phosphorescent organic electroluminescent devices, *Adv. Mater.* 17 (2005) 285–289.
- [27] L.S. Cui, S.C. Dong, Y. Liu, Q. Li, Z.Q. Jiang, L.S. Liao, A simple systematic design of phenylcarbazole derivatives for host materials to high-efficiency phosphorescent organic light-emitting diodes, *J. Mater. Chem. C* 1 (2013) 3967–3975.
- [28] P. Kautny, D. Lumpi, Y. Wang, A. Tissot, J. Bintinger, E. Horkel, B. Stöger, C. Hametner, H. Hagemann, D. Ma, J. Fröhlich, Oxadiazole based bipolar host materials employing planarized triarylamine donors for RGB PHOLEDs with low efficiency roll-off, *J. Mater. Chem. C* 2 (2014) 2069–2081.
- [29] H. Puntischer, P. Kautny, B. Stoeger, A. Tissot, C. Hametner, H.R. Hagemann, J. Fröhlich, T. Baumgartner, D. Lumpi, Structure-property studies of P-triarylamine-substituted dithieno[3,2-b:2',3'-d]phospholes, *RSC Adv.* 5 (2015) 93797–93807.
- [30] J. Lv, Q. Liu, J. Tang, F. Perdih, K. Kranjc, A facile synthesis of indolo[3,2,1-jk]carbazoles via palladium-catalyzed intramolecular cyclization, *Tetrahedron Lett.* 53 (2012) 5248–5252.
- [31] P. Kautny, D. Lumpi, Y. Wang, A. Tissot, J. Bintinger, E. Horkel, B. Stöger, C. Hametner, H. Hagemann, D. Ma, J. Fröhlich, Oxadiazole based bipolar host materials employing planarized triarylamine donors for RGB PHOLEDs with low efficiency roll-off, *J. Mater. Chem. C* 2 (2014) 2069–2081.
- [32] R. Anémian, D.C. Cupertino, P.R. Mackie, S.G. Yeates, Solution phase studies towards the synthesis of triarylamine oligomers using a germanium linker on a solid support, *Tetrahedron Lett.* 46 (2005) 6717–6721.
- [33] H. Xu, K. Yin, W. Huang, Highly improved electroluminescence from a series of novel EuIII complexes with functional single-coordinate phosphine oxide ligands: tuning the intramolecular energy transfer, morphology, and carrier injection ability of the complexes, *Chem. A Eur. J.* 13 (2007) 10281–10293.
- [34] M.J. Frisch, G.W. Trucks, H.B. Schlegel, G.E. Scuseria, M.A. Robb, J.R. Cheeseman, G. Scalmani, V. Barone, B. Mennucci, G.A. Petersson, H. Nakatsuji, M. Caricato, X. Li, H.P. Hratchian, A.F. Izmaylov, J. Bloino, K.N. Kudin, V.N. Staroverov, R. Kobayashi, J. Normand, K. Raghavachari, A. Rendell, J.C. Burant, S.S. Iyengar, J. Tomasi, M. Cossi, N. Rega, N.J. Millam, M. Klene, J.E. Knox, J.B. Cross, V. Bakken, C. Adamo, J. Jaramillo, R. Gomperts, R.E. Stratmann, O. Yazyev, A.J. Austin, R. Cammi, C. Pomelli, J.W. Ochterski, R.L. Martin, K. Morokuma, V.G. Zakrzewski, G.A. Voth, P. Salvador, J.J. Dannenberg, S. Dapprich, A.D. Daniels, Oe Farkas, J.B. Foresman, J.V. Ortiz, J. Cioslowski, D.J. Fox, Gaussian 09, Revision D.01, Gaussian, Inc., Wallingford CT, 2009.
- [35] C. Lee, W. Yang, R.G. Parr, Development of the Colle-Salvetti correlation-energy formula into a functional of the electron density, *Phys. Rev. B* 37 (1988) 785–789.
- [36] A.D. Becke, Density-functional thermochemistry. III. The role of exact exchange, *J. Chem. Phys.* 98 (1993) 5648–5652.
- [37] R. Krishnan, J.S. Binkley, R. Seeger, J.A. Pople, Self-consistent molecular orbital methods. XX. A basis set for correlated wave functions, *J. Chem. Phys.* 72 (1980) 650–654.
- [38] R. Dennington, T. Keith, J. Millam, GaussView, Version 5, Semichem Inc., Shawnee Mission KS, 2009.
- [39] Bruker Computer Programs: APEX2, SAINT, SADABS, and SHELXTL, Bruker AXS Inc., Madison WI, 2013.
- [40] L. Palatinus, G. Chapuis, SUPERFLIP – a computer program for the solution of crystal structures by charge flipping in arbitrary dimensions, *J. Appl. Crystallogr.* 40 (2007) 786–790.
- [41] V. Petříček, M. Dusek, L. Palatinus, Jana2006. The Crystallographic Computing System, Institute of Physics, Praha, Czech Republic, 2006.
- [42] S.I. Wharton, J.B. Henry, H. McNab, A.R. Mount, The production and characterisation of novel conducting redox-active oligomeric thin films from electrooxidised Indolo[3,2,1-jk]carbazole, *Chem. Eur. J.* 15 (2009) 5482–5490.
- [43] ICzCz: C30H18N2, Mr = 406.5, orthorhombic, Pca21, a = 18.372(8) Å, b = 4.0466(17) Å, c = 25.957(11) Å, V = 1929.8(14) Å³, Z = 4, μ = 0.082 mm⁻¹, T = 100 K, 23 375 measured, 5594 independent and 4603 observed [I > 3σ(I)] reflections, 289 parameters, wR [all data] = 0.0767, R [I > 3σ(I)] = 0.0624; CCDC reference number 1442064.
- [44] A.L. Spek, Structure validation in chemical crystallography, *Acta Crystallogr. D.* 65 (2009) 148–155.
- [45] H.H. Li, Y. Wang, K. Yuan, Y. Tao, R.F. Chen, C. Zheng, X.H. Zhou, J.F. Li, W. Huang, Efficient synthesis of pi-extended phenazasilines for optical and electronic applications, *Chem. Commun.* 50 (2014) 15760–15763.
- [46] Z. Ge, T. Hayakawa, S. Ando, M. Ueda, T. Akiike, H. Miyamoto, T. Kajita, M.-a. Kakimoto, Novel bipolar bathophenanthroline containing hosts for highly efficient phosphorescent OLEDs, *Org. Lett.* 10 (2008) 421–424.
- [47] M. Mas-Torrent, C. Rovira, Role of molecular order and solid-state structure in organic field-effect transistors, *Chem. Rev.* 111 (2011) 4833–4856.
- [48] D. Zhang, L. Duan, D. Zhang, J. Qiao, G. Dong, L. Wang, Y. Qiu, Extremely low driving voltage electrophosphorescent green organic light-emitting diodes based on a host material with small singlet-triplet exchange energy without p- or n-doping layer, *Org. Electron.* 14 (2013) 260–266.
- [49] D. Zhang, L. Duan, Y. Li, H. Li, Z. Bin, D. Zhang, J. Qiao, G. Dong, L. Wang, Y. Qiu, Towards high efficiency and low roll-off orange electrophosphorescent devices by fine tuning singlet and triplet energies of bipolar hosts based on Indolocarbazole/1, 3, 5-Triazine hybrids, *Adv. Funct. Mater.* 24 (2014) 3551–3561.
- [50] E. Mondal, W.-Y. Hung, H.-C. Dai, K.-T. Wong, Fluorene-based asymmetric bipolar universal hosts for white organic light emitting devices, *Adv. Funct. Mater.* 23 (2013) 3096–3105.
- [51] P. Kautny, Z. Wu, B. Stöger, A. Tissot, E. Horkel, J. Chen, D. Ma, H. Hagemann, J. Fröhlich, D. Lumpi, Controlling singlet-triplet splitting in carbazole-oxadiazole based bipolar phosphorescent host materials, *Org. Electron* 17

- (2015) 216–228.
- [52] Y. Tao, Q. Wang, C. Yang, C. Zhong, K. Zhang, J. Qin, D. Ma, Tuning the optoelectronic properties of carbazole/oxadiazole hybrids through linkage modes: hosts for highly efficient green electrophosphorescence, *Adv. Funct. Mater.* 20 (2010) 304–311.
- [53] J. Lee, N. Chopra, S.-H. Eom, Y. Zheng, J. Xue, F. So, J. Shi, Effects of triplet energies and transporting properties of carrier transporting materials on blue phosphorescent organic light emitting devices, *Appl. Phys. Lett.* 93 (2008) 123306.
- [54] S.T. Hoffmann, P. Schrogel, M. Rothmann, R.Q. Albuquerque, P. Strohriegel, A. Kohler, Triplet excimer emission in a series of 4,4'-Bis(N-carbazolyl)-2,2'-biphenyl derivatives, *J. Phys. Chem. B* 115 (2011) 414–421.
- [55] K.L. Woon, Z.A. Hasan, B.K. Ong, A. Ariffin, R. Griniene, S. Grigalevicius, S.-A. Chen, Triplet states and energy back transfer of carbazole derivatives, *Rsc Adv.* 5 (2015) 59960–59969.

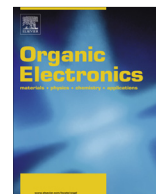
2.4. Manuscript #4

Controlling singlet-triplet splitting in carbazole-oxadiazole based bipolar phosphorescent host materials

Paul Kautny, Zhongbin Wu, Berthold Stöger, Antoine Tissot, Ernst Horkel, Jiangshan Chen, Dongge Ma, Hans Hagemann, Johannes Fröhlich, Daniel Lumpi

Organic Electronics, **2015**, 17, 216-228

Reproduced with the kind permission of Elsevier B. V.



Controlling singlet–triplet splitting in carbazole–oxadiazole based bipolar phosphorescent host materials

Paul Kautny^a, Zhongbin Wu^b, Berthold Stöger^c, Antoine Tissot^d, Ernst Horkel^a, Jiangshan Chen^{b,*}, Dongge Ma^b, Hans Hagemann^d, Johannes Fröhlich^a, Daniel Lumpi^{a,*}

^a Institute of Applied Synthetic Chemistry, Vienna University of Technology, Getreidemarkt 9/163, A-1060 Vienna, Austria

^b State Key Laboratory of Polymer Physics and Chemistry, Changchun Institute of Applied Chemistry, Chinese Academy of Sciences, Changchun 130022, China

^c Institute of Chemical Technologies and Analytics, Vienna University of Technology, Getreidemarkt 9/164, A-1060 Vienna, Austria

^d Département de Chimie Physique, Université de Genève, 30, quai E. Ansermet, 1211 Geneva 4, Switzerland

ARTICLE INFO

Article history:

Received 17 October 2014

Received in revised form 24 November 2014

Accepted 29 November 2014

Available online 12 December 2014

Keywords:

PHOLED

High triplet energy

Low efficiency roll-off

Sterically induced torsion

Structure–property relationship

ABSTRACT

A rational molecular design strategy for carbazole–oxadiazole based bipolar host materials was developed to improve the device efficiency of blue phosphorescent organic light-emitting diodes (PHOLED). Steric effects of strategically placed methyl groups led to an increase of triplet energies (**o**-2MPCzPOXD: 2.66 eV and **o**-3MPCzPOXD: 2.73 eV versus the initial host material **o**-PczPOXD: 2.62 eV) while less pronouncedly affecting singlet energies and, therefore, retaining low driving voltages, high power efficiencies and remarkably low efficiency roll-offs in PHOLEDs. The maximum quantum efficiencies (EQE) for blue devices (Flrpic) were significantly raised for **o**-2MPCzPOXD (13.6%) and **o**-3MPCzPOXD (11.5%) versus **o**-PczPOXD (9.0%) although yielding comparable values for green devices (Ir(ppy)₃; 12.9% and 15.4% versus 13.2%). Supported by theoretical calculations a structure–property relationship was established from photo-physical properties, PHOLED performance measurements and structural characterization from single crystal data.

© 2014 Elsevier B.V. All rights reserved.

1. Introduction

Organic Light Emitting Diodes (OLEDs) received great attention during the last two decades due to potential applications in flat panel displays and solid state lighting [1–10]. The introduction of phosphorescent emitters by Forrest et al. in 1998 [11,12] significantly enhanced the efficiency of OLEDs due to the fact that phosphorescent transition metal emitters harvest singlet and triplet excitons simultaneously. Thus, phosphorescent OLEDs (PHOLEDs) can theoretically achieve 100% internal quantum efficiency [13,14].

In fact, triplet emitters have to be dispersed in an organic host matrix to avoid concentration quenching [15,16]. Bipolar host materials proved to be especially useful due to balanced charge transport properties resulting in simplified device structure and broader recombination zones [7,17,18]. To efficiently confine triplet excitons on the dopant higher triplet energies (E_T) of the host materials compared to the phosphorescent dopant are required [19–21]. However, the combination of p- and n-type moieties in a molecule significantly decreases the triplet energy of host materials [7,17].

Therefore, the molecular design of bipolar host materials focuses on the interruption of the conjugated π -system to reduce the donor–acceptor interaction [7,10,17]. While aiming for increased triplet energies of host materials, the enhancement of singlet energies should be limited in order to achieve the desired device performances. Thus,

* Corresponding authors. Tel.: +86 431 85262807 (J. Chen), +43 1 58801 163719 (D. Lumpi).

E-mail addresses: jschen@ciac.ac.cn (J. Chen), daniel.lumpi@tuwien.ac.at (D. Lumpi).

<http://dx.doi.org/10.1016/j.orgel.2014.11.027>

1566-1199/© 2014 Elsevier B.V. All rights reserved.

methodologies to independently tune singlet and triplet energies are highly desirable.

Recently, we reported on the concept of planarizing tri-arylamine (TAA) donor structures in TAA–oxadiazole–TAA based materials significantly enhancing the *ortho*-linkage effect [22]. Utilizing phenylcarbazole (PCz) resulted in **o-PCzPOXD** as an efficient bipolar host material for green [Ir(ppy)₃] PHOLEDs with a remarkably low efficiency roll off. However, lower efficiencies were observed in blue (Flrpic) devices as a consequence of a slightly lower E_T value (**o-PCzPOXD** = 2.62 eV) compared to Flrpic (=2.65 eV [7]).

The objective of this work is to increase the E_T values of **o-PCzPOXD** while retaining low driving voltages and high power efficiencies in the device by elevating the singlet energy (E_S) less pronounced. This task is being tackled by sterically induced torsion introducing methyl groups at specific sites of the PCz core (Scheme 1) in order to reduce the overall electronic conjugation. Hence, due to the widespread applications of TAA donor structures in many fields of material science the strategy is of general interest for the design of novel donor–acceptor scaffolds. In addition, a distinct correlation between the molecular structures and the observed material properties is revealed.

2. Materials and methods

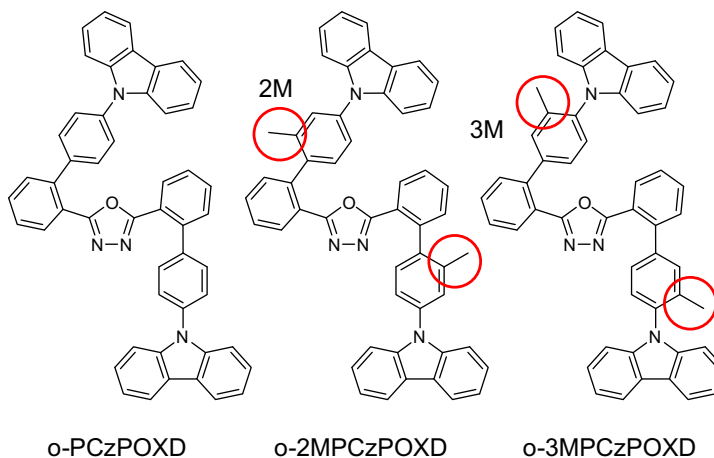
2.1. General information

All reagents and solvents were purchased from commercial suppliers and used without further purification. Anhydrous solvents were prepared by filtration through drying columns. Column chromatography was performed on silica 60 (Merck, 40–63 μm). NMR spectra were recorded on a Bruker Avance DRX-400 Spectrometer or a Bruker Avance 200 Spectrometer. High resolution mass spectra (HRMS) were obtained from a Thermo Scientific LTQ Orbitrap XL hybrid FTMS (Fourier Transform Mass Spectrometer) and Thermo Scientific MALDI LTQ Orbitrap interface; α -cyano-4-hydroxycinnamic acid was used as matrix. Thermogravimetric (TG) and differential scanning calorimetry (DSC) measurements were carried out with a heating rate of 5 K/

min in a flowing argon atmosphere (25 ml/min). For the TG measurements, a Netzsch TG 209 F9 Tarsus system with open aluminum oxide crucibles was used. For the DSC measurements, a Netzsch DSC 200 F3 Maia, working with aluminum pans with pierced lids, was employed. UV/VIS absorption and fluorescence emission spectra were recorded in DCM solutions (5 μM) with a Perkin Elmer Lambda 750 spectrometer and an Edinburgh FLS920, respectively. Time resolved experiments were obtained using a Quantel Brilliant tripled Nd-YAG laser (355 nm, 20 Hz repetition rate, pulse width \sim 5 ns). Spectra were measured using a SPEX 270 monochromator equipped with both photomultiplier and CCD. This set-up is controlled using a home-built Labview-based program which allows using different instruments such as photon counting, oscilloscope, and additional mechanical shutters. For the measurement of the triplet emission, a mechanical shutter was triggered by the pulsed laser. A pretrigger period of 0.5 ms was followed by a 1 ms aperture and a rest time of 300–500 ms allowed obtaining the measurements shown in the [Supplementary Material](#). The slit of the monochromator was also opened further (up to 0.5 mm) to measure the triplet emission. Cyclic voltammetry was performed using a three electrode configuration consisting of a Pt working electrode, a Pt counter electrode and an Ag/AgCl reference electrode and a PGSTAT128 N, ADC164, DAC164, External, DI048 potentiostat provided by Metrohm Autolab B.V. Measurements were carried out in a 0.5 mM solution in anhydrous DCM with Bu_4NBF_4 (0.1 M) as supporting electrolyte. The solutions were purged with nitrogen for 15 min prior to measurement. HOMO energy levels were calculated from the onset of the oxidation peaks. The onset potential was determined by the intersection of two tangents drawn at the background and the rising of the oxidation peaks.

2.2. Synthetic details

9-(4-Bromo-3-methyl-phenyl)-9H-carbazole (**1**) [23] and 2,5-bis(2-bromophenyl)-1,3,4-oxadiazole (**8**) [24] were synthesized according to previously published procedures whereas 1-fluoro-2-methyl-4-nitrobenzene (**3**) was



Scheme 1. Molecular structure of **o-PCzPOXD**, **o-2MPCzPOXD** and **o-3MPCzPOXD**.

purchased by Apollo Scientific and used without further purification.

2.2.1. 9-[3-Methyl-4-(4,4,5,5-tetramethyl-1,3,2-dioxaborolan-2-yl)phenyl]-9H-carbazole (**2**)

The synthesis of **2** was accomplished analogously to published procedures [25]. To a solution of 9-(4-bromo-3-methylphenyl)-9H-carbazole (**1**) (4.37 g, 13.0 mmol, 1.00 eq.) in anhydrous THF (45 ml) under argon atmosphere *n*-BuLi (6.24 ml, 15.6 mmol, 1.20 eq., 2.5 M in hexanes) was added dropwise at -78°C . Subsequently the reaction mixture was stirred at -80°C for 1 h before Pinbop[®] (2.90 g, 15.6 mmol, 1.20 eq.) was added and the reaction was allowed to warm to room temperature slowly. After stirring overnight the solvent was removed under reduced pressure and the residue was partitioned between aqueous HCl (1N) and DCM. The aqueous phase was extracted with DCM, the combined organic layers were dried over anhydrous Na_2SO_4 and concentrated *in vacuo*. **2** (3.80 g, 9.9 mmol, 76%) was isolated as white bulky crystals after crystallization from EtOH. ^1H NMR (200 MHz, CD_2Cl_2): $\delta = 8.16$ (d, $J = 7.6$ Hz, 2H), 8.01 (dd, $J = 6.5, 2.2$ Hz, 1H), 7.51–7.39 (m, 6H), 7.34–7.26 (m, 2H), 2.67 (s, 3H), 1.41 (s, 12H) ppm. ^{13}C NMR (50 MHz, CD_2Cl_2 , FID KAP180/43): $\delta = 147.7$ (s), 141.2 (s), 140.3 (s), 138.0 (d), 128.3 (d), 126.5 (d), 124.0 (s), 123.5 (d), 120.7 (d), 120.5 (d), 110.5 (d), 84.3 (s), 25.3 (q), 22.6 (q) ppm (C–B) was not detected). Calculated: m/z 534.89951 $[\text{M}]^+$, 383.20511. Found: MS (MALDI): m/z 383.20610 $[\text{M}]^+$.

2.2.2. 9-(2-Methyl-4-nitrophenyl)-9H-carbazole (**4**)

The synthesis of **4** was done analogously to a published procedure [26]. Carbazole (8.36 g, 50.0 mmol, 1.00 eq.) and K_2CO_3 (7.60 g, 55.0 mmol, 1.10 eq.) were suspended in anhydrous DMAc (100 ml) and cyclohexane (38 ml) in a 250-ml three necked flask equipped a Dean–Stark trap. The mixture was heated to 100°C for 3.5 h under argon atmosphere. After complete removal of water, the residual cyclohexane was distilled off and 1-fluoro-2-methyl-4-nitrobenzene (**3**) (8.53 g, 55.0 mmol, 1.10 eq.) was added. Then the mixture was heated to rf for 2.5 h before hydrochloric acid (180 ml, 1 M) was added, leading to the formation of a yellow precipitate. The reaction mixture was filtrated and the crude product was purified by crystallization from toluene/light petroleum (3:4) yielding **4** (9.50 g, 31.4 mmol, 63%) as yellow crystals. ^1H NMR (200 MHz, CD_2Cl_2): $\delta = 8.39$ (d, $J = 2.4$ Hz, 1H), 8.29–8.17 (m, 3H), 7.59 (d, $J = 8.6$ Hz, 1H), 7.48–7.29 (m, 4H), 7.05 (d, $J = 8.0$, 2H), 2.11 (s, 3H) ppm. ^{13}C NMR (50 MHz, CD_2Cl_2): $\delta = 148.1$ (s), 142.7 (s), 141.0 (s), 139.7 (s), 130.8 (d), 127.3 (d), 126.8 (d), 124.0 (s), 123.1 (d), 121.0 (d), 120.9 (d), 110.2 (d), 18.4 (q) ppm. Calculated: m/z 302.10498 $[\text{M}]^+$. Found: MS (MALDI): m/z 302.10609 $[\text{M}]^+$.

2.2.3. 4-(9H-Carbazole-9-yl)-3-methylbenzenamine (**5**)

Compound **5** was synthesized accordingly to a published procedure [27]. **4** (8.82 g, 29.2 mmol, 1.00 eq.) and $\text{SnCl}_2 \times 2\text{H}_2\text{O}$ (23.04 g, 102.1 mmol, 3.50 eq.) in EtOH were heated to rf for 2.5 h until full conversion (TLC). Subsequently aqueous NaOH (300 ml, 30%) was added and the reaction mixture was extracted with toluene. The

combined organic layers were washed with H_2O , dried over anhydrous Na_2SO_4 and concentrated under reduced pressure. The crude product was purified by column chromatography (light petroleum:DCM 70:30 \rightarrow 50:50) yielding **5** (6.07 g, 22.3 mmol, 76%) as orange solid. ^1H NMR (200 MHz, CD_2Cl_2): $\delta = 8.17$ (ddd, $J = 7.6, 1.2, 0.8$ Hz, 2H), 7.41 (ddd, $J = 8.1, 7.2, 1.3$ Hz, 2H), 7.27 (ddd, $J = 7.6, 7.2, 1.2$ Hz, 2H), 7.13–7.05 (m, 3H), 6.76–6.66 (m, 2H), 3.90 (bs, 2H), 1.83 (s, 3H) ppm. ^{13}C NMR (50 MHz, CD_2Cl_2): $\delta = 147.8$ (s), 142.2 (s), 138.8 (s), 130.5 (d), 126.6 (s), 126.3 (d), 123.3 (s), 120.7 (d), 119.8 (d), 117.5 (d), 113.9 (d), 110.3 (d), 17.8 (q) ppm. Calculated: m/z 272.13080 $[\text{M}]^+$, 273.13862 $[\text{M}+\text{H}]^+$. Found: MS (MALDI): m/z 272.13162 $[\text{M}]^+$, 273.13845 $[\text{M}+\text{H}]^+$.

2.2.4. 9-(4-Iodo-2-methylphenyl)-9H-carbazole (**6**)

The synthesis of **6** was accomplished accordingly to a published procedure [28]. Amine **5** (5.58 g, 20.5 mmol, 1.00 eq.) was suspended in 3.5 N aqueous HCl (35 ml), stirred mechanically and cooled to -5°C in an ice-salt cooling bath. To this solution NaNO_2 (1.48 g, 21.5 mmol, 1.05 eq.) dissolved in H_2O (7 ml) was slowly added, keeping the temperature below 0°C . After 1.5 h small amounts of urea were added 10 min before the diazonium salt was reacted with 3 M aqueous KI solution (3.74 g, 22.5 mmol, 1.10 eq.) under cooling. KI was added slowly in such a manner, that only slight foam formation was observed. After the addition of KI the reaction was stirred for 2 h at 0°C and overnight at room temperature. Then the aqueous phase was extracted with Et_2O . The combined organic layers were washed with aqueous $\text{Na}_2\text{S}_2\text{O}_5$ solution, dried over anhydrous Na_2SO_4 and concentrated under reduced pressure. **6** (3.43 g, 9.0 mmol, 44%) was obtained after column chromatography (light petroleum:DCM 100:0 \rightarrow 98:2) followed by crystallization from EtOH as white solid. ^1H NMR (200 MHz, CD_2Cl_2): $\delta = 8.18$ (ddd, $J = 7.5, 1.1, 0.8$ Hz, 2H), 7.89 (d, 1.8 Hz, 1H), 7.62 (dd, $J = 8.2, 2.0$ Hz, 1H), 7.42 (ddd, $J = 8.0, 7.3, 1.1$ Hz, 2H), 7.30 (ddd, $J = 7.5, 7.3, 1.0$ Hz, 2H), 7.13 (dd, $J = 8.2, 1.8$ Hz, 1H), 7.05 (ddd, $J = 8.0, 1.0, 0.8$ Hz, 2H), 1.93 (s, 3H) ppm. ^{13}C NMR (50 MHz, CD_2Cl_2): $\delta = 141.4$ (s), 141.1 (d), 140.4 (s), 137.1 (d), 136.5 (s), 131.6 (d), 126.6 (d), 123.6 (s), 120.8 (d), 120.3 (d), 110.2 (d), 94.7 (s), 17.6 (q) (q) ppm. Calculated: m/z 383.01654 $[\text{M}]^+$. Found: MS (MALDI): m/z 383.01771 $[\text{M}]^+$.

2.2.5. 9-[2-Methyl-4-(4,4,5,5-tetramethyl-1,3,2-dioxaborolan-2-yl)phenyl]-9H-carbazole (**7**)

Compound **7** was synthesized analogously to **2**. Starting from **6** (3.09 g, 8.0 mmol, 1.00 eq.), *n*-BuLi (3.84 ml, 9.6 mmol, 1.20 eq.) and Pinbop[®] (1.79 g, 9.6 mmol, 1.20 eq.) **7** (2.07 g, 5.4 mmol, 67%) was isolated as white crystals after crystallization from EtOH. ^1H NMR (200 MHz, CD_2Cl_2): $\delta = 8.17$ (ddd, $J = 7.5, 1.2, 0.8$ Hz, 2H), 7.92 (d, $J = 0.8$ Hz, 1H), 7.81 (dd, $J = 7.7, 0.8$ Hz, 1H), 7.45–7.33 (m, 3H), 7.27 (ddd, $J = 7.5, 7.4, 0.9$ Hz, 2H), 7.03 (ddd, $J = 8.0, 0.9, 0.8$ Hz, 2H), 1.98 (s, 3H), 1.39 (s, 12H) ppm. ^{13}C NMR (50 MHz, CD_2Cl_2): $\delta = 141.5$ (s), 139.2 (s), 138.6 (d), 137.0 (s), 134.1 (d), 129.0 (d), 126.5 (d), 123.6 (s), 120.8 (d), 120.1 (d), 110.3 (d), 84.6 (s), 25.3 (q), 17.8 (q) ppm (C–B) was not detected). Calculated: m/z 383.20511 $[\text{M}]^+$. Found: MS (MALDI): m/z 383.20614 $[\text{M}]^+$.

2.2.6. 9,9'-[1,3,4-Oxadiazole-2,5-diylbis[2-methyl-1,1'-biphenyl]-2',4-diyl]bis[9H-carbazole] (o-2MPCzPOXD)

o-2MPCzPOXD was synthesized using standard Suzuki cross-coupling conditions [29]. Dibromide **8** (0.76 g, 2.0 mmol, 1.00 eq.), **2** (1.92 g, 5.0 mmol, 2.50 eq.), K₂CO₃ (5 ml, 2 M aqueous solution) and Pd(PPh₃)₄ (0.12 g, 0.1 mmol, 0.05 eq.) were added to degassed THF (40 ml) under argon counterflow. The mixture was heated to reflux under argon atmosphere until full conversion (TLC), poured on H₂O and repeatedly extracted with DCM. The combined organic layers were dried over anhydrous Na₂SO₄ and the solvent was removed *in vacuo* after filtration. **o-2MPCzPOXD** (0.70 g, 1.0 mmol, 48%) was isolated after column chromatography (light petroleum:DCM 70:30) as white solid. ¹H NMR (400 MHz, CD₂Cl₂): δ = 8.16 (d, *J* = 7.8 Hz, 4H), 7.88–7.83 (m, 2H), 7.66–7.61 (m, 2H), 7.47–7.27 (m, 22H), 2.10–2.09 (m, 6H) ppm. ¹³C NMR (100 MHz, CD₂Cl₂): δ = 165.1 (s), 165.0 (s), 141.4 (s), 141.1(9) (s), 141.1(5) (s), 140.3(2) (s), 140.2(5) (s), 138.6 (s), 138.5 (s), 137.5 (s), 131.9 (d), 131.8(7) (d), 131.8(3) (d), 131.3 (d), 131.1 (d), 129.7 (d), 129.6 (d), 128.7 (d), 128.5(5) (d), 128.5(0) (d), 126.5 (d), 124.6 (d), 124.5 (d), 123.8(2) (s), 123.8(1) (s), 123.7(8) (s), 120.7 (d), 120.4 (d), 110.4(2) (d), 110.3(7) (d), 20.5 (q), 20.4 (q) ppm (due to high rotational barriers induced by the methyl groups, signals from two conformational isomers were detected). Calculated: *m/z* 732.28836 [M]⁺, 733.29619 [M+H]⁺, 755.27813 [M+Na]⁺. Found: MS (MALDI): *m/z* 732.28880 [M]⁺, 733.29514 [M+H]⁺, 755.27849 [M+Na]⁺.

2.2.7. 9,9'-[1,3,4-Oxadiazole-2,5-diylbis[3-methyl-1,1'-biphenyl]-2',4-diyl]bis[9H-carbazole] (o-3MPCzPOXD)

o-3MPCzPOXD was synthesized analogously to **o-2MPCzPOXD**. Starting from **8** (0.65 g, 1.7 mmol, 1.00 eq.), **7** (1.63 g, 4.25 mmol, 2.50 eq.), K₂CO₃ (4.25 ml, 2 M aqueous solution) and Pd(PPh₃)₄ (0.10 g, 0.1 mmol, 0.05 eq.) **o-3MPCzPOXD** (1.02 g, 1.4 mmol, 82%) was isolated after column chromatography (light petroleum: DCM 50:50) as white solid. ¹H NMR (400 MHz, CD₂Cl₂): δ = 8.14 (d, *J* = 7.9 Hz, 4H), 7.98 (d, *J* = 7.6 Hz, 2H), 7.76 (dd, *J* = 7.6, 7.6, 2H), 7.63–7.58 (m, 4H), 7.32–7.24 (m, 12H), 7.17 (dd, *J* = 8.0, 1.6 Hz, 2H), 6.78 (d, 7.9 Hz, 4H), 1.86 (s, 6H) ppm. ¹³C NMR (100 MHz, CD₂Cl₂): δ = 165.7 (s), 141.9 (s), 141.5(8) (s), 141.5(7) (s), 137.6 (s), 135.8 (s), 132.4 (d), 132.1 (d), 131.5 (d), 130.6 (d), 129.3 (d), 128.8 (d), 128.4 (d), 126.6 (d), 123.5 (s), 123.4 (s), 120.8 (d), 120.1 (d), 110.1 (d), 17.8 (q) ppm. Calculated: *m/z* 732.28836 [M]⁺, 733.29619 [M+H]⁺, 755.27813 [M+Na]⁺. Found: MS (MALDI): *m/z* 732.28893 [M]⁺, 733.29548 [M+H]⁺, 755.27905 [M+Na]⁺.

2.3. Computational details

All (TD)DFT computations were performed using the Gaussian 09 package, revision D.01 [30]. Density functional theory (DFT) and time-dependent (TD)DFT calculations were performed using the Becke three parameters hybrid functional with Lee–Yang–Perdew correlation (B3LYP) [31,32], in combination with Pople basis sets (6-31G*, 6-311+G*) [33]. Geometry optimizations were performed in gas phase and without symmetry constraints. For the

calculation of HOMO/LUMO levels, ground state (S₀) geometries were optimized applying the 6-311+G* basis set. The determination of triplet energy (E_T) was achieved by the calculation of the T₁ excitation energy applying TDDFT level and the 6-311+G* basis to a S₀ geometry optimized at DFT level using the 6-31G* basis set. To calculate the contribution of the molecular subunits to HOMO and LUMO levels, wavefunctions of the optimized geometries were decomposed to atomic level (using Hirshfeld partition by percentage) [34] and then summed up according to relevant functional structure moieties. Orbital plots were generated using GaussView [35].

2.4. Single crystal diffraction

Crystals of **2**, **4**, **7**, **o-2MPCzPOXD** and **o-3MPCzPOXD** suitable for single crystal diffraction were selected under a polarizing microscope, embedded in perfluorinated oil and attached to Kapton[®] mounts. Intensity data were collected in a dry stream of nitrogen at 100 K on a Bruker KAPPA APEX II diffractometer system. Data were reduced using SAINT-Plus [36] and an empirical absorption correction using the multi-scan approach implemented in SADABS [36] was applied. The crystal structures were solved by charge-flipping implemented in SUPERFLIP [37] and refined against *F* with the JANA2006 [38] software package. The non-H atoms were refined with anisotropic displacement parameters (ADPs). The H atoms were placed at calculated positions and refined as riding on the parent C atoms. Both methyl groups in **o-2MPCzPOXD** and **o-3MPCzPOXD** were modeled as disordered around two different positions. The lengths of the C–C bonds connecting the disordered methyl groups to the remaining molecule were restrained to 1.510(1) Å. The atoms of one carbazole and the connected benzene in **o-2MPCzPOXD** featured highly anisotropic displacement parameters indicating disorder. Nevertheless the atoms could not be resolved into distinct positions. Instead, the atoms of the carbazole were refined with anharmonic ADPs leading to distinctly improved residuals.

2.5. Device fabrication and measurement

All the devices were fabricated on glass substrates pre-coated with 180 nm indium tin oxide (ITO) with a sheet resistance of 10 Ω per square. The ITO substrates were degreased in an ultrasonic solvent bath and then dried at 120 °C for 30 min. Before loaded into the deposition chamber, the ITO surface was treated with UV–ozone for 15 min. All layers were grown in succession by thermal evaporation without breaking the vacuum (<5 × 10^{−4} Pa). The device structures were described in the text. The organic materials and metal oxide were evaporated at the rate in a range of 1–2 Å/s, and the metals were evaporated at the rate of 8–10 Å/s. The overlap between ITO and Al electrodes was 4 mm × 4 mm which is the active emissive area of the devices. Current–voltage–brightness characteristics were measured by using a Keithley source measurement unit (Keithley 2400 and Keithley 2000) with a calibrated silicon photodiode. The EL spectra were measured by a Spectrascan PR650 spectrophotometer. EQEs were

calculated from the luminance, current density, and EL spectrum, assuming a Lambertian distribution. All the measurements were carried out in ambient atmosphere.

3. Results and discussion

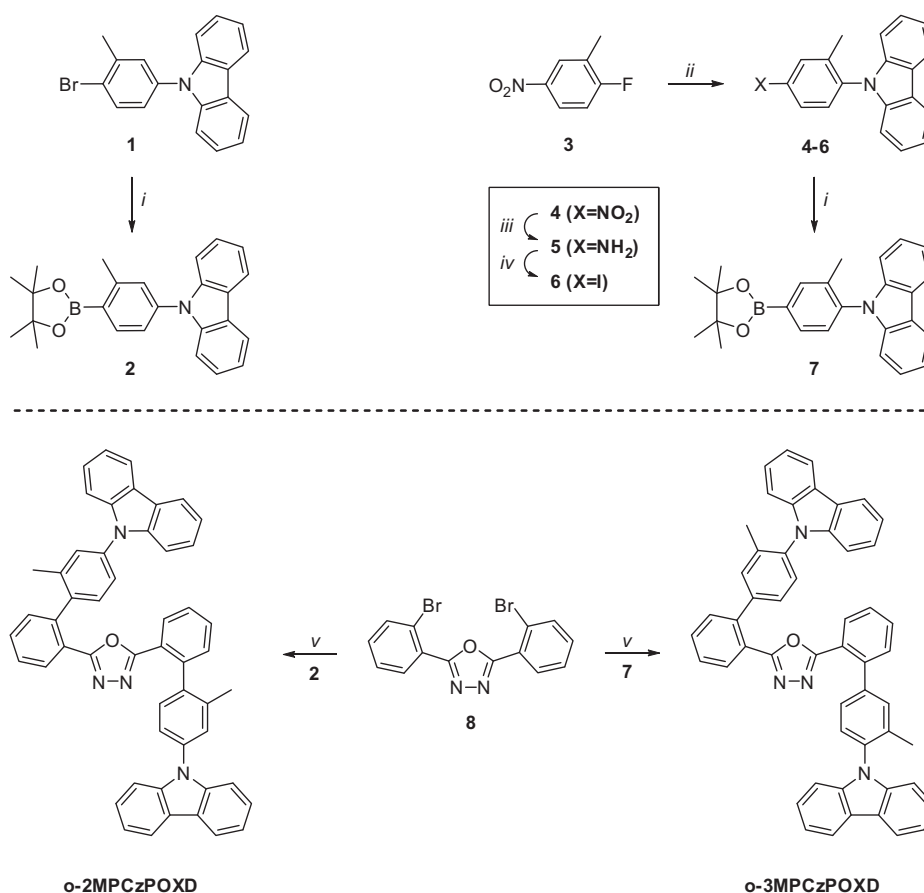
3.1. Molecular design

The concept of introducing sterically demanding groups in order to tune intramolecular torsion angles to achieve high E_T -values was applied to uni- and bipolar host materials [21,39–43]. However, the modification of torsion angles inevitably influences not only triplet but also singlet states and thus may lead to undesirably increased singlet–triplet splitting due to reorganization of the molecular orbitals [39]. Recently, Monkman et al. showed that by thoughtful and selective placement of sterically demanding groups this effect can be limited [44]. In this work we aim to increase the E_T while retaining reasonably low singlet energy values by the introduction of methyl groups to the molecular scaffold of **o-PCzPOXD**. Based on theoretical calculations we chose to attach the methyl groups to the phenyl ring of the phenylcarbazole fragment (Scheme 1). Due to the placement of the methyl groups between the

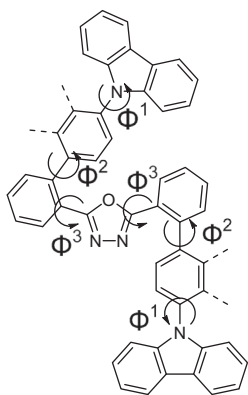
carbazole donor and the oxadiazole acceptor the overall conjugation should be decreased while the location of HOMO and LUMO levels should remain on the respective molecular subunit in order to preserve the original electronic structure.

3.2. Synthesis

The synthetic approach toward target host materials **o-2MPCzPOXD** and **o-3MPCzPOXD**, which relies on Pd-catalyzed Suzuki cross-coupling reactions as key step, is outlined in Scheme 2. Whereas a synthetic protocol toward bromide **1** is available, **6** was synthesized starting from commercially available 1-fluoro-2-methyl-4-nitrobenzene (**3**). Conversion of **3** with carbazole yielded the corresponding nitro compound **4**, which was subsequently reduced to amine **5**. Iodo-compound **6** was obtained by diazotization of **5** and treatment of the diazonium intermediate with KI. Lithiation of **1** and **6** and conversion of the organo-lithium-intermediates with isopropyl pinacol borate yielded the corresponding pinacol boronic esters **2** and **7**. In the final step the boronic esters were reacted with dibromide **8** in a Suzuki cross-coupling reaction giving target molecules **o-2MPCzPOXD** and **o-3MPCzPOXD** in 48% and 82%



Scheme 2. Synthesis of **o-2MPCzPOXD** and **o-3MPCzPOXD**: (i) (a) THF, $-78\text{ }^\circ\text{C}$, *n*-BuLi (1.2 eq.), (b) isopropyl pinacol borate (1.2 eq.); (ii) (a) DMAc/cyclohexane (5:2), carbazole (1.0 eq.), K₂CO₃ (1.1 eq.), reflux (b) **3** (1.1 eq.) reflux; (iii) EtOH, SnCl₂ × 2H₂O (3.5 eq.), reflux; (iv) (a) H₂O, HCl, NaNO₂ (1.05 eq.), $-5\text{ }^\circ\text{C}$, (b) KI (1.1 eq.); (v) boronic acid ester **2/7** (2.5 eq.), K₂CO₃ (5.0 eq., 2 M aq.), Pd(PPh₃)₄ (5 mol%), THF, reflux.



Scheme 3. Schematic representation of torsion angles Φ^{1-3} .

yields, respectively. The steric demand of the methyl group next to the reaction center hampers the formation of **o-2MPCzPOXD** resulting in distinctly lower yields. The molecular structure of all newly synthesized compounds was confirmed by ^1H and ^{13}C NMR measurements and high resolution mass spectroscopy. Unexpectedly two signals for the methyl group in **o-2MPCzPOXD** were observed in ^1H NMR spectra. Moreover, two distinct signals were found for a majority of the carbon atoms in ^{13}C NMR measurements indicating that the interconversion of both possible conformational diastereomers with the methyl-groups *cis* or *trans* with respect to the plane of the POXD core is significantly hindered. Furthermore, **2** [45] **4** [46], **7** [47], **o-2MPCzPOXD** [48] and **o-3MPCzPOXD** [49] were structurally characterized by single crystal X-ray diffraction (see [Supplementary Material](#)).

3.3. Molecular structures

The influence of additional methyl-groups on the torsion angles Φ^1 , Φ^2 and Φ^3 (Scheme 3, Table 1) in the molecular structure of the host materials (Fig. 1) was determined from single crystal data. Although single crystals feature packing effects, the results can be extrapolated to amorphous materials and even solutions.

As already described for **o-PCzPOXD** [50] the PCz moieties are located *cis* relative to the POXD cores for all compounds. Different conformational isomers of **o-2MPCzPOXD** as well as **o-3MPCzPOXD** were observed in the difference Fourier maps and, therefore, the methyl groups were modeled as disordered around two different positions. The two possible positions of the methyl groups (C21 and C28 respectively C21' and C28') are unequally occupied. In single crystals of

o-3MPCzPOXD atomic sites C21 (94.8(3)%) and C28 (87.7(5)%), which are located *cis* with respect to the plane of the POXD core, are preferably occupied compared to C21' (5.2(3)%) and C28' (12.3(5)%). This finding can be explained by the close vicinity of C21 and C28' within the molecular structure leading to unfavorable interactions. Furthermore, the incorporation of not only the conformational *cis*-isomer but also of the *trans*-isomers can be concluded from the diverging site occupancies of C21 and C28. Similar observations were made for **o-2MPCzPOXD** crystals in which C21 (77.5(5)%) and C28 (79.5(5)%) are more frequently occupied compared to C21' (22.5(5)%) and C28' (20.5(5)%). However, the diverging occupancies are within the error of measurement. A difference of 2% of a carbon atom corresponds to approximately 0.1 electrons and the presence of the *trans*-isomer of **o-2MPCzPOXD** can thus not be concluded from the obtained data.

In case of **o-3MPCzPOXD** the torsion angles Φ^1 of the least squares planes of the carbazole moieties and the PCz-benzenes are significantly increased (79.34(4)°/82.35(4)°) compared to **o-PCzPOXD** (57.68(5)°/56.38(5)°) as result of the methyl groups next to the carbazoles. In contrast, the variation of Φ^1 for **o-2MPCzPOXD** (58.69(8)°/58.26(15)°) is negligible compare to **o-PCzPOXD**. The inverse situation is observed for Φ^2 , which is enlarged in **o-2MPCzPOXD** (64.44(11)°/66.97(12)°) versus **o-PCzPOXD** (54.12(6)°/53.49(6)°), whereas no change was observed for **o-3MPCzPOXD** (54.18(5)°/51.85(5)°). Moreover, altered torsion angles Φ^3 were found for **o-2MPCzPOXD**, whereupon one is smaller (19.48(12)°) and one larger (43.83(12)°) compared to **o-PCzPOXD** (32.44(8)°/33.63(8)°) and **o-3MPCzPOXD** (38.36(6)°/32.34(6)°). The increased respective torsion angles of the aromatic moieties next to the methyl-groups in **o-2MPCzPOXD** and **o-3MPCzPOXD** significantly reduce the overall conjugation of the π -system and, in particular, the conjugation between the carbazole donors and the POXD acceptors. Therefore, decreased intramolecular charge transfer and, as a result, higher triplet energies are expected for the methyl-modified host materials.

3.4. Theoretical calculations

To gain insight on the electronic properties of the materials on the molecular level, studies applying density functional theory (DFT) and time-dependent DFT (TDDFT) calculations were performed. According to the DFT calculations, absolute HOMO/LUMO values are in a small range of 5.50–5.55/2.02–2.04 eV, which correlates well with the experimental data (Table 3). Contour plots for **o-PCzPOXD**, **o-2MPCzPOXD** and **o-3MPCzPOXD**, comparing the HOMO

Table 1

Characteristic torsion angles of host materials.

	o-PCzPOXD	o-2MPCzPOXD	o-3MPCzPOXD
Φ^1	57.68(5)°/56.38(5)°	58.69(8)°/58.26(15)° ^a	79.34(4)°/82.35(4)°
Φ^2	54.12(6)°/53.49(6)°	64.44(11)°/66.97(12)° ^a	54.18(5)°/51.85(5)°
Φ^3	32.44(8)°/33.63(8)°	19.48(12)°/43.83(12)°	38.36(6)°/32.34(6)°

^a Inexact because the benzene and carbazole moieties are disordered.

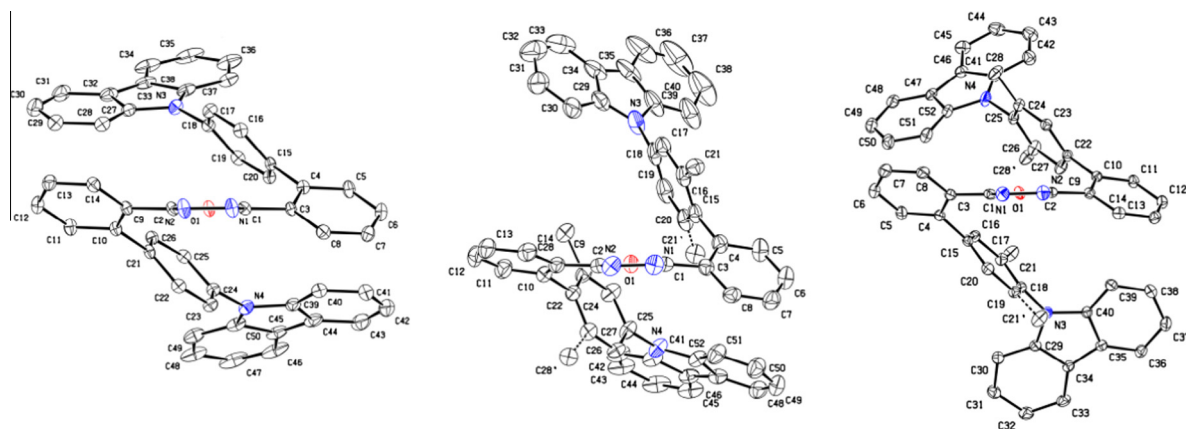


Fig. 1. Molecular structures of **o-PCzPOXD** (left), **o-2MPCzPOXD** (middle) and **o-3MPCzPOXD** (right); C, N and O atoms are represented by white, blue and red ellipsoids drawn at 50% probability levels, H atoms were omitted for clarity. (For interpretation of the references to color in this figure legend, the reader is referred to the web version of this article.)

Table 2

Contribution of molecular subunits to HOMO and LUMO levels.

	HOMO (%)			LUMO (%)		
	PCz	2MPCz	3MPCz	PCz	2MPCz	3MPCz
Cz	89	89	95	0	0	0
P	10	11	5	4	2	3
POXD	1	1	0	89	95	91
P'	0	0	0	6	3	5
Cz'	0	0	0	1	0	1

and LUMO distributions, are depicted in Fig. 2. As expected, HOMO levels are mainly located at one of the carbazole (Cz) moieties and the adjacent benzene (P) linker, whereas LUMOs reside at the POXD core. The spatial separation of the frontier orbitals was found to be more efficiently realized in the methyl substituted derivatives. To get a better quantitative description of this separation, the contribution of the different structural elements (Cz, P, POXD, P', Cz') to the HOMO and LUMO was calculated. The results are given in Table 2. Comparing **o-2MPCzPOXD** to **o-PCzPOXD** the HOMO distribution is nearly unchanged. For both compounds approximately 89% of the electron

density is located at one carbazole moiety and 10–11% are situated at the benzene linker. In contrast the LUMO distribution is modified by the additional methyl group and is distinctly better confined at the POXD motive (PCz: 89%; 2MPCz: 95%). Notably these findings directly correlate to the increased torsion angle Φ^2 of **o-2MPCzPOXD**. Whereas the phenylcarbazole subunit and thus the HOMO distribution is essentially unaffected by the methyl group the torsion angle Φ^2 between the phenylcarbazole donor and POXD acceptor is increased, confining the LUMO to the POXD core. Analogously, the LUMO distribution is nearly unchanged in **o-3MPCzPOXD** compared to **o-PCzPOXD**, whereas the HOMO is basically restricted to the carbazole moiety (PCz: 89%; 3MPCz: 95%) owing to the increased torsion angle Φ^1 . Therefore, the additional methyl groups do not cause a reorganization of the molecular orbitals but the enhanced torsion angles lead to a better confinement of the HOMO and LUMO distribution to the corresponding molecular subunit. Due to the better spatial resolution higher E_T are expected for **o-2MPCzPOXD** and **o-3MPCzPOXD** and indeed the calculated E_T values increase from **o-PCzPOXD** (2.83 eV) to **o-3MPCzPOXD** (2.91 eV) and **o-2MPCzPOXD** (2.92 eV).

Table 3

Physical data of synthesized materials.

	$T_g/T_m/T_d$ (°C) ^a	opt. BG (eV) ^{b,c}	$\lambda_{PL,max}$ (nm) ^c	HOMO/LUMO (eV)		E_T (eV)	
				Exp. ^d	Cal. ^e	Exp. ^f	Cal. ^g
o-PCzPOXD [22]	125/252/395	3.51	428	−5.64/−2.12	−5.55/−2.04	2.62	2.83
o-2MPCzPOXD	128/238/401	3.53	427	−5.60/−2.07	−5.50/−2.02	2.66	2.92
o-3MPCzPOXD	n.o. ^h /314/415	3.57	420	−5.66/−2.09	−5.55/−2.02	2.73	2.91

^a Determined from DSC/TGA analysis.

^b Determined from the absorption onset.

^c Measured in DCM (5 μ M) at r.t.

^d HOMO levels were calculated from the onset of the oxidation peak. CV-measurements were carried out in a 0.5 mM solution in anhydrous DCM with Bu_4NBF_4 (0.1 M) as supporting electrolyte; LUMO levels were calculated from HOMO levels and the optical band gap.

^e Calculated applying density functional theory level (B3LYP/6-311+G*).

^f Estimated from the highest energy vibronic transition in toluene at 77 K.

^g Calculated applying the time-dependent density functional theory level (B3LYP/6-311+G*).

^h Not observed.

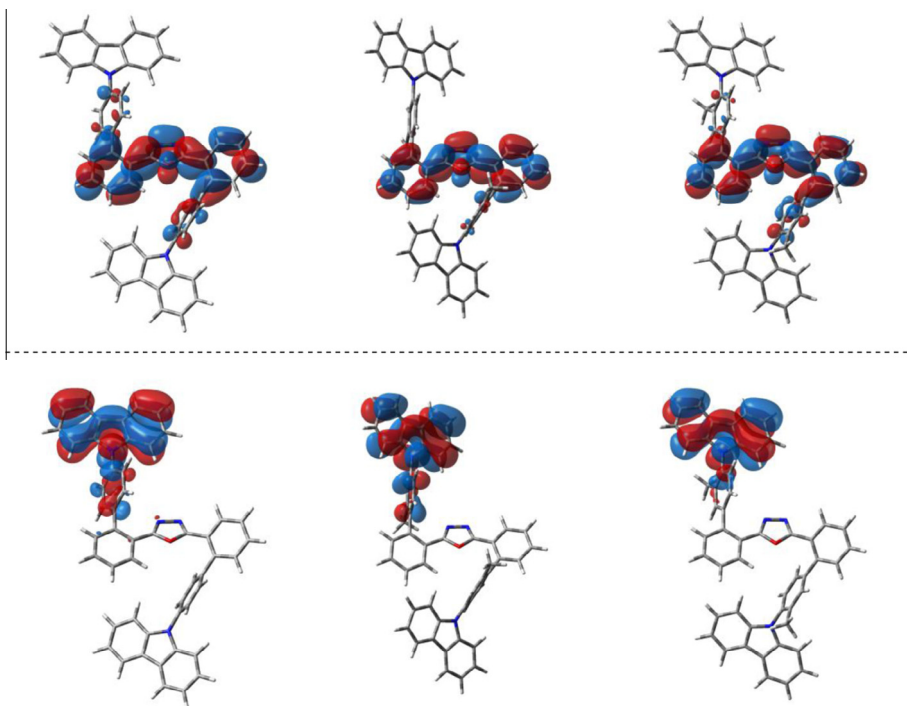


Fig. 2. Spatial distribution of HOMO (bottom) and LUMO (top) of **o-PCzPOXD** (left), **o-2MPCzPOXD** (middle) and **o-3MPCzPOXD** (right).

3.5. Photo-physical properties

In order to investigate the impact of the additional methyl groups in **o-2MPCzPOXD** and **o-3MPCzPOXD** on the photo-physical properties UV/VIS absorption as well as fluorescence and phosphorescence emission spectra have been recorded (Fig. 3). Absorption spectra of the methyl substituted materials and **o-PCzPOXD** are highly similar. All compounds show a sharp absorption peak at 290 nm which can be attributed to transitions of the carbazole moiety [51] (ϵ ($1 \text{ mol}^{-1} \text{ cm}^{-1}$) = $\sim 57,000$ (**o-PCzPOXD**), $\sim 50,000$ (**o-2MPCzPOXD**), $\sim 43,000$ (**o-3MPCzPOXD**). Longer wavelength absorption results from charge transfer transition from electron-rich carbazole to electron-withdrawing oxadiazole [52]. For **o-2MPCzPOXD** and **o-3MPCzPOXD** the intensity of this transition is distinctly decreased compared to **o-PCzPOXD** indicating a decreased degree of charge transfer. The absorption onset of the newly developed materials is slightly blue shifted from **o-PCzPOXD** (353 nm) to **o-2MPCzPOXD** (351 nm) and **o-3MPCzPOXD** (347 nm), corresponding to an optical band gap of 3.51, 3.53 and 3.57 eV.

Due to the slight electron-donating nature of the methyl group, methyl substituted phenylcarbazoles are expected to be stronger electron-donors compared to plain phenylcarbazole. Therefore, applying the new MPCz donors to the oxadiazole acceptor, slightly red shifted emission may be expected. However, this effect is over-compensated by the increased molecular torsion induced by the steric demand of the methyl substituents leading to slightly blue shifted emission maxima of **o-2MPCzPOXD** (427 nm) and **o-3MPCzPOXD** (420 nm) compared to **o-PCzPOXD** (428 nm).

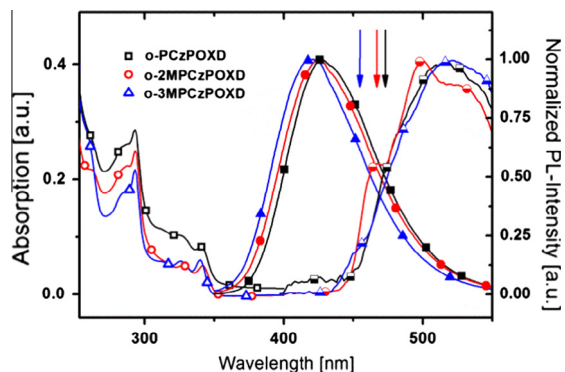


Fig. 3. UV-VIS absorption (hollow symbols), normalized fluorescence spectra at room temperature (full symbols) and normalized phosphorescence spectra at 77 K (half-full symbols) of **o-PCzPOXD** (squares), **o-2MPCzPOXD** (circles) and **o-3MPCzPOXD** (triangles).

Strikingly, this effect is much more pronounced in phosphorescent emission spectra of methyl-substituted host materials and the highest vibronic sub-bands are blue shifted from **o-PCzPOXD** (473 nm) to **o-2MPCzPOXD** (466 nm) and **o-3MPCzPOXD** (454 nm), corresponding to E_T of 2.62, 2.66 and 2.73 eV. Therefore, the E_T of the newly developed materials was raised by 0.11 eV, whereas the HOMO–LUMO gap was increased by only 0.06 eV and thus the singlet–triplet splitting even slightly reduced by 0.05 eV. Notably the increase of E_T from **o-PCzPOXD** to **o-2MPCzPOXD** and **o-3MPCzPOXD** correlates with the increased torsion angles as discussed in the crystallographic section. These results suggest that the methyl substituted

host materials are distinctly better suited for light blue emitting Flrpic, since the E_T of the target materials is raised over the crucial value of 2.65 eV, allowing for an exothermic energy transfer from the host to the dopant. Accordingly, the effect on driving voltages of the PHOLED devices is expected to be negligible, due to the low overall increase of the HOMO–LUMO gap. All photo-physical characteristics are summarized in Table 3.

3.6. Thermal properties

The thermal and morphological stability (Table 3) of **o-2MPCzPOXD** and **o-3MPCzPOXD** were investigated by DSC and TGA (Supplementary Material Figs. S 15 and 16). The decomposition temperatures (T_d – corresponding to the temperatures of 5% mass loss) of **o-2MPCzPOXD** and **o-3MPCzPOXD** are 401 °C and 415 °C and therefore slightly higher compared to **o-PCzPOXD** (395 °C) [22]. The glass transition temperature (T_g) of **o-2MPCzPOXD** (128 °C) was found to be similar to that of **o-PCzPOXD** (125 °C) [22]; no glass transition was detected for **o-3MPCzPOXD** but exothermic crystallization was observed at 212 °C during cooling.

3.7. Electro-chemical properties

The electrochemical properties (Table 3) of the newly developed materials were studied by cyclic voltammetry (CV). Both materials exhibit irreversible oxidation (Fig. 4) typically for 3,6-unprotected carbazole materials [53]. The HOMO levels were calculated from the onset of the oxidation waves relative to ferrocene and are located at –5.60 and –5.66 eV for **o-2MPCzPOXD** and **o-3MPCzPOXD**, respectively. These values indicate no significant injection barrier for holes from the adjacent layers and are in a characteristic range for oxadiazole/carbazole-based bipolar materials [44,52]. Upon cathodic scans no reduction peaks were observed. Thus, the LUMO levels were calculated from the HOMOs and the onset of absorption and are located at –2.07 and –2.09 eV for **o-2MPCzPOXD** and **o-3MPCzPOXD**. These values deviate only slightly from the HOMO (–5.64 eV) and LUMO (–2.12 eV) of **o-PCzPOXD** [22] revealing negligible influence of the additional methyl groups on the absolute location of the levels, as predicted by the theoretical calculations.

3.8. Electroluminescent properties

To investigate the bipolarity of the materials, hole-only devices (HODs; structure: ITO/MoO₃ (10 nm)/TCTA (20 nm)/POXD (40 nm)/TCTA (20 nm)/MoO₃ (10 nm)/Al) and electron-only devices (EODs; structure: ITO/LiF (1 nm)/TPBI (20 nm)/POXD (40 nm)/TPBI (20 nm)/LiF (1 nm)/Al) were fabricated. Current–voltage curves are given in Fig. 5. **o-PCzPOXD** featured highly balanced charge carrier density. Despite similar charge carrier injection barriers the charge transport properties were distinctly less balanced for **o-2MPCzPOXD** and **o-3MPCzPOXD**. Hole current densities were slightly higher in HODs of **o-2MPCzPOXD** and **o-3MPCzPOXD** compared to **o-PCzPOXD**. In contrast electron current densities in EODs decreased in the order **o-PCzPOXD** > **o-2MPCzPOXD** > **o-3MPCzPOXD**.

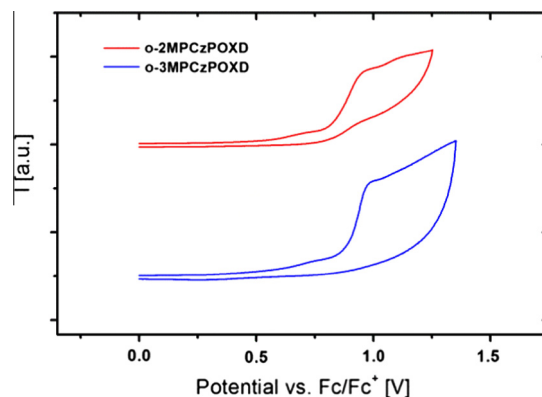


Fig. 4. CV curves of **o-2MPCzPOXD** and **o-3MPCzPOXD**.

The significantly lower electron current densities of **o-2MPCzPOXD** and **o-3MPCzPOXD** may be attributed to the additional methyl groups which are located in close vicinity above and below the POXD plane as can be seen in Fig. 1. The steric demand of these methyl groups may impede the intermolecular overlap of LUMO orbitals located on the POXD core and thus decrease the electron current density. However, more complex factors influencing the molecular arrangements and therefore charge transport properties of the molecules in film cannot be ruled out.

In order to evaluate the applicability of **o-2MPCzPOXD** and **o-3MPCzPOXD** in comparison to **o-PCzPOXD** as host materials in red, green and blue PHOLEDs, devices with the architecture of ITO/MoO₃/NPB (70 nm)/TCTA (5 nm)/EML (10 nm)/TPBI (35 nm)/LiF/Al have been fabricated. The emissive layers consist of coevaporated hosts **o-PCzPOXD** (I), **o-2MPCzPOXD** (II) or **o-3MPCzPOXD** (III) and red (**R** – 6% Ir(MDQ)₂(acac)), green (**G** – 8% Ir(ppy)₃) or blue (**B** – 12% Flrpic) guest emitter. NPB is used as hole transporting layer while TPBI is applied as electron transporting and hole blocking layer due to its low lying HOMO level [54–57]. Additionally a thin TCTA layer is inserted between the hole transporting and emitting layer in order to confine triplet excitons more effectively in the EML as result of a larger triplet energy of TCTA compared to NPB [55]. All

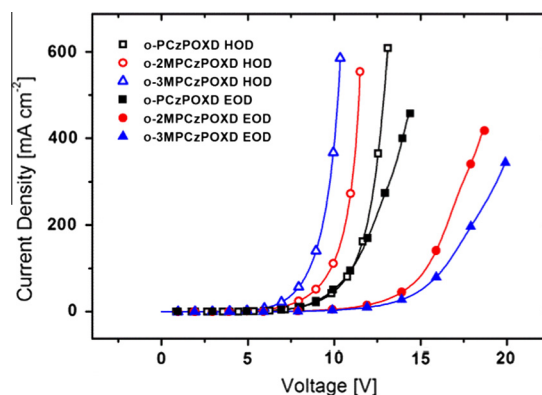


Fig. 5. Current–voltage (I – V) curves of hole- (hollow symbols) and electron-only (full symbols) devices.

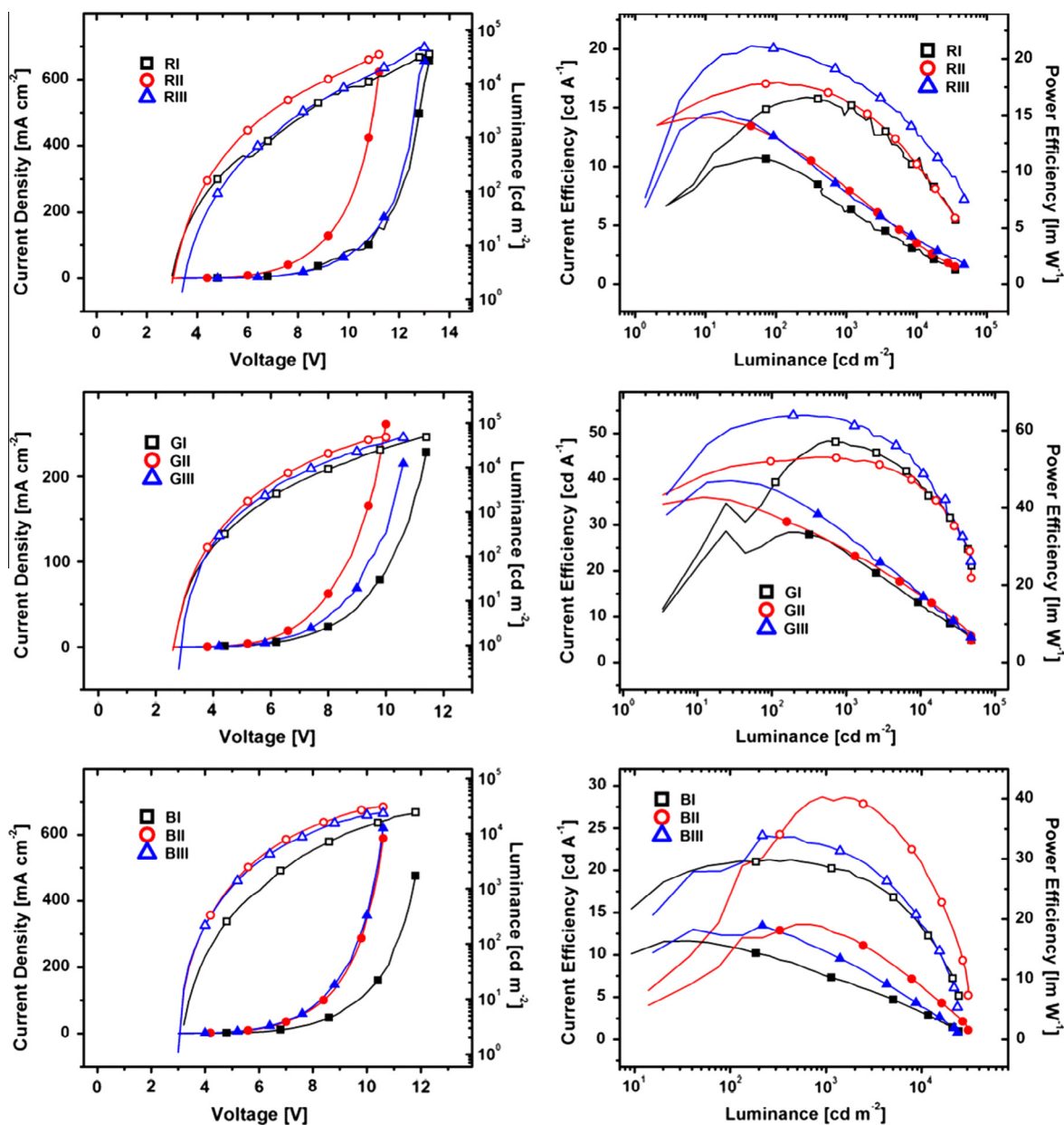


Fig. 6. Current density–voltage–luminance (full symbols: current density; hollow symbols: luminance) and current efficiency–luminance–power efficiency (full symbols: power efficiency; hollow symbols: current efficiency) curves of devices **RI-III**, **GI-III** and **BI-III**.

devices exhibited low turn-on voltages between 2.8 and 3.4 V. Current density–voltage–luminance and current efficiency–luminance–power efficiency charts are depicted in Fig. 6 and the key EL parameters of all devices are summarized in Table 4.

Among green devices **GIII** exhibited the best performance with a maximum current efficiency (CE) of 54.0 cd A⁻¹, a maximum power efficiency (PE) of 47.8 lm W⁻¹ and a maximum external quantum efficiency (EQE) of 15.4%, whereas **GI** and **GII** showed comparable but slightly lower efficiency values. Most notably, the efficiency roll-off in **GI-III** was extremely low as already observed for other

oxadiazole based bipolar host materials employing planarized arylamine donors [22]. At a practical brightness of 1000 cd m⁻² **GI-III** featured CE of 44.5–52.7 cd A⁻¹ corresponding to efficiency roll-offs of 0.7–2.4%. Even at a brightness of 5000 cd m⁻² the CE values were still as high as 41.3–46.5 cd A⁻¹ (roll-off: 7.8–13.9%). Devices **RI-III** displayed similar performance with CE_{max} of 20.3–15.9 cd A⁻¹, PE_{max} of 15.3–11.2 lm W⁻¹ and EQE_{max} of 12.8–11.4% whereupon the best results were acquired for **RIII**. In analogy to green devices **RI-III** exhibited low efficiency roll-off of 25.8–27.9% at 5000 cd m⁻². In summary, **o-PCzPOXD**, **o-2MPCzPOXD** and **o-3MPCzPOXD** featured comparable

Table 4

Electroluminescent properties of devices **RI-III**, **GI-III**, and **BI-V**.

	V_{on} (V)	CE (cd A^{-1}) ^a	PE (lm W^{-1}) ^a	EQE (%) ^a
RI	3.0	15.3/14.4/11.8/15.9	10.9/6.4/4.1/11.2	11.0/10.2/8.2/11.4
RII	3.0	17.2/15.3/12.4/17.2	12.8/8.3/5.1/14.8	12.8/11.2/8.8/12.8
RIII	3.4	20.1/17.6/14.7/20.3	13.1/7.9/5.1/15.3	12.7/10.8/8.8/12.8
GI	2.8	39.3/47.4/43.3/48.3	32.5/27.6/19.4/34	10.7/12.9/11.8/13.2
GII	2.8	43.9/44.5/41.3/44.8	38.3/29.1/20.9/42.8	12.6/12.7/11.8/12.9
GIII	2.8	53.6/52.7/46.5/54.0	44.3/33.1/22.1/47.8	15.4/15.2/13.4/15.4
BI	3.2	20.8/20.5/16.8/21.3	15.5/10.8/6.6/16.6	8.8/8.7/7.1/9.0
BII	3.0	20.6/28.7/25.1/28.7	16.7/18.8/12.3/19.2	9.7/13.6/11.9/13.6
BIII	3.0	20.9/22.8/18.0/24.3	17.3/14.3/8.6/18.9	9.5/10.1/8.6/11.5
BIV	3.0	15.9/11.5/-/15.9	12.5/6.3/-/13.3	7.8/5.7/-/7.8
BV	3.0	16.5/11.1/-/16.7	12.9/5.8/-/14.9	7.7/5.2/-/7.8

^a Measured at a brightness of 100 cd m^{-2} /1000 cd m^{-2} /5000 cd m^{-2} /max.

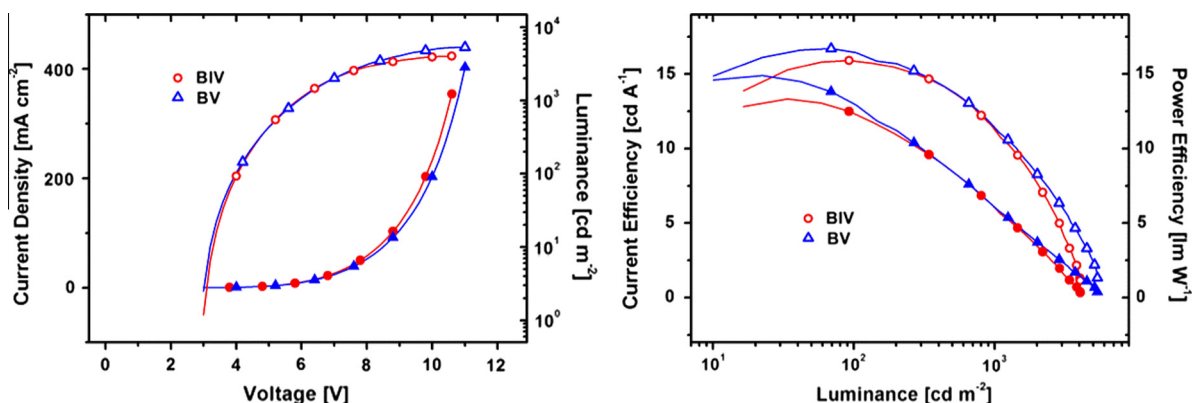


Fig. 7. Current density–voltage–luminance (full symbols: current density; hollow symbols: luminance) and current efficiency–luminance–power efficiency (full symbols: power efficiency; hollow symbols: current efficiency) curves of devices **BIV** and **BV**.

performance in red and green devices; no negative effects arise from the introduced methyl groups and, with the exception of **G2**, devices incorporating **o-2MPCzPOXD** and **o-3MPCzPOXD** showed slightly higher efficiency values compared to **o-PCzPOXD**. Most importantly, the power efficiency of devices employing **o-2MPCzPOXD** and **o-3MPCzPOXD** is not decreased as result of the slightly higher singlet band gap compared to **o-PCzPOXD**.

While red and green devices showed similar performance values the results for blue devices (Flrpic as phosphorescent emitter) are distinctly different. Significantly improved efficiencies were achieved in **o-2MPCzPOXD** and **o-3MPCzPOXD** based devices revealing an EQE_{max} increase from 9.0% (**o-PCzPOXD**) to 11.5% (**o-3MPCzPOXD**) and 13.6% (**o-2MPCzPOXD**), which corresponds to an efficiency improvement of 27.8% and 51.1%, respectively. These findings are clearly attributed to the increased E_T of **o-2MPCzPOXD** and **o-3MPCzPOXD** as result of the additional methyl groups and, thus, better confinement of triplet excitons on the phosphorescent emitter. Strikingly, for **o-2MPCzPOXD** this effect is even more pronounced at high brightness and **BII** exhibited EQE of 13.6% (+56.3% compared to **o-PCzPOXD**) at 1000 cd m^{-2} and 11.9% (+67.6%) at 5000 cd m^{-2} . Furthermore, low efficiency roll-off was observed for **BI-III**. At 1000 cd m^{-2} **BII** featured CE of

28.7 cd A^{-1} (roll-off: 0.0%) whereas at 5000 cd m^{-2} CE was still as high as 25.1 cd A^{-1} (roll-off: 12.5%). Despite the higher E_T of **o-3MPCzPOXD** **BIII** showed slightly lower efficiencies compared to **BII**. In contrast to red and green devices direct charge trapping on the emitter is not feasible in **BII** and **BIII** due to the low HOMO level of Flrpic (−5.8 eV). Thus, charge balance should play a dominated role regarding to device performance and the more balanced charge transport properties of **o-2MPCzPOXD** (Fig. 5) explains the better performance of the **BII** device (for energy level diagrams see [Supplementary Material](#)). Additionally the PE of both **BII** and **BIII** were significantly improved compared to **BI** at high brightness, which is of particular importance regarding the practical applicability of host materials in commercial devices. **BII** exhibits a CE of 18.8 lm W^{-1} at 1000 cd m^{-2} and 12.3 lm W^{-1} at 5000 cd m^{-2} displaying an improvement of 74.1% and 86.4% compared to **o-PCzPOXD**, respectively.

Although Flrpic is by far the most frequently used phosphorescent emitter for the characterization of new host materials, Flrpic emits in the sky-blue region. However, for the realization of full-color displays and white lighting with good color rendering index, high quality blue light is indispensable. Recent reports on Flr6 devices based on host materials [58] with relatively low E_T compared to blue

emitting Flr6 (E_T : 2.72 eV) [59] encouraged us to investigate **o-2MPCzPOXD** and **o-3MPCzPOXD** as host materials for that purpose. Thus, devices **BIV (o-2MPCzPOXD)** and **BV (o-3MPCzPOXD)** with the architecture of ITO/MoO₃/NPB (70 nm)/TCTA (5 nm)/EML (10 nm)/TmPyPB (35 nm)/LiF/Al applying Flr6 as dopant have been fabricated. TmPyPB is applied as electron transporting layer due to its slightly higher E_T (2.78 eV) compared to TPBI (2.74 eV) [7]. Current density–voltage–luminance and current efficiency–luminance–power efficiency curves are depicted in Fig. 7 and the key EL parameters of all devices are summarized in Table 4. Devices **BIV** and **BV** exhibited similar performance with CE_{\max} of 15.9 and 16.7 cd A⁻¹, PE_{\max} of 13.3 and 14.9 lm W⁻¹ and EQE_{\max} of 7.8% and 7.8%, respectively. Although these values are lower than previously reported efficiencies [58] the fabrication of Flr6 based devices **BIV** and **BV** demonstrates the broadened applicability of **o-2MPCzPOXD** and **o-3MPCzPOXD** as a result of sterically induced torsion.

4. Conclusion

The investigations reveal the strategic objective of tuning the triplet energy virtually independently from the singlet energy for the specific adjustment of material properties accompanied with PHOLED performance of bipolar host materials. The strategy of rational molecular design applying sterically induced torsion to raise triplet energies, which is of particular importance for high-energy emitters, has been demonstrated for carbazole–oxadiazole based **o-PCzPOXD**. As a result, the triplet energies were affected more pronouncedly compared to the singlet energy values in novel materials **o-2MPCzPOXD** and **o-3MPCzPOXD** leading to significantly improved device performances for blue devices while showing similar efficiencies for the green devices. Ongoing research will focus on molecular design concepts to more efficiently separate the tuning of triplet energies from the impact on singlet energy values and the adaptation to further donor–acceptor motives, which is of relevance for the functional organic materials community in general.

Acknowledgement

This work was supported in part by the Swiss National Science Foundation, the Vienna University of Technology research funds and the Austrian Federal Ministry of Science, Research and Economy. The X-ray center of the Vienna University of Technology is acknowledged for providing access to the single-crystal diffractometer. G. Faflek is acknowledged for support regarding the CV measurements and K. Föttinger for assisting the photo-physical analysis.

Appendix A. Supplementary material

Supplementary data (¹H/¹³C NMR spectra, TGA/DSC measurements, electro- and photoluminescence spectra and X-ray crystallography) associated with this article

can be found, in the online version, at <http://dx.doi.org/10.1016/j.orgel.2014.11.027>.

References

- [1] C.W. Tang, S.A. VanSlyke, Organic electroluminescent diodes, *Appl. Phys. Lett.* 51 (1987) 913–915.
- [2] S.R. Forrest, The path to ubiquitous and low-cost organic electronic appliances on plastic, *Nature* 428 (2004) 911–918.
- [3] Y. Sun, N.C. Giebink, H. Kanno, B. Ma, M.E. Thompson, S.R. Forrest, Management of singlet and triplet excitons for efficient white organic light-emitting devices, *Nature* 440 (2006) 908–912.
- [4] S. Reineke, F. Lindner, G. Schwartz, N. Seidler, K. Walzer, B. Lüssem, K. Leo, White organic light-emitting diodes with fluorescent tube efficiency, *Nature* 459 (2009) 234–238.
- [5] M.C. Gather, A. Köhnen, K. Meerholz, White organic light-emitting diodes, *Adv. Mater.* 23 (2011) 233–248.
- [6] L. Xiao, Z. Chen, B. Qu, J. Luo, S. Kong, Q. Gong, J. Kido, Recent progresses on materials for electrophosphorescent organic light-emitting devices, *Adv. Mater.* 23 (2011) 926–952.
- [7] Y. Tao, C. Yang, J. Qin, Organic host materials for phosphorescent organic light-emitting diodes, *Chem. Soc. Rev.* 40 (2011) 2943–2970.
- [8] H. Sasabe, J. Kido, Recent progress in phosphorescent organic light-emitting devices, *Eur. J. Org. Chem.* 2013 (2013) 7653–7663.
- [9] S. Reineke, M. Thomschke, B. Lüssem, K. Leo, White organic light-emitting diodes: status and perspective, *Rev. Mod. Phys.* 85 (2013) 1245–1293.
- [10] K.S. Yook, J.Y. Lee, Organic materials for deep blue phosphorescent organic light-emitting diodes, *Adv. Mater.* 24 (2012) 3169–3190.
- [11] M.A. Baldo, D.F. O'Brien, Y. You, A. Shoustikov, S. Sibley, M.E. Thompson, S.R. Forrest, Highly efficient phosphorescent emission from organic electroluminescent devices, *Nature* 395 (1998) 151–154.
- [12] M.A. Baldo, S. Lamansky, P.E. Burrows, M.E. Thompson, S.R. Forrest, Very high-efficiency green organic light-emitting devices based on electrophosphorescence, *Appl. Phys. Lett.* 75 (1999) 4–6.
- [13] M.A. Baldo, D.F. O'Brien, M.E. Thompson, S.R. Forrest, Excitonic singlet–triplet ratio in a semiconducting organic thin film, *Phys. Rev. B* 60 (1999) 14422–14428.
- [14] C. Adachi, M.A. Baldo, M.E. Thompson, S.R. Forrest, Nearly 100% internal phosphorescence efficiency in an organic light-emitting device, *J. Appl. Phys.* 90 (2001) 5048–5051.
- [15] M.A. Baldo, C. Adachi, S.R. Forrest, Transient analysis of organic electrophosphorescence. II. Transient analysis of triplet–triplet annihilation, *Phys. Rev. B* 62 (2000) 10967–10977.
- [16] C. Murawski, K. Leo, M.C. Gather, Efficiency roll-off in organic light-emitting diodes, *Adv. Mater.* 25 (2013) 6801–6827.
- [17] A. Chaskar, H.-F. Chen, K.-T. Wong, Bipolar host materials: a chemical approach for highly efficient electrophosphorescent devices, *Adv. Mater.* 23 (2011) 3876–3895.
- [18] S.O. Jeon, J.Y. Lee, Phosphine oxide derivatives for organic light emitting diodes, *J. Mater. Chem.* 22 (2012) 4233–4243.
- [19] R.J. Holmes, B.W. D'Andrade, S.R. Forrest, X. Ren, J. Li, M.E. Thompson, Efficient, deep-blue organic electrophosphorescence by guest charge trapping, *Appl. Phys. Lett.* 83 (2003) 3818–3820.
- [20] R.J. Holmes, S.R. Forrest, Y.-J. Tung, R.C. Kwong, J.J. Brown, S. Garon, M.E. Thompson, Blue organic electrophosphorescence using exothermic host–guest energy transfer, *Appl. Phys. Lett.* 82 (2003) 2422–2424.
- [21] S. Tokito, T. Iijima, Y. Suzuri, H. Kita, T. Tsuzuki, F. Sato, Confinement of triplet energy on phosphorescent molecules for highly-efficient organic blue-light-emitting devices, *Appl. Phys. Lett.* 83 (2003) 569–571.
- [22] P. Kautny, D. Lumpi, Y. Wang, A. Tissot, J. Bintinger, E. Horkel, B. Stöger, C. Hametner, H. Hagemann, D. Ma, J. Fröhlich, Oxadiazole based bipolar host materials employing planarized triarylamine donors for RGB PHOLEDs with low efficiency roll-off, *J. Mater. Chem. C* 2 (2014) 2069–2081.
- [23] M.K. Kim, J. Kwon, T.-H. Kwon, J.-I. Hong, A bipolar host containing 1,2,3-triazole for realizing highly efficient phosphorescent organic light-emitting diodes, *New J. Chem.* 34 (2010) 1317–1322.
- [24] L.G. Liu, Y.F. Xu, X.H. Qian, Q.C. Huang, Novel analogs of α -terthienyl, thienyl 1,3,4-thia(oxa)diazoles as potential photoactivated insecticides: synthesis and bioactivity, *Chin. Chem. Lett.* 15 (2004) 7–10.
- [25] R. Anémian, D.C. Cupertino, P.R. Mackie, S.G. Yeates, Solution phase studies toward the synthesis of triarylamine oligomers using a

- germanium linker on a solid support, *Tetrahedron Lett.* 46 (2005) 6717–6721.
- [26] W.-Y. Lee, T. Kurosawa, S.-T. Lin, T. Higashihara, M. Ueda, W.-C. Chen, New donor–acceptor oligoimides for high-performance nonvolatile memory devices, *Chem. Mater.* 23 (2011) 4487–4497.
- [27] H.G. Dunlop, S.H. Tucker, Attempts to prepare optically active tervalent nitrogen compounds. Part I. Syntheses of 1: 9-phenylencarbazole and derivatives, *J. Chem. Soc.* 399 (1939) 1945–1956 (Resumed).
- [28] S.Y. Cho, A.C. Grimsdale, D.J. Jones, S.E. Watkins, A.B. Holmes, Polyfluorenes without monoalkylfluorene defects, *J. Am. Chem. Soc.* 129 (2007) 11910–11911.
- [29] N. Miyaura, A. Suzuki, Palladium-catalyzed cross-coupling reactions of organoboron compounds, *Chem. Rev.* 95 (1995) 2457–2483.
- [30] M.J. Frisch, G.W. Trucks, H.B. Schlegel, G.E. Scuseria, M.A. Robb, J.R. Cheeseman, G. Scalmani, V. Barone, B. Mennucci, G.A. Petersson, H. Nakatsuji, M. Caricato, X. Li, H.P. Hratchian, A.F. Izmaylov, J. Bloino, G. Zheng, J.L. Sonnenberg, M. Hada, M. Ehara, K. Toyota, R. Fukuda, J. Hasegawa, M. Ishida, T. Nakajima, Y. Honda, O. Kitao, H. Nakai, T. Vreven, J.A. Montgomery Jr., J.E. Peralta, F. Ogliaro, M. Bearpark, J.J. Heyd, E. Brothers, K.N. Kudin, V.N. Staroverov, R. Kobayashi, J. Normand, K. Raghavachari, A. Rendell, J.C. Burant, S.S. Iyengar, J. Tomasi, M. Cossi, N. Rega, N.J. Millam, M. Klene, J.E. Knox, J.B. Cross, V. Bakken, C. Adamo, J. Jaramillo, R. Gomperts, R.E. Stratmann, O. Yazyev, A.J. Austin, R. Cammi, C. Pomelli, J.W. Ochterski, R.L. Martin, K. Morokuma, V.G. Zakrzewski, G.A. Voth, P. Salvador, J.J. Dannenberg, S. Dapprich, A.D. Daniels, Oe. Farkas, J.B. Foresman, J.V. Ortiz, J. Cioslowski, D.J. Fox, Gaussian 09, Revision D.01, Gaussian Inc, Wallingford CT, 2009.
- [31] C. Lee, W. Yang, R.G. Parr, Development of the Colle–Salvetti correlation-energy formula into a functional of the electron density, *Phys. Rev. B* 37 (1988) 785–789.
- [32] A.D. Becke, Density-functional thermochemistry. III. The role of exact exchange, *J. Chem. Phys.* 98 (1993) 5648–5652.
- [33] R. Krishnan, J.S. Binkley, R. Seeger, J.A. Pople, Self-consistent molecular orbital methods. XX. A basis set for correlated wave functions, *J. Chem. Phys.* 72 (1980) 650–654.
- [34] T. Lu, F. Chen, Multiwfn: a multifunctional wavefunction analyzer, *J. Comput. Chem.* 33 (2012) 580–592.
- [35] R. Dennington, T. Keith, J. Millam, GaussView, Version 5, Semichem Inc., Shawnee Mission KS, 2009.
- [36] Bruker Computer Programs: APEX2, SAINT, SADABS, and SHELXTL, Bruker AXS Inc., Madison WI, 2013.
- [37] L. Palatinus, G. Chapuis, SUPERFLIP – a computer program for the solution of crystal structures by charge flipping in arbitrary dimensions, *J. Appl. Crystallogr.* 40 (2007) 786–790.
- [38] V. Petříček, M. Dušek, L. Palatinus, Jana2006. The Crystallographic Computing System, Institute of Physics, Praha, Czech Republic, 2006.
- [39] Z. Ge, T. Hayakawa, S. Ando, M. Ueda, T. Akiike, H. Miyamoto, T. Kajita, M.-A. Kakimoto, Spin-coated highly efficient phosphorescent organic light-emitting diodes based on bipolar triphenylamine-benzimidazole derivatives, *Adv. Funct. Mater.* 18 (2008) 584–590.
- [40] J. He, H. Liu, Y. Dai, X. Ou, J. Wang, S. Tao, X. Zhang, P. Wang, D. Ma, Nonconjugated carbazoles: a series of novel host materials for highly efficient blue electrophosphorescent OLEDs, *J. Phys. Chem. C* 113 (2009) 6761–6767.
- [41] D. Wagner, S.T. Hoffmann, U. Heinemeyer, I. Münster, A. Köhler, P. Strohhriegl, Triazine based bipolar host materials for blue phosphorescent OLEDs, *Chem. Mater.* 25 (2013) 3758–3765.
- [42] C.W. Lee, J.Y. Lee, High quantum efficiency and color stability in white phosphorescent organic light emitting diodes using a pyridine modified carbazole derivative, *Dyes Pigm.* 103 (2014) 34–38.
- [43] S. Hofmann, M. Hummert, R. Scholz, R. Luschinetz, C. Murawski, P.-A. Will, S.I. Hintschich, J. Alex, V. Jankus, A.P. Monkman, B. Lüssem, K. Leo, M.C. Gather, Engineering blue fluorescent bulk emitters for OLEDs: triplet harvesting by green phosphors, *Chem. Mater.* 26 (2014) 2414–2426.
- [44] Y. Zheng, A.S. Batsanov, V. Jankus, F.B. Dias, M.R. Bryce, A.P. Monkman, Bipolar molecules with high triplet energies: synthesis, photophysical, and structural properties, *J. Org. Chem.* 76 (2011) 8300–8310.
- [45] (2): $C_{25}H_{26}BNO_2$, $M_r = 383.3$, monoclinic, $C2/c$, $a = 25.4870(9) \text{ \AA}$, $b = 8.1586(3) \text{ \AA}$, $c = 20.4034(7) \text{ \AA}$, $\beta = 100.7543(15)^\circ$, $V = 4168.1(3) \text{ \AA}^3$, $Z = 8$, $\mu = 0.076 \text{ mm}^{-1}$, $T = 100 \text{ K}$, 62,430 measured, 6102 independent and 5013 observed [$I > 3\sigma(I)$] reflections, 262 parameters, $wR(F)$ (all data) = 0.0695, R [$I > 3\sigma(I)$] = 0.0425; CCDC reference number 1008518.
- [46] (4): $C_{19}H_{14}N_2O_2$, $M_r = 302.3$, triclinic, $P\bar{1}$, $a = 7.7738(3) \text{ \AA}$, $b = 12.6026(5) \text{ \AA}$, $c = 15.4833(7) \text{ \AA}$, $\alpha = 104.4551(18)^\circ$, $\beta = 92.579(2)^\circ$, $\gamma = 90.6132(18)^\circ$, $V = 1467.02(11) \text{ \AA}^3$, $Z = 4$, $\mu = 0.09 \text{ mm}^{-1}$, $T = 100 \text{ K}$, 52,514 measured, 10,725 independent and 8379 observed [$I > 3\sigma(I)$] reflections, 415 parameters, $wR(F)$ (all data) = 0.0621, R [$I > 3\sigma(I)$] = 0.0440; CCDC reference number 1008519.
- [47] (7): $C_{25}H_{26}BNO_2$, $M_r = 383.3$, monoclinic, $P2_1$, $a = 6.8278(3) \text{ \AA}$, $b = 30.3994(12) \text{ \AA}$, $c = 20.0477(8) \text{ \AA}$, $\beta = 90.251(3)^\circ$, $V = 4161.1(3) \text{ \AA}^3$, $Z = 8$, $\mu = 0.076 \text{ mm}^{-1}$, $T = 100 \text{ K}$, 105,394 measured, 18,036 independent and 15,608 observed [$I > 3\sigma(I)$] reflections, 1040 parameters, $wR(F)$ (all data) = 0.0620, R [$I > 3\sigma(I)$] = 0.0501; CCDC reference number 1008517.
- [48] (o-2MCzPOXD): $C_{52}H_{36}N_4O$, $M_r = 732.9$, monoclinic, $P2_1/c$, $a = 17.2182(9) \text{ \AA}$, $b = 24.396(3) \text{ \AA}$, $c = 9.2030(18) \text{ \AA}$, $\beta = 99.915(4)^\circ$, $V = 3808.0(9) \text{ \AA}^3$, $Z = 4$, $\mu = 0.077 \text{ mm}^{-1}$, $T = 100 \text{ K}$, 134,420 measured, 9136 independent and 5450 observed [$I > 3\sigma(I)$] reflections, 644 parameters, $wR(F)$ (all data) = 0.1143, R [$I > 3\sigma(I)$] = 0.0619; CCDC reference number 1008521.
- [49] (o-3MCzPOXD): $C_{52}H_{36}N_4O$, $M_r = 732.9$, monoclinic, Cc , $a = 27.9396(4) \text{ \AA}$, $b = 9.3735(6) \text{ \AA}$, $c = 15.5140(8) \text{ \AA}$, $\beta = 109.512(2)^\circ$, $V = 3829.7(3) \text{ \AA}^3$, $Z = 4$, $\mu = 0.076 \text{ mm}^{-1}$, $T = 100 \text{ K}$, 61,608 measured, 11,251 independent and 10,864 observed [$I > 3\sigma(I)$] reflections, 528 parameters, $wR(F)$ (all data) = 0.0471, R [$I > 3\sigma(I)$] = 0.0337; CCDC reference number 1008520.
- [50] B. Stöger, P. Kautny, D. Lumpi, E. Zobet, J. Fröhlich, The pseudo-inversion symmetry of 9,9'-(1,3,4-oxadiazole-2,5-diylidylidene)-2,2',4'-diylbis[9H-carbazole] in the light of OD theory, *Z. Kristallogr. – Cryst. Mater.* 229 (2014) 378–384.
- [51] Z. Ge, T. Hayakawa, S. Ando, M. Ueda, T. Akiike, H. Miyamoto, T. Kajita, M.-A. Kakimoto, Novel bipolar bathophenanthroline containing hosts for highly efficient phosphorescent OLEDs, *Org. Lett.* 10 (2008) 421–424.
- [52] Y. Tao, Q. Wang, C. Yang, C. Zhong, K. Zhang, J. Qin, D. Ma, Tuning the optoelectronic properties of carbazole/oxadiazole hybrids through linkage modes: hosts for highly efficient green electrophosphorescence, *Adv. Funct. Mater.* 20 (2010) 304–311.
- [53] E. Mondal, W.-Y. Hung, H.-C. Dai, K.-T. Wong, Fluorene-based asymmetric bipolar universal hosts for white organic light emitting devices, *Adv. Funct. Mater.* 23 (2013) 3096–3105.
- [54] M. Ikai, S. Tokito, Y. Sakamoto, T. Suzuki, Y. Taga, Highly efficient phosphorescence from organic light-emitting devices with an exciton-block layer, *Appl. Phys. Lett.* 79 (2001) 156–158.
- [55] D.-H. Lee, Y.-P. Liu, K.-H. Lee, H. Chae, S.M. Cho, Effect of hole transporting materials in phosphorescent white polymer light-emitting diodes, *Org. Electron.* 11 (2010) 427–433.
- [56] M.E. Kondakova, T.D. Pawlik, R.H. Young, D.J. Giesen, D.Y. Kondakov, C.T. Brown, J.C. Deaton, J.R. Lenhard, K.P. Klubek, High-efficiency, low-voltage phosphorescent organic light-emitting diode devices with mixed host, *J. Appl. Phys.* 104 (2008) 094501-1–094501-17.
- [57] S.H. Kim, J. Jang, K.S. Yook, J.Y. Lee, M.-S. Gong, S. Ryu, G.-K. Chang, H.J. Chang, Triplet host engineering for triplet exciton management in phosphorescent organic light-emitting diodes, *J. Appl. Phys.* 103 (2008) 054502-1–054502-4.
- [58] C. Fan, L. Zhu, T. Liu, B. Jiang, D. Ma, J. Qin, C. Yang, Using an organic molecule with low triplet energy as a host in a highly efficient blue electrophosphorescent device, *Angew. Chem.* 126 (2014) 2179–2183.
- [59] X. Ren, J. Li, R.J. Holmes, P.I. Djurovich, S.R. Forrest, M.E. Thompson, Ultrahigh energy gap hosts in deep blue organic electrophosphorescent devices, *Chem. Mater.* 16 (2004) 4743–4747.

2.5. Manuscript #5

Using dicyanoanthracene triflates as superior precursors: modifying properties by sterically hindered aryl substituents

Florian Glöcklhofer, Paul Kautny, Patrick Fritz, Berthold Stöger, Johannes Fröhlich

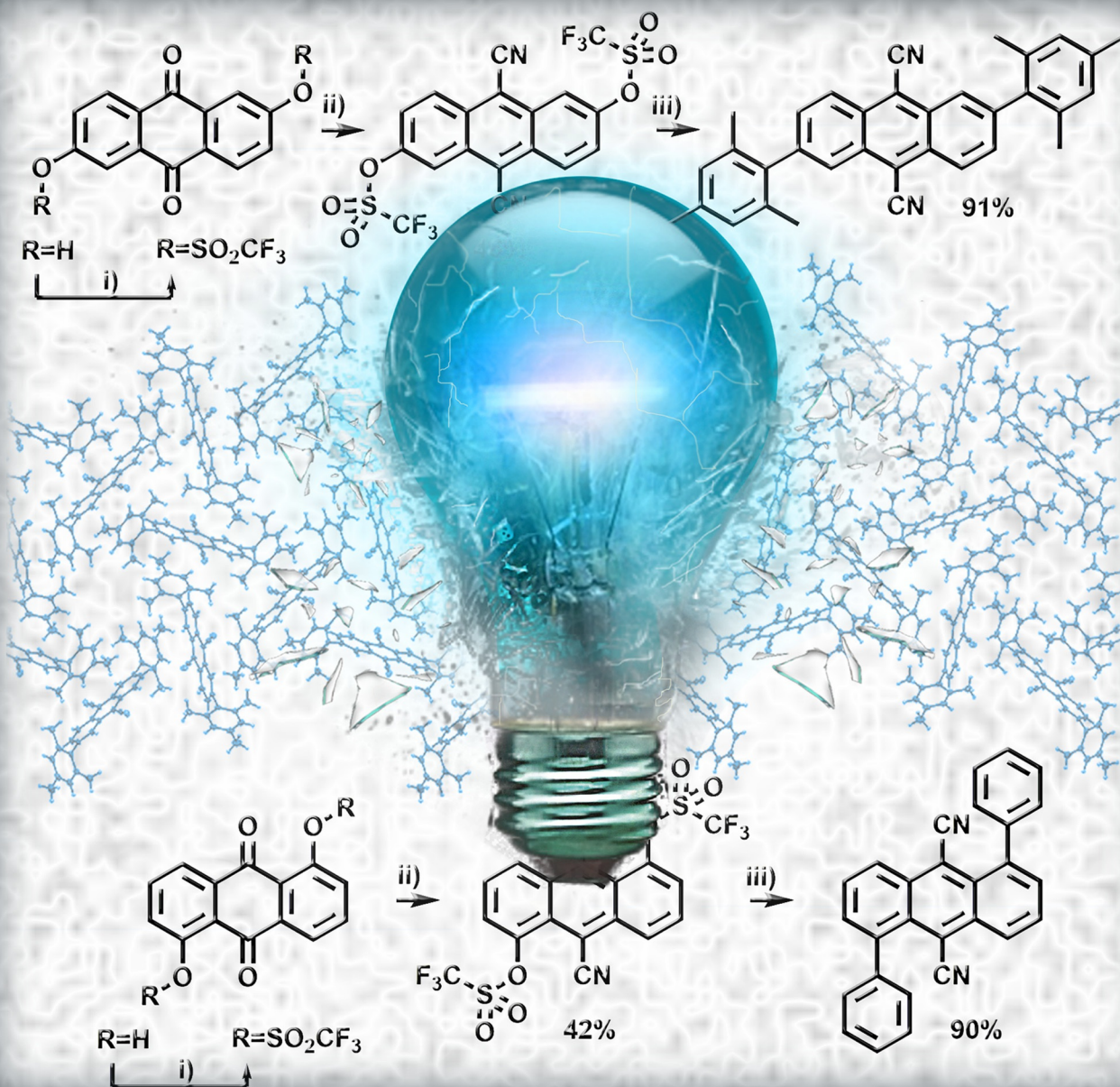
ChemPhotoChem, **2017**, 1, 51-55

Reproduced with the kind permission of John Wiley & Sons, Inc.

CHEMISTRY OF LIGHT INTERACTION

CHEMPHOTOCHEM

ACROSS THE WHOLE SPECTRUM



2/2017

Cover Picture:

F. Glöcklhofer et al.

Using Dicyanoanthracene Triflates as Superior Precursors:
Modifying Properties by Sterically Hindered Aryl Substituents

A Journal of



WILEY-VCH

www.chemphotochem.org



Using Dicyanoanthracene Triflates as Superior Precursors: Modifying Properties by Sterically Hindered Aryl Substituents

Florian Glöcklhofer,^{*[a]} Paul Kautny,^[a] Patrick Fritz,^[a] Berthold Stöger,^[b] and Johannes Fröhlich^[a]

The preparation of 9,10-dicyanoanthracene triflates is reported. Taking advantage of the high reactivity of these precursors in Suzuki coupling reactions, sterically hindered substituents were introduced. The impact of the substituents on the crystallographic and photophysical properties was investigated. The results highlight the usefulness of the new triflate derivatives and the substituents for the development of 9,10-dicyanoanthracene-based materials.

The international community has agreed on significantly cutting the greenhouse gas emissions in an initiative to fight climate change.^[1] Developing new technologies for a more responsible and efficient consumption of energy is an important part of this agreement. Organic light emitting diodes for lighting applications represent such a new technology that could improve the energy efficiency.^[2] Thus, there is an ongoing quest for new emitters to further develop this technology.

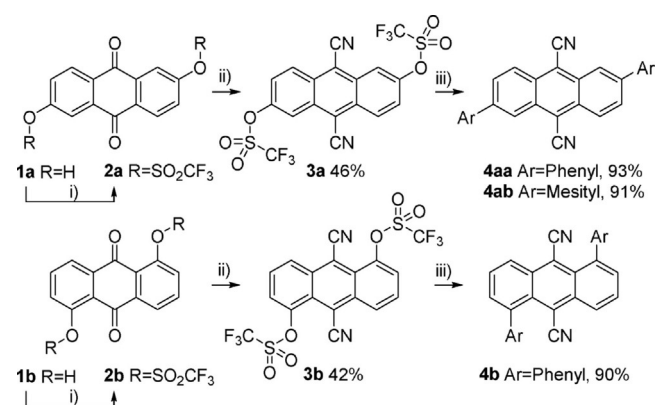
Anthracene is one of the most investigated building blocks for fluorescent emitters, due to the facile synthesis and the good emission properties of many anthracene derivatives.^[3] However, the particularly promising 9,10-dicyanoanthracene (DCA) has been neglected in studies of organic light emitting diodes for a reason. The planar molecular structure allows for strong intermolecular interactions and favors aggregation. This ultimately results in a broad and distinctly red-shifted emission and in low efficiency in the solid state compared to the very high fluorescence quantum yield of the blue emission in solution.^[4]

Additional bulky, sterically hindered substituents can prevent this aggregation and the close assembly of the anthracene cores. The resulting twisted molecular configuration after introduction of such substituents can also decrease the expansion

of the π -electron system, which otherwise drastically impacts the emission properties and again leads to a red-shifted emission.^[5]

Until recently, there was no reasonable possibility to carry out such modifications on a DCA core. This changed when we reported on a new synthesis of cyanoarenes from the corresponding quinones.^[6] For the first time, this synthesis enables a straightforward preparation of halogenated DCAs, which can be used as precursors for the introduction of aryl substituents by coupling reactions. However, the introduction of sterically hindered substituents is often ambitious and the very poor solubility of the halogenated DCAs represents an additional challenge for a fast and efficient reaction. Consequently, the aim of this work was to develop DCA precursors with a higher reactivity in Suzuki coupling reactions.

Triflates are known to be valuable alternatives to halogenated precursors. Although they were reported to be less reactive,^[7] we expected a higher solubility and thus an improved reactivity for the DCA triflates compared to the halogenated analogues. In order to verify this assumption, 2,6-triflate **3a** and 1,5-triflate **3b** were selected for preparation (Scheme 1). **3a** allows for a comparison to the previously used brominated precursor by coupling with phenylboronic acid,^[6a] but also enables us to investigate the introduction of sterically hindered substituents by coupling with mesitylboronic acid. Coupling



Scheme 1. i) Synthesis of anthraquinone triflates **2a** and **2b**. Conditions: triflic anhydride, pyridine, overnight, 0 °C to RT.^[8] ii) Preparation of dicyanoanthracene triflates **3a** and **3b**. Conditions: a) TMSCN, *n*-butyllithium, 15 min, RT; b) addition to anthraquinone triflate, DMF, 3 h, RT; c) addition of MeCN, PBr₃, overnight, 50 °C. iii) Suzuki coupling with boronic acids. Conditions: Pd(PPh₃)₄, aq. K₂CO₃, THF, under argon, 30 min (**4a**, **4b**)/ 90 min (**4b**), reflux.

[a] F. Glöcklhofer, P. Kautny, P. Fritz, Prof. Dr. J. Fröhlich
Institute of Applied Synthetic Chemistry
TU Wien
Getreidemarkt 9/163
1060 Vienna (Austria)
E-mail: florian.gloecklhofer@tuwien.ac.at

[b] Dr. B. Stöger
Institute of Chemical Technologies and Analytics
TU Wien
Getreidemarkt 9/164
1060 Vienna (Austria)

Supporting information and the ORCID identification number(s) for the author(s) of this article can be found under <http://dx.doi.org/10.1002/cptc.201600018>.

3b and phenylboronic acid reveals the influence of steric hindrance by the spatial proximity of the cyano groups.

The synthesis of triflates **3a** and **3b** was carried out in two steps (Scheme 1). In the first step, anthraquinone triflates **2a** and **2b** were prepared starting from the two dihydroxy anthraquinones **1a** and **1b** (anthraflavic acid and anthrarufin). In contrast to the preparation of the halogenated analogues, this reaction can be easily carried out on a multigram scale.^[6] In the second step, the cyano groups were introduced. This reaction proceeds via the intermediate formation of silylated cyanohydrins using trimethylsilyl cyanide (TMSCN) and subsequent aromatization.^[6] Lithium cyanide was used to catalyze the formation of the silylated cyanohydrins. This catalyst was prepared in situ by adding *n*-butyllithium to the TMSCN prior to the addition to the anthraquinone substrates. The *trans* configuration of the cyanohydrin intermediate of **3b** was confirmed by X-ray diffraction (see the Supporting Information). The aromatization was carried out by diluting the reaction with acetonitrile and adding PBr₃ as reagent. As expected, **3a** and **3b** are significantly more soluble than the halogenated DCAs, enabling purification by column chromatography.

The structures of both DCA triflates were confirmed by X-ray diffraction (Figure 1, see the Supporting Information for detailed crystal descriptions). The triflate groups are not bulky enough to inhibit π - π interactions in **3a**, as shown by short C-C distances of 3.41 Å. In **3b**, the intermolecular contact is established through the cyanide groups.

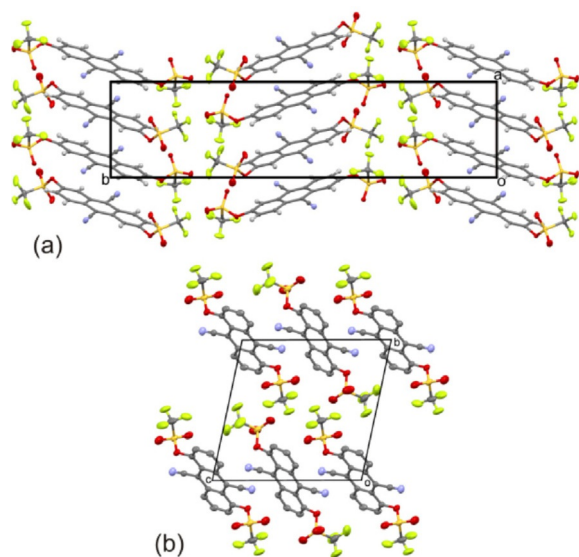


Figure 1. The crystal structures of a) **3a** and b) **3b**. C (grey), N (blue), O (red), S (yellow), and F (green) atoms are represented by ellipsoids drawn at the 50% probability levels. H atoms and the disorder of the **3b** molecules were omitted for clarity.

Screening reactions confirmed the significantly enhanced reactivity of **3a** and **3b** in Suzuki coupling reactions (Table 1). Using Pd(PPh₃)₄ as catalyst, an aqueous K₂CO₃ solution as base, and THF as solvent, full conversion was observed for the formation of **4aa** in less than 90 min at room temperature. At

Table 1. Screening reactions for the Suzuki coupling of triflates **3a** and **3b** (1.00 equiv) and boronic acids (2.50 equiv) carried out on a 0.05 mmol scale in a heating block.^[a]

Product	Triflate	Boronic acid	Substituent positions	Reaction temperature	Reaction time ^[b]
4aa	3a	Phenyl	2,6	RT	< 90 min
				55 °C	< 15 min
4ab	3a	Mesityl	2,6	RT	overnight
4b	3b	Phenyl	1,5	55 °C	< 60 min
				RT	< 90 min
				55 °C	< 15 min

[a] Conditions: Pd(PPh₃)₄ (0.05 equiv), K₂CO₃ (5.00 equiv, 2.0 M in H₂O), THF (0.05 M), under argon. [b] Time until full conversion of both triflate functionalities, determined by thin-layer chromatography.

55 °C the same reaction was complete in less than 15 min, considerably faster than the previously observed 3 h for the brominated precursor under the same conditions.^[6a]

As expected, the introduction of the sterically hindered mesityl substituents to obtain **4ab** was more ambitious; but still, this reaction was complete after stirring overnight at room temperature. At 55 °C full conversion was observed in less than 60 min. In contrast, the steric hindrance caused by the cyano groups did not affect the reaction rate for the synthesis of **4b**.

Considering these results, the synthesis of **4aa**, **4ab**, and **4b** on a preparative scale was carried out under reflux (Scheme 1). Yields of 90% and more were obtained for all three target compounds after purification by column chromatography.

Analysis of single crystals revealed that for **4aa** the molecules are connected by strong π - π interactions (C7-C7: 3.397 Å) to rods extending along [001] (Figure 2). This is no surprise, due to the absence of sterically hindered substituents.

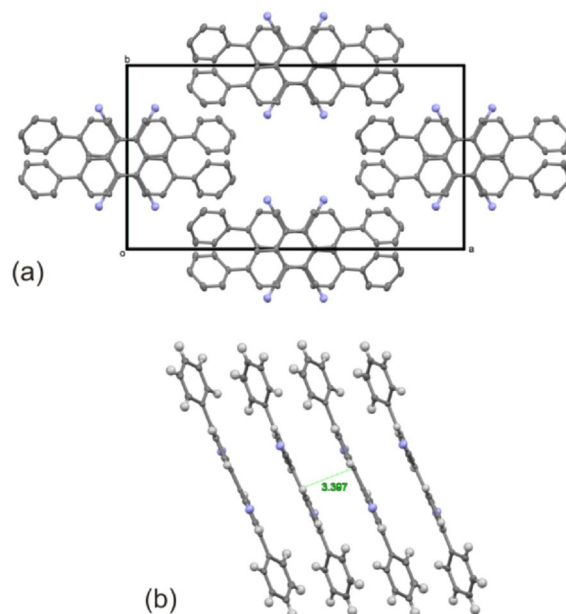


Figure 2. a) The crystal structure of **4aa** (viewed down [001]). H atoms and the disordered solvent molecules were omitted for clarity. b) Rods of **4aa** molecules connected by π - π interactions extending along [001]. Color codes as in Figure 1.

4aa crystallizes with 0.575CHCl₃ molecules in space group C2/c. One crystallographically unique **4aa** molecule is located on a center of inversion ($Z' = 1/2$). The phenyl substituents are slightly inclined with respect to the anthracene ring (angle of least-square planes: 29.96(8)°). In the free space of the packing, CHCl₃ solvent molecules are located, which are disordered around a two-fold axis.

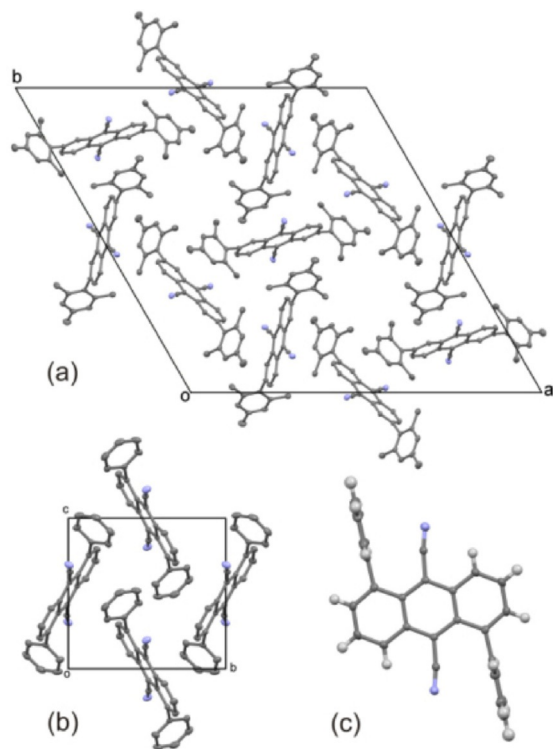


Figure 3. The crystal structures of **4ab** (a) (viewed down [001]) and **4b** (b) (viewed down [100]). c) Molecular structure of **4b**, H atoms are represented by spheres of arbitrary radius. Color codes as in Figure 1.

For compounds **4ab** and **4b** the π -stacking is efficiently inhibited by the sterically hindered substituents (Figure 3). **4ab** crystallizes from CDCl₃ in the $R\bar{3}$ space group with one **4ab** molecule located on a center of inversion. A solvent molecule is disordered around the $\bar{3}$ rotoinversion. **4b** crystallizes in the $P2_1/c$ space group with one molecule located on a center of inversion. The substituents of both compounds are virtually perpendicular to the anthracene (angle of least-squares planes: 88.38(7)° (**4ab**) and 89.26(4)° (**4b**)). The phenyl substitution next to the cyano group results in a remarkable bending of the latter (C-C-N: 172.11(11)° for **4b**; 179.00(16)° for **4ab**). The absence of π -stacking validates the general strategy and is in sharp contrast to both **4aa** and the unsubstituted DCA.^[9]

UV/VIS absorption and photoluminescent emission spectra of the target compounds and the unsubstituted DCA were recorded to investigate the impact of the phenyl and mesityl substituents on the photophysical properties. Key parameters are summarized in Table 2. All compounds exhibit a distinct absorption maximum (between 261 nm and 306 nm) and four less intense absorption bands (between 356 nm and 447 nm) in solution (Figure 4, left). The latter are systematically red-shifted for the substituted DCA derivatives. The bands of the phenyl substituted **4aa** and **4b** are located in close proximity, whereas the corresponding transitions of **4ab** are less red-shifted. This is also reflected in the absorption onsets and the related optical band gaps (ΔE_{opt}). **4aa** (2.67 eV) and **4b** (2.65 eV) exhibit the smallest band gap, while the value of **4ab** (2.79 eV) is located exactly in between these values and the band gap of the DCA (2.92 eV). These results indicate that the π -electron system of the DCA is expanded by the two additional phenyl substituents. However, this effect is significantly reduced in **4ab**, due to increased torsion resulting from the steric demand of the mesityl substituents.

With some exceptions, similar results were obtained for the photoluminescence in *n*-heptane solution (Figure 4, middle).

Product	$\lambda_{abs,Sol}$ ^[a] [nm]	$\lambda_{PL,Sol}$ ^[a] [nm]	$Q_{PL,Sol}$ ^[a]	$\lambda_{PL,Pow}$ ^[b] [nm]	ΔE_{opt} ^[a] [eV]	HOMO/LUMO ^[c] [eV]	ΔE_{cal} ^[c] [eV]
DCA	261 /356/374/395/418 ^[d]	419 /445/473 ^[d]	90 % ^[4b]	516 ^[d]	2.92	-6.42/-3.32	3.10
4aa	306 /376/396/421/447 ^[d]	460 /488/529 ^[d]	79 % ^[e]	601 ^[d]	2.67	-6.15/-3.25	2.90
4ab	272 /366/383/405/429 ^[d]	447 /469 ^[d]	81 % ^[e]	456 / 482 /507 ^[d]	2.79	-6.26/-3.20	3.06
4b	274 /364/382/416/437 ^[d]	476 /499 ^[d]	71 % ^[e]	529 ^[d]	2.65	-6.07/-3.15	2.92

[a] Determined in *n*-heptane solutions. [b] Determined from powder samples. [c] Calculated applying density functional theory level (B3LYP/6-311G(d,p)). [d] Values in bold face denote maxima. [e] Relative to DCA.

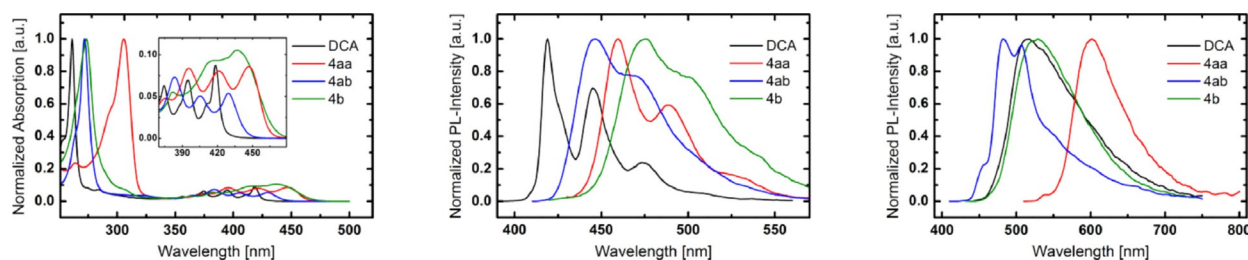


Figure 4. UV/Vis absorption (left) and photoluminescent emission spectra in *n*-heptane solutions (middle) and from powders (right) of **4aa**, **4ab**, **4b** and DCA.

The emission of **4aa** is significantly redshifted ($\lambda_{\text{max}}=460$ nm) compared to the DCA ($\lambda_{\text{max}}=419$ nm); the emission maximum of **4ab** ($\lambda_{\text{max}}=447$ nm) is located in between. In contrast to the absorption, **4b** ($\lambda_{\text{max}}=476$ nm) exhibits a more pronounced red-shift than **4aa**. The photoluminescence quantum yields ($Q_{\text{PL, Sol}}$) in solution relative to DCA (90%)^[4b] are affected by the substituents, but the quantum yields are still high.

DFT calculations were employed to shed further light on the properties of the materials. The trends for the calculated HOMO/LUMO gaps and for the experimentally determined optical band gaps in solution are in excellent agreement. For both phenyl-substituted compounds, the HOMO clearly expands onto the aryl substituents (Figure 5, top and bottom),

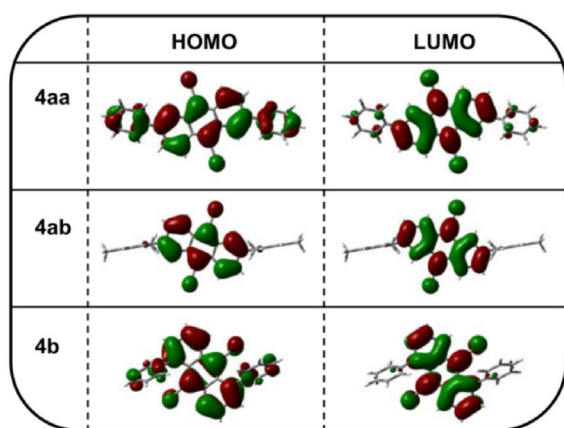


Figure 5. Spatial distribution of HOMO and LUMO levels of **4aa**, **4ab** and **4b**.

which explains the increased energy level and the smaller band gap compared to the DCA. In contrast, the HOMO of **4ab** is exclusively located on the DCA core (Figure 5, middle) as a result of the perpendicular orientation of the sterically demanding mesityl substituents. Similar observations were made for the LUMO levels, but with a distinctly stronger localization of the orbital at the DCA core for all materials under investigation. The DFT calculations also revealed through-space interactions of the phenyl substituents and the cyano groups in **4b** (see the Supporting Information), which is a possible explanation for the pronounced red-shift of the emission in solution and for the expansion of the HOMO onto the substituents despite their perpendicular orientation.

The advantages of the sterically hindered substituents come to the fore when switching from the solution to the solid state. Photoluminescence spectra of powder samples (Figure 4, right) proved the tremendous effect of the packing motif on the solid-state emission. The emission maximum of **4ab** (482 nm) is red-shifted by only 35 nm compared to the solution. In contrast, the maximum of the π -stacked plain DCA (516 nm) is distinctly shifted by 97 nm, resulting in a reversed order of the emission maxima compared to the measurements in solution. The packing effects also result in a reversed order of the emission maxima of the phenyl substituted DCAs; **4b** (529 nm) exhibits a shift of 53 nm, the maximum of **4aa**

(601 nm) is shifted by 141 nm. The large red-shift of **4aa** is attributed to the strong π - π interactions observed in the crystal structure.

In conclusion, our investigations illustrate the tremendous effect of sterically hindered aryl substituents on the properties of DCA. The acquired knowledge will guide the molecular design of DCA-based materials for organic light emitting diodes and other applications. The careful selection of substituents, which take into account the packing effects, but also the charge transport properties, is considered a promising approach. The newly developed, highly reactive DCA triflates will enable a facile preparation of new DCA-based materials.

Experimental Section

Experimental and instrumental details for the synthesis and characterization of all compounds, as well as for the DFT calculations, are provided in the Supporting Information. CCDC-1500690-1500694 and 1517671 contain the supplementary crystallographic data for this paper.

General procedure for the synthesis DCA triflates **3a** and **3b**

n-Butyllithium (0.10 equiv, 2.5 M in hexanes) was added carefully to rigorously stirred TMSCN (2.20 equiv) in a sealed reaction vial at room temperature. After 15 min, the resulting mixture was added to anthraquinone triflate **2a/2b** (1.00 equiv), again at room temperature. Dry DMF (0.5 mL mmol⁻¹ starting material) was used to fully transfer the residues of the mixture. The reaction was stirred at room temperature for 3 h. MeCN (3.0 mL mmol⁻¹ starting material) and PBr₃ (1.20 equiv) were added and the reaction was heated to 50 °C overnight. The reaction was then allowed to cool to room temperature, diluted with CH₂Cl₂ and directly filtered over a pad of silica (conditioned with CH₂Cl₂ and some drops of MeCN) using CH₂Cl₂ as eluent. After evaporation of the solvent, the residue was purified by column chromatography (using petroleum ether:CH₂Cl₂, 7:3 to 3:2 v/v, as eluent). Yields: 46% (**3a**), 42% (**3b**).

General procedure for the synthesis of **4aa**, **4ab**, and **4b**

DCA triflate **3a/3b** (1.00 equiv) and phenyl-/mesitylboronic acid (2.50 equiv) were mixed in degassed THF (0.05 M) under an argon atmosphere and the mixture was heated to reflux. An aqueous K₂CO₃ solution (5.00 equiv, 2.0 M) and Pd(PPh₃)₄ (0.05 equiv) were added and the reaction was stirred for 30 min (**4aa**, **4b**)/90 min (**4ab**). After cooling to room temperature, the reaction was poured on water and extracted four times with CH₂Cl₂. The combined organic layers were dried over sodium sulfate and the solvent was evaporated in vacuo. After evaporation of the solvent, the residue was purified by column chromatography (petroleum ether:CH₂Cl₂ 3:2 v/v). Yields of 90% and more were obtained for all three target compounds.

Acknowledgements

This work was supported in part by the TU Wien "Innovative Projects" research funds. The X-ray center of the TU Wien is acknowledged for providing access to the single-crystal diffractometer. We gratefully thank Manuel Spettel for contributing to synthetic experiments and Christian Hametner for NMR measurements.

Keywords: cross-coupling reactions · cyanides · fluorescence · fused-ring systems · steric hindrance

- [1] UNFCCC, Adoption of the Paris Agreement FCCC/CP/2015.L.9/Rev.1 **2015**.
- [2] a) S. Reineke, F. Lindner, G. Schwartz, N. Seidler, K. Walzer, B. Lüssem, K. Leo, *Nature* **2009**, *459*, 234–238; b) S. Reineke, M. Thomschke, B. Lüssem, K. Leo, *Rev. Mod. Phys.* **2013**, *85*, 1245–1293; c) N. Thejokalyani, S. J. Dhoble, *Renewable Sustainable Energy Rev.* **2014**, *32*, 448–467.
- [3] a) J. Huang, J.-H. Su, H. Tian, *J. Mater. Chem.* **2012**, *22*, 10977–10989; b) M. Zhu, C. Yang, *Chem. Soc. Rev.* **2013**, *42*, 4963–4976.
- [4] a) S. Ateşli, A. Yildiz, *J. Chem. Soc. Faraday Trans. 1* **1983**, *79*, 2853–2861; b) S. Schoof, H. Güsten, C. Von Sonntag, *Ber. Bunsen-Ges.* **1978**, *82*, 1068–1073.
- [5] a) K. H. So, H.-T. Park, S. C. Shin, S.-G. Lee, D. H. Lee, K.-H. Lee, H.-Y. Oh, S.-K. Kwon, Y.-H. Kim, *Bull. Korean Chem. Soc.* **2009**, *30*, 1611–1615; b) K.-R. Wee, W.-S. Han, J.-E. Kim, A.-L. Kim, S. Kwon, S. O. Kang, *J. Mater. Chem.* **2011**, *21*, 1115–1123; c) M. A. Reddy, A. Thomas, K. Srinivas, V. J. Rao, K. Bhanuprakash, B. Sridhar, A. Kumar, M. N. Kamalasanan, R. Srivastava, *J. Mater. Chem.* **2009**, *19*, 6172–6184; d) C.-L. Wu, C.-H. Chang, Y.-T. Chang, C.-T. Chen, C.-T. Chen, C.-J. Su, *J. Mater. Chem. C* **2014**, *2*, 7188–7200.
- [6] a) F. Glöckhofer, M. Lunzer, B. Stöger, J. Fröhlich, *Chem. Eur. J.* **2016**, *22*, 5173–5180; b) F. Glöckhofer, M. Lunzer, J. Fröhlich, *Synlett* **2015**, *26*, 950–952.
- [7] T. Ohe, N. Miyauchi, A. Suzuki, *J. Org. Chem.* **1993**, *58*, 2201–2208.
- [8] J. E. Gautrot, P. Hodge, D. Cupertino, M. Helliwell, *New J. Chem.* **2007**, *31*, 1585–1593.
- [9] J. Xiao, Z. Yin, B. Yang, Y. Liu, L. Ji, J. Guo, L. Huang, X. Liu, Q. Yan, H. Zhang, Q. Zhang, *Nanoscale* **2011**, *3*, 4720–4723.

Manuscript received: September 16, 2016

Revised: November 11, 2016

Accepted Article published: December 5, 2016

Final Article published: January 4, 2017

2.6. Manuscript #6

Thieno[3,4-*c*]pyrrole-4,6-dione as novel building block for host materials
in red PhOLEDs

Paul Kautny, Chenyang Zhao, Dominik Schopf, Berthold Stöger, Ernst Horkel, Jiangshan Chen,
Dongge Ma, Johannes Fröhlich, Daniel Lumpi

Journal of Materials Chemistry C, **2017**, 5, 1997-2004

Reproduced with the kind permission of the Royal Society of Chemistry.

PAPER



Cite this: *J. Mater. Chem. C*, 2017,
5, 1997

Received 3rd December 2016,
Accepted 31st January 2017

DOI: 10.1039/c6tc05248g

rsc.li/materials-c

Thieno[3,4-c]pyrrole-4,6-dione as novel building
block for host materials for red PhOLEDs†

Paul Kautny,^{*a} Chenyang Zhao,^b Dominik Schopf,^a Berthold Stöger,^c Ernst Horkel,^a
Jiangshan Chen,^{*b} Dongge Ma,^b Johannes Fröhlich^a and Daniel Lumpi^a

In the presented work the electron accepting thieno[3,4-c]pyrrole-4,6-dione is introduced as a novel building block for donor–acceptor based host materials for Phosphorescent Organic Light Emitting Diodes (PhOLEDs). A series of three regioisomers consisting of the thieno[3,4-c]pyrrole-4,6-dione acceptor and carbazole donors linked *via* a phenylene linker was prepared and the impact of the phenylene substitution pattern on the molecular properties was analyzed. Regarding their applicability as host materials, the newly developed materials were investigated in red PhOLED devices achieving a high current efficiency of 30.6 cd A⁻¹ corresponding to an external quantum efficiency of 17.7% and a high power efficiency of 23.8 lm W⁻¹. Thus, we present the first successful application of the thieno[3,4-c]pyrrole-4,6-dione building block in host materials for PhOLEDs.

Introduction

Since the first reports on electroluminescence from organic materials,^{1,2} great efforts have been made in the development of organic light emitting diodes (OLEDs).^{3–8} The application of transition metal emitters in phosphorescent OLEDs (PhOLEDs)^{9,10} and of organic compounds capable of thermally activated delayed fluorescence (TADF)¹¹ boosted the efficiency of OLED devices.^{12–16} Therefore, one major goal of research is the development of new host materials for these emitters.^{17–21} In particular, the application of bipolar host materials consisting of donor and acceptor subunits proved successful, owing to their balanced charge transport properties and thus simplified device structures and broad recombination zones.^{22–24}

The primary source of electron donating groups for optoelectronic materials are aromatic amines, such as triphenylamines,^{3,9,25–29} carbazoles,^{10,17,28,30–33} indolocarbazoles,^{34–37} phenoxazines^{15,38–40} and dihydroacridines.^{15,41} In contrast, the nature of the electron accepting moieties exhibits more variations. Among the most frequently used acceptors are oxadiazoles,^{27,33,38,42–44} phenantrolines,^{31,45} pyridines,^{32,46}

benzimidazoles,^{26,28,47} 1,3,5-triazines,^{39,48,49} 1,2,4-triazoles,^{29,38,50} phosphine oxides,^{51–53} sulfones,^{15,54} ketones,^{40,41} carbolines^{55,56} and benzonitriles.^{11,57}

The thieno[3,4-c]pyrrole-4,6-dione (TPD) (Scheme 1) has been successfully employed as electron accepting unit in donor–acceptor polymers for organic photovoltaics in combination with various donor units.^{58–62} Moreover, the application of a TPD based polymer in an organic field effect transistor has been reported.⁶³ So far however, this particular unit has not been exploited as acceptor in materials for OLEDs.

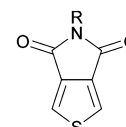
This circumstance prompted us to explore the possibility to utilize the TPD building block in donor–acceptor host materials for PhOLEDs. Hence, this study presents the first application of TPD in host materials in combination with the well-established carbazole donor. The variation of the linkage mode between the two molecular subunits allowed for a modification of the molecular properties of the derivatives. Suchlike developed compounds were employed as host materials in efficient red PhOLED devices (CE_{max}: 30.6 cd A⁻¹, PE_{max}: 23.8 lm W⁻¹, EQE_{max}: 17.7%), demonstrating the applicability of the TPD

^a Institute of Applied Synthetic Chemistry, TU Wien, Getreidemarkt 9/163,
A-1060 Vienna, Austria. E-mail: paul.kautny@tuwien.ac.at

^b State Key Laboratory of Polymer Physics and Chemistry, Changchun Institute of
Applied Chemistry, Chinese Academy of Sciences, Changchun, 130022, China.
E-mail: jschen@ciac.ac.cn

^c Institute of Chemical Technologies and Analytics, TU Wien, Getreidemarkt 9/164,
A-1060 Vienna, Austria

† Electronic supplementary information (ESI) available: NMR spectra, DSC, TGA and CV analysis and crystallographic information. CCDC 1519402. For ESI and crystallographic data in CIF or other electronic format see DOI: 10.1039/c6tc05248g



Thieno[3,4-c]pyrrole-4,6-dione

TPD

Scheme 1 Molecular structure of thieno[3,4-c]pyrrole-4,6-dione (TPD).

unit as electron withdrawing organic building block for optoelectronic applications.

Results and discussion

Synthesis

Three different TPD based host materials (*p*-PCzTPD, *m*-PCzTPD and *o*-PCzTPD), in which the TPD unit is connected to the carbazole donors by phenylene linkers, were prepared (Scheme 2). Thereby three different linkage modes (*para*, *meta*, *ortho*) were realized using the phenylene linker. The unsubstituted imide of the TPD unit was protected with an octyl chain, also facilitating the handling of the materials during the synthetic process. The key synthetic step in the preparation of the new materials was a Suzuki cross coupling reaction of dibrominated TPD **1** and the suitable substituted boronic acid esters **2a–c** (Scheme 2). Products *p*-PCzTPD and *m*-PCzTPD were obtained with yields of 67% and 70%, respectively. In contrast the reaction towards *o*-PCzTPD proceeded significantly slower and with a low yield of 17% due to the high steric demand resulting from the *ortho* linkage mode. All materials were characterized by ^1H and ^{13}C NMR and high resolution mass spectrometry.

In the case of *p*-PCzTPD the molecular structure was unequivocally confirmed by X-ray crystal analysis (Fig. 1). Both phenylene linkers are close to coplanar with the TPD core [angles between the least square (LS) planes: $\Phi_2 = 15.04(11)^\circ$ and $\Phi_3 = 18.08(11)^\circ$] and thus fully conjugated with the central aromatic system. In contrast, the carbazole moieties and the phenylene linkers are more pronouncedly inclined [angles between the LS planes: $\Phi_1 = 54.53(12)^\circ$ and $\Phi_4 = 61.68(11)^\circ$] due to the steric interaction of the *ortho* hydrogen atoms.

Thermal properties

The thermal behaviour of the developed materials was studied to evaluate their applicability as host materials for PhOLEDs (Table 1). *m*-PCzTPD and *p*-PCzTPD exhibited high decomposition temperatures (T_d – corresponding to 5% mass loss) of 438 °C and 448 °C during thermogravimetric analysis (Fig. S7, ESI †). In contrast, the T_d of *o*-PCzTPD was lower (369 °C). The glass transition temperatures (T_g) of the compounds were determined by differential scanning calorimetry, to estimate the morphological stability of thin films of the materials. Whereas *o*-PCzTPD exhibited a rather low T_g of 62 °C, the T_g s increased with increasingly linear

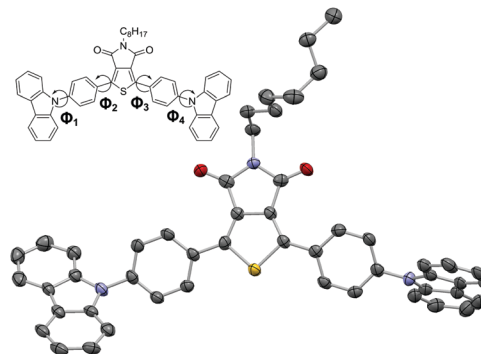


Fig. 1 Molecular structure of *p*-PCzTPD. C, N, O and S atoms are represented by gray, blue, red and yellow ellipsoids drawn at 70% probability levels. H atoms are omitted for clarity.

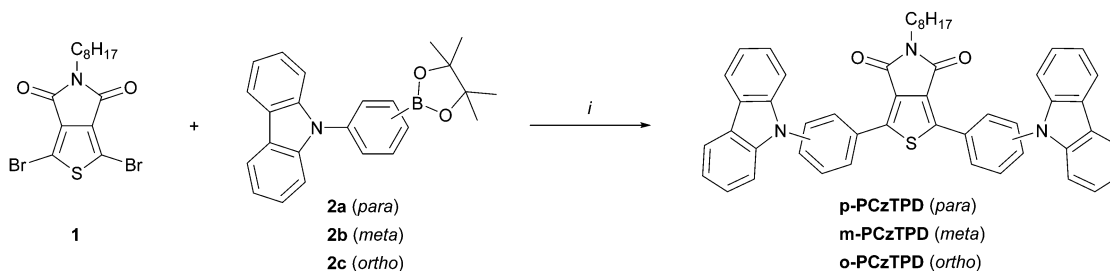
shape of the molecules to 84 °C for *m*-PCzTPD and 102 °C for *p*-PCzTPD (Fig. S8, ESI †).

Photophysical properties

UV/Vis absorption, room temperature photoluminescence and low temperature phosphorescence spectra were recorded to investigate the impact of the substitution pattern on the photophysical properties of the materials (Fig. 2). The key photophysical data is summarized in Table 1. All derivatives exhibit a distinct absorption peak at 292 nm, which can be attributed to a transition centered on the carbazole moieties.³¹ Moreover, weaker transitions at approximately 325 nm and 340 nm, which are typical for phenylcarbazole derivatives,⁶⁴ are found for all compounds. Fully conjugated *p*-PCzTPD features an additional broad absorption peak with a peak maximum at 386 nm. This peak can be attributed to an intramolecular charge transfer transition between the electron rich carbazoles and the TPD acceptor unit. Owing to the decreased effective conjugation resulting from the *ortho* and *meta* linkages,³³ this transition is absent in *o*-PCzTPD and *m*-PCzTPD. In analogy, the absorption onsets are shifted towards lower energy from *o*-PCzTPD (3.34 eV) to *m*-PCzTPD (3.18 eV) and *p*-PCzTPD (2.84 eV).

The fluorescence of the materials is distinctly red shifted compared to the absorption, and emission maxima are located at 476 nm (*p*-PCzTPD), 506 nm (*m*-PCzTPD) and 485 nm (*o*-PCzTPD).

To determine the triplet energy (E_T) of the developed materials low temperature phosphorescence was recorded. The order of the



Scheme 2 Synthesis of TPD based host materials; (i) **1** (1.0 eq., 25 mM), **2a–c** (2.5 eq.), Pd(PPh $_3$) $_4$ (0.05 eq.), K $_2$ CO $_3$ (5.0 eq., 2 M aqueous solution), THF, reflux.

Table 1 Physical data of the synthesized host materials

	$T_g/T_m/T_d^a$ [°C]	Opt. BG ^{b,c} [eV]	$\lambda_{PL,max}^c$ [nm]	HOMO/LUMO [eV]		E_T [eV]	
				Exp. ^d	Cal. ^e	Exp. ^f	Cal. ^g
<i>p</i>-PCzTPD	102/208/448	2.84	476	−5.68/−2.84	−5.68/−2.57	2.09	2.11
<i>m</i>-PCzTPD	84/195/438	3.18	506	−5.70/−2.52	−5.71/−2.56	2.21	2.31
<i>o</i>-PCzTPD	62/133/369	3.34	485	−5.65/−2.31	−5.75/−2.13	2.33	2.62

^a Determined by thermogravimetric analysis and differential scanning calorimetry. T_m : melting temperature. ^b Estimated from the absorption onset. ^c Measurements were carried out in CH_2Cl_2 (5 μM) at room temperature. ^d HOMO levels were determined from the onset of the oxidation peak obtained during cyclic voltammetric measurements (0.5 mM solution in anhydrous CH_2Cl_2 with Bu_4NBF_4 (0.1 M) as supporting electrolyte); LUMO levels were calculated from the HOMO levels and the optical bandgap. ^e Calculated applying density functional theory level (B3LYP/6-311+G*). ^f Estimated from the highest energy vibronic transition in solid solution of toluene/EtOH (9:1) at 77 K. ^g Calculated applying time dependent density functional theory level (B3LYP/6-311+G*).

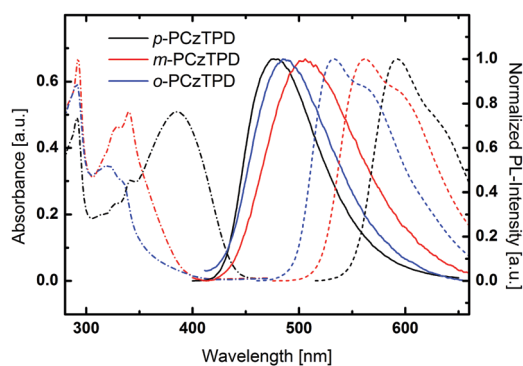


Fig. 2 UV-Vis absorption (dashed and dotted lines), normalized fluorescence at room temperature (solid lines) and normalized phosphorescence spectra at 77 K (dashed lines) of the materials under investigation.

emission maxima follows the absorption onset. Thus, ***o*-PCzTPD** features the highest E_T of 2.33 eV, whereas the E_T of ***m*-PCzTPD** is slightly lower (2.21 eV) and ***p*-PCzTPD** exhibits the lowest E_T of 2.09 eV. In ***p*-PCzTPD**, the pronounced donor–acceptor interaction between the carbazoles and the TPD, which is also evident in the absorption behaviour of the material, lowers the E_T s *via* intramolecular charge transfer.²² The theoretically calculated E_T display the same trend, the absolute values for ***m*-PCzTPD** and ***o*-PCzTPD** are, however, higher than the experimentally determined energies. A closer inspection of the $S_0 \rightarrow T_1$ transition reveals that in case of ***m*-PCzTPD** and ***o*-PCzTPD** transitions from low lying molecular orbitals contribute significantly to the lowest excited triplet state. These transitions may be slightly overestimated in the applied model, leading to the prediction of too high E_T s of the two derivatives. Ultimately, the application of different linkage modes allowed to control the degree of the overall conjugation in ***m*-PCzTPD** and ***o*-PCzTPD**. Therefore, the intramolecular charge transfer could be decreased, resulting in higher E_T s. Notably, in this series the *ortho* derivative ***o*-PCzTPD** exhibits a higher E_T than *meta* linked ***m*-PCzTPD**, which is unlike the behaviour of related host materials based on 1,3,4-oxadiazole acceptor units.^{33,65}

Electrochemical properties

The levels of the Highest Occupied Molecular Orbitals (HOMOs) of the materials were determined by cyclic voltammetry (CV). All derivatives exhibited irreversible oxidation, as commonly observed for carbazole based materials, owing to the instability of the

formed cations.⁶⁶ The HOMO levels were calculated from the onset of the oxidation peaks relative to the oxidation of ferrocene and span a narrow range between −5.65 eV and −5.70 eV (Fig. S9, ESI†), indicating no significant barrier for hole injection from the adjacent layers. The Lowest Unoccupied Molecular Orbital (LUMO) levels of the materials were estimated from the HOMO levels and the optical bandgaps and are located between −2.84 eV and −2.31 eV, whereby ***p*-PCzTPD** features the lowest value owing to the lower bandgap of this compound.

Computational investigations

Density functional theory was applied to obtain a deeper understanding of the electronic layouts of the investigated materials on the molecular level. In general, the calculated HOMO and LUMO energy values are in good agreement with the experimental results (Table 1). Moreover, the energetic order of the triplet energies of the developed host materials was reliably reproduced by the theoretical calculations, albeit slightly higher energies were predicted for ***m*-PCzTPD** and ***o*-PCzTPD** compared to the experimental values.

The spatial distributions of the HOMOs and LUMOs are depicted in Fig. 3. In the case of the fully conjugated ***p*-PCzTPD**, the HOMO level expands over the whole aromatic backbone of the molecule with a distinctive localization of electron density on the central TPD unit. The LUMO of ***p*-PCzTPD** is more localized with major contributions coming from the TPD acceptor and the

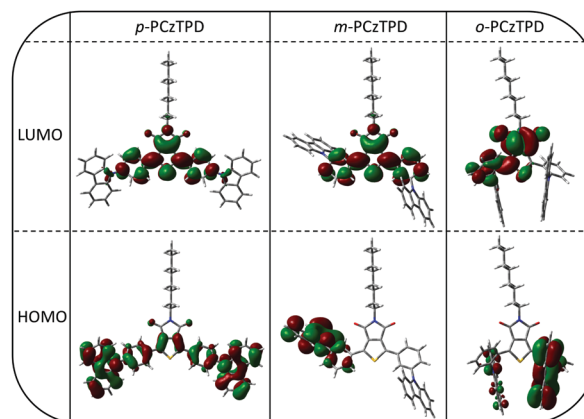


Fig. 3 Spatial distribution of the HOMOs and LUMOs of ***p*-PCzTPD**, ***m*-PCzTPD** and ***o*-PCzTPD**.

adjacent phenyl moieties. Looking at *m*-PCzTPD, the morphology of the HOMO is distinctly different. The electron density of the orbital is solely located on one of the carbazole units and the neighbouring phenyl ring owing to the decreased overall conjugation. In contrast, the shape of the LUMO is essentially unaffected by the altered linkage mode of the donor units. Consequently, the decreased spatial overlap of the two molecular orbitals leads to a lower degree of intramolecular charge transfer in *m*-PCzTPD, as reflected by the absence of a distinct charge transfer transition in the absorption spectra and also an increased E_T .²²

In the case of *o*-PCzTPD, however, the overall situation changed as a result of the geometric structure of the molecule. The calculated shape of the aromatic part of *p*-PCzTPD is in excellent agreement with the molecular structure determined by X-ray diffraction. Accordingly, the optimized torsion angles between the aromatic subunits deviate only slightly from the experimentally determined values (Table 2). Similar torsion angles were observed for *m*-PCzTPD. In contrast the molecular structure of *o*-PCzTPD is distinctly different. Both carbazole units are oriented away from the TPD, owing to the steric demand of the carbonyl oxygen atoms (Fig. 3). This leads to a rotation of the phenylene linkers to avoid a close proximity of the carbazoles. Therefore, the torsion angles Φ_2 and Φ_3 between the TPD and the adjacent phenyl rings are distinctly enlarged to 49.43° and 53.46° and also the torsion angles between the phenylene linkers and the carbazole are larger than in the other two derivatives (Table 2). The highly twisted structure of *o*-PCzTPD restricts the HOMO to one of the carbazoles with only minor electron density on the neighbouring phenylene linker

as well as on the opposite carbazole. Notably, also the distribution of the LUMO is altered compared to the other derivatives. The LUMO is exclusively located on the TPD acceptor and the phenylene linker opposite of the carbazole that is hosting the HOMO. The increased spatial separation of the two molecular orbitals impedes their electronic exchange and thus explains the increased E_T of *o*-PCzTPD compared to *m*-PCzTPD. Thus, the *ortho* linkage effect³³ is further enhanced for these particular class of materials, owing to the steric demand of the TPD, which leads to an increased electronic separation of the molecular subunits, even compared to the corresponding *meta* derivatives.

Electroluminescent properties

The title compounds were employed in PhOLED devices, to investigate their practical applicability as host materials. Owing to the higher E_T of the three materials compared to red emitting Ir(MDQ)₂(acac) (2.0 eV),⁶⁷ Ir(MDQ)₂(acac) was chosen as phosphorescent emitter for this purpose. PhOLED devices were fabricated with the structure of ITO/MoO₃ (8 nm)/TAPC (75 nm)/EML (12 nm)/BPhen (70 nm)/LiF/Al (Fig. S10, ESI†). The EMLs consisted of host materials *p*-PCzTPD (**R1**), *m*-PCzTPD (**R2**) or *o*-PCzTPD (**R3**) doped with Ir(MDQ)₂(acac). A dopant concentration of 5% was applied without further optimization. TAPC was employed as hole transporting layer and BPhen was utilized as electron transporting and hole blocking layer. Current density–voltage–luminance and current efficiency–luminance–power efficiency curves of the three devices are depicted in Fig. 4 and the key electroluminescent properties are summarized in Table 3.

All devices exhibited electroluminescent emission exclusively from the Ir(MDQ)₂(acac) dopant (Fig. S11, ESI†), indicating that exciton transfer from the host to the dopant or direct charge trapping on the phosphorescent emitter was effective. Moreover, all devices exhibited turn-on voltages between 3.2 V and 4.0 V. The slightly lower turn on voltage of 3.2 V of **R1** can be attributed to the lower bandgap and in particular the low lying LUMO level of *p*-PCzTPD compared to its regioisomers.

Among the three devices, *m*-PCzTPD based **R2** exhibited the best performance with a high maximum current efficiency (CE) of 30.8 cd A⁻¹ corresponding to a satisfying maximum external

Table 2 Characteristic torsion angles Φ_1 – Φ_4 of the least square planes of the aromatic ring systems of the materials under investigation

	Φ_1 [°] (Cz1–Ph1)	Φ_2 [°] (Ph1–TPD)	Φ_3 [°] (TPD–Ph2)	Φ_4 [°] (Ph2–Cz2)
<i>p</i> -PCzTPD ^a	54.53(12)	15.04(11)	18.08(11)	61.68(11)
<i>p</i> -PCzTPD ^b	55.67	19.14	20.30	55.52
<i>m</i> -CzTPD ^b	59.65	25.75	23.47	61.64
<i>o</i> -CzTPD ^b	67.16	49.43	53.46	67.91

^a Determined by single-crystal X-ray diffraction. ^b Calculated applying density functional theory level (B3LYP/6-311+G*).

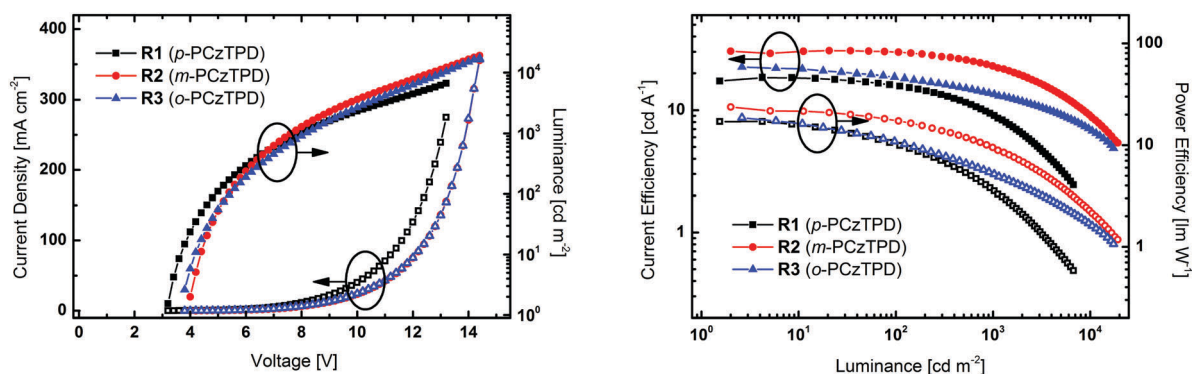


Fig. 4 Current density–voltage–luminance (left; luminance: full symbols, current density: hollow symbols) and current efficiency–luminance–power efficiency (right; current efficiency: full symbols, power efficiency: hollow symbols) curves of devices **R1**–**R3**.

Table 3 Electroluminescent properties of devices **R1–3**

	V_{on} [V]	CE^a [cd A^{-1}]	PE^a [lm W^{-1}]	EQE^a [%]
R1	3.2	15.9/9.1/18.5	10.1/3.6/17.1	10.1/5.8/11.8
R2	4.0	29.7/22.5/30.6	17.3/9.1/23.8	17.2/13.0/17.7
R3	3.8	18.4/13.6/22.5	10.7/5.2/18.6	10.5/7.7/12.9

^a Measured at a brightness of 100 cd m^{-2} /measured at a brightness of 1000 cd m^{-2} /maximum efficiency.

quantum efficiency (EQE) of 17.7% and a maximum power efficiency (PE) of 23.8 lm W^{-1} . Compared to **R2** devices **R1** and **R3** displayed somewhat lower efficiencies with a CE_{max} of 18.5 cd A^{-1} and 22.2 cd A^{-1} and a PE_{max} of 11.8 lm W^{-1} and 12.9 lm W^{-1} , respectively. The lower efficiency of **R1** may be attributed to the fact that the E_{T} of *p*-PCzTPD is rather close to the E_{T} of the red (MDQ)₂(acac) dopant (2.0 eV),⁶⁷ which is also in accordance with the higher efficiency roll-off of **R1** compared to **R2** and **R3**. Although the performance of **R3** is slightly better compared to **R1**, it does not reach the efficiency values of **R2** despite a higher E_{T} of the host material. Nonetheless, the efficiency roll-off above a brightness of 1000 cd m^{-2} is less pronounced in **R3**.

Conclusions

In this study we incorporated the electron accepting thieno[3,4-*c*]pyrrole-4,6-dione building block in donor–acceptor host materials for PhOLEDs and prepared three isomeric derivatives for this purpose. The newly developed materials displayed favourable molecular properties for the application in red PhOLED devices and prototype devices employing Ir(MDQ)₂(acac) as phosphorescent emitter featured satisfying current and power efficiencies. Thus, we have successfully demonstrated the applicability of the thieno[3,4-*c*]pyrrole-4,6-dione as acceptor in host materials for PhOLEDs and introduced this particular molecular unit as novel building block for functional organic materials for OLEDs.

Experimental section

General information

All reagents and solvents were purchased from commercial suppliers and used without further purification. Column chromatography was performed on silica 60 (Merck, 40–63 μm). NMR spectra were recorded on a Bruker Avance DRX-400 Spectrometer. A Thermo Scientific LTQ Orbitrap XL hybrid FTMS (Fourier Transform Mass Spectrometer) equipped with a Thermo Scientific MALDI source was used for high resolution mass spectrometry. The thermal analysis was carried out with a heating rate of 10 K min^{-1} in a flowing argon atmosphere (25 mL min^{-1}). TG measurements were performed on a Netzsch TG 209 F9 Tarsus system with open aluminium oxide crucibles. DSC measurements were performed on a Netzsch DSC 200 F3 Maia, working with aluminium pans with pierced lids. UV/Vis absorption and fluorescence emission spectra were recorded in DCM solutions ($5 \mu\text{M}$) with a Perkin Elmer Lambda 750 spectrometer and an Edinburgh FLS920, respectively. The time resolved low temperature phosphorescence spectra were

recorded in solid solutions (1 mg mL^{-1} ; toluene : EtOH = 9 : 1) at 77 K with a Perkin Elmer Instruments LS 50B luminance spectrometer. Cyclic voltammetry was performed using a three electrode configuration consisting of a Pt working electrode, a Pt counter electrode and an Ag/AgCl reference electrode and a PGSTAT128N, ADC164, DAC164, External, DI048 potentiostat provided by Metrohm Autolab B.V. Measurements were carried out in a 0.5 mM solution in anhydrous DCM with Bu_4NBF_4 (0.1 M) as supporting electrolyte. The solutions were purged with nitrogen for 15 minutes prior to measurement. HOMO energy levels were calculated from the onset of the oxidation peaks, which was determined from the intersection of two tangents drawn at the background and the rising of the oxidation peaks.

Synthetic details

General procedure for the synthesis of the host materials: Host materials *p*-PCzTPD, *m*-PCzTPD and *o*-PCzTPD were prepared using a Suzuki cross coupling reaction. A three necked flask was flushed with argon and charged with dibromide **1** (1.0 eq.) and boronic acid esters **2a–c** (2.5 eq.) before degassed THF (2.5 mM) and aqueous K_2CO_3 (5.0 eq. , 2 M) were added. Subsequently, $\text{Pd}(\text{PPh}_3)_4$ (0.05 eq.) was added and the reaction mixture was heated to reflux until full conversion (TLC, 72 h). After cooling to room temperature the reaction mixture was poured on water and extracted with CH_2Cl_2 three times. The combined organic layers were dried over Na_2SO_4 and concentrated under reduced pressure. Purification of the crude product was accomplished by column chromatography.

1,3-Bis[4-(9*H*-carbazol-9-yl)phenyl]-5-octyl-4*H*-thieno[3,4-*c*]pyrrole-4,6(5*H*)-dione (*p*-PCzTPD). Starting from **1** (169 mg , 0.40 mmol), **2a** (370 mg , 1.00 mmol), K_2CO_3 (277 mg , 2.00 mmol) and $\text{Pd}(\text{PPh}_3)_4$ (23 mg , 0.02 mmol) *p*-PCzTPD was isolated after column chromatography (light petrol/toluene = 1/2) as yellow solid (199 mg , 0.27 mmol , 67%). $^1\text{H NMR}$ (400 MHz , CD_2Cl_2): $\delta = 8.46$ (d, $J = 8.5 \text{ Hz}$, 4H), 8.17 (d, $J = 7.6 \text{ Hz}$, 4H), 7.76 (d, $J = 8.5 \text{ Hz}$, 4H), 7.56 (d, $J = 8.0 \text{ Hz}$, 4H), 7.46 (t, $J = 7.6 \text{ Hz}$, 4H), 7.33 (t, $J = 7.6 \text{ Hz}$, 4H), 3.71 (t, $J = 7.0 \text{ Hz}$, 2H) 1.72 (q, $J = 6.9 \text{ Hz}$, 2H), 1.44 – 1.24 (m, 10H), 0.88 (t, $J = 6.9 \text{ Hz}$, 3H) ppm. $^{13}\text{C NMR}$ (100 MHz , CD_2Cl_2): $\delta = 163.4$ (s), 144.3 (s), 141.0 (s), 139.9 (s), 131.7 (s), 130.3 (d), 129.9 (s), 127.6 (d), 126.7 (d), 124.2 (s), 121.0 (d), 120.9 (d), 110.4 (d), 39.2 (t), 32.4 (t), 29.8 (t), 29.8 (t), 29.0 (t), 27.5 (t), 23.2 (t), 14.4 (q) ppm. HRMS (MALDI): m/z calculated for $\text{C}_{50}\text{H}_{41}\text{N}_3\text{O}_2\text{S}$: 747.29140 [M]⁺, 748.29922 [$\text{M} + \text{H}$]⁺; found: 747.29229 [M]⁺, 748.29565 [$\text{M} + \text{H}$]⁺.

1,3-Bis[3-(9*H*-carbazol-9-yl)phenyl]-5-octyl-4*H*-thieno[3,4-*c*]pyrrole-4,6(5*H*)-dione (*m*-PCzTPD). Starting from **1** (412 mg , 0.97 mmol), **2b** (899 mg , 2.43 mmol), K_2CO_3 (672 mg , 4.86 mmol) and $\text{Pd}(\text{PPh}_3)_4$ (56 mg , 0.05 mmol) *m*-PCzTPD was isolated after column chromatography (light petrol/ CH_2Cl_2 = 3/1 \rightarrow 1/1) as yellow solid (510 mg , 0.68 mmol , 70%). $^1\text{H NMR}$ (400 MHz , CD_2Cl_2): $\delta = 8.41$ (s, 2H), 8.21 – 8.16 (m, 6H), 7.76 – 7.67 (m, 4H), 7.54 (d, $J = 8.2 \text{ Hz}$, 4H), 7.45 (t, $J = 7.3 \text{ Hz}$, 4H), 7.32 (t, $J = 7.3 \text{ Hz}$, 4H), 3.63 (t, $J = 7.2 \text{ Hz}$, 2H) 1.64 (q, $J = 7.3 \text{ Hz}$, 2H), 1.36 – 1.19 (m, 10H), 0.85 (t, $J = 6.7 \text{ Hz}$, 3H) ppm. $^{13}\text{C NMR}$ (100 MHz , CD_2Cl_2): $\delta = 163.3$ (s), 144.3 (s), 141.2 (s), 139.0 (s), 132.9 (s), 132.1 (s), 131.1 (d), 129.0 (d), 127.5 (d), 127.1 (d), 126.7 (d), 124.1 (s), 120.8 (d),

120.8 (d), 110.4 (d), 39.2 (t), 32.4 (t), 29.7 (t), 29.7 (t), 28.9 (t), 27.5 (t), 23.2 (t), 14.4 (q) ppm. HRMS (MALDI): m/z calculated for $C_{50}H_{41}N_3O_2S$: 747.29140 $[M]^+$, 748.29922 $[M + H]^+$, 770.28117 $[M + Na]^+$, found: 747.29282 $[M]^+$, 748.29733 $[M + H]^+$, 770.28271 $[M + Na]^+$.

1,3-Bis[2-(9H-carbazol-9-yl)phenyl]-5-octyl-4H-thieno[3,4-c]pyrrole-4,6(5H)-dione (o-PCzTPD). Starting from **1** (566 mg, 1.34 mmol), **2c** (1233 mg, 3.31 mmol), K_2CO_3 (922 mg, 6.67 mmol) and $Pd(PPh_3)_4$ (77 mg, 0.07 mmol) **o-PCzTPD** was isolated after column chromatography (light petrol/ $CH_2Cl_2 = 1/1$) as yellow solid (172 mg, 0.23 mmol, 17%). 1H NMR (400 MHz, CD_2Cl_2): $\delta = 7.96$ (d, $J = 7.2$ Hz, 4H), 7.87–7.45 (m, 2H), 7.53–7.48 (m, 4H), 7.26–7.24 (m, 2H), 7.19–7.11 (m, 8H), 6.75 (d, $J = 7.6$ Hz, 4H), 3.61 (t, $J = 7.3$ Hz, 2H) 1.55 (q, $J = 7.2$ Hz, 2H), 1.37–1.21 (m, 10H), 0.91 (t, $J = 6.7$ Hz, 3H) ppm. ^{13}C NMR (100 MHz, CD_2Cl_2): $\delta = 162.8$ (s), 141.8 (s), 141.7 (s), 135.9 (s), 132.6 (d), 132.0 (s), 131.8 (d), 129.9 (d), 129.8 (s), 128.9 (d), 126.4 (d), 124.0 (s), 120.6 (d), 120.6 (d), 110.2 (d), 38.7 (t), 32.4 (t), 29.8 (t), 29.8 (t), 28.8 (t), 27.4 (t), 23.2 (t), 14.5 (q) ppm. HRMS (MALDI): m/z calculated for $C_{50}H_{41}N_3O_2S$: 747.29140 $[M]^+$, 748.29922 $[M + H]^+$, 770.28117 $[M + Na]^+$, found: 747.29249 $[M]^+$, 748.29516 $[M + H]^+$, 770.28228 $[M + Na]^+$.

Computational details

The (TD)DFT computations were performed using the Gaussian 09 package, revision D.01.⁶⁸ Density functional theory (DFT) and time-dependent (TD)DFT calculations were performed using the Becke three parameters hybrid functional with Lee–Yang–Perdew correlation (B3LYP),^{69,70} in combination with Pople basis sets (6-31G*, 6-311+G*⁷¹). The geometry optimizations were performed in gas phase and without symmetry constraints. For the calculation of HOMO/LUMO levels, the ground state (S_0) geometries were optimized applying the 6-311+G* basis set. The determination of the triplet energy was achieved by the calculation of the T_1 excitation energy applying TDDFT level and the 6-311+G* basis to a S_0 geometry optimized at DFT level using the 6-31G* basis set. Orbital plots were generated using GaussView.⁷²

Single crystal diffraction

A crystal of **p-PCzTPD** suitable for single crystal diffraction was selected under a polarizing microscope, embedded in perfluorinated oil and attached to Kapton[®] micromounts. Intensity data were collected in a dry stream of nitrogen at 100 K on a Bruker KAPPA APEX II diffractometer system. Data were reduced using SAINT-Plus⁷³ and an empirical absorption correction using the multi-scan approach implemented in SADABS⁷³ was applied. The crystal structures were solved by charge-flipping implemented in SUPERFLIP⁷⁴ and refined against F with the JANA2006⁷⁵ software package. The non-H atoms were refined with anisotropic displacement parameters. The H atoms were placed at calculated positions and refined as riding on the parent C atoms.

Device fabrication and measurement

All synthesized materials were additionally purified by crystallization (light petrol with minor amounts of toluene) prior to device fabrication. OLED fabrication and testing: the fabricated

devices were grown on clean glass substrates pre-coated with ITO with a sheet resistance of $10 \Omega \text{ sq}^{-1}$. After cleaning with detergent and deionized water, they were dried in an oven at 120°C for 30 minutes and then treated with UV-ozone for 15 minutes. All layers were grown in succession by thermal evaporation without breaking the vacuum ($\sim 10^{-4}$ Pa). The evaporation rates for the organic layer were in a range of $1\text{--}2 \text{ \AA s}^{-1}$, LiF and Al were evaporated with a rate of approximately 0.1 and 5.0 \AA s^{-1} , respectively. All measurements were carried out in ambient atmosphere. The current–voltage–brightness characteristics were recorded using a Keithley source measurement unit (Keithley 2400 and Keithley 2000) with a calibrated silicon photodiode. The electroluminescence (EL) spectra were measured with a Spectrascan PR650 spectrophotometer.

Acknowledgements

This work was supported in part by the TU Wien “Innovative Projects” research funds and the Austrian Federal Ministry of Science, Research and Economy. The X-ray centre of the TU Wien is acknowledged for providing access to the single-crystal diffractometer. P. K. and J. F. gratefully acknowledge financial support by the Austrian Science Fund (FWF) (Grant No. I 2589-N34). J. C. and D. M. gratefully acknowledge financial support by the National Natural Science Foundation of China (Grant No. 11661131001).

Notes and references

- M. Pope, P. Magnante and H. P. Kallmann, *J. Chem. Phys.*, 1963, **38**, 2042–2043.
- W. Helfrich and W. G. Schneider, *Phys. Rev. Lett.*, 1965, **14**, 229–231.
- C. W. Tang and S. A. VanSlyke, *Appl. Phys. Lett.*, 1987, **51**, 913–915.
- J. H. Burroughes, D. D. C. Bradley, A. R. Brown, R. N. Marks, K. Mackay, R. H. Friend, P. L. Burn and A. B. Holmes, *Nature*, 1990, **347**, 539–541.
- D. Braun and A. J. Heeger, *Appl. Phys. Lett.*, 1991, **58**, 1982–1984.
- S. R. Forrest, *Nature*, 2004, **428**, 911–918.
- M. C. Gather, A. Köhnen and K. Meerholz, *Adv. Mater.*, 2011, **23**, 233–248.
- S. Reineke, M. Thomschke, B. Lüssem and K. Leo, *Rev. Mod. Phys.*, 2013, **85**, 1245–1293.
- M. A. Baldo, D. F. O’Brien, Y. You, A. Shoustikov, S. Sibley, M. E. Thompson and S. R. Forrest, *Nature*, 1998, **395**, 151–154.
- M. A. Baldo, S. Lamansky, P. E. Burrows, M. E. Thompson and S. R. Forrest, *Appl. Phys. Lett.*, 1999, **75**, 4–6.
- H. Uoyama, K. Goushi, K. Shizu, H. Nomura and C. Adachi, *Nature*, 2012, **492**, 234–238.
- Y. Sun, N. C. Giebink, H. Kanno, B. Ma, M. E. Thompson and S. R. Forrest, *Nature*, 2006, **440**, 908–912.
- S. Reineke, F. Lindner, G. Schwartz, N. Seidler, K. Walzer, B. Lüssem and K. Leo, *Nature*, 2009, **459**, 234–238.
- Y. Tao, K. Yuan, T. Chen, P. Xu, H. H. Li, R. F. Chen, C. Zheng, L. Zhang and W. Huang, *Adv. Mater.*, 2014, **26**, 7931–7958.

- 15 Q. Zhang, B. Li, S. Huang, H. Nomura, H. Tanaka and C. Adachi, *Nat. Photonics*, 2014, **8**, 326–332.
- 16 W.-C. Chen, C.-S. Lee and Q.-X. Tong, *J. Mater. Chem. C*, 2015, **3**, 10957–10963.
- 17 R. J. Holmes, S. R. Forrest, Y.-J. Tung, R. C. Kwong, J. J. Brown, S. Garon and M. E. Thompson, *Appl. Phys. Lett.*, 2003, **82**, 2422–2424.
- 18 S. Tokito, T. Iijima, Y. Suzuri, H. Kita, T. Tsuzuki and F. Sato, *Appl. Phys. Lett.*, 2003, **83**, 569–571.
- 19 L. Xiao, Z. Chen, B. Qu, J. Luo, S. Kong, Q. Gong and J. Kido, *Adv. Mater.*, 2011, **23**, 926–952.
- 20 K. S. Yook and J. Y. Lee, *Adv. Mater.*, 2012, **24**, 3169–3190.
- 21 H. Sasabe and J. Kido, *Eur. J. Org. Chem.*, 2013, 7653–7663.
- 22 Y. Tao, C. Yang and J. Qin, *Chem. Soc. Rev.*, 2011, **40**, 2943–2970.
- 23 A. Chaskar, H.-F. Chen and K.-T. Wong, *Adv. Mater.*, 2011, **23**, 3876–3895.
- 24 S. O. Jeon and J. Y. Lee, *J. Mater. Chem.*, 2012, **22**, 4233–4243.
- 25 B. E. Koene, D. E. Loy and M. E. Thompson, *Chem. Mater.*, 1998, **10**, 2235–2250.
- 26 Z. Ge, T. Hayakawa, S. Ando, M. Ueda, T. Akiike, H. Miyamoto, T. Kajita and M.-a. Kakimoto, *Adv. Funct. Mater.*, 2008, **18**, 584–590.
- 27 Y. Tao, Q. Wang, Y. Shang, C. Yang, L. Ao, J. Qin, D. Ma and Z. Shuai, *Chem. Commun.*, 2009, 77–79.
- 28 C. H. Chen, W. S. Huang, M. Y. Lai, W. C. Tsao, J. T. Lin, Y. H. Wu, T. H. Ke, L. Y. Chen and C. C. Wu, *Adv. Funct. Mater.*, 2009, **19**, 2661–2670.
- 29 Y. Tao, Q. Wang, L. Ao, C. Zhong, C. Yang, J. Qin and D. Ma, *J. Phys. Chem. C*, 2010, **114**, 601–609.
- 30 Y. Kuwabara, H. Ogawa, H. Inada, N. Noma and Y. Shiota, *Adv. Mater.*, 1994, **6**, 677–679.
- 31 Z. Ge, T. Hayakawa, S. Ando, M. Ueda, T. Akiike, H. Miyamoto, T. Kajita and M.-a. Kakimoto, *Org. Lett.*, 2008, **10**, 421–424.
- 32 S.-J. Su, H. Sasabe, T. Takeda and J. Kido, *Chem. Mater.*, 2008, **20**, 1691–1693.
- 33 Y. Tao, Q. Wang, C. Yang, C. Zhong, K. Zhang, J. Qin and D. Ma, *Adv. Funct. Mater.*, 2010, **20**, 304–311.
- 34 H.-C. Ting, Y.-M. Chen, H.-W. You, W.-Y. Hung, S.-H. Lin, A. Chaskar, S.-H. Chou, Y. Chi, R.-H. Liu and K.-T. Wong, *J. Mater. Chem.*, 2012, **22**, 8399–8407.
- 35 P. Kautny, D. Lumpi, Y. Wang, A. Tissot, J. Bintinger, E. Horkel, B. Stöger, C. Hametner, H. Hagemann, D. Ma and J. Fröhlich, *J. Mater. Chem. C*, 2014, **2**, 2069–2081.
- 36 D. Zhang, L. Duan, C. Li, Y. Li, H. Li, D. Zhang and Y. Qiu, *Adv. Mater.*, 2014, **26**, 5050–5055.
- 37 P. Kautny, Z. Wu, J. Eichelner, E. Horkel, B. Stöger, J. Chen, D. Ma, J. Fröhlich and D. Lumpi, *Org. Electron.*, 2016, **34**, 237–245.
- 38 J. Lee, K. Shizu, H. Tanaka, H. Nomura, T. Yasuda and C. Adachi, *J. Mater. Chem. C*, 2013, **1**, 4599–4604.
- 39 H. Tanaka, K. Shizu, H. Nakanotani and C. Adachi, *Chem. Mater.*, 2013, **25**, 3766–3771.
- 40 S. Y. Lee, T. Yasuda, Y. S. Yang, Q. Zhang and C. Adachi, *Angew. Chem., Int. Ed.*, 2014, **126**, 6520–6524.
- 41 Q. Zhang, H. Kuwabara, W. J. Potscavage, S. Huang, Y. Hatae, T. Shibata and C. Adachi, *J. Am. Chem. Soc.*, 2014, **136**, 18070–18081.
- 42 Y. Hamada, C. Adachi, T. Tsutsui and S. Saito, *Jpn. J. Appl. Phys., Part 1*, 1992, **31**, 1812–1816.
- 43 C. Adachi, T. Tsutsui and S. Saito, *Appl. Phys. Lett.*, 1989, **55**, 1489–1491.
- 44 P. Kautny, Z. Wu, B. Stöger, A. Tissot, E. Horkel, J. Chen, D. Ma, H. Hagemann, J. Fröhlich and D. Lumpi, *Org. Electron.*, 2015, **17**, 216–228.
- 45 D. F. O'Brien, M. A. Baldo, M. E. Thompson and S. R. Forrest, *Appl. Phys. Lett.*, 1999, **74**, 442–444.
- 46 S.-J. Su, Y. Takahashi, T. Chiba, T. Takeda and J. Kido, *Adv. Funct. Mater.*, 2009, **19**, 1260–1267.
- 47 Z. Gao, C. S. Lee, I. Bello, S. T. Lee, R.-M. Chen, T.-Y. Luh, J. Shi and C. W. Tang, *Appl. Phys. Lett.*, 1999, **74**, 865–867.
- 48 H. Inomata, K. Goushi, T. Masuko, T. Konno, T. Imai, H. Sasabe, J. J. Brown and C. Adachi, *Chem. Mater.*, 2004, **16**, 1285–1291.
- 49 D. R. Lee, M. Kim, S. K. Jeon, S.-H. Hwang, C. W. Lee and J. Y. Lee, *Adv. Mater.*, 2015, **27**, 5861–5867.
- 50 J. Kido, C. Ohtaki, K. Hongawa, K. Okuyama and K. Nagai, *Jpn. J. Appl. Phys., Part 2*, 1993, **32**, L917–L920.
- 51 P. E. Burrows, A. B. Padmameruma, L. S. Sapochak, P. Djurovich and M. E. Thompson, *Appl. Phys. Lett.*, 2006, **88**, 183503.
- 52 S. O. Jeon, K. S. Yook, C. W. Joo and J. Y. Lee, *Adv. Funct. Mater.*, 2009, **19**, 3644–3649.
- 53 C. Han, G. Xie, H. Xu, Z. Zhang, L. Xie, Y. Zhao, S. Liu and W. Huang, *Adv. Mater.*, 2011, **23**, 2491–2496.
- 54 H. Wang, L. Xie, Q. Peng, L. Meng, Y. Wang, Y. Yi and P. Wang, *Adv. Mater.*, 2014, **26**, 5198–5204.
- 55 C. W. Lee and J. Y. Lee, *Adv. Mater.*, 2013, **25**, 5450–5454.
- 56 Y. Im and J. Y. Lee, *Chem. Commun.*, 2013, **49**, 5948–5950.
- 57 T. Nakagawa, S.-Y. Ku, K.-T. Wong and C. Adachi, *Chem. Commun.*, 2012, **48**, 9580–9582.
- 58 C. Piliago, T. W. Holcombe, J. D. Douglas, C. H. Woo, P. M. Beaujuge and J. M. J. Fréchet, *J. Am. Chem. Soc.*, 2010, **132**, 7595–7597.
- 59 T.-Y. Chu, J. Lu, S. Beaupré, Y. Zhang, J.-R. Pouliot, S. Wakim, J. Zhou, M. Leclerc, Z. Li, J. Ding and Y. Tao, *J. Am. Chem. Soc.*, 2011, **133**, 4250–4253.
- 60 C. B. Nielsen, R. S. Ashraf, B. C. Schroeder, P. D'Angelo, S. E. Watkins, K. Song, T. D. Anthopoulos and I. McCulloch, *Chem. Commun.*, 2012, **48**, 5832–5834.
- 61 M.-C. Yuan, M.-Y. Chiu, S.-P. Liu, C.-M. Chen and K.-H. Wei, *Macromolecules*, 2010, **43**, 6936–6938.
- 62 X. Guo, N. Zhou, S. J. Lou, J. Smith, D. B. Tice, J. W. Hennek, R. P. Ortiz, J. T. L. Navarrete, S. Li, J. Strzalka, L. X. Chen, R. P. H. Chang, A. Facchetti and T. J. Marks, *Nat. Photonics*, 2013, **7**, 825–833.
- 63 X. Guo, R. P. Ortiz, Y. Zheng, M.-G. Kim, S. Zhang, Y. Hu, G. Lu, A. Facchetti and T. J. Marks, *J. Am. Chem. Soc.*, 2011, **133**, 13685–13697.
- 64 H. Li, Y. Wang, K. Yuan, Y. Tao, R. Chen, C. Zheng, X. Zhou, J. Li and W. Huang, *Chem. Commun.*, 2014, **50**, 15760–15763.
- 65 Y. Tao, Q. Wang, L. Ao, C. Zhong, J. Qin, C. Yang and D. Ma, *J. Mater. Chem.*, 2010, **20**, 1759–1765.
- 66 E. Mondal, W.-Y. Hung, H.-C. Dai and K.-T. Wong, *Adv. Funct. Mater.*, 2013, **23**, 3096–3105.

- 67 G. Schwartz, S. Reineke, T. Rosenow, K. Walzer and K. Leo, *Adv. Funct. Mater.*, 2009, **19**, 1319–1333.
- 68 M. J. Frisch, G. W. Trucks, H. B. Schlegel, G. E. Scuseria, M. A. Robb, J. R. Cheeseman, G. Scalmani, V. Barone, B. Mennucci, G. A. Petersson, H. Nakatsuji, M. Caricato, X. Li, H. P. Hratchian, A. F. Izmaylov, J. Bloino, G. Zheng, J. L. Sonnenberg, M. Hada, M. Ehara, K. Toyota, R. Fukuda, J. Hasegawa, M. Ishida, T. Nakajima, Y. Honda, O. Kitao, H. Nakai, T. Vreven, J. A. Montgomery Jr., J. E. Peralta, F. Ogliaro, M. J. Bearpark, J. Heyd, E. N. Brothers, K. N. Kudin, V. N. Staroverov, R. Kobayashi, J. Normand, K. Raghavachari, A. P. Rendell, J. C. Burant, S. S. Iyengar, J. Tomasi, M. Cossi, N. Rega, N. J. Millam, M. Klene, J. E. Knox, J. B. Cross, V. Bakken, C. Adamo, J. Jaramillo, R. Gomperts, R. E. Stratmann, O. Yazyev, A. J. Austin, R. Cammi, C. Pomelli, J. W. Ochterski, R. L. Martin, K. Morokuma, V. G. Zakrzewski, G. A. Voth, P. Salvador, J. J. Dannenberg, S. Dapprich, A. D. Daniels, Ö. Farkas, J. B. Foresman, J. V. Ortiz, J. Cioslowski and D. J. Fox, *Gaussian 09, Revision D.01*, Gaussian, Inc., Wallingford, CT, USA, 2009.
- 69 C. Lee, W. Yang and R. G. Parr, *Phys. Rev. B: Condens. Matter Mater. Phys.*, 1988, **37**, 785–789.
- 70 A. D. Becke, *J. Chem. Phys.*, 1993, **98**, 5648–5652.
- 71 R. Krishnan, J. S. Binkley, R. Seeger and J. A. Pople, *J. Chem. Phys.*, 1980, **72**, 650–654.
- 72 R. Dennington, T. Keith and J. Millam, *GaussView, Version 5*, Semichem, Inc., Shawnee Mission, KS, 2009.
- 73 *Bruker computer programs: APEX2, SAINT and SADABS*, Bruker AXS Inc., Madison, WI, 2015.
- 74 L. Palatinus and G. Chapuis, *J. Appl. Crystallogr.*, 2007, **40**, 786–790.
- 75 V. Petříček, M. Dušek and L. Palatinus, *Z. Kristallogr. – Cryst. Mater.*, 2014, **229**, 345–352.

2.7. Manuscript #7

Structure-property relationships in Click-derived donor-triazole-acceptor materials

Paul Kautny, Dorian Bader, Berthold Stöger, Georg A. Reider, Johannes Fröhlich, Daniel Lumpi

Chemistry-A European Journal, **2016**, 22, 18887-18898

Reproduced with the kind permission of John Wiley & Sons, Inc.

Charge Transfer

Structure–Property Relationships in Click-Derived Donor–Triazole–Acceptor Materials

Paul Kautny,^{*[a]} Dorian Bader,^[a] Berthold Stöger,^[b] Georg A. Reider,^[c] Johannes Fröhlich,^[a] and Daniel Lumpi^[a]

Abstract: To shed light on intramolecular charge-transfer phenomena in 1,2,3-triazole-linked materials, a series of 1,2,3-triazole-linked push–pull chromophores were prepared and studied experimentally and computationally. Investigated modifications include variation of donor and/or acceptor strength and linker moiety as well as regioisomers. Photo-

physical characterization of intramolecular charge-transfer features revealed ambipolar behavior of the triazole linker, depending on the substitution position. Furthermore, non-centrosymmetric materials were subjected to second-harmonic generation measurements, which revealed the high nonlinear optical activity of this class of materials.

Introduction

Great efforts have been made in the design and synthesis of novel organic push–pull molecules owing to a wide range of technologically relevant applications. Bipolar organic materials, consisting of an electron-donating and -withdrawing subunit, are of crucial importance for organic light-emitting diodes (OLEDs),^[1] imaging,^[2] organic photovoltaics (OPVs),^[3] dyes, and nonlinear optical (NLO) materials^[4] for two-photon absorption^[5] or second-harmonic generation (SHG)^[6] to name a few. The electronic structure and, as a consequence, intrinsic properties of the individual molecules are dominated by the donor–acceptor interaction through intramolecular charge transfer (ICT).^[1a–c, 5a, 7]

Generally, the design of push–pull chromophores relies on a donor– π linker–acceptor architecture. Thus, the properties of the materials can be modified by careful selection of donor and/or acceptor units as well as by the modulation of the degree of electronic exchange between the donor and acceptor groups through the conjugated linker moiety.^[1a,b, 5a, 6a] To control ICT, molecular design offers a variety of specific linkage modes, such as 1) the introduction of sp^3 -hybridized bridges,^[8] 2) twisted configurations of molecules that result from sterically demanding groups,^[9] 3) *ortho* linkage of the electron-with-

drawing and -donating groups,^[10] and 4) *meta* linkage of the two molecular subunits to lower conjugation.^[10a,b, 11] Moreover, the choice of a specific linker moiety can be used effectively to control the donor–acceptor exchange. However, these particular methods are often difficult to realize and/or require tedious synthetic work.

In contrast, copper(I)-catalyzed azide–alkyne cycloaddition (CuAAC) is a well-investigated, robust synthetic methodology for joining two molecular subunits through 1,2,3-triazole formation. Whereas CuAAC, which is generally regarded as the most successful example of click chemistry,^[12] has been extensively exploited in many fields of organic synthesis,^[12, 13] reports on bipolar organic materials that incorporate 1,2,3-triazoles as functional π -conjugated moieties are rare. Such synthesized click-derived push–pull molecules have been employed as NLO materials,^[14] fluorophores,^[15] materials for two-photon absorption,^[16] fluorescent metal sensors,^[17] and electro-optical materials.^[18] CuAAC provides an intriguingly simple possibility to join various donor and acceptor combinations to establish the 1,2,3-triazole linker. However, the intrinsically weak electron-accepting properties of the triazole^[16, 18a, 19] and influence on ICT through the triazole linker have to be considered in the molecular design of the materials. Although a significant influence of the triazole substitution pattern on the electrochemical and photophysical properties has been reported,^[15b–e, 17e, 20] no extensive combinatorial study of a large set of donors and acceptors, including donor–acceptor exchange, can be found in the literature.

The aim of this work was to investigate the effects of donor and/or acceptor variations, as well as of triazole substitution pattern, on the photophysical properties of simple donor–triazole–acceptor molecules and gain a detailed insight into ICT phenomena to establish a structure–property relationship for this particular molecular scaffold.

[a] P. Kautny, D. Bader, Prof. Dr. J. Fröhlich, Dr. D. Lumpi
Institute of Applied Synthetic Chemistry, TU Wien
Getreidemarkt 9/163, 1060 Vienna (Austria)
E-mail: paul.kautny@tuwien.ac.at

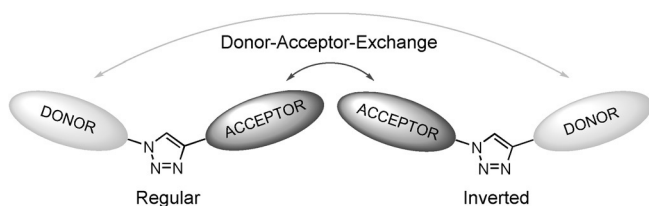
[b] Dr. B. Stöger
Institute of Chemical Technologies and Analytics, TU Wien
Getreidemarkt 9/164-SC, 1060 Vienna (Austria)

[c] Prof. Dr. G. A. Reider
Photonics Institute, TU Wien
Gußhausstraße 27–29, 1040 Vienna (Austria)

Supporting information and the ORCID number(s) for the author(s) of this article are available under <http://dx.doi.org/10.1002/chem.201603510>.

Results and Discussion

Our investigations are based on a large matrix of donor-acceptor molecules. We systematically increased donor (benzene < anisole < dimethylaniline (DMA)) and acceptor (benzene < pyridine < pyrimidine) strength to explore the ICT. Moreover, we examined the effects of donor-acceptor exchange, by inverting the triazole substitution pattern. In the following discussion, the two groups of regioisomers are referred to as the regular (electron donor at 1-N of the triazole linker) and inverted (electron donor at 4-C of the triazole linker) linked series (Scheme 1). An overview of all synthesized materials is given in Scheme 2.

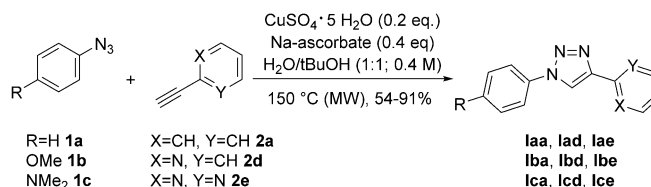


Scheme 1. Representation of the investigated 1,2,3-triazole-linked donor-acceptor materials.

Synthesis

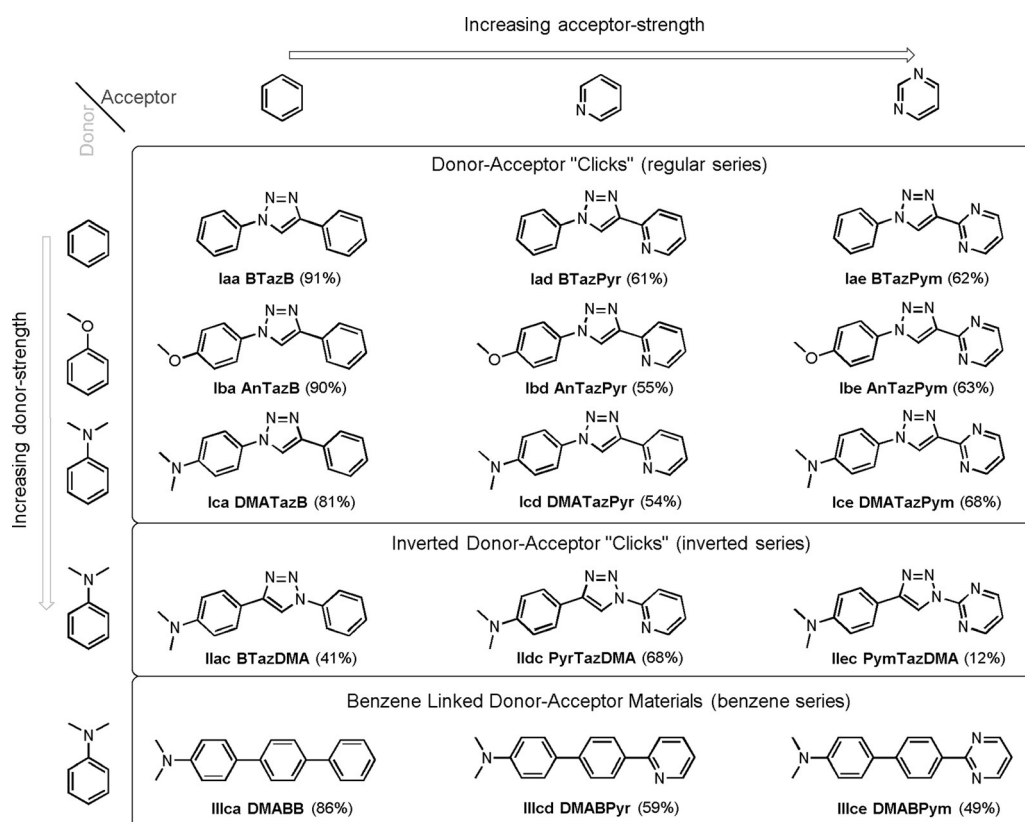
By employing standard CuAAC conditions, the synthesis of the regular series was accomplished by using $\text{CuSO}_4 \cdot 5\text{H}_2\text{O}$ as the

copper source and sodium ascorbate for the in situ reduction of Cu^{II} in a mixture of H_2O and $t\text{BuOH}$ (1:1; Scheme 3). Application of a reaction microwave (MW) reactor allowed for short reaction times (30–60 min). Whereas reactions starting from alkyne **2a** proceeded with excellent yields (81–91%), a tendency towards lower yields (54–68%) was observed in the conversion of electron-poor alkynes **2d** and **2e** (Scheme 3).

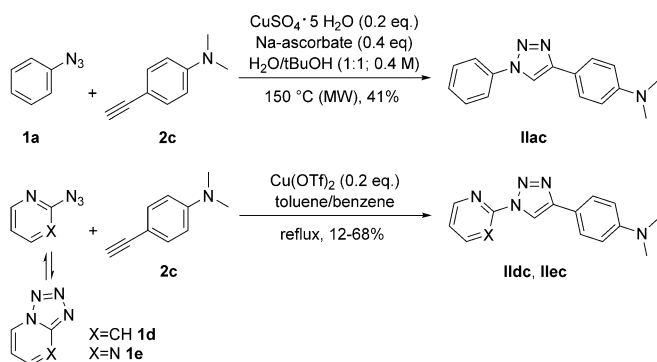


Scheme 3. Synthesis of the 1,2,3-triazole-linked donor-acceptor materials (regular series).

In case of the inverted series, DMA was employed as the sole donor, owing to its superior electron-donating properties (Scheme 4). The synthesis of pyridine- and pyrimidine-based **lldc** and **llec** required the application of 2-azidopyridine (**1d**) and 2-azidopyrimidine (**1e**). Whereas compound **llac** could be synthesized under standard click conditions (Scheme 4), this methodology was not applicable for azides **1d** and **1e** because they were in a tautomeric equilibrium with the corresponding ring-closed tetrazoles, and thus, exhibited significant-



Scheme 2. Overview of all materials under investigation.



Scheme 4. Synthesis of the 1,2,3-triazole-linked donor–acceptor materials (inverted series).

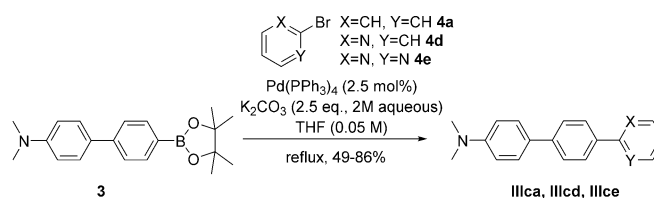
ly decreased reactivity. Single crystals of both tetrazoles were obtained from solutions of **2d** and **2e** in CDCl_3 upon slow evaporation of the solvent.

Nevertheless, by utilizing $\text{Cu}(\text{OTf})_2$ ($\text{OTf} = \text{triflate}$) as catalyst azides, compounds **1d** and **1e** could be reacted with **2c** by heating at reflux in toluene containing traces of benzene^[21] for 24–28 h to obtain **11dc** and **11ec** in 68 and 12% yield, respectively (Scheme 4).

Additionally, a benzene-linked donor–acceptor series was prepared to compare 1,2,3-triazole and benzene as linking moieties. DMA was likewise employed as the sole electron-donating group for this series and the strength of the electron acceptor was varied. Synthesis of the benzene-linked materials was realized in a Suzuki cross-coupling reaction starting from boronic ester **3** and the corresponding brominated acceptor moieties **4a**, **4d**, and **4e** (Scheme 5).

Photophysical characterization

To explore the effects of the systematic structural modifications on the photophysical properties of the materials, UV/Vis absorptions and emissions were recorded. In the following dis-



Scheme 5. Synthesis of the benzene-linked donor–acceptor materials.

cussion, all compounds are named according to the nomenclature defined in Scheme 2. All materials based on the DMA donor exhibited photoluminescence, with the exception of **PymTazDMA**, whereas among the other materials weak emission was only observed in the case of **AnTazPyr**. To examine the differences in the excited states of the compounds, photoluminescence spectra in eight solvents with increasing polarity (cyclohexane, dibutyl ether, diisopropyl ether, diethyl ether, dichloromethane, butanol, ethanol, acetonitrile) have been recorded. However, in butanol and ethanol, no or only very weak emission was obtained from triazole-linked materials that incorporated pyridine or pyrimidine units, probably owing to specific protic interactions between the solvent and chromophores.^[15c,22] Key photophysical properties are summarized in Table 1 and all spectra of the individual compounds are given in the Supporting Information.

First, compounds of the regular series were investigated. Within this series, materials with a DMA donor unit exhibit similar absorption spectra in dichloromethane with broad maxima between $\lambda = 302$ and 309 nm. In contrast, the absorption profiles of materials with weaker donors seem to be predominately determined by the acceptor unit connected to the triazole at the 4-position. Although **BTazB** and **AnTazB** feature structured absorptions with several shoulders between $\lambda = 260$ and 290 nm, compounds **BTazPyr** and **AnTazPyr** exhibit a single absorption maximum at $\lambda = 287$ nm, albeit with low intensity in the case of **BTazPyr**. Pyrimidine-based **BTazPym** and **AnTazPym** feature one broad absorption peak at $\lambda = 255$ and

Table 1. Key photophysical properties of the materials.

	$\lambda_{\text{abs}}^{[a]}$ [nm]	$\epsilon^{[a]}$ [$\text{M}^{-1} \text{cm}^{-1}$]	$\lambda_{\text{PL,max}}^{[a]}$ [nm]	$\Delta E_{\text{opt.}}^{[a]}$ [eV]	$k^{[b]}$ [cm^{-1}]
BTazB	250.5, 266 (sh), ^[c] 272 (sh), ^[c] 282 (sh), ^[c] 289 (sh) ^[c]	23 140	n.o. ^[d]	4.04	–
BTazPyr	286.5	4020	n.o. ^[d]	4.02	–
BTazPym	255	25 120	n.o. ^[d]	4.18	–
AnTazB	256, 267 (sh), ^[c] 273 (sh), ^[c] 282 (sh), ^[c] 289 (sh) ^[c]	25 600	n.o. ^[d]	3.98	–
AnTazPyr	287	27 180	392.5	3.92	6087
AnTazPym	263	24 380	n.o. ^[d]	3.99	–
DMATazB	286 (sh), ^[c] 302	20 940	396	3.57	12 729
DMATazPyr	306	23 920	413.5	3.53	22 048
DMATazPym	309	20 020	454	3.49	27 609
DMABB	325	34 320	419.5	3.37	13 028
DMABPyr	337	27 640	449	3.22	18 636
DMABPym	351	30 000	472	3.10	20 865
BTazDMA	270 (sh), ^[c] 302	28 480	438	3.47	23 228
PyrTazDMA	271 (sh), ^[c] 296, 305 (sh), ^[c] 345 (sh) ^[c]	27 660	470.5	3.31	26 593
PymTazDMA	268 (sh), ^[c] 287, 310 (sh), ^[c] 345 (sh) ^[c]	16 760	n.o. ^[d]	3.20	–

[a] Determined in dichloromethane (5 μM). [b] Slope of the linear correlation of the Stokes shift with the solvent orientation polarizability determined from the Lippert–Mataga plots. [c] Shoulder. [d] Not observed.

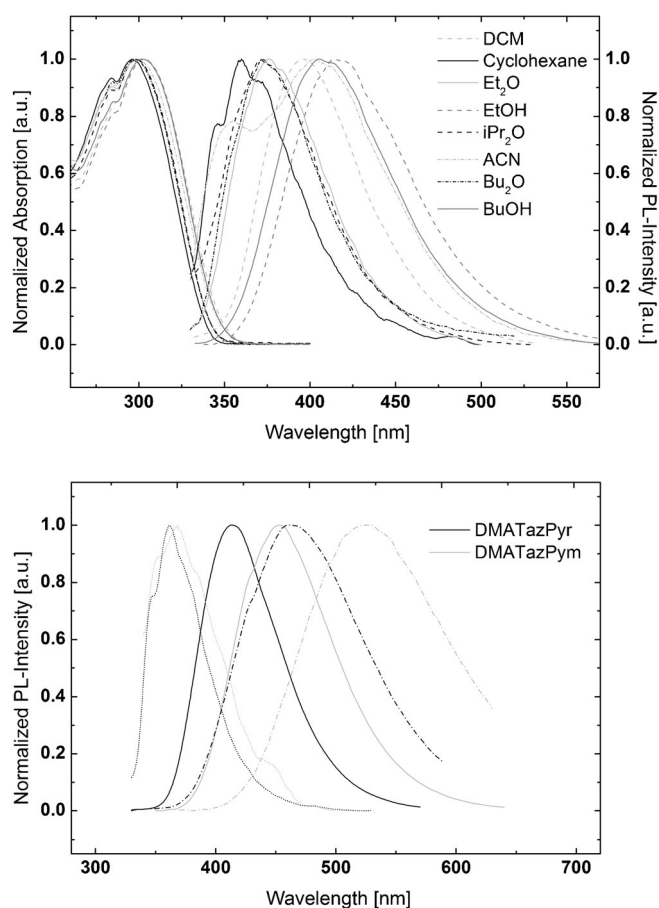


Figure 1. Top: UV/Vis absorption and photoluminescence emission spectra of **DMATazB** in various solvents (DCM = dichloromethane, ACN = acetonitrile). Bottom: photoluminescence emission spectra of **DMATazPyr** and **DMATazPym** in cyclohexane (.....), dichloromethane (—), and acetonitrile (---).

265 nm, respectively. Strikingly, the absorption onset, and thus, optical band gap of materials of the regular series is solely determined by the donor moiety and varies only insignificantly within the respective groups. Although materials with a benzene donor (**BTazB**, **BTazPyr**, **BTazPym**) exhibit optical band gaps between $\lambda = 297$ and 308 nm, onset values of the anisole derivatives are shifted to slightly higher wavelength ($\lambda = 311$ –316 nm). In contrast, the absorption onsets of compounds with DMA donors are distinctly redshifted and located between $\lambda = 347$ and 356 nm.

Whereas the absorption spectra are basically independent of the solvent polarity, the emission spectra of DMA-substituted materials of the regular series exhibit distinct solvatochromic effects, as typically observed for ICT emission.^[22] However, the extent of the solvatochromic shift strongly depends on the strength of the acceptor group (Figure 1). In cyclohexane, the emission maxima of **DMATazB**, **DMATazPyr**, and **DMATazPym** are vibronically resolved and located over a narrow range at $\lambda = 360$, 361.5, and 368.5 nm. In contrast, they are shifted to $\lambda = 396$, 413.5, and 454 nm in dichloromethane and $\lambda = 402.5$, 460.5, and 524.5 nm in acetonitrile, corresponding to an overall redshift of 42.5, 99, and 156 nm from cyclohexane to acetonitrile for **DMATazB**, **DMATazPyr**, and **DMATazPym**, respectively.

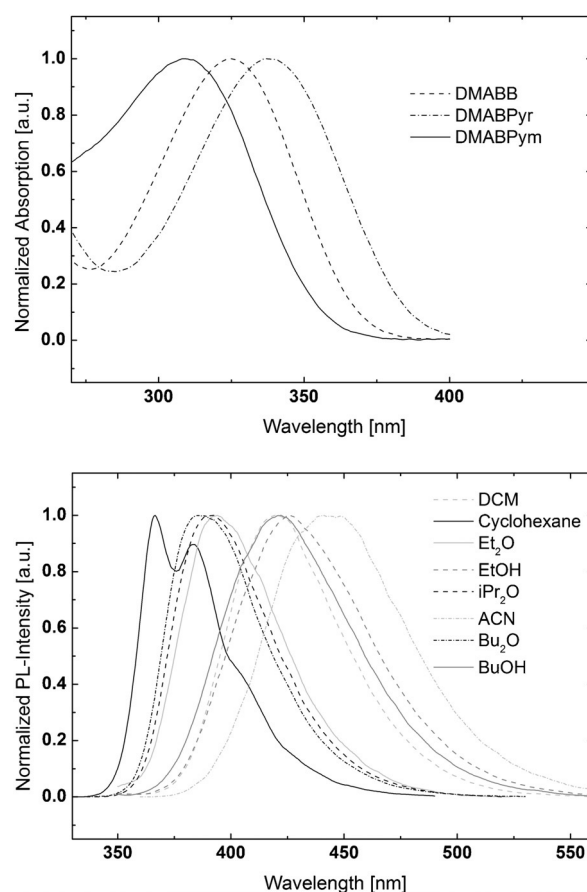


Figure 2. Top: UV/Vis absorption spectra of **DMABB**, **DMABPyr**, and **DMABPym** in dichloromethane. Bottom: photoluminescence emission spectra of **DMABB** in various solvents.

The increasingly redshifted emission can be attributed to the higher acceptor strength of pyridine and pyrimidine, and thus, an increased degree of charge transfer upon photoexcitation. Furthermore, an additional interesting emission feature was observed for **DMATazB**. In polar acetonitrile, a second high-energy emission band emerges at $\lambda = 354$ nm (Figure 1). Such dual behavior is indicative of a mixed emission from a locally excited (LE) and ICT state; a feature that has been previously reported for structurally related chromophores.^[15b]

As a second step, the benzene-linked compounds were analyzed to identify varied photophysical properties relative to the regular series and correlate these alterations to the modified linkage mode. In contrast to the regular series, the absorption maxima and absorption onsets of benzene-linked materials are not only dependent on the donor unit, but exhibit progressive bathochromic shifts for stronger acceptor units (Figure 2). Accordingly, the absorption maxima of **DMABB**, **DMABPyr**, and **DMABPym** in dichloromethane are located at $\lambda = 325$, 337, and 351 nm; thus spanning a significantly larger range (26 nm corresponding to 0.28 eV) than that of the regular series (7 nm, 0.09 eV). This particular behavior can be explained by a donor–acceptor interaction in the ground state that is absent or distinctly reduced in the regular series. Moreover, the absorption maximum of **DMABB**, which is the compound with the weak-

est electron-accepting moiety within the series, is redshifted by 23 nm relative to that of the corresponding compound **DMATazB**. The observation of an acceptor dependence and overall redshift of the absorption are indicative of a higher degree of conjugation in the benzene-linked donor–acceptor materials. Thus, the incorporation of the triazole moiety in the regular series effectively decreased the electronic conjugation of the molecules in the ground state.

In analogy to the regular triazole series, all benzene-linked materials exhibited distinct solvatochromism, as depicted for **DMABB** in Figure 2. To provide a better insight into the solvent dependency of the emission and for better comparability of the different series the solvatochromic behavior of the materials the Lippert–Mataga equation^[23] [Eq. (1)] was applied:

$$(\nu_a - \nu_f) = \frac{2(\mu_e - \mu_g)^2}{hca^3} \Delta f + \text{const.} \quad (1)$$

in which $(\nu_a - \nu_f)$ is the Stokes shift, h is the Planck constant, c is the speed of light, a is the solvent cavity (Onsager) radius, and μ_g and μ_e correspond to the ground- and excited-state dipole moments, respectively. The orientation polarizability, Δf , as a measure of solvent polarity is related to the refractive index by Equation (2):

$$\Delta f = \frac{\varepsilon - 1}{2\varepsilon + 1} - \frac{n^2 - 1}{2n^2 + 1} \quad (2)$$

in which ε is the dielectric constant and n is the refractive index of the solvent. Equation (1) predicts a linear dependence between the Stokes shift and solvent polarity, for which the slope depends on the square of the dipole moment difference of the ground and excited states, and thus, indicates the degree of charge transfer upon photoexcitation. Because the molecular weight and shape of the investigated molecules are similar, slopes of the Lippert–Mataga plots are a direct measure of charge transfer in the individual molecules.

As seen in Figure 3, all materials indeed display a linear correlation of the Stokes shift and solvent polarity and steeper slopes were observed for materials that incorporated stronger acceptor units due to increased charge transfer. However, a comparison of both series unveils more complex behavior. Compounds **DMATazB** and **DMABB** exhibit nearly identical slopes of 12729 and 13028 cm^{-1} ; these values indicate similar degrees of charge transfer upon excitation. In contrast, the corresponding congeners with stronger acceptor units display different emission properties. Within the regular series, the slope values are distinctly increased to 22048 and 27609 cm^{-1} for the pyridine and pyrimidine acceptors, respectively, which suggests significantly enhanced charge transfer in these derivatives. In contrast, and in analogy to the absorption maxima, the benzene series exhibits an overall redshifted emission from **DMABB** to **DMABPyr** to **DMABPym**, which is already evident in cyclohexane. Furthermore, the additional redshift of the emission of the individual acceptor-substituted molecules caused by $\Delta\mu_{eg}$ is smaller than that of the regular series, as deduced from the lower slope values of **DMABPyr** (18636 cm^{-1})

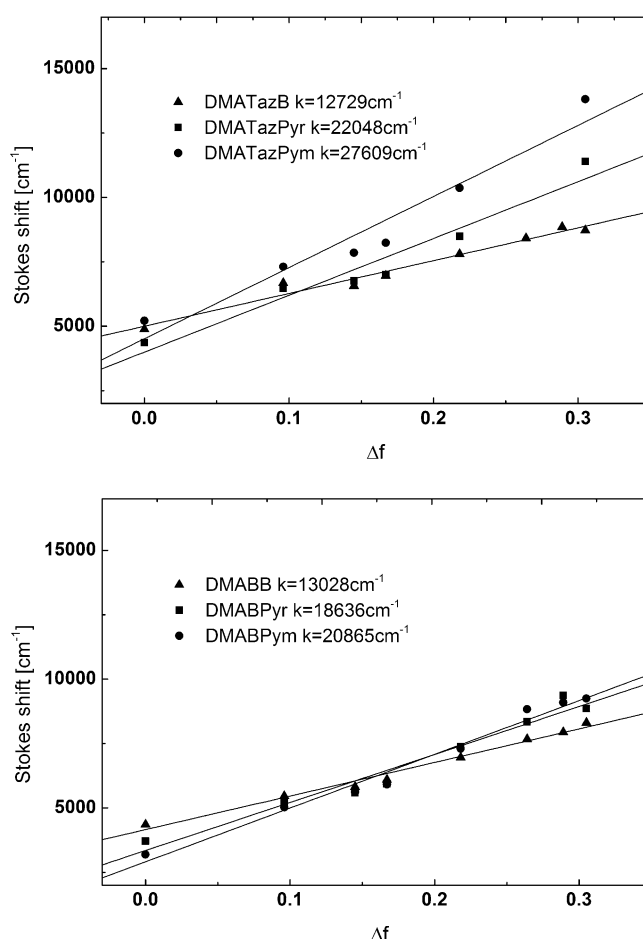
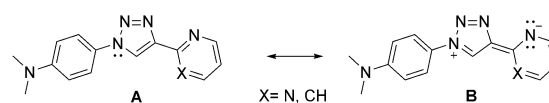


Figure 3. Lippert–Mataga plots of **DMATazB**, **DMATazPyr**, and **DMATazPym** (top), as well as of **DMABB**, **DMABPyr**, and **DMABPym** (bottom).

and **DMABPym** (20865 cm^{-1}); this indicates a lower degree of charge transfer.

From these findings, it can be concluded that the triazole linker decreases conjugation in the ground state, but enhances charge transfer upon photoexcitation. Notably, increased charge transfer is only observed in acceptor-substituted **DMATazPyr** and **DMATazPym**, whereas the charge-transfer properties of **DMATazB** are comparable to those of **DMABB**. Thus, it can be concluded that the triazole linker increases the donor strength of DMA, resulting in enhanced donor–acceptor interaction. The donor properties of the triazole linker can be rationalized by a contribution from mesomeric structure **B** (Scheme 6) to the excited state, as previously suggested for metallochromic materials.^[15e, 17d]

Finally, the photophysical properties of the inverted series were determined. In contrast to the DMA-substituted deriva-



Scheme 6. Mesomeric structures of **DMATazPyr** and **DMATazPym**.

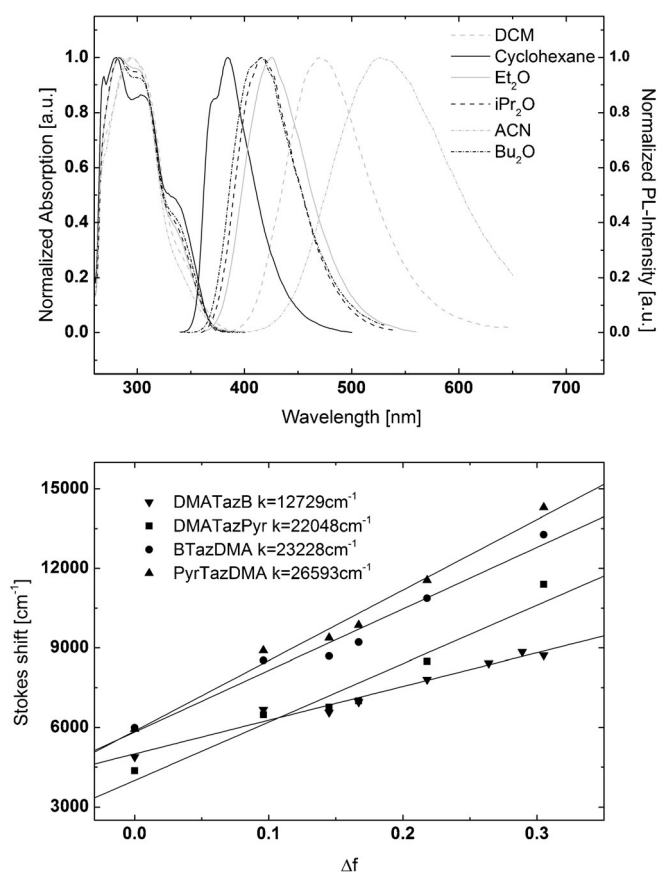


Figure 4. Top: UV/Vis absorption and photoluminescence emission spectra of PyrTazDMA in various solvents. Bottom: Lippert–Mataga plots of DMATazB, DMATazPyr, BTazDMA, and PyrTazDMA.

tives of the regular series, all materials of the inverted series display structured absorption spectra in solvents with low polarity, whereas the individual peaks diminish with increasing solvent polarity, as depicted for PyrTazDMA in Figure 4 as an example. In analogy to the benzene series, the absorption onsets of the inverted materials are gradually redshifted from BTazDMA to PyrTazDMA and PymTazDMA; this indicates a donor–acceptor interaction in the ground state that is not present in the regular series.

Whereas BTazDMA and PyrTazDMA exhibit strong solvatochromic behavior, no photoluminescent emission was detected for PymTazDMA. Emission maxima of BTazDMA and PyrTazDMA are redshifted relative to the corresponding derivatives of the regular series; a feature that has been previously reported for pairs of triazole regioisomers.^[15c] Strikingly, the value of the slope for BTazDMA ($23\,228\text{ cm}^{-1}$) is significantly higher than that of DMATazB ($12\,729\text{ cm}^{-1}$). The additional increase from BTazDMA to PyrTazDMA ($26\,593\text{ cm}^{-1}$) is due to the stronger electron-accepting moiety of the pyridine. However, it is distinctly lower than the corresponding two derivatives of the regular series. From the observation of a strong solvatochromic effect for BTazDMA without an additional acceptor unit, and the moderated increase of solvatochromism for the pyridine-substituted derivative PyrTazDMA, it can be concluded that the triazole itself operates as an electron-accepting moiety in the inverted series.

In summary, these investigations revealed that the triazole linkage significantly decreased conjugation in the ground state, but increased charge-transfer phenomena upon photoexcitation due to an enhancement of donor or acceptor properties. The kind of electronic interaction triggered by the ambipolar triazole moiety, in turn, can be controlled by the triazole substitution pattern.

Theoretical calculations

To gain further insight into the electronic properties of the investigated materials, theoretical studies applying DFT have been performed. The spatial distribution of the HOMOs and LUMOs of the compounds are depicted in Figure 5 and the Supporting Information.

HOMOs and LUMOs are uniformly distributed over the whole molecules in materials without strong acceptor and/or donor units. In contrast, increasing spatial separation can be found for materials with distinctive donor–acceptor combinations. This spatial separation of the HOMO and LUMO is indicative of a charge-transfer process upon photoexcitation, as described in the spectroscopic section. However, looking at the DMA-substituted congeners in detail, a more complex situation is observed (Figure 5). In DMABPym, the HOMO and LUMO are mainly located on the DMA and pyrimidine units, respectively,

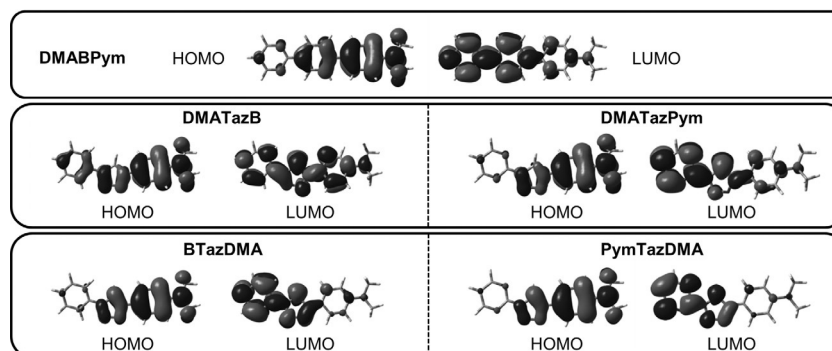


Figure 5. Spatial distribution of HOMO and LUMO levels of DMABPym, DMATazB, DMATazPym, BTazDMA, and PymTazDMA.

Table 2. Key crystallographic properties, supramolecular features, and relative SHG yields of the compounds under investigation.

	Space group	Centro-symmetry	Weak hydrogen bonds				π - π interactions		Relative SHG yield ^[a]
			Taz→Taz	Taz→Pym	Pym→Taz	Pym→Pym	Head-tail	Head-head	
BTazB ^[25]	<i>C2/c</i>	yes	chains					–	
BTazPyr ^[26]	<i>P2₁/n</i>	yes	chains					–	
BTazPym	<i>Cc</i>	no	chains			chains		80	
AnTazB	<i>P2₁2₁2₁</i>	no	chains			chains		3.4	
AnTazPyr	<i>P2₁2₁2₁</i>	no	chains			chains		6.0	
AnTazPym	<i>P2₁/c</i>	yes		chains		chains		–	
DMATazB ^[27]	<i>P2₁/n</i>	yes	chains					–	
DMATazPyr ^[28]	<i>P2₁</i>	no				pairs		0.2	
DMATazPym	<i>P2₁/c</i>	yes			pairs	pairs	chains ^[b]	–	
BTazDMA ^[27]	<i>P1</i>	yes					pairs	–	
PyrTazDMA	<i>P2₁/c</i>	yes				pairs	chains ^[b]	–	
PymTazDMA	<i>P2₁/c</i>	yes			pairs	pairs	chains ^[b]	–	

[a] Relative to potassium dihydrogen phosphate (KDP). [b] Formed by pairs of molecules.

but spread over the whole molecule and significant electron density is located on the opposite end of the molecule. A higher degree of separation is observed in **DMATazPym** and **PymTazDMA**, which indicates increased charge-transfer features; this is in agreement with experimental findings. In particular, the LUMO level of **PymTazDMA** is localized on the pyrimidine and triazole rings. This kind of localization was also found for the LUMO of **BTazDMA**. Likewise, the HOMO level of **BTazDMA** is confined to the DMA and triazole units. Thus, theoretical calculations suggest a pronounced charge transfer in **BTazDMA**, which is in agreement with spectroscopic characterization. In contrast, no such separation is observed in the corresponding derivative of the regular series, **DMATazB**. Therefore, this particular electronic layout can be directly attributed to the altered substitution of the triazole linker. A strong localization of the LUMO in **BTazDMA** in the absence of a strong electron-withdrawing unit indicates the establishment of an electron-accepting moiety at the benzene-triazole fragment. This particular behavior can be attributed to the substitution pattern of the triazole due to the absence of any other molecular modifications and is again in agreement with spectroscopic characterization.

Crystallography and NLO properties

Recently, our group reported a novel class of NLO-active materials with high SHG yields.^[14] These materials are based on click-functionalized ene-yne compounds with an 1,2,3-triazole linker as an essential building block. To further explore the scope of this class of materials, we investigated our present compounds with regard to their SHG efficiency. Because SHG requires non-centrosymmetric crystallization,^[24] single crystals of all triazole-linked materials were subjected to single-crystal XRD. Unfortunately, no usable crystals could be grown for the benzene-linked series. The crystal structures of **BTazB**,^[25] **BTazPyr**,^[26] **DMATazB**,^[27] **DMATazPyr**,^[28] and **BTazDMA**^[27] are known from the work of other groups. Additionally, we grew crystals and determined the structures of **AnTazB**, **AnTazPym**, **AnTazPyr**, **BTazPym**, **DMATazPym**, **PymTazDMA**, and **PyrTazDMA**. Moreover, we redetermined the structure of **DMATazB**, not

being aware of the previously published structural data.^[27] Key crystallographic properties of the materials are summarized in Table 2.

Compound **DMATazPyr** is made up of $Z' = 4$ crystallographically independent molecules. All other structures are made up of one independent molecule, located on a general position. Notably, common structural features were observed in some of the derivatives.

Compounds **AnTazB** and **AnTazPyr** are isostructural, which shows that pyridine can be used as a substitute for benzene. Likewise, compounds **DMATazPym**, **PymTazDMA**, and **PyrTazDMA** are isostructural, which shows that the substitution pattern of the triazole linker can be inverted and pyridine can be substituted by pyrimidine, without affecting the structure type. Whereas the inversion of the triazole has virtually no impact on the structure, additional hydrogen in the pyridine ring imposes a distinct stretching in the [100] direction (**DMATazPym**: $a = 8.4266(7)$ Å, **PymTazDMA**: $a = 8.5714(5)$ Å, **PyrTazDMA**: $a = 9.1392(8)$ Å). A more surprising structural relationship is observed for **BTazPyr** and **DMATazB**. Although the dimethylamine group in **DMATazB** requires additional space (**BTazPyr**: $V = 1078.45$ Å³, **DMATazB**: $V = 1315.84$ Å³), both structures can still be considered as isostructural (Figure S4.1 in the Supporting Information). The remaining structures (**BTazB**, **BTazPym**, **AnTazPym**, **DMATazPyr**, and **BTazDMA**) are unique.

Supramolecular features constitute, on one hand, weak hydrogen bonds of the triazole and pyrimidine hydrogen atoms, and, on the other hand, π - π interactions of the aromatic rings, as summarized in Table 2. The most commonly observed feature is hydrogen bonding connecting triazole moieties, forming infinite chains, for example, as in **BTazPyr** (Figure 6, left). Triazole to pyrimidine and pyrimidine to pyrimidine hydrogen bonds are only observed in **AnTazPym** (chains, Figure 6, right). Pyrimidine to triazole hydrogen bonds exist only in **DMATazPym** and **PymTazDMA** to form pairs of molecules. The absence of this particular intermolecular bonding in isostructural **PyrTazDMA** proves that these weak hydrogen bonds are not structure determining.

The π - π interactions are observed in **DMATazPyr** (pairs) and **DMATazPym**, **PymTazDMA**, and **PyrTazDMA**. In the last of

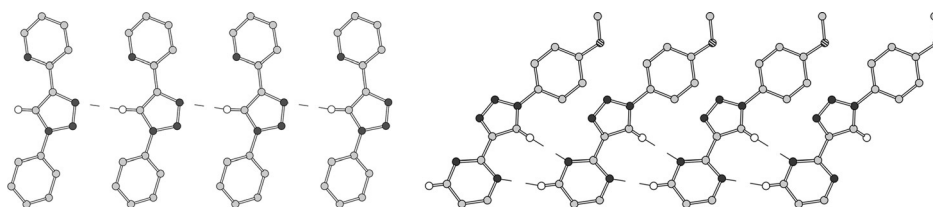


Figure 6. Supramolecular arrangement of **BTazPyr** (left) and **AnTazPym** (right) molecules in chains connected through Taz→Taz hydrogen bonds (**BTazPyr**) or Taz→Pym and Pym→Taz hydrogen bonds (**AnTazPyr**). Carbon, nitrogen, and oxygen atoms are represented by light gray, dark gray, and striped spheres of arbitrary radius. Hydrogen atoms not involved in hydrogen bonding are omitted for clarity. Hydrogen bonds are indicated by dashed lines.

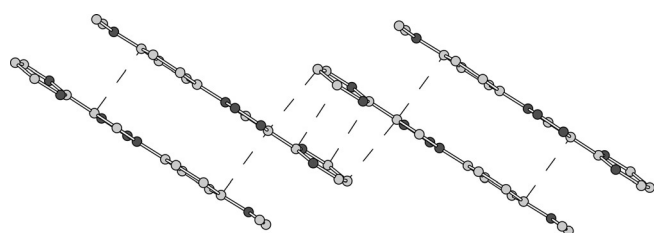


Figure 7. Supramolecular arrangement of **DMATazPym** determined by intermolecular π - π interactions. Colors are the same as those used in Figure 6. Intermolecular C-C contacts in the 3.3–3.4 Å range are indicated by dashed lines.

these, the resulting pairs are also connected by head-to-head π - π interactions (through pyrimidine/pyridine) to chains (Figure 7). Head-to-head π - π interactions through the benzene rings are also observed in **BTazDMA**; these form pairs of molecules. However, no intermolecular interaction between pairs is observed. Finally, the **BTazPym**, **AnTazB**, and **AnTazPyr** molecules are connected through head-to-tail π - π interactions to chains (Figure S4.2 in the Supporting Information).

All materials that crystallize as non-centrosymmetric crystals were investigated regarding their capability of SHG. The strong dependence of the macroscopic SHG yield on the exact alignment of the individual molecules with respect to the symmetry elements of the crystal has to be taken into account when different materials are compared.^[29] However, in the case of **AnTazB** and **AnTazPyr**, isostructural crystallization allows for the direct comparison of the two materials. Whereas **AnTazB** exhibits a SHG efficiency of 3.4 times the value of KDP, this value is higher for **AnTazPyr** (6.0×KDP). In analogy to DMA-substituted materials, stronger charge-transport features can be expected for **AnTazPyr** than those of **AnTazB**, owing to the presence of the pyridine acceptor. Thus, the increased SHG efficiency directly reflects the increased $\Delta\mu_{eg}$ value, as predicted by the two-state model.^[29] Investigation of the NLO properties of **BTazPym** revealed a significantly higher SHG yield of 80 times the value of KDP. We could therefore further improve the NLO performance compared with the most efficient click-functionalized thiophene- or selenophene-ring fragmentation^[14b] products reported previously by our group. Hence, our investigations further expand the scope of click-derived materials for NLO applications. In particular, the inverted triazole architecture, which ensures high $\Delta\mu_{egr}$, provides an appealing strategy in the design of new NLO materials because hyperpo-

larizability in the donor-acceptor materials is predominantly determined by ICT features.^[29]

Conclusion

We have synthesized a complete set of 1,2,3-triazole-linked donor-acceptor materials and provided a thorough photo-physical and theoretical characterization. Our findings reveal an intriguing relationship between intramolecular charge-transfer properties and triazole substitution patterns in donor-acceptor materials. Accordingly, triazole can be utilized not only as a linker unit, but also to increase either the electron-donating properties of the donor or to establish electron-accepting properties in a conjugated system without a defined acceptor moiety. Thus, our investigations provide guidelines for the incorporation of the 1,2,3-triazole unit as a linker in conjugated materials and are of great importance for the design of new functional click-derived materials for manifold applications.

Experimental Section

X-ray structure determination

Crystals of **BTazPym** (hexane/EtOH = 100:1), **AnTazB** (EtOH), **AnTazPyr** (hexane), **AnTazPym** (EtOH), **DMATazB** (EtOH), **DMATazPym** (EtOH), **PyrTazDMA** (EtOH), and **PymTazDMA** (EtOH) were crystallized from saturated boiling solvents. XRD intensities were collected at $T = 100$ K in a dry stream of nitrogen on Bruker Smart APEX (**AnTazPym** and **DMATazPym**) or Bruker Kappa APEX II (all other) diffractometer systems by using graphite-monochromatized $\text{Mo}_{K\alpha}$ radiation ($\lambda = 0.71073$ Å) and fine-sliced φ and ω scans. Data were reduced to intensity values with SAINT^[30] and an absorption correction was applied with the multiscan approach implemented in SADABS.^[30] The structures were solved by charge flipping by using SUPERFLIP^[31] and refined against F with JANA2006.^[32] Non-hydrogen atoms were refined anisotropically. The hydrogen atoms were placed in calculated positions and thereafter refined as riding on the parent atoms. Owing to a lack of anomalous scatterers, the Friedel opposites of non-centrosymmetric crystals were merged and the absolute structure was not determined. Molecular graphics were generated with the program MERCURY.^[33]

CCDC 1471390 (**AnTazB**), 1471391 (**AnTazPym**), 1471392 (**AnTazPyr**), 1471393 (**BTazPym**), 1471394 (**DMATazB**), 1471395 (**DMATazPym**), 1471396 (**PymTazDMA**), and 1471397 (**PyrTazDMA**) contain the supplementary crystallographic data for this paper. These data are provided free of charge by The Cambridge Crystallographic Data Centre.

SHG measurements

Second-order NLO properties of the substances were studied with second-harmonic measurements from powder samples. Powdered samples of the materials with a grain size of less than 1 μm were prepared with a mortar. A relative measurement of the NLO coefficients was possible with this technique because the second-harmonic efficiency scaled quadratically with the nonlinear coefficient, providing that the particle size was significantly less than the nonlinear coherence length (which was more than 10 μm in all practical cases).^[34] Subsequently, the powders were positioned between two microscope slides and irradiated with the output of an ultrafast Yb:KGW-Laser (Light Conversion, pulse duration 70 fs, average power 600 mW, repetition rate 75 MHz, wavelength $\lambda = 1034\text{ nm}$), moderately focused with a 100 mm focusing lens. The diffusely reflected second-harmonic radiation was collected with a NA = 0.1 lens, separated from fundamental radiation with a color filter, and spectrally analyzed with a 0.25 m grating monochromator and a photomultiplier detector. The sample plane was positioned somewhat out of the focal plane (towards the lens) to prevent any damage to the sample. After each measurement, the samples were carefully checked for the absence of damage or thermal modification. For quantification of the SHG yields, (Z)-4-(2-(methylthio)-1-propenyl)-1-phenyl-1,2,3-triazole^[14a] was employed as a reference material (SHG yield of reference = SHG yield of KDP $\times 2$).

Synthesis

All reagents and solvents were purchased from commercial suppliers and used without further purification. Azidobenzene (**1a**),^[35] 1-azido-4-methoxybenzene (**1b**),^[36] 4-azido-*N,N*-dimethylbenzenamine (**1c**),^[36] **1d**,^[37] **1e**,^[37] 4-ethynyl-*N,N*-dimethylbenzenamine (**2c**),^[38] 2-ethynylpyridine (**2d**),^[38] 2-ethynylpyrimidine (**2e**),^[38] *N,N*-dimethyl-4'-(4,4,5,5-tetramethyl-1,3,2-dioxaborolan-2-yl)-[1,1'-bi-phenyl]-4-amine (**3**)^[39] were prepared in analogy to published procedures and the physical data of the prepared materials was compared with literature values. Anhydrous solvents were prepared by filtration through drying columns. Column chromatography was performed on silica 60 gel (Merck, 40–63 μm). Experiments under MW irradiation were performed in a Biotage Initiator Sixty MW reactor. Melting points were determined by using a MPA100 Opti-Melt automated melting point system from Stanford Research Systems. NMR spectra were recorded on a Bruker Avance DRX-400 spectrometer. A Thermo Scientific LTQ Orbitrap XL hybrid Fourier transform mass spectrometer equipped with a Thermo Fischer Exactive Plus Orbitrap (LC-ESI+) and a Shimadzu IT-TOF mass spectrometer were used for HRMS. UV/Vis absorption and fluorescence emission spectra in solution (5 μm) were recorded with a PerkinElmer Lambda 750 spectrometer and an Edinburgh FLS920 instrument, respectively. DFT calculations were performed by using the Gaussian 09 package.^[40] applying the Becke three-parameter hybrid functional with Lee–Yang–Perdew correlation (B3LYP)^[41] in combination with Pople basis sets 6-31G(d,p).^[42] Geometry optimizations were performed in the gas phase and without symmetry constraints. Orbital plots were generated by using GaussView.^[43]

General procedure for CuAAC

CuSO₄·5H₂O (0.2 equiv) and sodium ascorbate (0.4 equiv) were added to a solution of alkyne (1.0 equiv) and azide (1.0 equiv) in H₂O/*t*BuOH (1:1; ca. 0.4 M) in a MW reaction vial immediately before the vial was sealed and the reaction mixture was heated to 150 $^{\circ}\text{C}$ until full conversion (TLC; 30–60 min). The resulting precipitate was dissolved in H₂O and DCM and the aqueous phase was

extracted with DCM. The combined organic layers were dried over Na₂SO₄ and concentrated under reduced pressure. Purification of the crude product was accomplished by filtration over a small amount of silica gel.

BTazB: Starting from ethynylbenzene (**2a**; 255 mg, 2.50 mmol, 1.00 equiv), **1a** (298 mg, 2.50 mmol, 1.00 equiv), CuSO₄·5H₂O (125 mg, 0.50 mmol, 0.2 equiv), and sodium ascorbate (198 mg, 1.00 mmol, 0.40 equiv), **BTazB** (506 mg, 91%) was obtained as a yellow solid. M.p. 181.0–182.3 $^{\circ}\text{C}$; ¹H NMR (400 MHz, CD₂Cl₂): $\delta = 8.27$ (s, 1H), 7.92 (d, $J = 8.1\text{ Hz}$, 2H), 7.81 (d, $J = 8.1\text{ Hz}$, 2H), 7.58 (dd, $J = 8.0\text{ Hz}$, 7.3 Hz, 2H), 7.51–7.45 (m, 3H) 7.37 ppm (t, $J = 7.3\text{ Hz}$, 1H); ¹³C NMR (100 MHz, CD₂Cl₂): $\delta = 148.7$, 137.7 131.0, 130.3, 129.5, 129.3, 128.9, 126.2, 121.0, 118.4 ppm; HRMS (ESI): m/z calcd for C₁₄H₁₁N₃: 221.09475 [*M*]⁺, 222.10257 [*M*+H]⁺, 244.08452 [*M*+Na]⁺; found: 221.09438 [*M*]⁺, 222.10196 [*M*+H]⁺, 244.08379 [*M*+Na]⁺.

AnTazB: Starting from **2a** (153 mg, 1.50 mmol, 1.00 equiv), **1b** (224 mg, 1.50 mmol, 1.00 equiv), CuSO₄·5H₂O (75 mg, 0.30 mmol, 0.2 equiv), and sodium ascorbate (119 mg, 0.60 mmol, 0.40 equiv), **AnTazB** (339 mg, 90%) was obtained as a white solid. M.p. 165.5–166.8 $^{\circ}\text{C}$; ¹H NMR (400 MHz, CD₂Cl₂): $\delta = 8.17$ (s, 1H), 7.90 (d, $J = 8.2\text{ Hz}$, 2H), 7.70 (d, $J = 9.0\text{ Hz}$, 2H), 7.46 (dd, $J = 8.2\text{ Hz}$, 7.4 Hz, 2H), 7.37 (t, $J = 7.4\text{ Hz}$, 1H), 7.06 (d, $J = 9.0\text{ Hz}$, 2H), 3.87 ppm (s, 3H); ¹³C NMR (100 MHz, CD₂Cl₂): $\delta = 160.5$, 148.5, 131.2, 131.1, 129.5, 128.8, 126.2, 122.7, 118.6, 115.3, 56.2 ppm; HRMS (ESI): m/z calcd for C₁₅H₁₃N₃O: 251.10531 [*M*]⁺, 252.11314 [*M*+H]⁺, 274.09508 [*M*+Na]⁺; found: 251.10486 [*M*]⁺, 252.11195 [*M*+H]⁺, 274.09465 [*M*+Na]⁺.

DMATazB: Starting from **2a** (112 mg, 1.10 mmol, 1.00 equiv), **1c** (178 mg, 1.10 mmol, 1.00 equiv), CuSO₄·5H₂O (55 mg, 0.22 mmol, 0.20 equiv), and sodium ascorbate (87 mg, 0.44 mmol, 0.40 equiv), **DMATazB** (236 mg, 81%) was obtained as a yellow solid. M.p. 168.1–169.4 $^{\circ}\text{C}$; ¹H NMR (400 MHz, CD₂Cl₂): $\delta = 8.13$ (s, 1H), 7.90 (d, $J = 8.1\text{ Hz}$, 2H), 7.60 (d, $J = 9.0\text{ Hz}$, 2H), 7.46 (dd, $J = 8.1\text{ Hz}$, 7.4 Hz, 2H), 7.36 (t, $J = 7.4\text{ Hz}$, 1H), 6.81 (d, $J = 9.0\text{ Hz}$, 2H), 3.02 ppm (s, 6H); ¹³C NMR (100 MHz, CD₂Cl₂): $\delta = 151.3$, 148.2, 131.4, 129.4, 128.6, 127.2, 126.2, 122.3, 118.4, 112.8, 40.8 ppm; HRMS (ESI): m/z calcd for C₁₆H₁₆N₄: 264.13695 [*M*]⁺, 265.14477 [*M*+H]⁺, 287.12672 [*M*+Na]⁺; found: 264.13679 [*M*]⁺, 265.14342 [*M*+H]⁺, 287.12584 [*M*+Na]⁺.

BTazPyr: Starting from **2d** (113 mg, 1.10 mmol, 1.00 equiv), **1a** (131 mg, 1.10 mmol, 1.00 equiv), CuSO₄·5H₂O (55 mg, 0.22 mmol, 0.20 equiv), and sodium ascorbate (87 mg, 0.44 mmol, 0.40 equiv), **BTazPyr** (148 mg, 61%) was obtained as a yellow solid. M.p. 90.7–92.0 $^{\circ}\text{C}$; ¹H NMR (400 MHz, CD₂Cl₂): $\delta = 8.63$ (s, 1H), 8.60 (d, $J = 4.7\text{ Hz}$, 1H), 8.21 (d, $J = 8.0\text{ Hz}$, 1H), 7.85–7.80 (m, 3H), 7.57 (dd, $J = 8.3\text{ Hz}$, 7.6 Hz, 2H), 7.48 (t, $J = 7.6\text{ Hz}$, 1H), 7.27 ppm (dd, $J = 7.6$, 4.7 Hz, 1H); ¹³C NMR (100 MHz, CD₂Cl₂): $\delta = 150.7$, 150.2, 149.6, 137.7, 137.4, 130.4, 129.4, 123.6, 121.0, 120.7, 120.6 ppm; HRMS (ESI): m/z calcd for C₁₃H₁₀N₄: 222.09000 [*M*]⁺, 223.09782 [*M*+H]⁺, 245.07977 [*M*+Na]⁺; found: 222.08914 [*M*]⁺, 223.09716 [*M*+H]⁺, 245.07908 [*M*+Na]⁺.

AnTazPyr: Starting from **2d** (105 mg, 1.02 mmol, 1.00 equiv), **1b** (152 mg, 1.02 mmol, 1.00 equiv), CuSO₄·5H₂O (51 mg, 0.20 mmol, 0.20 equiv), and sodium ascorbate (81 mg, 0.41 mmol, 0.40 equiv), **AnTazPyr** (141 mg, 55%) was obtained as an orange solid. M.p. 127.9–128.4 $^{\circ}\text{C}$; ¹H NMR (400 MHz, CD₂Cl₂): $\delta = 8.59$ (d, $J = 4.7\text{ Hz}$, 1H), 8.53 (s, 1H), 8.20 (d, $J = 8.1\text{ Hz}$, 1H), 7.81 (dd, $J = 8.1$, 7.4 Hz,

1 H), 7.72 (d, *J* = 9.2 Hz, 2H), 7.26 (d, *J* = 7.4, 4.7 Hz, 1H), 7.06 (d, *J* = 9.2 Hz, 2H), 3.87 ppm (s, 3H); ¹³C NMR (100 MHz, CD₂Cl₂): δ = 160.6, 150.8, 150.1, 149.4, 137.4, 131.1, 123.5, 122.6, 120.8, 120.6, 115.4, 56.2 ppm; HRMS (ESI): *m/z* calcd for C₁₄H₁₂N₄O: 252.10056 [M]⁺, 253.10839 [M+H]⁺, 275.09033 [M+Na]⁺; found: 252.10027 [M]⁺, 253.10734 [M+H]⁺, 275.08946 [M+Na]⁺.

DMATazPyr: Starting from **2d** (88 mg, 0.85 mmol, 1.00 equiv), **1c** (138 mg, 0.85 mmol, 1.00 equiv), CuSO₄·5H₂O (42 mg, 0.17 mmol, 0.20 equiv), and sodium ascorbate (67 mg, 0.34 mmol, 0.40 equiv), **DMATazPyr** (121 mg, 54%) was obtained as a yellow solid. M.p. 150.7–151.5 °C; ¹H NMR (400 MHz, CD₂Cl₂): δ = 8.59 (d, *J* = 4.7 Hz, 1H), 8.48 (s, 1H), 8.19 (d, *J* = 8.1 Hz, 1H), 7.80 (dd, *J* = 8.1, 7.4 Hz, 1H), 7.62 (d, *J* = 9.4 Hz, 2H), 7.25 (d, *J* = 7.4, 4.7 Hz, 1H), 6.81 (d, *J* = 9.2 Hz, 2H), 3.02 ppm (s, 6H); ¹³C NMR (100 MHz, CD₂Cl₂): δ = 151.3, 151.0, 150.1, 149.1, 137.3, 127.1, 123.3, 122.2, 120.6, 120.5, 112.8, 40.8 ppm; HRMS (ESI): *m/z* calcd for C₁₅H₁₅N₅: 265.13220 [M]⁺, 266.14002 [M+H]⁺, 288.12197 [M+Na]⁺; found: 265.13254 [M]⁺, 266.13866 [M+H]⁺, 288.12122 [M+Na]⁺.

BTazPym: Starting from **2e** (156 mg, 1.50 mmol, 1.00 equiv), **1a** (179 mg, 1.50 mmol, 1.00 equiv), CuSO₄·5H₂O (75 mg, 0.30 mmol, 0.20 equiv), and sodium ascorbate (119 mg, 0.60 mmol, 0.40 equiv), **BTazPym** (209 mg, 62%) was obtained as a yellow solid. M.p. 150.8–154.2 °C; ¹H NMR (400 MHz, CD₂Cl₂): δ = 8.83 (d, *J* = 4.9 Hz, 2H), 8.74 (s, 1H), 7.84 (d, *J* = 8.9 Hz, 2H), 7.58 (dd, *J* = 8.9 Hz, 7.4 Hz, 2H), 7.50 (t, *J* = 7.4 Hz, 1H), 7.27 ppm (t, *J* = 4.9 Hz, 1H); ¹³C NMR (100 MHz, CD₂Cl₂): δ = 159.6, 158.1, 148.6, 137.5, 130.4, 129.6, 123.7, 121.1, 120.4 ppm; HRMS (ESI): *m/z* calcd for C₁₂H₉N₅: 223.08525 [M]⁺, 224.09307 [M+H]⁺, 246.07502 [M+Na]⁺; found: 223.08420 [M]⁺, 224.09245 [M+H]⁺, 246.07437 [M+Na]⁺.

AnTazPym: Starting from **2e** (141 mg, 1.35 mmol, 1.00 equiv), **1b** (201 mg, 1.35 mmol, 1.00 equiv), CuSO₄·5H₂O (67 mg, 0.27 mmol, 0.20 equiv), and sodium ascorbate (107 mg, 0.54 mmol, 0.40 equiv), **AnTazPym** (216 mg, 63%) was obtained as a beige solid. M.p. 162.1–163.4 °C; ¹H NMR (400 MHz, CD₂Cl₂): δ = 8.82 (d, *J* = 4.8 Hz, 2H), 8.65 (s, 1H), 7.73 (d, *J* = 9.1 Hz, 2H), 7.25 (t, *J* = 4.8 Hz, 1H), 7.07 (d, *J* = 9.1 Hz, 2H), 3.87 ppm (s, 3H); ¹³C NMR (100 MHz, CD₂Cl₂): δ = 160.7, 159.7, 158.1, 148.3, 130.8, 123.8, 122.7, 120.3, 115.4, 56.2 ppm; HRMS (ESI): *m/z* calcd for C₁₃H₁₁N₅O: 253.09581 [M]⁺, 254.10364 [M+H]⁺, 276.08558 [M+Na]⁺; found: 253.09527 [M]⁺, 254.10248 [M+H]⁺, 276.08474 [M+Na]⁺.

DMATazPym: Starting from **2e** (135 mg, 1.30 mmol, 1.00 equiv), **1c** (211 mg, 1.30 mmol, 1.00 equiv), CuSO₄·5H₂O (65 mg, 0.26 mmol, 0.20 equiv), and sodium ascorbate (103 mg, 0.52 mmol, 0.40 equiv), **DMATazPym** (234 mg, 68%) was obtained as a brown solid. M.p. 201.8–202.9 °C; ¹H NMR (400 MHz, CD₂Cl₂): δ = 8.81 (d, *J* = 4.9 Hz, 2H), 8.60 (s, 1H), 7.63 (d, *J* = 9.2 Hz, 2H), 7.24 (t, *J* = 4.9 Hz, 1H), 6.81 (d, *J* = 9.2 Hz, 2H), 3.02 ppm (s, 6H); ¹³C NMR (100 MHz, CD₂Cl₂): δ = 159.9, 158.0, 151.4, 148.0, 126.9, 123.5, 122.3, 120.2, 112.7, 40.8 ppm; HRMS (ESI): *m/z* calcd for C₁₄H₁₄N₆: 266.12745 [M]⁺, 267.13527 [M+H]⁺, 289.11722 [M+Na]⁺; found: 266.12824 [M]⁺, 267.13384 [M+H]⁺, 289.11640 [M+Na]⁺.

BTazDMA: Starting from **2c** (232 mg, 1.60 mmol, 1.00 equiv), **1a** (192 mg, 1.60 mmol, 1.00 equiv), CuSO₄·5H₂O (80 mg, 0.32 mmol, 0.20 equiv), and sodium ascorbate (127 mg, 0.64 mmol, 0.40 equiv), **BTazDMA** (173 mg, 41%) was obtained as a yellow solid after column chromatography (petroleum ether (PE)/DCM, 1%). M.p. 175.0–176.6 °C; ¹H NMR (400 MHz, CD₂Cl₂): δ = 8.11 (s, 1H), 7.81–7.74 (m, 4H), 7.56 (dd, *J* = 8.6 Hz, 7.4 Hz, 2H), 7.46 (t, *J* = 7.4 Hz,

1H), 6.80 (d, *J* = 8.9 Hz, 2H), 3.00 ppm (s, 6H); ¹³C NMR (100 MHz, CD₂Cl₂): δ = 151.3, 149.3, 137.9, 130.3, 129.0, 127.2, 120.9, 118.8, 116.7, 112.9, 40.8 ppm; HRMS (ESI): *m/z* calcd for C₁₆H₁₆N₄: 264.13695 [M]⁺, 265.14477 [M+H]⁺, 287.12672 [M+Na]⁺; found: 264.13640 [M]⁺, 265.14382 [M+H]⁺, 287.12537 [M+Na]⁺.

PyrTazDMA

The synthesis of **PyrTazDMA** was accomplished according to a published procedure.^[21] Compounds **1d** (180 mg, 1.50 mmol, 1.00 equiv), **2c** (240 mg, 1.65 mmol, 1.10 equiv), and Cu(OTf)₂ (108 mg, 0.30 mmol, 0.20 equiv) in toluene (6 mL, abs. degassed) and benzene (11 mg) were heated to reflux for 28 h. The reaction mixture was poured on H₂O and extracted with DCM. Subsequently, the combined organic layers were dried over Na₂SO₄ and concentrated under reduced pressure. The crude product was purified by column chromatography (DCM/Et₂O, 2%) to yield **PyrTazDMA** (269 mg, 68%) as a yellow solid. M.p. 154.8–156.7 °C; ¹H NMR (400 MHz, CD₂Cl₂): δ = 8.68 (s, 1H), 8.52 (d, *J* = 4.7 Hz, 1H), 8.20 (d, *J* = 8.2 Hz, 1H), 7.94 (dd, *J* = 8.2, 7.4 Hz, 1H), 7.79 (d, *J* = 9.0 Hz, 2H), 7.36 (d, *J* = 7.4, 4.7 Hz, 1H), 6.80 (d, *J* = 9.2 Hz, 2H), 3.00 ppm (s, 6H); ¹³C NMR (100 MHz, CD₂Cl₂): δ = 151.3, 150.0, 149.1, 148.9, 139.6, 127.2, 123.9, 118.8, 115.6, 114.1, 112.9, 40.8 ppm; HRMS (ESI): *m/z* calcd for C₁₅H₁₅N₅: 265.13220 [M]⁺, 266.14002 [M+H]⁺, 288.12197 [M+Na]⁺; found: 265.13243 [M]⁺, 266.13860 [M+H]⁺, 288.12115 [M+Na]⁺.

PymTazDMA

The synthesis of **PymTazDMA** was accomplished according to a published procedure.^[21] Compounds **1e** (157 mg, 1.30 mmol, 1.00 equiv), **2c** (208 mg, 1.43 mmol, 1.10 equiv), and Cu(OTf)₂ (94 mg, 0.26 mmol, 0.20 equiv) in toluene (6 mL, abs. degassed) and benzene (3 drops) were heated to reflux for 24 h. The reaction mixture was poured on H₂O and extracted with DCM. Subsequently, the combined organic layers were dried over Na₂SO₄ and concentrated under reduced pressure. The crude product was purified by column chromatography (DCM/Et₂O, 25%) to yield **PymTazDMA** (40 mg, 12%) as a yellow solid. M.p. 212 °C (dec); ¹H NMR (400 MHz, CD₂Cl₂): δ = 8.87 (d, *J* = 4.8 Hz, 2H), 8.69 (s, 1H), 7.80 (d, *J* = 9.0 Hz, 2H), 7.40 (t, *J* = 4.8 Hz, 1H), 6.81 (d, *J* = 9.0 Hz, 2H), 3.01 ppm (s, 6H); ¹³C NMR (100 MHz, CD₂Cl₂): δ = 159.8, 155.2, 151.4, 148.9, 127.3, 121.1, 118.3, 117.1, 112.9, 40.7 ppm; HRMS (ESI): *m/z* calcd for C₁₄H₁₄N₆: 266.12745 [M]⁺, 267.13527 [M+H]⁺, 289.11722 [M+Na]⁺; found: 266.12788 [M]⁺, 267.13403 [M+H]⁺, 289.11658 [M+Na]⁺.

General procedure for the Suzuki cross-coupling reactions

Arylbromide (1.00 equiv), **3** (1.00 equiv), K₂CO₃ (2.50 equiv, 2 M degassed aqueous solution), and [Pd(PPh₃)₄] (2.5 mol%) were added to degassed THF (50 mm). The mixture was heated to reflux under an argon atmosphere until full conversion (TLC, ca. 20 h). Subsequently, the solvent was evaporated and the residue was dissolved in DCM and H₂O. The aqueous phase was repeatedly extracted with DCM, the combined organic layers were dried over anhydrous Na₂SO₄, and the solvent was removed in vacuo after filtration.

DMABB: Starting from bromobenzene (**4a**; 196 mg, 1.25 mmol, 1.00 equiv), **3** (404 mg, 1.25 mmol, 1.00 equiv), K₂CO₃ (432 mg, 3.13 mmol, 2.50 equiv, 2 M aqueous solution), and [Pd(PPh₃)₄] (36 mg, 31 μmol, 2.5 mol%), **DMABB** (293 mg, 86%) was obtained as a yellow solid after column chromatography (PE/DCM, 40%). M.p. 239.8–241.7 °C; ¹H NMR (400 MHz, CD₂Cl₂): δ = 7.67–7.65 (m,

- [25] a) M. A. Sridhar, N. K. Lokanath, J. S. Prasad, K. S. Rangappa, N. V. Anil Kumar, D. G. Bhadre Gowda, *Mol. Cryst. Liq. Cryst. Sci. Technol. Sect. A* **1998**, 319, 137–146; b) R. Marsh, *Acta Crystallogr. Sect. A* **2004**, 60, 252–253.
- [26] D. Schweinfurth, R. Pattacini, S. Strobel, B. Sarkar, *Dalton Trans.* **2009**, 9291–9297.
- [27] C. Katan, P. Savel, B. M. Wong, T. Roisnel, V. Dorcet, J.-L. Fillaut, D. Jacquemin, *Phys. Chem. Chem. Phys.* **2014**, 16, 9064–9073.
- [28] D. Schweinfurth, S. Strobel, B. Sarkar, *Inorg. Chim. Acta* **2011**, 374, 253–260.
- [29] J. L. Oudar, D. S. Chemla, *J. Chem. Phys.* **1977**, 66, 2664–2668.
- [30] Bruker computer programs: APEX2, SAINT and SADABS (Bruker AXS Inc., Madison, WI, 2015).
- [31] L. Palatinus, G. Chapuis, *J. Appl. Crystallogr.* **2007**, 40, 786–790.
- [32] V. Petříček, M. Dušek, L. Palatinus, *Z. Kristallogr. - Cryst. Mater.* **2014**, 229, 345–352.
- [33] C. F. Macrae, P. R. Edgington, P. McCabe, E. Pidcock, G. P. Shields, R. Taylor, M. Towler, J. van de Streek, *J. Appl. Crystallogr.* **2006**, 39, 453–457.
- [34] S. K. Kurtz, T. T. Perry, *J. Appl. Phys.* **1968**, 39, 3798–3813.
- [35] A. Cwiklicki, K. Rehse, *Arch. Pharm.* **2004**, 337, 156–163.
- [36] K. D. Grimes, A. Gupte, C. C. Aldrich, *Synthesis* **2010**, 1441–1448.
- [37] F. Li, Y. Park, J. M. Hah, J. S. Ryu, *Bioorg. Med. Chem. Lett.* **2013**, 23, 1083–1086.
- [38] a) S. Ladouceur, A. M. Soliman, E. Zysman-Colman, *Synthesis* **2011**, 3604–3611; b) P. LaBeaume, K. Wager, D. Falcone, J. Li, V. Torchilin, C. Castro, C. Holewa, A. E. Kallmerten, G. B. Jones, *Bioorg. Med. Chem.* **2009**, 17, 6292–6300.
- [39] R. Anémian, D. C. Cupertino, P. R. Mackie, S. G. Yeates, *Tetrahedron Lett.* **2005**, 46, 6717–6721.
- [40] Gaussian 09, Revision D.01, M. J. Frisch, G. W. Trucks, H. B. Schlegel, G. E. Scuseria, M. A. Robb, J. R. Cheeseman, G. Scalmani, V. Barone, B. Menucci, G. A. Petersson, H. Nakatsuji, M. Caricato, X. Li, H. P. Hratchian, A. F. Izmaylov, J. Bloino, G. Zheng, J. L. Sonnenberg, M. Hada, M. Ehara, K. Toyota, R. Fukuda, J. Hasegawa, M. Ishida, T. Nakajima, Y. Honda, O. Kitao, H. Nakai, T. Vreven, J. A. Montgomery Jr., J. E. Peralta, F. Ogliaro, M. J. Bearpark, J. Heyd, E. N. Brothers, K. N. Kudin, V. N. Staroverov, R. Kobayashi, J. Normand, K. Raghavachari, A. P. Rendell, J. C. Burant, S. S. Iyengar, J. Tomasi, M. Cossi, N. Rega, N. J. Millam, M. Klene, J. E. Knox, J. B. Cross, V. Bakken, C. Adamo, J. Jaramillo, R. Gomperts, R. E. Stratmann, O. Yazyev, A. J. Austin, R. Cammi, C. Pomelli, J. W. Ochterski, R. L. Martin, K. Morokuma, V. G. Zakrzewski, G. A. Voth, P. Salvador, J. J. Dannenberg, S. Dapprich, A. D. Daniels, Ö. Farkas, J. B. Foresman, J. V. Ortiz, J. Cioslowski, D. J. Fox, Gaussian, Inc., Wallingford, CT, USA, **2009**.
- [41] a) C. Lee, W. Yang, R. G. Parr, *Phys. Rev. B* **1988**, 37, 785–789; b) A. D. Becke, *J. Chem. Phys.* **1993**, 98, 5648–5652.
- [42] R. Krishnan, J. S. Binkley, R. Seeger, J. A. Pople, *J. Chem. Phys.* **1980**, 72, 650–654.
- [43] R. Dennington, T. Keith, J. Millam, Semichem, Inc., Shawnee Mission, KS, **2009**.

Received: July 25, 2016

Published online on November 15, 2016

2.8. Manuscript #8

Ethyne-linked push-pull chromophores: implications of crystal structure and molecular electronics on the quadric nonlinear activity

Paul Kautny, Helene Kriegner, Dorian Bader, Michal Dušek, Georg A. Reider, Johannes Fröhlich, Berthold Stöger

submitted for publication

Ethyne-linked push-pull chromophores: Implications of crystal structure and molecular electronics on the quadric nonlinear activity

Paul Kautny,^{†,} Helene Kriegner,[†] Dorian Bader,[†] Michal Dušek,[‡] Georg A. Reider,[§] Johannes Fröhlich,[†] Berthold Stöger[¶]*

[†]Institute of Applied Synthetic Chemistry, TU Wien, Getreidemarkt 9/163, A-1060 Vienna, Austria

[‡]Institute of Physics of the Czech Academy of Sciences, Na Slovance 2, 18221 Prague 8, Czech Republic

[§]Photonics Institute, TU Wien, Gußhausstraße 27-29, A-1040 Vienna, Austria

[¶]X-Ray Centre, TU Wien, Getreidemarkt 9, A-1060 Vienna, Austria

Three ethyne-linked push-pull materials consisting of a dimethylaniline donor and acceptors of increasing electron withdrawing strength were prepared as nonlinear optical chromophores. While all derivatives exhibit non-centrosymmetric crystallization behavior, one compound features a remarkable packing with $Z' = 16$ molecules in the asymmetric unit forming two interpenetrating subsystems. Inspection of the nonlinear optical activity of single crystalline powders revealed an extraordinarily efficient second harmonic generation of one of the materials

with a 1200 fold increased second harmonic response compared to potassium dihydrogen phosphate (KDP). The second harmonic generation efficiency of the materials under investigation has been related to both the intrinsic molecular properties, as well as the alignment of the individual chromophores within the crystal packing, highlighting the importance of a multidisciplinary approach to understand the properties of nonlinear optical materials.

INTRODUCTION

π -conjugated organic donor-acceptor materials have been extensively investigated in the last couple of years due to manifold technologically relevant applications. Various push-pull derivatives consisting of an electron rich (donor) and an electron withdrawing (acceptor) subunit have been prepared for organic photovoltaics (OPVs),¹ nonlinear optical (NLO) materials,² imaging³ and organic light emitting diodes (OLEDs)⁴ to name a few. Nonlinear optical materials are of particular importance for the telecommunication technology and quantum electronics. Nonlinear effects result in various phenomena, such as second harmonic generation (SHG), optical three-wave mixing, parametric amplification, the electro-optic effect and downconversion.⁵ The donor-acceptor architecture of bipolar organic materials provides the potential for a high macroscopic second-order susceptibility due to the high polarizability of the delocalized π -electrons on the molecular scale.^{2e,6} Beside the molecular properties, the macroscopic SHG of organic crystals is dependent on the condition that crystallization occurs in one of the non-centrosymmetric crystal classes (except 432).⁷ Unfortunately, the strong dipole-dipole interaction between single bipolar molecules often leads to undesired antiparallel packing resulting in the occurrence of an inversion center and thus centrosymmetric crystallization or at least in almost complete cancellation of the individual polarization.⁸

Recently, we reported a set of 1,2,3-triazole and benzene-linked donor-acceptor materials and found significant intramolecular charge transfer upon photoexcitation in this class of compounds. Furthermore, we investigated the NLO properties of selected non-centrosymmetric crystalline powders of these materials and observed high SHG efficiencies up to 80 times the value of KDP.⁹ In this work we present a related series of three push-pull materials based on an *N,N*-dimethylaniline donor and different acceptors with increasing electron withdrawing properties (benzene<pyridine<pyrimidine) connected by an ethyne linker. All three compounds exhibited non-centrosymmetric crystallization and were probed for NLO activity yielding an extraordinarily high SHG efficiency of one of the derivatives. This result was subsequently related to the molecular properties of the materials as well as the exact spatial alignment of the molecules within the crystals under investigation. In addition, one of the materials featured an intriguing crystal structure with a very high Z' (16 molecules in the asymmetric unit), which is made up of two interpenetrating substructures.

EXPERIMENTAL SECTION

X-ray structure determination. Crystals of the title molecules were selected under a polarizing microscope, embedded in perfluorinated oil and attached to Kapton[®] micromounts. Data of **2** and **3** were collected at 100 K in a dry stream of nitrogen on a Bruker KAPPA APEX II CCD diffractometer system¹⁰ using graphite monochromatized MoK_α radiation. Data reduction was performed with SAINT-Plus¹⁰ and corrections for absorption effects were applied with SADABS.¹⁰ Crystals of **1** featured intense smearing of reflections. To minimize smearing, data of a tiny plate (0.02×0.10 mm) of **1** were collected at 95 K on a four-circle SuperNova diffractometer by Rigaku Oxford Diffraction using CuK_α radiation from a microfocus X-ray tube collimated by mirrors. Owing to very weak diffraction intensities, a full sphere of reciprocal

space was collected up to $d=0.9 \text{ \AA}$ with a long exposition time of 100 s/° . Moreover, data quality was hampered by an intense diffuse background caused by disorder and arcing of reflections at higher diffraction angles owing to prominent mosaicity. Data reduction and absorption correction was performed using the CrysAlis¹¹ 38.43 software package.

All three structures were solved using the dual-space method implemented in SHELXT¹² and refined with JANA2006¹³ against F^2 . The absolute structures were not determined owing to a lack of resonant scatterers. The models of **2** and **3** were refined with routine methods. The structure of **1** possesses pseudo-orthorhombic metrics, but a structure solution was only possible in the monoclinic Pc space group. An attempt to model the crystal as a twin by pseudo-merohedry [reflection at (100)] did not significantly improve residuals. 16 independent molecules were identified in the SHELXT output. In the difference electron density after the first refinement cycles, for each molecule a different minor orientation [related by reflection at (010)] was observed. A model of these minor orientations was generated from the coordinates of the major orientation and every molecule was refined as disordered. One of the molecules even had to be refined as disordered with three positions. Since the minor positions in most cases only made up ca. 20%, the geometry was improved by distance and angle restraints. Nevertheless, such refinements did not converge owing to bad parameter-to-data ratios. Therefore, the geometries of the minor positions were fixed and only the orientation of the molecules refined. To achieve reasonable geometries, the benzene rings and ethyne fragments of the minor positions were adopted from the structural data of **2**. For each minor position only one atomic displacement parameter (ADP) was refined, which was applied to all atoms. If the thus obtained ADPs were nevertheless unreasonable, they were constrained to be equivalent to those of the major position [with respect to a reflection at (010)].

Details on crystal data and structure refinement are compiled in Table 1. Molecular graphics were drawn with Mercury v. 3.7.¹⁴

Table 1. Details on crystal data and structure refinement.

	1	2	3
formula	C ₁₆ H ₁₅ N	C ₁₅ H ₁₄ N ₂	C ₁₄ H ₁₃ N ₃
<i>M</i> (g mol ⁻¹)	221.3	222.3	223.3
crystal system	monoclinic	orthorhombic	orthorhombic
space group	<i>Pc</i>	<i>Pna2</i> ₁	<i>Pna2</i> ₁
<i>a</i> (Å)	27.1667(17)	16.664(3)	11.8904(15)
<i>b</i> (Å)	19.1320(11)	10.359(4)	9.005(2)
<i>c</i> (Å)	19.2831(9)	7.460(6)	11.0057(19)
β (°)	90.196(5)	90	90
<i>V</i> (Å ³)	10022.4(10)	1287.7(12)	1178.5(4)
<i>Z</i> , <i>Z'</i>	32, 16	4, 1	4, 1
<i>D</i> _{calc} (g cm ⁻³)	1.1733	1.1467	1.2585
radiation	CuK α	MoK α	MoK α
μ (mm ⁻¹)	0.518	0.068	0.077
<i>F</i> ₀₀₀	3776	472	472
(sin θ/λ) _{max} (Å ⁻¹)	0.627	0.749	0.759
reflns	59443	8828	13757
reflns unique	25594	3423	3959
reflns observed [<i>I</i> > 3 σ (<i>I</i>)]	7536	2692	3559

R_{int}	0.1138	0.0347	0.0420
parameters	2033	154	154
R_{obs}	0.0763	0.0454	0.0448
wR_{all}	0.2086	0.1001	0.1174
S	1.24	1.80	1.80
$\Delta\rho_{\text{min}}$ ($\text{e } \text{\AA}^{-3}$)	-0.46	-0.20	-0.23
$\Delta\rho_{\text{max}}$ ($\text{e } \text{\AA}^{-3}$)	0.49	0.29	0.29

SHG measurements. The second order nonlinear optical properties of the materials were studied with second harmonic measurements from powder samples. Powdered samples of the materials with a grain size of less than 1 μm were prepared with a mortar. Using this technique a relative measurement of the nonlinear optical coefficients is possible since the SH efficiency scales quadratically with the nonlinear coefficient provided that the particle size is significantly less than the so-called nonlinear coherence length (which is more than 10 μm in all practical cases).¹⁵ The powders were positioned between two microscope slides and irradiated with the output of an ultrafast Yb:KGW-Laser (High Q Lasers and Light Conversion respectively) with a pulse repetition rate of 3 kHz, a pulse duration of 300 femtoseconds and an average power of 400 mW operating at a center wavelength of 1033 nm. The laser beam was directed onto the sample without focusing, resulting in an exposed sample area of about 1 cm^2 and an optical peak power of about 440 MW/ cm^2 , well below typical values of the damage threshold for dielectrics. The diffusely reflected SH-radiation was collected with a NA = 0.1 lens, separated from fundamental radiation with a color filter, and spectrally analyzed with a 0.25 m grating monochromator and a photomultiplier detector. After the measurement, all samples were carefully checked for the absence of damage or thermal modification. For quantification of the SHG yields (Z)-4-(2-

(methylthio)-1-propenyl)-1-phenyl-1,2,3-triazole¹⁶ (SHG-yield = SHG-yield (KDP) x 2) was used as a reference material.

Synthesis. All reagents and solvents were purchased from commercial suppliers and used without further purification. 4-Ethynyl-*N,N*-dimethylbenzenamine was prepared analogously to published procedures.¹⁷ Anhydrous solvents were prepared by filtration through drying columns. Column chromatography was performed on silica 60 (Merck, 40-63 μm). NMR spectra were recorded on a Bruker Avance DRX-400 Spectrometer. An Agilent 6230 LC TOFMS mass spectrometer equipped with an Agilent Dual AJS ESI-Source was used for HRMS. UV/VIS absorption and fluorescence emission spectra in solution (5 μM) were recorded with a Perkin Elmer Lambda 750 spectrometer and an Edinburgh FLS920, respectively.

***N,N*-Dimethyl-4-(2-phenylethynyl)benzenamine (1).** 4-Bromo-*N,N*-dimethylbenzenamine (1.00 g, 5.00 mmol, 1.00 eq.) and ethynylbenzene (0.51 g, 5.00 mmol, 1.00 eq.) were dissolved in degassed Et₃N (15 ml) in a three-necked flask under argon atmosphere. Pd(PPh₃)₄ (115 mg, 0.1 mmol, 0.02 eq.) and CuI (38 mg, 0.2 mmol, 0.04 eq.) were added and the reaction mixture was heated to reflux for 3 h until full conversion (TLC). Subsequently, the reaction mixture was poured on 1N HCl (100 ml) and repeatedly extracted with CH₂Cl₂. The combined organic layers were dried over anhydrous Na₂SO₄ and concentrated under reduced pressure. Purification of the crude product was accomplished by column chromatography (light petrol/CH₂Cl₂ = 85/15) yielding **1** as beige solid (0.17 g, 0.8 mmol, 16%). Single crystals of **1** were obtained by crystallization from boiling EtOH. ¹H-NMR (400 MHz, CD₂Cl₂): δ = 7.48 (dd, J =7.8, 1.8 Hz, 2H), 7.40-7.27 (m, 5H), 6.67 (d, J =8.9 Hz, 2H), 2.99 (s, 6H) ppm. ¹³C-NMR (100 MHz, CD₂Cl₂): δ = 150.8, 133.1, 131.6, 128.9, 128.0, 124.7, 112.3, 110.1, 91.1, 87.6, 40.5 ppm. HRMS (ESI): m/z calculated for C₁₆H₁₅N: 222.1277 [M+H]⁺; found: 222.1281 [M+H]⁺.

***N,N*-Dimethyl-4-[2-(2-pyridinyl)ethynyl]benzenamine (2).** A three-necked flask was charged with 4-ethynyl-*N,N*-dimethylbenzenamine (284 mg, 1.96 mmol, 1.00 eq.), Pd(PPh₃)₂Cl₂ (28 mg, 0.04 mmol, 0.02 eq.) and CuI (10 mg, 0.05 mmol, 0.03 eq.) and flushed with argon. Subsequently, degassed DIPA (50 ml) and 2-bromopyridine (640 mg, 4.05 mmol, 2.07 eq.) were added and the reaction mixture was heated to reflux for 3 h until full conversion (TLC). After cooling to room temperature the reaction mixture was poured on a saturated aqueous NH₄Cl solution and repeatedly extracted with CH₂Cl₂. The combined organic layers were dried over anhydrous Na₂SO₄ and concentrated under reduced pressure. Purification of the crude product was accomplished by column chromatography (light petrol/ethyl acetate = 70/30 → 50/50) yielding **2** as beige solid (160 mg, 0.72 mmol, 37%). Single crystals of **2** were obtained by crystallization from a mixture of boiling *n*-hexane and EtOH. ¹H-NMR (400 MHz, CD₂Cl₂): δ= 8.55 (ddd, *J*=4.7, 1.6, 0.8 Hz, 1H), 7.65 (ddd, *J*=7.7, 7.7, 1.8 Hz, 1H), 7.47-7.42 (m, 3H), 7.19 (ddd, *J*=7.4, 4.7, 1.2 Hz, 1H), 6.68 (d, *J*=9.0 Hz, 2H), 3.00 (s, 6H) ppm. ¹³C-NMR (100 MHz, CD₂Cl₂): δ= 151.2, 150.4, 144.7, 136.5, 133.6, 127.2, 122.5, 112.2, 108.8, 91.2, 87.7, 40.5 ppm. HRMS (ESI): *m/z* calculated for C₁₅H₁₄N₂: 223.1230 [M+H]⁺; found: 223.1241 [M+H]⁺.

***N,N*-Dimethyl-4-[2-(2-pyrimidinyl)ethynyl]benzenamine (3).** 2-Bromopyrimidine (525 mg, 3.30 mmol, 1.50 eq.) and 4-ethynyl-*N,N*-dimethylbenzenamine (319 mg, 2.20 mmol, 1.00 eq.) were dissolved in degassed Et₃N (5.5 ml) in a three-necked flask under argon atmosphere. Pd(PPh₃)₄ (127 mg, 0.11 mmol, 0.05 eq.) and CuI (61 mg, 0.32 mmol, 0.10 eq.) were added and the reaction mixture was heated to reflux for 2.5 h until full conversion (TLC). Subsequently, the reaction mixture was poured on 1N HCl (50 ml) and repeatedly extracted with CH₂Cl₂. The combined organic layers were dried over anhydrous Na₂SO₄ and concentrated under reduced pressure. Purification of the crude product was accomplished by column chromatography

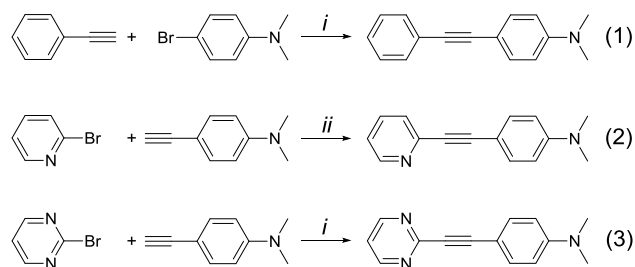
(CH₂Cl₂/Et₂O = 99/1) yielding **3** as orange solid (287 mg, 1.29 mmol, 58%). Single crystals of **3** were obtained by crystallization from boiling EtOH. ¹H-NMR (400 MHz, CD₂Cl₂): δ= 8.67 (d, *J*=4.9 Hz, 2H), 7.50 (d, *J*=9.0 Hz, 2H), 7.16 (t, *J*=4.9 Hz, 1H), 6.68 (d, *J*=9.0 Hz, 2H), 3.01 (s, 6H) ppm. ¹³C-NMR (100 MHz, CD₂Cl₂): δ= 157.7, 154.4, 151.7, 134.4, 119.5, 112.2, 107.7, 90.3, 87.8, 40.4 ppm. HRMS (ESI): *m/z* calculated for C₁₄H₁₃N₃: 224.1182 [M+H]⁺; found: 224.1193 [M+H]⁺.

Theoretical calculations. DFT calculations were performed using the Gaussian 09 package revision D.01.¹⁸ applying the long range corrected CAM-B3LYP functional¹⁹ in combination with Pople basis sets 6-311++G(d,p)²⁰ in order to have polarized and diffuse functions included. Geometry optimizations were performed in gas phase. First-order hyperpolarizability tensors were visualized using a method adapted from Tuer *et al.*²¹. The graphical representations were rendered using the POV-Ray software package.²²

RESULTS AND DISCUSSION

Synthesis

Based on our previous results on small molecules with high NLO activity,⁹ the design of the materials under investigation was based on a donor-acceptor architecture. Dimethylaniline was chosen as electron donating unit and connected to the acceptor unit by an ethyne linker. Compounds **1**, **2** and **3** were synthesized starting from the corresponding terminal alkynes and brominated precursors applying standard conditions for Sonogashira cross-coupling reactions (Scheme 1). To investigate the influence of an increased donor-acceptor interaction on the molecular properties, the strength of the electron accepting unit was continuously increased from benzene (**1**) to pyridine (**2**) and pyrimidine (**3**), while the electron donating unit remained unchanged (dimethylaniline).



Scheme 1. Synthesis of compounds **1-3**. *i*: Pd(PPh₃)₄, CuI, Et₃N; *ii*: Pd(PPh₃)₂Cl₂, CuI, DIPA.

Photophysical properties

UV/Vis absorption and photoluminescent emission spectra of the materials in various solvents were recorded to explore the impact of the altered acceptor strength on the photophysical properties. Peak maxima and the onsets of the absorption spectra of all materials are relatively independent of the polarity of the solvent as exemplarily depicted for **2** in Figure 1. While one single broad absorption peak is observed in most solvents, a finer structure can be found in nonpolar cyclohexane. In contrast to the absorption the emission of the materials displayed a strong dependency on the solvent environment and a distinct solvatochromic behavior was observed (Figure 1), thus indicating the presence of a relatively polar excited state due to intramolecular charge transfer upon photoexcitation.²³ In analogy to the absorption a vibronically resolved emission was found for all materials in cyclohexane. In contrast broad emission bands, typical for charge transfer emission, were observed in all other solvents.

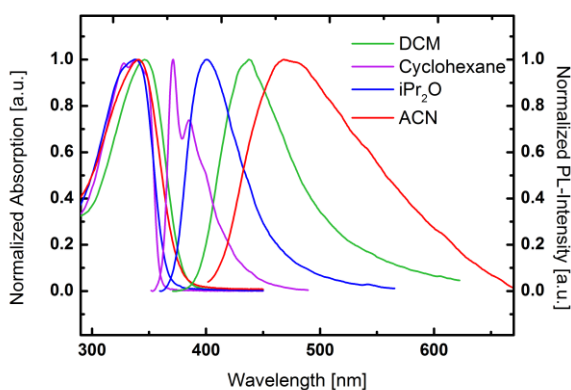


Figure 1. UV/Vis absorption and photoluminescent emission spectra of **2** in various solvents (DCM=dichloromethane, ACN=acetonitrile).

With increasing acceptor strength a distinct redshift of the absorption maxima could be found. While **1** exhibits a peak maximum at 332 nm in dichloromethane the absorption bands are shifted to 346 nm and 359 nm for **2** and **3**, respectively (Figure 2, left). Along with this finding go likewise red-shifted absorption onsets at 360 nm (**1**), 378 nm (**2**) and 392 nm (**3**) and thus reduced optical band gaps as a result of the enhanced donor-acceptor interactions. Key photophysical properties of the materials in DCM are summarized in Table 2. Compared to the corresponding benzene-linked dimethylaniline-benzene-acceptor derivatives⁹ the onset values are shifted to slightly lower wavelengths indicating a decreased degree of conjugation as a result of the substitution of the benzene unit by one acetylene fragment.

Table 2. Photophysical properties of the materials under investigation in DCM (5 μ M).

	λ_{abs} [nm]	ϵ [$M^{-1} cm^{-1}$]	ΔE_{opt} [eV]	λ_{em} [nm]
1	332	26200	3.44	390
2	346	30500	3.28	426

All materials featured red-shifted emission compared to their absorption maxima. Notably, the Stokes shift of all materials increased significantly with increasing solvent polarity, as typically observed for charge transfer transitions.²³ To quantify the intramolecular charge transfer properties the photophysical behavior of the materials was analyzed by application of the Lippert-Mataga equation²⁴

$$(v_a - v_f) = \frac{2(\mu_e - \mu_g)^2}{hca^3} \Delta f + \text{const.}$$

in which $(v_a - v_f)$ describes the Stokes shift, h the Planck constant, c the speed of light and a the solvent cavity (Onsager) radius. μ_g and μ_e correspond to the ground state dipole moment and excited state dipole moment, respectively. The orientation polarizability Δf as a measure of the solvent polarity is defined by the equation

$$\Delta f = \frac{\varepsilon - 1}{2\varepsilon + 1} - \frac{n^2 - 1}{2n^2 + 1}$$

in which ε is the dielectric constant and n is the refractive index of the solvent. According to the Lippert-Mataga equation the slope of the linear correlation between the Stokes shift and Δf is dependent on $(\Delta\mu)^2$ and can thus be regarded as a measure for the degree of the intramolecular charge transfer during the photoexcitation process. Indeed all materials obey the predicted linear correlation (Figure 2, right) and exhibit high slope values indicative for a charge transfer transition. The nearly identical molecular weight of the investigated materials allows to directly compare the slope values as a measure for $\Delta\mu$. As expected, the slopes increase with growing acceptor strength due to enhanced donor-acceptor interactions. While the increase is moderate from **1** (17791 cm⁻¹) to **2** (21176 cm⁻¹), particularly **3** (31898 cm⁻¹) features a high slope value indicative for a strong intramolecular charge transfer process. Notably, the increased $\Delta\mu$ also

suggests a higher SH efficiency of the materials with stronger electron acceptors according to the two-state model.²⁵ Within the limits of accuracy of the method these values are – corrected for the Onsager radius – in the same range as those of the corresponding benzene linked donor-acceptor materials, whereat **3** features slightly increased charge transfer compared to its benzene derivative.⁹ Hence, compared to benzene the ethyne linker slightly decreases the overall conjugation in the ground state as deduced from the absorption measurements but allows for pronounced charge transfer upon photoexcitation.

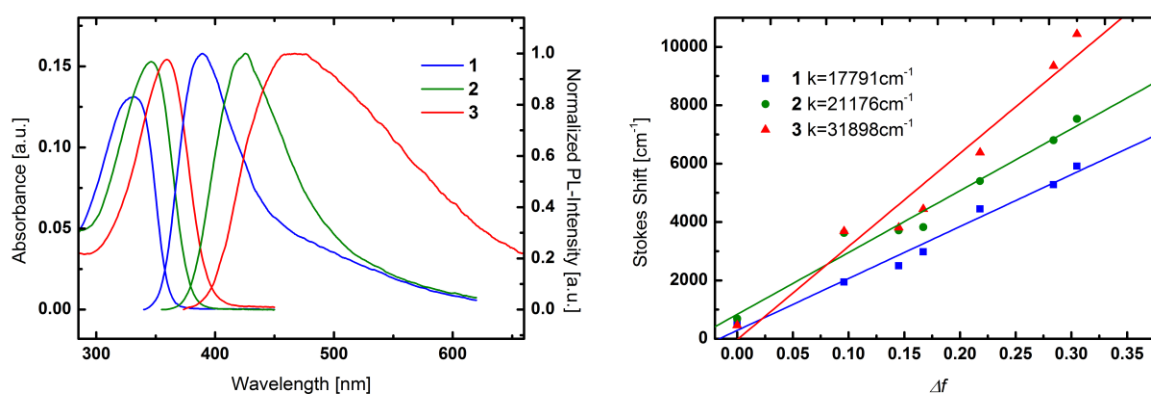


Figure 2. left: UV/Vis absorption and photoluminescent emission spectra of **1**, **2** and **3** in dichloromethane. right: Lippert-Mataga plots of **1**, **2** and **3**.

Crystallography

Overview. In the crystalline state, all three title molecules are essentially flat (Figure 3). The angles between the least squares (LS) planes of the aromatic rings are 4.38(7)^o (**2**) and 5.08(6)^o (**3**). The dimethylamine group is virtually coplanar with the connected benzene ring [largest distance of C atom to LS plane of benzene: 0.1234(14) Å (**2**) and 0.1391(14) Å (**3**)]. The geometry of **1** is qualitatively the same, but values are not given here owing to a lack of high-

quality structural data. The axis along the $\text{—C}\equiv\text{C—}$ triple bond will henceforth be called the molecular axis, the plane of the aromatic rings the molecular plane.

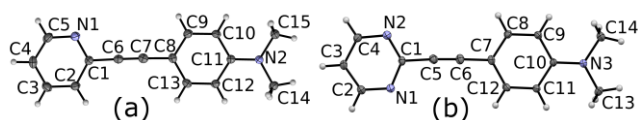


Figure 3. Molecular structures of (a) **2** and (b) **3**. C (gray) and N (blue) atoms are represented by ellipsoids drawn at the 50% probability levels; H atoms by white spheres of arbitrary radius.

2 and **3** both crystallize in the $Pna2_1$ space group with $Z' = 1$ molecule on the general position. The structures can therefore be considered as isopointal,²⁶ but the packing in both structures is unrelated. **1** crystallizes with a remarkable packing of $Z' = 16$ molecules in the asymmetric unit. In many cases, N can substitute for C—H in aromatic rings without a change of the structure type. Here, short intermolecular C—H \cdots N contacts in **2** and **3** induce different structure types. Indeed, **3** [$V/Z = 294.6(1) \text{ \AA}^3$] packs tighter than **2** [$V/Z = 321.9(3) \text{ \AA}^3$]. Interestingly, although short C—H \cdots N contacts cannot exist in **1** [$V/Z = 313.2(3) \text{ \AA}^3$] the peculiar packing leads to a density between those of **2** and **3**.

Crystal structures of 2 and 3. Even though they cannot be considered as being of the same structure type, the crystal structures of **2** and **3** share some commonalities. Besides equivalent symmetry and Z' , both are made up of layers normal to the polar direction [001] (Figure 4). The layers feature $p1n1$ symmetry²⁷ and adjacent layers are related by the n and 2_1 operations of the $Pna2_1$ space group.

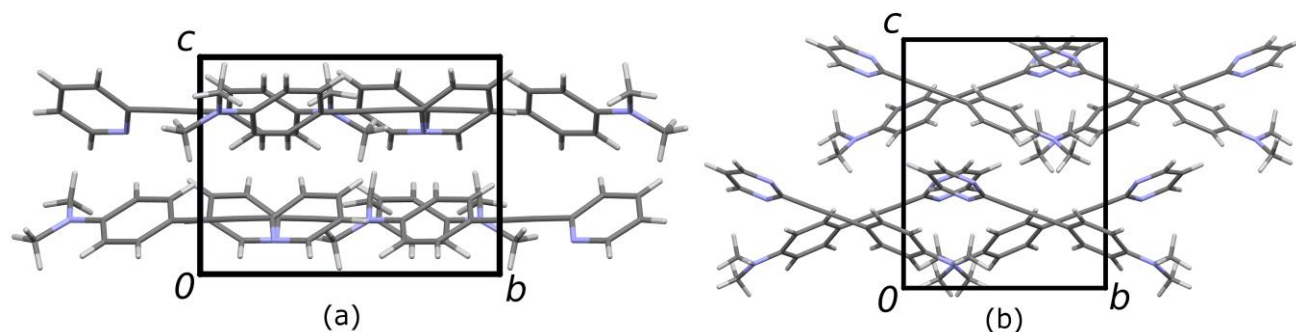


Figure 4. Packing of (a) **2** and (b) **3** viewed down [100] showing distinct layers parallel to (001).

Crystallo-chemically, the layers are unrelated, which significantly affects the SHG efficiency (see below). In **2** [Figure 4 (a)], the molecular axis is virtually parallel to the layer plane. In consequence, the layers are narrow [layer width $c/2 = 3.730(3)$ Å]. Inside these layers the molecules contact *via* a short methyl-H to pyridine-N contacts [C15—H \cdots N1: 2.720 Å, Figure 5 (a)], making this arrangement impossible for **1**.

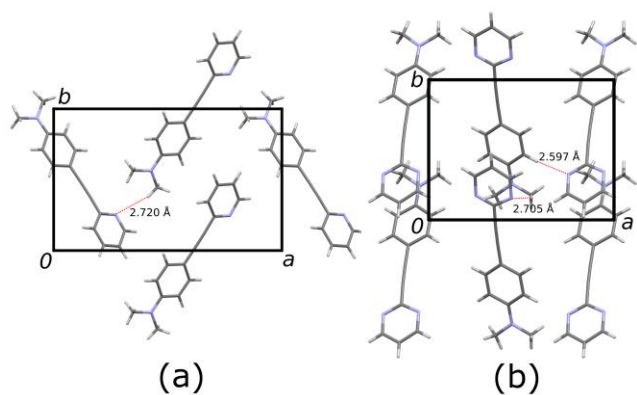


Figure 5. The layers of Figure 4 projected on the layer plane (001).

The **3** molecules, on the other hand, are distinctly inclined with respect to the plane of the layers [Figure 4 (b)], which are in consequence distinctly wider [layer width $c/2 = 5.5029(9)$ Å]. The molecules connect *via* a short benzene-H to pyrimidine-N contacts [C9—H \cdots N1: 2.597 Å, Figure 5 (b)]. The N2 atom of the pyrimidine is located above (with respect to [001]) a methyl

group [C14—H···N1: 2.705 Å]. This short contact probably prohibits **2** from crystallizing with this structure type.

Crystal structure of 1. **1** crystallizes in the *Pc* space group with pseudo-orthorhombic metrics. The asymmetric unit contains $Z' = 16$ molecules. Moreover, each molecule can appear in two orientations related by reflection at (010). Since there are 16 molecules, each containing 16 C atoms, a hexadecimal naming scheme was used. The molecules are named with a hexadecimal digit 0-*f*, which makes up the second place of each atom name. The third place of C-atom names is likewise a hexadecimal digit, which describes the atom in the structure according to the scheme in Figure 6. Minor positions are described by prime (') characters appended to the atom names.

The crystal structure features pseudo-orthorhombic metrics [$\beta = 90.196(5)^\circ$]. For simplicity, planes and directions will be given as if the metrics were perfectly orthorhombic.

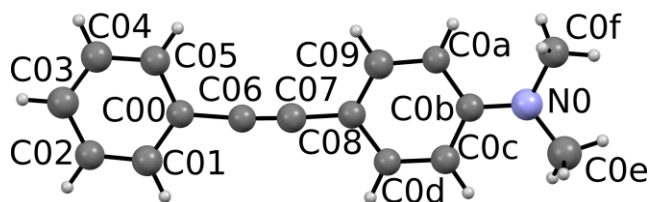


Figure 6. Molecular structure of **1** (molecule 0).

The structure is made up of two kinds of molecules. For twelve (4-*f*) the molecular axis is approximately aligned in [010] direction. These molecules form a three-dimensional packing where molecules contact *via* the benzene and dimethylaniline units. The “thin” ethyne parts of the molecules leave place for distinct channels extending along [100] in which the remaining four (0-3) molecules are located.

Thus, the structure is an interpenetration of two subsystems. To describe the complex packing and explain the disorder it is crucial to understand pseudo-symmetry and interactions of these subsystems. One might consider molecules 4-*f* the host network and 0-3 the guest molecules. Nevertheless, a clearer presentation of pseudo-symmetry is achieved by regarding the framework of the 0-3 molecules, which will be done first. These considerations will also rule out the existence of missed symmetry, *i.e.* prove the high Z' . Only the major (ca. 80%) orientations will be used in these considerations.

Looking at molecules 0-3, two distinct wavy layers extending in the (001) plane can be identified, which will be called *L1* and *L2* (red lines in Figure 7). In these layers the 0-3 molecules are arranged in rods extending along [100], connected by dimethylamine \leftrightarrow benzene contacts. The rods are spaced in [010] direction by a full lattice translation. They are connected by the 4-*f* molecules with the molecular axis in [010] direction. These 4-*f* molecules can be classified into three kinds, *viz.* those connecting benzene rings (4-7), those connecting the ethyne bridges (8-*b*) and those connecting the dimethylamine groups (*c-f*).

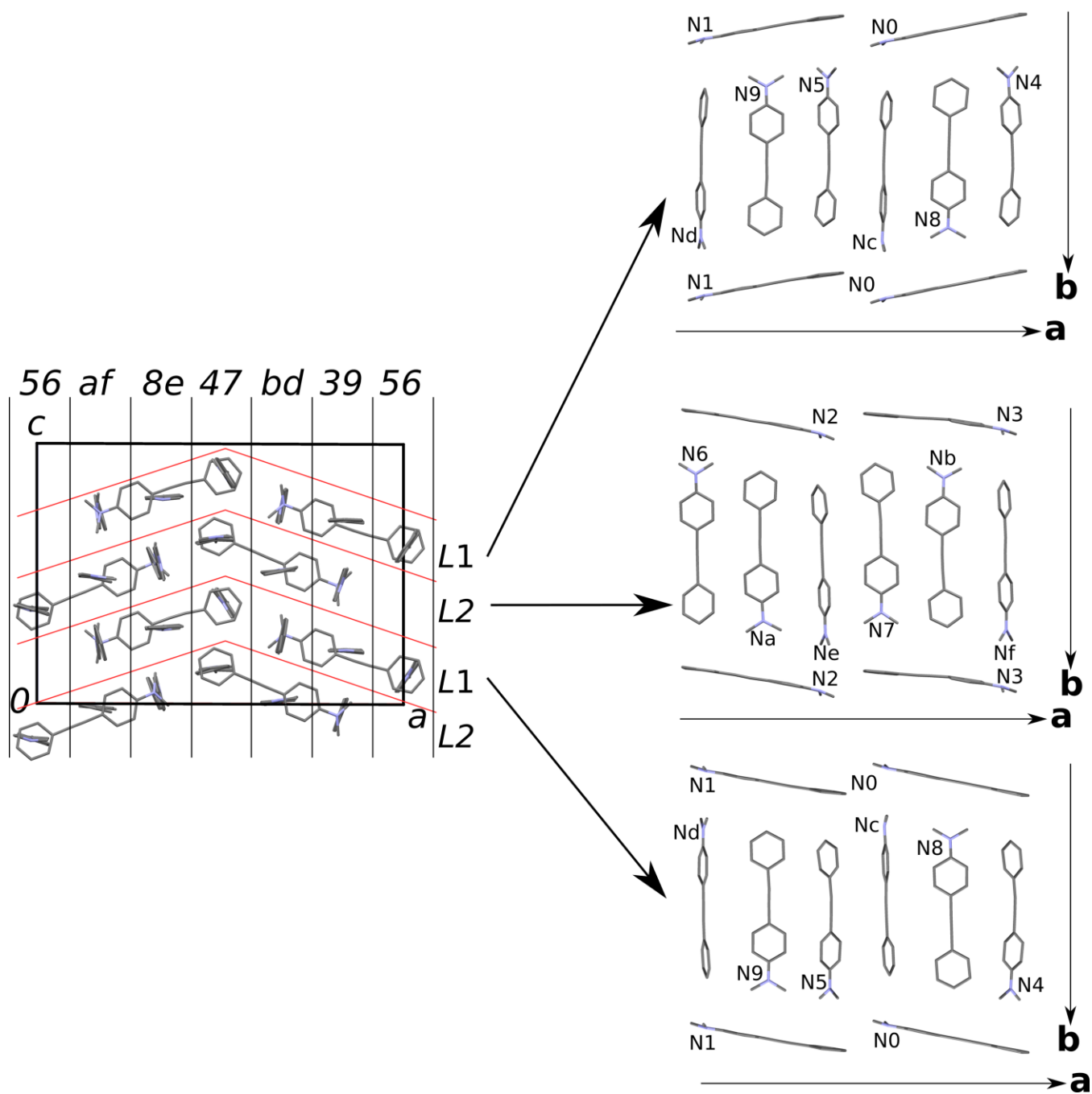


Figure 7. Left: packing of **1** viewed down [010]. Layers parallel to (001) and (100) are indicated using black and red lines. Right: three adjacent *L1* and *L2* layers projected on the layer plane (001).

The two rods are each made up of two molecules ($L1$: 0, 1 and $L2$: 2, 3), which are related by a pseudo- $a_{[001]}$ glide reflection. The origin of the model was chosen [no restriction in the (010) plane] such that the pseudo- $a_{[001]}$ glide planes of $L1$ and $L2$ are approximately at $z = 0$ and $z = \frac{1}{2}$. To assess the degree of pseudo symmetry, the appropriate $a_{[001]}$ operation was applied to each layer. An overlay of the original and transformed layers is given in Figure 8.

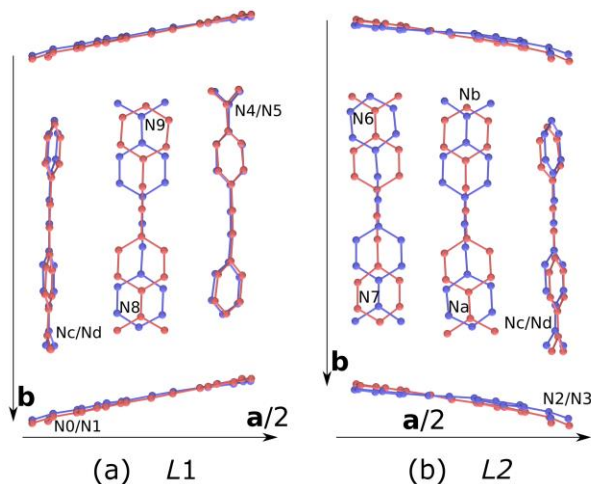


Figure 8. Overlay of the (a) $L1$ and (b) $L2$ layers in **1** with their image by $a_{[001]}$ pseudo-symmetry. The original and transformed parts are drawn in red and blue, respectively.

Indeed, the 0-3 molecules match virtually perfectly and with respect to these molecules, the layers possess $p11a$ layer symmetry.²⁷ In the $L1$ layer the 4/5 and c/d pairs of molecules likewise are in agreement with the $p11a$ symmetry. But the 8/9 molecules feature opposite orientation with respect to the molecular axis. If the orientation of the molecules with respect to the molecular axis is symbolized by \uparrow and \downarrow signs, the $L1$ layer is described by the period 6 sequence $\dots\downarrow\uparrow\uparrow\downarrow\downarrow\uparrow\dots$

The $L2$ layer is described by $\dots\downarrow\uparrow\uparrow\downarrow\uparrow\dots$. Thus, only the ef molecules are oriented in the same direction, whereas the pairs 6/7 and a/b break the $p11a$ symmetry [Figure 8 (b)].

In consequence, $L1$ and $L2$ indeed only possess $p1$ layer symmetry with eight independent molecules each. Moreover, the orientation sequences of $L1$ and $L2$ differ and both layers cannot be equivalent. $Z' = 16$ is therefore realized without a doubt.

The difference in molecule orientation of $L1$ and $L2$ is due to a single pair of molecules $N5/N7$. Disregarding this pair, $L1$ and $L2$ are related by pseudo-symmetry (Figure 9). If the minor differences of $L1$ and $L2$ are disregarded, $L1$ and $L2$ layers are alternately related by 2_1 operations with an axis parallel to $[010]$ and $\bar{1}$ inversions. Note that the combination of the 2_1 and $\bar{1}$ pseudo-symmetries results in the c glide reflection of the actual Pc crystal symmetry. Thus, there are two kinds of $L1 \leftrightarrow L2$ contacts. In the first, the 0-3 molecules are tilted in the same direction with respect to $[010]$, in the second in opposite direction (Figure 7, right).

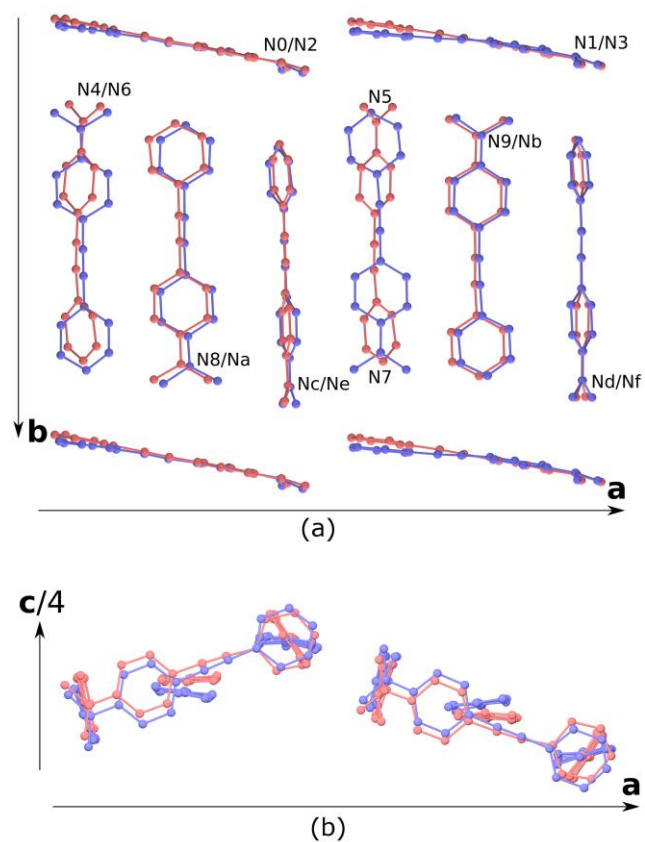


Figure 9. Overlay of the *L1* (red) and *L2* (blue) layers in **1** after application of a 2_1 operation with axis parallel to [010] to *L1* projected (a) on the layer plane and (b) along [010].

Such a structure composed of (pseudo)-equivalent layers where contacts are non-equivalent is a non-OD polytype.²⁸ Since each layer can contact in two ways to adjacent layers, stacking faults are expected. A stacking fault leads to a structure that is reflected at (010), corresponding to the minor molecular positions. Thus, at least from the point of view of the 0-3 molecules, the observed disorder is plausible.

To understand the root cause of the differences of *L1* and *L2*, it is necessary to pay closer attention to the 4-*f* molecules. In Figure 9 (b) it is seen that the planes of the 8-*b* (ethyne connecting) molecules and the *c-f* (dimethylamine connecting) molecules are approximately parallel and perpendicular to the layer plane (001), respectively. For the 4-7 (benzene connecting) molecules, on the other hand, 6/7 in *L2* are parallel to (001) but 4/5 in *L1* adopt a more perpendicular orientation. This differing orientation of the 4-7 molecules in *L1* and *L2* is connected to the intermolecular contacts in [001] direction, as indicated by black lines in Figure 7. In [001] direction, 8-*b* (ethyne connecting) molecules connect to *c-f* (dimethylamine connecting) molecules and vice-versa. Thus, molecules are alternately (approximately) perpendicular and parallel to (001). The 4-7 (benzene connecting) connect in [001] direction to other 4-7 molecules. To maintain the perpendicular/parallel scheme, orientation of these molecules with respect to [001] has to alternate.

Indeed, the 4-*f* molecules form layers parallel to (100). There are six of these layers, all with approximate p_x112_1 (the subscript “*x*” indicates the direction lacking translation) symmetry, indicated by black lines in Figure 7. The layers are named according to their molecules as 39, 47, 56, 8*e*, *af* and *bd*. They can be categorized in two groups, *viz.* of benzene-connecting molecules

(47, 56) and ethyne- and dimethylamine-connecting (39, 8e, af, bd). The layers are made up of two kinds of rods, of the molecules parallel and perpendicular to (001), respectively (Figure 10). In the benzene-connecting layers (47, 56), the molecules parallel to (100) deviate more from this idealized orientation. Nevertheless, all six layers are geometrically very similar (Figure 11). And therefore the packing of the 4-*f* molecules can be considered as a polytype made up of layers parallel to (100) with a repetition period of six.

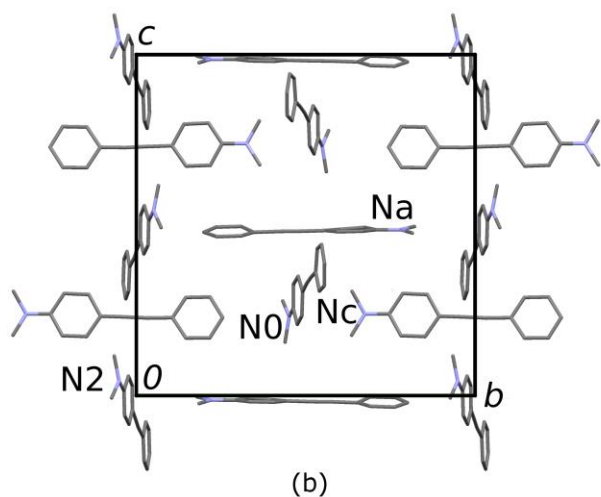
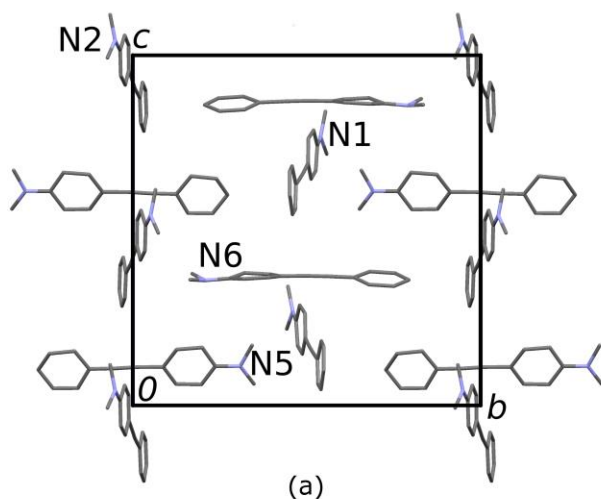


Figure 10. Examples of the two kinds of layers parallel to (100). (a) Molecules connecting ethyne and dimethylamine functionalities (here: 56) and (b) molecules connecting benzene rings (here: *ac*). For orientation, the 0-3 molecules piercing through these layers are also shown.

If the molecules would adopt the idealized orientation [perfectly parallel and perpendicular to (100), respectively], both kinds of rods are symmetric by reflection at (001). The rods contact in two non-equivalent ways, *i.e.* in head-to-head or head-to-tail fashion (Figure 10). Thus, the layers of the 4...*f* molecules can in turn be considered as non-OD polytypes made up of two kinds of rods. Application of the $m_{\{001\}}$ operation on the rods leads to an alternative arrangement, which again corresponds to the observed disorder [reflection at (010)]. The disorder is in agreement with the packing of the 4-*f* molecules.

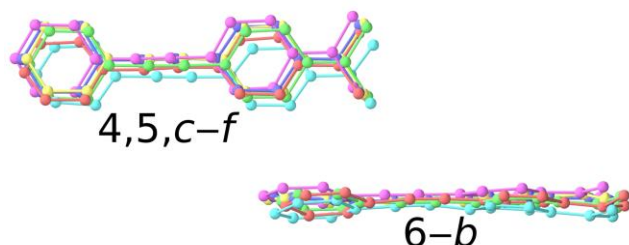


Figure 11. Overlay of the layers of 4 . . . *f* molecules parallel to (100).

In summary, the unusually high $Z' = 16$ is caused by the interaction of two subsystems and the disorder is due to pseudo symmetry of these subsystems. In a recent review on high- Z' structures,²⁹ special attention was paid to different factors: commensurate modulation, symmetry reduction, polytypes, hydrogen networks and especially a combination of these factors. Indeed, the *L1* and *L2* layers can be derived from higher symmetry layers with $p11a$ symmetry. Both, *L1* and *L2*, can be described as a two-fold superstructures (*i.e.* commensurate modulation). The packing of the 4-*f* molecules can be considered a long-period polytype. Nevertheless, it would be

incorrect to attribute the high Z' to a combination of factors, because all these factors are a direct consequence of the interaction of the two subsystems 0-3 and 4-*f*. As such, the crystals of **1** should be considered as the commensurate analogue of a composite crystal,³⁰ *i.e.* a single reason is sufficient to describe the high Z' in this case.

As has been mentioned above, the **1** molecules are disordered and can appear in two distinct orientations (the minor orientation being indicated by an added prime character). So far, the disorder was only described qualitatively as being a consequence of pseudo-symmetry and polytypism. A closer look at the actual occupancies reveals even more complexities. In Figure 12 the major and minor orientations of the molecules are shown for the *L1* and *L2* layers. In Table 3 the occupancy ratios of the individual positions are compiled. If one of the 0-3 molecules adopts a certain orientation (e.g. 0 or 0'), then the adjacent 0-3 molecule in [100] direction must adopt the corresponding orientation (e.g. 1 or 1') for steric reasons (overlap of H atoms of the methyl and benzene fragments). Indeed, the occupancy ratios of all 0-3 molecules refined to very similar values and were ultimately restrained to the same value to achieve a chemically reasonable model. The orientations of the 0-3 subsystem refined to an approximate 4:1 occupancy ratio (Table 3, first row). Likewise, the *c-f* (dimethylamine connecting) molecules must adopt the orientation corresponding to the connected 0-3 molecules, because the opposite orientation has unreasonably short H...H interactions of the methyl groups of both molecules. These occupancies were therefore likewise restrained to those of the 0-3 molecules.

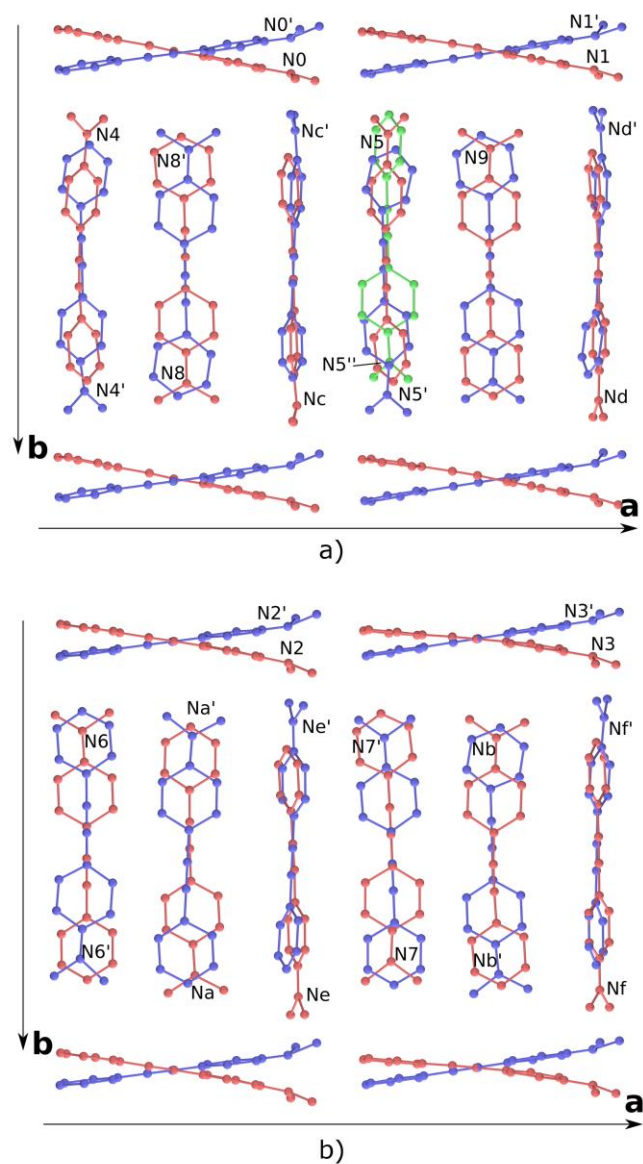


Figure 12. Overlay of the major (red) and minor (blue: ', green: '') orientations in the crystal structure of **1** in the (a) *L1* and (b) *L2* layers.

Table 3. Occupation ratios of the molecule orientations in single crystals of **1**. The ratios are given as red:blue:green with respect to the colors of Figure 12.

Molecules	Ratio
-----------	-------

0-4, <i>a-f</i>	80.6:19.4(1)
5	55.6:19.4:25.9(4)
6	52.4:47.6(7)
7	56.1:43.9(7)
8	72.2:27.8(7)
9	63.2:36.8(6)

The situation is more complex for the remaining molecules. The 5 molecule, which connects benzenes of 1 molecules, was refined as being disordered about three positions, viz. 5 (major), 5' and 5'' (both minor). Here, 5 and 5'' can only be realized with 1 and 5' only with 1'. The occupancies were restrained accordingly. Thus, in addition to the 4:1 disorder of the 0-3 framework, the major 5 position can additionally feature two orientations with an approximate 2:1 ratio. Notably, in the alternative 5'' orientation, the *L1* layer adopts the orientation sequence of the *L2* layer (compare with Figure 9). Most likely, the 5' position also features an additional alternative orientation (which might be called 5'''), but its total electron density is too low to be evidenced in the given data. A similar situation is observed for the 6 molecule, which connects two benzenes of molecule 2. Here, the 6'' and 6''' orientations could not be resolved because they are too close to the 6' and 6, respectively. Instead, the disorder is reflected by displacement ellipsoids with a principal axis significantly enlarged in the [010] direction. The ratio of the occupancy of both orientations of 6 is close to 1:1, showing that it is close to independent from the orientation of the remainder of the structure. The alternative orientation gives a layer with the orientation sequence ...↑↑↑↑↓↑... (see above). The 7 molecule (connecting the benzene of the 3 molecules) can likewise adopt two orientations for a given orientation of the 3 molecules. The displacement ellipsoids are less enlarged than for 6, because the orientations are even closer.

Supposing that the additional disorder is identical for both orientations of the 3 molecule, the 7:7'' occupancy ratio is approximately 3:2. If 7'' is realized, the *L2* layer adopts the orientation sequence of the *L1* layer. The occupancy ratio of the remaining benzene connecting molecule (4), on the other hand, refined to values very close to those of the 0-3 molecules. It was therefore restrained to the same ratio without noticeable influence on the residuals.

Finally, the 8-b (ethyne connecting) molecules feature different behavior in *L1* and *L2*. In *L1* (molecules 8, 9) they possess additional disorder. The ratio of major to minor orientation for a given orientation of the connected molecules is 85:15 (8:8'') and 72:28 (9:9''). The occupancy ratios of the *a* and *b* molecules in *L2*, on the other hand, refine nearly to those of the connected molecules and were also restrained to the same values.

In summary, even though the disorder in the crystal structure of **1** can be qualitatively attributed to the non-OD polytypism of both subsystems, the actual occupancy ratios are very complex owing to the intricate interactions of both subsystems.

NLO properties

As all three developed materials exhibit non-centrosymmetric crystallization, they were probed for SHG. Powdered samples of the compounds were irradiated with the output of an ultrafast Yb:KGW-Laser. The second-harmonic radiation was collected and compared to the signal of reference compound (*Z*)-4-(2-(methylthio)-1-propenyl)-1-phenyl-1,2,3-triazole (2 x SHG intensity of KDP) (Figure 13).¹⁶

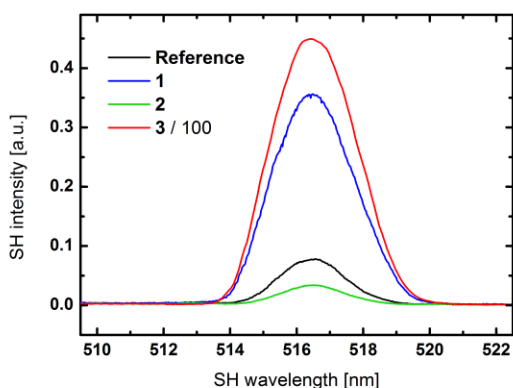


Figure 13. SHG spectra of **1**, **2**, **3** and reference material (*Z*)-4-(2-(methylthio)-1-propenyl)-1-phenyl-1,2,3-triazole. The original SH spectra of **3** was downscaled by a factor of 100. The relatively large line width of the SHG signals results from the inherent spectral bandwidth of the ultrashort laser pulses.

Derivatives **1** ($\sim 4 \times$ SHG intensity of reference material) and **2** ($\sim 0.5 \times$ SHG intensity of reference material) exhibited similar SHG efficiency compared to the reference material. In contrast, pyrimidine based **3** featured a very high SH emission and compound **3** displayed a 600 fold increased SHG intensity compared to the reference material. This value corresponds to approximately 1200 times the SH intensity of KDP. Thus, **3** exhibits by far the highest SHG intensity of this class of materials.^{9,16,31}

The intensity of the SHG correlates to the hyperpolarizability, which in turn is related to the dipole moment difference of the materials between the ground state and the excited state.²⁵ Nonetheless, these differences in $\Delta\mu$ are not sufficient to explain the distinctly different SHG efficiencies of the ethyne-linked molecules. The polarization in donor-acceptor materials predominantly originates from the movements of electrons from the donor to the acceptor in the electric field.^{25,32} This delocalization occurs along a charge transfer axis connecting the donor

and the acceptor. However, the orientation of this axis of the single molecules with respect to the symmetry elements of the crystal has to be taken into account.³³ While the contributions to an overall hyperpolarization of molecules whose charge transfer axis are aligned parallel to a polar direction of the crystal add up, those contributions of molecules that are oriented parallel to a non-polar direction of the single crystal cancel each other.

To explain the orders-of-magnitude variation of the SHG efficiency, we investigated hyperpolarizabilities of the individual chromophores and their actual orientation in the unit cells of the three materials. In this section the conventions of tensor calculus are used.³⁴ Typographically, we will not distinguish between a vector/tensor and its components and the Einstein summation convention applies. The static first-order hyperpolarizability tensors β_{ijk} of the title molecules were calculated using the Gaussian 09 package. For **2** and **3**, calculations were performed on the molecular conformation in the crystal structure and on a gas-phase optimized configuration. The non-H atoms in the original and the optimized configurations differ generally by less than 0.15 Å, only for the dimethylamine group a deviation of up to 0.22 Å is observed. Accordingly, no significant differences were observed for the β_{ijk} . For **1**, only an optimized conformation was used, owing to a lack of reliable structural data. Here, the optimized conformation differs up to 0.4 Å from the conformations determined by diffraction.

The β_{ijk} tensors of the single molecules are visualized²¹ in Figure 14 & 15, top row. The quadric response to the applied electric field is represented by arrows whose origins are located on a sphere around the molecule. Each point of the sphere corresponds to the direction of the applied field. The length of the vectors is additionally encoded in color (red: longest; blue: shortest). The vectors of all molecules are on the same scale. In all three cases the same qualitative behavior is observed. A field applied perpendicular to the molecular axis exhibits

only a linear response (blue belt of vanishing arrows). For strong fields along the molecular axis, on the other hand, the induced polarization is distinctly skewed in the DMA→acceptor direction compared to the linear response (red arrows at the poles). This finding is in perfect agreement with the assumption that the charge transfer from the donor to the acceptor is the leading force for the polarization.^{25,32}

A useful quantification of the quadric nonlinear response of the molecule is the first hyperpolarizability vector²¹ β_i^{tot} , whose components are related to the β_{ijk} tensor by

$$\beta_i^{tot} = \sum_{j=1}^3 \beta_{ijj}$$

In all cases β_i^{tot} is virtually parallel to the molecular axis and points in the DMA→acceptor direction (yellow arrows in Figure 14 & 15, top row). In the case of **3** and **1**, β_i^{tot} is also parallel to the dipole moment of the molecule, which is directed along the molecular axis owing to the *mm2* point symmetry. **2** exhibits the lower *m* symmetry, due to the desymmetrization of the molecule by the incorporation of one single nitrogen atom in the pyridine ring. Accordingly, the dipole moment points from the center of the molecule towards the N atom of the pyridine and therefore is distinctly not parallel to β_i^{tot} . Hence, the dipole moment is an inadequate criterion for the estimation of the non-linear character of a molecule and thus a proper main charge transfer axis³³ has to be chosen carefully.

The absolute value $|\beta_i^{tot}|$ of all three title molecules is compiled in Table 4, left side. The total hyperpolarizability increases **1**<**2**<**3**, with the first-order hyperpolarizability of **3** being nearly twice that of **1**. This result is in perfect accordance with the photophysical characterization and represents an increased degree of charge transfer with increasing acceptor strength.

Table 4. $|\beta_i^{tot}|$ in atomic units ($e^3 a_0^3 / E_h^2$; e : elementary charge; a_0 : Bohr radius; E_h : ionization energy of hydrogen) for the different molecules before and after application of the point symmetry restraints of the crystal. The percentage in parentheses is with respect to $|\beta_i^{tot}|$ for the free molecule. The last line lists the $|\beta_i^{tot}|$ of the β_{ijk} tensor averaged over the 16 crystallographic independent **1** molecules (neglecting disorder).

	Free molecule		Symmetry restrained	
	Crystal	Gas phase	Crystal	Gas phase
2	5875.13	5250.16	13.65 (0.23%)	83.65 (1.59%)
3	7055.02	6710.53	2632.86 (37.32%)	2535.19 (37.78%)
1 , mol. 0	-	3763.87	-	3728.08 (99.05%)
1 , mol. 1	-	3763.87	-	3672.93 (97.58%)
1 , mol. 2	-	3763.87	-	3738.43 (99.32%)
1 , mol. 3	-	3763.87	-	3711.00 (98.60%)
1 , mol. 4	-	3763.87	-	214.66 (5.70%)
1 , mol. 5	-	3763.87	-	208.62 (6.54%)
1 , mol. 6	-	3763.87	-	245.64 (6.53%)
1 , mol. 7	-	3763.87	-	229.59 (6.10%)
1 , mol. 8	-	3763.87	-	228.65 (6.08%)
1 , mol. 9	-	3763.87	-	217.14 (5.77%)
1 , mol. a	-	3763.87	-	266.17 (7.07%)
1 , mol. b	-	3763.87	-	208.75 (5.55%)
1 , mol. c	-	3763.87	-	177.52 (4.72%)

1, mol. d	-	3763.87	-	267.13 (7.10%)
1, mol. e	-	3763.87	-	347.58 (9.24%)
1, mol. f	-	3763.87	-	235.58 (6.28%)
1 (average)	-	3763.87	-	40.53 (1.08%)

Obviously, the orders-of-magnitude difference in SHG activity cannot be explained by the absolute value $|\beta_i^{tot}|$ alone. The orientation of the β_i^{tot} vector with respect to the symmetry elements of the crystal or, more precisely, the non-polar direction has to be taken into account as well.

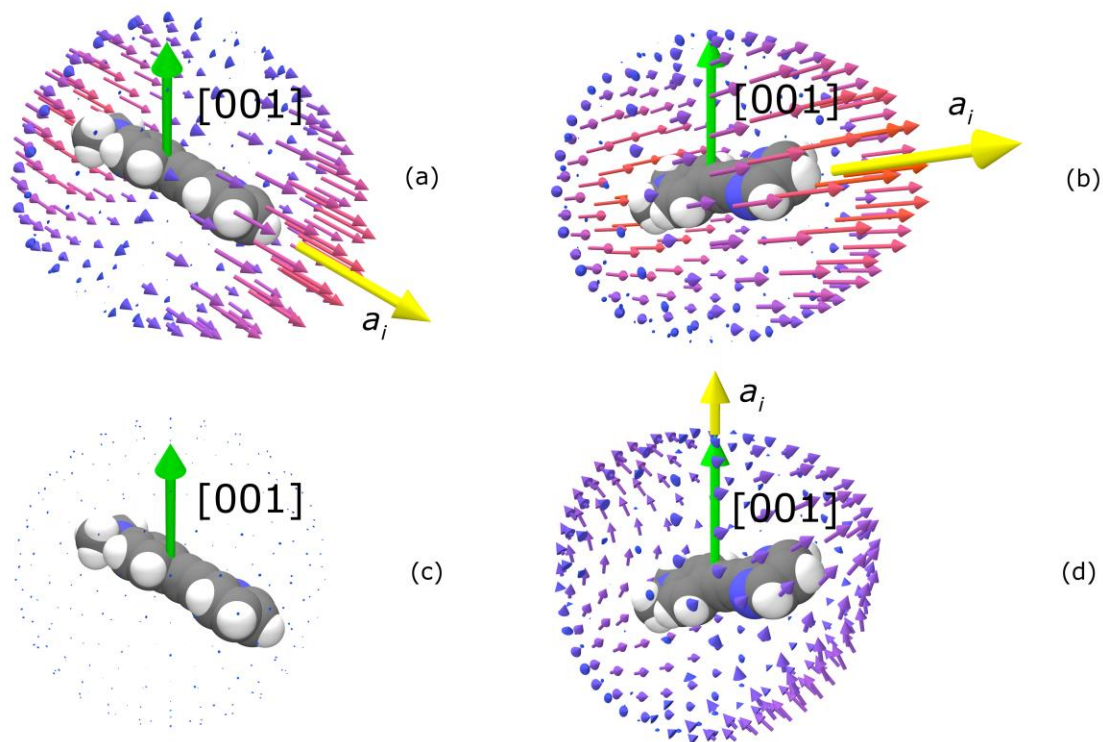


Figure 14. Representation of the first-order hyperpolarizability β_{ijk} of **2** [a and c (symmetry restrained)] and **3** [b and d (symmetry restrained)]. The quadric response is represented by arrows with the origins located on a sphere around the molecule, whereby the points on the sphere indicate the direction of the applied field. A yellow arrow represents the total first-order

hyperpolarizability β_i^{tot} . Its length is scaled by a factor 2 with respect to the other arrows and its origin is placed on the same sphere. The polar [001] axis is indicated by a green arrow. In the second row the symmetry restrictions according to the $mm2$ point symmetry of the crystals were applied to β_{ijk} .

2 and **3** both crystallize in the $Pna2_1$ space group (point group $mm2$), with the polar axis [001], which is indicated by a green arrow in Figure 14. If written in the 3×6 β_{ij} matrix form commonly used for piezoelectricity tensors ($\beta_{i1} = \beta_{i11}, \dots, \beta_{i6} = 2\beta_{i12}$), the overall β_{ij} of the crystal takes the form

$$\begin{pmatrix} 0 & 0 & 0 & 0 & 2\beta_{31} & 0 \\ 0 & 0 & 0 & 2\beta_{32} & 0 & 0 \\ \beta_{31} & \beta_{32} & \beta_{33} & 0 & 0 & 0 \end{pmatrix}$$

The total first-order hyperpolarizability β_i^{tot} in this case is parallel to [001].

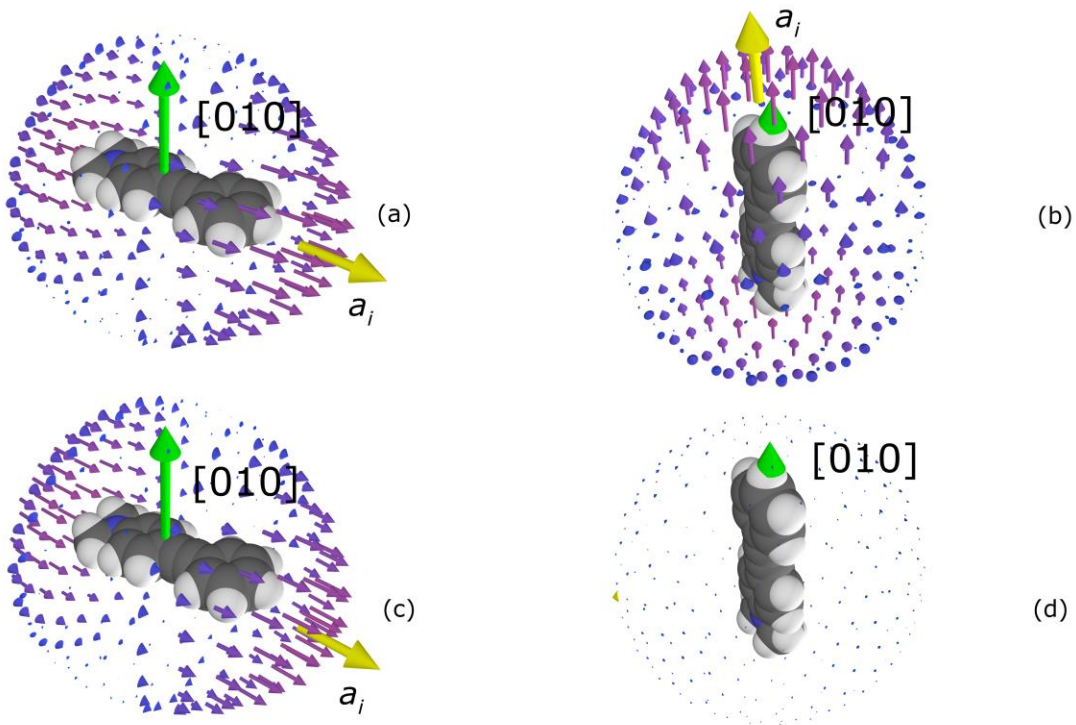


Figure 15. Representation of the first-order hyperpolarizability β_{ijk} of molecules **0** [a and c (symmetry restrained)] and **1**. Symbols as in Figure 14. The green arrow indicates the non-polar [010] axis. In the second row the symmetry restrictions according to the m point symmetry of the crystals were applied to β_{ijk} .

To calculate the overall β_{ijk} tensor of the **2** and **3** crystals, the atomic coordinates of the single-crystal model were transformed into an orthonormal coordinate system. The matrix of direction cosines a_{ij} ,³⁴ transforming the coordinates x_i of the DFT-calculation molecules (crystal conformation and optimized conformation) into orthonormal crystal coordinates \tilde{x}_i according to

$$\tilde{x}_i = a_{il}x_l$$

were determined by minimizing the least-square distances of atoms in both orientations. The β_{ijk} tensor was transformed into crystal coordinates by

$$\widetilde{\beta}_{ijk} = a_{il}a_{jm}a_{kn}\beta_{lmn}$$
³⁴

and the symmetry-restrained elements were cleared. The transformed tensors are compiled in the supplementary materials. The tensors and the corresponding β_i^{tot} are visualized in Figure 14, second row.

The molecular axis of **2** is virtually perpendicular to [001] [angle —C≡C— with (001): 2.2°]. Thus, the non-linear response is virtually non-existent at < 1% of the possible total hyperpolarizability (Table 4). The **3** molecules, on the other hand, are distinctly inclined [angle —C≡C— with (001): 19.5°]. Here, after symmetry correction a distinct hyperpolarizability in [001] direction remains (37–38%, Table 4). Even though β_i^{tot} of the crystal is parallel to [001], the individual first-order hyperpolarizability responses need not be parallel to [001] [Figure 14 (d)].

1 crystallizes in the Pc space group (point group m). Here, the monoclinic axis $[010]$, which is indicated by a green arrow in Figure 15, is non-polar. The total hyperpolarizability β_i^{tot} lies in the (010) plane and the overall β_{ij} takes the form

$$\begin{pmatrix} \beta_{11} & \beta_{12} & \beta_{13} & 0 & 2\beta_{31} & 0 \\ 0 & 0 & 0 & 2\beta_{32} & 0 & 2\beta_{12} \\ \beta_{31} & \beta_{32} & \beta_{33} & 0 & 2\beta_{13} & 0 \end{pmatrix}$$

As above, the direction cosines a_{ij} were calculated for the 16 molecules in the crystal (disregarding disorder). The symmetry-restricted β_{ijk} are depicted in Figure 15, second row, for two characteristic molecules. The four molecules 0-3 [Figure 15 (c)] are nearly perfectly aligned for a high first-order hyperpolarizability with the molecular axis located in the (010) plane. Thus, after symmetry restriction approximately 98% of the total hyperpolarizability remains (Table 4). The molecular axis of the twelve remaining molecules 4-*f* [Figure 15 (d)], on the other hand, are close to perpendicular to (010) . In consequence, the symmetry-restrained total hyperpolarizability is small (approximately 6%, Table 4).

Even though the molecules 0-3 constitute only 25% of the total molecules 0-*f*, one still might expect a total hyperpolarizability on the same order of magnitude as for **3**. However, the molecules 0, 1 and 2, 3 are oriented in opposite direction with respect to the molecular axis. Indeed, as shown above, the structure can be decomposed into layers which are related by pseudo-inversion symmetry. Even though not being a symmetry operation of the crystal, such a pseudo-symmetry is effective at prohibiting first-order hyperpolarizability. To estimate the total hyperpolarizability, the average of the 16 symmetry-restrained β_{ijk} tensors was calculated. A vanishing β_i^{tot} (1% of the original magnitude, Table 4, last line) was obtained.

Notably, not only the order of the materials regarding their SHG efficiency is reliably reproduced by this analysis but also the calculated relative total hyperpolarizabilities (**1** : **2** : **3** =

1 : 0.34 : 65) are within the margin of error of the applied methodology in excellent agreement with the measured SHG intensities (**1 : 2 : 3** = 1 : 0.13 : 125)

CONCLUSION

We have prepared a series of three novel NLO chromophores based on a simple donor-acceptor design. All of the materials displayed distinct charge transfer properties as observed during the photophysical properties and furthermore exhibited non centrosymmetric crystallization behavior. Notably, one of the compounds crystallized with a high $Z' = 16$ molecules. Furthermore, one of these materials exhibited a very high second harmonic generation with an 1200 fold efficiency improvement compared to potassium dihydrogen phosphate. Based on the crystal structure and theoretical calculations the different intensities of the SHG of the materials could be rationalized, highlighting the importance of both the molecular properties, as well as the spatial alignment of the materials in the solid phase to understand the nonlinear response of such chromophores.

ASSOCIATED CONTENT

Supporting Information. Photophysical data, hyperpolarizability tensors. This material is available free of charge via the Internet at <http://pubs.acs.org>.

CCDC 1537726–1537728 contain the supplementary crystallographic data and can be accessed free of charge from the Cambridge Crystallographic Data Centre (CCDC).

AUTHOR INFORMATION

Corresponding Author

*E-mail: paul.kautny@tuwien.ac.at

ACKNOWLEDGMENT

This work was supported in part by the TU Wien “Innovative Projects” research funds. P. Getreuer is acknowledged for supporting the synthesis of the materials. The X-ray centre of the TU Wien is acknowledged for providing access to the single-crystal diffractometer. L. Czollner is acknowledged for performing the HRMS measurement. E. Horkel is acknowledged for assistance with theoretical calculations. The authors thank he authors thank V. Petříček for fruitful discussions on rigid body refinements with Jana2006.

REFERENCES

1. (a) Mishra, A.; Bäuerle, P. *Angew. Chem., Int. Ed.* **2012**, *51* (9), 2020-2067; (b) Roncali, J. *Acc. Chem. Res.* **2009**, *42* (11), 1719-1730.
2. (a) Cho, M. J.; Choi, D. H.; Sullivan, P. A.; Akelaitis, A. J. P.; Dalton, L. R. *Prog Pol. Sci.* **2008**, *33* (11), 1013-1058; (b) Kato, S.-i.; Diederich, F. *Chem. Commun.* **2010**, *46* (12), 1994-2006; (c) He, G. S.; Tan, L.-S.; Zheng, Q.; Prasad, P. N. *Chem. Rev.* **2008**, *108* (4), 1245-1330; (d) Dalton, L. R.; Sullivan, P. A.; Bale, D. H. *Chem. Rev.* **2009**, *110* (1), 25-55; (e) Marder, S. R. *Chem. Commun.* **2006**, (2), 131-134.
3. (a) Qian, X.; Xiao, Y.; Xu, Y.; Guo, X.; Qian, J.; Zhu, W. *Chem. Commun.* **2010**, *46* (35), 6418-6436; (b) Lord, S. J.; Conley, N. R.; Lee, H.-I. D.; Nishimura, S. Y.; Pomerantz, A. K.; Willets, K. A.; Lu, Z.; Wang, H.; Liu, N.; Samuel, R.; Weber, R.; Semyonov, A.; He, M.; Twieg, R. J.; Moerner, W. E. *ChemPhysChem* **2009**, *10* (1), 55-65.
4. (a) Tao, Y.; Yang, C.; Qin, J. *Chem. Soc. Rev.* **2011**, *40* (5), 2943-2970; (b) Chaskar, A.; Chen, H.-F.; Wong, K.-T. *Adv. Mater.* **2011**, *23* (34), 3876-3895; (c) Tao, Y.; Yuan, K.; Chen, T.; Xu, P.; Li, H. H.; Chen, R. F.; Zheng, C.; Zhang, L.; Huang, W. *Adv. Mater.* **2014**, *26* (47), 7931-7958.

5. Yariv, A.; Yeh, P., *Photonics: Optical Electronics in Modern Communications (The Oxford Series in Electrical and Computer Engineering)*. Oxford University Press, Inc.: 2006.
6. (a) Zyss, J. *J. Chem. Phys.* **1979**, *71* (2), 909-916; (b) Marder, S. R.; Kippelen, B.; Jen, A. K. Y.; Peyghambarian, N. *Nature* **1997**, *388* (6645), 845-851.
7. Kleinman, D. A. *Phys. Rev.* **1962**, *126* (6), 1977-&.
8. (a) Wu, W.; Qin, J.; Li, Z., New design strategies for second-order nonlinear optical polymers and dendrimers. *Polymer* **2013**, *54* (17), 4351-4382; (b) Souza, T. E.; Rosa, I. M. L.; Legendre, A. O.; Paschoal, D.; Maia, L. J. Q.; Dos Santos, H. F.; Martins, F. T.; Doriguetto, A. *C. Acta Crystallogr. Sect. B* **2015**, *71* (4), 416-426.
9. Kautny, P.; Bader, D.; Stöger, B.; Reider, G. A.; Fröhlich, J.; Lumpi, D. *Chem. –Eur. J.* **2016**, *22* (52), 18887-18898.
10. APEXII, RLATT, SAINT, SADABS and TWINABS, 2014.
11. CrysAlis CCD, 2006.
12. Sheldrick, G., *Acta Crystallogr. Sect. A* **2015**, *71* (1), 3-8.
13. Petříček, V.; Dušek, M.; Palatinus, L. *Z. Kristallogr. – Cryst. Mate.* **2014**; *229*, 345-352.
14. Macrae, C. F.; Bruno, I. J.; Chisholm, J. A.; Edgington, P. R.; McCabe, P.; Pidcock, E.; Rodriguez-Monge, L.; Taylor, R.; van de Streek, J.; Wood, P. A. *J. Appl. Crystallogr.* **2008**, *41* (2), 466-470.
15. Kurtz, S. K.; Perry, T. T. *J. Appl. Phys.* **1968**, *39* (8), 3798-3813.
16. Lumpi, D.; Stöger, B.; Hametner, C.; Kubel, F.; Reider, G.; Hagemann, H.; Karpfen, A.; Fröhlich, J. *CrystEngComm* **2011**, *13* (24), 7194-7197.

17. (a) Ladouceur, S.; Soliman, A. M.; Zysman-Colman, E. *Synthesis* **2011**, (22), 3604-3611;
(b) LaBeaume, P.; Wager, K.; Falcone, D.; Li, J.; Torchilin, V.; Castro, C.; Holewa, C.; Kallmerten, A. E.; Jones, G. B. *Bioorg. Med. Chem.* **2009**, *17* (17), 6292-6300.
18. Gaussian 09, Revision D.01, M. J. Frisch, G. W. Trucks, H. B. Schlegel, G. E. Scuseria, M. A. Robb, J. R. Cheeseman, G. Scalmani, V. Barone, B. Mennucci, G. A. Petersson, H. Nakatsuji, M. Caricato, X. Li, H. P. Hratchian, A. F. Izmaylov, J. Bloino, G. Zheng, J. L. Sonnenberg, M. Hada, M. Ehara, K. Toyota, R. Fukuda, J. Hasegawa, M. Ishida, T. Nakajima, Y. Honda, O. Kitao, H. Nakai, T. Vreven, J. A. Montgomery Jr. , J. E. Peralta, F. Ogliaro, M. J. Bearpark, J. Heyd, E. N. Brothers, K. N. Kudin, V. N. Staroverov, R. Kobayashi, J. Normand, K. Raghavachari, A. P. Rendell, J. C. Burant, S. S. Iyengar, J. Tomasi, M. Cossi, N. Rega, N. J. Millam, M. Klene, J. E. Knox, J. B. Cross, V. Bakken, C. Adamo, J. Jaramillo, R. Gomperts, R. E. Stratmann, O. Yazyev, A. J. Austin, R. Cammi, C. Pomelli, J. W. Ochterski, R. L. Martin, K. Morokuma, V. G. Zakrzewski, G. A. Voth, P. Salvador, J. J. Dannenberg, S. Dapprich, A. D. Daniels, .: Farkas, J. B. Foresman, J. V. Ortiz, J. Cioslowski, D. J. Fox, Gaussian, Inc., Wallingford, CT, USA, 2009.
19. Yanai, T.; Tew, D. P.; Handy, N. C. *Chem. Phys. Lett.* **2004**, *393* (1-3), 51-57.
20. (a) Krishnan, R.; Binkley, J. S.; Seeger, R.; Pople, J. A. *J. Chem. Phys.* **1980**, *72* (1), 650-654; (b) Frisch, M. J.; Pople, J. A.; Binkley, J. S. *J. Chem. Phys.* **1984**, *80* (7), 3265-3269.
21. Tuer, A.; Krouglov, S.; Cisek, R.; Tokarz, D.; Barzda, V. *J. Comput. Chem.* **2011**, *32* (6), 1128-1134.
22. Persistence of Vision Raytracer (Version 3.6) Persistence of Vision Pty. Ltd., Williamstown, Victoria, Australia.
23. Grabowski, Z. R.; Rotkiewicz, K.; Rettig, W. *Chem. Rev.* **2003**, *103* (10), 3899-4032.

24. Mataga, N.; Kaifu, Y.; Koizumi, M. *Bull. Chem. Soc. Jpn.* **1956**, 29 (4), 465-470.
25. Oudar, J. L.; Chemla, D. S. *J. Chem. Phys.* **1977**, 66 (6), 2664-2668.
26. Lima-de-Faria, J.; Hellner, E.; Liebau, F.; Makovicky, E.; Parthe, E. *Acta Crystallogr. Sect. A* **1990**, 46 (1), 1-11.
27. *Subperiodic Groups*, volume E of International Tables For Crystallography; Kopsky V.; Litvin D. B., Eds.; IUCr: Chester, 2006.
28. Ferraris G.; Makovicky E.; Merlino, S. *Crystallography of Modular Materials*, volume 15 of IUCr Monographs on Crystallography; Oxford University Press: Oxford, 2008.
29. Brock, C. *Acta Crystallogr. Sect. B* **2016**, 72 (6), 807-821.
30. van Smaalen, S. *Incommensurate Crystallography*, volume 21 of IUCr Monographs on Crystallography; Oxford University Press, Oxford, 2007.
31. Lumpi, D.; Glöcklhofer, F.; Holzer, B.; Stöger, B.; Hametner, C.; Reider, G. A.; Fröhlich, J. *Cryst. Growth Des.* **2014**, 14 (3), 1018-1031.
32. Oudar, J. L. *J. Chem. Phys.* **1977**, 67 (2), 446-457.
33. (a) Oudar, J. L.; Zyss, J. *Phys. Rev. A* **1982**, 26 (4), 2016-2027; (b) Zyss, J.; Oudar, J. L. *Phys. Rev. A* **1982**, 26 (4), 2028-2048.
34. Nye, J. F. *Physical Properties of Crystals*; Clarendon Press: Oxford, 1985.

2.9. Manuscript #9

Functional organic click-materials: application in phosphorescent organic light emitting diodes

Paul Kautny, Chenyang Zhao, Thomas Kader, Berthold Stöger, Ernst Horkel, Jiangshan Chen, Dongge Ma, Johannes Fröhlich, Daniel Lumpi

RSC Advances, **2017**, 7, 12150-12160

Reproduced with the kind permission of the Royal Society of Chemistry.

PAPER


 CrossMark
 click for updates
Cite this: *RSC Adv.*, 2017, 7, 12150Received 14th December 2016
Accepted 10th February 2017

DOI: 10.1039/c6ra28212a

rsc.li/rsc-advances

Functional organic click-materials: application in phosphorescent organic light emitting diodes†

 Paul Kautny,^{*a} Chenyang Zhao,^b Thomas Kader,^a Berthold Stöger,^c Ernst Horkel,^a Jiangshan Chen,^{*b} Dongge Ma,^b Johannes Fröhlich^a and Daniel Lumpi^a

In the presented work click chemistry is utilized to introduce 1,2,3-triazoles as a functional linker in organic donor–acceptor materials. A systematic series of materials was prepared and characterized to investigate the effect of the linkage mode on the molecular properties. The 1,2,3-triazole linker allowed control of the degree of intramolecular charge transfer over a wide range depending on the substitution pattern of the triazole moiety. The prepared materials were successfully employed as host materials for green and red dopants in phosphorescent organic light emitting diodes. Thus, this work presents the first application of this novel linkage mode in the design and synthesis of functional π -conjugated organic donor–acceptor materials and their application in organic light emitting diodes.

Introduction

Controlling the conjugation in organic molecules is one of the major challenges in the design of new materials for the rapidly evolving field of organic materials sciences,^{1–7} as the molecular properties of such compounds are predominantly determined by the π -conjugated system.^{1,2,7,8} One of these new technologies, which is now entering our everyday life in small portable displays and also large area TV screens,⁹ is organic light emitting diodes (OLEDs).¹⁰ Tremendous efforts have been made to advance OLEDs and in particular the introduction of phosphorescent heavy transition metal complexes as emitters significantly boosted the device efficiency of OLEDs.^{11,12}

In contrast to purely fluorescent materials, phosphorescent emitters harvest singlet and triplet excitons for light emission simultaneously, thus allowing for theoretically 100% internal quantum efficiency.^{13,14} Those metal complexes are typically dispersed in an organic host material to avoid concentration quenching.^{15,16} The application of bipolar host materials proved particularly successful to provide balanced charge transfer properties and thus high device efficiency.^{1,3,17}

Unfortunately, the combination of electron rich donor and electron poor acceptor subunits in one host molecule lowers the triplet band gap (E_T) *via* intramolecular charge transfer, resulting in undesired energy transfer from the guest emitter to the host.^{1,3} This effect particularly hampers the applicability of bipolar host materials for large band gap blue emitters.¹⁸ An improved efficiency of blue emitting components is, however, a prerequisite for the application of OLEDs in energy efficient solid-state lighting.^{9,19,20}

Thus, the focus of current research is on the control of this undesired interaction. In order to minimize these donor–acceptor exchange *via* the conjugated π -system and to retain high E_T s various strategies have been proposed. Among those are (i) the introduction of saturated sp^3 hybridized bridges;^{21,22} (ii) induction of large twist angles by applying sterically demanding groups^{23,24} or *ortho* linkage of molecular subunits;^{25–27} (iii) decreased π -conjugation as result of *meta* linkage.^{25,26,28} Nonetheless, the challenge to design and prepare large band gap host materials remains.²⁹

In particular, complex synthetic efforts are often required to join donor and acceptor units within one molecule, realizing a specific linkage mode at the same time. In contrast, copper(I)-catalyzed azide–alkyne cycloaddition (CuAAC) represents the most successful example of click chemistry³⁰ and provides a convenient methodology to join two molecular building blocks by 1,2,3-triazole formation.³¹ Whereas widely applied in many fields of organic synthesis^{32,33} the application of this specific linkage mode and 1,2,3-triazoles as integral π -conjugated moiety in functional organic materials^{34–43} and in particular in host materials for PhOLEDs⁴⁴ are relatively scarce. In contrast, 1,2,4-triazoles have been frequently employed as electron accepting units in the design of bipolar host materials.^{25,45–48} Furthermore, triazoles have been used as ligands for phosphorescent iridium complexes.^{49–51}

^aInstitute of Applied Synthetic Chemistry, TU Wien, Getreidemarkt 9/163, A-1060 Vienna, Austria. E-mail: paul.kautny@tuwien.ac.at

^bState Key Laboratory of Polymer Physics and Chemistry, Changchun Institute of Applied Chemistry, Chinese Academy of Sciences, Changchun, 130022, China. E-mail: jschen@ciac.ac.cn

^cInstitute of Chemical Technologies and Analytics, TU Wien, Getreidemarkt 9/164, A-1060 Vienna, Austria

† Electronic supplementary information (ESI) available: NMR spectra, DSC and TGA analysis, cyclic voltammetry, theoretical calculations and crystallographic information. CCDC 1497478–1497479. For ESI and crystallographic data in CIF or other electronic format see DOI: 10.1039/c6ra28212a

In our previous work on small molecules we showed that the application of 1,2,3-triazole linkers allows for the subtle control of the photophysical properties of donor–acceptor materials.⁵² Thus, we envisioned to employ this strategy in the design of wide band gap host materials.

Results and discussion

Molecular design

The aim of this work was to incorporate the 1,2,3-triazole as functional linker in a large π -conjugated system in order to decrease the overall conjugation and utilize the CuAAC as key step for the assembly of the molecular subunits. This strategy allows for a building block approach enabling the convenient synthesis of a large set of molecules.

The CuAAC was applied to connect electron rich triphenylamine (TPA) or phenylcarbazole (PCz) units to a central electron poor core system (Scheme 1). To explore the effect of the triazole linker on the overall conjugation and intramolecular charge transfer phenomena an electron accepting pyridine as well as benzene were chosen as core units. Furthermore, different substitution patterns of the central core units as well as of the triazole linker were investigated.

Beside the mere function as linkage unit the intrinsically weak electron accepting properties of the 1,2,3-triazole unit^{38,44} have to be considered in the molecular design of the materials. Thus, the triazole units will enhance the electron accepting properties of the core unit in case of pyridine acceptors or establish an electron accepting subunit itself in case of the benzene core.

Synthesis

TPA was chosen as primary electron rich subunit, owing to its superior electron donation properties. The TPA-substituted materials **3a**, **3b**, **3d** and **3e** were synthesized starting from azide **1i** and the corresponding dialkynes (Scheme 2). Standard condition using $\text{CuSO}_4 \cdot 5\text{H}_2\text{O}$ and sodium ascorbate in a mixture of H_2O and *t*-BuOH (1 : 1) were employed and the application of a microwave reactor allowed for high reaction temperatures of 150 °C and convenient reaction times (30–60 min) yielding the target materials in reasonable to excellent yields (52–91%). In case of **3d** single crystals were obtained by

crystallization from EtOH, permitting the unambiguous determination of the triazole substitution pattern (Fig. 1 left). The five central aromatic units deviate only slightly from coplanarity with torsion angles of the least square planes of 10.03(10)° and 8.74(10)° for the pyridine–triazole and triazole–benzene fragments, respectively. Only one angle is listed in each case because the molecule is symmetric by twofold rotation with an axis passing through the pyridine fragment.

Whereas the synthesis of the *para*- and *meta*-substituted benzene derivatives **3a** and **3b** proceeded smoothly, the corresponding *ortho*-substituted product could not be isolated. Instead a significant amount of a byproduct, that exhibited twice the number of signals in the carbon NMR spectrum, was obtained. Single crystals grown from acetonitrile enabled the assignment of structure **3c** (Scheme 2). Surprisingly, **3c** featured a mixed triazole substitution pattern (Fig. 1 right). Apparently, the primary installed bulky TPA-substituted 1,4-triazole unit inhibits the formation of the second 1,4-substituted triazole moiety, but favours the 1,5-substituted cycloaddition product. Nonetheless, the isolated product allows for an interesting comparison of the molecular properties of **3c** and the purely 1,4-substituted derivatives.

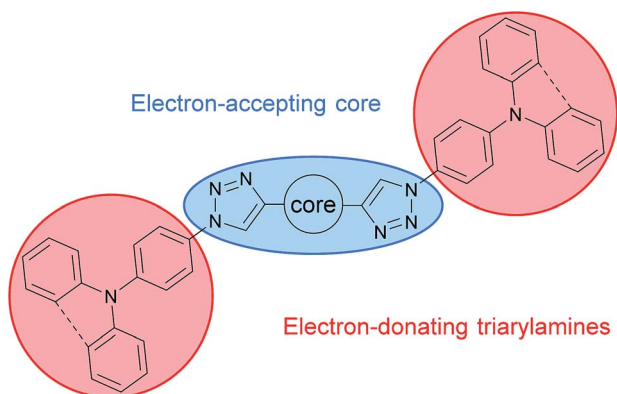
Accordingly, a twofold 1,5-substituted material was prepared.

To maximize the donor–acceptor interaction electron poor pyridine was chosen as core and TPA as electron donating unit. A transition metal free methodology was utilized in the conversion of **2d** and **1i** applying tetramethylammonium hydroxide as alkaline promotor for cycloaddition.⁵³ In such a manner **4d** could be isolated with a low yield (18%).

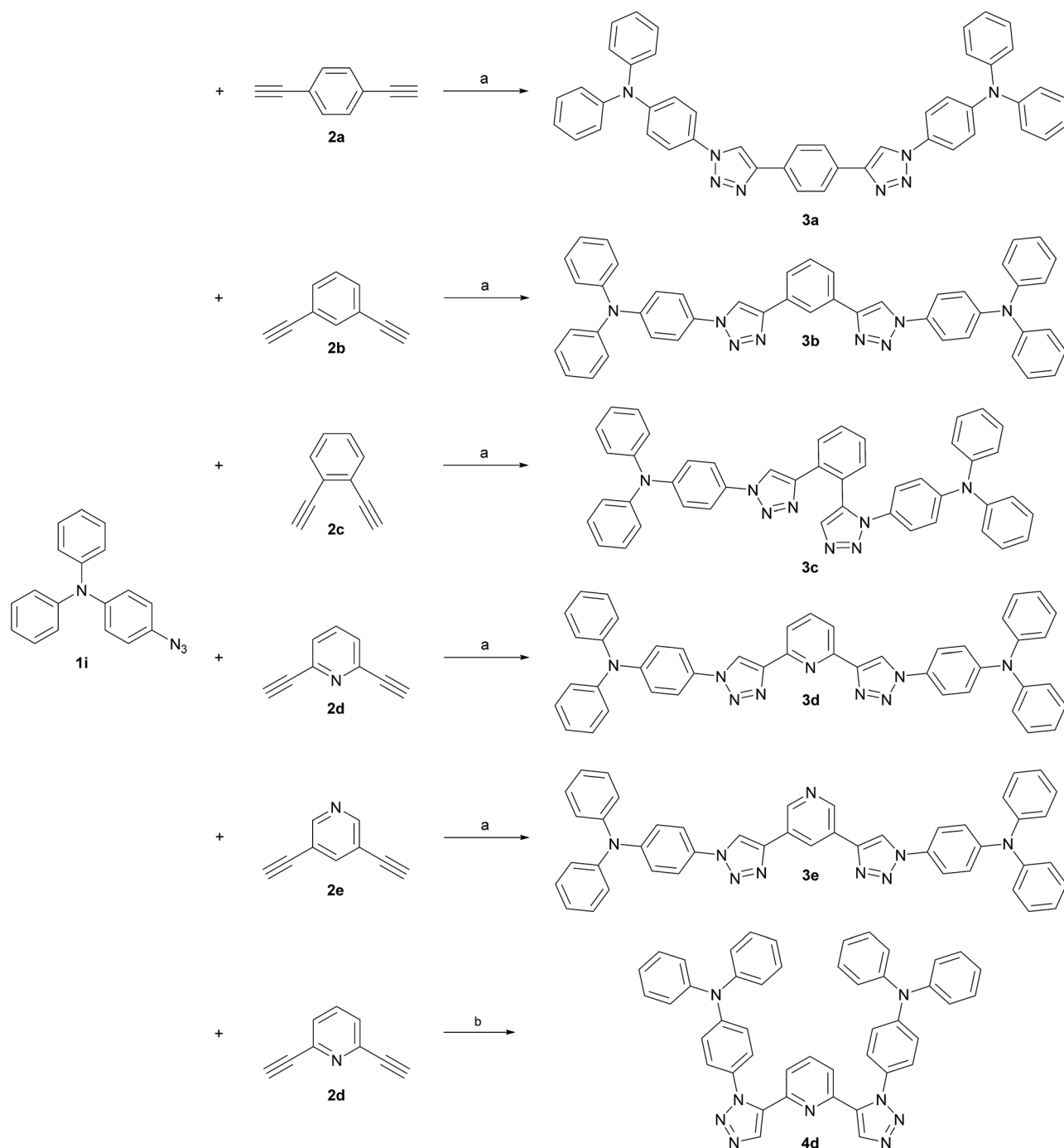
Finally, two phenylcarbazole (PCz)-substituted derivatives were prepared to investigate the influence of weaker electron donors. Dialkynes **2b** and **2d** were chosen as templates for the central core (Scheme 3), since the *meta* relationship between the alkyne groups allows for a better comparability between the benzene and pyridine congeners. Identical reaction conditions were applied as for the synthesis of the 1,4-substituted TPA derivatives and **5b** and **5d** were isolated in 65% and 68% yield, respectively.

Photophysical properties

UV/Vis absorption and photoluminescence (PL) spectra of all compounds as solutions in dichloromethane (5 μM) as well as low temperature phosphorescence spectra were recorded to investigate the impact of the conducted molecular variations on the photophysical properties of the materials. All TPA-substituted host materials exhibited two absorption maxima (Fig. 2). The high energy band is located around 300 nm and can be attributed to a π – π^* transition centered at the TPA unit, while the peaks at longer wavelengths between 330 nm and 340 nm are due to charge transfer (CT) transitions between the electron rich TPA units and the electron withdrawing central cores. Notably, the intensity of this CT transition decreases for the 1,5-substituted derivatives. While for 1,4-substituted materials the CT transition is more intense compared to the π – π^* transition, intensities are equal for **3c** and inverted for **4d**. The optical band gaps of all TPA materials are relatively similar and located between 3.31 and 3.37 eV.



Scheme 1 Molecular design of 1,2,3-triazole linked host materials.



Scheme 2 Synthesis of TPA-substituted host materials. (a) *t*-BuOH/H₂O (1 : 1, 0.4 M), CuSO₄·5H₂O (0.20 eq.), sodium ascorbate (0.40 eq.), 150 °C microwave irradiation; (b) DMSO (0.25 M), tetramethylammonium hydroxide (0.1 eq., 25 wt% in H₂O), 80 °C.

Inspecting the PL spectra of benzene based **3a** and **3b**, nearly identical emission spectra were observed (Fig. 2 left) with peak maxima at 418 nm. In contrast, the emission of **3c**, featuring mixed 1,4 and 1,5 substitution pattern, is much broader. Remarkably, the emission onset is the same compared to the purely 1,4-substituted derivatives, however the emission extends to longer wavelength regions.

In analogy to the materials with benzene core, nearly identical emission features of **3d** and **3e** were observed in case of the

pyridine based host materials, albeit with peak maxima at somewhat higher wavelengths of 424 nm and 425 nm, respectively. In contrast, the emission of **4d** is distinctly red shifted compared to the 1,4-substituted derivatives. However, in the case of purely 1,5-substituted **4d** also the onset of the emission is shifted compared to **3c** with mixed substitution pattern.

Most strikingly, though, the absorption and emission properties of both *meta*-substituted derivative **3b** and **3d** are nearly identical. Additionally, no influence of the substitution pattern

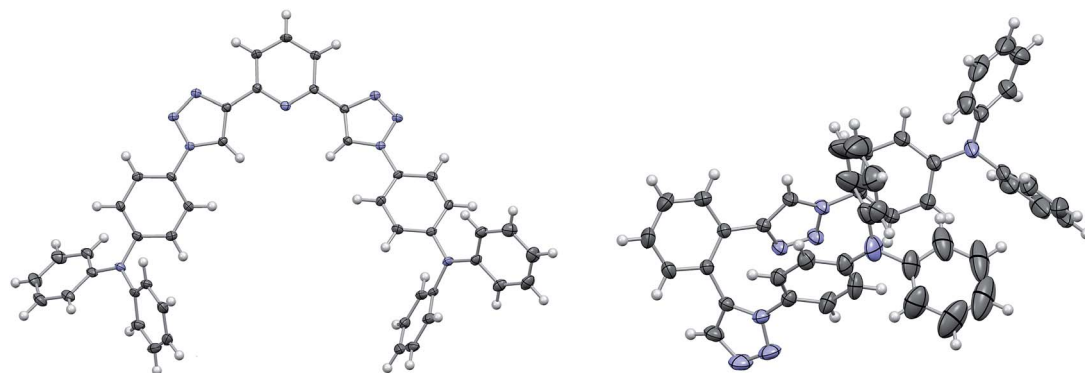
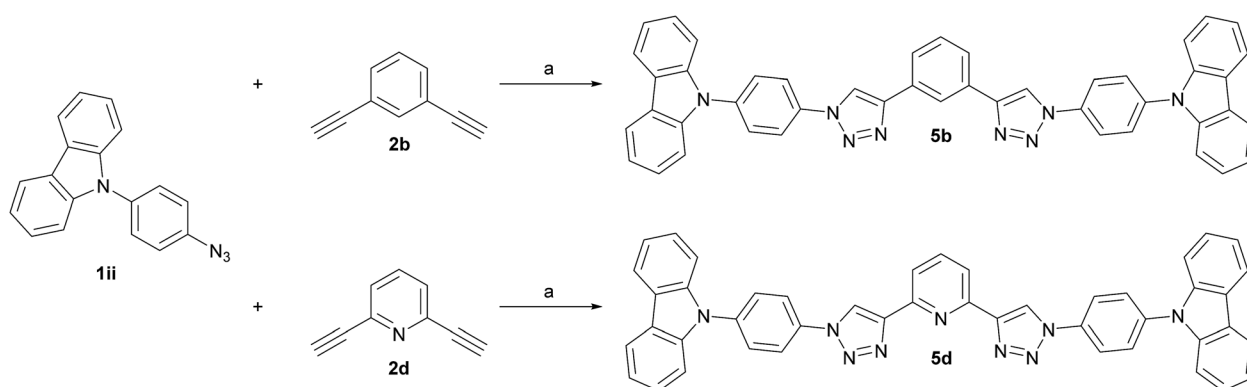


Fig. 1 Molecular structures of **3d** (left) and **3c** (right). C and N atoms are represented by grey and blue ellipsoids drawn at 50% probability levels, H atoms by white spheres of arbitrary radius. The atoms of one diphenylamine fragment of **3c** feature enlarged displacement parameters owing to disorder, which could not be resolved.



Scheme 3 Synthesis of PCz-substituted host materials. (a) *t*-BuOH/H₂O (1 : 1, 0.4 M), CuSO₄·5H₂O (0.20 eq.), sodium ascorbate (0.40 eq.), 150 °C microwave irradiation.

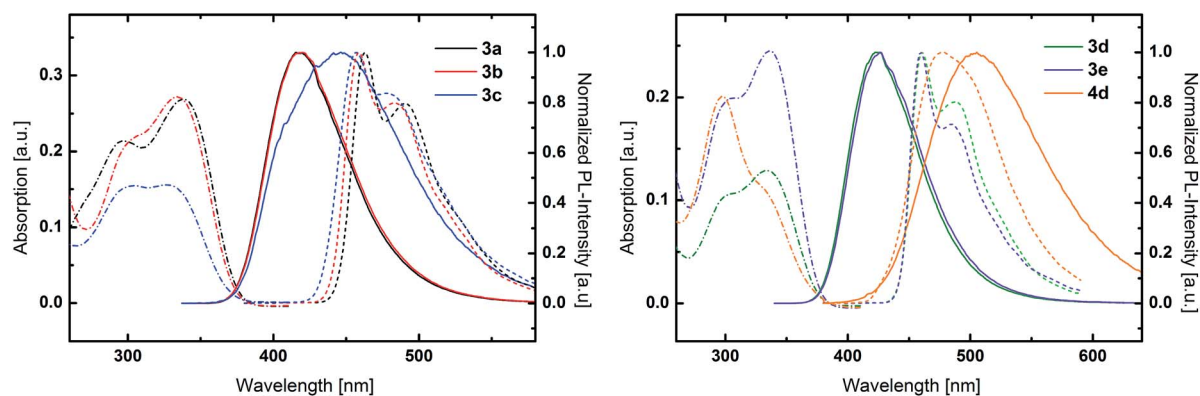


Fig. 2 UV/Vis absorption (dashed and dotted lines), normalized fluorescence spectra at room temperature (solid lines) and normalized phosphorescence spectra at 77 K (dashed lines) of TPA-substituted materials **3a**, **3b** and **3c** (left) and **3d**, **3e** and **4d** (right).

of the central aromatic ring on the photophysical properties was observed for **3a** and **3b** as well as **3d** and **3e**. Thus, the constitution and nature of the central aromatic core seems to be electronically insignificant due to the decreased conjugation as result of the triazole linkage.⁵² The negligible differences in the emission of the benzene and pyridine derivatives indicate that

CT takes place between the peripheral TPA donors and an electron accepting core, which is established by the triazole moiety. In contrast, the central aromatic unit only plays a minor role, due to the restricted overall conjugation, which is unlike the behavior of molecules with less extended π -systems.⁵² Notably, the decreased overall conjugation can be solely

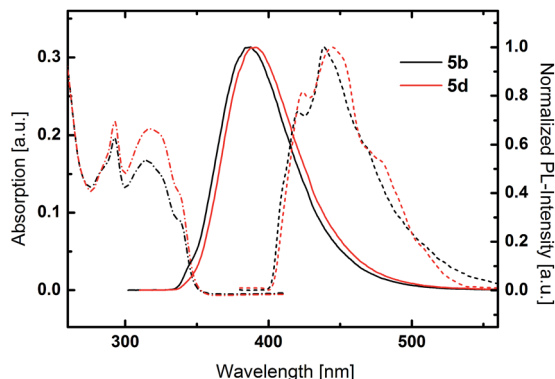


Fig. 3 UV/Vis absorption (dashed and dotted lines), normalized fluorescence spectra at room temperature (solid lines) and normalized phosphorescence spectra at 77 K (dashed lines) of PCz-substituted materials **5b** and **5d**.

attributed to the triazole linkage effect and is independent of any steric effect as conjugation is feasible in **3d** due to the favorable planar configuration of the central aromatic units (Fig. 1).

PCz based host materials exhibited a sharp absorption peak at 293 nm due to the π - π^* transition centered at the PCz unit (Fig. 3). The fine-structured absorption features at longer wavelengths resemble the absorption spectra of plain phenylcarbazole.⁵⁴ No distinct CT band can be observed as result of the decreased donor strength of PCz compared to TPA. In relation to the TPA based derivatives **5b** and **5d** display distinctly blue shifted emission with maxima at 387 nm and 390 nm. Again an insignificant difference between the benzene and pyridine was observed.

Low temperature phosphorescence spectra were recorded at 77 K, to determine the triplet energies (E_T s) of the potential host materials. Unlike the room temperature PL, low temperature phosphorescence featured vibronically resolved emission spectra (Fig. 2 and 3). Within the benzene series **3a** and **3b** exhibited similar E_T s of 2.68 eV and 2.70 eV. Surprisingly, **3c** displayed identical emission features indicating that the relevant triplet states are of similar nature. Analogously, pyridine based materials **3d** and **3e** featured E_T s of 2.69 eV and 2.70 eV, respectively. However, 1,5-substituted **4d** displayed diverse behavior with a broad phosphorescence emission without vibronic resolution and a lower E_T of 2.59 eV. Notably, the red shift of the phosphorescence emission is distinctly lower compared to the room temperature PL, which exhibits a large Stokes-shift in medium polar dichloromethane. This particular effect indicates that the red shifted emission is only partly due to the intramolecular charge transfer but also induced by a strong structural relaxation that is inhibited in the solid phase and/or specific interaction with the solvent. In analogy to room temperature PL also the triplet emission of the PCz-substituted host materials are blue shifted compared to the TPA derivatives and are located at very high values of 2.95 eV and 2.92 eV, respectively.

Thermal and electrochemical properties

The thermal properties of the materials were investigated by TGA and DSC. DSC analysis (Fig. S17 and S18 left†) revealed the

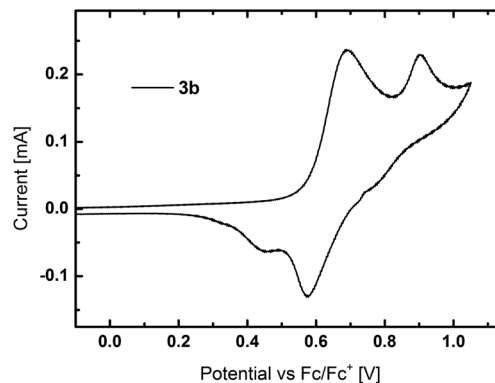


Fig. 4 CV curve of **3b**.

formation of stable films with glass transition temperatures (T_g s; determined from the second heating cycle of the DSC experiments) between 112 °C and 130 °C for the TPA-substituted derivatives. The introduction of PCz donors resulted in significantly increased T_g s of 182 °C and 171 °C for **5b** and **5d**, respectively.

Unlike the satisfying film properties, the thermal durability of the compounds was found to be average (Fig. S18 right and S19†). In contrast to the T_g s the decomposition temperatures T_d s (corresponding to the temperature of 5% mass loss) are not determined by the electron donor but the core ring system. Within the benzene series the T_d s span a narrow range between 332 °C and 338 °C, whereas the range of the T_d s of pyridine based materials is wider with **3d** (293 °C) and 1,5-substituted **4d** (355 °C) featuring the lowest and highest thermal stability, respectively.

Cyclic voltammetry (CV) was used to investigate the electrochemical properties of the materials (Fig. S20†). All TPA containing derivatives exhibited separated oxidation peaks, which are attributed to the two TPA units as exemplarily shown for **3b** in Fig. 4. Whereas the first oxidation is reversible, a further increase of voltage led to the formation of reactive species. The HOMO levels of all TPA based compounds are located in a narrow range from -5.35 eV to -5.39 eV. The sole exception is **3a** with a slightly higher lying HOMO at -5.27 eV. In contrast to the TPA compounds, PCz based host materials displayed irreversible oxidation, as typically observed for carbazole derivatives due to the instability of the formed cations.⁵⁵ Owing to the less electron rich PCz moieties, the HOMO levels of **5b** and **5d** are located at lower energies of -5.66 eV and -5.71 eV, respectively. The suitable located HOMO energies indicate no significant barrier for charge injection from adjacent layers in PhOLED devices.

The LUMO levels were calculated from the location of the HOMO and the optical bandgap and are located between -1.95 eV and -2.15 eV. Surprisingly, the incorporation of pyridine into the central core unit only negligibly influenced the energetic location of the LUMOs and the LUMO levels of pyridine based derivatives are only slightly lower compared to the corresponding benzene based congeners.

Computational investigations

Density functional theory (DFT) and time-dependent DFT (TDDFT) calculations were applied to obtain further insight into

Table 1 Physical data of the synthesized materials

	$T_g/T_m/T_d^a$ [°C]	Opt. BG ^{b,c} [eV]	$\lambda_{\max,PL}^c$ [nm]	HOMO/LUMO [eV]		E_T [eV]	
				Exp. ^d	Cal. ^e	Exp. ^f	Cal. ^g
3a	130/312/336	3.32	418	-5.27/-1.95	-5.46/-1.58	2.68	2.74
3b	121/n.o. ^h /338	3.34	418	-5.38/-2.04	-5.46/-1.53	2.70	2.79
3c	112/n.o. ^h /338	3.37	446	-5.37/-2.00	-5.42/-1.58	2.71	2.80
3d	122/220/293	3.31	424	-5.36/-2.06	-5.53/-1.64	2.69	2.79
3e	125/n.o. ^h /335	3.31	425	-5.35/-2.04	-5.52/-1.63	2.70	2.78
4d	112/n.o. ^h /355	3.33	505	-5.39/-2.06	-5.66/-1.91	2.59	2.87
5b	182/317/332	3.56	387	-5.66/-2.10	-5.83/-1.85	2.95	2.94
5d	171/323/340	3.56	390	-5.71/-2.15	-5.89/-2.01	2.92	3.01

^a Determined from TGA and DSC analysis; T_m - melting point, determined from the first cycle of the DSC experiments. ^b Estimated from the absorption onset. ^c Measured in DCM (5 μ M) at room temperature. ^d Calculated from the onset of the oxidation peak and the optical bandgap. ^e Calculated applying the density functional theory level (B3LYP/6-311+G*). ^f Estimated from the highest energy vibronic transition in solid solutions (1 mg ml⁻¹; toluene : EtOH = 9 : 1) at 77 K. ^g Calculated applying the time-dependent density functional theory level (B3LYP/6-311+G*). ^h Not observed.

the electronic layout of the developed materials. In general, the calculated HOMO and LUMO energy levels as well as E_T s are in good agreement with the experimental values (Table 1).

As expected the HOMO levels of the materials are mainly located at the electron rich triarylamine groups with the exception of **3a** (Fig. S21–S25[†]), as exemplarily depicted for **3b**, **5b** and **5d** (Fig. 5). This localization can be explained by the prevention of full conjugation resulting from the triazole linker, as already observed for smaller asymmetric chromophores.⁵²

The spatial extension of the HOMO levels of **5b** and **5d** is even smaller compared to the TPA derivatives, due to the decreased electron donating character of the PCz moiety. In case of **3a** the increased expansion of the HOMO onto the benzene core is due to the *para* substitution of the central aromatic moiety, which allows for better overall conjugation. Notably, this extension of the MO leads to a higher experimental determined HOMO energy compared to the corresponding *meta* and *ortho* derivatives. Furthermore, there are no significant differences between the extension of the HOMO levels between the benzene and pyridine based materials, which is again in agreement with the experimental results.

In analogy to the HOMOs, the LUMOs are mainly located on the three central aromatic rings and extend to the first phenyl

rings of the triarylamine moieties. In case of the materials with benzene cores the strong localization of the LUMO levels indicates the establishment of an electron accepting subunit caused by the triazole linkers without the presence of an additional electron withdrawing group.

For the 1,5-linked compound **4d**, a stronger localization of the MOs is found as result of the strongly twisted conformation and thus decreased conjugation, leading to slightly decreased energy levels. Furthermore, in **3c** with mixed substitution pattern the HOMO is exclusively located on the TPA unit connected to the 1,5-substituted triazole and the corresponding triazole itself, due to the asymmetric architecture of the molecule.

Electroluminescent properties

Prototype PhOLED devices were fabricated to explore the practical applicability of the developed materials. Compounds **3b** and **3d** were chosen as representative examples for device fabrication. Their common substitution pattern allows for a direct comparability. Furthermore, the good solubility of the two materials permits device fabrication from solution. As the E_T s of **3b** and **3d** are higher than those of green and red dopants, green emitting Ir(ppy)₂(acac) and red emitting Ir(MDQ)₂(acac) were chosen as emitters. Accordingly, prototype PhOLEDs were

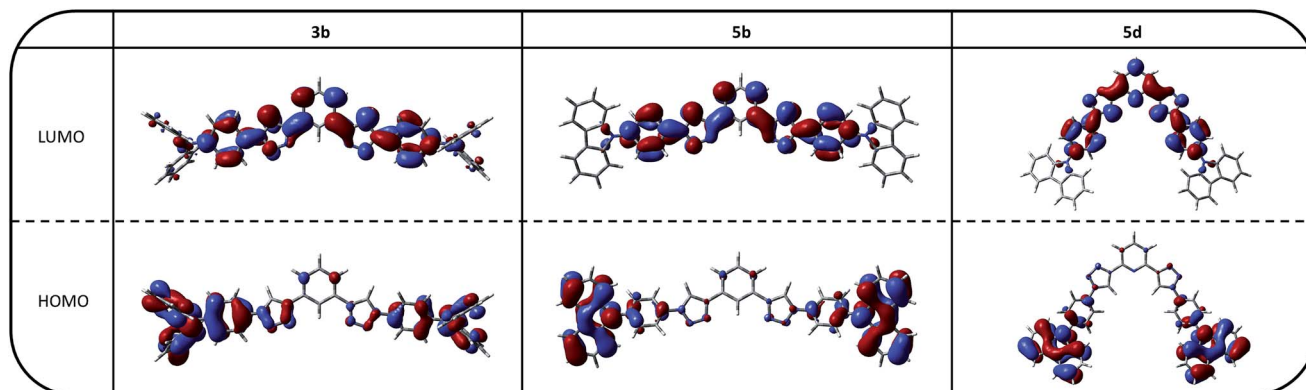


Fig. 5 Spatial distribution of HOMOs and LUMOs of **3b**, **5b** and **5d**.

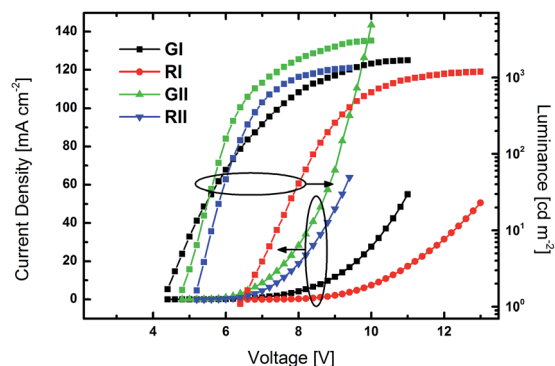


Fig. 6 Luminance–voltage–current density curves of devices GI, RI, GII and RII.

fabricated with the device architecture of ITO/PEDOT:PSS (45 nm)/EML (35 nm)/TPBi (GI–II: 50 nm; RI–II: 60 nm)/LiF/Al. PEDOT:PSS was employed as a hole injection and hole transporting layer, while TPBi was utilized as electron transporting and hole blocking layer. The emissive layers were made up of host materials **3b** (GI and RI) and **3d** (GII and RII) with emitters Ir(ppy)₂(acac) (G) and Ir(MDQ)₂(acac) (R) at a doping concentration of 8%.

Luminance–voltage–current density curves are depicted in Fig. 6 and current efficiency–luminance and power efficiency–luminance curves are depicted in Fig. 7. The key electroluminescent properties of the devices are summarized in Table 2.

All devices exclusively exhibited emission from the phosphorescent emitters (Fig. S26[†]), indicating that energy transfer from the host to the dopant was effective and that excitons were successfully confined on the emitters. Green devices GI and GII exhibited turn-on voltages (V_{on}) of 4.4 and 4.0 V, respectively, while the V_{on} s of RI and RII were slightly higher at 6.4 and 5.4 V. Notably, the current density in GII and RII, utilizing host material **3d** with a pyridine core, were significantly higher at lower voltage than in devices based on **3b** (Fig. 6). Among the green devices GI displayed the better performance with a maximum current efficiency (CE_{max}) of 35.0 cd A⁻¹ and a maximum power efficiency (PE_{max}) of 24.1 lm W⁻¹, while the

Table 2 Electroluminescent properties of devices GI, RI, GII and RII

	V_{on} [V]	CE^a [cd A ⁻¹]	PE^a [lm W ⁻¹]
GI	4.4	35.0/28.0	24.1/14.0
GII	5.0	18.7/17.7	12.2/9.4
RI	6.4	14.7/13.8	5.9/5.1
RII	5.4	14.1/14.0	7.4/7.0

^a Maximum value at 100 cd m⁻².

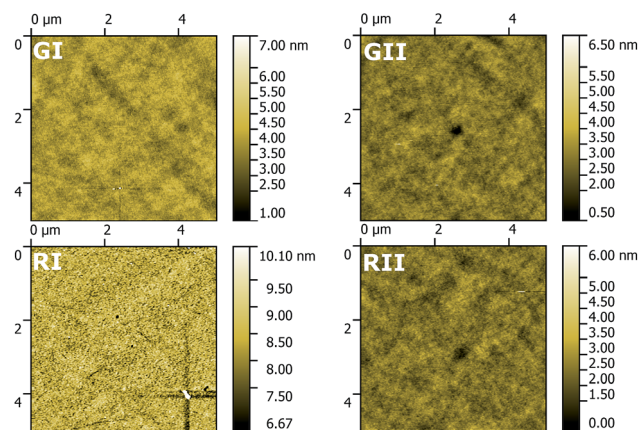


Fig. 8 Top-view AFM images of the EMLs of GI, GII, RI and RII.

values were lower for GII. In contrast RI and RII featured basically the same CE characteristics with CE_{max} of 14.7 and 14.1 cd A⁻¹, respectively. However, the PE of RII was slightly higher compared to RI, due to the lower driving voltage of RII.

Thin films of the four EMLs were investigated using AFM to explore their morphology (Fig. 8). In the case of all four EMLs films with a comparable low roughness (root mean square = 0.38, 0.35, 0.46 and 0.36 nm for GI, GII, RI and RII) were obtained. However, films based on **3b** and in particular GI are distributed more uniformly compared to films based on **3d**. This behaviour probably reduces the leak current, thus resulting in the superior device efficiency of GI compared to GII.

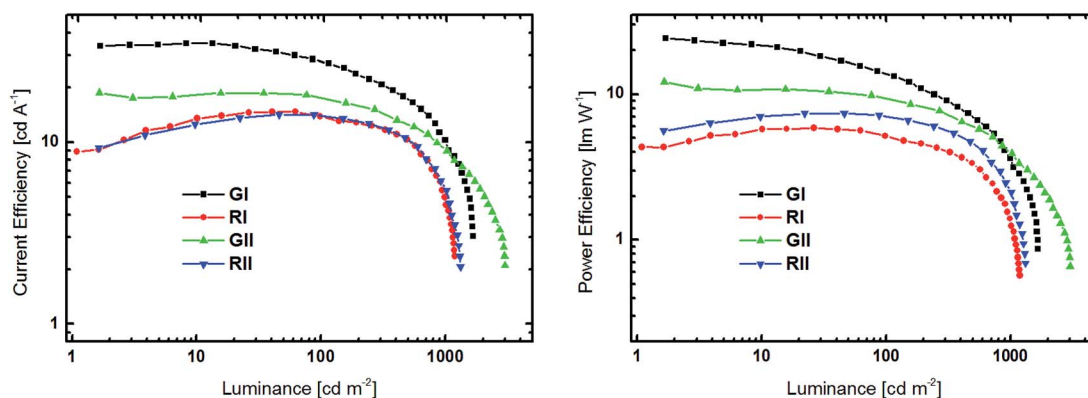


Fig. 7 Current efficiency–luminance (left) and power efficiency–luminance (right) curves devices GI, RI, GII and RII.

Conclusions

We have successfully demonstrated the application of a novel click linkage mode for the preparation of large band gap conjugated donor–acceptor materials. Beside the convenient synthetic approach this strategy allowed the modulation of the molecular properties, which solely depend on the substitution pattern of the employed 1,2,3-triazole linker but are independent of the nature and substitution pattern of the core units. The prepared materials were successfully employed as host materials in red and green prototype PhOLED devices to demonstrate a first practical application of this class of materials. The intriguingly simple preparation in combination with the significant impact on the molecular properties predestines the presented approach as a novel tool to tune the molecular properties of π -conjugated materials. Therefore, we present a useful methodology for the field of organic materials chemistry, also beyond optoelectronics.

Experimental section

General information

All reagents and solvents were purchased from commercial suppliers and used without further purification. Anhydrous solvents were prepared by filtration through drying columns. Experiments under microwave irradiation were performed in a Biotage Initiator Sixty microwave reactor. Column chromatography was performed on silica 60 (Merck, 40–63 μm). NMR spectra were recorded on a Bruker Avance DRX-400 Spectrometer. A Thermo Scientific LTQ Orbitrap XL hybrid FTMS (Fourier Transform Mass Spectrometer) equipped with an APCI source was used for high resolution mass spectrometry. Thermogravimetric (TG) and differential scanning calorimetry (DSC) measurements were carried out with a heating rate of 10 K min^{-1} in a flowing argon atmosphere (25 ml min^{-1}). For the TG measurements, a Netzsch TG 209 F9 Tarsus system with open aluminium oxide crucibles was used. For the DSC measurements, a Netzsch DSC 200 F3 Maia, working with aluminium pans with pierced lids was employed. UV/Vis absorption and fluorescence emission spectra were recorded in DCM solutions (5 μM) with a Perkin Elmer Lambda 750 spectrometer and an Edinburgh FLS920, respectively. Time resolved low temperature phosphorescence spectra were recorded in solid solutions (1 mg ml^{-1} ; toluene : EtOH = 9 : 1) at 77 K with a Perkin Elmer Instruments LS 50B luminance spectrometer. Cyclic voltammetry was performed using a three electrode configuration consisting of a Pt working electrode, a Pt counter electrode and an Ag/AgCl reference electrode and a PGSTAT128N, ADC164, DAC164, External, DI048 potentiostat provided by Metrohm Autolab B.V. Measurements were carried out in a 0.5 mM solution in anhydrous DCM with Bu_4NBF_4 (0.1 M) as supporting electrolyte. The solutions were purged with nitrogen for 15 minutes prior to measurement. HOMO energy levels were calculated from the onset of the oxidation peaks. The onset potential was determined by the intersection of two tangents drawn at the background and the rising of the oxidation peaks.

Synthetic details

4-Azido-*N,N*-diphenylbenzenamine **1i**⁵⁶ and 9-(4-azidophenyl)-9*H*-carbazole **1ii**⁵⁷ have been prepared from the corresponding boronic acid esters⁵⁸ and physical data acquired for the synthesized materials were identical with literature values. 1,4-Diethynylbenzene **2a**, 1,2-diethynylbenzene **2c**, 2,6-diethynylpyridine **2d** and 3,5-diethynylpyridine **2e** have been prepared by Sonogashira coupling starting from the corresponding dibromoaryls and trimethylsilylacetylene followed by desilylation.

General procedure for the CuAAC (“click”) reaction

A microwave reaction vessel was charged with dialkyne (1.00 eq.) and azide (2.50 eq.) in *t*-BuOH/ H_2O (1 : 1, 0.4 M). Immediately before the start of the reaction $\text{CuSO}_4 \cdot 5\text{H}_2\text{O}$ (0.20 eq.) and sodium ascorbate (0.40 eq.) were added, the vial was sealed with a septum and heated to 150 $^\circ\text{C}$ under microwave irradiation. After complete conversion (TLC; 30–60 min) the reaction mixture was poured on water and extracted with dichloromethane. The combined organic layers were dried over Na_2SO_4 and concentrated under reduced pressure. Purification of the crude products was accomplished by column chromatography.

4,4'-(1,4-Phenylendi-1*H*-1,2,3-triazol-4,1-diyl)bis[*N,N'*-diphenylbenzenamine] (**3a**)

Starting from **1i** (573 mg, 2.00 mmol), **2a** (101 mg, 0.80 mmol), $\text{CuSO}_4 \cdot 5\text{H}_2\text{O}$ (40 mg, 0.16 mmol) and sodium ascorbate (63 mg, 0.32 mmol) **3a** (346 mg, 0.50 mmol, 62%) was isolated after column chromatography (dichloromethane/ Et_2O = 99 : 1 \rightarrow 94 : 6). $^1\text{H-NMR}$ (400 MHz, CD_2Cl_2): δ = 8.23 (s, 2H), 8.01 (s, 4H), 7.63 (d, J = 8.8 Hz, 4H), 7.32 (t, J = 7.9 Hz, 8H), 7.20–7.09 (m, 16H) ppm. $^{13}\text{C-NMR}$ (100 MHz, CD_2Cl_2): δ = 149.1 (s), 148.1 (s), 147.7 (s), 131.5 (s), 131.0 (s), 130.1 (d), 126.7 (d), 125.6 (d), 124.4 (d), 123.7 (d), 122.1 (d), 118.5 (d) ppm. HRMS (APCI): m/z calculated for $\text{C}_{46}\text{H}_{34}\text{N}_8$: 698.29009 [M]⁺, 699.29792 [$\text{M} + \text{H}$]⁺; found: 698.28987 [M]⁺, 699.29685 [$\text{M} + \text{H}$]⁺.

4,4'-(1,3-Phenylendi-1*H*-1,2,3-triazol-4,1-diyl)bis[*N,N'*-diphenylbenzenamine] (**3b**)

Starting from **1i** (143 mg, 0.50 mmol), **2b** (25 mg, 0.20 mmol), $\text{CuSO}_4 \cdot 5\text{H}_2\text{O}$ (10 mg, 0.04 mmol) and sodium ascorbate (16 mg, 0.08 mmol) **3b** (128 mg, 0.18 mmol, 91%) was isolated after column chromatography (dichloromethane/ Et_2O = 97 : 3 \rightarrow 93 : 7). $^1\text{H-NMR}$ (400 MHz, CD_2Cl_2): δ = 8.45 (s, 1H), 8.30 (s, 2H), 7.92 (dd, J_1 = 7.7 Hz, J_2 = 1.8 Hz, 2H), 7.63 (d, J = 8.8 Hz, 4H), 7.56 (t, J = 7.7 Hz, 1H), 7.32 (t, J = 7.9 Hz, 8H), 7.19–7.09 (m, 16H) ppm. $^{13}\text{C-NMR}$ (100 MHz, CD_2Cl_2): δ = 149.1 (s), 148.1 (s), 147.7 (s), 131.8 (s), 131.5 (s), 130.1 (d), 130.1 (d), 126.0 (d), 125.6 (d), 124.3 (d), 123.6 (d), 123.4 (d), 122.0 (d), 118.7 (d) ppm. HRMS (APCI): m/z calculated for $\text{C}_{46}\text{H}_{34}\text{N}_8$: 698.29009 [M]⁺, 699.29792 [$\text{M} + \text{H}$]⁺; found: 698.28976 [M]⁺, 699.29685 [$\text{M} + \text{H}$]⁺.

4-[4-[2-[1-[4-(Diphenylamino)phenyl]-1*H*-1,2,3-triazol-5-yl]phenyl]-1*H*-1,2,3-triazol-1-yl]-*N,N*-diphenylbenzenamine (**3c**)

Starting from **1i** (573 mg, 2.00 mmol), **2c** (101 mg, 0.80 mmol), $\text{CuSO}_4 \cdot 5\text{H}_2\text{O}$ (40 mg, 0.16 mmol) and sodium ascorbate (63 mg,

0.32 mmol) **3c** (158 mg, 0.23 mmol, 28%) was isolated after column chromatography (dichloromethane/Et₂O = 97 : 3 → 91 : 9). ¹H-NMR (400 MHz, CD₂Cl₂): δ = 7.92 (d, *J* = 7.9 Hz, 1H), 7.85 (s, 1H), 7.66–7.56 (m, 1H), 7.52–7.47 (m, 2H), 7.37 (d, *J* = 8.9 Hz, 2H), 7.33–7.23 (m, 8H), 7.13–7.03 (m, 15H), 6.80–6.78 (m, 4H) ppm. ¹³C-NMR (100 MHz, CD₂Cl₂): δ = 149.2 (s), 148.8 (s), 147.7 (s), 147.6 (s), 146.3 (s), 137.3 (s), 134.8 (d), 131.9 (d), 131.2 (s), 131.1 (s), 130.8 (d), 130.4 (s), 130.1 (d), 130.0 (d), 129.8 (d), 129.2 (d), 125.8 (s), 125.6 (d), 125.5 (d), 124.7 (d), 124.4 (d), 124.2 (d), 123.5 (d), 122.8 (d), 122.2 (d), 120.0 (d). HRMS (APCI): *m/z* calculated for C₄₆H₃₄N₈: 698.29009 [M]⁺, 698.28980 [M + H]⁺, found: 698.28987 [M]⁺, 699.29675 [M + H]⁺.

4,4'-(2,6-Pyridindi-1*H*-1,2,3-triazol-4,1-diyl)bis[*N,N'*-diphenylbenzenamine] (**3d**)

Starting from **1i** (143 mg, 0.50 mmol), **2d** (25 mg, 0.20 mmol), CuSO₄·5H₂O (10 mg, 0.04 mmol) and sodium ascorbate (16 mg, 0.08 mmol) **3d** (116 mg, 0.17 mmol, 83%) was isolated after column chromatography (dichloromethane/Et₂O = 96 : 4). ¹H-NMR (400 MHz, CD₂Cl₂): δ = 8.62 (s, 2H), 8.16 (d, *J* = 8.0 Hz, 2H), 7.94 (t, *J* = 7.9 Hz, 1H), 7.67 (d, *J* = 8.8 Hz, 4H), 7.32 (t, *J* = 7.9 Hz, 8H), 7.20–7.09 (m, 16H) ppm. ¹³C-NMR (100 MHz, CD₂Cl₂): δ = 150.6 (s), 149.2 (s), 149.2 (s), 147.7 (s), 138.4 (d), 131.5 (s), 130.1 (d), 125.6 (d), 124.4 (d), 123.6 (d), 122.1 (d), 120.7 (d), 119.9 (d) ppm. HRMS (APCI): *m/z* calculated for C₄₅H₃₃N₉: 700.29317 [M + H]⁺, found: 700.29304 [M + H]⁺.

4,4'-(3,5-Pyridindi-1*H*-1,2,3-triazol-4,1-diyl)bis[*N,N'*-diphenylbenzenamine] (**3e**)

Starting from **1i** (129 mg, 0.45 mmol), **2e** (23 mg, 0.18 mmol), CuSO₄·5H₂O (9 mg, 0.04 mmol) and sodium ascorbate (14 mg, 0.07 mmol) **3e** (65 mg, 0.09 mmol, 52%) was isolated after column chromatography (dichloromethane/Et₂O = 95 : 5 → 82 : 18). ¹H-NMR (400 MHz, CD₂Cl₂): δ = 9.09 (s, 2H), 8.74 (t, *J* = 1.9 Hz, 1H), 8.36 (s, 2H), 7.63 (d, *J* = 8.8 Hz, 4H), 7.32 (t, *J* = 7.9 Hz, 8H), 7.20–7.09 (m, 16H) ppm. ¹³C-NMR (100 MHz, CD₂Cl₂): δ = 149.3 (s), 147.7 (s), 147.0 (d), 145.3 (s), 131.2 (s), 130.1 (d), 130.0 (d), 127.2 (s), 125.6 (d), 124.4 (d), 123.5 (d), 122.1 (d), 119.2 (d) ppm. HRMS (APCI): *m/z* calculated for C₄₅H₃₃N₉: 699.28534 [M]⁺, 700.29317 [M + H]⁺. Found: 699.28400 [M]⁺, 700.29201 [M + H]⁺.

4,4'-(2,6-Pyridindi-1*H*-1,2,3-triazol-5,1-diyl)bis[*N,N'*-diphenylbenzenamine] (**4d**)

The synthesis of **4d** was accomplished following a previously published procedure.⁵³ **1i** (515 mg, 1.80 mmol, 2.40 eq.) and **2d** (95 mg, 0.75 mmol, 1 eq.) were dissolved in 3 ml degassed DMSO in a reaction vial. Subsequently, tetramethylammonium hydroxide (27 mg, 0.075 mmol, 0.1 eq., 25 wt% in H₂O) was added and the reaction mixture was heated to 80 °C in a heating block for 27 h. The reaction mixture was poured on H₂O and repeatedly extracted with dichloromethane. The combined organic layers were dried over Na₂SO₄ and concentrated under reduced pressure. **4d** (95 mg, 0.14 mmol, 18%) was isolated after column chromatography (dichloromethane/Et₂O = 98 : 1 → 91 : 9). ¹H-NMR (400 MHz, CD₂Cl₂): δ = 7.88 (s, 2H), 7.74 (t, *J* = 8.1 Hz, 1H), 7.34–7.29 (m, 10H), 7.17–7.05 (m, 20H) ppm. ¹³C-NMR (100 MHz, CD₂Cl₂): δ =

149.6 (s), 147.6 (s), 147.2 (s), 138.3 (d), 137.0 (s), 134.7 (d), 130.9 (s), 130.1 (d), 127.0 (d), 125.8 (d), 124.5 (d), 122.8 (d), 122.6 (d) ppm. HRMS (APCI): *m/z* calculated for C₄₅H₃₃N₉: 699.28534 [M]⁺, 700.29317 [M + H]⁺, found: 699.28455 [M]⁺, 700.29232 [M + H]⁺.

9,9'-[1,3-Phenyldiylbis(1*H*-1,2,3-triazol-4,1-diyl-4,1-phenylen)]bis[9*H*-carbazole] (**5b**)

Starting from **1ii** (745 mg, 2.62 mmol), **2b** (134 mg, 1.06 mmol), CuSO₄·5H₂O (53 mg, 0.21 mmol) and sodium ascorbate (83 mg, 0.42 mmol) **5b** (533 mg, 0.77 mmol, 72%) was isolated after column chromatography (dichloromethane/Et₂O = 99 : 1 → 97 : 3). ¹H-NMR (400 MHz, CD₂Cl₂): δ = 8.59 (t, *J* = 1.6 Hz, 1H), 8.52 (s, 2H), 8.18 (d, *J* = 7.8 Hz, 4H), 8.11 (d, *J* = 8.9 Hz, 4H), 8.02 (dd, *J*₁ = 7.7, *J*₂ = 1.9 Hz, 2H), 7.83 (d, *J* = 8.8 Hz, 4H), 7.65 (t, *J* = 7.8 Hz, 1H), 7.52–7.45 (m, 8H), 7.34 (td, *J*₁ = 7.3, *J*₂ = 1.4 Hz, 4H) ppm. ¹³C-NMR (100 MHz, CD₂Cl₂): δ = 148.6 (s), 141.2 (s), 138.7 (s), 136.3 (s), 131.6 (s), 130.3 (d), 128.9 (d), 126.8 (d), 126.3 (d), 124.1 (s), 123.6 (d), 122.5 (d), 120.9 (d), 120.9 (d), 118.8 (d), 110.2 (d) ppm. HRMS (APCI): *m/z* calculated for C₄₆H₃₀N₈: 695.26662 [M + H]⁺, found: 695.26575 [M + H]⁺.

9,9'-[2,6-Pyridindiylbis(1*H*-1,2,3-triazol-4,1-diyl-4,1-phenylen)]bis[9*H*-carbazole] (**5d**)

Starting from **1ii** (142 mg, 0.50 mmol), **2d** (25 mg, 0.20 mmol), CuSO₄·5H₂O (10 mg, 0.04 mmol) and sodium ascorbate (16 mg, 0.08 mmol) **5d** (94 mg, 0.13 mmol, 68%) was isolated after column chromatography (dichloromethane/Et₂O = 99 : 1 → 95 : 5). ¹H-NMR (400 MHz, CD₂Cl₂): δ = 8.86 (s, 2H), 8.26 (d, *J* = 8.1 Hz, 2H), 8.19–8.13 (m, 8H), 8.02 (t, *J* = 7.9 Hz, 1H), 7.84 (d, *J* = 8.4 Hz, 4H), 7.52–7.44 (m, 8H), 7.33 (t, *J* = 7.3 Hz, 4H) ppm. ¹³C-NMR (100 MHz, CD₂Cl₂): δ = 150.5 (s), 149.7 (s), 141.2 (s), 138.8 (s), 138.6 (d), 136.3 (s), 128.9 (d), 126.8 (d), 124.1 (s), 122.6 (d), 121.0 (d), 120.9 (d), 120.9 (d), 120.3 (d), 110.2 (d) ppm. HRMS (APCI): *m/z* calculated for C₄₅H₂₉N₉: 695.25404 [M]⁺, 696.26187 [M + H]⁺, found: 695.25171 [M]⁺, 696.26094 [M + H]⁺.

Computational details

All (TD)DFT computations were performed using the Gaussian 09 package, revision D.01.⁵⁹ Density functional theory (DFT) and time-dependent (TD)DFT calculations were performed using the Becke three parameters hybrid functional with Lee–Yang–Perdew correlation (B3LYP),^{60,61} in combination with Pople basis sets (6-31G*, 6-311+G*).⁶² Geometry optimizations were performed in gas phase and without symmetry constraints. For the calculation of HOMO/LUMO levels, ground state (S₀) geometries were optimized applying the 6-311+G* basis set. The determination of triplet energy (*E*_T) was achieved by the calculation of the *T*₁ excitation energy applying TDDFT level and the 6-311+G* basis to a S₀ geometry optimized at DFT level using the 6-31G* basis set. Orbital plots were generated using GaussView.⁶³

Single crystal diffraction

Crystals suitable for single crystal diffraction were selected under a polarizing microscope, embedded in perfluorinated oil and attached to Kapton® micromounts. Intensity data were collected

in a dry stream of nitrogen at 100 K on a Bruker KAPPA APEX II diffractometer system. Data were reduced using SAINT-Plus⁶⁴ and an empirical absorption correction using the multi-scan approach implemented in SADABS⁶⁴ was applied. The crystal structures were solved by charge-flipping implemented in SUPERFLIP⁶⁵ and refined against F with the JANA2006 (ref. 66) software package. The non-H atoms were refined with anisotropic displacement parameters. The H atoms were placed at calculated positions and refined as riding on the parent C atoms.

Device fabrication and measurement

All devices were fabricated on glass substrates pre-coated with a 180 nm thick layer of indium tin oxide (ITO) having a sheet resistance of 10 Ω per square. The ITO substrates were ultrasonically cleaned with detergent, deionized water, acetone and isopropanol, and then dried by blowing nitrogen over them. A layer of 45 nm thick PEDOT:PSS was spin-coated onto the pre-cleaned ITO substrates, and then baked at 120 °C in a vacuum oven for 30 min to extract residual water. Afterwards, the samples were moved into a glove box under a nitrogen-protected environment (oxygen and water contents less than 1 ppm), and the emissive layers (EMLs) were spin-coated on top of PEDOT:PSS from chlorobenzene and then annealed at 100 °C in a vacuum oven for 10 min to remove the residual solvent; the resulting thickness of EMLs is about 35 nm. Following that, the samples were transferred to a thermal evaporator chamber (pressure less than 5×10^{-4} Pa) connected to the glove box without exposure to the atmosphere. TBPI, LiF and Al were deposited sequentially by thermal evaporation. The overlap between ITO and Al electrodes was 16 mm² as the active emissive area of the devices. The luminance–voltage–current density characteristics were measured by a Keithley source measurement unit (Keithley 2400 and Keithley 2000) with a calibrated silicon photodiode. The EL spectra were measured by SpectraScan PR650 spectrophotometer. The film thickness was determined by Dektak 6M Profiler (Veeco Metrology Inc.). All the measurements were carried out in ambient atmosphere.

Acknowledgements

This work was supported in part by the TU Wien “Innovative Projects” research funds and the Austrian Federal Ministry of Science, Research and Economy. The X-ray centre of the Vienna University of Technology is acknowledged for providing access to the single-crystal diffractometer. The authors acknowledge P. Gauss, E. Schönegger and D. Liu for contributing to the synthesis of the materials and C. Hametner for assistance during NMR characterization. P. K., T. K. and J. F. gratefully acknowledge financial support by the Austrian Science Fund (FWF) (grant No. I 2589-N34). J. C. and D. M. gratefully acknowledge financial support by the National Natural Science Foundation of China (grant No. 11661131001).

Notes and references

- 1 Y. Tao, C. Yang and J. Qin, *Chem. Soc. Rev.*, 2011, **40**, 2943–2970.
- 2 Y. Tao, K. Yuan, T. Chen, P. Xu, H. Li, R. Chen, C. Zheng, L. Zhang and W. Huang, *Adv. Mater.*, 2014, **26**, 7931–7958.
- 3 A. Chaskar, H.-F. Chen and K.-T. Wong, *Adv. Mater.*, 2011, **23**, 3876–3895.
- 4 A. Mishra and P. Bäuerle, *Angew. Chem., Int. Ed.*, 2012, **51**, 2020–2067.
- 5 M. J. Cho, D. H. Choi, P. A. Sullivan, A. J. P. Akelaitis and L. R. Dalton, *Prog. Polym. Sci.*, 2008, **33**, 1013–1058.
- 6 S.-i. Kato and F. Diederich, *Chem. Commun.*, 2010, **46**, 1994–2006.
- 7 G. S. He, L.-S. Tan, Q. Zheng and P. N. Prasad, *Chem. Rev.*, 2008, **108**, 1245–1330.
- 8 Y. Shirota, *J. Mater. Chem.*, 2000, **10**, 1–25.
- 9 S. Reineke, *Nat. Mater.*, 2015, **14**, 459–462.
- 10 C. W. Tang and S. A. VanSlyke, *Appl. Phys. Lett.*, 1987, **51**, 913–915.
- 11 M. A. Baldo, D. F. O'Brien, Y. You, A. Shoustikov, S. Sibley, M. E. Thompson and S. R. Forrest, *Nature*, 1998, **395**, 151–154.
- 12 M. A. Baldo, S. Lamansky, P. E. Burrows, M. E. Thompson and S. R. Forrest, *Appl. Phys. Lett.*, 1999, **75**, 4–6.
- 13 M. A. Baldo, D. F. O'Brien, M. E. Thompson and S. R. Forrest, *Phys. Rev. B: Condens. Matter Mater. Phys.*, 1999, **60**, 14422–14428.
- 14 C. Adachi, M. A. Baldo, M. E. Thompson and S. R. Forrest, *J. Appl. Phys.*, 2001, **90**, 5048–5051.
- 15 M. A. Baldo, C. Adachi and S. R. Forrest, *Phys. Rev. B: Condens. Matter Mater. Phys.*, 2000, **62**, 10967–10977.
- 16 C. Murawski, K. Leo and M. C. Gather, *Adv. Mater.*, 2013, **25**, 6801–6827.
- 17 S. O. Jeon and J. Y. Lee, *J. Mater. Chem.*, 2012, **22**, 4233–4243.
- 18 K. S. Yook and J. Y. Lee, *Adv. Mater.*, 2012, **24**, 3169–3190.
- 19 S. Reineke, M. Thomschke, B. Lüssem and K. Leo, *Rev. Mod. Phys.*, 2013, **85**, 1245–1293.
- 20 W.-C. Chen, C.-S. Lee and Q.-X. Tong, *J. Mater. Chem. C*, 2015, **3**, 10957–10963.
- 21 M. Guan, Z. Q. Chen, Z. Q. Bian, Z. W. Liu, Z. L. Gong, W. Baik, H. J. Lee and C. H. Huang, *Org. Electron.*, 2006, **7**, 330–336.
- 22 L. Zeng, T. Y.-H. Lee, P. B. Merkel and S. H. Chen, *J. Mater. Chem.*, 2009, **19**, 8772–8781.
- 23 Y. Zheng, A. S. Batsanov, V. Jankus, F. B. Dias, M. R. Bryce and A. P. Monkman, *J. Org. Chem.*, 2011, **76**, 8300–8310.
- 24 P. Kautny, Z. Wu, B. Stöger, A. Tissot, E. Horkel, J. Chen, D. Ma, H. Hagemann, J. Fröhlich and D. Lumpi, *Org. Electron.*, 2015, **17**, 216–228.
- 25 Y. Tao, Q. Wang, L. Ao, C. Zhong, C. Yang, J. Qin and D. Ma, *J. Phys. Chem. C*, 2010, **114**, 601–609.
- 26 Y. Tao, Q. Wang, C. Yang, C. Zhong, K. Zhang, J. Qin and D. Ma, *Adv. Funct. Mater.*, 2010, **20**, 304–311.
- 27 P. Kautny, D. Lumpi, Y. Wang, A. Tissot, J. Binting, E. Horkel, B. Stöger, C. Hametner, H. Hagemann, D. Ma and J. Fröhlich, *J. Mater. Chem. C*, 2014, **2**, 2069–2081.
- 28 Z. Ge, T. Hayakawa, S. Ando, M. Ueda, T. Akiike, H. Miyamoto, T. Kajita and M.-a. Kakimoto, *Org. Lett.*, 2008, **10**, 421–424.
- 29 C.-L. Ho and W.-Y. Wong, *New J. Chem.*, 2013, **37**, 1665–1683.

- 30 A. Qin, J. W. Y. Lam and B. Z. Tang, *Chem. Soc. Rev.*, 2010, **39**, 2522–2544.
- 31 V. V. Rostovtsev, L. G. Green, V. V. Fokin and K. B. Sharpless, *Angew. Chem., Int. Ed.*, 2002, **41**, 2596–2599.
- 32 F. Amblard, J. H. Cho and R. F. Schinazi, *Chem. Rev.*, 2009, **109**, 4207–4220.
- 33 J. E. Hein and V. V. Fokin, *Chem. Soc. Rev.*, 2010, **39**, 1302–1315.
- 34 I. Stengel, A. Mishra, N. Pootrakulchote, S. J. Moon, S. M. Zakeeruddin, M. Grätzel and P. Bäuerle, *J. Mater. Chem.*, 2011, **21**, 3726–3734.
- 35 M. Juricek, M. Felici, P. Contreras-Carballada, J. Lauko, S. R. Bou, P. H. J. Kouwer, A. M. Brouwer and A. E. Rowan, *J. Mater. Chem.*, 2011, **21**, 2104–2111.
- 36 R. M. Meudtner, M. Ostermeier, R. Goddard, C. Limberg and S. Hecht, *Chem.–Eur. J.*, 2007, **13**, 9834–9840.
- 37 Y. H. Lau, P. J. Rutledge, M. Watkinson and M. H. Todd, *Chem. Soc. Rev.*, 2011, **40**, 2848–2866.
- 38 M. Parent, O. Mongin, K. Kamada, C. Katan and M. Blanchard-Desce, *Chem. Commun.*, 2005, 2029–2031.
- 39 D. Lumpi, F. Glöcklhofer, B. Holzer, B. Stöger, C. Hametner, G. A. Reider and J. Fröhlich, *Cryst. Growth Des.*, 2014, **14**, 1018–1031.
- 40 S. Ast, T. Fischer, H. Müller, W. Mickler, M. Schwichtenberg, K. Rurack and H. J. Holdt, *Chem.–Eur. J.*, 2013, **19**, 2990–3005.
- 41 S. S. Bag and R. Kundu, *J. Org. Chem.*, 2011, **76**, 3348–3356.
- 42 A.-S. Cornec, C. Baudequin, C. Fiol-Petit, N. Plé, G. Dupas and Y. Ramondenc, *Eur. J. Org. Chem.*, 2013, **2013**, 1908–1915.
- 43 D. J. V. C. van Steenis, O. R. P. David, G. P. F. van Strijdonck, J. H. van Maarseveen and J. N. H. Reek, *Chem. Commun.*, 2005, 4333–4335.
- 44 M. K. Kim, J. Kwon, T.-H. Kwon and J. I. Hong, *New J. Chem.*, 2010, **34**, 1317–1322.
- 45 D. Liu, D. Li, M. Wang and W. Li, *J. Mater. Chem. C*, 2016, **4**, 7260–7268.
- 46 M.-k. Leung, Y.-H. Hsieh, T.-Y. Kuo, P.-T. Chou, J.-H. Lee, T.-L. Chiu and H.-J. Chen, *Org. Lett.*, 2013, **15**, 4694–4697.
- 47 J. Zhuang, W. Su, W. Li, Y. Zhou, Q. Shen and M. Zhou, *Org. Electron.*, 2012, **13**, 2210–2219.
- 48 J. Zhuang, W. Li, W. Su, M. Zhou and Z. Cui, *New J. Chem.*, 2014, **38**, 650–656.
- 49 Y. Chi and P.-T. Chou, *Chem. Soc. Rev.*, 2010, **39**, 638–655.
- 50 Y. Zhao, J. Tang, H. Zhang and Y. Ma, *Eur. J. Inorg. Chem.*, 2014, **2014**, 4843–4851.
- 51 J. Feldman, G. D. Vo, C. D. McLaren, T. C. Gehret, K.-H. Park, J. S. Meth, W. J. Marshall, J. Buriak, L. M. Bryman, K. D. Dobbs, T. H. Scholz and S. G. Zane, *Organometallics*, 2015, **34**, 3665–3669.
- 52 P. Kautny, D. Bader, B. Stöger, G. A. Reider, J. Fröhlich and D. Lumpi, *Chem.–Eur. J.*, 2016, **22**, 18887–18898.
- 53 S. W. Kwok, J. R. Fotsing, R. J. Fraser, V. O. Rodionov and V. V. Fokin, *Org. Lett.*, 2010, **12**, 4217–4219.
- 54 H. Li, Y. Wang, K. Yuan, Y. Tao, R. Chen, C. Zheng, X. Zhou, J. Li and W. Huang, *Chem. Commun.*, 2014, **50**, 15760–15763.
- 55 J. F. Ambrose and R. F. Nelson, *J. Electrochem. Soc.*, 1968, **115**, 1159–1164.
- 56 Q. Zhang, Z. Ning and H. Tian, *Dyes Pigm.*, 2009, **81**, 80–84.
- 57 A. Hörner, D. Volz, T. Hagendorn, D. Füniss, L. Greb, F. Rönicke, M. Nieger, U. Schepers and S. Bräse, *RSC Adv.*, 2014, **4**, 11528–11534.
- 58 K. D. Grimes, A. Gupte and C. C. Aldrich, *Synthesis*, 2010, 1441–1448.
- 59 M. J. Frisch, G. W. Trucks, H. B. Schlegel, G. E. Scuseria, M. A. Robb, J. R. Cheeseman, G. Scalmani, V. Barone, B. Mennucci, G. A. Petersson, H. Nakatsuji, M. Caricato, X. Li, H. P. Hratchian, A. F. Izmaylov, J. Bloino, G. Zheng, J. L. Sonnenberg, M. Hada, M. Ehara, K. Toyota, R. Fukuda, J. Hasegawa, M. Ishida, T. Nakajima, Y. Honda, O. Kitao, H. Nakai, T. Vreven, J. A. Montgomery Jr, J. E. Peralta, F. Ogliaro, M. J. Bearpark, J. Heyd, E. N. Brothers, K. N. Kudin, V. N. Staroverov, R. Kobayashi, J. Normand, K. Raghavachari, A. P. Rendell, J. C. Burant, S. S. Iyengar, J. Tomasi, M. Cossi, N. Rega, N. J. Millam, M. Klene, J. E. Knox, J. B. Cross, V. Bakken, C. Adamo, J. Jaramillo, R. Gomperts, R. E. Stratmann, O. Yazyev, A. J. Austin, R. Cammi, C. Pomelli, J. W. Ochterski, R. L. Martin, K. Morokuma, V. G. Zakrzewski, G. A. Voth, P. Salvador, J. J. Dannenberg, S. Dapprich, A. D. Daniels, Ö. Farkas, J. B. Foresman, J. V. Ortiz, J. Cioslowski and D. J. Fox, *Gaussian 09, Revision D.01*, Gaussian, Inc., Wallingford, CT, USA, 2009.
- 60 C. Lee, W. Yang and R. G. Parr, *Phys. Rev. B: Condens. Matter Mater. Phys.*, 1988, **37**, 785–789.
- 61 A. D. Becke, *J. Chem. Phys.*, 1993, **98**, 5648–5652.
- 62 R. Krishnan, J. S. Binkley, R. Seeger and J. A. Pople, *J. Chem. Phys.*, 1980, **72**, 650–654.
- 63 R. Dennington, T. Keith and J. Millam, *GaussView, Version 5*, Semichem, Inc., Shawnee Mission, KS, 2009.
- 64 *Bruker computer programs: APEX2, SAINT and SADABS*, Bruker AXS Inc., Madison, WI, 2015.
- 65 L. Palatinus and G. Chapuis, *J. Appl. Crystallogr.*, 2007, **40**, 786–790.
- 66 V. Petříček, M. Dušek and L. Palatinus, *Z. Kristallogr.–Cryst. Mater.*, 2014, **229**, 345–352.

2.10. Manuscript #10

Thiophene ring-fragmentation reactions: Principles and scale-up towards NLO materials

Daniel Lumpi, Johannes Steindl, Sebastian Steiner, Victor Carl, Paul Kautny, Michael Schön, Florian Glöcklhofer, Brigitte Holzer, Berthold Stöger, Ernst Horkel, Christian Hametner, Georg Reider, Marko D. Mihovilovic, Johannes Fröhlich

Tetrahedron, **2017**, 73, 472-280

Reproduced with the kind permission of Elsevier B. V.



Thiophene ring-fragmentation reactions: Principles and scale-up towards NLO materials



Daniel Lumpi^{a,*}, Johannes Steindl^a, Sebastian Steiner^a, Victor Carl^a, Paul Kautny^a, Michael Schön^a, Florian Glöcklhofer^a, Brigitte Holzer^a, Berthold Stöger^b, Ernst Horkel^a, Christian Hametner^a, Georg Reider^c, Marko D. Mihovilovic^a, Johannes Fröhlich^a

^a Institute of Applied Synthetic Chemistry, TU Wien, Getreidemarkt 9/163, A-1060 Vienna, Austria

^b Institute of Chemical Technologies and Analytics, TU Wien, Getreidemarkt 9/164-SC, A-1060 Vienna, Austria

^c Photonics Institute, TU Wien, Gusshausstraße 27-29, A-1040 Vienna, Austria

ARTICLE INFO

Article history:

Received 26 September 2016

Received in revised form

10 December 2016

Accepted 12 December 2016

Available online 18 December 2016

Keywords:

Thiophene ring-opening

Reaction mechanism

Reaction kinetics

Inline monitoring

Second harmonic generation

ABSTRACT

A systematic study on the thiophene ring-fragmentation (TRF) reaction, yielding the Z-isomer of ene-yne type compounds, is presented. The investigations focus on the origins and pathways of potential side-reactions, resulting in an advanced synthetic protocol featuring enhanced selectivity and efficiency. The fragmentation threshold temperatures as well as reaction kinetics have been investigated utilizing inline infrared spectroscopy revealing unexpected results particularly concerning the reaction order (zero-order process). With regard to safety, selectivity, and up-scaling a flow-chemistry procedure for the TRF reaction has been developed. Finally, the technological relevance of the ene-yne structural motif is extended by a new design concept for NLO-chromophores showing the highest second harmonic generation efficiencies reported for these scaffolds.

© 2016 Elsevier Ltd. All rights reserved.

1. Introduction

The base induced ring-opening reaction of heterocycles is a well-established methodology in organic chemistry.¹ In particular, the organo-metal intermediated ring-fragmentation of thiophene derivatives, leading to “ene-yne” type compounds, is one of the best-studied ring-opening reactions.^{1–3} Early observations of the formation of “unsaturated aliphatic products” from 3-thienyllithium date back to 1962,⁴ however, the mechanism has not been understood at that time. The first report on controlled ring-fragmentation was given by Gronowitz et al. in 1969 on the selenophene structure.⁵ These findings were followed by publications of S. Gronowitz et al.⁶ and K. Jakobsen⁷ demonstrating thiophene ring-opening reactions; similar studies on benzo[b]thiophene were presented by B. Iddon et al.⁸ Recent extensions of the strategy represent double-sided ring-opened species *via* a tandem fragmentation process.^{9–11}

Thiophene ring-fragmentations (TRF) (Scheme 1) proceed with

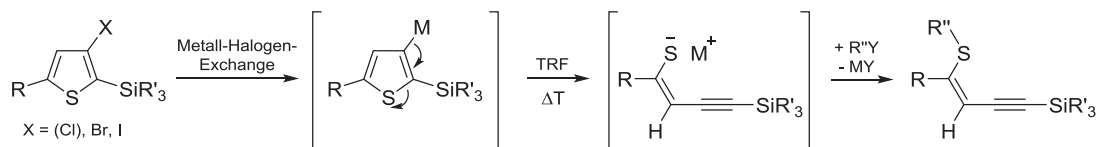
remarkable stereoselectivity yielding Z-isomers, selectively^{1–3,5–11}; alternative approaches to synthesize these scaffolds typically suffer from poor regio- or/and stereoselectivity.¹ Driven by the broad variety of potential applications, intense research in the development of stereoselective approaches *via* e.g. carbo- or hydrothiolation, in order to obtain Z-organylthioenynes but also vinyl sulfides,^{12–17} has been reported.

The scope of possible modifications, functionalizations (e.g. cycloaddition, Sonogashira-coupling, Michael-addition, nucleophilic substitution, oxidation) and applications of TRF-products was demonstrated to be widespread.¹⁸ Another important factor for applications, e.g. in materials science, is the potential to selectively oxidize the alkylthio group.^{18,19} This strategy enables to convert the +M- (alkylthio) directly into a –M-substituent (sulfoxide or sulfone), thus significantly influencing electronic properties.²⁰

Moreover, ene-yne substructures are found in natural products (e.g. Anthemis species)^{21–23} and, thus, represent attractive building blocks for total synthesis. Organylthioenynes are also useful synthons in organic synthesis, as these scaffolds can be utilized as precursors to enedynes and other functionalized olefins.¹⁴ Vinyl sulfides are widely applied in organic synthesis as versatile intermediates¹² and were identified in several biologically active

* Corresponding author.

E-mail address: daniel.lumpi@tuwien.ac.at (D. Lumpi).



Scheme 1. Generally accepted reaction mechanism of thiophene ring-fragmentation.

molecules.^{12–14,24–26} In particular, aromatic vinyl-sulfide derivatives are found in various pharmaceutically active drugs against important diseases such as Alzheimer's, Parkinson's, diabetes, AIDS, and cancer.^{14,27,28} For potential pharmaceutical applications the selectivity of the synthetic approach with respect to double bond geometry is an important issue.

Recently, our group has reported on ene-yne derived nonlinear optical (NLO) materials capable of second harmonic (SH) generation.^{29–31} Direct functionalization of TRF-products via copper(I)-catalyzed azide-alkyne cycloaddition (CuAAC)^{32,33} applying phenylazide yielded NLO materials featuring twice the SH-efficiency of potassium dihydrogen phosphate (KH₂PO₄ - KDP).³⁰ Furthermore, replacing sulfur by selenium resulted in 20-fold higher SH-efficiency due to an increased electron density leading to enhanced hyperpolarizability.³¹

Applications in the field of materials science in particular necessitate efficient and reliable synthetic access to TRF-products. Here, we present a systematic study on the thiophene ring-opening approach focusing on origins and pathways of potential side reactions. As a result, an advanced procedure leading to significantly improved Z-selectivity and efficiency is being developed. We investigated the reaction kinetics of the TRF, applying inline monitoring via infrared spectroscopy and implemented flow chemistry for safe and convenient scalability of the process. In addition, the development of an improved design concept for NLO-chromophores, yielding the highest SH-generation efficiencies reported for TRF-based products up to date, underlines the technological relevance of ene-yne compounds.

2. Results and discussion

2.1. Thiophene ring-fragmentation

In the course of our research on NLO materials, utilizing (*Z*)-trimethyl(4-(methylthio)pent-3-en-1-ynyl)silane (**3a**, Scheme 2) as an ene-yne scaffold, deviations from the synthetic protocol³⁰ (e.g. loss of inert atmosphere) resulted in an unexpected *E/Z*-isomerization of **3a** toward the *E*-species **3f** (typically in the range of 1–5%). For this reason, the impact of the reaction components on the isomerization was evaluated. It could be shown that neither the used dry solvent (Et₂O), the reactants (**2a**, *n*-BuLi, MeI) nor the organic by-products (*n*-BuBr) are associated with this process. However, the addition of LiI, which is formed during quenching of the TRF reaction using MeI, results in an isomerization of **3a**. By evaluating various salts containing Li⁺- or I⁻-ions (LiCl, LiBr, LiClO₄, LiI, NaI, KI and TBAI – see Supplementary Data) it was established that the iodide anion is responsible for this side-reaction. Interestingly, this reaction showed enhanced rates in the presence of oxygen; argon atmosphere significantly limits this effect.

From these experiments we concluded that the formation of elemental iodine (I₂), even if only present in traces, is the origin of the formation of the *E*-species. This I₂-induced process of double bond isomerization is well-described in literature.³⁴ Indeed, a control experiment revealed that the addition of I₂ (1 mol%) induces this reaction (Fig. 1); full exclusion of light suppresses the isomerization.

To further quantify this side reaction, **3a** and the corresponding *E*-isomer **3f** were subjected to UV-light assisted isomerization experiments. The reactions were carried out in standard NMR tubes using an I₂ solution in CDCl₃ at concentrations of 1.0 mol% and a standard light source.³⁵ The results for 1.0 mol% I₂ are illustrated in Fig. 1. The experiment yielded the same *E/Z*-ratio starting from both, the pure *Z*- and *E*-isomer, indicating that complete equilibration is reached during the I₂-induced isomerization. Additional experiments using 10.0 mol% I₂ and starting material **3a** revealed that an equilibrium state between the *Z*- and *E*-isomer is already reached within 15 s of light irradiation.

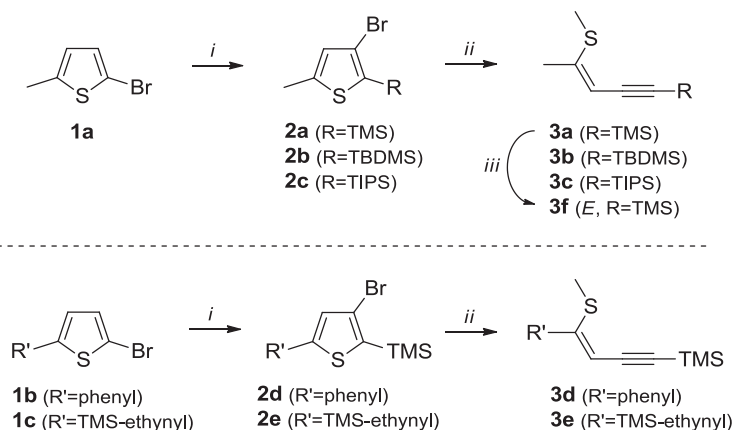
The equilibrium state consists of 16% **3a** (*Z*-isomer) compared to an 84% **3f** (*E*-isomer), corresponding to the thermodynamic energy level difference between the *Z*- and the *E*-isomer as indicated by DFT calculations. This fact clearly points out the importance of the TRF approach to obtain the thermodynamically less favored isomer. Moreover, the strategy potentially allows obtaining the corresponding *E*-structure in good yields. Indeed, repeating this experiment on preparative scale (using a 1.0 mol% I₂ solution) resulted in 76% of pure (*E*)-trimethyl(4-(methylthio)pent-3-en-1-ynyl)silane (**3f**) after column chromatography.

Hence, various alternative methylation sources were assessed. These experiments revealed that iodomethane (MeI) clearly outperforms the applied analogs (trifluoromethanesulfonate (MeOTf), dimethyl sulfate (Me₂SO₄) and methyl 4-methylbenzenesulfonate (MeOTs)) with regard to efficiency and selectivity. Further information on potential side reactions is given in chapter 2 in the Supplementary Data (acid-induced isomerization pathways).

As a consequence, the second approach was to avoid the formation of I₂. On the one hand, the removal of I⁻ with Ag⁺-salts (e.g. Ag₂CO₃) and, on the other hand, the addition of a reducing agent were attempted for this purpose. In both cases, the formation of *E*-isomer was entirely suppressed. Particularly the application of Na₂SO₃ as the reducing agent prior to the addition of MeI proved to be advantageous. This new procedure for TRF, also applying slightly modified reaction parameters, combines both the prevention of the isomerization and the ease of workup. In addition to the significant improvement in stereospecificity an enhanced isolated yield of 86% (vs. 76–81% using the old procedure)³⁰ for **3a** was obtained, which shows the efficiency of the protocol.

To demonstrate the scope of the developed protocol, various substrates for TRF reactions were evaluated (Scheme 2). The modifications of **2a** include the introduction of more stable silyl groups R (from TMS to TBDMS and TIPS) and variation in the substituent R' in the thiophene 5-position (from sp³ to sp² and sp hybridization). The diversity of suitable silyl groups is an important factor with regard to specific functionalization. The alteration towards sp² and sp centers for R' derives from the current interest in these compounds as organic functional π-systems (e.g. NLO materials).

Detailed synthetic protocols for the synthesis of precursors **2a–e** via Halogen-Dance reactions³⁶ and TRF towards **3a–e** are given in the experimental section. Applying the novel TRF protocol all ring-opening reactions were accomplished successfully and in good yields of 75–86% without any formation of *E*-isomer; the proof for the formation of the *Z*-isomers has been given by X-ray diffraction



Scheme 2. Synthesis of compounds **3a-f**; i: HD-reaction; ii: new TRF-protocol; iii: I_2 -induced isomerization.

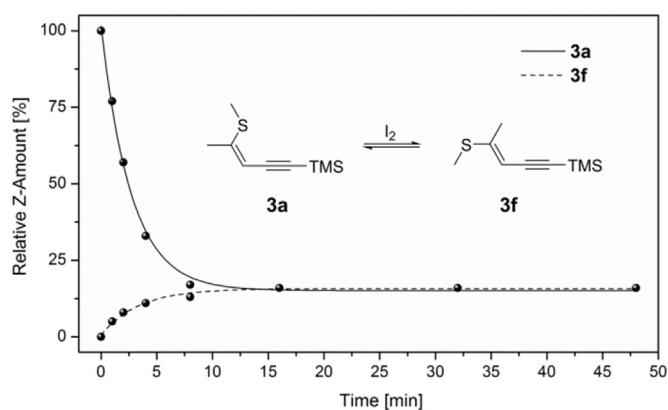


Fig. 1. I_2 -induced isomerization of ene-yne compounds **3a** and **3f** (1.0 mol% I_2 solution in $CDCl_3$); curve fitting performed using standard exponential fit parameters.

on various examples.^{37,38} A tendency towards lower yields for larger silyl groups (**3a/3b/3c** = 86%/82%/75%) and an increase in yields for sp to sp^2 and sp^3 hybridization of R' (**3e/3d/3a** = 77%/81%/86%) has been observed (see Table 1).

2.2. Kinetic investigations

Although the TRF reaction has been extensively studied regarding the substrate scope, no kinetic data is available. Based on previous investigations³⁹ on organo-lithium compounds an ATR-IR probe was applied for inline reaction monitoring to explore the ring-opening process under dynamic conditions in order to gain insight on fragmentation threshold temperatures and reaction kinetics. Recent progress in the development of mid-IR transparent

Table 1
Isolated yields and fragmentation temperatures of TRF products **3a-e**.

	Isolated Yield ^a [%]	TRF Temperature ^b [°C]
3a	86	−50
3b	82	−47
3c	75	n.o. ^c
3d	81	−24
3e	77	−42

^a i) Et_2O (0.2 M), $-40^\circ C$, $n-BuLi$ (1.1 eq.), ii) rt, 30 min, iii) $-40^\circ C$, Na_2SO_3 (1.2 eq.), iv) MeI (1.5 eq.), rt.

^b Defined by 5% threshold temperature.

^c Not observed due to low solubility.

fibres⁴⁰ and sensor assembly render it possible to achieve reliable data even under non-isothermal conditions. This allows for a monitoring of the TRF reaction in a warm-up phase yielding the onset temperature of the ring-opening. The inline approach (both *in-situ* and real-time) is of critical importance for this study, since alternative techniques typically suffer from sample alteration during sampling.³⁹

In the initial experiments the fragmentation threshold temperatures were matter of interest. For this purpose the respective substrates (**2a**, **2b**, **2d**, **2e**) were lithiated *via* metal-halogen exchange using $n-BuLi$ (1.1 eq.) at $-60^\circ C$ in anhydrous Et_2O (0.2 M). The fragmentation of the TIPS-substituted derivative **2c** could not be monitored under the applied conditions due to the low solubility in Et_2O at $-60^\circ C$. After completion of the lithiation process the temperature was raised to $\sim 0^\circ C$ at a constant rate ($0.5^\circ C/min$). Indeed, the formation of intense new absorption bands, particularly in the fingerprint region ($650-900\text{ cm}^{-1}$), were reproducibly observed for all substrates at certain temperatures. These bands reveal a significant correlation to peaks located between 2100 and 2200 cm^{-1} (highly specific for C–C triple bonds), which confirms the onset of the TRF reaction forming the ene-yne moiety. However, due to the self-absorption of the applied ATR-unit these bands were not utilized for quantitative analyses. The obtained concentration profiles during the ring-opening of **2a** are exemplarily depicted in Fig. 2 (profiles for all fragmentation products are given in the Supplementary Data). Remarkably, the obtained ring-opening temperatures (defined by a 5% intensity threshold relative to the baseline) are in contrast to literature values. Whereas thiophene ring-fragmentations are typically reported to occur at room-temperature,^{1–3} we observed reaction on-set temperatures of $-50^\circ C$, $-47^\circ C$ and $-42^\circ C$ for **2a**, **2b** and **2e**, respectively. Only the fragmentation of **2d** was found to take place at higher temperature ($-24^\circ C$), which is attributed to stabilizing effects of the phenyl substituent (see Table 1).

Furthermore, we investigated the TRF of **2a** under isothermal conditions ($-45^\circ C$, $-40^\circ C$ and $-35^\circ C$). A linear time dependence was observed for the product formation at all temperatures (Fig. 3) indicating a zero-order reaction, typically found for saturated catalytic processes. The reaction rates plotted against $1/T$ also show the linear dependence required by the Arrhenius equation, confirming this assumption (Supplementary Data). This finding is in obvious disagreement with the reaction mechanism depicted in Scheme 1, which implies a first-order reaction. To gain further insights we applied an excess $n-BuLi$ and altered the concentration (0.13 M) of **2a**, however, did not find any significant influence of the variations on the reaction rate. At this point, the reason for the zero-

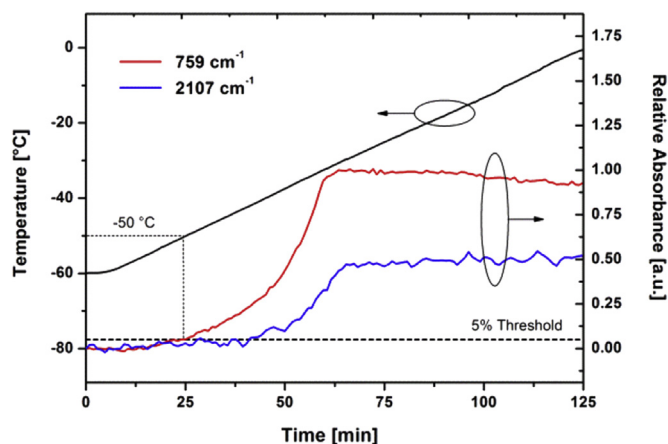


Fig. 2. Normalized integrals of selected absorption bands of **3a** and temperature gradient during TRF of **2a**.

order kinetics is not understood and remains to be clarified by future research.

2.3. Flow chemistry

Problems associated with solvent interactions, highly exothermic reactions and other safety issues limit the applicability of organolithium reagents to low temperature regimes. Unfortunately, the scale-up of cryogenic reactions employing hazardous reagents such as organometallic compounds under strictly inert conditions tend to be troublesome and error-prone. However, excellent heat transfer and short residence times (t^R) allow those reactions to be conducted safely in a microflow reactor. Inspired by previous reports on ring-fragmentation under flow conditions,⁴¹ we therefore aimed to incorporate the TRF to an automated flow process, providing wide scalability and safe operation conditions. Furthermore, the application of such a microflow reactor guarantees fully inert atmosphere which is of crucial importance in order to avoid the formation of the undesired *E*-isomer. Low fragmentation temperatures observed during IR-experiments allow for short residence times in a microflow reactor under convenient temperature (Fig. 4).

A stainless steel microreactor was fabricated (Fig. 5), consisting of individual pre-cooling zones for reagents (200 μ L volume each), T-shaped mixers and two microfluidic reaction zones – one for the

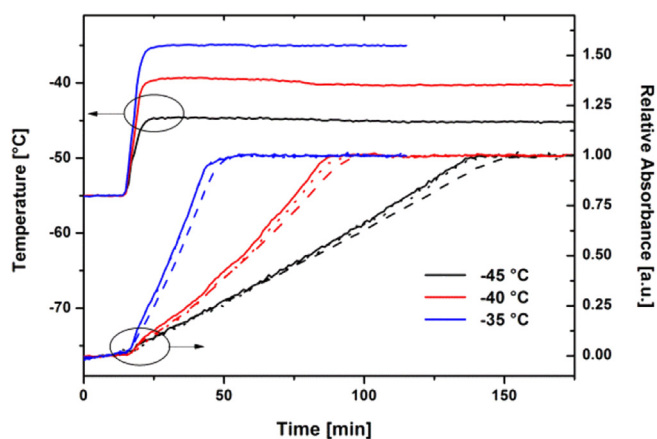


Fig. 3. Normalized integrals of absorption bands at 1249 cm^{-1} (solid), 854 cm^{-1} (dashed) and 759 cm^{-1} (dotted) of **3a** during TRF under isothermal conditions.

lithiation (1 mL volume) and one for the quench (1.5 mL volume). In order to allow reaction temperatures down to -40 °C, a dual-stage Peltier-assisted cooling module was developed (FlowChiller), and attached to the bottom of the stainless steel reactor.

Precooled solutions of **2a** (1.0 eq., 0.1 mol L^{-1} in Et_2O) and *n*-BuLi (1.1 eq., 1.6 mol L^{-1} in hexanes) were mixed and lithiation as well as TRF was accomplished in the lithiation reactor. Subsequently, a solution of MeI (1.8 eq., 0.35 mol L^{-1} in Et_2O) was added and methylation of the thiolate took place in the quench-reactor. Finally, after leaving the microflow reactor, the reaction mixture was collected in a vial containing a Na_2SO_3 solution to avoid isomerization induced by atmospheric oxygen. Reaction temperature (-40 °C, -20 °C, 0 °C and room temperature) as well as t^R (5–60 s) in the lithiation reactor were varied in order to identify ideal reaction conditions. Overall recovery of product, starting material and dehalogenated starting materials was approximately 75–80% at room temperature and almost quantitative beneath -20 °C. While virtually no product formation was observed at -40 °C (as expected from kinetic data), low conversion (34% yield) towards **3a** took place at $t^R = 60$ s at -20 °C. Notably, in both experiments only small amounts of dehalogenated by-product were formed, while the majority of the recovered material was starting compound **2a** indicating that TRF proceeds rapidly compared to the initial lithiation in the investigated temperature regime. At 0 °C significantly increased product formation was observed for higher values of t^R , while best results were obtained at room temperature (Fig. 6). Fragmentation is basically completed after 20 s and the highest yield (73%) was found at $t^R = 30$ s. Remarkably, no formation of the *E*-isomer was observed in any of our experiments. Variation of t^R in the quench-reactor did not significantly influence the outcome of the experiment. More detailed results of the screening are given in Table S2 and S3 in the Supplementary Data.

Applying the optimized conditions, a run on a preparative scale (12 mmol, room temperature, $t^R = 60$ s) was conducted. After purification by column chromatography, **3a** could be obtained in 56% yield.

2.4. Non linear optical properties

Recently, we showed that replacing sulfur by selenium in enyne derived NLO-materials significantly boosts the SH-efficiency. This outcome can be attributed to increased density of delocalized electrons in the conjugated π -system and thus enhanced hyperpolarizability.³¹ However, the application of selenium is accompanied by drawbacks such as the toxicity of organo-selenium compounds and complex synthesis of the required precursors. We therefore adopted a novel design strategy to increase the electron-density in the conjugated π -system. By attaching electron-donating substituents to the phenyl subunit, the molecular architecture was extended to a donor-acceptor-donor structure as depicted in Scheme 3.

The syntheses of **5i-iii** were accomplished *via* CuAAC starting from **3a** and the corresponding azides **4i-iii** in moderate to good yields (**5i**: 82%, **5ii**: 34%, **5iii**: 57%). A fundamental prerequisite for SHG (second harmonic generation) is the crystallization in a non-centrosymmetric crystal class, with the exception of 432.⁴² Unfortunately, **5ii**⁴³ and **5iii**⁴⁴ both crystallized in the centrosymmetric space group $P2_1/c$. In contrast, enantiomeric crystals of **5i**⁴⁵ (space group $P2_1$, Flack parameter 0.00(2)) were grown by slow solvent evaporation (EtOH) > 25 °C. A second centrosymmetric polymorph of **5i**⁴⁶ (space group: $P2_1/c$) was obtained by growing crystals from a saturated EtOH solution upon cooling to ~ 5 °C.

The molecules in the $P2_1$ polymorph of **5i** ($Z' = 1$) crystallize in layers parallel to (001), whereby the molecules are significantly

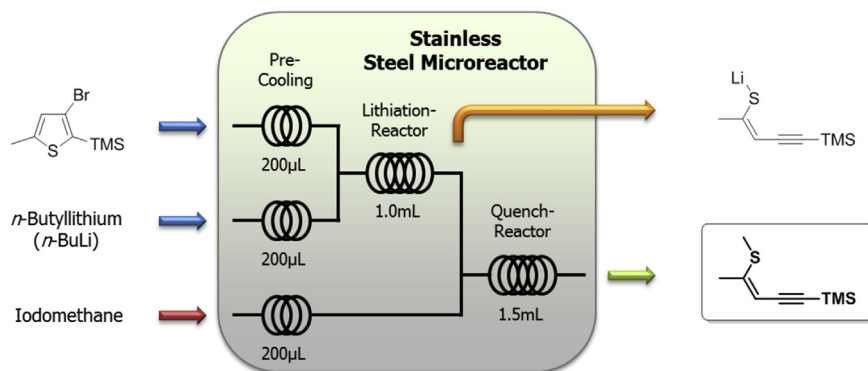


Fig. 4. Microreactor setup for continuous-flow experiments.

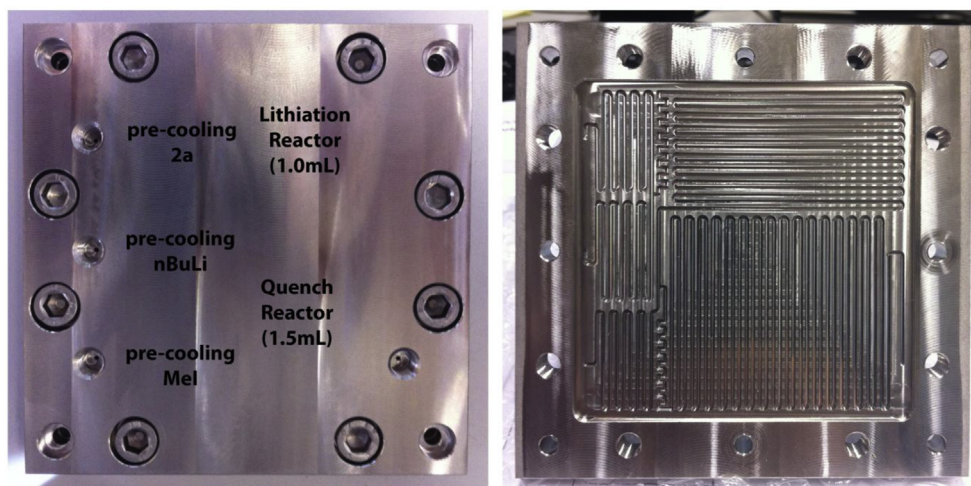


Fig. 5. Stainless steel microreactor equipped with pre-cooling zones, a lithiation reaction zone and a quench reaction zone.

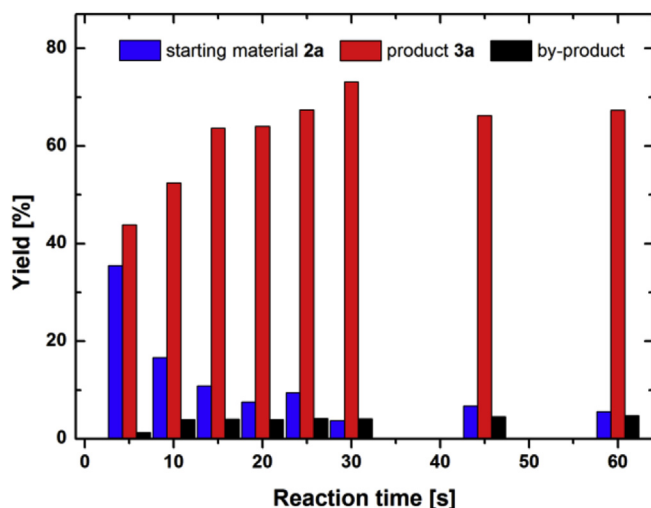
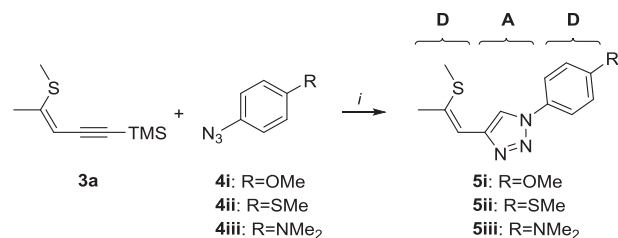


Fig. 6. Reaction course at room temperature and reaction times from 5 to 60 s.

inclined with respect to the stacking direction (Fig. 7). Inside these layers, molecules related by translation along **a** are connected via face-to-face contacts of benzene to triazole rings (distance of least squares planes defined by the benzene rings of two adjacent molecules 3.519 Å).

The $P2_1/c$ polymorph ($Z' = 1$) is crystallo-chemically unrelated to the $P2_1$ polymorph. The conformations of the molecules in both polymorphs differ regarding the orientation of the methoxy group and the molecule in the $P2_1$ polymorph is considerably more twisted: The least squares planes defined by the non-H atoms of the benzene ring and the triazole ring form an angle of 26.7° , while the benzene and $\text{CH}=\text{CS}-\text{CH}_3$ -fragment form an angle of 18.9° . The analogous angles in the $P2_1/c$ polymorph are 9.0° and 8.7° .

Enantiomorphic crystals of **5i** were subjected to SHG measurements (Fig. 8). Compared to parent compound **I** (Scheme 3; $\text{R} = \text{H}$) **5i** ($\text{R} = \text{OMe}$) exhibits 35-fold increased SHG-efficiency or ~ 80 -times the value of KDP (potassium dihydrogen phosphate). The nonlinear performance of **5i** is the highest reported for TRF-derived



Scheme 3. Synthesis of "Click"-functionalized ene-yne derivatives **5i-iii** via CuAAC; i : $\text{CuSO}_4 \cdot 5\text{H}_2\text{O}$, Na ascorbate, KF; D = Electron Donor, A = Electron Acceptor.

NLO chromophores so far and underlines the efficiency of the proposed donor-acceptor-donor design.

3. Conclusion

Systematic investigations on the thiophene ring-fragmentation reaction focusing on improved selectivity as well as enhanced efficiency have been presented. The application of state of the art inline reaction monitoring technique revealed novel insights to fragmentation on-set temperatures and reaction kinetics. As a result, reliable synthetic procedures for lab-scale (Na_2SO_3 method) as well as mid- to large-scale (flow chemistry) were established. In addition a new design concept for ene-yne based NLO materials was developed, which strengthens the relevance of TRF products in the field of functional organic materials.

4. Experimental section

4.1. Synthesis

4.1.1. General procedures and methods

All reactions were performed in oven-dried glassware. Reagents were purchased from common commercial sources and used without prior purification. Anhydrous solvents were prepared by filtration through drying columns. Column chromatography was performed on silica 60 (40–63 μm) using distilled solvents as given. Melting points were recorded on an Automated Melting Point System and are corrected.

NMR spectra were recorded at 400 MHz for ^1H and 100 MHz for ^{13}C for all target compounds (ene-yne) and at 200 MHz for ^1H and 50 MHz for ^{13}C for intermediates. Data for ^1H NMR are reported as follows: chemical shift in parts per million (ppm) from TMS (tetramethylsilane) with the residual solvent signal as an internal reference (CDCl_3 $\delta = 7.26$ ppm), multiplicity (s = singlet, d = doublet, t = triplet and m = multiplet), coupling constant in Hz and integration. ^{13}C NMR spectra are reported in ppm from TMS

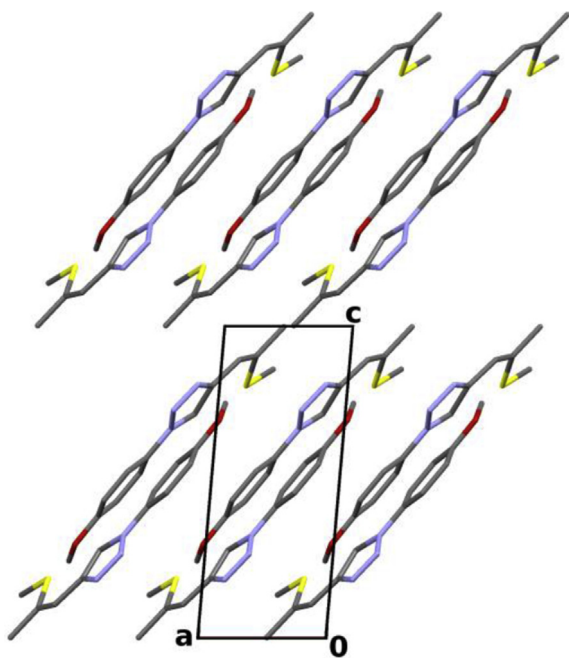


Fig. 7. The crystal structure of the $P2_1$ polymorph of **5i** viewed down [010]; C, N, O and S atoms are grey, blue, red and yellow, respectively; H atoms have been omitted for clarity.

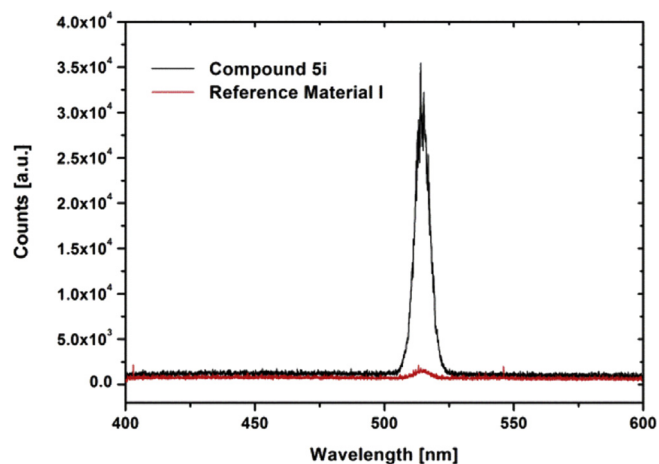


Fig. 8. SHG spectra of **5i** and reference material I; the lineshape is a replica of the emission spectrum of the femtosecond laser used in the experiment and shows the relatively large bandwidth typical for femtosecond lasers.

using the central peak of the solvent as reference (CDCl_3 $\delta = 77.0$ ppm); multiplicity with respect to proton (deduced from APT experiments, s = quaternary C, d = CH, t = CH_2 , q = CH_3).

4.1.2. General procedure for the halogen dance (HD) reaction³⁶

To a solution of diisopropylamine (DIPA, 1.4 eq.) in anhydrous THF under argon *n*-BuLi (1.2 eq.) was slowly added at -30 to -40 °C. After 30–60 min the thiophene species (**1**, 1.0 eq.) was added in anhydrous THF at -70 °C and the reaction stirred for 1.5–2 h. Subsequently, the appropriate silyl chloride (1.2 eq.) was added as a solution in anhydrous THF and the mixture stirred at rt overnight. The reaction was poured on water, extracted with Et_2O , the organic phases were dried over anhydrous Na_2SO_4 and concentrated under reduced pressure.

4.1.3. General procedure for the thiophene ring-fragmentation (TRF) reaction

To a solution of **2a-c** (1.0 eq.) in anhydrous Et_2O (~ 0.2 M) under argon atmosphere at -40 to -60 °C *n*-BuLi (1.1 eq.) was injected dropwise. After the addition the reaction was immediately warmed to rt, stirred for 30 min and again cooled to -40 °C. At this point the addition of first Na_2SO_3 (1.2 eq.) then MeI (1.5 eq.) was accomplished and the temperature subsequently raised to rt. After a reaction time of 20–60 min the mixture was poured on water, extracted with Et_2O , the combined organic layers were washed with brine, dried over anhydrous Na_2SO_4 and concentrated *in vacuo*. Purification was performed by column chromatography (light petroleum).

4.1.4. General procedure for CuAAC

To a suspension of **3a** (1.2 eq.), azide (1.0 eq.), Na ascorbate (0.4 eq.) and $\text{CuSO}_4 \cdot 5\text{H}_2\text{O}$ (0.2 eq.) in $t\text{-BuOH}/\text{H}_2\text{O}$ (1:1, ~ 0.4 M) in a microwave reaction vial was added KF (1.4 eq.) at room temperature. Subsequently, the reaction vial was sealed and heated to 150 °C for 30 min in a reaction microwave. Then the reaction mixture was poured on H_2O and extracted with Et_2O . The combined organic layers were washed with brine, dried over anhydrous Na_2SO_4 and concentrated under reduced pressure. Final purification was accomplished by column chromatography.

4.1.5. Synthetic details

The syntheses of 2-bromo-5-methylthiophene (**1a**),⁴⁷ 2-bromo-5-phenylthiophene (**1b**),^{48,49} 2-bromo-5-[2-(trimethylsilyl)]

ethynyl]-thiophene (**1c**),^{50,51} 3-bromo-5-methyl-2-(trimethylsilyl)thiophene (**2a**),³⁰ 1-azido-4-methoxybenzene (**4i**),⁵² 1-azido-4-(methylthio)benzene (**4ii**)⁵² and 4-azido-*N,N*-dimethylbenzenamine (**4iii**)⁵² were performed according to published protocols.

4.1.6. 3-Bromo-2-[(1,1-dimethylethyl)dimethylsilyl]-5-methylthiophene (**2b**)

DIPA (5.20 g, 51.4 mmol) in anhydrous THF (150 mL), *n*-BuLi (18.0 mL, 45.0 mmol, 2.5 M in hexanes), **1a** (6.70 g, 37.8 mmol) in anhydrous THF (20 mL), TBDMS-Cl (15.0 mL, 45.0 mmol, 3 M in anhydrous THF) and purification by bulb-to-bulb distillation *in vacuo* yielded **2b** (8.07 g, 73%) as slightly yellow oil. BP: 73–74 °C (0.18 mbar). ¹H NMR (400 MHz, CDCl₃): δ = 6.78 (s, 1H), 2.47 (s, 3H), 0.96 (s, 9H), 0.38 (s, 6H) ppm. ¹³C NMR (100 MHz, CDCl₃): δ = 145.6 (s), 131.1 (d), 130.1 (s), 117.0 (s), 26.8 (q), 18.2 (s), 15.1 (q), –4.3 (q) ppm. Anal. Calcd for C₁₁H₁₉BrSSi: C, 45.35; H, 6.57; *m/z* 290.02 [M]⁺. Found: C, 45.58; H, 6.61; MS (EI, quadrupole): *m/z* 290.07 [M]⁺.

4.1.7. 3-Bromo-2-[tris(1-methylethyl)silyl]-5-methylthiophene (**2c**)

DIPA (1.09 g, 10.8 mmol) in anhydrous THF (80 mL), *n*-BuLi (3.8 mL, 9.6 mmol, 2.5 M in hexanes), **1a** (1.41 g, 8.0 mmol) in anhydrous THF (20 mL), TIPS-Cl (1.85 g, 9.6 mmol) in anhydrous THF (15 mL) and purification by column chromatography (light petroleum) yielded **2c** (2.14 g, 80%) as white solid. MP: 48.4–49.5 °C. ¹H NMR (400 MHz, CDCl₃): δ = 6.79 (s, 1H), 2.48 (s, 3H), 1.55 (sept., *J* = 7.5 Hz, 3H), 1.13 (d, *J* = 7.5 Hz, 18H) ppm. ¹³C NMR (100 MHz, CDCl₃): δ = 145.5 (s), 131.2 (d), 128.0 (s), 116.9 (s), 18.8 (q), 15.1 (q), 12.4 (d) ppm. Anal. Calcd for C₁₄H₂₅BrSSi: C, 50.43; H, 7.56; *m/z* 332.06 [M]⁺. Found: C, 50.64; H, 7.65; MS (EI, quadrupole): *m/z* 332.06 [M]⁺.

4.1.8. 3-Bromo-5-phenyl-2-(trimethylsilyl)thiophene (**2d**).⁵³

DIPA (6.86 g, 67.8 mmol) in anhydrous THF (160 mL), *n*-BuLi (24.1 mL, 60.2 mmol, 2.5 M in hexanes), **1b** (12.0 g, 50.2 mmol) in anhydrous THF (40 mL) were mixed as described in the general procedure and stirred for 2 h at 40 °C. After the addition of TMS-Cl (6.54 g, 60.2 mmol) in anhydrous THF (60 mL) and purification by bulb-to-bulb distillation under reduced pressure **2d** (14.76 g, 94%) was isolated as colorless oil. BP: ~110 °C (0.05 mbar). Physical properties in agreement with literature.⁵³

4.1.9. 3-Bromo-2-(trimethylsilyl)-5-[2-(trimethylsilyl)ethynyl]thiophene (**2e**)

Alterations to the general procedure. A precooled (–40 °C) solution of LDA (DIPA (0.49 g, 4.8 mmol), *n*-BuLi (1.9 mL, 4.6 mmol, 2.4 M in hexanes, anhydrous THF (40 mL)) was added to as stirred suspension of **1c** (1.00 g, 3.9 mmol) in anhydrous THF (40 mL) at –35 °C under argon atmosphere. After a reaction time of 30 min TMS-Cl (0.60 g, 5.6 mmol) in anhydrous THF (5 mL) was injected rapidly and the mixture warmed to rt. Standard work-up (general procedure) and column chromatography (light petroleum) gave **2e** (0.84 g, 66%) as slightly yellow oil. BP: ~111 °C (0.2 mbar). ¹H NMR (400 MHz, CDCl₃): δ = 7.17 (s, 1H), 0.38 (s, 9H), 0.23 (s, 9H) ppm. ¹³C NMR (100 MHz, CDCl₃): δ = 137.6 (s), 136.7 (d), 128.3 (s), 116.1 (s), 101.3 (s), 95.9 (s), –0.3 (q), –0.9 (q) ppm. Anal. Calcd for C₁₂H₁₉BrSSi₂: C, 43.49; H, 5.78; *m/z* 329.99 [M]⁺. Found: C, 43.87; H, 5.47; MS (EI, quadrupole): *m/z* 329.96 [M]⁺.

4.1.10. Trimethyl[(3*Z*)-4-(methylthio)-3-penten-1-yn-1-yl]silane **3a**

Starting from **2a** (2.98 g, 12.0 mmol), *n*-BuLi (5.3 mL, 13.2 mmol, 2.5 M in hexanes), Na₂SO₃ (1.81 g, 14.4 mmol) and MeI (2.55 g, 18.0 mmol) pure *Z*-isomer **3a** (1.90 g, 86%) was isolated as a colorless to slightly yellow liquid after a reaction time of 20 min at rt subsequent to the addition of the methyl-species. Physical data is in accordance to published values.³⁰

4.1.11. (1,1-Dimethylethyl)dimethyl[(3*Z*)-4-(methylthio)-3-penten-1-yn-1-yl]silane **3b**

Starting from **2b** (583 mg, 2.0 mmol), *n*-BuLi (0.9 mL, 2.2 mmol, 2.5 M in hexanes), Na₂SO₃ (303 mg, 2.4 mmol) and MeI (426 mg, 3.0 mmol) **3b** (370 mg, 82%) was isolated as a yellow low melting solid after a reaction time of 60 min at rt after the addition of MeI. ¹H NMR (400 MHz, CDCl₃): δ = 5.43 (s, 1H), 2.36 (s, 3H), 2.07 (s, 3H), 0.97 (s, 9H), 0.13 (s, 6H) ppm. ¹³C NMR (100 MHz, CDCl₃): δ = 149.4 (s), 102.9 (d), 102.3 (s), 99.5 (s), 26.1 (q), 22.3 (q), 16.6 (s), 14.0 (q), –4.5 (q) ppm. Anal. Calcd for C₁₂H₂₂SSi: *m/z* 227.1284 [M + H]⁺. Found: MS (APCI, TOF): *m/z* 227.1281 [M + H]⁺.

4.1.12. Tris(1-methylethyl)[(3*Z*)-4-(methylthio)-3-penten-1-yn-1-yl]silane **3c**

Starting from **2c** (500 mg, 1.5 mmol), *n*-BuLi (0.65 mL, 1.7 mmol, 2.5 M in hexanes), Na₂SO₃ (227 mg, 1.8 mmol) and MeI (319 mg, 2.3 mmol) **3c** (302 mg, 75%) was isolated as colorless low melting solid after a reaction time of 60 min at rt subsequently to the addition of the methyl-species. ¹H NMR (400 MHz, CDCl₃): δ = 5.46 (s, 1H), 2.36 (s, 3H), 2.08 (s, 3H), 1.10 (m, 21H) ppm. ¹³C NMR (100 MHz, CDCl₃): δ = 149.0 (s), 103.4 (s), 103.2 (d), 97.6 (s), 22.2 (q), 18.7 (q), 14.0 (q), 11.3 (d) ppm. Anal. Calcd for C₁₅H₂₈SSi: *m/z* 269.1754 [M + H]⁺. Found: MS (APCI, TOF): *m/z* 269.1746 [M + H]⁺.

4.1.13. Trimethyl[(3*Z*)-4-(methylthio)-4-phenyl-3-buten-1-yn-1-yl]silane **3d**

Starting from **2d** (623 mg, 2.0 mmol), *n*-BuLi (0.9 mL, 2.2 mmol, 2.5 M in hexanes), Na₂SO₃ (303 mg, 2.4 mmol) and MeI (426 mg, 3.0 mmol) **3d** (397 mg, 81%) was isolated as yellow oil after a reaction time of 30 min at rt after the addition of MeI. ¹H NMR (400 MHz, CDCl₃): δ = 7.41–7.33 (m, 5H), 5.76 (s, 1H), 2.13 (s, 3H), 0.26 (s, 9H) ppm. ¹³C NMR (100 MHz, CDCl₃): δ = 152.6 (s), 138.2 (s), 128.7 (d), 128.5 (d), 128.0 (d), 107.5 (d), 103.2 (s), 102.2 (s), 16.1 (q), 0.0 (q) ppm. Anal. Calcd for C₁₄H₁₈SSi: *m/z* 247.0971 [M + H]⁺. Found: MS (ESI, TOF): *m/z* 247.0958 [M + H]⁺.

4.1.14. [(3*Z*)-3-(Methylthio)-3-hexen-1,5-diyne-1,6-diyne]bis(trimethylsilane) **3e**

Starting from **2e** (331 mg, 1.0 mmol), *n*-BuLi (0.45 mL, 1.1 mmol, 2.5 M in hexanes), Na₂SO₃ (151 mg, 1.2 mmol) and MeI (213 mg, 1.5 mmol) **3e** (206 mg, 77%) was obtained as slightly orange low-melting solid after a reaction time of 30 min at rt subsequently to the addition of MeI. ¹H NMR (400 MHz, CDCl₃): δ = 5.87 (s, 1H), 2.42 (s, 3H), 0.22 (m, 18H) ppm. ¹³C NMR (100 MHz, CDCl₃): δ = 133.9 (s), 111.3 (d), 109.1 (s), 104.1 (s), 100.9 (s), 99.4 (s), 15.7 (q), –0.1 (q), –0.2 (q) ppm. Anal. Calcd for C₁₃H₂₂SSi₂: *m/z* 267.1054 [M + H]⁺. Found: MS (ESI, TOF): *m/z* 267.1045 [M + H]⁺.

4.1.15. Isomerization procedure towards trimethyl[(3*E*)-4-(methylthio)-3-penten-1-yn-1-yl]silane **3f**

3a (220 mg, 1.2 mmol, 1.0 eq.) was dissolved in a solution of I₂ (12 μmol, 1.0 mol%) in CHCl₃ (~7 mL) in NMR glass tubes and irradiated with an external light source for 20 min (IntelliRay 600, 50% intensity) resulting in a relative *E*-isomer content of 86%. Subsequently, the mixture was diluted with CHCl₃ and extracted with an aqueous Na₂SO₃ solution. The organic layer was dried over anhydrous Na₂SO₄ and the solvent removed under reduced pressure. Column chromatography (light petroleum) yielded compound **3f** (167 mg, 76%) as slightly yellow oil. ¹H NMR (400 MHz, CDCl₃): δ = 5.12 (s, 1H), 2.25 (s, 3H), 2.14 (s, 3H), 0.19 (s, 9H) ppm. ¹³C NMR (100 MHz, CDCl₃): δ = 150.9 (s), 102.5 (s), 99.0 (d), 97.7 (s), 20.6 (q), 14.7 (q), 0.1 (q) ppm. Anal. Calcd for C₉H₁₆SSi: *m/z* 185.0815 [M + H]⁺. Found: MS (APCI, TOF): *m/z* 185.0810 [M + H]⁺.

4.1.16. 4-[(1Z)-2-(Methylthio)-1-propen-1-yl]-1-(4-methoxyphenyl)-1H-1,2,3-triazol 5i

Starting from **3a** (1.55 g, 8.4 mmol), **4i** (1.04 g, 7.0 mmol), Na ascorbate (0.56 g, 2.8 mmol), CuSO₄·5H₂O (0.35 g, 1.4 mmol) and KF (0.57 g, 9.8 mmol) **5i** (1.50 g, 82%) was obtained after column chromatography (light petroleum/Et₂O 1:1). ¹H NMR (400 MHz, CD₂Cl₂): δ = 8.31 (s, 1H), 7.66 (d, *J* = 9.0 Hz, 2H), 7.04 (d, *J* = 9.0 Hz, 2H), 6.61 (d, *J* = 1.1 Hz, 1H), 3.86 (s, 3H), 2.42 (s, 3H), 2.27 (d, *J* = 1.1 Hz, 3H) ppm. ¹³C NMR (100 MHz, CD₂Cl₂): δ = 160.3 (s), 145.6 (s), 135.9 (s), 131.2 (s), 122.6 (d), 120.6 (d), 115.2 (d), 115.1 (d), 56.2 (q), 23.8 (q), 14.7 (q) ppm. Anal. Calcd for C₁₃H₁₅N₃OS: *m/z* 262.1009 [M + H]⁺. Found: MS (ESI, TOF): *m/z* 262.1010 [M + H]⁺.

4.1.17. 4-[(1Z)-2-(Methylthio)-1-propen-1-yl]-1-[(4-methylthio)phenyl]-1H-1,2,3-triazol 5ii

Starting from **3a** (288 mg, 1.56 mmol), **4ii** (215 mg, 1.30 mmol), Na ascorbate (103 mg, 0.52 mmol), CuSO₄·5H₂O (65 mg, 0.26 mmol) and KF (106 mg, 1.82 mmol) **5ii** (121 mg, 34%) was obtained after column chromatography (light petroleum/Et₂O 3:2). ¹H NMR (400 MHz, CD₂Cl₂): δ = 8.35 (s, 1H), 7.69 (d, *J* = 8.6 Hz, 2H), 7.39 (d, *J* = 8.6 Hz, 2H), 6.62 (s, 1H), 2.54 (s, 3H), 2.42 (s, 3H), 2.27 (s, 3H) ppm. ¹³C NMR (100 MHz, CD₂Cl₂): δ = 145.7, 140.2, 136.3, 134.8, 127.6, 121.3, 120.4, 114.9, 23.8, 16.0, 14.7 ppm. Anal. Calcd for C₁₃H₁₅N₃S₂: *m/z* 278.0780 [M + H]⁺. Found: MS (ESI, TOF): *m/z* 278.0783 [M + H]⁺.

4.1.18. N,N-dimethyl-4-[4-[(1Z)-2-(methylthio)-1-propen-1-yl]-1H-1,2,3-triazol-1-yl]benzenamine 5iii

Starting from **3a** (288 mg, 1.56 mmol), **4iii** (211 mg, 1.30 mmol), Na ascorbate (103 mg, 0.52 mmol), CuSO₄·5H₂O (65 mg, 0.26 mmol) and KF (106 mg, 1.82 mmol) **5iii** (203 mg, 57%) was obtained after column chromatography (light petroleum/Et₂O 3:2). ¹H NMR (400 MHz, CD₂Cl₂): δ = 8.26 (s, 1H), 7.56 (d, *J* = 9.0 Hz, 2H), 6.79 (d, *J* = 9.0 Hz, 2H), 6.61 (s, 1H), 3.01 (s, 6H), 2.41 (s, 3H), 2.26 (s, 3H) ppm. ¹³C NMR (100 MHz, CD₂Cl₂): δ = 151.1 (s), 145.3 (s), 135.4 (s), 127.3 (s), 122.2 (d), 120.5 (d), 115.4 (d), 112.7 (d), 40.8 (q), 23.8 (q), 14.7 (q) ppm. Anal. Calcd for C₁₄H₁₈N₄S: *m/z* 275.1325 [M + H]⁺. Found: MS (ESI, TOF): *m/z* 275.1323 [M + H]⁺.

4.2. IR monitoring

The ATR-IR fibre system consisted of a ReactIRTM 15 spectrometer equipped with an MCT (mercury cadmium telluride) detector (Mettler Toledo) connected to a DiComp Probe (Mettler Toledo, dimensions: 6.3 mm DSub AgX DiComp, 8 inches (203 mm) wetted length with a 1.5 m total length of AgX fiberconduit, optical window: 2500 to 650 cm⁻¹, temperature range: -80–180 °C, pH range: 1–14, wetted materials: alloy C276, diamond, gold). Spectra were recorded over the duration of the entire reaction at a spectral resolution of 4 cm⁻¹, averaging 76 scans yielding a temporal resolution of 30 s. The fibre probe was integrated in a double-walled cooling reactor (~10 mL volume) *via* feed-trough equipped with an argon inlet and a septum. The reaction vessel was charged with anhydrous solvent (Et₂O) and cooled by cryostat (Julabo) to -60 °C. After a steady temperature in the reactor was reached the background spectrum was recorded, the measurement started and the lithium species added. Subsequently the respective reactant was rapidly added *via* a syringe (concentrations and equivalents identical to the preparative experiments).

4.3. Flow chemistry

Screening experiments in the flow were carried out using three New Era NE-1000 syringe pumps. **2a** (4.98 g, 20.0 mmol) and *n*-dodecane (1.25 g) were dissolved in anhydrous Et₂O (200 mL) and a

50 mL (60 mL) syringe was filled with the solution. Methyl iodide (4.82 g, 33.9 mmol) was dissolved in anhydrous Et₂O (100 mL) and a 20 mL (24 mL) syringe was filled with the solution. A 10 mL syringe was filled with *n*-butyllithium (1.6 mol/L in hexanes). Na₂SO₃ (3.16 g, 25 mmol) was dissolved in deionized water (100 mL) and sixteen screw-cap vials were charged with Na₂SO₃ solution (1.35 mL each). The syringes were connected to the reactor inlets *via* Luer-Slip adapters as follows: starting material to inlet 1; *n*-butyllithium to inlet 2 and Mel to inlet 3. The chip reactor was placed on the FlowChiller⁵⁴ and the temperature was monitored. The outlet tube was placed in a waste bottle. Then 2 mL of every solution were pushed into the system. The desired flow rates were entered into the pumps. After starting the pumps, the dead volume time was awaited. Then the outlet tube was placed in the first vial and two subsequent samples were collected. Upon completion the vial was screwed tight and shaken vigorously. In such manner four sets of experiments were conducted at room temperature, 0 °C, -20 °C and -40 °C. Preparation of the vials and sample collection was conducted as described above. For GC analysis 256 μL of organic layer from every sample were transferred to a GC vial, diluted with 744 μL ethyl acetate, and analyzed. For the pre-scale experiment, reagents were prepared in the same way, whereas the syringe pumps were replaced with continuous pumps (Syrris Africa) and the reaction time was prolonged. After separation of the layers the diethyl ether was evaporated under reduced pressure. Purification of the crude product was accomplished *via* column chromatography (MPLC, light petrol, then ethyl acetate), yielding 1.258 g (56%) of pure product **3a** as a yellowish oil.

4.4. X-ray diffraction

Diffraction data of single crystals of **5i** (two polymorphs), **5ii** and **5iii** were collected on a Bruker KAPPA APEX II diffractometer system equipped with a CCD detector at 100 K under a dry stream of nitrogen using fine sliced ϕ - and ω -scans.⁵⁵ Data were reduced using SAINT-Plus⁵⁵ and corrected for absorption using SADABS.⁵⁵ The structures were solved with charge-flipping implemented in SUPERFLIP⁵⁶ and refined against *F* using Jana2006.⁵⁷ All non-H atoms were refined with anisotropic atomic displacement parameters. H atoms were located in difference Fourier maps and refined freely in **5i** (both polymorphs) and **5iii**. In **5ii** the H atoms were placed at calculated positions and refined as riding on the parent C atom.

4.5. Second harmonic generation

The second order nonlinear optical properties of the substances were screened with second harmonic measurements from powder samples, produced by grinding the sample crystals with a mortar to a particle size below <1 μm. A relative measurement of the nonlinear optical coefficients is possible with this technique since the SH efficiency scales quadratically with the nonlinear coefficient in this particle size regime.⁵⁸ The powder samples, sandwiched between microscope slides, were irradiated with the output of an ultrafast Yb:KGW-Laser (Light Conversion, pulse duration 70 fs, average power 600 mW, repetition rate 75 MHz, wavelength 1034 nm), moderately focused with a 100 mm focusing lens. The diffusely reflected SH-radiation was collected with a NA = 0.1 lens, separated from fundamental radiation with a color filter, and spectrally analyzed with a 0.25 m grating monochromator and a photomultiplier detector. The sample plane was positioned somewhat out of the focal plane (towards the lens) so as to prevent any damage to the sample. After each measurement, the samples were carefully checked for the absence of damage or thermal modification.

Acknowledgment

This work was supported in part by the TU Wien “Innovative Projects” research funds and the Austrian Federal Ministry of Science, Research and Economy. The authors acknowledge M. Lunzer, D. Wurm, D. Koch, B. Pokorny, D. Möstl, F. Krenn and A. Kempf for supporting the synthetic experiments. The authors also thank W. Skranc for preliminary work on this topic. N. Jankowski is acknowledged for conducting the ion chromatography and E. Rosenberg for performing the high resolution mass spectrometry (HRMS). The X-ray centre of the TU Wien is acknowledged for providing access to the single-crystal diffractometer.

Appendix A. Supplementary data

Supplementary data related to this article can be found at <http://dx.doi.org/10.1016/j.tet.2016.12.025>.

References

- Gronowitz S, Frejd T. *Chem Heterocycl Compd*. 1978;14:353–367.
- Iddon B. *Heterocycles*. 1983;20:1127–1171.
- Gilchrist TL. In: Alan RK, ed. *Advances in Heterocyclic Chemistry*. Academic Press; 1987:41–74.
- Moses P, Gronowitz S. *Arkiv Kemi*. 1961;18:119–132.
- Gronowitz S, Frejd T. *Acta Chem Scand*. 1969;23:2540–2542.
- Gronowitz S, Frejd P. *Acta Chem Scand*. 1970;24:2656–2658.
- Jakobsen HJ. *Acta Chem Scand*. 1970;24:2663–2664.
- Dickinson RP, Iddon B. *Tetrahedron Lett*. 1970;975–978.
- Fuller LS, Iddon B, Smith KA. *Chem Commun*. 1997:2355–2356.
- Fuller LS, Iddon B, Smith KA. *J Chem Society-Perkin Trans*. 1999;1:1273–1277.
- Bobrovsky R, Hametner C, Kalt W, Fröhlich J. *Heterocycles*. 2008;76:1249–1259.
- Santana AS, Carvalho DB, Casemiro NS, et al. *Tetrahedron Lett*. 2012;53:5733–5738.
- Arisawa M, Igarashi Y, Tagami Y, Yamaguchi M, Kabuto C. *Tetrahedron Lett*. 2011;52:920–922.
- Alves D, Sachini M, Jacob RG, et al. *Tetrahedron Lett*. 2011;52:133–135.
- Xu H, Gu SJ, Chen WZ, Li DC, Dou JM. *J Org Chem*. 2011;76:2448–2458.
- Dabdoub MJ, Dabdoub VB, Lenardou EJ, et al. *Synlett*. 2009:986–990.
- Murai T, Fukushima K, Mutoh Y. *Org Lett*. 2007;9:5295–5298.
- Skranc, W., report PhD Thesis, TU Wien, 1999.
- Bohlmann F, Haffer G. *Chem Berichte*. 1969;102:4017–4024.
- Glöckhofer F, Lumpi D, Kohlstädt M, Yurchenko O, Würfel U, Fröhlich J. *React Funct Polym*. 2015;86:16–26.
- Bohlmann F, Skuballa W. *Chem Berichte*. 1970;103:1886–1893.
- Bohlmann F, Burkhardt T, Zdero C. *Naturally Occurring Acetylenes*. London, New York: Academic Press; 1973.
- Karlsson JO, Gronowitz S, Frejd T. *J Org Chem*. 1982;47:374–377.
- Lam HW, Cooke PA, Pattenden G, Bandaranayake WM, Wickramasinghe WA. *J Chem Society-Perkin Trans*. 1999;1:847–848.
- Marcantoni E, Massaccesi M, Petrini M, et al. *J Org Chem*. 2000;65:4553–4559.
- Kuligowski C, Bezenine-Lafollee S, Chaume G, et al. *J Org Chem*. 2002;67:4565–4568.
- Liu G, Huth JR, Olejniczak ET, et al. *J Med Chem*. 2001;44:1202–1210.
- Nielsen SF, Nielsen EO, Olsen GM, Liljefors T, Peters D. *J Med Chem*. 2000;43:2217–2226.
- Lumpi D, Horkel E, Stoeger B, et al. Novel ene-yne compounds as quadratic nonlinear optical materials. In: *Proc SPIE*. Photonics, Devices, and Systems V. vol. 8306. October 11, 2011:830615. <http://dx.doi.org/10.1117/12.912457>.
- Lumpi D, Stöger B, Hametner C, et al. *CrystEngComm*. 2011;13:7194–7197.
- Lumpi D, Glöckhofer F, Holzer B, et al. *Cryst Growth & Des*. 2014;14:1018–1031.
- Tornøe CW, Christensen C, Meldal M. *J Org Chem*. 2002;67:3057–3064.
- Rostovtsev VV, Green LG, Fokin VV, Sharpless KB. *Angew Chem Int Ed*. 2002;41:2596–2599.
- Moussebo C, Dale J. *J Chem Soc C Org*. 1966:260–264.
- NMR tubes (Schott Duran), CDCl₃ (Euriso-Top), standard light source (Intel-liRay 600, Uvitron International, 600 W metal halide type lamp, intensity level 50 %). Prior to the experiment CDCl₃ was extracted with saturated aqueous NaHCO₃ solution and dried over molecular sieve to prevent side effects from acidic residues.
- Fröhlich J, Hametner C, Kalt W. *Monatsh für Chem/Chem Mon*. 1996;127:325–330.
- Lumpi D, Kautny P, Stöger B, Fröhlich J. *IUCrj*. 2015;2:584–600.
- Lumpi D, Kautny P, Stöger B, Fröhlich J. *Acta Crystallogr, Sect B Struct Sci, Cryst Eng Mater*. 2016;72:753–762.
- Lumpi D, Wagner C, Schöpf M, et al. *Chem Commun*. 2012;48:2451–2453.
- Harrington JA. *Handbook of Optics*. 3 ed. The McGraw-Hill Companies; 2010.
- Asai T, Takata A, Ushioji Y, Iinuma Y, Nagaki A, Yoshida J. *Chem Lett*. 2011;40:393–395.
- Klapper H, Hahn T. In: Hahn T, ed. *International Tables for Crystallography*. Dordrecht: Springer; 2005:804.
- Sii): C₁₃H₁₅N₃S₂, M_r = 277.4, monoclinic, P2₁/c, a = 12.1159(4) Å, b = 14.6389(9) Å, c = 7.6543(7) Å, β = 107.959(4)°, V = 1291.44(15) Å³, Z = 4, μ = 0.397 mm⁻¹, T = 100 K, 15795 measured, 2924 independent and 1738 observed [I > 3σ(I)] reflections, 164 parameters, wR (all data) = 0.0658, R [I > 3σ(I)] = 0.0509; CCDC reference number 1453300.
- Siii): C₁₄H₁₈N₄S, M_r = 274.4, monoclinic, P2₁/c, a = 11.0084(2) Å, b = 8.08390(10) Å, c = 15.7948(3) Å, β = 105.7583(8)°, V = 1352.76(4) Å³, Z = 4, μ = 0.231 mm⁻¹, T = 100 K, 53619 measured, 4901 independent and 3986 observed [I > 3σ(I)] reflections, 244 parameters, wR (all data) = 0.0454, R [I > 3σ(I)] = 0.0345; CCDC reference number 1453301.
- (5i), polymorph I: C₁₃H₁₅N₃OS, M_r = 261.3, monoclinic, P2₁, a = 4.6978(3) Å, b = 11.8173(8) Å, c = 11.4978(8) Å, β = 94.974(3)°, V = 635.90(7) Å³, Z = 2, μ = 0.246 mm⁻¹, T = 100 K, 39787 measured, 7967 independent and 7364 observed [I > 3σ(I)] reflections, 223 parameters, wR (all data) = 0.0288, R [I > 3σ(I)] = 0.0252, Flack parameter 0.00(2); CCDC reference number 1453298.
- (5i), polymorph II: C₁₃H₁₅N₃OS, M_r = 261.3, monoclinic, P2₁/c, a = 12.5889(5) Å, b = 9.1066(4) Å, c = 11.0679(5) Å, β = 94.6707(16)°, V = 1264.63(9) Å³, Z = 4, μ = 0.247 mm⁻¹, T = 100 K, 53752 measured, 4634 independent and 4163 observed [I > 3σ(I)] reflections, 223 parameters, wR (all data) = 0.0493, R [I > 3σ(I)] = 0.0300; CCDC reference number 1453299.
- Nakayama J, Konishi T, Murabayashi S, Hoshino M. *Heterocycles*. 1987;26:1793–1796.
- Vachal P, Toth LM. *Tetrahedron Lett*. 2004;45:7157–7161.
- Goldberg Y, Alper H. *J Org Chem*. 1993;58:3072–3075.
- Skranc, W., Diploma Thesis, TU Wien, 1996.
- Huang C, Zhen CG, Su SP, Loh KP, Chen ZK. *Org Lett*. 2005;7:391–394.
- Grimes KD, Gupta A, Aldrich CC. *Synthesis Stuttgart*. 2010:1441–1448.
- Kobatake S, Imagawa H, Nakatani H, Nakashima S. *New J Chem*. 2009;33:1362–1367.
- M. Schoen, M. D. Mihovilovic, M. Schnuerch PCT Int. Appl., 2013, WO 2013006878 A1 20130117.
- Bruker Analytical X-ray Instruments, Inc., Madison, WI, USA: SAINT and SADABS 2008.
- Palatinus L, Chapuis G. *J Appl Crystallogr*. 2007;40:786–790.
- Petricek V, Dusek M, Palatinus L. *Z Krist – Cryst Mater*. 2014;229:345–352.
- Kurtz SK, Perry TT. *J Appl Phys*. 1968;39:3798–3813.

2.11. Manuscript #11

Crystal chemistry of layered structures formed by linear rigid silyl-capped molecules

Daniel Lumpi, Paul Kautny, Berthold Stöger, Johannes Fröhlich

IUCrJ, **2015**, 2, 584-600

Reproduced with the kind permission of the International Union of Crystallography.

Crystal chemistry of layered structures formed by linear rigid silyl-capped molecules

Daniel Lumpi,^a Paul Kautny,^a Berthold Stöger^{b*} and Johannes Fröhlich^a

^aInstitute of Applied Synthetic Chemistry, Vienna University of Technology, Vienna, Austria, and ^bInstitute of Chemical Technologies and Analytics, Vienna University of Technology, Vienna, Austria. *Correspondence e-mail: bstoeger@mail.tuwien.ac.at

Received 24 February 2015

Accepted 16 June 2015

Edited by C.-Y. Su, Sun Yat-Sen University, China

Keywords: arene spacers; incommensurately modulated structures; layer interfaces; order–disorder polytypes; Hirshfeld surface fingerprint plots.

CCDC references: 927469; 927470; 927472; 927473; 928106; 928107; 928108; 928110; 1407074; 1407075; 1407076

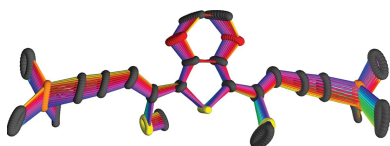
Supporting information: this article has supporting information at www.iucrj.org

The crystallization behavior of methylthio- or methylsulfonyl-containing spacer extended *Z,Z*-bis-ene–yne molecules capped with trimethylsilyl groups obtained by (tandem) thiophene ring fragmentation and of two non-spacer extended analogs were investigated. The rigid and linear molecules generally crystallized in layers whereby the flexibility of the layer interfaces formed by the silyl groups leads to a remarkably rich crystal chemistry. The molecules with benzene and thiophene spacers both crystallized with *C2/c* symmetry and can be considered as merotypes. Increasing the steric bulk of the core by introduction of ethylenedioxythiophene (EDOT) gave a structure incommensurately modulated in the [010] direction. Further increase of steric demand in the case of a dimethoxythiophene restored periodicity along [010] but resulted in a doubling of the *c* vector. Two different polytypes were observed, which feature geometrically different layer interfaces (non-OD, order–disorder, polytypes), one with a high stacking fault probability. Oxidation of the methylthio groups of the benzene-based molecule to methylsulfonyl groups led to three polymorphs (two temperature-dependent), which were analyzed by Hirshfeld surface d_c/d_i fingerprint plots. The analogously oxidized EDOT-based molecule crystallized as systematic twins owing to its OD polytypism. Shortening of the backbone by removal of the aryl core resulted in an enantiomorphic structure and a further shortening by removal of a methylthio-ene fragment again in a systematically twinned OD polytype.

1. Introduction

The controlled formation of layers plays an important role in the design of materials. For example, hybrid organic–inorganic layered perovskites (Mitzi, 2001) are natural quantum well structures and can be tuned to specific electronic, magnetic and optical properties. The combination of layers with different properties enables the synthesis of multi-functional composites (Coronado *et al.*, 2000). In the field of organic electronics the formation of layers has been shown to be a viable strategy to improve conductivity (Anthony *et al.*, 2001). Efficient charge transport in organic materials is governed by nearest-neighbor electronic coupling. The intermolecular coupling is maximized when a face-to-face orientation of aromatic molecules is realized, as a consequence of enhanced interactions of the π -electron clouds of adjacent molecules (Mueller & Bunz, 2007).

Anthony *et al.* (2001) modified pentacene by connecting it at the central C atoms to triisopropylsilyl (TIPS) groups *via* rigid ethyne bridges. As opposed to plain pentacene, the resulting TIPS-pentacene molecules crystallized in layers (Fig. 1), whereby the pentacene cores are arranged in face-to-



OPEN  ACCESS

face orientation. As a result, a significantly lower resistivity perpendicular to the pentacene was reported (Anthony *et al.*, 2001). Hence, TIPS-pentacene yielded promising solution-processed OFET (organic field effect transistor) devices (Park *et al.*, 2007). In addition to the modified stacking arrangement the structures showed improved stability and solubility. On this basis a general molecular design for improved π -stacking was proposed by Anthony *et al.* (2002), and intense research in the field of substituted acene derivatives arose from these findings and is of ongoing interest (Anthony, 1994, 2008).

Besides technological importance, layered structures are interesting from a crystallographic point of view. Polymorphs (different crystal structures of the same composition) that crystallize in different arrangements of equivalent layers are called polytypes. Polytypes are ubiquitous in all classes of solid materials and are often the cause of crystallographically challenging problems, like twinning (the systematic association of equivalent macroscopic domains with different orientations; Hahn, 2006b) and stacking disorder. In order-disorder (OD) polytypes (Dornberger-Schiff & Grell-Niemann, 1961; Ferraris *et al.*, 2008) pairs of layers are equivalent and therefore all polytypes are locally equivalent. The symmetry of a polytype is described by groupoids, a generalization of the group concept (Fichtner, 1986). For OD polytypes these groupoids are classified into OD groupoid families (Fichtner, 1977b), in analogy to space group types. These were tabulated for the special case of OD structures composed of layers of one kind with identical lattices (Fichtner, 1977a).

Nevertheless, many issues remain unsolved. For example, OD structures composed of layers with different lattices have received only a little attention. Yet in some structures, like $K_2HAsO_4 \cdot 2.5H_2O$ (Stöger, Weil & Zobetz, 2012), the different lattices of the layers are the decisive factor giving rise to OD

polytypism. Moreover, we have discovered structures that follow the basic principle of OD theory, namely locally equivalent stacking possibilities, but do not follow the strict definition of OD theory (Stöger, Kautny *et al.*, 2012; Stöger & Weil, 2013). Also, as we will show in this work, polytypes that are not locally equivalent must not be overlooked. The symmetry groupoids of these kinds of polytypes are virtually unexplored. Thus, to shed new light on OD theory and related kinds of polytypism, we are in search of suitable model compounds. A fundamental advantage of organic over inorganic compounds is the ease of introduction of systematic geometric and electronic modifications.

An ideal basis for the crystal engineering of layered structures seemed to be spacer-extended ene-yne molecules synthesized by tandem thiophene ring-fragmentation (TRF) reactions (Bobrovsky *et al.*, 2008) owing to the generality and flexibility of the TRF protocol. The makeup of these molecules resembles the TIPS-pentacene described above, though with smaller aromatic rings and a side chain extended by an ene fragment and a methylthio group (Fig. 2). An interesting aspect of these ene-yne scaffolds is the possibility to selectively oxidize the methylthio group to modify electronic properties, but also introduce structure-directing hydrogen-bond acceptors.

The first reports on controlled TRF reactions go back to Gronowitz & Torbjörn (1970) and Jakobsen (1970). They were explored in detail by Gronowitz & Frejd (1978), Iddon (1983) and Gilchrist (1987). This approach enables the selective yield of *Z*-isomers of ene-yne compounds as determined by the cyclic structure of thiophene. The exploration of tandem fragmentation reactions affording double-sided ring-opened (ene-yne) products was first reported by Fuller *et al.* (1999) on substituted thieno[3,2-*b*]thiophenes.

The first synthesized molecule of the class depicted in Fig. 2 was BSEM (**1**) [benzene spacer-extended with methylthio group; spacer = benzene, SiR_3 = trimethylsilyl (TMS)]. As expected, in analogy to TIPS-pentacene and related molecules (Anthony *et al.*, 2001, 2002), BSEM (**1**) crystallizes in distinct molecular layers delimited by the bulky and flexible silyl groups. Therefore, this molecule was chosen as the starting point of the systematic crystallographic studies presented in this work.

It has to be noted that, in traditional crystal engineering, directed intermolecular interactions, notably *via* hydrogen bonding or, less commonly, halogen bonds, are used to induce controlled 'self-assembly' of molecules (Aakeröy *et al.*, 2010). In the case at hand, no such bonding exists, since the layer-

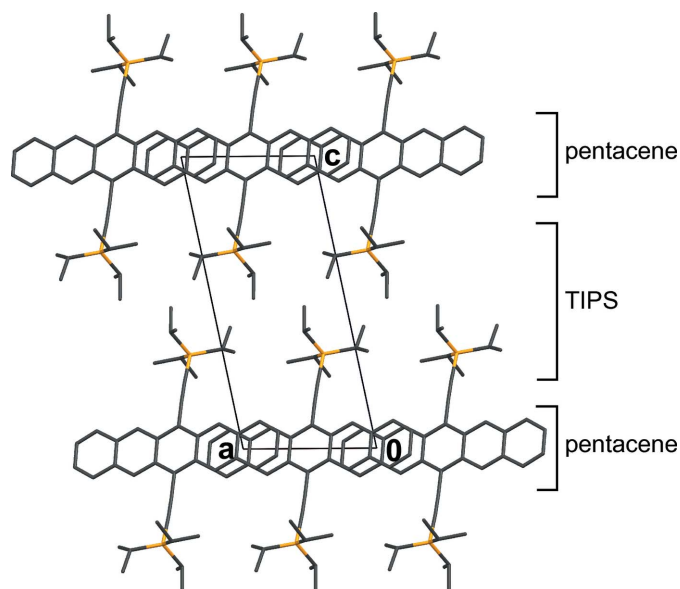


Figure 1
Crystal structure of TIPS-pentacene (*PT*) featuring distinct layers of pentacene cores and TIPS groups connected by $-C\equiv C-$ bridges viewed down [010]. Coordinates taken from Anthony *et al.* (2001). H atoms and disorder of the TIPS groups were omitted for clarity.

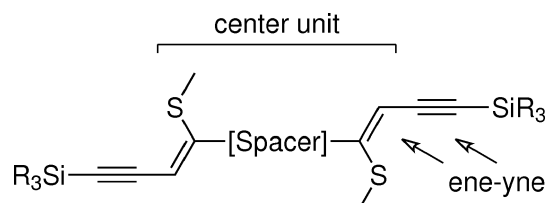


Figure 2
General structure of spacer-extended ene-yne molecules.

delimiting moieties are trialkylsilyl groups. Nevertheless, the special makeup of the molecules clearly induces crystallization as layered structures, and therefore variations of the spacer-extended ene-yne compounds can be considered as a form of crystal engineering.

2. Results and discussion

2.1. Molecular modifications

The scope of molecular modifications and expected impacts on the layer structures are schematized in Fig. 3. The main focus is modification of the spacer to control the intermolecular spacing and width of the layer backbone, with special attention paid to the effects on the layer interface. The latter is also determined by the nature of the silyl groups. Finally, the possibility of introducing potential structure-directing hydrogen-bond acceptors by oxidation of the methylthio groups is used to create new kinds of layer structures.

2.1.1. Spacer modifications. The variations of the spacer unit are illustrated in Fig. 4. Firstly, the *para*-substituted benzene (*mmm*) spacer was replaced by the electron-rich 2,5-substituted thiophene (*2mm*) to TSEM (**2**). Thiophene is, from a technological point of view, an interesting core, since poly-

thiophene has been successfully applied in the field of organic semiconductors.

To analyze the effects of a bulkier spacer extending into the layer plane, we enlarged the spacer to a 3,4-ethylenedioxythiophene (EDOT) bicycle, which is, like thiophene, commonly used in the field of organic semiconductors, to give ESEM (**3**). Surprisingly, the resulting crystal structure was incommensurately modulated. Such a structure can be described by a periodic basic structure and periodic modulation functions, but since the periodicities are incommensurate, the overall structure is only quasi-periodic (Janssen *et al.*, 2007; van Smaalen, 2007). A review of incommensurately modulated organic molecular structures was given by Schönleber (2011).

To better understand the reasons for the modulation, we synthesized the ring-opened 3,4-dimethoxythiophene compound DSEM (**4**) featuring even more steric bulk. After numerous failed crystallization attempts, we were able to obtain two non-incommensurate polymorphs, which can be considered as polytypes, from the same crystallization dish and which will be designated as polytype I and II, respectively.

2.1.2. Oxidation to sulfonyl compounds. The electronic makeup of the molecules was modified by oxidation of the thioether functionality to the corresponding sulfonyl functions (Lumpi *et al.*, 2014). We obtained crystals of the disulfonyl analog of BSEM (**1**): oxBSEM (**1b**) and the fully oxidized trisulfonyl analog of ESEM (**3**): oxESEM (**3b**).

For oxBSEM (**1b**) we observed three polymorphs: polymorph I reversibly transforms into polymorph II upon cooling below *ca* 150 K. Polymorph III is unrelated to the former two and features no phase transition from 100 K up to the melting point. So far we were unable to determine the crystallization conditions needed to selectively obtain either polymorph.

2.1.3. Backbone modifications. An important argument of OD theory concerns the layer thickness: only for thick layers can interatomic interactions over a layer width be ignored. Thus, in a further modification we shortened the backbone

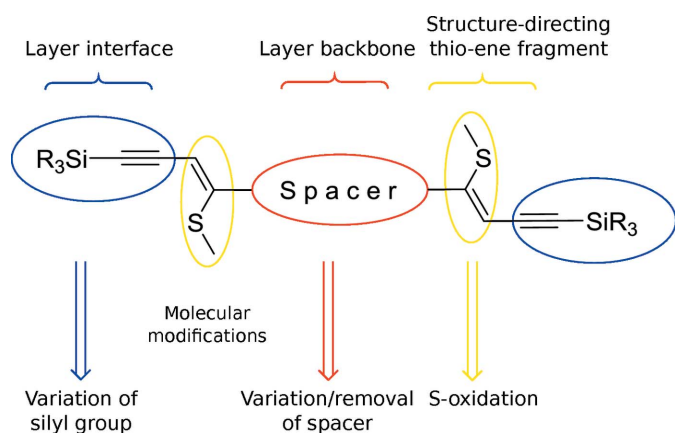


Figure 3
Scope of molecular modifications (bottom) and expected impact on the structures (top).

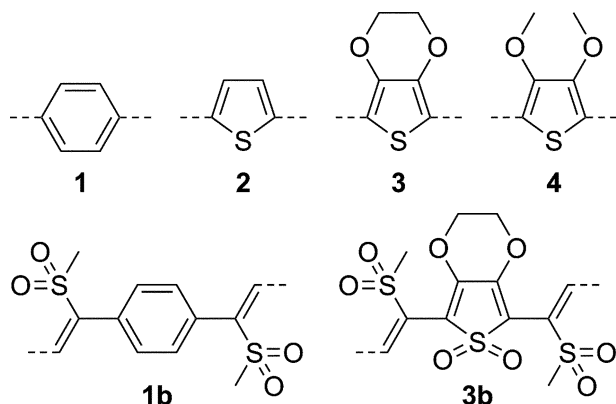


Figure 4
Spacer-extended ene-yne molecules.

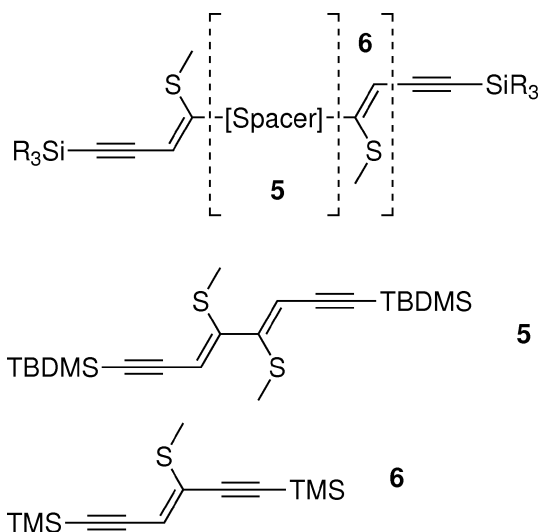


Figure 5
Non-spacer-extended ene-yne molecules.

(Fig. 5). At first the spacer was removed to NSEM (non-spacer-extended with methylthio group; Bobrovsky *et al.*, 2008). We were unable to obtain single crystals suitable for structure determination of the TMS-containing molecule. Therefore, we synthesized and grew crystals of the corresponding *tert*-butyl-dimethylsilyl (TBDMS) compound NSEM-TBDMS (**5**).

Finally, we shortened the backbone further by removing a $-\text{CH}=\text{C}(\text{SMe})-$ fragment to the single-sided ring-opened product ASYM (**6**). The name ASYM indicates a lack of symmetry in the direction of the main axis of the molecule. Despite the name, the molecule does not possess a stereogenic center and it can be considered as symmetric by reflection. Besides the short length, the compound seemed especially

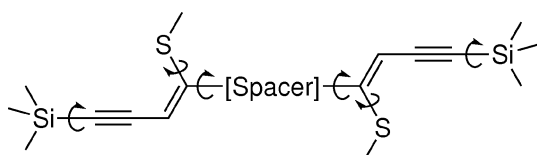


Figure 6
Rotational degrees of freedom in spacer-extended molecule.

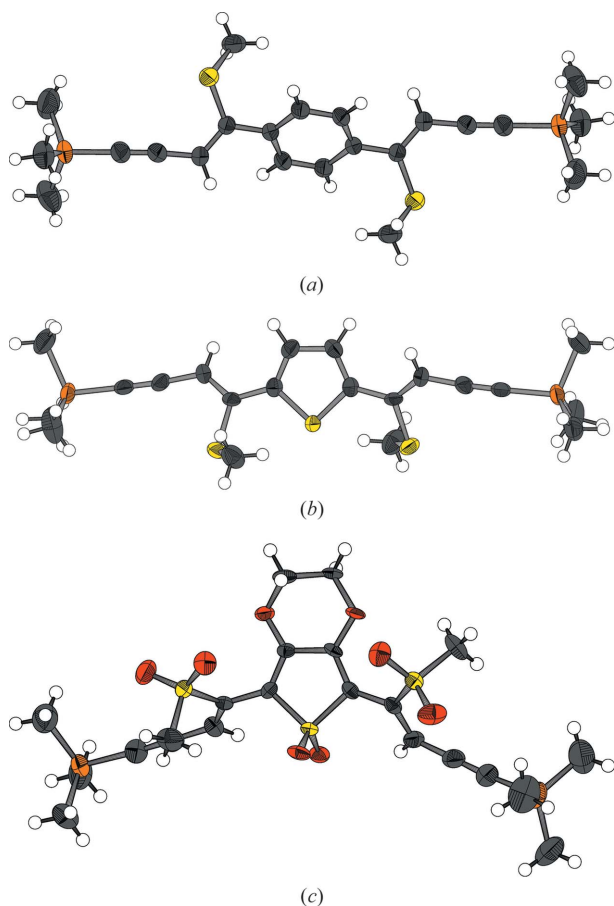


Figure 7
Characteristic geometries of molecules featuring (a) a benzene spacer, (b) a thiophene spacer and methylthio groups, (c) a thiophene dioxide spacer and methylsulfonyl groups. C, O, S and Si atoms are represented by gray, red, yellow and orange ellipsoids drawn at 90% probability levels, H atoms by white spheres of arbitrary radius.

interesting in the light of OD theory, since the latter differentiates between polar and nonpolar layers. By growing crystals of a molecule that is polar with respect to the main axis, we were hoping to obtain polar layers, yet even ASYM (**6**) crystallized in nonpolar layers.

2.2. Molecular structures

The molecules presented in this work are essentially rigid, but possess three kinds of pivotal points, as depicted in Fig. 6. The main pivotal point is the connection of the side chains to the aromatic spacers (or the connection of the side chains in the case of non-spacer-extended molecules). Moreover, the methylthio (or methylsulfonyl) groups as well as the silyl groups can freely rotate. Nevertheless, the overall forms of the molecules feature little possibility for variation.

In Table 1 the rotation angles about the freely rotatable bonds of the title compounds are compiled.

In general, the geometries of the molecules are similar. The most notable trend is that in molecules with a benzene spacer the $\text{C}=\text{C}(-\text{spacer})\text{C}=\text{C}$ torsion angle is 180° (all molecules are symmetric by inversion), *i.e.* the methylthio or methylsulfonyl groups are located at opposite sides of the molecules (Fig. 7a). In molecules with a thiophene or a thiophene dioxide spacer, on the other hand, the torsion angle is small, *i.e.* the methylthio or methylsulfonyl groups face the same direction. Whereas in the methylthio/thiophene containing molecules [TSEM (**2**), ESEM (**3**) and DSEM (**4**)] the S atoms of the methylthio groups are in close vicinity to the S atom of the thiophene ring (Fig. 7b), in the oxidized trisulfone compound oxESEM (**3b**) the methylsulfonyl groups are located at the opposite side of the aromatic ring owing to steric repulsion (Fig. 7c).

With the exception of the non-spacer-extended molecules [NSEM-TBDMS (**5**), ASYM (**6**)], the methylthio and methylsulfonyl groups feature a distinct inclination to the plane of the ene fragment. In contrast, in NSEM-TBDMS (**5**) and ASYM (**6**) one methylthio unit is nearly perfectly aligned with the ene fragment. Whereas the CH_3 unit of the methylthio groups is generally turned towards the spacer ($\text{C}=\text{C}-\text{S}-\text{CH}_3$ torsion angle $> 90^\circ$), the methylsulfonyl groups face the side chain ($\text{C}=\text{C}-\text{SO}_2-\text{CH}_3$ torsion angle $< 90^\circ$). An exception is polymorph II of oxBSEM (**1b**), whereby the two unique molecules show the two behaviors, respectively.

The silyl group is in most cases in a *gauche* conformation to the side chain with inclination angles of ~ 10 – 30° . Only the TMS groups in one out of two molecules in polymorph II of oxBSEM (**1b**) and one out of two TMS groups in ASYM (**6**) are in a nearly perfect *anti* position (176.7 and 178.4° , respectively).

2.3. Layer stacking

With the exception of polymorph III of oxBSEM (**1b**), all structures crystallize in distinct crystallochemical layers, whereby the silyl groups are located at the layer interfaces. In Table 2 the symmetry of the layers and the operations relating adjacent layers are compiled. Here and in the following text,

Table 1

Torsion angles in the title compounds (°).

For structures with two crystallographically different molecules each molecule is listed in a separate row. For the incommensurately modulated ESEM (**3**) minimum and maximum values are indicated. For thiophene spacers the S atom was used as terminal atom, for benzene spacers the C atom with a torsion angle > 90°. For the C–Si(–C≡C–)C=C torsion angle the atom with the angle closest to 0° or 180° was chosen.

Molecule	C=C–spacer	C=C(–spacer–)C=C	C=C–S–CH ₃	C–Si(–C≡C–)C=C
BSEM	144.26 (8)	180	138.00 (6)	30.09 (8)
TSEM	152.0 (3)	68.5 (5)	129.3 (3)	28.8 (4)
ESEM	156.36–165.31 (12)	47.4–52.4 (3)	149.81–162.53 (17)	149.81–162.53 (17)
DSEM, polytype I	156.66 (19), 163.93 (17)	50.2 (3)	121.71 (19), 111.17 (19)	160.0 (2), 158.9 (2)
DSEM, polytype II	157.1 (4), 162.7 (4)	51.4 (7)	124.7 (4), 111.2 (5)	160.8 (4), 22.1 (5)
oxBSEM, polymorph I	132.80 (11)	180	57.32 (11)	151.46 (10)
	131.49 (10)	180	62.46 (9)	24.84 (10)
oxBSEM, polymorph II	127.7 (4)	180	71.8 (4)	176.7 (5)
	128.5 (4)	180	109.2 (4)	29.9 (3)
oxBSEM, polymorph III	124.93 (17)	180	84.82 (15)	23.9 (18)
oxESEM	44.6 (3), 63.7 (3)	14.9 (3)	80.0 (2), 66.8 (2)	159.6 (2), 151.0 (2)
	46.2 (3), 64.2 (3)	17.2 (3)	78.8 (2), 67.8 (3)	159.6 (2), 153.4 (2)
NSEM-TBDMS	–	76.32 (12)	179.50 (7), 164.04 (8)	170.82 (7), 10.18 (8)
ASYM	–	–	179.3 (2)	166.7 (2), 178.4 (2)

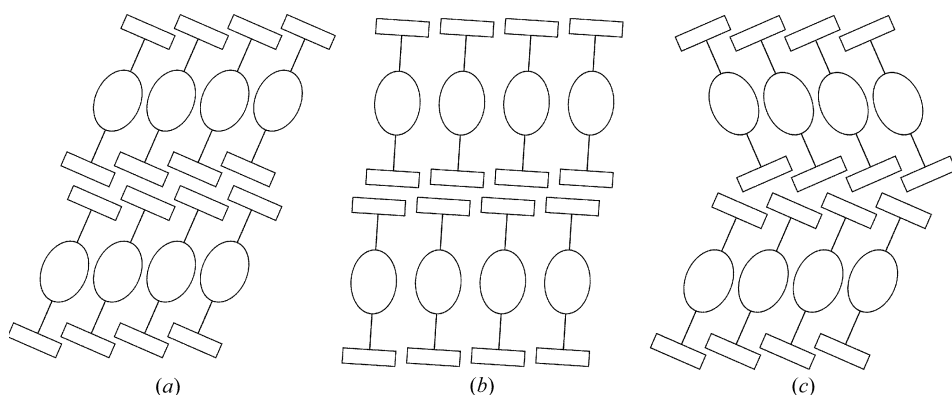


Figure 8

Scheme of the layer contacts of the title compounds observed in (a) the common case, (b) oxESEM (**3b**) and (c) polytype II of DSEM (**4**) and NSEM-TBDMS (**5**). Sylil groups are represented by rectangles, the yne fragments by lines and the center unit of the molecules (spacer, methylthio/methylsulfonyl and ene fragment) by ellipses.

layer group types are designated with lower case Bravais symbols reflecting the two-dimensionality of the lattice (Kopsky & Litvin, 2006) and parentheses indicating the direction of missing translation symmetry as is customary in OD theory (Dornberger-Schiff & Grell-Niemann, 1961).

The main axis of the molecules is in general distinctly inclined with respect to the stacking direction and the molecules in adjacent layers are inclined in the same direction as schematized in Fig. 8(a). In oxESEM (**3b**), on the other hand, the molecules feature only a little inclination, resulting in a layer stacking comparable to the scheme in Fig. 8(b). The layer stacking in polytype II of DSEM (**4**) and in NSEM-TBDMS (**5**) are exceptions: The molecules in adjacent layers are inclined in opposite directions (Fig. 8c). Indeed, these two are the only structures presented in this work that lack inversion symmetry relating adjacent layers (Table 2).

2.4. Structural relationships

Before describing the individual crystal structures in detail (§2.5), here an overview of the structural relationships of the crystals under investigation is given. The relationships and interesting crystallographical features are summarized

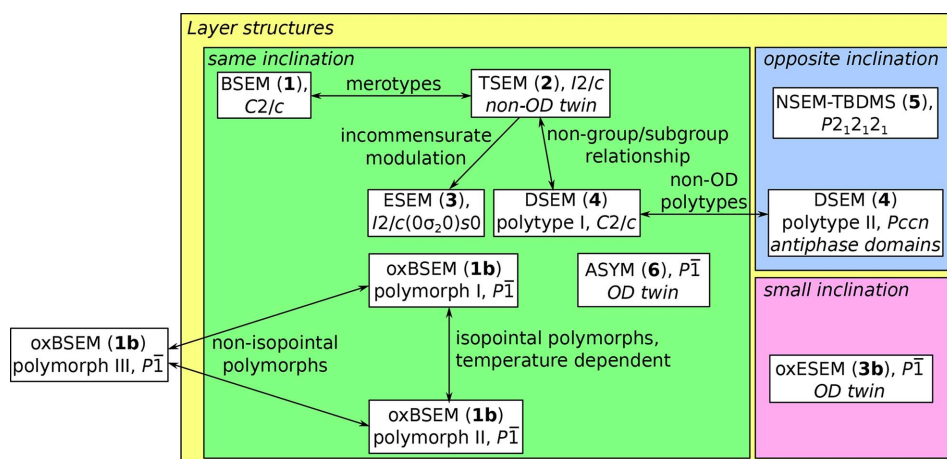


Figure 9

Structural relationships of the crystals under investigation. Structures crystallizing as layers are marked by a yellow backdrop; those with same and opposite inclination in adjacent layers or little inclination (see Fig. 8) by green, blue and pink backdrops, respectively. Twinning or antiphase domains are indicated in cursive.

in Fig. 9. The 11 structures can be partitioned into two families and three unrelated structures.

The first family is made up of the structures of BSEM (1) and of the analogs obtained by substitution of the aromatic spacer [TSEM (2), ESEM (3) and DSEM (4)]. BSEM (1) and TSEM (2) are merotypes, *i.e.* belong to a family of structures that possess layers common to all members, but also layers found only in certain members (Makovicky, 1997). Although the term originates from the crystallography of minerals, an interpretation of molecular organic structures in terms of merotypism has for example been given by our group (Stöger, Kautny *et al.*, 2012).

Increase of the steric bulk of the thiophene spacer in TSEM (2) to EDOT in ESEM (3) leads to an incommensurately modulated structure with a basic structure isostructural (Kálmán *et al.*, 1993) with TSEM (2). The modulation is a compromise between the need for additional space by the EDOT spacer and the retention of the structure of the inter-layer contacts formed by the TMS groups.

On further increase of the steric bulk to dimethoxythiophene in DSEM (4), periodicity is restored. Although structurally related, the symmetries of TSEM (2) and DSEM (4) are not related by a group/subgroup relationship. Crystals of two DSEM (4) polytypes were grown in which layers connect in geometrically different ways (non-OD polytypes). Owing to these alternative stacking possibilities, the second polymorph crystallizes as antiphase domains (domains related by translation symmetry; Wondratschek, 1976), leading to weak diffraction intensities. Different possible kinds of connecting layers are also the likely reason for the non-OD twinning (the interface is geometrically different from the individuals) of TSEM (2).

Oxidation of the methylthio groups and removal of the spacer leads to unrelated structures. oxBSEM (1b) exists as three polymorphs making up the second family. Two poly-

Table 2

Symmetry of the overall structures and the molecular layers and operations relating adjacent layers in the crystals under investigation.

For the incommensurately modulated ESEM (3), symmetry and operations of the basic structure are listed. Pseudosymmetry of OD structures is not listed.

Structure	Space group	Layer group	Operations relating adjacent layers
BSEM	$C2/c$	$p(1)2/c1$	$\bar{1}$, $t_{(a+b)/2}$, 2_1 [010], n [010]
TSEM	$I2/c$	$p(1)2/c1$	$\bar{1}$, $t_{(a+b+c)/2}$, 2_1 [010], a [010]
ESEM, basic structure	$I2/c$	$p(1)2/c1$	$\bar{1}$, $t_{(a+b+c)/2}$, 2_1 [010], a [010]
DSEM, polytype I	$C2/c$	$p(1)2_1/c1$	$\bar{1}$, $t_{(a+b)/2}$, 2_1 [010], n [010]
DSEM, polytype II	$Pccn$	$p(1)2_1/c1$	2_1 [100], c [100], 2 [001], n [001]
oxBSEM, polymorph I	$P\bar{1}$	$p\bar{1}\bar{1}(\bar{1})$	$\bar{1}$, t_c
oxBSEM, polymorph II	$P\bar{1}$	$p\bar{1}\bar{1}(\bar{1})$	$\bar{1}$, t_c
oxESEM	$P\bar{1}$	$p\bar{1}\bar{1}(\bar{1})$	$\bar{1}$, t_c
NSEM-TBDMS	$P2_12_12_1$	$p12_1(1)$	2_1 [100], 2_1 [001]
ASYM	$P\bar{1}$	$p\bar{1}(\bar{1})\bar{1}$	$\bar{1}$, t_b

morphs (I and II) are structurally related. Whereas the arrangement of the molecules is retained, one out of two molecules inverts orientation. Thus, although the term is usually reserved for inorganic structures, both polymorphs can be considered isopointal (same space group and Wyckoff positions of molecules; de Faria *et al.*, 1990), but not isostructural. Polymorph III is structurally unrelated and the only analyzed structure that is not composed of layers.

Of the remaining three structures, oxESEM (3b) and ASYM (6) crystallize as OD twins, since their layers possess higher symmetry than adjacent layers. In these twins, the layer interface can be considered as a fragment of a different polytype that is locally equivalent to the twin individuals.

Finally, NSEM-TBDMS (5) is the only structure crystallizing in a Sohncke space group (the crystal is enantiomorphic).

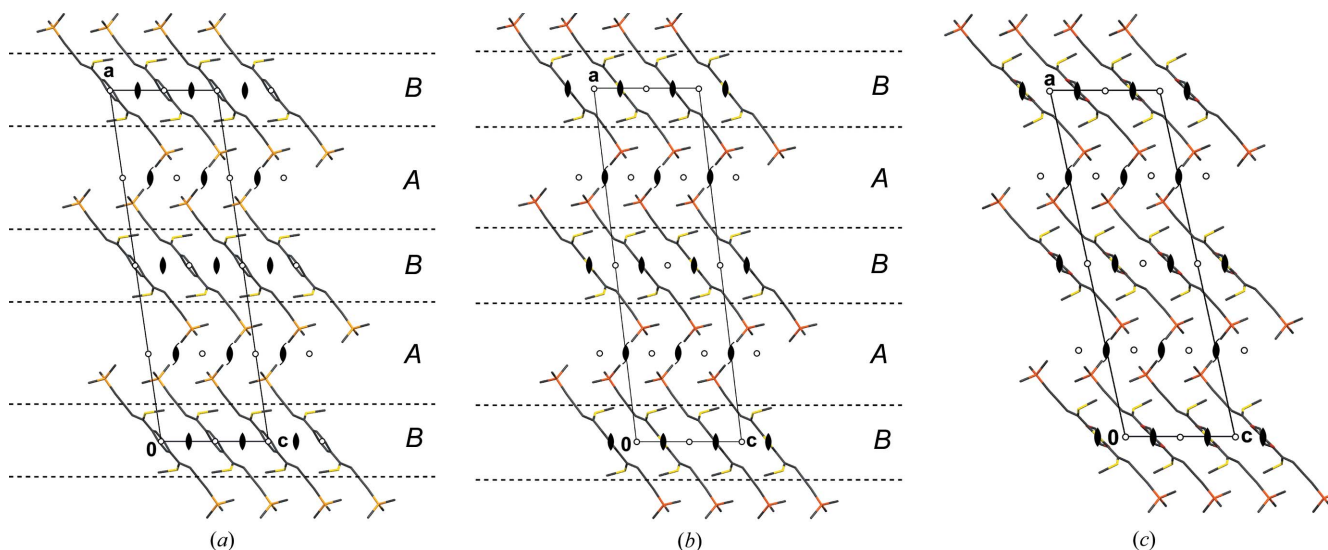


Figure 10

The crystal structures of (a) BSEM (1), (b) TSEM (2) and (c) the basic structure of ESEM (3) viewed down the monoclinic axis [010]. Color codes as in Fig. 7. H atoms have been omitted for clarity. Symmetry elements with the exception of the glide planes are indicated by the graphical symbols standardized in *International Tables for Crystallography* (Hahn, 2006a). Boundaries between the A and B layers are indicated by dashed lines.

2.5. Crystal structure details

2.5.1. BSEM (1) and TSEM (2). In the structures of BSEM (1) and TSEM (2) the molecules are arranged in layers parallel to (100) with $p(1)2_1/c1$ symmetry (Figs. 10a and 10b). Yet, owing to the intrinsically different symmetries of the *para*-substituted benzene (mmm) and 2,5-substituted thiophene ($mm2$) rings, the molecules are located on different Wyckoff positions: Whereas the BSEM (1) molecules are symmetric by inversion, the TSEM (2) molecules are located on the twofold rotation axes. Adjacent BSEM (1) and TSEM (2) molecules are related by the mutual operation: twofold rotations for BSEM (1) and inversions for TSEM (2).

Despite this difference, the outer parts of the layers are virtually identical in both structures. Moreover, adjacent layers connect in equivalent ways *via* 2_1 screws, n glides, inversions and the centering translations (Figs. 10a and 10b).

Thus, to relate their symmetry, the crystal structures of BSEM (1) and TSEM (2), are ‘sliced’ into two kinds of layers, which do not correspond to layers in the chemical sense. The *A* layers [$p(1)2_1/c1$], which are composed of the $-C\equiv C-$ TMS fragments of adjacent molecules, are equivalent in both structures. The *B* layers [$p(1)2_1/c1$] containing the center unit (aromatic rings, ene fragment and methylthio groups) on the other hand are fundamentally different (Figs. 10a and 10b).

Since the *A* and *B* layers of both structures crystallize in the same layer group type, BSEM (1) and TSEM (2) possess the same space-group symmetry. Yet, in a comparable cell setting, the *B* layers are translated along $c/4$ in TSEM (2) compared with BSEM (1), thus the former is described in the non-standard $I2/c$ setting of $C2/c$.

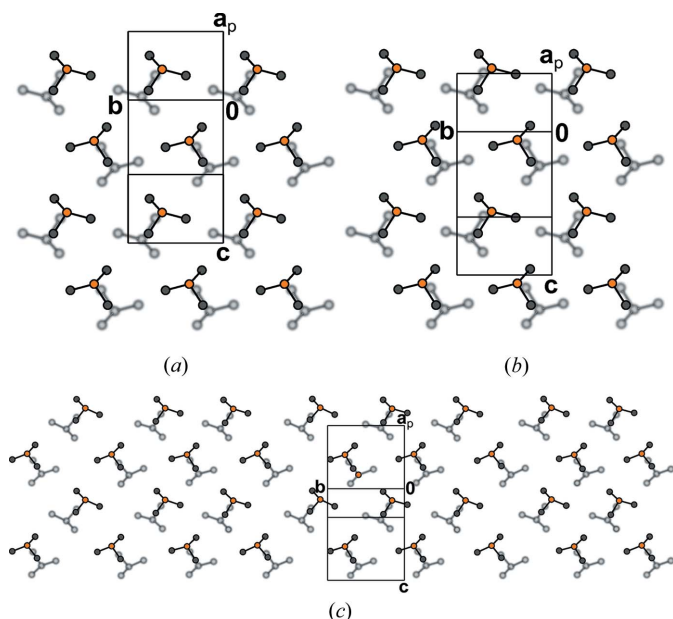


Figure 11 Contact of TMS groups in two adjacent layers of (a) BSEM (1), (b) TSEM (2) and (c) ESEM (3) projected on the layer plane (100). Groups of the lower layer are gray and blurred, other color codes as in Fig. 7. H atoms have been omitted for clarity. The extent of the unit cell [of the basic structure in the case of ESEM (3)] is indicated by black lines.

The BSEM (1) molecule is slightly longer than the TSEM (2) molecule (Si–Si distance of 16.36 *versus* 16.07 Å). However, since the inclination of the BSEM (1) molecules with respect to the layer plane is slightly more pronounced, the molecular layer width is smaller ($a\sin\beta/2 = 16.89$ *versus* 17.10 Å) and the packing in the [001] direction less dense [$c = 10.3442$ (18) *versus* 10.1978(8) Å]. The benzene rings require more space in the [010] direction compared with the thiophene rings, as observed by an increased lattice parameter b of 6.8690 (12) *versus* 6.7415 (4) Å. These small structural modifications have nearly no impact on the layer interface (Figs. 11a and 11b).

The crystal of TSEM (2) was twinned by reflection at (001). Often, OD theory is a convenient tool to understand twinning in layered structures (Stöger *et al.*, 2013): the twin domain is interpreted as an alternative but locally equivalent stacking sequence. Application of OD theory to TSEM (2) did not lead to such a convincing interpretation, since no local pseudo-symmetry is present. From a crystallochemical point of view, the only plausible twin interface is the boundary of the molecular layers. The molecule contact would then resemble more closely Fig. 8(c) than Fig. 8(a). Thus, the twin interface is

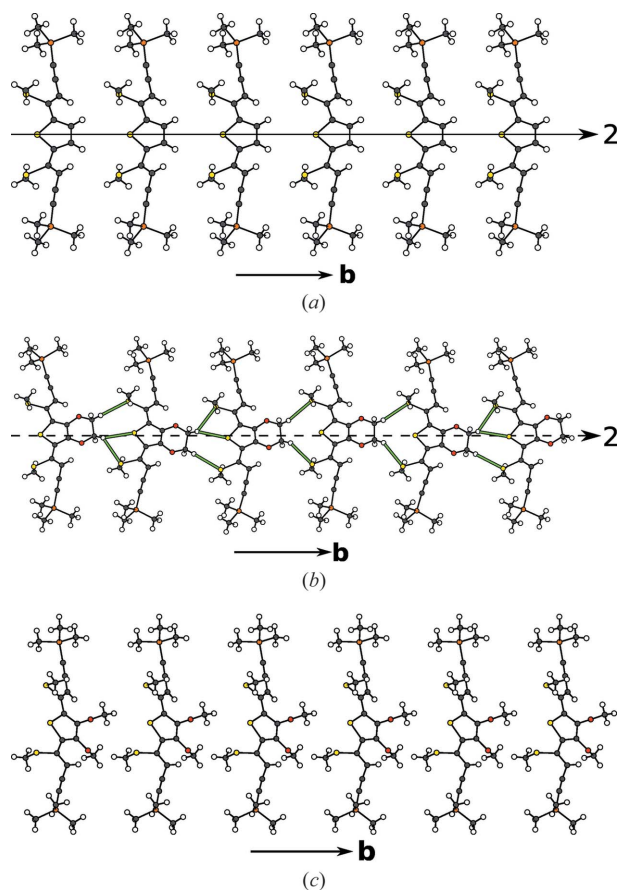
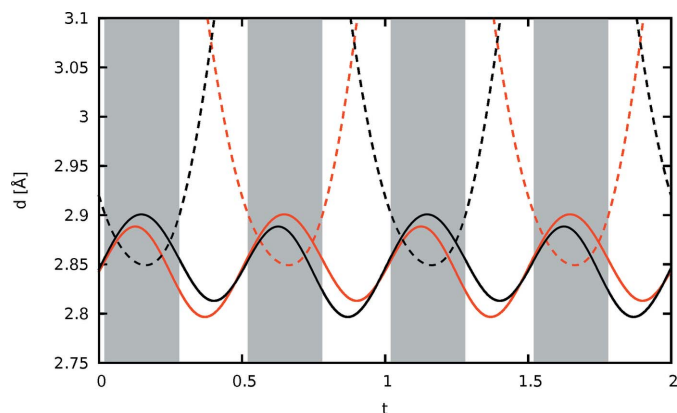


Figure 12 Chain of (a) TSEM (3), (b) ESEM (3) and (c) DSEM (4) molecules running along [010]. Color codes as in Fig. 7. In (b) intermolecular H...S contacts up to 2.91 Å are indicated by green rods to highlight the different types of intermolecular contacts. An arrow indicates a twofold rotation of the chain. If it is dashed it is valid only for the basic structure.


Figure 13

Distance of the equatorial H112 atoms of the ethylenedioxy bridge in ESEM (3) to the S atoms in the adjacent molecules plotted against t . The curves of the two H112 atoms are red and black, respectively. The distances to the S atoms of the methylthio groups and the thiophene ring are drawn using continuous and dashed lines, respectively. Gray backdrops mark the ranges where an H atom protrudes into the cavity formed by the three S atoms of the adjacent molecule.

geometrically different from the twin individuals. The possibility of such a twinning is demonstrated by the DSEM (4) polytypes (§2.5.3).

2.5.2. ESEM (3). The basic structure of ESEM (3) is isostructural with TSEM (2) (Fig. 10c). Compared with TSEM (2), the ESEM (3) molecules are more strongly inclined with respect to the layer plane, resulting in a larger monoclinic angle of $\beta = 102.301(2)^\circ$ versus $\beta = 96.889(5)^\circ$ and smaller layer widths ($a\sin\beta = 31.72$ versus 34.19 \AA). As expected, the lattice parameter b increases significantly from $6.7415(4)$ to $8.4003(5) \text{ \AA}$ owing to the additional space needed by the ethylenedioxy group.

The actual structure is incommensurately modulated with a modulation wavevector of $\mathbf{q} = \sigma_2\mathbf{b}^*$ with $\sigma_2 = 0.6223(1) \simeq 5/8$.

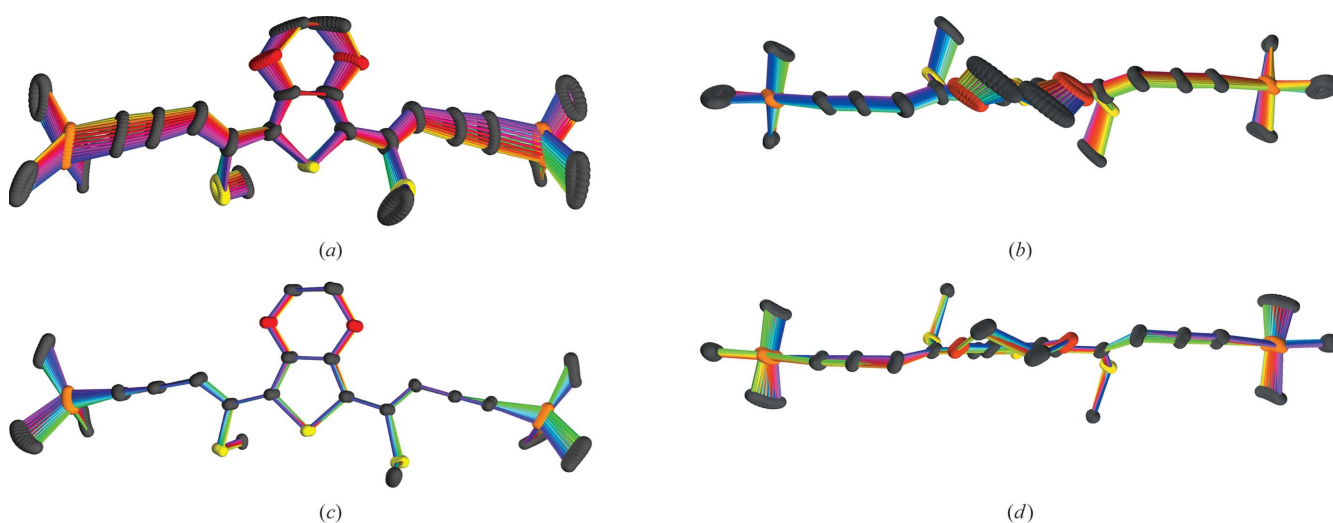
Although incommensurately modulated structures are non-periodic, they can be conveniently described by embedding into $3+n$ superspace (Janssen *et al.*, 2007; van Smaalen, 2007). The superspace of ESEM (3) has $3+1$ -dimensional superspace group symmetry (van Smaalen *et al.*, 2013; Stokes *et al.*, 2011) $I2/c(0\sigma_2)0s0$, a non-standard setting of $B2/b(00\sigma_3)s0$, No. 15.3 (Janssen *et al.*, 2006).

Since \mathbf{q} is parallel to the layer planes, the layers are equivalent. Adjacent layers are related by a 2_1 screw with intrinsic translation along $\mathbf{a}_{s2}/2 + \mathbf{a}_{s4}/2$, corresponding to an increase of the internal coordinate t by $(\sigma_2 + 1)/2$.

The twofold rotation of the molecules in the basic structure features an intrinsic translation along $\mathbf{a}_{s4}/2$ in internal space. Thus, half of each molecule is completed by a second half located at $t + 1/2$. The individual molecules are therefore generally not symmetric by twofold rotation and the actual S1 atoms are not located on the twofold rotation axis.

In Figs. 12(b) and 12(c) the progression from the unmodulated chains of molecules along [010] in TSEM (2) to the modulated chains in ESEM (3) is depicted. On the one hand, the steric repulsion of the ethylenedioxy groups and the S atoms requires more space in the [010] direction, on the other hand the layer contacts *via* the TMS groups remain similar to those of TSEM (2) (Figs. 11b and 11c). To accommodate for both, the structure reacts by different rotations of adjacent molecules in an incommensurate way.

The distance of the equatorial H112 atoms of the ethylenedioxy group to the S atoms is plotted against the internal coordinate t in Fig. 13. Roughly two regions can be distinguished. For approximately half of the t values, marked by a gray backdrop in Fig. 13, an H112 atom is close to the thiophene S. Adjacent molecules are inclined to each other and the H112 atom protrudes into the cavity defined by the three S atoms. For the remaining t values, the molecules feature little inclination and the two H112 atoms connect only to the S atoms of the methylthio atom. In Fig. 12(b) H–S distances up


Figure 14

Overlap of an ESEM (3) molecule at 24 equidistant t values (*a*, *c*) projected approximately on the molecular plane and (*b*, *d*) viewed down the twofold axis of the basic structure. In (*a*, *b*) the orientation of the molecules from the actual structure is unchanged; In (*c*, *d*) the molecules are rotated to minimize the interatomic distances of the thiophene rings. Bond colors with similar hue signify close t values, complementary colors a shift of $t + 1/2$.

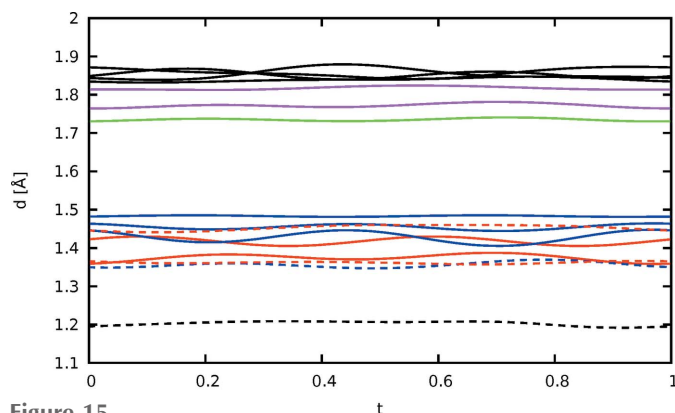


Figure 15
All intramolecular bond lengths in ESEM (3) involving non-H atoms plotted against t . Symmetry-equivalent distances located at $t + 1/2$ are not listed. Color codes: Si–C: black; C–S aliphatic: pink; C–S aromatic: green; C–C single bond (spacer to ene, ene to yne and yne to TMS): blue; C–O: red dashed; C–C aromatic: red; C–C double bond: blue dashed; C–C triple bond: black dashed.

to an arbitrary value of 2.91 Å are indicated to highlight the two kinds of contacts.

Owing to the rigidity of the ESEM (3) molecules small rotations of the EDOT core translate into larger displacements of the TMS groups (Figs. 14a and 14b). Therefore, the connection of adjacent layers *via* the TMS groups features a wide variation of interatomic distances (Fig. 11). This surprising flexibility of the interlayer contacts enables incommensurate modulation.

The variation of the geometry of the ESEM (3) molecules is pictured in Figs. 14(c) and 14(d). The interatomic distances are

close to constant (Fig. 15) and in good agreement with the expected values (Allen *et al.*, 2006). Whereas the core of the molecule is virtually identical in all molecules, the side arms (yne fragment, TMS group) feature significant bending (Fig. 14c), needed to contact adjacent layers.

2.5.3. DSEM (4). Like in TSEM (2) and ESEM (3), the DSEM (4) molecules in both polytypes are arranged in rods running along the [010] direction (Fig. 12c). In contrast to ESEM (3), periodicity in the [010] direction is restored by rotating all molecules in a rod in the same direction (Fig. 12c). The symmetry of the rods is thus reduced from $\mu_b 121$ to $\mu 1$. The rods form pairs which are related by inversion and adjacent pairs are related by 2_1 screws. As a consequence the **c** lattice vector is doubled compared with TSEM (2). Owing to the different arrangements of the rods the DSEM (4) layers cannot be considered as superstructures of the TSEM (2) layers and indeed, their symmetry groups ($p(1)2_1/c1$ with doubled **c** and $p(1)2/c1$) are not related by a group/subgroup relationship.

Although the DSEM (4) polytypes are non-OD polytypes, in the following discussion the naming conventions of OD theory will be used (Ferraris *et al.*, 2008): the layers are designated as A_n , whereby the n is a serial index. \mathbf{a}_0 is the vector normal to the layer planes with the length of one layer thickness.

Given an A_n layer, the adjacent A_{n+1} layer can appear in two different orientations. A_n and A_{n+1} are either related by the operations listed in Table 2, line 4, or those in line 5. The symmetry elements are indicated in Fig. 16.

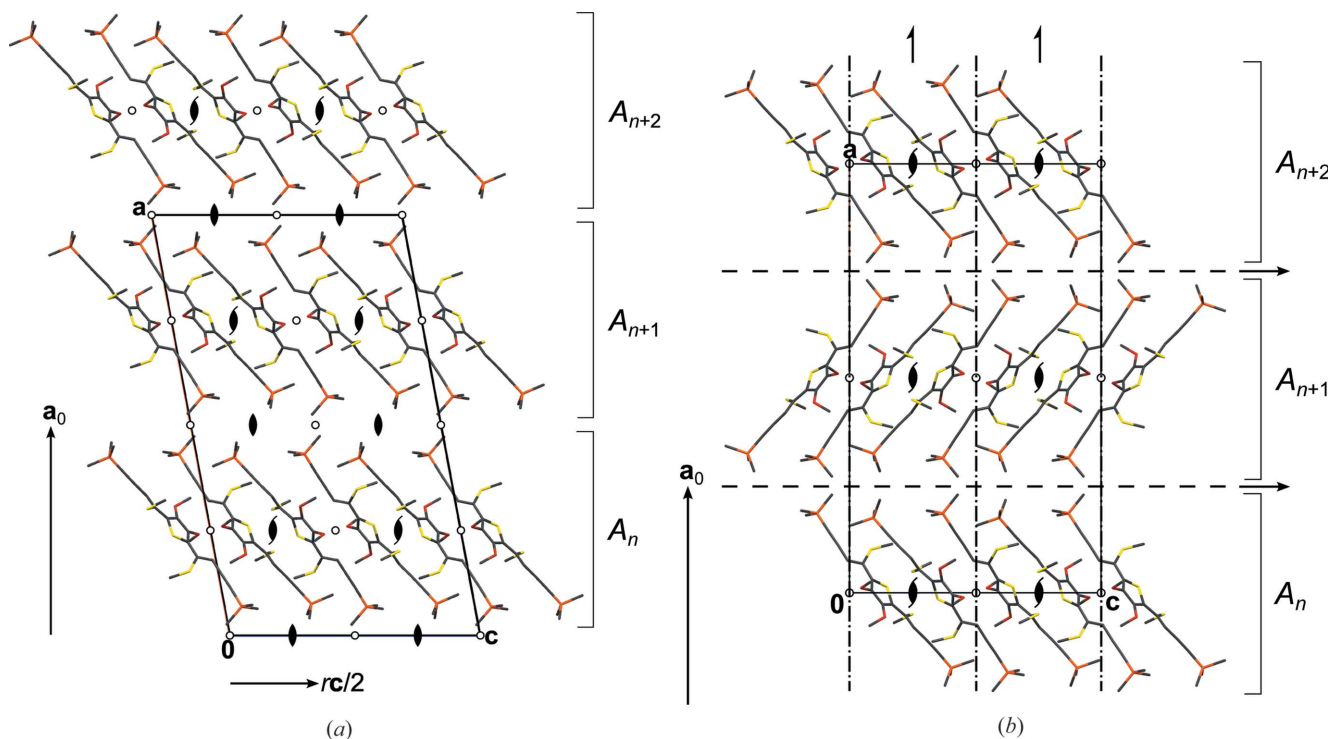


Figure 16
The crystal structures of polytypes (a) I and (b) II of DSEM (4) viewed down [010]. Color codes and symbols as in Fig. 7. H atoms have been omitted for clarity. The A_n layers are indicated to the right by brackets.

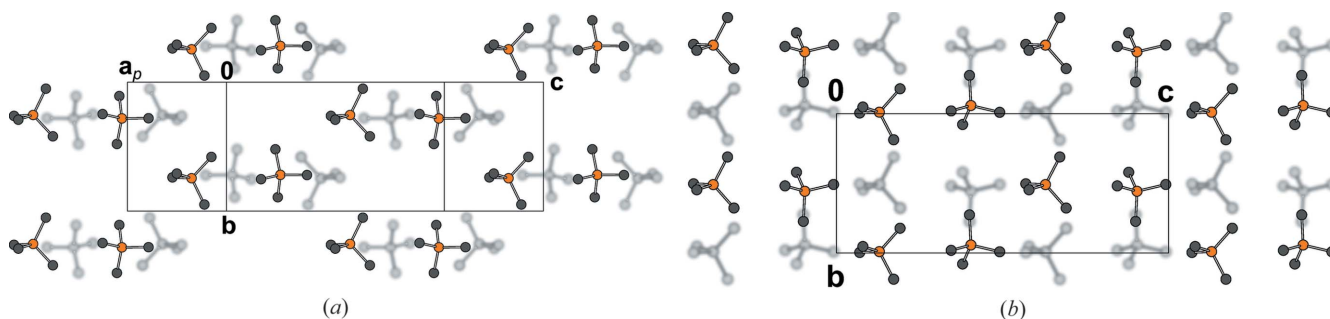


Figure 17

Geometrically non-equivalent contacts of two layers in polytypes (a) I and (b) II of DSEM (4) projected on the layer plane (100). The TMS groups and the connecting sp^1 hybridized C atom are shown. Atoms of the lower layer are gray and blurred, color codes of the top layer as in Fig. 7. H atoms have been omitted for clarity.

Thus, the layers can be connected to an infinity of polytypes, which are not OD polytypes because (A_n, A_{n+1} layer pairs are not necessarily equivalent [$p(1)2/c1$ and $p(c)2$ symmetry, respectively]). The polytypes differ from other non-OD polytypes we discussed before (Stöger *et al.*, 2012a; Stöger & Weil, 2013). In the latter, which we designated as ‘non-classic OD’ polytypes, every polytype is at every point locally equivalent to all other polytypes, *i.e.* every point belongs to at least two equivalence regions (Grell, 1984). In DSEM (4), on the other hand, the contact plane of the layers differs geometrically among polytypes as depicted in Fig. 17. As in the case of ESEM (3) this demonstrates a remarkable flexibility of the layer contacts and confirms the assumption that the twinning of TSEM (2) is likewise caused by non-equivalent layer contacts.

Although the symmetry groupoids of these kind of non-OD polytypes were not elaborated up to now, the OD concept of polytypes with a *maximum degree of order* (MDO) (Dornberger-Schiff, 1982) can nevertheless be applied. There are

two polytypes that cannot be decomposed into simpler polytypes. They are generated by continuous application of either set of operations relating the adjacent layers. The MDO₁ polytype has $C2/c$ symmetry and lattice vector $2\mathbf{a}_0 + (r-1)\mathbf{c}$; MDO₂ $Pccn$ symmetry and lattice vector $2\mathbf{a}_0$.

The observed polytypes I and II are MDO₁ and MDO₂, respectively. Indeed, it is well documented for OD structures that ordered polytypes are in the vast majority of cases MDO. Fragments of the MDO₂ polytype in MDO₁ result in twinning by reflection at a plane normal to [001]. No such twinning was observed in the investigated crystal. Stacking faults in MDO₂, on the other hand, results in antiphase domains (Wondratschek, 1976), since the MDO₂ domains are related by translation. Although in principle not directly observable in diffraction patterns, we suspect that such stacking faults exist and cause the systematic low scattering power of the polytype II crystals.

As opposed to OD structures, where ordered polytypes usually feature desymmetrization of the layers compared to the idealized description (Đurovič, 1979), the *A* layers in both MDO polytypes of DSEM (4) possess the $p(1)2_1/c$ symmetry of the idealized description. A deviation from the idealized model is nevertheless observed by a slight variation of the lattice parameters and layer widths across structures [$a\sin\beta = 33.765$ versus 33.630 (10) Å, $b = 8.1665$ (5) versus 8.271 (2) Å and $c = 20.0791$ (12) versus 19.717 (6) Å] and a small deviation of the molecular conformations (Fig. 18). As expected, the largest deviation is observed for the TMS groups, which are located in geometrically different environments in both polytypes.

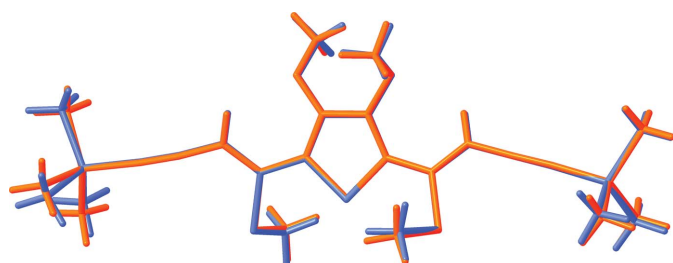


Figure 18

Overlap of the DSEM (4) molecules in polytypes I and II, drawn in red and blue, respectively.

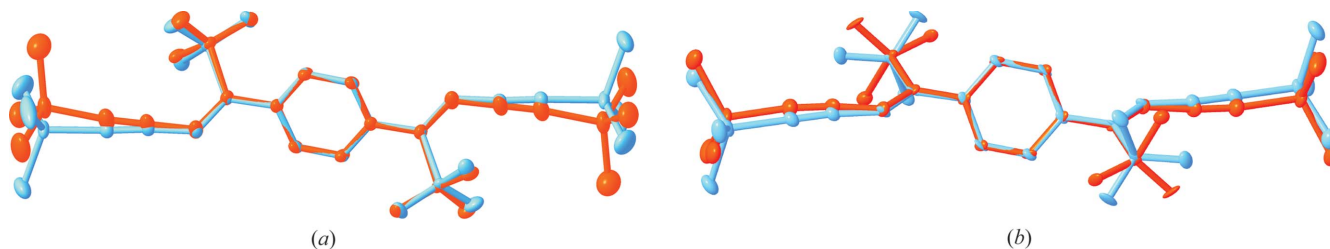


Figure 19

Overlap of the independent oxBSEM (1b) molecules in (a) the high-temperature polymorph I and (b) the low-temperature polymorph II. The molecules are drawn in red and blue, respectively. H atoms have been omitted for clarity.

2.5.4. oxBSEM (1b), polymorphs I and II. Both polymorphs consist of two crystallographically different oxBSEM (**1b**) molecules (Fig. 19), called *A* and *B*, both located on centers of inversion ($Z' = 2/2$). In both polymorphs, the crystallographically independent molecules feature different conformations: The molecules in polymorph I differ by the conformation of the TMS groups with respect to the remaining molecule, whereas in polymorph II the major difference pertains to the orientation of the methylsulfonyl groups (Fig. 19). Nevertheless, the torsion angle differences between all four conformations (Table 1) are too small for the molecules to be considered as conformers according to the criteria of Cruz-Cabeza & Bernstein (2014). Thus, the changes in these polymorphs are only conformational adjustments, though to a rather large degree in the molecule of polymorph II that has a different orientation of the methylsulfonyl groups.

The molecules are arranged in layers parallel to (001) with $p(\bar{1})\bar{1}$ symmetry, whereby the *B* molecules form rods along [100], connected by the *A* molecules (Fig. 20).

The most striking difference between the two polymorphs is the orientation of the *A* molecules, which are rotated by nearly 180° . In projection along [100], the S atoms of the methylsulfonyl groups are nearly superimposed in polymorph II,

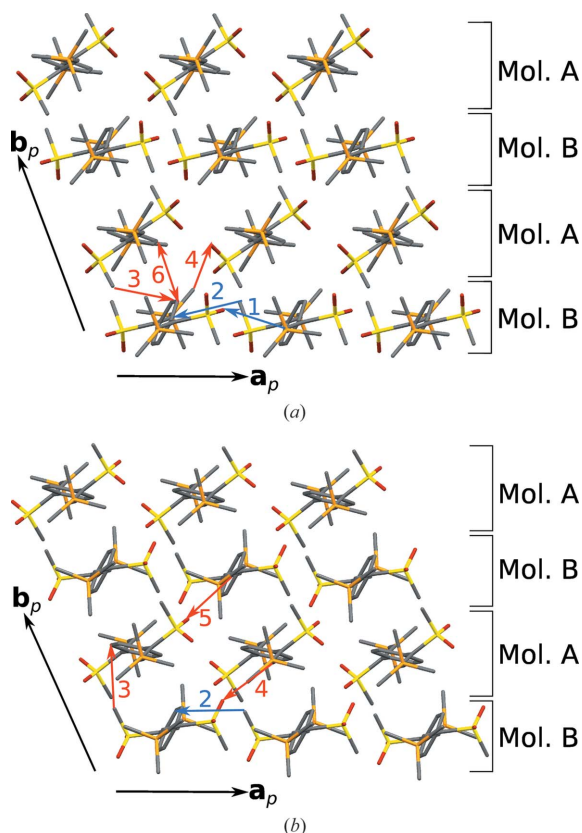


Figure 20
Layers in polymorphs (a) I and (b) II of oxBSEM (**1b**) viewed approximately along the main axis of the molecules. Color codes as in Fig. 7. H atoms have been omitted for clarity. C–H...O and C–H...C contacts are indicated by arrows originating from the ‘donor’ C atoms, C–H...H–C contacts by double-sided arrows connecting the C atoms.

while in polymorph I the methylsulfonyl groups of subsequent molecules point in opposite directions (Fig. 21).

Thus, the I \leftrightarrow II phase transition has to be considered reconstructive, which is consistent with the destruction of large single crystals on cooling. The transformation is accompanied by an inclination of the molecules with respect to the stacking direction (Figs. 21b and 21d). In consequence, the layer interfaces are fundamentally different in the two polymorphs (Fig. 22), demonstrating again the flexibility in layer arrangements allowed by the TMS groups.

Although methylsulfonyl groups are potential hydrogen bond acceptors, the oxBSEM (**1b**) molecules do not possess classical hydrogen-bond donors. Indeed, attempts to analyze the phase transition by listing the weak hydrogen bonds of the two polymorphs were inconclusive, since these lists depend on rather arbitrary distance and angle limits. A more holistic and unbiased approach for the description of molecular interactions in polymorphs, which was established in the last decade, is the analysis of molecular Hirshfeld surfaces

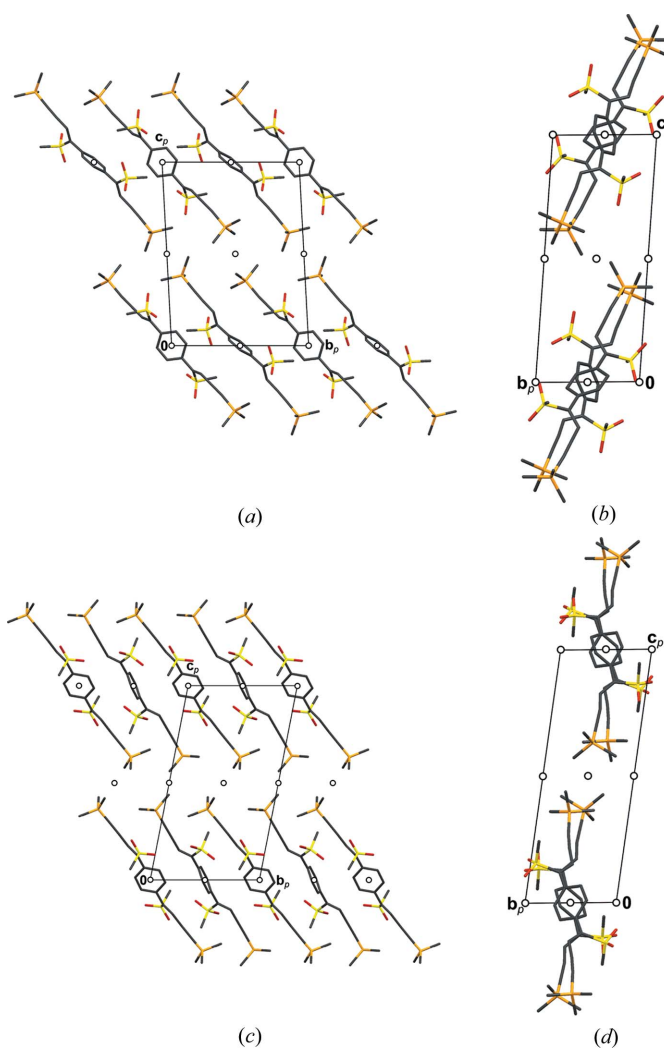


Figure 21
Crystal structures of the polymorphs (a, b) I and (c, d) II of oxBSEM (**1b**), viewed down (a, c) [010] and (b, d) [100]. Color codes as in Fig. 7. H atoms have been omitted for clarity.

Table 3

Prominent intermolecular contacts in the d_i/d_e fingerprint plots of the I and II polymorphs of oxBSEM (**1b**) marked in Fig. 23.

Region	Polymorph I		Polymorph II	
	Atoms	Molecular groups	Atoms	Molecular groups
1	C5'–H5'···O2'	ene–sulfone		
2	C11'–H112'···C7'	Methylsulfone–yne	C11'–H113'···C3'	Methylsulfone–benzene
3	C11–H111···C3'	Methylsulfone–benzene	C11'–H112'···C2	Methylsulfone–benzene
4	C9'–H93'···O2	TMS–sulfone	C5–H5···O2'	Ene–sulfone
5	–	–	C5'–H5'···O1	Ene–sulfone
6	C3–H3'···H3–C3	Benzene–benzene	–	–

(Spackman & Jayatilaka, 2009). The d_e/d_i fingerprint plots (Spackman & McKinnon, 2002) of the two molecules in both polymorphs are depicted in Fig. 23. As expected, contacts not involving H atoms, as well as those involving S and Si atoms, are negligible. First conclusions can be drawn from the shape of the plots: In both polymorphs, the individual plots are not symmetric by reflection at the $d_e = d_i$ line, but the plots of the crystallographically independent molecules are approximately related by such an operation. Thus, the closest contacts are mostly between non-equivalent molecules along the [010] direction. An exception are the regions 1 and 2 in Fig. 23, which correspond to C=C–H···O and SC–H···C≡C contacts of equivalent molecules along [100] (Fig. 20).

Surprisingly, the fingerprint plot of the *A* molecule of polymorph I resembles the plot of the *B* molecule of polymorph II and *vice versa*. Thus, one could say that the roles of the donor and acceptor are reversed on phase transition, although overall the type of interatomic interaction remains similar. The most prominent interactions are indicated in Fig. 23 and correlated to the actual atoms in Fig. 20 and Table 3. A striking feature that is only observed in polymorph I is region 6, a very short C–H···H–C contact (2.30 Å) between two aromatic protons. Thus, although there is no definite proof, one might speculate that, on cooling, the structure contracts until these H atoms are too close and the structure becomes unstable. This conjecture would not have been insinuated without the analysis of fingerprint plots.

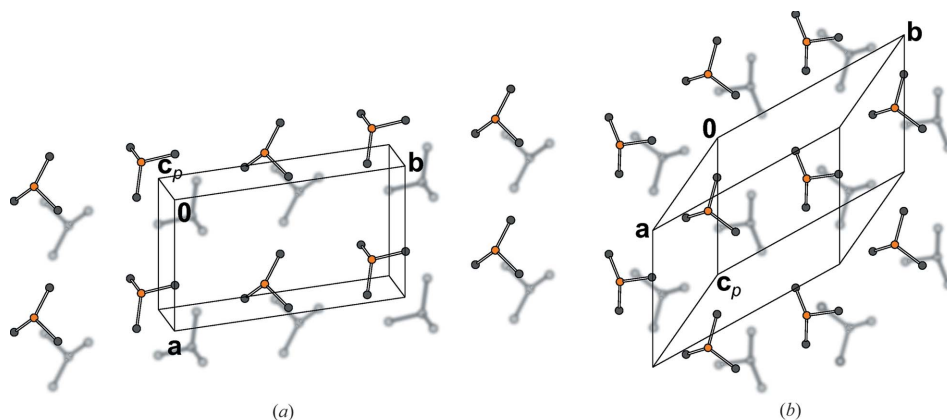


Figure 22

Layer contacts in the polymorphs (a) I and (b) of oxBSEM (**1b**) projected on the layer plane (100). Only the TMS groups are shown. Atoms of the lower layer are gray and blurred, color codes of the top layer as in Fig. 7. H atoms have been omitted for clarity.

2.5.5. oxBSEM (**1b**), polymorph III.

The molecules in polymorph III of oxBSEM (**1b**) are not arranged in distinct silyl-group delimited layers (Fig. 24). One crystallographically unique oxBSEM (**1b**) molecule is located on a center of inversion. It can again not be considered a different conformer. As expected, the Hirshfeld fingerprint plot (Fig. 21e) is nearly symmetric by reflection at $d_e = d_i$. It most closely resembles the plot of the *A*

molecule in polymorph II, but the H···C contacts are distinctly less prominent, indicating an energetically more favorable packing. Indeed, polymorph III has higher symmetry (same space group type, but $Z' = 1/2$ versus 2/2) and distinctly higher density (1.267 versus 1.229 g cm⁻³ at 100 K). Thus, the I ↔ II transition is an example of Ostwald's rule stating that a system does not change into the thermodynamically stable, but the nearest metastable state.

2.5.6. oxESEM (3b). The oxESEM (**3b**) molecules are arranged in layers parallel to (001) with (idealized) $p2_1/b1(1)$ symmetry (Fig. 25), which are, despite possessing the same layer group type, structurally unrelated to the layers in BSEM (**1**), TSEM (**2**), the basic structure of ESEM (**3**) and DSEM (**4**).

One crystallographically unique molecule is located on a general position. The layers are stacked in such a way that the *b*-glide planes do not overlap. In consequence oxESEM (**3b**) belongs to a category I OD family composed of layers of one kind. The OD groupoid family symbol reads according to the notation introduced by Dornberger-Schiff & Grell-Niemann (1961) as

$$p \quad 2_1/b \quad 1 \quad (1) \\ \{ \quad 2_r/n_{1,2} \quad \bar{1} \quad (\bar{1}) \}.$$

It has to be noted that in this case \mathbf{c}_0 is conveniently chosen not normal to the layer planes, to reflect the monoclinic point group $2/m11$ of the OD family (Fichtner, 1979), whereby a

second metric parameter describing the relative layer positions vanishes. In one possible arrangement of the (A_n, A_{n+1}) layer pair, A_{n+1} is related to A_n by a 2_r screw with intrinsic translation along $\mathbf{ra}/2$ or equivalently by an $n_{1,2}$ glide with intrinsic translation along $(\mathbf{b}/2) + \mathbf{c}_0$. The other geometrically equivalent arrangements are derived using the NFZ relationship (Đurovič, 1997): Given an A_n layer, an adjacent $A_{n\pm 1}$ layer can appear in $Z = N/F = [p11(1);pb1(1)] = 2$ orientations, related by the *b* glides of A_n . $p11(1)$ and $pb1(1)$ are the groups of those layer operations that do not invert the orien-

tation of the layers with respect to the stacking direction [called λ - τ partial operations (POs) in the OD literature].

These stacking possibilities give rise to two MDO polytypes: MDO₁ ($P\bar{1}$, $\mathbf{c} = \mathbf{c}_0 + [(r-1)/2]\mathbf{a}$) and MDO₂ ($P2_1/n11$, $\mathbf{c} = 2\mathbf{c}_0$), obtained by continuous application of the 2_r screws and $n_{1,2}$ glides, respectively. The symmetry of the two polytypes is schematized in Fig. 26.

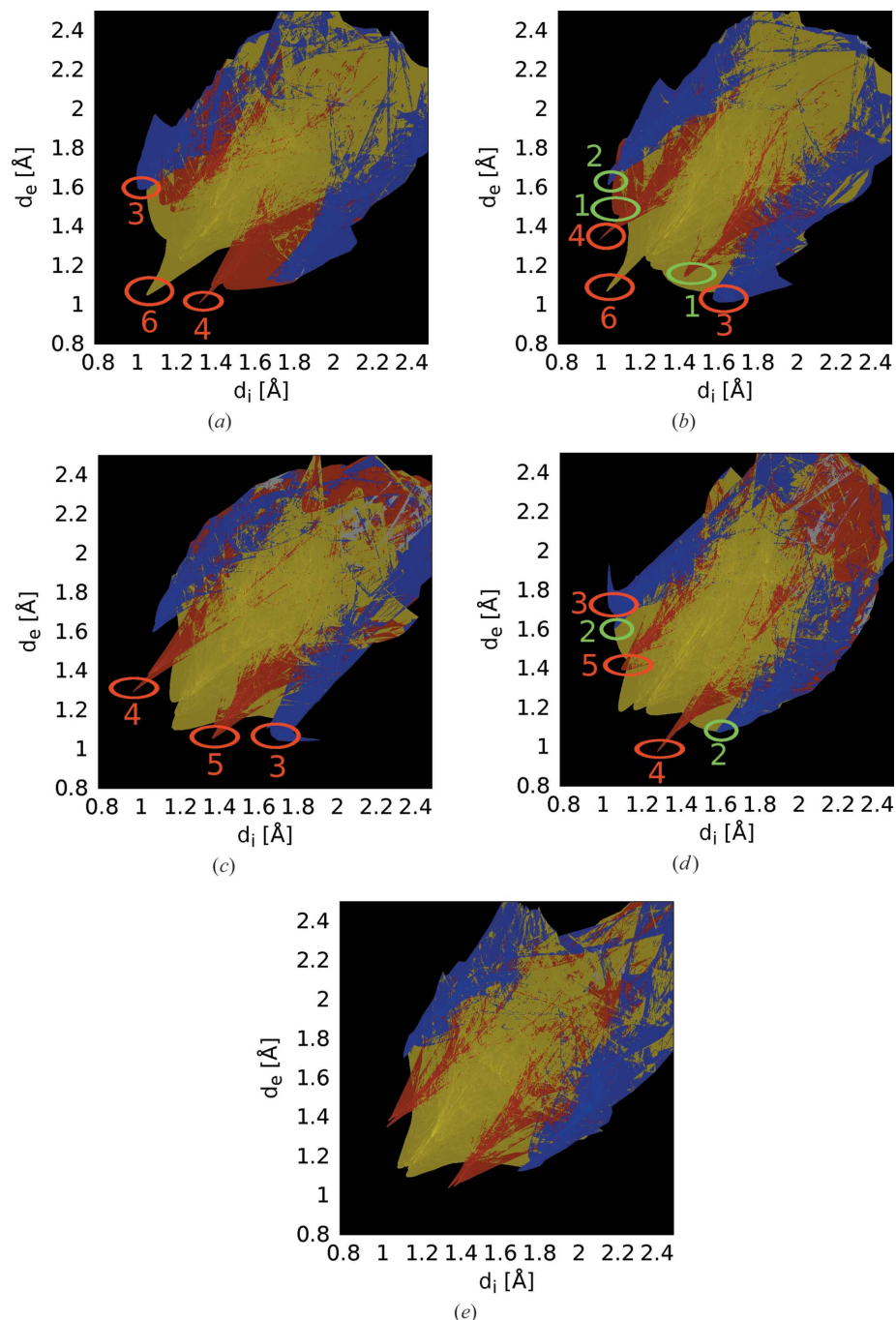


Figure 23
 d_i/d_e fingerprint plots of the oxBSEM (**1b**) molecules in polymorphs (a, b) I, (c, d) II and (e) III, calculated with *CrystalExplorer* (Wolff *et al.*, 2012). Regions where H...H, H...O and H...C dominate are drawn in yellow, red and blue, respectively, other regions in gray. Brighter colors indicate a higher proportion of the surface. Regions discussed in the text connecting two B molecules or A and B molecules are marked by green and red ellipses, respectively.

The major polytype of the crystals under investigation is the MDO₁ polytype. Fragments of the MDO₂ polytype were observed indirectly by systematic twinning. The twin element corresponds to the plane of the *b* glides of the *A* layers. This kind of twinning is fundamentally different from that in TSEM (**2**) or the polytypism of DSEM (**4**). The latter is only possible owing to the flexibility of the layer contacts, whereas in oxESEM (**3b**) the layer contacts are equivalent in all polytypes.

In the major MDO₁ polytype, the symmetry of the *A* layers is reduced by an index of 2 from $p2_1/b1(1)$ to $p\bar{1}1(\bar{1})$. This translates to a small deviation of $\gamma = 89.771(2)^\circ$ from the ideal value of 90° imposed by the rectangular layer lattice and a small deviation of the atoms from the positions compared with the idealized $p2_1/b1(1)$ layers. Significant deviations from ideal symmetry are limited to the TMS groups, which are located at the layer interfaces [deviations of 0.272 Å (Si2) up to 0.508 Å (C10)]. This is expected, since the layer interfaces are located in an environment which deviates from the ideal layer symmetry. The closer the atoms are located to the center of the layers, the smaller the deviation. The C atoms of the yne fragment connecting to the TMS group deviate by 0.130 Å (C8) and 0.138 Å (C16), all other atoms by less than 0.100 Å.

2.5.7. NSEM-TBDMS (5). Although achiral, the NSEM-TBDMS (**5**) molecules crystallize in the Sohncke group $P2_12_12_1$. The crystal under investigation was enantiomerically pure [Flack parameter 0.03 (3)]. An estimation of the number of achiral molecules crystallizing in Sohncke groups was given by Pidcock (2005).

Whereas the central part of the molecule is nearly symmetric by twofold rotation, the TBDMS groups feature a distinctly different orientation with respect to the methylthio groups, resulting in molecules with 1 symmetry (Figs. 27a and 27b). The molecules are arranged in layers parallel to (001) with $p12_1(1)$ symmetry. The layers in turn are connected by 2_1 screws with axes parallel to [100] and [010] (Fig. 27c).

2.5.8. ASYM (6). The ASYM (**6**) molecules are located on general positions. Despite being polar with respect to the main direction, they are

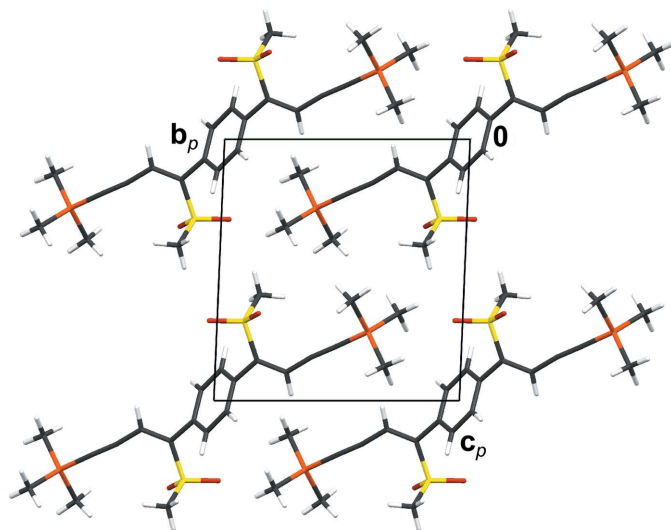


Figure 24
Crystal structure of polymorph III of oxBSEM (**1b**) viewed down [100]. Color codes as in Fig. 7.

arranged in nonpolar layers parallel to (010) with $p\bar{1}(\bar{1})\bar{1}$ symmetry (Fig. 28).

In contrast to the other layered structures, the TMS groups are not as clearly located at the layer interface: every second group is moved away from the surface into the layers. This can be attributed to ASYM (**6**) being the shortest of the molecules under investigation.

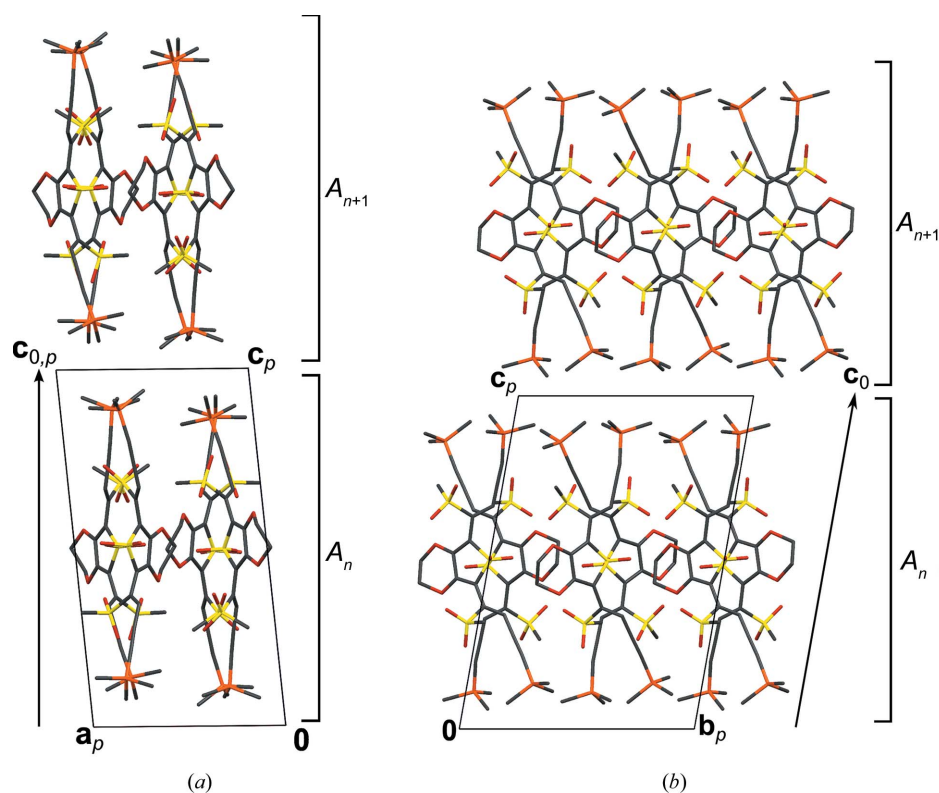


Figure 25
The crystal structure of oxESEM (**3b**) viewed down (a) [010] and (b) [100]. The location of the A_n layers is indicated by brackets to the right. Color codes as in Fig. 7.

The systematic twinning of ASYM (**6**) can be explained by local pseudosymmetry: With the exception of one TMS group, the molecules are practically symmetric by reflection at (100) (Fig. 28*b*). Thus the structure can be 'sliced' into OD layers (Grell, 1984) of two kinds, which do not correspond to layers in the crystallochemical sense (Fig. 28). The A^1 layers contain the parts of the molecule that possess mirror symmetry, whereas the A^2 layers are made up of the remaining TMS groups.

As a consequence, the structure belongs to a category IV OD family composed of nonpolar layers of two kinds. The corresponding OD groupoid family symbol reads according to the notation introduced by Grell & Dornberger-Schiff (1982) as

$$\begin{array}{cc} A^1 & A^2 \\ p2_1/m(1)1 & p\bar{1}(\bar{1})\bar{1}. \\ [0, s] & \end{array}$$

Accordingly, the structure is made up of an alternating stacking of A^1 and A^2 layers, with $p2_1/m(1)1$ and $p\bar{1}(\bar{1})\bar{1}$ symmetry, respectively. \mathbf{b}_0 is chosen not normal to the layer planes so that one metric parameter vanishes. In one possible arrangement of the (A_n^1, A_{n+1}^2) layer pair, the origin of A^2 is reached from the origin of A^1 by translation along $(\mathbf{b}_0/2) + \mathbf{sa}$.

According to the NFZ relationship, given an A_n^1 layer, the adjacent $A_{n\pm 1}^2$ layers can appear in $Z = N/F = [pm(1)1:p1(1)1] = 2$ orientations, related by the m operation of the A_n^1 layer. For the A^2 layers on the other hand, there is only one way to connect to the A^1 layers, since all $\lambda\text{-}\tau$ POs of A^2 ($p1(1)1$) apply likewise to A^1 .

These stacking possibilities give rise to two MDO polytypes: MDO₁ ($P\bar{1}$, $\mathbf{b} = \mathbf{b}_0 + 2\mathbf{sa}$) is obtained by continuous application of the inversion operations of the A^1 layers; MDO₂ ($P2_1/b11$, $\mathbf{b} = 2\mathbf{b}_0$) by application of the 2_1 screws. The symmetry of the two polytypes is schematized in Fig. 29.

The bulk of the ASYM (**6**) crystals under investigation are made up of the MDO₁ polytype, whereas fragments of the MDO₂ polytype are located at the twin interface. A twin element corresponds to the mirror plane of the A^1 layers. Again, all polytypes are locally equivalent and no flexibility of the layer contact is needed for twinning.

In MDO₁, the symmetry of the A^1 layers is reduced by an index of 2 from $p2_1/m(1)1$ to $p\bar{1}(\bar{1})\bar{1}$. This is reflected by a deviation of $\beta = 92.510(2)^\circ$ from the ideal value of 90° according to the rectangular layer lattice, and by a slight deviation of

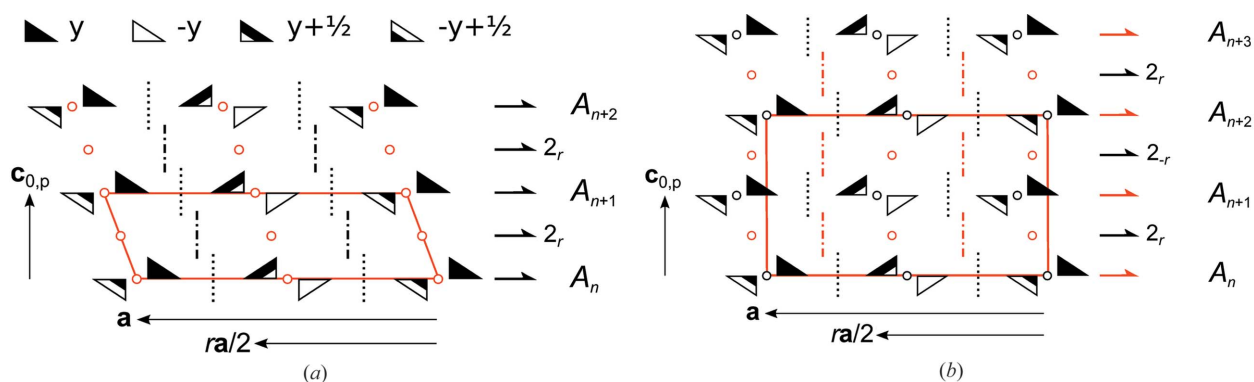


Figure 26

Schematic representation of the symmetry of the (a) MDO₁ and (b) MDO₂ polytypes of oxESEM (**3b**). Triangles are black on one and white on the other side. (Partial) symmetry operations of a layer and relating adjacent layers are indicated by the graphical symbols standardized in *International Tables for Crystallography* (Hahn, 2006a). Additionally for operations with non-crystallographic intrinsic translations the printed symbol is given.

the molecules from their idealized positions. Under the assumption of $\beta = 90^\circ$, the only non-negligible deviations ($> 0.1 \text{ \AA}$) of non-H atoms from the idealized positions of the A¹ layers are observed for the atoms of the TMS group that are not located on the mirror plane (C10, C11, deviation of 0.11 \AA) and for the C3 atom, which connects to the TMS group in the A² layer (deviation of 0.12 \AA).

The deviation of β from the ideal value of 90° by 2.51° is remarkably large and distinctly larger than in the case of oxESEM (**3b**). As a consequence, the lattices of the twin domains do not match (deviation of 5°) and the crystals are distinctly distorted at the twin interface. The orthorhombic MDO₂ fragment at the twin interface possesses an ideal angle of 90° and it therefore enables the passage of the two extremes of the MDO₁ domains.

In contrast to oxESEM (**3b**), the desymmetrization does not result in two crystallographically unique molecules, but rather in a desymmetrization of the A¹ parts of the molecule from m to 1 symmetry.

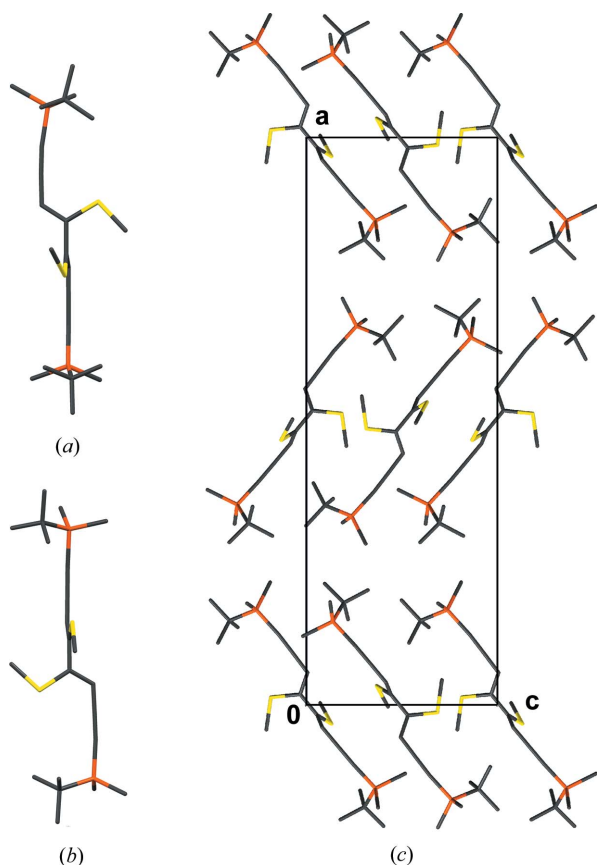


Figure 27

(a, b) The NSEM-TBDMS (**5**) molecule viewed down two different directions, showing the different conformations of the methylthio group with respect to the TBDMS groups (top group: *gauche*, bottom group: *eclipsed*) and (c) crystal structure of NSEM-TBDMS (**5**) viewed down [100]. H atoms have been omitted for clarity. Color codes as in Fig. 7.

3. Experimental

Detailed syntheses and spectroscopic characterizations of all compounds are given by Lumpi (2013). Single crystals of BSEM (**1**) (*i*-PrOH, EtOH), oxBSEM (**1b**) (EtOH), ESEM (**3**) (EtOH, in a glove-box with N₂ atmosphere), oxESEM (**3b**) (MeOH) and DSEM (**4**) (EtOH) were obtained by slow evaporation at room temperature. Crystallization of TSEM (**2**) from solvents failed to give single crystals suitable for single-crystal diffraction. Tiny single crystals were instead afforded by crystallization of the oily sample at $\sim 293 \text{ K}$ over a time period of several months.

Single-crystal data were collected and processed on a Bruker Kappa APEXII diffractometer system (Bruker, 2008). Data were reduced using the *SAINT-Plus* (Bruker, 2008) and *EVAL* (Duisenberg *et al.*, 2003) suites and corrected for absorption effects with *SADABS* or *TWINABS* (Bruker, 2008). Structures were solved with *SUPERFLIP* (Palatinus & Chapuis, 2007) and refined with *JANA2006* (Petříček *et al.*, 2014). More details on single-crystal diffraction and structure refinement are available as supplementary materials.

4. Conclusion and outlook

We set out to create layered structures, expecting to obtain OD polytypes due to different local layer symmetry. We were indeed successful with the systematic twins oxESEM (**3a**) and ASYM (**6**). Surprisingly though, we observed numerous other

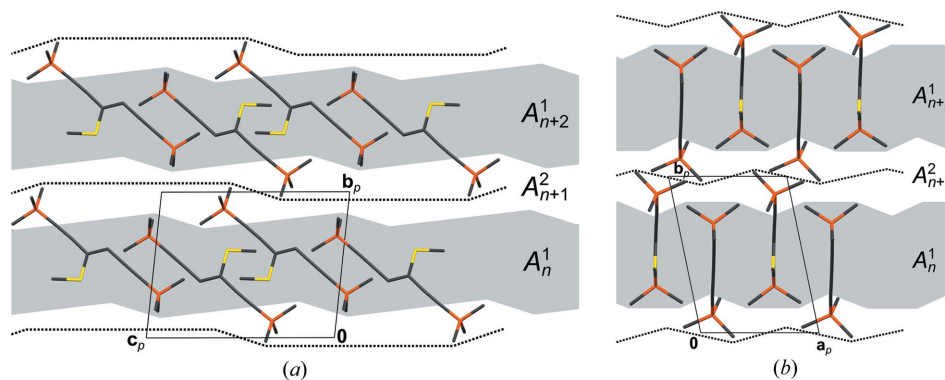


Figure 28
The crystal structure of ASYM (6) viewed down (a) [100] and (b) [001]. The A^1 and A^2 OD layers are marked by a gray and white backdrop, respectively. The boundaries of the crystallochemical layers are indicated by dotted lines. Color codes as in Fig. 7.

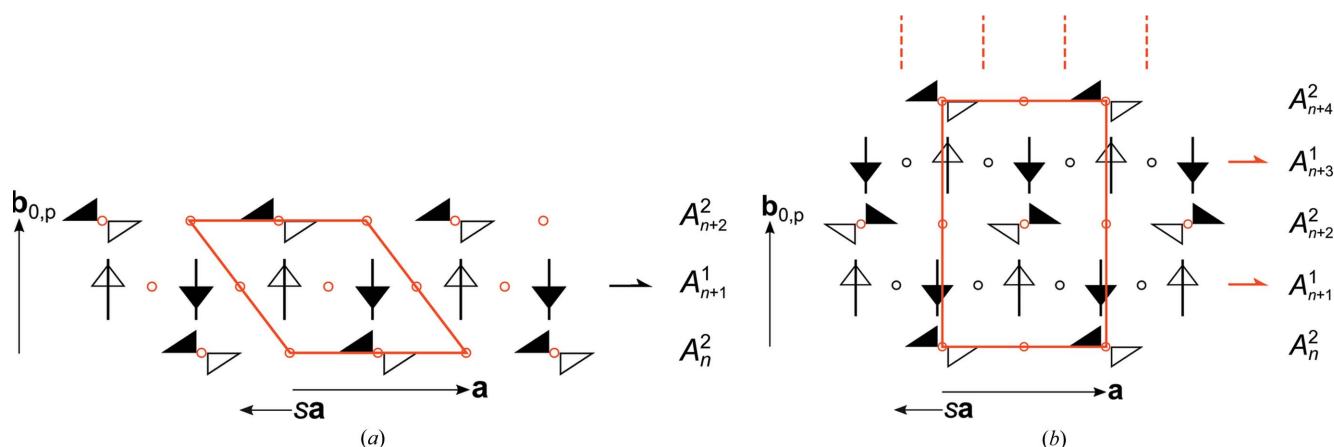


Figure 29
Schematic representation of the symmetry of the (a) MDO₁ and (b) MDO₂ polytypes of ASYM (6). Symbols as in Fig. 26.

crystallographic phenomena, which are not caused by local layer symmetry but by the remarkable flexibility of the layer contacts. On the one hand, a given layer contact can accommodate significant distortion leading to the incommensurate modulation of ESEM (3). On the other hand, identical layers can connect in fundamentally different ways as observed in the non-OD polytypism of TSEM (2) and DSEM (4) and the layer contacts can accommodate the different molecular arrangements observed in the temperature-dependent polymorphism of oxBSEM (1b).

These phenomena demonstrate the necessity of a generalization of space-group symmetry to local symmetry. These so far unexplored groupoids are necessary not only for the description of polytypism, but also of structural relationships like the merotypism of BSEM (1) and TSEM (2).

Future synthetic work will focus on the core of the layers (alterations of the aromatic spacer and an elongation of the methylthio groups), as well as the application of other silyl groups like TBDMS or TIPS to induce different layer contacts as in NSEM-TBDMS (5). Besides studying crystallographic phenomena, the application of acene or polythiophene derivatives may also enable the application of the layer motifs in the field of functional organic materials. To achieve this goal

an adjustment of the steric bulk of the cores and the size of the silyl groups will be needed to obtain an optimum face-to-face stacking of the extended aromatic cores. Moreover, the merotypism of BSEM (1) and TSEM (2) presents an opportunity for the controlled epitaxial growth of different kinds of molecules, a crucial point in the design of devices.

Acknowledgements

The authors are indebted to V. Carl, D. Koch, J. Steindl and D. Wurm for supporting the synthetic experiments. The authors also thank W. Skranc for preliminary work on the discussed topic. The help of Martin Lutz with the use of the EVAL software package is highly appreciated. The X-ray centre of the Vienna University of Technology is acknowledged for providing access to the single-crystal diffractometer. This publication was supported by TU Vienna research funds.

References

- Aakeröy, C. B., Champness, N. R. & Janial, C. (2010). *Cryst. Eng. Commun.* **12**, 22–43.
- Allen, F. H., Watson, D. G., Brammer, L., Orpen, A. G. & Taylor, R. (2006). *International Tables for Crystallography*, Vol. C, ch. 9.5, pp. 790–881. Heidelberg: Springer.

- Anthony, J. E. (1994). *Induced π -Stacking in Acenes*, Vol. 1, *Functional Organic Materials – Syntheses, Strategies and Applications*, ch. 14. Weinheim: Wiley-VCH Verlag.
- Anthony, J. E. (2008). *Angew. Chem. Int. Ed.* **47**, 452–483.
- Anthony, J. E., Brooks, J. S., Eaton, D. L. & Parkin, S. R. (2001). *J. Am. Chem. Soc.* **123**, 9482–9483.
- Anthony, J. E., Eaton, D. L. & Parkin, S. R. (2002). *Organic Lett.* **4**, 15–18.
- Bobrovsky, R., Hametner, C., Kalt, W. & Fröhlich, J. (2008). *Heterocycles*, **76**, 1249–1259.
- Bruker (2008). *APEX2, RLATT, SAINT, SADABS and TWINABS*. Bruker AXS Inc., Madison, Wisconsin, USA.
- Coronado, E., Galán-Mascarós, J. R., Gómes-García, C. J. & Laukhin, V. (2000). *Nature*, **408**, 447–449.
- Cruz-Cabeza, A. J. & Bernstein, J. (2014). *Chem. Rev.* **114**, 2170–2191.
- Dornberger-Schiff, K. (1982). *Acta Cryst.* **A38**, 483–491.
- Dornberger-Schiff, K. & Grell-Niemann, H. (1961). *Acta Cryst.* **14**, 167–177.
- Duisenberg, A. J. M., Kroon-Batenburg, L. M. J. & Schreurs, A. M. M. (2003). *Appl. Cryst.* **36**, 220–229.
- Đurovič, S. (1979). *Krist. Tech.* **14**, 1047–1053.
- Đurovič, S. (1997). *EMU Notes Mineral.* **1**, 3–28.
- Faria, J. L. de, Hellner, E., Liebau, F., Makovicky, E. & Parthé, E. (1990). *Acta Cryst.* **A46**, 1–11.
- Ferraris, G., Makovicky, E. & Merlino, S. (2008). *Crystallography of Modular Materials*, Vol. 15, *IUCr Monographs on Crystallography*. Oxford University Press.
- Fichtner, K. (1977a). *Krist. Tech.* **12**, 1263–1267.
- Fichtner, K. (1977b). *Beitr. Algebra. Geom.* **6**, 71–99.
- Fichtner, K. (1979). *Krist. Tech.* **14**, 1453–1461.
- Fichtner, K. (1986). *Comput. Math. Appl. B*, **12**, 751–762.
- Fuller, L. S., Iddon, B. & Smith, K. A. (1999). *J. Chem. Soc. Perkin Trans.* pp. 1273–1278.
- Gilchrist, T. L. (1987). *Adv. Heterocycl. Chem.* **41**, 41–74.
- Grell, H. (1984). *Acta Cryst.* **A40**, 95–99.
- Grell, H. & Dornberger-Schiff, K. (1982). *Acta Cryst.* **A38**, 49–54.
- Gronowitz, S. & Frejd, T. (1978). *Chem. Heterocycl. Compd.* **14**, 353–367.
- Gronowitz, S. & Torbjörn, F. (1970). *Acta Chem. Scand.* **24**, 2656–2658.
- Hahn, T. (2006a). *International Tables for Crystallography*, Vol. A, ch. 1.4, pp. 7–11. Heidelberg: Springer.
- Hahn, T. (2006b). *International Tables for Crystallography*, Vol. D, ch. 3.3, pp. 393–448. Heidelberg: Springer.
- Iddon, B. (1983). *Heterocycles*, **20**, 1127–1171.
- Jakobsen, H. J. (1970). *Acta Chem. Scand.* **24**, 2663–2665.
- Janssen, T., Chapuis, G. & de Boissieu, M. (2007). *Aperiodic Crystals – From Modulated Phases to Quasicrystals*, Vol. 21, *IUCr Monographs on Crystallography*. Oxford University Press.
- Janssen, T., Janner, A., Looijenga-Vos, A. & de Wolff, P. M. (2006). *International Tables for Crystallography*, Vol. C, ch. 9.8, pp. 907–955. Heidelberg: Springer.
- Kálmán, A., Párkányi, L. & Argay, G. (1993). *Acta Cryst.* **B49**, 1039–1049.
- Kopsky, V. & Litvin, D. B. (2006). *International Tables for Crystallography*, Vol. E. Heidelberg: Springer.
- Lumpi, D. (2013). Dissertation, Vienna University of Technology, Austria.
- Lumpi, D., Glöcklhofer, F., Holzer, B., Stöger, B., Hametner, C., Reider, G. A. & Fröhlich, J. (2014). *Cryst. Growth Des.* **14**, 1018–1031.
- Makovicky, E. (1997). *EMU Notes Mineral.* **1**, 315–343.
- Mitzi, D. B. (2001). *J. Chem. Soc. Dalton Trans.* pp. 1–12.
- Mueller, T. J. J. & Bunz, U. H. F. (2007). *Functional Organic Materials – Syntheses, Strategies and Applications*. IUCr Monographs on Crystallography. Weinheim: Wiley-VCH Verlag.
- Park, S. K., Jackson, T. N., Anthony, J. E. & Mourey, D. A. (2007). *Appl. Phys. Lett.* **91**, 063514.
- Pidcock, E. (2005). *Chem. Commun.* pp. 3457–3459.
- Palatinus, L. & Chapuis, G. (2007). *J. Appl. Cryst.* **40**, 786–790.
- Petříček, V., Dušek, M. & Palatinus, L. (2014). *Z. Kristallogr.* **229**, 345–352.
- Schönleber, A. (2011). *Z. Kristallogr.* **226**, 499–517.
- Smaalen, S. van (2007). *Incommensurate Crystallography*, Vol. 20, *IUCr Monographs on Crystallography*. Oxford University Press.
- Smaalen, S. van, Stokes, H. T. & Campbell, B. J. (2013). *Acta Cryst.* **A69**, 75–90.
- Spackman, M. A. & Jayatilaka, D. (2009). *CrystEngComm*, **11**, 19–32.
- Spackman, M. A. & McKinnon, J. J. (2002). *CrystEngComm*, **4**, 378–392.
- Stöger, B., Kautny, P., Lumpi, D., Zobetz, E. & Fröhlich, J. (2012). *Acta Cryst.* **B68**, 667–676.
- Stöger, B., Pokorny, B., Lumpi, D., Zobetz, E. & Fröhlich, J. (2013). *Z. Kristallogr.* **228**, 106–112.
- Stöger, B. & Weil, M. (2013). *Mineral. Petrol.* **107**, 253–263.
- Stöger, B., Weil, M. & Zobetz, E. (2012). *Z. Kristallogr.* **227**, 859–868.
- Stokes, H. T., Campbell, B. J. & van Smaalen, S. (2011). *Acta Cryst.* **A67**, 45–55.
- Wolff, S. K., Grimwood, D. J., McKinnon, J. J., Turner, M. J., Jayatilaka, D. & Spackman, M. A. (2012). *CrystalExplorer*, Version 3.1. University of Western Australia.
- Wondratschek, H. (1976). *Acta Cryst.* **A32**, 664–666.

2.12. Manuscript #12

Crystal chemistry of trialkylsilyl-capped (3Z)-4-(methylthio)-3-penten-1-yne: polymorphism, twinning and ambiguity of order-disorder descriptions

Daniel Lumpi, Paul Kautny, Berthold Stöger, Johannes Fröhlich

Acta Crystallographica Section B, **2016**, 72, 753-762

Reproduced with the kind permission of the International Union of Crystallography.

Crystal chemistry of trialkylsilyl-capped (3*Z*)-4-(methylthio)-3-penten-1-yne: polymorphism, twinning and ambiguity of order–disorder descriptions

Daniel Lumpi,^a Paul Kautny,^a Berthold Stöger^{b*} and Johannes Fröhlich^a

^aInstitute of Applied Synthetic Chemistry, TU Wien, Vienna, Austria, and ^bInstitute of Chemical Technologies and Analytics, TU Wien, Vienna, Austria. *Correspondence e-mail: bstoeger@mail.tuwien.ac.at

Received 2 May 2016

Accepted 6 July 2016

Edited by S. Parsons, University of Edinburgh, Scotland

Keywords: layer structures; twinning; order–disorder theory; desymmetrization; polymorphism; Hirshfeld fingerprint plots.

CCDC references: 1491092; 1491093; 1491094; 1491095

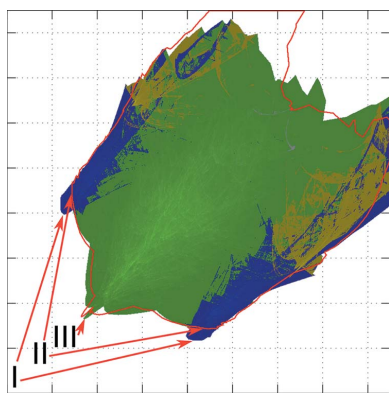
Supporting information: this article has supporting information at journals.iucr.org/b

The crystallization behavior of trimethylsilyl-capped (3*Z*)-4-(methylthio)-3-penten-1-yne (1-TMS) and the triisopropylsilyl and *tert*-butyldimethylsilyl analogues (1-TIPS) and (1-TBDMS) was investigated. (1-TMS) crystallizes in the Sohncke space group $P2_12_12_1$ with $Z' = 1$. (1-TIPS) exists as two polymorphs, both crystallizing in $P\bar{1}$ with $Z' = 2$ independent molecules. Polymorph (I) is an order–disorder (OD) twin. Two interpretations in terms of $M = 1$ or $M = 2$ kinds of OD layers are possible, with different degrees of idealization. Polymorph (II) is fully ordered (non-twinned). Its structure can be derived from polymorph (I) by inverting the orientation of every second molecule. (1-TBDMS) ($P\bar{1}$, $Z' = 2$) is an OD twin, where the OD description is unambiguously in $M = 1$ kinds of layers.

1. Introduction

In recent work (Lumpi *et al.*, 2015) we studied the controlled formation ('crystal engineering') of layered structures by crystallizing molecules derived from **A** (Fig. 1). These molecules are obtained by tandem thiophene ring fragmentation. They are made up of a central aromatic spacer, which is extended on opposite sides by linear ene-yne chains in *Z*-configuration with an attached methylthio group. The ene-yne/methylthio fragments were obtained by thiophene ring fragmentation. The yne-functionality in turn is capped by bulky trialkylsilyl (SiR_3) groups. All of the investigated molecules crystallized in distinct crystallochemical layers, whereby the trialkylsilyl groups form the layer interfaces (Fig. 2*a*). The structures featured a rich crystal chemistry, such as incommensurate modulation, OD and non-OD polytypism, twinning and polymorphism.

One of the investigated modifications was the shortening of the conjugated π -system by, at first, removal of the central aromatic spacer of **A** to give **B** and, in a next step, removal of a $\text{C}=\text{C}(\text{SMe})$ -fragment resulting in **C** (Fig. 1). **B** and **C** still crystallized in layered structures, but in **C** one of two trialkylsilyl groups was moved away from the layer interface (Fig. 2*b*). In a continuation of this line of work, we investigated the crystallization behavior of molecules with further reduced conjugation length. A suitable candidate molecule seemed to be (1-TMS) (TMS = trimethylsilyl), obtained by removal of a CSiMe_3 -fragment of **C** (Fig. 1). The molecule has been previously synthesized as a precursor to potentially NLO active triazole derivatives (Lumpi *et al.*, 2014). However, its crystal structure has not been determined up to now, owing to a melting point below room temperature. By cooling chromatographically purified (1-TMS) to 255 K, we obtained crystals suitable for single-crystal diffraction. The trend from



© 2016 International Union of Crystallography

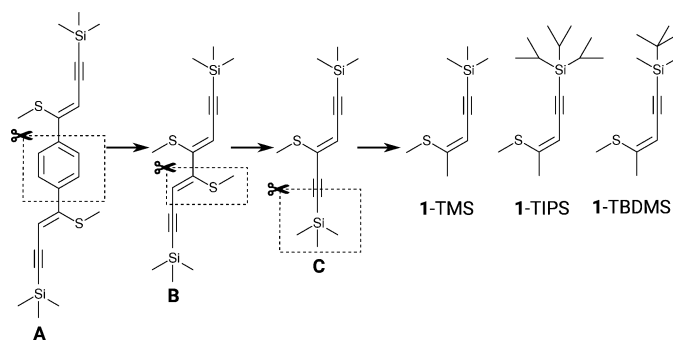


Figure 1

Schematic representation of the molecular shortening investigated in the preceding study (Lumpi *et al.*, 2015) and chemical structure of the molecules in the current study.

B to C, a breaking up of the distinct layer structure, found its closure in the crystal structure of (1-TMS), as the latter is not made up of trialkylsilyl-delimited layers. Intrigued, we were interested if layered crystallization could be restored by application of more bulky trialkylsilyl groups. We applied the widely used triisopropylsilyl (TIPS) and *tert*-butyldimethylsilyl (TBDMS) groups to obtain (1-TIPS) and (1-TBDMS) (Fig. 1). Indeed, these molecules crystallized in layers and their interesting crystallization behavior, *viz.* OD-twinning and polymorphism is reported here.

The first crystal of (1-TIPS) that we structurally characterized was twinned. Since the collected data set was of mediocre quality, we attempted to locate a better diffracting crystal. Surprisingly, we found a non-twinned crystal of a different polymorph. The polymorphs will henceforth be designated as

(I) (twinned) and (II) (non-twinned), respectively. The twinning and lack thereof can be explained by application of the OD theory (Dornberger-Schiff & Grell-Niemann, 1961), *i.e.* by the existence and absence of local pseudosymmetry, respectively. Much to our chagrin, we were unable to isolate a further polymorph (I) crystal of better quality. In X-ray powder diffraction experiments from 100 K to room temperature we could only evidence polymorph (II).

The crystals of (1-TBDMS) were likewise twinned owing to OD polytypism. Here, multiple characterized crystals were all of the same polymorph and all twinned.

2. Experimental

2.1. Synthesis

Synthesis and spectroscopic characterization of all three investigated compounds is given in Lumpi *et al.* (2011) and Lumpi (2013). Crystals were in all cases grown by cooling the neat chromatographed oil to 255 K.

2.2. Data collection and refinement

Crystals were selected under a polarizing microscope and attached to Kapton® micromounts. To avoid melting of (1-TMS) during manipulation, a small vessel with boiling N₂ was placed next to the microscope. The cold vapors provided adequate cooling. The thus prepared crystals were quickly immersed in a dry stream of 100 K N₂ on a Bruker KAPPA APEX II diffractometer system (Bruker, 2015).

Complete data sets were collected in fine sliced ω - and φ -scan modes. For the twinned (1-TIPS) [polymorph (I)] and (1-TBDMS), orientation matrices of two individuals were obtained after separating the reflections using the RLATT tool (Bruker, 2015). In the former, the lattices can be related by $(\mathbf{a}', \mathbf{b}', \mathbf{c}') = (\mathbf{a}, -0.0602\mathbf{a} - \mathbf{b}, -0.6124\mathbf{a} - \mathbf{c})$, corresponding to a twofold rotation about [100]. In the latter, the orientation relationship is $(\mathbf{a}', \mathbf{b}', \mathbf{c}') = (\mathbf{a}, \mathbf{b}, 0.0098\mathbf{a} + 0.0195\mathbf{b} - \mathbf{c})$, which is a reflection at (001).

Data were reduced with *SAINT-Plus* (Bruker, 2015) and corrected for absorption effects with the multi-scan approach implemented in *SADABS* or *TWINABS* (Bruker, 2015). The structures were solved with charge-flipping implemented in *SUPERFLIP* (Palatinus & Chapuis, 2007) and refined with *JANA2006* (Petříček *et al.*, 2014). The structures of (1-TIPS) (both polymorphs) and (1-TBDMS) are made up of $Z' = 2$ crystallographically independent mole-

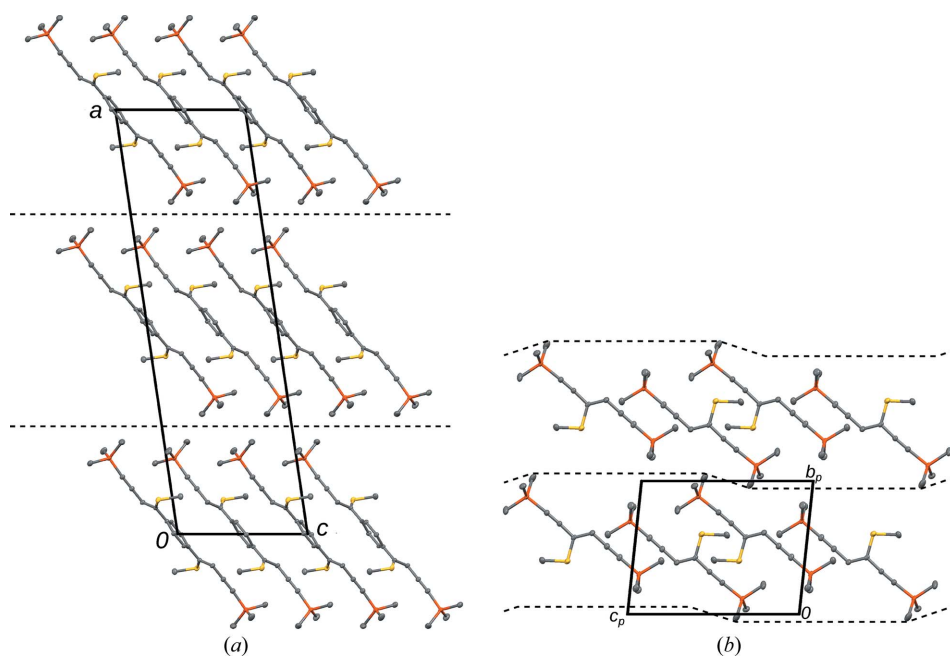


Figure 2

(a) Example of the characteristic layer structure formed by linear, rigid, *bis*-silyl capped molecules (**A**, $C2/c$). (b) Beginning breakup of the distinct layer structure in the shortened **C** ($P1$). C (gray), S (yellow) and Si (orange) atoms are represented by ellipsoids drawn at the 50% probability levels. H atoms were omitted for clarity. Coordinates taken from Lumpi *et al.* (2015).

Table 1
Experimental details.

For all structures: Experiments were carried out at 100 K with Mo $K\alpha$ radiation using a Bruker KAPPA APEX II CCD. Absorption was corrected for by multi-scan methods, *SADABS* and *TWINABS*. H-atom parameters were constrained.

	(1-TMS)	(1-TIPS)		(1-TBDMS)
		Polymorph (I)	Polymorph (II)	
Crystal data				
Chemical formula	C ₉ H ₁₆ SSi	C ₁₅ H ₂₈ SSi	C ₁₅ H ₂₈ SSi	C ₁₂ H ₂₂ SSi
M_r	184.4	268.5	268.5	226.5
Crystal system, space group	Orthorhombic, $P2_12_12_1$	Triclinic, $P\bar{1}$	Triclinic, $P\bar{1}$	Triclinic, $P\bar{1}$
a, b, c (Å)	5.6366 (4), 11.0112 (8), 17.8309 (14)	7.962 (2), 13.842 (3), 15.326 (3)	9.4082 (7), 11.2004 (8), 16.3446 (12)	6.2535 (7), 7.2501 (8), 32.335 (4)
α, β, γ (°)	90, 90, 90	92.330 (6), 99.313 (10), 90.721 (11)	79.108 (3), 83.424 (3), 89.300 (3)	92.496 (6), 91.452 (6), 107.191 (6)
V (Å ³)	1106.69 (14)	1665.1 (7)	1680.1 (2)	1398.1 (3)
Z, Z'	4, 1	4, 2	4, 2	4, 2
μ (mm ⁻¹)	0.35	0.25	0.25	0.28
Crystal size (mm)	0.52 × 0.46 × 0.07	0.55 × 0.25 × 0.02	0.58 × 0.25 × 0.02	0.64 × 0.34 × 0.04
Data collection				
T_{\min}, T_{\max}	0.84, 0.98	0.93, 1.00	0.88, 0.99	0.89, 0.99
No. of measured, independent and observed [$I > 3\sigma(I)$] reflections	38 182, 3254, 2933	17 126, 4002, 2725	68 578, 7746, 5684	22 518, 4971, 4548
R_{int}	0.040	0.042	0.044	0.046
$(\sin \theta/\lambda)_{\text{max}}$ (Å ⁻¹)	0.706	0.658	0.653	0.661
Refinement				
$R[F^2 > 2\sigma(F^2)], wR(F^2), S$	0.025, 0.028, 1.52	0.057, 0.054, 1.74	0.039, 0.043, 1.95	0.044, 0.055, 2.37
No. of reflections	3254	4002	7746	4971
No. of parameters	101	308	307	254
$\Delta\rho_{\text{max}}, \Delta\rho_{\text{min}}$ (e Å ⁻³)	0.20, -0.15	0.36, -0.36	0.30, -0.37	0.30, -0.35
Twin operation	$\bar{1}$	$2_{[100]}$	–	$m_{(001)}$
Twin volume ratio	58.42 (6)	72.42:27.58 (15)	–	59.95:40.05 (13)
Absolute structure	1894 of Friedel pairs used in the refinement	–	–	–
Absolute structure parameter	0.42 (6)	–	–	–

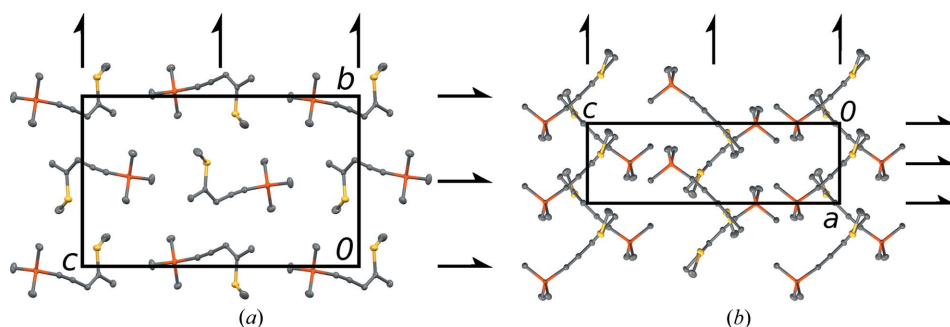


Figure 3
The crystal structure of (1-TMS) viewed down (a) [100] and (b) [010]. Atom color codes as in Fig. 2. Symmetry elements are indicated by the usual graphical symbols (Hahn, 2006).

cules. To facilitate comparison and highlight pseudo-symmetry, the atoms in the pairs of molecules were named identically up to a prime character (S1 and S1' *etc.*). Crystallographic data and refinement details are compiled in Table 1.

3. Results and discussion

3.1. (1-TMS)

As has been stated in §1, in contrast to the parent *bis*-ene-yne compounds (Lumpi *et al.*, 2015), (1-TMS) does not crys-

tallize in distinct trialkylsilyl group delimited layers. Instead, one crystallographically unique molecule is arranged as shown in Fig. 3. The molecular conformation is similar to the structurally related molecules in this class (Lumpi *et al.*, 2014, 2015). The methylthio group is rotated slightly out of the plane defined by the ene-yne chain [CH=C–S–CH₃ torsion angle of 160.23 (10)° *versus* 180° for a flat conformation].

(1-TMS) crystallizes in the Sohncke group $P2_12_12_1$, *i.e.* the crystalline domains are chiral. A survey of flexible, non-chiral molecules crystallizing in Sohncke groups was given by Pidcock (2005). The crystal under investigation was twinned *via* inversion with approximately equal volume fractions [Flack parameter 0.42 (6)]. The twin law is made up of the $\bar{1}$, $m_{[100]}$, $m_{[010]}$ and $m_{[001]}$ operations, *i.e.* the left coset of 222 (the point group of the crystal) with the inversion operation.

The key to understanding twinning is often a symmetry analysis. A twin operation may be interpreted as the linear part of:

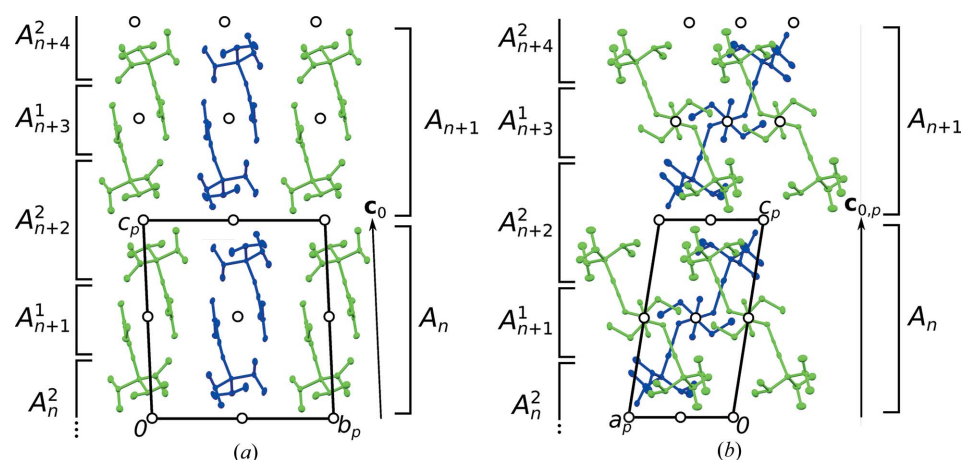


Figure 4 The crystal structure of polymorph (I) of (1-TIPS) viewed down (a) [100] and (b) [010]. The molecules are colored according to symmetry equivalence. Symbols as in Fig. 3. Layers according to the OD descriptions in terms of $M = 1$ (§3.2.1) and $M = 2$ (§3.2.3) kinds of layers are indicated to the right and left, respectively.

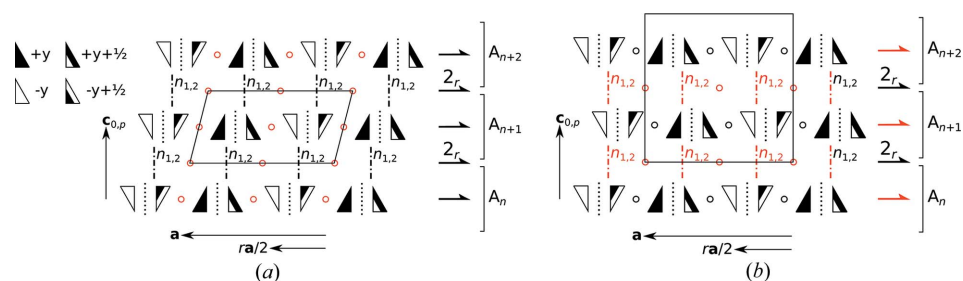


Figure 5 Scheme of the (local) symmetry of the (a) MDO₁ and (b) MDO₂ polytypes of polymorph (I) of (1-TIPS), viewed down [010]. (1-TIPS) molecules are represented by triangles which are white on one and black on the other side. A translation of $\mathbf{b}/2$ (in addition to the y -component of \mathbf{c}_0) is indicated by a small triangle of opposite color. Symmetry operations of layers and operations relating adjacent layers are indicated by the common graphical symbols (Hahn, 2006). In the case of non-crystallographic intrinsic translations (other than half of a primitive lattice vector) the symbols for 2_1 screw rotations and n glide reflections are used and the printed symbol is given. Operations valid for the whole polytype are painted in red.

a symmetry operation of a related higher symmetry structure, as in ferroic species (Aizu, 1970);

a local pseudo-symmetry operation (see discussion on OD twins below);

a pseudo-symmetry operation of a subset of the atoms/molecules in the structure (Marzouki *et al.*, 2014).

In all these cases, a higher-symmetry part of the structure enables the structural continuity of one twin individual to the next.

In (1-TMS) no such pseudo-symmetry is apparent and inspection of the platy crystal under a polarizing microscope was not enlightening. As we have shown for the molecules TSEM and DSEM (Lumpi *et al.*, 2015), in some cases the twin interface is different from the bulk, *i.e.* there are geometrically different, but energetically equivalent, ways of arranging structural modules (layers, rods or blocks). (1-TMS) seems to be such a case and until a different arrangement is found, the nature of the twin interface will remain unknown.

3.2. (1-TIPS), polymorph (I)

3.2.1. OD structure of one kind of layer. The (1-TIPS) molecules in polymorph (I) are arranged in distinct crystallochemical layers parallel to (001). The TIPS groups are located at the layer interfaces, the remainder of the molecules at the center (Fig. 4). The layers possess $p\bar{1}(1)$ symmetry [parentheses identify the direction without translational symmetry (Dornberger-Schiff & Grell-Niemann, 1961)]. They are made up of $Z' = 2$ crystallographically independent molecules, which are colored differently in Fig. 4, both located on the general position.

The independent molecules are related by pseudo-symmetry (although see §3.2.2), *viz.* a $b_{[100]}$ pseudo-glide reflection. The glide planes of adjacent layers do not coincide and therefore the structure belongs to a category I OD family composed of layers of one kind with the OD groupoid symbol

$$\left\{ \begin{array}{l} p \quad 2_1/b \quad 1 \quad (1) \\ \quad \quad \quad 2_r/n_{1,2} \quad \bar{1} \quad (\bar{1}) \end{array} \right\}$$

according to the notation of Dornberger-Schiff & Grell-Niemann (1961). The symbol indicates that the structure is composed of layers with the symmetry $p2_1/b1(1)$, which are designated as A_n , where n is a sequential number. These layers correspond to the crystallochemical

layers described above. The second line of the symbol describes one possible way in which adjacent layers can be related: by inversion, a 2_r screw rotation (with intrinsic translation $\mathbf{ra}/2$) and an $n_{1,2}$ glide reflection (with intrinsic translation $\mathbf{b}/2 + \mathbf{c}_0$). The vector \mathbf{c}_0 is used as a reference to describe the connectivity of adjacent layers. It is chosen normal to \mathbf{a} , but not normal to \mathbf{b} (Fig. 4) to reflect the monoclinic point group of the OD family (Fichtner, 1977) with the monoclinic axis parallel to the layer planes. Thus, an additional metric parameter s is avoided (Fichtner, 1979).

According to the NFZ relationship (Đurovič, 1997), there are $Z = N/F = [\mathcal{G}_n : \mathcal{G}_n \cap \mathcal{G}_{n+1}] = [p\bar{1}(1) : p1(1)] = 2$ equivalent ways of placing the layer A_{n+1} given the position of A_n . \mathcal{G}_n is the group of operations of the layer A_n that do not reverse the orientation with respect to the stacking direction and $\mathcal{G}_n \cap \mathcal{G}_{n+1}$ the subgroup of those operations also valid for the adjacent A_{n+1} layer. The $Z = 2$ positions of the A_{n+1} layer are related by the $b_{[100]}$ glide reflection of A_n .

Thus, the A_n layers can be arranged to an infinity of locally (at least two layer widths) equivalent polytypes. Of these, two are of a maximum degree of order (MDO; Dornberger-Schiff, 1982). They play an important role in OD theory since, by a large margin, the most commonly observed polytypes are of the MDO type. All other polytypes can be decomposed into fragments of the MDO polytypes.

MDO_1 [$P\bar{1}$, $\mathbf{c} = \mathbf{c}_0 + (r-1)\mathbf{a}/2$, Fig. 5a] is generated by repeated application of the $\bar{1}$ operations; MDO_2 ($P2_1/n11$, $\mathbf{c} = 2\mathbf{c}_0$, Fig. 5b) by repeated application of $n_{1,2}$ glide reflections.

(1-TIPS) is a classical OD twin (Dornberger-Schiff & Grell-Niemann, 1961). The individuals are of the MDO_1 polytype, whereas a fragment of the MDO_2 polytype is located at the twin interface. The possible orientations and twin laws are obtained by coset decomposition of the $\bar{1}$ point group of the MDO_1 polytype in the $2/m11$ point group of the OD family. In agreement with the experimental data, there are two cosets (and therefore individuals), viz. $\{1, \bar{1}\}$ and $\{2_{[010]}, m_{[010]}\}$, the latter being the twin law.

The metric parameter r is calculated from the measured lattice parameters of the MDO_1 polytype as $r = (2c/a) \cos \beta + 1 = 0.377$. Since r is not close to a rational with a small denominator, only $0kl$ are family reflections (i.e. reflections that emerge from all polytypes).

3.2.2. Desymmetrization. A characteristic phenomenon of OD structures is desymmetrization of ordered polytypes in comparison to the idealized description (the *archetype* structure). In the MDO_1 polytype of polymorph (I) of (1-TIPS) the symmetry of the actual A_n layers is related to the archetype layers by a *translationengleiche* symmetry reduction of index 2 from $p2_1/b1(1)$ to $p\bar{1}\bar{1}(\bar{1})$.

A simple measure of desymmetrization is the rather large deviation from the rectangular metrics of the layer lattice [$\gamma = 90.721$ (11)°]. Thus, the lattice mismatch at the twin composition plane is $\sim 1.4^\circ$. The structural continuity is enabled by a fragment of the MDO_2 polytype with an ideal angle of $\gamma = 90^\circ$. An even more extreme case of layer lattice desymmetrization ($\beta = 92.5^\circ$ instead of 90°) in the same class of compounds was observed for **C** (Lumpi *et al.*, 2015).

For a more detailed quantification of the desymmetrization, γ was idealized as 90° and the $b_{[100]}$ glide reflection applied to the A_0 layer. An excerpt of an overlap of the original and the transformed layer is depicted in Fig. 6. Compared with other OD structures analyzed by our group, the deviation from idealized symmetry is substantial. Whereas the deviation of the backbone of the molecules (ene-yne chain, methylthio group, Si atom) is in line with comparable structures (distance of atoms in both layers: 0.100–0.311 Å), the ${}^i\text{Pr}$ groups of the TIPS unit deviate more markedly (0.236–1.131 Å). Notably, the C7–C9 ${}^i\text{Pr}$ group features a different orientation in both layers (Fig. 6). It is expected that desymmetrization is more pronounced for the ${}^i\text{Pr}$ groups, since they are located at the layer interface and therefore in an environment of different symmetry. Nevertheless, the deviation is large enough to cast doubt on the validity of the OD description in terms of one layer.

3.2.3. OD structure of two kinds of layers. Owing to the excessive desymmetrization of the ${}^i\text{Pr}$ groups, it may be appropriate to consider the ${}^i\text{Pr}$ groups as distinct layers. The structure of polymorph (I) of (1-TIPS) is then composed of $M = 2$ kinds of layers, A^1 (C10–C15, S1) and A^2 (C1–C9, Si), which do not correspond to layers in the crystallochemical sense. Although such a description in terms of non-crystallochemical layers has been criticized (Ferraris *et al.*, 2008), it has to be noted that the fundamental arguments of OD theory (local equivalence of polytypes) are independent from such crystallochemical considerations.

The structure then belongs to a category IV OD family composed of layers of two kinds with the OD groupoid family symbol

$$\begin{array}{ccc} A^1 & & A^2 \\ p2_1/b1(1) & & p\bar{1}\bar{1}(\bar{1}) \\ & [(r-1)/4, 0] & \end{array}$$

according to the notation of Grell & Dornberger-Schiff (1982). The structure is made up of an alternating stacking of A^1 and A^2 layers with $p2_1/b1(1)$ and $p\bar{1}\bar{1}(\bar{1})$ symmetry, respectively (Fig. 4). In one stacking possibility, the origins of A_n^1 and A_{n+1}^2 are related by a translation $(r-1)\mathbf{a}/4 + \mathbf{c}_0/2$. The r is chosen to be identical to the r in §3.2.1. Here, the NFZ relationship reads for the $A_n^1 \rightarrow A_{n+1}^2$ layer contact as $Z = [pb1(1) : p11(1)] = 2$, i.e. given the A_n^1 layer, there are two possibilities of placing A_{n+1}^2 , which are related by the $b_{[100]}$ glide reflection of A_n^1 . For the $A_{n+1}^2 \rightarrow A_{n+2}^1$ contact, on the other hand, $Z = [p11(1) : p11(1)] = 1$ and therefore, for a fixed A_{n+1}^2 , the location of the adjacent A_{n+2}^1 is also fixed.

As a consequence, given A_n^1 , A_{n+2}^1 can be placed at two positions, which correspond precisely to the stacking possibilities of the description in terms of one layer given in §3.2.1. Thus, formally, both descriptions are equivalent and possess the same MDO polytypes, which will not be listed again. The major difference pertains to the desymmetrization: in the two-

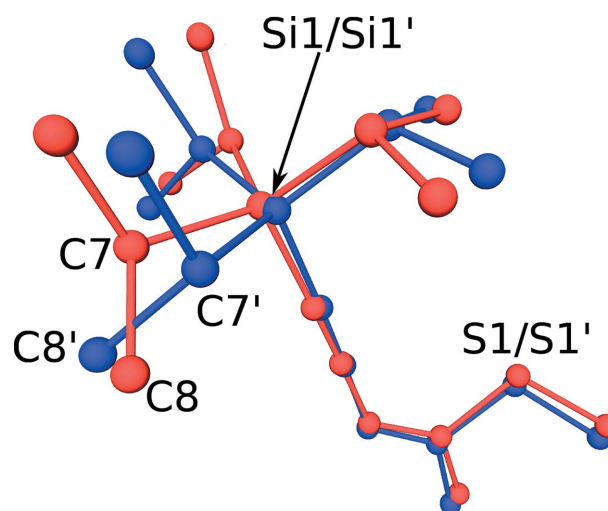


Figure 6
Excerpt of the overlap of the A_0 layer in polymorph (I) of (1-TIPS) and its image by the $b_{[100]}$ pseudo-glide reflection. The molecules of both layers are painted in red and blue, respectively.

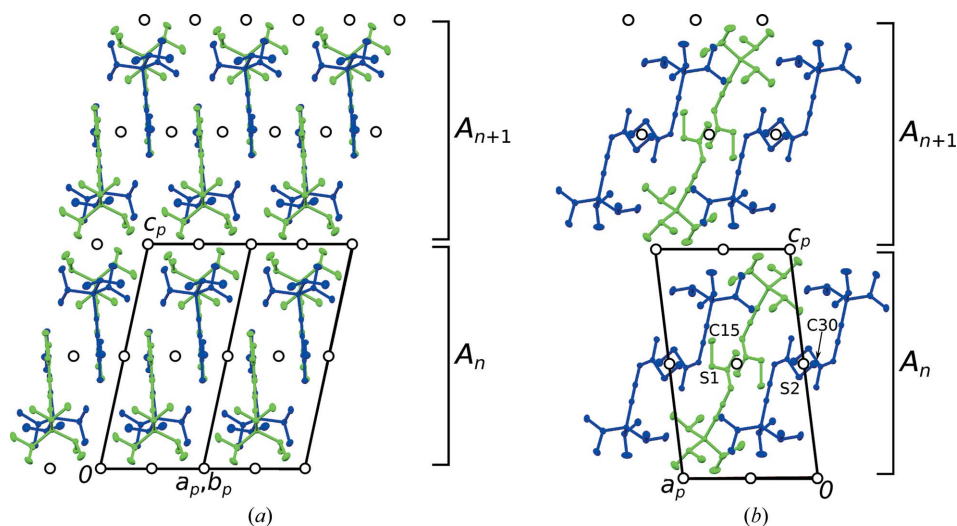


Figure 7
The crystal structure of polymorph (II) of (1-TIPS) viewed down (a) [110] and (b) [010]. Atom color codes and symbols as in Fig. 3.

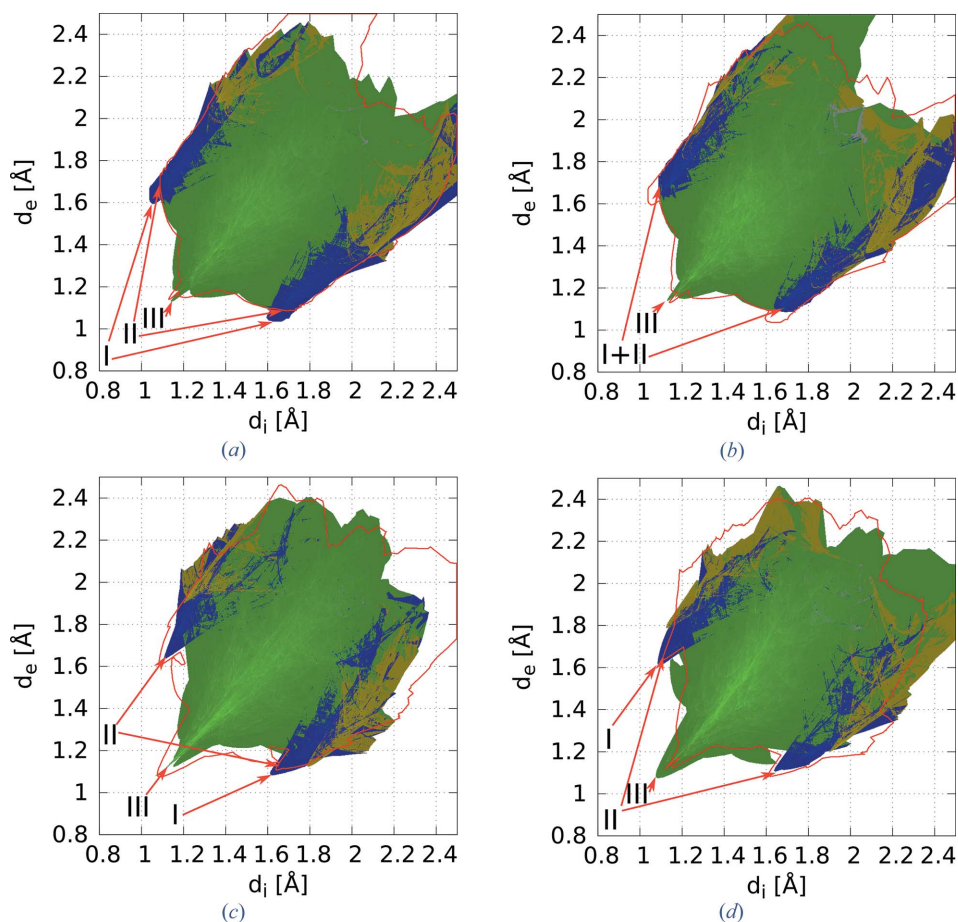


Figure 8
Hirshfeld d_i/d_e fingerprint plots of the molecules in (a, b) polymorph (I) and (c, d) polymorph (II) of (1-TIPS) calculated with *CrystalExplorer* (Wolff *et al.*, 2012). Regions of the histograms where H···H, C···H and S···H contacts dominate are drawn in green, blue and yellow, respectively. Other kinds of contacts are drawn in gray. A brighter color signifies a larger proportion of the Hirshfeld surface. For comparison, each plot is overlaid with the outline of the fingerprint plot of the other molecule in the same polymorph.

layer description the symmetry of the A^2 layers is not reduced. Desymmetrization affects only the A^1 layers [*translationengleiche* symmetry reduction by an index of 2 from $p2_1/b1(1)$ to $p\bar{1}1(\bar{1})$] and thus distinctly less idealization is needed.

In the end, the choice of description is a matter of taste and depends on the degree of desymmetrization that is considered acceptable. In the two-layer description, the layer interface of the one-layer description is considered a separate layer. This ambiguity in the description of OD structures is different from the ambiguity of layer choice discussed by Grell (1984). In the latter, the archetype structures of both descriptions are identical. By selecting different layers, the symmetry operations of a layer in one description may instead be considered as operations relating adjacent layers. Here, on the other hand, the archetype structures according to both OD descriptions differ, because for the one-layer description a higher degree of idealization is necessary.

3.3. (1-TIPS), polymorph (II)

Polymorph (II) of (1-TIPS) is isopointal (Lima-de-Faria *et al.*, 1990) with polymorph (I) [space group $P\bar{1}$ and $Z' = 2$ independent molecules on the general position]. The molecules in polymorph (II) are again arranged in layers parallel to (001) (Fig. 7), here with the plane of the ene-yne fragment approximately normal to [110]. In contrast to polymorph (I), the molecules are not related by a pseudo-symmetry operation. The molecules with the primed atom names (blue in Fig. 7) are moved slightly away from the layer interface and, more importantly, the orientations of the methylthio groups are different in both molecules (see §3.4). Thus, polymorph (II) lacks pseudo-symmetry and the symmetry of the layers is $p\bar{1}1(\bar{1})$.

Adjacent layers are related by inversion and according to the *NFZ* relationship $Z = N/F = [p11(1) : p11(1)] = 1$. There is only one way of placing adjacent layers, or in terms of OD theory, the structure is *fully ordered*.

3.4. Comparison of both polymorphs of (1-TIPS)

Comparing polymorphs of molecular compounds is difficult if they lack structure-directing moieties, such as hydrogen (or halogen) bond donors and acceptors. Care must be taken not to use arbitrary cut-off distances when considering intermolecular interactions. The analysis of Hirshfeld surfaces (Spackman & Jayatilaka, 2009) was developed as a way to objectify such a comparison. Hirshfeld surfaces are the surfaces in a crystal where the atoms of two molecules

contribute equally to the electron density. Multiple properties can be mapped onto these surfaces. Especially interesting for the analysis of polymorphs are the distances d_i and d_e to the center of gravity of the closest atoms inside and outside of the surface, respectively. When plotted in a two-dimensional histogram, these d_i/d_e fingerprint plots (Spackman & McKinnon, 2002) are characteristic for the closest coordination of a molecule in a polymorph.

In Fig. 8 the d_i/d_e fingerprint plots of the four (1-TIPS) molecules (two per polymorph) are given. The first – and expected – observation is that in all four cases the $H \cdots H$ contacts are dominant. Secondly, the plots of both molecules in polymorph (I) are more similar than the plots of the molecules in polymorph (II). This fact is likewise unsurprising, because the molecules in polymorph (I) are related by pseudo-symmetry and are located in (pseudo-)equivalent chemical environments.

Although the plots of the molecules in polymorph (I) are very similar, effects of desymmetrization (see §3.2.2) are apparent. Notably, shorter $C \cdots H$ contacts are observed in the

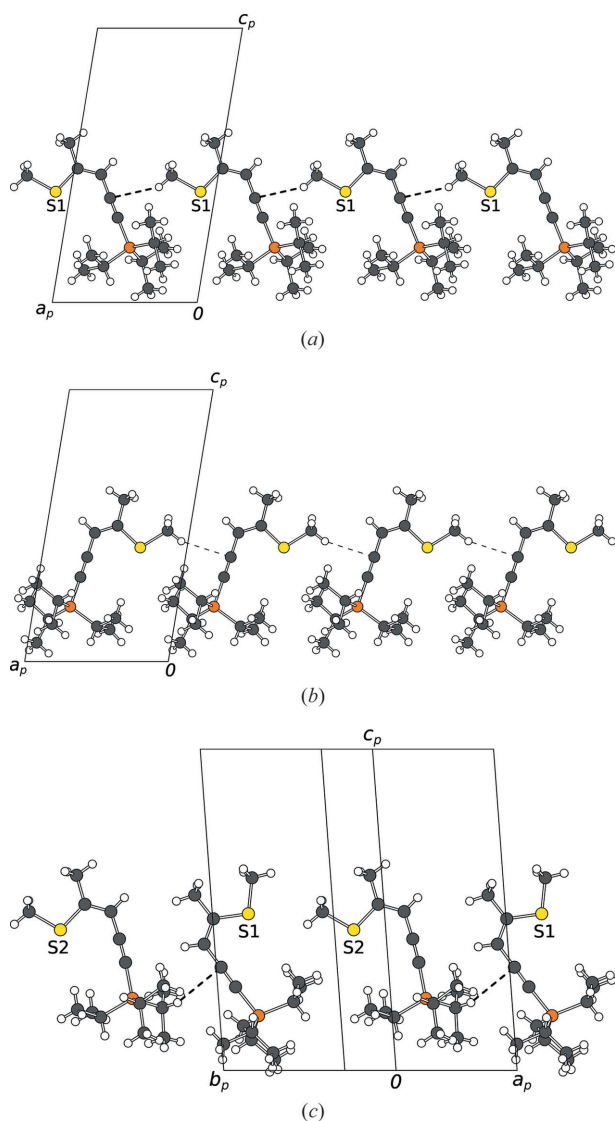


Figure 9
(1-TIPS) molecules connected by short $H \cdots C$ contacts (*a*, *b*) in polymorph (I), forming rods extending along $[100]$ and (*c*) in polymorph (II), forming molecule pairs arranged in rods extending along $[1\bar{1}0]$. The rods in (*a*) and (*b*) are related by a pseudo $b_{[100]}$ glide reflection. Atoms are represented by spheres of arbitrary radius, with color codes as in Fig. 3. H atoms are shown in white.

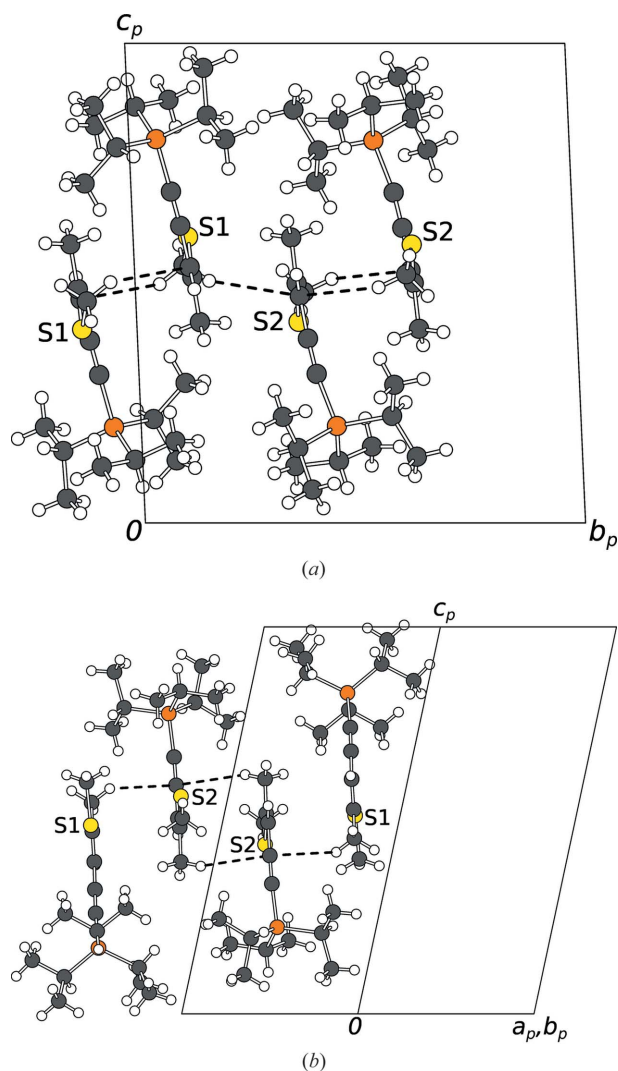


Figure 10
The rods of Fig. 9 viewed down the rod axis and interconnected by short $H \cdots C$ contacts. Atom color codes as in Fig. 9.

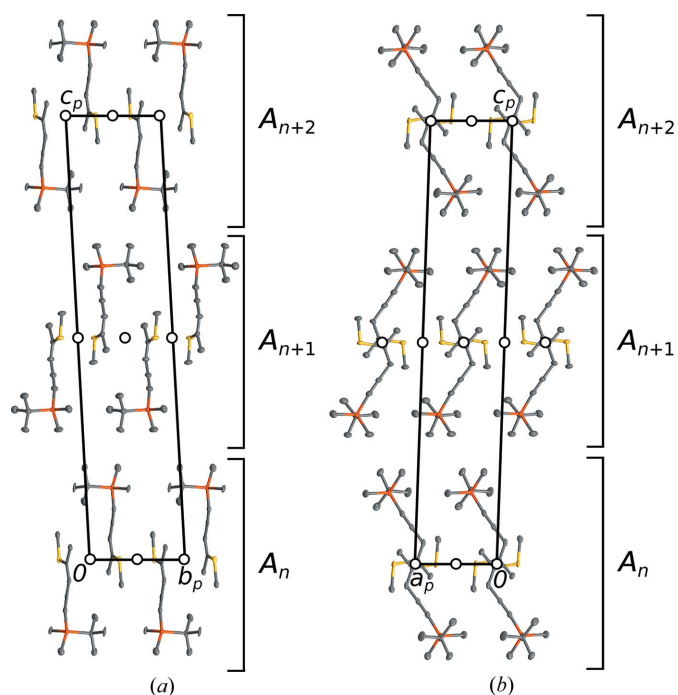


Figure 11
The crystal structure of (1-TBDMS) viewed down (a) [110] and (b) [010]. Atom color codes and symbols as in Fig. 3.

plot of molecule 1 compared to molecule 2 (region I in Figs. 8a and b). The plots are symmetric at the $d_i = d_e$ -line with respect to this region, indicating that these contacts are between the crystallographic equivalent molecules. Indeed, these are contacts between the methylthio group and an sp -hybridized C atom of the yne group, forming rods extending along [100] as shown in Figs. 9(a) and (b).

Polymorph (II) possesses similar $C \cdots H$ contacts [region (I) in Figs. 8(c) and (d)]. Here the plots are not symmetric at the

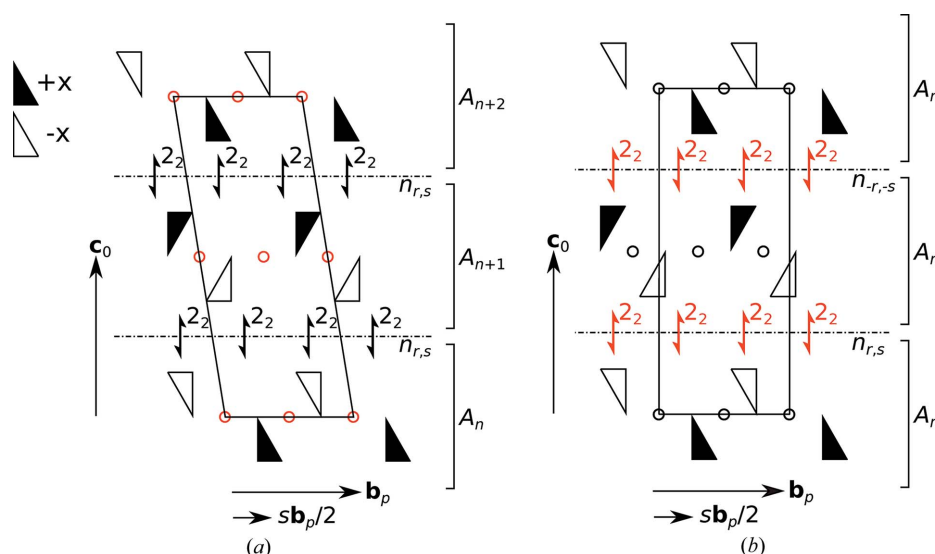


Figure 12
Scheme of the (local) symmetry of the (a) MDO₁ and (b) MDO₂ polytypes of (1-TBDMS) viewed down [010]. Symbols as in Fig. 5.

$d_i = d_e$ line with respect to this region, but the plots of both molecules are related by such an operation, suggesting that this contact connects two crystallographically independent molecules. Indeed, it corresponds to a $C-H \cdots C$ contact from an ⁱPr group of molecule 2 to an sp -hybridized C atom of the yne group of molecule 1, thus forming pairs (Fig. 9c). These pairs are arranged in rods extending along [110]. In these rods, the orientation of molecule 2 is nearly unchanged compared with the rods in polymorph (I), but molecule 1 is flipped with respect to the rod direction. As a consequence of this rotation, the TMS group of the molecule 1 protrudes from the layer interface. One can say that the crystallochemical layers in polymorph (II) can be derived from the layers in polymorph I by flipping every second molecule. The existence of a corresponding phase transition remains speculative owing to a lack of polymorph I material.

Additional $C \cdots H$ contacts (region II in Fig. 8) connect molecules perpendicular to the rod direction (Fig. 10): In polymorph (I) the methylthio groups connect to sp^2 -hybridized C atoms. In polymorph (II) the terminal methyl groups next to the ene fragment connect the sp -hybridized C atoms.

The small spike of very short $H \cdots H$ distances (region III in Fig. 8) originates from intermolecular TMS group contacts. In polymorph (I), crystallographically different molecules inside the layers are connected ($C9-H3C9 \cdots H3C5'-C5'$: 2.498 Å). In polymorph (II) two pairs of crystallographically equivalent molecules are connected across the layer boundary ($C8-H2C8 \cdots H3C9-C9$: 2.477 Å; $C9'-H1C9' \cdots H1C9'-C9'$: 2.312 Å).

3.5. (1-TBDMS)

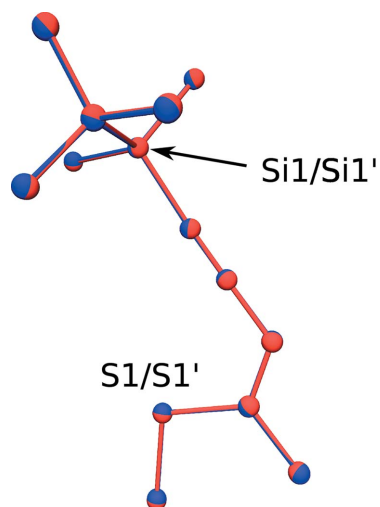
Like both polymorphs of (1-TIPS), the (1-TBDMS) molecules crystallize in distinct crystallochemical layers parallel to (001), which are connected *via* the silyl groups (here TBDMS).

Again, $Z' = 2$ crystallographically independent molecules are located on the general position. In contrast to the TIPS polymorphs, which are composed of equivalent layers of two molecules, (1-TBDMS) is composed of two independent layers with one unique molecule each (Fig. 11).

These two layers are related by pseudo-symmetry operations and therefore the structure belongs to a category I OD family composed of layers of one kind with the OD groupoid family symbol

$$p \quad \bar{1} \quad \bar{1} \quad (\bar{1}) \\ \{ \quad - \quad - \quad (2/n_{r,s}) \}$$

Accordingly, the structure is composed of A_n layers with $p\bar{1}\bar{1}(\bar{1})$ symmetry, which correspond to the crystallochemical layers. In one

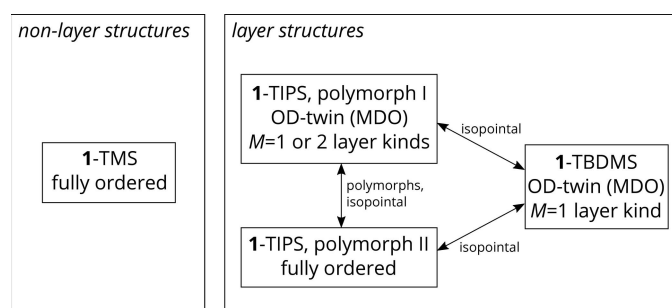

Figure 13

Excerpt of the overlap of the A_0 and A_1 layers in the actual MDO_1 polytype of (1-TBDMS). A 2_2 screw rotation was applied to A_0 to superpose both layers.

possible stacking arrangement, A_n is related to A_{n+1} by a 2_2 screw rotation with intrinsic translation \mathbf{c}_0 or, equivalently, an $n_{r,s}$ glide reflection with an intrinsic translation $r\mathbf{a}/2 + s\mathbf{b}/2$. \mathbf{c}_0 is the vector perpendicular to the layer planes with the length of one layer width. Since the intrinsic translation of the $n_{r,s}$ operation is neither a primitive nor half of a primitive lattice vector $[(r, s) \notin \mathbb{Z}^2]$, $n_{r,s}$ maps A_n on A_{n+1} , but does not map A_{n+1} on A_n . In such a case, the NFZ relationship reads as $Z = 2N/F = 2[p\bar{1}\bar{1}(\bar{1}) : p\bar{1}\bar{1}(\bar{1})] = 2$ and, given an A_n layer, there are two equivalent ways of placing the adjacent A_{n+1} layer, obtained by application of $n_{r,s}$ or $n_{-r,-s}$ glide reflections. The two possible positions of A_{n+1} are related the translation $r\mathbf{a} + s\mathbf{b}$.

Two of the polytypes are MDO: MDO_1 [$P\bar{1}$, $\mathbf{c} = 2\mathbf{c}_0 + (r-1)\mathbf{a} + (s-1)\mathbf{b}$, Fig. 12a] is generated by repeated application of $n_{r,s}$; MDO_2 ($P112_1$, $\mathbf{c} = 2\mathbf{c}_0$, Fig. 12b) by an alternating application of $n_{r,s}$ and $n_{-r,-s}$.

(1-TBDMS) is, like polymorph (I) of (1-TIPS), an OD twin. The individuals are of the MDO_1 polytype and a fragment of MDO_2 is located at the composition plane. Coset decom-


Figure 14

Overview of the analyzed crystal structures, their degree of order and structural relationships.

position of the $112/m$ point group of the OD family by the $\bar{1}$ point group of the MDO_1 polytype gives the two cosets $\{1, \bar{1}\}$, $\{2_{(001)}, m_{(001)}\}$, corresponding to two individuals [the rotation axis and mirror plane are given as normal and parallel to the (001) plane]. The second coset is the twin law. The metric parameters r and s are derived trigonometrically from the lattice parameters as $r = (c/a) \cos \beta + 1 = 0.869$ and $s = (c/b) \cos \alpha + 1 = 0.806$.

Desymmetrization of the MDO_1 polytype results in a splitting of the A_n layers into two crystallographically independent layers. To quantify the desymmetrization, the 2_2 operation with axis $(\frac{1}{4}, \frac{1}{4}, z)$ was applied to the A_0 layer. An excerpt of the overlap of the image of A_0 and the A_1 layer is depicted in Fig. 13. The molecules of both layers overlap nearly perfectly. A remarkably small maximum distance of 0.028 Å is observed for the C4/C4' pair. Thus, in contrast to polymorph (I) of (1-TIPS) there is no doubt about the validity of the OD description in terms of one OD layer.

4. Conclusion

As in the preceding study (Lumpi *et al.*, 2015), the capping of rigid ene-yne fragments with bulky trialkylsilyl groups induced crystallization in distinct layers delimited by the silyl groups. But here, since the molecules were only capped single-sidedly, the molecules did not span a full layer-width.

Also, as previously, the layered structures have proven to feature a rich crystal chemistry, such as polymorphism and twinning as summarized in Fig. 14. Both observed twins can be convincingly explained by application of the OD theory, underlining the importance of local symmetry.

The comparison of both polymorphs of (1-TIPS) shows that application of the OD theory is even useful in the case of fully ordered structures. It can explain the absence of twinning and establish structural relations beyond group/subgroup relationships. The case of polymorph (I) also highlights a fundamental issue of the approach: an OD description is a subjective interpretation in the sense that a decision has to be made how much idealization is acceptable.

Acknowledgements

The X-ray centre of the TU Vienna is acknowledged for providing access to the single-crystal and powder diffractometers. This publication was supported by TU Wien research funds.

References

- Aizu, K. (1970). *Phys. Rev. B*, **2**, 754–772.
 Bruker (2015). *APEXII, RLATT, SAINT, SADABS* and *TWINABS*. Bruker X-ray Instruments Inc., Madison, Wisconsin, USA.
 Dornberger-Schiff, K. (1982). *Acta Cryst.* **A38**, 483–491.
 Dornberger-Schiff, K. & Grell-Niemann, H. (1961). *Acta Cryst.* **14**, 167–177.
 Đurovič, S. (1997). *EMU Notes Mineral.* **1**, 3–28.
 Ferraris, G., Makovicky, E. & Merlino, S. (2008). *IUCr Monographs on Crystallography*, Vol. 15. Oxford University Press.
 Fichtner, K. (1977). *Beitr. Algebra. Geom.* **6**, 71–99.

- Fichtner, K. (1979). *Krist. Tech.* **14**, 1453–1461.
- Grell, H. (1984). *Acta Cryst.* **A40**, 95–99.
- Grell, H. & Dornberger-Schiff, K. (1982). *Acta Cryst.* **A38**, 49–54.
- Hahn, T. (2006). *International Tables For Crystallography*, Vol. A, ch. 1.4, pp. 7–11. Heidelberg: Springer.
- Lima-de-Faria, J., Hellner, E., Liebau, F., Makovicky, E. & Parthé, E. (1990). *Acta Cryst.* **A46**, 1–11.
- Lumpi, D. (2013). Dissertation. Vienna University of Technology, Austria.
- Lumpi, D., Glöcklhofer, F., Holzer, B., Stöger, B., Hametner, C., Reider, G. A. & Fröhlich, J. (2014). *Cryst. Growth Des.* **14**, 1018–1031.
- Lumpi, D., Kautny, P., Stöger, B. & Fröhlich, J. (2015). *IUCrJ*, **2**, 584–600.
- Lumpi, D., Stöger, B., Hametner, C., Kubel, F., Reider, G. A., Hagamann, H. R., Karpfen, A. & Fröhlich, J. (2011). *CrystEngComm*, **24**, 7194–7197.
- Marzouki, M. A., Souvignier, B. & Nespolo, M. (2014). *IUCrJ*, **1**, 39–48.
- Palatinus, L. & Chapuis, G. (2007). *J. Appl. Cryst.* **40**, 786–790.
- Petříček, V., Dušek, M. & Palatinus, L. (2014). *Z. Kristallogr.* **229**, 345–352.
- Pidcock, E. (2005). *Chem. Commun.* pp. 3457–3459.
- Spackman, M. A. & Jayatilaka, D. (2009). *CrystEngComm*, **11**, 19–32.
- Spackman, M. A. & McKinnon, J. J. (2002). *CrystEngComm*, **4**, 378–392.
- Wolff, S. K., Grimwood, D. J., McKinnon, J. J., Turner, M. J., Jayatilaka, D. & Spackman, M. A. (2012). *CrystalExplorer*, Version 3.1. University of Western Australia, Australia.

2.13. Manuscript #13

Charge transfer states in triazole linked donor-acceptor materials: strong effects of chemical modification and solvation

Paul Kautny, Florian Glöcklhofer, Thomas Kader, Jan-Michael Mewes, Berthold Stöger, Johannes Fröhlich, Daniel Lumpi, Felix Plasser

submitted for publication

Charge transfer states in triazole linked donor-acceptor materials: strong effects of chemical modification and solvation

Received 00th January 20xx,
Accepted 00th January 20xx

DOI: 10.1039/x0xx00000x

www.rsc.org/

Paul Kautny,^a Florian Glöcklhofer,^a Thomas Kader,^a Jan-Michael Mewes,^b Berthold Stöger,^c Johannes Fröhlich,^a Daniel Lumpi*^a and Felix Plasser*^d

A series of 1,2,3-triazole linked donor-acceptor chromophores are prepared by Click Chemistry from ene-yne starting materials. The effect of three distinct chemical variations are investigated: enhancing the acceptor strength through oxidation of the sulphur atom, alteration of the double bond configuration, and variation of the triazole substitution pattern. A detailed photophysical characterization shows that these alterations have a negligible effect on the absorption while dramatically altering the emission wavelengths. In addition, strong solvatochromism is found leading to significant red shifts in the case of polar solvents. The resulting electronic structure properties are analyzed in detail by time-dependent density functional theory as well as the *ab initio* algebraic diagrammatic construction method for the polarization propagator in connection with a new formalism allowing to model the influence of solvation onto long-lived excited states and their emission energies. These calculations highlight the varying degree of intramolecular charge transfer character present for the different molecules and show that the amount of charge transfer is strongly modulated by the conducted chemical modifications, by the solvation of the chromophores, and by the structural relaxation in the excited state.

Introduction

The development of organic push-pull materials consisting of π -conjugated electron donating and electron withdrawing subunits has attracted a lot of attention during the last decades due to a wide range of technologically relevant applications in organic light emitting diodes (OLEDs),¹⁻⁴ organic photovoltaics (OPVs),^{5,6} nonlinear optical (NLO) materials⁷ for two-photon-absorption⁸ or second harmonic generation (SHG)⁹ and many others. The molecular properties of these materials are dominated by the interaction of the donor and acceptor moieties *via* intramolecular charge transfer (ICT).^{1,4,8,10} Therefore, the careful choice and modification of the donor and acceptor as well as the nature of the conjugated linker unit is of crucial importance in order to modulate the degree of ICT and efficiently control and tune the intrinsic electronics of the molecules.^{1,3,8,9} In particular, the emergence of novel techniques for the utilization of excited triplet states in OLEDs for the generation of light *via* fluorescence^{11,12} requires an

accurate molecular design of donor-acceptor materials. In the case of thermally activated delayed fluorescence (TADF) the splitting between the S_1 and T_1 states has to be minimized.^{4,13} Materials with hybridized local and charge transfer states (HLCT) can utilize high lying triplet states *via* hot exciton processes.¹⁴ Both processes have in common that the interplay between the donor and the acceptor has to be exactly controlled to achieve the required properties of the excited states.

Copper-catalyzed azide-alkyne cycloaddition (CuAAC) offers the unique possibility to join two molecular subunits establishing a 1,2,3-triazole linker at the same time.¹⁵ This methodology, which is generally regarded as the most successful example of Click Chemistry,¹⁶ has been widely exploited in many fields of organic chemistry.¹⁶⁻¹⁸ Whereas in most of these studies the formed triazole is merely a linking unit, the utilization of the heterocycle itself as integral functional unit is rare and reports on the application of 1,2,3-triazoles as weakly electron deficient functional π -conjugated linkers are relatively scarce. Nonetheless, click derived materials have been employed as optical¹⁹⁻²⁴ and nonlinear optical materials,²⁵ for sensor applications,²⁶ metal coordination^{27,28} and in dye sensitized solar cells.²⁹

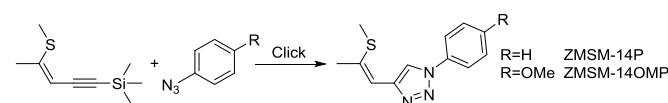
^a Institute of Applied Synthetic Chemistry, TU Wien, Getreidemarkt 9/163, A-1060 Vienna, Austria; E-mail: daniel.lumpi@tuwien.ac.at

^b Centre for Theoretical Chemistry and Physics, The New Zealand Institute for Advanced Study (NZIAS), Massey University Albany, Private Bag 102904, Auckland 0745, New Zealand

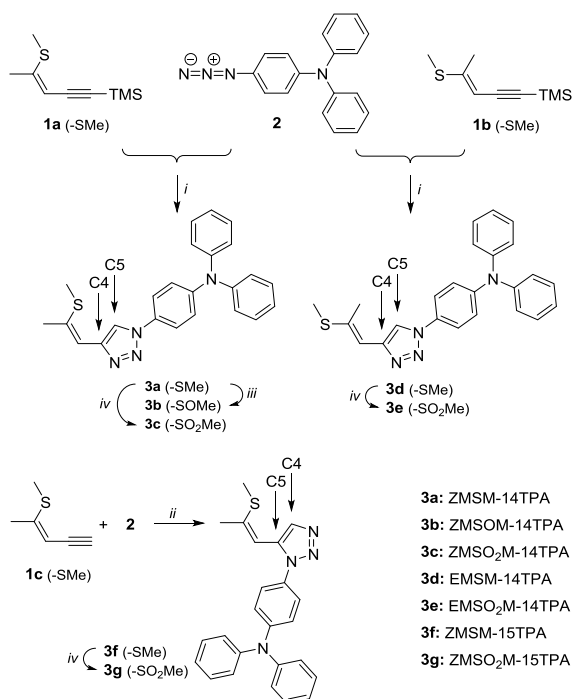
^c X-ray Centre, TU Wien, Getreidemarkt 9, A-1060 Vienna, Austria

^d Institute of Theoretical Chemistry, Faculty of Chemistry, University of Vienna, Währinger Str. 17, A-1090 Vienna, Austria; E-mail: felix.plasser@univie.ac.at

Electronic Supplementary Information (ESI) available: UV/VIS absorption and emission spectra, maxima of the spectra, optimized molecular structures of the investigated materials and crystallographic information. CCDC 1536607-1536609 See DOI: 10.1039/x0xx00000x



Scheme 1. Schematized synthetic approach to and molecular structure of ZMSM-14P and ZMSM-14pMOP.



Scheme 2. Synthesis of target compounds **3a-g**. *i*: $\text{CuSO}_4 \cdot 5\text{H}_2\text{O}$, Na-ascorbate, KF, $t\text{-BuOH}/\text{H}_2\text{O}$ (1:1), 150 °C. *ii*: $[\text{CpRuCl}]_4$, DMF, 110 °C. *iii*: DMDO (1 eq.), acetone, -40 °C. *iv*: DMDO (2.5 eq.), acetone, 25 °C. The C4 and C5 atoms on the triazole ring are indicated by arrows.

In the last years, some of us introduced Click-functionalized thio-ene-yne compounds, derived from thiophene ring fragmentation,³⁰⁻³² as nonlinear optical materials.^{33, 34} Phenyl substituted derivative ZMSM-14P (Scheme 1) exhibited second harmonic generation (SHG) with twofold higher efficiency compared to reference compound potassium dihydrogen phosphate (KDP).³³ Application of a donor type azide (ZMSM-14MOP) further increased the SHG efficiency by 40 times (80x KDP) compared to parent ZMSM-14P.³⁵ Furthermore, the incorporation of 1,2,3-triazoles as linker proved to be advantageous in the design of bipolar materials with high nonlinear activity³⁶ and tailored photophysical properties.^{36, 37} The application of thio-ene-yne compounds as starting materials for the synthesis of Click-derived functional materials allows for easy and versatile modification of molecular properties due to various chemical transformations of this particular structural scaffold. The possibility to selectively isomerize the double bond from *Z* to the thermodynamically more favourable *E* configuration³⁵ alters the spatial

arrangement of the functional groups, whereas sulphur oxidation converts the electron donating substituent to a strongly electron withdrawing sulfone.^{38, 39} Additionally, methods for the selective preparation of either 1,4- or 1,5-substituted triazoles in the course of the azide-alkyne cycloaddition offer further potential to control the electronic as well as the steric makeup.

The aim of this work was to investigate the impact of systematic structural modifications on the properties of push-pull chromophores derived from a thio-ene-yne precursor and an electron donating group. On the basis of this molecular layout the effects of double bond configuration, triazole substitution position as well as sulphur oxidation state were matter of interest. The molecules were synthesized, characterized spectroscopically and studied by computation. Specifically, the effects of solvation were investigated using spectroscopic methods in various solvents as well as computations applying a recently implemented self-consistent solvation model^{40, 41} in connection with the ab initio algebraic diagrammatic construction (ADC) method for the polarization propagator.^{42, 43}

Results and Discussion

Synthesis

Target molecules **3a**, **3d** and **3f** were synthesized via cycloaddition reactions of **1a-1c** and azidotriphenylamine **2** (Scheme 2). **1a** was stereoselectively synthesized by thiophene ring fragmentation yielding exclusively the *Z* configured isomer due to the cyclic structure of thiophene. Subsequently, **1b** and **1c** were obtained by isomerization and deprotection, respectively. 1,4-Substituted triazoles **3a** and **3d** were synthesized employing standard CuAAC conditions in a reaction microwave reactor. Oxidation of the thioether with DMDO yielded sulfoxide **3b** and sulfones **3c** and **3e** in excellent yields. Triazole **3f** featuring a 1,5-substitution pattern was selectively prepared by a Ru catalysed cycloaddition and the corresponding sulfone **3g** was again obtained by oxidation with DMDO. Double bond configurations and triazole substitution patterns could be unequivocally established by X-ray analysis of single crystals of **3a**, **3d** and **3f** as depicted in Figure 1.

An overview of the crystal-chemistry of the parent compounds lacking the diphenylamine group has been previously given.³⁴ The twist angles between the triazole and benzene rings

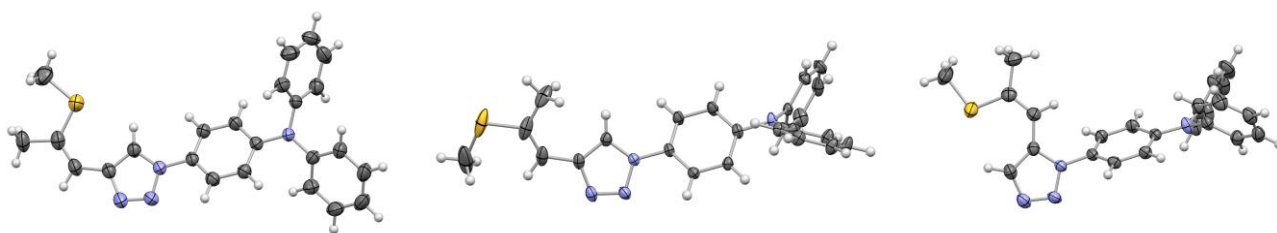


Figure 1. Molecular structures of ZMSM-14TPA (left), EMSM-14TPA (middle) and ZMSM-15TPA (right); C, N and S atoms are represented by grey, blue and yellow ellipsoids drawn at 90% (ZMSM-14TPA and ZMSM-15TPA) or 60% (EMSM-14TPA) probability levels, H atoms by spheres of arbitrary radius. In case of EMSM-14TPA the minor (14%) conformer is omitted for clarity.

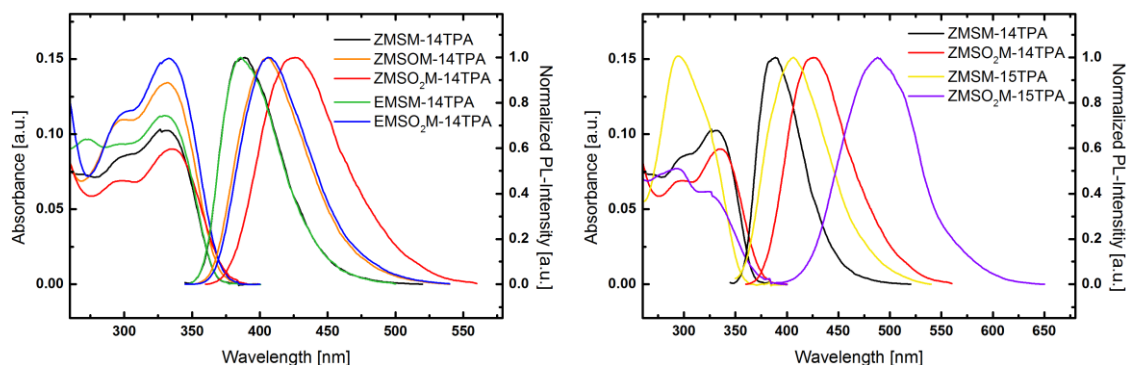


Figure 2. Experimental UV/VIS absorption and photoluminescence spectra of the investigated molecules recorded in diethyl ether.

feature a widespread distribution [angle between least-squares (LS) planes: $19.73(5)^\circ$ (**3a**); $27.68(8)^\circ$ (**3d**); $64.62(5)^\circ$ (**3f**)]. As previously observed,³⁴ the twist angle is larger for the 1,5-substituted derivative **3f**, owing to steric interactions of the triazole substituents. Here, it is significantly larger than in the parent 1,5-substituted compound [$39.48(6)^\circ$]. So far, in all structurally characterized compounds of this class, the propenyl group was oriented in the same direction with respect to the triazole ring ($C_{\text{ta}z}-C_{\text{ta}z}-C=C$ torsion angle $<90^\circ$). In principle, the same orientation is observed for the title compounds [$11.14(17)^\circ$ (**3a**); $17.6(3)^\circ$ (**3d**); $19.0(2)^\circ$ (**3f**)]. Remarkably, **3d** co-crystallizes with 14.0(2)% of a distinct conformer [torsion angle $150.4(13)^\circ$]. Because the positions of the carbon atoms in this minor conformer are not well determined, it will not be expanded upon. In all cases, the double bond is close to coplanar with the triazole ring [angles of C=C segment to LS plane: $9.73(6)^\circ$ (**3a**); $11.97(14)^\circ$ (**3d**); $14.90(7)^\circ$ (**3f**)]. The methylthio group is likewise nearly coplanar with the aromatic system. As noted before,³⁴ it is oriented in opposite direction in *Z* and *E* configured molecules [$C=C-S-C$ torsion angle $172.17(8)^\circ$ (**3a**); $10.8(2)^\circ$ (**3d**); $176.69(9)^\circ$ (**3f**)]. By contrast, the methyl groups are moved out of the molecular plane for the oxidized variants as shown by X-ray diffraction of the parent compounds (without the diphenylamine group)³⁴ and by computation for the molecules investigated here (see below).

Photophysical Characterization

UV/VIS absorption and photoluminescence emission spectra of all compounds in diethylether (Et_2O) were recorded to investigate the influence of the structural modifications on the molecular properties of the materials. All 1,4-substituted materials exhibit similar absorption behaviour and the absorption profiles of the materials are dominated by two transitions (Figure 2 left). Among those, the low energy transition features the highest absorbance and is located at 331.5 and 329.5 nm for **ZMSM-14TPA** and **EMSM-14TPA**, respectively. Single oxidation of the sulphur atom has a negligible effect on the location of the absorption maximum, which is located at 332 nm for the sulfoxide **ZMSOM-14TPA**. Twofold oxidation of the sulphur atom leads to a slight red

shift in case of sulfones **ZMSO₂M-14TPA** (335.5 nm) and **EMSO₂M-14TPA** (333 nm) compared to the parent compounds. Analogously, absorption onsets are shifted to somewhat lower energies from **ZMSM-14TPA** (366 nm) and **EMSM-14TPA** (365.5 nm) to **ZMSO₂M-14TPA** (373.5 nm) and **EMSO₂M-14TPA** (370.5 nm). The high energy band present in all five materials is observed as more or less distinctive shoulder between 296.5 and 301.5 nm and can be attributed to a characteristic triphenylamine centred $\pi-\pi^*$ transition.

While **ZMSM-14TPA** and **EMSM-14TPA** display nearly identical photoluminescent emission with maxima at 389 and 386 nm, the emission of the oxidized derivatives is distinctly red-shifted. In contrast to the methylthio-compounds the oxidized *E* and *Z* isomers exhibit different emission properties. Whereas the emission maximum of **ZMSO₂M-14TPA** is located at 426 nm and thus shifted by 37 nm compared to parent **ZMSM-14TPA**, **EMSO₂M-14TPA** features a less prominent red-shift and emits at 406.5 nm (20.5 nm shift compared to **EMSM-14TPA**). Coincidentally, the emission of **EMSO₂M-14TPA** resembles the emission features of **ZMSOM-14TPA**. Thus, single oxidation of the methylthio group of **ZMSM-14TPA** accomplishes approximately the same spectral shift of the photoluminescent emission as twofold sulphur oxidation of the corresponding *E* isomer.

According to these results, the double bond configuration seems to have negligible influence on the absorption and emission properties of **ZMSM-14TPA** and **EMSM-14TPA**. However, a decisive impact of the double bond configuration on the photophysical properties of the oxidized derivatives is observed.

Compared to 1,4-substituted derivatives, 1,5-substituted **ZMSM-15TPA** and its oxidized derivative **ZMSO₂M-15TPA** exhibit strongly differing behaviour (Figure 2 right). Whereas in 1,4-substituted materials the low energy transitions exhibit maximum absorbance values, these bands are merely present as shoulders located at 324.5 and 323.5 nm for **ZMSM-15TPA** and **ZMSO₂M-15TPA**, respectively. Absorption maxima in contrast are represented by the triphenylamine centred $\pi-\pi^*$ transitions at 294.5 and 293.5 nm, a feature that has been previously observed.³⁷ Notably, the absorption onset of **ZMSM-15TPA** is shifted to higher energy (354 nm) compared

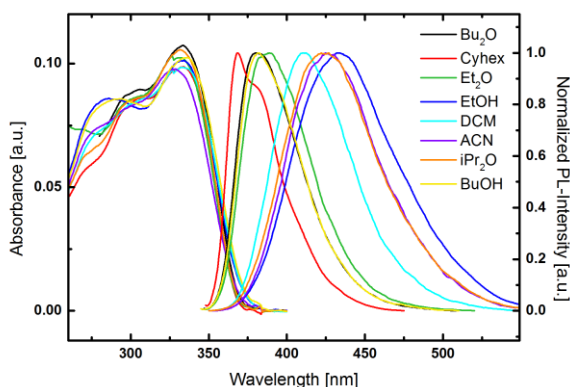


Figure 3. UV/VIS absorption and photoluminescence emission spectra of **ZMSM-14TPA** in various solvents (Cyhex=cyclohexane, DCM=dichloromethane, ACN=acetonitrile).

to **ZMSM-14TPA** (366 nm) indicative of a decreased degree of conjugation due to the highly twisted conformation of **ZMSM-15TPA**.

The photoluminescence of both 1,5-substituted derivatives is distinctly red-shifted with respect to the 1,4-substituted congeners. **ZMSM-15TPA** exhibits an emission maximum at 406 nm, 17 nm red-shifted compared to **ZMSM-14TPA**. In the case of oxidized **ZMSO₂M-15TPA** this shift is even more pronounced (62 nm) with an emission maximum at 488 nm. Thus, the substitution pattern of the triazole moiety distinctly influences the photophysical properties of the cycloaddition products.

The solvatochromic behaviour of the materials was investigated to provide a better insight into the nature of the excited states of the compounds and to examine the impact of structural modifications on the photophysical properties of individual molecules. Therefore, photoluminescence spectra in eight solvents with increasing polarity (cyclohexane, dibutyl ether, diisopropyl ether, diethyl ether, dichloromethane, butanol, ethanol, acetonitrile) were recorded. In contrast to the absorption spectra, which are to a large extent independent of the solvent polarity, the photoluminescent emission of all materials exhibits distinct solvatochromic effects, as exemplarily depicted for **ZMSM-14TPA** (Figure 3).

This solvatochromic behaviour indicates a charge-transfer transition for the emission of the materials.⁴⁴ Notably, no or only very weak emission was observed in protic butanol and ethanol for oxidized derivatives **ZMSO₂M-14TPA**, **EMSO₂M-14TPA** and **ZMSO₂M-15TPA**, most likely due to specific interactions between the solvent and the sulfone group.^{23,44}

To observe the impact of the solvatochromic effects on the individual materials the emission maxima were plotted against the orientation polarizability

$$\Delta f = \frac{\varepsilon - 1}{2\varepsilon + 1} - \frac{n^2 - 1}{2n^2 + 1}$$

as a measure of the solvent polarity (Figure 4) where ε is the dielectric constant and n is the refractive index of the solvent. All materials exhibited continuously red-shifted emission with increasing solvent polarity. Notably, a kink was observed at approximately $\Delta f = 0.15$ for all compounds and the wavelength of the emission maxima increased rapidly in solvents with a high Δf . This kink is similar to the one typically observed for materials with hybridized local and charge transfer (HLCT) states.^{12, 45-47} However, it can already be anticipated at this point that the mechanism is somewhat different considering that none of the investigated molecules possesses a chromophore with a low energy locally excited state. In analogy to the results for the diethyl ether solutions, basically no differences in the emission properties of **ZMSM-14TPA** and **EMSM-14TPA** were observed in any of the investigated solvents. Furthermore, the sulfone derivative **ZMSO₂M-14TPA** featured red-shifted emission in all solvents compared to the oxidized derivative with E double bond configuration (**EMSO₂M-14TPA**). Notably, this shift is more pronounced in solvents with high polarity, while the emissions in solvents with low Δf are similar. These results indicate a more pronounced charge transfer character of the excited state of **ZMSO₂M-14TPA** in highly polar solvents compared to **EMSO₂M-14TPA**, a feature that can be solely attributed to the different double bond configuration. The emission maxima of **ZMSO-14TPA** are more or less identical to those of **EMSO₂M-14TPA** in solvents with low and intermediate polarity, however the emission maximum of the former is distinctly blue shifted

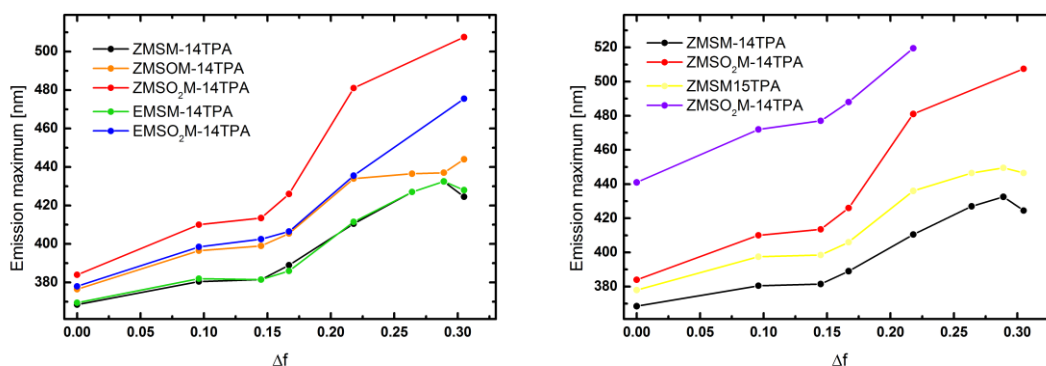


Figure 4. Emission maxima of the investigated molecules recorded in different solvents plotted against the orientation polarizability Δf used as a measure for the polarity of the solvents.

Table 1 Measured and computed photophysical properties of the investigated materials: Wavelengths (λ) and oscillator strengths (f) for absorption and emission.

	λ_{obs} [nm] ^a	λ_{em} [nm] ^a	λ_{obs} [nm] ^b	f_{obs}^b	Transition ^c	λ_{em} [nm] ^b	f_{em}^b
ZMSM-14TPA	273, 296, 307, 333.5 ^d	368.5	297, 323, 325	0.25, 0.09, 0.73	TPA, TPA, CT(N ₃)	379	0.40
ZMSOM-14TPA	301, 335	376.5	297, 322, 331	0.26, 0.07, 0.75	TPA, TPA, CT(N ₃)	387	0.38
ZMSO ₂ M-14TPA	298.5, 338	384	295, 321, 332	0.23, 0.04, 0.76	TPA, TPA, CT(N ₃)	404	0.28
EMSM-14TPA	277.5, 296, 306.5, 333	369.5	298, 322, 325	0.24, 0.21, 0.75	TPA, TPA, CT(N ₃)	378	0.49
EMSO ₂ M-14TPA	300, 337	378	294, 321, 329	0.23, 0.05, 0.81	TPA, TPA, CT(N ₃)	411	0.19
ZMSM-15TPA	297 , 325.5	378	296 , 319, 322	0.25 , 0.36, 0.31	TPA, TPA, CT(N ₃)	385	0.40
ZMSO ₂ M-15TPA	296 , 331	441	292 , 296, 320, 340	0.22 , 0.14, 0.10, 0.40	TPA, CT(S), TPA, CT(S)	431	0.35

^a Determined from cyclohexane solutions; ^b computed at the ω PBEh/6-31+G* level of theory in vacuo; ^c TPA – centred on TPA, CT(N₃) – partial charge transfer state from TPA to the triazole ring, CT(S) – charge transfer extending into the sulphur-containing side chain; ^d Bold indicates maximum.

in acetonitrile. Strikingly, the emission colour of the materials could be tuned over a very wide range from 368.5 to 507.5 nm depending on the solvent and chemical modification (double bond configuration and sulphur oxidation) of the basic molecular structure.

In the case of the 1,5-substituted derivatives both **ZMSM-15TPA** and **ZMSO₂-15TPA** exhibited clearly red-shifted emission in all solvents compared to the corresponding 1,4-substituted materials (Figure 4, right). This particular behavior suggests a distinctly altered nature of the excited state towards a higher charge transfer character for the 1,5-substituted materials. Notably, the emission maximum of **ZMSO₂-15TPA** in dichloromethane is located at 519.5 nm and therefore red-shifted compared to even the emission of **ZMSO₂-14TPA** in acetonitrile (507.5 nm) despite the distinctly lower polarity of the solvent.

Computational Characterization of the Excited States

In this section, the excited state characters are first discussed based on time-dependent density functional theory (TDDFT) calculations performed in the gas phase. Subsequently, more detailed results on solvation effects will be reported using the

wavefunction based ADC(2) method. More details on the employed methods are given in the Experimental Section. A comparison between the gas phase TDDFT results and experimental measurements in cyclohexane solution is presented in Table 1. A good agreement is observed between the experimental and computational absorption wavelengths with no discrepancies above 10 nm. In the case of all 1,4-substituted derivatives the same picture is obtained for the lowest three excited states. In these cases, the most intense transition, with an oscillator strength of about 0.75, derives from the lowest singlet state (S_1) lying around 330 nm, in agreement with experiment. The next transition (S_2) is energetically very close to S_1 and possesses no appreciable oscillator strength. The S_3 state is energetically well separated, around 295 nm, and possesses an oscillator strength of around 0.25. This state, which is exclusively located on the TPA moiety, is responsible for the shoulders seen in the spectra (Figure 3 left).

To characterize these excitations, the natural transition orbitals (NTOs)^{48, 49} for the first three singlet states of **ZMSM-14TPA** are presented in Figure 5. The excitation hole is almost indistinguishable between all three cases, being equally distributed over the TPA unit with a strong contribution on the nitrogen atom. Consequently, the differences between these states are exclusively due to the structure of the excited electron. In the case of the S_1 state, the excited electron is delocalized between the TPA unit and the triazole ring. Thus,

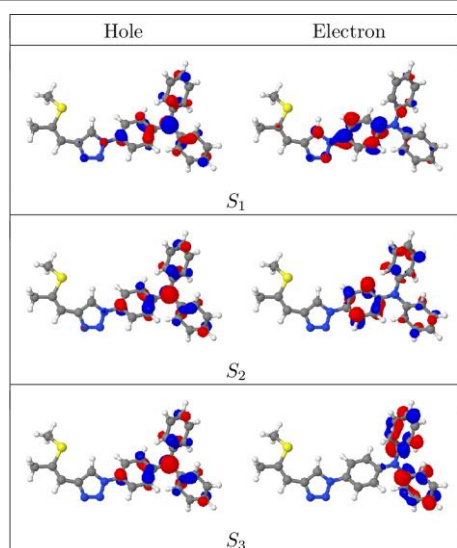


Figure 5. Natural transition orbitals (NTOs) characterizing the lowest three excited singlet states of **ZMSM-14TPA** computed at the TDDFT/ ω PBEh level of theory (cutoff value 0.05). The NTOs shown account for more than 95% of the respective total excitation process.

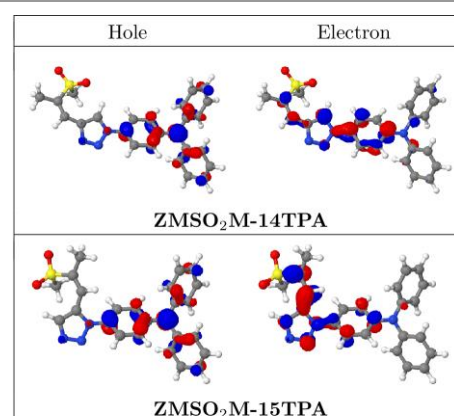


Figure 6. Natural transition orbitals (NTOs) characterizing the lowest excited singlet states of **ZMSO₂M-14TPA** and **ZMSO₂M-15TPA** computed at the TDDFT/ ω PBEh level of theory (cutoff value 0.05). The NTOs shown account for more than 95% of the respective total excitation process.

this state possesses partial charge transfer character, as suggested by the solvatochromic shifts of the materials. It should be noted at this point that the electron NTO, and similarly the lowest unoccupied molecular orbital (LUMO), has a strong contribution at the C5 atom of the triazole ring but only a vanishing contribution on the C4 atom (for numbering of the triazole ring see Scheme 2). Thus, the side chain is more or less electronically isolated when it is attached in the 4-position. The S_2 and S_3 states are both entirely localized on the TPA unit. For comparison, the NTOs of the S_1 state of the oxidized analogue **ZMSO₂M-14TPA** are shown in Figure 6 (top). These closely resemble the NTOs of **ZMSM-14TPA** with the exception that the charge transfer to the sulphur-containing side chain is somewhat enhanced.

Moving to the 1,5-substituted derivatives, changes are observed in the properties of the absorbing states. In the case of **ZMSM-15TPA** the computations still predict the same ordering of the excited states as in the previous cases (cf. Table 1). However, the oscillator strength of the S_1 state is decreased significantly to a value of only 0.31 while the S_2 obtains a larger oscillator strength of 0.36. This reduction in oscillator strength reflects the experimental absorption spectrum (Figure 3) in the sense that the intensity of the CT state is reduced. However, in the experimental absorption spectrum the effect is more pronounced as the TPA band at 297 nm, corresponding to the computed S_3 state, is the strongest band overall (Figure 2, right). Even more drastic changes are observed in the absorption spectrum of **ZMSO₂M-15TPA**. For the S_1 and S_3 states the excited electron is delocalized from the TPA unit through the triazole ring to the sulphur-containing side chain (cf. Figure 6, bottom). Thus, the charge-separation is significantly enhanced when compared to all other molecules studied here. The S_2 and S_4 states are centered on the TPA and are quite similar to the TPA-based states of the other molecules. The difference between the 1,4- and 1,5-substituted molecules can be rationalized by inspection of the spatial distribution of the involved NTOs (Figure 6). Whereas electronic conjugation is suppressed when the side chain is attached to the C4 position, there is a strong contribution of the LUMO at C5 allowing for efficient conjugation and more extended charge separation for the S_1 state of **ZMSO₂M-15TPA**.

In Table 1 also the experimental emission wavelengths are given along with the computed values obtained at the TDDFT level of theory for the S_1 -optimized structures. These agree well with the exception that the emission wavelengths of **ZMSO₂M-14TPA** and **EMSO₂M-14TPA** are somewhat overestimated by the computations. The emissive state generally possesses similar character to the S_1 state at the Franck-Condon geometry, i.e. the hole is localized on the TPA unit while the electron delocalizes into the triazole unit. However, the reduction in oscillator strength from 0.7-0.8 to about 0.3-0.4 indicates that the wavefunctions do indeed change after optimization of the S_1 geometry. A more detailed consideration shows that this goes along with an increase in CT character (see below). An inspection of the NTOs reveals that a

significant contribution of the sulphur-containing side chain is only present in the case of **ZMSO₂M-15TPA**.

The accurate computational modelling of UV emission in polar solvents is a challenging task due to the fact that the orientation polarization of the solvent can relax during the lifetime of the excited state prior to the emission, which can lead to a large electrostatic stabilization in particular for polar states with charge-transfer character. To account for this effect in the calculations, we alter the level of theory and compute the emission properties in solution at the ab initio ADC(2) level of theory in connection with a newly implemented state-specific polarizable-continuum model (SS-PCM).^{40, 41} This model enables a self-consistent treatment of the mutual electrostatic polarization of solvent and solute on the basis of accurate ab initio wavefunctions. The solvents cyclohexane ($\epsilon=2.03$, $\epsilon_\infty=2.02$) and acetonitrile ($\epsilon=35.7$, $\epsilon_\infty=1.81$) are chosen as the limiting cases of low and high polarity, respectively. The results of these computations are collected in Figure 7. In Figure 7 (a), the vertical excitation energies (blue) and emission energies (red) are plotted for cyclohexane and acetonitrile solvation, experimental reference values are shown in grey. The computed absorption energies are quite insensitive toward either chemical modification or solvation and all absorption energies lie between 3.9 and 4.1 eV, with the exception of **ZMSO₂M-15TPA** whose absorption is somewhat red-shifted for both solvents. With the exception of **ZMSO₂M-15TPA**, the computed vertical excitation energies are

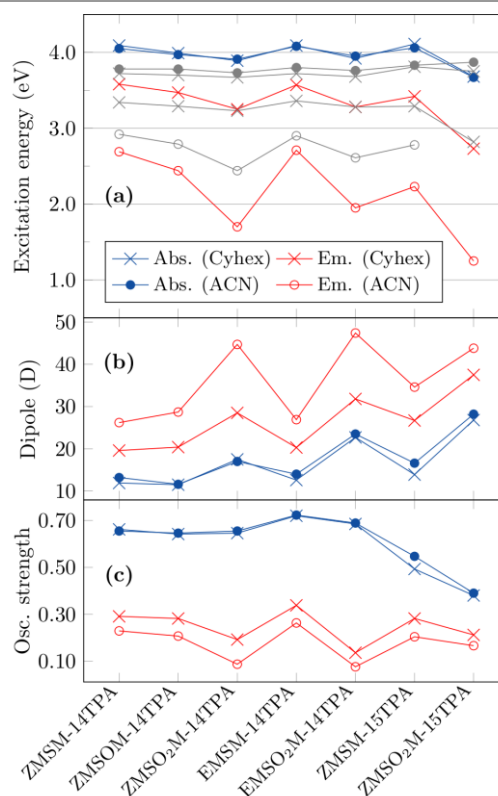


Figure 7. Results of the ab initio ADC(2) computations: (a) excitation energies, (b) excited-state dipole moments and (c) oscillator strengths determined for absorption (blue) and emission (red) of the S_1 state in cyclohexane (x) and acetonitrile (•). Experimental reference values in (a) are shown in grey.

always somewhat above the experimental band maxima. Previous experience shows that the agreement could be improved through enhancing the basis set⁵⁰ or through the inclusion of vibrational effects,⁵¹ however, such enhanced computations are not feasible for the systems investigated here. The computed emission in cyclohexane (red crosses) shows good agreement with experiment. In the case of acetonitrile (red circles), the general strong red shift is correctly reproduced by the computations although it is somewhat exaggerated. Nonetheless, the general ordering of the emission energies is reproduced including the enhanced red shift of **ZMSO₂M-14TPA** with respect to the isomeric sulfone **EMSO₂M-14TPA**. Figure 7 indicates that the emission of **ZMSO₂M-15TPA** is even further red-shifted than its 1,4-substituted isomer. In this case no experimental reference value is available but the result agrees with the overall experimental trends (Fig. 4, right).

The excited-state dipole moments are shown in Figure 7 (b). For the absorbing states, there is almost no difference between cyclohexane (blue crosses) and acetonitrile (blue circles) solvation. In the case of **ZMSM-14TPA**, **ZMSOM-14TPA**, and **EMSM-14TPA** the dipole moments are generally between 10 and 15 D while higher values are obtained for the sulfones and the 1,5-substituted derivatives. Upon relaxation of the geometry in the *S*₁ state, a strong enhancement of the dipole moments is observed. In the case of cyclohexane (red circles) the dipole moments are enhanced by ~10 D while another increase of ~10 D is obtained in acetonitrile. The largest dipole moments are present in the case of the sulfones. Interestingly, **EMSO₂M-14TPA** (47.4 D) shows an enhanced dipole moment as compared to **ZMSO₂M-15TPA** (44.7 D) despite its weaker solvatochromic shift. To understand this observation, it is worth noting that **EMSO₂M-14TPA** possesses a quite large dipole moment of 12.7 D already in the ground state when equilibrated in acetonitrile solution whereas the dipole moment of **ZMSO₂M-15TPA** (4.9 D) is significantly smaller. This difference most probably derives from the more linear structure of **EMSO₂M-14TPA**, which allows for an enhanced separation of the charges in space. To understand this situation in more detail, we also compute an alternative measure for charge transfer, the exciton size (*d_{exc}*), which is determined as the root-mean-square electron-hole separation.⁵² In acetonitrile solution the exciton size for **ZMSO₂M-14TPA** is 8.97 Å while a value of 8.54 Å is obtained for **EMSO₂M-14TPA**, i.e. in this case the enhanced charge separation of the Z-isomer can be directly seen.

It is also of interest to consider the oscillator strengths of the different molecules, see Figure 7 (c). All 1,4-substituted molecules possess oscillator strengths around 0.7 for absorption, while less than half of this value is obtained for emission. The oscillator strengths are lower in acetonitrile than in cyclohexane and they are especially low for the 1,4-substituted sulfones. The 1,5-substituted systems show similar trends but the effects are somewhat less pronounced. In summary, the oscillator strengths roughly behave in an opposite manner to the dipole moments, i.e. increased charge transfer goes along with reduced intensity. Interestingly, the

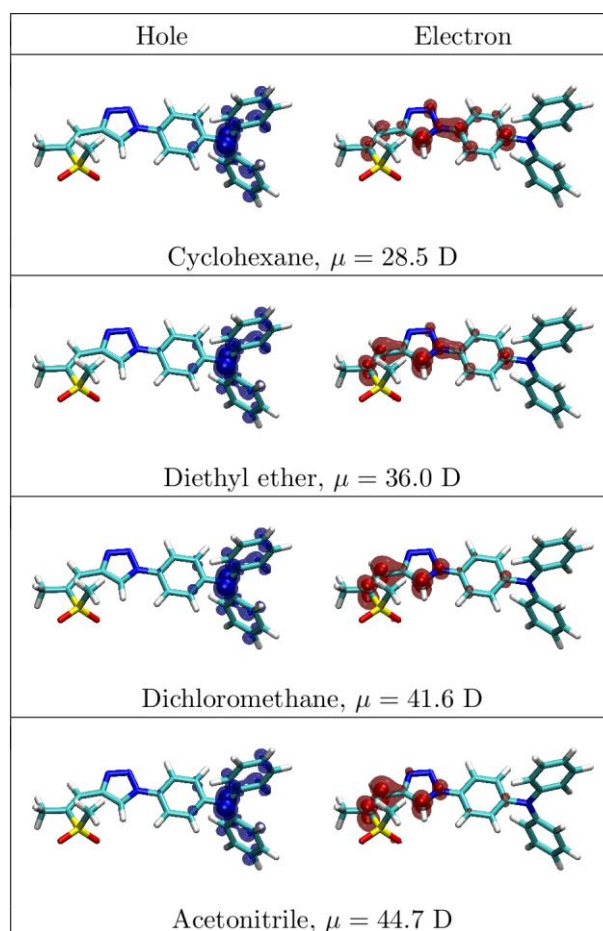


Figure 8. Hole and electron densities and excited state dipole moments (μ) characterizing the emitting *S*₁ state of **ZMSO₂M-14TPA** computed in four different solvents at the ab initio ADC(2) level of theory.

same inverse relationship between charge transfer and intensity has been reported recently by an experimental study of exciplex emission.⁵³

Finally, it is instructive to compare the present results with the HLCT model reported in the literature.^{12, 45-47} The HLCT model assumes one predominantly locally excited state with a dipole moment around 6 D and a CT state possessing a dipole moment around 13 D.⁴⁷ In the present case the dipole moments are significantly enhanced as all states possess significant CT character already in cyclohexane. Thus, a somewhat different mechanism is operative here despite a similar behaviour of the emission wavelengths when plotted against Δf (Figure 4).

As a next step, a closer look will be taken into the wavefunctions underlying the observed solvatochromic shifts. The excitation is visualized in terms of separate densities of the excited electron and the excitation hole, which are constructed by summing over the involved NTOs.⁵⁴ The discussion is started for the **ZMSO₂M-14TPA** molecule, considering that this molecule generally exhibits the strongest solvatochromic effects in the experimental measurements. In Figure 8, the electron and hole densities for this molecule are shown for four different solvents of varying dielectric

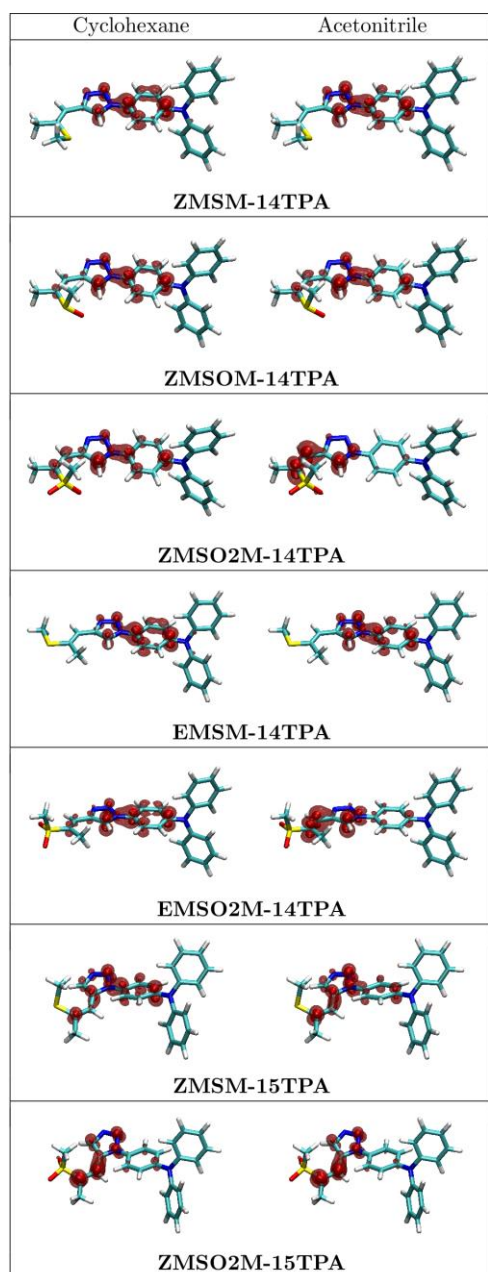


Figure 9. Densities of the excited electron characterizing the emitting S_1 state of the molecules studied here computed in cyclohexane and acetonitrile solution at the ab initio ADC(2) level of theory.

constants. The hole density is more or less unaffected by the solvent. It is located on the TPA unit similar to the S_1 state at the Franck-Condon geometry (Figure 6) with the exception that the contribution of the bridging phenyl ring is reduced. The excited electron is gradually pulled toward the sulfone group with increasing polarity of the solvent. The amount of charge separation can be quantified by the excited state dipole moment (μ), also given in Figure 8, which reflects the gradual increase in charge transfer character occurring when the solvent polarity is increased. A large dipole moment of 28.5 D is already observed in cyclohexane and a gradual increase to 44.7 D is obtained after increasing the polarity of the solvent.

A pictorial representation of the excited states of the all investigated molecules is given in Figure 9. Considering that the hole density is virtually unaltered in all these cases (cf. Figure 8) only the density of the excess electron is plotted here. Figure 9 summarizes the previous discussions. In the case of the unoxidized molecules **ZMSM-14TPA** and **EMSM-14TPA** the electron does not delocalize beyond the triazole ring and the changes occurring upon changing the solvent are only minor. Upon single oxidation to **ZMSOM-14TPA**, the charge transfer is somewhat enhanced while more dramatic effects are observed for the 1,4-substituted sulfones **ZMSO₂M-14TPA** and **EMSO₂M-14TPA**. While the differences between the E and Z isomers are quite subtle it is of interest to inspect their molecular structures in more detail. Figure 9 reveals that for both isomers the methyl group points out of the plane of the conjugated π -system. This allows for the formation of non-standard intramolecular hydrogen bonds between the sulfone group and either the triazole proton (**ZMSO₂M-14TPA**) or the vinyl proton (**EMSO₂M-14TPA**).³⁴ Figure 9 also shows the more elongated shape of **EMSO₂M-14TPA** as compared to **ZMSO₂M-14TPA**. Both factors, different hydrogen bonds and alterations in the overall molecular shape can certainly be the root of the observed differences in emission behaviour. A closer inspection of the densities of the 1,4-substituted systems reveals that the contribution of the C4 carbon, serving as a bridge head, is negligible in all cases. Thus, an effective conjugation break exists between the triazole unit and the side chain. Substitution at the C5 atom leads to enhanced conjugation between the different units. Therefore, the 1,5-substituted molecules show enhanced charge transfer already in cyclohexane solution. In the case of **ZMSM-15TPA**, there is a further enhancement of the charge transfer upon solvation in acetonitrile. By contrast, the charge separation in **ZMSO₂M-15TPA** is almost complete in cyclohexane and no further changes in the wavefunctions are observed upon solvation in acetonitrile. This finding is also in agreement with the fact that despite the overall red shift of the emission of **ZMSO₂M-15TPA** compared to **ZMSO₂M-14TPA** in all solvents, the difference in the emission maxima is reduced from cyclohexane (3366 cm^{-1}) to dichloromethane (1542 cm^{-1}) as depicted in Figure 4.

Summary and Conclusion

The photophysical properties of seven triazole based donor-acceptor materials were investigated and it was shown that this particular building block offers a variety of possibilities to tune the molecular properties: i) oxidation converts the electron rich thiomethyl group to an electron withdrawing sulfone and reliably enhances intramolecular charge transfer; ii) 1,4-substitution of the triazole electronically isolates the substituent connected to the C4 of the triazole and thus suppresses charge transfer compared to 1,5-substitution; iii) the double bond configuration significantly impacts the molecular structure of the sulfone derivatives with implications on their photophysical properties. Owing to these investigations the thio-ene-yne scaffold represents a versatile

and now well explored building block for the design of functional organic materials.

The effects of solvation were investigated by measuring absorption and emission spectra in various solvents. Strong solvatochromatic shifts were observed for the emitting states while the absorption remained more or less constant for all systems investigated. The excited state wavefunctions responsible for this behaviour were analysed in detail by high-level *ab initio* computations. The computations revealed that chemical modification significantly alters the amount of intramolecular charge transfer. It was shown that the wavefunctions are altered between the absorbing and emitting states with enhanced charge transfer for the latter. Furthermore, enhanced solvent polarity leads to a gradually increased amount of charge transfer.

The observed tunability of the investigated materials certainly makes them good candidates for future materials engineering purposes. With regard to the practical applicability of these materials, it is worth noting that the state character in the actual device will be sensitive to the dielectric constant of the employed film. While tuning in the device is not as simple as in solution, the dielectric constant could be modified through either changing the host material or through adding polar side chains to the molecules employed.⁵⁵

Experimental Section

The syntheses of trimethyl[(3*Z*)-4-(methylthio)-3-penten-1-yn-1-yl]silane (**1a**),³⁵ trimethyl[(3*E*)-4-(methylthio)-3-penten-1-yn-1-yl]silane (**1b**),³⁵ 4-(Methylthio)-(3*Z*)-3-penten-1-yne,⁵⁶ 4-azido-*N,N*-diphenylbenzenamine (**2**)⁵⁷ and 3,3-dimethyldioxirane⁵⁸ were performed in analogy to published procedures. Column chromatography was performed on silica 60 (Merck, 40-63 μ m). NMR spectra were recorded on a Bruker Avance III HD spectrometer or on a Bruker Avance DRX-400 spectrometer. UV/Vis absorption and fluorescence emission spectra were recorded in 5 μ M solutions with a Perkin Elmer Lambda 35 spectrometer and a Perkin Elmer LS 50 B, respectively. An Agilent 6230 LC TOFMS mass spectrometer equipped with an Agilent Dual AJS ESI-Source was used for HRMS.

General CuAAC (click) procedure. To a *t*-BuOH/H₂O (1:1 0.4 M) suspension of **1a/b** (1.0 eq.), 4-azido-*N,N*-diphenylbenzenamine **2** (1.25 eq.), CuSO₄·5H₂O (20 mol%) and sodium ascorbate (40 mol%) in a microwave reaction vessel KF (1.2 eq.) was added at room temperature. Subsequently, the vessel was sealed and heated to 150 °C under microwave irradiation for 25 min. The reaction mixture was diluted with water and extracted repeatedly with Et₂O. The combined organic layers were washed with brine and dried over anhydrous Na₂SO₄.

4-[4-[(1*Z*)-2-(methylthio)-1-propen-1-yl]-1*H*-1,2,3-triazol-1-yl]-*N,N*-diphenylbenzenamine **3a (ZMSM-14TPA).** Starting from **1a** (332 mg, 1.80 mmol, 1.0 eq.), **2** (644 mg, 2.25 mmol, 1.25 eq.), CuSO₄·5H₂O (90 mg, 0.36 mmol, 20 mol%), sodium ascorbate (143 mg, 0.72 mmol, 40 mol%) and KF (125 mg, 2.16 mmol, 1.2 eq.) **3a** (483 mg, 67 %) was obtained as a brownish

solid after column chromatography (light petroleum/Et₂O (20 % -> 30 %)). Single crystals of **3a** were grown from EtOH. ¹H NMR (400 MHz, CD₂Cl₂): δ = 8.32 (s, 1H), 7.59 (d, *J* = 8.9 Hz, 2H), 7.31 (t, *J* = 7.9 Hz, 4H), 7.17 – 7.07 (m, 8H), 6.62 (s, 1H), 2.42 (s, 3H), 2.27 (s, 3H) ppm. ¹³C NMR (100 MHz, CD₂Cl₂): δ = 148.7 (s), 147.8 (s), 145.6 (s), 136.0 (s), 131.8 (s), 130.0 (d), 125.4 (d), 124.2 (d), 123.8 (d), 122.0 (d), 120.4 (d), 115.0 (d), 23.8 (q), 14.7 (q) ppm. HRMS (ESI): *m/z* calculated for C₂₄H₂₂N₄S: *m/z* 399.1638 [M + H]⁺, 421.1457 [M + Na]⁺; found: 399.1654 [M + H]⁺, 421.1435 [M + Na]⁺.

4-[4-[(1*E*)-2-(Methylthio)-1-propen-1-yl]-1*H*-1,2,3-triazol-1-yl]-*N,N*-diphenylbenzenamine **3d (EMSM-14TPA).** Starting from **1b** (184 mg, 1.00 mmol, 1.0 eq.), **2** (358 mg, 1.25 mmol, 1.25 eq.), CuSO₄·5H₂O (50 mg, 0.20 mmol, 20 mol%), sodium ascorbate (79 mg, 0.40 mmol, 40 mol%) and potassium fluoride (70 mg, 1.20 mmol, 1.2 eq.) and **3d** (249 mg, 62 %) as obtained as a brownish solid after column chromatography (light petroleum/Et₂O (20 % -> 30 %)). Single crystals of **3d** were grown from EtOH. ¹H NMR (400 MHz, CD₂Cl₂): δ = 7.81 (s, 1H), 7.57 (d, *J* = 8.9 Hz, 2H), 7.31 (t, *J* = 7.8 Hz, 4H), 7.17 – 7.07 (m, 8H), 6.17 (s, 1H), 2.39 (s, 3H), 2.27 (s, 3H) ppm. ¹³C NMR (100 MHz, CD₂Cl₂): δ = 148.9 (s), 147.8 (s), 146.3 (s), 138.8 (s), 131.6 (s), 130.0 (d), 125.4 (d), 124.3 (d), 123.7 (d), 122.0 (d), 118.9 (d), 108.9 (d), 21.1 (q), 15.5 (q) ppm. HRMS (ESI): *m/z* calculated for C₂₄H₂₂N₄S: *m/z* 399.1638 [M + H]⁺; found: 399.1653 [M + H]⁺.

4-[5-[(1*Z*)-2-(methylthio)-1-propen-1-yl]-1*H*-1,2,3-triazol-1-yl]-*N,N*-diphenylbenzenamine **3f (ZMSM-15TPA).** The synthesis of **3f** was conducted in analogy to a published procedure.⁵⁹ A microwave reaction vessel was charged with [CpRuCl]₄ (14 mg, 27 μ mol, 2.5 mol%) and sealed. **3a** (120 mg, 1.07 mmol, 1.0 eq) and **2** (367 mg, 1.28 mmol, 1.2 eq.) were dissolved in 2 ml and 3 ml DMF under argon and added to the reaction vessel *via* a septum. Subsequently, the vessel was heated to 110 °C under microwave irradiation for 2 h. The solvent was reduced under reduced pressure and the residue partitioned between water and DCM. The aqueous layer was extracted with DCM and the combined organic layers were dried over anhydrous Na₂SO₄. **3f** (247 mg, 58 %) as obtained as a brownish solid after column chromatography (light petroleum/DCM (20 %) -> DCM/Et₂O (6%)). Single crystals of **3f** were grown by slow evaporation of a CD₂Cl₂ solution. ¹H NMR (600 MHz, CD₂Cl₂): δ = 8.12 (s, 1H), 7.34-7.31 (m, 4H), 7.27 (d, *J* = 8.9 Hz, 2H), 7.18 – 7.10 (m, 8H), 6.13 (s, 1H), 2.43 (s, 3H), 2.22 (d, *J* = 1.5 Hz, 3H) ppm. ¹³C NMR (150 MHz, CD₂Cl₂): δ = 149.5 (s), 147.7 (s), 141.5 (s), 134.5 (s), 133.4 (d), 130.1 (s), 130.1 (d), 127.0 (d), 125.8 (d), 124.5 (d), 122.8 (d), 108.4 (d), 24.2 (q), 14.7 (q) ppm. HRMS (ESI): *m/z* calculated for C₂₄H₂₂N₄S: *m/z* 399.1638 [M + H]⁺; found: 399.1652 [M + H]⁺.

General oxidation protocol using DMDO (3,3-dimethyldioxirane). The appropriate amount of DMDO as a precooled solution in acetone (DMDO concentration determined *via* NMR experiments) was added to **3a/b/c**. After a reaction time of 30 min the acetone was removed under reduced pressure yielding the desired sulfone species.

4-[4-[(1*Z*)-2-(Methylsulfinyl)-1-propen-1-yl]-1*H*-1,2,3-triazol-1-yl]-*N,N*-diphenylbenzenamine **3b (ZMSOM-14TPA).**

According to the general procedure precooled DMDO (8.8 mL, 0.54 mmol, 62 mM in acetone, 1.0 eq.) was added to a solution of **3a** (217 mg, 0.54 mmol, 1.0 eq.) in acetone and the mixture stirred for 30 min at rt. Due to incomplete consumption of **3a** (TLC) further DMDO (2.0 mL, 0.12 mmol, 62 mM in acetone, 0.2 eq.) was injected. After another 15 min at rt the solvent was removed and the product purified by column chromatography (EE) resulting in slightly beige solid **3b** (181 mg, 80 %). ^1H NMR (400 MHz, CD_2Cl_2): δ = 7.97 (s, 1H), 7.54 (d, J = 9.1 Hz, 2H), 7.32 (t, J = 7.7 Hz, 4H), 7.16 – 7.09 (m, 8H), 6.82 (s, 1H), 2.74 (s, 3H), 2.23 (s, 3H) ppm. ^{13}C NMR (100 MHz, CD_2Cl_2): δ = 149.3 (s), 147.7 (s), 146.7 (s), 143.2 (s), 131.0 (s), 130.1 (d), 125.6 (d), 124.5 (d), 123.4 (d), 122.2 (d), 121.8 (d), 119.8 (d), 38.9 (q), 13.6 (q) ppm. HRMS (ESI): m/z calculated for $\text{C}_{24}\text{H}_{22}\text{N}_4\text{O}_2\text{S}$: m/z 415.1587 $[\text{M} + \text{H}]^+$, 437.1407 $[\text{M} + \text{Na}]^+$; found: 415.1603 $[\text{M} + \text{H}]^+$, 437.1403 $[\text{M} + \text{Na}]^+$.

4-[4-[(1Z)-2-(Methylsulfonyl)-1-propen-1-yl]-1H-1,2,3-triazol-1-yl]-N,N-diphenylbenzenamine 3c (ZMSO₂M-14TPA).

According to the general procedure precooled DMDO (17.0 mL, 1.06 mmol, 62 mM in acetone, 2.4 eq.) was added to **3a** (173 mg, 0.44 mmol, 1.0 eq.). After stirring the mixture for 30 min at rt the solvent was evaporated yielding **3c** (178 mg, 95 %) as a beige solid. ^1H NMR (400 MHz, CD_2Cl_2): δ = 8.75 (s, 1H), 7.57 (d, J = 8.8 Hz, 2H), 7.31 (t, J = 7.9 Hz, 4H), 7.24 (s, 1H), 7.16 – 7.07 (m, 8H), 2.96 (s, 3H), 2.31 (s, 3H) ppm. ^{13}C NMR (100 MHz, CD_2Cl_2): δ = 149.4 (s), 147.7 (s), 141.8 (s), 136.7 (s), 131.0 (s), 130.1 (d), 128.6 (d), 125.6 (d), 124.7 (d), 124.4 (d), 123.4 (d), 122.4 (d), 41.4 (q), 21.7 (q) ppm. HRMS (ESI): m/z calculated for $\text{C}_{24}\text{H}_{22}\text{N}_4\text{O}_2\text{S}$: m/z 431.1536 $[\text{M} + \text{H}]^+$, 453.1356 $[\text{M} + \text{Na}]^+$; found: 431.1558 $[\text{M} + \text{H}]^+$, 453.1350 $[\text{M} + \text{Na}]^+$.

4-[4-[(1E)-2-(Methylsulfonyl)-1-propen-1-yl]-1H-1,2,3-triazol-1-yl]-N,N-diphenylbenzenamine 3e (EMSO₂M-14TPA).

According to the general procedure precooled DMDO (11.0 mL, 0.67 mmol, 62 mM in acetone, 2.4 eq.) was added to **3d** (110 mg, 0.28 mmol, 1.0 eq.). After a reaction time of 30 min at rt the solvent was removed yielding **3e** (120 mg, 99 %) as a beige solid. ^1H NMR (400 MHz, CD_2Cl_2): δ = 8.13 (s, 1H), 7.61 – 7.59 (m, 3H), 7.36 (t, J = 7.9 Hz, 4H), 7.21 – 7.13 (m, 8H), 3.00 (s, 3H), 2.61 (s, 3H) ppm. ^{13}C NMR (100 MHz, CD_2Cl_2): δ = 149.5 (s), 147.6 (s), 143.1 (s), 138.5 (s), 130.7 (s), 130.1 (d), 125.8 (d), 125.7 (d), 124.5 (d), 123.8 (d), 123.3 (d), 122.3 (d), 41.0 (q), 14.6 (q) ppm. HRMS (ESI): m/z calculated for $\text{C}_{24}\text{H}_{22}\text{N}_4\text{O}_2\text{S}$: m/z 431.1536 $[\text{M} + \text{H}]^+$; found: 431.1552 $[\text{M} + \text{H}]^+$.

4-[5-[(1Z)-2-(Methylsulfonyl)-1-propen-1-yl]-1H-1,2,3-triazol-1-yl]-N,N-diphenylbenzenamine 3g (ZMSO₂M-15TPA).

According to the general procedure precooled DMDO (10.3 mL, 0.36 mmol, 35 mM in acetone, 2.4 eq.) was added to **3f** (60 mg, 0.15 mmol, 1.0 eq.). After a reaction time of 30 min at rt the solvent was removed yielding **3g** (64 mg, 99 %) as a beige solid. ^1H NMR (600 MHz, CD_2Cl_2): δ = 8.26 (s, 1H), 7.34 (dd, J = 8.5, 7.3 Hz, 2H), 7.26 (d, J = 8.9 Hz, 2H), 7.18 (dd, J = 8.5, 1.3 Hz, 2H), 7.15 – 7.12 (m, 4H), 6.69 (s, 1H), 2.92 (s, 3H), 2.26 (d, J = 1.6 Hz, 3H) ppm. ^{13}C NMR (150 MHz, CD_2Cl_2): δ = 150.3 (s), 147.4 (s), 142.4 (s), 136.7 (d), 130.9 (s), 130.2 (d), 130.0 (s), 126.6 (d), 126.0 (d), 124.8 (d), 122.3 (d), 122.0 (d), 41.5 (q), 21.5 (q) ppm. HRMS (ESI): m/z calculated for

$\text{C}_{24}\text{H}_{22}\text{N}_4\text{O}_2\text{S}$: m/z 431.1536 $[\text{M} + \text{H}]^+$; found: 431.1557 $[\text{M} + \text{H}]^+$.

Computational Details

All DFT and TDDFT computations were performed with the range-separated ω PBEh functional^{60, 61} in connection with the 6-31+G* basis set.⁶² A range separation parameter of $\omega=0.1$ a.u. was chosen in order to reproduce the experimental energies. All ground and excited state geometry optimizations were performed at the ω PBEh/6-31+G* level in the gas phase. Based on the S_0 - and S_1 -optimized geometries, additional single-point computations employing the algebraic-diagrammatic construction method for the polarization propagator in second order of perturbation theory ADC(2)^{42, 43} were performed in connection with the Ahlrichs SV basis set.⁶³ In these calculations, the recently implemented, self-consistent, state-specific polarizable continuum solvation model (SS-PCM)^{40, 41} was employed to study the influence of solvation onto the emission energies. The SS-PCM was used in combination with the IEF-PCM kernel,⁶⁴ a reduced convergence criterion for the solvent-field iterations (3 instead of 4) and default parameters otherwise. The following dielectric constants (ϵ , ϵ_∞) were used to represent the solvents: cyclohexane (2.03, 2.02), diethyl ether (4.33, 1.83), dichloromethane (8.93, 2.03), acetonitrile (35.7, 1.81). All ADC calculations employ the resolution-of-the-identity and frozen core approximations. ADC dipole moments were computed using the intermediate state representation.⁶⁵ The wavefunctions were analysed in terms of the natural transition orbitals,^{48, 49} electron and hole densities,⁵⁴ and exciton sizes⁵² using an extended wavefunction analysis toolbox that has been made available for the ADC⁵⁴ and TDDFT⁶⁶ methods in Q-Chem. The computations were performed by means of a development version of the Q-Chem 4.4 package.⁶⁷ The SS-PCM module used will be released with the next version of Q-Chem.

Single crystal diffraction

X-ray diffraction data of **ZMSM-14TPA**, **EMSM-14TPA** and **ZMSM-15TPA** [CCDC entries 1536607-1536609] were collected at $T = 100$ K in a dry stream of nitrogen on a Bruker Kappa APEX II diffractometer system using graphite-monochromatized Mo- $K\alpha$ radiation ($\lambda = 0.71073$ Å) and fine sliced φ - and ω -scans. Data were reduced to intensity values with SAINT and an absorption correction was applied with the multi-scan approach implemented in SADABS.⁶⁸ The structures were solved by dual space methods implemented in SHELXT⁶⁹ and refined against F with JANA2006.⁷⁰ Non-hydrogen atoms were refined anisotropically. H atoms were placed in calculated positions and thereafter refined as riding on the parent C atoms. Residual electron density in **EMSM-14TPA** was attributed to a second orientation of the propenyl side chain. The side chain was therefore modelled as positionally disordered. The atoms of the minor (ca. 14%) orientation were refined with isotropic displacement parameters and distance restraints were applied to a C-C single and a C=C double bond.

Molecular graphics were generated with the program MERCURY.⁷¹ Crystal data and experimental details are given in the ESI.

Acknowledgements

This work was supported by the TU Wien research funds, by the Alexander-von-Humboldt Foundation, and by the VSC Research Center funded by the Austrian Federal Ministry of Science, Research and Economy (bmwfw). The X-ray centre of the TU Wien is acknowledged for providing access to the single-crystal diffractometer. Prof. P. Lieberzeit and A. Schnettelker are acknowledged for assistance during the photophysical characterization. L. Czollner is acknowledged for performing the HRMS measurement. The computational results presented have been achieved in part on the Vienna Scientific Cluster (VSC), Project No 70726.

Notes and references

- 1 Y. Tao, C. Yang and J. Qin, *Chem. Soc. Rev.*, 2011, **40**, 2943-2970.
- 2 A. Chaskar, H.-F. Chen and K.-T. Wong, *Adv. Mater.*, 2011, **23**, 3876-3895.
- 3 M. Zhu and C. Yang, *Chem. Soc. Rev.*, 2013, **42**, 4963-4976.
- 4 Y. Tao, K. Yuan, T. Chen, P. Xu, H. H. Li, R. F. Chen, C. Zheng, L. Zhang and W. Huang, *Adv. Mater.*, 2014, **26**, 7931-7958.
- 5 J. Roncali, *Acc. Chem. Res.*, 2009, **42**, 1719-1730.
- 6 A. Mishra and P. Bäuerle, *Angew. Chem., Int. Ed.*, 2012, **51**, 2020-2067.
- 7 M. J. Cho, D. H. Choi, P. A. Sullivan, A. J. P. Akelaitis and L. R. Dalton, *Prog. Pol. Sci.*, 2008, **33**, 1013-1058.
- 8 G. S. He, L.-S. Tan, Q. Zheng and P. N. Prasad, *Chem. Rev.*, 2008, **108**, 1245-1330.
- 9 L. R. Dalton, P. A. Sullivan and D. H. Bale, *Chem. Rev.*, 2009, **110**, 25-55.
- 10 Y. Shirota, *J. Mater. Chem.*, 2000, **10**, 1-25.
- 11 H. Uoyama, K. Goushi, K. Shizu, H. Nomura and C. Adachi, *Nature*, 2012, **492**, 234-238.
- 12 W. Li, D. Liu, F. Shen, D. Ma, Z. Wang, T. Feng, Y. Xu, B. Yang and Y. Ma, *Adv. Funct. Mater.*, 2012, **22**, 2797-2803.
- 13 Z. Yang, Z. Mao, Z. Xie, Y. Zhang, S. Liu, J. Zhao, J. Xu, Z. Chi and M. P. Aldred, *Chem. Soc. Rev.*, 2017, **46**, 915-1016.
- 14 D. Hu, L. Yao, B. Yang and Y. Ma, *Philos. Trans. R. Soc. A.*, 2015, **373**.
- 15 V. V. Rostovtsev, L. G. Green, V. V. Fokin and K. B. Sharpless, *Angew. Chem., Int. Ed.*, 2002, **41**, 2596-2599.
- 16 A. Qin, J. W. Y. Lam and B. Z. Tang, *Chem. Soc. Rev.*, 2010, **39**, 2522-2544.
- 17 F. Amblard, J. H. Cho and R. F. Schinazi, *Chem. Rev.*, 2009, **109**, 4207-4220.
- 18 J. E. Hein and V. V. Fokin, *Chem. Soc. Rev.*, 2010, **39**, 1302-1315.
- 19 D. J. V. C. van Steenis, O. R. P. David, G. P. F. van Strijdonck, J. H. van Maarseveen and J. N. H. Reek, *Chem. Commun.*, 2005, 4333-4335.
- 20 Y. Zhu, S. Guang, X. Su, H. Xu and D. Xu, *Dyes Pig.*, 2013, **97**, 175-183.
- 21 P. D. Jarowski, Y.-L. Wu, W. B. Schweizer and F. Diederich, *Org. Lett.*, 2008, **10**, 3347-3350.
- 22 S. S. Bag and R. Kundu, *J. Org. Chem.*, 2011, **76**, 3348-3356.
- 23 A.-S. Cornec, C. Baudequin, C. Fiol-Petit, N. Plé, G. Dupas and Y. Ramondenc, *Eur. J. Org. Chem.*, 2013, **2013**, 1908-1915.
- 24 M. K. Kim, J. Kwon, T. H. Kwon and J. I. Hong, *New J. Chem.*, 2010, **34**, 1317-1322.
- 25 M. Parent, O. Mongin, K. Kamada, C. Katan and M. Blanchard-Desce, *Chem. Commun.*, 2005, 2029-2031.
- 26 Y. H. Lau, P. J. Rutledge, M. Watkinson and M. H. Todd, *Chem. Soc. Rev.*, 2011, **40**, 2848-2866.
- 27 Y. J. Li, J. C. Huffman and A. H. Flood, *Chem. Commun.*, 2007, 2692-2694.
- 28 R. M. Meudtner, M. Ostermeier, R. Goddard, C. Limberg and S. Hecht, *Chem. – Eur. J.*, 2007, **13**, 9834-9840.
- 29 I. Stengel, A. Mishra, N. Pootrakulchote, S. J. Moon, S. M. Zakeeruddin, M. Grätzel and P. Bäuerle, *J. Mat. Chem.*, 2011, **21**, 3726-3734.
- 30 S. Gronowitz and T. Frejd, *Chem. Heterocycl. Compd.*, 1978, **14**, 353-367.
- 31 B. Iddon, *Heterocycles*, 1983, **20**, 1127-1171.
- 32 T. L. Gilchrist, in *Advances in Heterocyclic Chemistry*, ed. R. K. Alan, Academic Press, 1987, vol. Volume 41, pp. 41-74.
- 33 D. Lumpi, B. Stöger, C. Hametner, F. Kubel, G. Reider, H. Hagemann, A. Karpfen and J. Fröhlich, *CrystEngComm*, 2011, **13**, 7194-7197.
- 34 D. Lumpi, F. Glöckhofer, B. Holzer, B. Stöger, C. Hametner, G. A. Reider and J. Fröhlich, *Cryst. Growth Des.*, 2014, **14**, 1018-1031.
- 35 D. Lumpi, J. Steindl, S. Steiner, V. Carl, P. Kautny, M. Schön, F. Glöckhofer, B. Holzer, B. Stöger, E. Horkel, C. Hametner, G. Reider, M. D. Mihovilovic and J. Fröhlich, *Tetrahedron*, 2017, **73**, 472-480.
- 36 P. Kautny, D. Bader, B. Stöger, G. A. Reider, J. Fröhlich and D. Lumpi, *Chem. – Eur. J.*, 2016, **22**, 18887-18898.
- 37 P. Kautny, C. Zhao, T. Kader, B. Stöger, E. Horkel, J. Chen, D. Ma, J. Fröhlich and D. Lumpi, *RSC Adv.*, 2017, **7**, 12150-12160.
- 38 F. Glöckhofer, D. Lumpi, M. Kohlstädt, O. Yurchenko, U. Würfel and J. Fröhlich, *React. Funct. Polym.*, 2015, **86**, 16-26.
- 39 F. Glöckhofer, D. Lumpi, B. Stöger and J. Fröhlich, *New J. Chem.*, 2014, **38**, 2229-2232.
- 40 J. M. Mewes, Z. Q. You, M. Wormit, T. Kriesche, J. M. Herbert and A. Dreuw, *J. Phys. Chem. A*, 2015, **119**, 5446-5464.
- 41 J. M. Mewes, J. M. Herbert and A. Dreuw, *Phys. Chem. Chem. Phys.*, 2017, **19**, 1644-1654.
- 42 A. B. Trofimov and J. Schirmer, *J. Phys. B: At., Mol. Opt. Phys.*, 1995, **28**, 2299-2324.
- 43 F. Plasser, B. Thomitzni, S. A. Bappler, J. Wenzel, D. R. Rehn, M. Wormit and A. Dreuw, *J. Comput. Chem.*, 2015, **36**, 1609-1620.
- 44 Z. R. Grabowski, K. Rotkiewicz and W. Rettig, *Chem. Rev.*, 2003, **103**, 3899-4032.
- 45 L. Yao, S. Zhang, R. Wang, W. Li, F. Shen, B. Yang and Y. Ma, *Angew. Chem., Int. Ed.*, 2014, **126**, 2151-2155.
- 46 C. Wang, X. Li, Y. Pan, S. Zhang, L. Yao, Q. Bai, W. Li, P. Lu, B. Yang, S. Su and Y. Ma, *ACS Appl. Mater. Interfaces*, 2016, **8**, 3041-3049.
- 47 W. Li, Y. Pan, R. Xiao, Q. Peng, S. Zhang, D. Ma, F. Li, F. Shen, Y. Wang, B. Yang and Y. Ma, *Adv. Funct. Mater.*, 2014, **24**, 1609-1614.
- 48 R. L. Martin, *J. Chem. Phys.*, 2003, **118**, 4775-4777.
- 49 F. Plasser and H. Lischka, *J. Chem. Theory Comput.*, 2012, **8**, 2777-2789.
- 50 A. N. Panda, F. Plasser, A. J. A. Aquino, I. Burghardt and H. Lischka, *J. Phys. Chem. A*, 2013, **117**, 2181-2189.
- 51 F. Plasser, M. Barbatti, A. J. A. Aquino and H. Lischka, *J. Phys. Chem. A*, 2009, **113**, 8490-8499.
- 52 S. A. Bappler, F. Plasser, M. Wormit and A. Dreuw, *Phys. Rev. A*, 2014, **90**.
- 53 H. A. Al Attar and A. P. Monkman, *Adv. Mater.*, 2016, **28**, 8014-8020.

- 54 S. Mai, T. Muller, F. Plasser, P. Marquetand, H. Lischka and L. Gonzalez, *J. Chem. Phys.*, 2014, **141**.
- 55 S. Kraner, R. Scholz, C. Koerner and K. Leo, *J. Phys. Chem. C*, 2015, **119**, 22820-22825.
- 56 F. Bohlmann, W. Vonkaphe, C. Rybak and J. Reppling, *Chem. Ber./Recl.*, 1965, **98**, 1136.
- 57 Q. Zhang, Z. J. Ning and H. Tian, *Dyes Pig.*, 2009, **81**, 80-84.
- 58 H. Mikula, D. Svatunek, D. Lumpi, F. Glöckhofer, C. Hametner and J. Fröhlich, *Org. Process Res. Dev.*, 2013, **17**, 313-316.
- 59 L. K. Rasmussen, B. C. Boren and V. V. Fokin, *Org. Lett.*, 2007, **9**, 5337-5339.
- 60 J. P. Perdew, K. Burke and M. Ernzerhof, *Phys. Rev. Lett.*, 1996, **77**, 3865-3868.
- 61 M. A. Rohrdanz, K. M. Martins and J. M. Herbert, *J. Chem. Phys.*, 2009, **130**.
- 62 P. Hariharan and J. A. Pople, *Theor. Chim. Acta*, 1973, **28**, 213-222.
- 63 A. Schafer, H. Horn and R. Ahlrichs, *J. Chem. Phys.*, 1992, **97**, 2571-2577.
- 64 E. Cancès, B. Mennucci and J. Tomasi, *J. Chem. Phys.*, 1997, **107**, 3032-3041.
- 65 J. Schirmer, *Phys. Rev. A*, 1991, **43**, 4647-4659.
- 66 S. A. Mewes, F. Plasser and A. Dreuw, *J. Chem. Phys.*, 2015, **143**.
- 67 Y. H. Shao, Z. T. Gan, E. Epifanovsky, A. T. B. Gilbert, M. Wormit, J. Kussmann, A. W. Lange, A. Behn, J. Deng, X. T. Feng, D. Ghosh, M. Goldey, P. R. Horn, L. D. Jacobson, I. Kaliman, R. Z. Khaliullin, T. Kus, A. Landau, J. Liu, E. I. Proynov, Y. M. Rhee, R. M. Richard, M. A. Rohrdanz, R. P. Steele, E. J. Sundstrom, H. L. Woodcock, P. M. Zimmerman, D. Zuev, B. Albrecht, E. Alguire, B. Austin, G. J. O. Beran, Y. A. Bernard, E. Berquist, K. Brandhorst, K. B. Bravaya, S. T. Brown, D. Casanova, C. M. Chang, Y. Q. Chen, S. H. Chien, K. D. Closser, D. L. Crittenden, M. Diedenhofen, R. A. DiStasio, H. Do, A. D. Dutoi, R. G. Edgar, S. Fatehi, L. Fusti-Molnar, A. Ghysels, A. Golubeva-Zadorozhnaya, J. Gomes, M. W. D. Hanson-Heine, P. H. P. Harbach, A. W. Hauser, E. G. Hohenstein, Z. C. Holden, T. C. Jagau, H. J. Ji, B. Kaduk, K. Khistyayev, J. Kim, J. Kim, R. A. King, P. Klunzinger, D. Kosenkov, T. Kowalczyk, C. M. Krauter, K. U. Lao, A. D. Laurent, K. V. Lawler, S. V. Levchenko, C. Y. Lin, F. Liu, E. Livshits, R. C. Lochan, A. Luenser, P. Manohar, S. F. Manzer, S. P. Mao, N. Mardirossian, A. V. Marenich, S. A. Maurer, N. J. Mayhall, E. Neuscamman, C. M. Oana, R. Olivares-Amaya, D. P. O'Neill, J. A. Parkhill, T. M. Perrine, R. Peverati, A. Prociuk, D. R. Rehn, E. Rosta, N. J. Russ, S. M. Sharada, S. Sharma, D. W. Small, A. Sodt, T. Stein, D. Stuck, Y. C. Su, A. J. W. Thom, T. Tsuchimochi, V. Vanovschi, L. Vogt, O. Vydrov, T. Wang, M. A. Watson, J. Wenzel, A. White, C. F. Williams, J. Yang, S. Yeganeh, S. R. Yost, Z. Q. You, I. Y. Zhang, X. Zhang, Y. Zhao, B. R. Brooks, G. K. L. Chan, D. M. Chipman, C. J. Cramer, W. A. Goddard, M. S. Gordon, W. J. Hehre, A. Klamt, H. F. Schaefer, M. W. Schmidt, C. D. Sherrill, D. G. Truhlar, A. Warshel, X. Xu, A. Aspuru-Guzik, R. Baer, A. T. Bell, N. A. Besley, J. D. Chai, A. Dreuw, B. D. Dunietz, T. R. Furlani, S. R. Gwaltney, C. P. Hsu, Y. S. Jung, J. Kong, D. S. Lambrecht, W. Z. Liang, C. Ochsenfeld, V. A. Rassolov, L. V. Slipchenko, J. E. Subotnik, T. Van Voorhis, J. M. Herbert, A. I. Krylov, P. M. W. Gill and M. Head-Gordon, *Molecular Physics*, 2015, **113**, 184-215.
- 68 Bruker computer programs: APEX2, SAINT and SADABS (Bruker AXS Inc., Madison, WI, 2015).
- 69 G. Sheldrick, *Acta Crystallogr. Sect. A*, 2015, **71**, 3-8.
- 70 V. Petříček, M. Dušek and L. Palatinus, *Z. Kristallogr. - Cryst. Mater.*, 2014, **229**, 345.
- 71 C. F. Macrae, P. R. Edgington, P. McCabe, E. Pidcock, G. P. Shields, R. Taylor, M. Towler and J. van de Streek, *J. Appl. Crystallogr.*, 2006, **39**, 453-457.

3. Appendix

3.1. Manuscript #1 – Supporting Information

Oxadiazole based bipolar host materials employing planarized triarylamine donors for RGB PHOLEDs with low efficiency roll-off

Paul Kautny, Daniel Lumpi, Yanping Wang, Antoine Tissot, Johannes Bintinger, Ernst Horkel, Berthold Stöger, Christian Hametner, Hans Hagemann, Dongge Ma, Johannes Fröhlich

Journal of Materials Chemistry C, **2014**, 2, 2069-2081

Electronic Supporting Information

ESI

Oxadiazole based bipolar host materials employing planarized triarylamine donors for RGB PHOLEDs with low efficiency roll-off[†]

Paul Kautny,^a Daniel Lumpi,^{*a} Yanping Wang,^b Antoine Tissot,^c

Johannes Bintinger,^a Ernst Horkel,^a Berthold Stöger,^d Christian Hametner,^a

Hans Hagemann,^c Dongge Ma,^b and Johannes Fröhlich^a

daniel.lumpi@tuwien.ac.at

^a Institute of Applied Synthetic Chemistry, Vienna University of Technology, Getreidemarkt 9/163, A-1060 Vienna, Austria

^b State Key Laboratory of Polymer Physics and Chemistry, Changchun Institute of Applied Chemistry, Chinese Academy of Sciences, Changchun, 130022, China

^c Département de Chimie Physique, Université de Genève, 30, quai E. Ansermet, 1211 Geneva 4, Switzerland

^d Institute of Chemical Technologies and Analytics, Vienna University of Technology, Getreidemarkt 9/164, A-1060 Vienna, Austria

Content

A. NMR Spectra

B. TGA/DSC

C. Cyclic Voltammetry

D. Phosphorescence Measurements

E. DFT Calculations

F. EL Spectra

G. Crystal Structure of Compound 3c

A) NMR Spectra

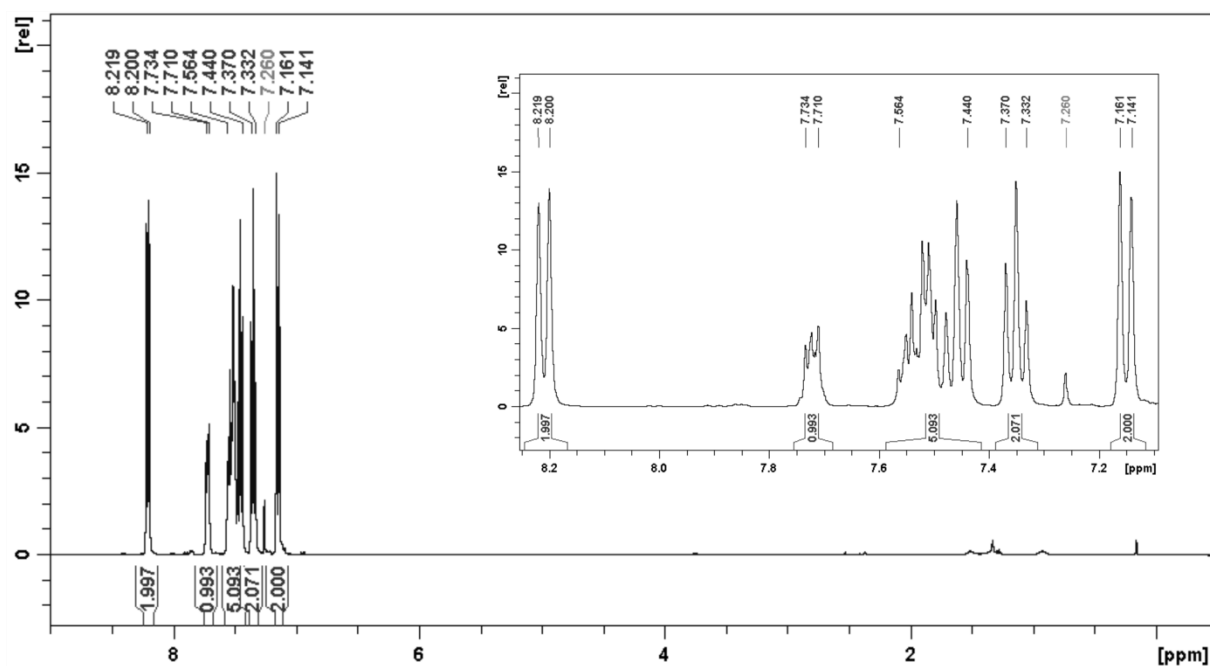


Figure S1. Proton NMR spectrum of compound **1ii**.

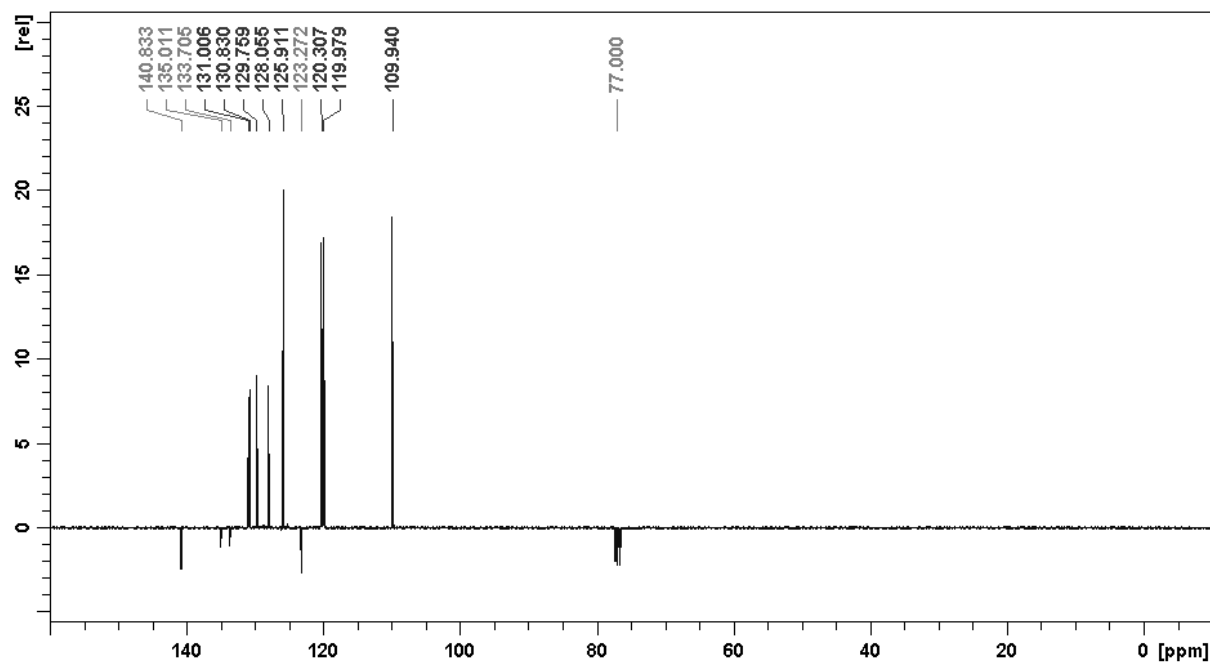


Figure S2. Carbon NMR spectrum of compound **1ii**.

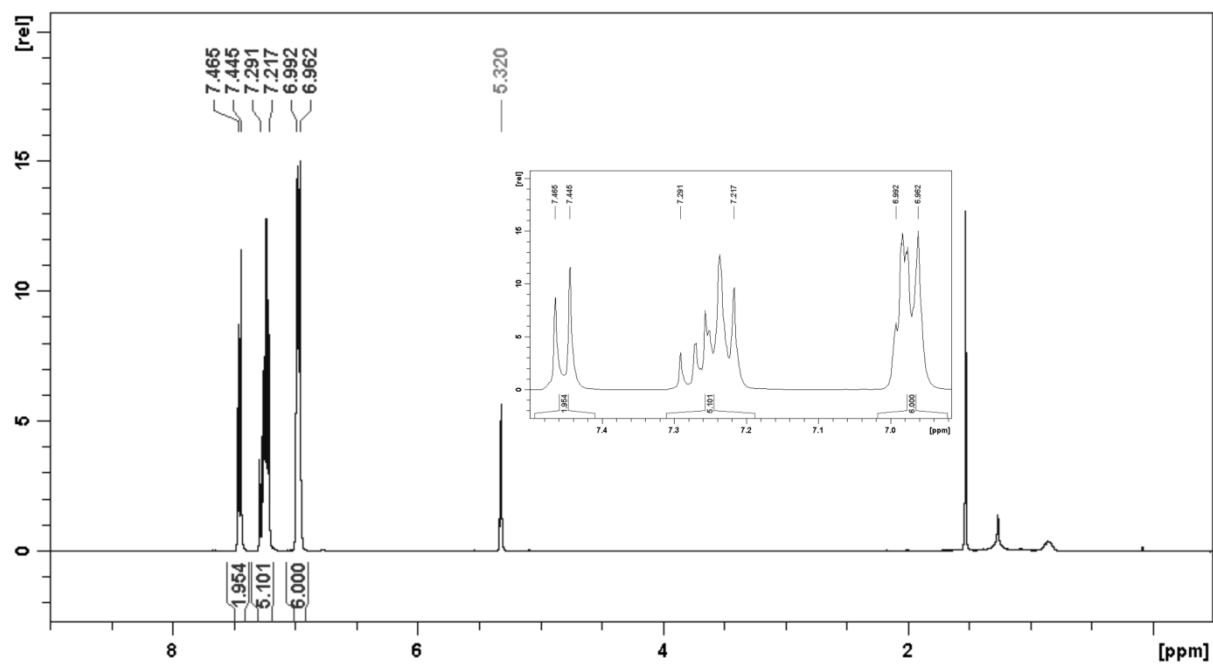


Figure S3. Proton NMR spectrum of compound **1iii**.

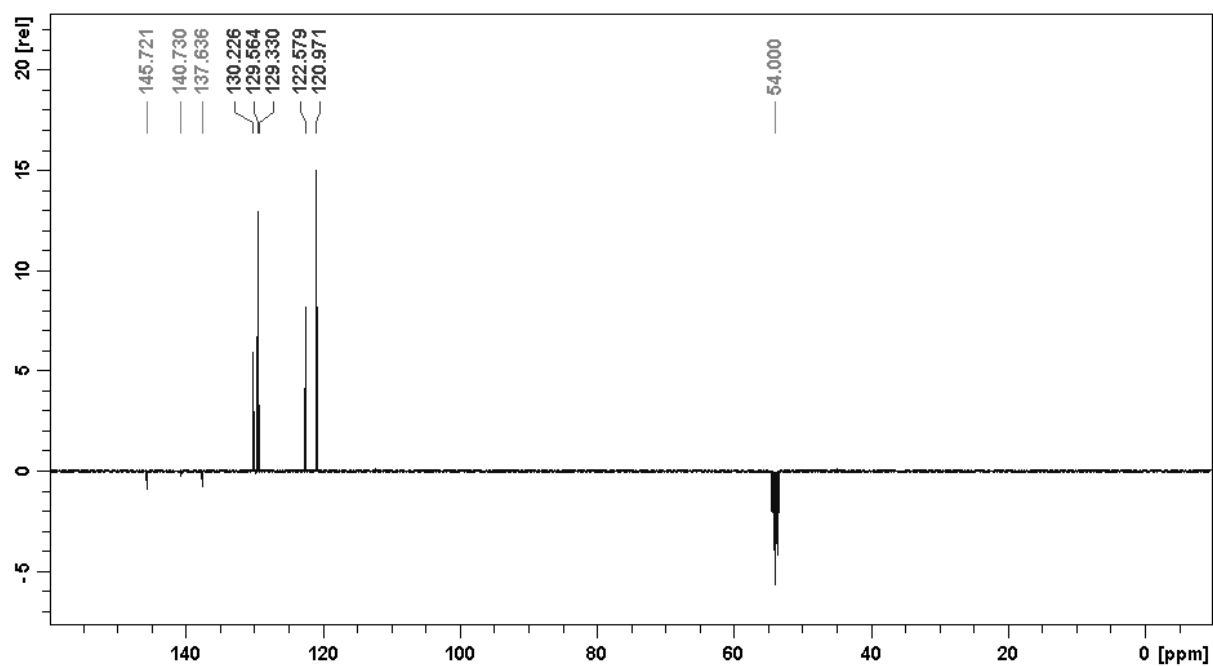


Figure S4. Carbon NMR spectrum of compound **1iii**.

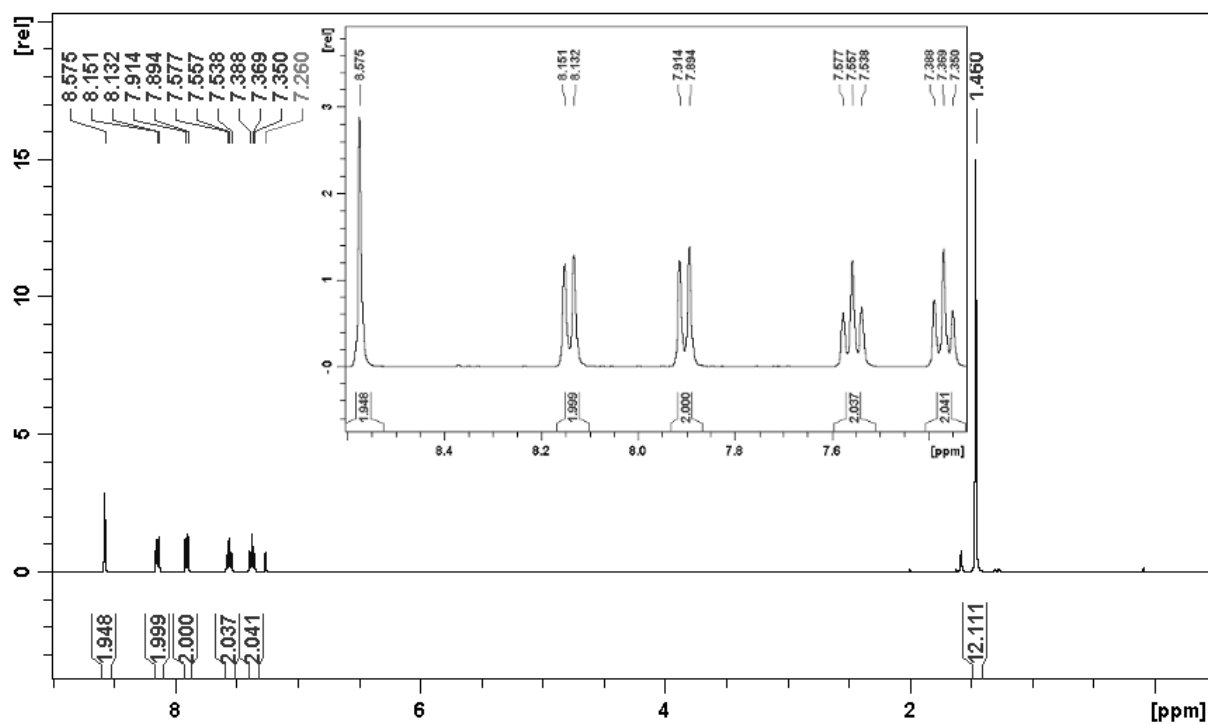


Figure S 5. Proton NMR spectrum of compound 3c.

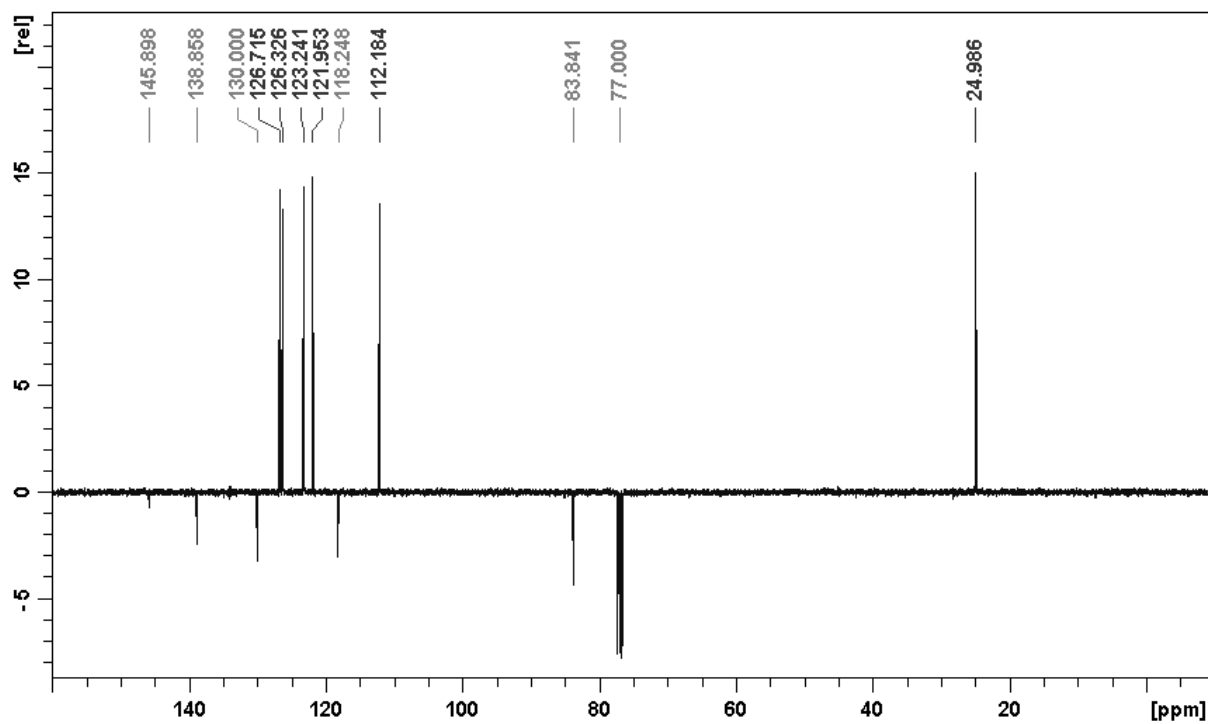


Figure S 6. Carbon NMR spectrum of compound 3c.

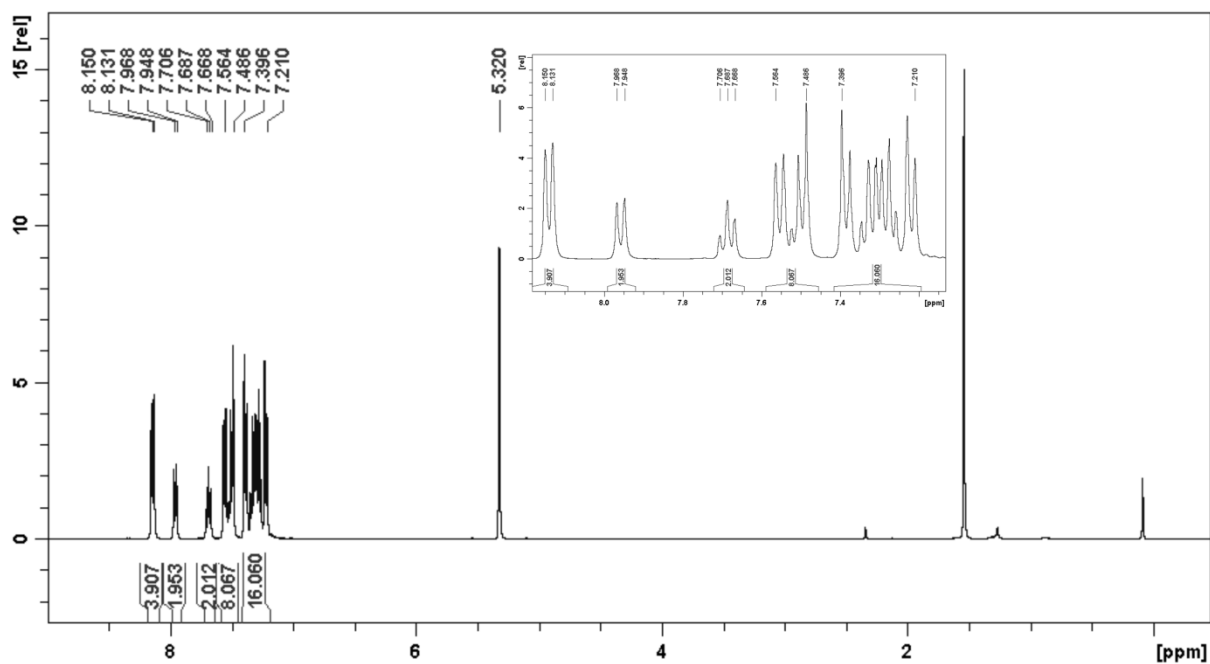


Figure S7. Proton NMR spectrum of compound o-PCzPOXD (5b).

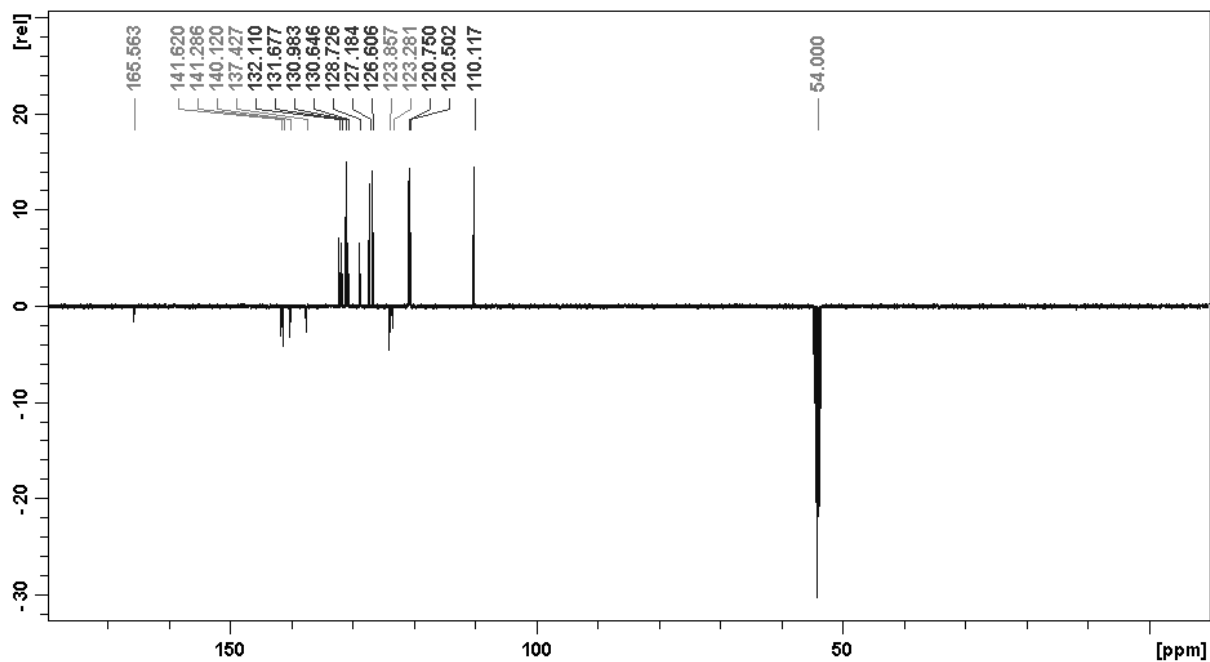


Figure S8. Carbon NMR spectrum of compound o-PCzPOXD (5b).

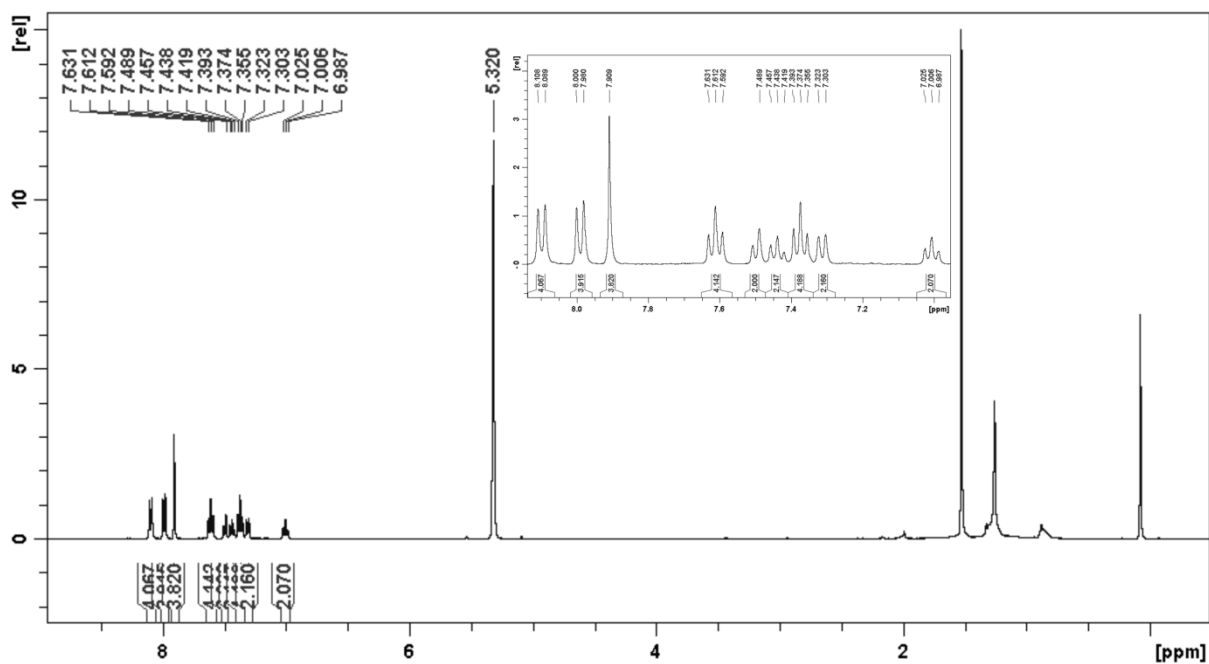


Figure S9. Proton NMR spectrum of compound o-ICzPOXD (**5c**).

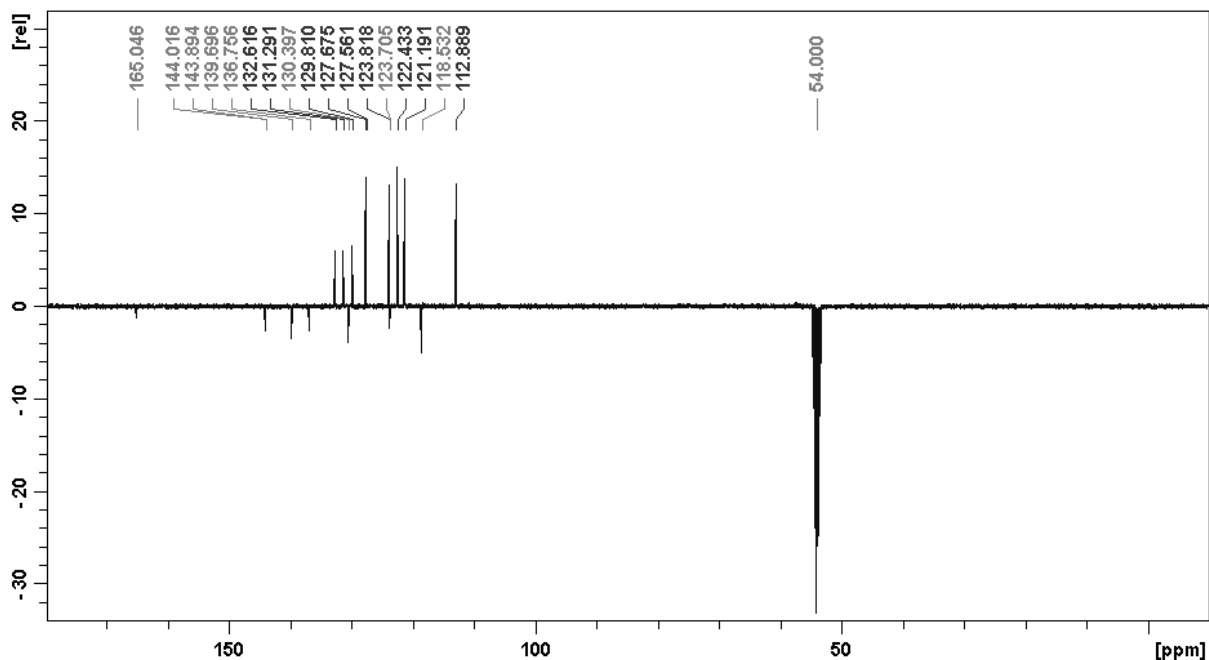


Figure S10. Carbon NMR spectrum of compound o-ICzPOXD (**5c**).

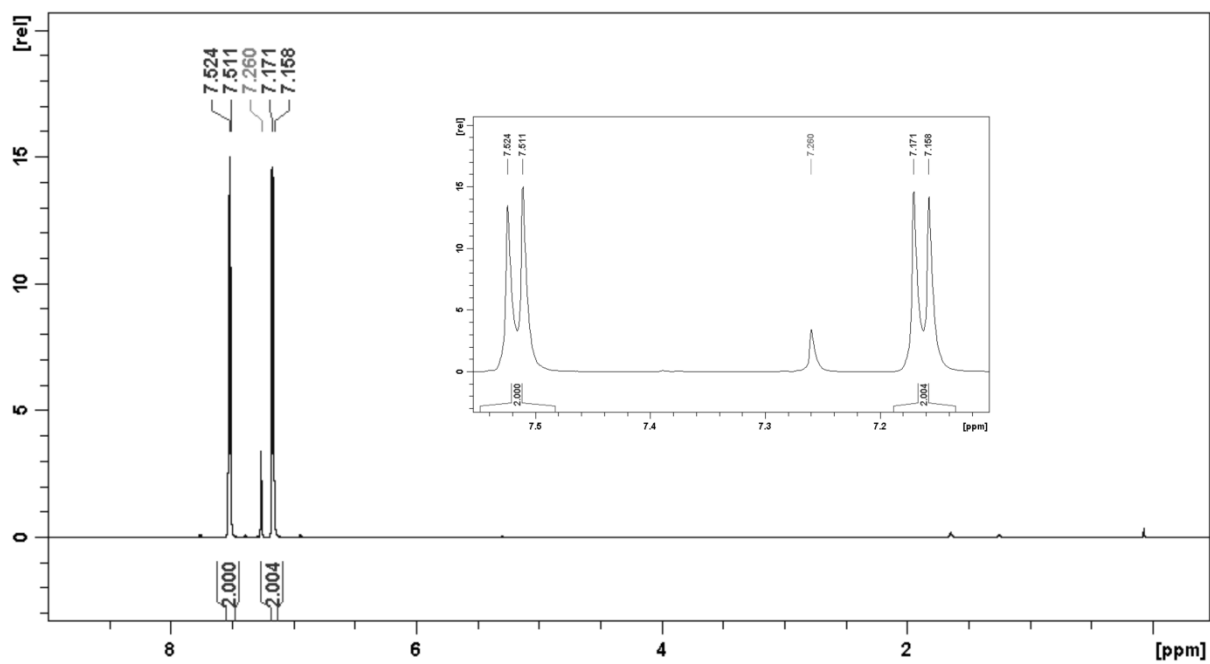


Figure S11. Proton NMR spectrum of compound 7i.

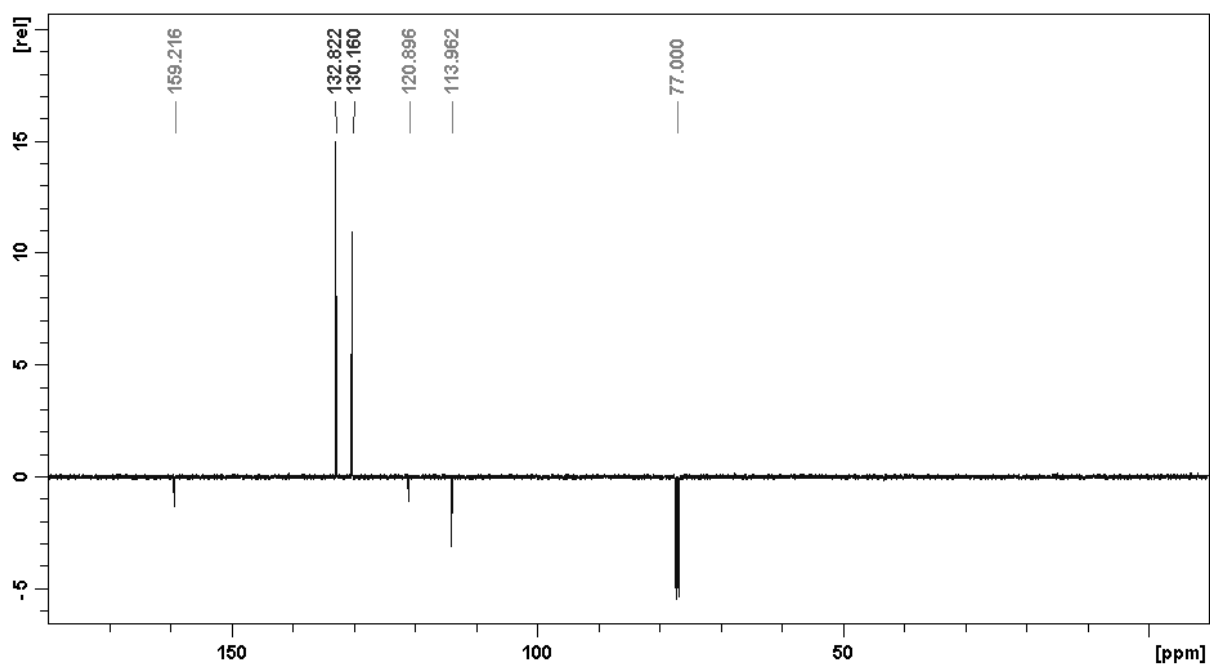


Figure S12. Carbon NMR spectrum of compound 7i.

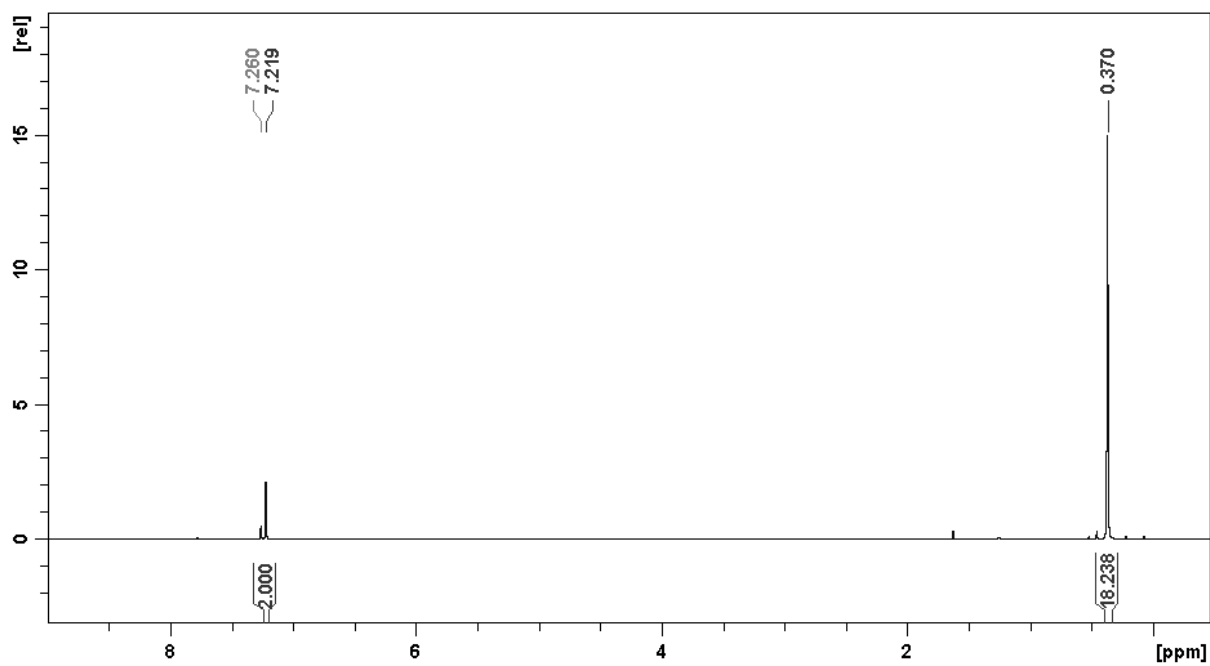


Figure S13. Proton NMR spectrum of compound 7ii.

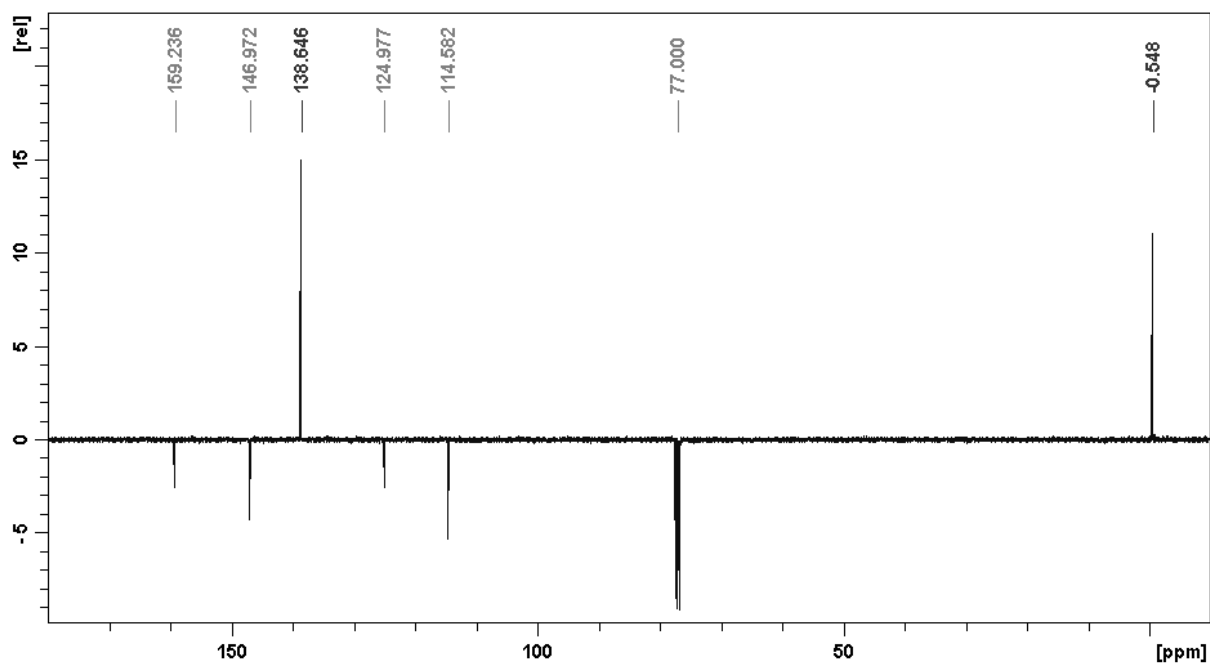


Figure S14. Carbon NMR spectrum of compound 7ii.

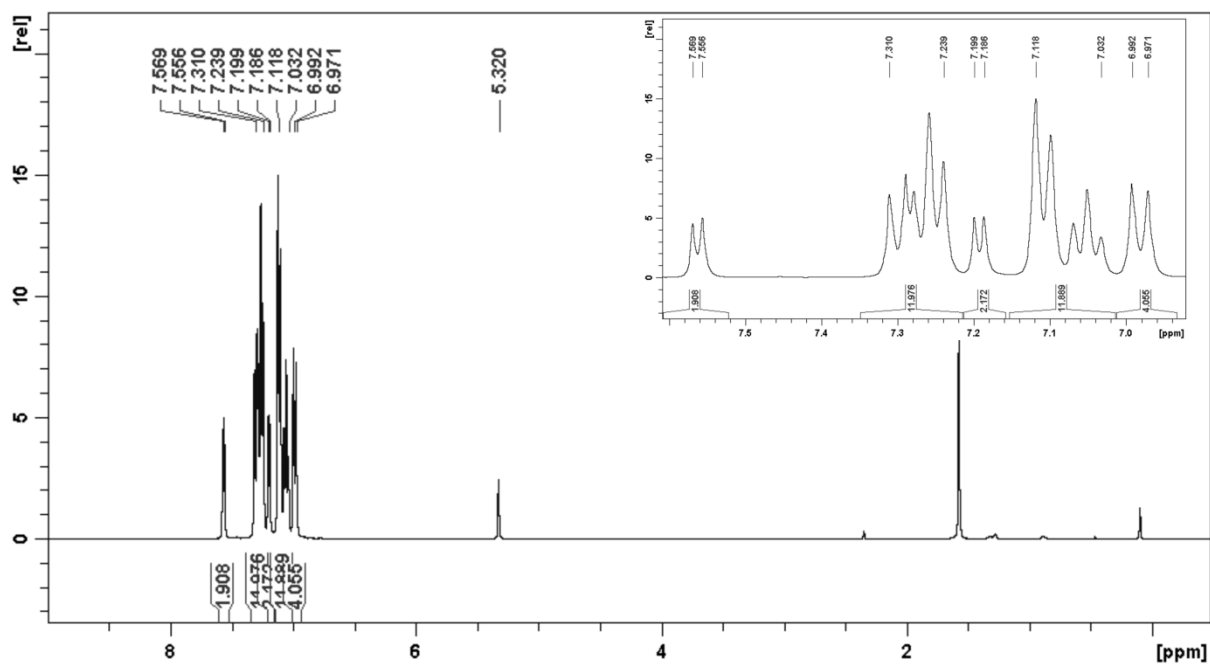


Figure S15. Proton NMR spectrum of compound o-TPATOXD (**8a**).

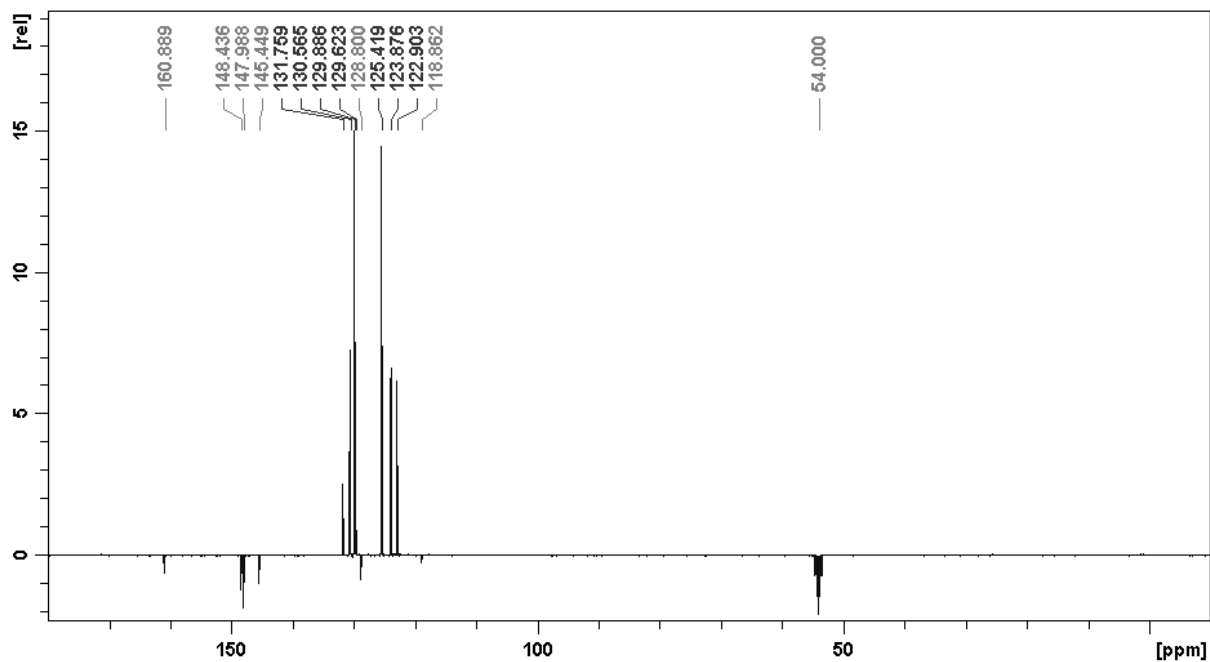


Figure S16. Carbon NMR spectrum of compound o-TPATOXD (**8a**).

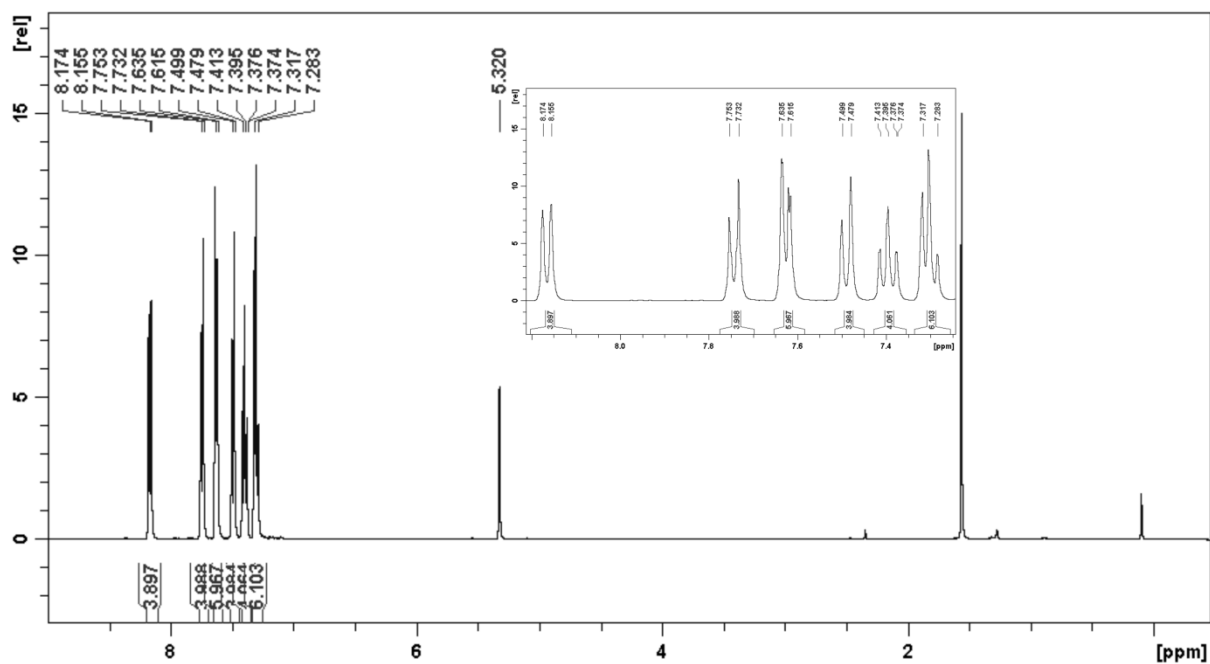


Figure S17. Proton NMR spectrum of compound o-PCzTOXD (**8b**).

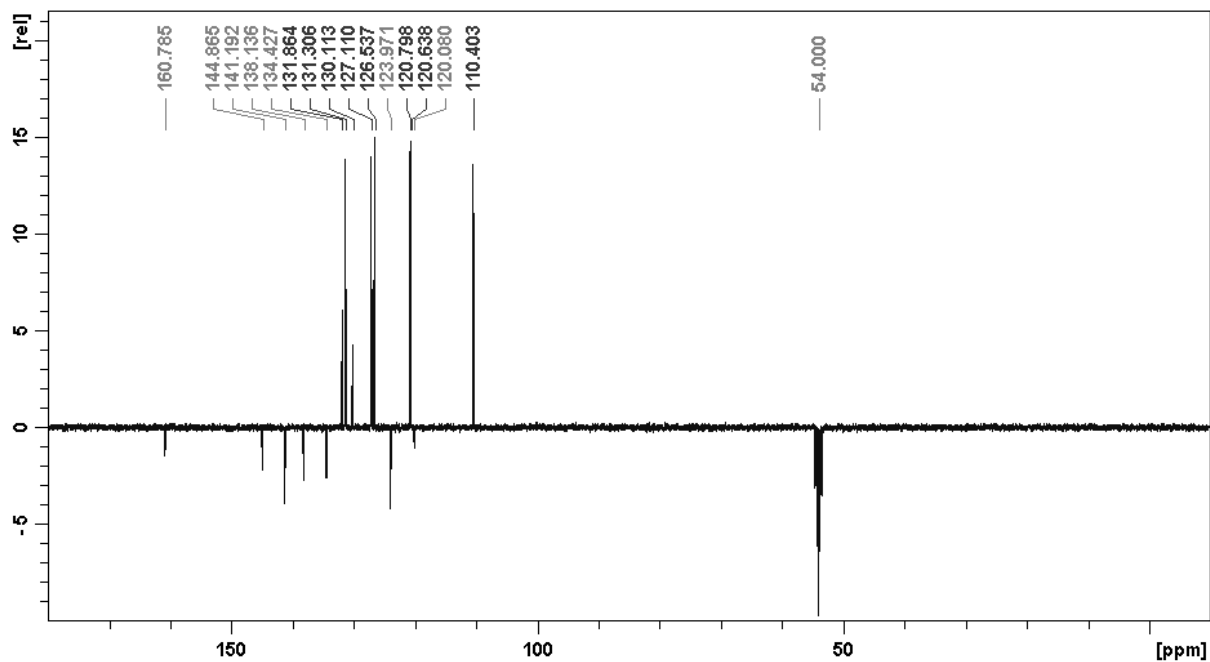


Figure S18. Carbon NMR spectrum of compound o-PCzTOXD (**8b**).

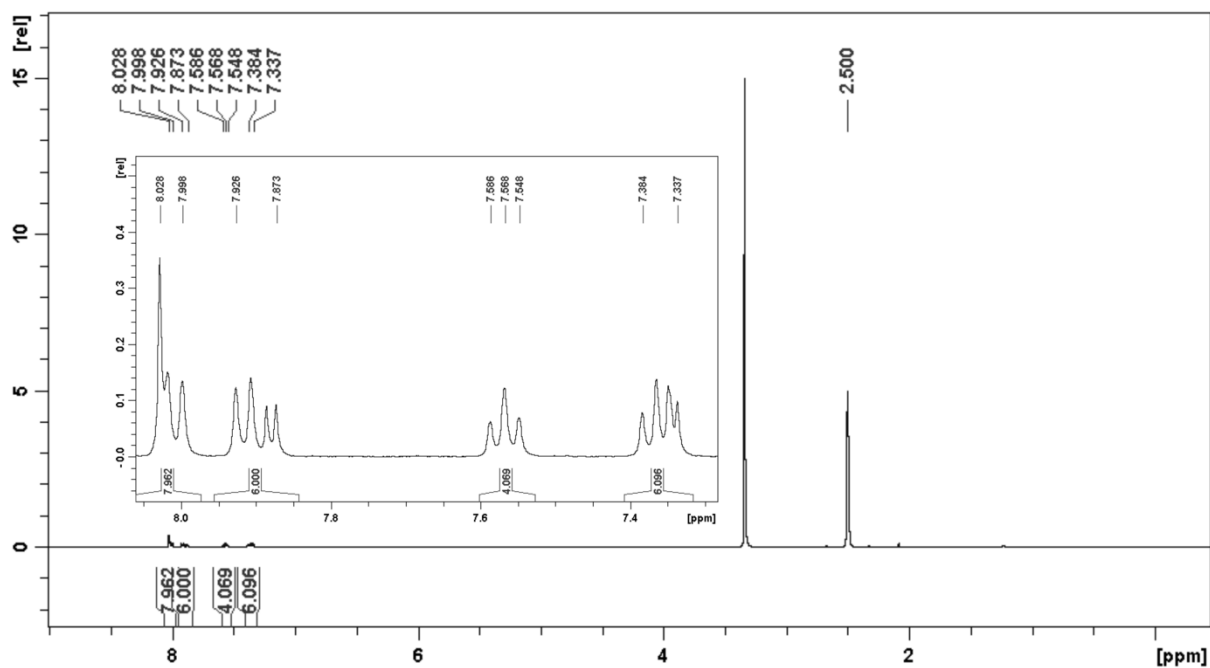


Figure S 19. Proton NMR spectrum of compound o-ICzTOXD (8c).

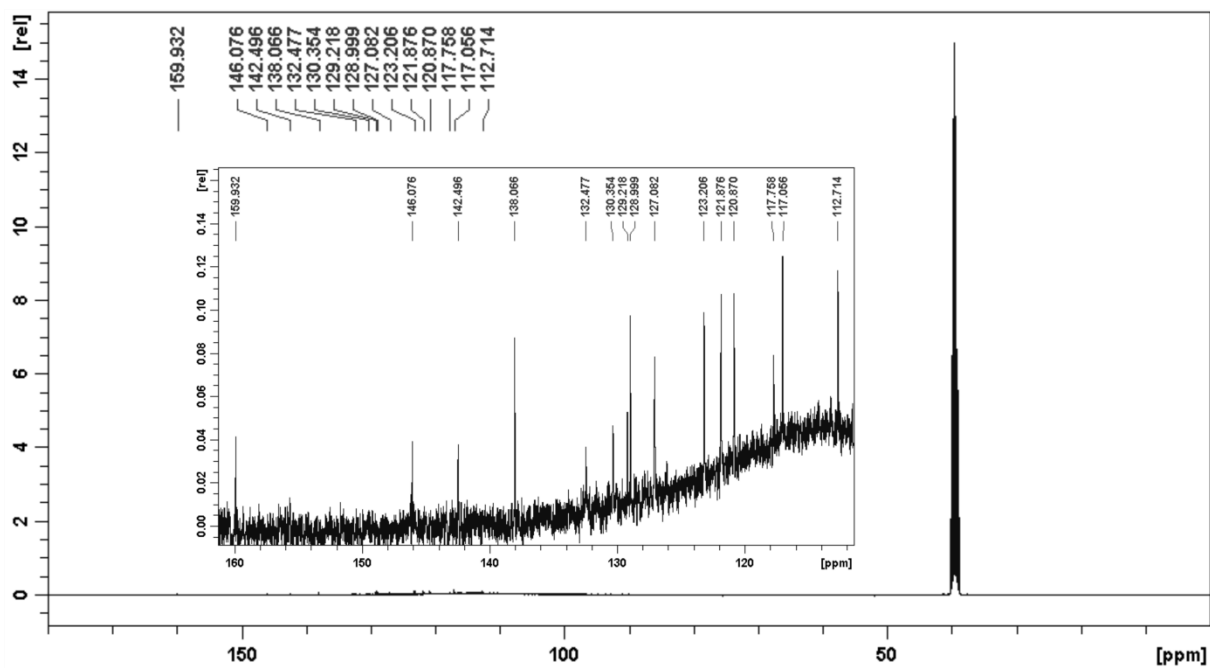
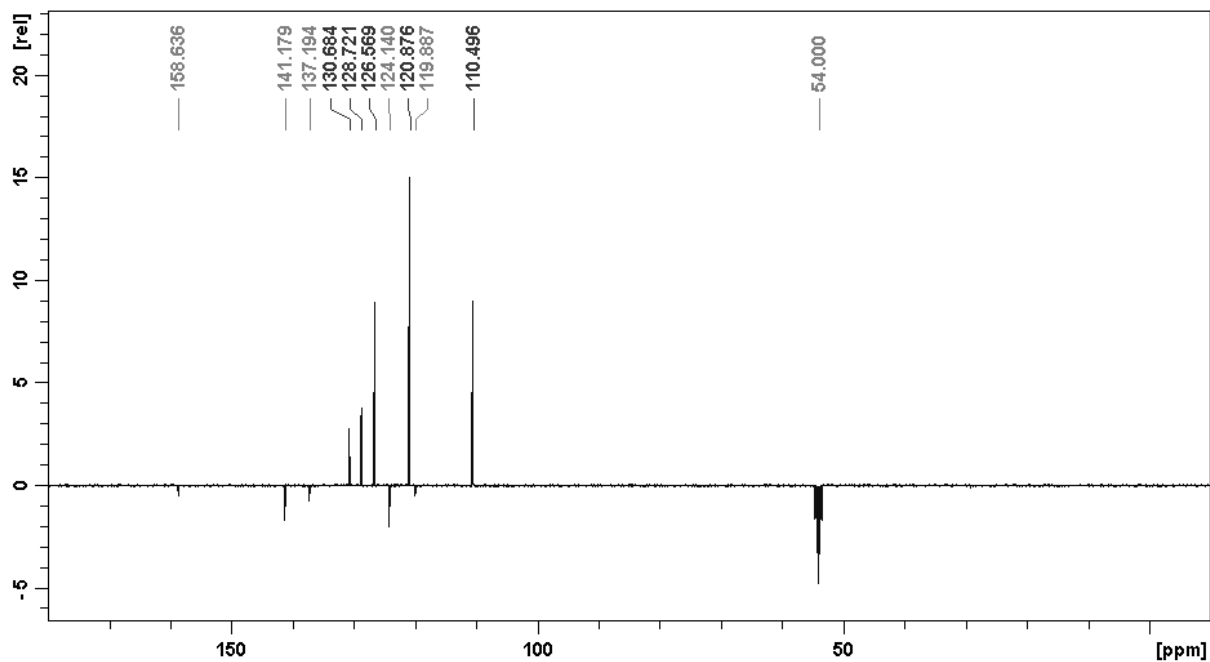
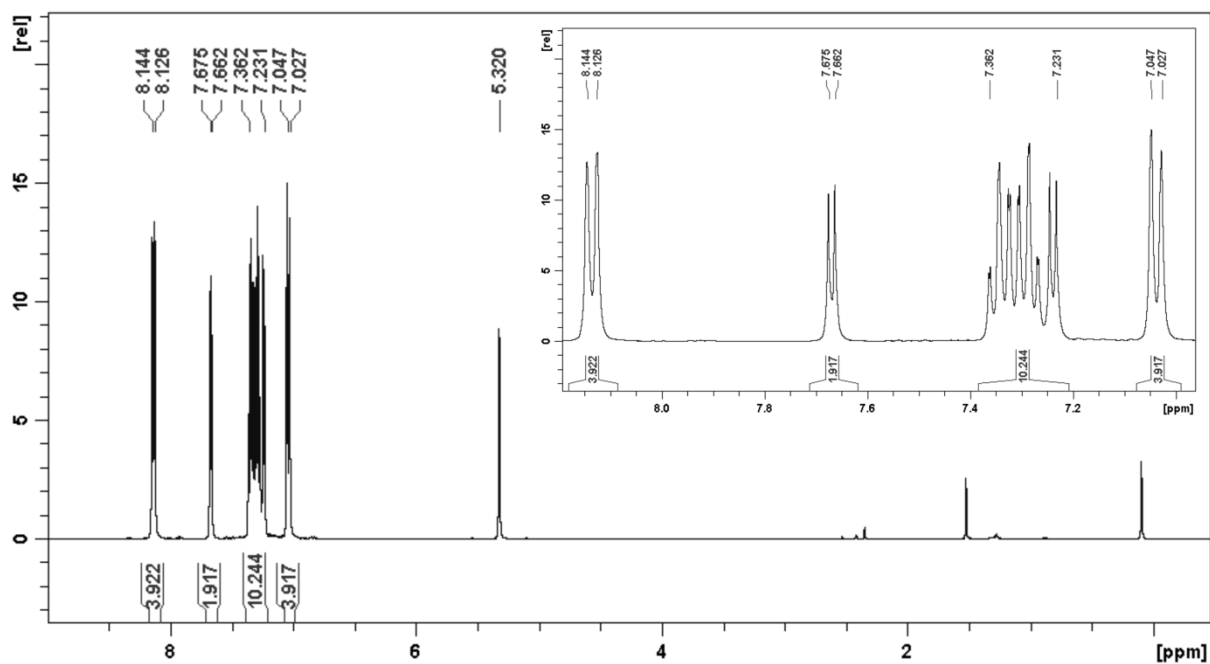


Figure S 20. Carbon NMR spectrum of compound o-ICzTOXD (8c).



B) TGA/DSC

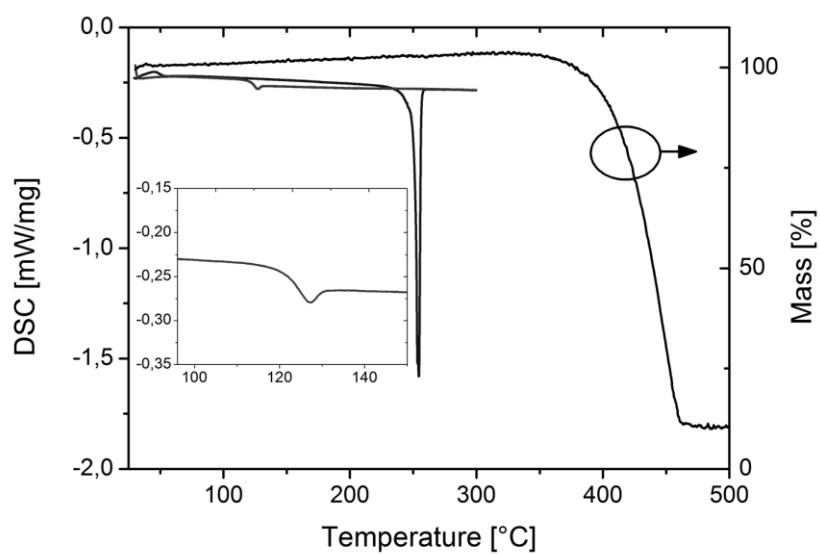


Figure S23. DSC and TG trace of o-PCzPOXD (**5b**) recorded at a heating rate of 5 °C min⁻¹.

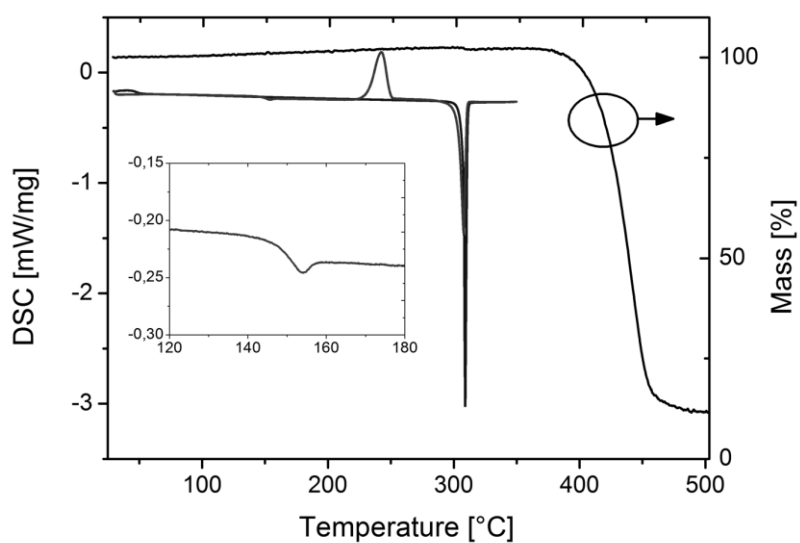


Figure S24. DSC and TG trace of o-ICzPOXD (**5c**) recorded at a heating rate of 5 °C min⁻¹.

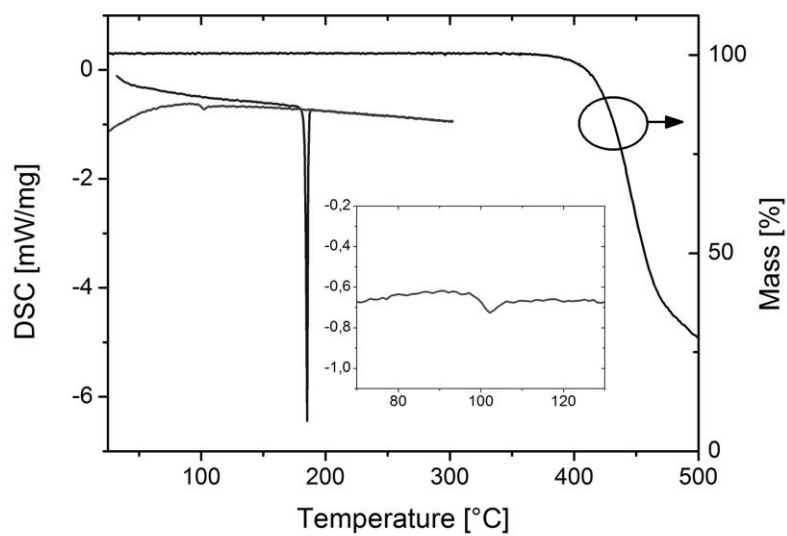


Figure S25. DSC and TG trace of o-TPATOXD (**8a**) recorded at a heating rate of 5 °C min⁻¹.

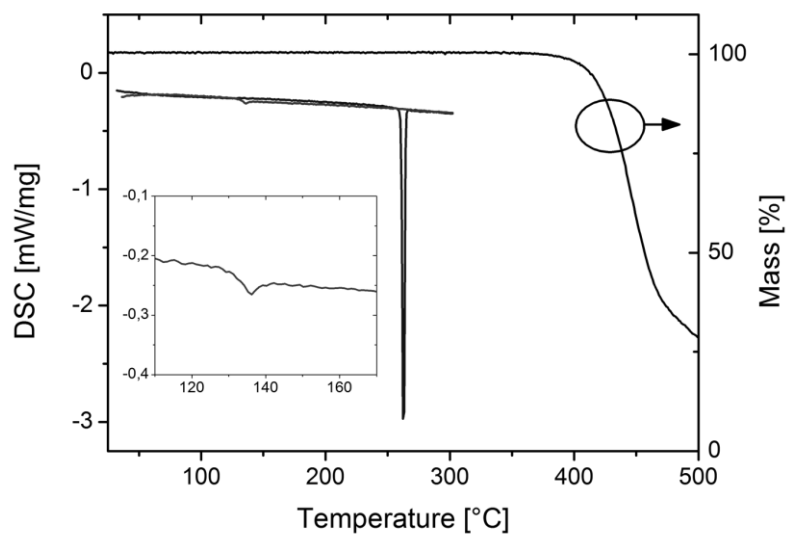


Figure S26. DSC and TG trace of o-PCzTOXD (**8b**) recorded at a heating rate of 5 °C min⁻¹.

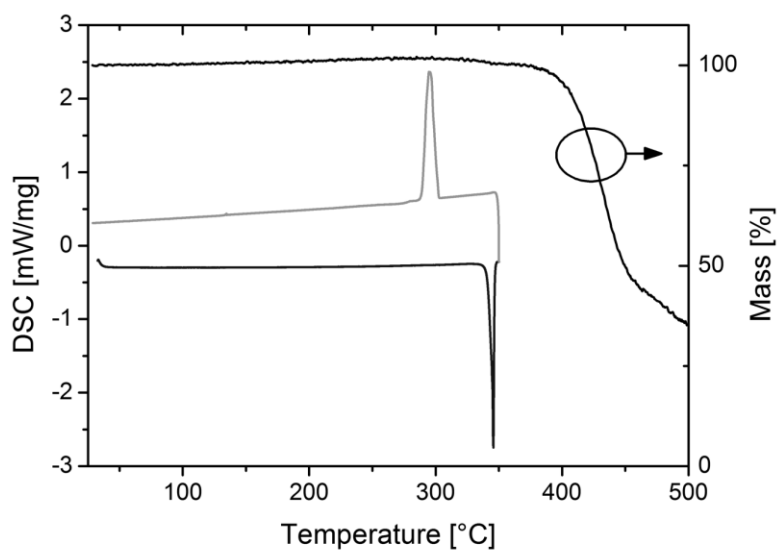


Figure S27. DSC and TG trace of o-ICzTOXD (**8c**) recorded at a heating rate of 5 °C min⁻¹.

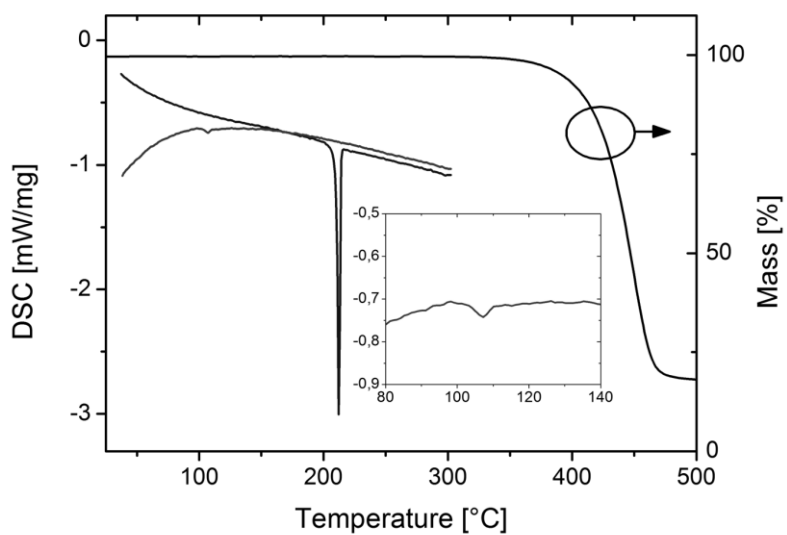


Figure S28. DSC and TG trace of o-CzTOXD (**8d**) recorded at a heating rate of 5 °C min⁻¹.

C)Cyclic Voltammetry

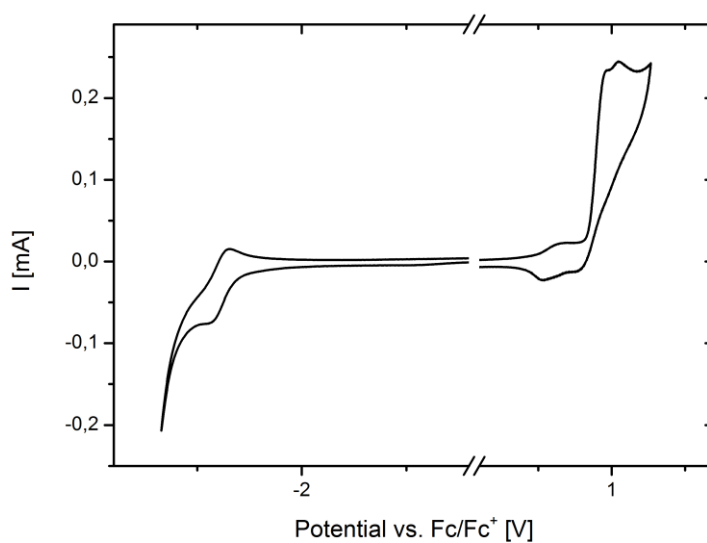


Figure S29. Cyclic voltammogram of o-PCzPOXD (**5b**).

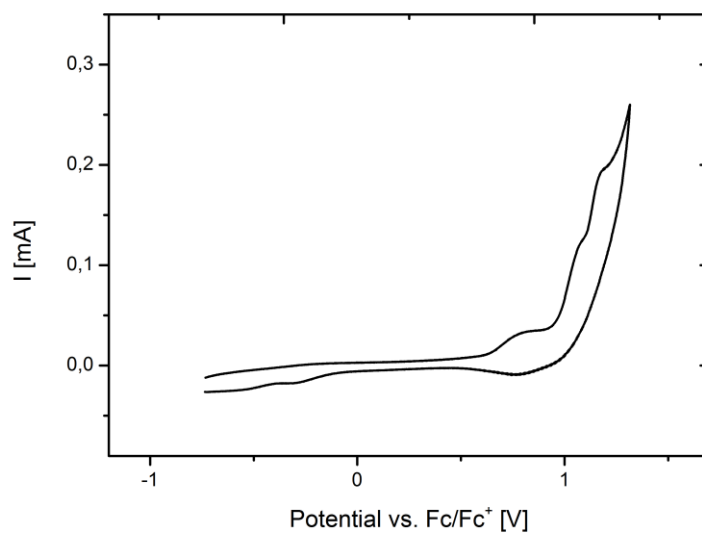


Figure S30. Cyclic voltammogram of o-ICzPOXD (**5c**).

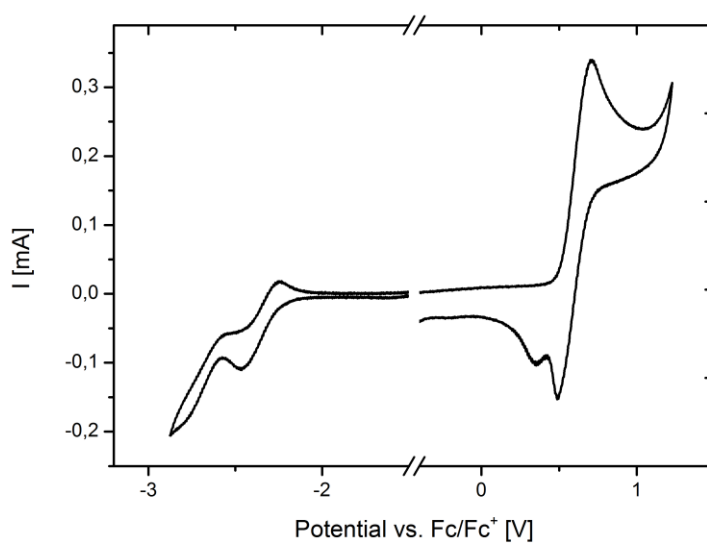


Figure S31. Cyclic voltammogram of o-TPATOXD (**8a**).

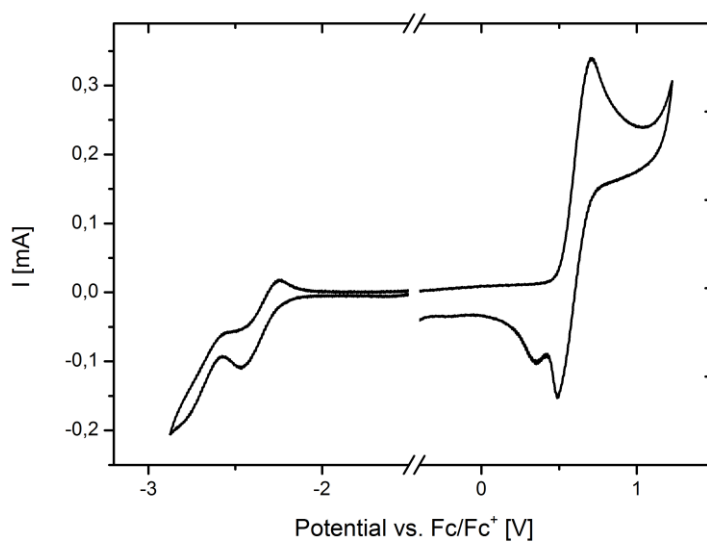


Figure S32. Cyclic voltammogram of o-PCzTOXD (**8b**).

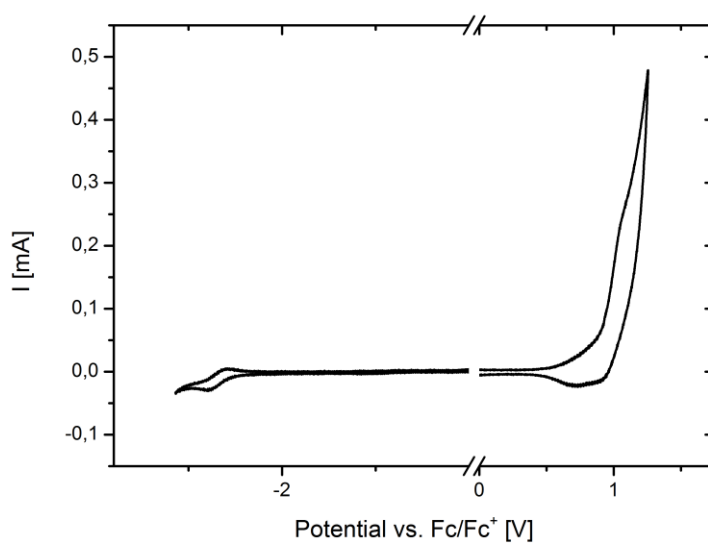


Figure S33. Cyclic voltammogram of o-ICzTOXD (**8c**).

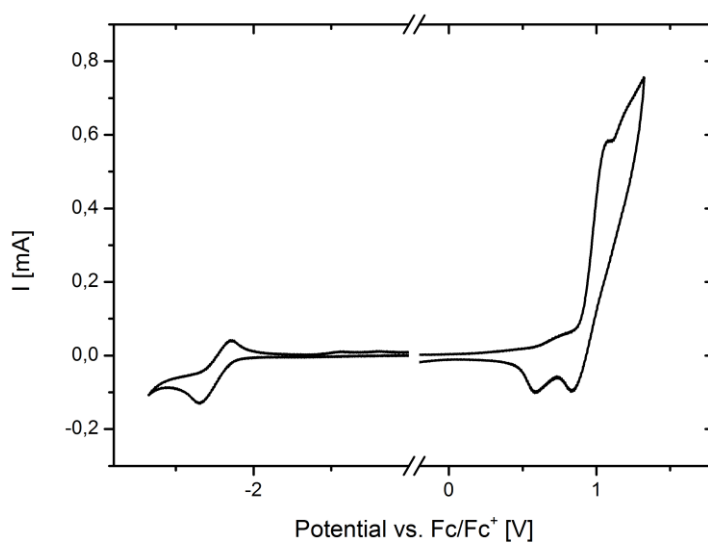


Figure S34. Cyclic voltammogram of o-CzTOXD (**8d**).

D) Phosphorescence Measurements

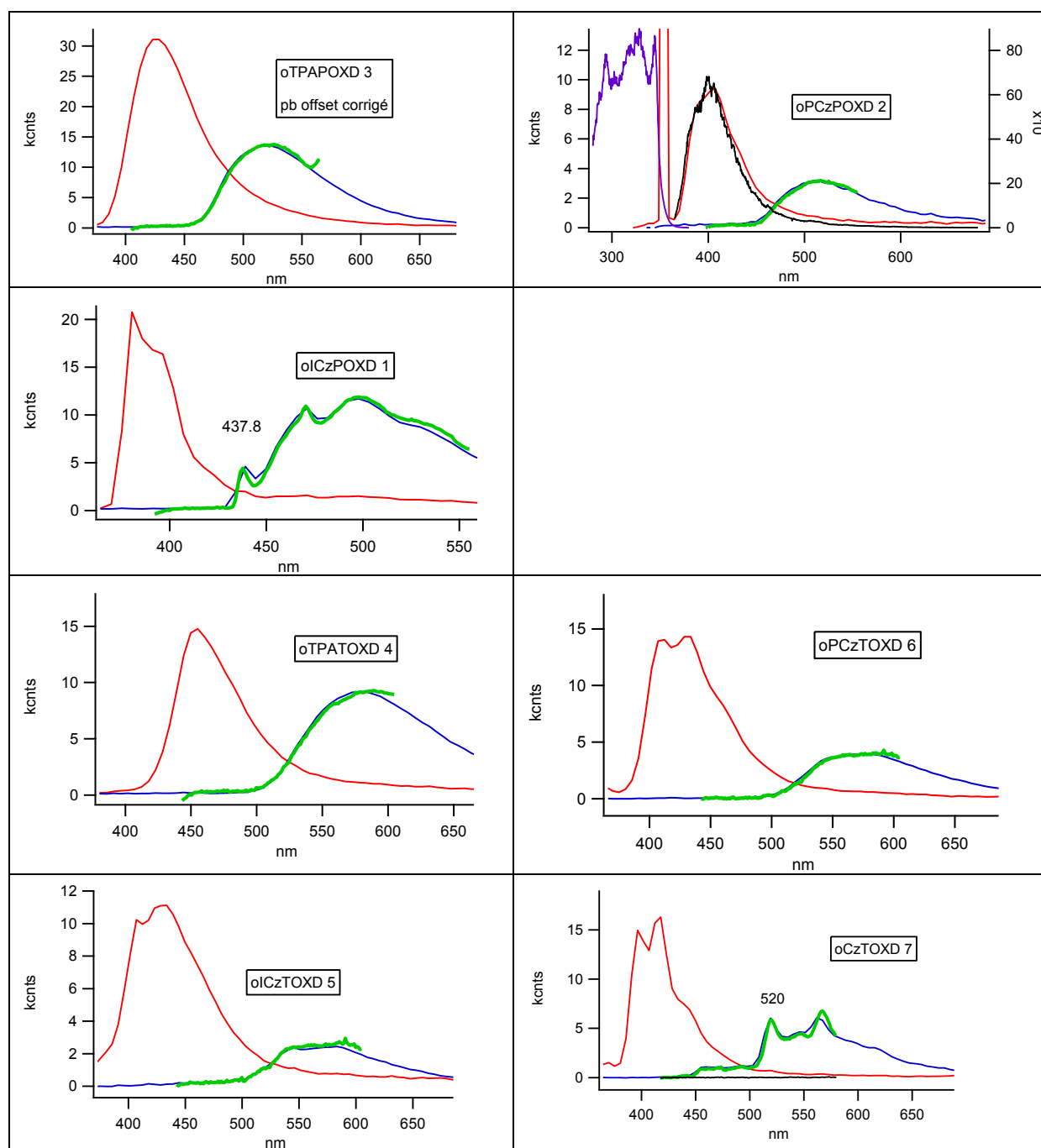


Figure S35. Singlet (red) and triplet (blue) emission spectra at 77 K with two different gratings to obtain higher resolution for the triplet emission (green).

Lifetime Measurements

The singlet and triplet lifetimes of target materials are summarized in Table S2. Some samples present single exponential decay, others a more complex behavior; results are derived from single and double exponential fits of the data. Note that the errors for the double exponential fits are significant.

Table S2. Singlet and triplet lifetimes measured in toluene solutions at ambient temperature.

Sample	Singlet Lifetime		Triplet Lifetime
	τ_1 [ns]	τ_2 [ns]	τ [ms]
o-TPAPOXD	3.25(0.003)		~790
o-PCzPOXD	0.90(0.04)	2.0(45)	335(6)
o-ICzPOXD	0.66(0.017)	64.7(12)	349(2)
o-TPATOXD	1.57(0.002)		12.3
o-PCzTOXD	0.84(0.004)		8.3
o-ICzTOXD	0.53(0.009)		8.2
o-CzTOXD	1.28(0.004)	2.02(0.17)	11.0

Experimental Parameter

The determination of the emission lifetime at room temperature was done with Dr. François-Alexandre Mianney using a picosecond 375 nm laser source in conjunction with a detection set-up as described in (Muller, P. A., Högemann, C., Allonas, X., Jacques, P., Vauthey, E., Chem. Phys. Letters 326 (2000) 321.) Low temperature experiments were performed in frozen dilute toluene solutions using a Janis closed cycle cryostat (at 5 K) and a liquid nitrogen dewar fitted with quartz windows for measurements at ~80 K.

Time resolved experiments were obtained using a Quantel Brilliant tripled Nd-YAG laser (355 nm, 20 Hz repetition rate, pulse width ~5ns). Spectra were measured using a SPEX 270 monochromator equipped with both photomultiplier and CCD. This set-up is controlled using a home-built Labview-based program which allows using different instruments such as photon counting, oscilloscope, and additional mechanical shutters.

Additional absorption measurements were performed with a Cary 5000 instrument at room temperature, as well as emission and excitation spectra at room temperature and liquid nitrogen temperature using a Fluorolog FL3-22 instrument.

E) DFT Calculations

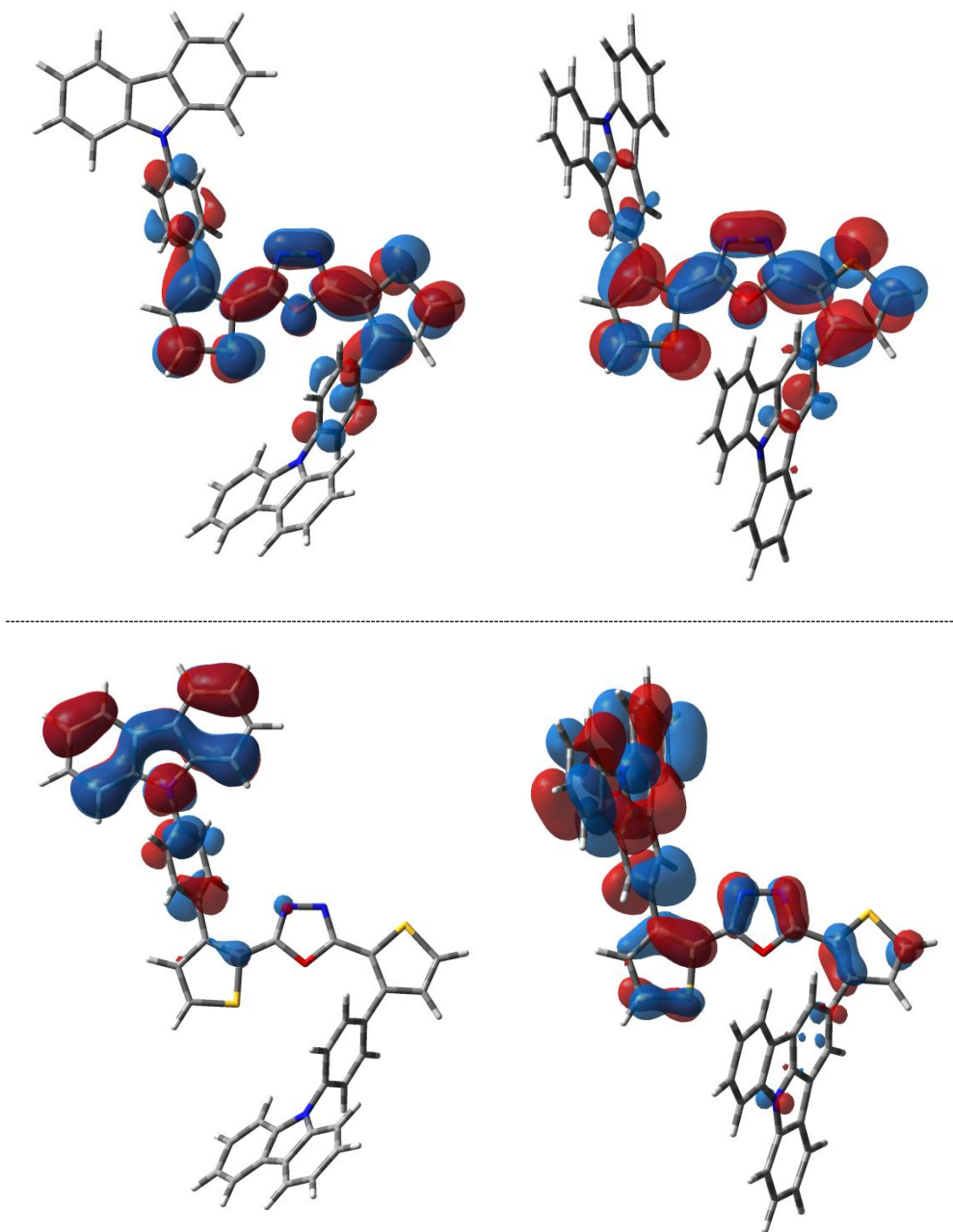


Figure S36. HOMO (bottom) and LUMO (top) of **o-PCzTOXD** (left) and **o-ICzTOXD** (right).

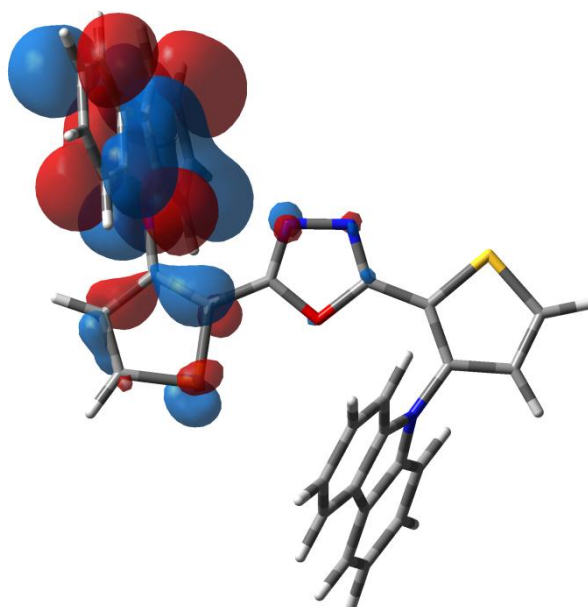
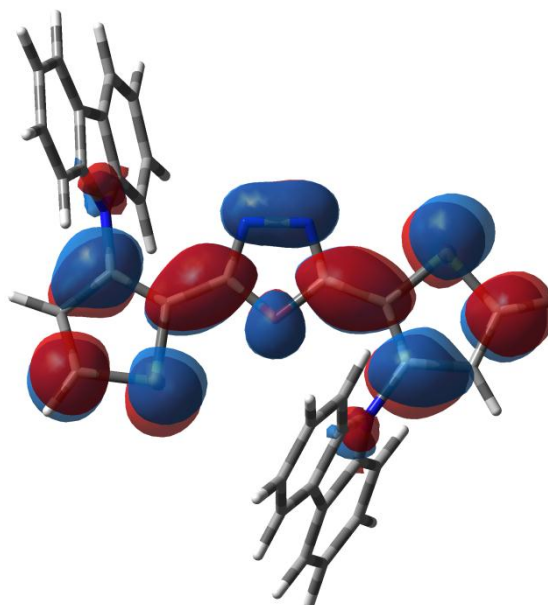
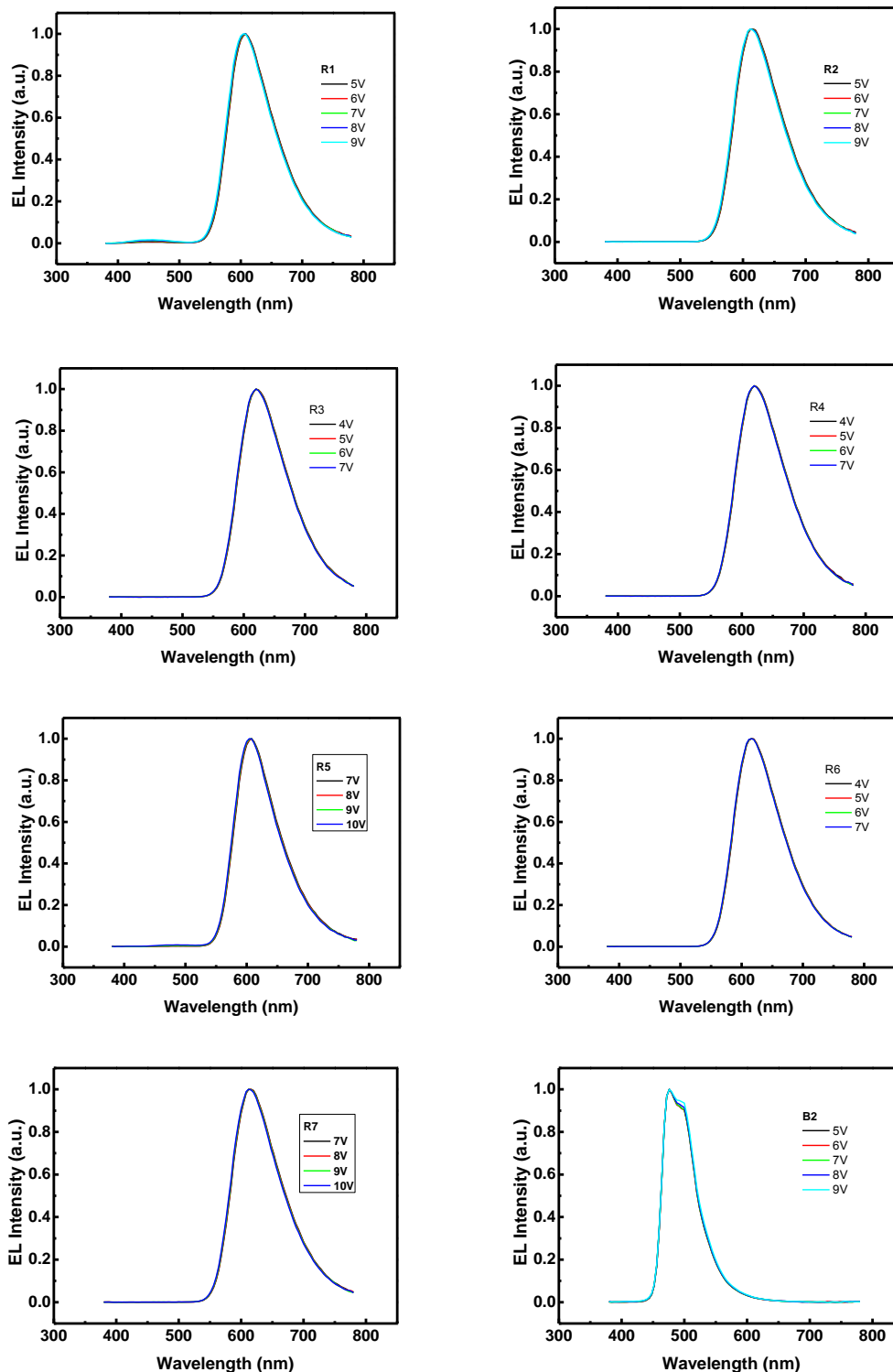


Figure S367. HOMO (bottom) and LUMO (top) of **o-CzTOXD**

F) EL Spectra



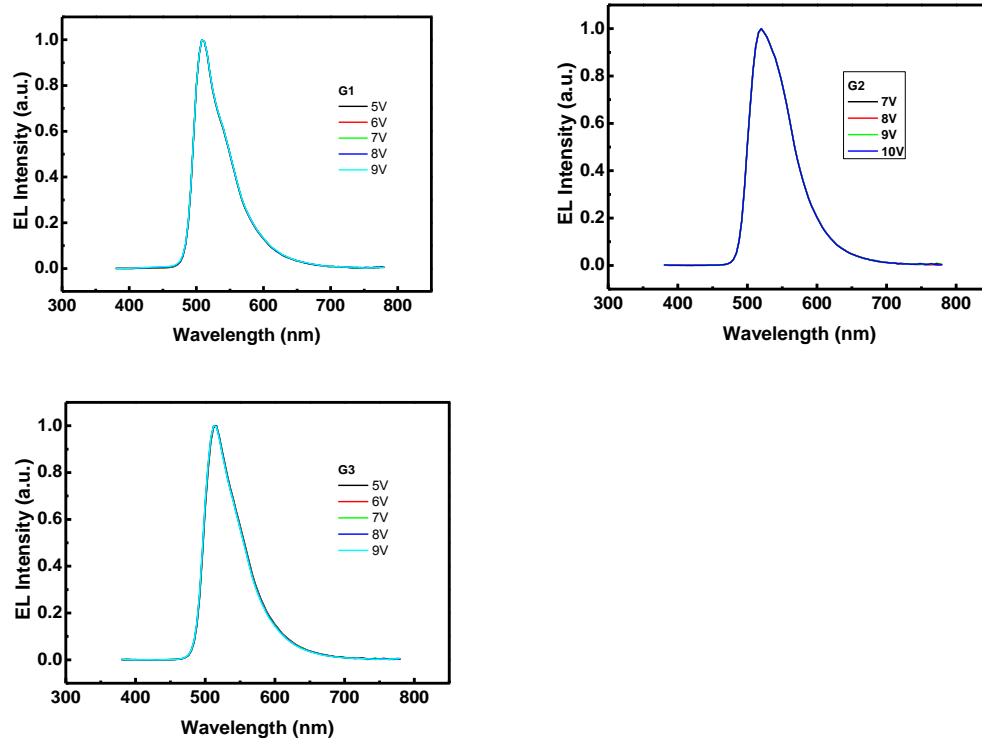


Figure S38. Electroluminescence (EL) spectra of all devices discussed in this study.

G) Crystal Structure of Compound **3c**

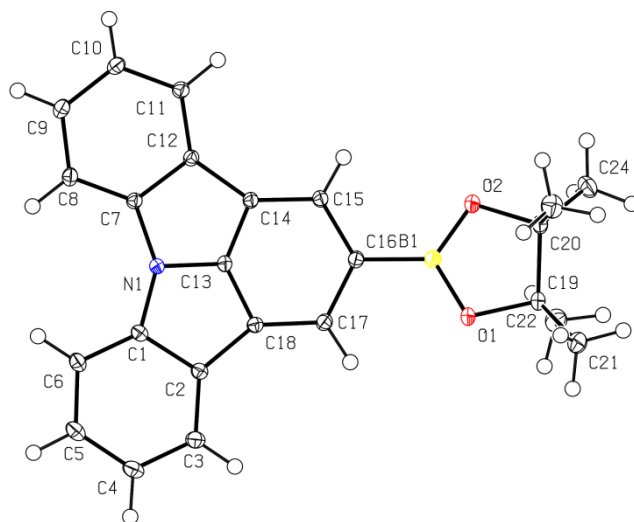


Figure S39. Molecular structure of **3c**; B, C, N, and O atoms are represented by yellow, white, blue and red ellipsoids drawn at 50% probability levels, H atoms by spheres of arbitrary radius.

3.2. Manuscript #2 – Supporting Information

Structure-property studies of *P*-triarylamine-substituted dithieno[3,2-*b*:2',3'-*d*]phospholes

Hannes Puntscher, Paul Kautny, Berthold Stöger, Antoine Tissot, Christian Hametner, Hans R. Hagemann, Johannes Fröhlich, Thomas Baumgartner, Daniel Lumpi

RSC Advances, **2015**, 5, 93797-93807

Electronic Supplementary Information

ESI

Structure-Property Studies of P-Triarylamine-Substituted Dithieno[3,2-*b*:2',3'-*d*]phospholes

Hannes Puntsher^{a,b,†}, Paul Kautny^{a,†}, Berthold Stöger^c, Antoine Tissot^d,
Christian Hametner^a, Hans R. Hagemann^d, Johannes Fröhlich^a,
Thomas Baumgartner^{b,*}, and Daniel Lumpi^{a,*}

^a Institute of Applied Synthetic Chemistry, Vienna University of Technology,
Getreidemarkt 9/163, A-1060 Vienna, Austria

^b Department of Chemistry & Centre for Advanced Solar Materials, University of
Calgary, 2500 University Dr. NW, Calgary AB, T2N 1N4, Canada

^c Institute of Chemical Technologies and Analytics, Vienna University of Technology,
Getreidemarkt 9/164, A-1060 Vienna, Austria

^d Département de Chimie Physique, Université de Genève, 30, quai E. Ansermet,
1211 Geneva 4, Switzerland

* tbaumga@ucalgary.ca, daniel.lumpi@tuwien.ac.at

[†] *contributed equally to this work*

Content

A. NMR Spectra

A.1 Proton and carbon spectra

A.2 Assignment of NMR signals and 1D NOE difference spectra of 3c and 3ci

B. Theoretical Data

C. Photo-physical Data

D. Crystallography

E. CV Measurements

A. NMR Spectra

A.1 Proton and carbon spectra

Figure S1. Proton NMR spectrum of compound 3a.

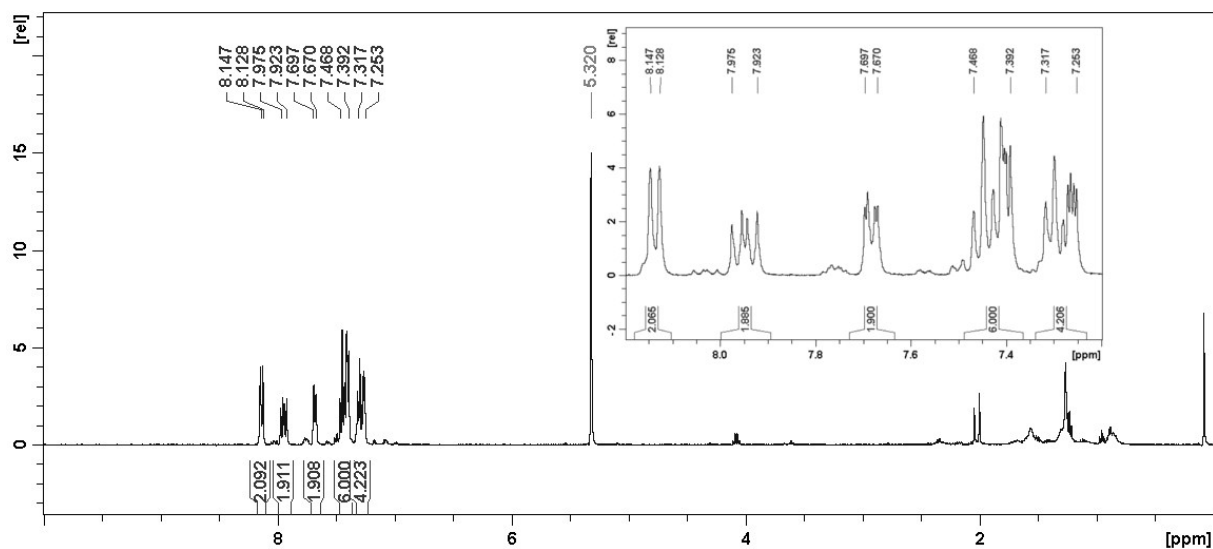


Figure S2. Carbon NMR spectrum of compound 3a.

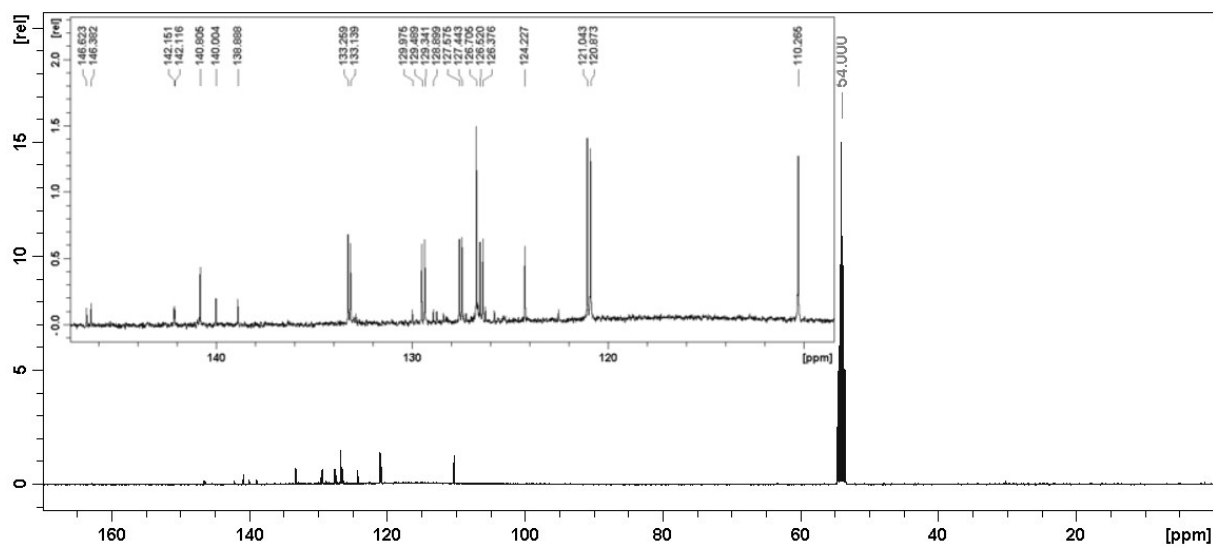


Figure S3. Proton NMR spectrum of compound 3ai.

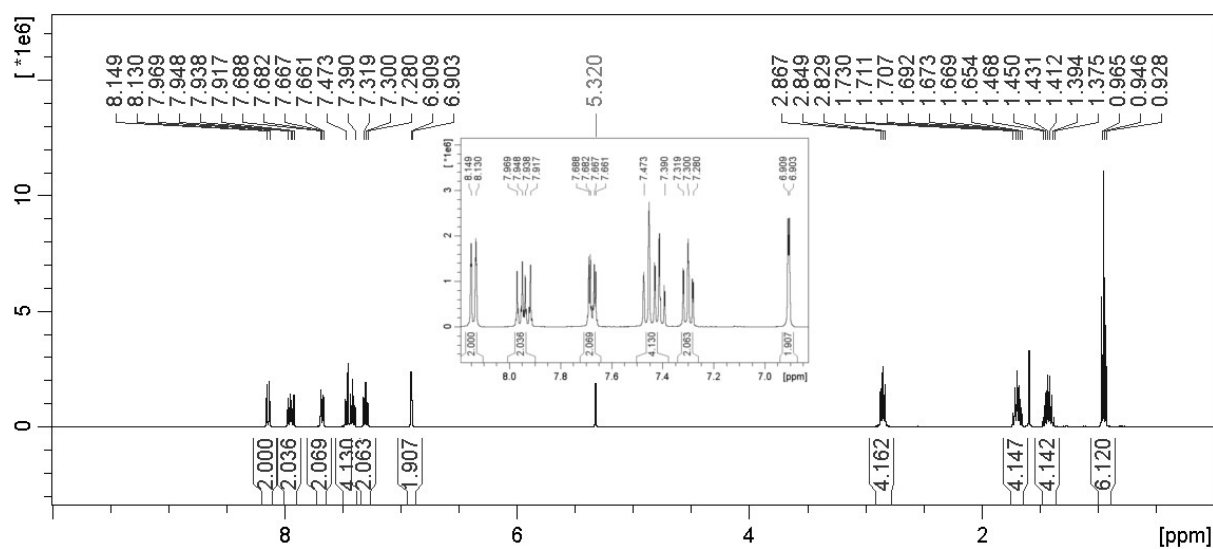


Figure S4. Carbon NMR spectrum of compound 3ai.

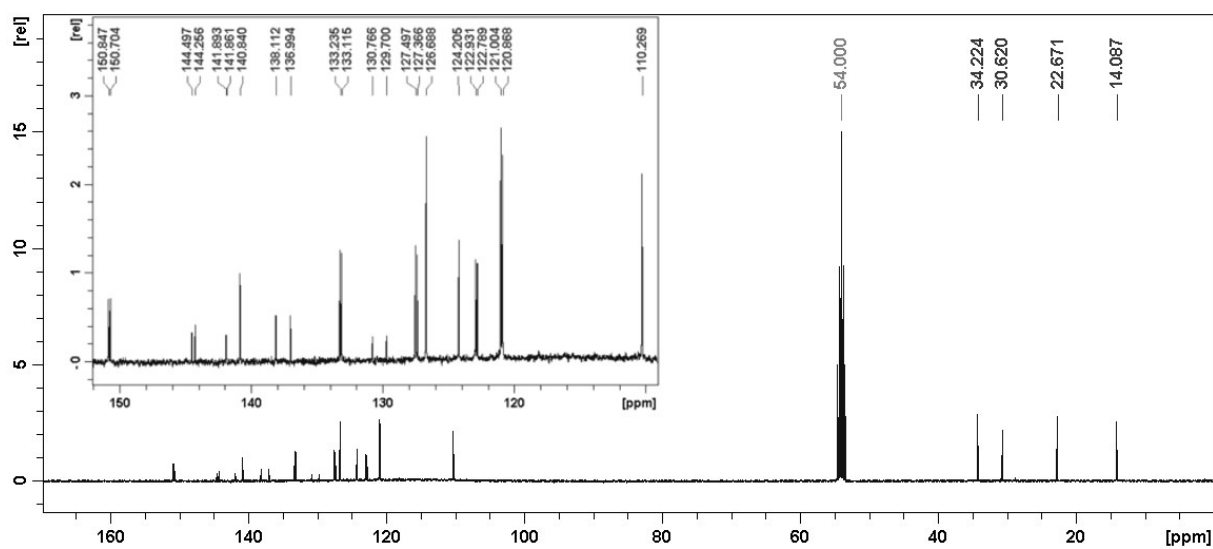


Figure S5. Proton NMR spectrum of compound 3b.

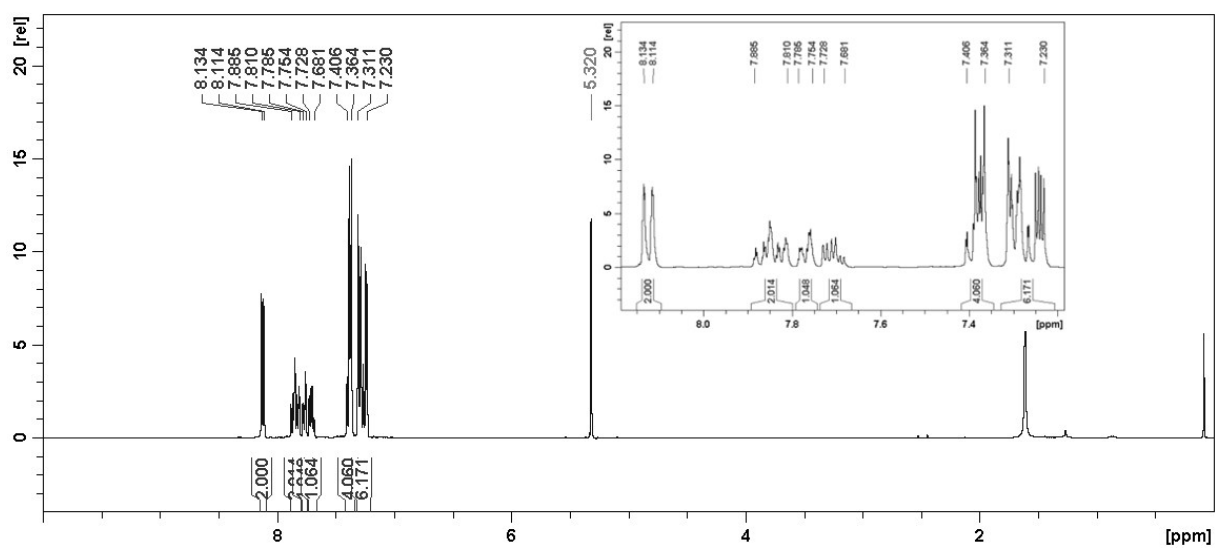


Figure S6. Carbon NMR spectrum of compound 3b.

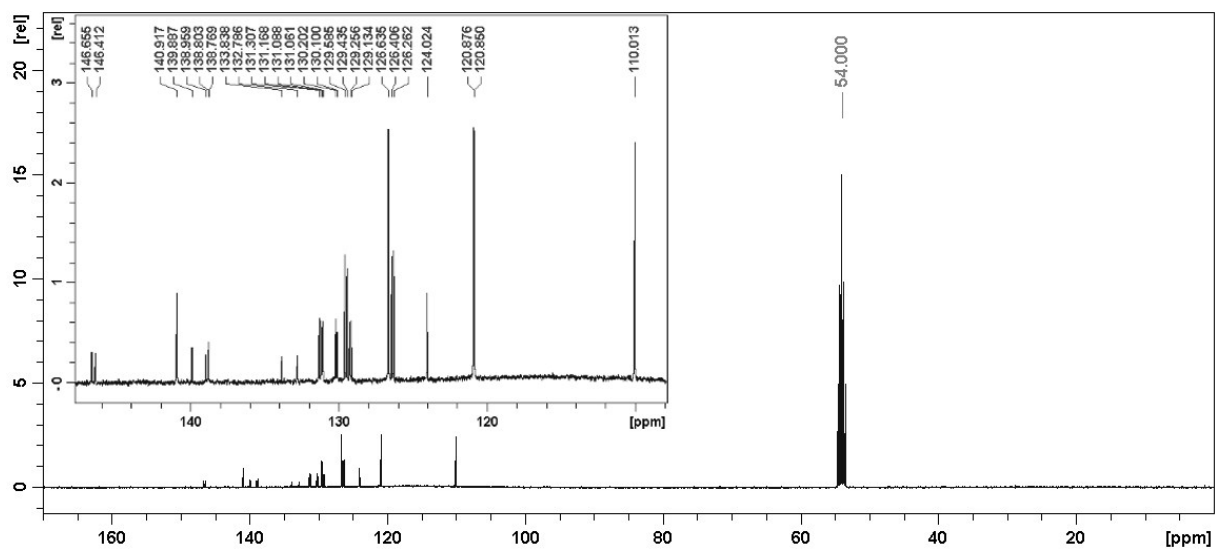


Figure S7. Proton NMR spectrum of compound **3bi**.

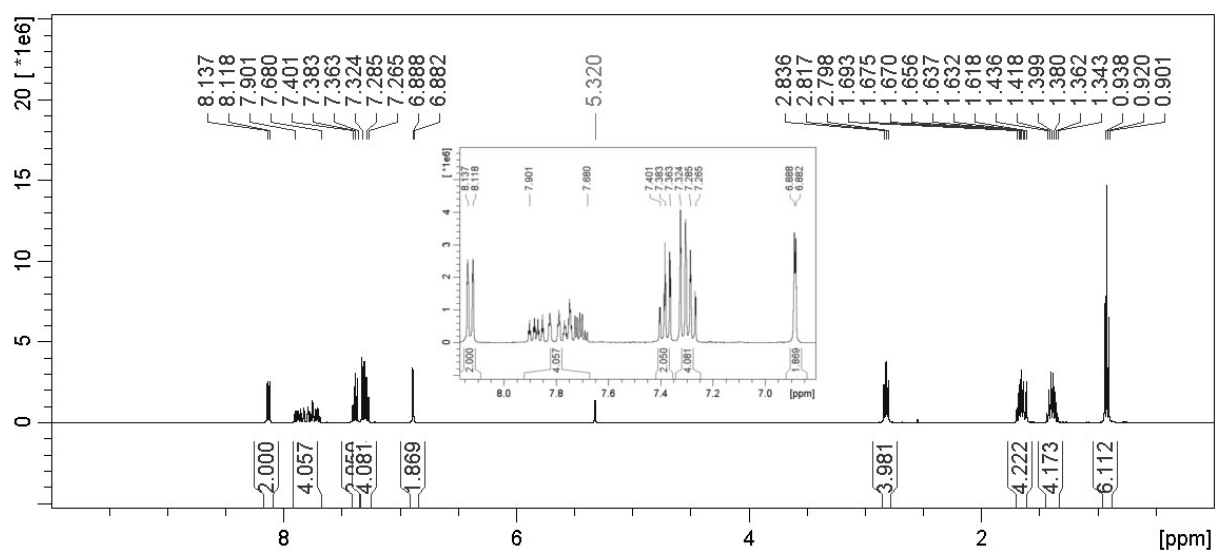


Figure S8. Carbon NMR spectrum of compound **3bi**.

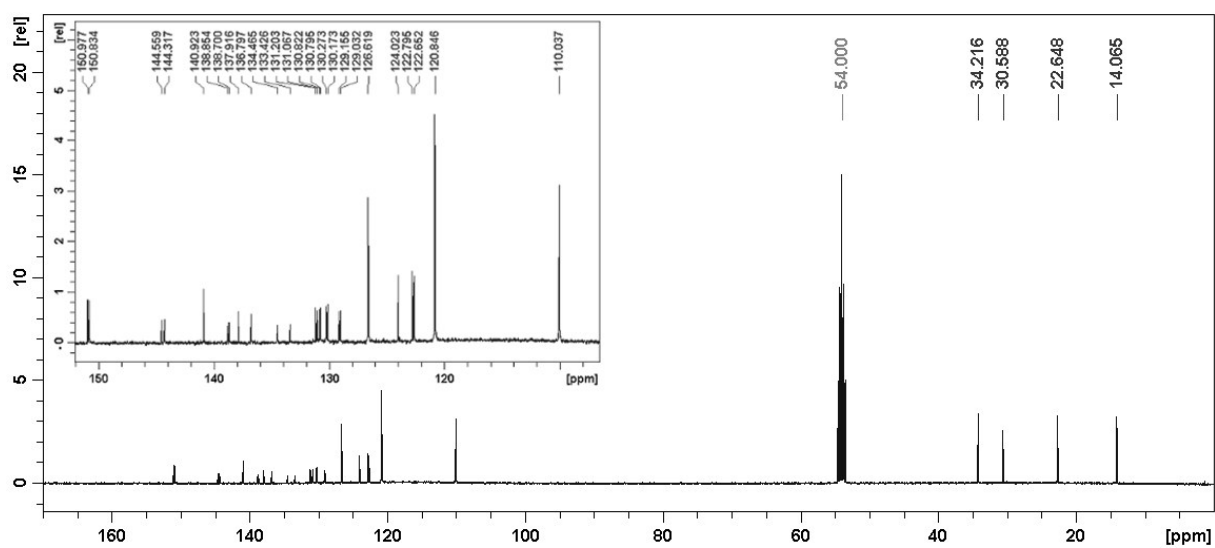


Figure S9. Proton NMR spectrum of compound 3c.

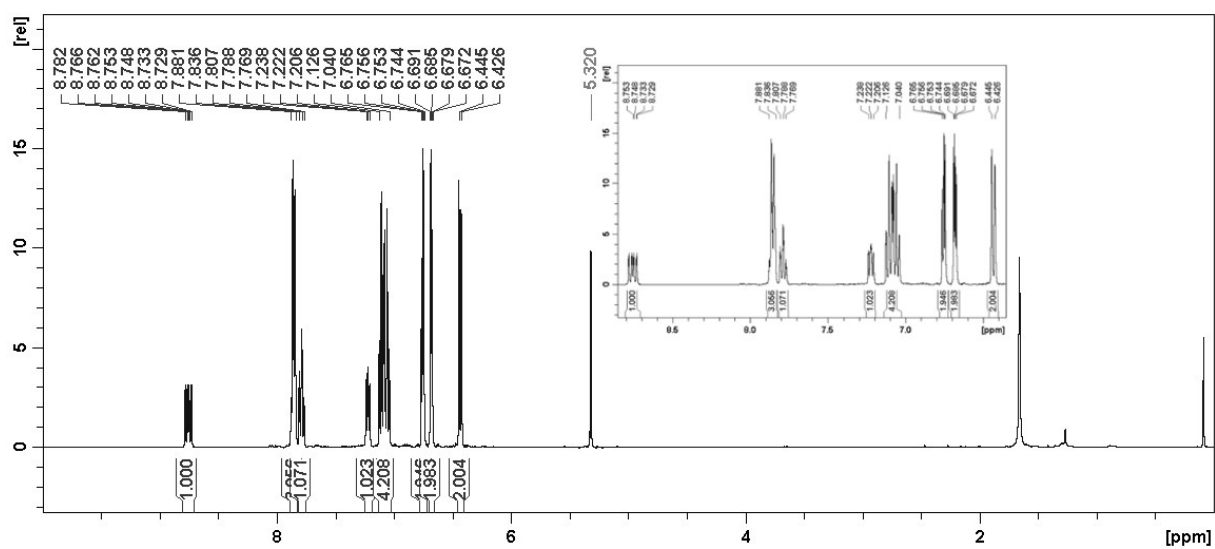


Figure S10. Carbon NMR spectrum of compound 3c.

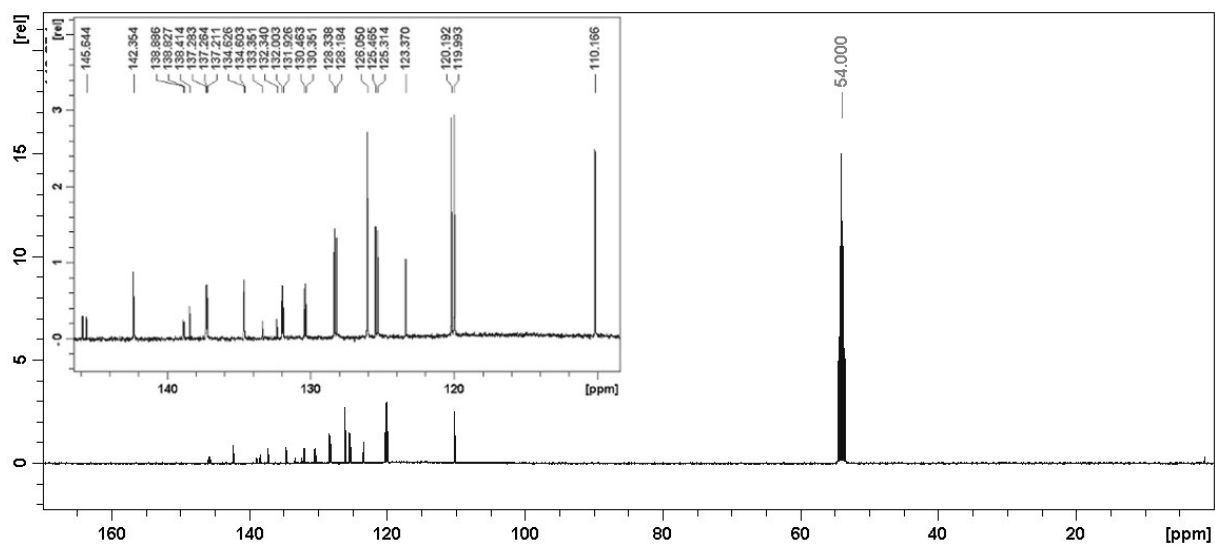


Figure S11. Proton NMR spectrum of compound 3ci.

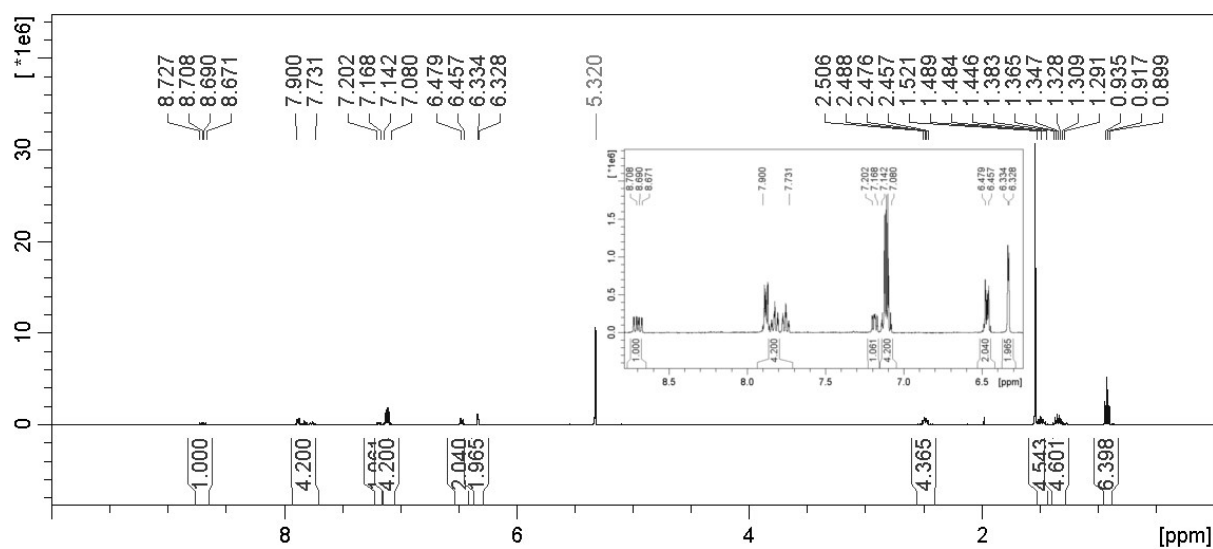


Figure S12. Carbon NMR spectrum of compound 3ci.

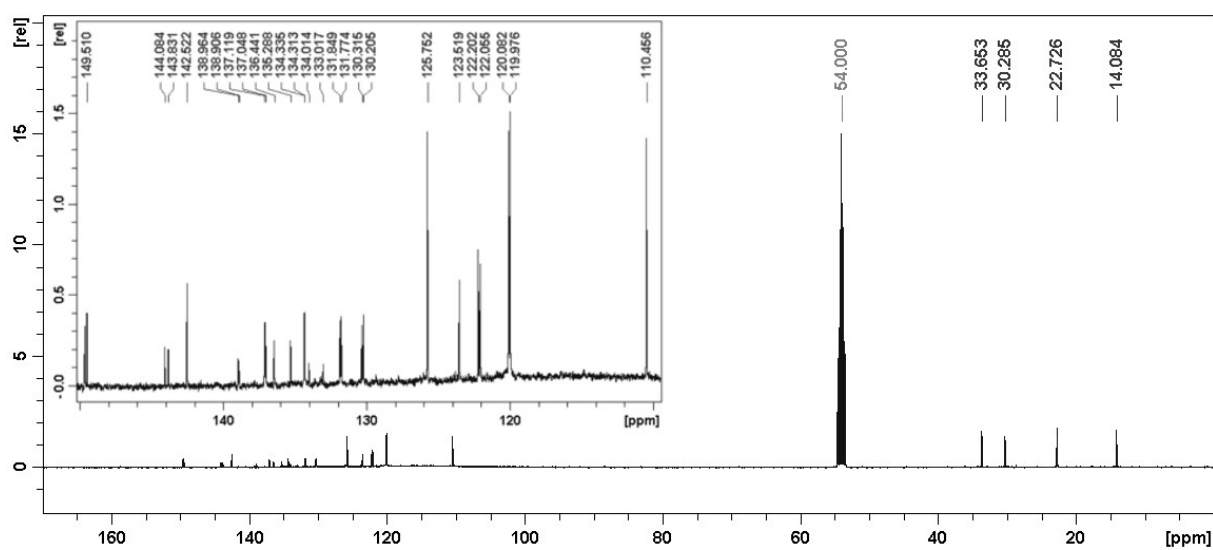


Figure S13. Proton NMR spectrum of compound 3d.

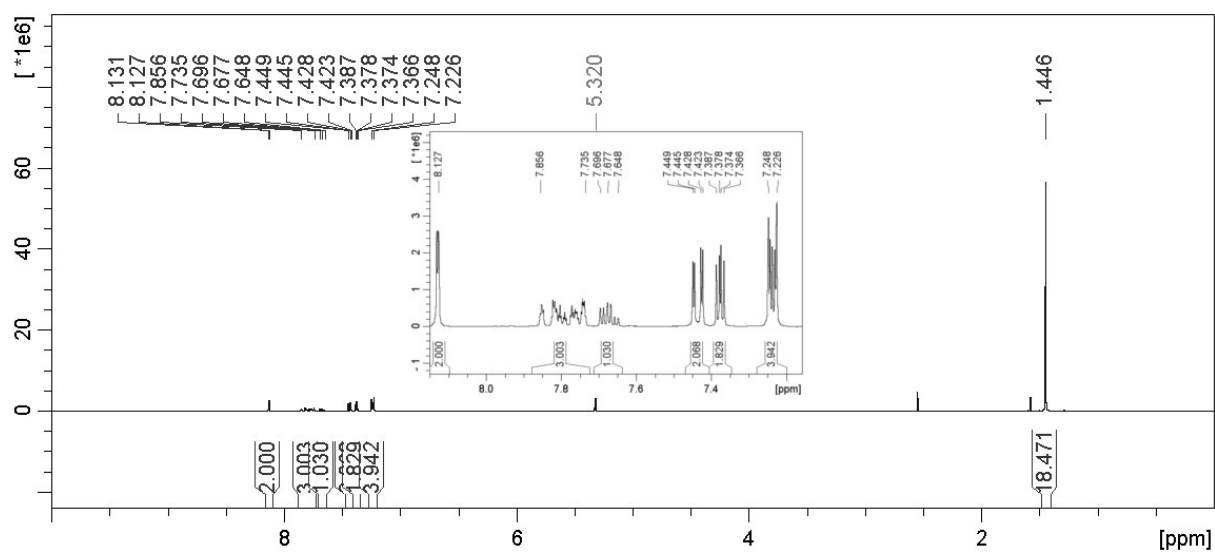


Figure S14. Carbon NMR spectrum of compound 3d.

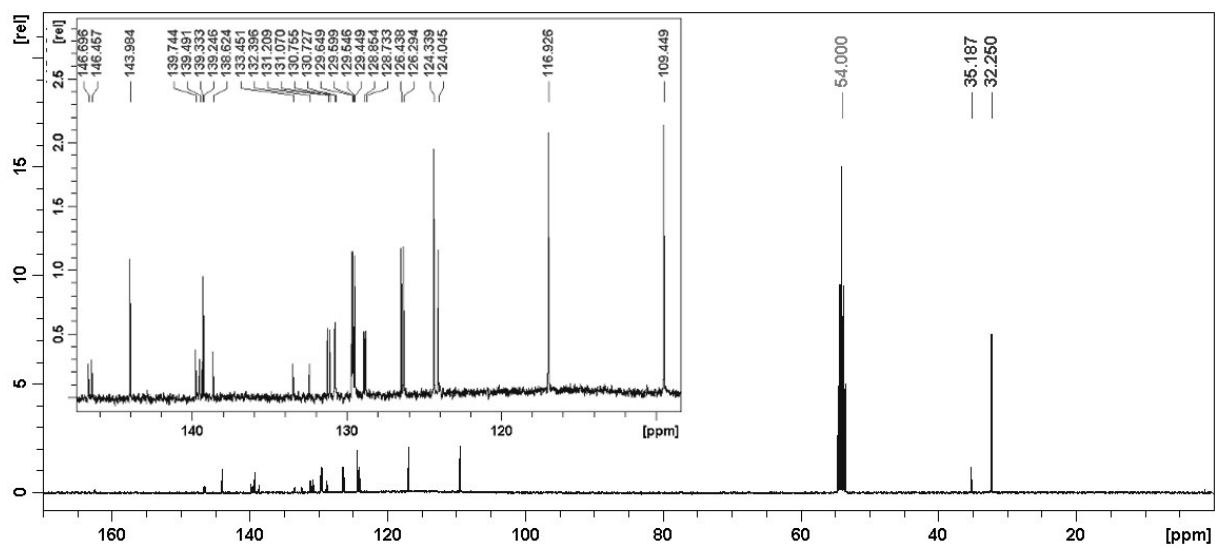


Figure S15. Proton NMR spectrum of compound 3di.

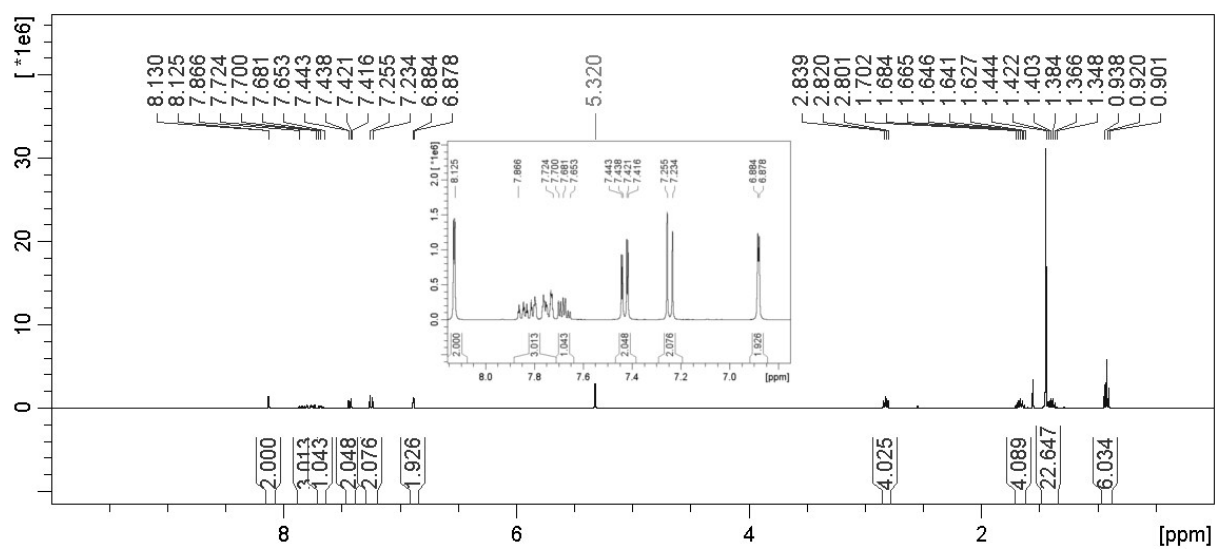


Figure S16. Carbon NMR spectrum of compound 3di.

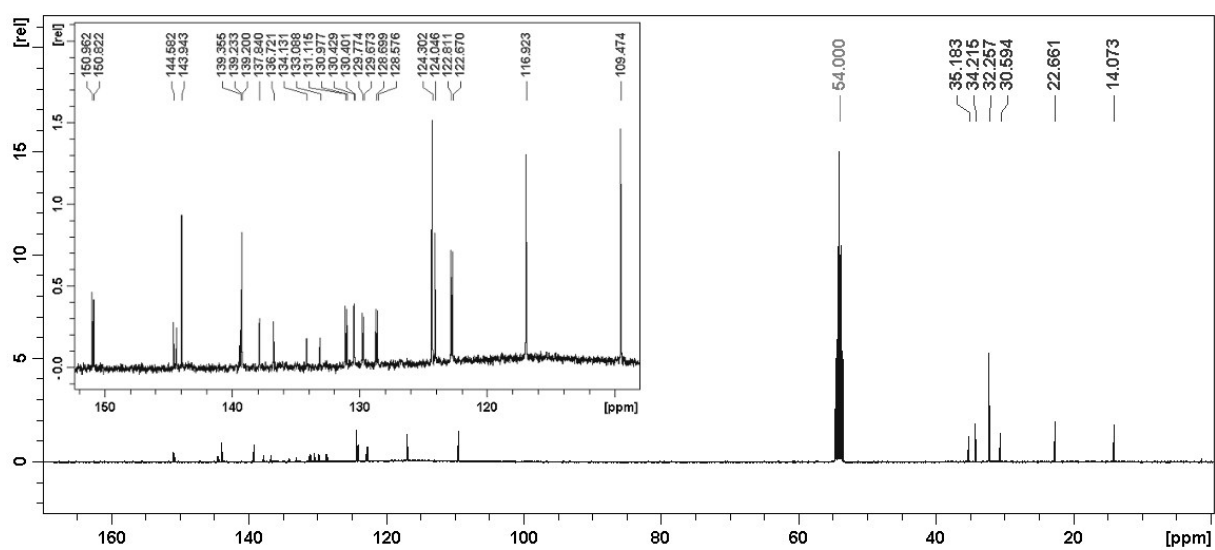


Figure S17. Proton NMR spectrum of compound 3e.

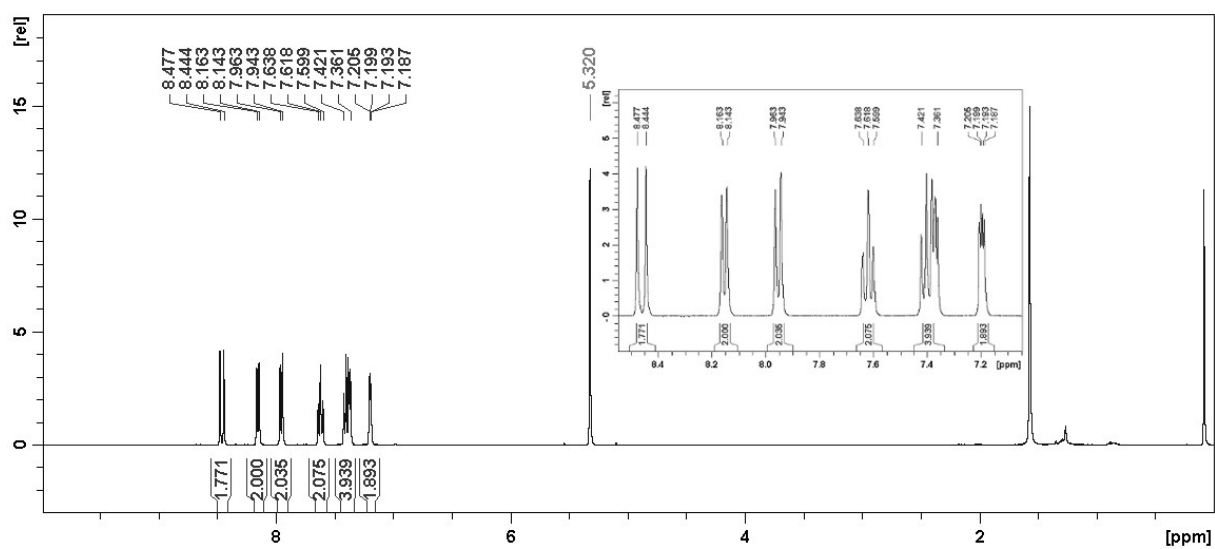


Figure S18. Carbon NMR spectrum of compound 3e.

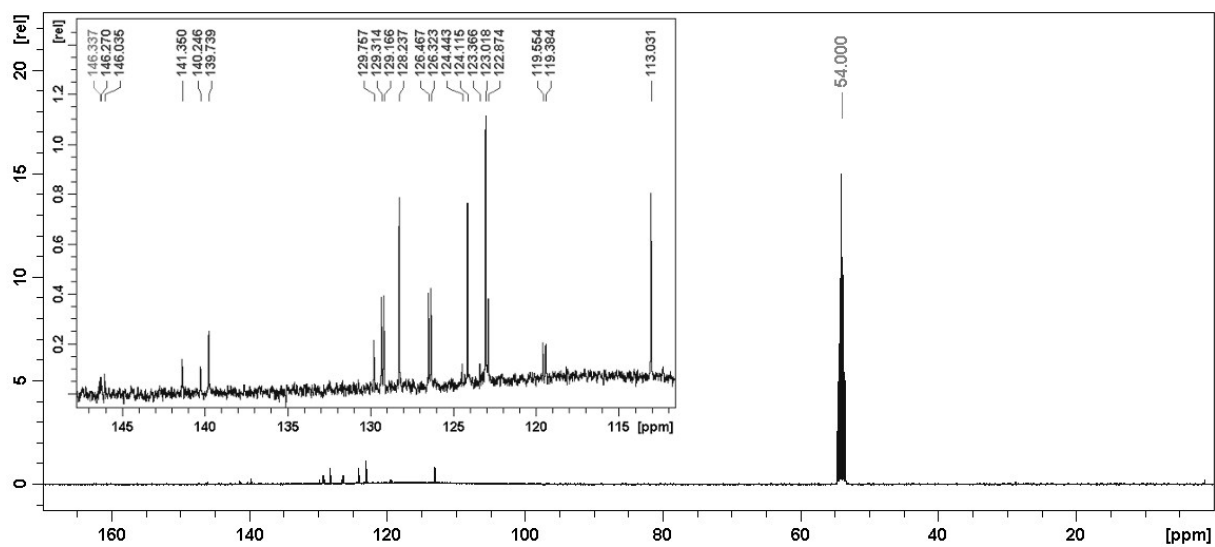


Figure S19. Proton NMR spectrum of compound 3ei.

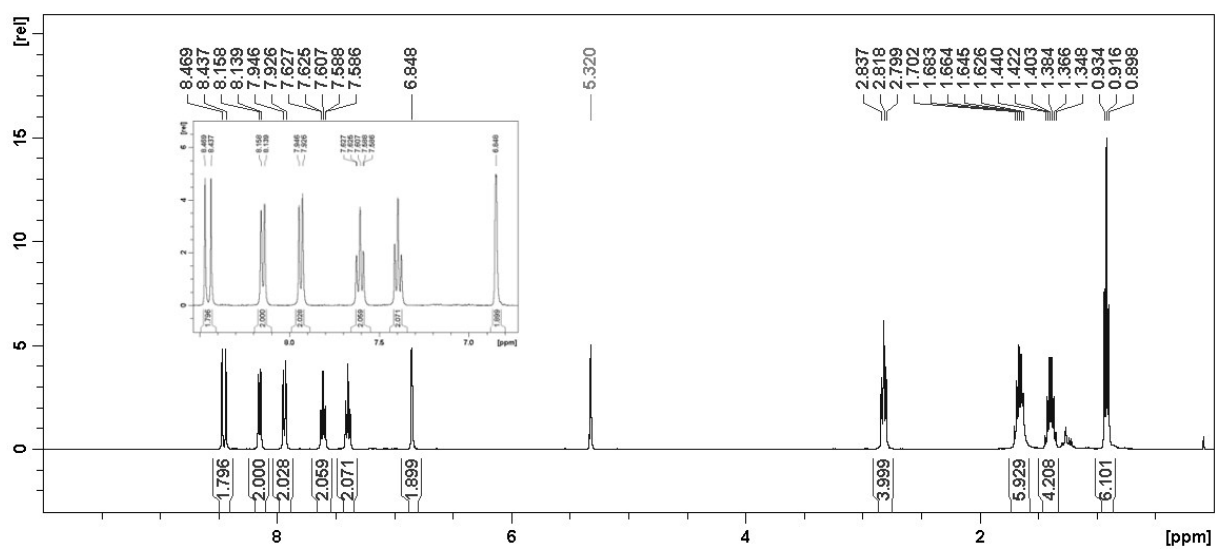
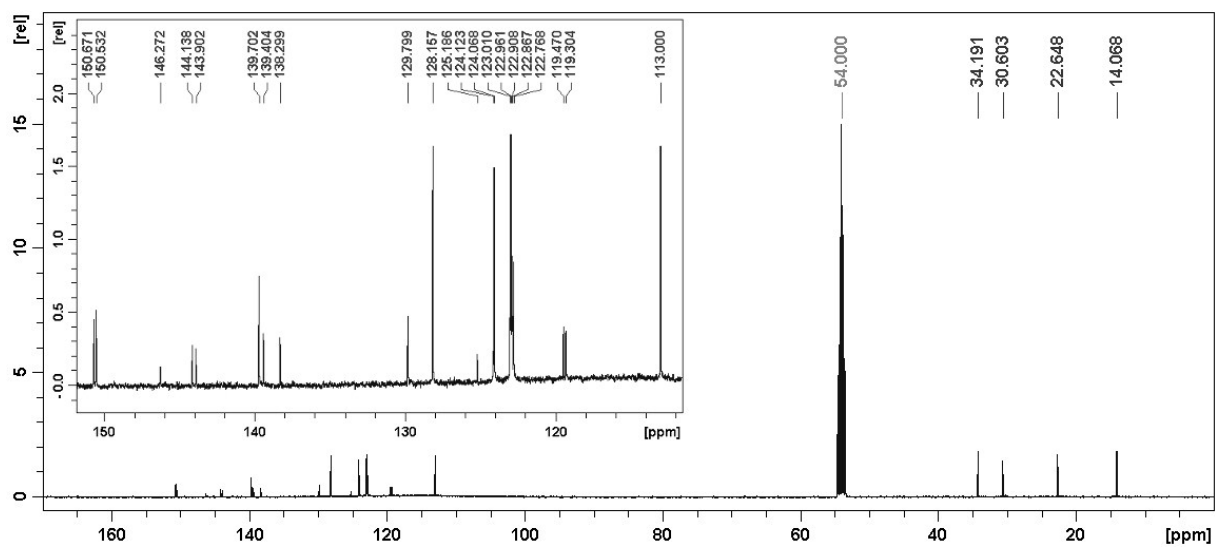


Figure S20. Carbon NMR spectrum of compound 3ei.



A.2 Assignment of NMR signals and 1D NOE difference spectra of 3c and 3ci

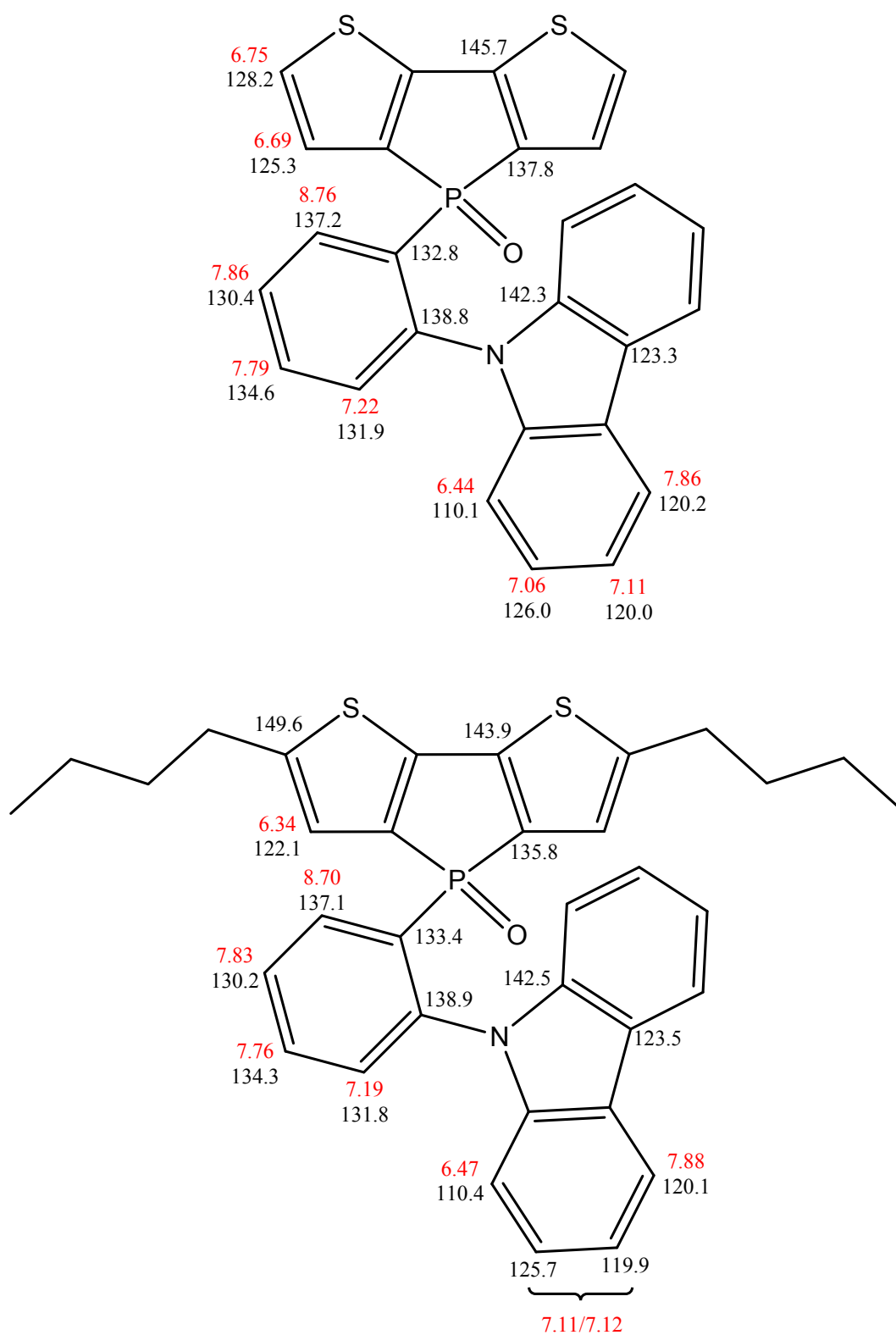


Figure S21. Assignment of proton (red) and carbon (black) NMR signals of **3c** (top) and **3ci** (bottom).

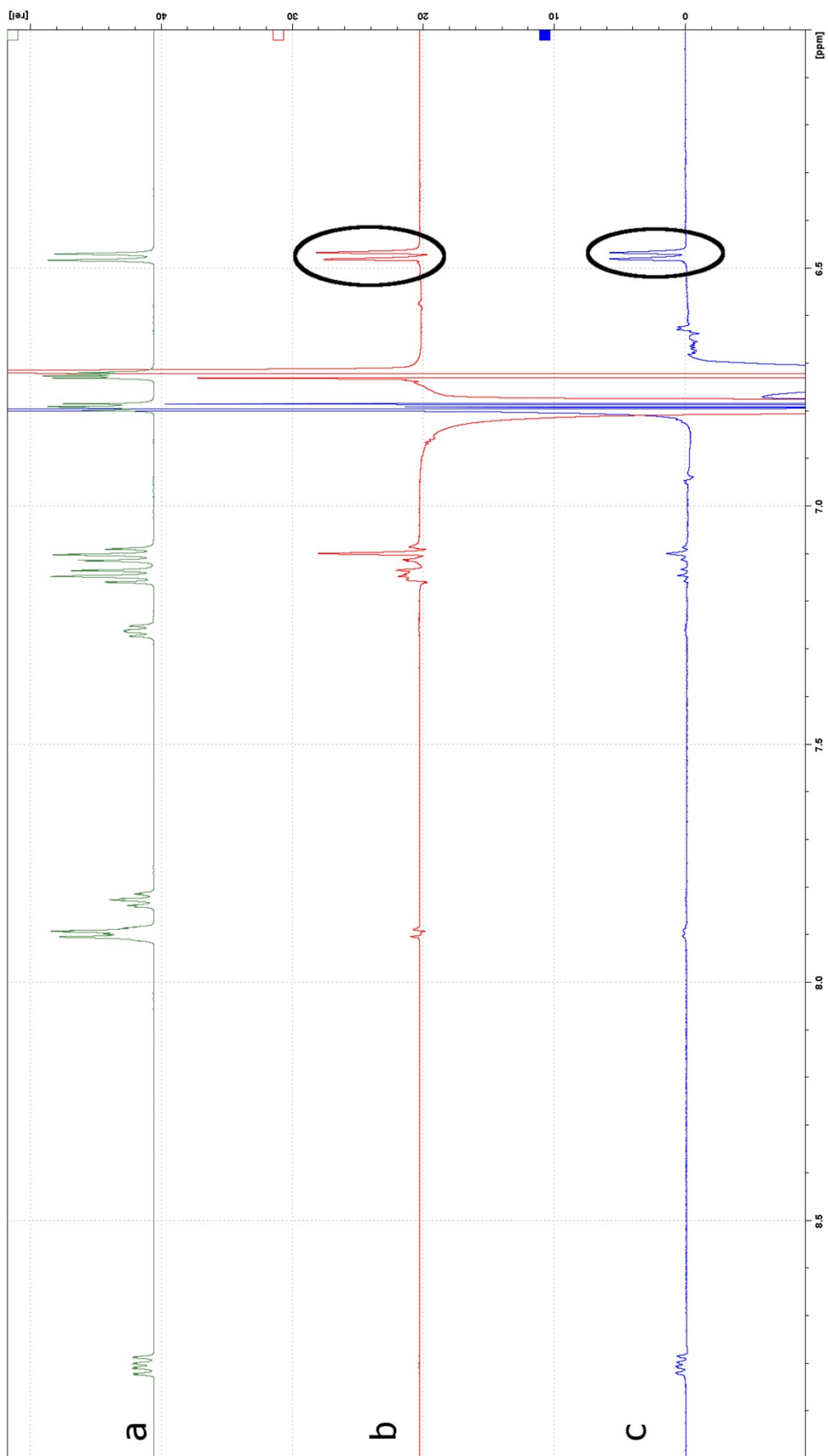


Figure S22. ^1H NMR (a) and 1D NOE difference spectrum of compound **3c** obtained upon irradiation of the thiophene α (b) and β (c) protons.

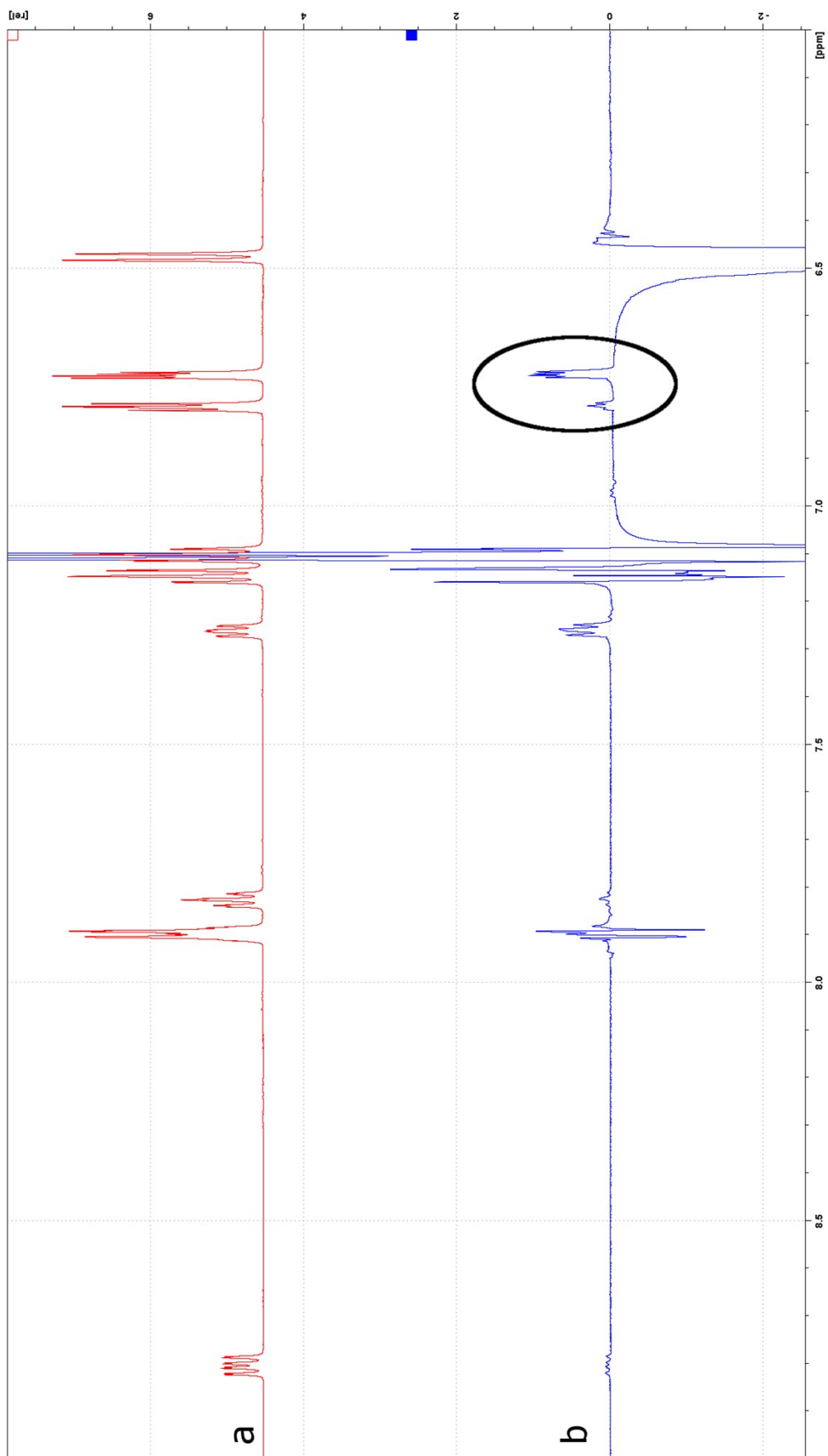


Figure S23. ¹H NMR (a) and 1D NOE difference spectrum of compound **3c** obtained upon irradiation of the carbazole 1 proton (b).

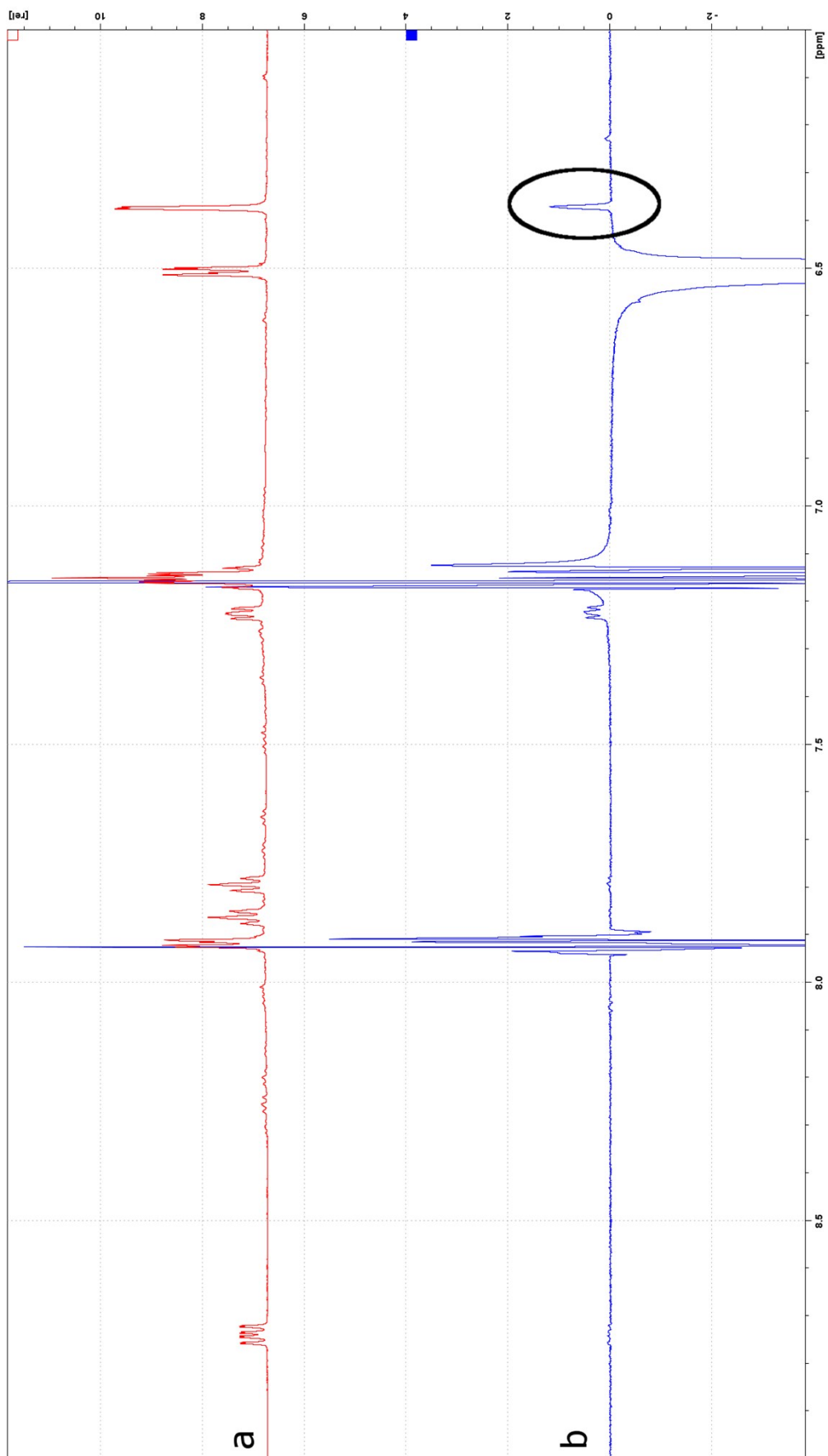


Figure S24. ¹H NMR (a) and 1D NOE difference spectrum of compound **3ci** obtained upon irradiation of the thiophene β (b) proton.

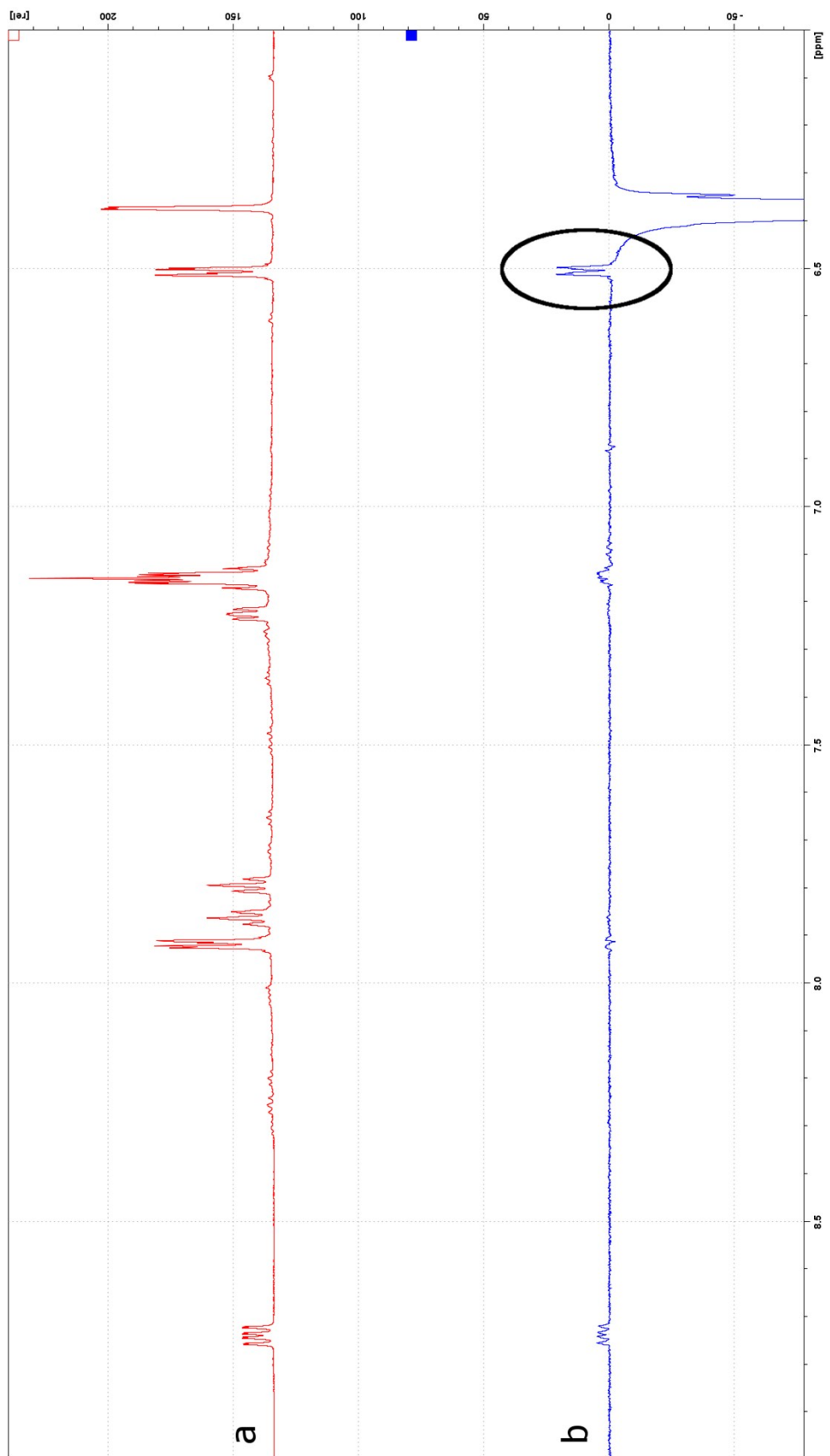


Figure S25. ¹H NMR (a) and 1D NOE difference spectrum of compound **3ci** obtained upon irradiation of the carbazole 1 proton (b).

B. Theoretical Data (B3LYP/6-31G+(d); Gaussian09)^{S1}

Figure S26. Frontier orbitals for the *para*- and *meta*-functionalized species.

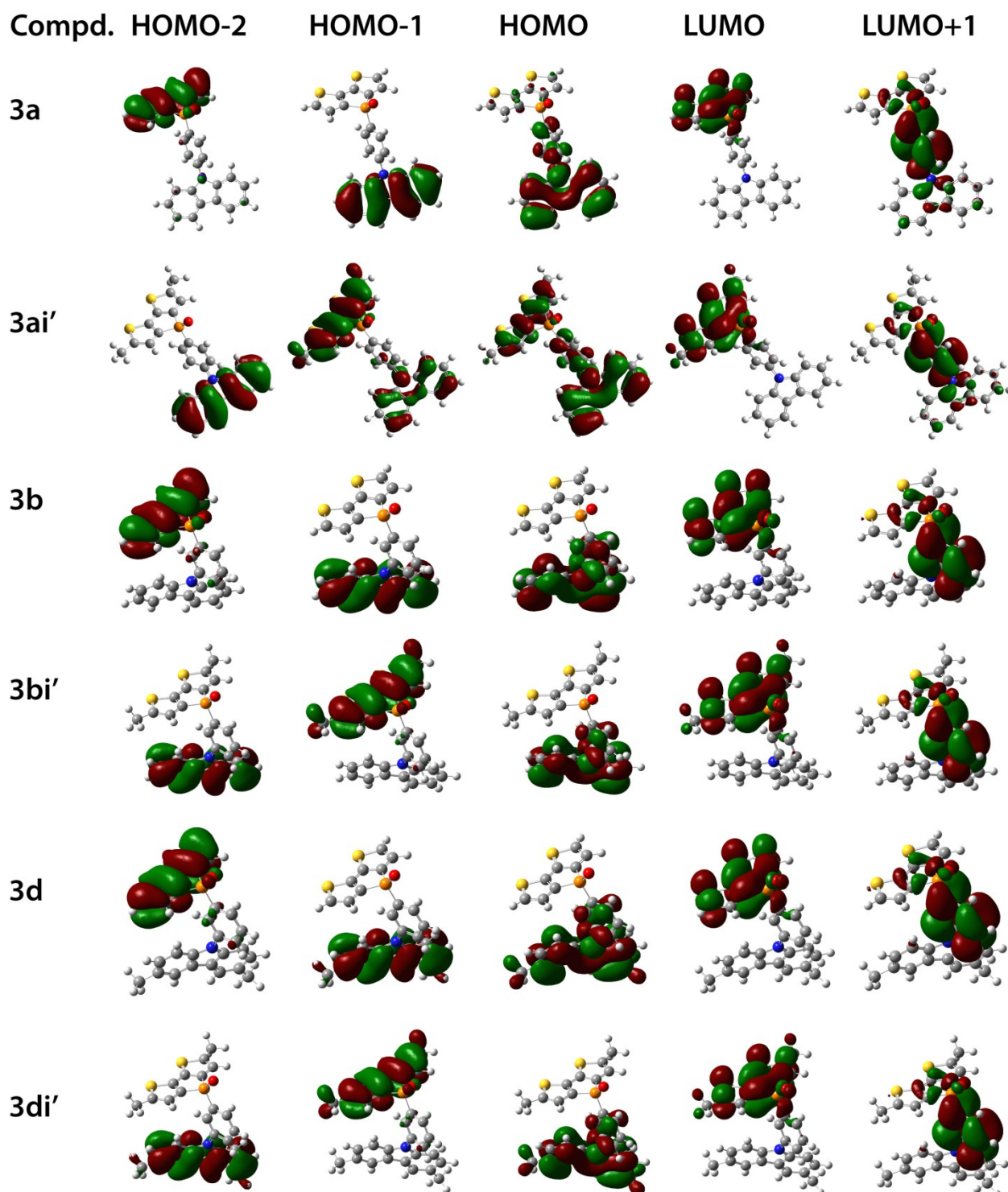


Figure S27. Frontier orbitals for the *ortho*-functionalized species.

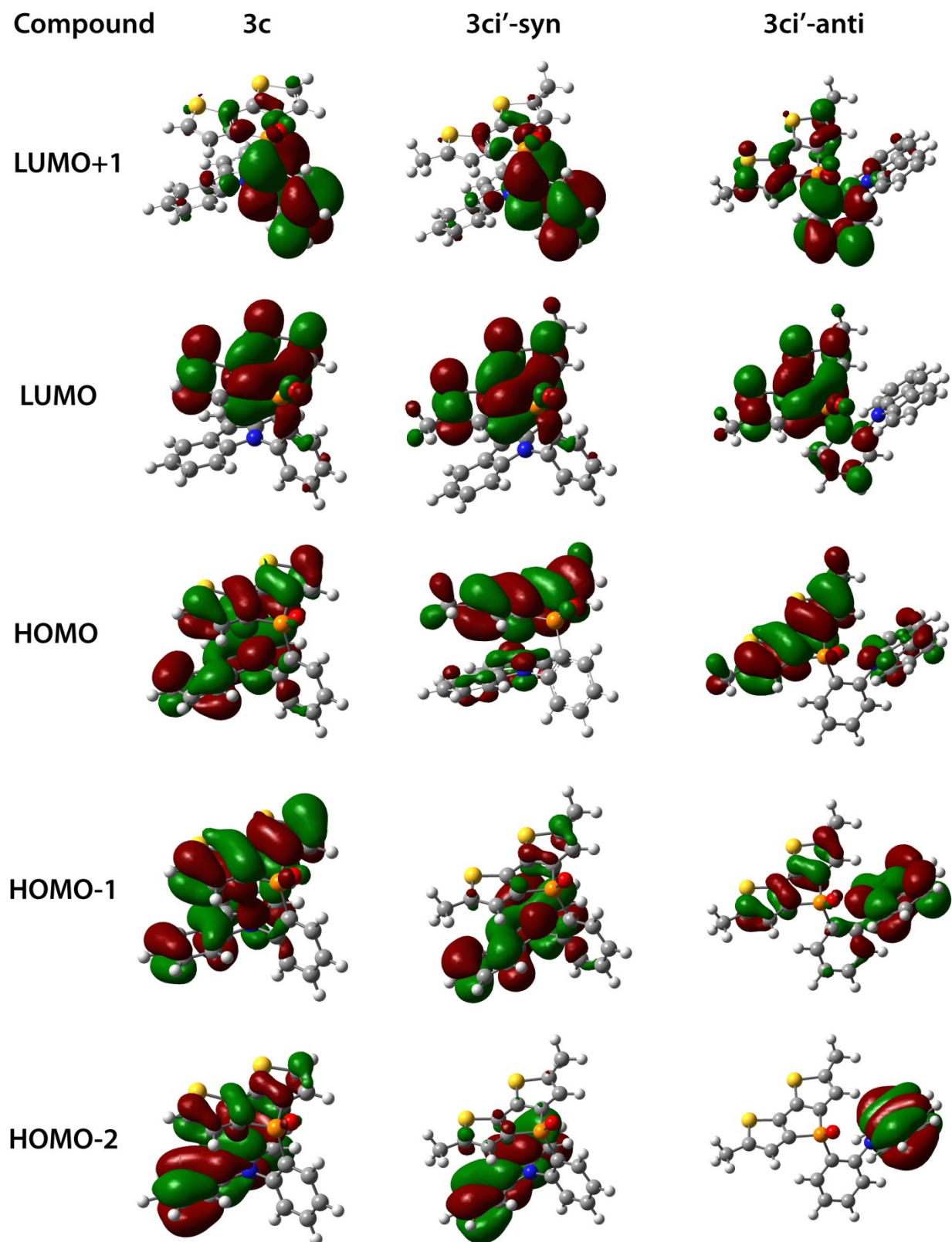


Figure S28. Frontier orbitals for the indolocarbazole-functionalized species.

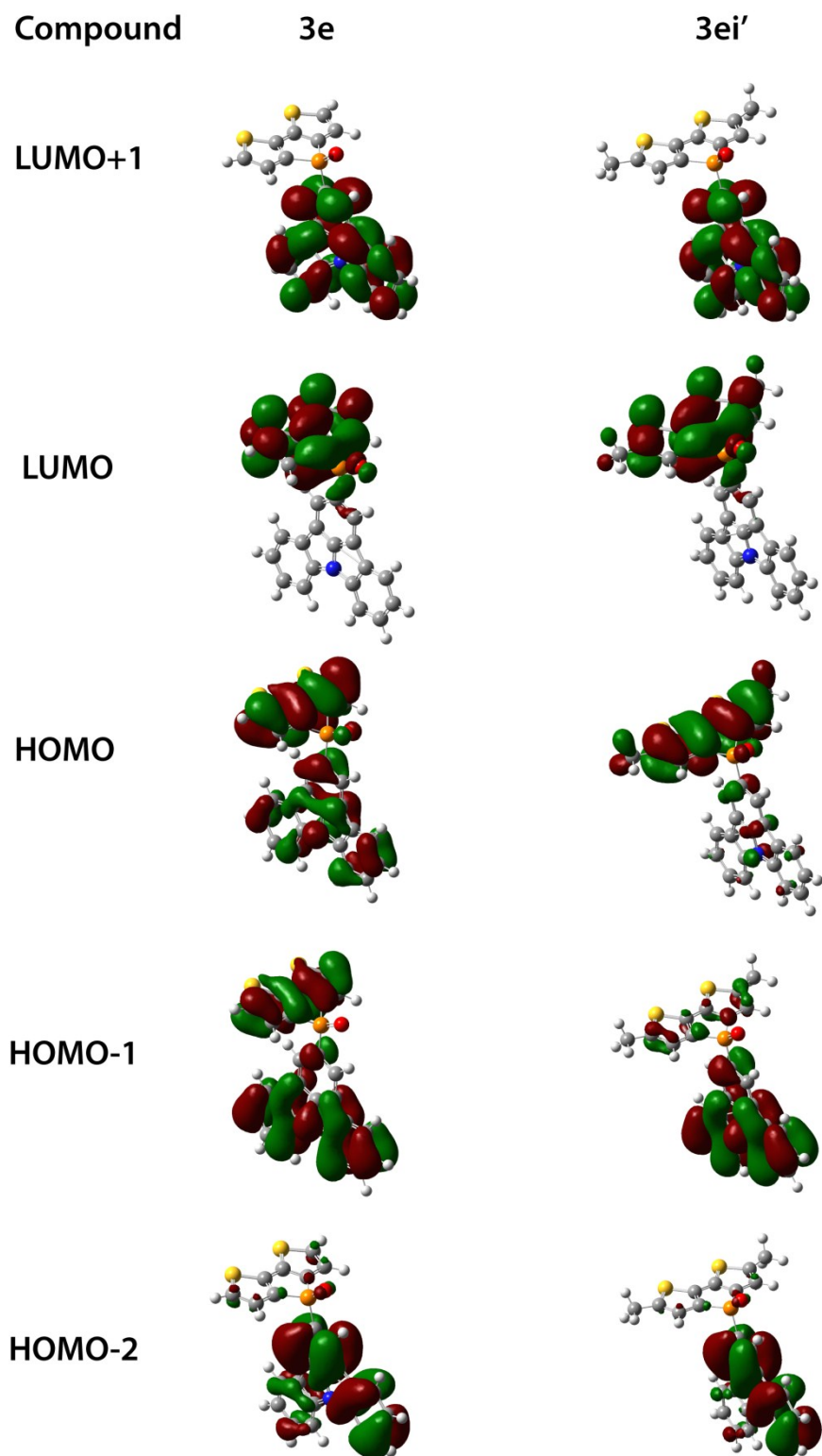


Table S1. Cartesian coordinates for **3a** from DFT calculations

Standard orientation:

Center Number	Atomic Number	Atomic Type	Coordinates (Angstroms)		
			X	Y	Z
1	6	0	4.382883	-2.581009	-2.066919
2	6	0	3.545569	-2.644026	-0.983359
3	6	0	3.527507	-1.426498	-0.249646
4	6	0	4.354227	-0.458184	-0.791427
5	16	0	5.166805	-1.027467	-2.209475
6	1	0	4.597721	-3.352156	-2.794442
7	1	0	2.975151	-3.528424	-0.722862
8	6	0	4.376865	0.799818	-0.061973
9	6	0	3.568428	0.832247	1.060384
10	16	0	5.225442	2.291424	-0.286023
11	6	0	3.630259	2.072755	1.751891
12	6	0	4.481636	2.959627	1.145291
13	1	0	3.080267	2.300674	2.657969
14	1	0	4.728288	3.967977	1.449495
15	15	0	2.715167	-0.777370	1.259022
16	6	0	0.956742	-0.507908	0.845710
17	6	0	-0.000299	-0.972289	1.756152
18	6	0	0.533633	0.135345	-0.326509
19	6	0	-1.359546	-0.789951	1.506566
20	1	0	0.331985	-1.464938	2.665012
21	6	0	-0.822075	0.304062	-0.588580
22	1	0	1.262675	0.492593	-1.049038
23	6	0	-1.778573	-0.155082	0.330587
24	1	0	-2.099428	-1.125130	2.226284
25	8	0	2.884862	-1.524730	2.547717
26	7	0	-3.159392	0.020507	0.066802
27	6	0	-4.134145	-0.987793	0.090261
28	6	0	-3.784779	1.230815	-0.265497
29	6	0	-5.391826	-0.418122	-0.231212
30	6	0	-5.169951	0.995366	-0.454875
31	6	0	-6.013751	2.063795	-0.779388
32	6	0	-5.474606	3.341048	-0.901989
33	1	0	-6.119303	4.177944	-1.154734
34	6	0	-4.102221	3.559815	-0.694187
35	1	0	-3.701214	4.565801	-0.783239
36	6	0	-3.240330	2.513681	-0.370813
37	6	0	-6.526097	-1.236184	-0.288546
38	6	0	-6.393460	-2.598336	-0.035861
39	1	0	-7.266685	-3.243137	-0.075748
40	6	0	-5.136393	-3.149533	0.264943
41	1	0	-5.050392	-4.216832	0.449775
42	6	0	-3.991819	-2.357395	0.329418
43	1	0	-3.024368	-2.794778	0.551934
44	1	0	-2.184616	2.695068	-0.199397
45	1	0	-7.077472	1.897468	-0.928162
46	1	0	-7.496756	-0.812344	-0.532495
47	1	0	-1.149699	0.775355	-1.509600

Table S2. Cartesian coordinates for **3b** from DFT calculations
Standard orientation:

Center Number	Atomic Number	Atomic Type	Coordinates (Angstroms)		
			X	Y	Z
1	6	0	-2.942852	-1.478503	3.288650
2	6	0	-2.739534	-2.126368	2.097784
3	6	0	-2.830644	-1.243900	0.987088
4	6	0	-3.102935	0.061811	1.356346
5	16	0	-3.250464	0.226201	3.072418
6	1	0	-2.935928	-1.893505	4.287545
7	1	0	-2.540391	-3.189579	2.025285
8	6	0	-3.218485	0.995924	0.247698
9	6	0	-3.039138	0.433371	-1.003781
10	16	0	-3.545454	2.692217	0.148377
11	6	0	-3.164976	1.377616	-2.059084
12	6	0	-3.437399	2.638077	-1.593050
13	1	0	-3.069828	1.140197	-3.112690
14	1	0	-3.592313	3.544637	-2.162552
15	15	0	-2.705390	-1.360056	-0.836292
16	6	0	-0.936268	-1.600699	-1.240583
17	6	0	-0.616383	-2.603678	-2.162513
18	6	0	0.078273	-0.826031	-0.665257
19	6	0	0.718054	-2.818605	-2.514409
20	1	0	-1.414462	-3.200570	-2.592850
21	6	0	1.411477	-1.033838	-1.031156
22	1	0	-0.154898	-0.064434	0.072731
23	6	0	1.728047	-2.032582	-1.964394
24	1	0	0.970746	-3.591827	-3.234552
25	1	0	2.763079	-2.175974	-2.258279
26	8	0	-3.587125	-2.331383	-1.561792
27	7	0	2.438267	-0.235103	-0.464299
28	6	0	3.580133	-0.712769	0.191795
29	6	0	2.490073	1.165365	-0.478608
30	6	0	4.370791	0.390781	0.601139
31	6	0	3.677304	1.587452	0.172021
32	6	0	3.960277	2.954578	0.272425
33	6	0	3.070384	3.873451	-0.275890
34	1	0	3.278404	4.937107	-0.202865
35	6	0	1.904641	3.437093	-0.928215
36	1	0	1.225277	4.169263	-1.356120
37	6	0	1.598299	2.082517	-1.041819
38	6	0	5.564542	0.163734	1.295840
39	6	0	5.947714	-1.144365	1.577303
40	1	0	6.872668	-1.332820	2.114768
41	6	0	5.144520	-2.225908	1.177072
42	1	0	5.455307	-3.239756	1.414395
43	6	0	3.952198	-2.027938	0.483723
44	1	0	3.332878	-2.868579	0.188709
45	1	0	0.698185	1.756731	-1.552657
46	1	0	4.866034	3.292733	0.769083
47	1	0	6.181223	0.999798	1.615371

Table S3. Cartesian coordinates for **3c** from DFT calculations
Standard orientation:

Center Number	Atomic Number	Atomic Type	Coordinates (Angstroms)		
			X	Y	Z
1	6	0	1.012261	-1.289584	-1.509569
2	6	0	0.646701	-0.045247	-1.997839
3	6	0	-0.277285	-0.120972	-3.074866
4	6	0	-0.607872	-1.418583	-3.377239
5	16	0	0.212979	-2.567800	-2.353909
6	1	0	-0.680495	0.734548	-3.604758
7	1	0	-1.296980	-1.775524	-4.131374
8	6	0	2.023788	-1.262438	-0.465242
9	6	0	2.472030	0.003641	-0.128271
10	16	0	2.846073	-2.491694	0.428599
11	6	0	3.494971	-0.012799	0.858332
12	6	0	3.802749	-1.290750	1.256776
13	1	0	3.991800	0.869099	1.248374
14	1	0	4.537623	-1.606573	1.985906
15	15	0	1.641341	1.248021	-1.177710
16	8	0	2.524637	2.086618	-2.061413
17	6	0	0.625385	2.359834	-0.105935
18	6	0	1.076357	3.692231	-0.102615
19	6	0	-0.487188	2.026597	0.691424
20	6	0	0.452355	4.665993	0.678015
21	1	0	1.919614	3.949519	-0.736812
22	6	0	-1.110983	3.009307	1.470368
23	6	0	-0.644027	4.323757	1.471431
24	1	0	0.821066	5.688145	0.660949
25	1	0	-1.970432	2.725154	2.071529
26	1	0	-1.138556	5.073456	2.083502
27	7	0	-1.044688	0.708071	0.722954
28	6	0	-0.806496	-0.244690	1.722535
29	6	0	-2.219710	0.347316	0.050547
30	6	0	-1.782833	-1.270020	1.628416
31	6	0	-2.686285	-0.891474	0.559393
32	6	0	-1.736134	-2.349527	2.520472
33	6	0	0.188382	-0.264047	2.703471
34	6	0	-0.739674	-2.381748	3.494868
35	1	0	-0.695207	-3.211398	4.195260
36	6	0	0.207271	-1.344431	3.585769
37	1	0	-2.473571	-3.146336	2.460687
38	1	0	0.971284	-1.383551	4.357921
39	1	0	0.924325	0.530559	2.776239
40	6	0	-3.845045	-1.463852	0.018802
41	6	0	-2.900744	1.033264	-0.958379
42	6	0	-4.059057	0.448666	-1.471738
43	1	0	-4.610680	0.962988	-2.254647
44	6	0	-4.525310	-0.790794	-0.995501
45	1	0	-4.216160	-2.415006	0.392720
46	1	0	-5.429421	-1.221694	-1.417284
47	1	0	-2.545082	1.990861	-1.327490

Table S4. Cartesian coordinates for **3d** from DFT calculations
Standard orientation:

Center Number	Atomic Number	Atomic Type	Coordinates (Angstroms)		
			X	Y	Z
1	6	0	0.155307	-2.851764	-2.718512
2	6	0	1.212314	-2.116525	-2.187941
3	6	0	0.970797	-1.148368	-1.201004
4	6	0	-0.337393	-0.921380	-0.762346
5	6	0	-1.399511	-1.643355	-1.319454
6	6	0	-1.154301	-2.615642	-2.295141
7	6	0	3.224893	-0.929222	-0.116457
8	6	0	4.057888	0.135194	0.303874
9	6	0	3.353502	1.364080	0.003998
10	6	0	2.118731	0.998023	-0.583595
11	7	0	2.044454	-0.400405	-0.656466
12	6	0	3.667720	2.718686	0.169796
13	6	0	2.771661	3.701934	-0.247441
14	6	0	1.555404	3.304379	-0.843729
15	6	0	1.212728	1.967988	-1.022290
16	6	0	3.605959	-2.260893	0.070867
17	6	0	4.840903	-2.506614	0.662376
18	6	0	5.702067	-1.467380	1.076624
19	6	0	5.295395	-0.146007	0.896035
20	6	0	-3.181490	-1.343712	1.008916
21	15	0	-3.139061	-1.367789	-0.822033
22	6	0	-3.414215	0.442605	-0.881620
23	6	0	-3.517748	0.944110	0.403835
24	6	0	-3.389471	-0.050936	1.456718
25	6	0	-3.547960	1.445375	-1.880260
26	6	0	-3.750931	2.688411	-1.338559
27	16	0	-3.782168	2.654104	0.406365
28	16	0	-3.460913	0.026296	3.183722
29	6	0	-3.208300	-1.697079	3.297584
30	6	0	-3.078155	-2.286900	2.067150
31	8	0	-4.086674	-2.269854	-1.553875
32	6	0	3.083086	5.170213	-0.069428
33	6	0	7.037564	-1.795449	1.703944
34	1	0	0.351358	-3.600230	-3.480381
35	1	0	2.226540	-2.274472	-2.538875
36	1	0	-0.514431	-0.186329	0.016156
37	1	0	-1.989617	-3.169957	-2.710268
38	1	0	4.614376	3.005689	0.620651
39	1	0	0.860303	4.070510	-1.178141
40	1	0	0.273024	1.697034	-1.490826
41	1	0	2.961339	-3.080977	-0.225675
42	1	0	5.151942	-3.537327	0.813685
43	1	0	5.939541	0.667303	1.220566
44	1	0	-3.506954	1.261499	-2.947250
45	1	0	-3.894813	3.628822	-1.851913
46	1	0	-3.175694	-2.163466	4.272232
47	1	0	-2.921785	-3.350341	1.931507
48	1	0	3.025809	5.712072	-1.020563
49	1	0	2.375348	5.651444	0.616323
50	1	0	4.087680	5.317345	0.336607
51	1	0	6.922068	-2.440880	2.582393
52	1	0	7.692855	-2.324754	1.001814
53	1	0	7.559875	-0.889528	2.023692

Table S5. Cartesian coordinates for **3e** from DFT calculations
Standard orientation:

Center Number	Atomic Number	Atomic Type	Coordinates (Angstroms)		
			X	Y	Z
1	6	0	3.387443	1.853667	-0.000230
2	6	0	4.397788	2.809009	-0.000308
3	6	0	5.689167	-0.768221	-0.000015
4	6	0	4.301631	-0.678785	-0.000021
5	7	0	3.459786	0.448830	-0.000128
6	6	0	1.996092	2.221689	-0.000229
7	6	0	1.658622	3.575200	-0.000304
8	6	0	2.672958	4.534343	-0.000382
9	6	0	4.021263	4.154390	-0.000384
10	6	0	6.258049	-2.044084	0.000119
11	6	0	5.462527	-3.197411	0.000245
12	6	0	4.069625	-3.107591	0.000242
13	6	0	3.465304	-1.849993	0.000111
14	6	0	-0.101034	0.493944	-0.000021
15	6	0	1.210023	0.979909	-0.000113
16	6	0	2.178173	-0.014531	-0.000056
17	6	0	2.067986	-1.395970	0.000082
18	6	0	0.746725	-1.861306	0.000168
19	6	0	-0.303467	-0.910373	0.000116
20	6	0	-3.957896	0.121393	3.202719
21	6	0	-2.989918	-0.723946	2.726003
22	6	0	-2.946992	-0.742811	1.305383
23	6	0	-3.887214	0.090743	0.727215
24	16	0	-4.838174	0.911406	1.918408
25	6	0	-3.887276	0.090491	-0.727190
26	6	0	-2.947082	-0.743240	-1.305146
27	6	0	-2.990244	-0.725000	-2.725767
28	6	0	-3.958360	0.120067	-3.202688
29	16	0	-4.838489	0.910560	-1.918589
30	15	0	-1.990693	-1.607684	0.000224
31	8	0	-1.991451	-3.108044	0.000417
32	1	0	5.444037	2.523464	-0.000311
33	1	0	6.311901	0.119714	-0.000114
34	1	0	0.615945	3.878754	-0.000306
35	1	0	2.414219	5.588495	-0.000438
36	1	0	4.792646	4.918431	-0.000445
37	1	0	7.339545	-2.139945	0.000126
38	1	0	5.936619	-4.173840	0.000346
39	1	0	3.460104	-4.006196	0.000339
40	1	0	-0.958960	1.159839	-0.000052
41	1	0	0.485849	-2.914772	0.000272
42	1	0	-4.218884	0.331982	4.230384
43	1	0	-2.343201	-1.308996	3.368949
44	1	0	-2.343583	-1.310276	-3.368563
45	1	0	-4.219487	0.330234	-4.230404

Table S6. Cartesian coordinates for **3ai'** from DFT calculations
Standard orientation:

Center Number	Atomic Number	Atomic Type	Coordinates (Angstroms)		
			X	Y	Z
1	6	0	4.454600	-0.920553	0.307510
2	6	0	5.697354	-0.421738	-0.157902
3	6	0	5.446227	0.898035	-0.698336
4	6	0	4.059394	1.149482	-0.545014
5	7	0	3.461132	0.039849	0.068289
6	6	0	4.341506	-2.199058	0.860541
7	6	0	5.500073	-2.966077	0.962544
8	6	0	6.742374	-2.480699	0.520907
9	6	0	6.846044	-1.213027	-0.043381
10	6	0	6.265524	1.874716	-1.275865
11	6	0	5.700839	3.079862	-1.682287
12	6	0	4.327560	3.319498	-1.507751
13	6	0	3.489698	2.364365	-0.936068
14	6	0	0.333087	-0.588988	1.976923
15	6	0	1.687071	-0.448728	1.676798
16	6	0	2.085502	-0.092467	0.382494
17	6	0	1.114182	0.129895	-0.605978
18	6	0	-0.236057	0.006947	-0.296150
19	6	0	-0.638880	-0.357163	0.996603
20	6	0	-4.164712	3.115771	0.652860
21	6	0	-3.310099	2.348061	1.404901
22	6	0	-3.250901	0.994029	0.976074
23	6	0	-4.066135	0.735783	-0.108845
24	16	0	-4.918689	2.155207	-0.618745
25	6	0	-4.047476	-0.642198	-0.570439
26	6	0	-3.217263	-1.482540	0.146352
27	6	0	-3.239418	-2.822192	-0.328999
28	6	0	-4.081089	-3.001829	-1.398804
29	16	0	-4.869132	-1.487629	-1.839813
30	15	0	-2.391212	-0.541815	1.482597
31	8	0	-2.534449	-1.013019	2.899325
32	6	0	-4.372952	-4.262077	-2.155009
33	6	0	-4.492766	4.569691	0.807225
34	1	0	3.386011	-2.587321	1.194446
35	1	0	5.437117	-3.961904	1.391183
36	1	0	7.626265	-3.103533	0.617257
37	1	0	7.804540	-0.842532	-0.395385
38	1	0	7.329574	1.694798	-1.399702
39	1	0	6.325593	3.844748	-2.132957
40	1	0	3.906858	4.270411	-1.821107
41	1	0	2.433470	2.563775	-0.794779
42	1	0	0.015101	-0.867416	2.976763
43	1	0	2.437965	-0.600826	2.444651
44	1	0	1.426203	0.382336	-1.613670
45	1	0	-0.977186	0.178926	-1.071434
46	1	0	-2.752084	2.750285	2.243040
47	1	0	-2.664939	-3.634695	0.101591
48	1	0	-3.781649	-5.082209	-1.739323
49	1	0	-5.429739	-4.544733	-2.089756
50	1	0	-4.121019	-4.172155	-3.217746
51	1	0	-5.556444	4.730924	1.015836
52	1	0	-3.922133	4.985664	1.641746
53	1	0	-4.242256	5.145838	-0.090731

Table S7. Cartesian coordinates for **3bi'** from DFT calculations
Standard orientation:

Center Number	Atomic Number	Atomic Type	Coordinates (Angstroms)		
			X	Y	Z
1	6	0	-2.942852	-1.478503	3.288650
2	6	0	-2.739534	-2.126368	2.097784
3	6	0	-2.830644	-1.243900	0.987088
4	6	0	-3.102935	0.061811	1.356346
5	16	0	-3.250464	0.226201	3.072418
6	1	0	-2.935928	-1.893505	4.287545
7	1	0	-2.540391	-3.189579	2.025285
8	6	0	-3.218485	0.995924	0.247698
9	6	0	-3.039138	0.433371	-1.003781
10	16	0	-3.545454	2.692217	0.148377
11	6	0	-3.164976	1.377616	-2.059084
12	6	0	-3.437399	2.638077	-1.593050
13	1	0	-3.069828	1.140197	-3.112690
14	1	0	-3.592313	3.544637	-2.162552
15	15	0	-2.705390	-1.360056	-0.836292
16	6	0	-0.936268	-1.600699	-1.240583
17	6	0	-0.616383	-2.603678	-2.162513
18	6	0	0.078273	-0.826031	-0.665257
19	6	0	0.718054	-2.818605	-2.514409
20	1	0	-1.414462	-3.200570	-2.592850
21	6	0	1.411477	-1.033838	-1.031156
22	1	0	-0.154898	-0.064434	0.072731
23	6	0	1.728047	-2.032582	-1.964394
24	1	0	0.970746	-3.591827	-3.234552
25	1	0	2.763079	-2.175974	-2.258279
26	8	0	-3.587125	-2.331383	-1.561792
27	7	0	2.438267	-0.235103	-0.464299
28	6	0	3.580133	-0.712769	0.191795
29	6	0	2.490073	1.165365	-0.478608
30	6	0	4.370791	0.390781	0.601139
31	6	0	3.677304	1.587452	0.172021
32	6	0	3.960277	2.954578	0.272425
33	6	0	3.070384	3.873451	-0.275890
34	1	0	3.278404	4.937107	-0.202865
35	6	0	1.904641	3.437093	-0.928215
36	1	0	1.225277	4.169263	-1.356120
37	6	0	1.598299	2.082517	-1.041819
38	6	0	5.564542	0.163734	1.295840
39	6	0	5.947714	-1.144365	1.577303
40	1	0	6.872668	-1.332820	2.114768
41	6	0	5.144520	-2.225908	1.177072
42	1	0	5.455307	-3.239756	1.414395
43	6	0	3.952198	-2.027938	0.483723
44	1	0	3.332878	-2.868579	0.188709
45	1	0	0.698185	1.756731	-1.552657
46	1	0	4.866034	3.292733	0.769083
47	1	0	6.181223	0.999798	1.615371

Table S8. Cartesian coordinates for **3ci'-syn** from DFT calculations
Standard orientation:

Center Number	Atomic Number	Atomic Type	Coordinates (Angstroms)		
			X	Y	Z
1	6	0	0.772486	-2.991562	2.741249
2	6	0	-0.583630	-2.946287	3.058953
3	6	0	-1.455184	-2.216251	2.254163
4	6	0	-0.984929	-1.525613	1.131788
5	6	0	0.385958	-1.559828	0.802328
6	6	0	1.246228	-2.307571	1.623134
7	6	0	0.881788	1.049016	-0.545193
8	15	0	1.049388	-0.765918	-0.721562
9	6	0	2.862517	-0.660663	-0.476316
10	6	0	3.224227	0.656380	-0.272624
11	6	0	2.126114	1.603547	-0.305312
12	6	0	3.981150	-1.539801	-0.519427
13	6	0	5.181710	-0.899604	-0.333269
14	16	0	4.940757	0.831868	-0.111885
15	16	0	2.045382	3.328397	-0.175258
16	6	0	0.306126	3.308165	-0.460046
17	6	0	-0.147832	2.025516	-0.638897
18	8	0	0.566468	-1.420826	-1.981944
19	6	0	6.559494	-1.488348	-0.313747
20	6	0	-0.481122	4.582626	-0.486013
21	6	0	-2.650084	0.306791	0.914718
22	6	0	-3.788667	0.565123	0.111558
23	6	0	-3.800809	-0.439593	-0.933025
24	6	0	-2.663174	-1.258732	-0.733214
25	7	0	-1.932827	-0.769642	0.369651
26	6	0	-4.677799	-0.720508	-1.988359
27	6	0	-4.416122	-1.813452	-2.807499
28	6	0	-3.285812	-2.619347	-2.586621
29	6	0	-2.392625	-2.355626	-1.551564
30	6	0	-2.351767	1.080706	2.038484
31	6	0	-3.211430	2.133157	2.347193
32	6	0	-4.337823	2.413220	1.554783
33	6	0	-4.631191	1.634941	0.437957
34	1	0	1.462638	-3.556874	3.360017
35	1	0	-0.964748	-3.478122	3.925434
36	1	0	-2.514433	-2.169195	2.485466
37	1	0	2.304199	-2.345092	1.390969
38	1	0	3.915181	-2.607717	-0.697170
39	1	0	-1.188493	1.802391	-0.834988
40	1	0	6.498899	-2.566051	-0.487310
41	1	0	7.200338	-1.059744	-1.092453
42	1	0	7.060838	-1.331182	0.648218
43	1	0	-0.182418	5.234465	-1.315155
44	1	0	-1.542494	4.349989	-0.603915
45	1	0	-0.365561	5.154553	0.441455
46	1	0	-5.552660	-0.098902	-2.156827
47	1	0	-5.087866	-2.046199	-3.628158
48	1	0	-3.095606	-3.462778	-3.243512
49	1	0	-1.501211	-2.953948	-1.412987
50	1	0	-1.478777	0.873536	2.648007
51	1	0	-3.002686	2.749574	3.216655
52	1	0	-4.987090	3.241956	1.820416
53	1	0	-5.505814	1.849543	-0.169520

Table S9. Cartesian coordinates for **3ci⁻-anti** from DFT calculations
Standard orientation:

Center Number	Atomic Number	Atomic Type	Coordinates (Angstroms)		
			X	Y	Z
1	6	0	0.211620	-1.633500	-1.242343
2	6	0	-0.381959	-0.595140	-1.936917
3	6	0	-1.658241	-0.934803	-2.462845
4	6	0	-2.040101	-2.219993	-2.158596
5	16	0	-0.801032	-3.035476	-1.209993
6	1	0	-2.278177	-0.265713	-3.050669
7	6	0	1.559077	-1.361347	-0.770831
8	6	0	2.043431	-0.107270	-1.092996
9	16	0	2.745139	-2.305612	0.062388
10	6	0	3.386921	0.095676	-0.673425
11	6	0	3.919829	-0.997185	-0.030978
12	1	0	3.954110	1.004865	-0.847481
13	15	0	0.791273	0.796150	-2.066427
14	8	0	1.187799	1.229646	-3.452499
15	6	0	0.216232	2.275428	-1.114655
16	6	0	0.456322	3.492861	-1.776240
17	6	0	-0.396222	2.312198	0.153991
18	6	0	0.108812	4.713927	-1.196943
19	1	0	0.913059	3.457797	-2.760972
20	6	0	-0.743833	3.540740	0.729726
21	6	0	-0.491928	4.739887	0.062759
22	1	0	0.305301	5.639519	-1.731588
23	1	0	-1.217261	3.539214	1.707854
24	1	0	-0.767162	5.684444	0.524672
25	7	0	-0.708953	1.126007	0.894132
26	6	0	0.062752	0.608514	1.942995
27	6	0	-2.000735	0.594778	1.004141
28	6	0	-0.710737	-0.334246	2.668211
29	6	0	-2.030326	-0.342925	2.067945
30	6	0	-0.139055	-0.999895	3.760590
31	6	0	1.374785	0.919618	2.308510
32	6	0	1.173592	-0.703643	4.124237
33	1	0	1.626356	-1.208986	4.973120
34	6	0	1.916862	0.252746	3.407293
35	1	0	-0.715718	-1.728620	4.325123
36	1	0	2.934746	0.479234	3.714462
37	1	0	1.954498	1.652404	1.756208
38	6	0	-3.222023	-1.021444	2.354490
39	6	0	-3.139350	0.887255	0.249001
40	6	0	-4.317651	0.208942	0.562785
41	1	0	-5.219609	0.422328	-0.005392
42	6	0	-4.360637	-0.742042	1.599429
43	1	0	-3.262666	-1.746427	3.163869
44	1	0	-5.293559	-1.254496	1.818970
45	1	0	-3.110850	1.620214	-0.551806
46	6	0	5.295028	-1.162396	0.545055
47	1	0	5.842129	-1.988508	0.073524
48	1	0	5.871524	-0.245425	0.384138
49	1	0	5.267616	-1.357332	1.624652
50	6	0	-3.317111	-2.922259	-2.512488
51	1	0	-3.923053	-2.275821	-3.155768
52	1	0	-3.136168	-3.859247	-3.053711
53	1	0	-3.911774	-3.160416	-1.621476

Table S10. Cartesian coordinates for **3di'** from DFT calculations
Standard orientation:

Center Number	Atomic Number	Atomic Type	Coordinates (Angstroms)		
			X	Y	Z
1	6	0	0.512388	-1.973145	-3.503781
2	6	0	1.534843	-1.379219	-2.767963
3	6	0	1.246916	-0.746130	-1.549031
4	6	0	-0.071743	-0.706182	-1.085740
5	6	0	-1.099936	-1.279283	-1.843323
6	6	0	-0.807846	-1.921111	-3.051706
7	6	0	3.476841	-0.765507	-0.393648
8	6	0	4.256538	0.160990	0.339649
9	6	0	3.505777	1.397892	0.386648
10	6	0	2.298079	1.173028	-0.316897
11	7	0	2.285315	-0.145467	-0.793095
12	6	0	3.757663	2.656589	0.946572
13	6	0	2.826057	3.684409	0.807343
14	6	0	1.637912	3.432266	0.087661
15	6	0	1.357364	2.194058	-0.480776
16	6	0	3.910750	-2.080272	-0.585939
17	6	0	5.143796	-2.442454	-0.053341
18	6	0	5.952619	-1.537386	0.667768
19	6	0	5.493883	-0.235170	0.862338
20	6	0	-2.904574	-1.695027	0.448350
21	15	0	-2.853827	-1.223348	-1.319146
22	6	0	-3.210693	0.522452	-0.897557
23	6	0	-3.341681	0.653312	0.471630
24	6	0	-3.172913	-0.580819	1.220443
25	6	0	-3.381035	1.751718	-1.591326
26	6	0	-3.642894	2.810566	-0.756804
27	16	0	-3.679627	2.290216	0.926759
28	16	0	-3.253312	-0.976317	2.904729
29	6	0	-2.920194	-2.673632	2.565427
30	6	0	-2.761796	-2.881939	1.217528
31	8	0	-3.752144	-1.936089	-2.285567
32	6	0	3.069882	5.048030	1.412014
33	6	0	7.289341	-1.984992	1.213041
34	6	0	-3.891239	4.243368	-1.118615
35	6	0	-2.845397	-3.673677	3.678792
36	1	0	0.743540	-2.463851	-4.444504
37	1	0	2.556432	-1.389329	-3.132815
38	1	0	-0.283389	-0.232899	-0.132378
39	1	0	-1.616483	-2.367775	-3.620973
40	1	0	4.683152	2.834966	1.488286
41	1	0	0.914756	4.235764	-0.028353
42	1	0	0.438010	2.035224	-1.033486
43	1	0	3.306588	-2.802231	-1.124223
44	1	0	5.495084	-3.461547	-0.195195
45	1	0	6.097047	0.472164	1.425965
46	1	0	-3.325425	1.860409	-2.668754
47	1	0	-2.555798	-3.861304	0.800452
48	1	0	3.012052	5.839859	0.656160
49	1	0	2.326228	5.285640	2.182225
50	1	0	4.057448	5.105673	1.878051
51	1	0	7.188619	-2.874615	1.845391
52	1	0	7.987363	-2.242497	0.407286
53	1	0	7.755982	-1.200439	1.815159
54	1	0	-3.813909	4.364659	-2.202314
55	1	0	-4.890129	4.576689	-0.815117
56	1	0	-3.163587	4.917516	-0.652665
57	1	0	-2.056771	-3.428280	4.399046

58	1	0	-3.788263	-3.743054	4.232966
59	1	0	-2.626419	-4.662309	3.266836

Table S11. Cartesian coordinates for **3ei'** from DFT calculations
Standard orientation:

Center Number	Atomic Number	Atomic Type	Coordinates (Angstroms)		
			X	Y	Z
1	6	0	-4.586716	-0.649419	-0.073290
2	6	0	-5.975234	-0.723746	-0.074250
3	6	0	-4.641846	2.812676	0.356091
4	6	0	-3.642923	1.853312	0.232114
5	7	0	-3.731894	0.460169	0.060764
6	6	0	-3.763831	-1.820416	-0.225597
7	6	0	-4.382457	-3.061678	-0.377660
8	6	0	-5.776286	-3.136240	-0.378650
9	6	0	-6.558600	-1.983581	-0.229119
10	6	0	-4.249490	4.144026	0.515335
11	6	0	-2.896828	4.506591	0.549725
12	6	0	-1.893925	3.543396	0.425801
13	6	0	-2.247175	2.203483	0.265359
14	6	0	-1.045569	-1.860935	-0.249548
15	6	0	-2.361440	-1.385174	-0.179949
16	6	0	-2.455448	-0.013591	-0.006621
17	6	0	-1.475664	0.962599	0.107314
18	6	0	-0.170235	0.466098	0.035657
19	6	0	0.015841	-0.929309	-0.139825
20	6	0	3.682759	0.515493	-3.174839
21	6	0	2.711039	-0.380799	-2.803993
22	6	0	2.663718	-0.607357	-1.401300
23	6	0	3.606994	0.123651	-0.705952
24	16	0	4.567192	1.101597	-1.766719
25	6	0	3.602001	-0.086861	0.732252
26	6	0	2.654989	-0.985798	1.182264
27	6	0	2.692133	-1.170539	2.591348
28	6	0	3.660039	-0.418706	3.210270
29	16	0	4.553407	0.545714	2.035467
30	15	0	1.696056	-1.640835	-0.236613
31	8	0	1.674143	-3.126059	-0.452171
32	6	0	4.034155	0.994169	-4.550593
33	6	0	4.000670	-0.353607	4.668048
34	1	0	-6.587927	0.163702	0.041006
35	1	0	-5.691397	2.540704	0.329975
36	1	0	-3.783067	-3.959569	-0.493999
37	1	0	-6.261453	-4.100010	-0.496930
38	1	0	-7.641119	-2.067260	-0.233138
39	1	0	-5.011814	4.910853	0.613809
40	1	0	-2.625739	5.550217	0.674523
41	1	0	-0.847683	3.833142	0.453468
42	1	0	-0.796495	-2.908509	-0.385208
43	1	0	0.695631	1.117388	0.109305
44	1	0	2.059264	-0.862471	-3.524341
45	1	0	2.035786	-1.837730	3.138875
46	1	0	3.920341	2.079645	-4.650743
47	1	0	5.066456	0.745072	-4.821456
48	1	0	3.373629	0.519936	-5.281326
49	1	0	3.333063	-1.013602	5.228288
50	1	0	5.030175	-0.673921	4.864498
51	1	0	3.888006	0.658836	5.072296

Reference for DFT calculations:

- S1. M. J. Frisch, G. W. Trucks, H. B. Schlegel, G. E. Scuseria, M. A. Robb, J. R. Cheeseman, J. A. Jr. Montgomery, T. Vreven, K. N. Kudin, J. C. Burant, J. M. Millam, S. S. Iyengar, J. Tomasi, V. Barone, B. Mennucci, M. Cossi, G. Scalmani, N. Rega, G. A. Petersson, H. Nakatsuji, M. Hada, M. Ehara, K. Toyota, R. Fukuda, J. Hasegawa, M. Ishida, T. Nakajima, Y. Honda, O. Kitao, H. Nakai, M. Klene, X. Li, J. E. Knox, H. P. Hratchian, J. B. Cross, V. Bakken, C. Adamo, J. Jaramillo, R. Gomperts, R. E. Stratmann, O. Yazyev, A. J. Austin, R. Cammi, C. Pomelli, J. W. Ochterski, P. Y. Ayala, K. Morokuma, G. A. Voth, P. Salvador, J. J. Dannenberg, V. G. Zakrzewski, S. Dapprich, A. D. Daniels, M. C. Strain, O. Farkas, D. K. Malick, A. D. Rabuck, K. Raghavachari, J. B. Foresman, J. V. Ortiz, Q. Cui, A. G. Baboul, S. Clifford, J. Cioslowski, B. B. Stefanov, G. Liu, A. Liashenko, P. Piskorz, I. Komaromi, R. L. Martin, D. J. Fox, T. Keith, M. A. Al-Laham, C. Y. Peng, A. Nanayakkara, M. Challacombe, P. M. W. Gill, B. Johnson, W. Chen, M. W. Wong, C. Gonzalez and J. A. Pople, Gaussian 09, Revision A.02, Gaussian, Inc.: Wallingford CT, **2009**.

C. Photo-physical Data

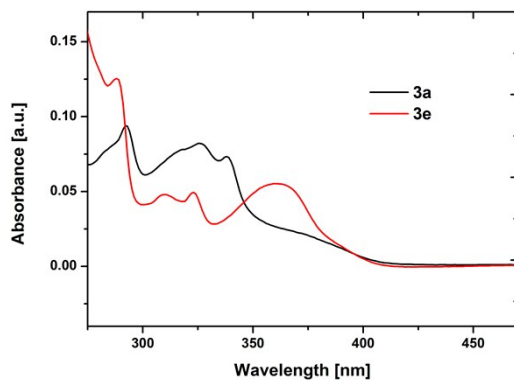


Figure S29. Absorption spectra of **3a** and **3e** recorded from 5 μ M solutions in DCM at r.t.

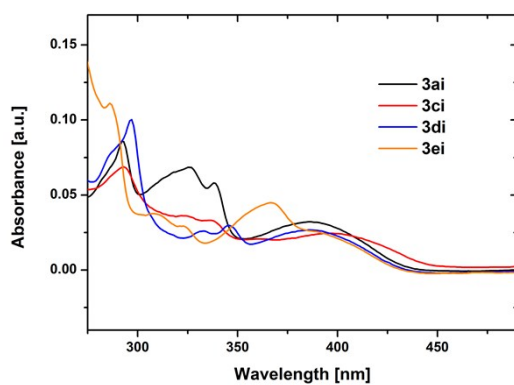


Figure S30. Absorption spectra of **3ai**, **3ci**, **3di** and **3ei** recorded from 5 μ M solutions in DCM at r.t.

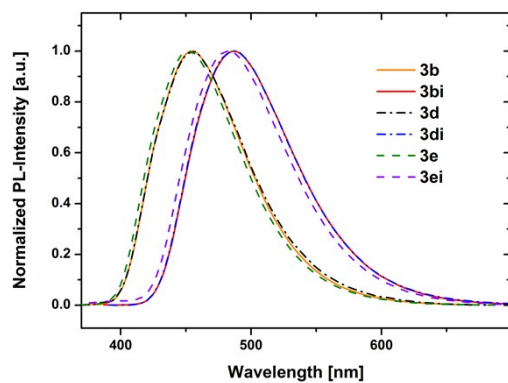


Figure S31. Normalized emission spectra of **3b**, **3bi**, **3d**, **3di**, **3e** and **3ei** recorded from 5 μ M solutions in DCM at r.t.

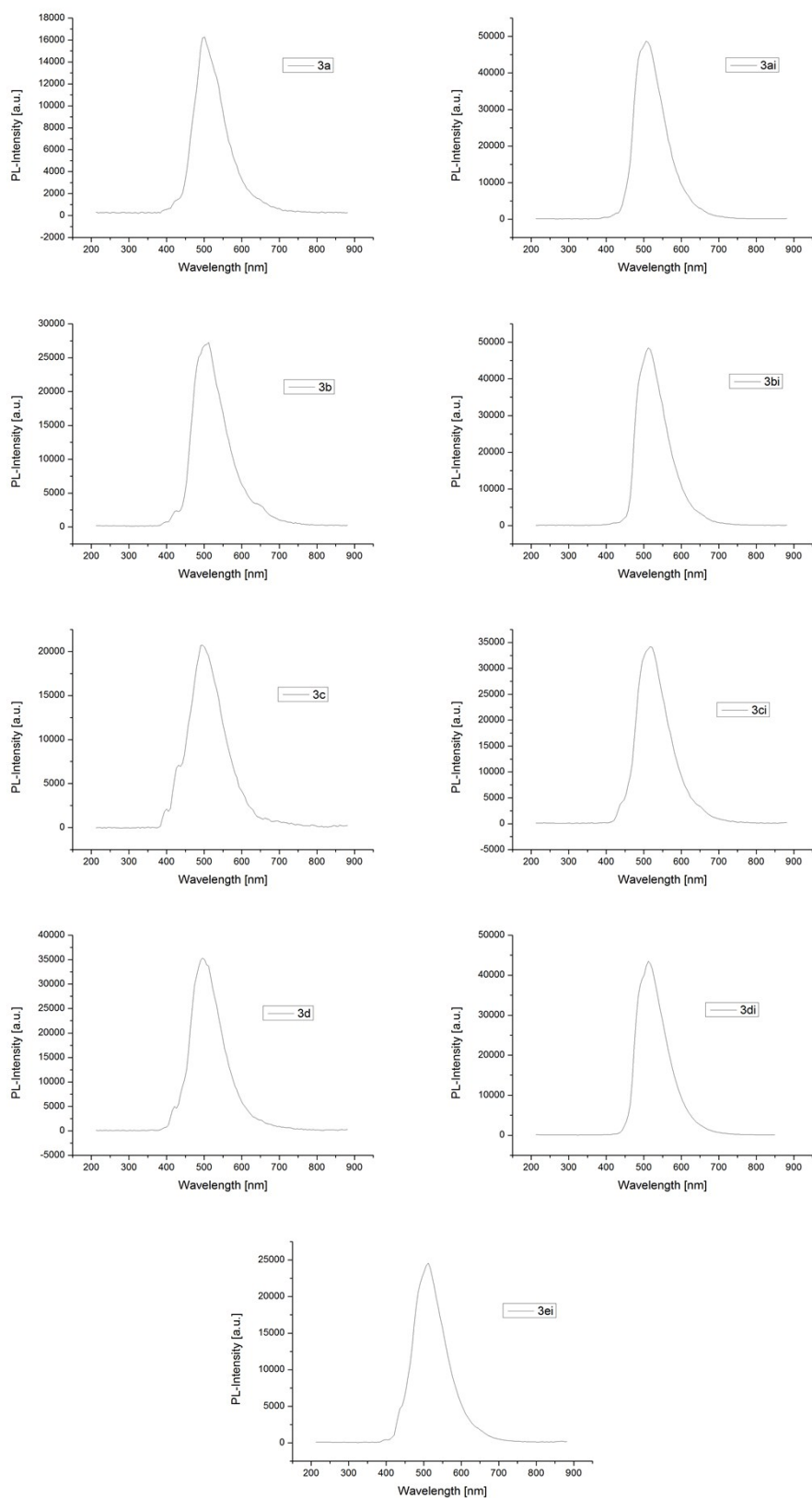


Figure S32. Low temperature phosphorescence spectra of compounds **3a-3di** and **3ei**.

D. Crystallography

Table S12. Details on data collection and refinement for **3c**.

formula	C ₂₆ H ₁₆ NOPS ₂
fw	453.5
cryst.size, mm	0.65 x 0.66 x 0.42
color, shape	yellow fragment
crystal system	monoclinic
space group	<i>P</i> 2 ₁ (no. 4)
<i>a</i> , Å	8.3295(6)
<i>b</i> , Å	14.1464(10)
<i>c</i> , Å	8.8132(6)
α , deg	90
β , deg	103.1530(19)
γ , deg	90
<i>V</i> , Å ³	1011.24(12)
<i>T</i> , K	100
<i>Z</i>	2
ρ_{calc} , g cm ⁻³	1.4894
μ , mm ⁻¹ (MoK α)	0.363
<i>F</i> (000)	468
absorption corrections, <i>T</i> _{min} - <i>T</i> _{max}	Multi-scan, 0.79–0.86
θ range, deg	2.37–32.72
no. of rflns measd	82676
<i>R</i> _{int}	0.0407
no. of rflns unique	7360
no. of rflns <i>I</i> > 3 σ (<i>I</i>)	7293
no. of params / restraints	281 / 0
<i>R</i> ₁ (<i>I</i> > 3 σ (<i>I</i>)) ^a	0.0198
<i>R</i> ₁ (all data)	0.0201
<i>wR</i> ₂ (<i>I</i> > 3 σ (<i>I</i>))	0.0272
<i>wR</i> ₂ (all data)	0.0273
GooF	1.92
Diff.Four.peaks	-0.20 / 0.28

E. CV Measurements

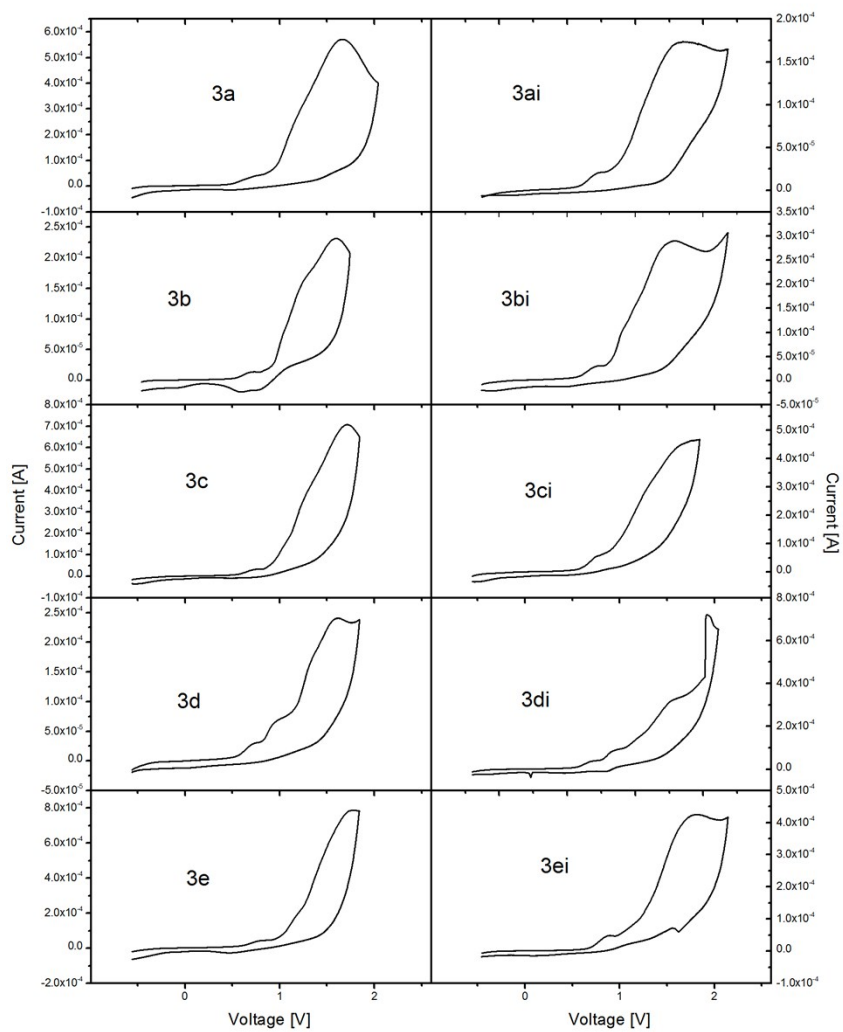


Figure S33. Cyclic voltammograms of compounds **3a(i)-3e(i)**.

3.3. Manuscript #3 – Supporting Information

Indolo[3,2,1-*jk*]carbazole based planarized CBP derivatives as host materials for PhOLEDs with low efficiency roll-off

Paul Kautny, Zhongbin Wu, Johanna Eichelter, Ernst Horkel, Berthold Stöger, Jiangshan Chen, Dongge Ma, Johannes Fröhlich, Daniel Lumpi

Organic Electronics, **2016**, 34, 237-245

Supplementary Material

Indolo[3,2,1-*jk*]carbazole based planarized CBP derivatives as host materials for PhOLEDs with low efficiency roll-off

Paul Kautny ^{a,‡}, Zhongbin Wu ^{b,‡}, Johanna Eichelter ^a, Ernst Horkel ^a,
Berthold Stöger ^c, Jiangshan Chen ^{b,*}, Dongge Ma ^b,
Johannes Fröhlich ^a, and Daniel Lumpi ^{a,*}

^a Institute of Applied Synthetic Chemistry, Vienna University of Technology,
Getreidemarkt 9/163, A-1060 Vienna, Austria

^b State Key Laboratory of Polymer Physics and Chemistry, Changchun Institute of
Applied Chemistry, Chinese Academy of Sciences, Changchun, 130022, China

^c Institute of Chemical Technologies and Analytics, Vienna University of Technology,
Getreidemarkt 9/164, A-1060 Vienna, Austria

[‡] contributed equally to this work

jschen@ciac.ac.cn

daniel.lumpi@tuwien.ac.at

Content

A. Molecular structure of CBP derivatives

B. NMR-spectra

C. Absorption and PL/EL-emission spectra

D. Device architecture

E. DSC and TGA analyses

References

A. Molecular structure of CBP derivatives

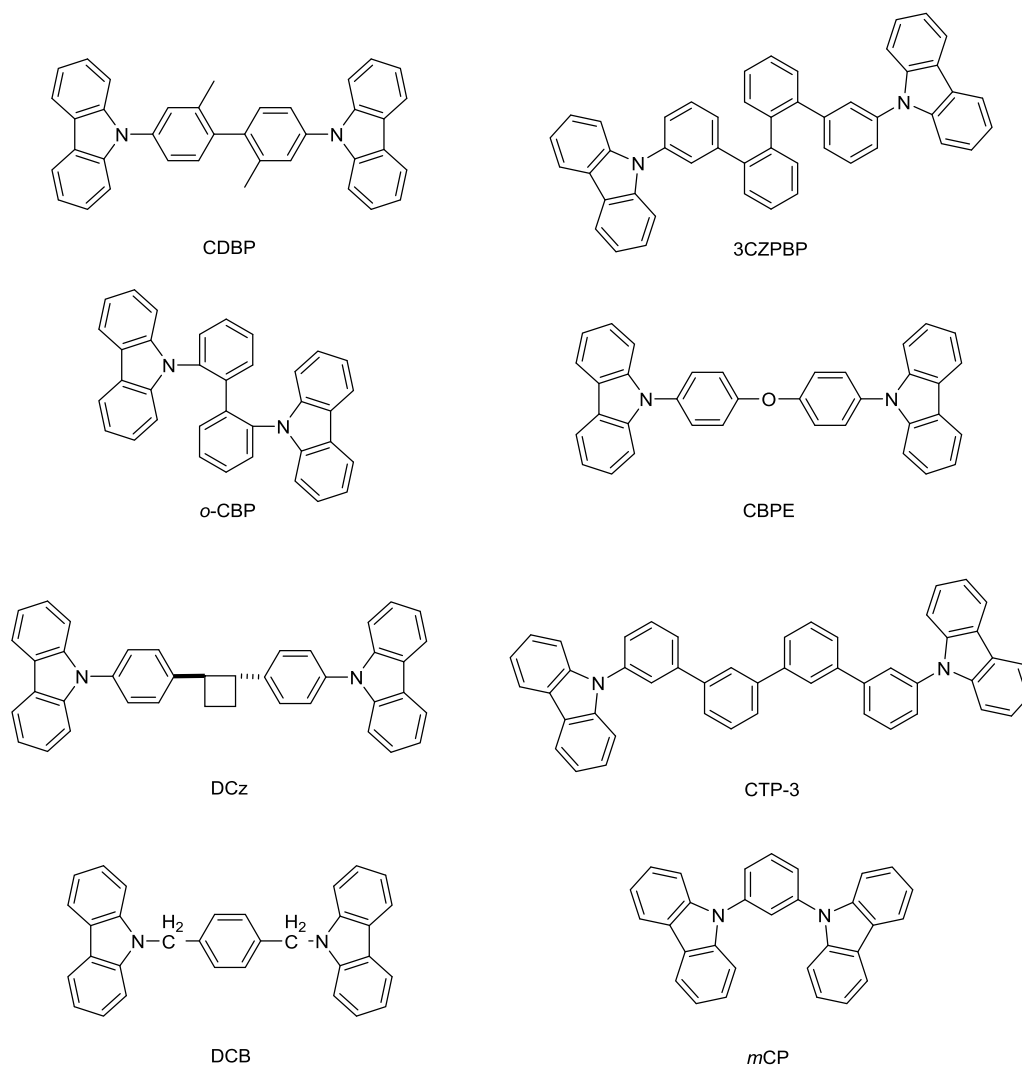


Fig. S1 Molecular structure of CBP derivatives CDBP¹, 3CZPBP², o-CBP³ CBPE⁴, DCz⁵, CTP-3⁶, DCB⁷ and mCP.⁸

B. NMR-spectra

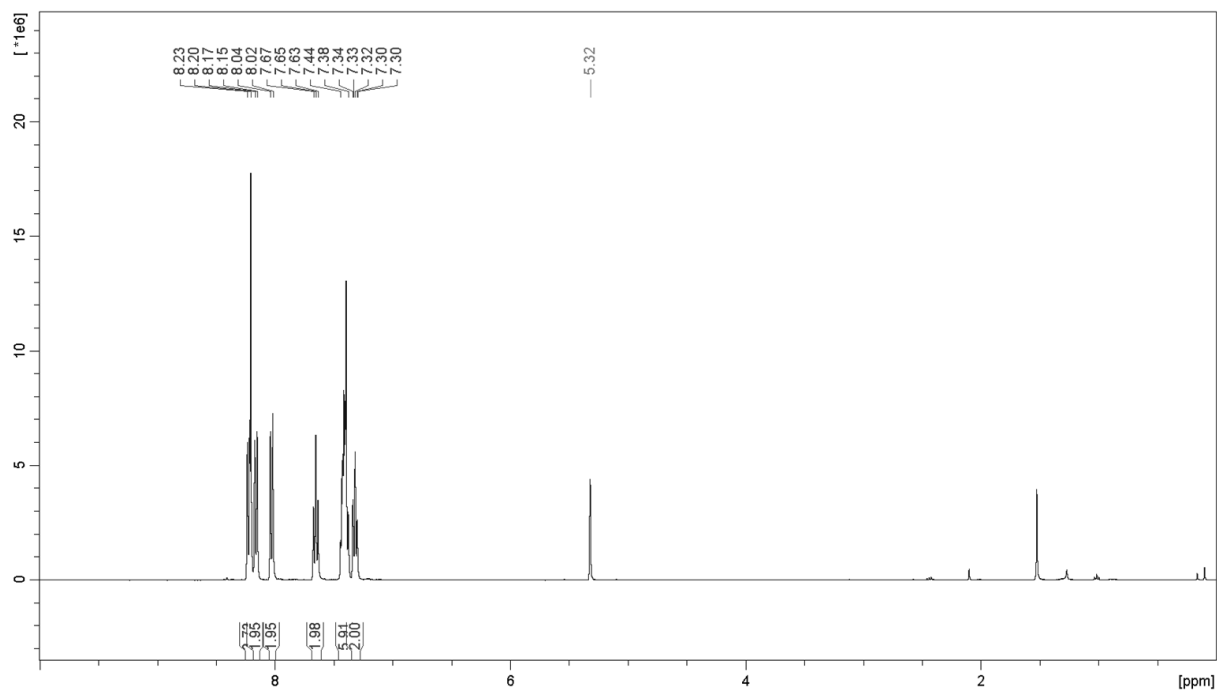


Fig. S2 Proton NMR spectrum of ICzCz.

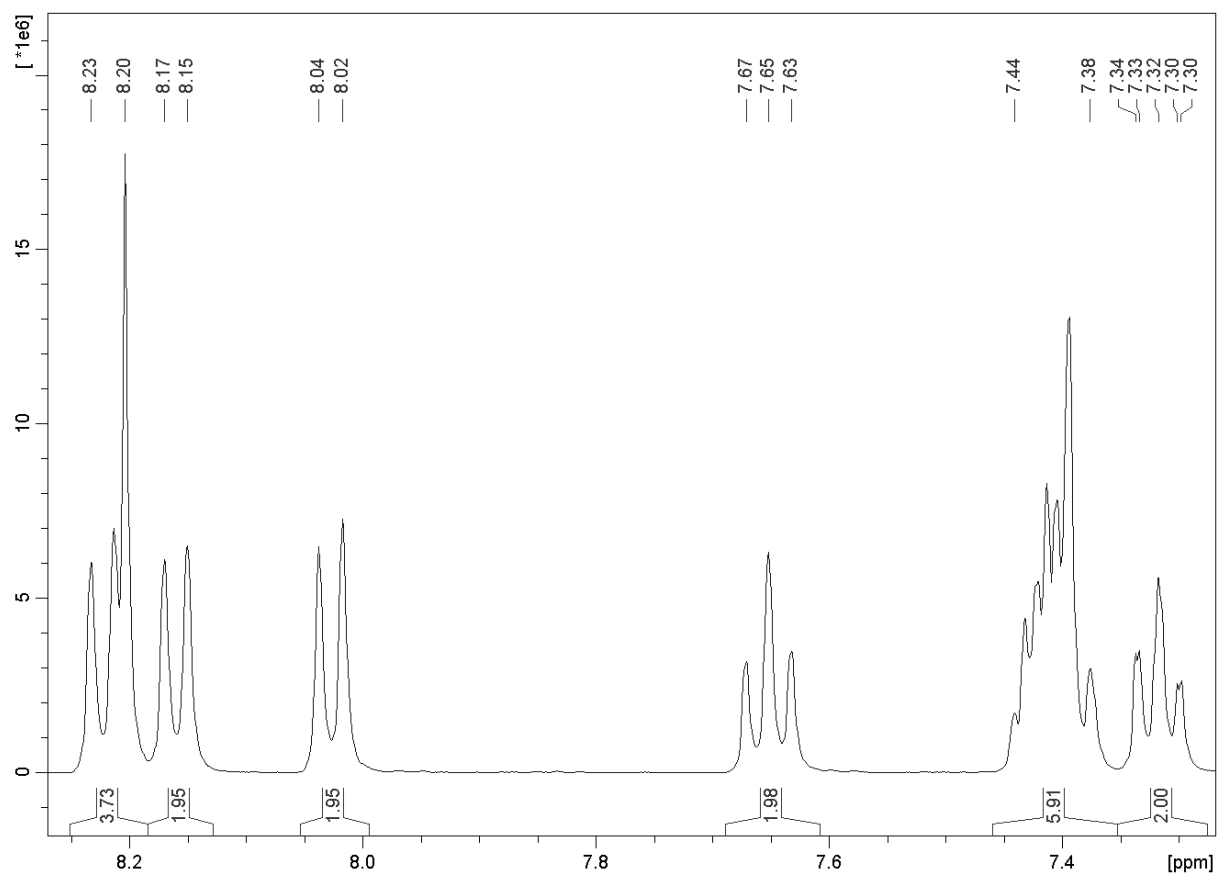


Fig. S3 Proton NMR spectrum of the aromatic region of ICzCz.

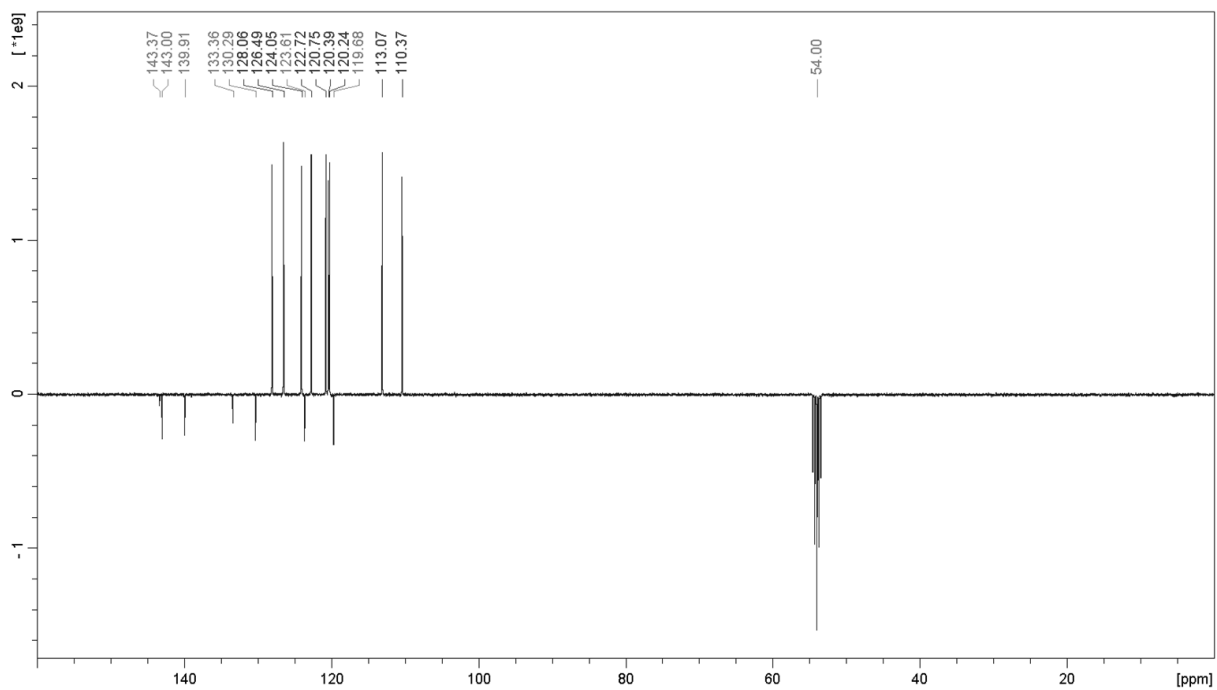


Fig. S4 Carbon NMR spectrum of ICzCz.

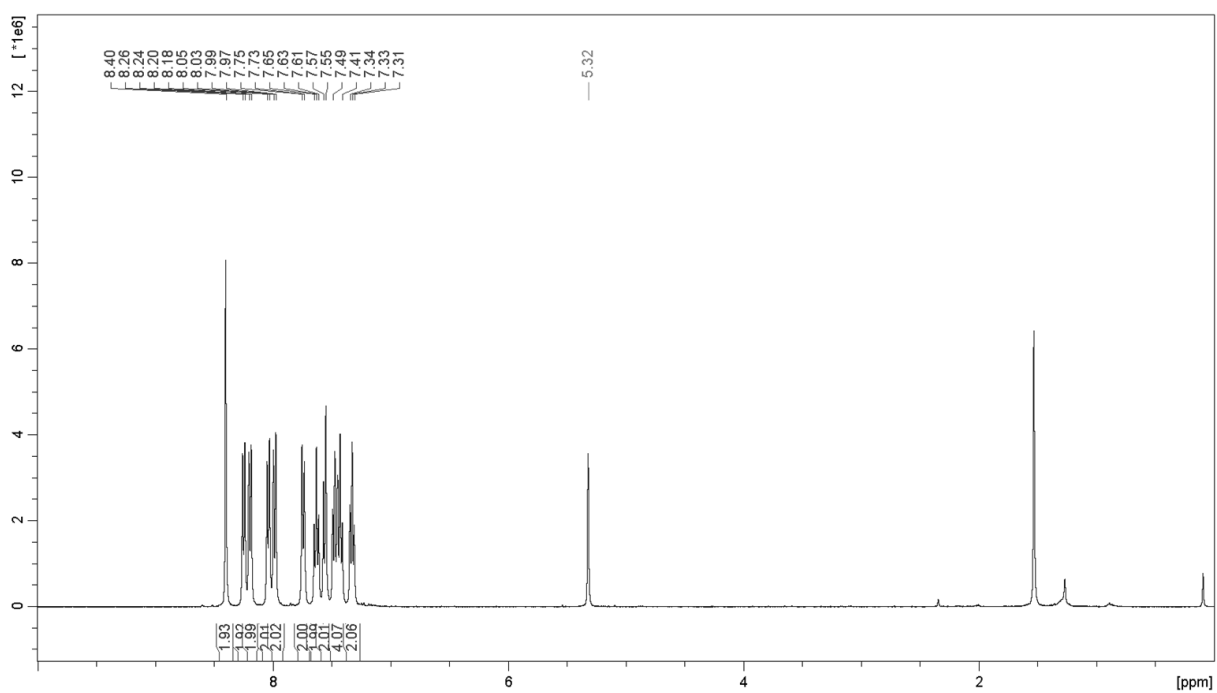


Fig. S5 Proton NMR spectrum of ICzPCz.

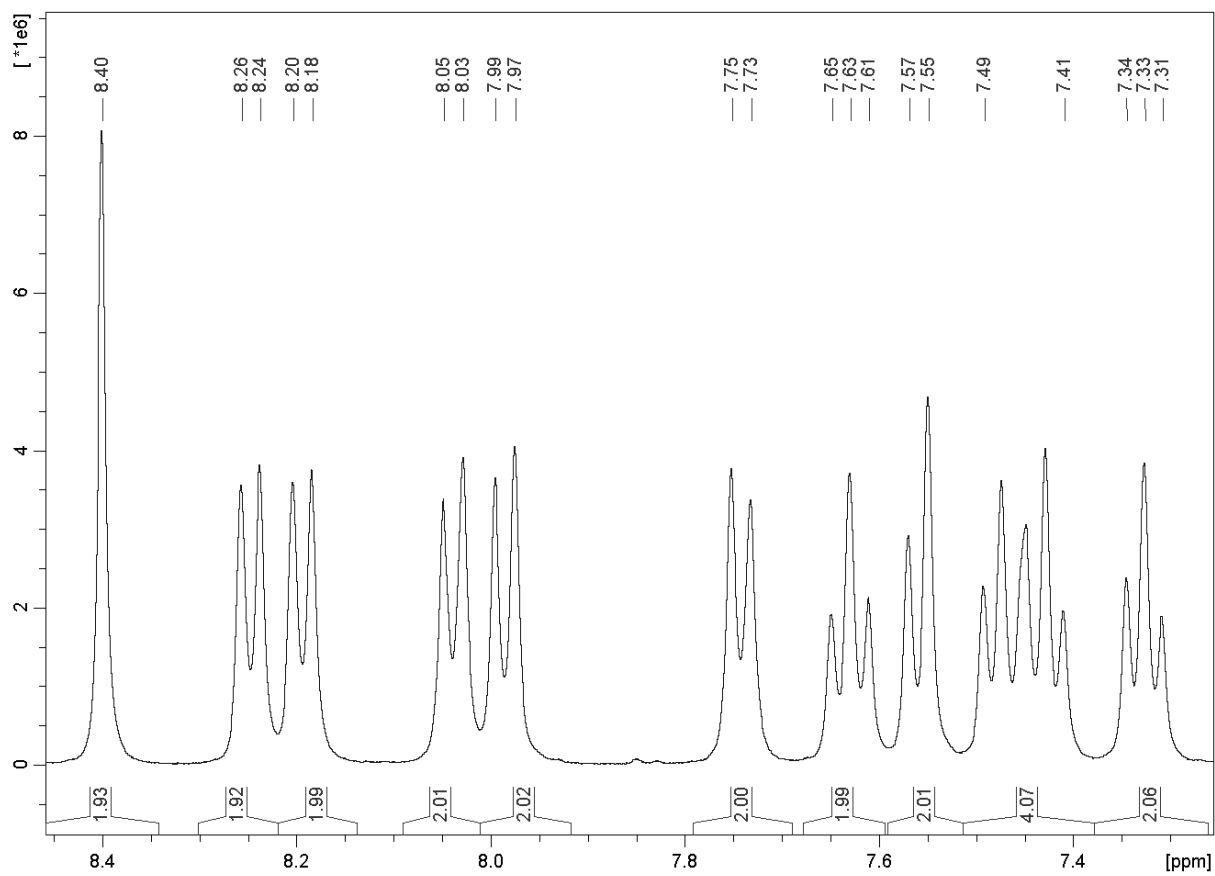


Fig. S6 Proton NMR spectrum of the aromatic region of **ICzPCz**.

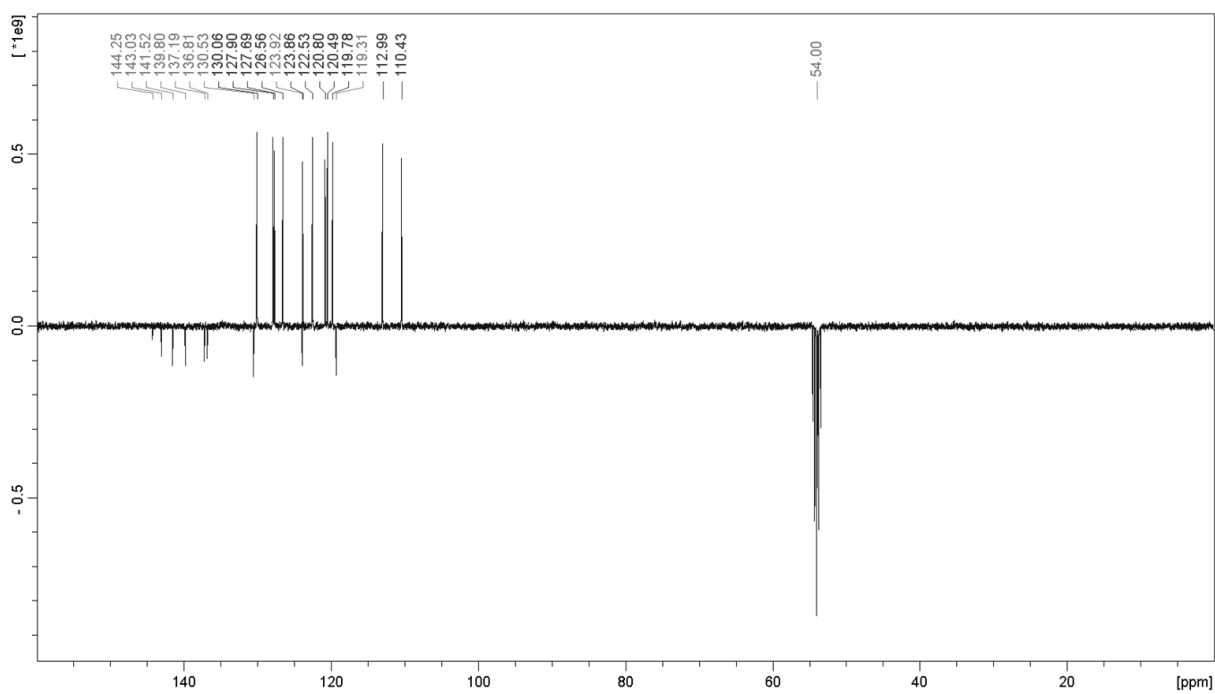


Fig. S7 Carbon NMR spectrum of **ICzPCz**.

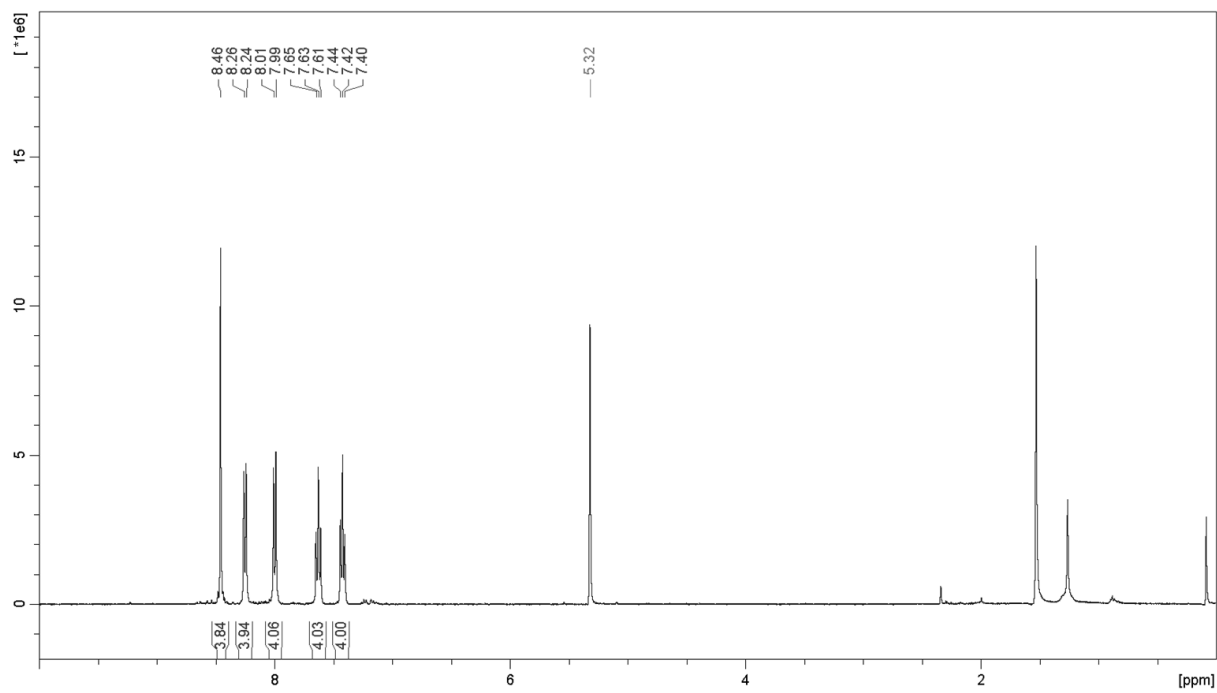


Fig. S8 Proton NMR spectrum of ICzICz.

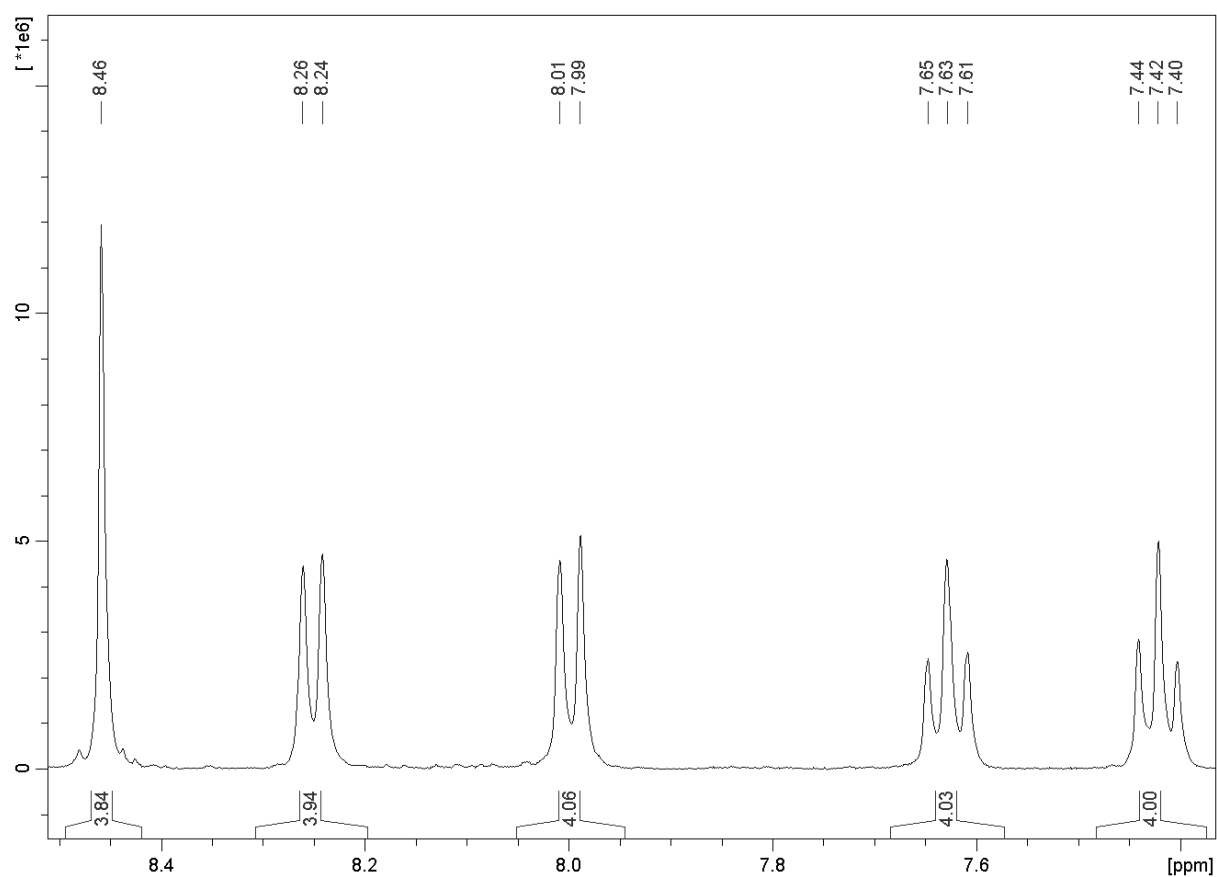


Fig. S9 Proton NMR spectrum of the aromatic region of ICzICz.

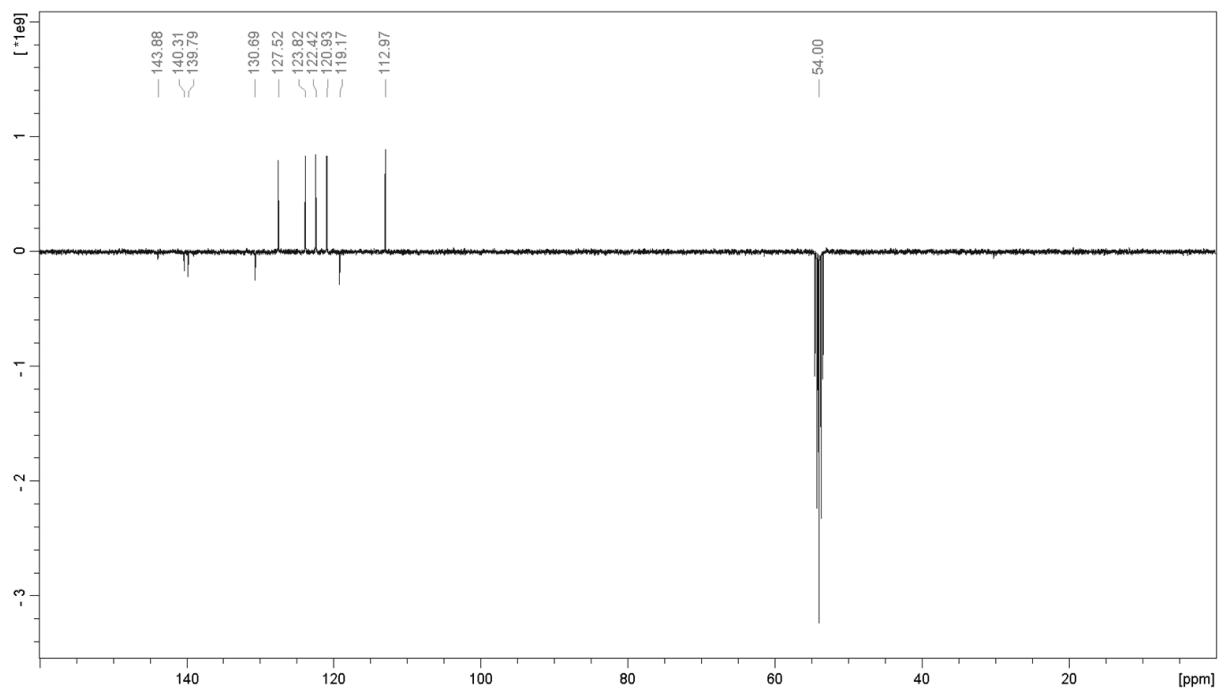


Fig. S10 Carbon NMR spectrum of ICzICz.

C. Absorption and PL/EL-emission spectra

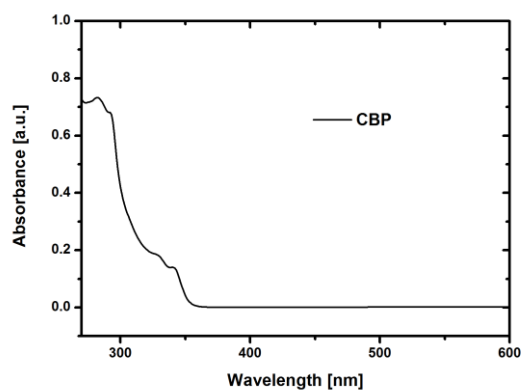


Fig. S11 UV-VIS absorption spectra of CBP.

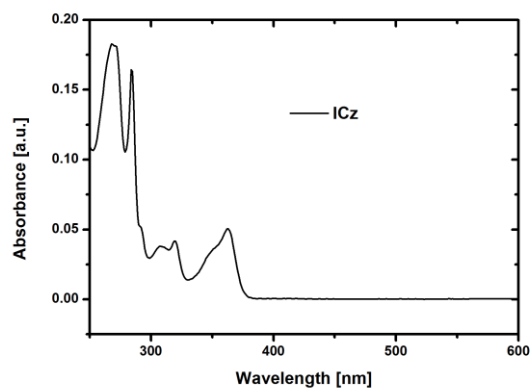


Fig. S12 UV-VIS absorption spectra of indolo[3,2,1-*jk*]carbazole.

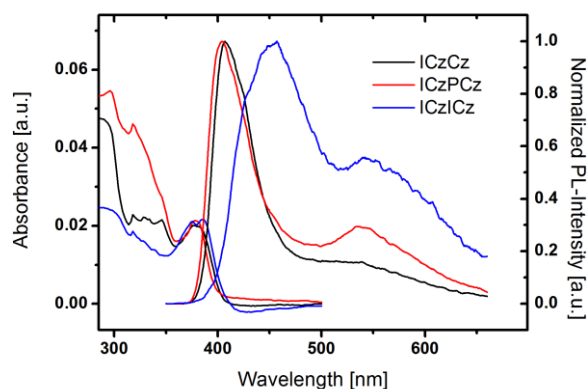


Fig. S13 UV-VIS absorption, and normalized fluorescence spectra of drop casted thin films of **ICzCz**, **ICzPCz** and **ICzICz**.

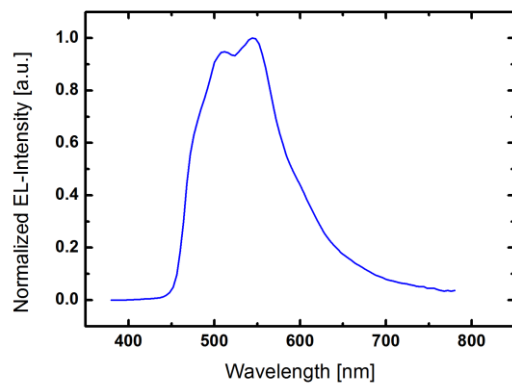


Fig. S14 EL-spectra of a ICzICz film doped with FIrPic.

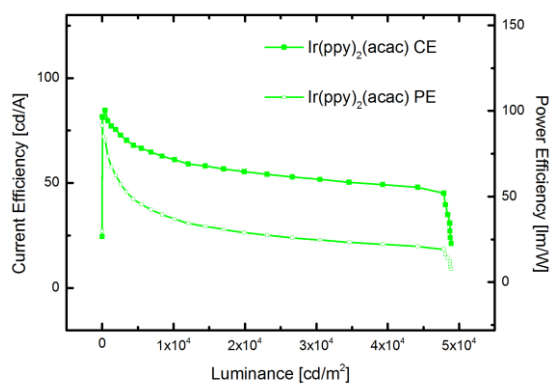


Fig. S15 Current efficiency–luminance–power efficiency (full symbols: current efficiency; hollow symbols: power efficiency) curves of a CBP based green device. Device architecture as displayed below.

D. Device architecture

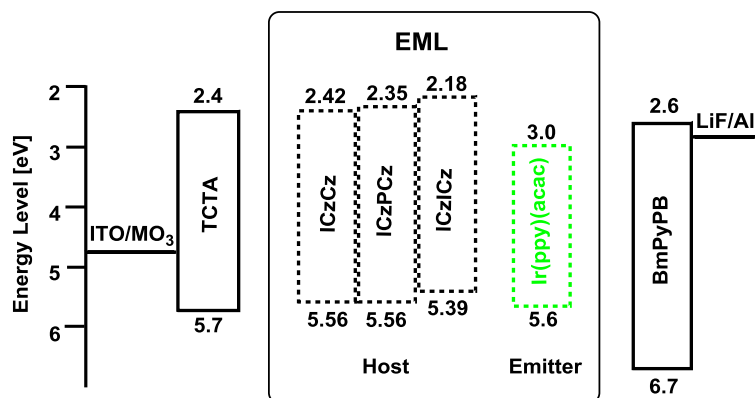


Fig. S16 Energy-level diagram for devices based on Ir(ppy)₂(acac).

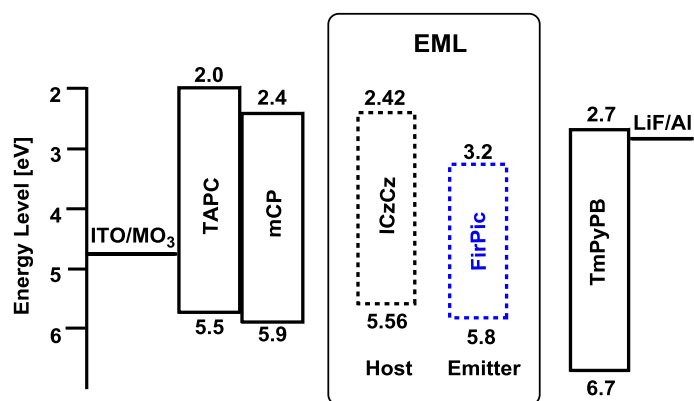


Fig. S17 Energy-level diagram for devices based on FIrPic.

E. DSC and TGA analyses

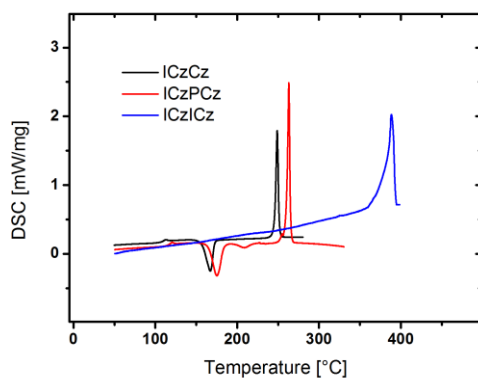


Fig. S18 DSC analysis of ICzCz, ICzPCz and ICzICz.

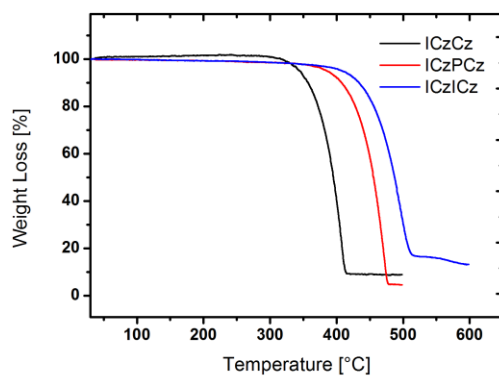


Fig. S19 TGA measurements of ICzCz, ICzPCz and ICzICz.

References

1. Tokito, S.; Iijima, T.; Suzuri, Y.; Kita, H.; Tsuzuki, T.; Sato, F., Confinement of triplet energy on phosphorescent molecules for highly-efficient organic blue-light-emitting devices. *Applied Physics Letters* **2003**, 83, (3), 569-571.
2. Agata, Y.; Shimizu, H.; Kido, J., Syntheses and properties of novel quarterphenylene-based materials for blue organic light-emitting devices. *Chemistry Letters* **2007**, 36, (2), 316-317.
3. Gong, S. L.; He, X.; Chen, Y. H.; Jiang, Z. Q.; Zhong, C.; Ma, D. G.; Qin, J. G.; Yang, C. L., Simple CBP isomers with high triplet energies for highly efficient blue electrophosphorescence. *Journal of Materials Chemistry* **2012**, 22, (7), 2894-2899.
4. He, J.; Liu, H.; Dai, Y.; Ou, X.; Wang, J.; Tao, S.; Zhang, X.; Wang, P.; Ma, D., Nonconjugated Carbazoles: A Series of Novel Host Materials for Highly Efficient Blue Electrophosphorescent OLEDs. *The Journal of Physical Chemistry C* **2009**, 113, (16), 6761-6767.
5. Whang, D. R.; You, Y.; Kim, S. H.; Jeong, W. I.; Park, Y. S.; Kim, J. J.; Park, S. Y., A highly efficient wide-band-gap host material for blue electrophosphorescent light-emitting devices. *Applied Physics Letters* **2007**, 91, (23).
6. Cui, L. S.; Dong, S. C.; Liu, Y.; Li, Q.; Jiang, Z. Q.; Liao, L. S., A simple systematic design of phenylcarbazole derivatives for host materials to high-efficiency phosphorescent organic light-emitting diodes. *Journal of Materials Chemistry C* **2013**, 1, (25), 3967-3975.
7. Lei, G. T.; Wang, L. D.; Duan, L.; Wang, J. H.; Qiu, Y., Highly efficient blue electrophosphorescent devices with a novel host material. *Synthetic Metals* **2004**, 144, (3), 249-252.
8. Holmes, R. J.; Forrest, S. R.; Tung, Y.-J.; Kwong, R. C.; Brown, J. J.; Garon, S.; Thompson, M. E., Blue organic electrophosphorescence using exothermic host-guest energy transfer. *Applied Physics Letters* **2003**, 82, (15), 2422-2424.

3.4. Manuscript #4 – Supporting Information

Controlling singlet-triplet splitting in carbazole-oxadiazole based bipolar phosphorescent host materials

Paul Kautny, Zhongbin Wu, Berthold Stöger, Antoine Tissot, Ernst Horkel, Jiangshan Chen, Dongge Ma, Hans Hagemann, Johannes Fröhlich, Daniel Lumpi

Organic Electronics, **2015**, 17, 216-228

Supplementary Material

Sterically Induced Torsion in Carbazole – Oxadiazole Based Bipolar Host Materials for PHOLEDs

Paul Kautny,^a Zhongbin Wu,^b Berthold Stöger,^c Antoine Tissot,^d Ernst Horkel,^a

Jiangshan Chen,^{*b} Dongge Ma,^b Hans Hagemann,^d

Johannes Fröhlich,^a and Daniel Lumpi^{*a}

^a Institute of Applied Synthetic Chemistry, Vienna University of Technology,
Getreidemarkt 9/163, A-1060 Vienna, Austria

^b State Key Laboratory of Polymer Physics and Chemistry, Changchun Institute of
Applied Chemistry, Chinese Academy of Sciences, Changchun, 130022, China

^c Institute of Chemical Technologies and Analytics, Vienna University of Technology,
Getreidemarkt 9/164, A-1060 Vienna, Austria

^d Département de Chimie Physique, Université de Genève, 30, quai E. Ansermet,
1211 Geneva 4, Switzerland

jschen@ciac.ac.cn

daniel.lumpi@tuwien.ac.at

Content

A. NMR Spectra

B. TGA/DSC

C. EL Spectra

D. PL Spectra

E. Crystal Structures

F. Device Architecture

A. NMR Spectra

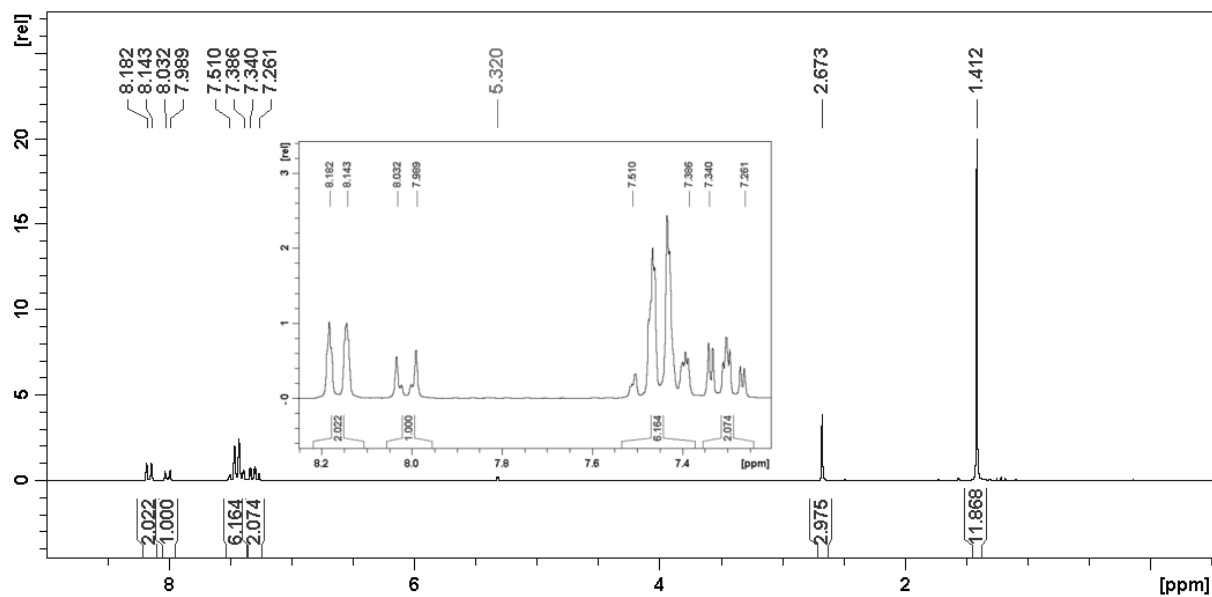


Figure S 1. Proton NMR spectrum of compound 2.

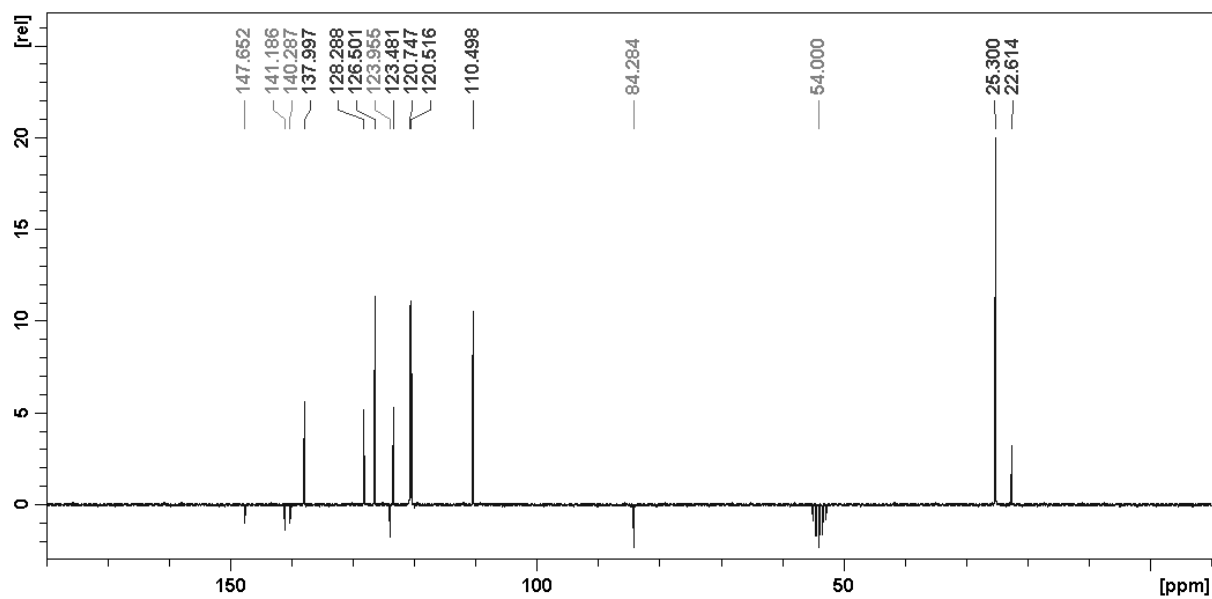


Figure S 2. Carbon NMR spectrum of compound 2.

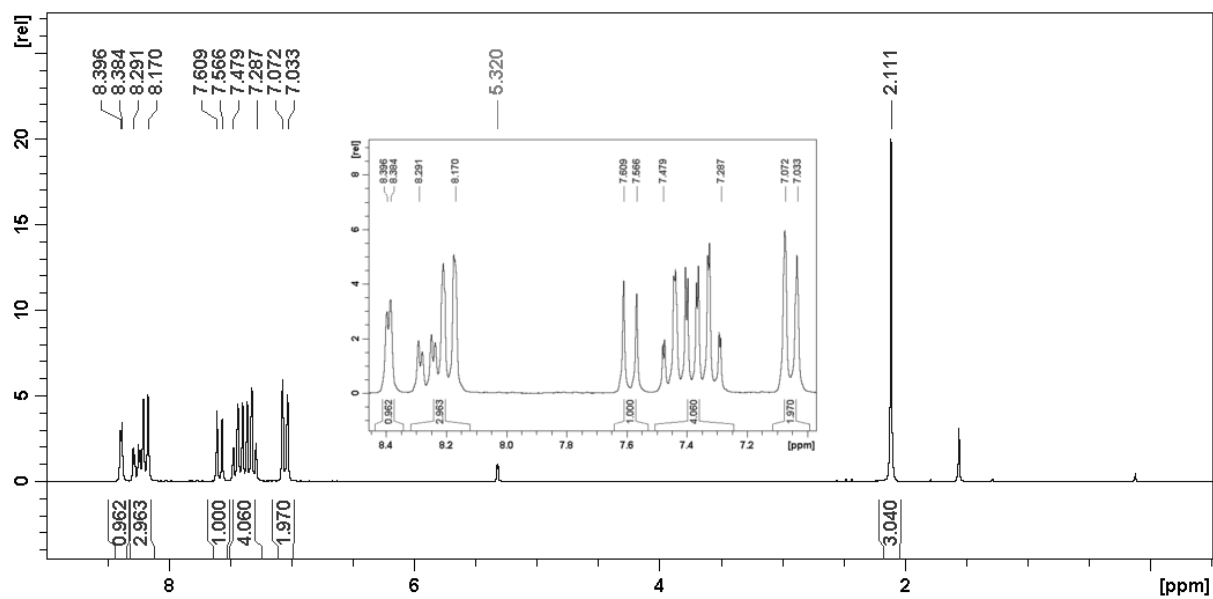


Figure S 3. Proton NMR spectrum of compound 4.

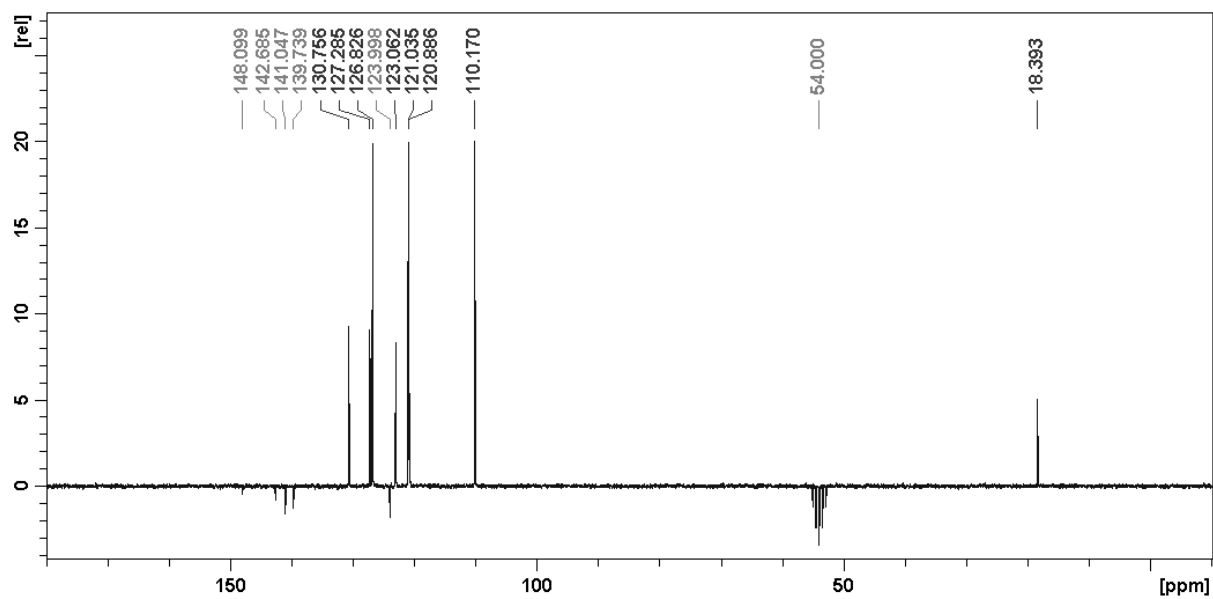


Figure S 4. Carbon NMR spectrum of compound 4.

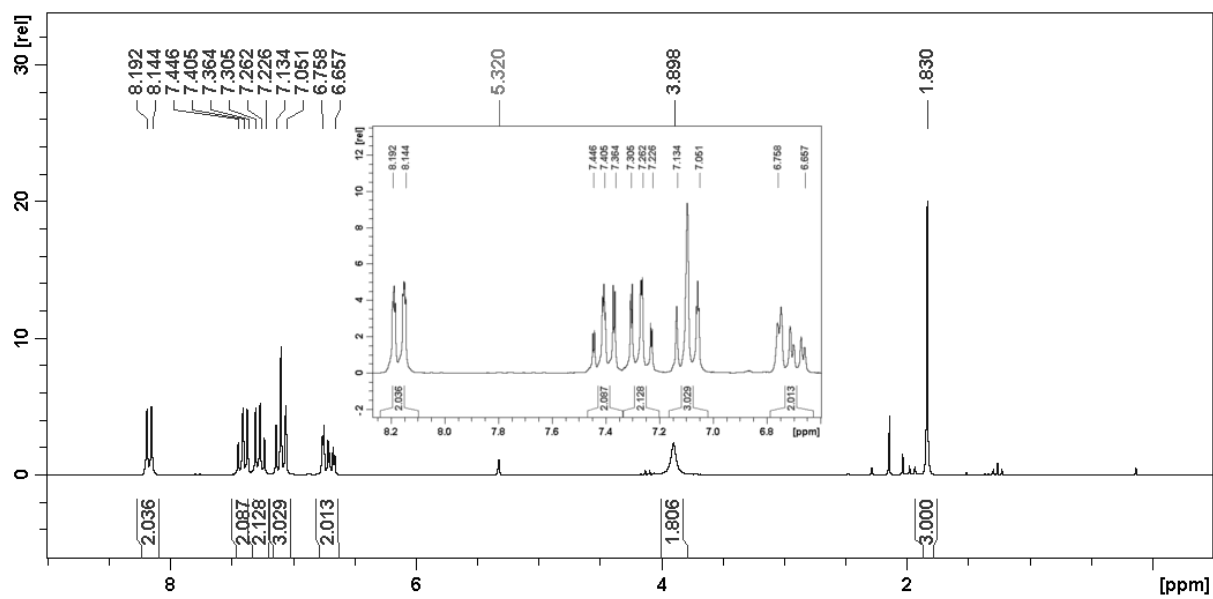


Figure S 5. Proton NMR spectrum of compound 5.

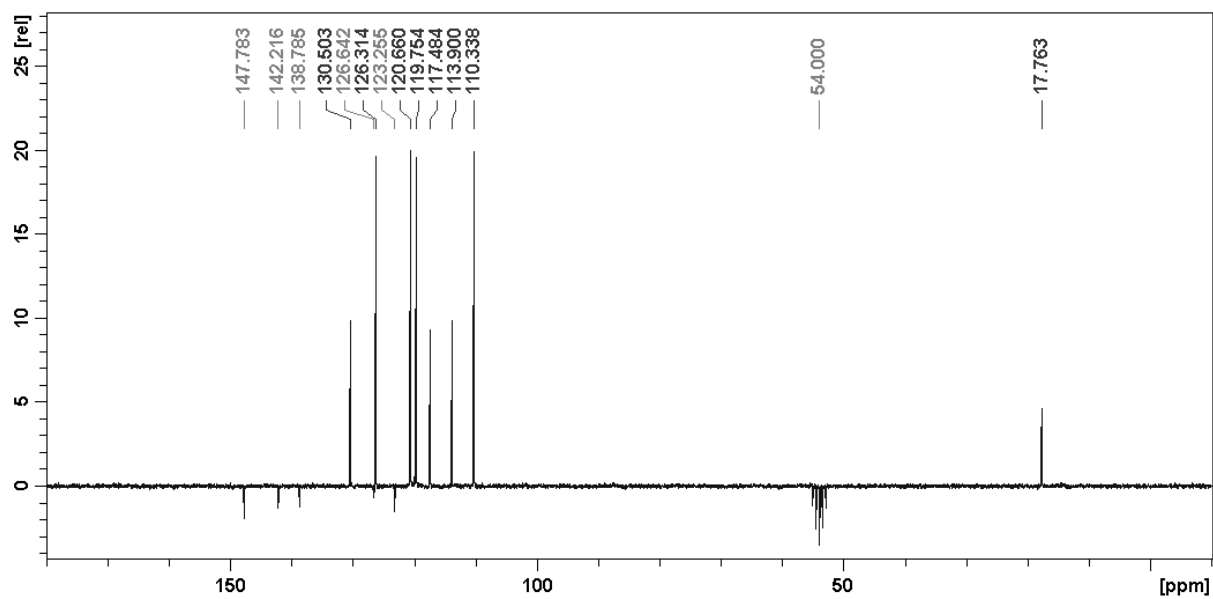


Figure S 6. Carbon NMR spectrum of compound 5.

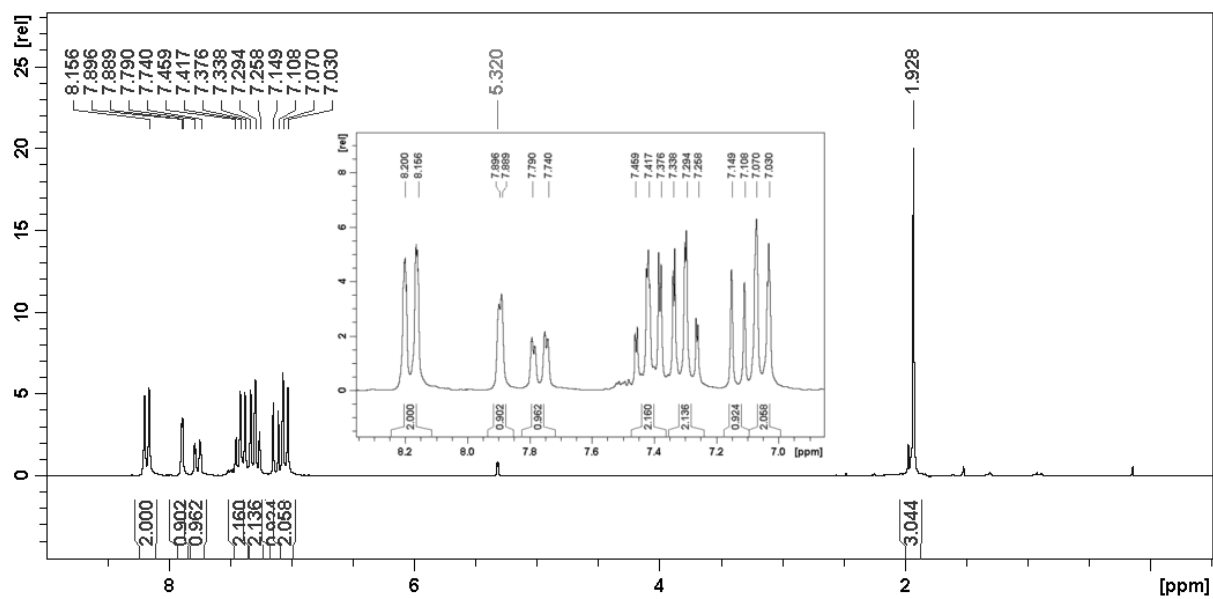


Figure S 7. Proton NMR spectrum of compound 6.

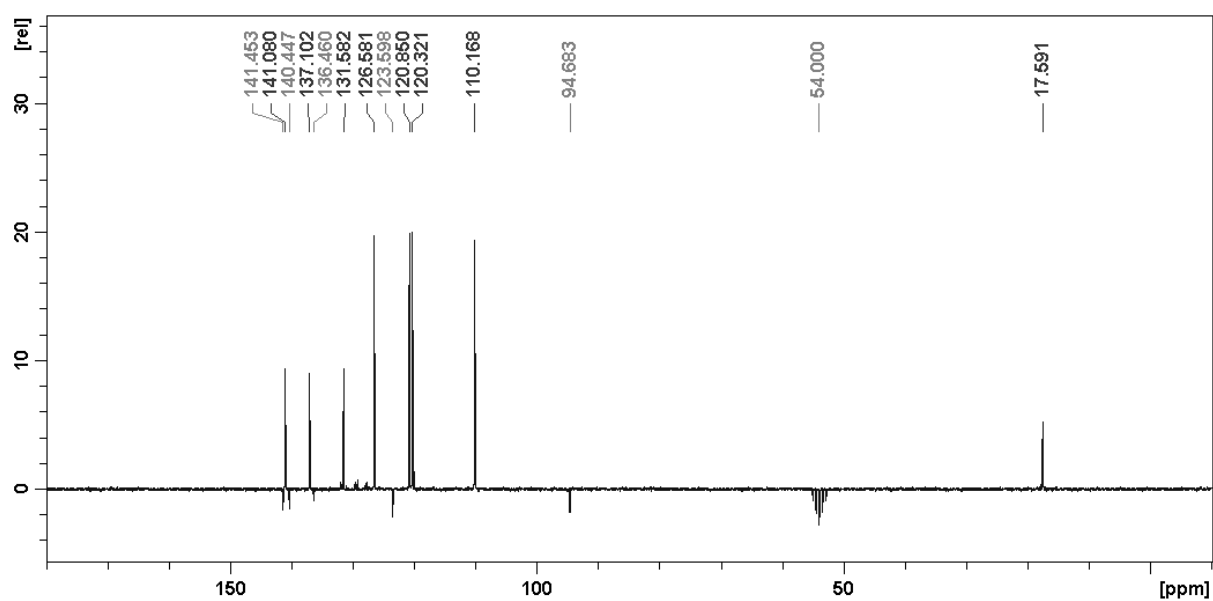


Figure S 8. Carbon NMR spectrum of compound 6.

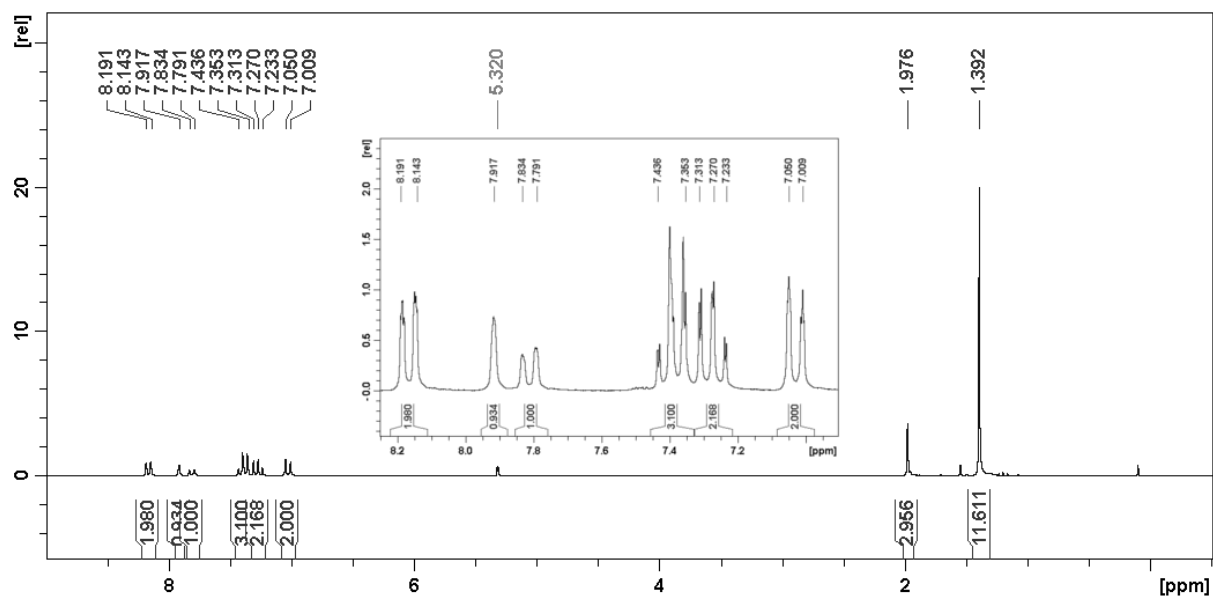


Figure S 9. Proton NMR spectrum of compound 7.

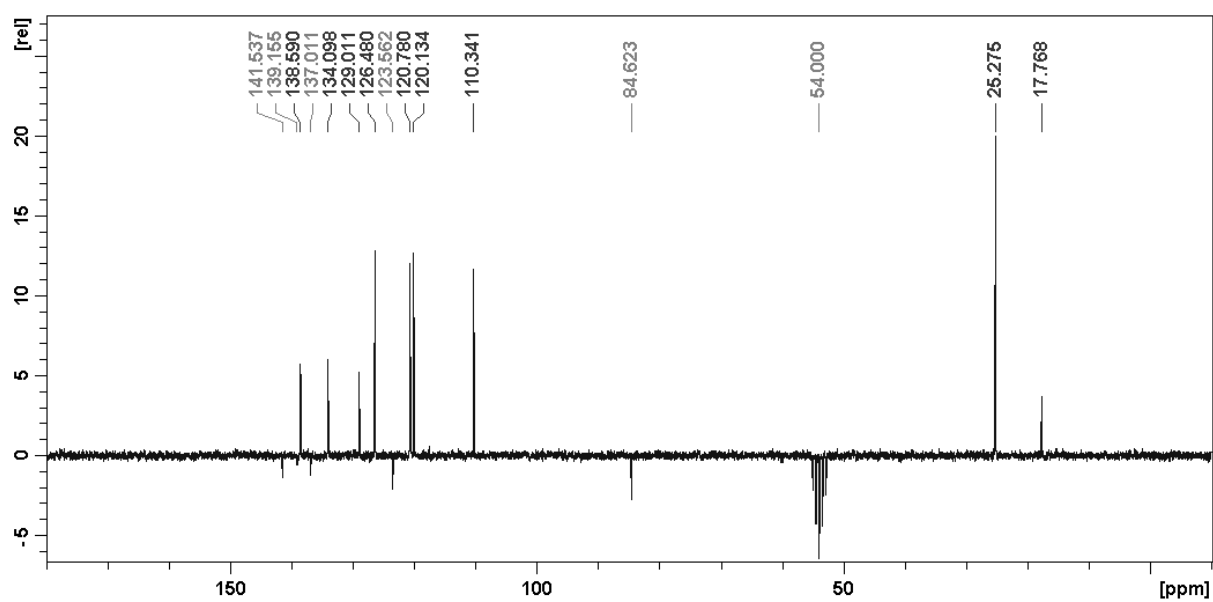


Figure S 10. Carbon NMR spectrum of compound 7.

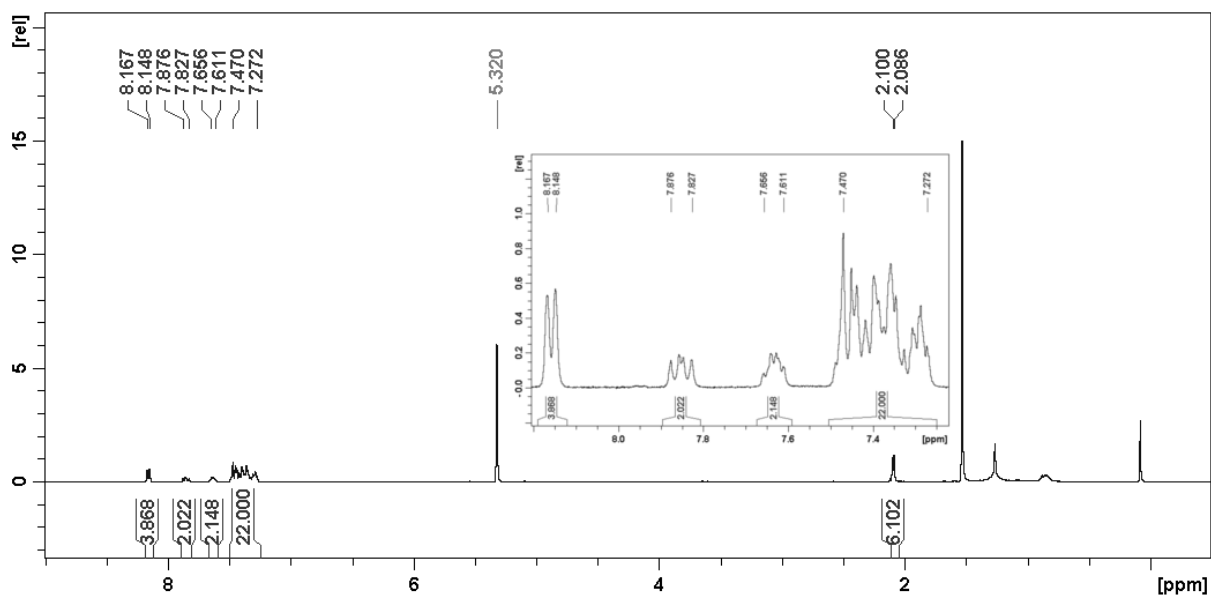


Figure S 11. Proton NMR spectrum of compound **o-2MPCzPOXD**.

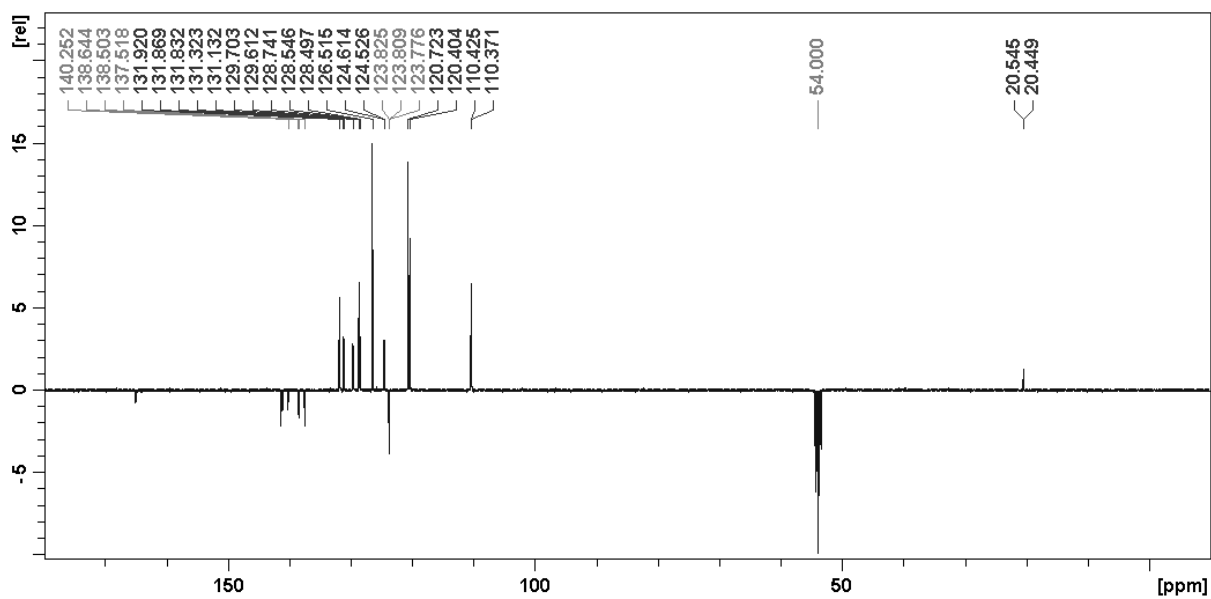


Figure S 12. Carbon NMR spectrum of compound **o-2MPCzPOXD**.

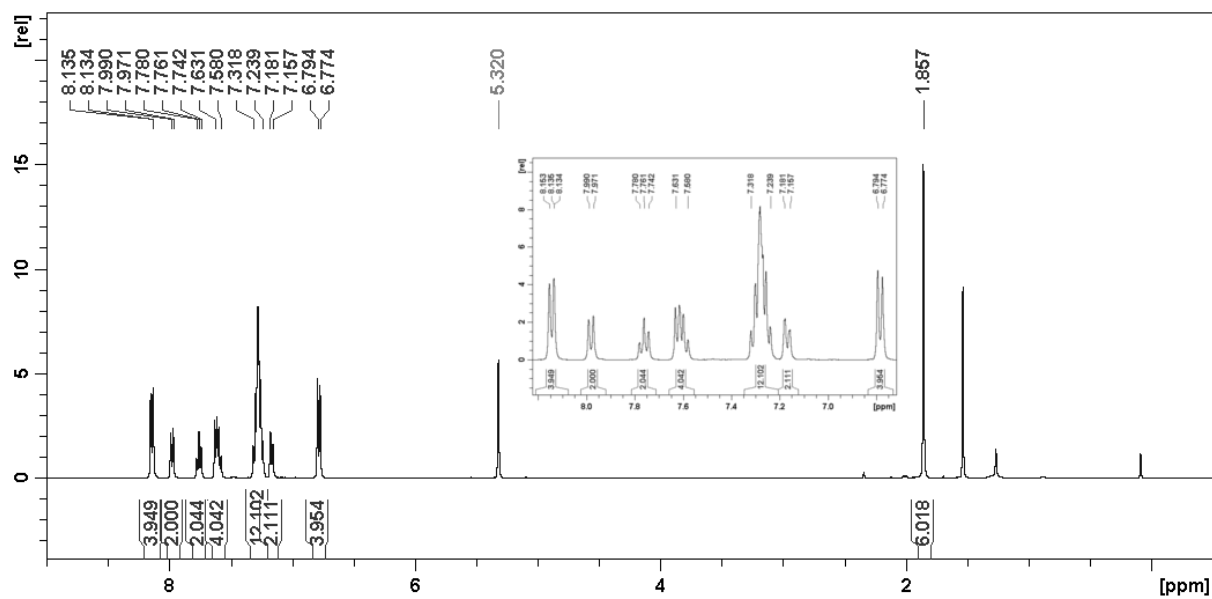


Figure S 13. Proton NMR spectrum of compound *o*-2MPCzPOXD.

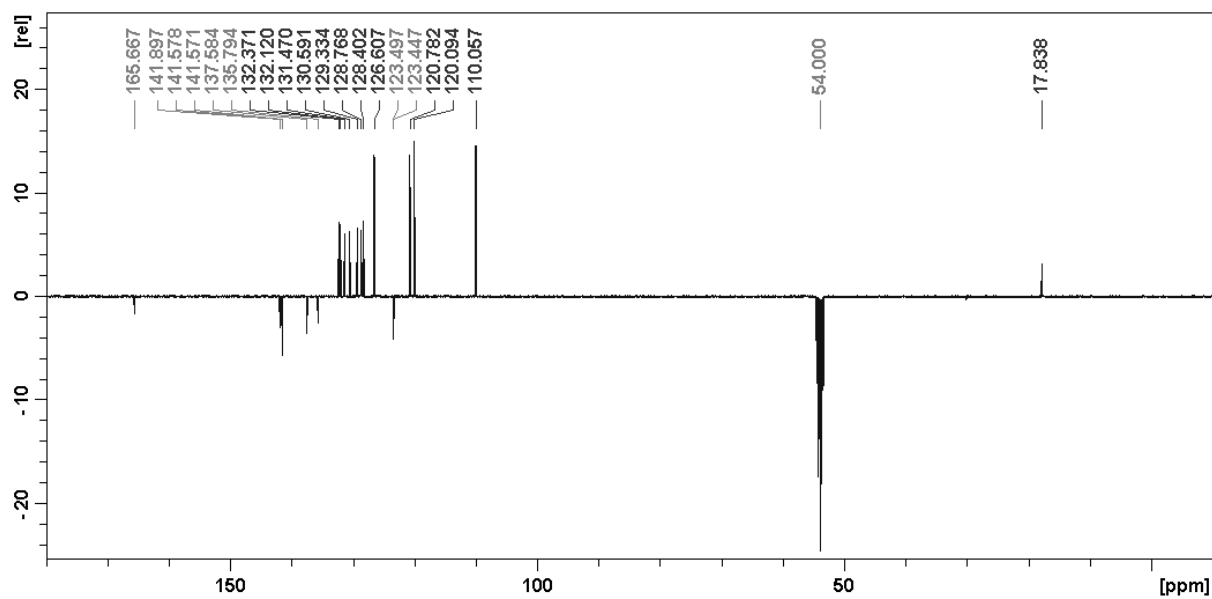


Figure S 14. Carbon NMR spectrum of compound *o*-2MPCzPOXD.

B. TGA/DSC

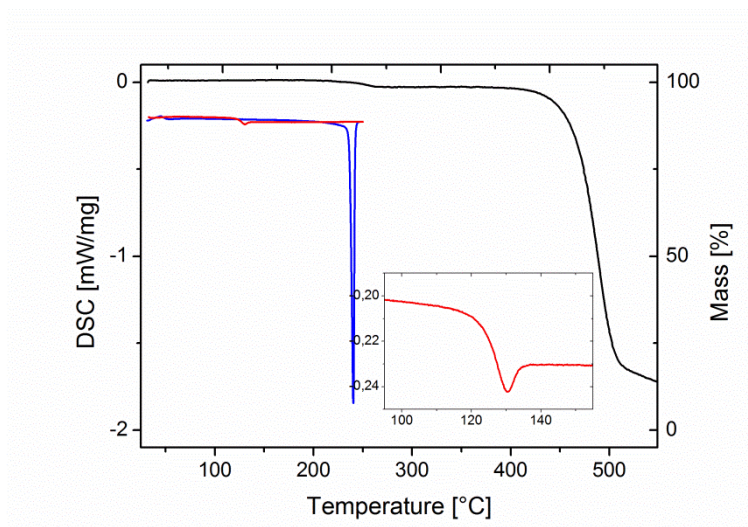


Figure S 15. DSC and TG trace of o-2MPCzPOXD recorded at a heating rate of $5\text{ }^{\circ}\text{C min}^{-1}$.

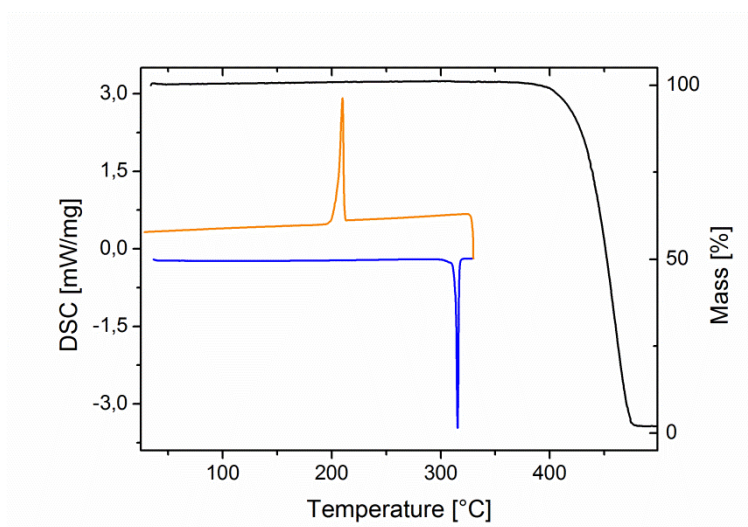


Figure S 16. DSC and TG trace of o-3MPCzPOXD recorded at a heating rate of $5\text{ }^{\circ}\text{C min}^{-1}$.

C. EL Spectra

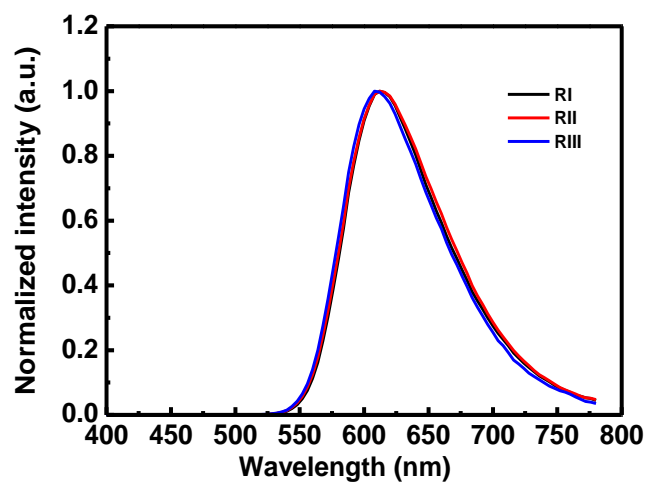


Figure S 17. EL spectra in the red OLEDs based on the hosts of **o-PCzPOXD** (RI), **o-2MPCzPOXD** (RII) and **o-3MPCzPOXD** (RIII).

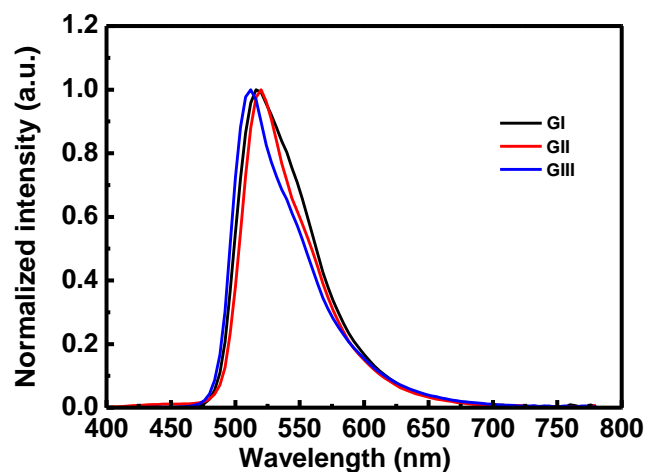


Figure S 18. EL spectra in the green OLEDs based on the hosts of **o-PCzPOXD** (GI), **o-2MPCzPOXD** (GII) and **o-3MPCzPOXD** (GIII).

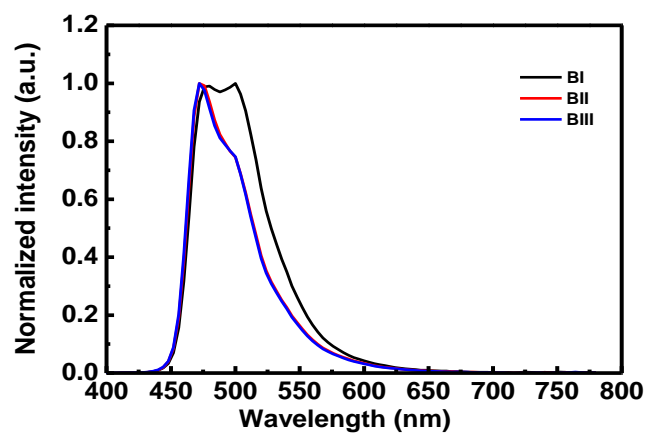


Figure S 19. EL spectra in the Flrpic-based blue OLEDs with **o**-PCzPOXD (BI), **o**-2MPCzPOXD (BII) and **o**-3MPCzPOXD (BIII) as the hosts.

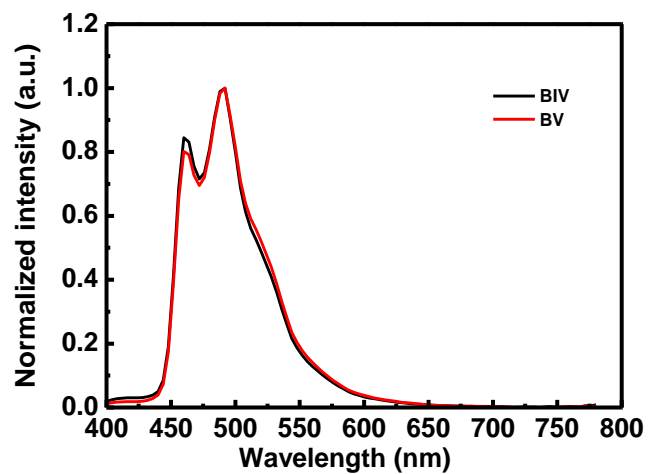


Figure S 20. EL spectra in the Flr6-based blue OLEDs with **o**-2MPCzPOXD (BIV) and **o**-3MPCzPOXD (BV) as the hosts.

D. PL Spectra

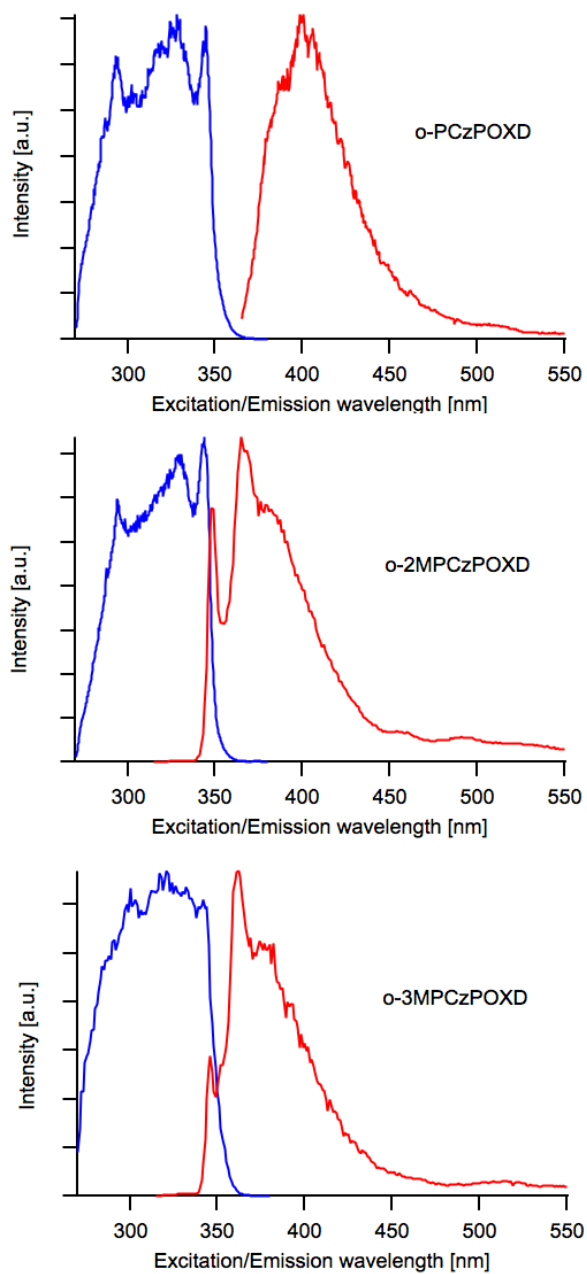


Figure S 21. Normalized excitation (blue) and fluorescence spectra at 77 K of **o-PCzPOXD**, **o-2MPCzPOXD** and **o-3MPCzPOXD** measured with a Fluorolog FL3-22 instrument.

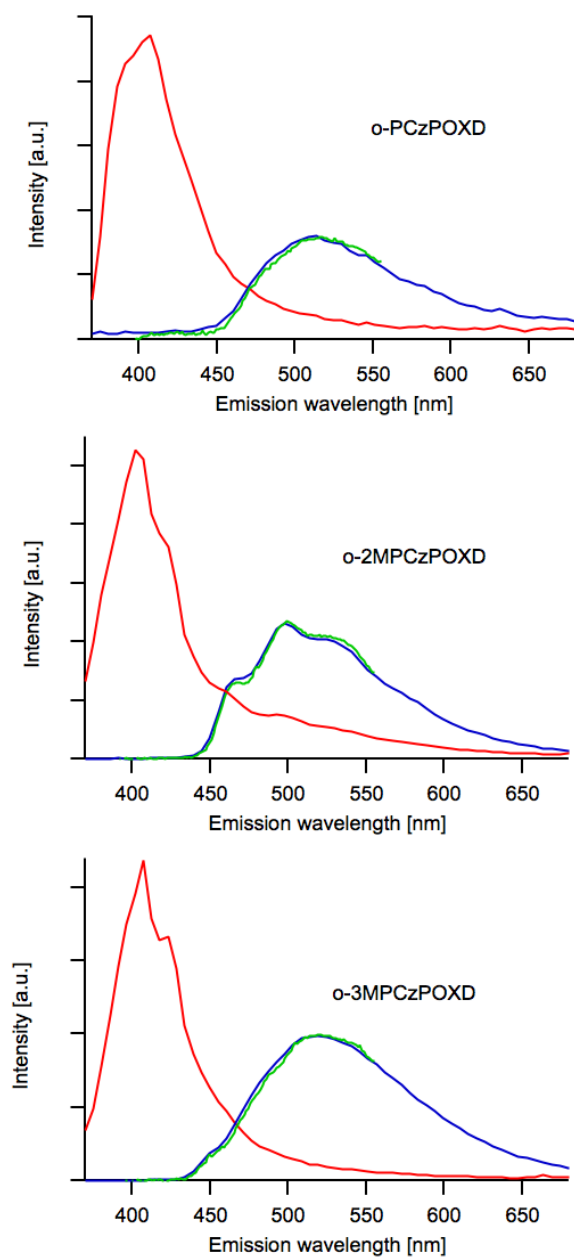


Figure S 22. Normalized low-resolution fluorescence (red), low-resolution phosphorescence (blue) and high-resolution phosphorescence spectra at 77 K of **o-PCzPOXD**, **o-2MPCzPOXD** and **o-3MPCzPOXD**. These measurements have been performed with our home-built setup described in the experimental section. A 370 nm cutoff filter is used for these measurements, preventing the detection of the high-energy part of the fluorescence spectra.

E. Crystal Structures

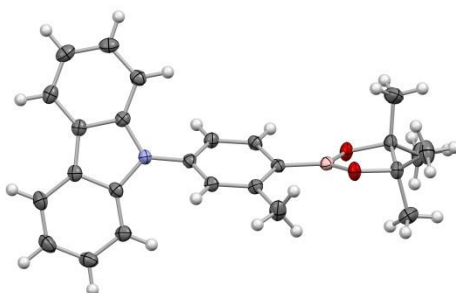


Figure S 23. Molecular structure of **2**. B, C, N, and O atoms are represented by pink, grey, blue and red ellipsoids drawn at 70% probability levels, H atoms by spheres of arbitrary radius.

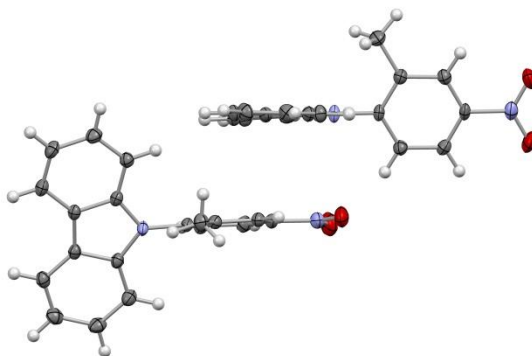


Figure S 24. Molecular structure of **4**. C, N, and O atoms are represented by grey, blue, red and yellow ellipsoids drawn at 70% probability levels, H atoms by spheres of arbitrary radius.

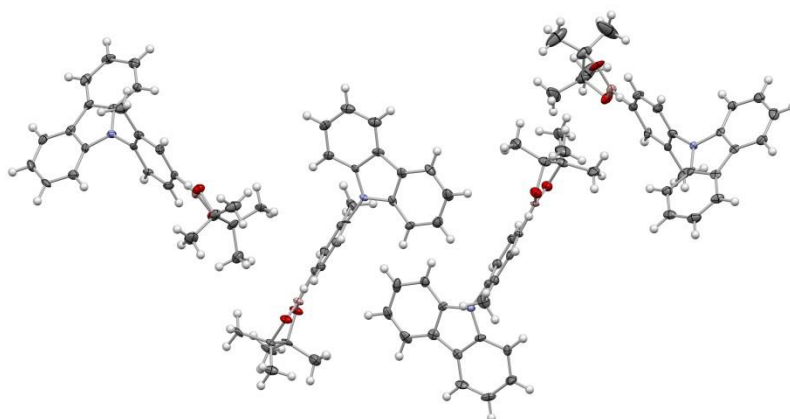


Figure S 25. Molecular structure of **7**. B, C, N, and O atoms are represented by pink, grey, blue and red ellipsoids drawn at 70% probability levels, H atoms by spheres of arbitrary radius.

F. Device Architecture

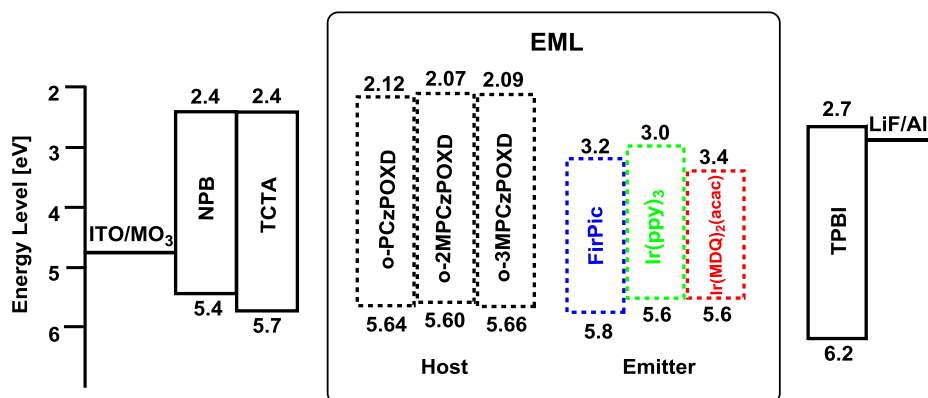


Figure S 26. Energy-level diagram for devices based on FirPic, Ir(ppy)₃ and Ir(MDQ)₂(acac).

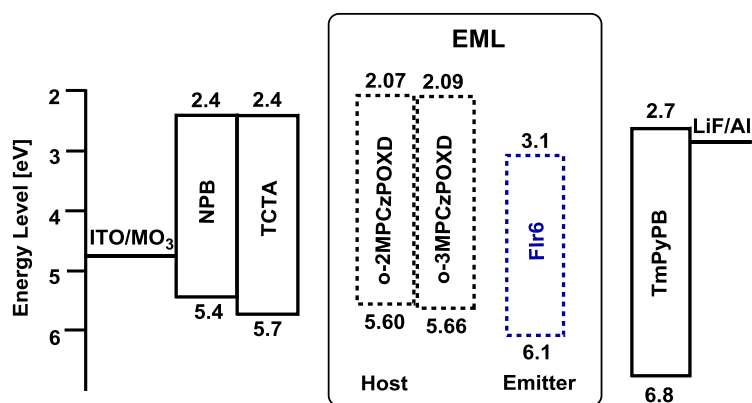


Figure S 27. Energy-level diagram for devices based on Fir6.

3.5. Manuscript #5 – Supporting Information

Using dicyanoanthracene triflates as superior precursors: modifying properties by sterically hindered aryl substituents

Florian Glöckhofer, Paul Kautny, Patrick Fritz, Berthold Stöger, Johannes Fröhlich

ChemPhotoChem, **2017**, 1, 51-55

Supporting Information

Using Dicyanoanthracene Triflates as Superior Precursors: Modifying Properties by Sterically Hindered Aryl Substituents

Florian Glöckhofer,^{*,[a]} Paul Kautny,^[a] Patrick Fritz,^[a] Berthold Stöger,^[b] and
Johannes Fröhlich^[a]

cptc_201600018_sm_miscellaneous_information.pdf

Table of contents:

1. Instrumentation	-1-
2. Synthesis	-3-
3. ^1H -, ^{13}C (APT)-NMR spectra	-7-
4. GC-MS measurements	-12-
5. Crystallography	-15-
6. DFT calculations	-18-
7. References	-19-

1. Instrumentation

NMR spectra were recorded at 600 MHz for ^1H and 150 MHz for ^{13}C on a Bruker Avance III HD spectrometer. Data for ^1H NMR is reported as follows: chemical shift in parts per million from TMS (tetramethylsilane), with the residual solvent signal as an internal reference (CDCl_3 δ = 7.26 ppm), multiplicity (s = singlet, d = doublet, dd = doublet of doublets, t = triplet, q = quartet, m = multiplet), coupling constant in Hz and integration. ^{13}C NMR data is reported in ppm from TMS using the central peak of the solvent as reference (CDCl_3 δ = 77.16 ppm); multiplicity with respect to H (s = quaternary C, d = CH, q = CH_3) or F (q = CF_3) deduced from APT experiments.

GC-MS measurements for reaction monitoring and substance identification were conducted using a system from Thermo Scientific (Trace 1300 Gas Chromatograph (30 m TR-5MS column), ICQ LT Single Quadrupole Mass Spectrometer (EI)). During the GC run, the oven was first kept at 100°C for 4 min and was then heated to 300°C with a rate of 30°C min⁻¹ for the rest of the run.

The m/z values and ratios of the two most intensive molecular ion peak signals are provided. A third value is given if the signal intensity reaches 10%+ of the most intensive molecular ion peak signal. For **3a** and **3b** no peak was detected in GC-MS measurements.

UV/VIS absorption was recorded on a Perkin Elmer Lambda 35 spectrometer. Samples for the measurements were prepared from saturated solutions in n-heptane, which were diluted in such a manner that the first absorption peaks exhibited an absorbance of 0.1-0.2. Further measurement conditions: slit = 2 nm, step = 0.5 nm, room temperature.

Photoluminescence emission spectra in n-heptane solution were recorded on an Edinburgh FLS920 spectrometer using samples prepared in the same way as for the UV/VIS absorption measurements and purged with argon for 15 min. Excitation wavelength: 365 nm. Further measurement parameters: ex. slit = 1 nm, em. slit = 1 nm, step = 0.5 nm, dwell time = 0.3 s, repeats = 3, temperatures between 23.1 and 24.1°C. No filters were used.

Photoluminescence quantum yields in solution were determined relative to DCA (90% quantum yield in n-heptane solution according to Schoof et al.^[S1]). The required photoluminescence emission spectra and the absorption at the excitation wavelength were determined using the same instruments and settings as above. The same samples were used for both measurements.

Photoluminescence emission spectra in the solid state were also recorded on an Edinburgh FLS920 spectrometer using a solid sample holder. Excitation wavelengths: 390 nm (DCA), 410 nm (**4aa**), 400 nm (**4ab**), 390 nm (**4b**). Further measurement parameters: ex. slit = 1 nm, em. slit = 1 nm, step = 0.5 nm, dwell time = 0.5 s, repeats = 3, temperatures between 23.1 and 24.1°C.

Elemental analysis was performed at the “Mikroanalytisches Laboratorium” (University of Vienna, Mag. Johannes Theiner). The deviation from the calculated values for **4ab** and **4b** is attributed to small residues of CH₂Cl₂, which remained also after prolonged vacuum treatment.

2. Synthesis

Reagents and solvents were purchased from commercial suppliers and used without further purification, except for PBr_3 , which was purified by distillation prior to use. Column chromatography and filtration over pads of silica were performed using silica 60 (Merck, 40-63 μm). Reactions were monitored by TLC (Merck, silica gel 60 F₂₅₄) whenever possible. 9,10-Dicyanoanthracene (DCA) was prepared by a published protocol and purified by column chromatography.^[S2]

2.1 Bistriflate of 2,6-dihydroxyanthraquinone 2a

Synthesis according to Gautrot *et al.*^[S3] The reaction was stirred mechanically. ¹H NMR data in accordance with the literature; (GC-)MS (70 eV): *m/z* (%): 504.0 (100) [M^+], 505.0 (20) [M^+], 506.0 (13) [M^+].

2.2 Bistriflate of 1,5-dihydroxyanthraquinone 2b

Synthesis following the protocol of Gautrot *et al.* for the synthesis of **2a**.^[S3] The reaction was stirred mechanically. ¹H NMR (600 MHz, CDCl_3): δ = 8.48 (dd, *J* = 7.9 Hz, 1.1 Hz, 2H; CH), 7.94 (t, *J* = 8.0 Hz, 2H; CH), 7.66 (d, *J* = 8.1 Hz, 2H; CH) ppm; ¹³C NMR (150 MHz, CDCl_3): δ = 179.7 (s; C), 147.6 (s; C), 136.1 (d; CH), 136.0 (s; C), 129.0 (d; CH), 128.6 (d; CH), 125.0 (s; C), 118.9 (q, *J* = 320.9 Hz; CF_3) ppm; (GC-)MS (70 eV): *m/z* (%): 504.0 (100) [M^+], 505.0 (16) [M^+], 506.0 (11) [M^+]; elemental analysis calcd (%) for $\text{C}_{16}\text{H}_6\text{F}_6\text{O}_8\text{S}_2$: C 38.11, H 1.20, N 0.00, S 12.71; found: C 38.47, H 1.21, N <0.05, S 12.50.

2.3 Bistriflate of 2,6-dihydroxy-9,10-dicyanoanthracene 3a

n-Butyllithium (0.12 ml, 0.30 mmol, 0.10 eq, 2.5 M in hexanes) was added carefully to rigorously stirred TMSCN (654.8 mg, 0.83 ml, 6.60 mmol, 2.20 eq) in a sealed reaction vial equipped with a septum at room temperature. After 15 min, the resulting mixture was added dropwise to 2,6-dihydroxyanthraquinone bistriflate **2a** (1513 mg, 3.00 mmol, 1.00 eq) in a round bottom flask, again equipped with a septum and at room temperature. Dry DMF (1.5 ml) was used to fully transfer the residues of the mixture. The reaction stirred at room temperature for 3 h. 9 ml dry MeCN and PBr_3 (974.5 mg, 0.34 ml, 3.60 mmol, 1.20 eq) were added and the reaction was slowly heated to 50°C overnight. The reaction was then allowed to cool to room

temperature, diluted with CH₂Cl₂ and directly filtered over a pad of silica (conditioned with CH₂Cl₂ and some drops of MeCN) using CH₂Cl₂ as eluent. After evaporation of the solvent, the residue was purified by column chromatography (petroleum ether:CH₂Cl₂ 7:3 → 3:2). **3a** (725.0 mg, 1.38 mmol, 46%) was obtained as bright yellow solid. ¹H NMR (600 MHz, CDCl₃): δ = 8.68 (d, J = 9.5 Hz, 2H; CH), 8.44 (d, J = 2.4 Hz, 2H; CH), 7.83 (dd, J = 9.5 Hz, 2.4 Hz, 2H; CH) ppm; ¹³C NMR (150 MHz, CDCl₃): δ = 150.1 (s; C), 132.6 (s; C), 131.4 (s; C), 129.8 (d; CH), 125.6 (d; CH), 118.9 (q, J = 321.0 Hz; CF₃), 118.0 (d; CH), 114.6 (s; C), 113.0 (s; C) ppm; (GC-)MS (70 eV): no signal detected; elemental analysis calcd (%) for C₁₈H₆F₆N₂O₆S₂: C 41.23, H 1.15, N 5.34, S 12.23; found: C 40.98, H 1.09, N 5.14, S 12.21.

2.4 Bistriflate of 1,5-dihydroxy-9,10-dicyanoanthracene **3b**

n-Butyllithium (0.20 ml, 0.50 mmol, 0.10 eq, 2.5 M in hexanes) was added carefully to rigorously stirred TMSCN (1091 mg, 1.38 ml, 11.00 mmol, 2.20 eq) in a sealed reaction vial equipped with a septum at room temperature. After 15 min, the resulting mixture was added dropwise to 1,5-dihydroxyanthraquinone bistriflate **2b** (2521 mg, 5.00 mmol, 1.00 eq) in a round bottom flask, again equipped with a septum and at room temperature. Dry DMF (2.5 ml) was used to fully transfer the residues of the mixture. The reaction stirred at room temperature for 3 h. 15 ml dry MeCN and PBr₃ (1624 mg, 0.57 ml, 6.00 mmol, 1.20 eq) were added and the reaction was slowly heated to 50°C overnight. The reaction was then allowed to cool to room temperature, diluted with CH₂Cl₂ and directly filtered over a pad of silica (conditioned with CH₂Cl₂ and some drops of MeCN) using CH₂Cl₂ as eluent. After evaporation of the solvent, the residue was purified by column chromatography (petroleum ether:CH₂Cl₂ 7:3 → 3:2). **3b** (1089 mg, 2.08 mmol, 42%) was obtained as bright yellow solid. ¹H NMR (600 MHz, CDCl₃): δ = 8.83 (dd, J = 8.4 Hz, 1.4 Hz, 2H; CH), 7.98 (dd, J = 7.7 Hz, 1.4 Hz, 2H; CH), 7.95 (t, J = 8.0 Hz, 2H; CH) ppm; ¹³C NMR (150 MHz, CDCl₃): δ = 143.9 (s; C), 135.2 (s; C), 129.9 (d; CH), 127.5 (d; CH), 125.4 (s; C), 122.8 (d; CH), 118.8 (q, J = 321.7 Hz; CF₃), 115.3 (s; C), 108.6 (s; C) ppm; (GC-)MS (70 eV): no signal detected; elemental analysis calcd (%) for C₁₈H₆F₆N₂O₆S₂: C 41.23, H 1.15, N 5.34, S 12.23; found: C 41.06, H 1.14, N 5.16, S 12.16.

2.5 2,6-Diphenyl-9,10-dicyanoanthracene 4aa

A three neck round bottom flask equipped with a reflux condenser was charged with 2,6-dihydroxy-9,10-dicyanoanthracene bistriflate **3a** (104.9 mg, 0.20 mmol, 1.00 eq) and phenylboronic acid (61.0 mg, 0.50 mmol, 2.50 eq). The flask was flushed with argon, 4 ml degassed THF were added and the reaction was heated to reflux. A degassed solution of K₂CO₃ (138.2 mg, 1.00 mmol, 5.0 eq) in 0.50 ml water (2.0 M) and Pd(PPh₃)₄ (11.6 mg, 0.01 mmol, 0.05 eq) were then added and the reaction was stirred for 30 min under argon atmosphere. After cooling to room temperature, the reaction was poured on water and extracted four times with CH₂Cl₂. The combined organic layers were dried over sodium sulfate and the solvent was evaporated in vacuo. After evaporation of the solvent, the residue was purified by column chromatography (petroleum ether:CH₂Cl₂ 3:2). **4aa** (70.4 mg, 0.19 mmol, 93%) was obtained as bright orange solid. ¹H NMR data in accordance with the literature;^[S1] (GC-)MS (70 eV): *m/z* (%): 380.2 (100) [*M*⁺], 381.2 (28) [*M*⁺].

2.6 2,6-Dimesityl-9,10-dicyanoanthracene 4ab

A three neck round bottom flask equipped with a reflux condenser was charged with 2,6-dihydroxy-9,10-dicyanoanthracene bistriflate **3a** (104.9 mg, 0.20 mmol, 1.00 eq) and mesitylboronic acid (82.0 mg, 0.50 mmol, 2.50 eq). The flask was flushed with argon, 4 ml degassed THF were added and the reaction was heated to reflux. A degassed solution of K₂CO₃ (138.2 mg, 1.00 mmol, 5.0 eq) in 0.50 ml water (2.0 M) and Pd(PPh₃)₄ (11.6 mg, 0.01 mmol, 0.05 eq) were then added and the reaction was stirred for 90 min under argon atmosphere. After cooling to room temperature, the reaction was poured on water and extracted four times with CH₂Cl₂. The combined organic layers were dried over sodium sulfate and the solvent was evaporated in vacuo. After evaporation of the solvent, the residue was purified by column chromatography (petroleum ether:CH₂Cl₂ 3:2). **4ab** (84.2 mg, 0.18 mmol, 91%) was obtained as bright yellow solid. ¹H NMR (600 MHz, CDCl₃): δ = 8.58 (d, J = 8.8 Hz, 2H; CH), 8.33 (s, 2H; CH), 7.67 (dd, J = 8.8 Hz, 1.5 Hz, 2H; CH), 7.04 (s, 4H; CH), 2.39 (s, 6H; CH₃), 2.06 (s, 12H; CH₃) ppm; ¹³C NMR (150 MHz, CDCl₃): δ = 143.4 (s; C), 138.0 (s; C), 137.0 (s; C), 135.8 (s; C), 132.7 (d; CH), 132.4 (s; C), 131.6 (s; C), 128.7 (d; CH), 126.4 (d; CH), 126.0 (d; CH), 116.2 (s; C), 111.2 (s; C), 21.3 (q; CH₃), 20.9 (q; CH₃) ppm; (GC-)MS (70 eV): *m/z* (%): 464.2 (100) [*M*⁺], 465.3 (33) [*M*⁺];

elemental analysis calcd (%) for C₃₄H₂₈N₂: C 87.90, H 6.07, N 6.03; found: C 86.46, H 6.33, N 5.77.

2.7 1,5-Diphenyl-9,10-dicyanoanthracene **4b**

A three neck round bottom flask equipped with a reflux condenser was charged with 1,5-dihydroxy-9,10-dicyanoanthracene bistriflate **3b** (262.2 mg, 0.50 mmol, 1.00 eq) and phenylboronic acid (152.4 mg, 1.25 mmol, 2.50 eq). The flask was flushed with argon, 10 ml degassed THF were added and the reaction was heated to reflux. A degassed solution of K₂CO₃ (345.5 mg, 2.50 mmol, 5.0 eq) in 1.25 ml water (2.0 M) and Pd(PPh₃)₄ (28.9 mg, 0.025 mmol, 0.05 eq) were then added and the reaction was stirred for 30 min under argon atmosphere. After cooling to room temperature, the reaction was poured on water and extracted four times with CH₂Cl₂. The combined organic layers were dried over sodium sulfate and the solvent was evaporated in vacuo. After evaporation of the solvent, the residue was purified by column chromatography (petroleum ether:CH₂Cl₂ 3:2). **4b** (171.3 mg, 0.45 mmol, 90%) was obtained as bright yellow solid. ¹H NMR (600 MHz, CDCl₃): δ = 8.56 (d, J = 8.8 Hz, 2H; CH), 7.79 (dd, J = 8.8 Hz, 6.9 Hz, 2H; CH), 7.67 (d, J = 6.9 Hz, 2H; CH), 7.62 – 7.55 (m, 6H; CH), 7.50 – 7.47 (m, 4H; CH) ppm; ¹³C NMR (150 MHz, CDCl₃): δ = 140.10 (s; C), 140.09 (s; C), 134.7 (s; C), 132.0 (d; CH), 130.7 (s; C), 130.5 (d; CH), 129.2 (d; CH), 129.0 (d; CH), 128.7 (d; CH), 126.3 (d; CH), 115.4 (s; C), 112.0 (s; C) ppm; (GC-)MS (70 eV): *m/z* (%): 380.1 (100) [*M*⁺], 381.2 (25) [*M*⁺]; elemental analysis calcd (%) for C₂₈H₁₆N₂: C 88.40, H 4.24, N 7.36; found: C 86.95, H 4.32, N 7.22.

3. ^1H -, ^{13}C -NMR spectra

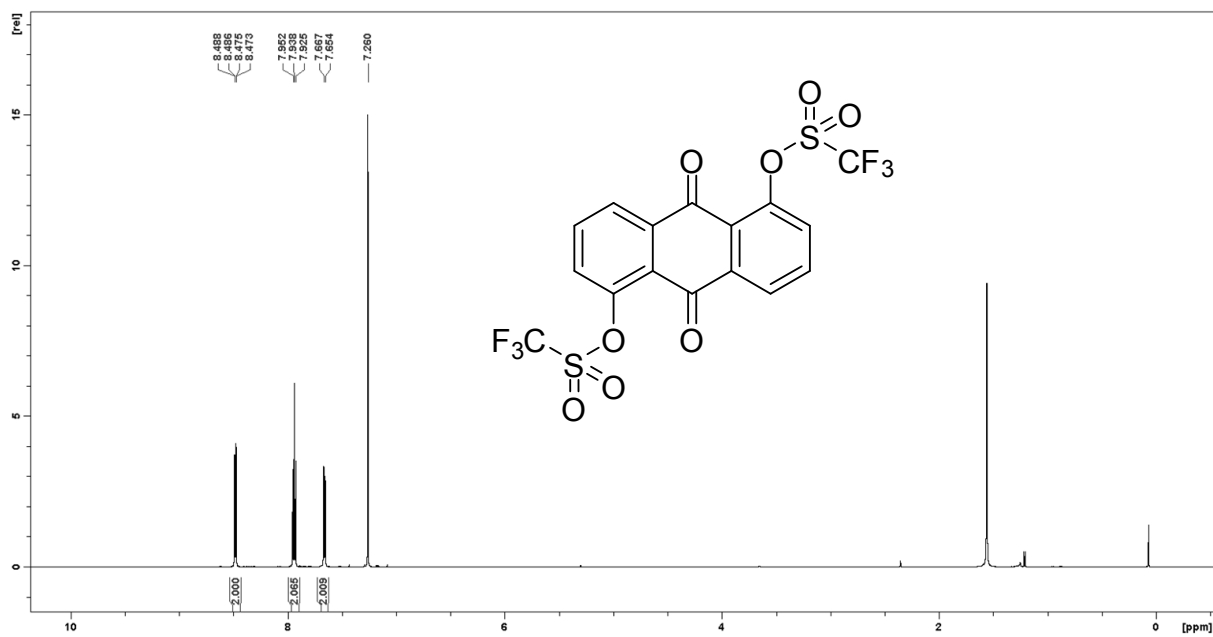


Figure S1: ^1H NMR (600 MHz, CDCl_3) of **2b**

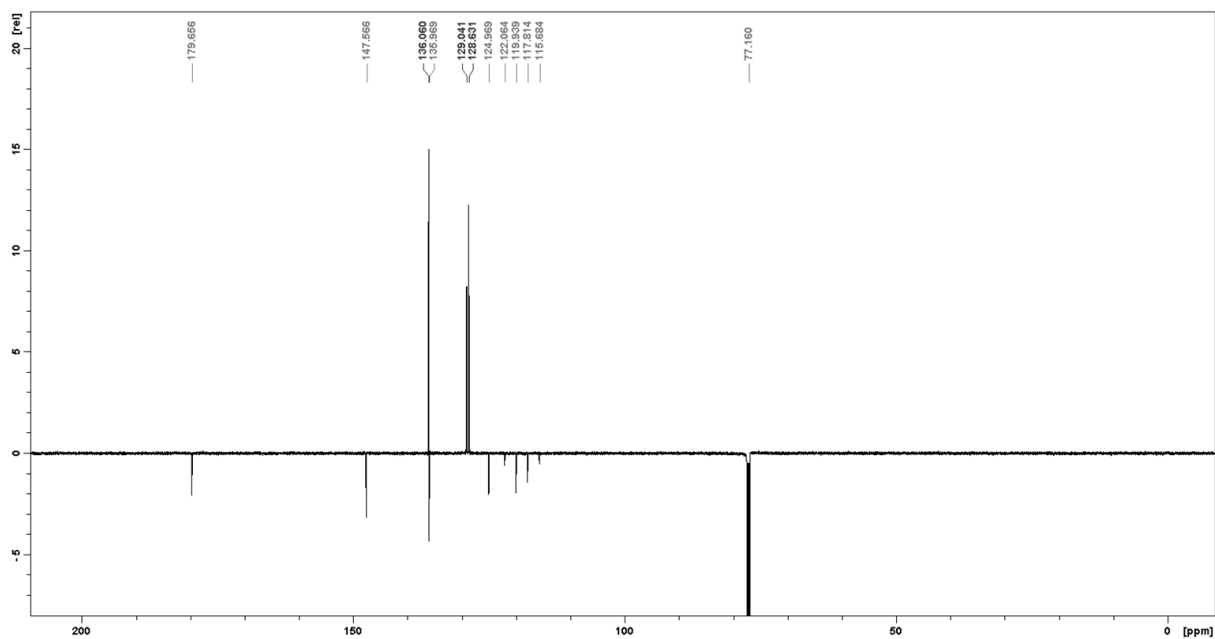


Figure S2: ^{13}C NMR (150 MHz, CDCl_3) of **2b**

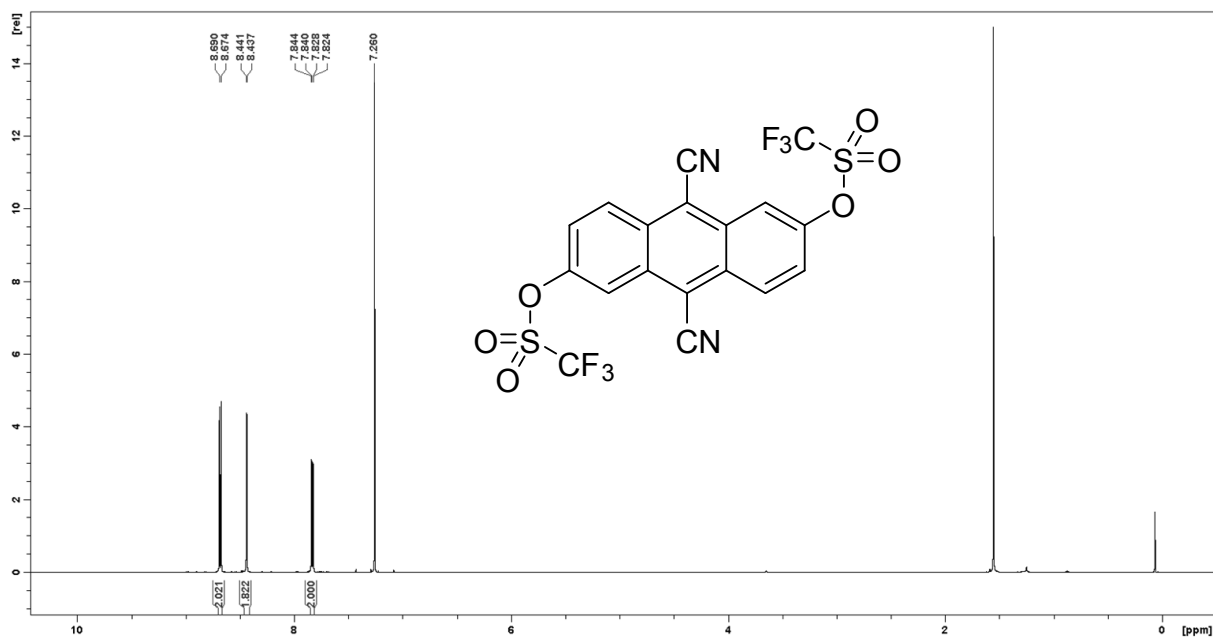


Figure S3: ^1H NMR (600 MHz, CDCl_3) of 3a

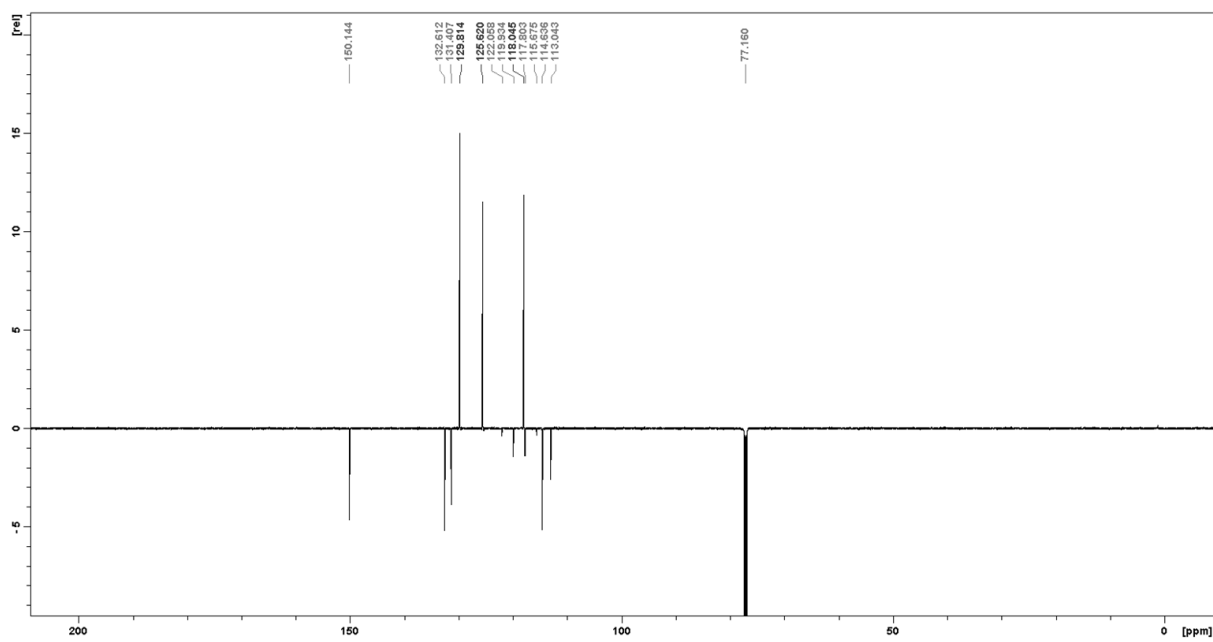


Figure S4: ^{13}C NMR (150 MHz, CDCl_3) of 3a

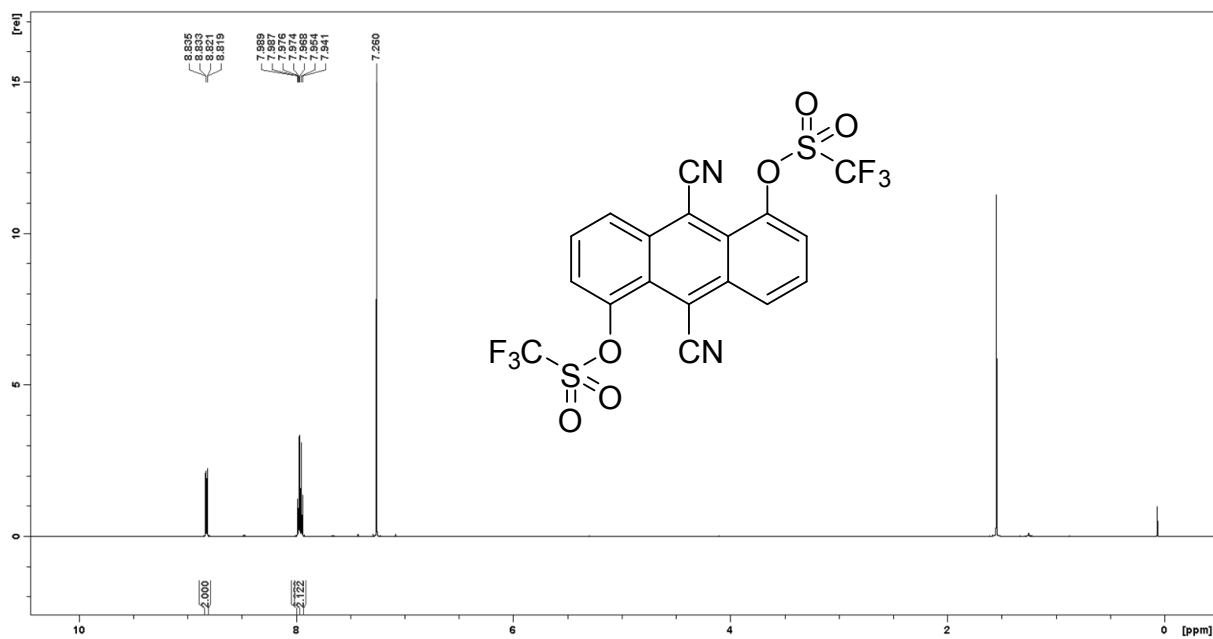


Figure S5: ¹H NMR (600 MHz, CDCl₃) of **3b**

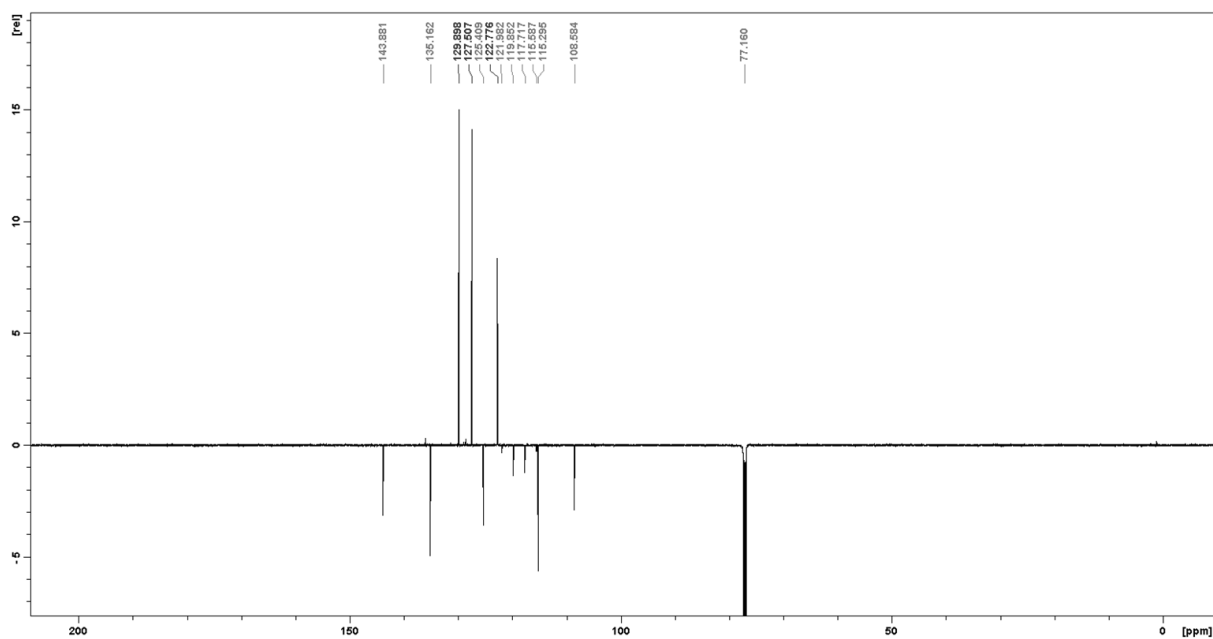


Figure S6: ¹³C NMR (150 MHz, CDCl₃) of **3b**

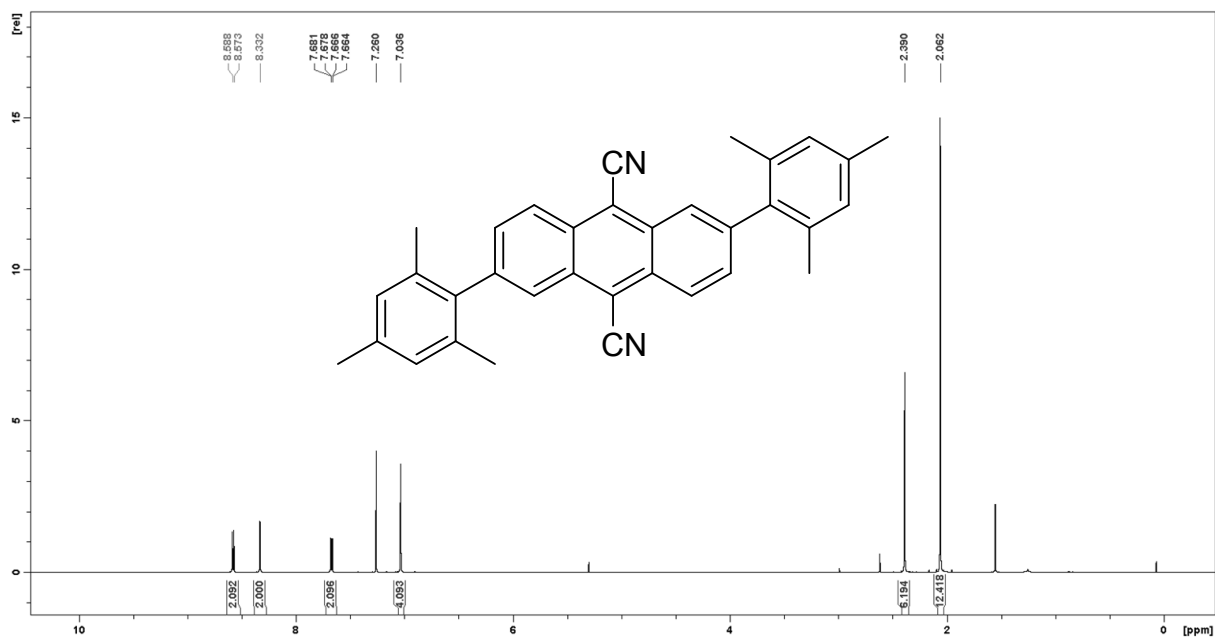


Figure S7: ^1H NMR (600 MHz, CDCl_3) of 4ab

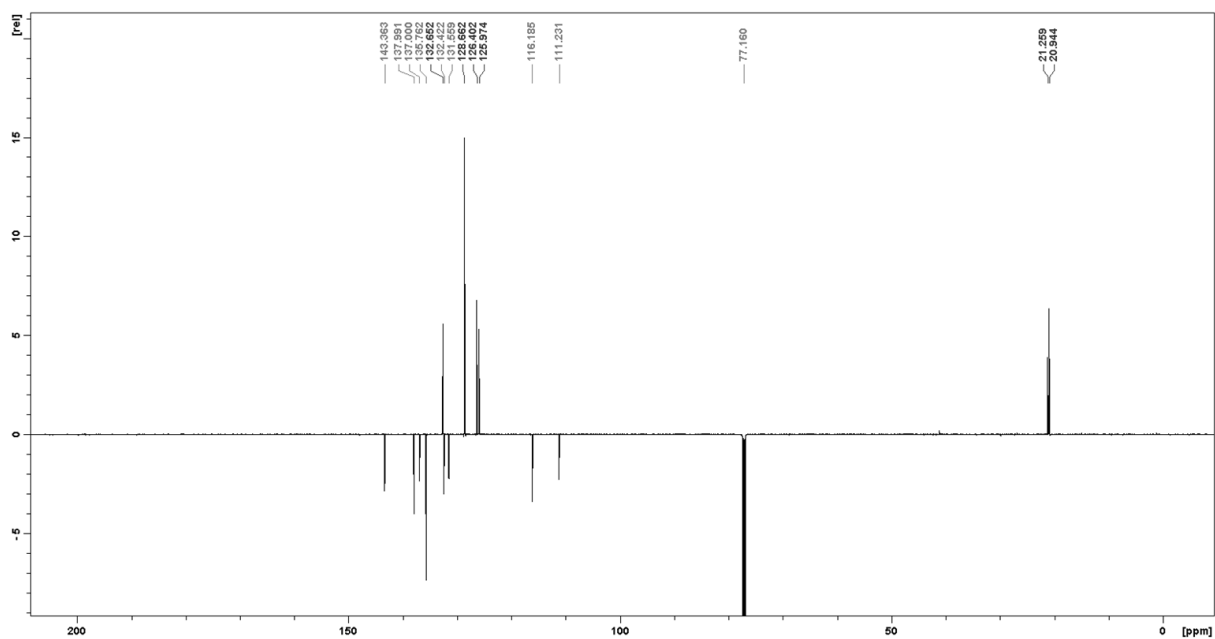


Figure S8: ^{13}C NMR (150 MHz, CDCl_3) of 4ab

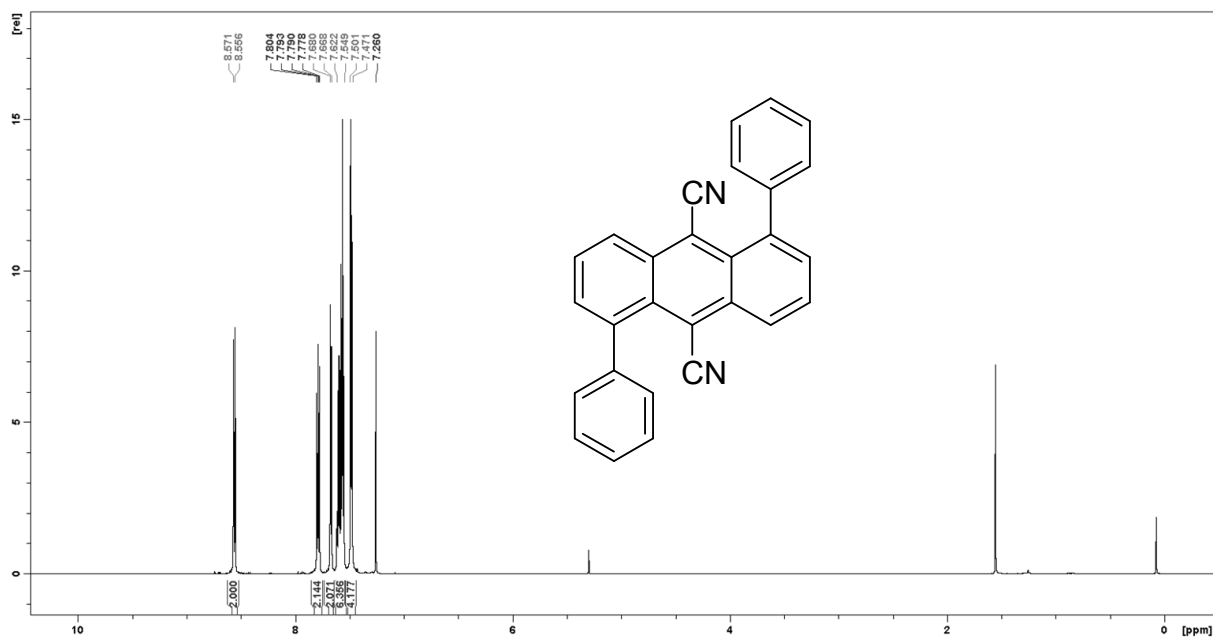


Figure S9: ^1H NMR (600 MHz, CDCl_3) of **4b**

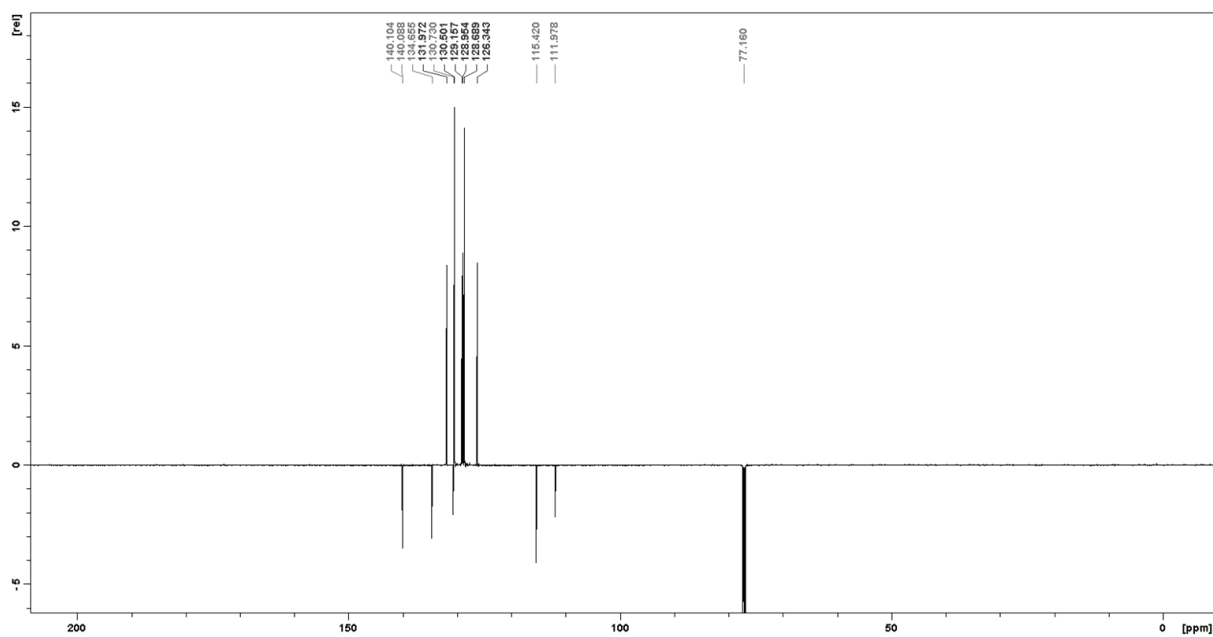


Figure S10: ^{13}C NMR (150 MHz, CDCl_3) of **4b**

4. GC-MS measurements

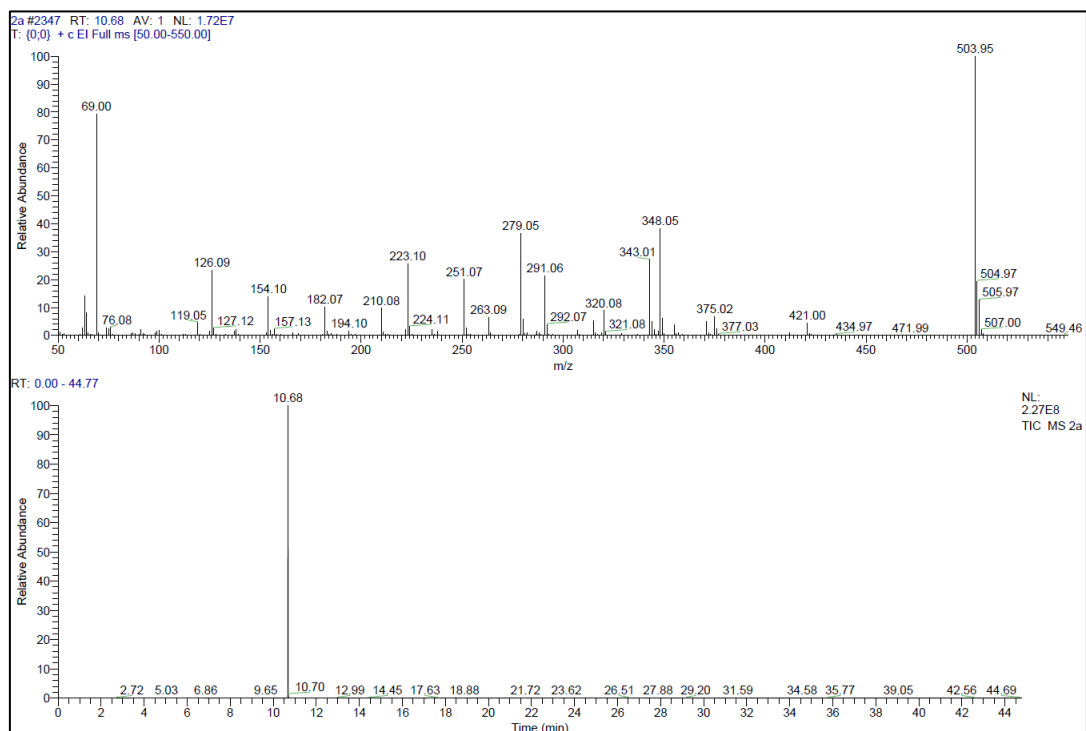


Figure S11: Mass spectrum (top) and gas chromatogram (bottom) of 2a

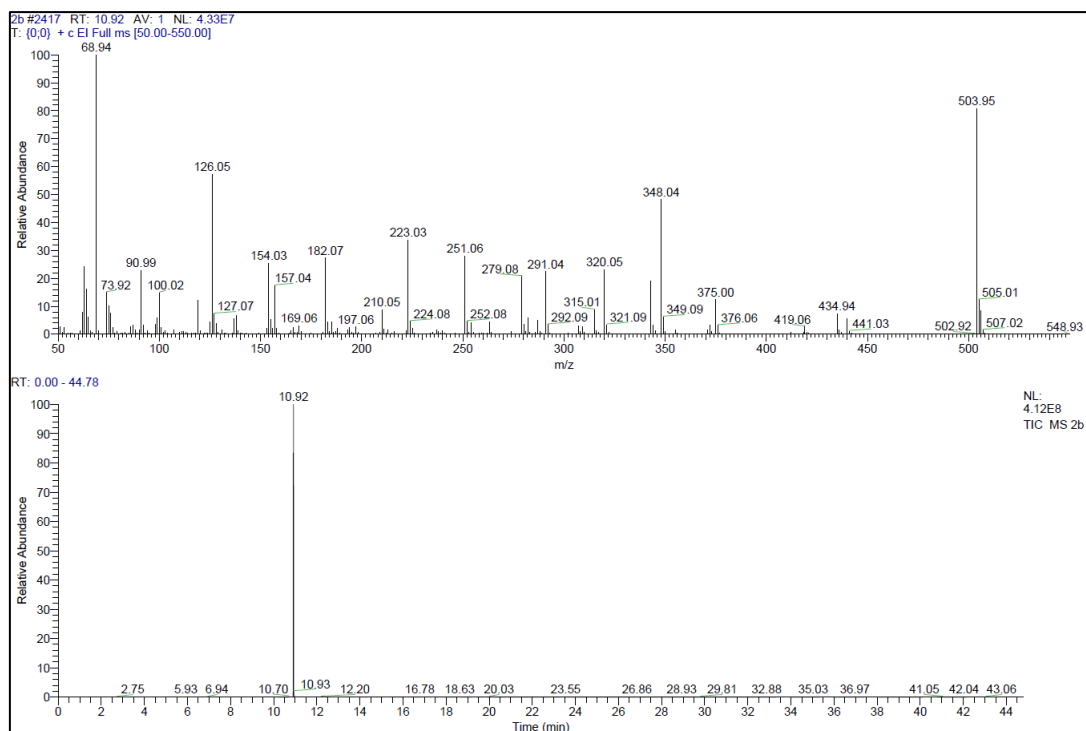


Figure S12: Mass spectrum (top) and gas chromatogram (bottom) of 2b

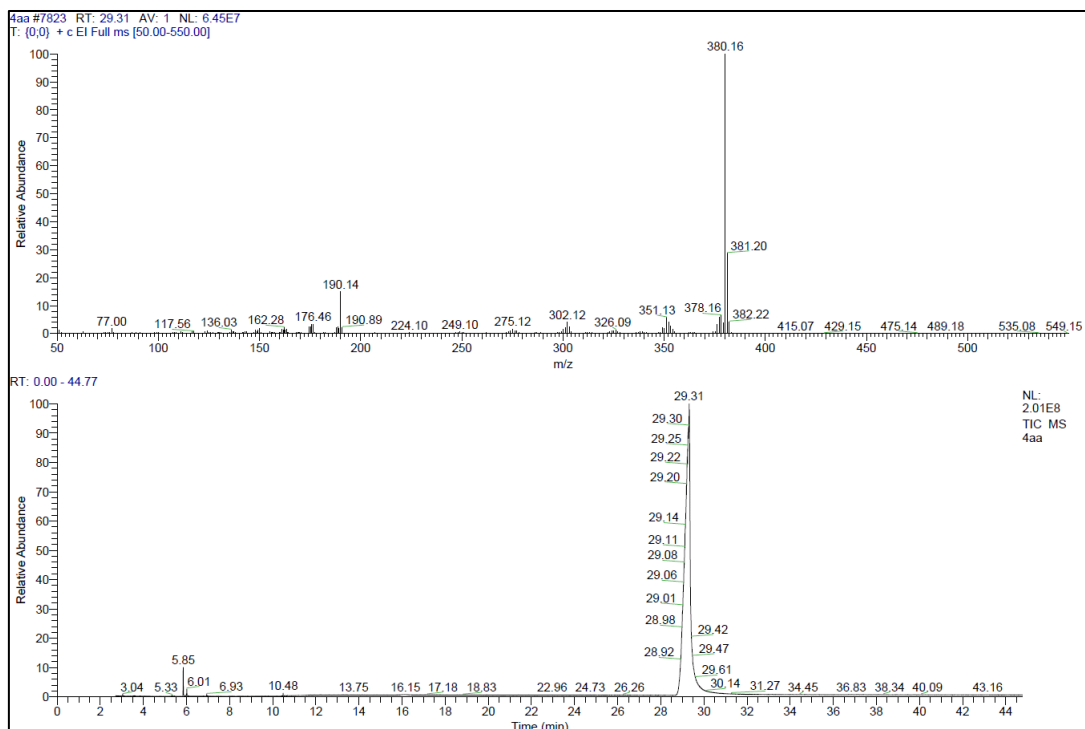


Figure S13: Mass spectrum (top) and gas chromatogram (bottom) of 4aa

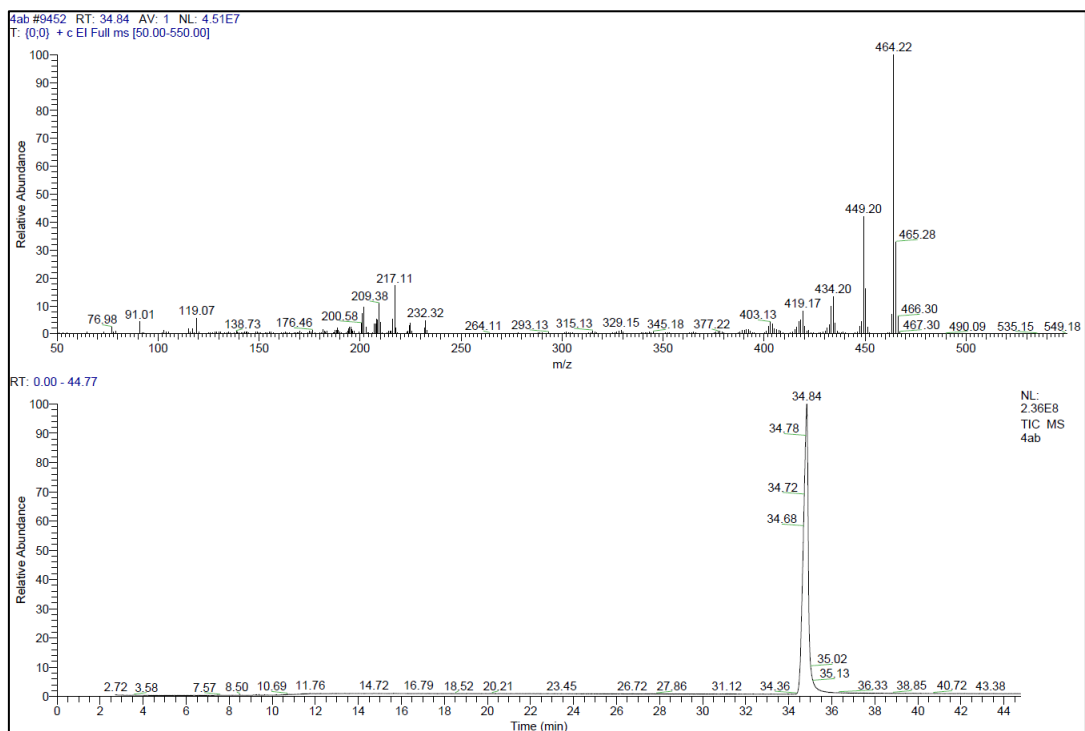


Figure S14: Mass spectrum (top) and gas chromatogram (bottom) of 4ab

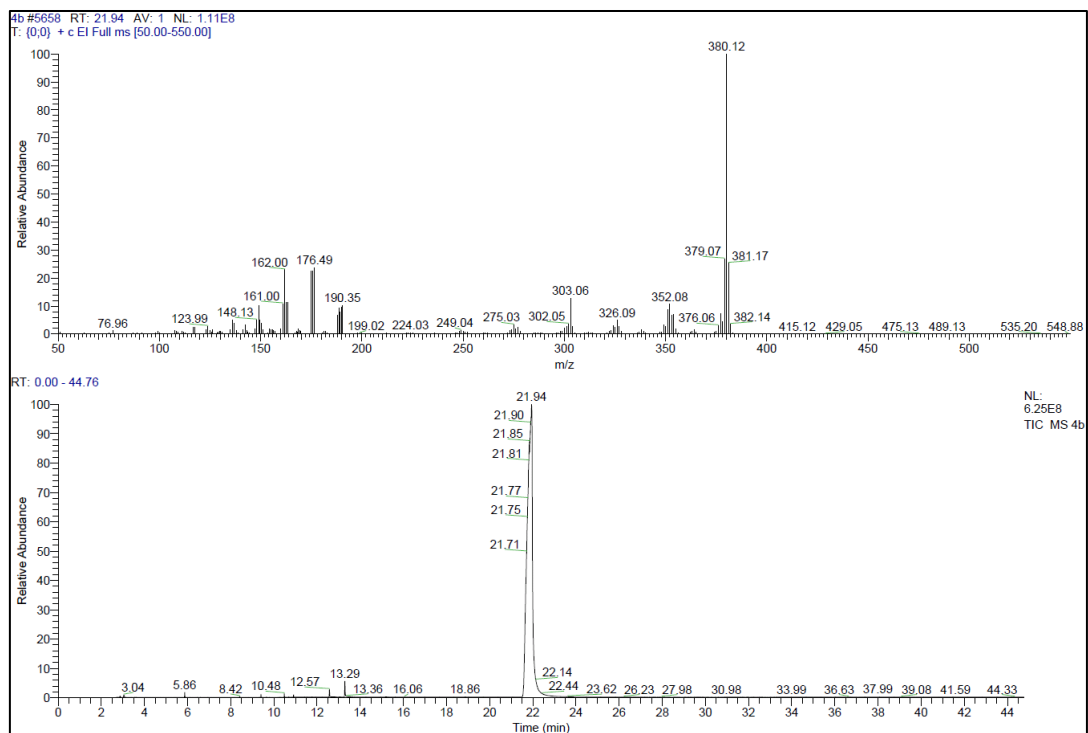


Figure S15: Mass spectrum (top) and gas chromatogram (bottom) of **4b**

5. Crystallography

Crystals of **3a**, **3b**, **4ab**· $\frac{1}{3}$ CDCl₃, **4b** and the cyanohydrin intermediate of **3b** were grown by slow evaporation of CDCl₃ solutions prepared for NMR spectroscopy. Crystals of **4aa**·0.575CHCl₃ were obtained by slow diffusion of ethanol into a solution of **4aa** in CHCl₃. X-ray diffraction data were collected at $T = 200$ K (**3b**, phase transition <200K) or $T = 100$ K (rest) in a dry stream of nitrogen on a Bruker Kappa APEX II diffractometer system using graphite-monochromatized Mo- $K\alpha$ radiation ($\lambda = 0.71073$ Å) and fine-sliced φ - and ω -scans. Data were reduced to intensity values with SAINT and an absorption correction was applied with the multi-scan approach implemented in SADABS.^[S4] The structures were solved by charge flipping implemented in SUPERFLIP^[S5] and refined against F with JANA2006.^[S6] Non-hydrogen atoms, with the exception of the C atom of the disordered CDCl₃ solvent molecule in **3b**, were refined anisotropically. The crystal of **3b** (space group $P2_1$) was modelled as a twin by inversion. The H atoms were placed in calculated positions and thereafter refined as riding on the parent atoms. Molecular graphics were generated with the program MERCURY.^[S7]

3a ($P2_1$) and **3b** ($P\bar{1}$) crystallize with two independent molecules located on the general position (**3a**) and centers of inversion (**3b**). Despite being located on a general position, the molecules in **3a** are pseudo-symmetric by inversion, which is also a twin operation. The molecules in **3b** are disordered, with 5.02(14) % of the molecules of the first kind being substituted for the other kind and vice-versa. Correlation of the disorder is evidenced by two-dimensionally diffuse scattering. The two molecules in each crystal feature distinctly different inclination of the triflate units [**3a**: C-C-O-S-torsion angle 73.31° and 74.19° vs. 36.56° and 41.88°; **3b**: 67.74° vs. 91.19°]. The molecules are arranged in distinct layers delimited by the triflate groups. Inside the **3a** layers the molecules arrange in face-to-face orientation to rods, whereby the contacts are between non-equivalent molecules (Figure S16). Short C-C distances of 3.41 Å show that the triflate groups are not bulky enough to inhibit π - π -interaction. In **3b**, molecules likewise form rods. Here the intermolecular contact is established via the cyanide groups (Figure S17).

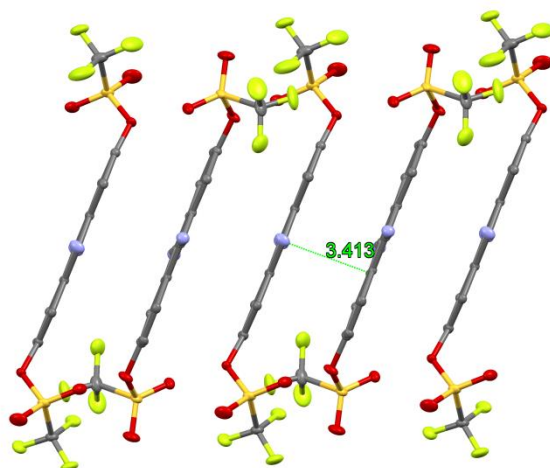


Figure S16: π -stacked rods of **3a** molecules. C (grey), N (blue), O (red), S (yellow), and F (green) atoms are represented by ellipsoids drawn at the 50% probability levels. H atoms were omitted for clarity.

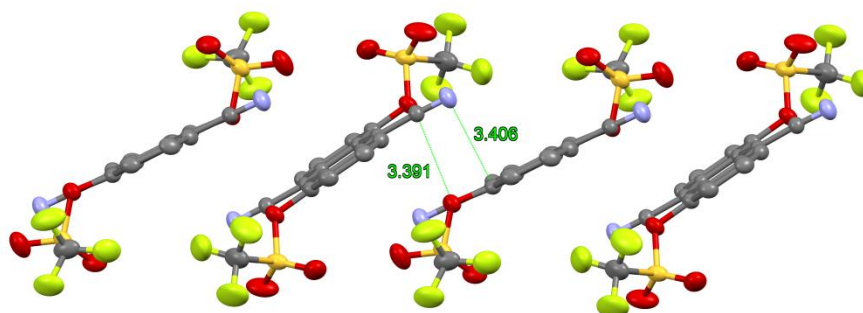


Figure S17: Rods of **3b** molecules contacting via interactions of the CN groups. C (grey), N (blue), O (red), S (yellow), and F (green) atoms are represented by ellipsoids drawn at the 50% probability levels. H atoms were omitted for clarity.

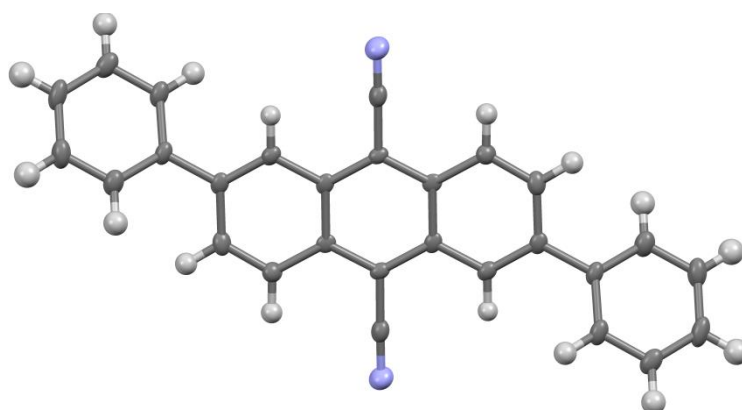


Figure S18: Molecular structure of **4aa**. C (grey) and N (blue) atoms are represented by ellipsoids drawn at the 50% probability levels; H atoms are represented by white spheres of arbitrary radius.

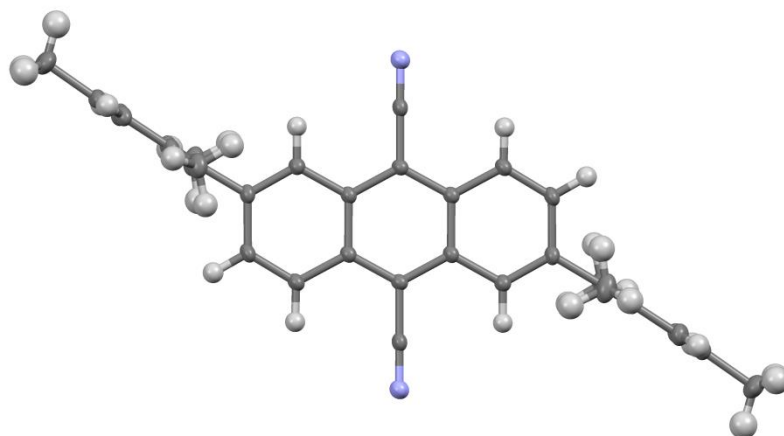


Figure S19: Molecular structure of **4ab**. C (grey) and N (blue) atoms are represented by ellipsoids drawn at the 50% probability levels; H atoms are represented by white spheres of arbitrary radius.

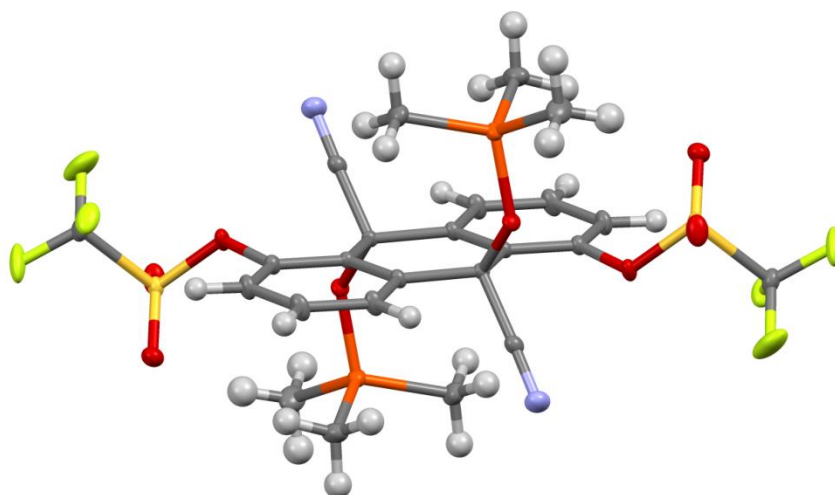


Figure S20: Molecular structure of the cyanohydrin intermediate of **3b**. C (grey), N (blue), O (red), Si (orange), S (yellow), and F (green) atoms are represented by ellipsoids drawn at the 50% probability levels; H atoms are represented by white spheres of arbitrary radius. The molecule is located on a center of inversion.

6. DFT calculations

DFT calculations were performed using the Gaussian 09 package revision D.01.^[S8] applying the Becke three parameters hybrid functional with Lee–Yang–Perdew correlation (B3LYP)^[S9] in combination with Pople basis sets 6-311G(d,p).^[S10] Geometry optimizations were performed in gas phase and without symmetry constraints. Orbital plots were generated using GaussView.^[S11]

Theoretical calculations show through space interactions of the phenyl substituents and the cyano groups in **4b**, indicating electronic communication of the two molecular subunits. This is most evident in the HOMO-3 (Figure S20 left) and LUMO+5 (Figure S20 right) of **4b**, which are derived from the benzene HOMO (Figure S21 left) and LUMO (Figure S20 right).

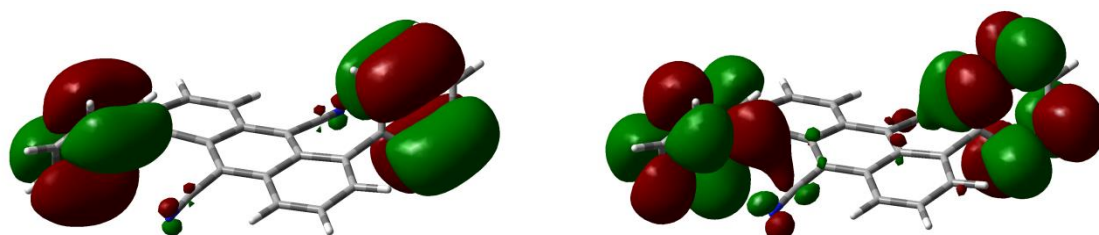


Figure S21: HOMO-3 (left) and LUMO+5 (right) of **4b**

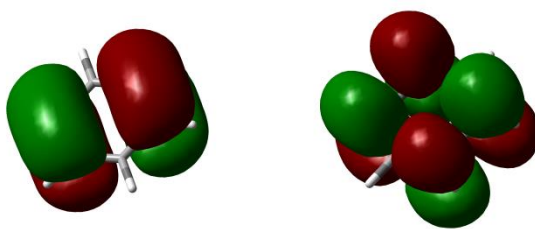


Figure S22: HOMO (left) and LUMO (right) of benzene

7. References

- [S1] S. Schoof, H. Güsten, C. Von Sonntag, *Berichte der Bunsengesellschaft für physikalische Chemie* **1978**, *82*, 1068-1073.
- [S2] F. Glöcklhofer, M. Lunzer, B. Stöger, J. Fröhlich, *Chem. Eur. J.* **2016**, *22*, 5173-5180.
- [S3] J. E. Gautrot, P. Hodge, D. Cupertino, M. Helliwell, *New J. Chem.* **2007**, *31*, 1585-1593.
- [S4] Bruker, *APEX2, SAINT-Plus and SADABS 2013*, Bruker AXS Inc., Madison, Wisconsin, USA.
- [S5] L. Palatinus, G. Chapuis, *J. Appl. Crystallogr.* **2007**, *40*, 786-790.
- [S6] V. Petříček, M. Dušek, L. Palatinus, *Z. Kristallogr. - Cryst. Mater.* **2014**, *229*, 345-352.
- [S7] C. F. Macrae, P. R. Edgington, P. McCabe, E. Pidcock, G. P. Shields, R. Taylor, M. Towler and J. van de Streek, *J. Appl. Crystallogr.* **2006**, *39*, 453-457.
- [S8] M. J. Frisch, G. W. Trucks, H. B. Schlegel, G. E. Scuseria, M. A. Robb, J. R. Cheeseman, G. Scalmani, V. Barone, B. Mennucci, G. A. Petersson, H. Nakatsuji, M. Caricato, X. Li, H. P. Hratchian, A. F. Izmaylov, J. Bloino, G. Zheng, J. L. Sonnenberg, M. Hada, M. Ehara, K. Toyota, R. Fukuda, J. Hasegawa, M. Ishida, T. Nakajima, Y. Honda, O. Kitao, H. Nakai, T. Vreven, J. A. Montgomery Jr., J. E. Peralta, F. Ogliaro, M. J. Bearpark, J. Heyd, E. N. Brothers, K. N. Kudin, V. N. Staroverov, R. Kobayashi, J. Normand, K. Raghavachari, A. P. Rendell, J. C. Burant, S. S. Iyengar, J. Tomasi, M. Cossi, N. Rega, N. J. Millam, M. Klene, J. E. Knox, J. B. Cross, V. Bakken, C. Adamo, J. Jaramillo, R. Gomperts, R. E. Stratmann, O. Yazyev, A. J. Austin, R. Cammi, C. Pomelli, J. W. Ochterski, R. L. Martin, K. Morokuma, V. G. Zakrzewski, G. A. Voth, P. Salvador, J. J. Dannenberg, S. Dapprich, A. D. Daniels, Ö. Farkas, J. B. Foresman, J. V. Ortiz, J. Cioslowski, D. J. Fox, Gaussian, Inc., Wallingford, CT, USA, **2009**.
- [S9] a) C. Lee, W. Yang, R. G. Parr, *Phys. Rev. B* **1988**, *37*, 785-789; b) A. D. Becke, *J. Chem. Phys.* **1993**, *98*, 5648-5652.
- [S10] R. Krishnan, J. S. Binkley, R. Seeger, J. A. Pople, *J. Chem. Phys.* **1980**, *72*, 650-654.
- [S11] R. Dennington, T. Keith, J. Millam, Semichem, Inc., Shawnee Mission, KS, **2009**.

3.6. Manuscript #6 – Supporting Information

Thieno[3,4-*c*]pyrrole-4,6-dione as novel building block for host materials
in red PhOLEDs

Paul Kautny, Chenyang Zhao, Dominik Schopf, Berthold Stöger, Ernst Horkel, Jiangshan Chen,
Dongge Ma, Johannes Fröhlich, Daniel Lumpi

Journal of Materials Chemistry C, **2017**, 5, 1997-2004

Thieno[3,4-*c*]pyrrole-4,6-dione as novel building block for host materials for red PhOLEDs

Supporting Information

Paul Kautny,^{*a} Chenyang Zhao,^b Dominik Schopf,^a Berthold Stöger,^c Ernst Horkel,^a Jiangshan Chen,^{*b} Dongge Ma,^b Johannes Fröhlich^a and Daniel Lumpi^a

^a Institute of Applied Synthetic Chemistry, TU Wien, Getreidemarkt 9/163, A-1060 Vienna, Austria; E-mail: paul.kautny@tuwien.ac.at

^b State Key Laboratory of Polymer Physics and Chemistry, Changchun Institute of Applied Chemistry, Chinese Academy of Sciences, Changchun, 130022, China; E-mail: jschen@ciac.ac.cn

^c Institute of Chemical Technologies and Analytics, TU Wien, Getreidemarkt 9/164, A-1060 Vienna, Austria

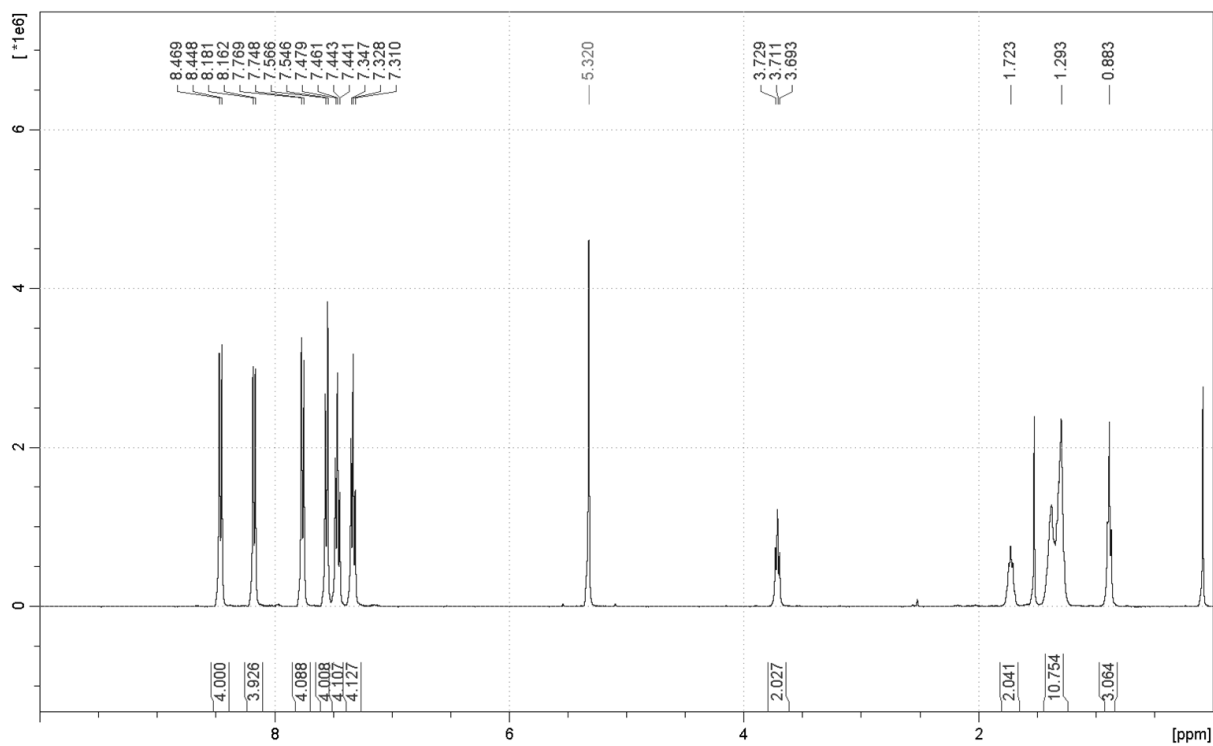


Fig. S1 Proton NMR spectrum of *p*-PCzTPD.

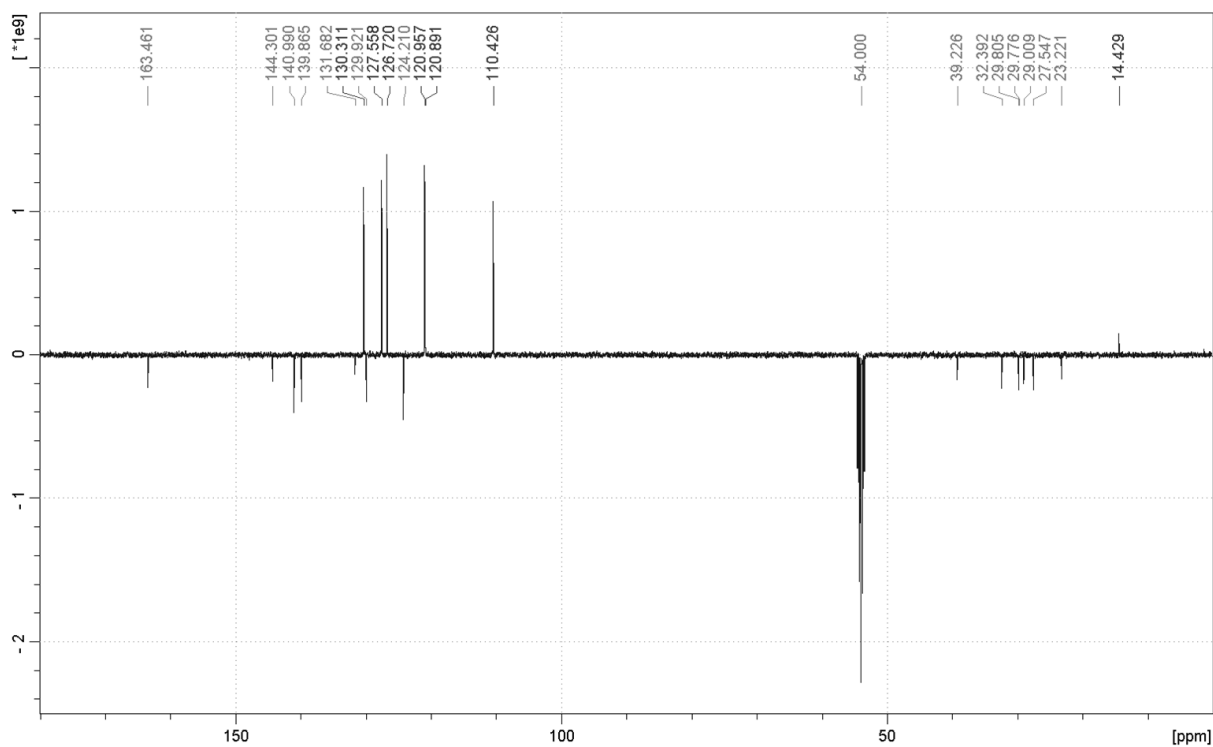


Fig. S2 Carbon NMR spectrum of *p*-PCzTPD.

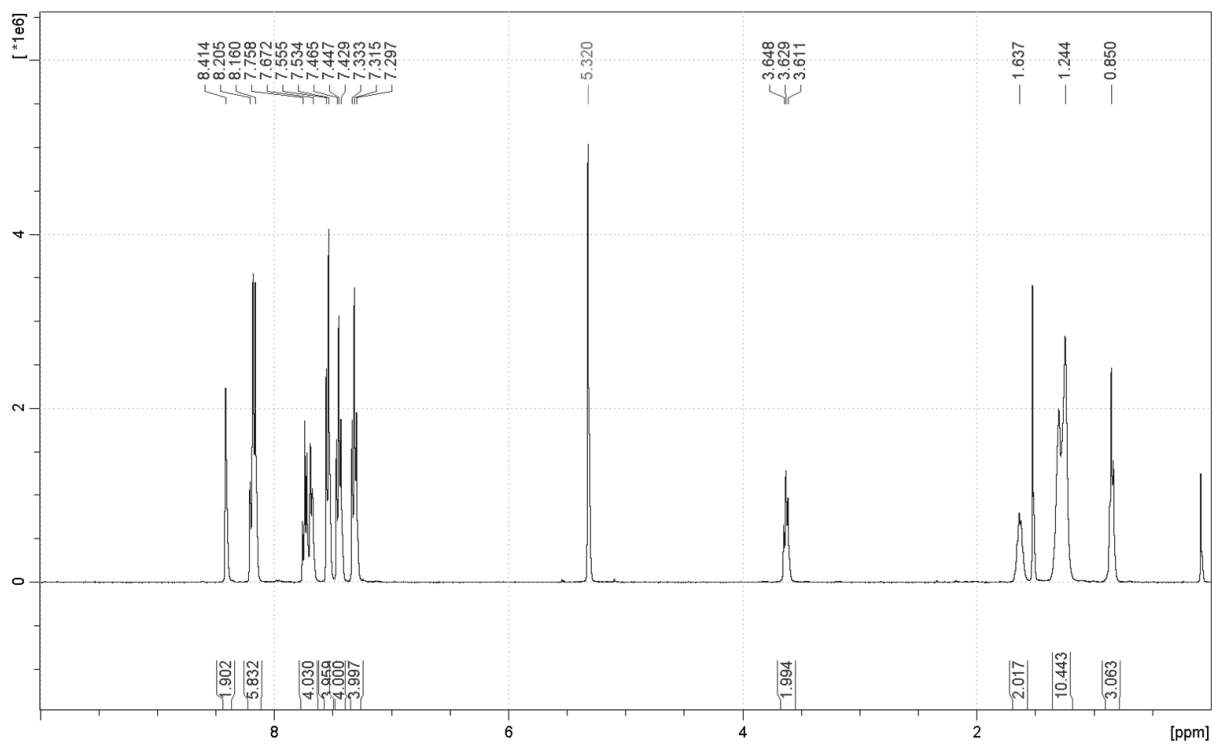


Fig. S3 Proton NMR spectrum of *m*-PCzTPD.

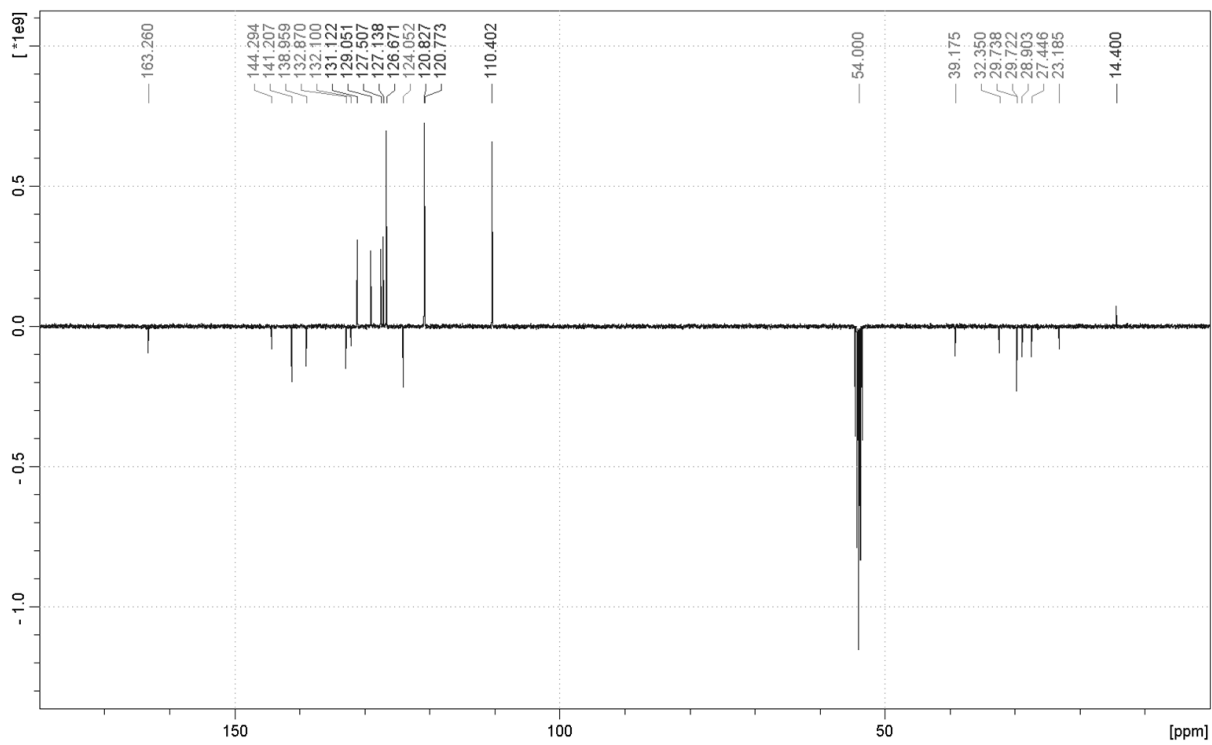


Fig. S4 Carbon NMR spectrum of *m*-PCzTPD.

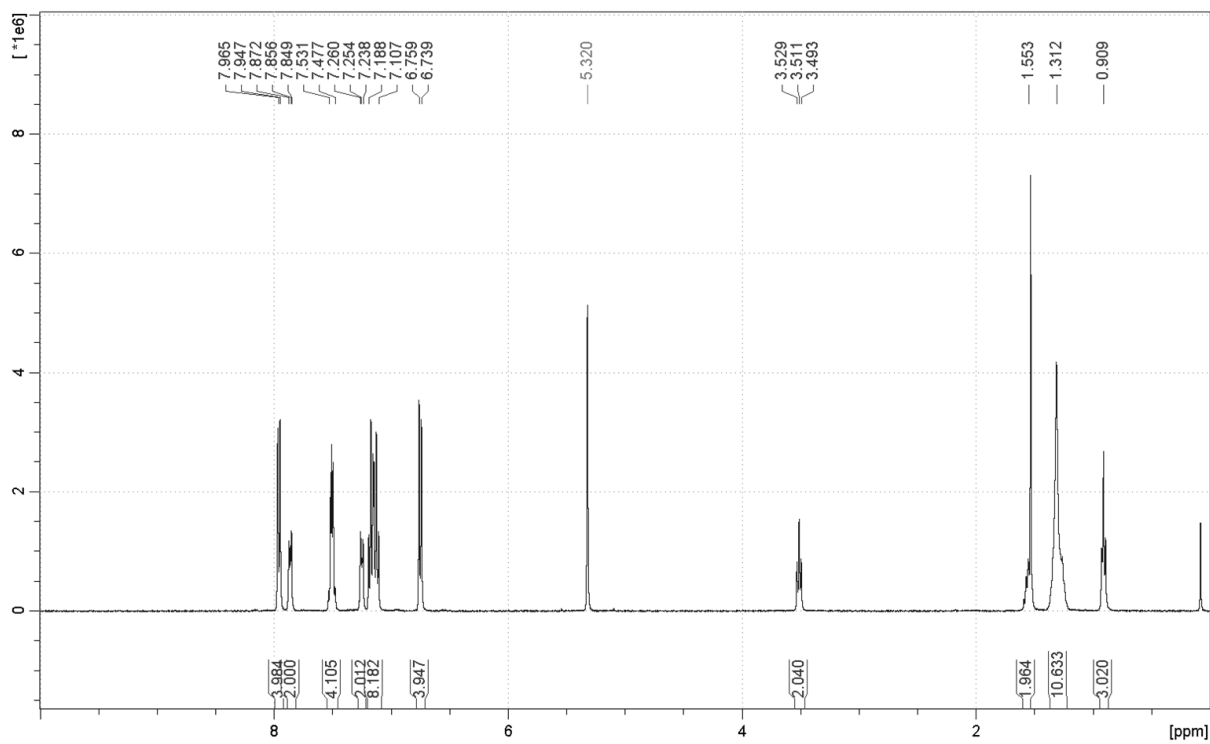


Fig. S5 Proton NMR spectrum of *o*-PCzTPD.

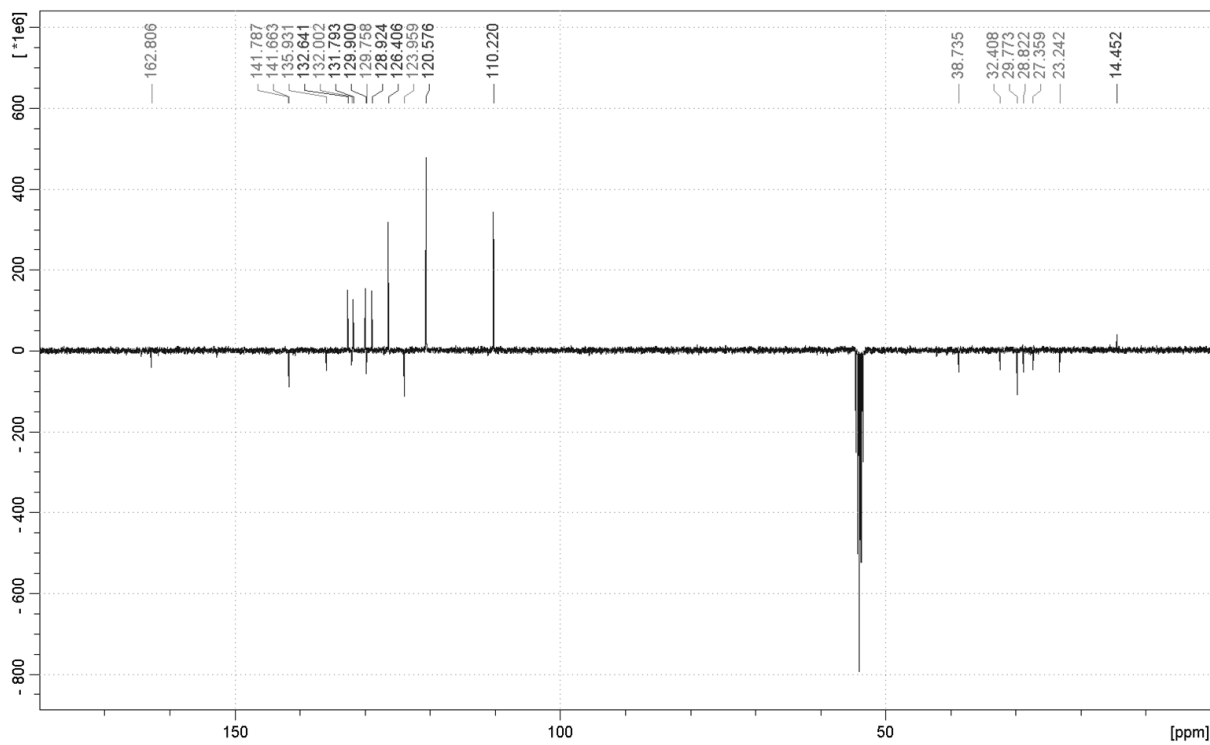


Fig. S6 Carbon NMR spectrum of *p*-PCzTPD.

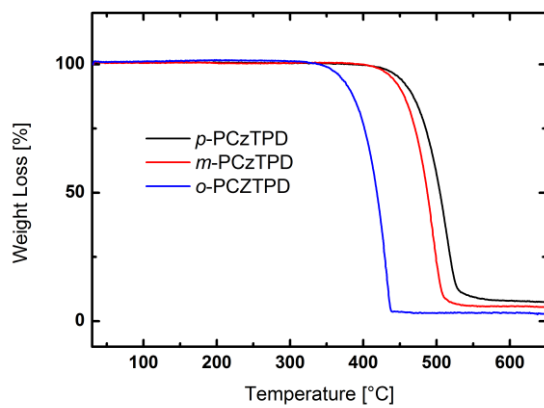


Fig. S8 TGA analysis of the developed materials.

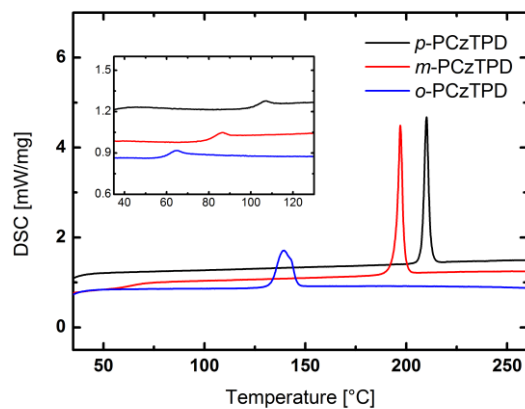


Fig. S7 DSC analysis of the developed materials.

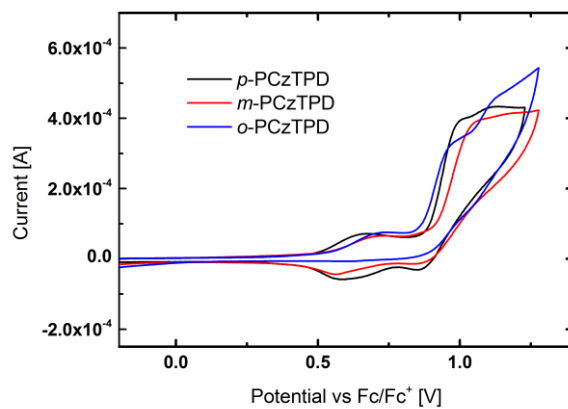


Fig. S9 CV curves of the developed materials.

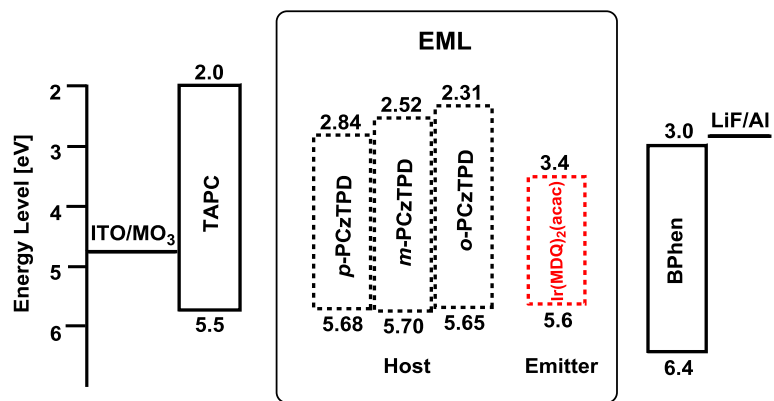


Fig. S10 Energy level diagram of the PhOLED devices.

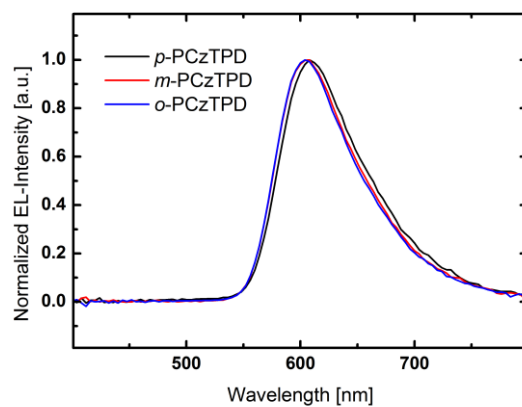


Fig. S11 EL spectra of the PhOLED devices.

3.7. Manuscript #7 – Supporting Information

Structure-property relationships in Click-derived donor-triazole-acceptor materials

Paul Kautny, Dorian Bader, Berthold Stöger, Georg A. Reider, Johannes Fröhlich, Daniel Lumpi

Chemistry-A European Journal, **2016**, 22, 18887-18898

CHEMISTRY

A **European** Journal

Supporting Information

Structure–Property Relationships in Click-Derived Donor–Triazole–Acceptor Materials

Paul Kautny,^{*[a]} Dorian Bader,^[a] Berthold Stöger,^[b] Georg A. Reider,^[c] Johannes Fröhlich,^[a]
and Daniel Lumpi^[a]

chem_201603510_sm_miscellaneous_information.pdf

1) NMR spectra

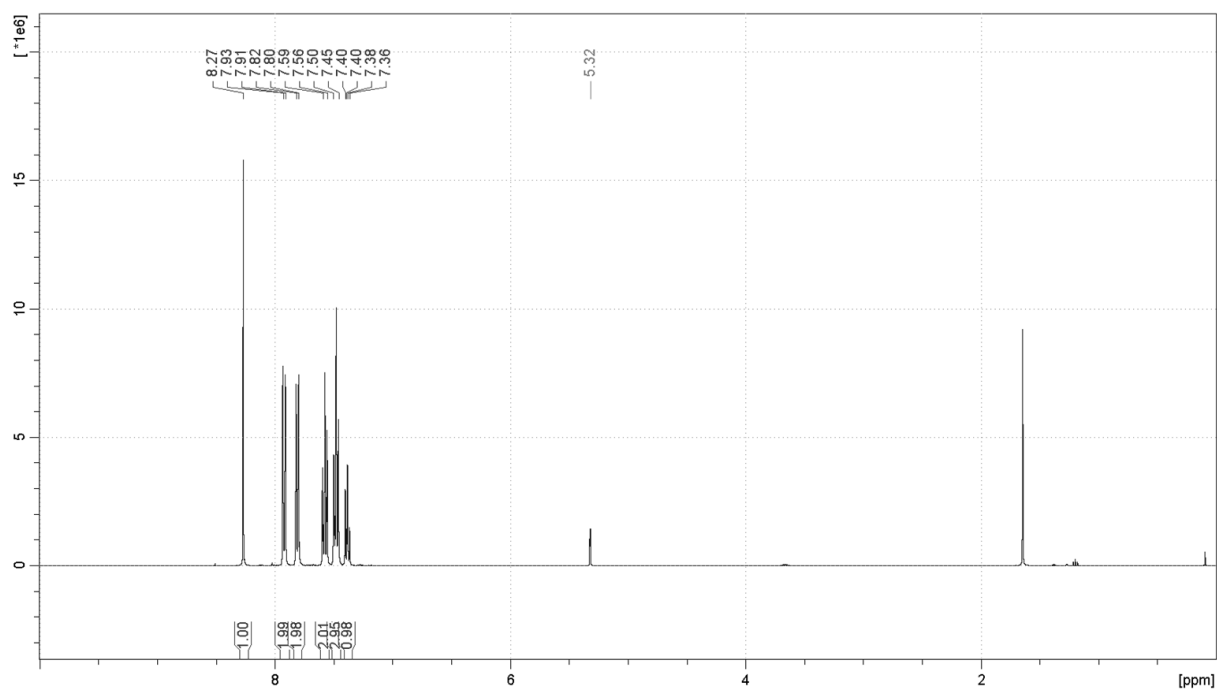


Figure S1.1. Proton NMR spectrum of compound **BTazB**.

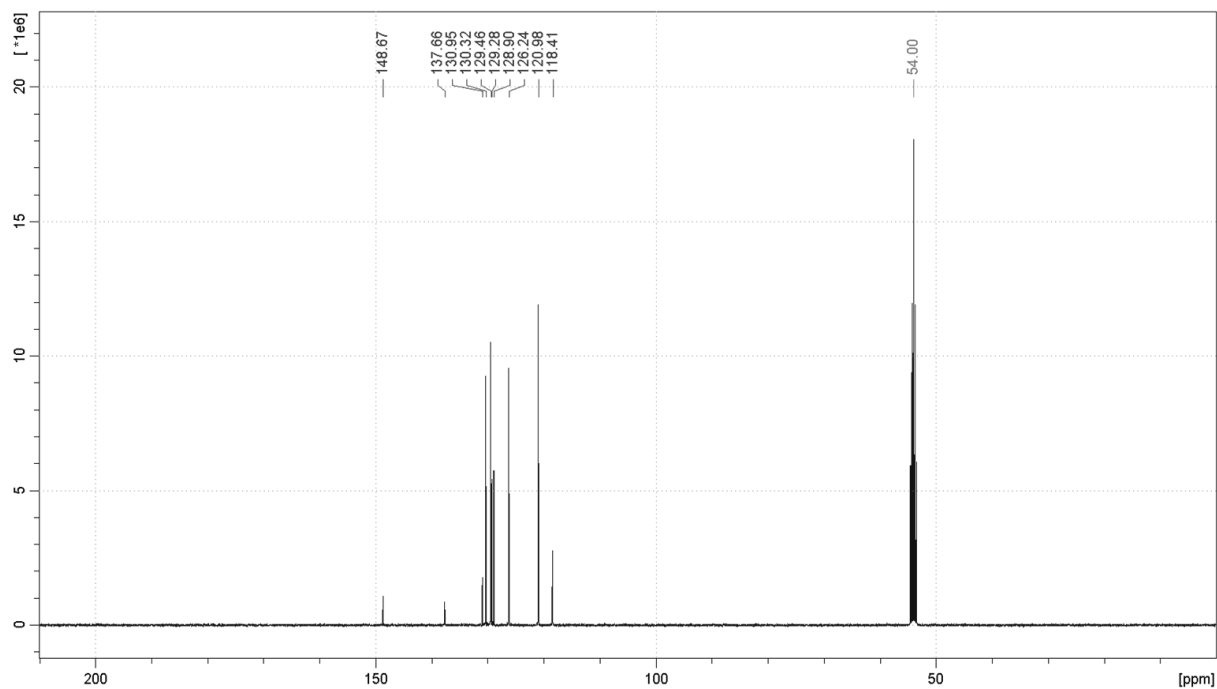


Figure S1.2. Carbon NMR spectrum of compound **BTazB**.

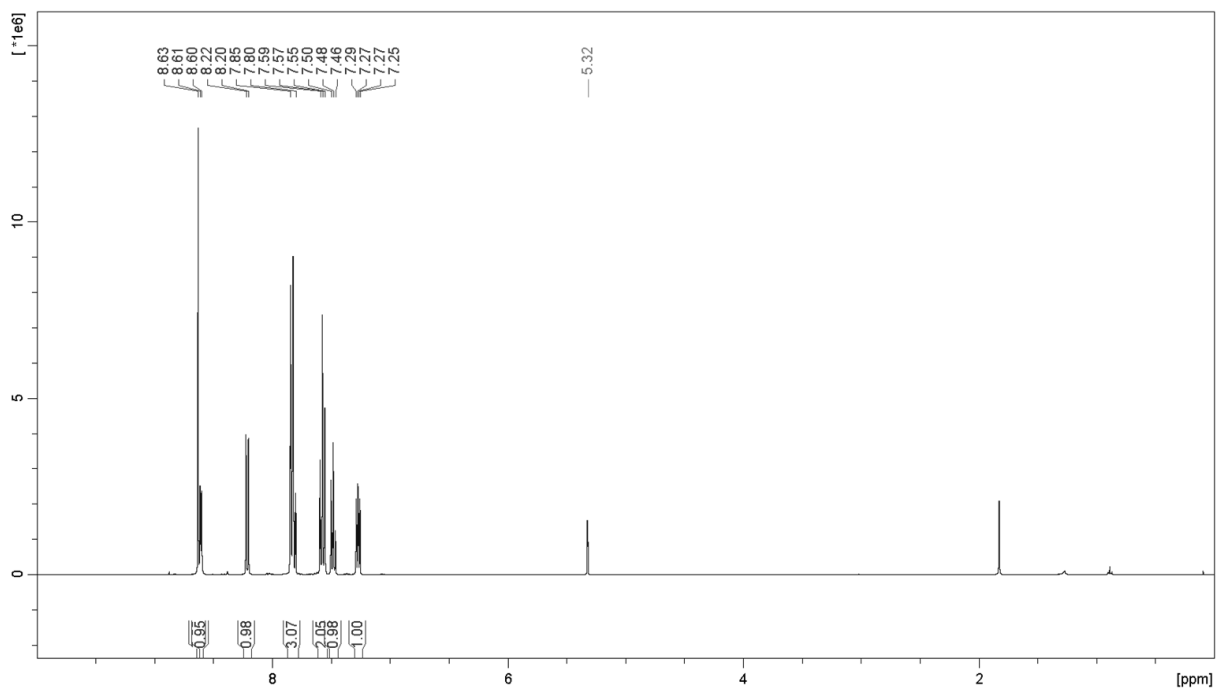


Figure S2.3. Proton NMR spectrum of compound **BTazPyr**.

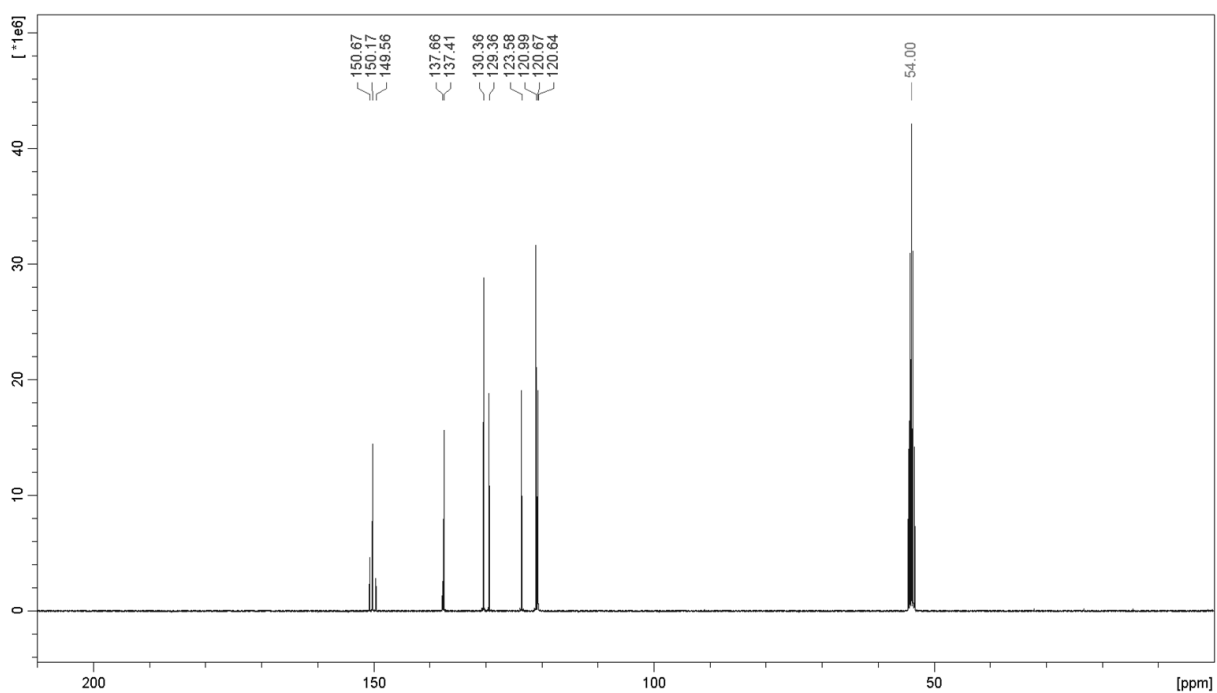


Figure S1.4. Carbon NMR spectrum of compound **BTazPyr**.

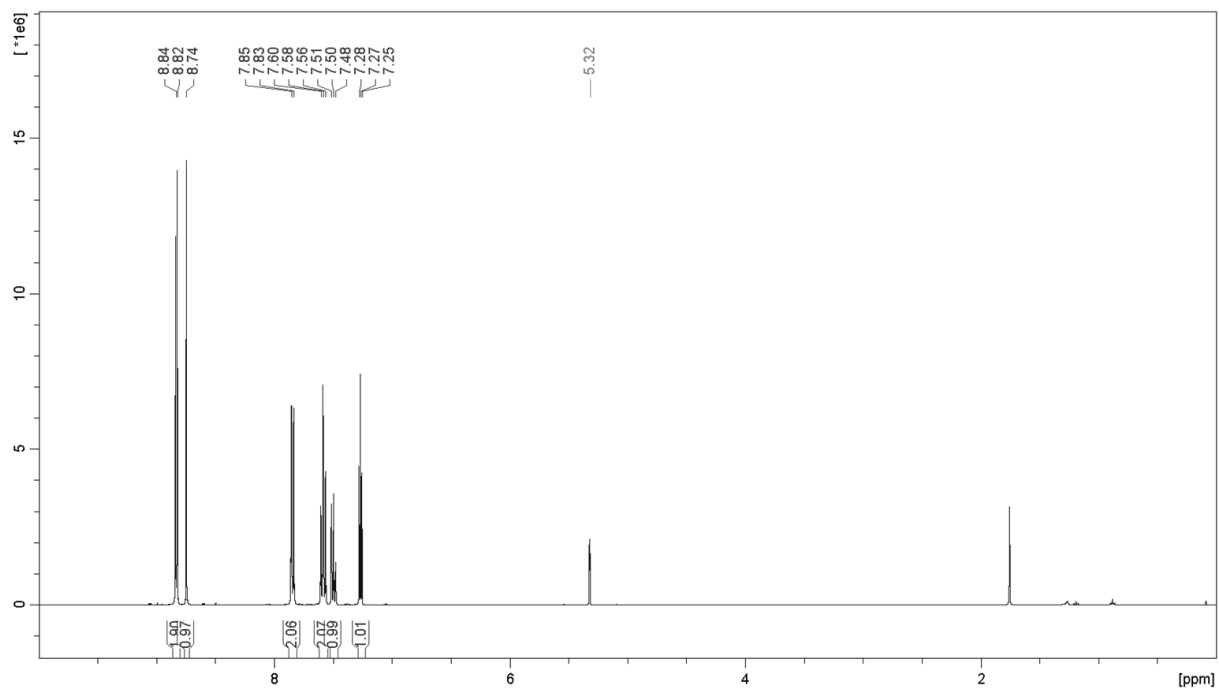


Figure S3.5. Proton NMR spectrum of compound **BTazPym**.

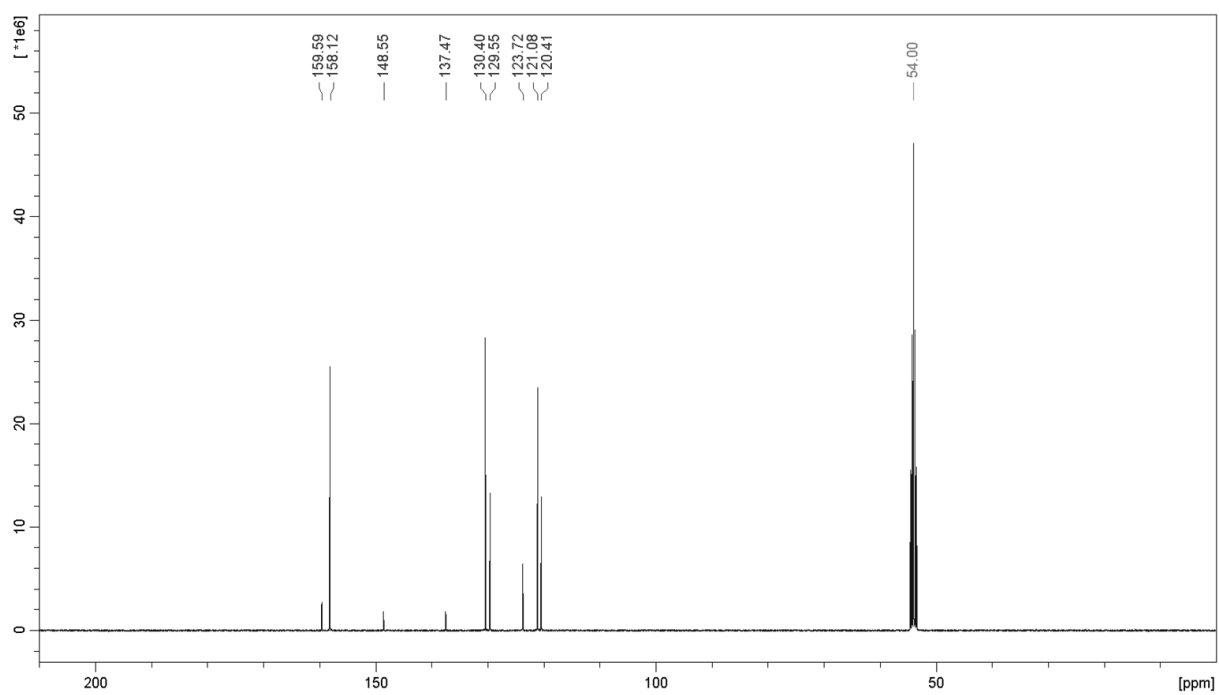


Figure S1.6. Carbon NMR spectrum of compound **BTazPym**.

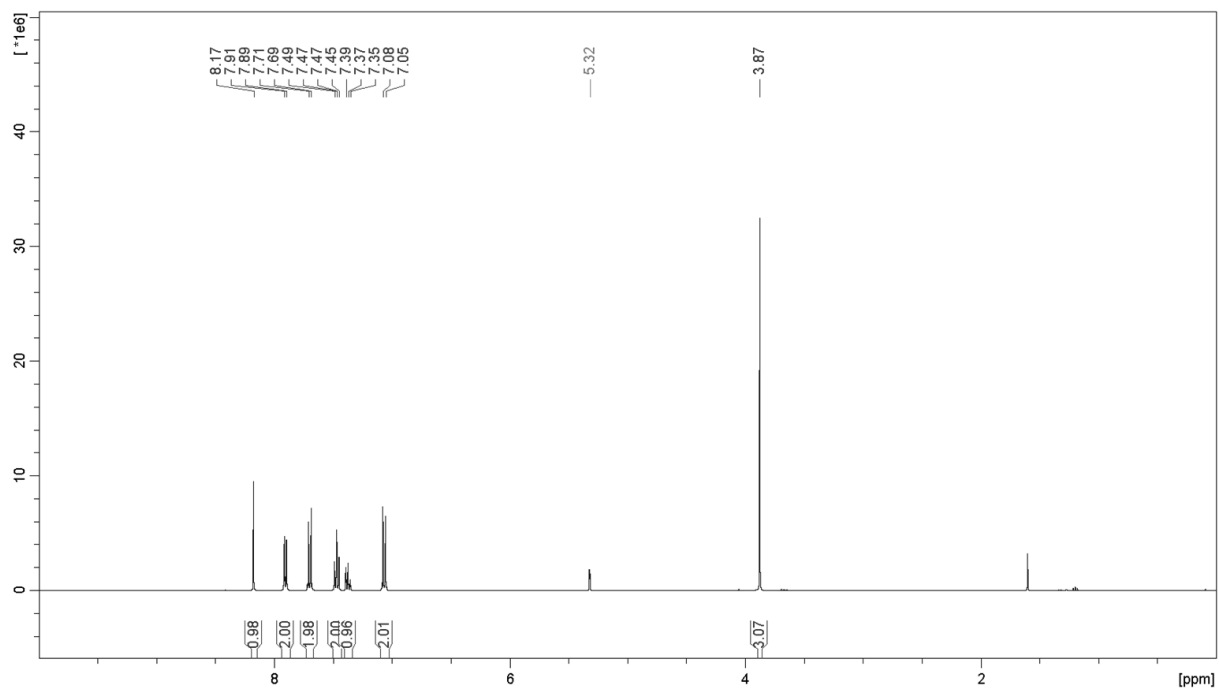


Figure S4.7. Proton NMR spectrum of compound **AnTazB**.

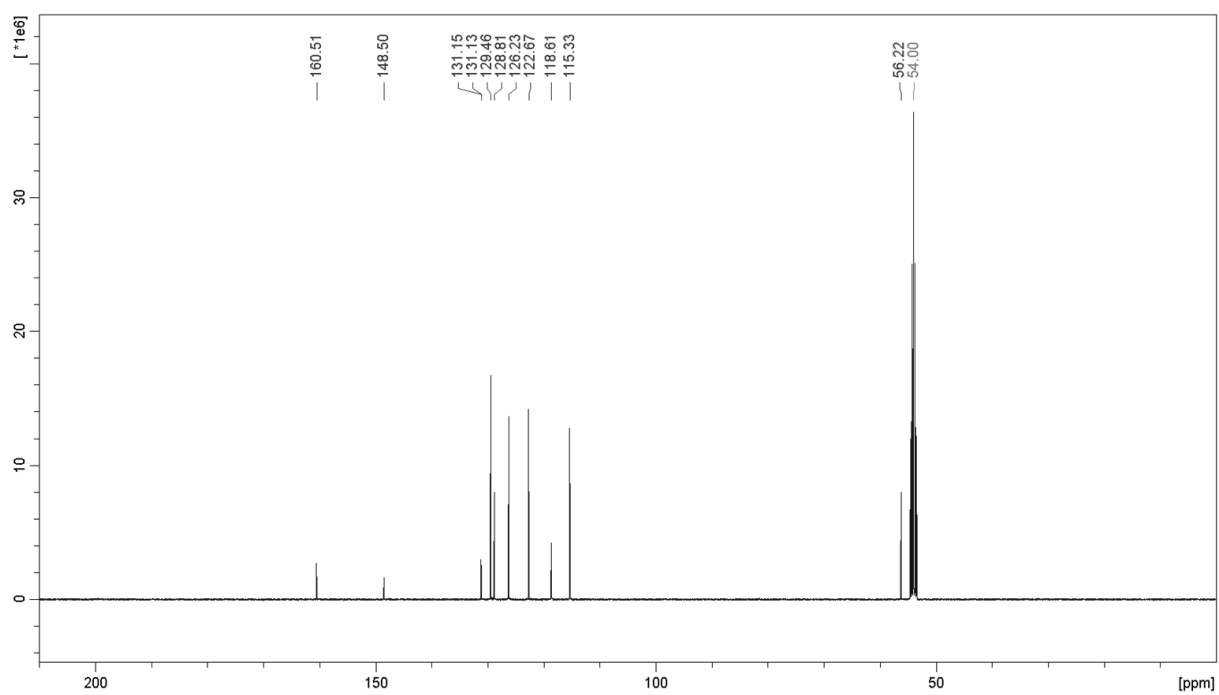


Figure S1.8. Carbon NMR spectrum of compound **AnTazB**.

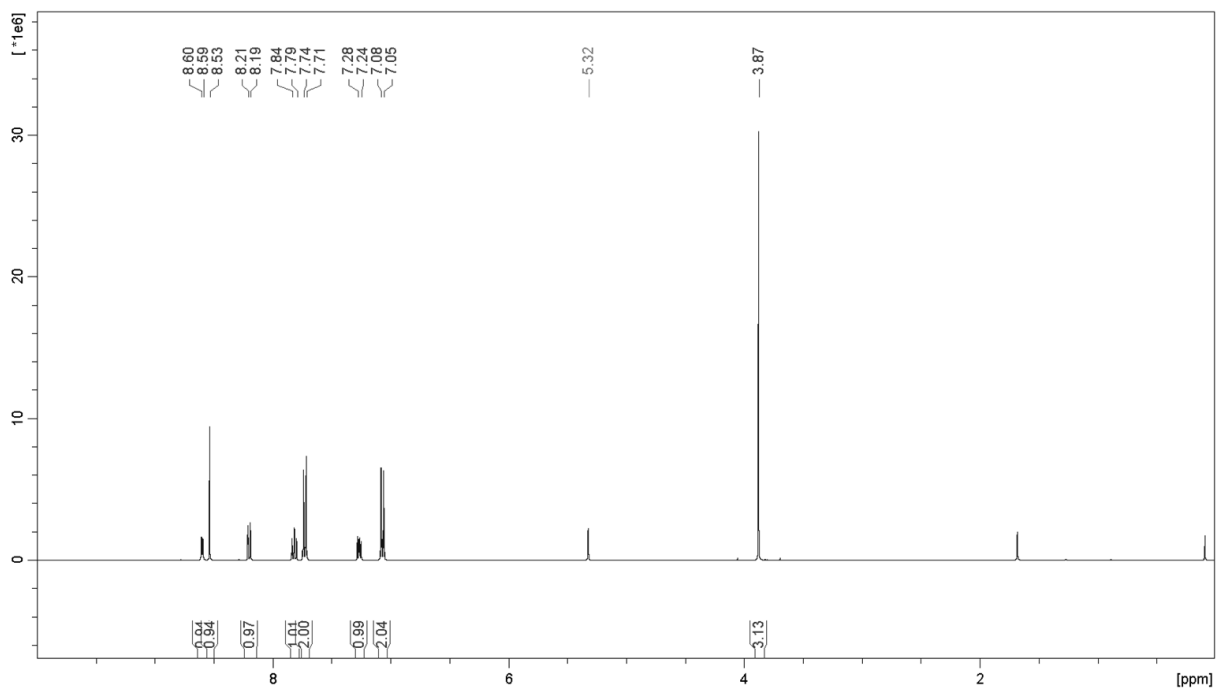


Figure S5.9. Proton NMR spectrum of compound **AnTazPyr**.

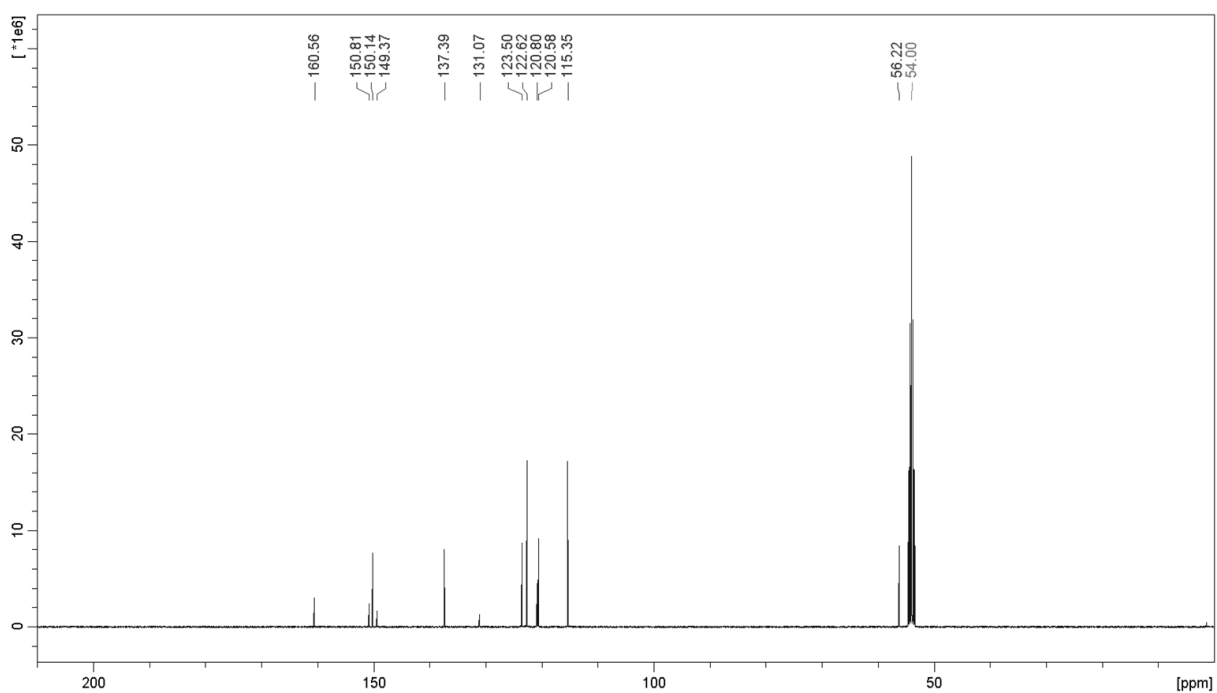


Figure S1.10. Carbon NMR spectrum of compound **AnTazPyr**.

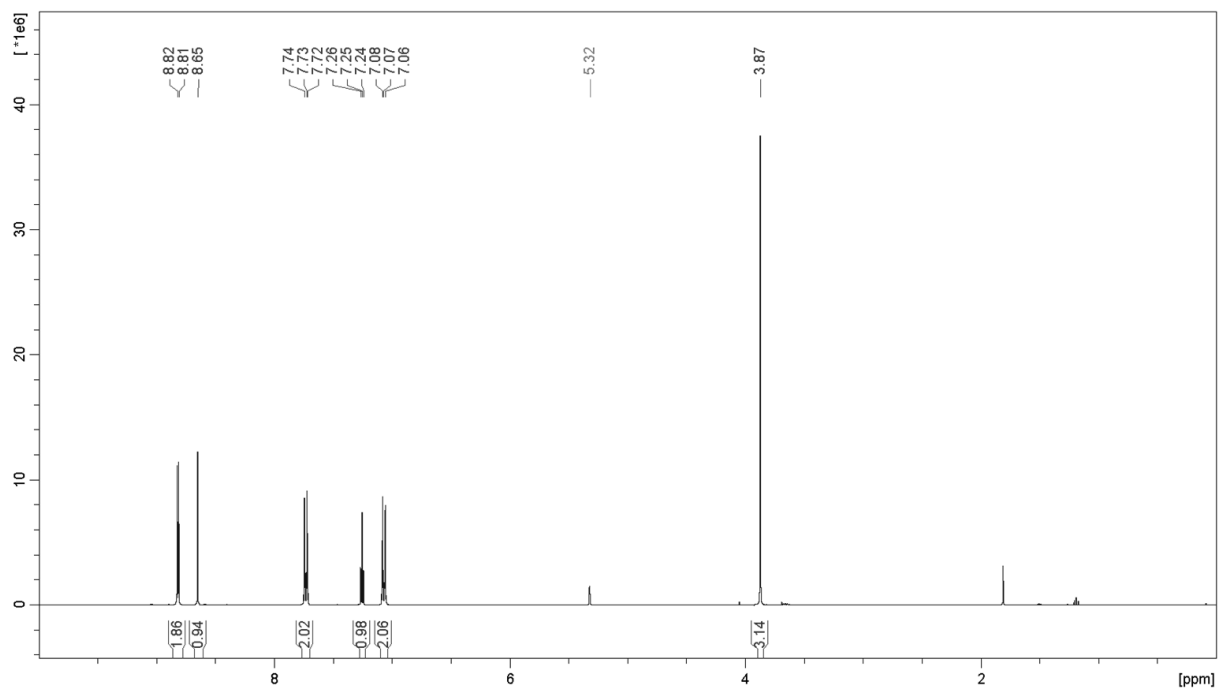


Figure S6.11. Proton NMR spectrum of compound **AnTazPym**.

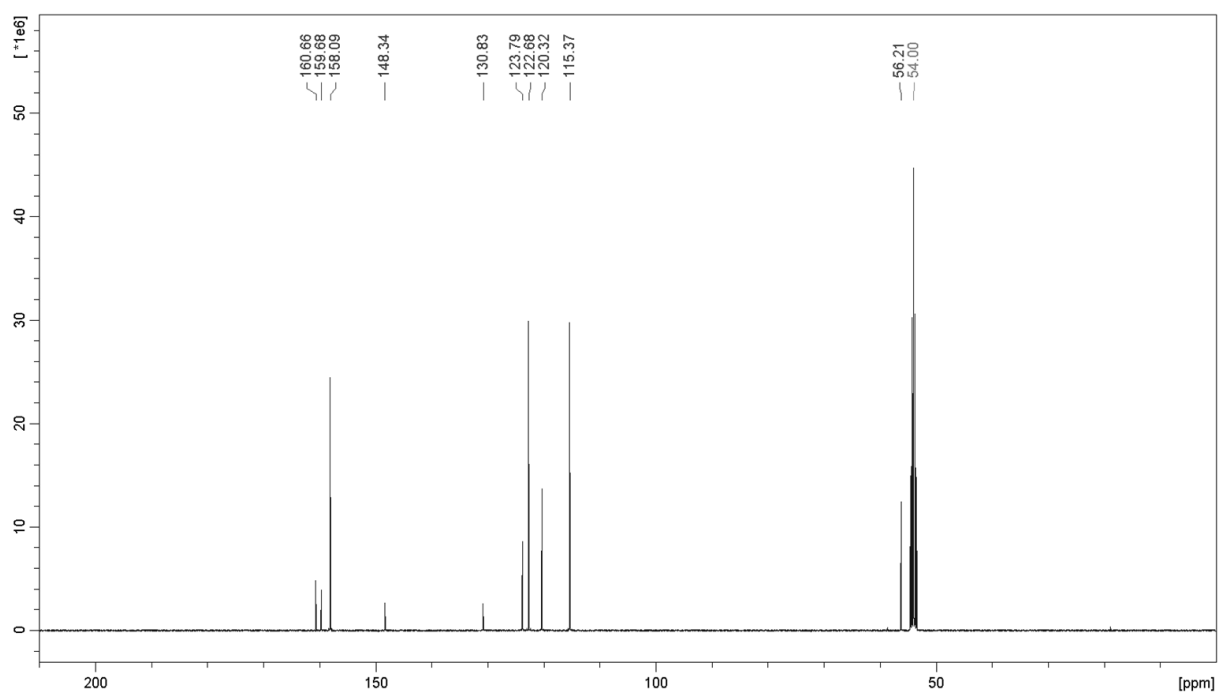


Figure S1.12. Carbon NMR spectrum of compound **AnTazPym**.

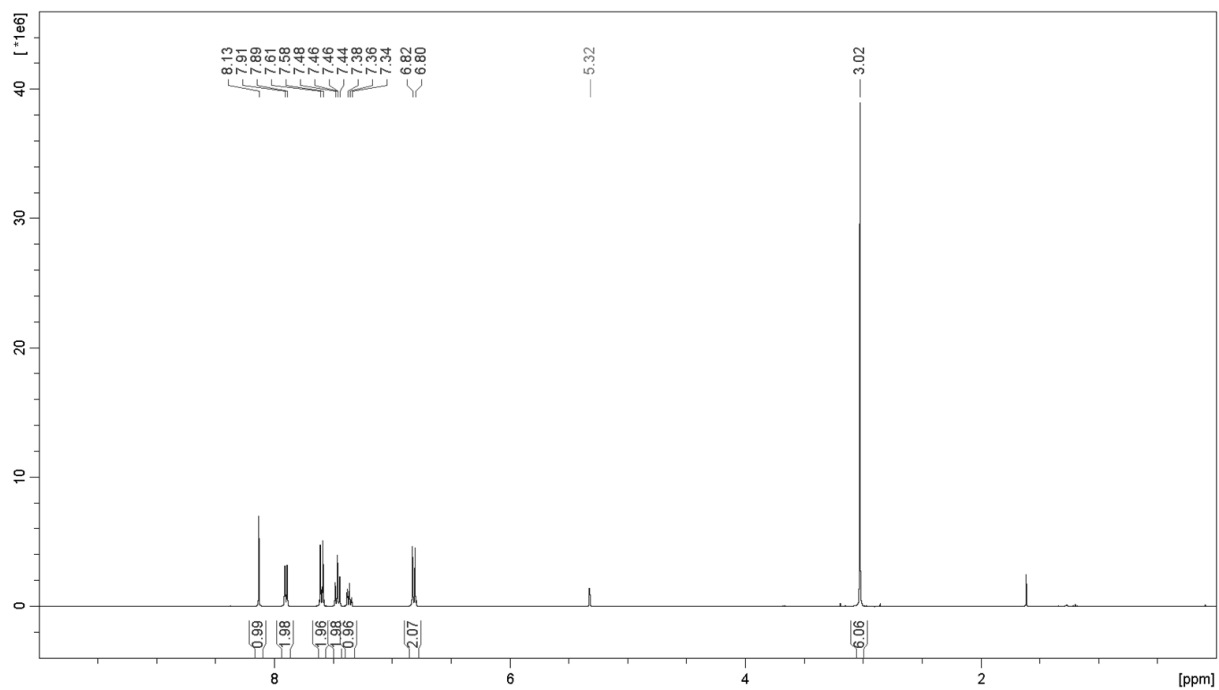


Figure S7.13. Proton NMR spectrum of compound **DMATazB**.

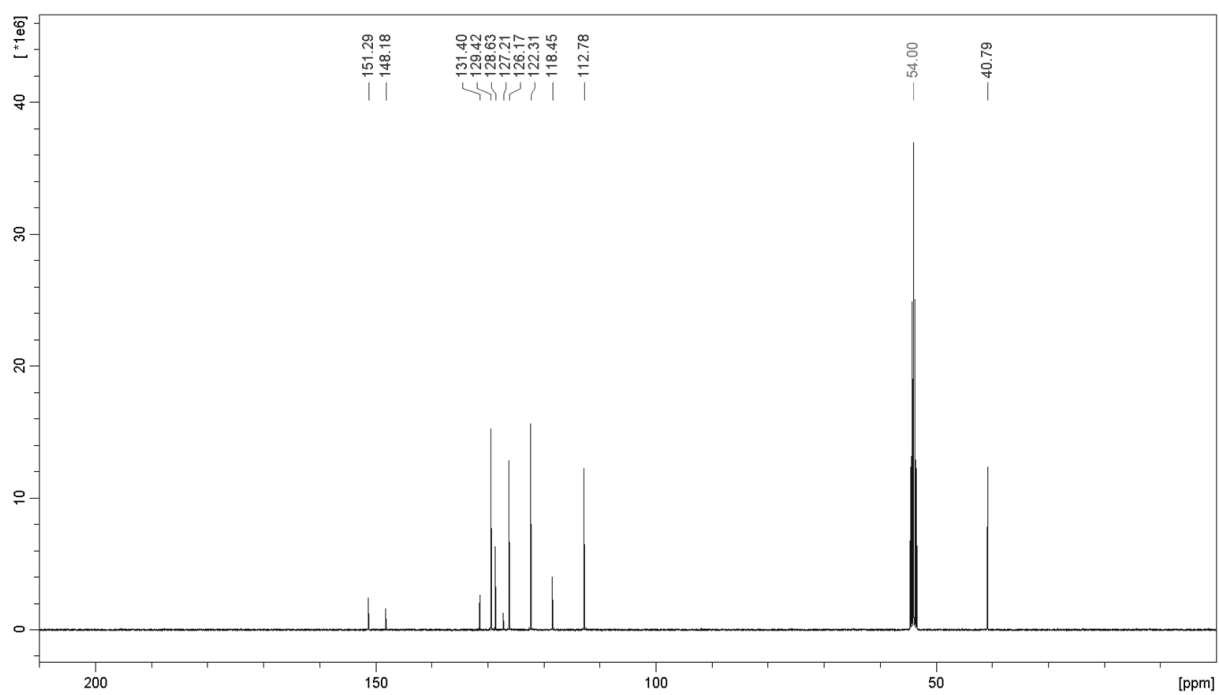


Figure S1.14. Carbon NMR spectrum of compound **DMATazB**.

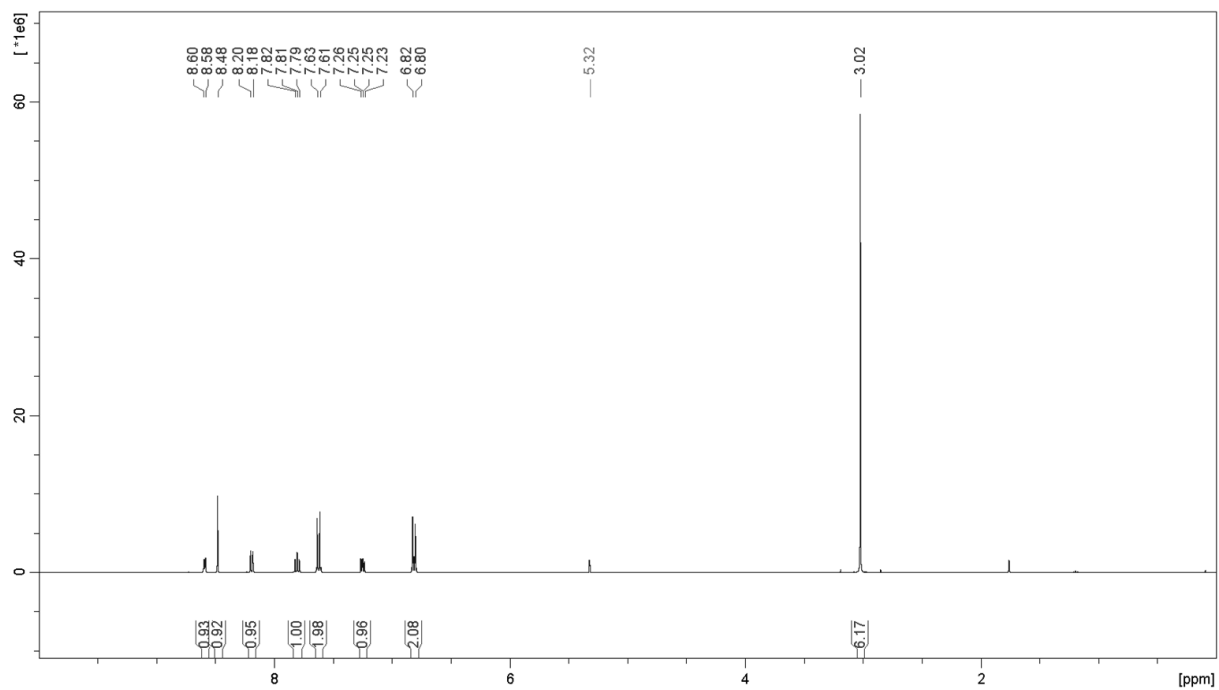


Figure S8.15. Proton NMR spectrum of compound **DMATazPyr**.

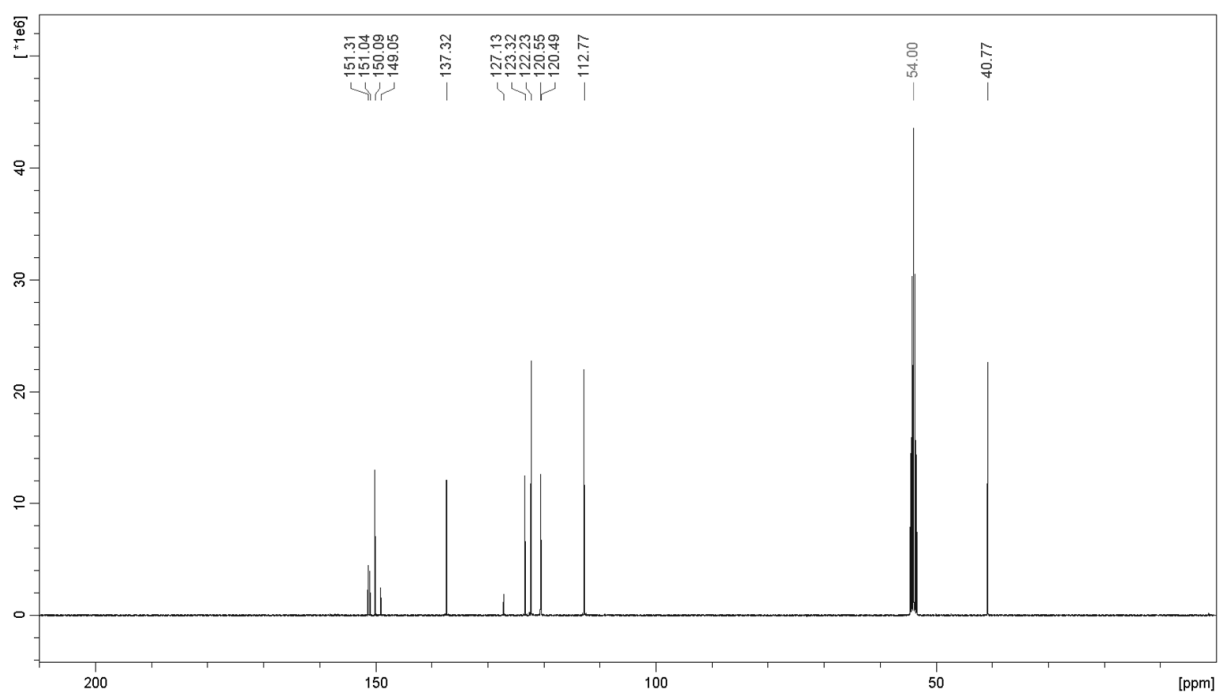


Figure S1.16. Carbon NMR spectrum of compound **DMATazPyr**.

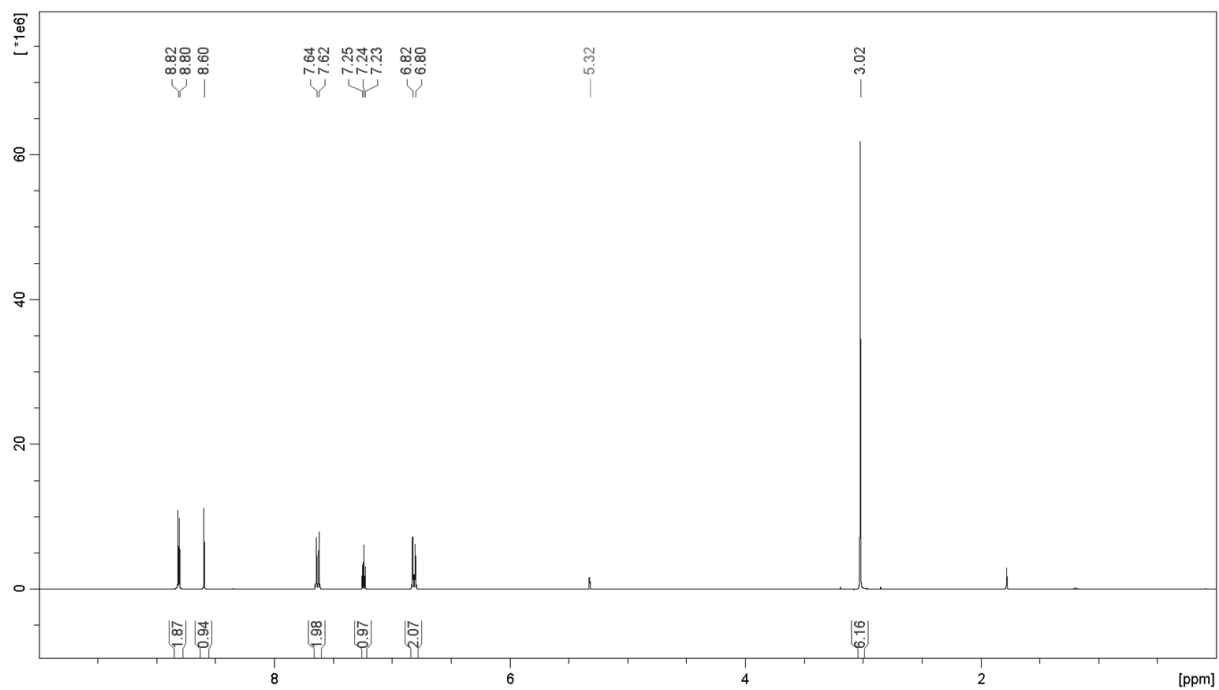


Figure S9.17. Proton NMR spectrum of compound **DMATazPym**.

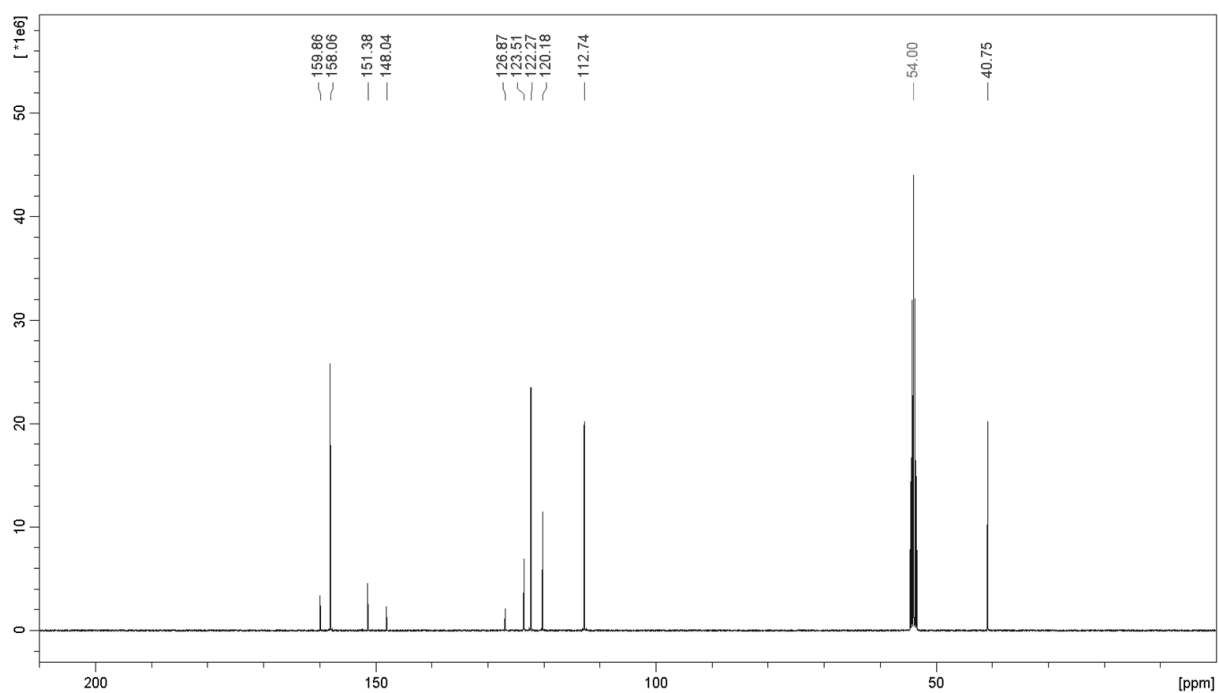


Figure S1.18. Carbon NMR spectrum of compound **DMATazPym**.

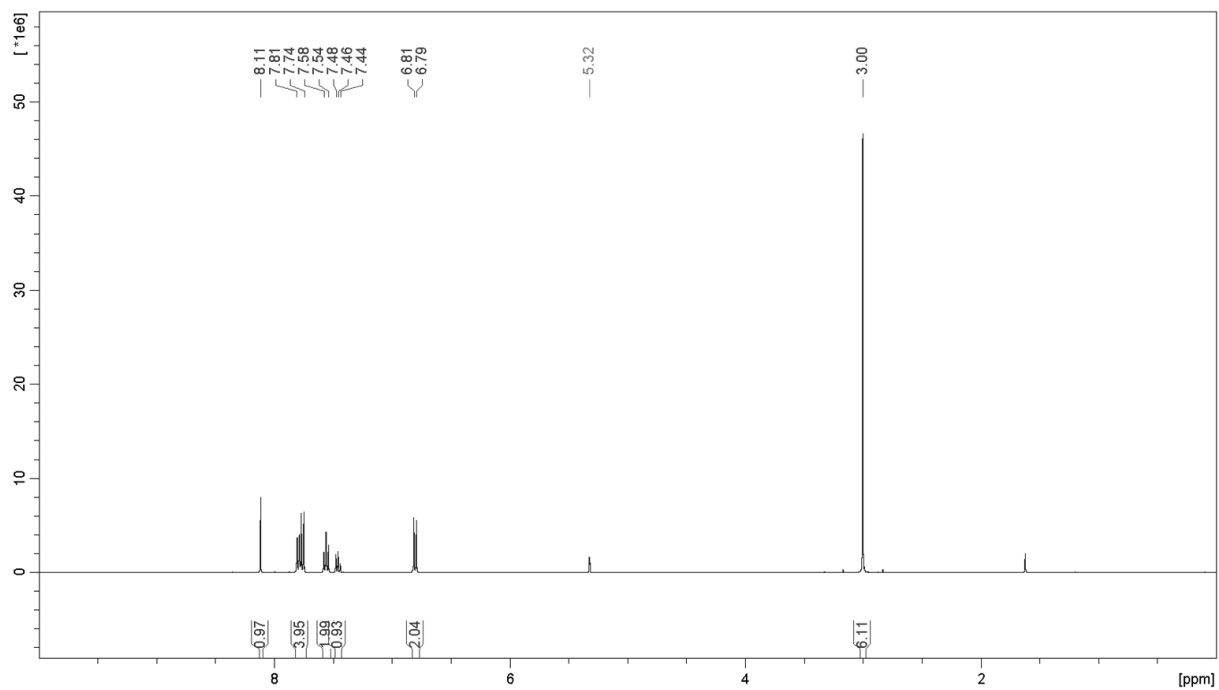


Figure S10.19. Proton NMR spectrum of compound **BTazDMA**.

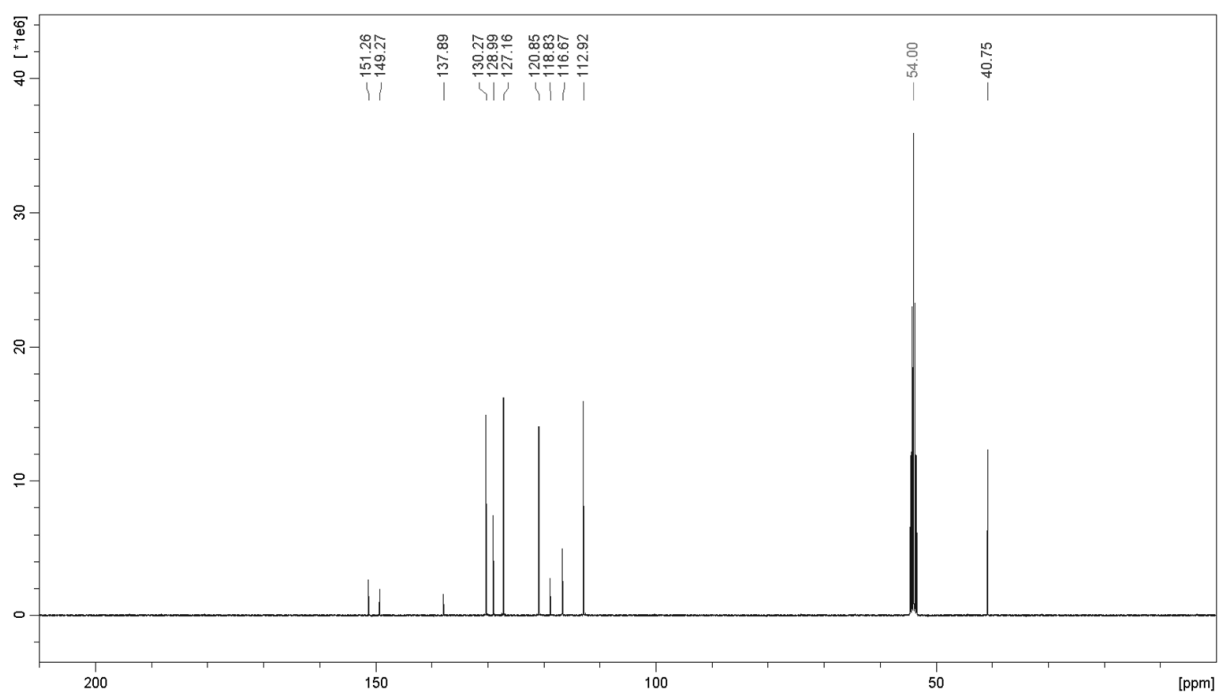


Figure S1.20. Carbon NMR spectrum of compound **BTazDMA**.

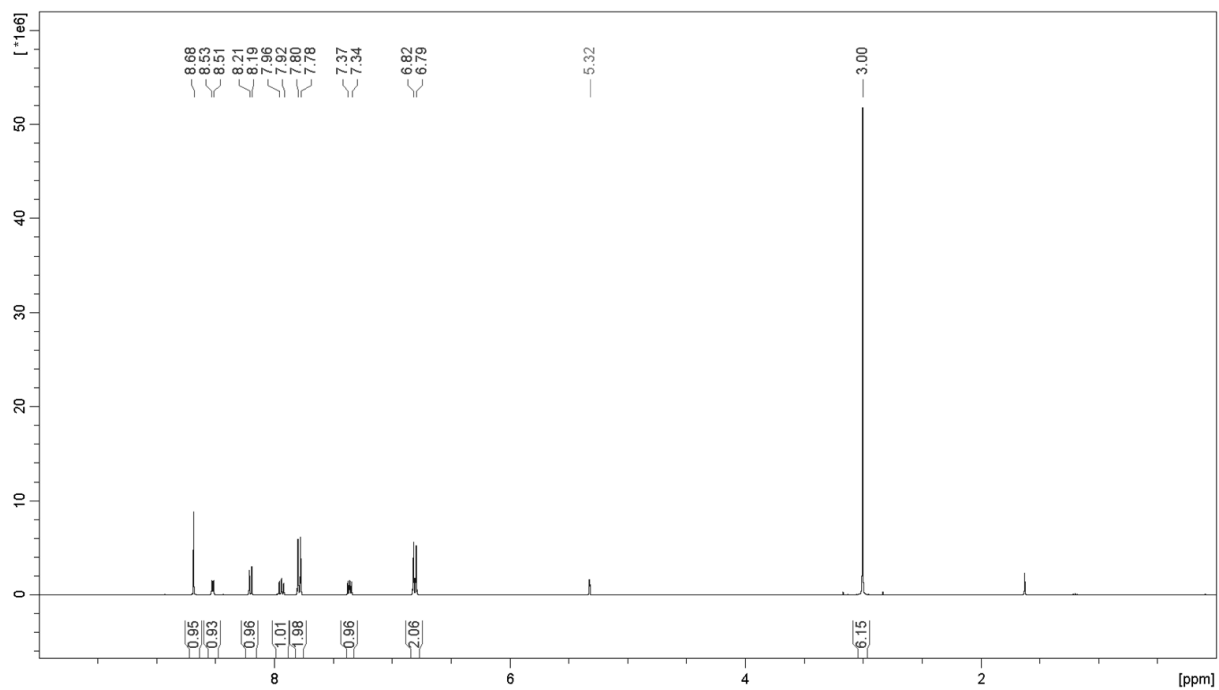


Figure S11.21. Proton NMR spectrum of compound **PyrTazDMA**.

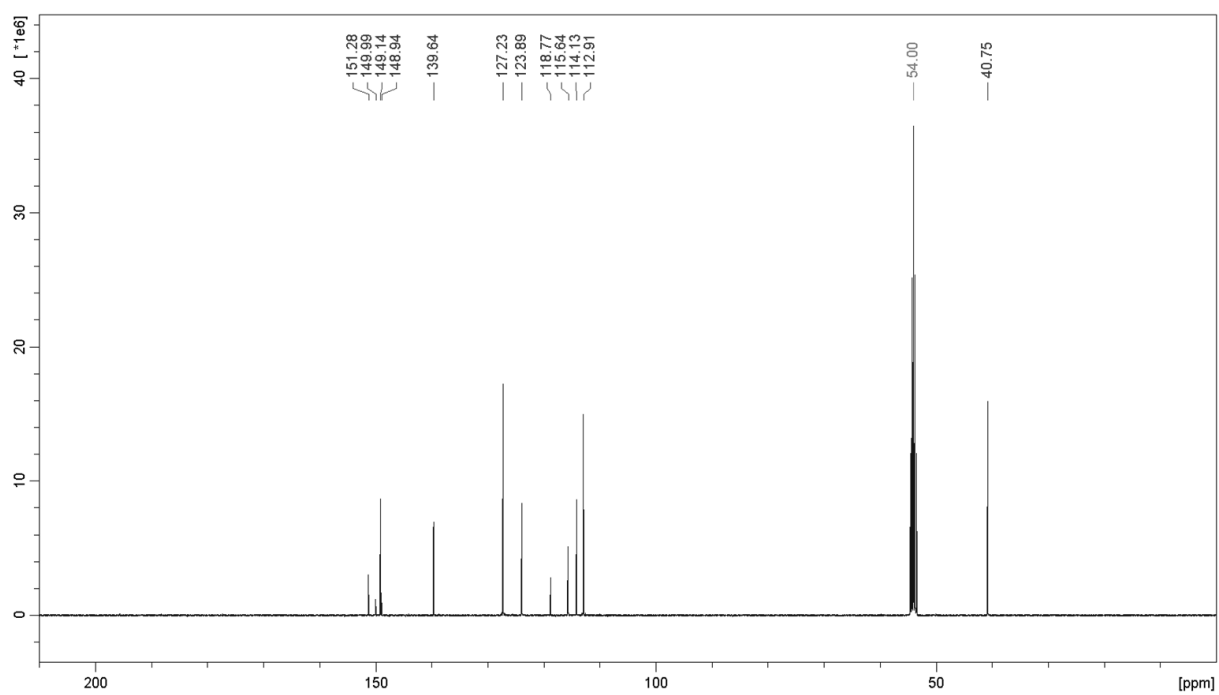


Figure S1.22. Carbon NMR spectrum of compound **PyrTazDMA**.

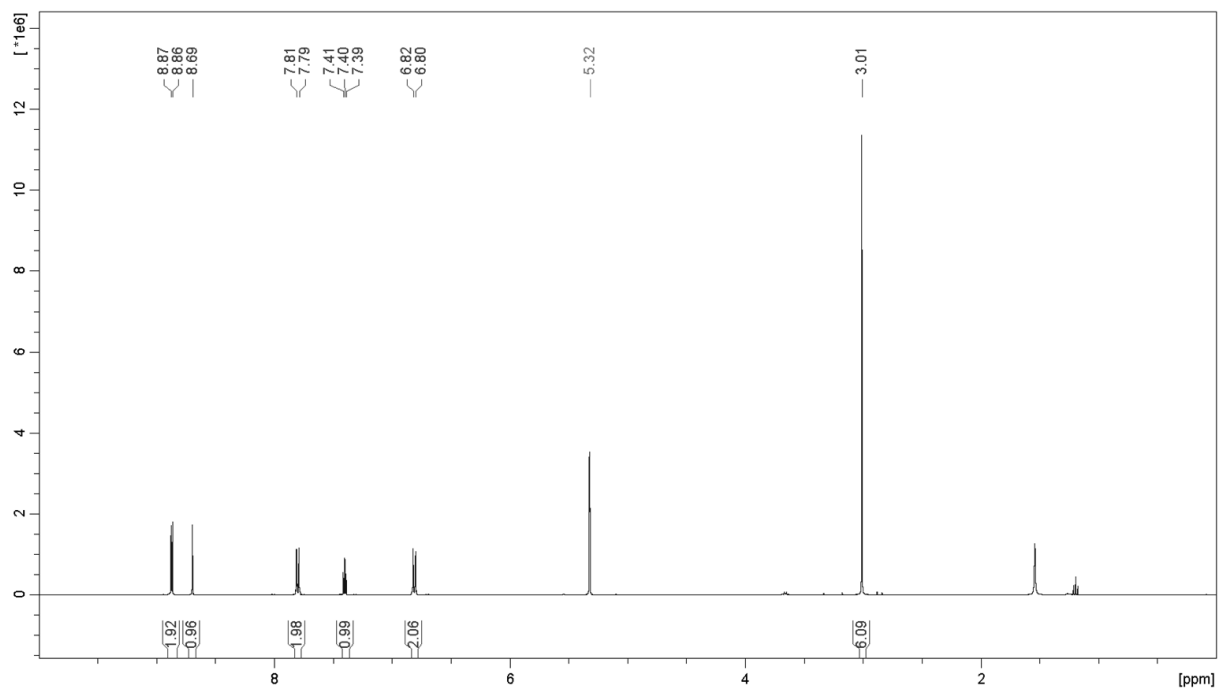


Figure S12.23. Proton NMR spectrum of compound **PymTazDMA**.

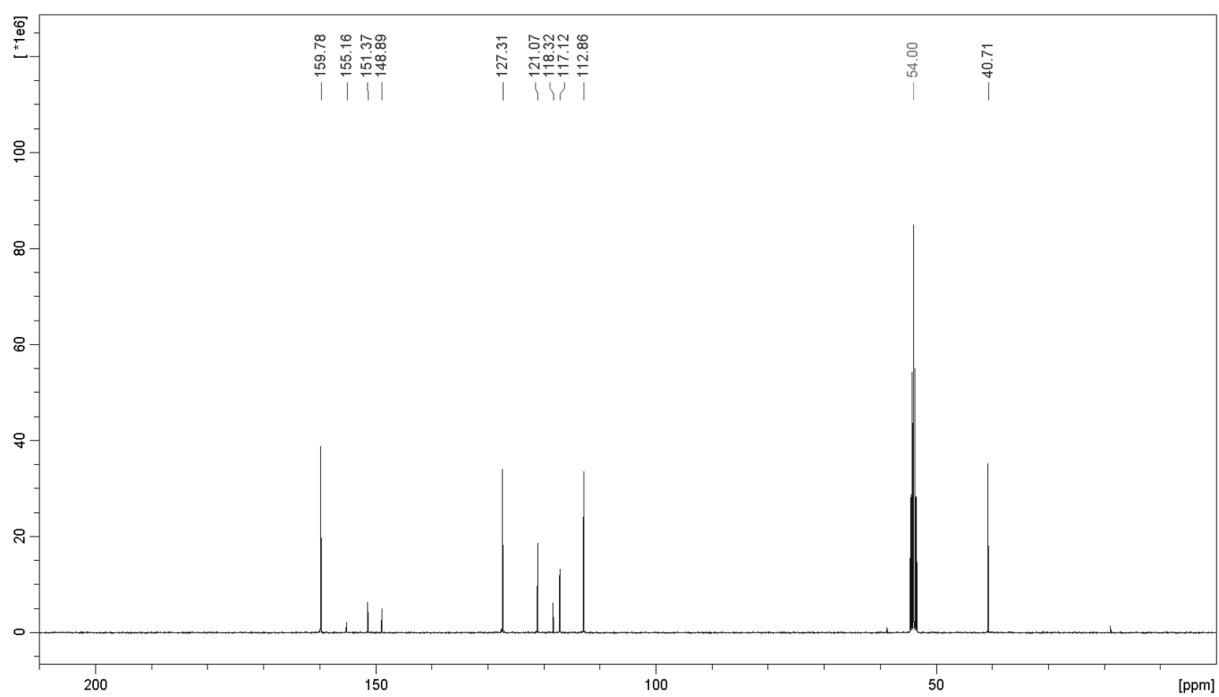


Figure S1.24. Carbon NMR spectrum of compound **PymTazDMA**.

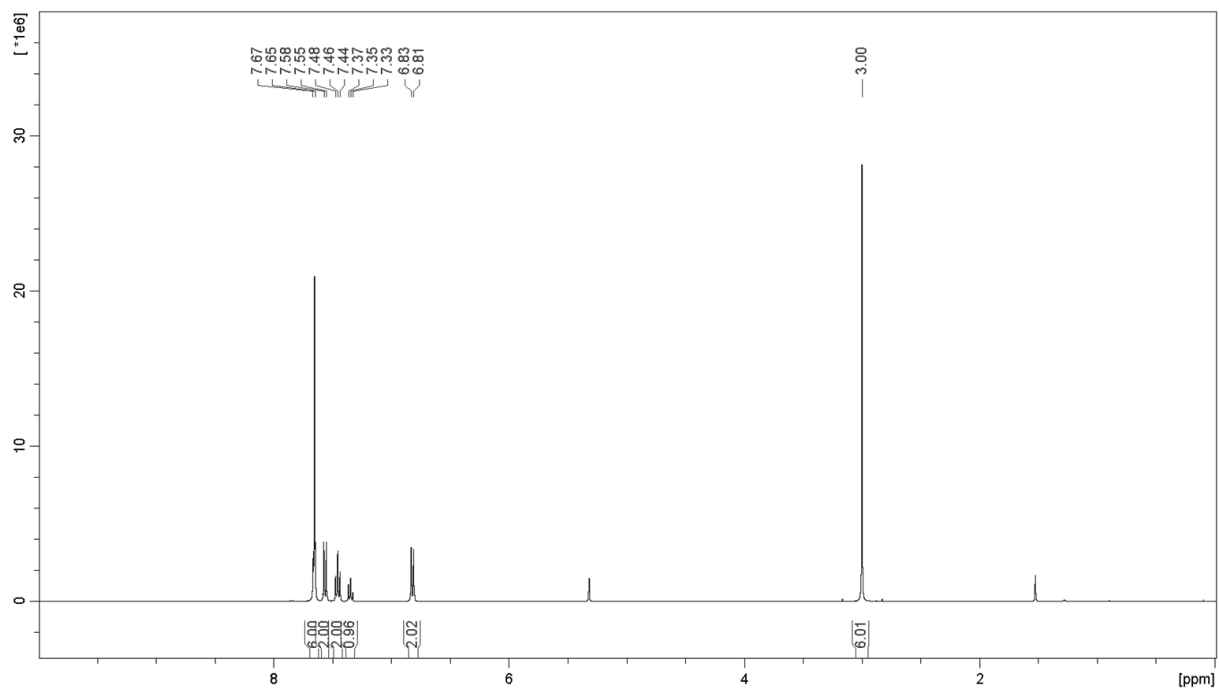


Figure S13.25. Proton NMR spectrum of compound **DMABB**.

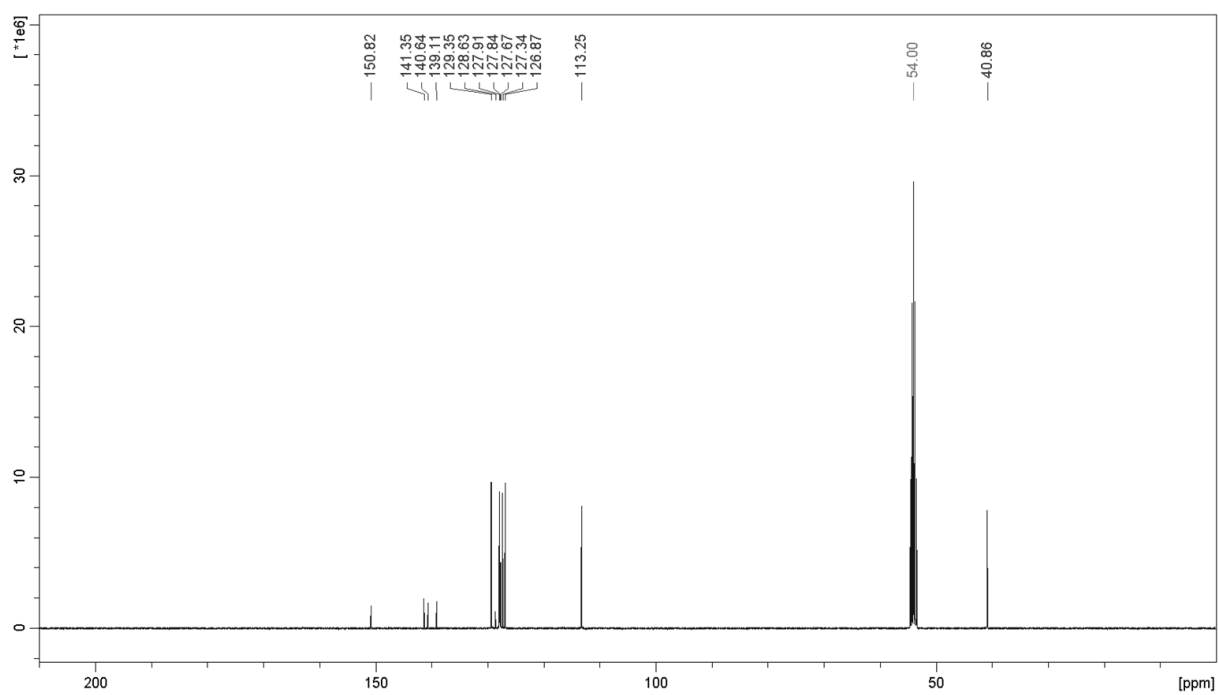


Figure S1.26. Carbon NMR spectrum of compound **DMABB**.

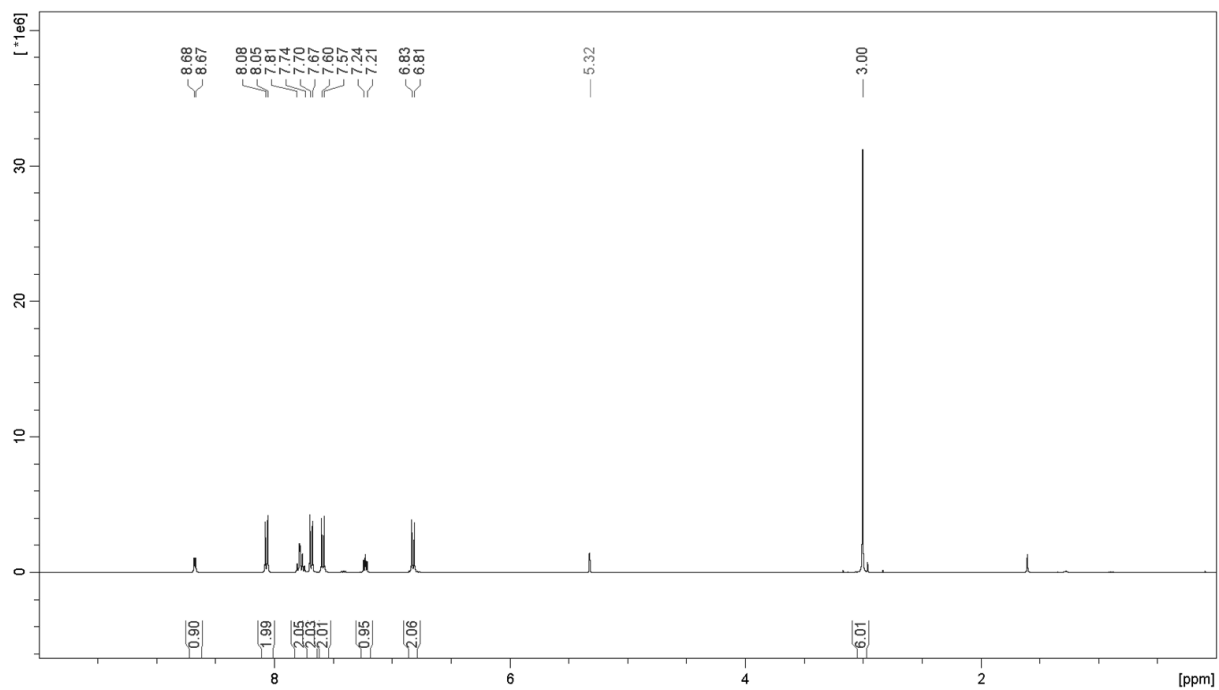


Figure S14.27. Proton NMR spectrum of compound **DMABPyr**.

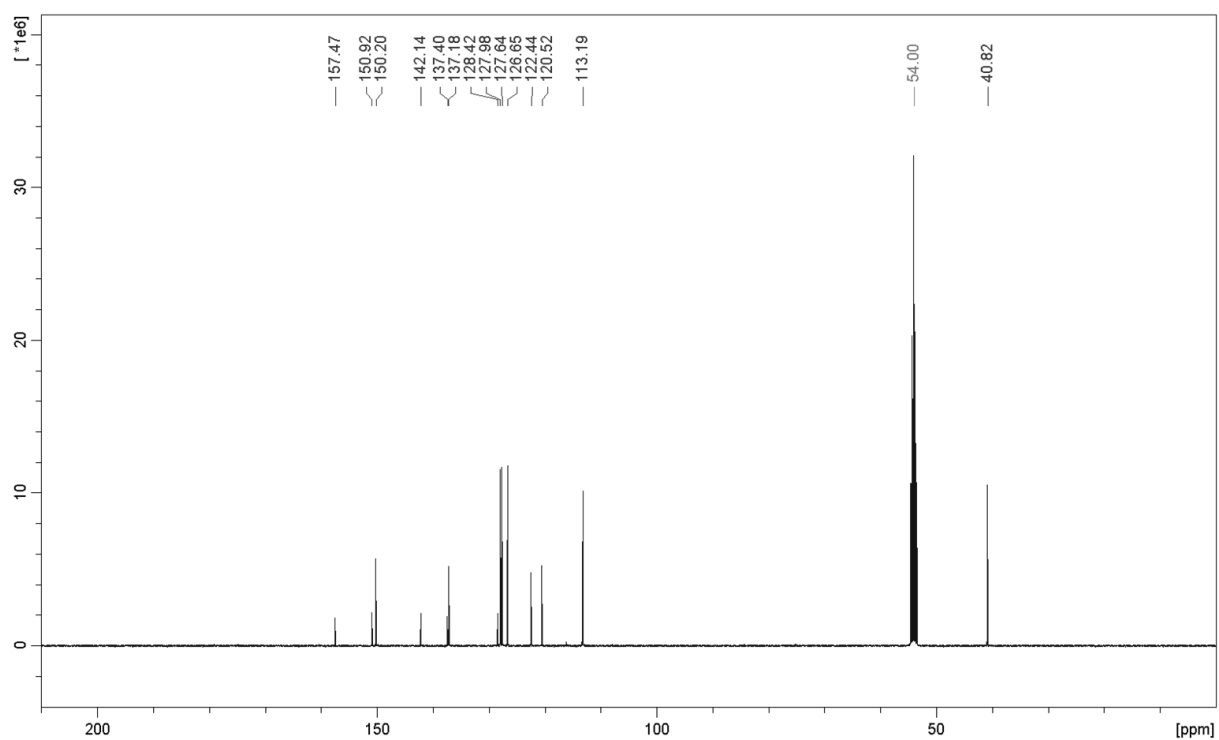


Figure S1.28. Carbon NMR spectrum of compound **DMABPyr**.

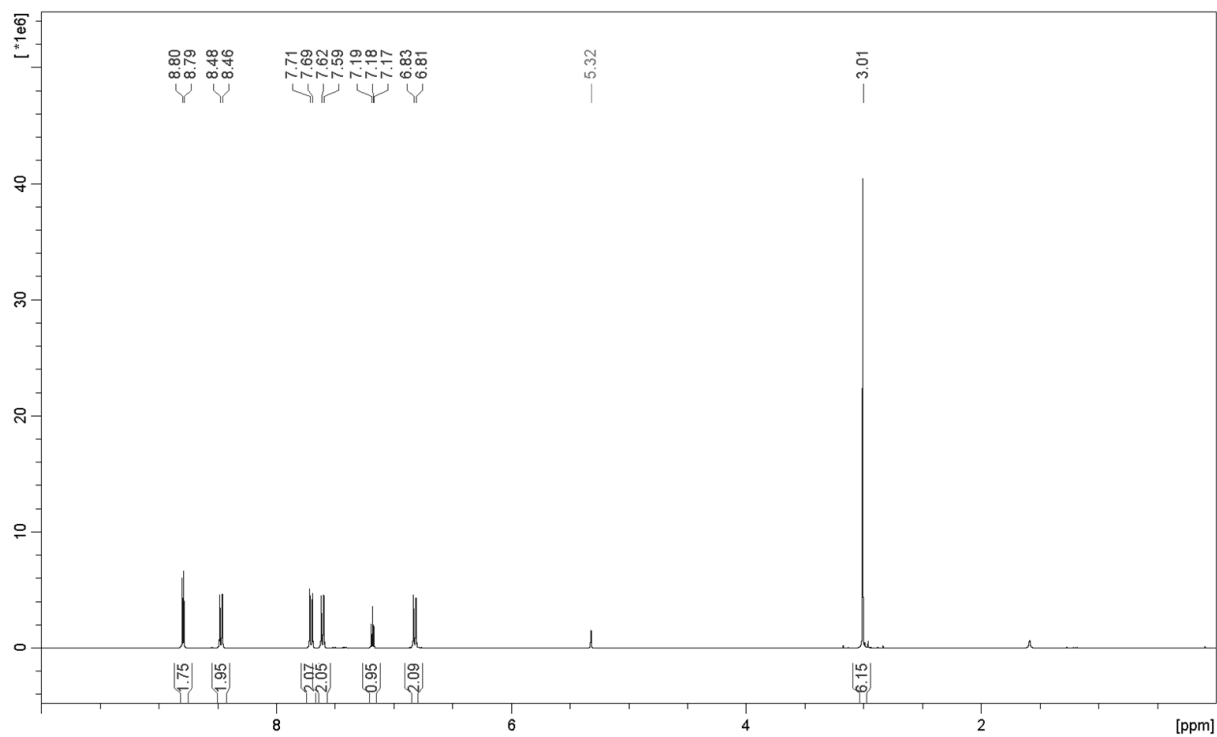


Figure S15.29. Proton NMR spectrum of compound **DMABPym**.

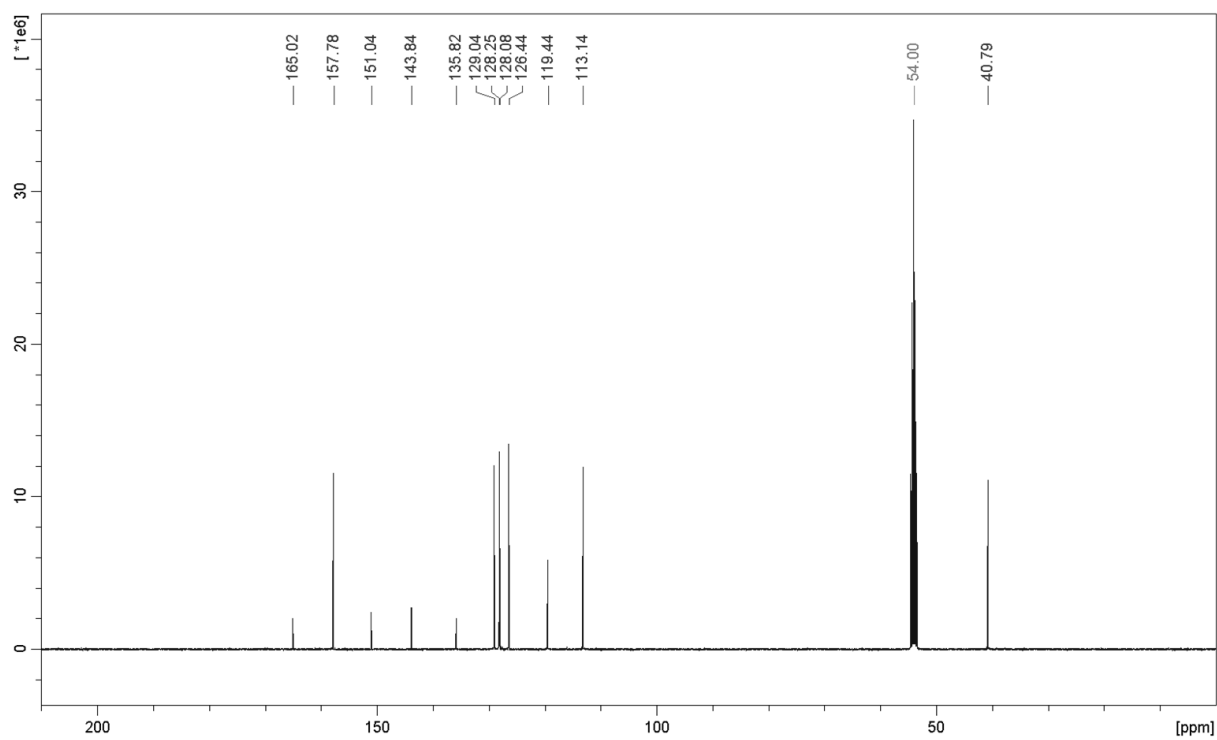


Figure S1.30. Carbon NMR spectrum of compound **DMABPym**.

2) Photophysical data

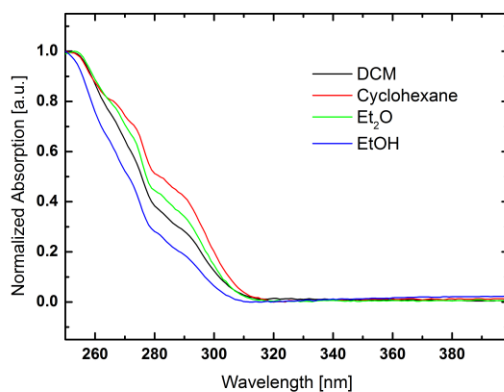


Figure S2.1. UV/VIS absorption spectra of **BTazB** in various solvents (DCM=dichloromethane)

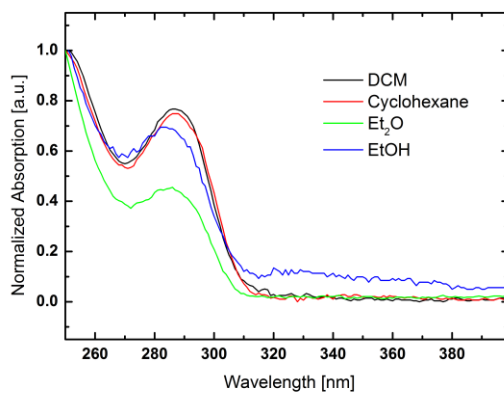


Figure S2.2. UV/VIS absorption spectra of **BTazPyr** in various solvents (DCM=dichloromethane)

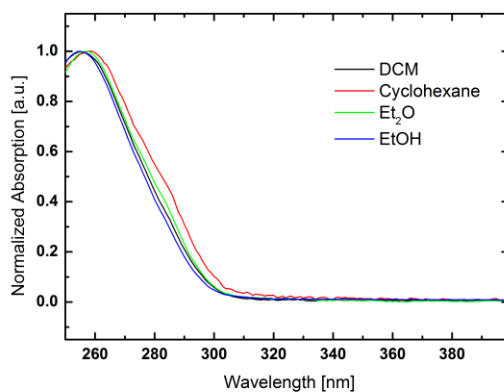


Figure S2.3. UV/VIS absorption spectra of **BTazPym** in various solvents (DCM=dichloromethane)

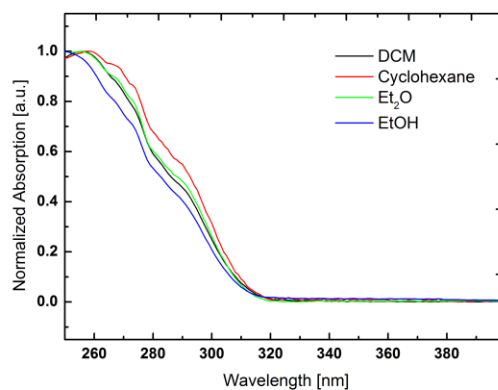


Figure S2.4. UV/VIS absorption spectra of **AnTazB** in various solvents (DCM=dichloromethane)

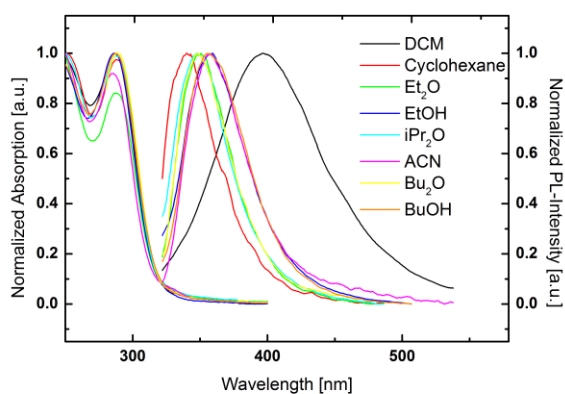


Figure S2.5. UV/VIS absorption and photoluminescence emission spectra of **AnTazPyr** in various solvents (DCM=dichloromethane, ACN=acetonitrile)

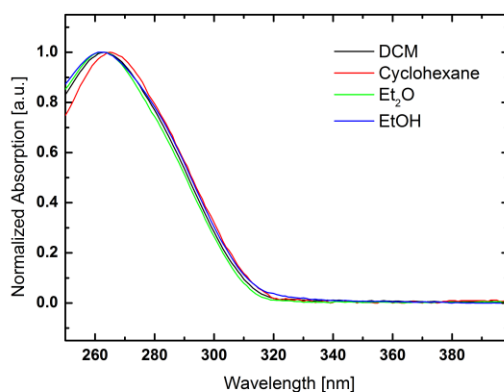


Figure S2.6. UV/VIS absorption spectra of **AnTazPym** in various solvents (DCM=dichloromethane)

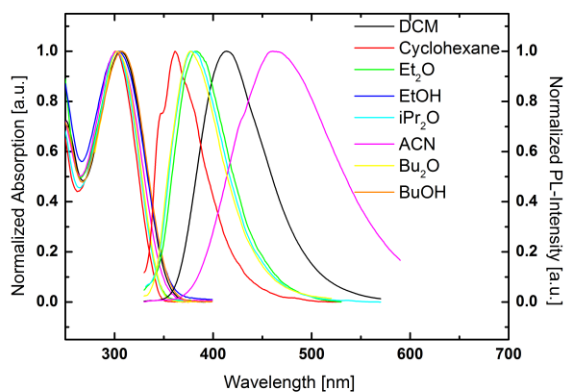


Figure S2.7. UV/VIS absorption and photoluminescence emission spectra of **DMATazPyr** in various solvents (DCM=dichloromethane, ACN=acetonitrile)

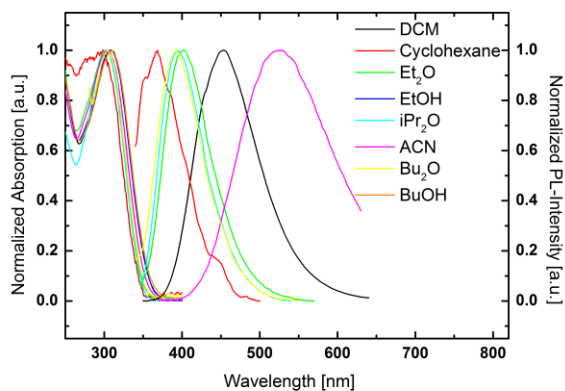


Figure S2.8. UV/VIS absorption and photoluminescence emission spectra of **DMATazPym** in various solvents (DCM=dichloromethane, ACN=acetonitrile)

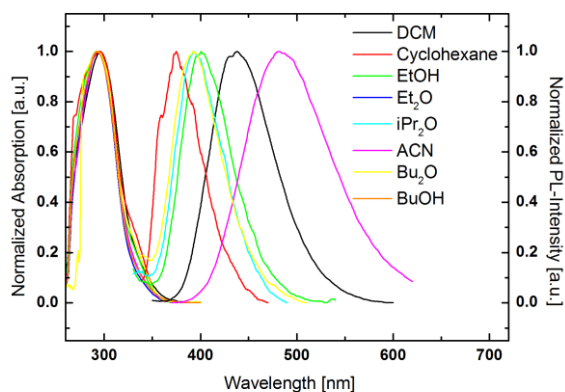


Figure S2.9. UV/VIS absorption and photoluminescence emission spectra of **BTazDMA** in various solvents (DCM=dichloromethane, ACN=acetonitrile)

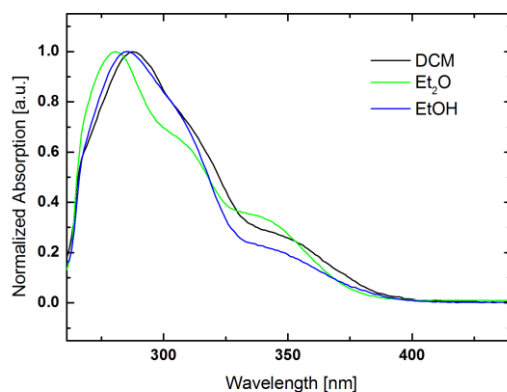


Figure S2.10. UV/VIS absorption spectra of **PymTazDMA** in various solvents (DCM=dichloromethane)

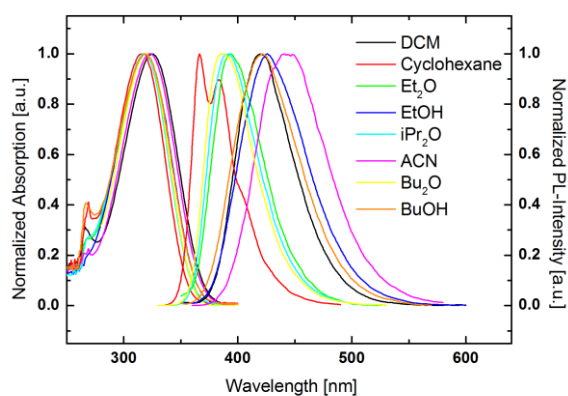


Figure S2.11. UV/VIS absorption and photoluminescence emission spectra of **DMABB** in various solvents (DCM=dichloromethane, ACN=acetonitrile)

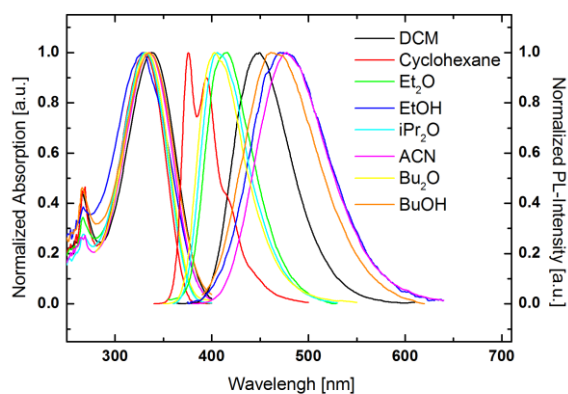


Figure S2.12. UV/VIS absorption and photoluminescence emission spectra of **DMABPy** in various solvents (DCM=dichloromethane, ACN=acetonitrile)

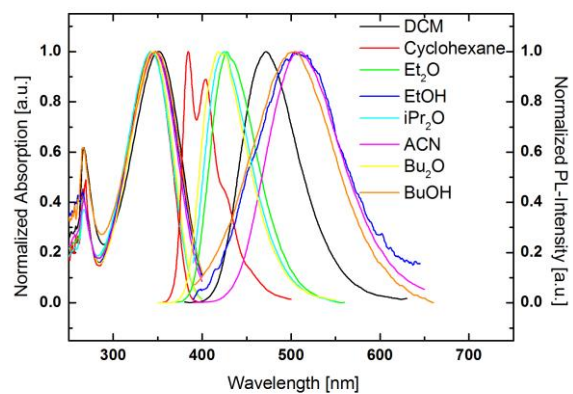


Figure S2.13. UV/VIS absorption and photoluminescence emission spectra of **DMABPym** in various solvents (DCM=dichloromethane, ACN=acetonitrile)

Table S2.1. Summary of the photophysical properties of the materials under investigation.

	Cyclohexane	Et ₂ O	EtOH	Bu ₂ O	iPr ₂ O	BuOH	ACN
Absorption							
BTazB	<250	253	<250	xxx	xxx	xxx	xxx
BTazPyr	287	286	282	xxx	xxx	xxx	xxx
BTazPym	258.5	257	255	xxx	xxx	xxx	xxx
AnTazB	258	256	255(sh)	xxx	xxx	xxx	xxx
AnTazPyr	288	288	286	287	288	287	285
AnTazPym	265	262.5	262	xxx	xxx	xxx	xxx
DMATazB	296	298	303	298	298	302	299
DMATazPyr	301	302	303	303	302	307	302
DMATazPym	298	302	308	305	302	310	304
BTazDMA	295.5	292.5	293	293.5	293.5	292.5	294.5
PyrTazDMA	304	299	293	302	301	293	294
PymTazDMA	xxx	280	286.5	xxx	xxx	xxx	xxx
DMABB	316	318	318	319.5	318.5	318.5	323.5
DMBBPyr	329.5	332	328	334	331.5	335	336
DMABPym	342	342.5	347.5	354.5	342	348	346.5
Emission							
BTazB	xxx	xxx	xxx	xxx	xxx	xxx	xxx
BTazPyr	xxx	xxx	xxx	xxx	xxx	xxx	xxx
BTazPym	xxx	xxx	xxx	xxx	xxx	xxx	xxx
AnTazB	xxx	xxx	xxx	xxx	xxx	xxx	xxx
AnTazPyr	337.5	348	356	346	345	352.5	354
AnTazPym	xxx	xxx	xxx	xxx	xxx	xxx	xxx
DMATazB	348	376	413.5	373	370.5	406	402.5
DMATazPyr	347	383	413	376.5	377.5	404.5	429 (sh), 460.5
DMATazPym	353.5	403	xxx	393	395	415.5	524.5
BTazDMA	359	400.5	501.5	392	393.5	476	482
PyrTazDMA	372	425.5	556	415.5	416.5	537	526.5
PymTazDMA	xxx	xxx	xxx	xxx	xxx	xxx	xxx
DMABB	366.5	394	426	386.5	391.5	422	441
DMBBPyr	375.5	414.5	470.5	403	405.5	462	477
DMABPym	384	427.5	505	418	424.5	504	511.5

3) Theoretical calculations



Figure S3.1. Spatial distribution of HOMO (left) and LUMO (right) levels of **BTazB**.



Figure S3.2. Spatial distribution of HOMO (left) and LUMO (right) levels of **BTazPyr**.



Figure S3.3. Spatial distribution of HOMO (left) and LUMO (right) levels of **BTazPym**.



Figure S3.4. Spatial distribution of HOMO (left) and LUMO (right) levels of **AnTazB**.



Figure S3.5. Spatial distribution of HOMO (left) and LUMO (right) levels of **AnTazPyr**.



Figure S3.6. Spatial distribution of HOMO (left) and LUMO (right) levels of **AnTazPym**.



Figure S3.7. Spatial distribution of HOMO (left) and LUMO (right) levels of **DMATazPyr**.



Figure S3.8. Spatial distribution of HOMO (left) and LUMO (right) levels of **PyrTazDMA**.



Figure S3.9. Spatial distribution of HOMO (left) and LUMO (right) levels of **DMABB**.



Figure S3.10. Spatial distribution of HOMO (left) and LUMO (right) levels of **DMABPyr**.

4) Crystallography

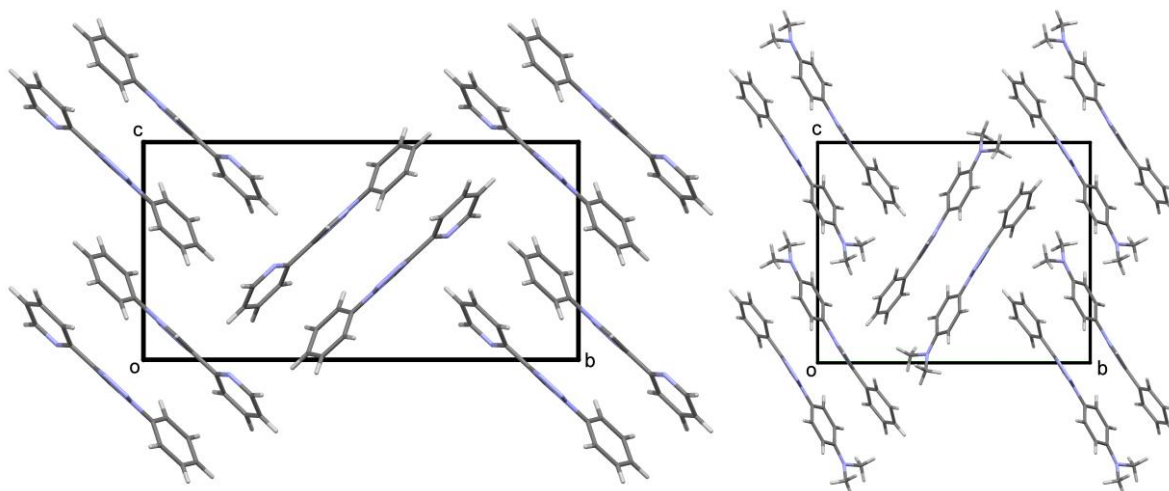


Figure S4.1. The crystal structures of **BTazPyr** (left) and **DMATazB** (right) viewed down [100]. C, H and N atoms are gray, white and blue, respectively. Coordinates of **BTazPyr** taken from D. Schweinfurth, R. Pattacini, S. Strobel, B. Sarkar, Dalton T 2009, 9291-9297.

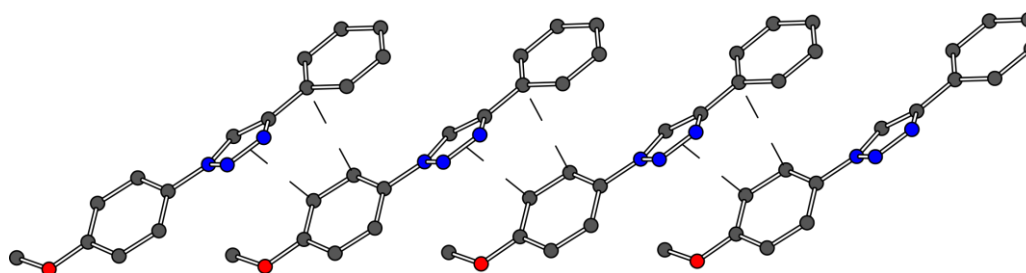


Figure S4.2. Chains of **AnTazPyr** molecule connected by head-to-tail π - π interactions. C, N and O atoms are represented by grey, blue and red spheres of arbitrary radius. H atoms are omitted for clarity. Hydrogen bonds are indicated by dashed lines.

3.8. Manuscript #8 – Supporting Information

Ethyne-linked push-pull chromophores: implications of crystal structure and molecular electronics on the quadric nonlinear activity

Paul Kautny, Helene Kriegner, Dorian Bader, Michal Dušek, Georg A. Reider, Johannes Fröhlich, Berthold Stöger

submitted for publication

Ethyne-linked push-pull chromophores: Implications of crystal structure and molecular electronics on the nonlinear activity

Supporting Information

Paul Kautny,^{†,} Helene Kriegner,[†] Dorian Bader,[†] Michal Dušek,[‡] Georg A. Reider,[§]
Johannes Fröhlich,[†] Berthold Stöger[¶]*

[†]Institute of Applied Synthetic Chemistry, TU Wien, Getreidemarkt 9/163, A-1060 Vienna, Austria

[‡]Institute of Physics of the Czech Academy of Sciences, Na Slovance 2, 18221 Prague 8, Czech Republic

[§]Photonics Institute, TU Wien, Gußhausstraße 27-29, A-1040 Vienna, Austria

[¶]X-ray Centre, TU Wien, Getreidemarkt 9, A-1060 Vienna, Austria

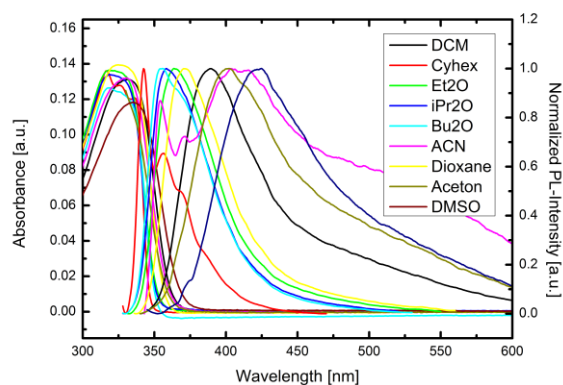


Figure S1. UV/Vis absorption and photoluminescent emission spectra of **1** in various solvents.

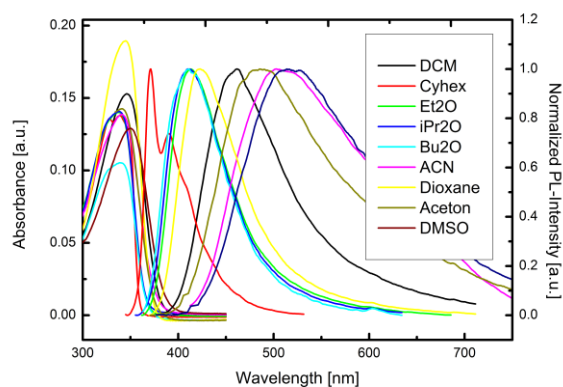


Figure S2. UV/Vis absorption and photoluminescent emission spectra of **2** in various solvents.

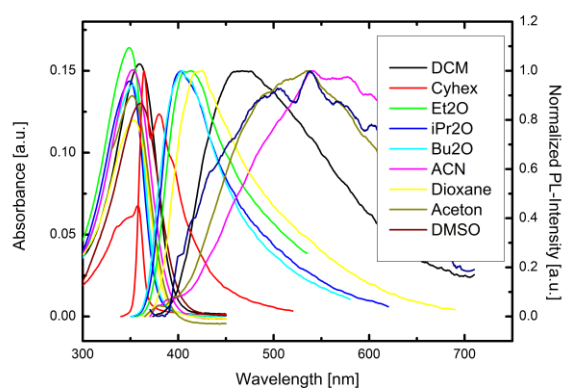


Figure S3. UV/Vis absorption and photoluminescent emission spectra of **3** in various solvents.

3.9. Manuscript #9 – Supporting Information

Functional organic click-materials: application in phosphorescent organic light emitting diodes

Paul Kautny, Chenyang Zhao, Thomas Kader, Berthold Stöger, Ernst Horkel, Jiangshan Chen, Dongge Ma, Johannes Fröhlich, Daniel Lumpi

RSC Advances, **2017**, 7, 12150-12160

Functional Organic Click-Materials: Application in Phosphorescent Organic Light Emitting Diodes

Paul Kautny,^{*a} Chenyang Zhao,^b Thomas Kader,^a Berthold Stöger,^c Ernst Horkel,^a
Jiangshan Chen,^{*b} Dongge Ma,^b Johannes Fröhlich^a and Daniel Lumpi^a

Supporting Information

^a Institute of Applied Synthetic Chemistry, TU Wien, Getreidemarkt 9/163, A-1060 Vienna, Austria; E-mail: paul.kautny@tuwien.ac.at

^b State Key Laboratory of Polymer Physics and Chemistry, Changchun Institute of Applied Chemistry, Chinese Academy of Sciences, Changchun, 130022, China; E-mail: jschen@ciac.ac.cn

^c Institute of Chemical Technologies and Analytics, TU Wien, Getreidemarkt 9/164, A-1060 Vienna, Austria

NMR spectra

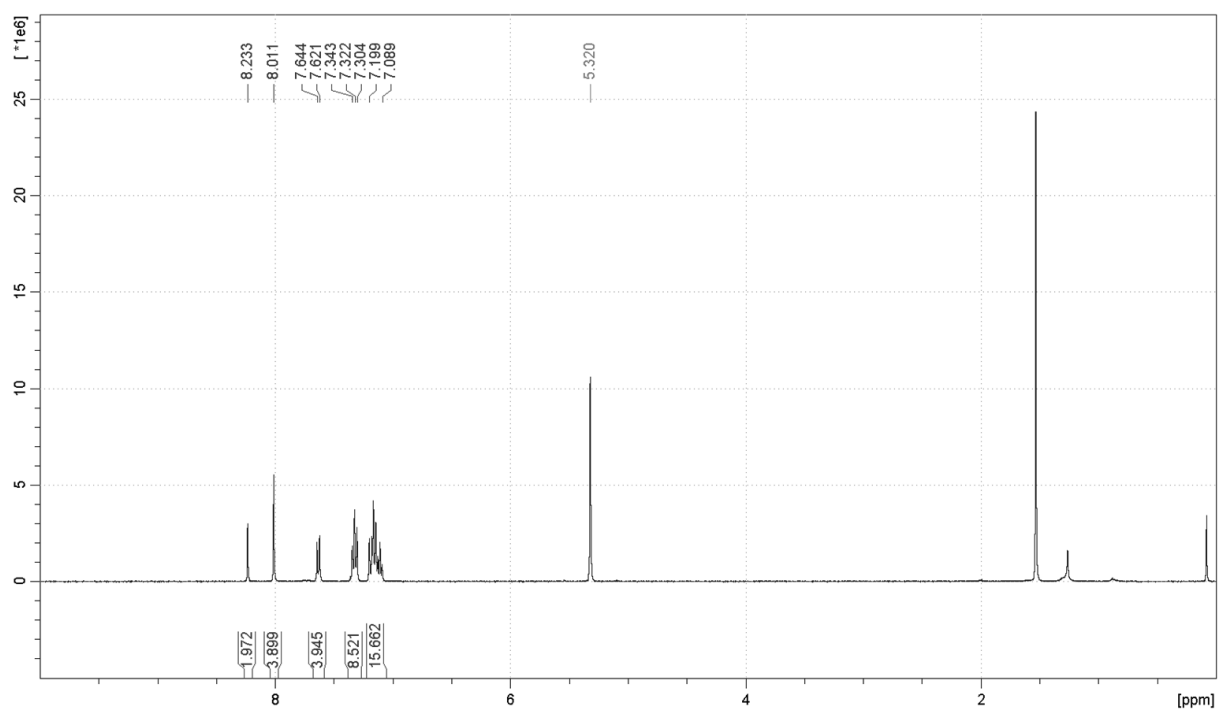


Figure S 1. Proton NMR spectrum of compound 3a.

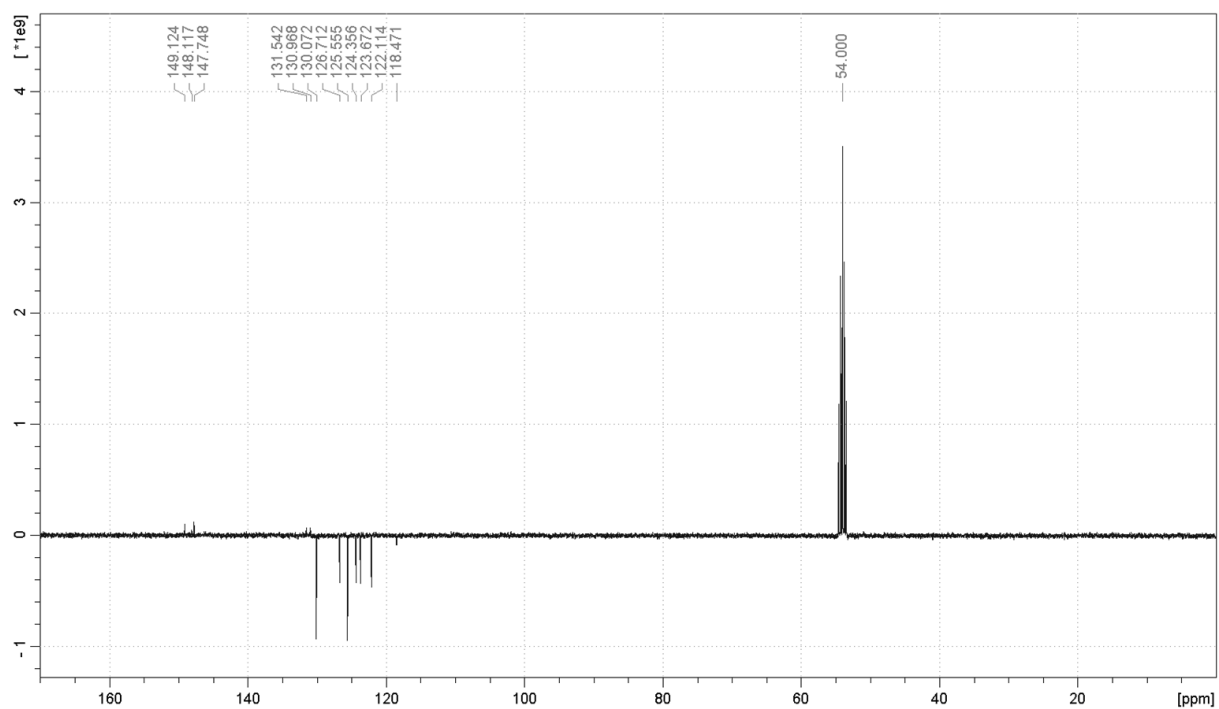


Figure S 2. Carbon NMR spectrum of compound 3a.

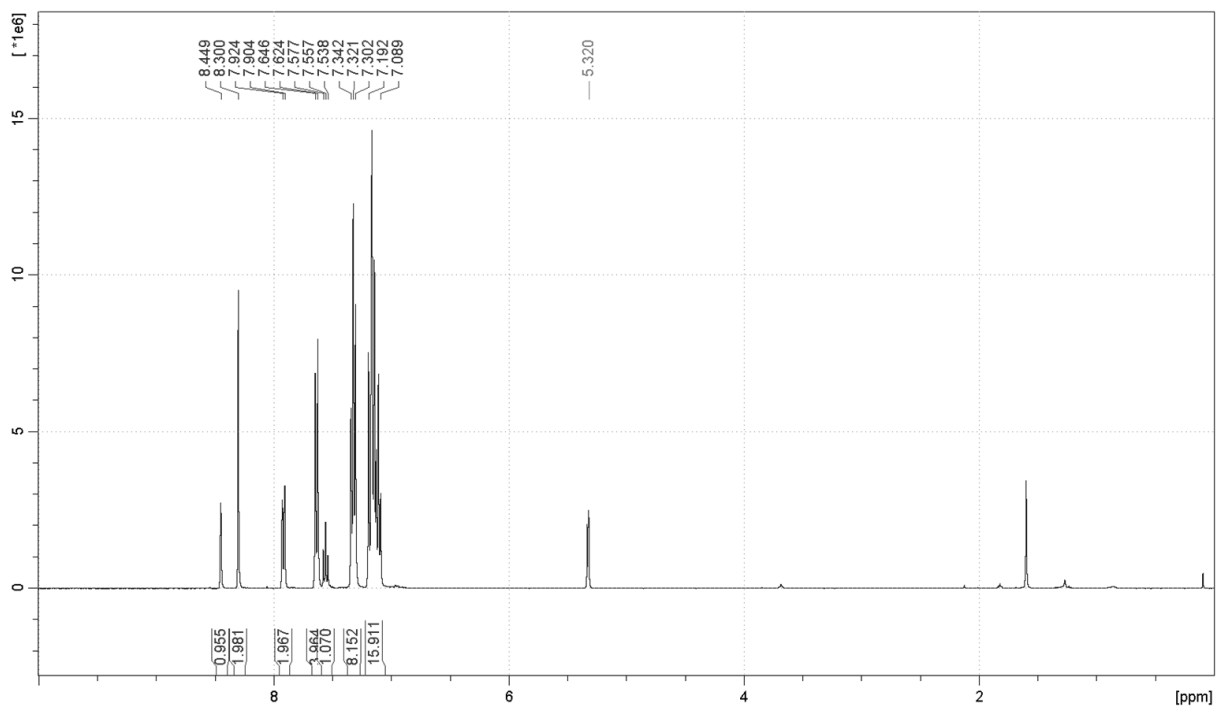


Figure S 3. Proton NMR spectrum of compound 3b.

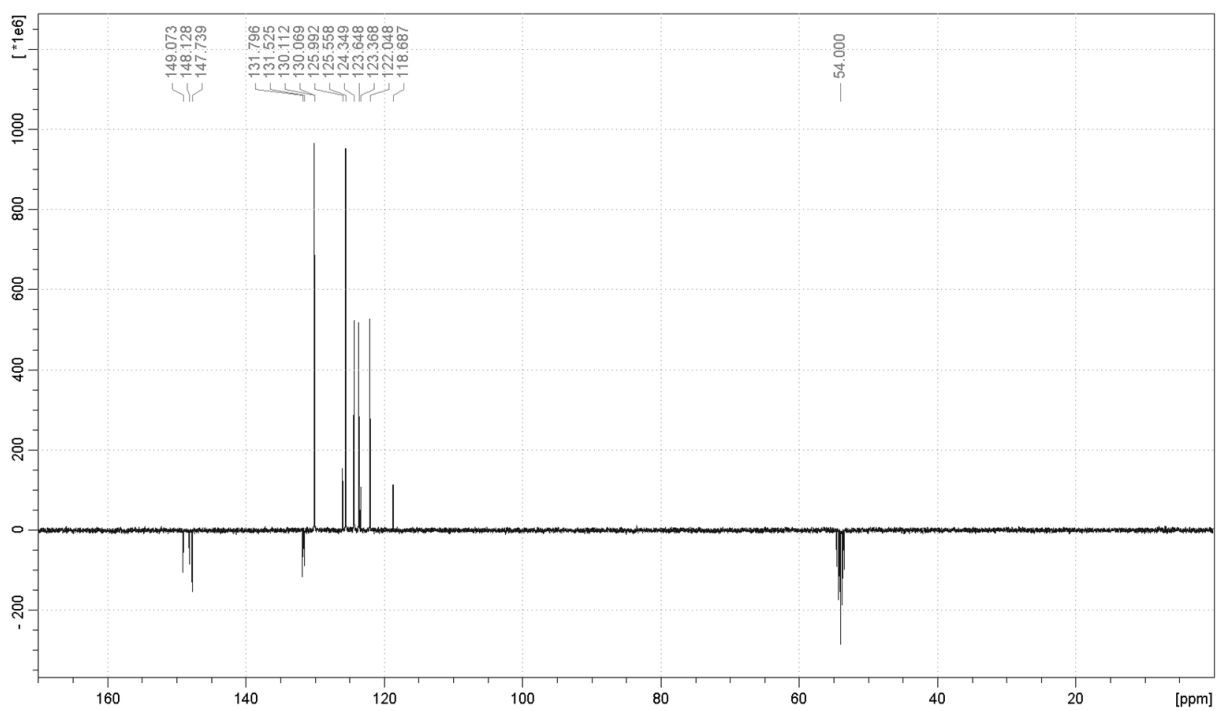


Figure S 4. Carbon NMR spectrum of compound 3b.

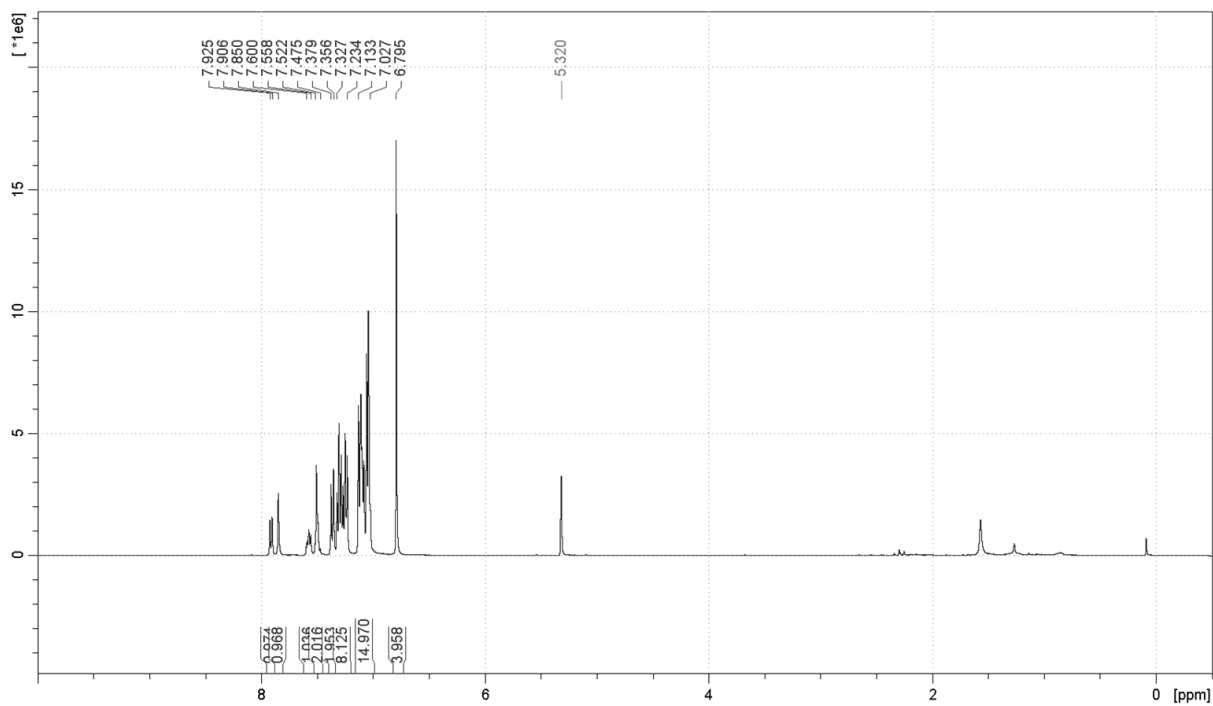


Figure S 5. Proton NMR spectrum of compound 3c.

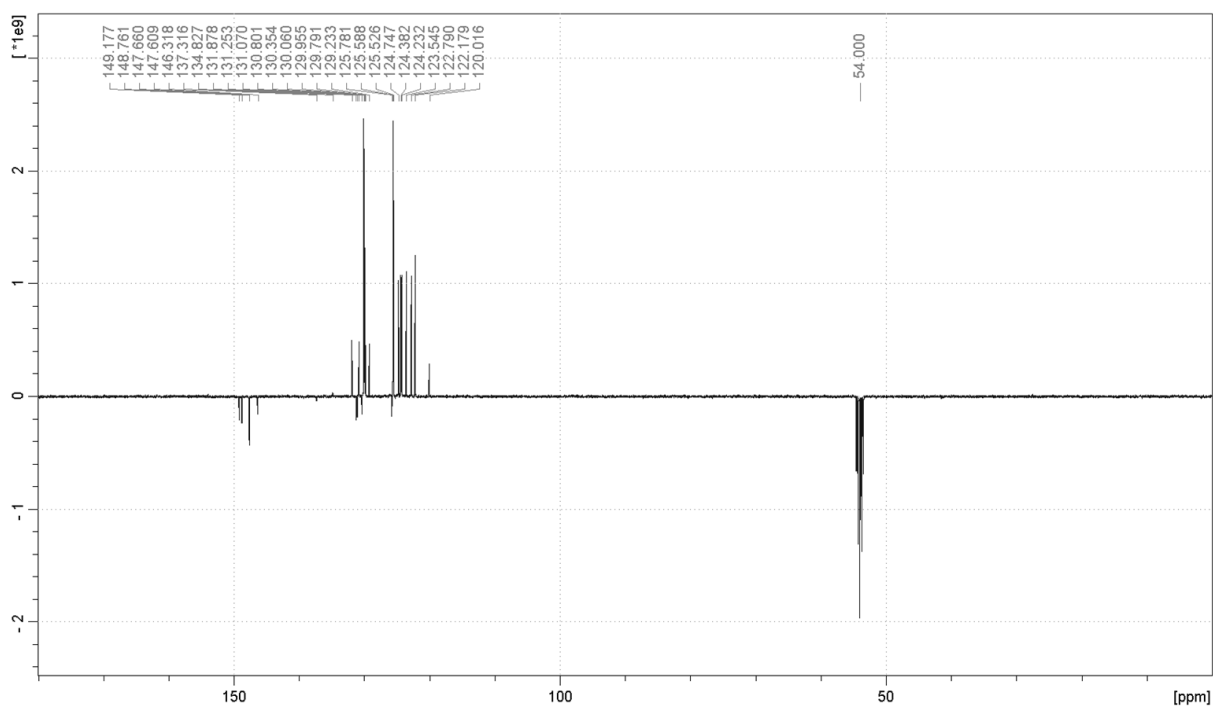


Figure S 6. Carbon NMR spectrum of compound 3c.

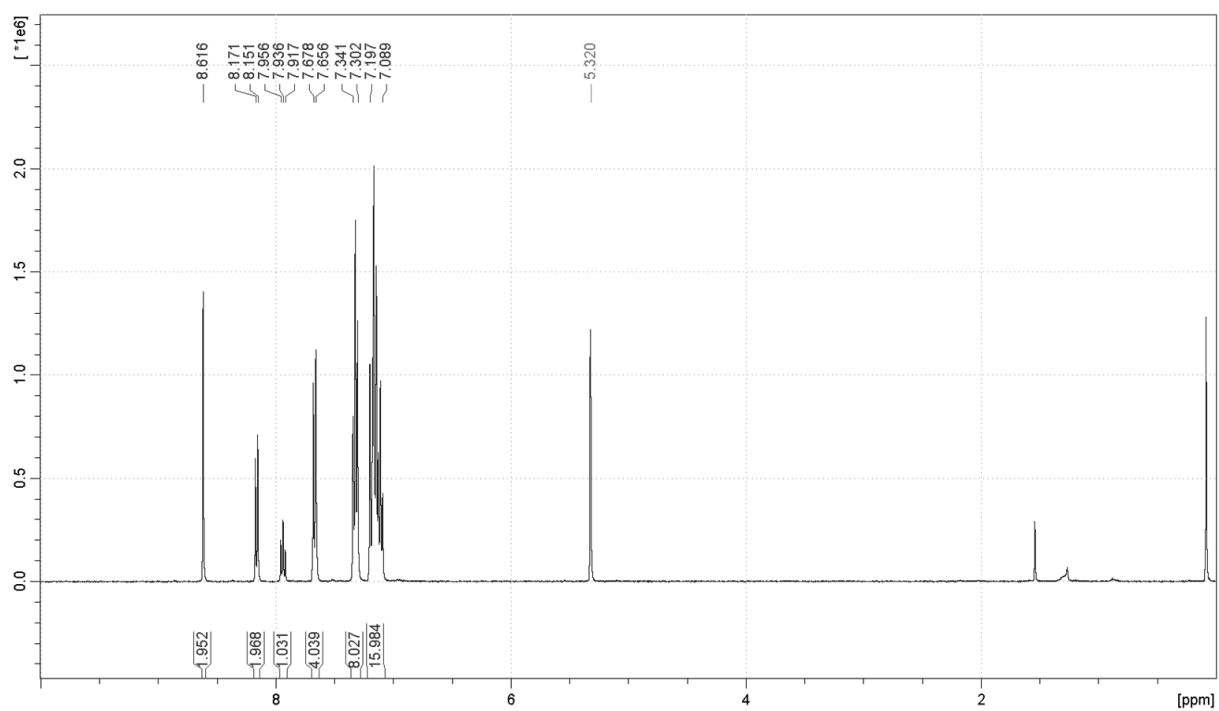


Figure S 7. Proton NMR spectrum of compound 3d.

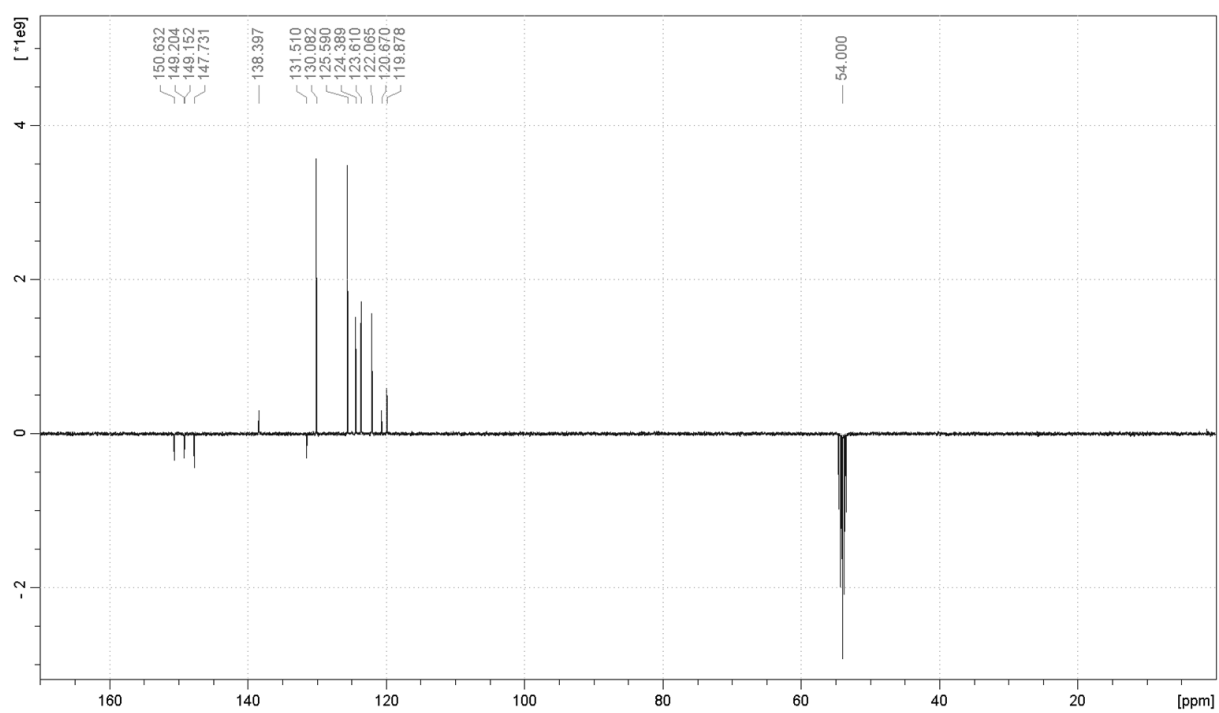


Figure S 8. Carbon NMR spectrum of compound 3d.

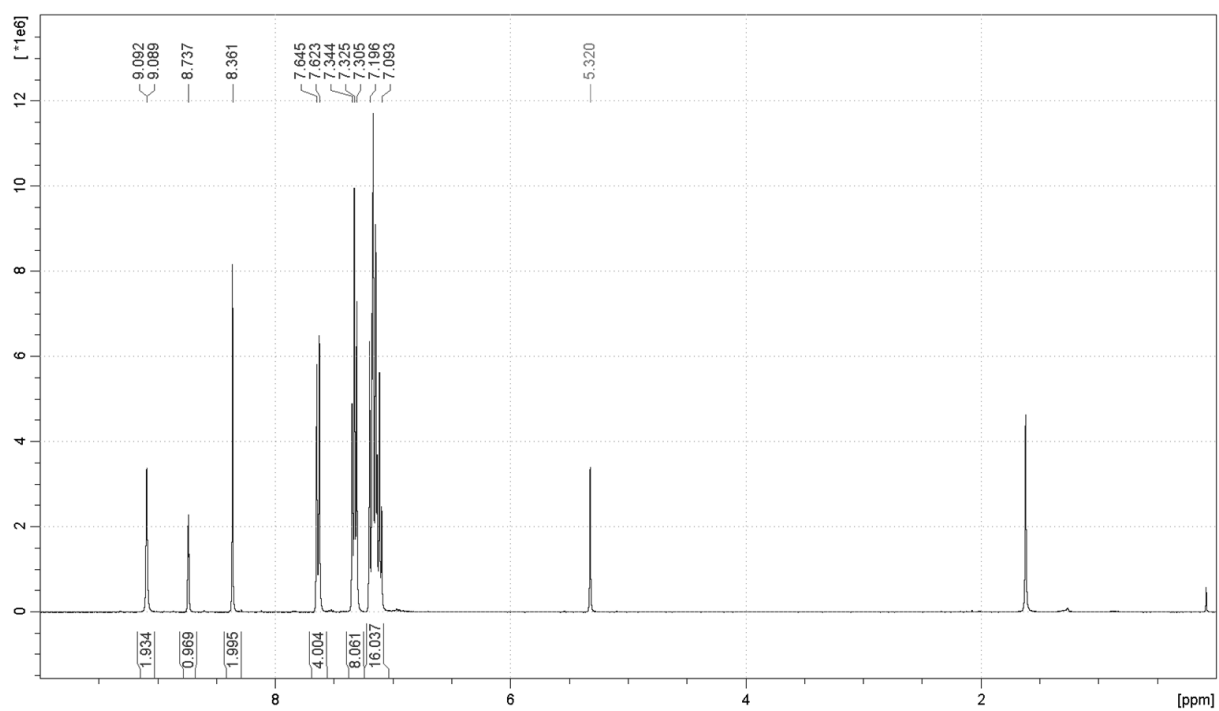


Figure S 9. Proton NMR spectrum of compound 3e.

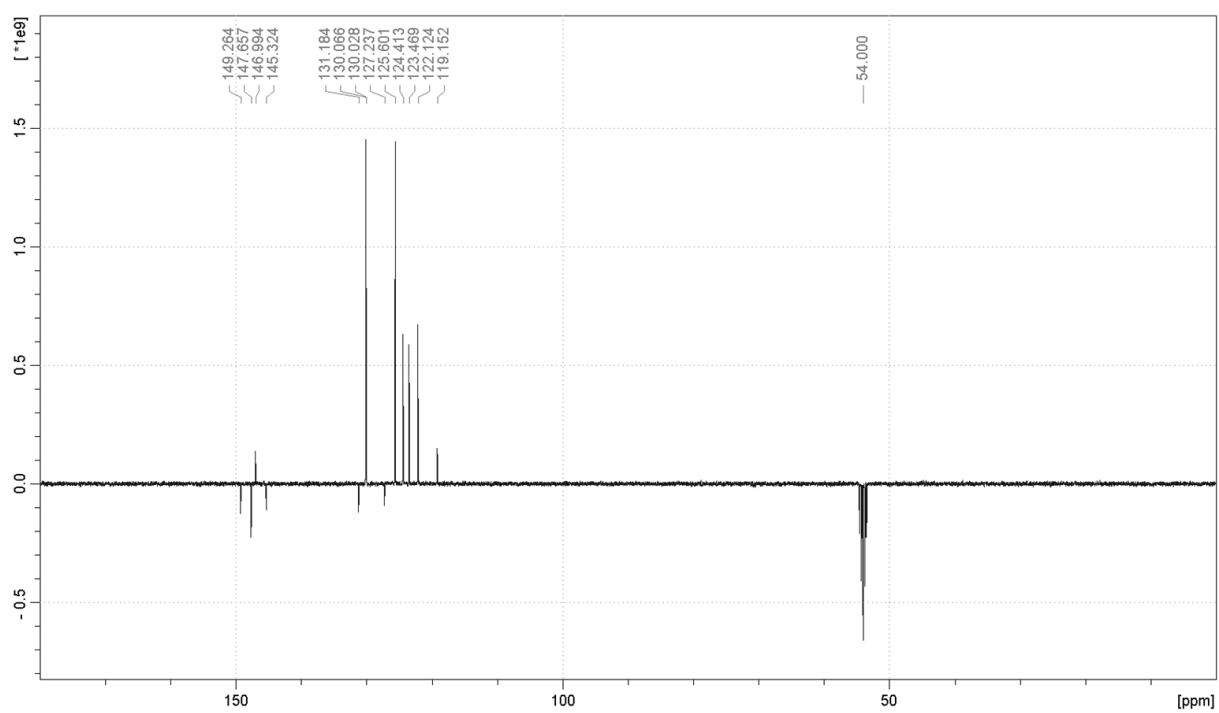


Figure S 10. Carbon NMR spectrum of compound 3e.

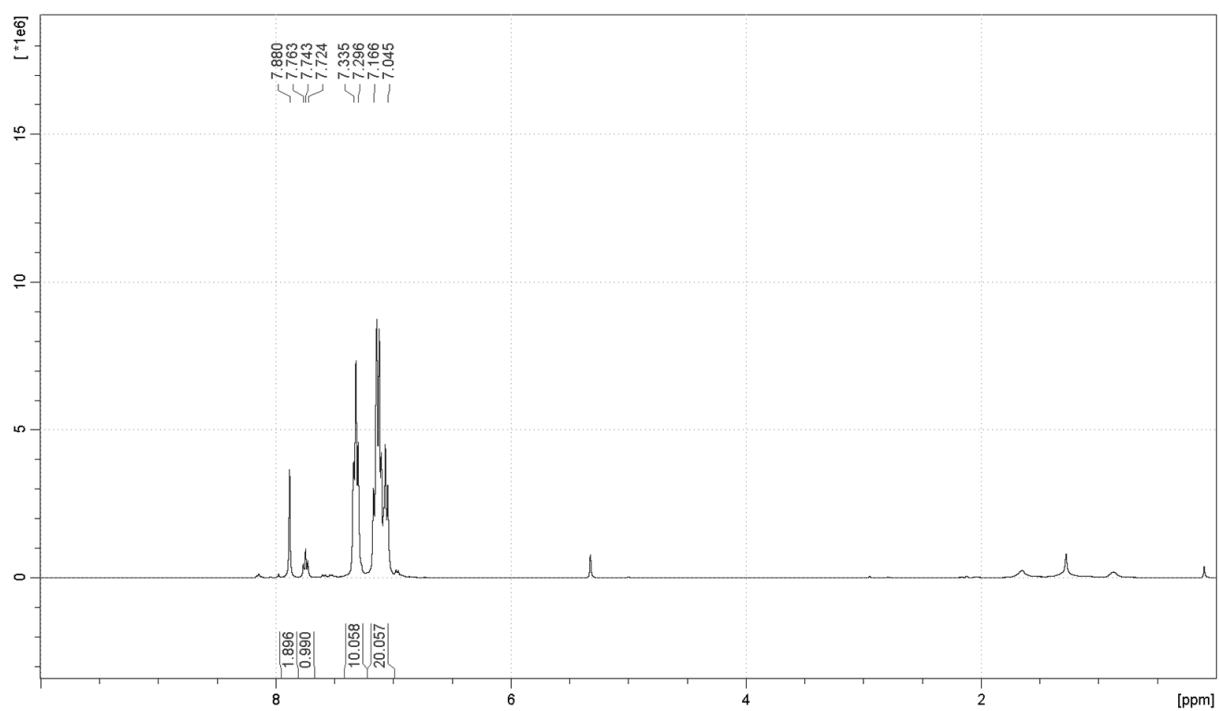


Figure S 11. Proton NMR spectrum of compound 4d.

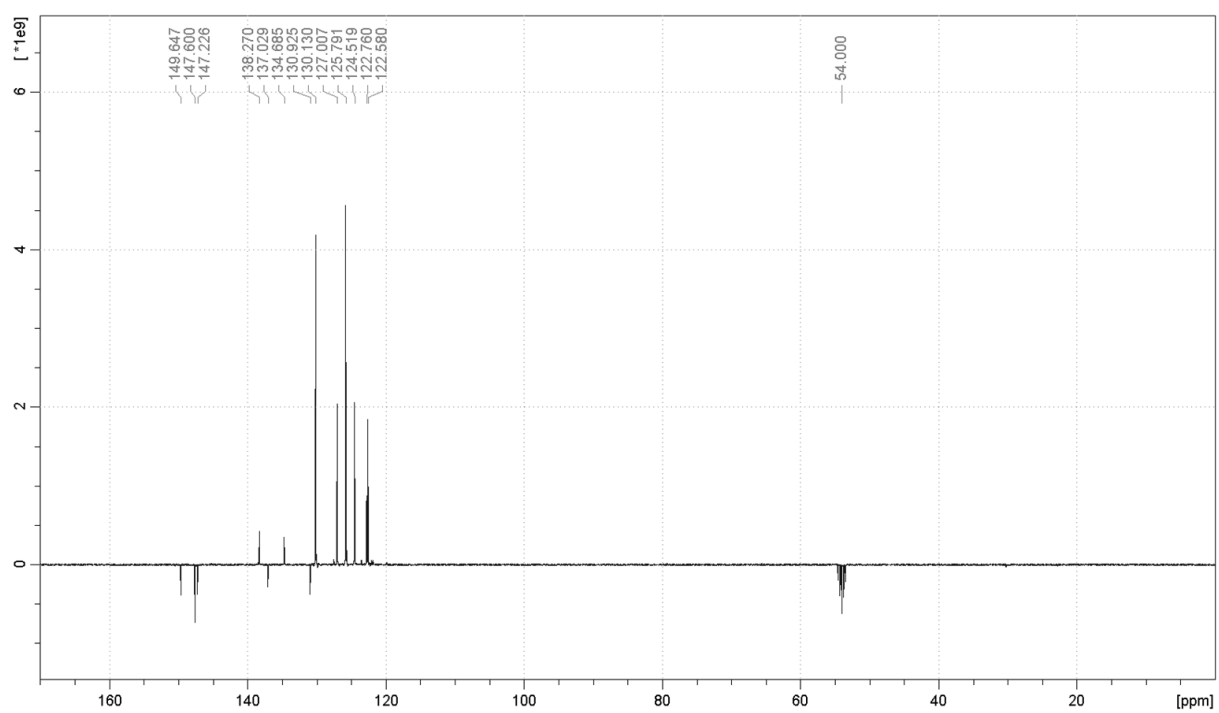


Figure S 12. Carbon NMR spectrum of compound 4d.

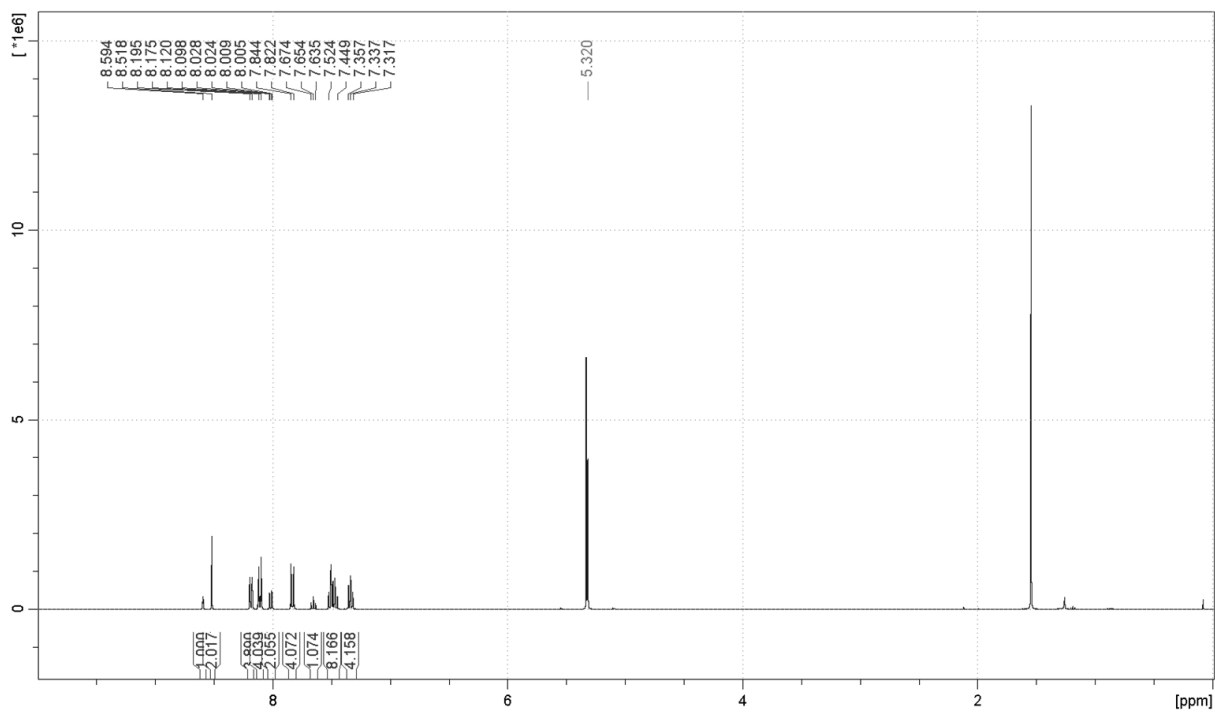


Figure S 13. Proton NMR spectrum of compound **5b**.

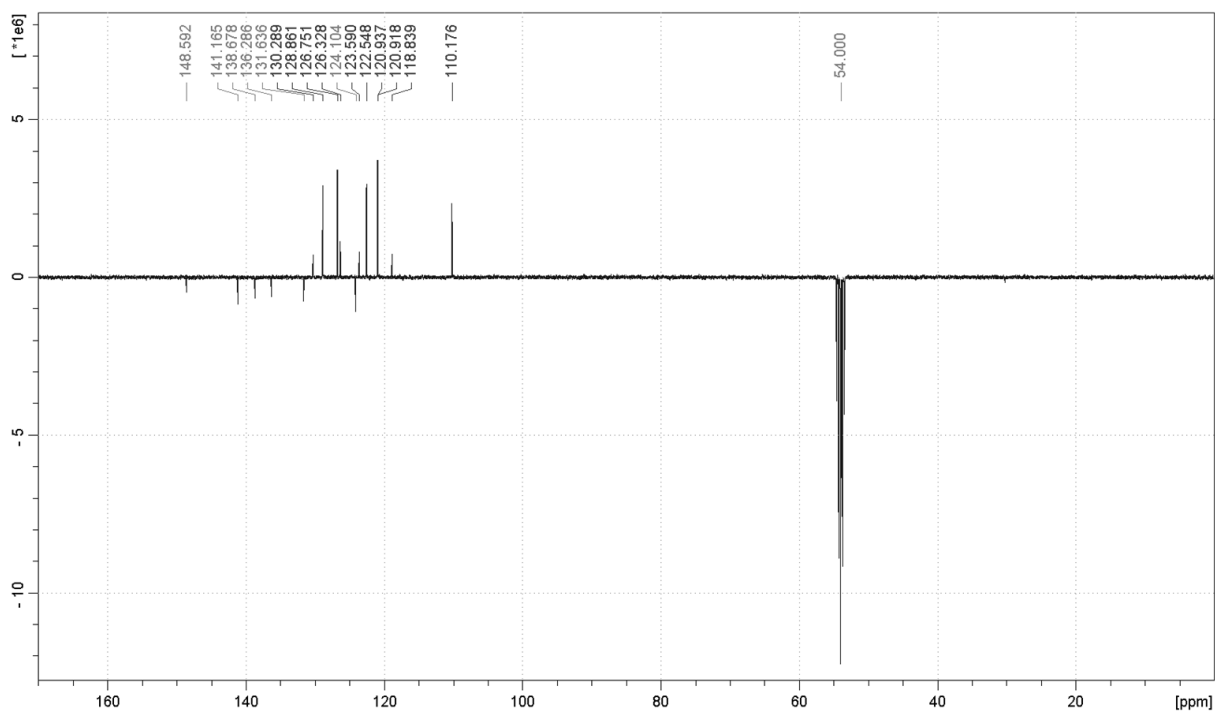


Figure S 14. Carbon NMR spectrum of compound **5b**.

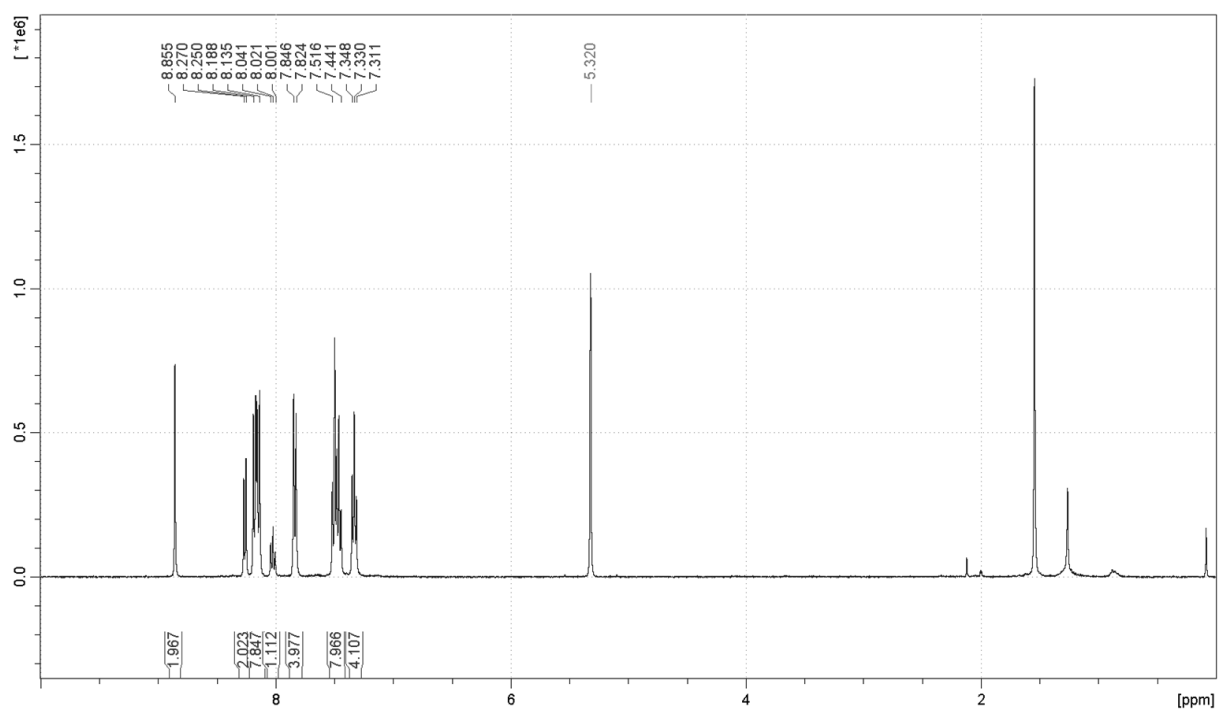


Figure S 15. Proton NMR spectrum of compound 5d.

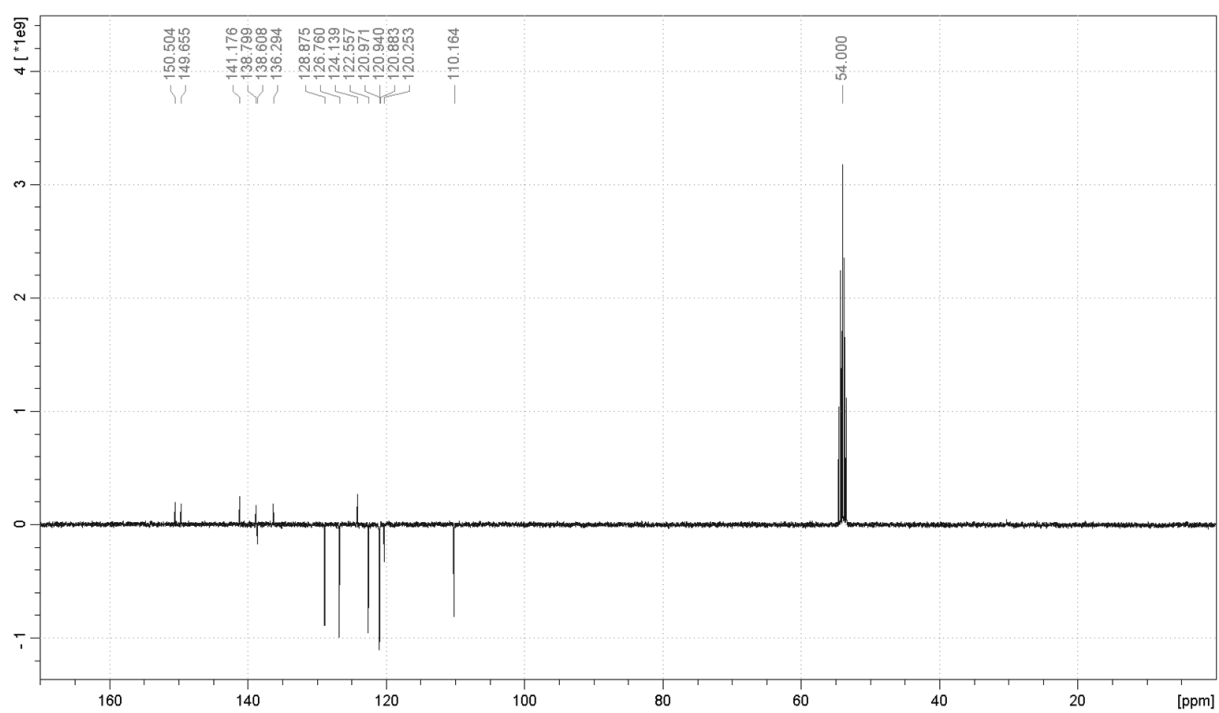


Figure S 16. Carbon NMR spectrum of compound 5d.

TGA/DSC

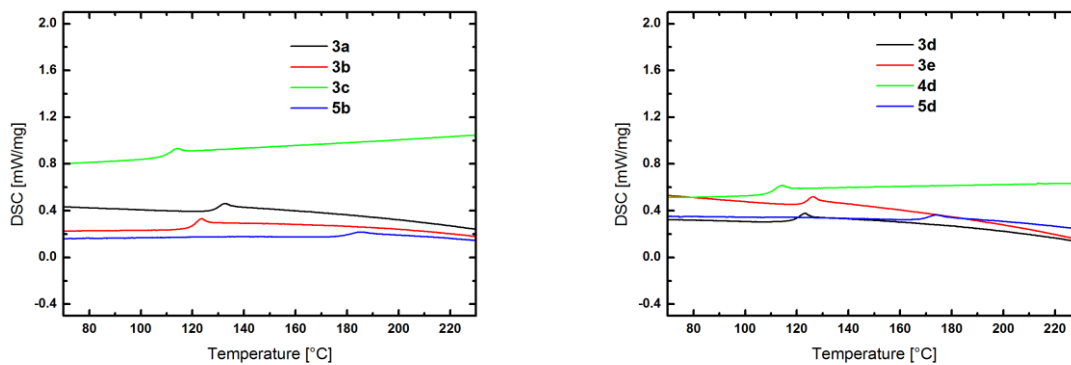


Figure S 17. DSC trace of the second heating cycle of **3a**, **3b**, **3c** and **5b** (left) and **3d**, **3e**, **4d** and **5d** (right) recorded at a heating rate of $10\text{ }^{\circ}\text{C min}^{-1}$.

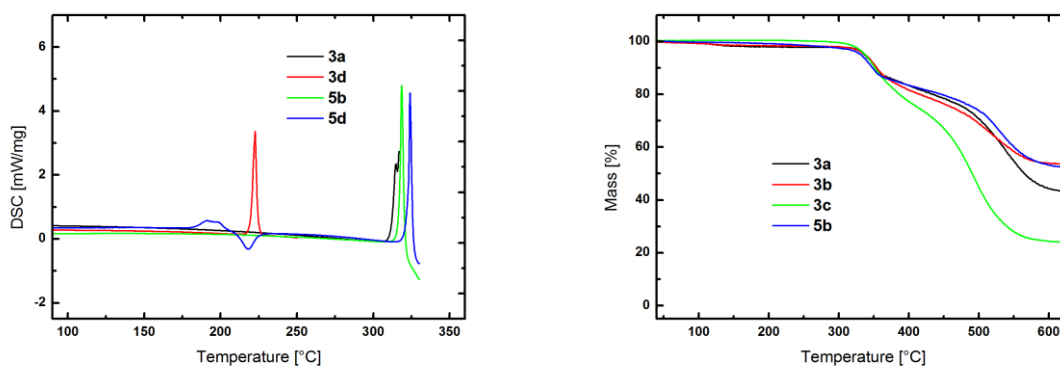


Figure S 18. DSC trace of the first heating cycle of **3a**, **3d**, **5b** and **5d** (left) and TGA trace of **3a**, **3b**, **3c** and **5b** (right) recorded at a heating rate of $10\text{ }^{\circ}\text{C min}^{-1}$.

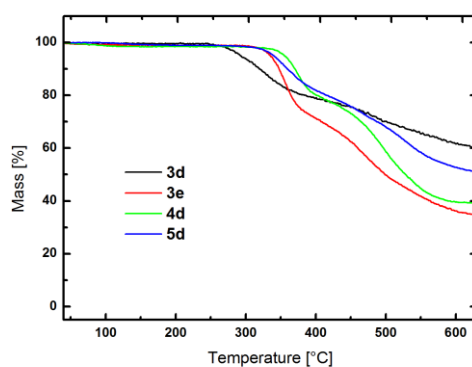


Figure S 19. TGA trace of **3d**, **3e**, **4d** and **5d** (right) recorded at a heating rate of $10\text{ }^{\circ}\text{C min}^{-1}$.

Cyclic voltammetry

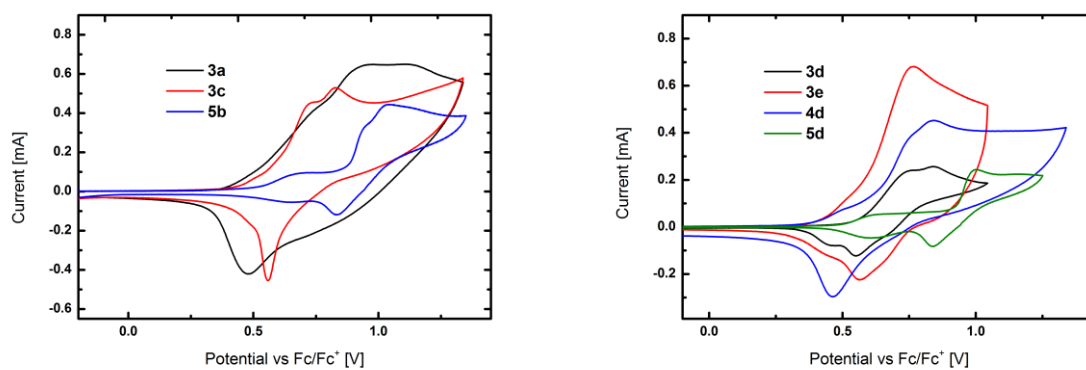


Figure S 20. CV curves of **3a**, **3c** and **5b** (left) and **3d**, **3e**, **4d** and **5d** (right).

Theoretical calculations



Figure S 21. Spatial distribution of the HOMO (left) and LUMO (right) of **3a**.



Figure S 22. Spatial distribution of the HOMO (left) and LUMO (right) of **3c**.



Figure S 23. Spatial distribution of the HOMO (left) and LUMO (right) of **3d**.



Figure S 24. Spatial distribution of the HOMO (left) and LUMO (right) of **3e**.



Figure S 25. Spatial distribution of the HOMO (left) and LUMO (right) of **4d**.

EL spectra

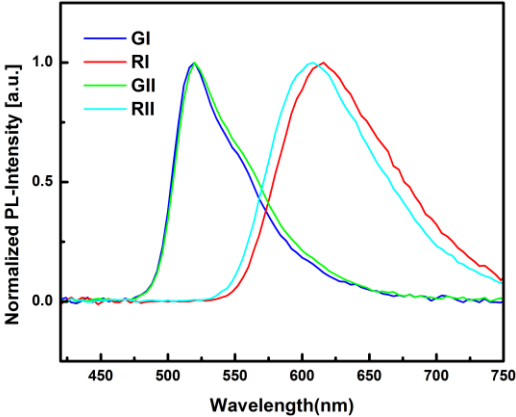


Figure S 26. EL spectra of devices RI, RII, GI and GII.

3.10. Manuscript #10 – Supporting Information

Thiophene ring-fragmentation reactions: Principles and scale-up towards NLO materials

Daniel Lumpi, Johannes Steindl, Sebastian Steiner, Victor Carl, Paul Kautny, Michael Schön, Florian Glöcklhofer, Brigitte Holzer, Berthold Stöger, Ernst Horkel, Christian Hametner, Georg Reider, Marko D. Mihovilovic, Johannes Fröhlich

Tetrahedron, **2017**, 73, 472-280

Supplementary Data

Thiophene Ring-Fragmentation Reactions: Principles and Scale-Up towards NLO Materials

Daniel Lumpi^{a,*}, Johannes Steindl^a, Sebastian Steiner^a, Victor Carl^a, Paul Kautny^a,
Michael Schön^a, Florian Glöcklhofer^a, Brigitte Holzer^a, Berthold Stöger^b, Ernst Horkel^a,
Christian Hametner^a, Georg Reider^c, Marko D. Mihovilovic^a, and Johannes Fröhlich^a

^a Institute of Applied Synthetic Chemistry, Vienna University of Technology,
Getreidemarkt 9/163, A-1060 Vienna, Austria

^b Institute of Chemical Technologies and Analytics, Vienna University of Technology,
Getreidemarkt 9/164-SC, A-1060 Vienna, Austria

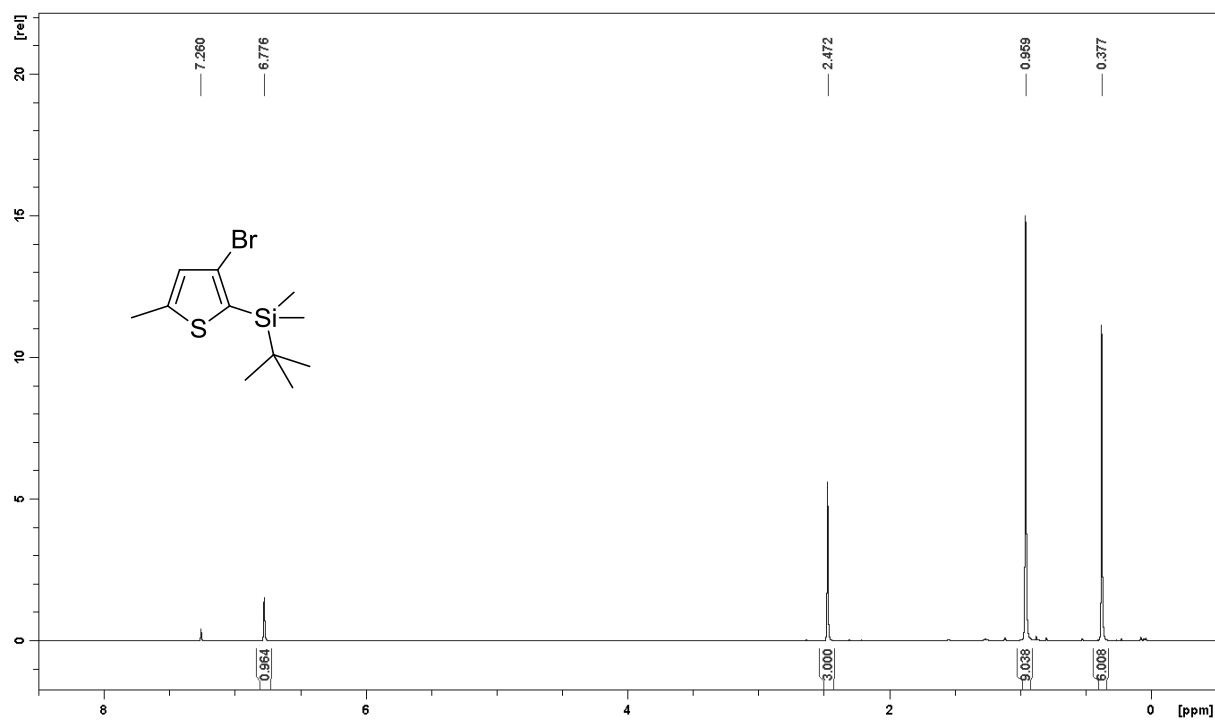
^c Photonics Institute, Vienna University of Technology,
Gußhausstraße 27-29, A-1040 Vienna, Austria

* daniel.lumpi@tuwien.ac.at

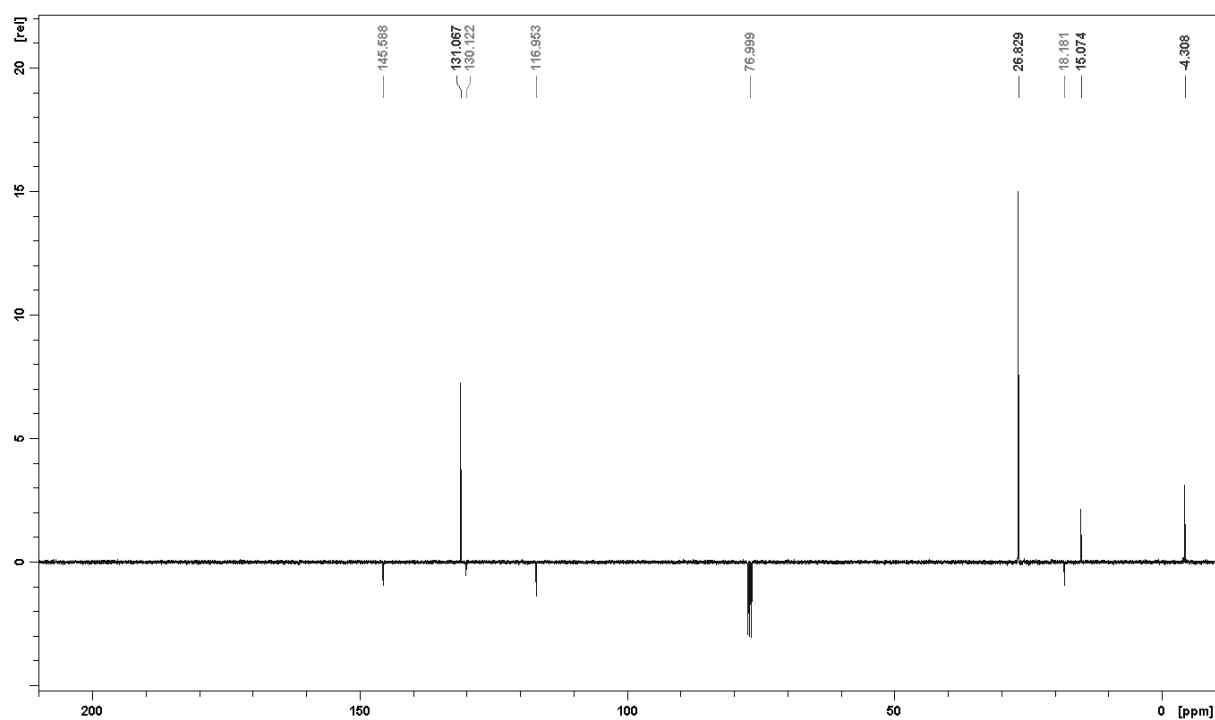
Table of contents:

1. Synthetic Part	-2-
2. Isomerization Experiments	-13-
3. Kinetic Investigations	-14-
4. Flow Experiments	-15-

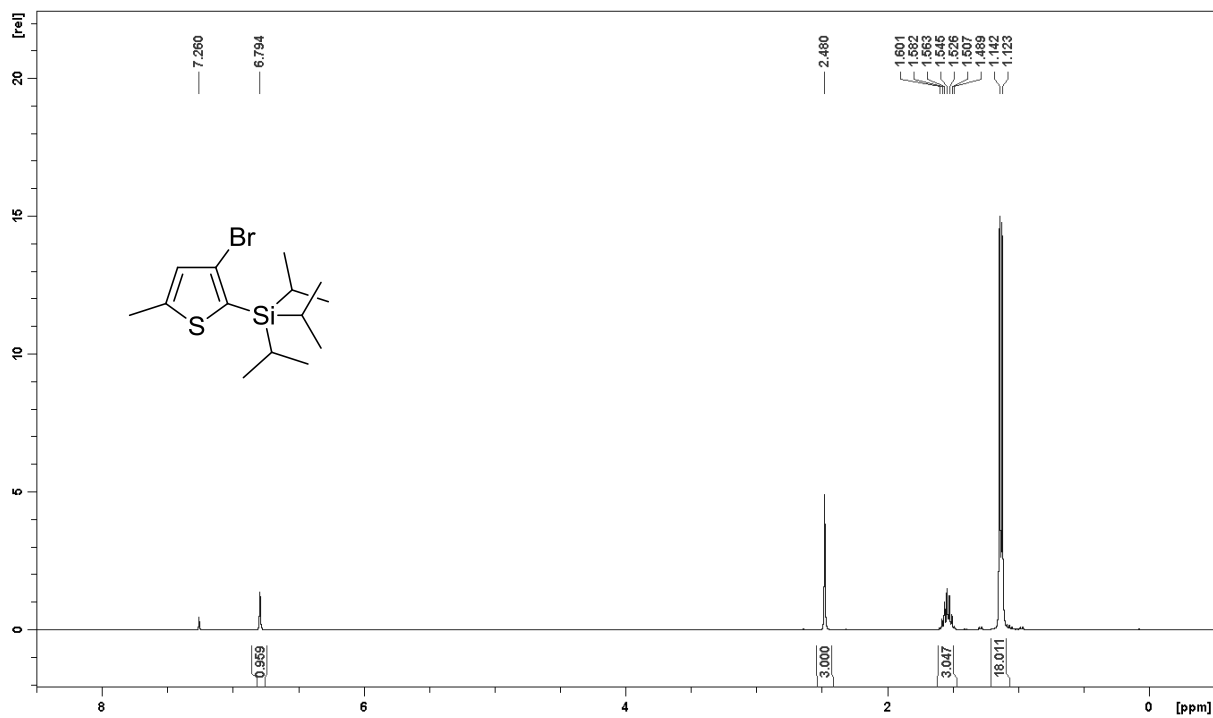
1. Synthetic Part



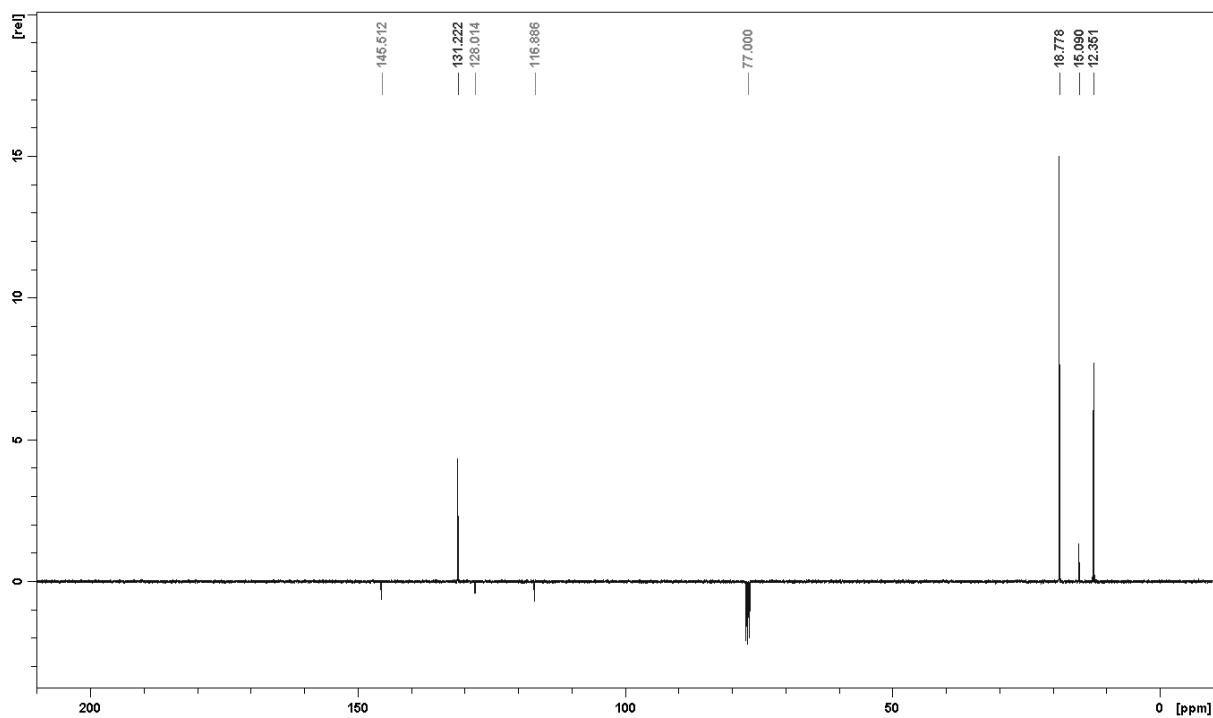
Spectrum 1.1. ^1H NMR (400 MHz, CDCl_3) of compound **2b**.



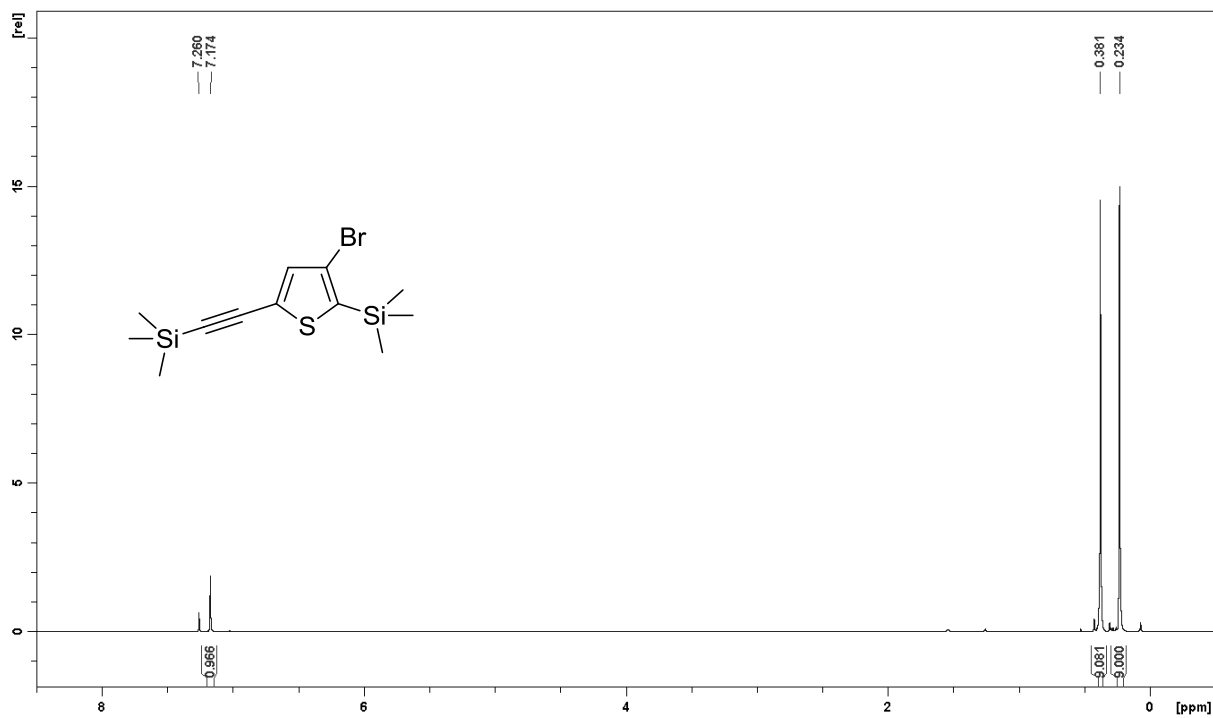
Spectrum 1.2. ^{13}C NMR (100 MHz, CDCl_3) of compound **2b**.



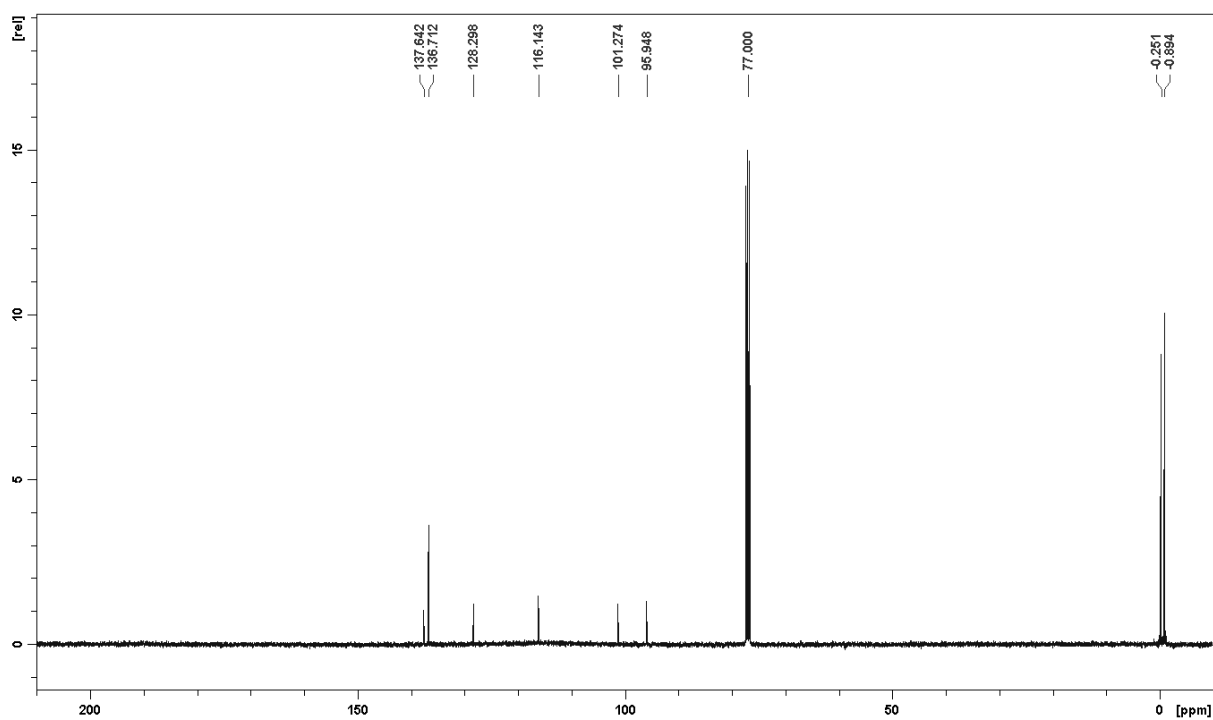
Spectrum 1.3. ^1H NMR (400 MHz, CDCl_3) of compound 2c.



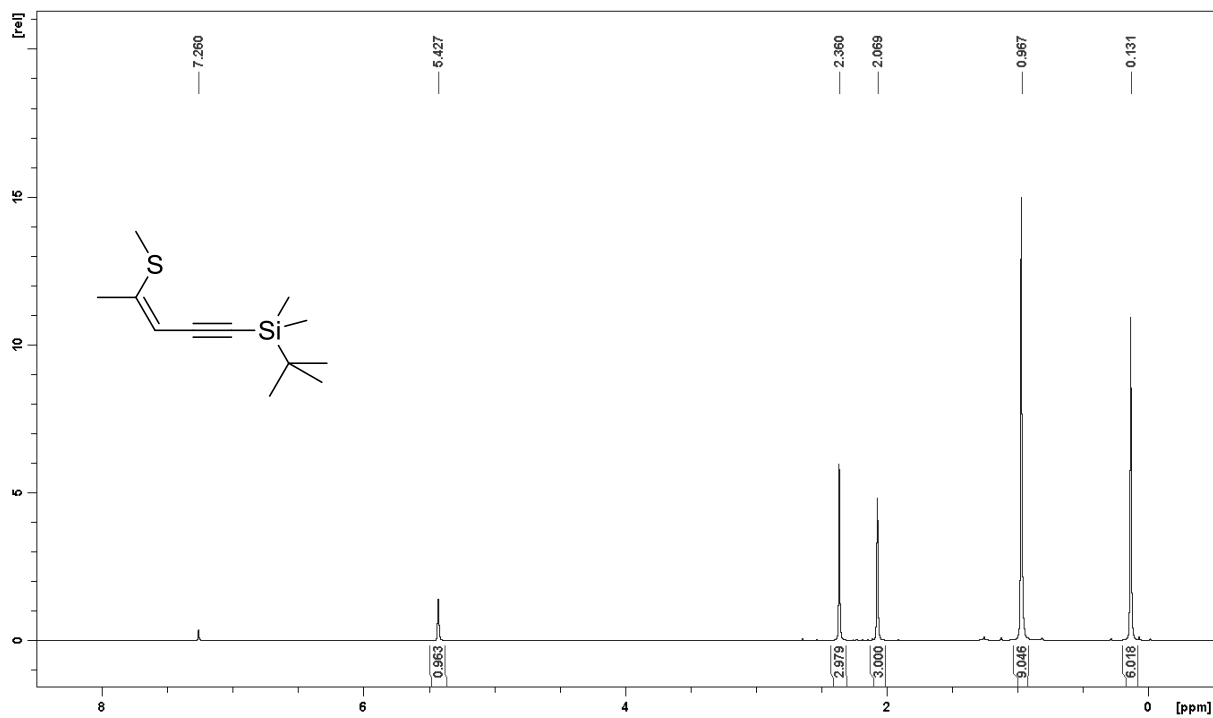
Spectrum 1.4. ^{13}C NMR (100 MHz, CDCl_3) of compound 2c.



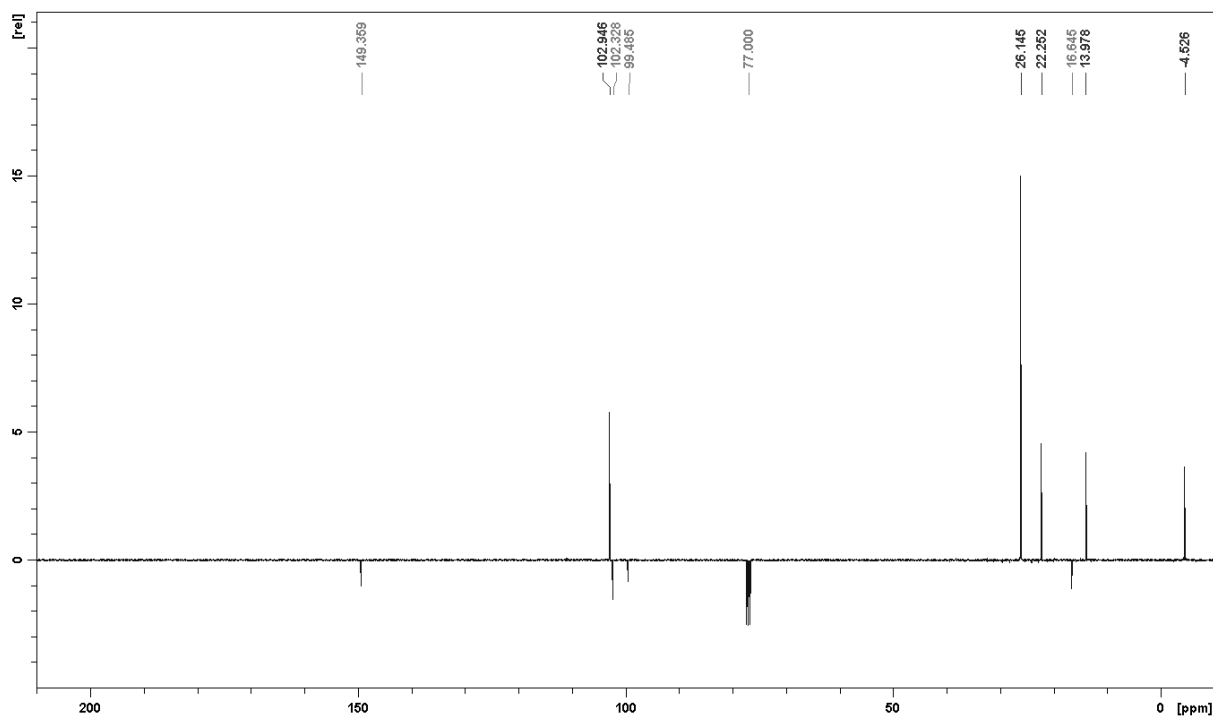
Spectrum 1.5. ^1H NMR (400 MHz, CDCl_3) of compound 2e.



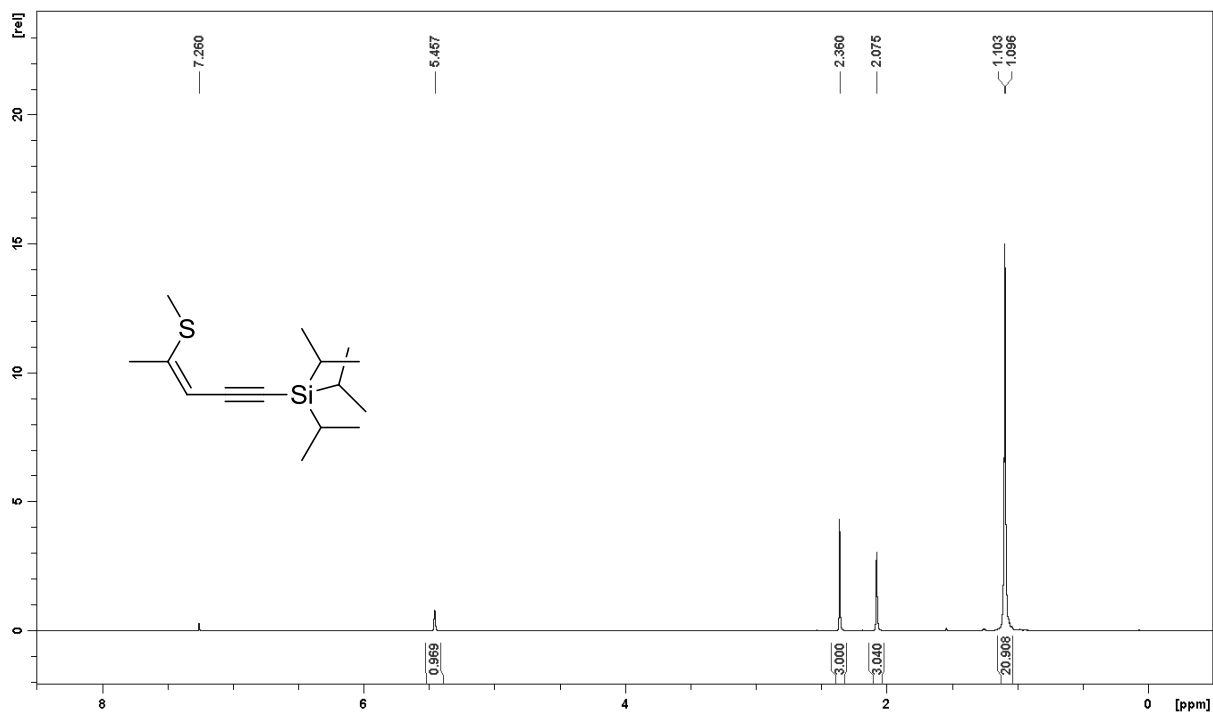
Spectrum 1.6. ^{13}C NMR (100 MHz, CDCl_3) of compound 2e.



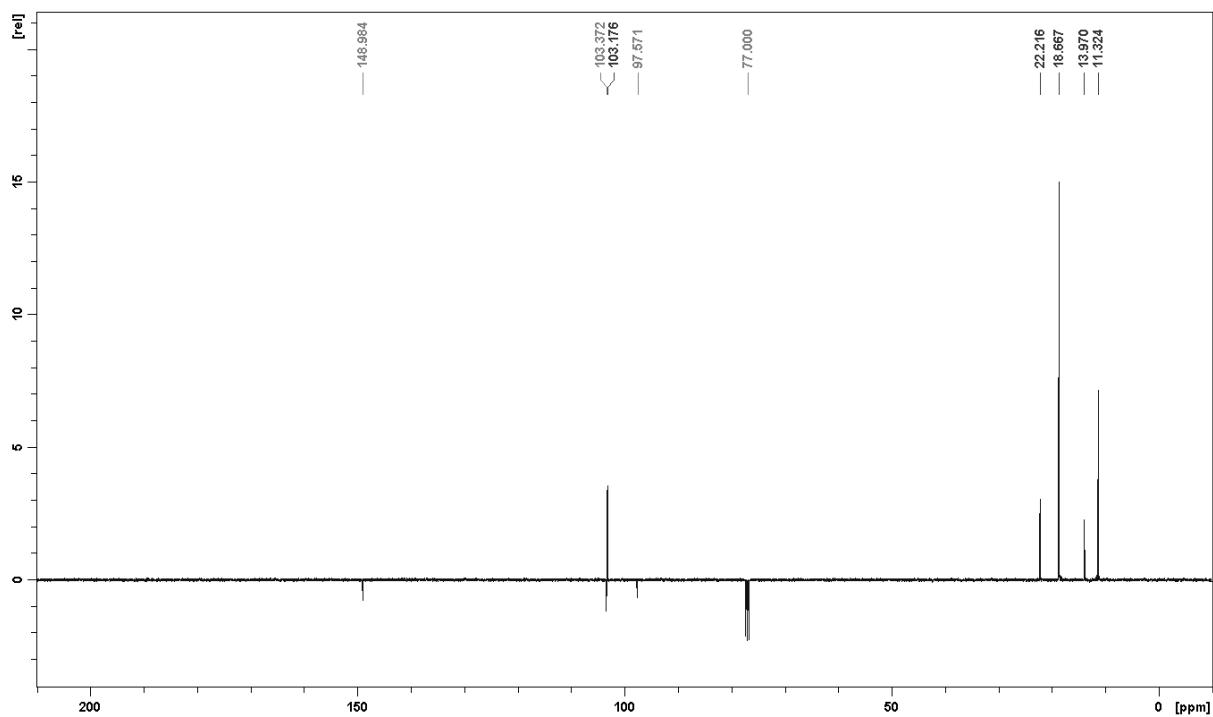
Spectrum 1.7. ^1H NMR (400 MHz, CDCl_3) of compound 3b.



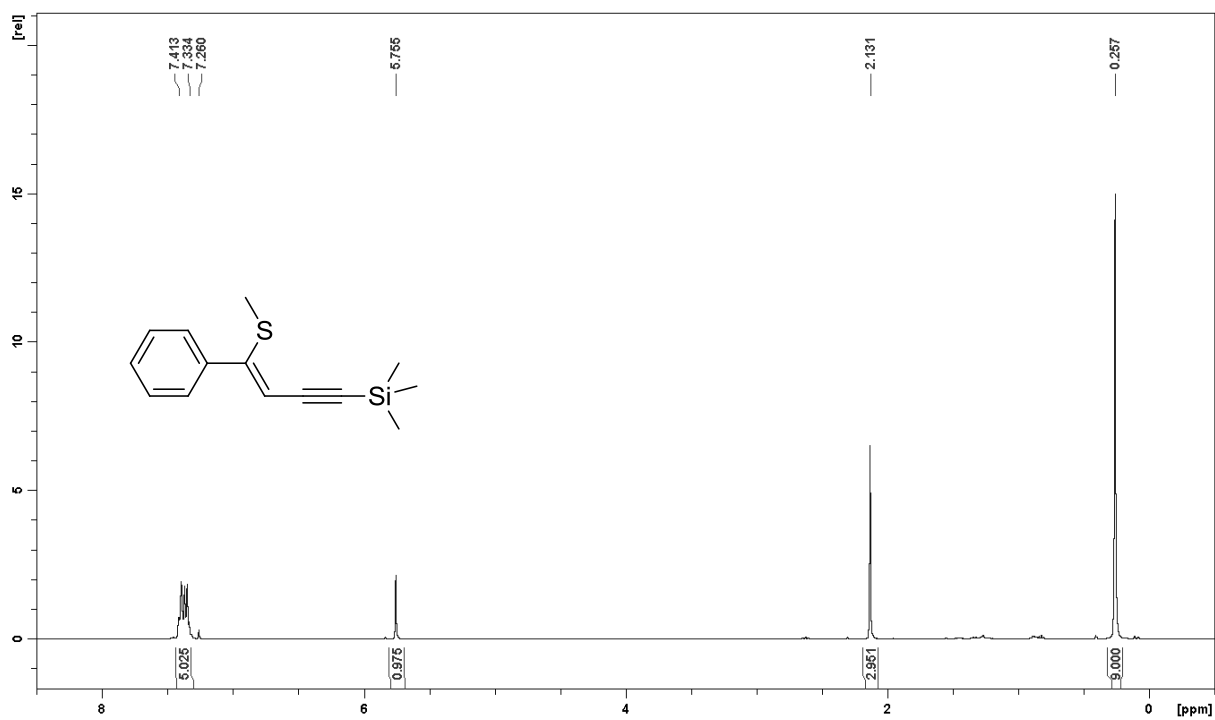
Spectrum 1.8. ^{13}C NMR (100 MHz, CDCl_3) of compound 3b.



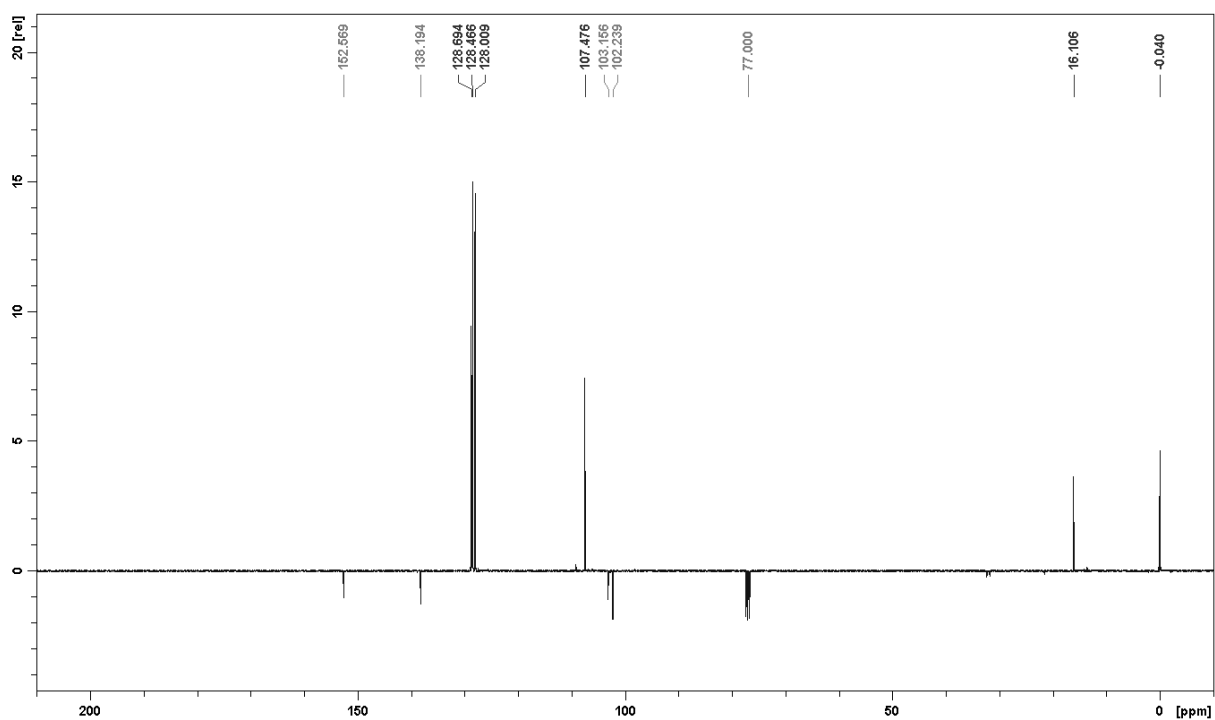
Spectrum 1.9. ^1H NMR (400 MHz, CDCl_3) of compound 3c.



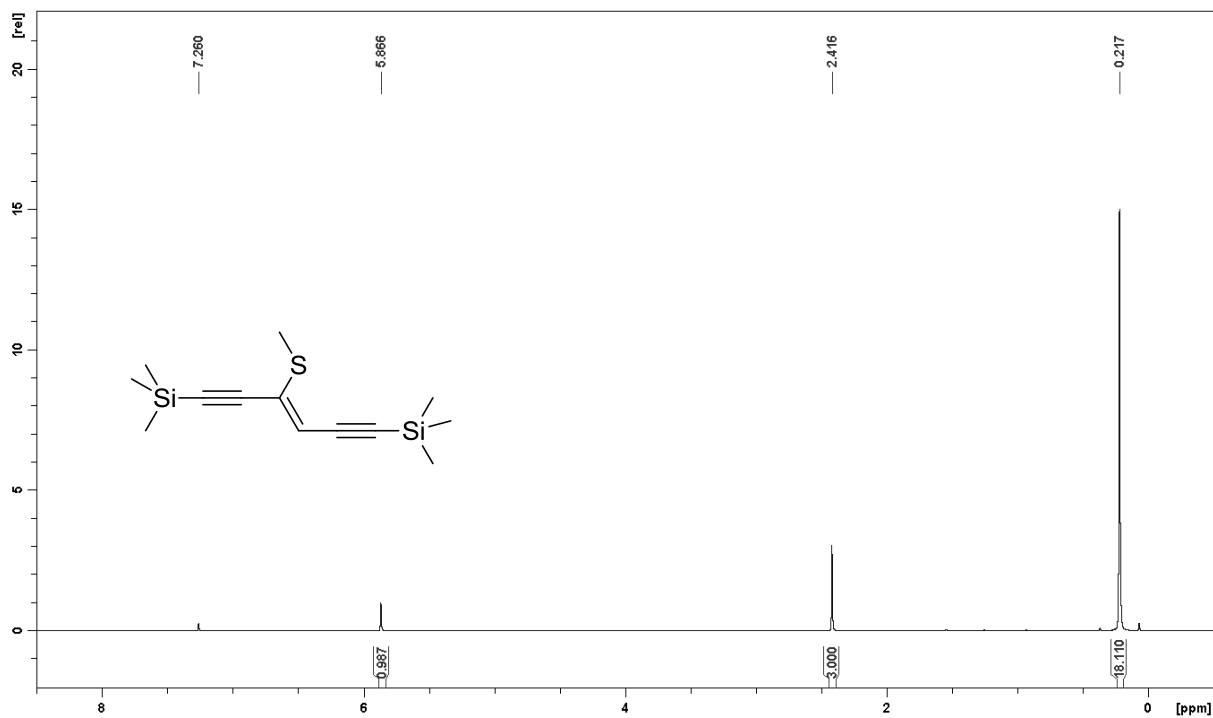
Spectrum 1.10. ^{13}C NMR (100 MHz, CDCl_3) of compound 3c.



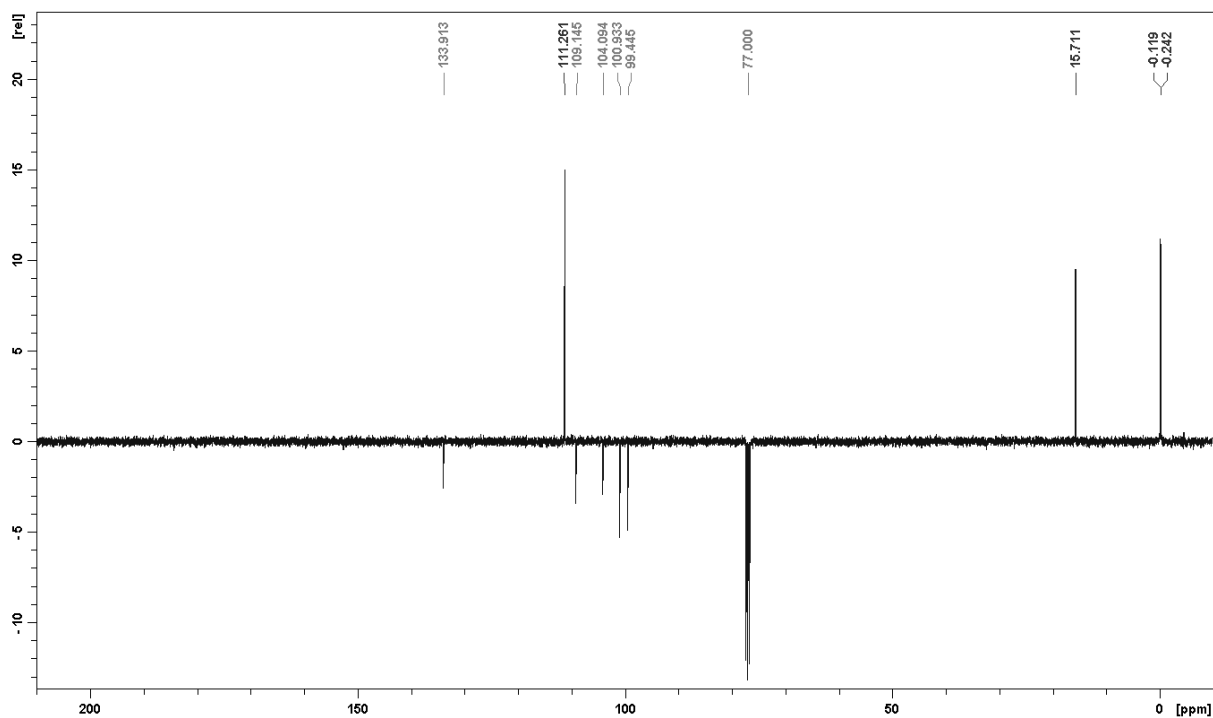
Spectrum 1.11. ^1H NMR (400 MHz, CDCl_3) of compound 3d.



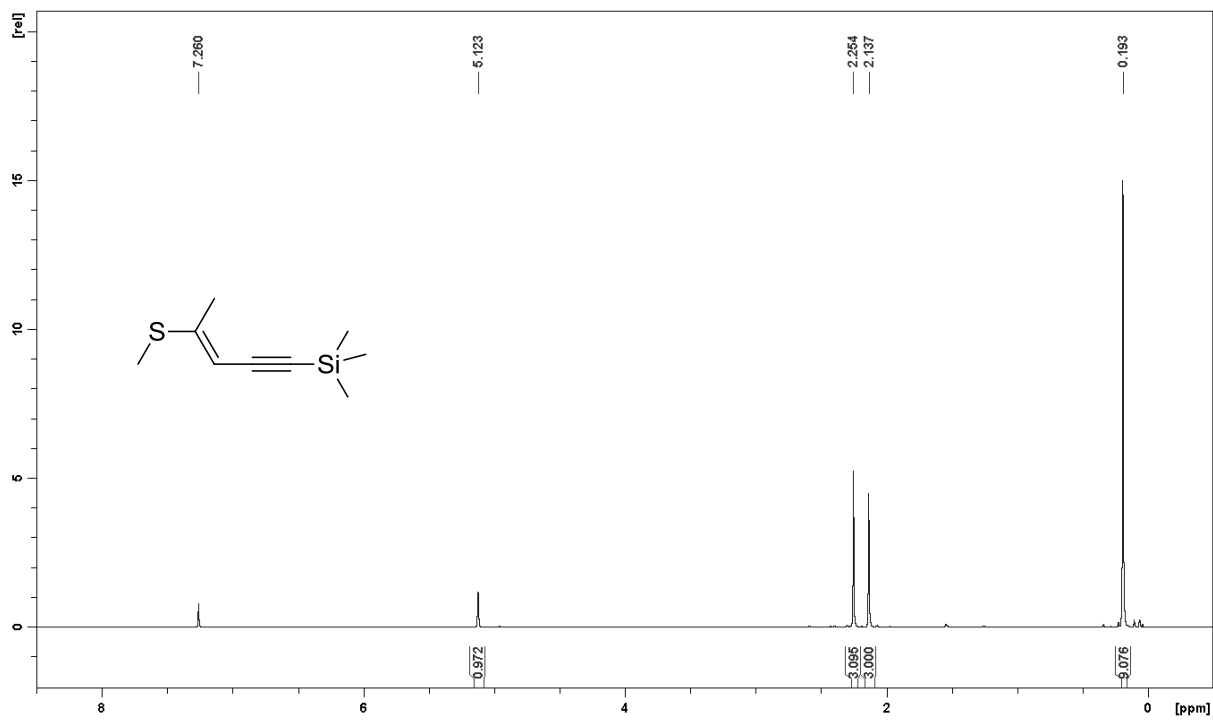
Spectrum 1.12. ^{13}C NMR (100 MHz, CDCl_3) of compound 3d.



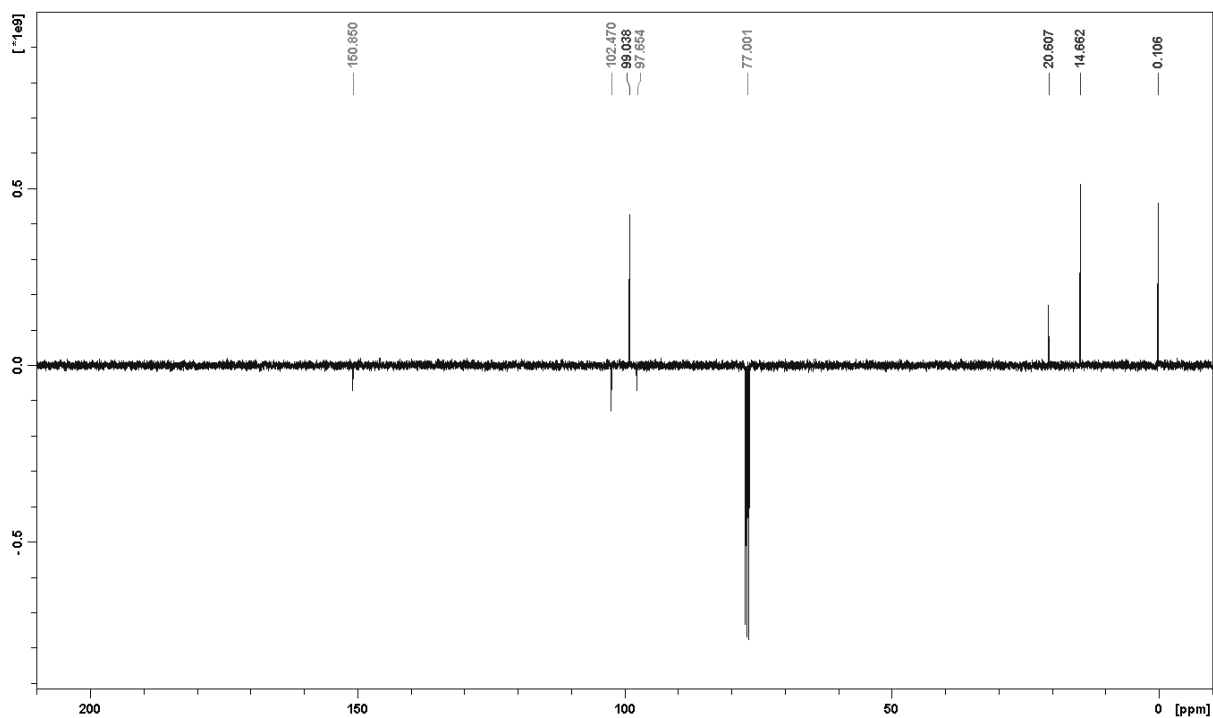
Spectrum 1.13. ^1H NMR (400 MHz, CDCl_3) of compound 3e.



Spectrum 1.14. ^{13}C NMR (100 MHz, CDCl_3) of compound 3e.



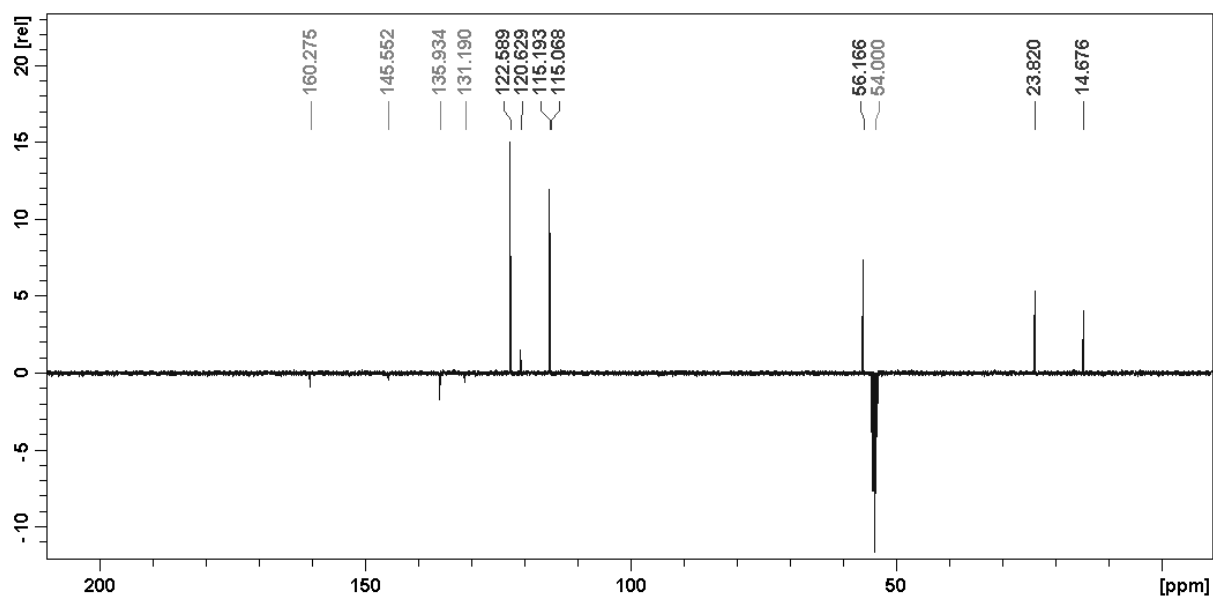
Spectrum 1.15. ^1H NMR (400 MHz, CDCl_3) of compound 3f.



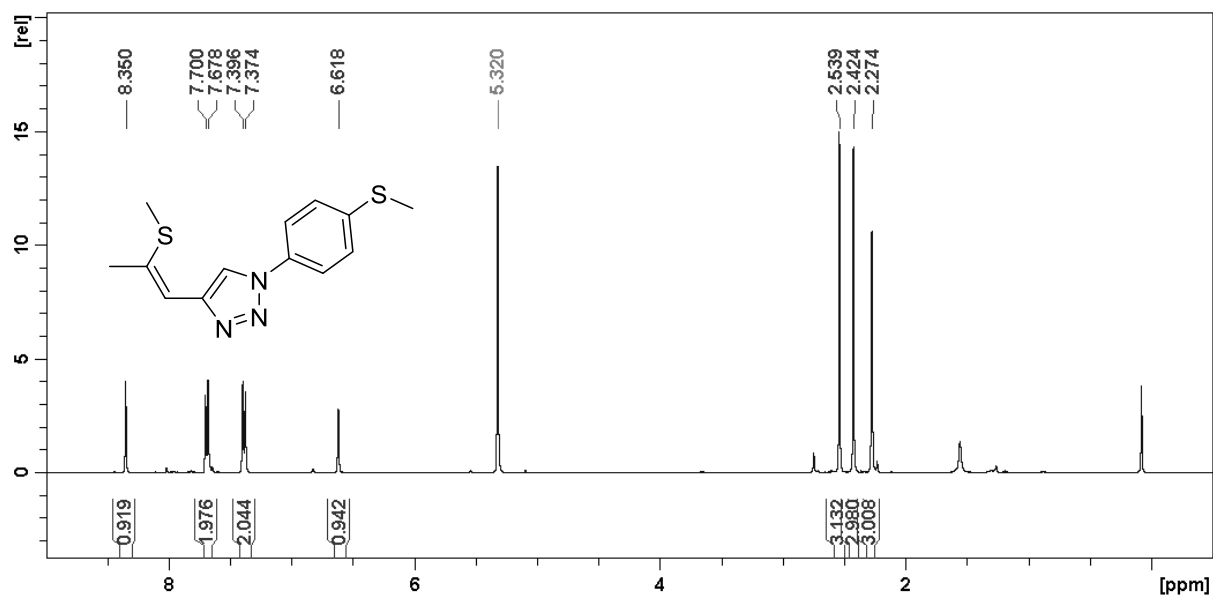
Spectrum 1.16. ^{13}C NMR (100 MHz, CDCl_3) of compound 3f.



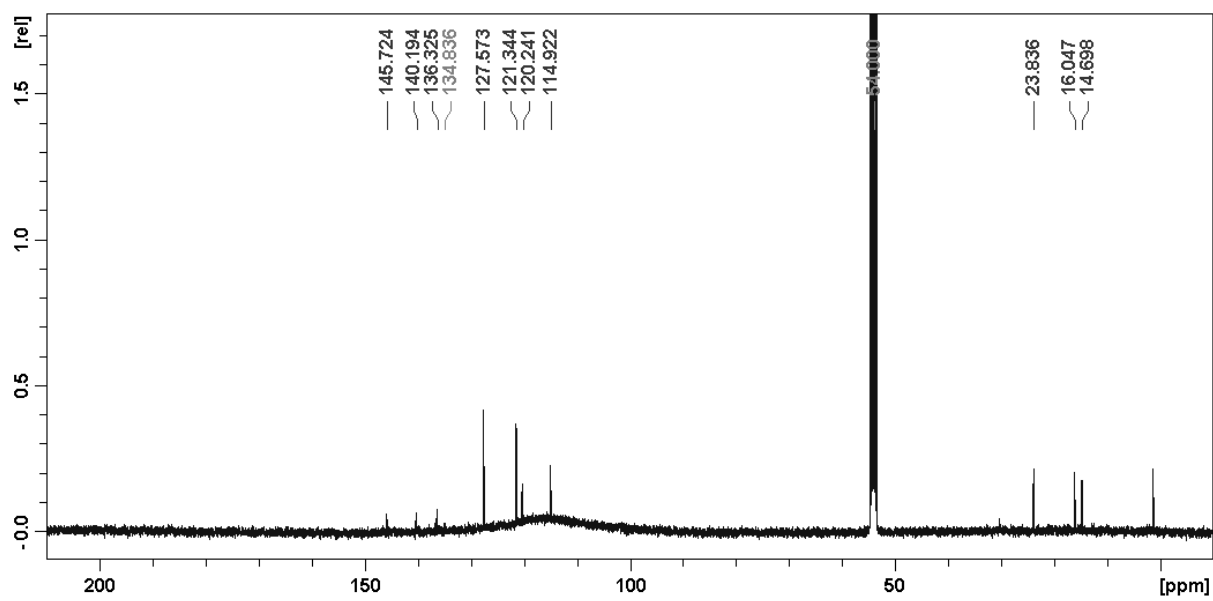
Spectrum 1.17. ^1H NMR (400 MHz, CD_2Cl_2) of compound 5i.



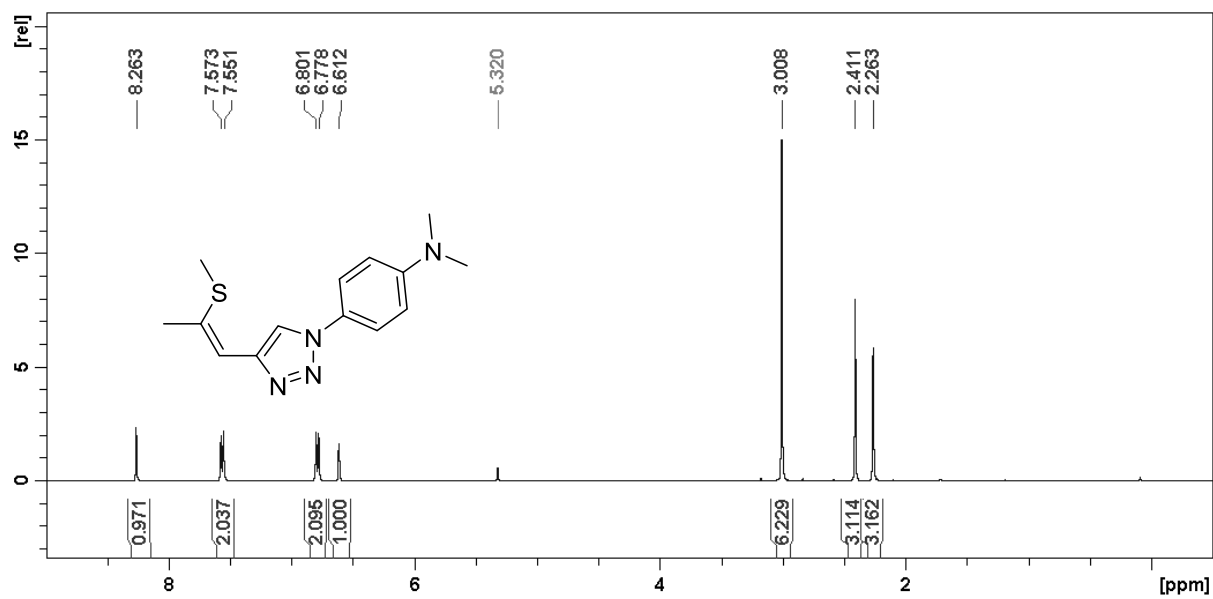
Spectrum 1.18. ^{13}C NMR (100 MHz, CD_2Cl_2) of compound 5i.



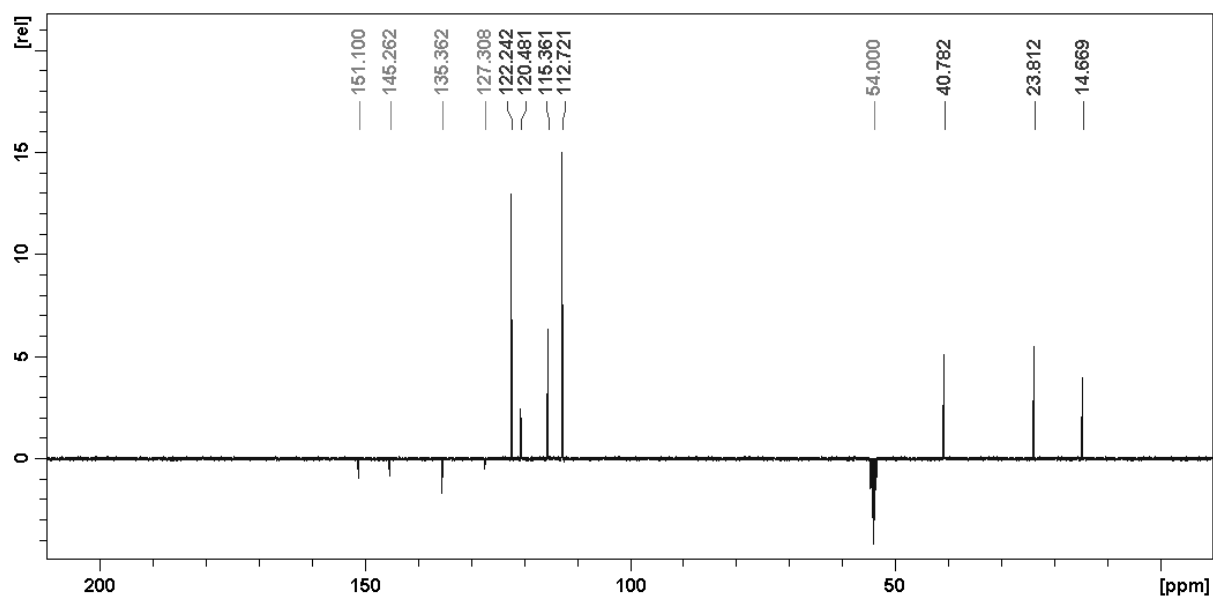
Spectrum 1.19. ^1H NMR (400 MHz, CD_2Cl_2) of compound 5ii.



Spectrum 1.20. ^{13}C NMR (100 MHz, CD_2Cl_2) of compound 5ii.



Spectrum 1.21. ^1H NMR (400 MHz, CD_2Cl_2) of compound 5iii.



Spectrum 1.22. ^{13}C NMR (100 MHz, CD_2Cl_2) of compound 5iii.

2. Isomerization Experiments

The acid-induced isomerization was first observed during NMR spectroscopy using CDCl_3 . Ion chromatography revealed a chloride content of ~ 280 ppm, which was attributed to the decomposition of CDCl_3 , resulting in the formation of DCI (Hill, D. G. *Journal of the American Chemical Society* **1932**, *54*, 32-40). A control experiment applying catalytic amounts of HCl (solution in dioxane) to **3a** in CHCl_3 quantitatively resulted in the same equilibrium values. The process was monitored for **3a** by NMR (Figure 2.1), which indicates a rather slow kinetic (compared to the I_2 -induced experiments) showing an isomerization state of 46 % *E*-isomer (**3f**) after five days. This effect was also observed during the evaluation of alternative methylation sources.

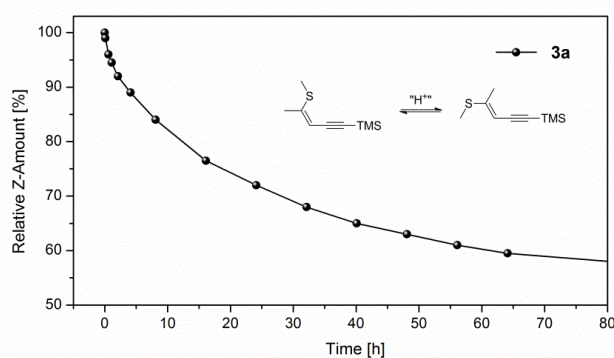


Figure 2.1. Acid-induced isomerization of ene-yne structure **3a**.

Isomerization experiments employing various Li^+ and/or I^- containing salts were conducted in Et_2O . 1.1 eq. of the salt were added to a solution of **3a**. All experiments were performed under ambient conditions and argon atmosphere. The formation of the *E*-isomer was monitored *via* NMR-spectroscopy. The finding that no isomerization was observed with NaI and KI is attributed to the low solubility of the salts in Et_2O .

Table S1. Various salts employed in the isomerization experiments of **3a**. x indicates formation of *E*-isomer.

	Ambient conditions	Argon atmosphere
LiCl		
LiBr		
LiI	x	
NaI		
KI		
LiClO ₄		
TBAI	x	

3. Kinetic Investigations

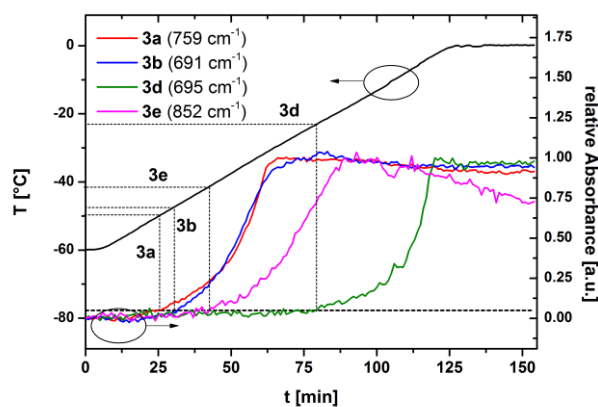


Figure 3.1. Normalized integrals of selected absorption bands of **3a,b,d,e** during TRF; temperature gradient applied during fragmentation of **2a** is depicted exemplarily.

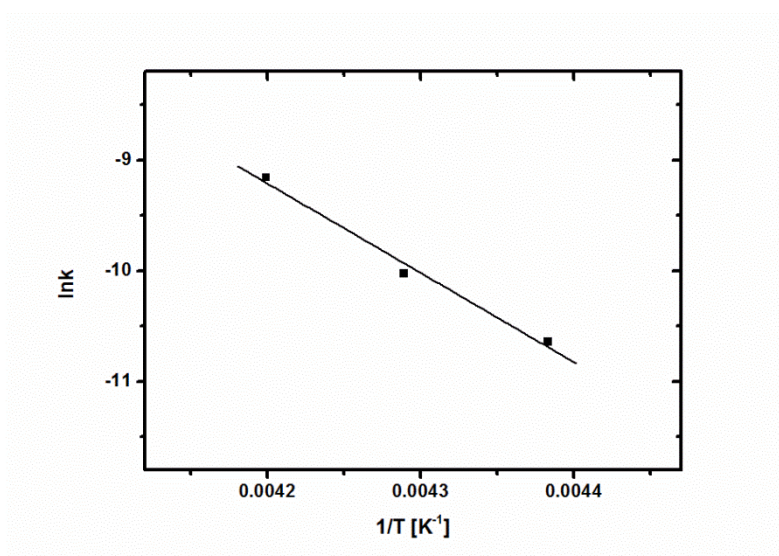


Figure 3.2. Arrhenius plot of TRF of **2a**.

4. Flow experiments

Table S2. Averaged yields at room temperature [%]

t_R [s]	byproduct	product	starting material	sum
5	1.3	43.9	35.5	80.7
10	4.0	52.4	16.7	73.1
15	4.0	63.7	10.8	78.5
20	4.0	64.1	7.6	75.6
25	4.2	67.4	9.4	81.1
30	4.1	73.2	3.8	81.0
45	4.5	66.2	6.7	77.5
60	4.8	67.4	5.6	77.7

Table S3. Averaged yields at 0°C [%]

t_R [s]	byproduct	product	starting material	sum
5	2.4	20.1	70.4	92.8
10	3.9	35.2	51.8	90.8
15	3.9	43.4	39.9	87.2
20	3.9	48.9	31.5	84.3
25	3.9	58.0	26.2	88.1
30	3.9	58.6	20.7	83.2
45	4.2	62.6	13.0	79.8
60	4.5	64.5	11.3	80.2

Table S3. Averaged yields at -20°C [%]

t_R [s]	byproduct	product	starting material	sum
5	8.8	3.2	91.7	103.7
10	9.5	8.0	82.3	99.8
15	5.1	16.5	77.4	99.1
20	4.0	20.4	71.5	95.8
25	4.4	24.0	67.8	96.2
30	4.5	27.0	63.5	95.1
45	4.8	35.2	52.3	92.2
60	5.5	33.5	47.0	86.0

Table S3. Averaged yields at -40°C [%]

t_R [s]	byproduct	product	starting material	sum
5	3.1	1.7	98.6	103.3
10	6.7	1.6	95.3	103.6
15	5.2	2.8	94.2	102.3
20	3.6	4.3	92.8	100.7
25	3.3	5.6	91.7	100.6
30	0.5	7.1	92.3	99.9
45	1.2	8.2	90.2	99.6
60	2.0	10.6	87.4	100.1

3.11. Manuscript #11 – Supporting Information

Crystal chemistry of layered structures formed by linear rigid silyl-capped molecules

Daniel Lumpi, Paul Kautny, Berthold Stöger, Johannes Fröhlich

IUCrJ, **2015**, 2, 584-600

IUCrJ

Volume 2 (2015)

Supporting information for article:

Crystal chemistry of layered structures formed by linear rigid silyl-capped molecules

Daniel Lumpi, Paul Kautny, Berthold Stöger and Johannes Fröhlich

Crystal chemistry of layered structures formed by linear rigid silyl-capped molecules - Experimental details

DANIEL LUMPI,^a PAUL KAUTNY,^a BERTHOLD STÖGER^{b*} AND

JOHANNES FRÖHLICH^a

^a*Institute of Applied Synthetic Chemistry, Vienna University of Technology, Vienna Austria, and* ^b*Institute of Chemical Technologies and Analytics, Vienna University of Technology, Vienna Austria. E-mail: bstoeger@mail.tuwien.ac.at*

1. Single crystal diffraction

Crystals of the title compounds were embedded in perfluorinated oil and attached to a thin glass fiber. Intensity data were collected using MoK α radiation ($\lambda = 0.71073$ Å) on a Bruker Kappa APEX II diffractometer with κ -geometry and a 0.7 mm collimator. Due to weak diffraction, notably of platy crystals, in some cases crystals of a size slightly exceeding the beam diameter were used to maximize intensities. It has been shown that this generally does not affect the refinement quality (Tan & Ng, 2014). Full spheres were collected in fine-sliced ω - and ϕ -scans up to a 2θ angle where reflections were still visible in preliminary scans, with the exception of polymorph III of oxBSEM, which was only measured up to $2\theta = 27.6^\circ$, albeit scattering to higher angles. In general frame data were reduced to intensity values with SAINT-Plus and corrected for absorption effects using the multi-scan approach implemented in SADABS or TWINABS (Bruker, 2008). The structures were solved by charge-flipping implemented in SUPERFLIP (Palatinus & Chapuis, 2007) and refined against F values

with JANA2006 (Petříček *et al.*, 2014). Non-H atoms were refined with anisotropic ADPs. H atoms were placed at computed positions and refined as riding on the parent C-atoms. Details of data collections and structure refinements are compiled in Tables 1–4. Deviations from the standard procedure and specific remarks will be given in the following sections.

Table 1. *Details on the crystal structure determinations of the methylthio compounds BSEM (1), TSEM (2), and both of DSEM (4).*

	BSEM	TSEM	DSEM, polytype I	DSEM, polytype II
formula	C ₂₂ H ₃₀ S ₂ Si ₂	C ₂₀ H ₂₈ S ₃ Si ₂	C ₂₂ H ₃₂ O ₂ S ₃ Si ₂	C ₂₂ H ₃₂ O ₂ S ₃ Si ₂
molecular weight	414.8	420.8	480.8	480.8
crystal color	clear yellow	clear yellow	clear yellow	clear yellow
crystal habit	plate	fragment	rhombic prism	plate
crystal size [mm ³]	0.77×0.25×0.03	0.09×0.07×0.01	0.87×0.66×0.03	0.60×0.51×0.01
temperature [K]	100	100	100	100
space group	<i>C2/c</i>	<i>I2/c</i>	<i>C2/c</i>	<i>Pccn</i>
<i>a</i> [Å]	34.148(6)	34.443(3)	34.344(2)	33.630(10)
<i>b</i> [Å]	6.8690(12)	6.7415(4)	8.1665(5)	8.271(2)
<i>c</i> [Å]	10.3442(18)	10.1978(8)	20.0791(12)	19.717(6)
α [°]	90	90	90	90
β [°]	98.343(8)	96.889(5)	100.532(2)	90
γ [°]	90	90	90	90
<i>V</i> [Å ³]	2400.7(7)	2350.8(3)	5536.7(6)	5484(3)
<i>Z</i>	4	4	8	8
<i>Z'</i>	$\frac{1}{2}$	$\frac{1}{2}$	1	1
density [g cm ⁻³]	1.147	1.189	1.153	1.164
θ range [°]	1.2–35.0	1.2–30.2	1.2–27.6	1.2–25.1
μ [mm ⁻¹]	0.326	0.419	0.369	0.373
Trans. coeff. <i>T</i> _{min} , <i>T</i> _{max}	0.91, 0.99	0.97, 1.00	0.74, 0.99	0.90, 1.00
reflections total	38270	29932	77428	48785
reflections unique	5255	3045	6397	4671
reflections obs. [<i>I</i> > 3 σ <i>I</i>]	4193	2366	4903	3185
parameters	118	115	262	262
<i>R</i> _{int}	0.0347	0.0643	0.0380	0.0792
<i>h</i>	-54→54	-45→48	-44→44	-9→9
<i>k</i>	-11→11	-9→9	-10→10	-13→13
<i>l</i>	-16→16	-14→14	-26→26	-17→17
$\Delta\rho$ _{max} [e Å ⁻³]	0.43	1.53	0.87	0.75
$\Delta\rho$ _{min} [e Å ⁻³]	-0.22	-1.41	-0.75	-0.74
Goof	2.19	2.56	3.02	3.22
<i>R</i> _{obs}	0.0307	0.0780	0.0489	0.0869
<i>wR</i> _{all}	0.0442	0.0625	0.0588	0.0848
twin operation	-	twofold rotation about [001]	-	-
twin volume fraction	-	50.39:49.61(17)	-	-

Table 2. Details on the crystal structure determinations of the methylsulfonyl compounds α BSEM (**1**) (polymorphs I, II and III) and α ESEM (**3b**).

	α BSEM, I	α BSEM, II	α BSEM, III	α ESEM
formula	$C_{22}H_{30}O_4S_2Si_2$	$C_{22}H_{30}O_4S_2Si_2$	$C_{22}H_{30}O_4S_2Si_2$	$C_{22}H_{30}O_8S_3Si_2$
molecular weight	478.8	478.8	478.8	574.8
crystal color	clear colorless	clear colorless	clear colorless	clear yellow
crystal habit	plate	plate	plate	block
crystal size [mm ³]	0.70×0.65×0.10	0.70×0.65×0.10	0.45×0.15×0.03	0.63×0.45×0.28
temperature [K]	150	100	100	100
space group	$P\bar{1}$	$P\bar{1}$	$P\bar{1}$	$P\bar{1}$
a [Å]	6.8197(3)	7.3096(2)	5.7300(3)	10.5399(4)
b [Å]	12.1073(5)	11.3935(3)	10.2961(5)	13.8276(5)
c [Å]	16.1123(7)	18.7425(6)	10.9801(6)	19.9987(8)
α [°]	92.3607(19)	73.167(2)	85.9433(17)	79.940(2)
β [°]	93.9781(19)	105.319(2)	79.7181(16)	84.589(2)
γ [°]	98.3425(19)	118.926(2)	80.1150(15)	89.771(2)
V [Å ³]	1311.34(10)	1293.21(7)	627.39(6)	2856.81(19)
Z	2	2	1	4
Z'	$\frac{2}{2}$	$\frac{2}{2}$	$\frac{1}{2}$	2
density [g cm ⁻³]	1.212	1.229	1.267	1.336
θ range [°]	1.3–35.1	1.15–30.15	1.89–27.6	1.0–30.1
μ [mm ⁻¹]	0.318	0.323	0.332	0.385
Trans. coeff. T_{\min} , T_{\max}	0.81,0.97	0.81,0.97	0.89,0.98	0.81,0.90
reflections total	57779	40880	16087	57022
reflections unique	11485	7541	2909	13689
reflections obs. [$I > 3\sigma I$]	8331	5106	2371	11291
parameters	271	271	136	632
R_{int}	0.0297	0.0625	0.0237	0.0348
h	-9→11	-10→10	-6→7	-14→14
k	-19→19	-15→16	-13→13	-19→19
l	-26→25	-26→26	-14→14	-28→28
$\Delta\rho_{\text{max}}$ [e Å ⁻³]	0.44	1.17	0.31	0.45
$\Delta\rho_{\text{min}}$ [e Å ⁻³]	-0.39	-0.70	-0.26	-0.60
Goof	2.15	3.05	2.19	1.96
R_{obs}	0.0350	0.0740	0.0300	0.0372
wR_{all}	0.0443	0.0925	0.0393	0.0422
twin operation	-	-	-	twofold rotation about [100]
twin volume fraction	-	-	-	60.92:39.08(7)

Table 3. *Details on the crystal structure determinations of the non-spacer extended compounds NSEM-TBDMS (5) and ASYM (6)*

	NSEM-TBDMS	ASYM
formula	C ₂₂ H ₃₈ S ₂ Si ₂	C ₁₃ H ₂₂ S ₁ Si ₂
molecular weight	422.8	266.6
crystal color	clear colorless	clear colorless
crystal habit	block	block
crystal size [mm ³]	0.70×0.56×0.50	0.82×0.61×0.20
temperature [K]	100	100
space group	<i>P</i> 2 ₁ 2 ₁ 2 ₁	<i>P</i> $\bar{1}$
<i>a</i> [Å]	7.7849(4)	7.2016(4)
<i>b</i> [Å]	10.5146(5)	9.7603(4)
<i>c</i> [Å]	31.2712(14)	12.2829(4)
α [°]	90	95.4952(16)
β [°]	90	92.510(2)
γ [°]	90	101.346(2)
<i>V</i> [Å ³]	2559.7(2)	840.86(6)
<i>Z</i>	4	2
<i>Z'</i>	1	1
density [g cm ⁻³]	1.097	1.052
θ range [°]	2.04–35.05	1.7–30.2
μ [mm ⁻¹]	0.306	0.313
Trans. coeff. <i>T</i> _{min} , <i>T</i> _{max}	0.78, 0.81	0.80, 0.94
reflections total	101389	21588
reflections unique	11125	4622
reflections obs. [<i>I</i> > 3 σ <i>I</i>]	10833	3651
parameters	236	146
<i>R</i> _{int}	0.0238	0.0345
<i>h</i>	-12→11	-9→9
<i>k</i>	-16→16	-13→13
<i>l</i>	-48→50	-17→17
$\Delta\rho$ _{max} [e Å ⁻³]	0.33	0.61
$\Delta\rho$ _{min} [e Å ⁻³]	-0.28	-0.39
Goof	2.72	2.27
<i>R</i> _{obs}	0.0267	0.0524
<i>wR</i> _{all}	0.0400	0.0549
Flack parameter	0.03(3)	-
twin operation	-	twofold rotation about [100]
twin volume fraction	-	83.78:16.22(11)

Table 4. *Details on the crystal structure determinations of the incommensurately modulated structure ESEM (3).*

	ESEM
formula	$C_{22}H_{30}O_2S_3Si_2$
molecular weight	478.8
crystal color	clear yellow
crystal habit	plate
crystal size [mm ³]	0.62×0.23×0.02
temperature [K]	100
superspace group	$I2/c(0\sigma_20)s0$
a [Å]	32.4653(8)
b [Å]	8.4003(5)
c [Å]	10.0737(3)
β [°]	102.301(2)
V [Å ³]	2684.20(19)
\mathbf{q}	0.6223(1) \mathbf{b}
Z	4
θ range [°]	1.8–27.5
μ [mm ⁻¹]	0.38
unique reflections (all, obs)	15382, 9184
unique main reflections (all, obs)	3080, 2307
unique first order sat (all, obs)	6156, 4248
unique second order sat (all, obs)	6146, 2629
observation criterion	$I > 3\sigma I$
parameters	510
R_{int}	0.0672
h	-41→41
k	-11→11
l	-13→12
m	-2→2
GooF	2.36
$R_{\text{obs}}/wR_{\text{all}}$	
all reflections	6.28/6.69
main reflections	5.87/6.47
first order satellites	4.78/4.91
second order satellites	11.35/12.71

1.1. *Twinning of TSEM (2), oxESEM (3b) and ASYM (6).*

For TSEM (2), oxESEM (3b) and ASYM (6), automatic unit cell determination failed at determining reasonable lattice parameters. Therefore the locations of the diffraction spots in reciprocal space were analyzed manually using RLATT (Bruker, 2008). In all three cases the spots could be assigned to two domains, related by rotation

of 180° about [001] (TSEM (**2**)) and [100] (oxESEM (**3b**), ASYM (**6**)). Intensity data of the twin domains were integrated concurrently and written to “HKLF5” files with overlap information.

1.2. TSEM (**2**).

TSEM (**2**) was refined in the non-standard space group setting $I2/c$ (standard setting $C2/c$) to highlight the close crystallographic relationship with BSEM (**1**). The standard setting is related to the chosen one by

$$(\mathbf{a}_{\text{std}}, \mathbf{b}_{\text{std}}, \mathbf{c}_{\text{std}}) = (\mathbf{a}, \mathbf{b}, \mathbf{c}) \begin{pmatrix} 1 & 0 & 0 \\ 0 & \bar{1} & 0 \\ 1 & 0 & \bar{1} \end{pmatrix}.$$

Due to the small size, the crystal was only weakly diffracting, leading to mediocre residuals and large peaks in the difference Fourier density.

1.3. DSEM (**4**).

The two polytypes of DSEM (**4**) were isolated from the same crystallization vessel. Polytype I grew on the walls and featured satisfactory diffraction quality. Polytype II was isolated from the bottom of the vessel among oil and featured weak diffraction intensities and diffuse scattering. Accordingly, the residuals were comparatively large.

1.4. oxBSEM (**1b**).

When mounting samples of oxBSEM (**1b**) on the diffractometer cooled in a stream of N₂ to our routine measurement temperature of 100 K, the crystals burst suggesting a phase transition. Therefore we slowly (2 K/min) cooled a crystal from room temperature to 150 K, while monitoring the lattice parameters. Since no phase transition was observed down to 150 K, a data set was collected at this temperature. On further cooling, a phase transition was apparent by fragmentation of the crystal accompanied by a dramatic worsening of reflection quality. Despite mediocre data quality we were

able to solve and refine the structure, though with high residuals and large peaks in the difference Fourier density.

To highlight the structural relationship between polymorphs I and II of oxBSEM (**1b**), the latter was refined using a non-reduced setting. The reduced setting is related to the chosen one by

$$(\mathbf{a}_{\text{red}}, \mathbf{b}_{\text{red}}, \mathbf{c}_{\text{red}}) = (\mathbf{a}, \mathbf{b}, \mathbf{c}) \begin{pmatrix} 1 & 1 & 1 \\ 0 & 1 & 0 \\ 0 & 0 & 1 \end{pmatrix}.$$

1.5. ESEM (3).

Since automatic indexing of the reflections failed, the locations of the diffraction spots in reciprocal space were analyzed manually using RLATT (Bruker, 2008). The strongest spots could be indexed using a *C*-centered monoclinic lattice. The remaining diffraction spots were interpreted as satellites located at $\pm\sigma_2\mathbf{b}^*$ and $\pm 2\sigma_2\mathbf{b}^*$ from main reflections, with irrational σ_2 close to $\frac{5}{8}$.

Data reduction turned out to be difficult, since first and second order satellites were close and reflections featured distinct enlargement in \mathbf{a}^* direction. The best overall result was obtained using EVAL14 (Duisenberg *et al.*, 2003), by tuning anisotropic mosaicity. Nevertheless, intensities of the strongest reflections were systematically overestimated, leading to slightly worse partial reliability factors of main reflections compared to first order satellites.

Systematic absences of the main reflections indicated a superspace group derived from *Ic* or *I2/c*. Since satellites $0k0m$ with $|m| = 1$ were absent, a structure solution in superspace group *I2/c*($0\sigma_20$)*s0* was attempted. The correctness of the choice was confirmed by the symmetry of the four-dimensional electron density obtained by charge-flipping as implemented in SUPERFLIP (Palatinus & Chapuis, 2007). The positions of all non-H atoms and first order displacive modulation functions were

directly located in SUPERFLIP output. To achieve decent reliability factors, notably concerning satellites, the positions of the non-H atoms were refined with second order harmonics. The ADPs of the heavy atoms S and Si were modulated with second order harmonics, for C and O atoms with first order harmonics. H atoms were placed at computed positions and refined as riding on the parent C-atoms. The methyl groups were fixed into *anti*-positions to obtain converging refinements.

The C9 atom of the TMS group features large ADPs in parts of internal space hinting towards disorder. Introducing discontinuous modulation functions for C9 (Legendre polynomials) led to distinctly more reasonable ADPs. Unfortunately attachment of H atoms to this C9 atom resulted in non-converging refinements and thus the continuous harmonics were used in the final refinements.

References

- Bruker Analytical X-ray Instruments, Inc., Madison, WI, USA, (2008). APEX2, RLATT, SAINT, SADABS and TWINABS.
- Duisenberg, A. J. M., Kroon-Batenburg, L. M. J. & Schreurs, A. M. M. (2003). *Appl. Cryst.* **36**, 220–229.
- Palatinus, L. & Chapuis, G. (2007). *J. Appl. Cryst.* **40**, 786–790.
- Petříček, V., Dušek, M. & Palatinus, L. (2014). *Z. Kristallogr.* **229**, 345–352.
- Tan, S. L. & Ng, S. W. (2014). *J. Appl. Cryst.* **47**, 1443–1444.

3.12. Manuscript #13 – Supporting Information

Charge transfer states in triazole linked donor-acceptor materials: strong effects of chemical modification and solvation

Paul Kautny, Florian Glöcklhofer, Thomas Kader, Jan-Michael Mewes, Berthold Stöger, Johannes Fröhlich, Daniel Lumpi, Felix Plasser

submitted for publication

Charge transfer states in triazole linked donor-acceptor materials: strong effects of chemical modifications and solvation

Electronic Supplementary Information

Paul Kautny,^a Florian Glöcklhofer,^a Thomas Kader,^a Jan-Michael Mewes,^b Berthold Stöger,^c Johannes Fröhlich,^a Daniel Lumpi*^a and Felix Plasser*^d

^a Institute of Applied Synthetic Chemistry, TU Wien, Getreidemarkt 9/163, A-1060 Vienna, Austria; E-mail: daniel.lumpi@tuwien.ac.at

^b Centre for Theoretical Chemistry and Physics, The New Zealand Institute for Advanced Study (NZIAS), Massey University, Albany, Private Bag 102904 Auckland 0745, New Zealand

^c X-ray Centre, TU Wien, Getreidemarkt 9, A-1060 Vienna, Austria

^d Institute of Theoretical Chemistry, Faculty of Chemistry, University of Vienna, Währingerst. 17, A-1090 Vienna, Austria; E-mail: felix.plasser@univie.ac.at

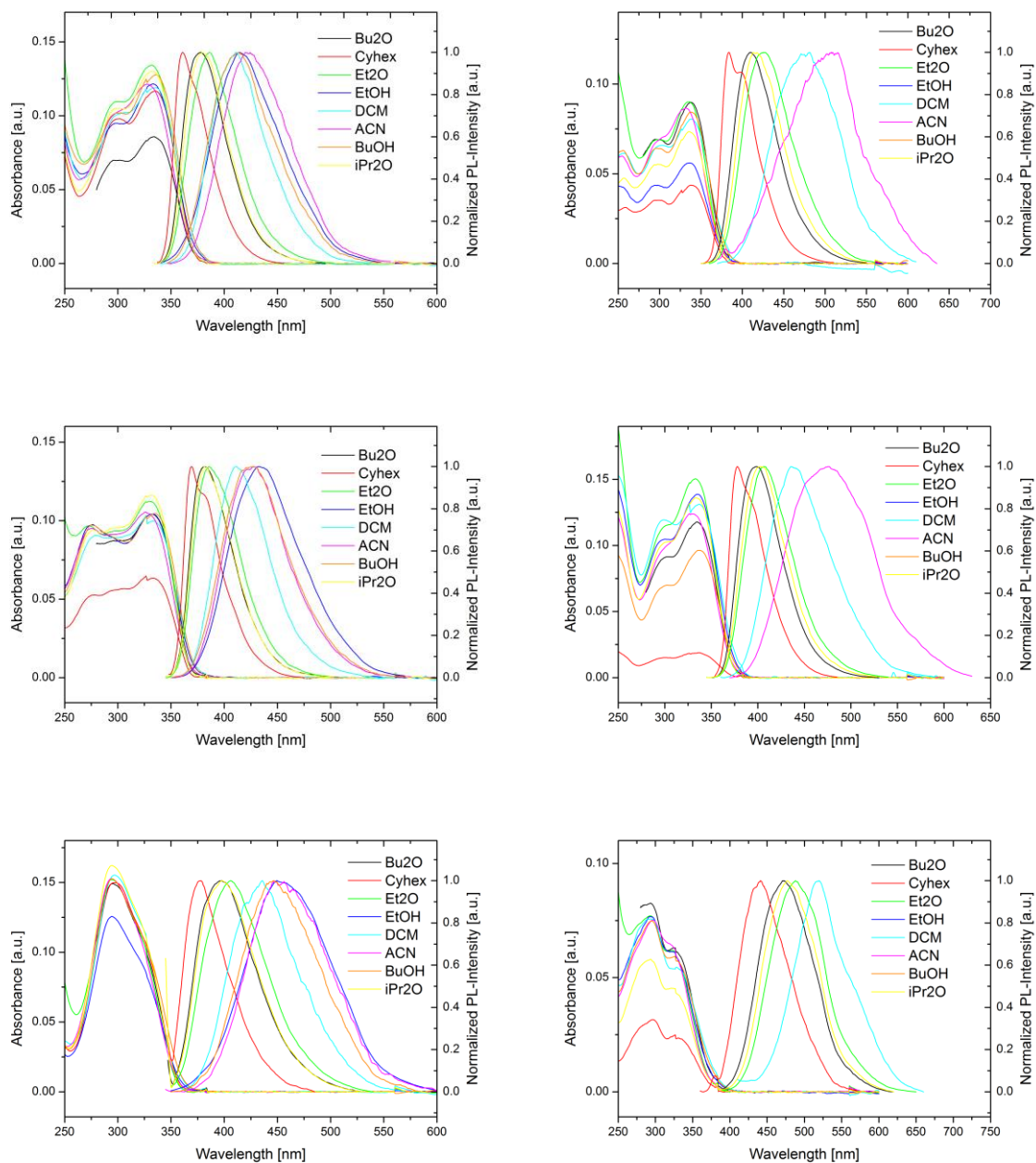


Figure S1. UV/VIS absorption and photoluminescence emission spectra of **ZMSOM-14TPA** (top left), **ZMSO₂M-14TPA** (top right), **EMSM-14TPA** (middle left), **EMSO₂M-14TPA** (middle right), **ZMSM-15TPA** (bottom left) and **ZMSO₂M-15TPA** (bottom right) in various solvents (Cyhex=cyclohexane, DCM=dichloromethane, ACN=acetonitrile).

Table S1. UV/Vis Absorption and fluorescence maxima of the materials in various solvents
(Cyhex=cyclohexane, DCM=dichloromethane, ACN=acetonitrile).

		Cyhex	Bu2O	iPr2O	Et2O	DCM	BuOH	EtOH	ACN
ZMSM-14TPA	Abs	333.5	333	332	331.5	333.5	335.5	333	328
	Em	368.5	380.5	381.5	389	410.5	427	432.5	424.5
ZMSOM-14TPA	Abs	335	334	332.5	332	335.5	336	333	328
	Em	376.5	396.5	399	405.5	434	436.5	437	444
ZMSO ₂ M-14TPA	Abs	338	338	336	335.5	338.5	338	336	332
	Em	384	410	413.5	426	481	---	---	507.5
EMSM-14TPA	Abs	333	332.5	331.5	329.5	333	335	332	326.5
	Em	369.5	382	381.5	386	411.5	427	432.5	428
EMSO ₂ M-14TPA	Abs	337	335	333.5	333	337	337	335	330
	Em	378	398.5	402.5	406.5	435.5	---	---	475.5
ZMSM-15TPA	Abs	325.5	329.5	324	294.5	297	324.5	325.5	324
	Em	378	397.5	398.5	406	436	446.5	449.5	446.5
ZMSO ₂ M-15TPA	Abs	331	325.5	323	293.5	266	325.5	323.5	320
	Em	441	472	477	488	519.5	---	---	---

Table S2. Atomic coordinates (Å) and total energies (a.u.) of **ZMSM-14TPA** optimized in the S_0 and S_1 states.

S_0				S_1			
DFT/ ω PBEh energy: -1543.530381578				TDDFT/ ω PBEh energy: -1543.401686816			
C	-6.99377	-2.50970	0.94822	C	-6.81471	-0.82237	2.71022
S	-5.78968	-1.52798	0.01427	S	-5.83671	-1.16936	1.21991
H	-6.53076	-3.49265	1.08428	H	-6.36230	-1.41186	3.51494
H	-7.93255	-2.64212	0.40163	H	-7.85961	-1.13075	2.60159
H	-7.18873	-2.07601	1.93452	H	-6.76291	0.23831	2.97882
C	-6.56499	0.05912	-0.11629	C	-6.56352	-0.08200	0.02116
C	-8.06451	0.10392	-0.19274	C	-8.06451	-0.04618	-0.04805
H	-8.44162	-0.52682	-1.00981	H	-8.48188	-1.05666	-0.16495
H	-8.40075	1.13191	-0.36836	H	-8.39188	0.56438	-0.89778
H	-8.53462	-0.24466	0.73662	H	-8.51039	0.38716	0.85864
C	-5.82493	1.18296	-0.23672	C	-5.80163	0.60159	-0.86527
C	-4.38803	1.36835	-0.18999	C	-4.36871	0.72946	-0.99651
H	-6.36306	2.11742	-0.39708	H	-6.33336	1.16349	-1.63513
C	-3.30621	0.50709	-0.11096	C	-3.27848	0.21120	-0.30099
N	-2.22142	1.32103	-0.10819	N	-2.18617	0.73887	-0.93063
N	-2.59549	2.61480	-0.18883	N	-2.58816	1.53924	-1.97065
N	-3.88685	2.64621	-0.24004	N	-3.88593	1.52404	-1.99725
C	-0.85198	0.96378	-0.05240	C	-0.84246	0.55717	-0.65922
H	-3.22268	-0.56850	-0.09607	H	-3.21522	-0.44294	0.55197
C	-0.45099	-0.18167	0.63640	C	-0.42132	-0.31842	0.38812
C	0.09790	1.76113	-0.69302	C	0.13259	1.23504	-1.43647
C	0.89208	-0.53773	0.67009	C	0.92358	-0.49932	0.63423
C	1.43886	1.40000	-0.66072	C	1.47432	1.05910	-1.18210
C	1.85718	0.24249	0.01492	C	1.88619	0.18621	-0.13527
H	-0.22485	2.65112	-1.22666	H	-0.20085	1.89344	-2.23291
H	-1.18139	-0.78198	1.17531	H	-1.14901	-0.85408	0.99053
H	1.20081	-1.42593	1.21665	H	1.24420	-1.17181	1.42893
N	3.21478	-0.13346	0.03514	N	3.28084	-0.05901	0.07173
H	2.17291	2.01489	-1.17657	H	2.21921	1.57253	-1.78781
C	3.57321	-1.50143	-0.06034	C	3.76262	-1.35625	-0.12666
C	4.23078	0.85130	0.10713	C	4.10725	0.99820	0.43426
C	5.37599	0.74424	-0.69378	C	5.47794	1.01680	0.08228
C	4.10807	1.93922	0.98288	C	3.54648	2.11498	1.09627
C	5.10912	2.90591	1.04325	C	4.35472	3.18670	1.44474
C	6.38028	1.70596	-0.61360	C	6.26530	2.10305	0.42773
C	6.25217	2.79438	0.25028	C	5.71410	3.18876	1.11926
H	3.22435	2.02350	1.61265	H	2.48690	2.10673	1.33442
H	5.47432	-0.09768	-1.37619	H	5.89634	0.19807	-0.49733
H	7.26400	1.60840	-1.24221	H	7.31402	2.11699	0.13818
H	4.99850	3.74603	1.72707	H	3.91885	4.03381	1.96993
H	7.03512	3.54817	0.30569	H	6.33796	4.03988	1.38364
C	2.91765	-2.34795	-0.96541	C	3.12642	-2.18820	-1.07230
C	4.59402	-2.02238	0.74684	C	4.81387	-1.87521	0.66149
C	4.95374	-3.36403	0.64294	C	5.23752	-3.18291	0.47191
C	3.27153	-3.69252	-1.04992	C	3.57511	-3.48729	-1.25940
C	4.29282	-4.20833	-0.25064	C	4.63119	-3.99232	-0.49432
H	2.13089	-1.94481	-1.59997	H	2.29979	-1.79052	-1.65449
H	2.75356	-4.33753	-1.75800	H	3.09296	-4.11476	-2.00586
H	5.10370	-1.36804	1.45128	H	5.25527	-1.26078	1.44256
H	4.57172	-5.25766	-0.32445	H	4.96748	-5.01724	-0.63564
H	5.74893	-3.75423	1.27619	H	6.03450	-3.58229	1.09605

Table S3. Atomic coordinates (Å) and total energies (a.u.) of **ZMOSM-14TPA** optimized in the S_0 and S_1 states.

S_0				S_1			
DFT/ ω PBEh energy: -1618.635052378				TDDFT/ ω PBEh energy: -1618.508807511			
C	-5.71624	-1.15923	2.05737	C	5.49309	-0.53194	2.36861
S	-6.00636	-1.57998	0.30838	S	5.92271	0.96592	1.42164
H	-5.40438	-2.07951	2.56210	H	5.14392	-0.20211	3.35307
H	-6.64676	-0.78804	2.50099	H	6.38679	-1.15660	2.47695
H	-4.92993	-0.40103	2.12659	H	4.70202	-1.08165	1.84854
C	-6.49471	0.09247	-0.21227	C	6.44385	0.13274	-0.09361
C	-7.98768	0.18461	-0.36342	C	7.93751	0.20684	-0.26251
H	-8.35103	-0.47652	-1.16229	H	8.28360	1.24388	-0.38043
H	-8.28695	1.21134	-0.60171	H	8.24789	-0.35825	-1.14923
H	-8.51143	-0.11309	0.55707	H	8.47514	-0.20935	0.60313
C	-5.67512	1.13079	-0.46198	C	5.64140	-0.48525	-0.99476
C	-4.23668	1.30786	-0.39313	C	4.21712	-0.67133	-1.08080
H	-6.16950	2.05750	-0.76361	H	6.15451	-0.95073	-1.83997
C	-3.15484	0.45369	-0.26921	C	3.12470	-0.16569	-0.37782
N	-2.07819	1.27044	-0.29672	N	2.04010	-0.73207	-0.98542
N	-2.45722	2.56334	-0.43285	N	2.45230	-1.55741	-2.01156
N	-3.74610	2.58672	-0.49583	N	3.74245	-1.50491	-2.05852
C	-0.70442	0.92831	-0.21481	C	0.69835	-0.56381	-0.71183
H	-3.11872	-0.62739	-0.22859	H	3.08884	0.59076	0.39310
C	-0.30836	-0.24506	0.42761	C	0.28282	0.28212	0.35996
C	0.25292	1.77326	-0.77881	C	-0.27787	-1.22176	-1.50337
C	1.03957	-0.57444	0.50093	C	1.06209	0.46143	0.61048
C	1.59871	1.43743	-0.70851	C	-1.61919	-1.04350	-1.24427
C	2.01475	0.25904	-0.06834	C	-2.02527	-0.19373	-0.18042
H	-0.06601	2.68174	-1.28219	H	0.05178	-1.86174	-2.31617
H	-1.04600	-0.89478	0.89363	H	1.01581	0.79454	0.97595
H	1.34354	-1.48507	1.01183	H	-1.37985	1.11127	1.42487
N	3.37758	-0.08833	-0.00100	N	-3.41973	0.05079	0.03618
H	2.33884	2.09146	-1.16368	H	-2.36709	-1.53711	-1.86261
C	3.76542	-1.44885	-0.10934	C	-3.89643	1.35429	-0.11680
C	4.37204	0.90736	0.15851	C	-4.24776	-1.01686	0.36754
C	5.57464	0.82171	-0.55656	C	-5.61365	-1.02969	-0.00086
C	4.17568	1.98247	1.03700	C	-3.69179	-2.14592	1.01106
C	5.16074	2.95636	1.18384	C	-4.50108	-3.22757	1.32503
C	6.56140	1.79000	-0.38928	C	-6.40223	-2.12589	0.30959
C	6.36048	2.86574	0.47666	C	-5.85623	-3.22562	0.98235
H	3.24877	2.05042	1.60310	H	-2.63545	-2.14090	1.26352
H	5.73137	-0.00934	-1.24100	H	-6.02704	-0.19837	-0.56616
H	7.48969	1.70776	-0.95236	H	-7.44718	-2.13594	0.00669
H	4.99172	3.78537	1.86925	H	-4.06949	-4.08508	1.83662
H	7.13032	3.62488	0.59983	H	-6.48073	-4.08429	1.21932
C	3.20544	-2.27055	-1.09660	C	-3.24888	2.22173	-1.02301
C	4.71863	-1.98276	0.76789	C	-4.95745	1.84304	0.67830
C	5.10742	-3.31536	0.65229	C	-5.37711	3.15747	0.53565
C	3.58693	-3.60673	-1.19449	C	-3.69326	3.52795	-1.16289
C	4.54163	-4.13590	-0.32468	C	-4.75732	4.00356	-0.39025
H	2.47053	-1.85527	-1.78336	H	-2.41709	1.84594	-1.61209
H	3.14355	-4.23381	-1.96625	H	-3.20130	4.18434	-1.87727
H	5.15351	-1.34514	1.53509	H	-5.40702	1.19935	1.43032
H	4.84258	-5.17835	-0.40833	H	-5.08987	5.03414	-0.49404
H	5.84984	-3.71718	1.33991	H	-6.18019	3.53377	1.16607
O	-4.66553	-1.99559	-0.26493	O	4.62695	1.74487	1.25707

Table S4. Atomic coordinates (Å) and total energies (a.u.) of **ZMSO₂M-14TPA** optimized in the S_0 and S_1 states.

S_0				S_1			
DFT/ ω PBEh energy: -1693.780560428				TDDFT/ ω PBEh energy: -1693.657570335			
C	-5.38994	-0.89746	2.00909	C	5.11098	-1.09464	1.98682
S	-5.78399	-1.24907	0.29537	S	5.71772	0.47302	1.35474
H	-5.11353	-1.85520	2.46242	H	4.79717	-0.91031	3.01971
H	-6.27846	-0.48920	2.49870	H	5.92660	-1.82238	1.95960
H	-4.55443	-0.19312	2.05681	H	4.26436	-1.42765	1.37906
C	-6.25100	0.35485	-0.37014	C	6.23539	0.10220	-0.30923
C	-7.71924	0.48620	-0.65281	C	7.72244	0.17271	-0.51793
H	-8.05161	-0.26668	-1.37738	H	8.11105	1.17763	-0.31146
H	-7.92917	1.48231	-1.05766	H	7.95452	-0.08212	-1.55843
H	-8.32415	0.33860	0.25091	H	8.26800	-0.51508	0.14134
C	-5.37469	1.36252	-0.54975	C	5.37394	-0.27727	-1.28788
C	-3.93974	1.49804	-0.37319	C	3.94397	-0.41389	-1.36708
H	-5.81405	2.30495	-0.88414	H	5.84533	-0.56297	-2.23073
C	-2.87415	0.61778	-0.28143	C	2.86636	-0.02794	-0.56685
N	-1.78626	1.41428	-0.19341	N	1.76409	-0.46903	-1.24510
N	-2.14072	2.71943	-0.23282	N	2.15110	-1.10202	-2.40813
N	-3.42501	2.77150	-0.34888	N	3.44023	-1.05354	-2.46800
C	-0.42105	1.03613	-0.11163	C	0.42890	-0.34556	-0.92336
H	-2.83232	-0.46003	-0.33467	H	2.83375	0.57068	0.32917
C	-0.05954	-0.16157	0.50553	C	0.03098	0.33371	0.26616
C	0.55906	1.86445	-0.65978	C	-0.56151	-0.89545	-1.77865
C	1.27661	-0.53746	0.56053	C	-1.30975	0.45512	0.57230
C	1.89358	1.48401	-0.60682	C	-1.89707	-0.77940	-1.46149
C	2.27510	0.27454	-0.00214	C	-2.28251	-0.09638	-0.28009
H	0.26676	2.79353	-1.14168	H	-0.24695	-1.41085	-2.68095
H	-0.81538	-0.79465	0.96573	H	0.77163	0.77290	0.92784
H	1.55395	-1.46791	1.05013	H	-1.61388	0.97986	1.47711
N	3.62218	-0.12422	0.03569	N	-3.67712	0.04288	0.03671
H	2.65102	2.12391	-1.05292	H	-2.65492	-1.20135	-2.11950
C	3.96059	-1.49703	-0.09266	C	-4.24901	1.31459	-0.00636
C	4.66036	0.83570	0.13786	C	-4.40627	-1.09392	0.36701
C	5.80604	0.72093	-0.66056	C	-5.79165	-1.18316	0.09142
C	4.56064	1.90110	1.04337	C	-3.73424	-2.21022	0.91553
C	5.58457	2.84117	1.13325	C	-4.44754	-3.35605	1.23178
C	6.83315	1.65535	-0.55115	C	-6.48332	-2.34347	0.39919
C	6.72744	2.72311	0.34086	C	-5.82116	-3.43074	0.98120
H	3.67717	1.98888	1.67308	H	-2.66537	-2.14580	1.09564
H	5.88677	-0.10498	-1.36443	H	-6.29580	-0.35925	-0.40678
H	7.71721	1.55271	-1.17833	H	-7.54339	-2.41276	0.16458
H	5.49251	3.66445	1.83984	H	-3.92682	-4.20327	1.67214
H	7.52817	3.45582	0.41924	H	-6.37064	-4.33911	1.21816
C	3.34375	-2.29356	-1.06660	C	-3.71877	2.28106	-0.88831
C	4.92508	-2.06542	0.74937	C	-5.29232	1.67526	0.87660
C	5.26720	-3.40906	0.61392	C	-5.81096	2.96099	0.84320
C	3.67869	-3.64060	-1.18382	C	-4.26345	3.55563	-0.92047
C	4.64325	-4.20509	-0.34793	C	-5.31037	3.90359	-0.06053
H	2.60154	-1.85109	-1.72818	H	-2.89666	2.00573	-1.54257
H	3.19129	-4.24847	-1.94434	H	-3.86319	4.28852	-1.61731
H	5.40507	-1.44622	1.50480	H	-5.64830	0.95907	1.61310
H	4.90742	-5.25617	-0.44631	H	-5.72023	4.91101	-0.07957
H	6.01887	-3.83852	1.27419	H	-6.59692	3.23904	1.54224
O	-6.98682	-2.08949	0.28351	O	6.92629	0.80919	2.12380
O	-4.55400	-1.73632	-0.35053	O	4.57877	1.40975	1.36939

Table S5. Atomic coordinates (Å) and total energies (a.u.) of EMSM-14TPA optimized in the S₀ and S₁ states.

S ₀				S ₁			
DFT/ωPBEh energy: -1543.530552918				TDDFT/ωPBEh energy: -1543.401988595			
C	5.57777	-2.01658	-0.06338	C	-5.54847	-1.30000	1.65107
C	6.33000	-0.71327	-0.02251	C	-6.28831	-0.45802	0.64581
S	8.07347	-0.96496	-0.03247	S	-8.03664	-0.59260	0.84672
C	5.74049	0.50091	0.01614	C	-5.69076	0.30792	-0.29594
C	4.31867	0.78855	0.02310	C	-4.27364	0.47923	-0.52885
H	6.34342	1.40499	0.04952	H	-6.29313	0.88664	-0.99264
C	3.17239	0.01064	-0.02337	C	-3.12404	-0.00913	0.09097
N	2.14898	0.90215	0.02569	N	-2.08868	0.53528	-0.61958
N	2.61987	2.16147	0.09735	N	-2.58100	1.31965	-1.62988
N	3.91209	2.09871	0.09701	N	-3.87921	1.27936	-1.56234
C	0.75480	0.65196	0.00850	C	-0.72521	0.38891	-0.44180
H	2.99793	-1.05366	-0.05020	H	-2.96849	-0.65149	0.94134
C	0.24213	-0.44544	-0.68405	C	-0.20661	-0.44686	0.59269
C	-0.11045	1.51418	0.68404	C	0.17368	1.07476	-1.30280
C	-1.12686	-0.68540	-0.69353	C	1.15687	-0.58025	0.75248
C	-1.47747	1.27002	0.67609	C	1.53345	0.94307	-1.13689
C	-2.00912	0.16585	-0.01036	C	2.04352	0.11135	-0.10091
H	0.29765	2.36539	1.22238	H	-0.23425	1.70154	-2.08974
H	0.90508	-1.09696	-1.24990	H	-0.87432	-0.98663	1.25784
H	-1.52040	-1.53464	-1.24723	H	1.55269	-1.21554	1.54356
N	-3.39383	-0.08382	-0.01619	N	3.45619	-0.05102	0.04548
H	-2.14405	1.93751	1.21722	H	2.22011	1.46175	-1.80361
C	-3.87983	-1.41587	-0.00399	C	4.00040	-1.33129	-0.08550
C	-4.32069	0.98902	-0.01592	C	4.24125	1.07164	0.29419
C	-5.45220	0.93784	0.80901	C	5.57989	1.14668	-0.15681
C	-4.12547	2.10464	-0.84171	C	3.66218	2.19067	0.93483
C	-5.04303	3.15280	-0.82992	C	4.42616	3.32576	1.16410
C	-6.37383	1.98192	0.80096	C	6.32230	2.29463	0.07007
C	-6.17356	3.09709	-0.01355	C	5.75636	3.38633	0.73960
H	-3.25192	2.14585	-1.48963	H	2.62503	2.13724	1.25281
H	-5.60550	0.07352	1.45219	H	6.00648	0.31881	-0.71749
H	-7.24862	1.92718	1.44692	H	7.34580	2.35031	-0.29516
H	-4.87735	4.01365	-1.47565	H	3.97719	4.17546	1.67397
H	-6.89145	3.91490	-0.01293	H	6.34455	4.28537	0.91084
C	-3.32526	-2.37061	0.85914	C	3.35987	-2.27094	-0.92151
C	-4.93214	-1.78883	-0.85075	C	5.12637	-1.72695	0.67106
C	-5.42271	-3.09223	-0.82714	C	5.61657	-3.01948	0.55541
C	-3.81026	-3.67649	0.86433	C	3.87409	-3.55457	-1.03564
C	-4.86329	-4.04472	0.02559	C	5.00297	-3.93690	-0.30417
H	-2.51458	-2.08281	1.52591	H	2.47754	-1.96632	-1.47745
H	-3.37044	-4.40663	1.54186	H	3.38686	-4.26647	-1.69851
H	-5.36475	-1.05000	-1.52249	H	5.57594	-1.02760	1.37177
H	-5.24514	-5.06363	0.03781	H	5.39154	-4.94962	-0.38829
H	-6.24171	-3.36656	-1.49008	H	6.47294	-3.32230	1.15470
C	8.75334	0.70508	0.00229	C	-8.70531	0.48509	-0.43487
H	6.25575	-2.87758	-0.06835	H	-6.23606	-1.86829	2.28825
H	4.95551	-2.07979	-0.96695	H	-4.92875	-0.67360	2.30756
H	4.92195	-2.11606	0.81244	H	-4.88989	-2.02017	1.14670
H	8.46685	1.23614	0.91700	H	-8.41425	0.14577	-1.43549
H	8.44418	1.28098	-0.87722	H	-8.38878	1.52415	-0.28874
H	9.84212	0.59152	-0.01406	H	-9.79513	0.43005	-0.34477

Table S6. Atomic coordinates (Å) and total energies (a.u.) of **EMSO₂M-14TPA** optimized in the S₀ and S₁ states.

S ₀				S ₁			
DFT/ωPBEh energy: -1693.782324261				TDDFT/ωPBEh energy: -1693.659700516			
C	5.07147	-1.73852	-0.00121	C	-5.05703	-0.52678	1.76950
C	5.71383	-0.38524	0.04591	C	-5.69330	-0.17884	0.45550
S	7.50359	-0.35708	0.13703	S	-7.46945	-0.22744	0.40397
C	5.10427	0.81311	0.06993	C	-5.06659	0.14564	-0.69790
C	3.67971	1.06648	0.04351	C	-3.65050	0.23796	-0.92792
H	5.72250	1.70925	0.12588	H	-5.67776	0.35902	-1.57479
C	2.56734	0.23874	0.01516	C	-2.52951	0.01846	-0.12074
N	1.51362	1.08554	0.01436	N	-1.46418	0.27494	-0.93548
N	1.93540	2.37028	0.04167	N	-1.91432	0.63762	-2.18587
N	3.22575	2.36069	0.06129	N	-3.20874	0.61054	-2.16339
C	0.12857	0.77876	-0.00155	C	-0.11061	0.20718	-0.67071
H	2.44048	-0.83304	0.03153	H	-2.41955	-0.27104	0.91079
C	-0.33538	-0.35346	-0.67135	C	0.36704	-0.24039	0.59800
C	-0.77112	1.61962	0.65483	C	0.82431	0.58201	-1.67305
C	-1.69222	-0.65239	-0.67411	C	1.72415	-0.31111	0.83908
C	-2.12624	1.31807	0.65201	C	2.17649	0.52176	-1.42326
C	-2.61116	0.17606	-0.00861	C	2.63970	0.07018	-0.15932
H	-0.40066	2.49871	1.17552	H	0.45207	0.92402	-2.63384
H	0.35456	-0.98790	-1.22476	H	-0.32547	-0.55243	1.37455
H	-2.04855	-1.52876	-1.21020	H	2.08637	-0.66790	1.80250
N	-3.98140	-0.12936	-0.00747	N	4.05465	-0.02389	0.08555
H	-2.82041	1.96911	1.17806	H	2.88869	0.81519	-2.19275
C	-4.41865	-1.47927	-0.00453	C	4.64835	-1.28564	0.10125
C	-4.95164	0.90662	-0.00902	C	4.78137	1.14567	0.27950
C	-6.06115	0.82847	0.84237	C	6.14646	1.23199	-0.08497
C	-4.82062	2.00625	-0.86754	C	4.12081	2.29391	0.77323
C	-5.77989	3.01645	-0.86076	C	4.82996	3.47016	0.95672
C	-7.02498	1.83405	0.82994	C	6.83318	2.42298	0.08749
C	-6.88805	2.93505	-0.01637	C	6.18579	3.54302	0.62084
H	-3.96490	2.06526	-1.53774	H	3.06409	2.23073	1.01374
H	-6.16448	-0.02575	1.50883	H	6.63499	0.37995	-0.55000
H	-7.88287	1.76064	1.49630	H	7.87539	2.48916	-0.21722
H	-5.66536	3.86631	-1.53159	H	4.31987	4.34333	1.35682
H	-7.63896	3.72267	-0.01903	H	6.73083	4.47524	0.75162
C	-3.83450	-2.41705	0.85746	C	4.06845	-2.32967	-0.65265
C	-5.45463	-1.88359	-0.85659	C	5.76793	-1.55778	0.92122
C	-5.89938	-3.20362	-0.84092	C	6.31110	-2.83345	0.94665
C	-4.27349	-3.73919	0.85467	C	4.63855	-3.59274	-0.63046
C	-5.30948	-4.13972	0.00932	C	5.76081	-3.85280	0.16324
H	-3.03846	-2.10326	1.53019	H	3.18759	-2.12216	-1.25273
H	-3.81197	-4.45677	1.53115	H	4.19974	-4.38582	-1.23154
H	-5.91092	-1.15660	-1.52564	H	6.16442	-0.78034	1.56941
H	-5.65556	-5.17140	0.01560	H	6.19159	-4.85131	0.18839
H	-6.70632	-3.50347	-1.50754	H	7.15684	-3.04208	1.59840
C	8.02410	-0.80266	-1.52186	C	-7.97709	1.26176	1.27364
H	5.81766	-2.53794	0.04591	H	-5.80974	-0.78664	2.52082
H	4.47599	-1.86516	-0.91674	H	-4.45040	0.30637	2.15289
H	4.40541	-1.87832	0.86166	H	-4.40140	-1.40193	1.66217
H	7.69654	-0.02735	-2.21962	H	-7.64189	2.13551	0.70831
H	7.60606	-1.77835	-1.78525	H	-7.55223	1.25635	2.28180
H	9.11726	-0.85833	-1.49474	H	-9.07032	1.23303	1.32667
O	7.91852	-1.44937	1.02895	O	-7.92399	-1.36451	1.22266
O	7.94921	1.02005	0.37938	O	-7.92641	-0.08582	-0.98571

Table S7. Atomic coordinates (Å) and total energies (a.u.) of **ZMSM-15TPA** optimized in the S_0 and S_1 states.

S_0				S_1			
DFT/ ω PBEh energy: -1543.527022286				TDDFT/ ω PBEh energy: -1543.395950146			
C	7.07617	-1.96753	-0.91673	C	-6.79934	-1.33475	2.15311
S	6.29039	-0.48843	-0.22458	S	-6.24835	-0.36699	0.72027
H	8.03452	-1.62276	-1.31899	H	-7.67721	-0.80960	2.54427
H	6.48892	-2.39193	-1.73749	H	-6.03335	-1.36428	2.93598
H	7.27547	-2.73087	-0.15828	H	-7.09859	-2.35244	1.88221
C	4.73734	-1.08582	0.36754	C	-4.78027	-1.21052	0.21423
C	4.63628	-2.52882	0.77377	C	-4.76730	-2.71075	0.29413
H	4.79818	-3.20692	-0.07432	H	-4.85926	-3.07310	1.32785
H	3.64091	-2.73773	1.18154	H	-3.82767	-3.10514	-0.11150
H	5.38068	-2.77945	1.54184	H	-5.59731	-3.15179	-0.27806
C	3.68303	-0.25167	0.52620	C	-3.73950	-0.52748	-0.34025
C	4.52394	2.19390	0.12081	C	-4.52102	1.89331	-0.88970
H	2.77858	-0.68968	0.94884	H	-2.90605	-1.14195	-0.68529
C	3.60058	1.16291	0.22672	C	-3.60532	0.87912	-0.59660
N	2.40338	1.81579	0.06868	N	-2.38282	1.50180	-0.83021
N	2.59222	3.13943	-0.11355	N	-2.58080	2.78583	-1.27440
N	3.87004	3.36347	-0.07939	N	-3.87167	2.99477	-1.30203
C	1.08403	1.29442	0.06451	C	-1.08731	1.06219	-0.62386
C	0.76353	0.16971	-0.69761	C	-0.77239	0.05223	0.31747
C	0.09132	1.94320	0.80105	C	-0.02271	1.72191	-1.31653
C	-0.54078	-0.31184	-0.71144	C	0.53402	-0.34850	0.51491
C	-1.21118	1.46087	0.78586	C	1.27956	1.31930	-1.11855
C	-1.54667	0.32540	0.03090	C	1.57672	0.27170	-0.22352
H	0.35063	2.82262	1.38526	H	-0.26354	2.53361	-1.99479
H	1.52770	-0.31017	-1.30523	H	-1.56138	-0.38298	0.92448
H	-0.78985	-1.17954	-1.31798	H	0.77006	-1.09918	1.26721
N	-2.87076	-0.15615	0.01175	N	2.93063	-0.12673	-0.00337
H	-1.98037	1.96409	1.36731	H	2.08714	1.80628	-1.66407
C	-3.12438	-1.54892	-0.02174	C	3.29023	-1.45102	-0.23380
C	-3.95550	0.75649	-0.02202	C	3.84596	0.83208	0.44062
C	-5.09393	0.53157	0.76376	C	5.19311	0.80241	0.01788
C	-3.90440	1.88973	-0.84487	C	3.39467	1.89013	1.25760
C	-4.96947	2.78707	-0.86814	C	4.28926	2.86271	1.67977
C	-6.16224	1.42460	0.72044	C	6.06976	1.79216	0.43869
C	-6.10534	2.55921	-0.09019	C	5.62816	2.81999	1.27794
H	-3.02559	2.06515	-1.46238	H	2.35046	1.92016	1.55650
H	-5.13583	-0.34765	1.40388	H	5.52402	0.02780	-0.66970
H	-7.04012	1.23679	1.33658	H	7.10152	1.77491	0.09345
H	-4.91400	3.66453	-1.51038	H	3.93848	3.66559	2.32455
H	-6.93828	3.25911	-0.11543	H	6.32006	3.59461	1.60163
C	-2.38758	-2.42371	0.78971	C	2.54551	-2.21704	-1.15997
C	-4.11848	-2.07050	-0.86136	C	4.33599	-2.06637	0.49292
C	-4.36993	-3.44044	-0.88276	C	4.64812	-3.39647	0.26215
C	-2.63347	-3.79387	0.74850	C	2.88207	-3.54404	-1.38537
C	-3.62715	-4.31109	-0.08411	C	3.93212	-4.14140	-0.68344
H	-1.62370	-2.02108	1.45197	H	1.73123	-1.74462	-1.70183
H	-2.05366	-4.46015	1.38540	H	2.31693	-4.11960	-2.11541
H	-4.69211	-1.39549	-1.49313	H	4.86470	-1.50304	1.25773
H	-3.82228	-5.38145	-0.10839	H	4.18217	-5.18572	-0.85750
H	-5.14527	-3.83023	-1.54038	H	5.44468	-3.86562	0.83606
H	5.60083	2.16083	0.20784	H	-5.60150	1.85283	-0.86691

Table S8. Atomic coordinates (Å) and total energies (a.u.) of **ZMSO₂M-15TPA** optimized in the S_0 and S_1 states.

S_0				S_1			
DFT/ ω PBEh energy: -1693.773861256				TDDFT/ ω PBEh energy: -1693.653860492			
C	-5.24932	-0.27115	1.92858	C	-5.27005	0.46811	2.05137
S	-5.73989	-0.81100	0.29199	S	-5.83671	-0.58980	0.71152
H	-6.18522	-0.11408	2.47502	H	-6.16919	0.92315	2.47929
H	-4.68643	0.66358	1.86734	H	-4.60786	1.24340	1.65618
H	-4.66597	-1.06604	2.40097	H	-4.76146	-0.14949	2.79652
C	-4.19433	-1.11505	-0.59312	C	-4.38467	-1.27813	0.00036
C	-4.08649	-2.50461	-1.14569	C	-4.36425	-2.78055	-0.04373
H	-4.18568	-3.26074	-0.35839	H	-4.55689	-3.23007	0.93863
H	-3.12236	-2.63058	-1.65069	H	-3.38384	-3.11980	-0.40239
H	-4.88731	-2.70211	-1.86970	H	-5.12527	-3.18684	-0.72556
C	-3.23967	-0.18111	-0.76538	C	-3.33170	-0.52420	-0.49735
C	-4.11653	2.25027	-0.30892	C	-4.04711	1.93803	-0.92964
H	-2.34233	-0.52755	-1.28429	H	-2.48590	-1.13332	-0.81811
C	-3.18933	1.22013	-0.38832	C	-3.16396	0.87141	-0.70564
N	-1.99535	1.86235	-0.16864	N	-1.91913	1.47823	-0.92831
N	-2.18964	3.17611	0.03714	N	-2.08781	2.80901	-1.31037
N	-3.46564	3.40949	-0.05533	N	-3.36043	3.04212	-1.28760
C	-0.67806	1.33301	-0.14038	C	-0.62939	1.05099	-0.68540
C	-0.38992	0.16831	0.57273	C	-0.33567	-0.01892	0.18770
C	0.34236	2.01088	-0.81031	C	0.44197	1.75717	-1.29189
C	0.90961	-0.32403	0.60545	C	0.97555	-0.39751	0.41586
C	1.63966	1.51880	-0.77618	C	1.74848	1.37405	-1.05889
C	1.94550	0.34288	-0.06887	C	2.02717	0.28629	-0.21605
H	0.10847	2.91922	-1.35993	H	0.21039	2.59617	-1.93915
H	-1.17401	-0.33816	1.13189	H	-1.13789	-0.52155	0.71625
H	1.13142	-1.22313	1.17514	H	1.19432	-1.20419	1.11326
N	3.26180	-0.14491	-0.03092	N	3.37235	-0.12365	0.00578
H	2.42914	2.04473	-1.30766	H	2.56529	1.90289	-1.54693
C	3.51275	-1.53976	0.02524	C	3.70715	-1.46845	-0.16762
C	4.35583	0.75861	0.02351	C	4.32023	0.83467	0.38701
C	5.49268	0.53545	-0.76374	C	5.65204	0.74857	-0.06611
C	4.31593	1.87185	0.87293	C	3.92541	1.91523	1.20053
C	5.39206	2.75508	0.91963	C	4.85792	2.87466	1.57039
C	6.57215	1.41371	-0.69745	C	6.56996	1.71972	0.30887
C	6.52645	2.53005	0.13875	C	6.18103	2.78278	1.13010
H	3.43808	2.04277	1.49325	H	2.89705	1.97604	1.54695
H	5.52484	-0.33088	-1.42178	H	5.94264	-0.05872	-0.73419
H	7.45001	1.22871	-1.31426	H	7.59261	1.65892	-0.05714
H	5.34700	3.61770	1.58232	H	4.55082	3.69888	2.21021
H	7.36823	3.21830	0.18219	H	6.90524	3.54176	1.41753
C	2.82156	-2.41943	-0.81906	C	3.01362	-2.23869	-1.12533
C	4.46341	-2.05121	0.91830	C	4.69903	-2.07618	0.63161
C	4.71724	-3.42031	0.96154	C	4.99272	-3.42035	0.45973
C	3.06852	-3.78874	-0.75677	C	3.32528	-3.58136	-1.28697
C	4.01870	-4.29696	0.13051	C	4.31261	-4.17925	-0.50003
H	2.09384	-2.02183	-1.52386	H	2.25670	-1.76497	-1.74481
H	2.52551	-4.46105	-1.41907	H	2.79670	-4.16513	-2.03720
H	5.00210	-1.36924	1.57301	H	5.19998	-1.49598	1.40276
H	4.21512	-5.36652	0.17121	H	4.54708	-5.23377	-0.62652
H	5.45904	-3.80440	1.65973	H	5.74480	-3.88801	1.09158
O	-6.46445	0.28902	-0.35799	O	-6.54915	0.29440	-0.23251
O	-6.38562	-2.11975	0.44846	O	-6.58019	-1.70059	1.33506
H	-5.18744	2.20179	-0.45193	H	-5.12821	1.90823	-0.91185

Table S9. Details for the crystal structure determinations.

	ZMSM-14TPA	4EMSM-14TPA	ZMSM-15TPA
formula	C ₂₄ H ₂₂ N ₄ S	C ₂₄ H ₂₂ N ₄ S	C ₂₄ H ₂₂ N ₄ S
fw	398.5	398.5	398.5
cryst.size, mm	0.73 x 0.54 x 0.44	0.65 x 0.51 x 0.35	0.66 x 0.43 x 0.26
color, shape	yellow, block	colourless, block	colourless, block
crystal system	triclinic	monoclinic	monoclinic
space group	<i>P</i> -1 (no. 2)	<i>C</i> 2/ <i>c</i> (no. 15)	<i>P</i> 2 ₁ / <i>n</i> (no. 14)
<i>a</i> , Å	8.1093(2)	20.8317(18)	8.8456(7)
<i>b</i> , Å	9.6000(3)	9.8784(9)	23.4528(18)
<i>c</i> , Å	13.0873(4)	20.8194(17)	10.1090(8)
α , °	89.2148(13)	90	90
β , °	90.597(3)	105.837(4)	104.403(2)
γ , °	86.5008(12)	90	90
<i>V</i> , Å ³	1012.63(5)	4121.7(6)	2031.2(3)
<i>T</i> , K	100	100	100
<i>Z</i> , <i>Z'</i>	2, 1	8, 1	4, 1
ρ_{calc} , g cm ⁻³	1.3070	1.2845	1.3032
μ , mm ⁻¹ (MoK α)	0.178	0.175	0.177
<i>F</i> (000)	420	1680	840
absorption corrections	multi-scan	multi-scan	multi-scan
<i>T</i> _{min} - <i>T</i> _{max}	0.89–0.93	0.90–0.94	0.91–0.96
θ range, deg	2.13–36.5	2.03–35.12	2.25–32.61
no. of rflns measd	36829	53546	25096
<i>R</i> _{int}	0.0286	0.0381	0.0231
no. of rflns unique	9847	9031	7412
no. of rflns <i>I</i> > 3 σ (<i>I</i>)	7581	6205	6390
no. of params / restraints	262 / 0	276 / 2	262 / 0
<i>R</i> (<i>I</i> > 3 σ (<i>I</i>)) ^a	0.0419	0.0676	0.0384
<i>R</i> (all data)	0.0566	0.0980	0.0448
<i>wR</i> (<i>I</i> > 3 σ (<i>I</i>))	0.0571	0.0916	0.0536
<i>wR</i> (all data)	0.0580	0.0952	0.0543
GooF	2.53	2.48	2.77
Diff.Four.peaks	-0.36 / 0.51	-1.11 / 1.21	-0.36 / 0.64
CCDC no.	-	-	-

$$^a R = \sum ||F_o| - |F_c|| / \sum |F_o|, wR = \sum w(|F_o| - |F_c|) / \sum w|F_o|, \text{GooF} = \{\sum [w(F_o^2 - F_c^2)^2] / (n-p)\}^{1/2}$$

3.13. Curriculum Vitae

Paul Kautny

Address: Mühlgrundgasse 3/25
1220 Wien

E-Mail: paul.kautny@tuwien.ac.at

Tel.: 0043 650 2608087

Date/place of birth: 26.08.1987 in Wels

Nationality: Austria

Education and qualification

03/2013 – 03/2017 Doctoral program in Technical Sciences – Technical Chemistry, TU Wien

04/2011 – 03/2013 Master program Technical Chemistry – Synthesis, TU Wien (with distinction)

09/2007 – 04/2011 Bachelor program Technical Chemistry, TU Wien (with distinction)

09/1997 – 06/2005 Stiftsgymnasium Kremsmünster

Additional qualification and scholarships

Languages German (native)
English (fluent in spoken and written)
Latin (6 years in school)

International experience Freshwater Senior Campus Sydney (02/2004)
Research stay at the Changchun Institute of Applied Chemistry of the Chinese Academy of Science – Ma group (11/2013)

Awards & scholarships Performance-oriented scholarship (TU Wien) – 2008 & 2010
2nd place at the International Forum-Competition of Young Researchers, St. Petersburg State Mining Institute, Topic: Nanotechnology.IT – 04/2011
Mobility grant „Kurzfristige wissenschaftliche Arbeiten im Ausland“ (TU Wien) - 2013
Research fellowship (TU Wien) – 06/2013 – 05/2014

Educational assignments

- Internal education assignments at the TU Wien (general chemistry introductory laboratory; synthesis laboratory course; advanced laboratory course in synthetic chemistry); chemistry

laboratory for students of technical college Wiener Neustadt (biotechnical procedure, Campus Tulln) at the TU Wien

- (Co-)supervision of Bachelor theses (11) and Diploma theses (4), TU Wien

Occupation

07/2003 & 07/2004	Internship at Gmundner Milch Sattledt
07/2005 – 12/2010	Civil service at the Red Cross Liezen and voluntary activities as paramedic at the Red Cross Kremsmünster
10/2006 – 07/2007 & 07/2008 – 09/2008	Librarian at the monastic library Kremsmünster
03/2012 – 07/2012	Tutor at the Vienna University of Technology
04/2014 – 03/2017	Research Assistant at the Institute of Applied Synthetic Chemistry – TU Wien

Publications

- o Bachelor thesis: [Synthese Linearer En-In-Systeme als Potentielle Linker für Organic Electronics](#)
- o Diploma thesis: [Synthesis of Novel Bipolar Heterocyclic Systems as Host Materials for Phosphorescent Organic Light Emitting Diodes](#)

Journal articles (peer-reviewed)

1. Thomas Kader, Paul Kautny, Berthold Stöger, Johannes Fröhlich; [OD- and non-OD-polytypism of 9-\(3-chloropyridin-4-yl\)-9H-carbazole](#); *Zeitschrift für Kristallographie - Crystalline Materials*, **accepted**
2. Paul Kautny, Chenyang Zhao, Dominik Schopf, Berthold Stöger, Ernst Horkel, Jiangshan Chen, Dongge Ma, Johannes Fröhlich, Daniel Lumpi; [Thieno\[3,4-c\]pyrrole-4,6-dione as novel building block for host materials in red PhOLEDs](#); *Journal of Materials Chemistry C*, **2017**, 5, 1997-2004.
3. Paul Kautny, Chenyang Zhao, Thomas Kader, Berthold Stöger, Ernst Horkel, Jiangshan Chen, Dongge Ma, Johannes Fröhlich, Daniel Lumpi; [Functional organic click-materials: application in phosphorescent organic light emitting diodes](#); *RSC Advances*, **2017**, 7, 12150-12160.
4. Florian Glöcklhofer, Paul Kautny, Patrick Fritz, Berthold Stöger, Johannes Fröhlich; [Using dicyanoanthracene triflates as superior precursors: modifying properties by sterically hindered aryl substituents](#); *ChemPhotoChem*, **2017**, 1, 51-55.
5. Paul Kautny, Thomas Schwartz, Berthold Stöger, Johannes Fröhlich; [An unusual case of OD-allotwinning: 9,9'-\(2,5-dibromo-1,4-phenylene\)bis\[9H-carbazole\]](#); *Acta Crystallographica Section B*, **2017**, 73, 65-73.
6. Daniel Lumpi, Johannes Steindl, Sebastian Steiner, Victor Carl, Paul Kautny, Michael Schön, Florian Glöcklhofer, Brigitte Holzer, Berthold Stöger, Ernst Horkel, Christian Hametner, Georg Reider, Marko D. Mihovilovic, Johannes Fröhlich; [Thiophene ring-fragmentation reactions: Principles and scale-up towards NLO materials](#); *Tetrahedron*, **2017**, 73, 472-280.
7. Daniel Lumpi, Paul Kautny, Berthold Stöger, Johannes Fröhlich; [Crystal chemistry of trialkylsilyl-capped \(3Z\)-4-\(methylthio\)-3-penten-1-yne: polymorphism, twinning and ambiguity of order-disorder descriptions](#); *Acta Crystallographica Section B*, **2016**, 72, 753-762.

8. Paul Kautny, Dorian Bader, Berthold Stöger, Georg A. Reider, Johannes Fröhlich, Daniel Lumpi; [Structure-property relationships in Click-derived donor-triazole-acceptor materials](#); *Chemistry-A European Journal*, **2016**, 22, 18887-18898.
9. Paul Kautny, Zhongbin Wu, Johanna Eichelter, Ernst Horkel, Berthold Stöger, Jiangshan Chen, Dongge Ma, Johannes Fröhlich, Daniel Lumpi; [Indolo\[3,2,1-jk\]carbazole based planarized CBP derivatives as host materials for PhOLEDs with low efficiency roll-off](#); *Organic Electronics*, **2016**, 34, 237-245.
10. Daniel Lumpi, Paul Kautny, Berthold Stöger, Johannes Fröhlich; [Crystal chemistry of layered structures formed by linear rigid silyl-capped molecules](#); *IUCrJ*, **2015**, 2, 584-600.
11. Hannes Puntsher, Paul Kautny, Berthold Stöger, Antoine Tissot, Christian Hametner, Hans R. Hagemann, Johannes Fröhlich, Thomas Baumgartner, Daniel Lumpi; [Structure-property studies of P-triarylamine-substituted dithieno\[3,2-b:2',3'-d\]phospholes](#); *RSC Advances*, **2015**, 5, 93797-93807.
12. Paul Kautny, Zhongbin Wu, Berthold Stöger, Antoine Tissot, Ernst Horkel, Jiangshan Chen, Dongge Ma, Hans Hagemann, Johannes Fröhlich, Daniel Lumpi; [Controlling singlet-triplet splitting in carbazole-oxadiazole based bipolar phosphorescent host materials](#); *Organic Electronics*, **2015**, 17, 216-228.
13. Berthold Stöger, Paul Kautny, Daniel Lumpi, Erich Zobetz, Johannes Fröhlich; [The pseudo-inversion symmetry of 9,9'-\(1,3,4-oxadiazole-2,5-diyl\)di\(1,1'-biphenyl\)-2',4'-diyl](#) bis[9H-carbazole] in the light of OD theory; *Zeitschrift für Kristallographie - Crystalline Materials*, **2014**, 229, 378-384.
14. Paul Kautny, Johannes Fröhlich, Berthold Stöger, Matthias Weil; [Isotypic crystal structures of 2,6-dibromo-N,N-bis\(4-nitrophenyl\)aniline and 2,6-dichloro-N,N-bis\(4-nitrophenyl\)aniline](#); *Acta Crystallographica Section E*, **2014**, 70, 65-67.
15. Paul Kautny, Thomas Kader, Berthold Stöger, Johannes Fröhlich; [9-\(4-Bromophenyl\)-9H-carbazole](#); *Acta Crystallographica Section E*, **2014**, 70, o330-o331.
16. Paul Kautny, Berthold Stöger; [1-Nitro-9H-carbazole](#); *Acta Crystallographica Section E*, **2014**, 70, o28.
17. Paul Kautny, Daniel Lumpi, Yanping Wang, Antoine Tissot, Johannes Binting, Ernst Horkel, Berthold Stöger, Christian Hametner, Hans Hagemann, Dongge Ma, Johannes Fröhlich; [Oxadiazole based bipolar host materials employing planarized triarylamine donors for RGB PHOLEDs with low efficiency roll-off](#); *Journal of Materials Chemistry C*, **2014**, 2, 2069-2081.
18. Berthold Stöger, Paul Kautny, Daniel Lumpi, Erich Zobetz, Johannes Fröhlich; [Solvatomorphism of 9,9'-\[1,3,4-thiadiazole-2,5-diylbis\(2,3-thiophendiyl-4,1-phenylene\)\]bis\[9H-carbazole\]: isostructurality, modularity and order-disorder theory](#); *Acta Crystallographica Section B*, **2012**, 68, 667-676.

Poster presentations

1. P. Kautny, F. Plasser, F. Glöcklhofer, T. Kader, B. Stöger, D. Lumpi, J. Fröhlich: [Photophysical and theoretical investigations of push-pull chromophores derived from thio-ene-yne compounds via CuAAC](#); ICSM2016 - International Conference on Science and Technology of Synthetic Metals, Guangzhou - China; 26.06.2016 - 01.07.2016; *ICSM2016 - Abstract Book*, (2016), S. 69.
2. T. Kader, P. Kautny, E. Horkel, J. Fröhlich: [Synthesis and Characterization of Novel Carboline based Annulated Arylamines](#); ICSM2016 - International Conference on Science and Technology of Synthetic Metals, Guangzhou - China; 26.06.2016 - 01.07.2016; *ICSM2016 - Abstract Book*, (2016), S. 69.
3. P. Kautny, Z. Wu, J. Eichelter, D. Lumpi, E. Horkel, B. Stöger, J. Chen, D. Ma, J. Fröhlich: [Indolo\[3,2,1-jk\]carbazole based Host-Materials for PHOLEDs](#); 12th International Symposium on Functional π -Electron Systems, University of Washington, Seattle, USA; 19.07.2015 -

- 24.07.2015; *Fπ-12 Program with links to Abstracts* (web page: http://depts.washington.edu/uwconf/fpi12/fpi12_abstracts.html, (2015), Paper-Nr. <http://depts.washington.edu/uwconf/fpi12/440.html>.
4. T. Kader, P. Kautny, D. Lumpi, J. Fröhlich: [Synthesis of Novel Bipolar Host Materials for Phosphorescent OLEDs](#); VSS 2015, Vienna; 25.06.2015 - 26.06.2015; *Book of Abstracts*, Richard Zemann, (2015), ISBN: 978-3-9504017-0-7; S. 136 - 137.
 5. P. Kautny, D. Lumpi, E. Horkel, J. Binting, C. Hametner, H. Hagemann, D. Ma, J. Fröhlich: [Tuning Singlet and Triplet Energies of Oxadiazole-Based Bipolar Host Materials for PHOLEDs by Structural Modification of Triarylamine Donor Units](#); 11th International Symposium on Functional π -Electron Systems, Arcachon (Bordeaux Area), France; 02.06.2013 - 07.06.2013; *Book of Abstracts*, (2013), 1 S.
 6. T. Kader, F. Glöcklhofer, D. Lumpi, J. Binting, P. Kautny, E. Horkel, B. Stöger, J. Fröhlich: [Investigations on Novel Click Derived Donor-Acceptor Materials for Organic Electronic Applications](#); 15th Blue Danube Symposium on Heterocyclic Chemistry, Sept. 1-5, 2013, Olomouc, Czech Republic, Olomouc; 01.09.2013 - 05.09.2013; *Book of Abstracts*, (2013), ISBN: 978-80-263-0502-6; S. P71.
 7. P. Kautny, D. Lumpi, T. Kader, B. Stöger, H. Hagemann, E. Horkel, J. Fröhlich: [Influence of Sterically Induced Torsion on Substance Properties of Oxadiazole-Carbazole Based Bipolar Host Materials for PHOLED Applications](#); 15th Blue Danube Symposium on Heterocyclic Chemistry, Sept. 1-5, 2013, Olomouc, Czech Republic, Olomouc; 01.09.2013 - 05.09.2013; *Book of Abstracts*, (2013), ISBN: 978-80-263-0502-6; S. P63.
 8. H. Puntischer, D. Lumpi, P. Kautny, T. Baumgartner, J. Fröhlich: [Synthesis of Novel Carbazole- and Indolocarbazole Functionalized Dithienophosphole Oxides as Functional Organic Materials](#); 15th Blue Danube Symposium on Heterocyclic Chemistry, Sept. 1-5, 2013, Olomouc, Czech Republic, Olomouc; 01.09.2013 - 05.09.2013; *Book of Abstracts*, (2013), ISBN: 978-80-263-0502-6; S. P21.
 9. P. Kautny, D. Lumpi, J. Binting, E. Horkel, C. Hametner, J. Fröhlich: [Synthesis of Novel Oxa- and Thiadiazole Containing Host Materials for PHOLED Emitters](#); 14th Blue Danube Symposium on Heterocyclic Chemistry, Podbanské, SK; 26.06.2011 - 29.06.2011; *Book of Abstracts - 14th Blue Danube Symposium on Heterocyclic Chemistry*, Vydavateľstvo STU - Publishing House of Slovak University of Technology, Bratislava, Slovakia (2011), ISBN: 978-80-227-3529-2; S. 74.
 10. D. Wurm, V. Carl, D. Lumpi, P. Kautny, E. Horkel, C. Hametner, J. Fröhlich: [Synthetic Pathways towards Spacer-Extended Ene-Yne Compounds: Cross Coupling Strategy](#); 14th Blue Danube Symposium on Heterocyclic Chemistry, Podbanské, SK; 26.11.2011 - 29.11.2011; *Book of Abstracts - 14th Blue Danube Symposium on Heterocyclic Chemistry*, Vydavateľstvo STU - Publishing House of Slovak University of Technology, Bratislava, Slovakia (2011), ISBN: 978-80-227-3529-2; S. 121.
 11. B. Pokorný, P. Kautny, D. Lumpi, E. Horkel, C. Hametner, J. Fröhlich: [Synthetic Pathways towards Spacer-Extended Ene-Yne Compounds: Ring Closing Strategy](#); 14th Blue Danube Symposium on Heterocyclic Chemistry, Podbanské, SK; 26.06.2011 - 29.06.2011; *Book of Abstracts - 14th Blue Danube Symposium on Heterocyclic Chemistry*, Vydavateľstvo STU - Publishing House of Slovak University of Technology, Bratislava, Slovakia (2011), ISBN: 978-80-227-3529-2; S. 101.
 12. D. Lumpi, P. Kautny, J. Binting, E. Horkel, C. Hametner, J. Fröhlich: [Novel Oxa- and Thiadiazole based Host Materials for PHOLED Applications: Synthesis and Characterization](#); 10th International Symposium on Functional π -Electron Systems (Fπ10), Beijing, CN; 13.10.2011 - 17.10.2011; *Abstracts - 10th International Symposium on Functional π -Electron Systems*, (2011), S. 228.

Oral presentations

1. P. Kautny, T. Kader, H. Puntsher, D. Lumpi, T. Baumgartner, J. Chen, D. Ma, J. Fröhlich: [Indolo\[3,2,1-jk\]carbazole as novel building block for organic electronics](#); Bioelectrochemistry And More, Wiener Neustadt; 13.06.2016 - 14.06.2016; *Bioelectrochemistry And More*, (2016).
2. P. Kautny, Z. Wu, J. Eichelter, D. Lumpi, E. Horkel, B. Stöger, J. Chen, D. Ma, J. Fröhlich: [Indolo\[3,2,1-jk\]carbazole based Host-Materials for PHOLEDs](#); Bioelectrochemistry And More, Wiener Neustadt; 25.06.2015 - 26.06.2015; *Bioelectrochemistry And More*, (2015).
3. P. Kautny, D. Lumpi, J. Binting, E. Horkel, C. Hametner, J. Fröhlich: [Molecular Design Of Novei Bipolar Organic Hybrids As Hosts Materials For PHOLED Emitters - Synthesis And Characterization](#); International Forum-Competition of Young Researchers, St. Petersburg State Mining Institute (Technical University), St. Petersburg, Russia; 25.04.2012 - 27.04.2012; *Abstracts Part 2*, (2012), ISBN: 978-5-94211-565-4; S. 170.
4. P. Kautny, D. Lumpi, E. Horkel, C. Hametner, J. Fröhlich: [Synthesis of Heteroaryl Linked Ene-Yne Compounds as Building Blocks for OLED-Materials](#); Topical Issues of Subsoil Usage, St. Petersburg, Russland; 20.04.2011 - 22.04.2011; *Proceedings of the International Forum - Competition of Youg Researchers "Topical Issues of Subsoil Usage"*, St. Petersburg Mining University, Band II/St. Petersburg (2011), ISBN: 978-5-94211-506-7; S. 199.